

DTIC
SELECTED
JUN 1 2 1995
F

11th Annual Review of Progress in

APPLIED COMPUTATIONAL ELECTROMAGNETICS

at the

Naval Postgraduate School

Monterey, CA

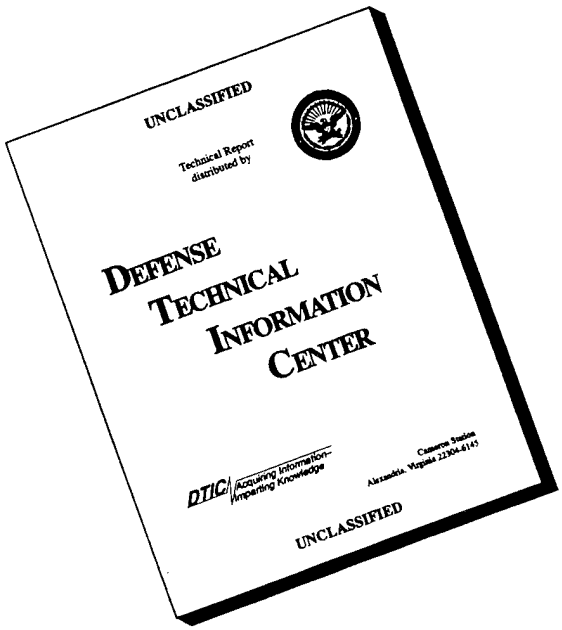
March 20-25, 1995

CONFERENCE PROCEEDINGS

This document has been approved for public release and sale; its distribution is unlimited.

19950608 143

DISCLAIMER NOTICE



THIS DOCUMENT IS BEST QUALITY AVAILABLE. THE COPY FURNISHED TO DTIC CONTAINED A SIGNIFICANT NUMBER OF PAGES WHICH DO NOT REPRODUCE LEGIBLY.

CONFERENCE PROCEEDINGS

VOLUME II

11th Annual Review of Progress in

APPLIED

COMPUTATIONAL

ELECTROMAGNETICS

at the

Naval Postgraduate School

Monterey, CA

March 20-25, 1995

Accesion For
NTIS CRA&I ☑
DTIC TAB ☐
Unannounced ☐
Justification .....
By .....
Distribution /
Availability Codes
Dist | Avail and / or Special
A-1

SYMPOSIUM PROGRAM COMMITTEE CHAIRMAN

Raymond Luebbers

Sponsored by

The Applied Computational Electromagnetics Society,

NPS, DOE/LLNL, Penn State University, University of Mississippi,

USAF, DOD AND DOE IN COOPERATION WITH IEEE, URSI, ASEE, SIAM AND AMTA

THE NAVAL POSTGRADUATE SCHOOL

DTIC QUALITY INSPECTED 5

Contents

Table of Contents i

1996 Call for Papers xii

1995 Symposium Program Committee xiii

Conference Chairman's Statement xiv

ACES President's Statement xv

ACES 95 Short Courses xvi

Agenda xvii

VOLUME I

SESSION 1: SCATTERING
Chairs: V. Cable and E. Miller

"A CGFFT Method Applied to the Scattering From Finite Size Microstrip Antenna" by A. McCowen 2

"Analysis of Scattering by Cluster of Nonspherical Particles Based on Complete Mathematic Models" by Y. Eremin, N. Orlov and V. Rozenberg 6

"Analytic Solution for Calculating the Radar Cross-Section and Related Parameters of a Conducting Right Circular Cylinder Surrounded by Multiple Layers of Lossy Dielectrics" by G.W. Jarriel, Jr., M.E. Baginski, and L. Riggs 8

"RCS of High Permittivity Cubes Computed with the TLM Method" by C. Eswarappa and W.J.R. Hoefer 13

"Scattering Analysis of Antenna Installations/Panels on a Curved Surface Using Uniform Field Integration Method" by J.J. Kim and O.B. Kesler 21

"Code Validation of Aircraft Scattering Parameters Using IR Thermograms" by J. Norgard, R. Sega, M. Seifert, T. Blocher, and A. Pesta 29

"A New Method for Solving Scattering Problems with Conducting Media in the Time Domain" by M. Schinke and K. Reiß 37

"Experience and Experiments at Cray Research with JUNCTION-2" by J.A. Crow and Q.M. Sheikh 45

"Quantitative Methods for Measuring and Improving the Performance of Electromagnetic Scattering Codes" by J.P. Meyers, A.J. Terzuoli, Jr., and G.C. Gerace 49

SESSION 2: LOW FREQUENCY
Chairs: K. Kunz and H. Sabbagh

"Numerical Modelling of EMC in Underground Power Cable Systems with the Hybrid FE-BE Method" by J. Shen and A. Kost 58

"New Contribution to the Study of Fault Currents Distribution in the Ground Systems" by H.O. Brodskyn, M.H. Giarolla, J.R. Cardoso, N.M. Abe, and A. Passaro 66

"On the Oscillatory Phenomena of Eddy Currents Along the, Ā, V- Ψ Interface" by Z. Cheng, Q. Hu, S. Gao, Z. Liu, M. Wu, and C. Ye 75

"A New MMP-Code for Static Field Computation" by M. Gnos and P. Leuchtmann 81

SESSION 2: continued

"Molten Aluminum Flow Induced by High Magnetic Fields" by W.P. Wheless, Jr., and C.S. Wheless 89

"The Electrostatic Characterization of a N-Element Planar Array Using the Singularity Expansion Method" by J.E. Mooney and L. Riggs 98

"A Volume-Integral Code for Electromagnetic Nondestructive Evaluation" by R.K. Murphy, H.A. Sabbagh, J.C. Treece, and L.W. Woo 109

SESSION 3: RESEARCH AND ENGINEERING FRAMEWORK FOR CEM
Organizer: K. Siarkiewicz

"Research and Engineering Framework (REF) for Computational Electromagnetics" (Invited Paper) by B. Hantman, K. Siarkiewicz, J. Labelle, and R. Jackson 118

"Research and Engineering Framework (REF) Data Dictionary Specifications for Computational Electromagnetics" (Invited Paper) by J.A. Evans 126

"DT_NURBS - A Geometry Engine for Integration of MMACE Data" (Invited Paper) by B. Ames and C. Whitcomb 127

"Standardized Grid Generation for the Research and Engineering Framework" (Invited Paper) by L.W. Woo, H.A. Sabbagh, J. LaBelle, and B. Hantman 135

"Visualization and Standards" (Invited Paper) by J.V. Cugini 143

"Visualization Tookkit for Computational Electromagnetics" (Invited Paper) by R.A. Joseph 151

"MMACE - Lessons for the Development of a CEM Computational Environment" (Invited Paper) by R.G. Hicks and K. Siarkiewicz 155

SESSION 4: INTERACTIVE TECHNICAL SESSIONS

SESSION 4A: EM THEORY I

"Pulse Basis Function Implementation of the Radiation Condition Integral Equations" by P.C. Colby 164

"Finite Difference Solutions of Geometrical Optics and Some Related Nonlinear PDEs Approximating High Frequency Helmholtz Equation" by E. Fatemi, B. Engquist, and S. Osher 172

"Conversion of Mechanical Energy to Electromagnetic Energy" by R.M. Bevensee ..... Presentation Only

"Block-Toeplitz-Structure-Based Solution Strategies for CEM Problems" by V.I. Ivakhnenko and E.E. Tyrtyshnikov 181

"The Two-Dimensional Finite Integral Technique Combined with the Measured Equation of Invariance Applied to Transverse Electric Open Region Scattering Problems" by G.K. Gothard and S.M. Rao 189

"Artificial Transparent Boundaries in Computational Quasioptics" by A.V. Popov 195

"A Statistical Electromagnetics (STEM) Research Initiation Report" by W.P. Wheless, Jr., C.B. Wallace, and W.D. Prather 202

SESSION 4A: continued

"Optimization of Aperiodic Conducting Grids" by R.L. Haupt 211

"Accurate MOM Scattering Calculations Using Massively Parallel Computation" by L.D. Vann and J.S. Bagby 216

"A New Angle on a Low Cost Ground Screen for Model Testing in the Undergraduate Antennas Laboratory (Looking at Near Vertical Incidence Skywaves (NVIS) for a Coast Guard Patrol Boat)" by M.E. McKaughan, W.M. Randall and B. Nutter 224

"Efficient Extraction of the Near-Field From CGFFT Methods Applied to Scatterers in the Resonance Region" by A.McCowen 229

SESSION 4B: VISUALIZATION & INTERFACES

"Computer Code for Field Calculation and Visualization in Quasioptics" by Y.V. Kopylov 234

"Dosimetry in a Voxel Model of the Head" by P.J. Dimbylow 240

"A Graphical User Interface for the NEC-BSC" by L.W. Henderson and R.J. Marhefka 245

"MF Communication and Broadcast Prediction System" by M.J. Packer and A.P. Tsitsopoulos 252

"A Finite Difference Time Domain Visualization Tool for Microsoft Windows ™" by A.Z. Elsherbeni, C.D. Taylor, Jr., and C.E. Smith 260

SESSION 4C: VALIDATION

"Transformable Scale Aircraft-Like Model for the Validation of Computational Electromagnetic Models and Algorithms: Initial Configuration and Results" by D.R. Pflug and D.E. Warren 268

"Measurement Study for Validation of Electromagnetics Scattering Codes on a Complex 3D Target" by T.L. Kienberger and D.E. Jurgens 276

"Validation Using a Moment Method Approach with Exact Object Representation" by J.A. Larsson, S. Ljung, and B. Wahlgren 286

"IR Measurements for Validating EM Analysis Tools" by M. Seifert, T. Blocher, and A. Pesta 294

SESSION 4D: EMI/EMC/EMP

"Analysis of Electromagnetic Interference at an Ocean Observation Post" by L. Bai and J.F. Dai 302

"Enforcing Correlation on Statistically Generated EM Cable Drivers" by R. Holland and R. St. John 308

"Analysis of Different Contributions to the Coupling Between Reflector Antennas on a Satellite" by C. Park and P. Ramanujam 321

"Simple Radiation Models in Lieu of EMC Radiated Emissions Testing" by R. Perez 323

SESSION 5: OPTIMIZATION TECHNIQUES IN APPLIED ELECTROMAGNETICS
Organizer: O.A. Mohammed

"An Optimization Approach to Reduce the Discretization Error in Finite Element Explicit Solution Scheme" (Invited Paper) by M. Feliziani, E. Latini, and F. Maradei 334

"Analysis and Design of a Reentrant Resonant Cavity Applicator for Radio Frequency Hyperthermia System" (Invited Paper) by Y. Kanai, T. Tsukamoto, K. Toyama, T. Kashiwa, Y. Saitoh, and M. Miyakawa 342

"Analysis of Loaded Cavities Using the Constitutive Error Approach" (Invited Paper) by R. Albanese, R. Fresa, R. Martone, and G. Rubinacci 350

"The Design of Electromagnetic Devices Using Knowledge Based Systems and Sensitivity Information" (Invited Paper) by D.A. Lowther, D.N. Dyck, and R. Rong 358

"A Computer Program for the Design of Superconducting Accelerator Magnets" (Invited Paper) by S. Russenschuck 366

"Application of Optimization to the Design of Electromechanical Devices" (Invited Paper) by J.K. Sykulski and Y.B. Cheng 378

"Genetic Algorithms for the Optimal Design of Electromagnetic Devices" (Invited Paper) by O.A. Mohammed and G.F. Üler 386

"Linear Constraints - Gradient Technique for the Inverse Problem of Design Optimization" (Invited Paper) by A.A. Arkadan and S. Subramaniam-Sivanesan 394

Session 6: COMPUTATIONAL ELECTROMAGNETICS APPLIED TO SHIP DESIGN
Organizers: J. Newcomb and J. Logan

"The Naval Sea Systems Command Electromagnetic Engineering Program" by D. Cebulski, N. Baron, and J. Eadie" ..... Presentation Only

"EM Engineering System Architecture" by J.A. Winston ..... Presentation Only

"EM Engineering Ray Tracing and Casting Model (RTC) by L. Gray ..... Presentation Only

"Ship Transition-Frequency EM Environment Analysis Requirements" by G.R. Piper ..... Presentation Only

"Finite Volume Time Domain Analysis of Ship Topside EM Environment Features" by W.F. Hall, A.H. Mohammadian, C.M. Rowell, and V. Shankar ..... Presentation Only

"EM Engineering Ship End-to-End Application" by L.R. Carlson, C.F. Juster, and G.R. Allen ..... Presentation Only

"EM Engineering Applied to Patrol Craft (PC-1)" (Invited Paper) by D. Tam, J. McGee, C. Azu, and M. Soyka 403

"Shipboard Antenna Pattern Visualization and Analysis"(Invited Paper) by L. Russell, J. Logan, J. Rockway, and D. Schwartz 410

SESSION 7: FINITE DIFFERENCE TIME DOMAIN
Organizer: J. Beggs

"Computational Analysis of Radiation from an Elliptical Shaped End Radiator" (Invited Paper) by S.A. Blocher, E.A. Baca, and J.H. Beggs 418

"A Time Domain in Harmonic Oscillator Model for an FDTD Treatment of Lossy Dielectrics" (Invited Paper) by K.S. Kunz 425

"FDTD Modeling of Electromagnetic Wave Interactions with Composite Random Sheets" (Invited Paper) by J.G. Maloney and B.L. Shirley 430

SESSION 7: continued

"An Improved Near to Far Field FDTD Algorithm" (Invited Paper) by K.S. Kunz 431

"Unstructured Finite-Volume Modeling in Computational Electromagnetics" (Invited Paper) by D.J. Riley and C.D. Turner 435

"Scattering from Coated Targets Using a Frequency-Dependent, Surface Impedance Boundary Condition in FDTD" by C.W. Penney, R.J. Luebbers, and J.W. Schuster 445

"Hybrid Finite Difference Time Domain and Finite Volume Time Domain in Solving Maxwell's Equations" (Invited Paper) by K.S. Yee and J.S. Chen 453

"Reducing the Number of Time Steps Needed for FDTD Antenna and Microstrip Calculations" (Invited Paper) by RJ. Luebbers and H.S. Langdon 465

"Numerical Simulations of Light Bullets, Using the Full Vector, Time Dependent, Nonlinear Maxwell Equations" by P.M. Goorjian and Y. Silberberg 472

SESSION 8: BERENGER'S BOUNDARY CONDITION
Organizer: J. Fang

"Ultrawideband Termination of Waveguiding and Multilayer Structures for FD-TD Simulations in 2-D and 3-D" (Invited Paper) by C.E. Reuter, R.M. Joseph, E.T. Thiele, D.S. Katz, and A. Taflove 476

"A 3-D Perfectly Matched Medium by Coordinate Stretching and Its Absorption of Static Fields" (Invited Paper) by W.C. Chew, W.H. Weedon, and A. Sezginer 482

"Perfectly Matched Anisotropic Absorbers for Finite Element Applications in Electromagnetics" by D.M. Kingsland, Z.S. Sacks, and J.F. Lee 490

"Modification of Berenger's Perfectly Matched Layer for the Absorption of Electromagnetic Waves in Layered Media" by M. Gribbons, S.K. Lee, and A.C. Cangellaris 498

"Performance of the Perfectly Matched Layer in Modeling Wave Propagation in Microwave and Digital Circuit Interconnects" by Z. Wu and J. Fang 504

SESSION 9: TIME DOMAIN/FDTD
Chairs: L. Long and J. Maloney

"A FVTD Algorithm for Maxwell's Equations on Massively Parallel Machines" by V. Ahuja and L.N. Long 513

"The Piecewise Linear Recursive Convulution Method for Incorporating Dispersive Media into FDTD" by D.F. Kelley and R.J. Luebbers 526

"Combining Different Coordinate Systems in the Time Domain Finite Difference Method" by M. Mrozowski, M. Okoniewski, M.A. Stuchly, and S.S. Stuchly 534

"Time Domain Response of Simulated 2D Composite Scatterers" by A.Z. Elsherbeni and P.M. Goggans 542

"An Object-Oriented Approach to Writing Computational Electromagnetics Codes" by M. Zimmerman and P. Mallasch 551

SESSION 10: "FAST ALGORITHMS FOR COMPUTATIONAL ELECTROMAGNETICS"
Organizers: E. Michelssen and W. Chew

"On the Use of Wavelet-Like Basis Functions in the Finite Element Analysis of Elliptic Problems" (Invited Paper) by R.K. Gordon 559

"Fast Wavelet Algorithm (FWA) for Moment Method Analysis of Electromagnetic Problems" (Invited Paper) by K. Sabetfakhri and L.P.B. Katehi 568

"Fast Far Field Approximation for Calculating the RCS of Large Objects" (Invited Paper) by C.C. Lu and W.C. Chew 576

"The Parameter Estimation Technique (PET): Speeding Up Dense Matrix Methods" (Invited Paper) by Ch. Hafner and J. Fröhlich 584

"A Novel Scheme for Massively Parallel Solution of Maxwell's Equation Using FDTD" (Invited Paper) by M.A. Jensen, Y.Rahmat-Samii, and A. Fijany 592

"Reduction of the Filling Time of Method of Moments Matrices" (Invited Paper) G. Vecchi, P. Pirinoli, L. Matekovits, and M. Orefice 600

"The Fast Multipole Method for Large 2d Scatterers" (Invited Paper) by L.R. Hamilton, J.J. Ottusch, M.A. Stalzer, R.S. Turley, J.L. Visher and S.M Wandzura 606

"A Multilevel Matrix Decomposition Algorithm for Analyzing Scattering From Large Structures" (Invited Paper) by E. Michielssen and M. Boag 614

"A 3D Fast Multipole Method for Electromagnetics with Multiple Levels" (Invited Paper) by B. Dembart and E. Yip 621

"Fast Multipole Method Solution of Combined Field Integral Equation" by J.M. Song and W.C. Chew 629

AUTHOR INDEX 637

VOLUME II

SESSION 11: MICROWAVE AND GUIDED WAVE
Chairs: P. Goggans and A. Terzuoli

"Computer-Simulation of Isotropic, Two-Dimensional Guided-Wave Propagation" by R.A. Speciale 639

"Analysis of Ultra-Short Pulse Propagation on Uniform and Tapered Printed Transmission Lines" by R.O. Veliz and J.R. Souza 648

"Wave-Field Patterns on Electrically Large Networks" by R.A. Speciale 656

"Scattering Characteristics of Dissimilar Waveguide Slot Couplers" by A.K. Singh and S. Christopher 664

"An Alternative Formulation of the Tranverse Resonance Technique" by A.G. Neto, S. Ariguel, H. Aubert, D. Bajon, and H. Baudrand 672

SESSION 12: MOM

Chairs: A. Peterson and R. Ziolkowski

"Moment Method Analysis of Dielectric Covered Radiating Slots Using Alternative Green's Function Approach" by S. Christopher, V.V.S. Prakash, A.K. Singh, and N. Balakrishnan 680

"Computation of E-Field Distribution of Low Gain Antenna on Conducting Body or Revolution" by J. Liu, J. Wang, and Y. Gao 687

"An Implementation of an Exact Scheme for Problem Decomposition Via the Use of Aperture Admittance" by D.L. Wilkes, C.C. Cha, and T. Krauss 695

"Parallelization of the Parametric Patch Moment Method Code" by X. Shen, G.E. Mortensen, C.C. Cha, G. Cheng, and G.C. Fox 702

"A Tool Box for Parallelization of Moments Method Codes" by E. Yip, B. Blakely, L. Johnson, D. Jurgens, and R. Kochhar 710

SESSION 13: RECENT DEVELOPMENTS IN FDTD ANALYSIS

Organizers: M. Piket-May and D. Katz

"Simulation of Microwave Circuits by FDTD Method" (Invited Paper) by C.N. Kuo, B. Houshmand, and T. Itoh 718

"Adaptation of FDTD Techniques to Acoustic Modeling" (Invited Paper) by J.G. Maloney and K.E. Cummings 724

"FDTD Investigation of the Antenna-Tissue Interaction for Cellular and Satellite Systems" (Invited Paper) by Y.Rahmat-Samii and M.A. Jensen 732

"FDTD Modeling of Ground-Penetrating Radar Antennas" by B.J. Zook 740

"FDTD Modeling of Ultrashort Optical Pulse Interactions with Nonresonant and Resonant Materials and Structures" (Invited Paper) by R.W. Ziolkowski 748

"Time Domain Analysis of Electromagnetic Wave Propagation in Nonlinear Dielectric Slab" by G. Miano, C. Serpico, L. Verolino, and F. Villone 753

"An Efficient Sub-gridding Algorithm for FDTD" by D.T. Shimizu, M. Okoniewski, and M.A. Stuchly 762

"Using the Integral Forms of Maxwell's Equations to Modify and Improve the FDTD (2,4) Scheme" by M.F. Hadi and M. Piket-May 767

"From the Berenger PML ABC to Micro-Lasers: Recent Advances in FD-TD Modeling Techniques" (Invited Paper) by A. Taflove 775

SESSION 14: PROPAGATION
Organizer: K. Chamberlin

"Terrain and Refractivity Effects in a Coastal Environment: Results From The VOCAR Experiment" by A. Barrios 784

"Capabilities and Limitations Associated with Using GTD to Model Propagation Path Loss in the Presence of Irregular Terrain" by K. Chamberlin 790

"Comparison of Electromagnetic Wave Propagation Computer Programs" by S.A. Fast and T.H. Koschmieder 798

"A Model for Estimating Electromagnetic Wave Attenuation in a Forest (EWAF) Environment" by C. Welch, C. Lemak, and L. Corrington 801

"Validation of the Radio Physical Optics Propagation Model" by R.A. Paulus 809

"VTRPE: A Variable Terrain Electromagnetic Parabolic Equation Model" by F.J. Ryan 816

"Estimating Tropospheric Refractivity Fields Using a Nonlinear Gauss-Markov Procedure and the PE Model" by D.B. Boyer and F.J. Ryan 824

"Modeling of Radio Wave Ducting Over Regular Boundary" by I.P. Zolotarev 830

SESSION 15: PARALLELIZATION OF EM CODES
Organizers: J. Volakis and A. Chatterjee

"Advances in Time-Domain CEM Using Massively Parallel Architectures" (Invited Paper) by C. Rowell, V. Shankar, W.F. Hall, and A. Mohammadian 839

"Parallel Solutions of Maxwell's Equations on the Meiko CS-2" by N. Madsen, B. Eme, D. Steich and G. Cook 847

"Parallelization of the CARLOS-3D Method of Moments Code" (Invited Paper) by J.M. Putnam, D.D. Car, and J.D. Kotulski 848

"Parallel Computing for Electromagnetism at ONERA" (Invited Paper) by A. de La Bourdonnaye, A. Cosnuau, X. Ferrières, P. Leca, and F.X. Roux 856

"The Performance of the Parallel Solution of the Quasi-Minimal Residual (QMR) Method on 2D Mesh Architectures" (Invited Paper) by L. Hamandi, F. Özgüner and R. Lee 864

"Advanced Parallel Solver Techniques" (Invited Paper) by A.S. King 872

"Parallelized FDTD for Antenna Radiation Pattern Calculations" by Z.M. Liu, A.S. Mohan, T.A. Aubrey, and W.R. Belcher 873

"Calculation of Electromagnetic Fields with the Multiple Multipole Method (MMP Method) on Parallel Computers" by C. Tudziers and H. Singer 881

"Implementation of the Finite-Difference Time-Domain Method on Parallel Computers" by R.S. David and L.T. Wille 889

SESSION 16: EM THEORY II
Chairs: K.Yee and R. Gordon

"FDTD Investigation of the Ability to Increase Electromagnetic Fields Around Head Tumors" by D.B. Dunn, A.J. Terzuoli, Jr., G.C. Gerace and C.M. Rappaport 898

"FDTD and PMM Based Design of a TEM Horn Antenna with Reduced Off-Boresight Fields" by D.J. Wolstenholme, A.J. Terzuoli, Jr., and G.C. Gerace 904

"Determination of the Complex Aperture Distribution of a Planar Spiral Antenna from 3-D Far-Field Radiation Pattern Data" by M. Kluskens, W. Lippincott, and M. Kragalott 910

"Analysis of Micro-Contamination of Silicon Wafers Based on Discrete Sources Method (DSM) by Y.A. Eremin and N.V. Orlov 925

"Analysis of Convergence Properties of Projection Methods for Solving CEM Applications" by V.I. Ivakhnenko, A.V. Kukk, E.E. Tyrtyshnikov, A.Y. Yeremin, and N.L. Zamarashkin 929

SESSION 17: ELECTROMAGNETIC MODELING TECHNIQUES FOR INTEGRATED OPTICS
Organizer: A. Cangellaris

"Analysis and Design of Guided-Wave Optical Devices Using Finite-Difference Time-Domain Method" (Invited Paper) by S.K. Chaudhuri and S.T. Chu 937

"Vectorial Analysis of Optical Waveguides by the Method of Lines" (Invited Paper) by R. Pregla and W.W. Pascher 943

"Vector Finite Element Analysis of Lossless and Lossy Dielectric Waveguides" (Invited Paper) by P. Cheung and A. Gopinath 951

"NL-FDTD Modeling of Linear and Nonlinear Corrugated Waveguiding Systems for Integrated Optics Applications" (Invited Paper) by R.W. Ziolkowski and J.B. Judkins 957

"Analysis of Coupled Nonlinear Optical Waveguides by Matrix Method" by V. Tripathi, A. Weisshaar, and H.S. Chang 962

SESSION 18: TOPICS IN FRACTAL AND WAVELET ELECTRODYNAMICS
Organizers: D.H. Werner and P.L. Werner

"An Overview of Fractal Electrodynamics Research" (Invited Paper) by D.H. Werner 964

"Fractal Arrays and Fractal Radiation Patterns" (Invited Paper) by P.L. Werner, D.H. Werner, and A.J. Ferraro 970

"Wavelet Transforms and Time/Time-scale Analysis" (Invited Paper) by R.K. Young and T.G. Golsberry 979

"Wavelet-based Processing to Efficiently Achieve Broadband Monostatic and/or Passive Cross-sensor Processing" (Invited Paper) by R.K. Young and L.H. Sibul 987

"The Intervallic Wavelets with Applications in the Surface Integral Equations" (Invited Paper) by G.W. Pan and J.Y. Du 993

"Radar Cross Section Data Reduction Using Wavelets" by A.S. Ali, S.E. Duval, and R.L. Haupt 1000

SESSION 19: NEC APPLICATIONS
Organizer: J.K. Breakall

"Computationally Efficient and Accurate Approximations for Impedance Matrix Elements of NEC-Type Method of Moments Formulations" by D.H. Werner, S.E. Metker, and J.A. Huffman 1009

"Development of the Coupled-Resonator Antenna Principle, A Computer Modeling Case History" by G.A. Breed 1017

"Antenna Design and Development Using NEC-WIN" by T.A. Erdley, J.J. Shapiro, J.S. Young, and J.K. Breakall 1025

"The "PAINT" System, A UTD/NEC Hybrid Package for Simulating Antenna Patterns Over 3-Dimensional Irregular Terrain" by J.S. Young and J.K. Breakall 1033

SESSION 20: FEM
Chairs: R. Burkholder and J. Karty

"Numerically Characterizing Electromagnetic Fields Local to the Edge of a Conducting Strip Using a Matched Asymptotic Technique and the Finite Element Method" by A.S. Ali and C.L. Holloway 1040

"An Enhanced "A Posteriori" Remeshing Algorithm for Adaptive Meshing of 2D Finite Element Problems" by P.Girdinio, A. Manella, and G. Molinari 1047

"Finite Element Analysis of Waveguides Using Edge-Based Magnetic Vector Potential and Nodal-Based Electric Scalar Potential" by J.F. Lee, G.Lizalek, and J. Brauer 1054

"A Scattering Analysis of Laser Beam Wave by Groove Pits on Optical Memory Disk by Using FEM with BEM" by Y. Miyazaki and K. Tanaka 1062

"3D Nodal-and Mixed-Based Elements for Unbounded Microwave Problems" by A. Nicolas, L. Nicolas, and J.L. Yao-bi 1070

"A Rationale for the Use of Mixed-Order Basis Functions Within Finite Element Solutions of the Vector Helmholtz Equation" by A.F. Peterson and D.R. Wilton 1077

"Finite Element Waveguide Simulator Techniques" by J.R. Sanford and N.M. Johansson 1085

"A Solution For Open Boundary Electromagnetic Field Problems by Mapped Infinite and Virtual Elements" by L.H.A. de Medeiros and A. Raizer 1094

SESSION 21: EM ANALYSIS TECHNIQUES FOR ELECTRICALLY LARGE CAVITIES
Organizer: D. Pflug

"Application of Modal and Plane Wave Expansions to Modeling Large Jet Engine Cavities" (Invited Paper) by J.L. Karty and J.M. Roedder 1103

"Scattering From Dielectric Loaded Cavities Using Shooting and Bouncing Rays" (Invited Paper) by M.C. Christensen, S.W. Lee, and D.J. Andersh 1111

"XPATCH Simulation of Large Inlet Structures" (Invited Paper) by R. Bhalla and H.Ling 1118

"An Iterative Physical Optics Approach for the EM Analysis of Cavities and Other Multi-Bounce Geometries" (Invited Paper) by R.J. Burkholder 1126

SESSION 21: continued

"Improved Ray Basis in the Hybrid Analysis of EM Scattering by Large Open Cavities" (Invited Paper) by R.J. Burkholder, P.H. Pathak, H.T. Chou, D.J. Andersh,and J. Fath 1134

"Overlapping Modal and Geometric Symmetries for Computing Jet Engine Inlet Scattering" (Invited Paper) by D.C. Ross, J.L. Volakis, H.T. Anastassiu, and D.J. Andersh 1142

SESSION 22: ACCURACY ESTIMATION IN ELECTROMAGNETIC MODELING
Organizer: S.M. Wandzura

"Assessing the Influence of Coefficient Accuracy, Matrix Condition Number, Size and Type, and Computer Precision on Matrix-Solution Accuracy" (Invited Paper) by E.K. Miller 1151

"Numerical Accuracy Issues in Finite Element Frequency Domain Solutions of Radar Scattering Problems" (Invited Paper) by J. D'Angelo 1163

"Accuracy in Computation of Matrix Elements of Singular Kernels" by S.M. Wandzura 1170

"Accuracy Estimation and High Order Methods" by L.R. Hamilton, J.J. Ottusch, M.A. Stalzer, R.S. Turley, J.L. Visher, and S.M. Wandzura 1177

"Accuracy Issues in Time-Domain CEM Using Structured/Unstructured Grid Formulations" (Invited Paper) by V. Shankar, W.F. Hall, and S. Palaniswamy 1185

"An Accuracy Study for the 3D Hybrid Finite Element Method of Moments SWITCH Code" (Invited Paper) by G.E. Antilla and Y.C. Ma 1193

"Modeling Accuracy of Method of Moments" by M.B. Gedera, L.N. Medgyesi-Mitschang, R. Pearlman, J.M. Putnam, D.S. Wang 1194

"Requiring Quantitative Accuracy Statements in EM Data" (Invited Paper) by E.K. Miller 1202

SESSION 23: PDE METHODS IN ELECTROMAGNETICS
Organizers: R. Lee and J.F. Lee

"Optimization Issues in Finite Element Codes for Solving Open Domain 3D Electromagnetic Problems" (Invited Paper) by A. Chatterjee and J.L. Volakis 1212

"A Characteristic-Based 3D Time Domain Maxwell Equation Solver" (Invited Paper) by J.J.S. Shang and K.C. Hill 1220

"Finite Element Solution of Eddy Current Problems in Electromagnetics" (Invited Paper) by O.A. Mohammed and G.F. Üler 1228

"Ten Years of Evolution of the FDTD-Like Conformal Techniques" (Invited Paper) by K.S. Yee 1241

"Whitney Elements Time Domain (WETD) Methods for Solving Three-Dimensional Waveguide Discontinuities" (Invited Paper) by J.F. Lee 1258

"An FDTD/FVTD 2D-Algorithm to Solve Maxwell's Equations" by J.S. Chen, J.V. Prodan, and K.S. Yee 1266

"Spectral Finite Methods for the Simulation of Electromagnetic Interactions with Electrically Long Structures" (Invited Paper) by A.C. Cangellaris and D. Hart 1280

AUTHOR INDEX 1288

THE APPLIED COMPUTATIONAL ELECTROMAGNETICS SOCIETY

1996 CALL FOR PAPERS 1996

The 12th Annual Review of Progress in Applied Computational Electromagnetics

March 18-22, 1996

Naval Postgraduate School, Monterey, CA

Share your knowledge and expertise with your colleagues

The Annual ACES Symposium is an ideal opportunity to participate in a large gathering of EM analysis enthusiasts. The purpose of the Symposium is to bring analysts together to share information and experience about the practical application of EM analysis using computational methods. The Symposium features four areas of interest: technical publication, demonstrations, vendor booths and short courses. All aspects of electromagnetic computational analysis are represented. The Symposium will also include invited speakers and interactive forums. Contact Richard Gordon (601) 232-5388 for details.

1996 ACES Symposium Chairman
Richard Gordon
University of Mississippi
EE Dept. Anderson Hall, Box 41
University, MS 38677
Phone: (601) 232-5388
Fax: (601) 232-7231
Email:eegordon@vm.cc.olemiss.edu

1996 ACES Symposium Administrator
Richard W. Adler
ECE Dept/Code ECAB
Naval Postgraduate School
833 Dyer Road, Room 437
Monterey, CA 93943-5121
Phone: (408) 646-1111
Fax: (408) 649-0300
Email:554-1304@mcimail.com

1996 ACES Symposium Co-Chairman
Jin-Fa Lee
EE Department
Worcester Polytechnic Institute
100 Institute Road
Worcester, MA 01609
Phone: (508) 831-5778
Fax: (508) 831-5491
E-mail: jinlee@ee.wpi.edu

1966 ACES Symposium Co-Chairman
Eric Michielssen
ECE Department
University of Illinois
1406 West Green Street
Urbana, IL 61801-2991
Phone: (217) 333-3803
Fax: (217) 333-8986
E-mail: michiels@decwa.ece.uiuc.edu

1996 ACES Symposium

Sponsored by: ACES, NPS, DOE/LLNL, UNIV OF MISSISSIPPI, USAF. DOD AND DOE IN COOPERATION WITH IEEE, URSI, ASEE, SIAM AND AMTA

THE NAVAL POSTGRADATE SCHOOL

1995 Symposium Program Committee

for the

11th Annual Review of Progress in

APPLIED COMPUTATIONAL ELECTROMAGNETICS

at the
Naval Postgraduate School
Monterey, CA

Chairman: Ray Luebbers
Penn State University
320 EE East
University Park, PA 16802
(814) 865-2362/Fax:7065
Email: lu4@psuuvm.psu.edu

Co-Chair: Richard K. Gordon
EE Dept. Univ. of Mississippi
Anderson Hall, Box 41
University, MS 38677
(601) 232-5388/Fax:7231
Email:eegordon@vm.cc.olemiss.edu

Publicity: Paul M. Goggans
EE Dept. Univ. of Mississippi
Anderson Hall, Box 41
University, MS 38677
(601) 232-5954/Fax:7231
Email:eepmg@cotton.vislab.olemiss.edu

Adviser: Dr. Richard W. Adler
ECE Dept. Code ECAB
Naval Postgraduate School
833 Dyer Road, Room 437
Monterey, CA. 93943-5121
(408) 646-1111/Fax: 649-0300
Email:554-1304@mcimail.com

Short Course Chairman: Robert Lee
EE Dept. Univ. of Mississippi
Anderson Hall, Box 41
2015 Neil Ave.
Columbus, OH 43210-1272
(614) 292-1433/Fax: 7596

1996 Symposium Chairman: Chair: Richard K. Gordon
EE Dept. Univ. of Mississippi
Anderson Hall, Box 41
University, MS 38677
(601) 232-5388/Fax: 7231
Email:eegordon@vm.cc.olemiss.edu

Conference Secretary: Mrs. Pat Adler

Advisory Committee:
Richard W. Adler, Naval Postgraduate School
Pat Foster, Microwave & Antenna System
Richard K. Gordon, Univ of Mississippi
Harold Sabbagh, Sabbagh Assoc., Inc.
Ed Miller, Ohio State University
Robert Bevensee, Consultant
Raymond Luebbers, Penn State University
Andrew Peterson, Georgia Institute of Tech.
Frank Walker, Boeing Defense & Space Group
Perry Wheless Jr., Univ. of Alabama
Duncan Baker, Univ. of Pretoria
James Breakall, Penn State University

A - C - E - S

1995

March 20-24, 1995
Monterey, CA

For more information please contact:

Technical Program Chairman
Raymond Luebbers
Dept. of Electrical Engineering
The Pennsylvania State University
University Park, PA 16802
Phone: (814) 865-2362
FAX: (814) 865-7065
Email: lu4@psuvm.psu.edu

Short Course Chairman
Robert Lee
Dept. of Electrical Engineering
The Ohio State University
Phone: 614-292-1433
FAX: 614-292-7596
Email: lee@ee.eng.ohio-state.edu

Symposium Administrator
Richard W. Adler
ECE Department/Code ECAB
Naval Postgraduate School
833 Dyer Road, Room 437
Monterey, CA 93943-5121
Phone: (408) 646-1111
FAX: (408) 649-0300
Email: 5541304@mcimail.com

Publicity Chairman
Paul M. Goggans
EE Department
University of Mississippi
Anderson Hall, Box 1
University, MS 38677
Phone: (601) 232-5954
FAX: (601) 232-7231
Email: eepmg@cotton.vislab.olemiss.edu

Publication Chairman
Richard K. Gordon
EE Dept., University of Mississippi
Anderson Hall, Box 41
University, MS 38677
Phone: (601) 232-5388
FAX: (601) 232-7231
Email: eegordon@vm.cc.olemiss.edu

APPLIED COMPUTATIONAL ELECTROMAGNETICS SOCIETY

The Eleventh Annual Review of Progress in Applied Computational Electromagnetics

Welcome to the 11th Annual Review of Progress in Applied Computational Electromagnetics.

While this year's conference retains the flavor of past meetings, some changes have been made. In particular, more of the sessions have been organized around a particular theme, with more invited papers than in previous years. The individuals responsible for these sessions are indicated in the agenda as Session Organizers, and their efforts are very much appreciated.

Special recognition should be given to several individuals who contributed significantly to the conference. Paul Goggans provided the advertising for the conference. Rob Lee once again did an excellent job of organizing the Short Courses. Richard Gordon received all the papers and put them together to produce these Proceedings. And of course Richard and Pat Adler must be recognized for arranging for the printing of the Proceedings, for providing access to the NPGS Facilities, and for all their other contributions to the conference.

Please enjoy your time in Monterey as much as possible, whether listening to a paper being presented, catching up on the latest "gossip" in the hallways, or enjoying the sights of Monterey.

Raymond Luebbers

Raymond Luebbers
Technical Program Chairman
1995 ACES Conference

ACES PRESIDENT'S STATEMENT

It's nice to be here in California in March, especially since we weren't entirely certain that there was going to be a California in March. This state seems to attract more than its fair share of calamities, ranging from floods, fires, mud slides, and OJ-things.

In any case, we're back at ACES'95, the Eleventh Annual Review of Progress in Applied Computational Electromagnetics, which reverts to the Naval Postgraduate School, our long-time home.

Ray Luebbers and his committee have put together an excellent program, one which embraces 'low frequency' CEM to 'high frequency 'CEM. The subject matter to be discussed ranges from the traditional scattering and radiation problems, so typical of ACES past, to optimization techniques in applied electromagnetics. This area has been of interest to designers of electrical machines, but we see that it is being applied to hyperthermia and superconducting accelerator magnets.

I am pleased to see ACES embrace all aspects of computational electromagnetics, for there is no single 'natural' milieu of CEM for ACES. The problems of CEM are many and varied. If one has an interest in solving Maxwell's equations, he should be at home at any frequency, in any environment.

You will note that Ken Siarkiewicz, a long-time dedicated supporter of ACES, has put together an interesting session entitled 'Research and Engineering Framework for CEM'. Ken then did himself proud by releasing $10,000 of MMACE (millimeter-wave, microwave advanced computational environment) funding so that ACES could properly support this session. This tells me two things: first, that Ken is a pretty good man to have on your side, and second, that ACES is increasingly being viewed as the preeminent vehicle to expose issues in computational electromagnetics.

ACES is reaching this stature because of the dedication of its members especially those who volunteer to do its work. When you publish next, think about the ACES Journal or Newsletter as the publication of choice. When you wish to give your profession extracurricular support, consider working for ACES. A lot of people have, and a lot more will.

Enjoy the Eleventh Annual Review.

Harold A. Sabbagh
Sabbagh Associates, Inc.
4635 Morningside Drive
Bloomington, IN 47408
(812) 339-8273
(812) 339-8292 FAX
email:has@sabbagh.com

ACES 1995 SHORT COURSES

MONDAY MARCH 20 — FULL-DAY COURSE

0830-1630 "Finite Elements for Electromagnetics"
by John Brauer, MacNeal Schwendler Corporation

0830-1630 "GEMACS From A-Z" by Buddy Coffey, Advanced EM.

0830-1630 "Physical Wavelets" by Gerald Kaiser, University of Massachusetts at Lowell.

HALF-DAY COURSE

1300-1630 "The Multiple Multipole Program (MMP): Theory, Practical Use and Latest Features"
by Pascal Leuchtmann, Swiss Federal Instiitute of Technology

1300-1630 "Verification and Validation of Computational Software" by E.K. Miller, Ohio University.

SATURDAY MARCH 25 — FULL-DAY COURSE

0830-1630 "Using Mathematical Software for Computational Electromagnetics"
by Jovan Lebaric, Naval Postgraduate School.

0830-1630 "Wire Antenna Modeling Using NEC" by Dick Adler, Naval Postgraduate School, Jim Breakall, Penn State University, and Gerry Burke, Lawrence Livermore National Lab.

0830-1630 "FDTD, Generalized FDTD and FVTD Techniques in Solving Maxwell's Equations"
by Kane Yee, Lockheed.

FINAL AGENDA

The Eleventh Annual Review of Progress in Applied Computational Electromagnetics

NAVAL POSTGRADUATE SCHOOL
20 - 25 MARCH, 1995

Raymond Luebbers, Technical Program Chairman

Richard Gordon, Proceedings Editor

Robert Lee, Short Course Chairman

Paul Goggans, Publicity Chairman

Richard Adler, Conference Facilitator

MONDAY 20 MARCH

0830-1630	**SHORT COURSE (FULL-DAY)** "Finite Elements for Electromagnetics"	**102 Glasgow** John Brauer, MacNeal-Schwendler Corporation
0830-1630	**SHORT COURSE (FULL-DAY)** "GEMACS from A-Z"	**122 Ingersoll** Buddy Coffey, Advanced EM
0830-1630	**SHORT COURSE (FULL-DAY)** "Physical Wavelets"	**101 A Spanagel** Gerald Kaiser, Univ. of Massachusetts at Lowell
1300-1630	**SHORT COURSE (HALF-DAY)** "The Multiple Multipole Program (MMP): Theory, Practical Use and Latest Features"	**325 Ingersoll** Pascal Leuchtmann, Swiss Federal Institute of Technology
1300-1630	**SHORT COURSE (HALF-DAY)** "Verification and Validation of Computational Software"	**323 Ingersoll** E. K. Miller, Ohio University
0800-2030	**CONFERENCE REGISTRATION**	**103 Glasgow Hall**

TUESDAY 21 MARCH

0700	**CONFERENCE REGISTRATION**	**103 Glasgow Hall**
0700-0800	**CONTINENTAL BREAKFAST**	
0800	**WELCOME** Raymond Luebbers	**102 Glasgow Hall**
SESSION 1: SCATTERING (parallel with Sessions 2 and 3) **CHAIRS: V. CABLE, E. MILLER**		**122 Ingersoll Hall**
0840	"A CGFFT Method Applied to the Scatttering from Finite Size Microstrip Antenna"	A. McCowen
0900	"Analysis of Scattering by Cluster of Nonspherical Particles Based on Complete Mathematic Models"	Y.A. Eremin, N.W. Orlov and V.I. Rozenberg
0920	"Analytic Solution for Calculating the Radar Cross-Section and Related Parameters of a Conducting Right Circular Cylinder Surrounded by Multiple Layers of Lossy Dielectrics"	G.W. Jarriel, Jr., M. E. Baginski, and Lloyd Riggs
0940	"RCS of High Permittivity Cubes Computed with the TLM Method"	C. Eswarappa and W.J.R. Hoefer
1000	**BREAK**	
1020	"Scattering Analysis of Antenna Installations/Panels on a Curved Surface Using Uniform Field Integration Method"	J.J. Kim and O.B. Kesler
1040	"Code Validation of Aircraft Scattering Parameters using IR Thermograms"	J. Norgard, R. Sega, M. Seifert, T. Blocher and A. Pesta

TUESDAY 21 MARCH

SESSION 1: SCATTERING (parallel with Sessions 2 and 3) (CONT) — **122 Ingersoll Hall**

1100	"A New Method for Solving Scattering Problems with Conducting Media in the Time Domain"	M. Schinke and K. Reiß
1120	"Experience and Experiments at Cray Research with JUNCTION-2"	J.A. Crow and Q.M. Sheikh
1140	"Quantitative Methods for Measuring and Improving the Performance of Electromagnetic Scattering Codes"	J.P. Meyers, A. J. Terzuoli, Jr., and G.C. Gerace
	LUNCH	

SESSION 2: LOW FREQUENCY (parallel with Sessions 1 and 3) — **117 Spanagel Hall**
CHAIRS: K. KUNZ, H. SABBAGH

0840	"Numerical Modelling of EMC in Underground Power Cable Systems with the Hybrid FE-BE Method"	J. Shen and A. Kost
0900	"New Contribution to the Study of Fault Currents Distribution in the Ground Systems"	H.O. Brodskyn, M.H. Giarolla, J.R. Cardoso, N.M. Abe and A. Passaro
0920	"On the Oscillatory Phenomena of Eddy Currents Along the Ã, V-Ψ Inferface"	Z. Cheng, Q. Hu, S. Gao, Z. Liu, M. Wu and C. Ye
0940	"A New MMP-Code for Static Field Computation"	M. Gnos and P. Leuchtmann
1000	**BREAK**	
1020	"Molten Aluminum Flow Induced by High Magnetic Fields"	W.P. Wheless, Jr. and C.S. Wheless
1040	"The Electrostatic Characterization of a N-Element Planar Array Using the Singularity Expansion Method"	J.E. Mooney and L. Riggs
1100	"A Volume-Integral Code for Electromagnetic Nondestructive Evaluation"	R.K. Murphy, H.A. Sabbagh, J.C. Treece and L. W. Woo
	LUNCH	

SESSION 3: RESEARCH AND ENGINEERING FRAMEWORK FOR CEM (parallel with Sessions 1 and 2) — **102 Glasgow Hall**
ORGANIZER: K. SIARKIEWICZ

0840	"Research and Engineering Framework (REF) for Computational Electromagnetics" (Invited)	B. Hantman, K. Siarkiewicz, J. Labelle and R. Jackson
0900	"Research & Engineering Framework (REF) Data Dictionary Specification for Computational Electromagnetics" (Invited)	J.A. Evans
0920	"DT_NURBS - A Geometry Engine for Integration of the MMACE Data" (Invited)	B. Ames and C. Whitcomb
0940	"Standardized Grid Generation for the Research and Engineering Framework" (Invited)	L.W. Woo, H. A. Sabbagh, J. LaBelle and B. Hantman
1000	**BREAK**	
1020	"Visualization and Standards" (Invited)	J. Cugini
1040	"A Visualization Toolkit for Computational Electromagnetics" (Invited)	B. Joseph
1100	"MMACE - Lessons for the Development of a CEM Computational Environment" (Invited)	R.G. Hicks and K.R. Siarkiewicz
	LUNCH	
1200	**BOARD OF DIRECTORS MEETING**	**Terrace Room, Herrmann Hall**

TUESDAY AFTERNOON 21 MARCH

1330-1730	**VENDOR BOOTHS AND WINE AND CHEESE BUFFET**	**Barbara McNitt Ballroom, Herrmann Hall**
1800	**HAPPY HOUR (NO HOST)**	**Barbara McNitt Ballroom, Herrmann Hall**
1900	**AWARDS BANQUET**	**Barbara McNitt Ballroom, Herrmann Hall**
1330-1530	**SHORT COURSE (PARTIAL DAY, NO FEE)** Bob Bevensee "Time Series Analyses of Equity Stock Prices and a Profitable Investment Strategy"	**102 Glasgow Hall**
1330-1530	**SESSION 4: INTERACTIVE TECHNICAL SESSION**	**Barbara McNitt Ballroom, Herrmann Hall**

SESSION 4A: EM THEORY I — **Barbara McNitt Ballroom, Herrmann Hall**

"Pulse Basis Function Implementation of the Radiation Condition Integral Equations"	P.C. Colby
"Finite Difference Solutions of Geometrical Optics and Some Related Nonlinear PDEs Approximating High Frequency Helmholtz Equation"	E. Fatemi, B. Engquist and S. Osher
"Conversion of Mechanical Energy to Electromagnetic Energy"	R.M. Bevensee
"Block-Toeplitz-Structure-Based Solution Strategies for CEM Problems"	V.I. Ivakhnenko and E.E. Tyrtyshnikov
"The Two-Dimensional Finite Integral Technique Combined with the Measured Equation of Invariance Applied to Transverse Electric Open Region Scattering Problems"	G.K. Gothard and S.M. Rao
"Artificial Transparent Boundaries in Computational Quasioptics"	A.V. Popov
"A Statistical Electromagnetics (STEM) Research Initiation Report"	W.P. Wheless, Jr., C.B. Wallace and W.D. Prather
"Optimization of Aperiodic Conducting Grids"	R.L. Haupt
"Accurate MOM Scattering Calculations Using Massively Parallel Computation"	L.D. Vann and J.S. Bagby
"A New Angle on a Low Cost Ground Screen for Model Testing in the Undergraduate Antennas Laboratory (Looking at Near Vertical Incidence Skywaves (NVIS) for a Coast Guard Patrol Boat)"	M.E. McKaughan, W.M. Randall and B. Nutter
"Efficient Extraction of the Near-Field from CGFFT Methods Applied to Scatterers in the Resonance Region"	A. McCowen

SESSION 4B: VISUALIZATION & INTERFACES — **Barbara McNitt Ballroom, Herrmann Hall**

"Computer Code for Field Calculation and Visualization in Quasioptics"	Y.V. Kopylov
"Dosimetry in a Voxel Model of the Head"	P.J. Dimbylow
"A Graphical User Interface for the NEC-BSC"	L.W. Henderson and R.J. Marhefka
"MF Communication and Broadcast Prediction System"	M.J. Packer and A.P. Tsitsopoulos
"A Finite Difference Time Domain Visualization Tool for Microsoft Windows™"	A. Z. Elsherbeni, C.D. Taylor, Jr. and C. E. Smith

SESSION 4C: VALIDATION — **Barbara McNitt Ballroom, Herrmann Hall**

"Transformable Scale Aircraft-Like Model for the Validation of Computational Electromagnetic Models and Algorithms: Initial Configuration and Results"	D.R. Pflug and D. Warren
"Measurement Study for Validation of Electromagnetic Scattering Codes on a Complex 3D Target"	T. Kienberger and D. Jurgens
"Validation Using a Moment Method Approach with Exact Object Representation"	J.A. Larsson, S. Ljung and B.Wahlgren
"IR Measurements for Validating EM Analysis Tools"	M. Seifert, T. Blocher and A. Pesta

TUESDAY AFTERNOON 21 MARCH

SESSION 4D: EMI/EMC/EMP — **Barbara McNitt Ballroom, Herrmann Hall**

"Analysis of Electromagnetic Interference at an Ocean Observation Post"	L. Bai and J.F. Dai
"Enforcing Correlation on Statistically Generated EM Cable Drivers"	R. Holland and R. St. John
"Analysis of Different Contributions to the Coupling Between Reflector Antennas on a Satellite"	C. Park and P. Ramanujam
"Simple Radiation Models in Lieu of EMC Radiated Emissions Testing"	R. Perez

WEDNESDAY MORNING 22 MARCH

0730 **CONTINENTAL BREAKFAST**

0800 **ACES BUSINESS MEETING** President Hal Sabbagh **102 Glasgow Hall**

SESSION 5: OPTIMIZATION TECHNIQUES IN APPLIED ELECTROMAGNETICS (parallel with Sessions 6 and 7) 361 Ingersoll Hall
ORGANIZER: O.A. MOHAMMED

0840	"An Optimization Approach to Reduce the Discretization Error in Finite Element Explicit Solution Sceme" (Invited)	M. Feliziani, E. Latini, F. Maradei
0900	"Analysis and Design of a Reentrant Resonant Cavity Applicator for Radio Frequency Hyperthermia System" (Invited)	Y. Kanai, T. Tsukamoto, K. Toyama, T. Kashiwa, Y. Saitoh and M. Miyakawa
0920	"Analysis of Loaded Cavities Using the Constitutive Error Approach" (Invited)	R. Albanese, R. Fresa, R. Martone and G. Rubinacci
0940	"The Design of Electromagnetic Devices using Knowledge Based Systems and Sensitivity Information" (Invited)	D.A. Lowther, D. N. Dyck and R. Rong
1000	**BREAK**	
1020	"A Computer Program for the Design of Superconducting Accelerator Magnets" (Invited)	S. Russenschuck
1040	"Application of Optimization to the Design of Electromechanical Devices" (Invited)	J.K. Sykulski and Y.B. Cheng
1100	"Genetic Algorithms for the Optimal Design of Electromagnetic Devices" (Invited)	O.A.Mohammed, G.F. Üler
1140	"Linear Constraints - Gradient Technique for the Inverse Problem of Design Optimization" (Invited)	A.A. Arakadan and S. Subramaniam-Sivanesan
	LUNCH	

SESSION 6: COMPUTATIONAL ELECTROMAGNETICS APPLIED TO SHIP DESIGN (parallel with Sessions 5 and 7) 102 Glasgow Hall
ORGANIZERS: J. NEWCOMB AND J. LOGAN

0840	"The Naval Sea Systems Command Electromagnetic Engineering Program" (Invited)	D. Cebulski, N. Baron and J. Eadie
0900	"EM Engineering System Architecture" (Invited)	J. Winston
0920	"EM Engineering Ray Tracing and Casting Model RTC" (Invited)	L. Gray
0940	"Ship Transition-Frequency EM Environment Analysis Requirements" (Invited)	G. Piper
1000	**BREAK**	
1020	"Finite Volume Time Domain Analysis of Ship Topside EM Environment Features" (Invited)	B. Hall, A. Mohammadian, C. Rowell and V. Shankar
1040	"EM Engineering Ship End-To-End Application" (Invited)	L. R. Carlson, C. F. Juster, G. R. Allen

WEDNESDAY MORNING 22 MARCH

SESSION 6: (CONT) COMPUTATIONAL ELECTROMAGNETICS APPLIED TO SHIP DESIGN (parallel with Sessions 5 and 7) 102 Glasgow

1100	"EM Engineering Applied to Patrol Craft (PC-1)" (Invited)	D. Tam, J. McGee, C. Azu and M. Soyka
1120	"Shipboard Antenna Pattern Visualization and Analysis" (Invited)	L.C. Russell, J.C. Logan, J.W. Rockway and D.F. Schwartz
	LUNCH	

SESSION 7: FINITE DIFFERENCE TIME DOMAIN (parallel with Sessions 5 and 6) 122 Ingersoll Hall
ORGANIZER: J. BEGGS

0840	"Computational Analysis of Radiation from an Elliptical Shaped End Radiator" (Invited)	S. A. Blocher, E. A. Baca and J. H. Beggs
0900	"A Time Domain Harmonic Oscillator Model for an FDTD Treatment of Lossy Dielectrics" (Invited)	K. S. Kunz
0920	"FDTD Modeling of Electromagnetic Wave Interactions with Composite Random Sheets" (Invited)	J.G. Maloney and B.L. Shirley
0940	"An Improved Near to Far Field FDTD Algorithm" (Invited)	K. S. Kunz
1000	**BREAK**	
1020	"Unstructured Finite-Volume Modeling in Computational Electromagnetics" (Invited)	D.J. Riley and C.D. Turner
1040	"Scattering from Coated Targets Using a Frequency-Dependent, Surface Impedance Boundary Condition in FDTD"	C.W. Penney, R.J. Luebbers and J.W. Schuster
1100	"Hybrid Finite Difference Time Domain and Finite Volume Time Domain in Solving Maxwell's Equations" (Invited)	K.S. Yee and J.S. Chen
1120	"Reducing the Number of Time Steps Needed for FDTD Antenna and Microstrip Calculations" (Invited)	R. Luebbers and H.S. Langdon
1140	"Numerical Simulations of Light Bullets, Using the Full Vector, Time Dependent, Nonlinear Maxwell Equations"	P. Goorjian and Y. Silberberg
	LUNCH	

WEDNESDAY AFTERNOON 22 MARCH

SESSION 8: BERENGER'S BOUNDARY CONDITION (parallel with Sessions 10 and 11) 102 Glasgow Hall
ORGANIZER: J. FANG

1320	"Ultrawideband Termination of Waveguilding and Multilayer Structures for FD-TD Simulations in 2-D and 3-D" (Invited)	C.E. Reuter, R.M. Joseph, E.T. Thiele, D.S. Katz and A. Taflove
1340	"A 3-D Perfectly Matched Medium by Coordinate Stretching and Its Absorption of Static Fields" (Invited)	W.C. Chew, W.H. Weedon and A. Sezginer
1400	"Perfectly Matched Anisotropic Absorbers for Finite Element Applications in Electromagnetics"	D.M. Kingsland, Z.S. Sacks and J.F. Lee
1420	"Modification of Berenger's Perfect Matched Layer for the Absorption of Electromagnetic Waves in Layered Media"	M. Gribbons, S.K. Lee and A.C. Cangellaris
1440	"Performance of the Perfectly Matched Layer in Modeling Wave Propagation in Microwave and Digital Circuit Interconnects"	Z. Wu and J. Fang
1500	**BREAK**	

WEDNESDAY AFTERNOON 22 MARCH

SESSION 9: TIME DOMAIN/FDTD (parallel with Sessions10, 11 and 12) **102 Glasgow Hall**
CHAIRS: L. LONG, J. MALONEY

1520	"A FVTD Algorithm for Maxwell's Equations on Massively Parallel Machines"	V. Ahuja and L.N. Long
1540	"The Piecewise Linear Recursive Convolution Method for Incorporating Dispersive Media into FDTD"	D.F. Kelley and R. J. Luebbers
1600	"Combining Different Coordinate Systems in the Time Domain Finite Difference Method"	M. Mrozowski, M. Okoniewski, M.A. Stuchly and S.S. Stuchly
1620	"Time Domain Response of Simulated 2D Composite Scatterers"	A.Z. Elsherbeni and P. Goggans
1640	"An Object-Oriented Approach to Writing Computational Electromagnetics Codes"	M. Zimmerman and P. Mallasch

SESSION 10: FAST ALGORITHMS FOR COMPUTATIONAL ELECTROMAGNETICS (parallel with Sessions 8, 9, 11, and 12)
ORGANIZERS: E. MICHIELSSEN AND W. CHEW **122 Ingersoll Hall**

1320	"On the Use of Wavelet-Like Basis Functions in the Finite Element Analysis of Elliptic Problems" (Invited)	R.K. Gordon
1340	"Fast Wavelet Algorithm (FWA) for Moment Method Analysis of Electromagnetic Problems" (Invited)	K. Sabetfakhri and L.P.B. Katehi
1400	"Fast Far Field Approximation for Calculating the RCS of Large Objects" (Invited)	C.C. Lu and W.C. Chew
1420	"The Parameter Estimation Technique (PET): Speeding Up Dense Matrix Methods" (Invited)	C. Hafner and J. Fröhlich
1440	"A Novel Scheme for Massively Parallel Solution of Maxwell's Equations using FDTD" (Invited)	M.A. Jensen, Y. Rahmat-Samii and A. Fijany
1500	**BREAK**	
1520	"Reduction of the Filling Time of Method of Moments Matrices" (Invited)	G. Vecchi, P. Pirinoli, L. Matekovits and M. Orefice
1540	"The Fast Multipole Method for Large 2d Scatterers" (Invited)	L.R. Hamilton, J.J. Ottusch, M.A. Stalzer, R.S. Turley, J.L. Visher and S.M. Wandzura
1600	"A Multilevel Matrix Decomposition Algorithm for Analyzing Scattering from Large Structures" (Invited)	E. Michielssen and A. Boag
1620	"A 3D Fast Multipole Method for Electromagnetics with Multiple Levels" (Invited)	B. Dembart and E. Yip
1640	"Fast Multipole Method Solution of Combined Field Integral Equaltion"	J.M. Song and W. C. Chew

SESSION 11: MICROWAVE AND GUIDED WAVE (parallel with Sessions 8 and 10) **361 Ingersoll Hall**
CHAIRS: P. GOGGANS, A. TERZUOLI

1320	"Computer-Simulation of Isotropic, Two-Dimensional Guided-Wave Propagation"	R.A. Speciale
1340	"Analysis of Ultra-Short Pulse Propagation on Uniform and Tapered Printed Transmission Lines"	R.A.O. Veliz and J.R. Souza
1400	"Wave-Field Patterns on Electrically Large Networks"	R.A. Speciale
1420	"Scattering Characteristics of Dissimilar Waveguide Slot Couplers"	A. Singh and K.S. Christopher
1440	"An Alternative Formulation of the Tranverse Resonance Technique"	A.G. Neto, S. Ariguel, H. Aubert, D. Bajon and H. Baudrand
1500	**BREAK**	

WEDNESDAY AFTERNOON 22 MARCH

SESSION 12: MOM (parallel with Sessions 9 and 10) **361 Ingersoll Hall**
CHAIRS: A. PETERSON, R. ZIOLKOWSKI

1520	"Moment Method Analysis of Dielectric Covered Radiating Slots Using Alternative Green's Function Approach"	S. Christopher, V.V.S. Prakash, A.K. Singh and N. Balakrishnan
1540	"Computation of E-field Distribution of Low Gain Antenna on Conducting Body of Revolution"	J. Liu, J. Wang and Y. Gao
1600	"An Implementation of an Exact Scheme for Problem Decomposition Via the Use of Aperture Admittance"	D.L. Wilkes, C-C. Cha and T. Krauss
1620	"Parallelization of the Parametric Patch Moment Method Code"	X. Shen, G.E. Mortensen, C.C. Cha, G. Cheng and G. C. Fox
1640	"A Tool Box for Parallelization of Moments Method Codes"	E. Yip, B. Blakely, L. Johnson, D. Jurgens and R. Kochhar

THURSDAY MORNING 23 MARCH

0730 **CONTINENTAL BREAKFAST**

SESSION 13: RECENT DEVELOPMENTS IN FDTD ANALYSIS (parallel with Sessions 14 and 15) 102 Glasgow Hall
ORGANIZERS: M. PIKET-MAY AND D. KATZ

0840	"Simulation of Microwave Circuits by FDTD Method" (Invited)	C.N. Kuo, B. Houshmand and T. Itoh
0900	"Adaptation of FDTD Techniques to Acoustic Modeling" (Invited)	J.G. Maloney and K.E. Cummings
0920	"FDTD Investigation of the Antenna-Tissue Interaction for Cellular and Satellite Systems" (Invited)	Y. Rahmat-Samii and M.A. Jensen
0940	"FDTD Modeling of Ground-Penetrating Radar Antennas"	B.J. Zook
1000	**BREAK**	
1020	"FDTD Modeling of Ultrashort Optical Pulse Interactions with Nonresonant and Resonant Materials and Structures" (Invited)	R.W. Ziolkowski
1040	"Time Domain Analysis of Electromagnetic Wave Propagation in Nonlinear Dielectric Slab"	G. Miano, C. Serpico, L. Verolino and F. Villone
1100	"An Efficient Sub-gridding Algorithm for FDTD."	D.T. Shimizu, M. Okoniewski and M.M. Stuchly
1120	"Using the Integral Forms of Maxwell's Equations to Modify and Improve the FDTD (2,4) Scheme"	M.F. Hadi and M. Piket-May
1140	"From the Berenger PML ABC to Micro-Lasers: Recent Advances in FD-TD Modeling Techniques" (Invited)	A. Taflove
	LUNCH	

SESSION 14: PROPAGATION (parallel with Sessions 13 and 15) **361 Ingersoll Hall**
ORGANIZER: K. CHAMBERLIN

0840	"Terrain and Refractivity Effects in a Coastal Environment: Results from the VOCAR Experiment"	A. Barrios
0900	"Capabilities and Limitations Associated With Using GTD to Model Propagation Path Loss in the Presence of Irregular Terrain"	K. Chamberlin
0920	"Comparison of Electromagnetic Wave Propagation Computer Programs"	S.A. Fast and T. H. Koschmieder
0940	"A Model for Estimating Electromagnetic Wave Attenuation in a Forest (EWAF) Environment"	C. Welch, C. Lemak, and L. Corrington
1000	**BREAK**	
1020	"Validation of the Radio Physical Optics Propagation Model"	R.A. Paulus

THURSDAY MORNING 23 MARCH

SESSION 14: PROPAGATION (parallel with Sessions 13 and 15) (CONT) — **361 Ingersoll Hall**

1040	"VTRPE: A Variable Terrain Electromagnetic Parabolic Equation Model"	F.J. Ryan
1100	"Estimating Tropospheric Refractivity Fields Using a Nonlinear Gauss-Markov Procedure and the PE Model"	D. Boyer and F.J. Ryan
1120	"Modeling of Radio Wave Ducting Over Regular Boundary"	I.P. Zolotarev
	LUNCH	

SESSION 15: PARALLELIZATION OF EM CODES (parallel with Sessions 13 and 14) — **122 Ingersoll Hall**
ORGANIZERS: J. VOLAKIS AND A. CHATTERJEE

0840	"Advances in Time-Domain CEM Using Massively Parallel Architectures" (Invited)	C. Rowell, V. Shankar, W.F. Hall and A. Mohammadian
0900	"Parallel Solutions of Maxwell's Equations on the Meiko CS-2" (Invited)	N. Madsen, B. Eme, D. Steich and G. Cook
0920	"Parallelization of the CARLOS-3D Method of Moments Code" (Invited)	J.M. Putnam, D.D. Car and J.D Kotulski
0940	"Parallel Computing for Electromagnetism at ONERA" (Invited)	A. de La Bourdonnaye, A. Cosnuau, X. Ferrières, P. Leca and F. X. Roux
1000	**BREAK**	
1020	"The Performance of the Parallel Solution of the Quasi-Minimal Residual (QMR) Method on 2D Mesh Architectures" (Invited)	L. Hamandi, F. Özgüner and R. Lee
1040	"Advanced Parallel Solver Techniques" (Invited)	A.S. King
1100	"Parallelized FDTD for Antenna Radiation Pattern Calculations"	Z.M. Liu, A.S. Mohan, T. Aubrey and W.R. Belcher
1120	"Calculation of Electromagnetic Fields with the Multiple Multipole Method (MMP Method) on Parallel Computers"	C. Tudziers and H. Singer
1140	"Implementation of the Finite-difference Time-Domain Method on Parallel Computers"	R.S. David and L.T. Wille
	LUNCH	

THURSDAY AFTERNOON 23 MARCH

SESSION 16: EM THEORY II (parallel with Sessions 18 and 20) — **361 Ingersoll Hall**
CHAIRS: K. YEE, R. GORDON

1320	"FDTD Investigation of the Ability to Increase Electromagnetic Fields Around Head Tumors"	D.B. Dunn, A.J. Terzuoli, Jr. G.C. Gerace and C.A. Rappaport
1340	"FDTD and PMM Based Design of a TEM Horn Antenna with Reduced Off-Boresight Fields"	D.J. Wolstenholme, A.J. Terzuoli, Jr. and G. C. Gerace
1400	"Determination of the Complex Aperture Distribution of a Planar Spiral Antenna from 3D Far-Field Radiation Pattern Data"	M. Kluskens, W. Lippincott and M. Kragalott
1420	"Analysis of Micro-Contamination of Silicon Wafers Based on Discrete Sources Method (DSM)"	Y.A. Eremin and N.W. Orlov
1440	"Analysis of Convergence Properties of Projection Methods for Solving CEM Applications"	V.I. Ivakhnenko, A.V. Kukk, E.E. Tyrtyshnikov, A.Y. Yeremin and N.L. Zamarashkin

THURSDAY AFTERNOON 23 MARCH

SESSION 17: ELECTROMAGNETIC MODELING TECHNIQUES FOR INTEGRATED OPTICS (parallel with Sessions 18, 19 and 20)
ORGANIZER: A. CANGELLARIS — **361 Ingersoll Hall**

1520	"Analysis and Design of Guided-wave Optical Devices Using Finite-Difference Time-Domain Method" (Invited)	S.I. Chaudhuri and S.T. Chu
1540	"Vectorial Analysis of Optical Waveguides by the Method of Lines"(Invited)	R. Pregla and W. Pascher
1600	"Vector Finite Element Analysis of Lossless and Lossy Dielectric Waveguides" (Invited)	P. Cheung and A. Gopinath
1620	"NL-FDTD Modeling of Linear and Nonlinear Corrugated Waveguiding Systems for Integrated Optics Applications" (Invited)	R.W. Ziolkowski and J.B. Judkins
1640	"Analysis of Coupled Nonlinear Optical Waveguides by Matrix Method"	V. Tripathi, A. Weisshaar and H.S. Chang

SESSION 18: TOPICS IN FRACTAL AND WAVELET ELECTRODYNAMICS (parallel with Sessions 16, 17and 20) 102 Glasgow Hall
ORGANIZERS: D.H. WERNER AND P.L. WERNER

1320	"An Overview of Fractal Electrodynamics Research" (Invited)	D.H. Werner
1340	"Fractal Arrays and Fractal Radiation Patterns" (Invited)	P.L. Werner, D.H. Werner and A.J. Ferraro
1400	"Wavelet Transforms and Time/Time-scale Analysis" (Invited)	R.K. Young and T.G. Golsberry
1420	"Wavelet-based Processing to Efficiently Achieve Broadband Monostatic and/or Passive Cross-sensor Processing" (Invited)	R.K. Young and L.H. Sibul
1440	"The Intervallic Wavelets with Application in the Surface Integral Equations" (Invited)	G.W. Pan and J.Y. Du
1500	**BREAK**	
1520	"Radar Cross Section Data Reduction Using Wavelets"	A.S. Ali, S.E. Duval and R.L. Haupt

SESSION 19: NEC APPLICATIONS (parallel with Session 17 and 20) — 102 Glasgow Hall
ORGANIZER: J. BREAKALL

1540	"Computationally Efficient and Accurate Approximations for Impedance Matrix Elements of NEC-Type Method of Moments Formulations"	D.H. Werner, S.E. Metker and J.A. Huffman
1600	"Development of the Coupled-Resonator Antenna Principle A Computer Modeling Case History"	G. Breed
1620	"Antenna Design & Development Using NEC-WIN"	T. A. Erdley, J. J. Shapiro, J. S. Young and J.K. Breakall
1640	"The "Paint" System A UTD/NEC Hybrid Package for Simulating Antenna Patterns Over 3-Dimensional Irregular Terrain"	J.S. Young and J.K. Breakall

SESSION 20: FEM (parallel with Sessions 16, 17, 18, and 19) — **122 Ingersoll Hall**
CHAIRS: R. BURKHOLDER, J. KARTY

1320	"Numerically Characterizing Electromagnetic Fields Local to the Edge of a Conducting Strip Using a Matched Asymptotic Technique and the Finite Element Method"	A.S. Ali and C. L. Holloway
1340	"An Enhanced "A Posteriori" Remeshing Algorithm for Adaptive Meshing of 2D Finite Element Problems"	P. Girdinio, A. Manella and G. Molinari
1400	"Finite Element Analysis of Waveguides Using Edge-Based Magnetic Vector Potential and Nodal-Based Electric Scalar Potential"	J. -F. Lee, G. Lizalek and J. Brauer
1420	"A Scattering Analysis of Laser Beam Wave by Groove Pits on Optical Memory Disk by Using FEM with BEM"	Y. Miyazaki and K. Tanaka
1440	"3D Nodal- and Mixed-Based Elements for Unbounded Microwave Problems"	A. Nicolas, L. Nicolas and J.L. Yao-bi
1500	**BREAK**	

THURSDAY AFTERNOON 23 MARCH

SESSION 20: FEM (parallel with Sessions 16, 17, 18, and 19) (CONT) — **122 Ingersoll Hall**

1520	"A Rationale for the Use of Mixed-order Basis Functions Within Finite Element Solutions of the Vector Helmholtz Equation"	A.F. Peterson and D.R. Wilton
1540	"Finite Element Waveguide Simulator Techniques"	J.R. Sanford and N.M. Johansson
1600	"A Solution for Open Boundary Electromagnetic Field Problems by Mapped Infinite and Virtual Elements"	L.H.A. de Medeiros and A. Raizer

FRIDAY MORNING, MARCH 24

0730 **CONTINENTAL BREAKFAST**

SESSION 21: EM ANALYSIS TECHNIQUES FOR ELECTRICALLY LARGE CAVITIES (parallel with Sessions 22 and 23) — **122 Ingersoll Hall**
ORGANIZER: D. PFLUG

0840	"Application of Modal and Plane Wave Expansions to Modeling Large Jet Engine Cavities" (Invited)	J. L. Karty and J.M. Roedder
0900	"Scattering from Dielectric Loaded Cavities Using Shooting and Bouncing Rays" (Invited)	M. Christensen, S. W. Lee D.J. Andersh
0920	"Xpatch Simulation of Large Inlet Structures" (Invited)	R. Bhalla and H. Ling
0940	"An Iterative Physical Optics Approach for the Em Analysis of Cavities and Other Multi-Bounce Geometries" (Invited)	R.J. Burkholder
1000	**BREAK**	
1020	"Improved Ray Basis in the Hybrid Analysis of EM Scattering by Large Open Cavities" (Invited)	R.J. Burkholder, P.H. Pathak, H.T. Chou, D. Andersh and J. Fath
1040	"Overlapping Modal and Geometric Symmetries for Computing Jet Engine Engine Inlet Scattering" (Invited)	D.C. Ross, J.L. Volakis, H. T. Anastassiu and D. Andersh
	LUNCH	

SESSION 22: ACCURACY ESTIMATION IN ELECTROMAGNETIC MODELING (parallel with Sessions 21 and 23) — **109 Glasgow Hall**
ORGANIZER: S.M. WANDZURA

0840	"Assessing the Influence of Coefficient Accuracy, Matrix Condition Number, Size and Type, and Computer Precision on Matrix-Solution Accuracy" (Invited)	E. K. Miller
0900	"Numerical Accuracy Issues in Finite Element Frequency Domain Solutions of Radar Scattering Problems" (Invited)	J. D'Angelo
0920	"Accuracy in Computation of Matrix Elements of Singular Kernels"	S.M. Wandzura
0940	"Accuracy Estimation and High Order Methods"	L.R. Hamilton, J.J. Ottusch, M.A. Stalzer, R.S. Turley, J.L. Visher and S. M. Wandzura
1000	**BREAK**	
1020	"Accuracy Issues in Time-Domain CEM Using Structured/Unstructured Formulations" (Invited)	V. Shankar, W. F. Hall and S. Palaniswamy
1040	"An Accuracy Study for the 3D Hybrid Finite Element Method of Moments SWITCH Code" (Invited)	G.E. Antilla and Y.C. Ma
1100	"Modeling Accuracy of 3D Method of Moments Techniques"	M.B. Gedera, L.N. Medgyesi-Mitschang, R.A. Pearlman, J.M. Putnam, D-S.Y. Wang
1120	"Requiring Quantitative Accuracy Statements in EM Data" (Invited)	E.K. Miller
	LUNCH	

FRIDAY MORNING, MARCH 24

SESSION 23: PDE METHODS IN ELECTROMAGNETICS (parallel with Sessions 21 and 22) 102 Glasgow Hall
ORGANIZERS: R. LEE AND J. -F. LEE

0840	"Optimization Issues in Finite Element Codes for Solving Open Domain 3D Electromagnetic Problems" (Invited)	A. Chatterjee and J.L. Volakis
0900	"A Characteristic-Based 3D Time Domain Maxwell Equation Solver" (Invited)	J.S. Shang and K.C. Hill
0920	"Finite Element Solution of Eddy Current Problems in Electromagnetics" (Invited)	O.A. Mohammed and G. F. Üler
0940	"Ten Years of Evolution of the FDTD-like Conformal Technique" (Invited)	K.S. Yee
1000	**BREAK**	
1020	"Whitney Elements Time Domain (WETD) Methods for Solving Three-Dimensional Waveguide Discontinuities" (Invited)	J. -F. Lee
1040	"An FDTD/FVTD 2D-algorithm to Solve Maxwell's Equations"	J.S. Chen, J.V. Prodan and K.S. Yee
1100	"Spectral Finite Methods for the Simulation of Electromagnetic Interactions with Electrically Long Structures" (Invited)	A.C. Cangellaris and D. Hart
	LUNCH	

SATURDAY, 25 MARCH SHORT COURSES

0830-1630 **SHORT COURSE (FULL-DAY)**
"Using Mathematical Software for Computational Electromagnetics"

101A Spanagel Hall
Jovan Lebaric, Naval Postgraduate School

0830-1630 **SHORT COURSE (FULL-DAY)**
"Wire Antenna Modeling Using NEC"

109 Glasgow Hall
Dick Adler, Naval Postgraduate School
Jim Breakall, Penn State University
Gerry Burke, Lawrence Livermore National Lab

0830-1630 **SHORT COURSE (FULL-DAY)**
"FDTD, Generalized FDTD and FVTD Techniques in Solving Maxwell's Equations"

102 Glasgow Hall
Kane Yee, Lockheed

SESSION 11:

MICROWAVE AND GUIDED WAVE

Chairs: P. Goggans, A. Terzuoli

COMPUTER-SIMULATION OF ISOTROPIC, TWO-DIMENSIONAL GUIDED-WAVE PROPAGATION

Ross A. Speciale

Redondo Beach, California

1 - PRINCIPLES OF THE SIMULATION METHOD.

A relatively simple computer-simulation method has been developed, for performing a first-approximation analysis of various two-dimensional guided-wave propagation processes. The method has been applied in two MATLAB programs.

One of the programs synthesizes a phase-conjugated EM-field that approximates, with its amplitude-distribution, the shape of a two-dimensional Dirac impulse-function. The second program synthesizes any given two-dimensional, complex aperture distribution, in terms of local amplitude and phase.

The developed simulation method uses (as an initial and qualitative first-approximation) a square, two-dimensional wave-guiding medium (such as the well known parallel-plate waveguide !), a medium characterized by: a) total uniformity in any arbitrary azimuthal direction, b) mathematical linearity, reciprocity, and losslessness, and c) complete isotropy, as defined by an azimuth-independent propagation constant.

The wave-propagation properties of the medium are thus characterized by total absence of internal scattering, of any wave-attenuation due to ohmic or radiation losses, and by a known azimuth-independent phase-constant. The developed method can be, however, easily modified to account for any known type of anisotropy of the wave-propagation medium, if such anisotropy can be defined by some functional azimuth-dependence of the propagation-constant. Further, any analytically-defined loss-mechanism can also be easily accounted for.

A large number of different, two-dimensional guided-wave field-patterns of increasing complexity have already been analyzed and synthesized. All the two-dimensional wave-field patterns generated so far, have been obtained as weighted linear combinations of the individual, two-dimensional wave-field patterns of large numbers of mutually-coherent sources. The sources were mostly aligned along the outer perimeter of the square wave-propagation domain, although the geometric pattern of the source locations is quite arbitrary.

Many examples of sharp phase-conjugation focusing in two-dimensions have been synthesized, using either two or four sets of external sources, all aligned along two or all four outer sides of the square domain. The sources are assumed, as a first approximation, to be all unconditionally-matched to the four sides of the two-dimensional wave-guiding medium, to be somehow mutually isolated, and to have totally different, mutually independent, and arbitrary amplitudes and phases.

The sides of the square wave-field domain, where no external sources are connected (if any), are assumed to be also unconditionally matched to an external, reflectionless, dissipative medium, that totally absorbs any incident wave-field.

An overwhelmingly large number of different, two-dimensional wave-field patterns can be obtained, simply by independently controlling the relative amplitudes and the relative phases of all the mutually-coherent external sources.

A large number of two-dimensional wave-patterns have already been generated, by using the developed simulation method, including many that are very sharply focused to very small and arbitrarily-located spots on the square wave-propagation domain, thus forming there narrow amplitude-peaks, resembling very sharply-focused, two-dimensional wave-caustics.

The developed simulation method provides very clear evidence of the possibility of arbitrarily reshaping the complex-amplitude distribution of a two-dimensional wave-field pattern, by simply controlling only the relative amplitudes and the relative phases of external sources, aligned around the perimeter of the considered wave-propagation domain. The geometrical shape of the domain perimeter, where the external sources are assumed to be connected, is obviously quite arbitrary, and it was chosen square just for expediency. It could, however be rectangular, hexagonal, circular, elliptic or any other desired shape. Further, the wave-propagation domain need not even be planar, but could for instance conform to a closed circular cylinder, thus leaving only the two opposing rims free for connecting external sources.

In this case, obviously, multi-path propagation of waves, circulating (clockwise or counter-clockwise) around the cylinder axis one or more times, should be taken into account, unless the curved propagation medium is assumed to be very lossy.

The wave-field domain could also conform to an open-truncated, spherical dome, with only one rim being accessible to external excitation sources.

The developed wave-field pattern simulation method is presently being used as a tool for establishing a deterministic wave-field synthesis procedure, that approximates any required wave-field distribution in a least-squares sense.

Recently generated preliminary results clearly show the applicability and powerful effectiveness of this least-squares synthesis procedure. Indeed, a Hansen's 'one-parameter' aperture-distribution for circular apertures, with an H-parameter value of 1.7254 (corresponding to -40 dB first-sidelobe level), was approximated, in a least-squares sense, with an RMS residual deviation of only a few parts in 10^{-4} (for a broadside, and for an off-broadside beam-steering direction).

2 - REPRESENTATION OF THE TWO-DIMENSIONAL MEDIUM.

The mathematically linear, reciprocal, uniform, isotropic, and lossless two-dimensional wave-guiding medium, that is the domain of the wave-propagation process, is analytically represented by a large-order, complex, square matrix M. The complex value of each matrix-element is used to represent the local complex field amplitude of any given wave-field pattern. The row- and column-indexes ' i ', and ' j ' of each matrix element are used to represent the discretized physical location of an arbitrary point in the considered square domain of wave-propagation.

The square-matrix representation of a uniform and isotropic, physical two-dimensional wave-guiding medium is thus implicitly used as either a discretized representation of a continuous, uniform, parallel-plane TEM-waveguide, or as a discretized representation of a continuous radiating aperture. In this analytical representation, each matrix element corresponds to a node of a discretized, geometrical square lattice, superimposed on the physical wave-field domain.

The order of the square matrix M, used in the performed simulations to represent the wave-field domain, was initially chosen to be 129 x 129, with the (65,65) point representing the domain's central point.

3 - SIMULATION OF THE FIELDS OF THE EDGE-FEEDING SOURCES.

All the analyzed two-dimensional wave-field patterns are generated by weighted linear superposition of different large sets of mutually-coherent, component wave-fields, each component being generated by one of the external edge-feeding sources, in the form of a single azimuthally-symmetric cylindrical wave.

The radial dependence of each injected cylindrical wave is analytically represented by the zero-order cylindrical Hankel function of the second kind :

$$H_0^{(2)}(k_R\, r) = J_0(k_R\, r) - i\, Y_0(k_R\, r) \qquad (\, i = \sqrt{-1}\,) \qquad (1)$$

where the symbol ' r ' represents the radius-vector distance of any given field-point (i , j) of the wave-propagation domain from the location (i_S , j_S) of any given edge-feeding source:

$$r = \sqrt{(i - i_S)^2 + (j - j_S)^2} \qquad (2)$$

and where k_R is the cylindrical wave-number, representing the asymptotic value of the phase-rotation of the wave-field per 'lattice-unit' (defined as the node-to-node spacing through the discretized square lattice, along its rows and columns).

The azimuthal dependence of a cylindrical wave, of any arbitrary type, is known to be expressed by $e^{i\,m\,\phi}$, where m is the well-known cylindrical symmetry index. For azimuthally-symmetric cylindrical waves, however, $m = 0$, so that the azimuthal dependence function reduces to $e^{i\,m\,\phi} = 1$.

The locations (i_S , j_S) of all the external edge-feeding sources are aligned and regularly spaced along the first and the last rows ($i_S = 1$, $j_S = 1,..,129$ and $i_S = 129$, $j_S = 1,..,129$), and aligned along the first and the last columns ($i_S = 1,...,129$, $j_S = 1$ and $i_S = 1,...,129$, $j_S = 129$) of the 129 x 129 complex matrix M , used to represent the resulting total wave-field pattern.

Consistently with the assumptions of losslessness and total isotropy, the medium is characterized by an azimuth-independent phase-constant, expressed in degrees of phase-rotation between adjacent matrix elements, or geometrically between the corresponding adjacent nodes of the discretized, square lattice. These assumptions lead to the choice of a constant, azimuth-independent value for the cylindrical wave-number k_R expressed, in radian per lattice-unit, by $k_R = 2\,\pi\,/\,\lambda_R$ (where λ_R is the wavelength of an infinite, two-dimensional 'planar' wave, propagating with a straight wavefront through the medium of the wave-propagation domain).

4 - FIELD SYMMETRY AND COMPUTATIONAL EFFICIENCY.

A highly efficient computation procedure is made possible by the intrinsic symmetries of the square wave-field domain, and of the regularly-spaced locations of the 129 external sources aligned along each of the four sides. Indeed, only the single component wave-field of any of the four corner-sources needs to be computed, while all the remaining component wave-fields are obtained by way of symmetry-operations, and wave-field-splicing operations.

The wave-field patterns of the four corner-sources *A*, *B*, *C*, and *D*, located at points (1,1), (129,1), (1,129), and (129,129), are generated first, with the complex amplitudes of all four corner-sources set to unity (and zero phase). These four basic wave-field patterns are stored in four complex 129 x 129 auxiliary matrices. Only the wave-field pattern of the source *A* is actually computed, by repeatedly evaluating the expression (1) through the 129 x 129 matrix *A* , with $i_S = j_S = 1$.

The wave-field pattern of source *B* is then generated by a reflection-symmetry operation, around the row $i = 65$, performed on the matrix *A* . The reflection is simply obtained by reversing the row-sequence of the matrix *A* into the matrix *B* . Similarly, the wave-field pattern of the source *C* is obtained by reversing the column-sequence of the matrix *A* , into the auxiliary matrix *C* . Finally the wave-field pattern of the source *D* is obtained by reversing the column-sequence of the matrix *B* , into the auxiliary matrix *D* .

The fundamental wave-fields of the four corner-sources are then used to build-up the copmponent wave-fields of all the other sources, by performing 127 matrix-splicing operations on each of the four sides of the square domain. For instance, the wave-field of a source *E* , located at point $i_S = i_S(E)$, $j_S = 1$ along the *A* -> *B* side of the square domain, is obtained by copying the set of rows 1 through 130 - $i_S(E)$, to the rows $i_S(E)$ through 129 of an auxiliary 129 x 129 complex matrix *T* , and then copying rows 130 - $i_S(E)$ through 128 of matrix B to rows 1 through $i_S(E) - 1$ of the same auxiliary matrix *T* . The obtained wave-field of source *E* , that is represented in the matrix *T* with unity source-amplitude and zero phase, is then multiplied by the specified complex weight *W(E)* , and added to the complex 129 x 129 matrix M , where the total wave-field pattern is progressively accumulated, as a weighted linear superposition of all the mutually-coherent, component wave-fields of the 516 sources.

The matrix-splicing operation described for the generic source *E* , arbitrarily located along the *A* -> *B* side, is similarly repeated for sources *F* , *G* , and *H* , arbitrarily located along the other three sides. The auxiliary matrix *T* is repeatedly re-used for temporary storage, prior to multiplication of the obtained spliced wave-field by the corresponding complex weight, and final accumulation in the matrix M .

5 - TWO-DIMENSIONAL PHASE-CONJUGATION FOCUSING.

Phase-conjugated focusing of the total wave-field pattern represented in the 129 x 129 complex matrix M , to an arbitrarily selected point of the square domain, is obtained by appropriately determining the required complex weights of all the sources aligned along each of the four sides. All the complex weights are generally different, unless the focus location is set to the domain central point (65,65).

To obtain a phase-focused pattern, the complex weight of each source is set to the value required to make the local amplitude of the corresponding component wave-field equal to unity (with zero phase), at the selected focus location (i_F , j_F). The required weight value is the reciprocal of the local complex amplitude of the component wave-field built-up in the auxiliary matrix *T* with unity source amplitude, at the selected focus location point (i_F , j_F).

The required magnitude of all the complex source weights is always larger than unity, as required to compensate for the radial amplitude decay of an $m = 0$ cylindrical wave, which asymptotically approximates a $1/r$ law. Similarly, the argument of all the complex source weights always represents a phase-lead, relative to the unweighted wave-field component, by an amount that continuously increases with increasing distance ' *r* ' , measured from the source location (i_S , j_S) to the selected focus-point (i_F , j_F). The complex weights of the four sources aligned on the same row i_F , and on the same column j_F of the focus-point have minimum magnitudes, and

minimum phase-conjugated leads, because of being located at the minimum distances ' r ' on the respective sides of the wave-field domain.

Figures 1, and 2 show two typical examples of two-dimensional, phase-conjugated focusing, in the form of *3D* amplitude displays. The sharpness of amplitude-peak has been found to be largely independent from the selected specific location of the focus-point.

6 - LEAST SQUARES FITTING OF PRESCRIBED APERTURE DISTRIBUTIONS.

The developed wave-pattern simulation method is presently being used as a tool for evaluating a deterministic aperture-distribution synthesis procedure, capable of approximating any required aperture distribution in a least-squares sense.

Recently generated preliminary results clearly show the applicability and powerful effectiveness of this least-squares synthesis procedure.

A Hansen's 'one-parameter' aperture-distribution for circular apertures, with an H-parameter value of 1.7254 (corresponding to - 40 dB first-sidelobe level), is approximated, in a least-squares sense, with an RMS residual deviation of only a few parts in 10^{-4} (for both a broadside and an off-broadside beam-steering direction).

The ultimate objective of this effort is to determine the feasibility of edge-feeding a two-dimensional, high-directivity, low-sidelobe, electronically-steered phased array, with a substantially reduced number of amplitude-, and phase-controlled microwave sources. The radiating elements of such a 'clustered' phased array [1,2] are fed through the nodes of an electrically-large, underlaying, two-dimensional, periodic slow-wave delay-structure [3-7], approximating in discretized form a uniform and isotropic wave-propagation medium.

Figures 3, and 4 show, as a typical result, the least-squares fitting of a separable Hansen one-parameter distribution, defined on a 61 x 61 square-lattice aperture by:

$$g(p_x, p_y) = I_0\left(H\sqrt{\pi^2 - p_x^2}\right) \cdot I_0\left(H\sqrt{\pi^2 - p_y^2}\right) \;/\; I_0^2(H\pi) \qquad (3)$$

where $p_x = 2\,\pi\,x\,/\,L$, $p_y = 2\,\pi\,y\,/\,L$ (with L = domain side length), and $H = 0.8899$ (for a - 25 dB sidelobe level).

7 - REFERENCES.

[1] US Patent No. 5,347,287 - September 13, 1994.

[2] US Patent Pending - September 12, 1994.

[3] Speciale R. A.,"Wave-Field Patterns on Electrically Large Networks," 1995 ACES Symposium Paper - Number S130, published in these Proceedings.

[4] Speciale R. A.,"Symmetry Analysis of Large Two-Dimensional Clusters of Coupled Cavity Resonators," 9th Annual Review of Progress in Applied Computational Electromagnetics, Naval Postgraduate School, Monterey, California, March 22-26, 1993, pp. 281-288.

[5] Speciale R. A., "Sectored Cylindrical Cavity Resonators," 8th Annual Review of Progress in Applied Computational Electromagnetics, Naval Postgraduate School, Monterey, California, March 16-20, 1992, pp. 274-281.

[6] Speciale R. A., "Wave Propagation on Infinite, Two-Dimensional Structures," 5th Annual Review of Progress in Applied Computational Electromagnetics, Naval Postgraduate School, Monterey, California, March 20-24, 1989, pp. 200-244.

[7] Speciale R. A.,"Projective Matrix Transformations in Microwave Network Theory," 1981 MTT-S International Microwave Symposium Digest, Los Angeles, California, June 15-19, 1981, IEEE Cat. No. 81CH1592-5, ISSN No. 0149-645X, pp. 510-512.

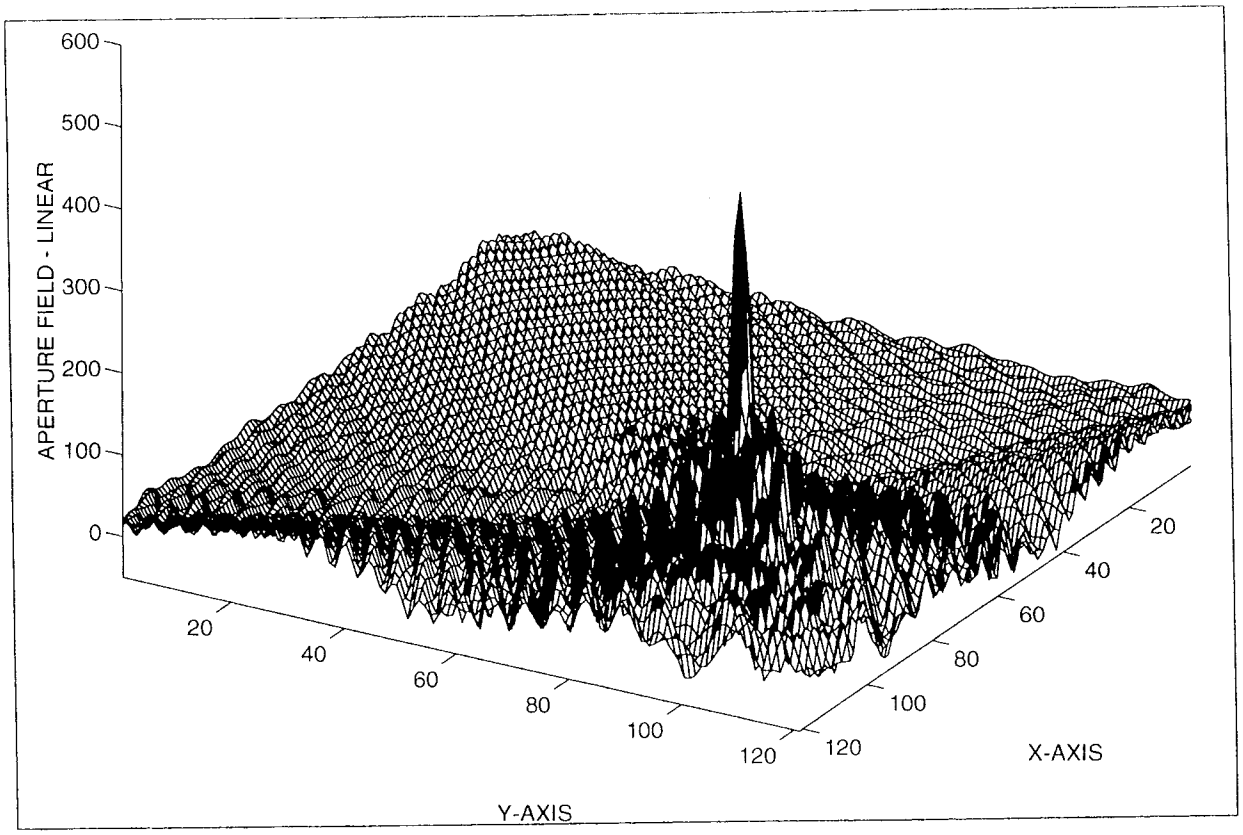


Figure 1 - Two-Dimensional, Phase-Conjugated Focusing of the Wave-Field Pattern of 516 Mutually-Coherent Edge-Feeding Sources : Focus at Point (97,97).

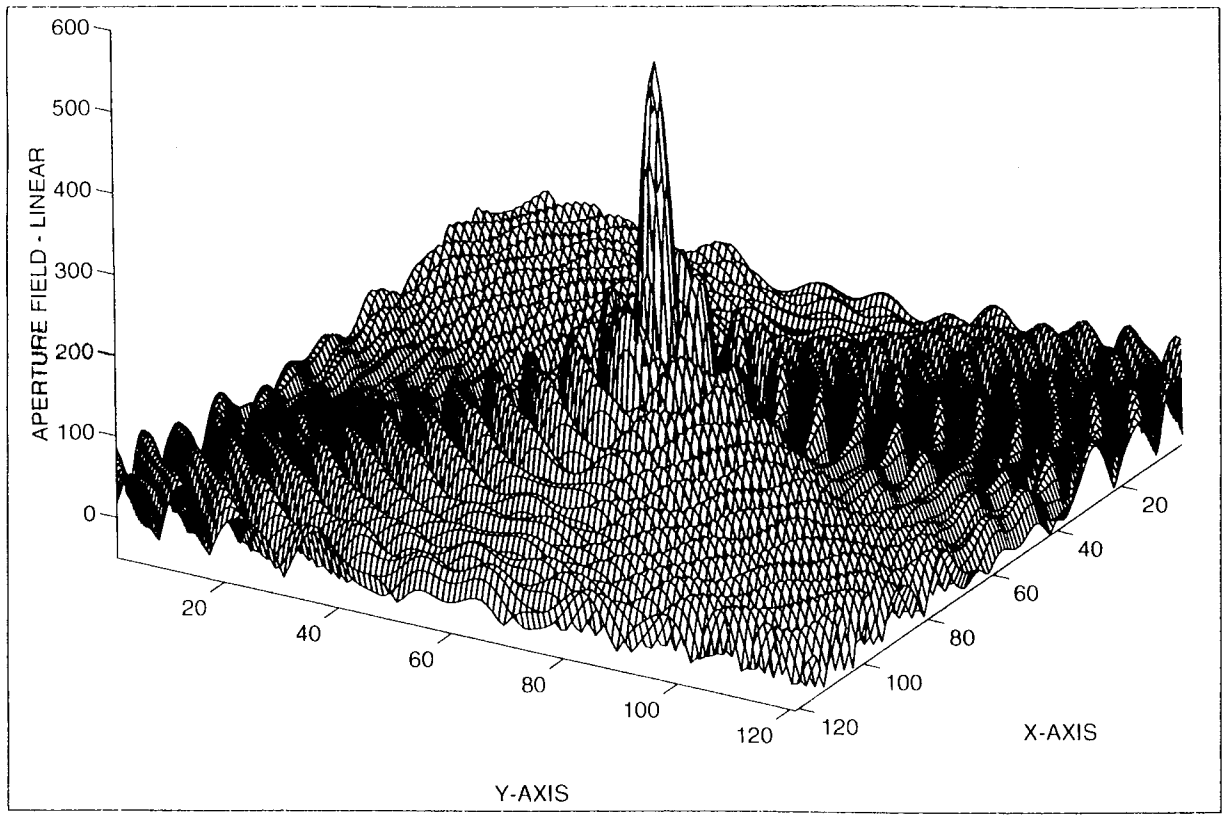


Figure 2 - Two-Dimensional, Phase-Conjugated Focusing of the Wave-Field Pattern of 516 Mutually-Coherent Edge-Feeding Sources : Focus at Point (65,65).

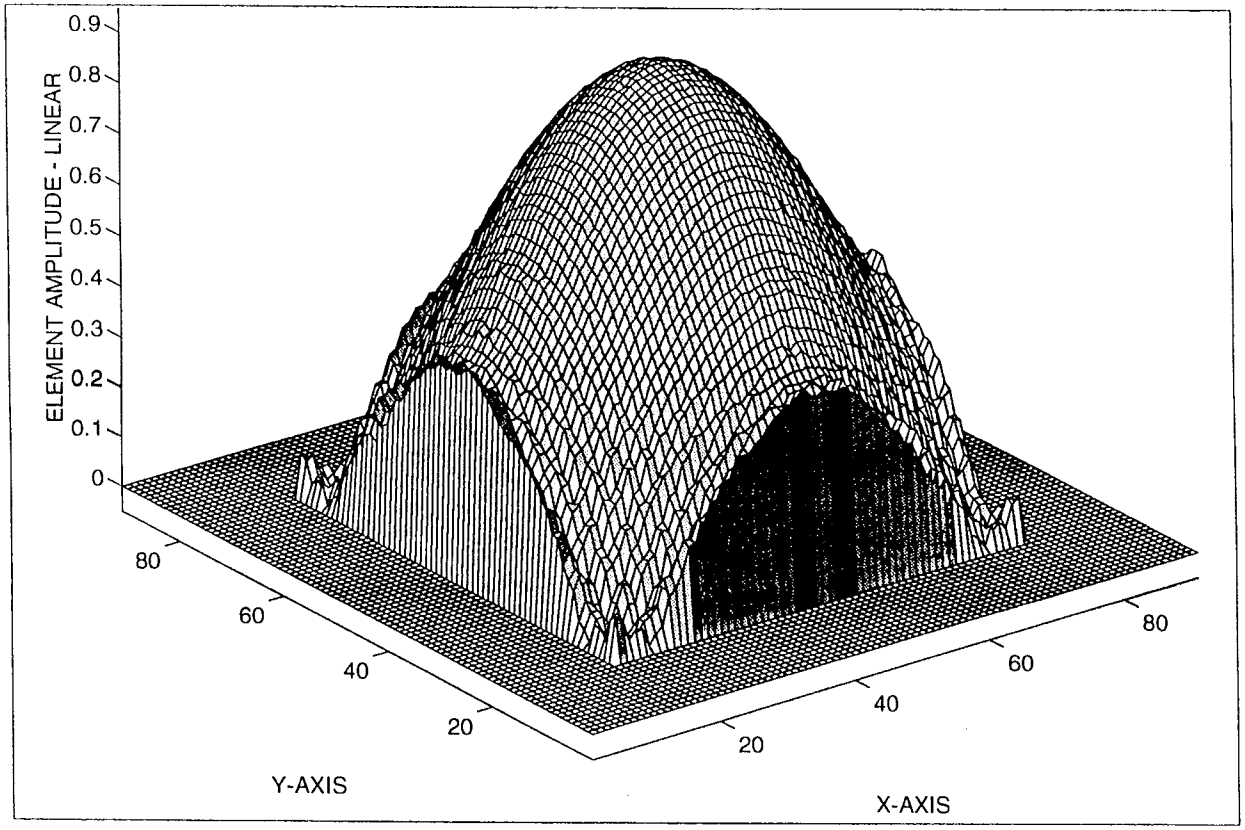


Figure 3 - Amplitude Distribution of a Least-Squares Fit to a 'Separable Hansen' g(x , y) Nominal Aperture Distribution, Defined on a 61 x 61 Square Lattice (H = 0.8899).

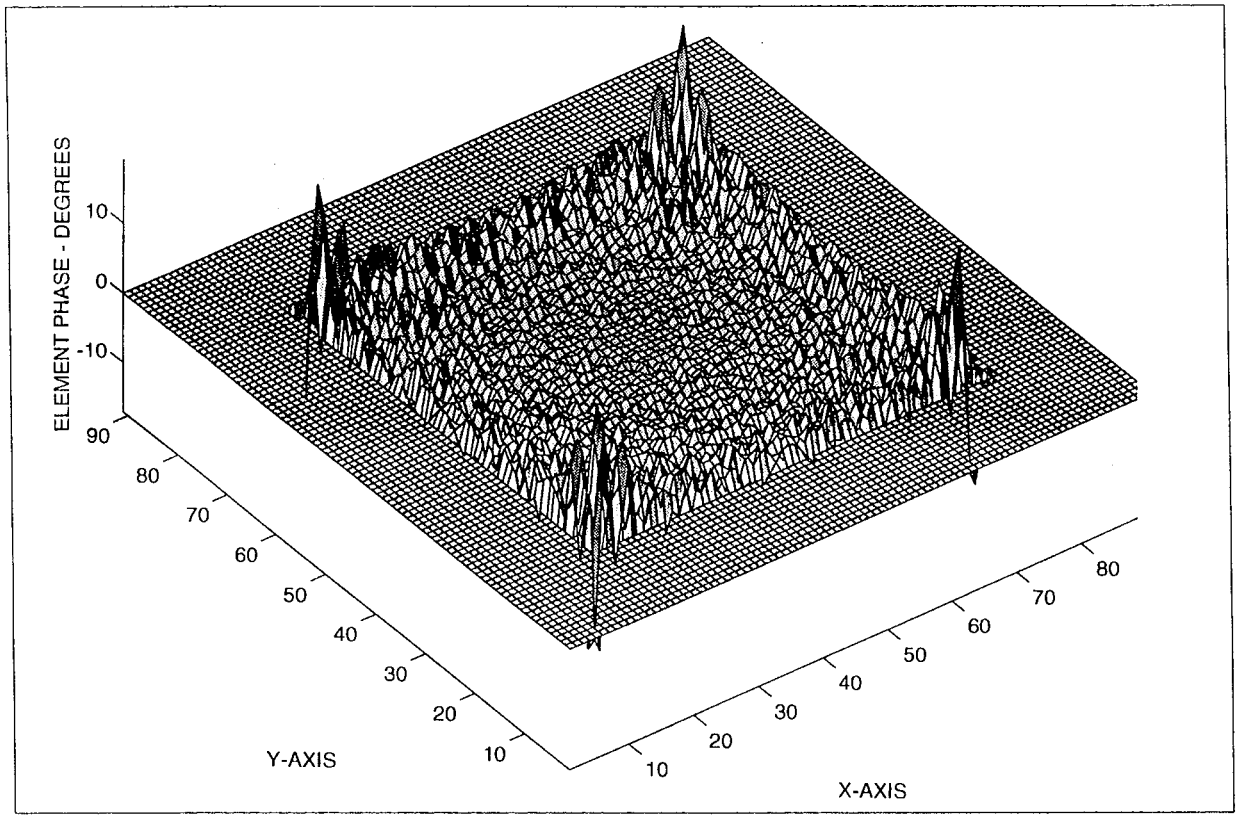


Figure 4 - Residual Phase Error of a Least-Squares Fit to a 'Separable Hansen' g(x , y) Nominal Aperture Distribution, Defined on a 61 x 61 Square Lattice (H = 0.8899).

ANALYSIS OF ULTRA-SHORT PULSE PROPAGATION ON UNIFORM AND TAPERED PRINTED TRANSMISSION LINES

R. Olivares Véliz and J. R. Souza

Center for Telecomunication Studies - CETUC
Pontifical Catholic University of Rio de Janeiro - PUC/Rio
Rua Marquês de São Vicente, 225, CEP 22453-900, Rio de Janeiro - RJ, Brazil

ABSTRACT

This paper presents a rigorous full-wave investigation of the propagation characteristics of very short electric pulses on uniform and tapered printed transmission lines by means of the Spectral Domain Approach (SDA). Initially, a frequency domain analysis is carried out to determine the variation of the propagation constant and characteristic impedance over a sufficiently wide frequency band. In the case of a tapered transmission line, it is also necessary to determine the variation of these parameters along the length of the line. Next, a time domain analysis is performed, using the Fourier Transform, to simulate the propagation of the pulse. Although different planar transmission line configurations were considered, results are presented here for microstrip lines, and for the combined CPW-slot line, which has a typical CPW configuration on one side of the substrate, and that of a slotline on the other side. Comparison is made between simulated and experimental results, with excellent agreement.

1.- INTRODUCTION

It is now possible to generate and manipulate pulses with pico- and sub-pico-second duration, due to the significant progress achieved by high speed optoelectronics. Such progress then represents a continuos challenge in the design and fabrication of the microwave circuits (MICs, MMICs, and HMICs) used in high speed systems, due to the requirements of increasingly larger band-widths. As the transmission line structures used in these circuits, such as microstrip lines and coplanar waveguides (CPW), do not support TEM propagation, the frequency components of a short electric pulse do not propagate at the same phase velocity. In consequence, the pulse shape is distorted as it propagates along the transmission line. A knowledge of the propagation characteristics of short electric pulses along dispersive transmission lines is necessary for the proper design of these circuits.

In the analyses found in the literature[1-4], only the frequency dependency of the propagation constant is considered, while the characteristic impedance is generally considered as invariant. In some of the analysis, empirical formulae are used to estimate the dispersion characteristics of the transmission lines. In this paper, the frequency dependency of both the propagation constant and the characteristic impedance is taken into account with the well known Spectral Domain Approach, which allows full non-TEM analysis. The temporal response of the transmission lines is calculated with algorithms based on the Fast Fourier Transform.

This paper then gives transfer functions for uniform and tapered microstrip and CPW-slot lines. An exponential impedance profile was considered for the tapered transmision lines. Results of the distortion of Gaussian and square pulses are shown and discussed. Also, comparison is made with experimental results, with excellent agreement.

2.- FORMULATION

The type of transmission lines considered here can be treated as a linear, time invariant system, whose temporal response, V(t,z), to an input signal V(t,z=0) can be written as[2]:

$$V(t,z=D) = \mathcal{F}^{-1}\{\mathcal{F}\,[V(t,z=0)]\cdot T(\omega, z=D)\} \tag{1}$$

where $\mathcal{F}$ represents the Fourier Transform, and T(ω,z=D), the transfer function of the transmission line.

In the case of lossless, uniform lines, this function simply introduces a phase change, which is equal to the product of the (imaginary) propagation constant, γ(ω), by the propagating distance, z=D. For lossy lines, an attenuation factor must be added, as γ(ω) is then complex. In the case of a non-uniform, or tapered, transmission line, the transfer function must incorporate the variation of the propagation constant and the characteristic impedance along the length of the line. For example, for a tapered transmission line, with an exponential impedance profile, as illustrated in Figure 1, T(ω,z=D) can be written as[1]:

$$T(\omega, z=D) = \left[1 - \frac{1}{4}\left[\ln\left(\frac{Z_2}{Z_1}\right)\cdot\frac{\sin[\theta(\omega,z=D)]}{\theta(\omega,z=D)}\right]^2\right]^{0.5}\exp\left[-j\theta(\omega, z=D)\right] \tag{2}$$

with $\theta(\omega, z=D) = \int_0^D \gamma(\omega, z)dz$. The impedances Z_1 and Z_2 represent the initial and final impedances of the transmission, line, respectively.

The equation (2), derived from the small reflection theory[5], assumes an exponential impedance profile for all frequencies; this assumption implies that the impedance is frequency invariant. Such approximation is only acceptable for a very narrow frequency band, wich in general is not compatible with ultra-short electric pulses. A new expression for T(ω,z) will be derived, based on the exact multiple reflection theory[5]. With this new expression, which is very adequate for numerical calculations, any impedance profile can be considered.

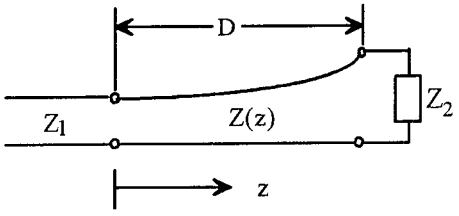


Figure 1: Tapered transmision line, with exponential impedance profile.

The non-uniform transmission line illustrated in Figure 1 can be represented by multiple sections of uniform lines with length ΔZ - as shown in Figure 2. Each section is described by its own characteristic impedance and propagation constant, wich can both have any dependence with frequency. This approximation is exact in the limit, when the number of sections tends to infinity. The equivalent impedance Z_{in} at the input of the i-th section is given by:

$$Z_{in_i} = Z_{o_i}[(Z_{in_{i+1}} + jZ_{o_i}\tan(\beta_i\Delta Z))/(Z_{o_i} + jZ_{in_{i+1}}\tan(\beta_i\Delta Z))] \tag{3}$$

With equation (3), all the impedances Z_{in} can be calculated recursively for the N sections. The total reflection coefficient at the input of the transmission line, Γ_{in}, is determined as:

$$\Gamma_{in} = (Z_{in_1} - Z_1)/(Z_{in_1} + Z_1) \tag{4}$$

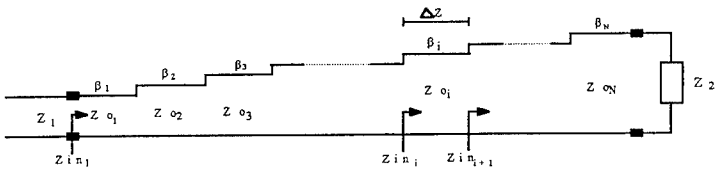


Figure 2: Multiple uniform section representation of a non-uniform transmission line.

From Γ_{in}, the voltage, T_V, and the effective power, T_P, transmission coefficients are calculated as:

$$T_V = 1 + \Gamma_{in} \tag{5}$$

$$T_P = \sqrt{1 - |\Gamma_{in}|^2} \tag{6}$$

It is now clear that the transfer function $T(\omega,z)$ can be obtained from (5), or (6), according to:

$$T(\omega, z = D) = T_{V/P} \exp[-j\theta(\omega, z = D)] \tag{7}$$

where

$$\theta(\omega, z = D) = \sum_{i=1}^{N} \beta_i \Delta Z \tag{8}$$

In the limit when ΔZ tends to zero, Riccati's equation is obtained, which gives the reflection coefficient $\Gamma(z)$ at any position along the transmission line[5]. The analytical solution of this equation is only possible in certain restricted cases, for specific impedance profiles. For an arbitrary impedance profile, numerical means of solutions are necessary.

The formulation presented here simplifies the numerical calculation of the input reflection coefficient. The accuracy of the calculation is determined by the length ΔZ chosen for the uniform sections. This formulation allows the consideration of multiple reflections, arbitrary impedance profile, and takes into account the fully dispersive nature of the transmission line. Equations (1) and (7) describe the algorithm developed to simulate the propagation of ultra-short pulses in uniform and non-uniform transmission lines. The frequency domain analysis of each section, i.e. the calculation of the propagation constant, $\beta_i(\omega)$, and of the characteristic impedance, $Z_{oi}(\omega)$, is performed with the Spectral Domain Approach (SDA[6,7]), while Fast Fourier Transform is used for the time domain analysis.

3.- RESULTS

3.1- Microstrip Lines

First, the SDA was used to determine the dispersion characteristics of uniform and non-uniform microstrip lines. Three lines were considered on a 0.635 mm thick substrate, with a dielectric constant ε_r=10.5. For the uniform line, a strip width of 0.588mm was chosen, so that the line impedance was 50Ω. For the non-uniform lines, the strip width varied continously from 0.588mm to 1.918mm in one line, and from 0.588mm to 3.300mm in the other one; both lines were 25mm long. The corresponding impedance transformation ratios are 2 and 3, respectively, with exponential impedance profiles. The design frequency was 10 GHz. Figures 3 and 4 show, for the second tapered line, the variation of the effective dielectric constant and of the characteristic impedance with position and with frequency. The dispersive nature of the structure is represented by the frequency dependent characteristic impedance and effective dielectric constant.

Next, pulse propagation was simulated. In all cases, a 30 ps (FWHM) Gaussian pulse was launched at z=0. The temporal response of the three microstrip lines at z=D=25mm is shown in Figure 5. It was observed that the transmission line dispersion, represented by the non-linear dependence between the effective dielectric constant and frequency, was the main cause of pulse distorsion. The variation of the impedance along the length of the lines does not change the pulse shape considerably, only introduces a time delay, and a small reduction in amplitude, due to mismatching. These effects are more pronounced for larger impedance transformation ratios. It was also observed that the variation of impedance with frequency has very little effect on the pulse shape, unless the pulse is extremely narrow. Both the frequency spectrum of the input pulse, represented by the amplitude of the normalized voltage signal $|V(f)/V(0)|$, and the magnitude of the total input reflection coefficient, $|\Gamma_{in}|$, are shown in Figure 6 for the tapered microstrip line with impedance transformation ratio $Z_2/Z_1=2$. Two situations are illustrated in this figure: considering the variation of the characteristic impedance with frequency (solid curve), and ignoring it (dashed curve). In the latter case, the input reflection coefficient reproduces that of a TEM tapered transmission line with exponential impedance profile, and behaves like the function $|\text{sen}(f)/f|$, which decays rapidly with frequency. When the variation of impedance with frequency is considered, the input reflection coefficient remains unaltered at the lower frequencies, but becomes oscillatory at the higher frequencies, where the components of the input pulse have negligible amplitude. That explains why the frequency dependent characteristic

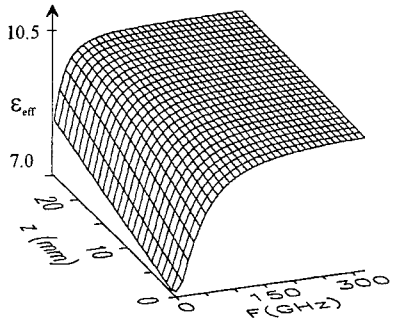


Figure 3: Variation of the effective dielectric constant with frequency and position along the tapered microstrip line with $Z_2/Z_1=3$.

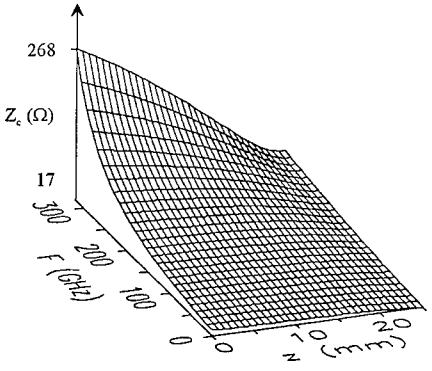


Figure 4: Variation of the characteristic impedance with frequency and position along the tapered microstrip line with $Z_2/Z_1=3$.

impedance does not have appreciable effect on the pulse shape. In the case where the input signal has much wider frequency spectrum, either due to extremely narrow pulses or to pulses modulated by a very high frequency carrier, the impedance dispersion must be taken into account.

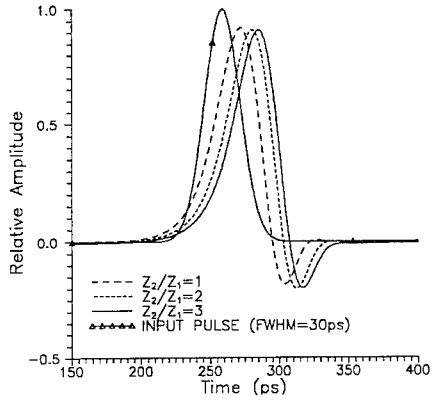


Figure 5: Propagation of Gaussian pulse along uniform and tapered microstrip lines considering the frequency dispersion of the effective dielectric constant and characteristic impedance.

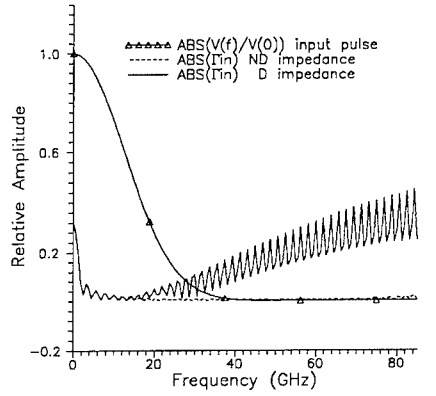


Figure 6: Frequency spectrum of the input pulse and variation of the total input reflection coefficient of a tapered microstrip line (Z_2/Z_1=2) with frequency, with (solid line) and without (dashed line) impedance dispersion.

3.2.-Experimental Results

To verify the adequacy of the formulation presented here, several experiments were carried out with the microstrip lines described in Section 3.1. In order to provide a 50Ω enviroment for the measurements, all the lines were mounted "back to back". A Hewlett-Packard 8133A pulse generator and an HP 1817A sampling oscilloscope were used in the experiments. The pulse at the generator output was measured, and then incorporated in the simulation algorithm. The experimental and simulated results are presented in Figures 7, 8, and 9, for an uniform 50Ω microstrip line, and for two tapered microstrip lines (impedance transformers: 50-25-50Ω and 50-16-50Ω), respectively.

Figure 7 shows the results obtained for the uniform microstrip line, where the dashed curve corresponds to the input pulse, which is approximately rectangular and exhibits distortion due to dispersion and reflections along the connecting cables. The other two curves in this figure correspond to the simulated and measured output pulses. A very good agreement is observed between the simulated and measured output pulses, except for a smaller amplitude in the latter. This is due to the fact that the microstrip losses (dielectric, ohmic and radiation losses) are not accounted for in the simulation. Also, the measured pulse incorporates effects due to the launchers and connectors, which introduce extra dispersion, and may be responsible for the variable time delay seen in the measured pulse when compared with the simulated one. Figures 8 and 9 show similar results for the two tapered microstrip lines. Once again, the simulated and measured pulses are in very good agreement.

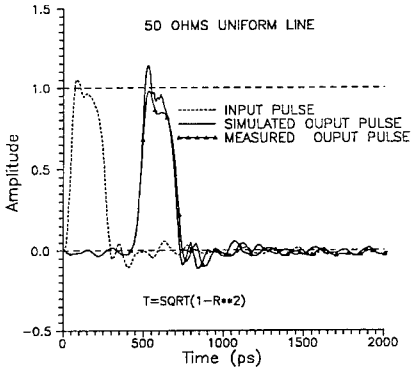


Figure 7: Simulated and measured pulses along a 50mm long uniform microstrip line (w=0.588, h=0.635mm, ε_r=10.5) .

3.3.-CPW-slot line

A combined CPW-slot line 50Ω-to-10Ω impedance transformer, 25mm in length, was also considered, on a 0.635mm thick substrate, with ε_r=38. For the SDA calculation, the transformer was divided in 20 sections of 1.25mm. After the frequency domain characterization, a 50ps FWHM Gausssian pulse was launched at the low impedance side of this transmission line transformer (TLT). The dispersed pulse is shown in Figure 10. For comparison, two other pulses are also shown in this figure: the one obtained after the same length of uniform line, whose transversal dimensions are those of the low impedance side, and one obtained without considering the transmission line dispersion. It is again seen in this figure that the main cause of pulse distortion is the transmission line dispersion, which introduces some ringing at the head and tail of the pulse, and so reduces its amplitude, due to a redistribuition of energy.

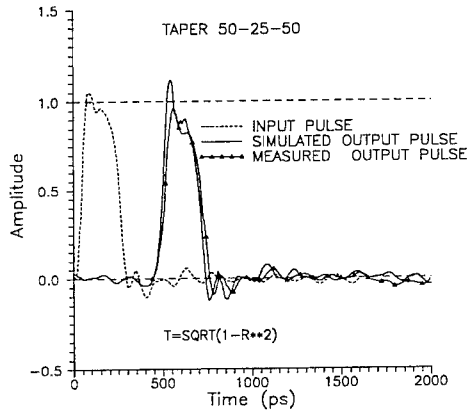


Figura 8: Simulated and measured pulses at a 50mm long tapered microstrip line (Z_2/Z_1=2, h=0.635mm, ε_r=10.5).

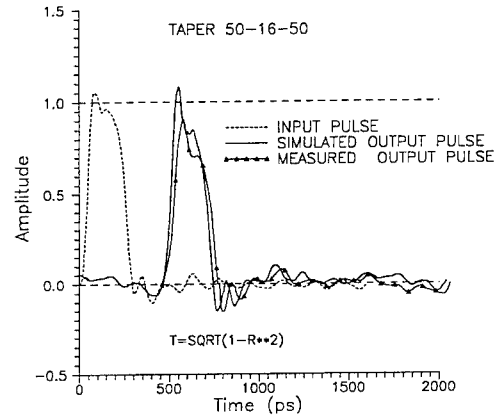


Figure 9: Simulated and measured pulses at a 50mm long tapered microstrip line (Z_2/Z_1=3, h=0.635mm, ε_r=10.5).

4.- CONCLUSIONS

This paper presented a rigorous investigation of the propagation characteristics of ultra-short electric pulses along uniform and tapered transmission lines, considering their fully dispersive nature. Both Gaussian and rectangular pulses were simulated. It was observed that the variation of the characteristic impedance with frequency affects the total input reflection coefficient, which acquires an oscillatory behaviour at the higher frequencies. However, it was shown that it does not contribute much for pulse distortion, except in the case of extremely narrow pulses, or pulses modulated by very high frequency carriers. In general, the major cause of pulse distortion is the non-linear relation between the

effective dielectric constant and frequency. The adequacy of the formulation was confirmed experimentally for microstrip lines: simulated and experimental results showed very good agreement.

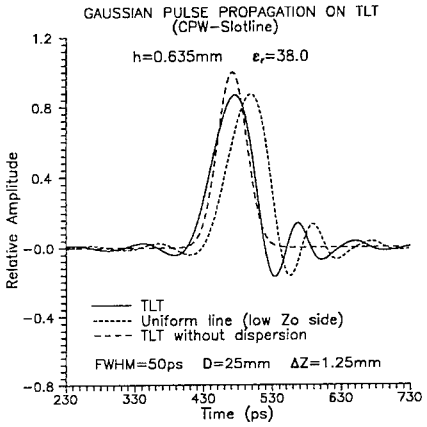


Figure 10: Dispersed pulses for exponential CPW-slot line taper.

ACKNOWLEDGEMENT

The authors would like to thank Prof. M. M. Mosso, of CETUC - PUC/Rio, for his cooperation in performing the measurements reported here. This work was supported by Telecomunicações Brasileiras S.A. - TELEBRÁS, under the Contract PUC-TELEBRÁS 513/93.

REFERENCES

1. P. Pramanick and R. R. Mansour: "Dispersion Characteristics of Square Pulse with Finite Rise Time in Single, Tapered, and Coupled Microstrip Lines", *IEEE Trans. Microwave Theory Tech.*, Vol. MTT-39, pp. 2117-2122, 1991.
2. M. Kobayashi and Y. Nemoto, "Analysis of Pulse Dispersion Distorsion Along Exponential and Tchebycheff Microstrip Tapers", *IEEE Trans. Microwave Theory Tech.*, Vol. MTT-42, pp. 834-839, 1994.
3. R. L. Veghte and C. A. Balanis: "Dispersion of transient signal in microstrip transmission lines", *IEEE Trans. Microwave Theory Tech.*, Vol. MTT-34, pp. 1427-1436, 1986.
4. T. Leung and C. A. Balanis: "Pulse distortion in open and shielded microstrip using the spectral domain method", *IEEE Trans. Microwave Theory Tech.*, Vol. MTT-36, pp. 1223-1228, 1988.
5. R. E. Collin, *"Foundation for Microwave Engineering"*, New York: McGraw Hill, 1992.
6. T. Uwano and T. Itoh, Spectral Domain Approach, in: *"Numerical Techniques for Microwave and Millimeter-Wave Passive Structures"*. T. Itoh (ed.), New York: John Wiley & Sons, 1989.
7. J. R. Souza: "Spectral Domain Analysis of Printed Transmission Lines in Multilayered Substrate and Superstrate Configuration", *Proc. 8th Annual Rev. Progress in Appl. Comp. Electromagn.*, pp 290-295, Monterey, CA, 1992.

WAVE-FIELD PATTERNS ON ELECTRICALLY LARGE NETWORKS.

Ross A. Speciale

Redondo Beach, California

1 - MULTIDIMENSIONAL GUIDED-WAVE PROPAGATION.

Recently formulated extensions of the old, classical concepts of *Image Impedance*, and of *Image Transfer Function*, from the basic theory of simple two-port networks to the broader context of large, complex systems of interconnected multiport networks, lead to new, and *far-reaching generalizations* of well known, elementary results.

The new, generalized results describe, in rigorous mathematical terms, the simultaneous propagation of multiple sets of *guided* electromagnetic *waves* through electrically large, *multi-dimensional delay-structures*, constructed by interconnecting large numbers of microwave multiport networks.

Closed form matrix expressions of new multidimensional quantities are given, that are conceptually equivalent to the classical *wave-impedance*, and *propagation-constant* of electrical transmission lines. All the given matrix expressions are cast in mutually complementary formulations, one set being suited to the *analysis* of wave-guiding system, the other set intended for system *synthesis* and *design*.

2 - PRACTICAL APPLICATIONS OF THE NEW RESULTS.

Numerous and varied applications of new analysis and synthesis methods, based on the here presented generalized theory of guided-wave propagation, have already been identified and studied in substantial depth. The most notable of these applications is perhaps the development of conceptually new, more affordable configurations for the *feed-networks* of large, two-dimensional, high directivity, low-sidelobe, electronically-steered *phased arrays* [1, 2].

3 - A VASTLY EXPANDED FIELD OF APPLICABILITY.

The generalized theory of guided wave propagation presented here, applies to 2D and 3D wave-guiding systems of interconnected multiport microwave networks, that may physically span tens, hundreds, or even thousands of free-space wavelengths in all linear dimensions. Further, the considered network systems may be simultaneously excited by *any* arbitrarily large *number* of mutually coherent *sources*, connected to the network system at an equally large number of input ports. The input ports may be located in *any* arbitrary or prescribed *pattern*, and the sources may conform to *any* given arbitrary or prescribed amplitude and phase *distribution*.

The new generalized theory of guided wave propagation is applicable to the analysis and synthesis of *practical* microwave guiding structures, built by interconnecting well-known, established types of basic microwave devices such as coaxial lines, waveguides, resonant cavities, couplers, hybrid junctions, power splitters, power combiners, matching networks, and any other type of microwave device known to be *linear*, at least below some given level of power density.

The emphasis of the new treatment is, however, on *periodic* structures having a substantial degree of *modularity*, as multi-atom molecules, or crystal lattices.

The combined modularity and periodicity of the considered microwave structures also implies some type of structural symmetry, including some of the point-symmetries of crystallography. The new generalized theory of guided wave propagation applies also to infinite or semi-infinite wave guiding systems, regarded as essentially limitless interconnections of elementary, partial *regions*, or *sub-arrays*.

4 - MULTI-DIMENSIONAL WAVE-FIELDS.

The 2D or 3D wave-field, generated by each of the external excitation sources, fills the whole guiding microwave network structure with position-dependent amplitudes and phases. The local wave amplitude and phase of each single-source wave-field depends on: a) the location of the selected observation point, b) the location of the source connection-point, c) the amplitude and phase settings of the given source, d) the wave-propagation properties of the microwave guiding structure, and e) the internal impedances of all the sources, and of the passive load-networks connected to the system external ports.

Further, because of the assumed system linearity and reciprocity, *linear superposition of the component wave-fields* of all the active system-excitation sources takes place, everywhere through the whole wave-guiding structure. The resulting, total 2D or 3D wave-field pattern is therefore a *weighted linear combination* of the wave-fields of all the active sources, with complex weights determined by the geometrical locations, relative amplitudes and relative phases of all the sources.

The old, well-known concept of *'artificial delay line'* is here generalized to 2D, and 3D microwave structures, by considering large-scale, periodic systems of interconnected *multiport* microwave devices, that may physically span large numbers of free-space wavelengths.

5 - ANALYTIC RESULTS.

The known open-circuit impedance matrix $Z_{(n+N)}$ of the ($n + N$) - port network **N** (shown in Figures 1 and 2) is *asymmetrically* - partitioned in four blocks Z_i having dimensions consistent with the ($n \mid N$) - split of the total number of ports, between the n - port interface 1 , and the N - port interface 2.

The matrix $Z_{(n+N)}$ is therefore partitioned in an $n \times n$ leading block Z_1 , and an $N \times N$ trailing block Z_4 , while the remaining blocks Z_2 , and Z_3 are both *rectangular* and with dimensions $n \times N$ and $N \times n$ respectively. Assuming, for instance, that $n < N$ the partitioned matrix $Z_{(n+N)}$ is represented in the form :

$$Z_{(n+N)} = \left|\begin{array}{c|c} Z_1 & Z_2 \\ \hline Z_3 & Z_4 \end{array}\right| \qquad (1)$$

where, because of the assumed reciprocity :

$$Z_1^T = Z_1 \qquad (2) \qquad Z_4^T = Z_4 \qquad (3) \qquad Z_3 = Z_2^T \qquad (4)$$

Two very fundamental matrix-algorithms describe mathematically the transformation of the open-circuit impedance matrices Z_{L1} , and Z_{L2} of totally general and arbitrary load-networks L_1 , and L_2 , to the corresponding input impedance matrices Z_{in2} , and Z_{in1} , expressed by :

$$Z_{in1} = Z_1 - Z_2 \cdot \left(Z_4 + Z_{L2} \right)^{-1} \cdot Z_3 \qquad (5)$$

$$Z_{in2} = Z_4 - Z_3 \cdot \left(Z_1 + Z_{L1} \right)^{-1} \cdot Z_2 \qquad (6)$$

Unconditional, bilateral matching of the network **N** is obtained if the matrices Z_{L1} , and Z_{L2} of the two load-networks L_1 , and L_2 are respectively equal to the two *Image Impedance Matrices* Z_{I1} , and Z_{I2} expressed as functions of the four blocks Z_i of the Z-matrix $Z_{(n+N)}$ by:

$$Z_{II} = \left(I_n - Z_2 \cdot Z_4^{-1} \cdot Z_3 \cdot Z_1^{-1} \right)^{1/2} \cdot Z_1 \qquad (7)$$

$$Z_{I2} = \left(I_N - Z_3 \cdot Z_1^{-1} \cdot Z_2 \cdot Z_4^{-1} \right)^{1/2} \cdot Z_4 \qquad (8)$$

Further, under the obtained unconditional, bilateral matching, the input voltages and currents are mapped, from one interface to the other, by the *Image Transfer Function Matrices* T_{IVF} , T_{IVB} , T_{IIF} , and T_{IIB} of the ($n + N$) - port network **N** , defined by:

$$V_j = T_{IVF} \cdot V_i \qquad (9) \qquad - I_j = T_{IIF} \cdot I_i \qquad (10)$$

$$V_i = T_{IVB} \cdot V_j \qquad (11) \qquad - I_i = T_{IIB} \cdot I_j \qquad (12)$$

where V_i and I_i are the n - dimensional *'voltage-'* and *'current-'* vectors at the n - port interface 1, and V_j and I_j are the N - dimensional *'voltage-'* and *'current-'* vectors at the N - port interface 2 .

The two *'forward'* image transfer function matrices T_{IVF} (for voltage vectors), and T_{IIF} (for current vectors), defined by the expressions (9) and (10) , are both N x n , and linearly map the *'input'* , n - dimensional voltage and current vectors V_i and I_i , of the n - port *'input'* interface 1, to the N - dimensional, *'output'* voltage and current vectors V_j , and I_j , of the N - port *'output'* interface 2 (Figure 1).

Similarly, the two *'backward'* image transfer function matrices T_{IVB} (for voltage vectors), and T_{IIB} (for current vectors), defined by the expressions (11) and (12) , are both n x N, and linearly map the *'input'* , N - dimensional voltage and current vectors V_j , and I_j , of the N - port *'input'* interface 2, to the n - dimensional, *'output'* voltage and current vectors V_i , and I_i , of the n - port *'output'* interface 1 (Figure 2).

The four Image Transfer Function Matrices T_{IVF} , T_{IIF} , T_{IVB} , and T_{IIB} are expressed as functions of the four blocks Z_i of the Z-matrix $Z_{(n+N)}$ by:

$$T_{IVF} = Z_3 \cdot Z_1^{-1} \cdot \left[I_n + \left(I_n - Z_2 \cdot Z_4^{-1} \cdot Z_3 \cdot Z_1^{-1} \right)^{1/2} \right]^{-1} \tag{13}$$

$$T_{IVB} = Z_2 \cdot Z_4^{-1} \cdot \left[I_N + \left(I_N - Z_3 \cdot Z_1^{-1} \cdot Z_2 \cdot Z_4^{-1} \right)^{1/2} \right]^{-1} \tag{14}$$

$$T_{IIF} = Z_4^{-1} \cdot \left[I_N + \left(I_N - Z_3 \cdot Z_1^{-1} \cdot Z_2 \cdot Z_4^{-1} \right)^{1/2} \right]^{-1} \cdot Z_3 \tag{15}$$

$$T_{IIB} = Z_1^{-1} \cdot \left[I_n + \left(I_n - Z_2 \cdot Z_4^{-1} \cdot Z_3 \cdot Z_1^{-1} \right)^{1/2} \right]^{-1} \cdot Z_2 \tag{16}$$

Two sets of closed-form expressions of the blocks Z_i of the open-circuit impedance matrix $Z_{(n+N)}$ of the ($n + N$) - port network $\mathbf{N}$, formulated as functions of two mutually equivalent sets of *image matrices*, have been found and are given by :

$$Z_1 = \left(I_n + T_{IVB} \cdot T_{IVF} \right) \cdot \left(I_n - T_{IVB} \cdot T_{IVF} \right)^{-1} \cdot Z_{II} \tag{17}$$

$$Z_2 = 2 \left(I_n - T_{IVB} \cdot T_{IVF} \right)^{-1} \cdot T_{IVB} \cdot Z_{I2} \tag{18}$$

$$Z_3 = 2 \left(I_N - T_{IVF} \cdot T_{IVB} \right)^{-1} \cdot T_{IVF} \cdot Z_{II} \tag{19}$$

$$Z_4 = \left(I_N + T_{IVF} \cdot T_{IVB} \right) \cdot \left(I_N - T_{IVF} \cdot T_{IVB} \right)^{-1} \cdot Z_{I2} \qquad (20)$$

$$Z_1 = Z_{I1} \cdot \left(I_n + T_{IIB} \cdot T_{IIF} \right) \cdot \left(I_n - T_{IIB} \cdot T_{IIF} \right)^{-1} \qquad (21)$$

$$Z_2 = 2\ Z_{I1} \cdot \left(I_n - T_{IIB} \cdot T_{IIF} \right)^{-1} \cdot T_{IIB} \qquad (22)$$

$$Z_3 = 2\ Z_{I2} \cdot \left(I_N - T_{IIF} \cdot T_{IIB} \right)^{-1} \cdot T_{IIF} \qquad (23)$$

$$Z_4 = Z_{I2} \cdot \left(I_N + T_{IIF} \cdot T_{IIB} \right) \cdot \left(I_N - T_{IIF} \cdot T_{IIB} \right)^{-1} \qquad (24)$$

These expressions solve the practical engineering problem of designing a wave-guiding microwave network structure that: a) is unconditionally and bilaterally *matched* to given multi-phase generators and multiport load-networks, and b) exhibits specified *amplitude* and *phase* transmissions of arbitrary, multiple sets of input waves, in both the forward and backward directions. A typical practical example is the design of the feed-network of a transmit/receive phased array.

Finally, four *'inverse'* image transfer function matrices R_{IVF} , R_{IVB} , R_{IIF} , and R_{IIB} defined by :

$$V_i = R_{IVF} \cdot V_j \qquad (25) \qquad\qquad V_j = R_{IVB} \cdot V_i \qquad (26)$$

$$I_i = - R_{IIF} \cdot I_j \qquad (27) \qquad\qquad I_j = - R_{IIB} \cdot I_i \qquad (28)$$

are expressed by :

$$R_{IVF} = - \left[I_n - \left(I_n - Z_2 \cdot Z_4^{-1} \cdot Z_3 \cdot Z_1^{-1} \right)^{-1/2} \right]^{-1} \cdot Z_2 \cdot Z_4^{-1} \cdot \left(I_N - Z_3 \cdot Z_1^{-1} \cdot Z_2 \cdot Z_4^{-1} \right)^{-1/2} \qquad (29)$$

$$R_{IVB} = -\left[I_N - \left(I_N - Z_3 \cdot Z_1^{-1} \cdot Z_2 \cdot Z_4^{-1} \right)^{-1/2} \right]^{-1} \cdot Z_3 \cdot Z_1^{-1} \cdot \left(I_n - Z_2 \cdot Z_4^{-1} \cdot Z_3 \cdot Z_1^{-1} \right)^{-1/2} \quad (30)$$

$$R_{IIF} = Z_1^{-1} \cdot \left[I_n - \left(I_n - Z_2 \cdot Z_4^{-1} \cdot Z_3 \cdot Z_1^{-1} \right)^{1/2} \right]^{-1} \cdot Z_2 \quad (31)$$

$$R_{IIB} = Z_4^{-1} \cdot \left[I_N - \left(I_N - Z_3 \cdot Z_1^{-1} \cdot Z_2 \cdot Z_4^{-1} \right)^{1/2} \right]^{-1} \cdot Z_3 \quad (32)$$

The *'inverse'* matrices R_{IVF} , and R_{IIF} are both n x N , while the *'inverse'* matrices R_{IVB} , and R_{IIB} are both N x n . The expressions (29) through (32) solve the practical engineering *synthesis* problem of determining the *input* excitation vectors V_j , and I_j required to generate *prescribed output* wave-field patterns V_j , and I_j .

Electrically-large, two-dimensional, reciprocal wave-guiding structures, with a square outer perimeter and lattice, exhibit C_{4V} rotation-, and reflection symmetries, and are represented by complex, symmetric, 4 x 4 block-circulant Z-matrices [4,5].

Similarly, structures with a regular-hexagonal outer perimeter and lattice exhibit C_{6V} symmetries, and are represented by complex, symmetric, 6 x 6 block-circulant matrices. The study of the symmetry-structure of the corresponding *Image-Impedance*, and *Image-Transfer-Function* matrices is the objective of current, intensive research.

6 - REFERENCES.

[1] US Patent No. 5,347,287 - September 13, 1994.

[2] US Patent Pending - September 12, 1994.

[3] Speciale R. A.,"Computer-Simulation of Isotropic, Two-Dimensional Guided-Wave Propagation," 1995 ACES Symposium Paper - Number S120, published in these Proceedings.

[4] Speciale R. A.,"Symmetry Analysis of Large Two-Dimensional Clusters of Coupled Cavity Resonators," 9th Annual Review of Progress in Applied Computational Electromagnetics, Naval Postgraduate School, Monterey, California, March 22-26, 1993, pp. 281-288.

[5] Speciale R. A., "Sectored Cylindrical Cavity Resonators," 8th Annual Review of Progress in Applied Computational Electromagnetics, Naval Postgraduate School, Monterey, California, March 16-20, 1992, pp. 274-281.

[6] Speciale R. A., "Wave Propagation on Infinite, Two-Dimensional Structures," 5th Annual Review of Progress in Applied Computational Electromagnetics, Naval Postgraduate School, Monterey, California, March 20-24, 1989, pp. 200-244.

[7] Speciale R. A.,"Projective Matrix Transformations in Microwave Network Theory," 1981 MTT-S International Microwave Symposium Digest, Los Angeles, California, June 15-19, 1981, IEEE Cat. No. 81CH1592-5, ISSN No. 0149-645X, pp. 510-512.

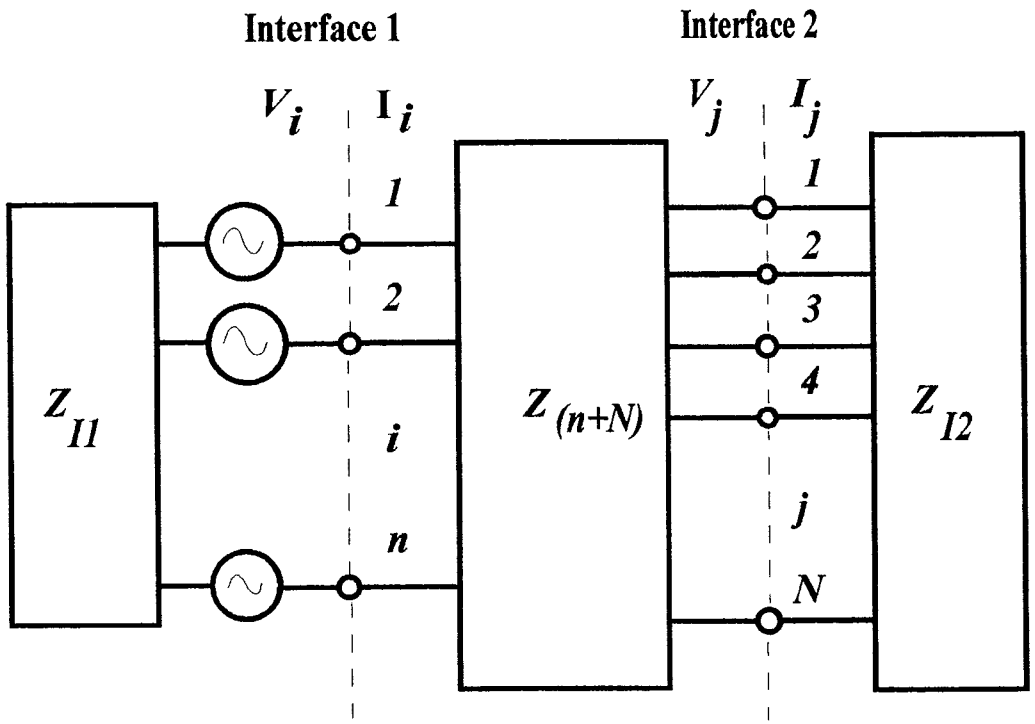


Figure 1 - Unconditional, Bilateral Image-Impedance Match: Forward-Wave, n-Phase Excitation, with Arbitrary Wave Amplitudes and Phases.

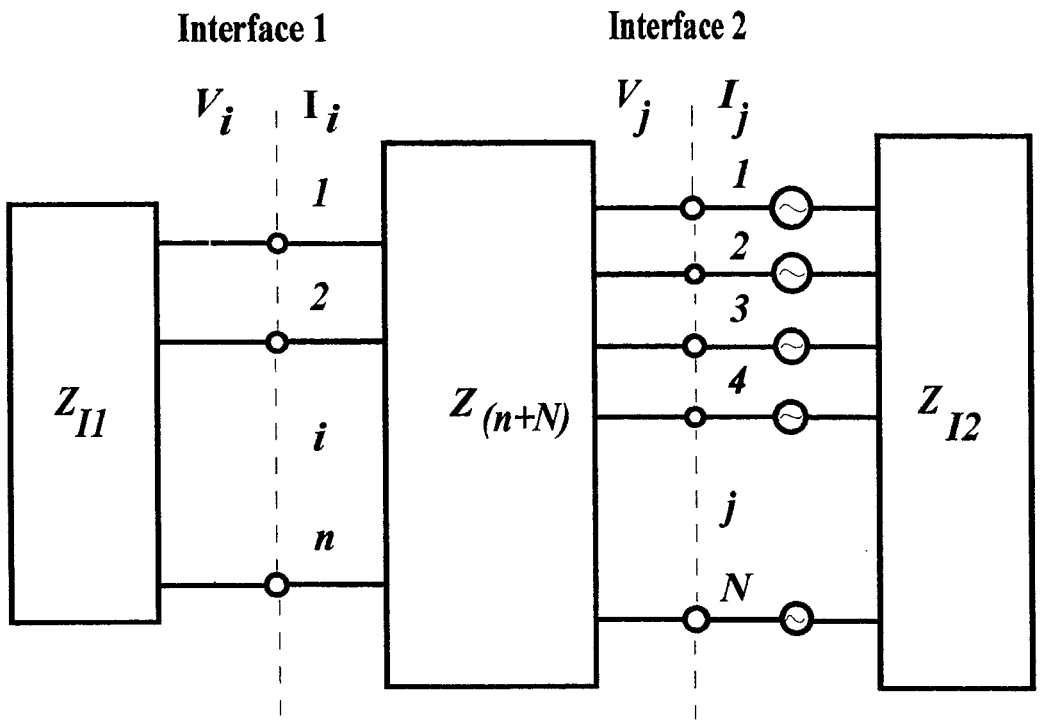


Figure 2 - Unconditional, Bilateral Image-Impedance Match: Backward-Wave, N-Phase Excitation, with Arbitrary Wave Amplitudes and Phases.

SCATTERING CHARACTERISTICS OF DISSIMILAR WAVEGUIDE SLOT COUPLERS

A.K.SINGH AND S. CHRISTOPHER

ELECTRONICS AND RADAR DEVELOPMENT ESTABLISHMENT
CV RAMAN NAGAR, BANGALORE (INDIA)

ABSTRACT : Characteristics of dissimilar orthogonal rectangular waveguides coupled through inclined coupling slot has been studied. A moment method solution is used with entire basis and testing functions. Numerical results for resonant length and scattering parameters over a rang of non-identical mainline and branchline waveguide dimensions are presented. Moment method code developed has been validated experimentally by designing novel test fixtures.

INTRODUCTION

Planar slotted arrays are widely used in radar and microwave communication systems because of their rugged, compact structure. Such planar arrays require coupling slots as feeding elements in addition to radiating elements. A centered-inclined slot located in the common broad wall of radiating and feeding (hereafter called branchline and mainline) waveguides is widely used coupling element because of its better off resonance behavior. A fully assembled slotted array with feed network is difficult to test because many of the desired points are inaccessible. Therefore, it often is desirable to test separate sub array sections using dimensions of actual array which requires isolated coupling slot characterization. Because of the electrical and mechanical constraints, most of the slotted arrays have non-identical, non-standard mainline and branchline dimensions. The low side lobe array design requires that the impedance of isolated coupling slot located in the common broad wall of two dissimilar waveguides be known to a high degree of accuracy.

Waveguide slot couplers have been discussed in the literature by many investigators [1-5]. A rigorous analysis of centered-inclined slot coupler has been made by Rengarajan [6], who developed integral equations for the slot E-field, taking into account finite wall thickness, with a solution obtained using method of moments. He presented numerical results for resonant length and scattering parameters over a range of slot inclinations, frequencies and waveguide dimensions. Most of his results deal with identical mainline and branchline waveguide dimensions. The present paper deals with dissimilar waveguide slot couplers . Formulation used involves the moment method solution of a pair of coupled integral equations containing dyadic Green functions of the homogeneous isotropic lossless filled mainline and branchline waveguides. Method of analysis is similar to [6] with certain modifications in slot resonant length and scattering parameters calculations. Due to the complexity of the boundary value problem encountered in the coupling slot modeling, all analytical and numerical analysis involve a set of reasonable approximations. Although moment method solution offers a high degree of accuracy and provides inexpensive alternative to measurements, it is essential to cross check computed data with some experiment to have an estimate on the error and to make appropriate adjustments in the final array design. Here an attempt has been made to validate theoretical data experimentally by designing novel test jigs.

THEORY

The slot is assumed to be excited by TE_{10} mode from a matched generator and terminated in a match load. The coordinate system of the structure is shown in Fig. 1a and 1b. The structure is divided into the regions A, B and C where A is mainline waveguide region, B is slot (or cavity) region and C is branchline region. In Region A and C, slot is completely shorted and magnetic current sheets $M_{\alpha 1}$ and $M_{\alpha 2}$ are placed in its location at $y = b^-$ and $y = b+t^+$. In region B, both the slot apertures are shorted by magnetic current sheets $-M_{\alpha 1}$ and $-M_{\alpha 2}$. The problem is solved by making use of couple of integral equations for slot electric field which can be arrived at by equating magnetic fields on the two sides of the slot interface. The slot electric field is assumed to be varying along the length with no variation across the width.

A pair of coupled integral equations obtained after enforcing the continuity of longitudinal magnetic fields across each slot aperture is

$$H_{\alpha}^{inc} + H_{\alpha 1}^{scat} = H_{\alpha 1}^{c} \qquad ...(1)$$

$$H_{\alpha 2}^{scat} - H_{\alpha 2}^{c} = 0 \qquad ...(2)$$

where H_{α}^{inc} is the TE_{10} incident tangential magnetic field, given by

$$H_{\alpha}^{inc} = A_{10} e^{j\beta_{10} z} \left[j\cos(\pi x/a_m)\cos\theta - \frac{\beta_{10}}{(\pi/a_m)} \sin(\pi x/a_m)\sin\theta \right] \qquad ...(3)$$

where a_m is the mainline waveguide "a" dimension.

The $H_{\alpha 1}^{scat}$ is the scattered magnetic field inside the waveguide and is expressed in terms of aperture magnetic current $M_{\alpha 1}$ through respective Green's function

$$H_{\alpha 1}^{scat} = \iint_{s'} [\cos\theta \quad \sin\theta] \, [G^{main}] \, [\cos\theta \quad \sin\theta]^T \, M_{\alpha 1} \, ds' \qquad ...(4)$$

The integration is performed over the interior slot aperture s_1.
$[G^{main}]$ is the internal mainline waveguide Green's function which is similar to that of [7] with a,b and k replaced by a_m , b_m and k_d where $k_d = k\sqrt{\varepsilon_m}$, ε_m is permittivity of the dielectric material in mainline waveguide.

$H_{\alpha 1}^{1}$ and $H_{\alpha 2}^{2}$ are the lower and the upper aperture fields in the cavity due to the magnetic currents $-M_{\alpha 1}$ and $-M_{\alpha 2}$ respectively and are given by

$$H_{\alpha 1}^{c} = -\iint_{s_1} G_{s\alpha\alpha}^{c} \, M_{\alpha 1} \, ds' - \iint_{s_2} G_{e\alpha\alpha}^{c} \, M_{\alpha 2} \, ds' \qquad ...(5)$$

$$H_{\alpha 2}^{c} = -\iint_{s_1} G_{e\alpha\alpha}^{c} \, M_{\alpha 1} \, ds' - \iint_{s_2} G_{s\alpha\alpha}^{c} \, M_{\alpha 2} \, ds' \qquad ..(6)$$

where $G^c_{e\alpha\alpha}$ and $G^c_{s\alpha\alpha}$ are cavity region Green's functions [8]

$H^{scat}_{\alpha 2}$ is the tangential magnetic field in the region C and is computed from magnetic current $M_{\alpha 2}$ using branchline internal waveguide Green's function G^{branch}, i.e.,

$$H^{scat}_{\alpha 2} = \iint [\sin\theta \quad \cos\theta\ ]\ [G^{branch}]\ [\sin\theta \quad \cos\theta\ ]^T \quad M_{\alpha 2}\ ds'$$

where $[G^{branch}]$ is expressed in terms of branchline waveguide dimensions a_b, b_b and dielectric constant ε_b.

The integral equations (1) and (2) are solved by method of moments using Galerkin's method of testing [9]. It has been found that around the first resonance the field within the slot is essentially sinusoidal and hence trigonometric functions can be chosen as basis functions. Let

$$M_{\alpha 1} = \sum_{q=1}^{N} A_q \quad \sin[q\pi(\alpha 1 + L)/(2L)]$$

$$M_{\alpha 2} = \sum_{q=1}^{N} B_q \sin[q\pi(\alpha 1 + L)/(2L)]$$

where A_q and B_q are unknown coefficients.

As Galarkin method is used, the weighting function should be of the same type as basis functions, namely

$$w_p = \sin[p\pi(\alpha 1 + L)/(2L)]$$

The basis function should satisfy the same boundary conditions as satisfied by the magnetic current sources in order to converge magnetic current expansion series. The moment method converts the integral equations into a matrix equation which is then solved for unknown coefficients A_q and B_q. The field distribution on the surface of the slot can be obtained once unknown coefficients are solved.

NUMERICAL RESULTS AND DISCUSSION

The centered-inclined slot is modeled as a series element The resonance condition is defined when slot magnetic current is purely real and thus avoiding previous ambiguous resonance condition [5]. The scattering parameters are modified in order to satisfy the power balance condition and proper normalization has been done in terms of mainline and branchline waveguide dimensions and corresponding impedance to make the scattering matrix symmetrical. Based on moment method analysis, a software package has been developed to compute slot length and other scattering parameters at resonance. Secant method of root finding has been used for faster convergence.

Fig.2 illustrates the variation of resonant length (2L) as a function of slot inclination (θ) for non-standard, non-identical mainline and branchline waveguide "a" dimensions. The resonant length increases with inclination and variation is more in the case of reduced height waveguide couplers. Fig. 3 shows the variation of resonant length with inclination where mainline is a standard waveguide while branchline is non-standard. Variation is same as in the previous case but slot resonant length is shorter compared to previous case. Fig. 4 and 5 show the back scattered wave amplitude, |S11| at resonance as a function of slot tilt angle for two different cases. Waveguide dimensions affect |S11| by a small amount. For both the cases |S11| = 0.5 at θ = 45 deg. where half the power is coupled in the branchline waveguide. Computed results show that $S11(\theta) = S11(90-\theta)$. In all these computations ε_m and ε_b is taken as 1.0. The effect of different ε_m and ε_b has also been studied. For standard half height waveguide slot coupler with ε_m = 2.0 and ε_b =1.0, computed results show 4.5% decrease

in resonant length for θ lying between 5 deg. and 15 degrees. For higher value of slot inclinations and ε_m, the series behavior of slot is found to be poor. When ε_m = 1.0 and ε_b = 2.0, the reduction in resonant length is significant : about 13% for θ lying between 5 and 35 degrees. A similar behavior is observed in the case of non-standard waveguide slot couplers also.

EXPERIMENTAL VALIDATION

To validate the moment method code developed, a novel test fixture containing two blocks with coupling insert plates has been devised. The dimensions of the waveguides are obtained by machining two identical solid aluminum block. In the first block, channel of required mainline waveguide dimensions (22.532 mm x 5.08 mm) is machined out. In the second block, channel of required branchline waveguide dimensions (19.953 mm x 5.08 mm) is machined out in such a manner that when the two blocks are connected together, the channels are orthogonal to each other. In order to have a common wall between the two blocks, a coupling insert plate, which has the same geometry as blocks, is designed. To obtain more than one data point, the test fixture accommodates several coupling slot geometries by virtue of different insert plates. Indexing pins of appropriate dimensions are provided to mach mainline, branchline and coupling insert plates. Apart from this, a number of screws at a number of places are used to avoid any leakage. A photograph of test jig along with coupling insert plate is shown in Fig.6. The test fixture can be viewed as a four port transmission line network. A transition from 22.532 x 5.08 mm to 22.86 x 5.08 mm and 19.953 x 5.08 mm to 22.86 x 5.08 mm was made and standard coax -to-waveguide adopter provided by HP were used to connect the test jig with HP 8510 vector network analyzer. The network analyzer is calibrated for two port using standard 8036 half height calibration kit. Coupling insert plates with slot tilts 15, 25, 27.5, 32.5 and 35 degrees were fabricated and extensive measurement were carried out for all the scattering parameters. The results for |S11| is shown in Table-I along with computed results. The agreement between computed and measured results are seen to be excellent.

CONCLUSION

Based on moment method analysis, a generalized software package has been developed. A great care has been taken to compute slot resonant length and scattering parameters for dissimilar waveguide slot couplers. The validity of the moment method code developed has been checked experimentally.

REFERENCES

[1] W.H Watson, *The Physical Principles of Waveguide Transmission and Antenna Systems,* London: Clarenden Press, 1949.

[2] T.Vu Khac and CT Carson," Coupling by slots in rectangular waveguides using with arbitrary wall thickness," *Electron Lett.*, vol. 8, no. 18, pp. 296-297, Sept. 1972.

[3] P.K. Perk et al," Shunt/series coupling slot in rectangular waveguide," in *IEEE Int. Antennas and Propagat. Symp. Dig.*, 1984, pp. 62-65.

[4] D.C. Senior," Higher order mode coupling effects in shunt series coupling junction of planar slot array antenna," Ph.D. dissertation,UCLA, 1986.

[5] S.R. Rengarajan," Characteristics of longitudinal transverse coupling slots in crossed rectangular waveguides," IEEE-MTT, vol. 37, pp. 1171-1177, 1989

[6] S.R. Rengarajan," Analysis of centered-inclined waveguide slot coupler," *IEEE-MTT*, vol. 37, no. 5, pp. 884-889, 1989.

[7] A.F. Stevenson," Theory of slots in rectangular waveguides," *J. Appl. Phys.*, Vol.19, pp. 24-38, 1948.

[8] S.R. Rengarajan," Compound radiating slots in the broad wall of rectangular waveguide," *IEEE-AP, Vol. 37, pp. 1116-1123, 1989*
[9] R.F. Harrington, *Field computations by Moment Method,* New York, McGraw Hill, 1969

ACKNOWLEDGMENT

Authors wish to thank Mr. K.U. Limaye, Scientist 'F', Electronics and Radar Development Establishment, Bangalore for his constant encouragement and valuable suggestions throughout the work and Mr. N.P. Ramasubba Rao, Director, Electronics and radar Development Establishment, Bangalore for his kind permission to publish this work.

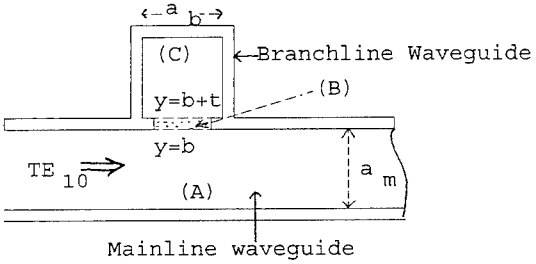


Fig. 1a Waveguide & Cavity Regions

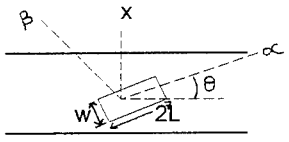


Fig. 1b Coordinate system of the slot

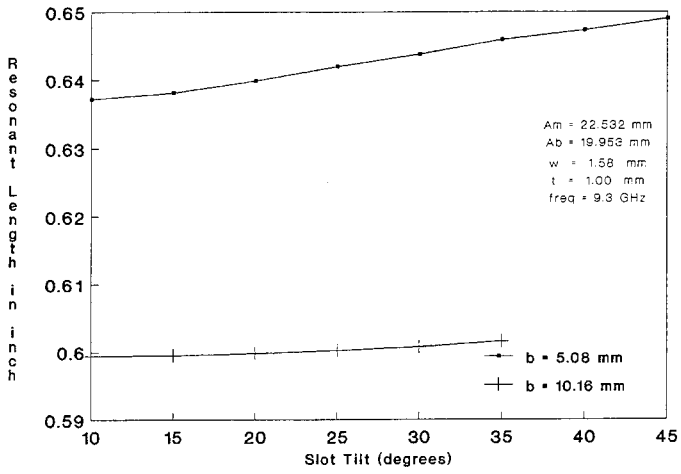


FIG.2 Variation of resonant length with slot tilt

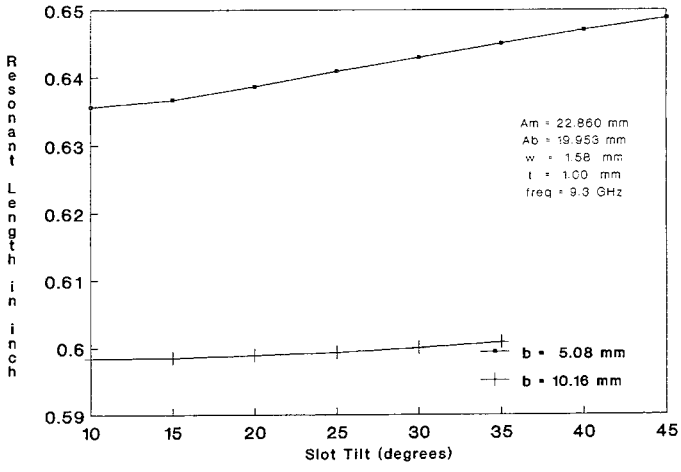


FIG.3 Variation of resonant length with slot tilt

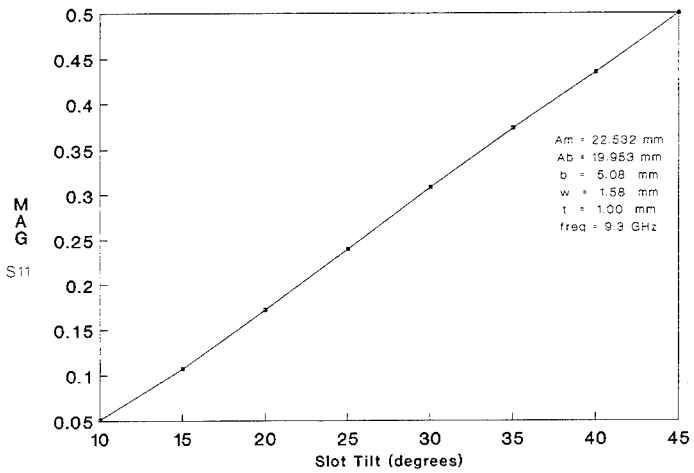


FIG.4 Variation of Mag. S11 with slot tilt

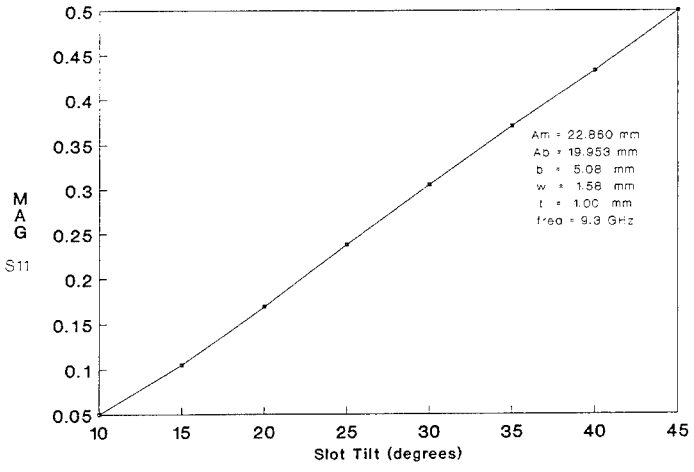


FIG.5 Variation of Mag. S11 with slot tilt

Table-I
EXPERIMENTAL VALIDATION OF THEORETICAL RESULTS

Waveguide Dimensions (mm)
Mainline : 22.532 * 5.08
Branchline : 19.953 * 5.08
Slot Dimensions (mm)
Width : 1.58
Thickness : 1.00
Frequency (GHz) : 9.60

Slot Tilt (deg.)	Resonant Length (mm)	|S11| in dB	
		Theoretical	Experimental
15.0	15.33	-20.44	-20.27
25.0	15.41	-13.19	-13.40
27.5	15.42	-12.01	-12.51
32.5	15.46	-10.01	-10.44
35.0	15.48	-09.17	-09.55

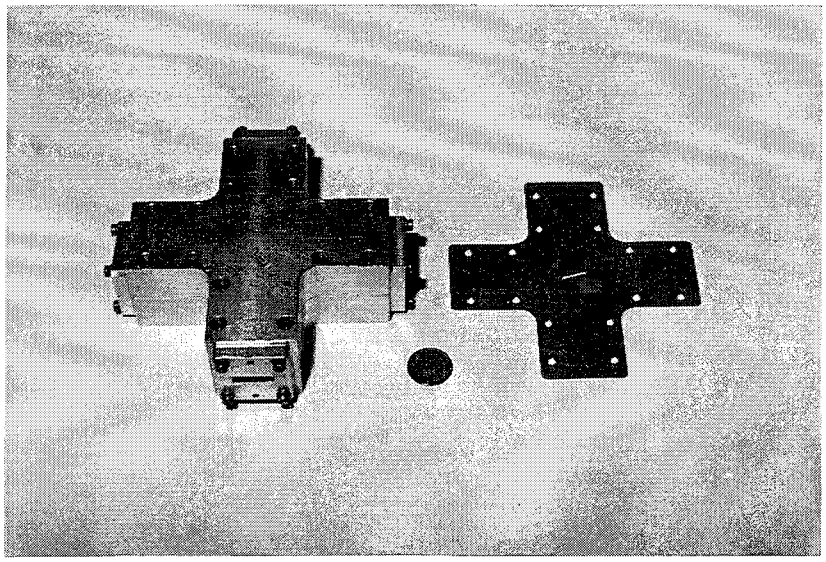


Fig. 6 PHOTOGRAPH OF TEST JIG WITH COUPLING INSERT PLATE

An Alternative Formulation of the Tranverse Resonance Technique

A. GOMES NETO †, *S. ARIGUEL* ‡, *H. AUBERT* ‡, *D. BAJON* ‡, *H. BAUDRAND* ‡

†Dept. of Electrical Engineering, Federal University of Paraíba,
C.P. 10064, Campina Grande, Paraíba, BRAZIL

‡Laboratoire d'Electronique, ENSEEIHT,
2 rue C. Camichel, Toulouse, FRANCE

Abstract

An alternative formulation of the transverse resonance technique is presented. The difference between the usual TRT and the formulation presented here is the considered transverse equivalent network. With the TRT proposed formulation mode solutions identification requires a less arduous work. Numerical results are presented for microstrip, coupled microstrips and conductor-backed coplanar waveguide.

I. Introduction

The transverse resonance technique (TRT) can be applied to a large class of microwave and millimeter-wave passive structures problems. It has been used not only to obtain dispersion characteristics, but also to the characterization of a large variety of discontinuity problems in planar and quasi-planar structures [1], [2]. In this paper an alternative formulation of the TRT is presented. With the proposed formulation open side structures can be exactly analyzed, boxed modes can be avoided and mode solutions identification requires a work less arduous. In this manner, not only dominant modes, but also higher order modes can be studied and distinguished from boxed modes. Numerical results obtained by the proposed TRT formulation are presented to microstrip, coupled microstrips and conductor-backed coplanar waveguide. They are in good agreement when compared to results obtained by other methods.

II. Theory

In the conventional formulation of the TRT, a suitable transverse equivalent network is established to compute the cutoff frequencies and possibly some additional characteristics of the structures [2]. The difference between the conventional and the proposed formulation is the adopted equivalent network, and consequently the admittance matrix expressions. In Fig. 1 equivalent networks and admittance matrix, for the usual TRT is preesented. The adopted equivalent network and admittance matrix expressions for the proposed TRT, is presented in Fig. 2. Mode coupling, which occurs at each step discontinuity, is represented by a generalized voltage source. Each transmission line section represents the different structure sections (two homogeneous waveguides and one inhomogeneous), and the admittances represent the boundary conditions. Matrix admittance elements are detailed in [3].

III. Numerical Results

In order to exemplify the proposed TRT formulation, numerical results are presented here to microstrip (MS), coupled microstrips (CMS) and conductor-backed coplanar waveguide (CBCW) (Fig. 3). The results were obtained by a computer program on a personal computer. In Fig. 4 results for the effective dielectric constant of a microstrip are presented. When compared to results of [4], a good agreement is observed not only to the dominant mode (EH_0), but also to the higher order modes.

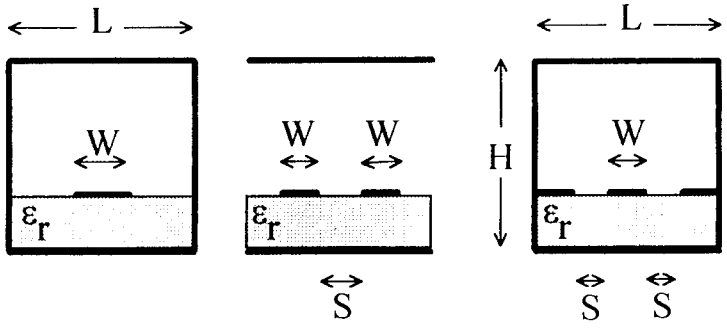


Figure 3: a) MS b) CMS c) CBCW

In Fig. 5 two different coupled microstrips are considered. In both cases, the obtained results for the first even and odd modes are in accordance with results of [5].

A conductor-backed coplanar waveguide is considered in Fig. 6. Numerical results are presented for the fundamental and higher order modes, and are in good agreement when compared to results of [6].

IV. Conclusions

An alternative TRT formulation is presented which constitutes a versatile method for the calculation of dispersion characteristics of pratical MIC, MHMIC and MMIC structures. The effort in mode solutions identification, especially higher order modes, is considerable reduced. The results presented are in accordance with results obtained by other authors.

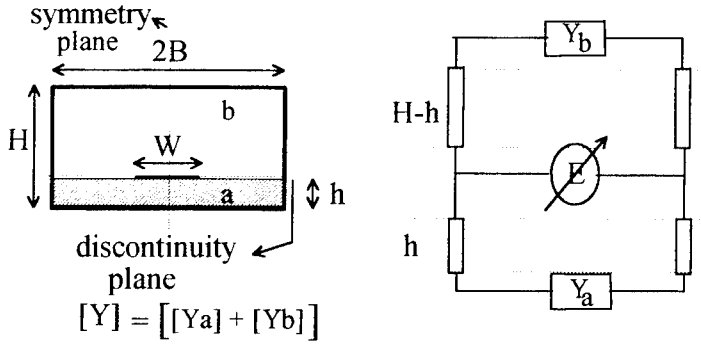


Figure 1: Usual TRT

One advantage of the proposed formulation is that open side structures can be analyzed exactly. When an open microstip is considered, by the usual formulation, two shorting end plates are placed at such distance of the center strip that their effects in microstrip electromagnetic fields can be negligible. The problem of this approach is the presence of "boxed modes" which makes the identification of specific microstrip modes an arduous work. When the present formulation is used, the two shorting end plates can be removed and infinite transmission lines are used instead. So, the work in mode identification is considerably reduced. In addition, equivalent networks and admittance matrix can be obtained for coupled microstrips, conductor-backed coplanar waveguide and other structures.

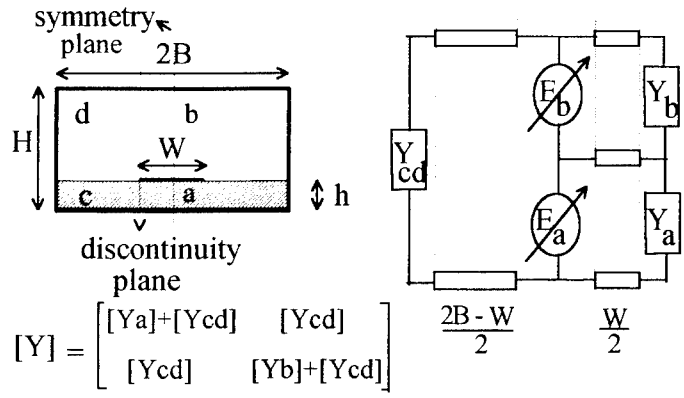
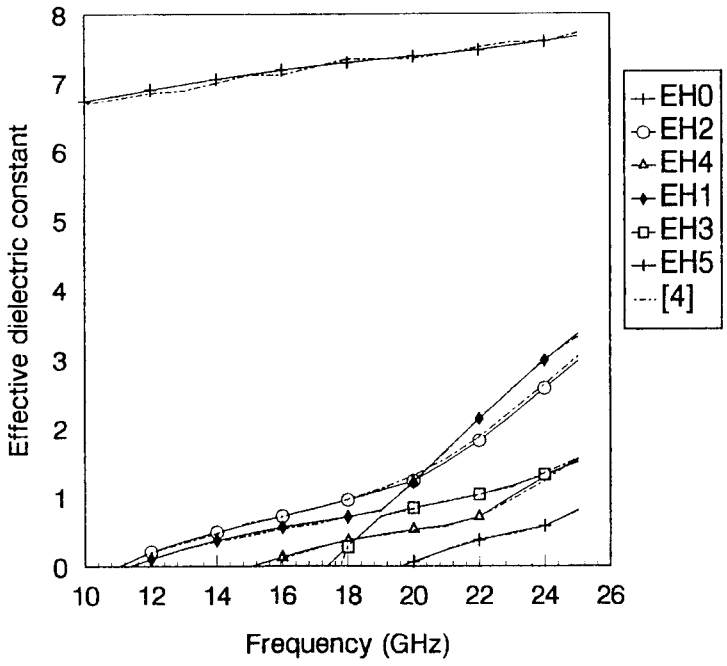
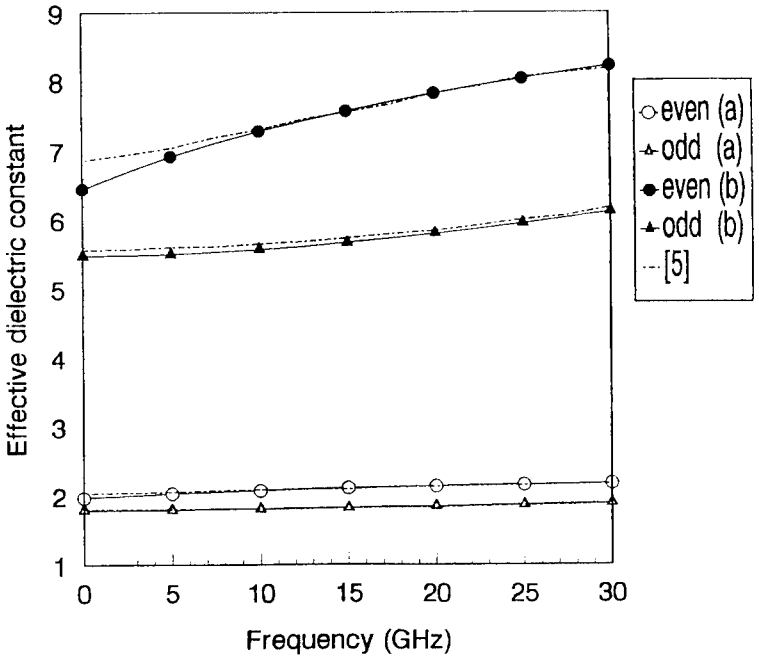


Figure 2: Proposed TRT



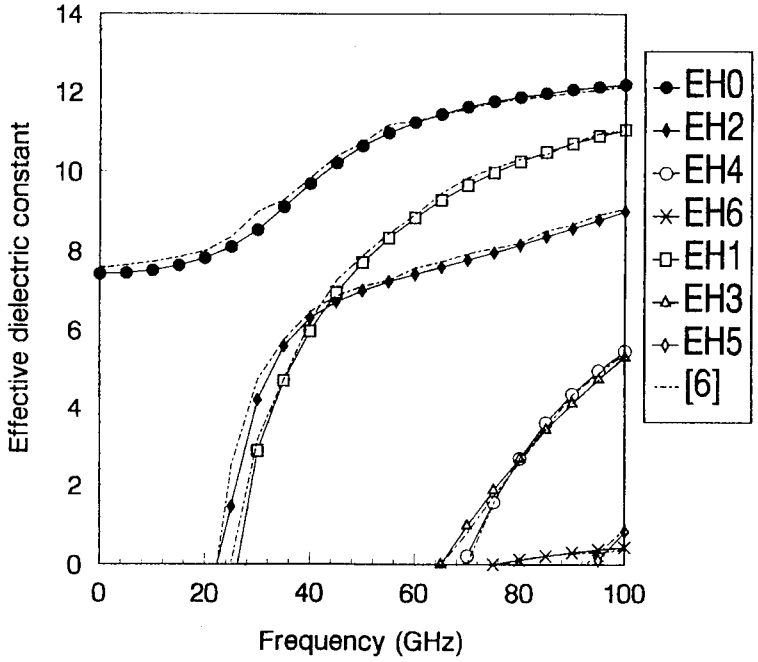
$H = 12.7mm, h = 1.27mm, W = 0.635mm, L = 12.7mm, \epsilon_r = 8.875$, [4]

Figure 4: MS - ϵ_{eff} x $Freq.(GHz)$



(a) $h = 0.79mm, W = 1.7775mm, S = 0.395mm, \epsilon_r = 2.35, H \approx 5h$, [5]
(b) $h = 0.64mm, W = 0.48mm, S = 0.32mm, \epsilon_r = 9.7, H \approx 5h$, [5]

Figure 5: CMS - ϵ_{eff} x $Freq.(GHz)$



$H = 0.80mm, h = 0.20mm, W = 0.14mm, S = 0.28m, L = 2.00mmm, \epsilon_r = 12.9$. [6]

Figure 6: CBCW - ϵ_{eff} x $Freq.(GHz)$

References

[1] Tatsuo Itoh. "Overview of quasi-planar transmission lines". *IEEE Transactions on Microwave Theory and Techniques*, 37:275–280, February 1989.

[2] R. Sorrentino. *Transverse Resonance Technique - in Numerical in Tecniques for Microwave and Millimeter-Wave Passive Structures*. cap. 11, T. Itoh, Ed., John Wiley and Sons, Inc., New York, New York, 1989.

[3] Alfrêdo Gomes Neto. *An Alternative Formulation of the Transverse Resonance Technique (in Portuguese)*. Dr. Tese, UFPB, Campina Grande, Paraíba, Brazil, December 1994.

[4] Eikichi Yamashita and Kazuhiko Atsuki. "Analysis of microstrip-like transmission lines by nouniform discretization of integral equations". *IEEE Transactions on Microwave Theory and Techniques*, 24:195–200, April 1976.

[5] M. Kirschning and R. H. Jansen. "Accurate wide-range design equations for the frequency-dependent characteristic of parallel coupled microstrip lines". *IEEE Transactions on Microwave Theory and Techniques*, 32:83–90, January 1984.

[6] S. Aditya, R. R. Kumar, and D. Chadha. "Modes of a shielded conductor-backed coplanar waveguide". *Electronics Letters*, 30:146–148, January 1994.

SESSION 12:

MOM

Chairs: A. Peterson, R. Ziolkowski

MOMENT METHOD ANALYSIS OF DIELECTRIC COVERED RADIATING SLOTS USING ALTERNATIVE GREEN'S FUNCTION APPROACH

S CHRISTOPHER, VVS PRAKASH, AK SINGH
AND N BALAKRISHNAN*

ELECTRONICS AND RADAR DEVELOPMENT ESTABLISHMENT
BANGALORE, INDIA
** INDIAN INSTITUTE OF SCIENCE, BANGALORE, INDIA*

ABSTRACT:- The dielectric covered radiating slot in the broad wall of the rectangular waveguide has been analyzed. An alternative method of using both electric and magnetic vector potentials for the derivation of spectral domain Green's function has been presented. The efficiency of the present method has been pointed out. To validate the analysis, the derived dielectric Green's function has been applied to shunt and series slots. The numerical results have been compared with the published results. The problems encountered in the numerical integration have been discussed.

1. INTRODUCTION

Waveguide slots are well suited for array applications because of their properties like control over amplitude, phase and polarization. A dielectric substrate layer over the exterior of the array is used extensively for practical considerations. The presence of dielectric cover (or) layer will detune the individual slots which in turn leads to pattern detoriation. Hence, the electrical properties of the radiating elements with dielectric sheet needs tobe studied. The dielectric covered slots were studied by Bailey in 1969[1]. He used a single basis function and derived expressions for slot admittance by using conservation of power at the slot aperture. The study of waveguide slots radiating into free space is well advanced. Rengarajan studied the centered-inclined slot radiating into free space[2]. Katehi characterized the dielectric covered longitudinal offset radiating slot using moment method[3].

This paper presents a detailed study on the dielectric covered longitudinal offset and centered-inclined radiating slots on the broad wall of rectangular waveguide. Moment method has been used for obtaining the resonant characteristics of the radiating element. A simplified method has been followed in the derivation of external Green's function. The region external to the waveguide is divided in to two layers and in each layer, the electromagnetic fields are expanded in terms of a set of vector wave functions namely $A_z(x,y,z)$ and $F_z(x,y,z)$ in contrast to the earlier method[3]. The tangential components of the fields are matched at the junctions of the two layers and the tangential magnetic field due to a dirac delta source at the slot aperture which in other words is the external Green's function has been found out. The resulting expression is less complicated and hence computationally less expensive when compared to the approach of using only the electric vector potential for the derivation[3].

2. THEORY

The geometry of the slot with dielectric cover is shown in Fig.1. The slot is assumed to be narrow so that the only significant component of the electric field lies in x-direction. The slot is covered by a dielectric layer of thickness 'h'.

Using Equivalence principle, the x-directed electric field is replaced by a z-directed magnetic current as

$$M = \hat{n} \times E \qquad \text{.....(1)}$$

In the absence of any media discontinuity, the z-directed magnetic current gives rise to only the z-component of magnetic vector potential F_Z. But when the magnetic current is placed at the media discontinuity, in addition to F_Z one more component of F has to be considered to satisfy boundary condition. One approach is to use F_Z and F_y components. Second approach is to expand the electromagnetic fields in terms of the vector potentials normal to the media discontinuity. Traditionally, the problem of dielectric covered slot in an infinite ground plane has been dealt using first approach[3]. The method presented in this paper uses both the electric and magnetic vector potentials for deriving the magnetic field Green's function.

For the sake of comparison, the spatial domain expression of the Green's function is given below. The tangential magnetic field at the slot aperture is given by[3],

$$H_{\tan} = \iint K_{zz}(r/r').M_s(r')ds' \qquad \text{....(2.a)}$$

where

$$K_{zz}(r/r') = k_d^2 G_{zz}^d + \frac{\partial^2}{\partial z^2} G_{zz}^d + \frac{\partial^2}{\partial y \partial z} G_{yz}^d \qquad \text{....(2.b)}$$

with G_{zz}^d *and* G_{yz}^d being the dielectric Green's functions given by,

$$G_{zz}^d = \frac{-j\omega\varepsilon_o\varepsilon_r}{2\pi k_d^2} \int J_o(\lambda \mid \bar{\rho} - \bar{\rho}' \mid) \frac{\lambda}{u} \frac{u\cosh[u(-h+y)] + \varepsilon_r u_o \sinh[u(-h+y)]}{\varepsilon_r u_o \cosh(uh) + u\sinh(uh)} d\lambda \qquad \text{....(3.a)}$$

$$G_{yz}^d = \frac{-j\omega\varepsilon_r}{2\pi k_d^2}(1-\varepsilon_r)\cos\phi \int J_1(\lambda \mid \bar{\rho} - \bar{\rho}' \mid) \frac{\lambda^2}{u\cosh(uh) + u_o \sinh(uh)} \frac{\sinh(uy)}{\varepsilon_r u_o \cosh(uh) + u\sinh(uh)} d\lambda$$

where $u_o = \sqrt{\lambda^2 - k_o^2}$ and $u = \sqrt{\lambda^2 - k_d^2}$ .....(3.b)

The above method of finding the Green's function of F_z *and* F_y leads to the presence of second order derivatives w.r.t. y and z. The computation of the partial derivatives of dielectric Green's functions is a difficult task. An alternate approach has been followed here to reduce the complexity of the tangential magnetic field at the slot aperture. In the approach outlined below, the problem is formulated in such a way that the Green's function for the magnetic field is found out directly, thus avoiding the partial derivatives.

The spatial domain and the spectral domain relation is

$$F(x,y,z) = \frac{1}{2\pi} \iint \tilde{F} e^{-jk_x x} e^{-jk_z z} dk_x dk_z \qquad \text{....(4.a)}$$

$$\tilde{F}(k_x,y,k_z)=\frac{1}{2\pi}\iint F e^{jk_x x}e^{jk_z z}dxdz \qquad \ldots.(4.b)$$

The electromagnetic fields in the dielectric layer and in the free space are expressed in terms of a set of vector potentials $A^i(x,y,z)$ and $F^i(x,y,z)$ where

$$A^i(x,y,z)=A^i_y(x,y,z)\hat{y} \qquad \ldots.(5)$$

$$F^i(x,y,z)=F^i_y(x,y,z)\hat{y} \qquad \ldots.(6)$$

which satisfies the wave equation:

$$(\nabla^2+k_o^2)f(x,y,z)=0 \qquad \ldots.(7)$$

where f(x,y,z) can be either $A^i(x,y,z)$ or $F^i(x,y,z)$.

The electromagnetic fields are related to the vector potentials as

$$H=\frac{\nabla \mathrm{X} A}{\mu}+\frac{1}{j\omega\mu}[\nabla(\nabla.F)+k_o^2F] \qquad \ldots.(8)$$

$$E=-\nabla \mathrm{X}F+\frac{1}{j\omega\mu\varepsilon}[\nabla(\nabla.A)+k_o^2A] \qquad \ldots.(9)$$

The corresponding Fourier transformed equations are

$$\tilde{E}^i_x=-jk_z\tilde{F}^i_y-\frac{k_x}{\omega\mu\varepsilon}\frac{\partial\tilde{A}^i_y}{\partial y} \qquad \tilde{E}^i_z=jk_x\tilde{F}^i_y-\frac{k_z}{\omega\mu\varepsilon}\frac{\partial\tilde{A}^i_y}{\partial y}$$

$$\tilde{H}^i_x=\frac{jk_z\tilde{A}^i_y}{\mu}-\frac{k_x}{\omega\mu}\frac{\partial\tilde{F}^i_y}{\partial y} \qquad \tilde{H}^i_z=\frac{-jk_x\tilde{A}^i_y}{\mu}-\frac{k_z}{\omega\mu}\frac{\partial\tilde{F}^i_y}{\partial y} \qquad \ldots.(10)$$

Solving Eq.(10), at y = 0, for $\frac{\partial\tilde{A}^i_y}{\partial y}$ and $\tilde{F}^i_y$ gives

$$\tilde{A}^i=\frac{\partial\tilde{A}^i_y}{\partial y}=\frac{-k_x\tilde{E}^i_x}{(k_x^2+k_z^2)}\omega\mu\varepsilon \qquad \ldots.(11.a)$$

$$\tilde{F}^i_y=\frac{jk_z\tilde{E}^i_x}{(k_x^2+k_z^2)} \qquad \ldots.(11.b)$$

The solution of wave equation Eq(7), subjected to appropriate boundary conditions gives rise to

$$\frac{\tilde{A}_y}{\tilde{A}^i_y}=\frac{j}{u_d}\frac{[u_d+j\varepsilon_r u_o\tan(hu_d)]}{[\varepsilon_r u_o+ju_d\tan(hu_d)]}=\frac{j}{u_d}f_a \qquad \ldots.(12.a)$$

$$\frac{\tilde{F}_y'}{\tilde{F}_y} = \frac{u_d}{j}\cdot\frac{[u_o + ju_d\tan(hu_d)]}{[u_d + ju_o\tan(hu_d)]} = \frac{u_d}{j} f_f \qquad \ldots.(12.b)$$

where $u_d^2 = k_d^2 - k_x^2 - k_z^2$ and $u_o^2 = k_o^2 - k_x^2 - k_z^2$.

Substituting the Eq.(11) to (12) in Eq.(10) leads to

$$\tilde{H}_z = [\frac{-\omega\varepsilon_o\varepsilon_r k_x^2}{(k_x^2 + k_z^2)u_d} f_a - \frac{k_z^2 u_d}{(k_x^2 + k_z^2)\omega\mu} f_f]\tilde{E}_x \qquad \ldots.(13)$$

The Eq.(13) gives the magnetic field in spectral domain and its counter part in spatial domain is obtained from Fourier inverse transformation. The advantage of this formulation is the complex spatial derivatives are avoided and the resulting expression is simplified. It expresses the magnetic field directly in terms of slot aperture electric field. The spectral functions f_a and f_f have multiple TE and TM poles. Their respective contributions can be computed from the two terms on the right hand side of Eq.(13). Using only the vector potential 'F' in the derivation of dielectric Green's function leads to the presence of both TE and TM singularities in the second term of the Eq.(13) in addition to the first term. This complicates the evaluation of integral.

RESULTS:

To validate the procedure, the above developed theory is applied to solve the problem of slot radiating in to finite dielectric slab. The expression for magnetic field derived in Eq.(14) has been used as external scattered magnetic field and for the internal scattered fields, Stevenson's Green's functions are used[4]. The unknown slot field is expanded into entire domain sinusoidal functions. The coupled integral equations resulting from matching the tangential magnetic fields at the top and bottom slot apertures are converted into matrix equation using moment method. The matrix equation is solved by direct inversion.

A generalized moment method code has been developed which uses the above presented alternative expressions for characterizing the longitudinal offset (shunt) and the centered-inclined (series) radiating slots. To validate the approach, the method presented here has been applied for computing the resonant length and the resonant conductance of an isolated shunt slot radiating into a dielectric slab of ε_r=2.62 and a thickness of 0.062" (Fig.2 and Fig.3). The results are presented for various slot offsets with and without wall thickness and are found to be in good agreement with published results[3]. For a centered-inclined radiating slot, the resonant length and the resonant conductance have been computed for ε_r=1.0 and ε_r=2.62. The results are presented in Fig.4 and Fig.5 over a range of slot tilts. For the case of ε_r=1.0, as can be observed, the data obtained by using the alternate Green's function matches well with the earlier published results[2]. Because of the lack of published literature, the dielectric covered centered-inclined radiating slot data has been presented without any comparison. Since the above developed theory has already been validated for longitudinal offset slot, the theory and the results generated are reliable for centered-inclined case also.

CONCLUSION:

A simplified expression has been derived for the dielectric Green's function of a slot radiating in to a finite dielectric slab. The above developed theory has been applied to characterize the longitudinal offset and the centered inclined radiating slots. It has been found that the Green's function presented in this paper reduces the computational complexity without effecting the accuracy of the moment method.

REFERENCES:

[1] M.C. Bailey,"The impedance properties of dielectric-covered narrow radiating slots in the broad face of a rectangular waveguide," IEEE Trans. Antennas Propagat., vol. AP-18,pp.596-603, Sept. 1970.

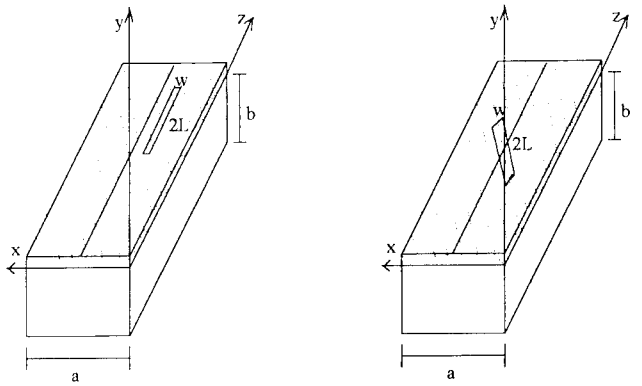
[2] S.R. Rengarajan," Scattering characteristics of centered-inclined slot in the broad wall of a rectangular waveguide," IEE Proc.H,1990,137, pp.343-348.

[3] P. B. Katehi," Dielectric - covered waveguide longitudinal slots with finite wall thickness", IEEE Trans. Antennas Propagat., pp.1039-1045, July 1990.

[4] A.F. Stevenson," Theory of slots in rectangular waveguides', J. Appl. Phys., 19, pp.24-38.

ACKNOWLEDGMENTS:

Authors wish to thank Mr. KU Limaye, Sc'F', LRDE for the facilities provided without which this work would not have been completed and Mr. NP Ramasubba Rao, Director, LRDE for his kind permission to publish this work.



(a) Longitudinal offset radiating slot (b) Centered-inclined radiating slot

Fig.1 Dielectric covered Slot in the Broad wall of Rectangular Waveguide

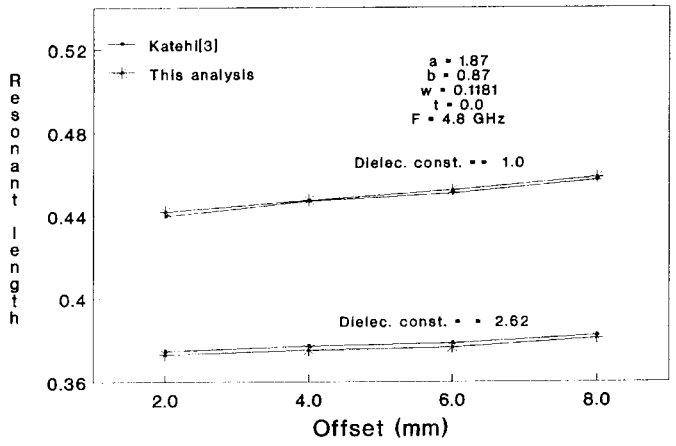


Fig.2 Resonant Length versus offset.

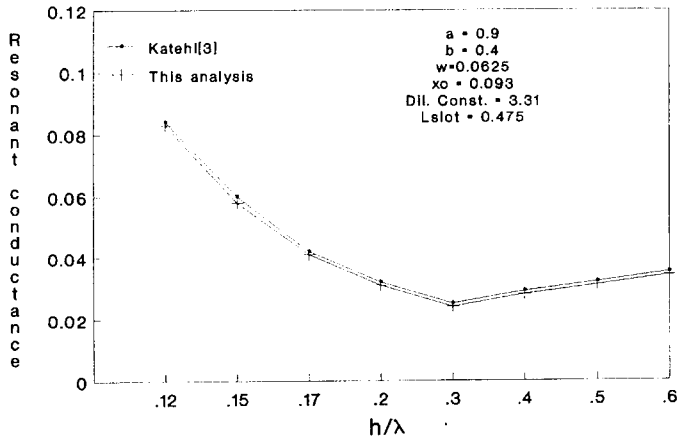


Fig.3 Resonant Conductance versus Dielectric thcikness.

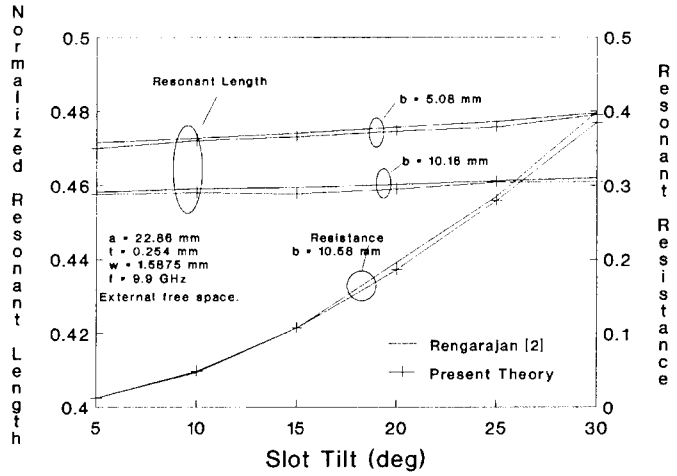


Fig.4 Norm. Resonant Length and Resistance .vs. Tilt

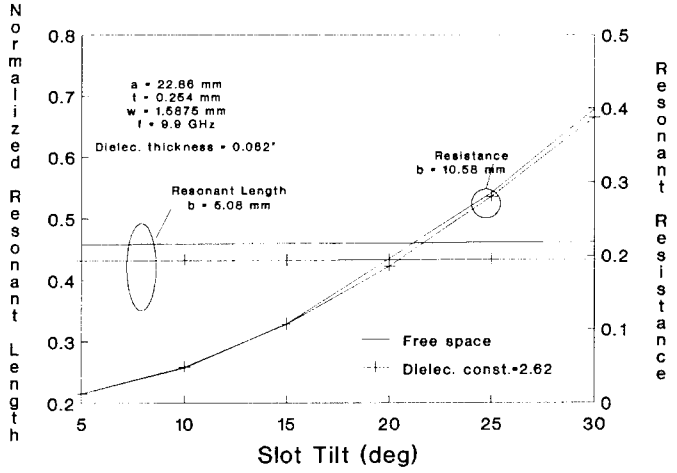


Fig.5 Norm. Resonant Length and Resistance .vs. Tilt

Computation of E-field Distribution of Low Gain Antenna on Conducting Body of Revolution*

Liu Jianxin
EMC Lab, Box 171, Beijing University of Post and Telecommunication, Beijing, China, 100088
Phone: 2013388-2451(work)
8379037(home)

Wang Jueqi
Institute of Spacecraft System Engineering, CAST, Box 2417-24, Beijing, China, 100081
Phone: 8378258(work)
2019988-612(home)

Gao Yougang
EMC Lab, Box 171, Beijing University of Post and Telecommunication, Beijing, China, 100088
Phone: 2013388-2451(work)
2019988-722(home)

Abstract

The E-field distribution of low gain antenna on conducting body will help to arrange antennas and solve Electromagnetic Compatibility (EMC) problems. In this article, resonant linear antenna on conducting body of revolution (BOR) is discussed. Moment method and Fourier analysis method are used to obtain the BOR surface current excited by the antenna. From the antenna current and the surface current, the E-field distribution on BOR surface is obtained. The distribution results are shown in figures, and the variation of E-field strength over the whole body surface can be expressed out clearly.

1 Introduction

With the developing of space technology, spacecrafts are becoming more and more complex. It is essential to arrange all the spacecraft antennas reasonably and solve the Electromagnetic Compatibility (EMC) problems. High gain antennas have narrow radiation patterns, and their influence on other antennas is small. On the other hand, low gain antennas have wide radiation patterns, their influence is strong. The distribution of surface current and E-field excited by a low gain antenna on the spacecraft surface is helpful to antenna arrangement and EMC. In articles [1][2][3], the computation and figures of surface current distribution excited by a resonant linear antenna on conducting body of revolution (BOR) have been discussed. In this article, we focus our discussion on the E-field distribution under the same conditions. For the reason of simplification, the current distribution on the resonant linear antenna is assumed to be sinusoidal standing wave distribution, the body's influence on the antenna current distribution is ignored, and the conducting body of revolution is limited with geometry for resonant region.

The time factor is $e^{j\omega t}$.

2 Analysis

The conducting body of revolution to be discussed here and its coordination are shown in Fig 1. A resonant linear antenna with arbitrary shape is attached on the body. By solving the magnetic field integral equation (MFIE), the surface current can be obtained[4]. From the integral of the antenna current on antenna itself and that of the surface current over BOR surface, the E-field distribution is obtained.

2.1 The Magnetic Field Integral Equation and Linearization[4]

From the Maxwell's equations, the following MFIE for the surface current density $\vec{\sigma}$ on the surface of a conducting body in an incident field with magnetic field strength $\vec{H}^{inc}$ may be derived:

$$\vec{\sigma}(p) = 2\vec{\sigma}^{pr}(p) - \frac{1}{2\pi}\iint_{s}\hat{n}\times\vec{\sigma}(q)\times\nabla\frac{e^{-jk\rho}}{\rho}ds' \qquad (2.1.1)$$

* This work was supported by National Nature Science Foundation of China.

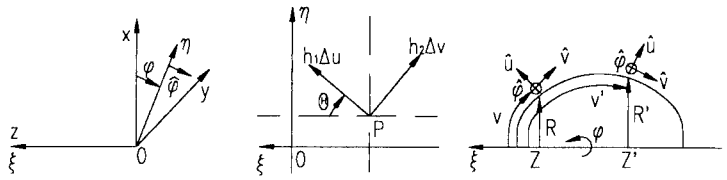


Fig 1 Conducting Body of Revolution and Its Coordination

Here, $\hat{n}$ is an outward unit normal vector to the surface, ρ is the distance between the observation point p and the source point q on area element ds', k is the wave number in free space, and $\vec{\sigma}^{pr}(\xi,\eta)=\hat{n}\times\vec{H}^{inc}(\xi,\eta)$. The integral is carried out on the body surface. The symbol ∇ denotes a gradient with respect to the primed coordinates.

In order to express the surface current density in terms of generatrix line length v and azimuth angle φ, a new coordinate system (u,v,φ) is introduced.

The $\vec{\sigma},\vec{\sigma}^{pr},e^{-jk\rho}/\rho$ can be expressed as Fourier series:

$$\vec{\sigma}(v,\varphi)=\sum_{m=-\infty}^{+\infty}\vec{\sigma}_m(v)e^{jm\varphi}=\sum_{m=-\infty}^{+\infty}(\sigma_{vm}(v)\hat{v}+\sigma_{\varphi m}(v)\hat{\varphi})e^{jm\varphi} \qquad (2.1.2)$$

$$\vec{\sigma}^{pr}(v,\varphi)=\sum_{m=-\infty}^{+\infty}\vec{\sigma}^{pr}_m(v)e^{jm\varphi}=\sum_{m=-\infty}^{+\infty}(\sigma^{pr}_{vm}(v)\hat{v}+\sigma^{pr}_{\varphi m}(v)\hat{\varphi})e^{jm\varphi} \qquad (2.1.3)$$

$$\frac{e^{-jk\rho}}{\rho}=\sum_{m=-\infty}^{+\infty}S_m(u,u',v,v')e^{jm(\varphi-\varphi')} \qquad (2.1.4)$$

Using (2.1.2), (2.1.3) and (2.1.4), the integral equation (2.1.1) can be transferred into the following integral equations for each Fourier harmonics (m) of v and φ components.

$$\sigma_{vm}=2\sigma^{pr}_{vm}-\int_{v'}(P_{m11}\sigma_{vm}+P_{m12}\sigma_{\varphi m})R'dv' \qquad (2.1.5)$$

$$\sigma_{\varphi m}=2\sigma^{pr}_{\varphi m}-\int_{v'}(P_{m21}\sigma_{vm}+P_{m22}\sigma_{\varphi m})R'dv' \qquad (2.1.6)$$

P_{m11}, P_{m12}, P_{m21}, P_{m22} are the functions of Θ, Θ', Z, Z', R, R', S_m.

Using pulse function for expansion and point-matching, the integral equations (2.1.5) and (2.1.6) become linear equations.

$$\begin{bmatrix}[I+C_{m11}] & [C_{m12}]\\ [C_{m21}] & [I+C_{m22}]\end{bmatrix}\begin{bmatrix}[\sigma_{vm}]\\ [\sigma_{\varphi m}]\end{bmatrix}=\begin{bmatrix}2[\sigma^{pr}_{vm}]\\ 2[\sigma^{pr}_{\varphi m}]\end{bmatrix} \qquad (2.1.7)$$

The primary surface current associated with the incident $\vec{H}^{inc}$ from the linear antenna is still unknown, and will be discussed in next section. Solving (2.1.7), the current distribution $\vec{\sigma}$ on BOR surface can be obtained.

2.2 The Formulas of Primary Surface Current Associated with the Incident H^{inc} from Arbitrary Linear Antenna[4]

A source, whose volume current density is $\vec{J}$, produces the incident $\vec{H}^{inc}$, which produces $\vec{\sigma}^{pr}$. The

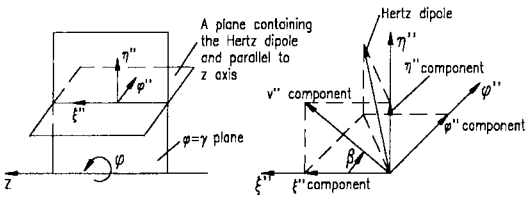


Fig 2 An arbitrary Hertz dipole

$\vec{\sigma}^{pr}$ can be expressed as the following integral:

$$\vec{\sigma}^{pr} = -\frac{1}{4\pi}\iiint_{v'} \hat{n} \times \vec{J} \times \nabla \frac{e^{-jk\rho}}{\rho} dv' \qquad (2.2.1)$$

Similar to (2.1.1), (2.2.1) can be expressed as the following:

$$\sigma^{pr}_{vm} = -\frac{1}{2}\int (P''_{m11} J_{v''m} + P''_{m12} J_{\varphi''m}) R'' du'' dv'' \qquad (2.2.2)$$

$$\sigma^{pr}_{\varphi m} = -\frac{1}{2}\int (P''_{m21} J_{v''m} + P''_{m22} J_{\varphi''m}) R'' du'' dv'' \qquad (2.2.3)$$

P''_{m11}, P''_{m12}, P''_{m21}, P''_{m22} are the functions of Θ, β, Z, Z'', R, R'', S''_m

The line current density on linear antenna should be expressed as volume current density, so that the σ^{pr}_{vm} and $\sigma^{pr}_{\varphi m}$ can be obtained through (2.2.2) and (2.2.3) respectively.

As shown in Fig 2, a Hertz dipole *idl* is expressed as following:

$$\begin{aligned} idl\hat{l} &= i_{\xi''} d\xi'' \hat{\xi}'' + i_{\eta''} d\eta'' \hat{\eta}'' + i_{\varphi''} R'' d\varphi'' \hat{\varphi}'' \\ &= i_{v''} dv'' \hat{v}'' + i_{\varphi''} R'' d\varphi'' \hat{\varphi}'' \end{aligned} \qquad (2.2.4)$$

$$i_{v''} dv'' = \sqrt{\cos^2 \alpha_{\xi''} + \cos^2 \alpha_{\eta''}}\, idl \qquad (2.2.5)$$

$$i_{\varphi''} R'' d\varphi'' = \cos\alpha_{\varphi''}\, idl \qquad (2.2.6)$$

$$tg\beta = \frac{\cos\alpha_{\eta''}}{\cos\alpha_{\xi''}} \qquad (2.2.7)$$

where $\alpha_{\xi''}$, $\alpha_{\eta''}$, $\alpha_{\varphi''}$ are the angles between the Hertz dipole and ξ'',η'',φ'' respectively.

$$J_{v''m} R'' du'' dv'' = \frac{i_{v''} e^{-jm\gamma}}{2\pi} \delta(v'' - v''_q) dv'' \qquad (2.2.8)$$

$$J_{\varphi''m} R'' du'' dv'' = \frac{i_{\varphi''} R'' e^{-jm\gamma}}{2\pi} \delta(v'' - v''_q) dv'' \qquad (2.2.9)$$

From (2.2.4) to (2.2.9), the integral equations (2.2.2) and (2.2.3) are transferred into the following equations for σ^{pr}_{vm} and $\sigma^{pr}_{\varphi m}$ respectively.

$$\sigma^{pr}_{vm} = -\frac{1}{4\pi}\int_l (P''_{m11}\sqrt{\cos^2\alpha_{\xi''} + \cos^2\alpha_{\eta''}} + P''_{m12}\cos\alpha_{\varphi''})e^{-jm\gamma}idl \qquad (2.2.10)$$

$$\sigma^{pr}_{\varphi m} = -\frac{1}{4\pi}\int_l (P''_{m21}\sqrt{\cos^2\alpha_{\xi''} + \cos^2\alpha_{\eta''}} + P''_{m22}\cos\alpha_{\varphi''})e^{-jm\gamma}idl \qquad (2.2.11)$$

The $\alpha_{\xi''}$, $\alpha_{\eta''}$, $\alpha_{\varphi''}$, γ, β are function of the antenna length l.

2.3 E-Field Computation Formulas

In this section, the E-field of an arbitrarily placed Hertz dipole is analyzed. The effect of the antenna current and the surface current on the body can be regarded as that of many Hertz dipoles with different site, orientation, phase and strength. The whole E-field distribution is then obtained from the sum of these dipoles' near fields.

Suppose a z-direction Hertz dipole $i\Delta l$ is at source point (x`,y`,z`), as shown in Fig.3, and the field point is (x,y,z). We have the following formulas for obtaining the E-field:

$$\vec{E} = -j\omega\vec{A} + \frac{\nabla\nabla\cdot\vec{A}}{j\omega\varepsilon\mu} = \frac{1}{j\omega\varepsilon\mu}(k^2\vec{A} + \nabla\nabla\cdot\vec{A}) \qquad (2.3.1)$$

$$\vec{A} = \frac{\mu}{4\pi}\iiint_V F_1\vec{J}dv = \frac{\mu i\Delta l}{4\pi}F_1\hat{z} \qquad (2.3.2)$$

$$R = \sqrt{(x-x')^2 + (y-y')^2 + (z-z')^2} \qquad (2.3.3)$$

$$F_1 = \frac{e^{-jkR}}{R} \qquad (2.3.4)$$

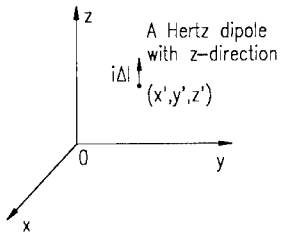


Fig 3 A Hertz dipole and the coordination

Here $\vec{A}$ has only z component. Then we have:

$$\vec{E} = \frac{1}{j\omega\varepsilon\mu}(k^2 A_z\hat{z} + \frac{\partial^2 A_z}{\partial x\partial z}\hat{x} + \frac{\partial^2 A_z}{\partial y\partial z}\hat{y} + \frac{\partial^2 A_z}{\partial z\partial z}\hat{z}) \qquad (2.3.5)$$

$$\frac{\partial A_z}{\partial x} = \frac{\mu i\Delta l}{4\pi}\frac{\partial F_1}{\partial R}\frac{\partial R}{\partial x} = \frac{\mu i\Delta l}{4\pi}(x-x')F_2 \qquad (2.3.6)$$

$$\frac{\partial A_z}{\partial y} = \frac{\mu i\Delta l}{4\pi}\frac{\partial F_1}{\partial R}\frac{\partial R}{\partial y} = \frac{\mu i\Delta l}{4\pi}(y-y')F_2 \qquad (2.3.7)$$

$$\frac{\partial A_z}{\partial z} = \frac{\mu i\Delta l}{4\pi}\frac{\partial F_1}{\partial R}\frac{\partial R}{\partial z} = \frac{\mu i\Delta l}{4\pi}(z-z')F_2 \qquad (2.3.8)$$

$$F_2 = -\frac{(jkR+1)}{R^3}e^{-jkR} \qquad (2.3.9)$$

$$\frac{\partial^2 A_z}{\partial x\partial z} = \frac{\mu i\Delta l}{4\pi}(x-x')\frac{\partial F_2}{\partial R}\frac{\partial R}{\partial z} = \frac{\mu i\Delta l}{4\pi}(x-x')(z-z')F_3 \qquad (2.3.10)$$

$$\frac{\partial^2 A_z}{\partial y \partial z} = \frac{\mu i \Delta l}{4\pi}(y-y')\frac{\partial F_2}{\partial R}\frac{\partial R}{\partial z} = \frac{\mu i \Delta l}{4\pi}(y-y')(z-z')F_3 \qquad (2.3.11)$$

$$\frac{\partial^2 A_z}{\partial z \partial z} = \frac{\mu i \Delta l}{4\pi}\left[(z-z')\frac{\partial F_2}{\partial R}\frac{\partial R}{\partial z} + F_2\frac{\partial (z-z')}{\partial z}\right] = \frac{\mu i \Delta l}{4\pi}\left[(z-z')^2 F_3 + F_2\right] \qquad (2.3.12)$$

$$F_3 = \frac{3 + 3jkR - k^2R^2}{R^5}e^{-jkR} \qquad (2.3.13)$$

Then, the E-field at point (x, y, z) produced by the z-direction Hertz dipole can be given as following:

$$\vec{E}_{z'} = E_{z'x}\hat{x} + E_{z'y}\hat{y} + E_{z'z}\hat{z} \qquad (2.3.14)$$

$$E_{z'x} = \frac{30i\Delta l}{jk}F_3(x-x')(z-z') \qquad (2.3.15)$$

$$E_{z'y} = \frac{30i\Delta l}{jk}F_3(y-y')(z-z') \qquad (2.3.16)$$

$$E_{z'z} = \frac{30i\Delta l}{jk}\left[k^2 F_1 + F_3(z-z')^2 + F_2\right] \qquad (2.3.17)$$

For the same reason, the Hertz dipole at point (x',y',z') being along x-direction or y-direction, produces E-field $\vec{E}_{x'}$ or $\vec{E}_{y'}$ at point (x,y,z) as following:

$$\vec{E}_{x'} = E_{x'x}\hat{x} + E_{x'y}\hat{y} + E_{x'z}\hat{z} \qquad (2.3.18)$$

$$E_{x'x} = \frac{30i\Delta l}{jk}\left[k^2 F_1 + F_3(x-x')^2 + F_2\right] \qquad (2.3.19)$$

$$E_{x'y} = \frac{30i\Delta l}{jk}F_3(y-y')(x-x') \qquad (2.3.20)$$

$$E_{x'z} = \frac{30i\Delta l}{jk}F_3(z-z')(x-x') \qquad (2.3.21)$$

$$\vec{E}_{y'} = E_{y'x}\hat{x} + E_{y'y}\hat{y} + E_{y'z}\hat{z} \qquad (2.3.22)$$

$$E_{y'x} = \frac{30i\Delta l}{jk}F_3(x-x')(y-y') \qquad (2.3.23)$$

$$E_{y'y} = \frac{30i\Delta l}{jk}\left[k^2 F_1 + F_3(y-y')^2 + F_2\right] \qquad (2.3.24)$$

$$E_{y'z} = \frac{30i\Delta l}{jk}F_3(z-z')(y-y') \qquad (2.3.25)$$

Regarding an Hertz dipole with arbitrary direction, its total field $d\vec{E}$ can be expressed as following.

$$i\Delta l\hat{l} = c_x i\Delta l\hat{x} + c_y i\Delta l\hat{y} + c_z i\Delta l\hat{z} \qquad (2.3.26)$$

where c_x, c_y and c_z are direction cosines of $\hat{l}$.

$$d\vec{E} = dE_x\hat{x} + dE_y\hat{y} + dE_z\hat{z} \qquad (2.3.27)$$

$$dE_x = \frac{30i\Delta l}{jk}\left\{c_x\left[k^2 F_1 + F_3(x-x')^2 + F_2\right] + c_y F_3(x-x')(y-y') + c_z F_3(x-x')(z-z')\right\} \quad (2.3.28)$$

$$dE_y = \frac{30i\Delta l}{jk}\left\{c_y\left[k^2 F_1 + F_3(y-y')^2 + F_2\right] + c_x F_3(y-y')(x-x') + c_z F_3(y-y')(z-z')\right\} \quad (2.3.29)$$

$$dE_z = \frac{30i\Delta l}{jk}\left\{c_z\left[k^2 F_1 + F_3(z-z')^2 + F_2\right] + c_x F_3(z-z')(x-x') + c_y F_3(z-z')(y-y')\right\} \quad (2.3.30)$$

The E-field over the body of revolution is composed of the linear antenna's field and the body surface current's field. For the linear antenna, given its geometry parameter and current distribution, its field is obtained from the integral of $d\vec{E}$ along antenna length.

$$\vec{E}_l = \int_{\substack{Antenna \\ length}} d\vec{E} \quad (2.3.31)$$

From section 2.1, the body surface current is obtained as (2.3.33) under the (u,v,φ) coordinates. For the convenience of calculation, they should be transferred into (x,y,z) coordinates, as shown in (2.3.32).

$$\begin{cases} i\Delta l c_x = (\sigma_v \cos\varphi' \cos\Theta' - \sigma_\varphi \sin\varphi')R'dv'd\varphi' \\ i\Delta l c_y = (\sigma_v \sin\varphi' \cos\Theta' - \sigma_\varphi \cos\varphi')R'dv'd\varphi' \\ i\Delta l c_z = -\sigma_v \sin\Theta' R'dv'd\varphi' \end{cases} \quad (2.3.32)$$

$$\begin{cases} \sigma_v = \sum_{m=-\infty}^{+\infty} \sigma_{vm} e^{jm\varphi'} \\ \sigma_\varphi = \sum_{m=-\infty}^{+\infty} \sigma_{\varphi m} e^{jm\varphi'} \end{cases} \quad (2.3.33)$$

From the integral of $d\vec{E}$ over the body surface, the field contributed by the surface current is obtained.

$$\vec{E}_{BOR} = \iint_{\substack{BOR \\ surface}} d\vec{E} \quad (2.3.34)$$

The total E-field, therefore, is:

$$\vec{E} = \vec{E}_l + \vec{E}_{BOR} \quad (2.3.35)$$

The normal component of the E-field on the conducting body of revolution is most concerned, and the computation formula is in (2.3.36).

$$E_{normal} = (E_x \cos\varphi + E_y \sin\varphi)\sin\Theta + E_z \cos\Theta \quad (2.3.36)$$

Now, we have obtained all the formulas about E-field distribution computation. In next section, some examples are present.

3 Computations

The E-field distribution of a monopole on infinite plane, as shown in Fig. 4, is first computed. The result is compared with which is obtained by image method. The monopole is λ/4 high and with the current $\sin(k(\lambda/4-l))$ on it. The results of two methods are listed in Table 1, and they match well to each other. This proves our method right and suitable for E-field distribution computation.

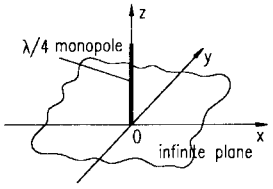


Fig 4 A monopole on infinite plane

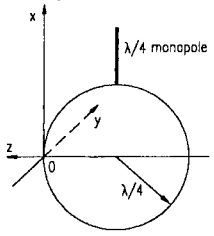


Fig 5 A monopole on conducting sphere

Another example is the E-field distribution of the same monopole on a conducting sphere whose radius is λ/4. The monopole's position and the associated coordination are shown in Fig 5. In Fig 6 and Fig 7, the E-Field normal component strength distribution along generatrix line length r and azimuth angle φ are plotted respectively. Shown in Fig 8 is a 3-dimension E-field distribution on the sphere surface. The three dimensions are the length r and the angle φ of the field position, and the E-field normal component strength. From these figures, it is clear that the E-field strength decreases rapidly with the increasing of the distance from the antenna.

Table 1 Results comparison of image method and the method in this article

Field Point	Image Method			Method in This Article		
(x,y,z)	E_x	E_y	E_z	E_x	E_y	E_z
(0.5,0.,0.5)	-38.71429	0.0	38.77425	-38.73227	0.0	38.78413
	+j15.63384	+j0.0	+j22.92286	+j15.61806	+j0.0	+j22.9743
(0.5,0.,0.25)	-40.89494	0.0	40.87492	-40.8786	0.0	40.89369
	+j11.29625	+j0.0	+j71.29628	+j11.30152	+j0.0	+j71.3437
(0.5,0.,0.1)	-19.6096	0.0	39.33406	-19.5676	0.0	39.3349
	-j9.390205	+j0.0	+j94.72982	-j9.36906	+j0.0	+j94.76012
(0.5,0.,0.05)	-10.05461	0.0	39.0087	-5.871329	0.0	39.60166
	-j5.122965	+j0.0	+j98.68033	-j6.735781	+j0.0	+j99.51534

4 Conclusion

We have discussed a method to obtain the linear low gain antenna's E-field distribution on a conducting body of revolution. The distribution variation trend can be clearly expressed out by the data computed, the 2-dimension figures and the 3-dimension figure. While we arrange other antennas, we can choose among those sites where the E-field is weak, and thus reduce the probability of antenna interference. On the other hand, if antenna is in the area with strong E-field, EMI may exist, and we can change the antenna to other site where the E-field is weaker.

Reference

[1]Wang Jueqi, Liu Jianxin, "The Radiation of a Arbitrary Hertz Dipole outside a Conducting Body of Revolution", Proceedings of the Chinese 8th Linear and Small Antennas Conference, pp224-227, November, 1992, Suzhou, China (in Chinese).

[2]Wang Jueqi, "Research on the Current Excited by Linear Antennas on the Satellite Surface", Proceedings of International Symposium on EMC, pp203-206, May, 1992, Beijing, China.

[3]Wang Jueqi, Liu Jianxin, "Illustration of Current Distribution on Satellite's Surface for EMC", Proceedings of Chinese EMC-94 Symposium, pp204-207, March, 1994, Nanjing, China (in Chinese).

[4] Liu Jianxin, Yan Lubin, Wang Jueqi, "Computation of Radiation Property of Quadrafiliar Volute on Conducting Body of Revolution", Proceedings of the 3rd International Symposium on Antennas and EM Theory, pp43-47, September, 1993, Nanjing, China.

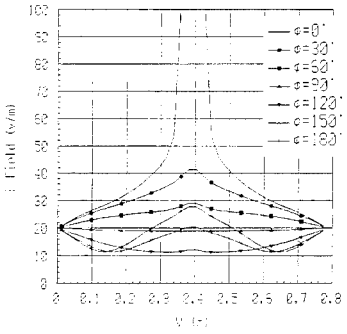


Fig 6 E-field distribution along generatrix line length

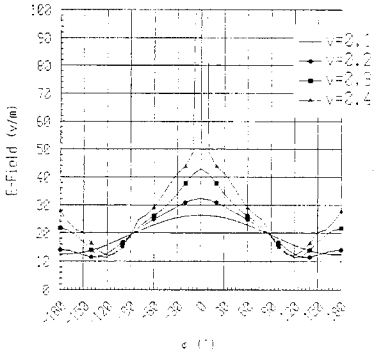


Fig 7 E-field distribution along azimuth angle

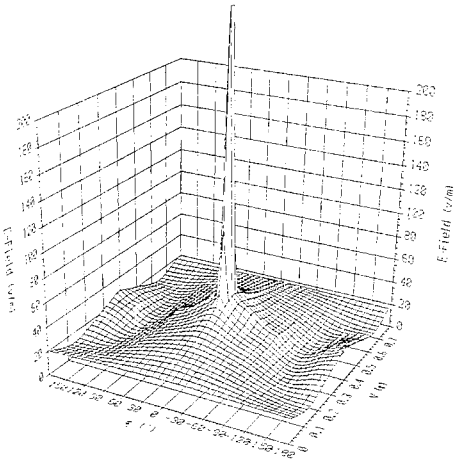


Fig 8 3-dimension figure of E-filed distribution

An Implementation of an Exact Scheme for Problem Decomposition Via the Use of Aperture Admittance

Debra L. Wilkes, Chung-Chi Cha, Thomas Krauss
Syracuse Research Corporation
Merrill Lane
Syracuse, NY 13210

1.0 Introduction

In this paper an approach is given for the practical solution of a class of large computational electromagnetics problems. While the application of a numerical method such as the Method of Moments (MOM) to a large problem is often not possible due to limitations in computer resources (speed and memory), this same problem can often be decomposed into smaller tractable problems. An excellent example of a target that is well suited to decomposition techniques is an aircraft where the jet engine cavities are naturally separated from the aircraft exterior by the aperture formed by the entrance to the inlet.

This decomposition can be performed without the loss of exactness by separating an original shape into an exterior surface and one or more interior regions. Each interior region is coupled to the exterior through an aperture. The solution of the interior problem(s) and the exterior problem can be performed independently as long as provisions are made to correctly pass the appropriate coupling information between the two solutions.

We can realize a computational saving by decomposing a large problem into two separate smaller problems. In addition to the computational savings, this problem decomposition allows for the convenient use of a hybrid approach where different techniques can be applied to their suitable respective portions of the target.

2.0 Formulation

The class of problems that are suitable for this type of problem decomposition is illustrated in Figure 1 which shows a generally shaped target with a cavity-like feature. The entire problem is decomposed into two separate problems: the interior problem and the exterior problem. The sources are assumed to exist in the exterior region. The interior region is bounded by the surface S_1 which is the cavity wall, and a surface S_a at the aperture. The exterior problem is defined by the surfaces S_2 and S_a. After the interior problem has been solved, we will apply the Method of Moments using subdomain basis functions to solve the exterior problem.

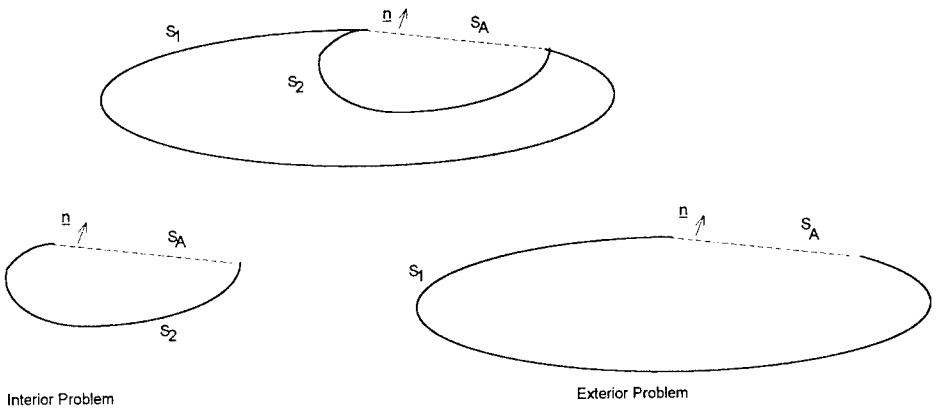


Figure 1. Decomposition of Original Problem into Two Separate Problems

In considering only the interior problem, the electric and magnetic fields cannot be determined. This is because the complete problem information is not available: the incident field and the shape of the exterior region are unknown. However, the uniqueness theorem tells us that the knowledge of the tangential electric field in the aperture, $\mathbf{E}_a$, is sufficient to determine all fields within the cavity. Consequentially, we can say that the tangential magnetic field in the aperture, $\mathbf{H}_a$, can be expressed as a function $\mathbf{E}_a$. This relationship can be expressed by using a generalized admittance of the aperture:

$$\mathbf{n}\mathbf{x}\mathbf{H}_a = \mathbf{Y}(\mathbf{E}_a) \qquad (1)$$

where $\mathbf{n}$ is the outward unit normal of the aperture and $\mathbf{Y}$ is the linear admittance operator that transforms $\mathbf{E}_a$ into $\mathbf{n}\mathbf{x}\mathbf{H}_a$. This admittance relates two "distributions." But when $\mathbf{E}_a$ and $\mathbf{n}\mathbf{x}\mathbf{H}_a$ are represented by their samples at discrete locations within the aperture, then $\mathbf{Y}$ will be of the form of a dense matrix. It should be noted that we have chosen this definition for $\mathbf{Y}$ instead of representing a relationship between $\mathbf{E}_a$ and $\mathbf{H}_a$. This was done to parallel the formulation used for an Impedance Boundary Condition (IBC). Thus, if $\mathbf{Y}$ was to be used to represent an IBC, it would take the form of a diagonal matrix since the IBC is a pointwise relationship between the two fields.

After the interior problem is solved, the next step begins with the hand-over of the admittance matrix to the exterior problem. We note that the interior problem may solved by an arbitrary means as long as is can be used to describe the aperture via the desired admittance matrix. We define the aperture characterization as consisting of the following information:

1. a set of N discrete points, $\{ \mathbf{P}_i \mid i = 1,...N\}$, in the aperture. The way in which they lie in the aperture is illustrated in Figure 2, which shows an aperture in a cylindrical body.

2. Two unit vectors, $(\mathbf{u}_i,\mathbf{v}_i)$, at each point in the aperture which are both tangent to the aperture surface

3. The aperture admittance matrix [Y] which is 2Nx2N in size which corresponds to the operator in Equation (1). The 2N samples correspond to the vector components alond the two specified directions at the N specified points. Thus, Equation (1) will have the form:

$$\begin{bmatrix} \mathbf{n}\times\mathbf{H}_a(\mathbf{P}_i)\cdot\mathbf{u}_i \\ \mathbf{n}\times\mathbf{H}_a(\mathbf{P}_i)\cdot\mathbf{v}_i \end{bmatrix} = \begin{bmatrix} \mathbf{Y}_{uu} & \mathbf{Y}_{uv} \\ \mathbf{Y}_{vu} & \mathbf{Y}_{vv} \end{bmatrix} \begin{bmatrix} \mathbf{E}_a(\mathbf{P}_i)\cdot\mathbf{u}_i \\ \mathbf{E}_a(\mathbf{P}_i)\cdot\mathbf{v}_i \end{bmatrix} \tag{2}$$

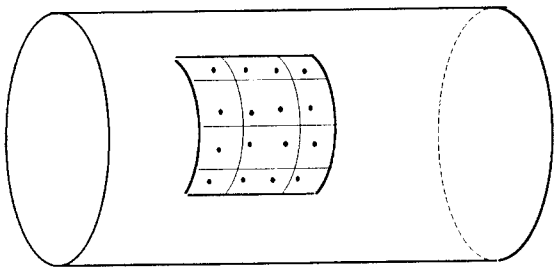


Figure 2. Distribution of Grid Points on an Aperture with a Rectangular Grid

The exterior problem is solved for using MOM where the equivalent electric and magnetic currents, $\mathbf{J} = \mathbf{n}\mathrm{x}\mathbf{H}_a$ and $\mathbf{M} = \mathbf{E}_a\mathrm{x}\mathbf{n}$, are the two unknown quantities. This solution will utilize the admittance matrix to reduce the equivalent currents in the aperture to one independent variable The equivalent currents are expanded using a set of subdomain basis functions $\{\mathbf{f}_k \mid k= 1,...M\}$ on the aperture surface:

$$\mathbf{J} = \Sigma \alpha_k \mathbf{f}_k \tag{3a}$$

$$\mathbf{M} = \Sigma \beta_k \mathbf{f}_k \tag{3b}$$

An illustration of an aperture divided up into rectangular subdomains was shown in FIgure 2. We will select **J** to be the independent variable and **M** to be the dependent variable. We can write Equation (2) as

$$\left[\langle \mathbf{w}_i, \mathbf{J}\rangle\right] = \left[\mathbf{Y}_{ij}\right]\left[\langle \mathbf{w}_j, \mathbf{n}\times\mathbf{M}\rangle\right] \tag{4}$$

where $\mathbf{w}_i$ represents both the **u** and **v** tangent vectors depending on the value of i. Substituting Equation (3) into (4), we get

$$\left[\langle \mathbf{w}_j, \mathbf{f}_k \rangle\right]\underline{\alpha} = \left[\mathbf{Y}_{ij}\right]\left[\langle \mathbf{w}_j, \mathbf{n} \times \mathbf{f}_k \rangle\right]\underline{\beta} \qquad k = 1,...M \tag{5}$$

or

$$[F]\,\underline{\alpha} = [Y]\,[G]\,\underline{\beta}$$

This equation can be solved for $\underline{\beta}$ using the method of least squares provided that $2N > M$. Using the superscript H to denote the Hermetian of a matrix, we find that

$$\underline{\beta} = [\,(YG)^H\,(YG)\,]^{-1}\,(YG)^H\,F\;\underline{\alpha} \tag{6}$$

With this expression that expresses the coefficients of the magnetic equivalent current in terms of the coefficients of the electric equivalent current, both currents can be described by the coefficients α_k. These coefficients can be solved for using the standard MOM formulation.

3.0 Software Implementation

This capability has been implemented in a general purpose Method of Moments code called PARAMOM (Parametric Method of Moments) which was developed by Syracuse Research Corporation. Here, the term parametric refers to the fact that the basis functions used are a modification of the RWG (Rao, Wilton and Glisson) triangular patch basis functions which lie on a curved parametric surface.

Briefly, the user supplies a data file with the aperture admittance matrix and the associated supporting information as defined in the previous section. A portion of the target is designated as the aperture surface. Thus it is important to have a target geometry model where the aperture "hole" was closed off with a surface. There are a few issues that arise in the implementation of this scheme into a computer code. These issues will be briefly discussed in the following paragraphs.

Issue 1: The coordinate systems for the interior and exterior problems are different. This problem was treated by the sufficient but somewhat rudimentary approach of allowing the user to specify a rotation and translation vector which transforms the aperture (local) coordinates into the entire target (global) coordinates.

Issue 2: The grid points may not lie exactly on the surface. An example of this is an aperture which lies in a slightly curved surface where the aperture admittance was generated assuming a planar aperture face. As long as the grid points do not lie too far off the actual surface in the target, this can be dealt with by using an algorithm that minimizes the distance between the grid point and the parametric surface to find the point on the surface that is closest to the grid point.

Issue 3: In order to form the matrix equation in Equation 5, we need dense, uniform distribution of grid points. There should be at least one grid point in each subdomain. Since both grids should be

sufficiently dense to accurately represent the tangential fields at a particular frequency, this should not be a problem.

4.0 Results and Conclusions

In this section, some results of radar cross sections (RCS) of a dielectric filled rectangular cavity are given. The shape is an open perfectly conducting (PEC) cube. The interior problem for this shape, as illustrated in Figure 3 can be solved for using a modal expansion of the interior fields to generate the aperture matrix.

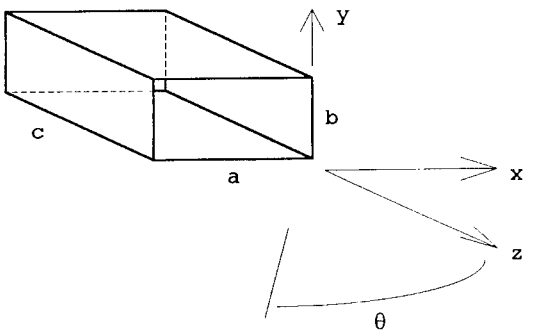


Figure 3. Geometry of Open Cavity

In the following figures, the monostatic RCS for an open PEC cube (a=b=c=.909λ) is shown for three cases: 1) ε_r=1 (air-filled) and θθ polarization, 2) ε_r=2 and θθ polarization, 3) ε_r=2 and φφ polarization. The results generated using the aperture admittance are compared against two other numerical methods. In Figure 4, the RCS for Case 1 is shown as computed by the aperture admittance formulation described in this paper and two other methods. One is to simply model the entire open-faced cube. The third method is to use the capability of the ParaMOM code to model bulk dielectrics using a surface formulation. The open box is filled with a dielectric region having the properties of free space. All three methods produce very similar results. The RCS of the corresponding closed cube is included for reference. Figure 5 shows the RCS for Cases 2 and 3. They are compared against the method that fills the cube with a bulk dielectric.

In conclusion, we have shown how a type of problem decomposition using an aperture formulation can be developed and implemented into a code which solves the exterior problem. This has been validated using a simple test shape. This can be easily extended to work with other interior formulations and more complicated shapes.

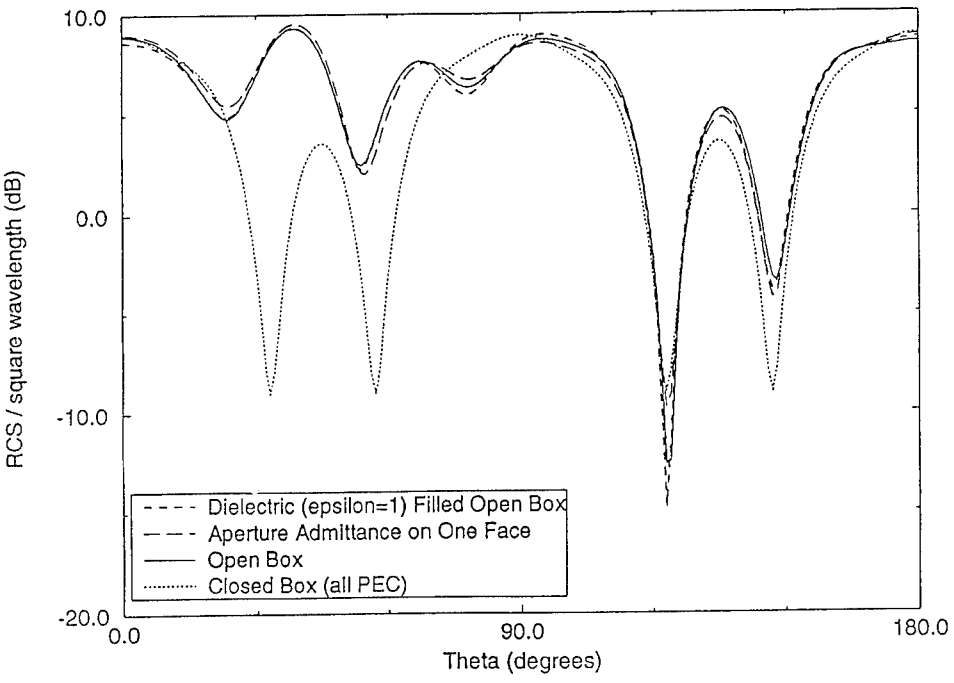
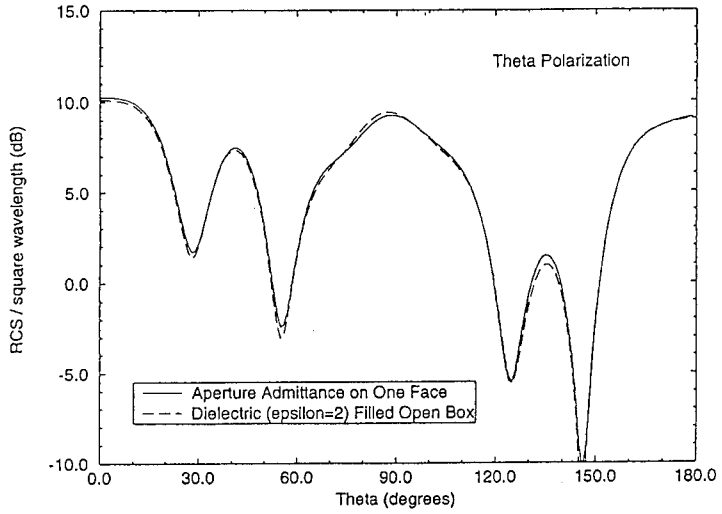
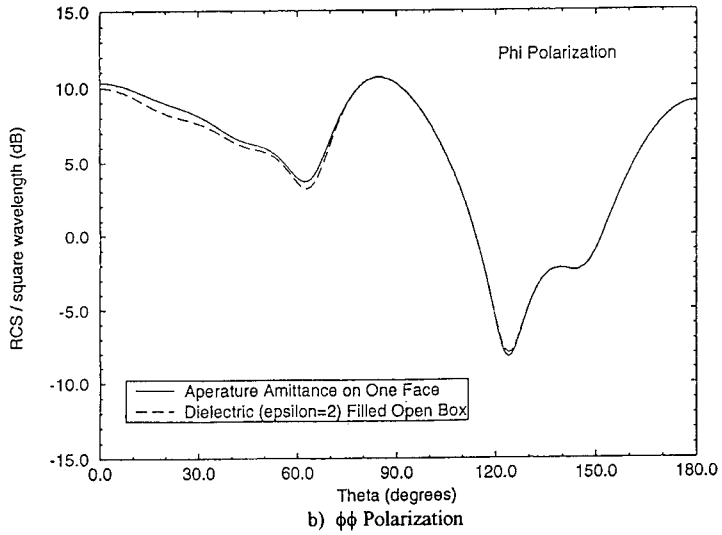


Figure 4. RCS of an Open Cube, L = .909λ, θθ Polarization



a) θθ Polarization



b) φφ Polarization

Figure 5. RCS of an Dielectric-Filled Open Cube, ε_r=2, L = .909λ

Parallelization of the Parametric Patch Moment Method Code*

Xianneng Shen
Cornell Theory Center
Cornell University
Ithaca, NY 14853-3801

Gerald E. Mortensen, Chung-Chi Cha
Syracuse Research Corporation
Merrill Lane
Syracuse, NY 13210

Gang Cheng, Geoffery C. Fox
Northeast Parallel Architecture Center
Syracuse University
Syracuse, NY 13244

December 1994

Abstract

In this paper, we discuss the development and implementation of computational electromagnetics techniques on a massively parallel architecture, Thinking Machine Corporation's CM-5. We focus on advanced numerical formulations and parallel implementation for electromagnetic scattering problems. The goal of this work is to combine state-of-the-art numerical algorithms and massively parallel processing to increase the maximum target size that can realistically be solved using the method of moments (MoM) technique.

We have parallelized ParaMoM, a MoM program which utilizes the parametric patch formulation developed at the Syracuse Research Corporation (SRC). ParaMoM-MPP, the parallel implementation of ParaMoM, has been demonstrated to produce good performance and accuracy.

1 Introduction

The problem we are addressing is the prediction of the radar cross section (RCS) of 3D arbitrarily shaped electrically large targets. We report results obtained by combining state-of-the-art CEM techniques and state-of-the-art massively parallel processing technologies. Practical RCS prediction using numerical methods has long been thought of as unrealistic. This is because numerical solutions, while exact in concept, demanded amounts of computation and memory too

*This work was supported by the Electromagnetic Code Consortium, ARPA and the Signature Technology Office of Wright Laboratory, Air force Material Command, (ASC) U. S. Air Force, Wright Patteron Air Force Base, Ohio 45433-5000.

large to accomplish in the past. The RCS prediction of a fighter-sized aircraft using MoM, for example, requires the solution of a matrix equation whose dimension can easily exceed 100,000. The impossibility of such computations also discouraged efforts to improve other aspects of CEM techniques. Successful developments of massively parallel processing (MPP) technologies have moved us into a position from which the opportunity now looks much better for solving the above-mentioned problem. Parallel computing not only drastically improves speed, it also prompts new developments in CEM techniques by bettering the prospects of real problem solutions.

In this paper, we discuss the development and implementation of an MoM code which computes RCS and antenna radiation on a Massively Parallel Processing (MPP) architecture. We utilize the parametric patch model proposed by Wilkes and Cha [2].The parametric formulation has been implemented by Syracuse Research Corporation (SRC) in a program called ParaMoM. ParaMoM utilizes curvilinear surface patches in conjunction with a new type of basis function suited to the curved domains. A brief overview of the parametric formulation is presented in Section 2.

The ParaMoM code has been parallelized on various MIMD distributed memory systems including Thinking Machine Corporation's CM-5 and the Intel Paragon. We present the details of the implementation on the CM-5, in Section 3.

The performance and scalability of ParaMoM-MPP are discussed in Section 4. Results for some of the Electromagnetic Code Consortium (EMCC) benchmark cases are shown and discussed in Section 4. The results obtained by ParaMoM-MPP are in good agreement with the EMCC benchmark measurement data.

We present our conclusions in Section 5.

2 An Overview of the ParaMoM Formulation

In this section we summarize the parametric patch formulation, originally proposed by Wilkes and Cha [2], used in the ParaMoM-MPP code. The parametric MoM formulation is defined for a class of surfaces which can be represented by two surface parameters (u and v). Each point on the target surface corresponds to a (u,v) coordinate pair. Most popular geometry modeling programs can produce such a parametric surface representation (e.g. NURBS or bicubic spline representations).

The basis functions used in the parametric formulation are similar to the well-known Rao-Wilton-Glisson (RWG) [3] functions but are defined in the parametric space of the surface. The basis function domains are triangles in the parametric (u,v) space. The potential integrals are performed on the basis function domains which conform to the curved target surface rather than the usual flat facet approximation. Therefore errors introduced by facetization are eliminated. The basis functions have all the desirable properties of the RWG functions, i.e. artificial charge accumulations at patch boundaries are avoided. When the patch dimensions become small compared to the radius of curvature, this basis function approaches the RWG basis function for a flat triangle. This basis function is defined in terms of a general surface parameterization, and it is not tied to any specific surface parameterization. This feature has allowed for simple modular inclusion of several different parameterizations in the method of moment procedure.

The ParaMoM-MPP code includes a number of capabilities and features. E-field, H-field, and Combined Field formulations are supported. An IBC formulation is included in the CM-5 version for use with material-coated targets. Parametric geometries are accepted in the standard

IGES 114 (bicubic) and IGES 128 (nurbs) formats, as well as the SRC-developed GPE format. Wire antennas may be attached to the target surface. Gridding and material specification are performed in the ParaMoM geometry preprocessor. Up to three symmetry planes may be utilized to reduce computational and memory requirements for symmetric targets.

3 Parallel Implementation

The ParaMoM [4] code has the following phases: Setup, Precomputation, Matrix fill, Right hand side vector fill, Matrix factorization, Back-substitution solution, and Far-field solution. The setup phase reads in the parameters required for the computation. Precomputation computes arrays of position vectors and basis functions at each integral point. The matrix fill phase fills the elements of the moment matrix which can be one of EFIE, MFIE, and CFIE decided at setup time. The right hand side vector fill phase computes the excitation (right-hand side vector). The matrix factorization phase decomposes the moment matrix into lower and upper triangular matrices, then back substitution is applied to solve the linear system. Finally far-field and RCS are calculated at the far-field solution phase.

The computational expenses of the setup phase, precomputation phase, RHS vector fill phase, and scattered-field computation phase are of order N, where N is the number of unknowns (proportional to surface area of target). The matrix fill phase is of order N^2, the matrix factorization is of order N^3, and the matrix solution is of order N^2. Because our primary interest in applying parallel computers lies in reducing the total time required to solve large problems (i.e., large N), we concentrate our energy on reducing the N^2 and N^3 processes. All phases of the program were parallelized in this effort.

The explicit message-passing approach has a number of advantages for the MoM application. Performance of a message-passing program is less dependent on the interconnection topology of the parallel machine than it is in data-parallel and shared-memory approaches. There is more direct control over the message volume and timing. Therefore, message-passing programs are more likely to port efficiently from one parallel architecture to another. In addition, the functions of the message-passing library are quite similar on all architectures; differences are mainly in syntax rather than in philosophy.

The CM-5 implementation utilizes the software supplied by Thinking Machine Corporation: the CMMD message passing library and the CMSSL matrix solver. The CMSSL library uses a data-parallel programming model and cannot be globally interfaced with the message-passing, matrix-filling algorithm. Therefore, in our implementation, the matrix fill and matrix factorization and solution (factor/solve) are two distinct program units. A high-speed device, such as the scalable data array (SDA) or DataVault, is used to link these two stages. The message-passing MoM matrix-filling program fills the matrix and writes it to a file in the format required for the factor/solve stage. The matrix is subsequently read in by the data-parallel matrix solver stage.

There is very little performance penalty for using separate program units for the filling and factor/solve because the DataVault or the SDA has very high data rates. As an illustration, the elapsed time for writing the moment matrix to a SDA file as measured by the CMMD timer is shown in Table 1. The writing operation is executed by the CMMD global write under CMMD synchronous sequential mode. One can see that the extra effort in using a high performance storage device to utilize both the message-passing paradigm and the data-parallel paradigm is

Table 1: The elapsed time of writing the moment matrix to a SDA file using CMMD global write under CMMD synchronous sequential mode (recorded using the CMMD timer).

$N^{\dagger}$	32-node		512-node	
	write	fill	write	fill
3000	1.19(s)	1207(s)	0.39(s)	94.1(s)
5000	2.93(s)	3295.2(s)	0.78(s)	237.9(s)
10000			1.47(s)	901(s)

justified.

There are a number of methods available to perform the solution of dense linear system of equations. In specialized problems, iterative approaches can be quite efficient in terms of memory and computation time. However, iterative techniques suffer when used to treat many right-hand side vectors. In this study, it is of interest to solve systems with a large number of right-hand side vectors (i.e., scatterers illuminated by multiple incident waves) and iterative methods were not considered. The Gaussian elimination method is employed under these conditions, since the computational intensive factorization need only be performed once.

In addition to computational cost concerns, it is necessary to consider memory requirements. On the class of computers we are considering, the main memory (RAM) is distributed among the nodes. The moment matrix is generally much too large to fit in the memory of one node, so it must be distributed equitably among the nodes. The matrix size is of order N^2, but all other arrays used in the ParaMoM code are of order N or lower.

To parallelize the ParaMoM code, we apply the problem partition approach which has received the most attention in scientific computing applications. In this approach, each processor executes substantially the same program, but on a portion of the problem data. Processors are loosely coupled throughout the computation, exchanging information whenever necessary. It is very suitable for solving large problems, where all available memory is required. The implementation difficulties are how to partition the problem to have a good load balance.

The task of filling the moment matrix is distributed among the nodes in the system. Each node has the responsibility of computing a number of columns of the matrix. The implementation of the setup phase utilizes parallel I/O to achieve parallel read. The implementation of the precomputation phase distributes the tasks of computing arrays between nodes, each node only compute a portion of the array then all nodes gather the results from all the nodes. The matrix fill implementation is illustrated in Figure 1. The RHS vector fill implementation distributes the vectors among the compute nodes. The matrix factorization and back substitution have different implementations on the different architectures. The CM-5 implementation uses CMSSL subroutines. The far-field and RCS computation implementation lets each node compute the far-field in terms of its local solution vector obtained by solving the moment matrix equation, then the contributions are summed and put in one node.

Parallel Moment Matrix Fill Algorithm

1. Loop over source patches from one to N_f;
2. Loop over three possible edges on the source patch;
   (a) Find out the global index of the edge;
   (b) Compute the index of the node in whose slab includes the column whose number is the same as the global edge index;
   (c) Compute the local index for the location of the column in the node;
   (d) The selected node increases its job counter by one and stores the information of the edge (the global edge index, the local edge index, and the local position in the node);
3. Those nodes whose job counter is 0 go back to 1;
4. Loop over field patches from one to N_f;
   (a) Compute all the integration points for the source-field patch pair interaction (Green's function);
   (b) Loop over source basis functions for that node, from 1 to its job counter;
      - Loop over all possible field basis functions (or edges on the field patch)
      - Use the formula derived in Chapter 2 to compute the elements of the moment matrix;
      - Sum all the contributions from the four pairs of patches associated with each source-field basis function;

End of the source patch loop.

Figure 1: The pseudo code of the parallel fill algorithm

4 Numerical Results

In this section we present the performance and scalability of ParaMoM-MPP and some numerical results computed by the ParaMoM-MPP code. We only show architectures here. Table 2 shows a performance comparison of ParaMoM on one processor SGI versus ParaMoM-MPP on various architectures.

The test targets used here were modeled using ACAD and gridded using the ParaMoM geometry preprocessor. All numerical results are compared with the measurements published by the EMCC (see references [6, 7]). For the results shown, the patch sampling rates used for the benchmark comparison runs are somewhat conservative and would be reasonable on a large problem. In most cases, the maximum edge length specified during target gridding was one-eighth of a wavelength.

Table 2: Time Comparisons

	SGI Indigo R4000 (estimated)	Paragon (98 nodes)	CM5 (512 ndoes)	SP1 (EST.) (58 nodes)
Fill Time(in secs)	57,000	888	901	871
speedup rel. to SGI	1	64	63	65
Factor Time(secs)	142,000	358	156	
speedup rel. to SGI	1	397	910	
Total Time(secs) Fill + Factor + I/O	199,000	1715	1067	
speedup rel. to SGI	1	116	186	

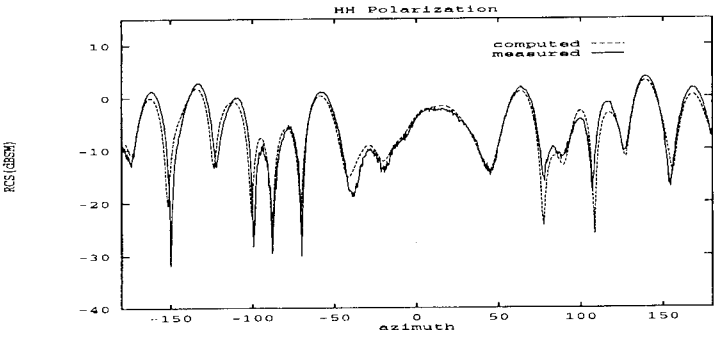


Figure 2: The RCS with HH polarization of a wedge cylinder with gap

The first example is the RCS from a flat plate in the shape of a wedge cylinder with gap. The incident wave has a frequency of 5.9 GHz with horizontal polarization. The receiver's polarization is also horizontal. The parametric patch model of the target has the maximum edge length $\frac{\lambda}{8}$, and the number of triangular patches is 1008 with 553 nodes and 1560 edges. The radius of circular part of the wedge cylinder is λ and the length of its straight side is two λ.

The monostatic radar cross section for horizontal transmitter and receiver polarizations (HH) is shown in Figure 2. The result is obtained by running the ParaMoM-MPP on a 80-node partition Intel NAS paragon. Six Mbytes of memory per node are required to run this target. There are 360 excitation vectors to compute the monostatic radar cross section. The computation takes 309 seconds by a wall clock. The RCS, in dB λ^2, plotted against the azimuthal angle is shown in Figure 2 in a 10°-elevation conical cut.

The parametric patch model for the "single ogive" target with three symmetry planes are used so one eighth of the body is actually modeled. The ogive is illuminated by an incident wave at 9 GHz. The single ogive is gridded into two different models. The first model utilizes three

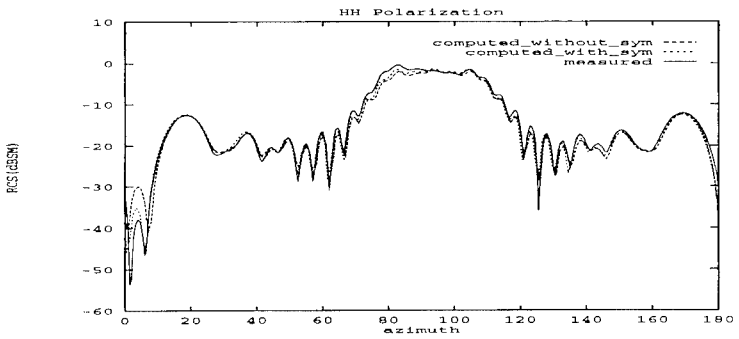


Figure 3: The RCS with HH polarization of a "single ogive"

symmetry planes, so only one eighth of the single ogive needs to be modeled. This one-eighth single ogive is modeled by 2088 curved triangles with 3208 edges and 1121 nodes. The maximum edge length is $\frac{\lambda}{12}$. The second model uses no symmetry plane. It consists of about 5000 curved patches, and 7332 edges.

The monostatic radar cross section characteristics for both HH and VV polarizations are plotted in dBSM as functions of the azimuthal angle in Figures 3 and 4. The elevation angle is zero. In Figures 3 and 4, and computed_without_sym denotes the model uses no symmetry planes, computed_with_sym denotes the target modeled with three symmetry planes. Although the number of the curved patches of the model without symmetry planes is much less dense than that with symmetry planes, Figures 3 and 4 shows good agreement. This demonstrates that the parametric patch method of moments with relatively fewer unknowns still obtains good accuracy. There are 360 RHS vectors for this problem. This problem is run on a 64-node partition of the NAS Paragon. The symmetry model requires 9 Mbytes per node and takes 9648 seconds to complete the run. The model without symmetry planes requires 21 Mbytes per node and takes 3918 seconds to complete the run.

5 Conclusion

In this paper we describe the parallelization of ParaMoM, a MoM code which computes the RCS of 3-D arbitrarily shaped conducting bodies utilizing a parametric curved patch model.

We describe the development and implementation of ParaMoM-MPP, the parallel version of ParaMoM, a MoM code which computes the RCS of 3-D arbitrarily shaped conducting bodies utilizing a parametric curved patch model. The performance data listed in Section 4 shows good performance on three platforms. We demonstrate the accuracy of the code through comparison of computed data with published EMCC test case measurements.

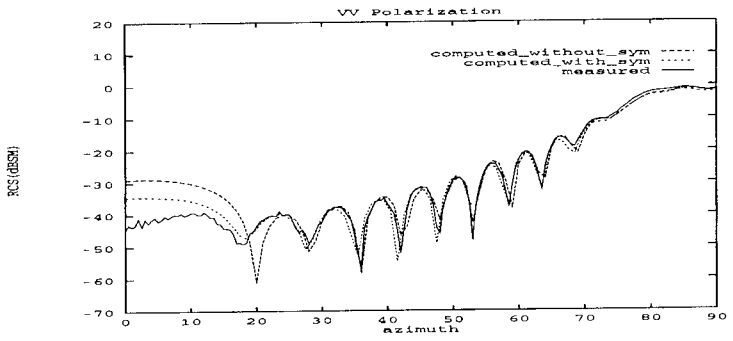


Figure 4: The RCS with VV polarization of a "single ogive"

References

[1] Roger F. Harrington, *Matrix Methods for Field Problems*, Proc. IEEE, Vol. 55, No. 2, pp. 136–149, Feb. 1967.

[2] Debra L. Wilkes and Chung-Chi Cha, *Method of Moments Solution with Parametric Curved Triangular Patches*, IEEE Antennas and Propagation International Symposium Digest, pp. 1512–1515, 1991

[3] S.M. Rao, D. R. Wilton and A. W. Glisson, *Electromagnetic Scattering by Surfaces of Arbitrary Shape*, IEEE Trans. Antennas Propagat., Vol. AP-30, pp. 409–418, May 1982.

[4] Syracuse Research Corporation, Parametric Method of Moments (ParaMoM) RCS Prediction Package User's Manual, Version 1.0, SRC Technical Report TD 92-1321, October 1992.

[5] Thinking Machines Corporation, CMSSL for CM Fortran, Version 3.1, June 1993.

[6] Alex C. Woo, Helen T. G. Wang, Michael J. Schuh, and Michael L. Sanders, *Benchmark Plate Radar Targets for the Validation of Computational Electromagnetics Programs*, IEEE Antennas Propagat. Magazine, Vol. 34, No. 6, pp. 52–56, Dec. 1992.

[7] Alex C. Woo, Helen T. G. Wang, Michael J. Schuh, and Michael L. Sanders, *Benchmark Plate Radar Targets for the Validation of Computational Electromagnetics Programs*, IEEE Antennas Propagat. Magazine, Vol. 35, No. 1, pp. 84–89, Feb. 1993.

A Tool Box for Parallelization of Moments Method Codes

E. Yip, B. Blakely, L. Johnson, D. Jurgens, R. Kochhar
The Boeing Company,
P.O. Box 3999. Mail Stop 4C-01
Seattle, Wa.

January 4, 1995

Abstract

In this paper, we present a library of tools for parallelizing moment method codes written for sequential machines. These codes are FERM, IBC3D, CARLOS-3D and SIG2D. We created the tools to parallelize the first 3D MOM code and used the same set of tools to parallelize other MOM codes with little effort. Our procedure includes:

1. An adequate understanding of the original code,
2. Code modification to conform to the input of the toolbox library,
3. Direct application of the subroutines in the tool box library and
4. Validation.

1 Introduction

Two years ago, we parallelized a 3D MOM (Methods of Moments) code, FERM, (Finite Element Radiation Modeling) to run on the iPSC/860. At the time, we did not anticipate any part of code would be reused for another project. Shortly afterwards, we needed to migrate another 3D MOM code, IBC3D, from the VAX to the iPSC/860. We found that we could reuse a lot of the subroutines used in the parallelization of FERM. We grouped these subroutines into a "toolbox" called BESLIB (Boeing Electromagnetics Subroutine Library.) Since then, we have used BESLIB to migrate two other codes, CARLOS-3D and SIG2D, from sequential machines to the iPSC/860.

In §2, we discuss the basic parallelization algorithm for MOM codes. In §3, we present the usage of BESLIB and the specifics in the parallelization of each of the MOM codes, FERM, IBC3D, CARLOS-3D and SIG2D and the corresponding validation and timing results of each of these codes. In §4, we present the plans for future improvement of BESLIB.

2 MOM Codes for MIMD Machines

In the parallelization of MOM codes, we are concerned with the following issues:

1. Maximize the performance of the linear equation solver,
2. Minimize message passing and redundant arithmetic during the matrix generation stage and
3. Load balancing during the matrix generation stage.

The factorization of the impedance matrix is the most costly part of a MOM code. It is also application independent. Most hardware vendors provide out-of-core matrix equation solvers that are tuned for optimal performance of their machines. It is important that the solver has adequate computing resources for maximum performance. Since the solver does not need the geometric and electric data of the physical problem, it is best to have the factorization and solution of the impedance matrix as a separate program module so that the computation block size can be maximized. To address problem (1) above, we separate our MOM codes into three program modules:

- Impedance matrix equation generation,
- Impedance matrix factorization-solution and
- Postprocessing.

(Post processing includes RCS calculation, antenna excitation calculation and graphic output of the currents.)

We use the ProSolver$^{(TM)}$-DES[13] as our impedance matrix equation solver. ProSolver$^{(TM)}$-DES requires the matrix to be stored in a two-level block form. The matrix is stored as a 2D mesh of disk sections. Each disk section is a 2D mesh of node sections. We generate the impedance matrix in ProSolver$^{(TM)}$-DES format. Often the units of computation and the unknowns are different. For example, in the 3D codes, if one uses the Rao Wilton-Glisson (RWG) basis function, the units of computation are the triangle patches and the unknowns correspond to the interior edges of the triangulation of the model. We studied several different parallelization schemes of this problem[11]. For the 3D codes using the RWG basis function, the best scheme is to reoder the patches with the Reverse Cuthill-Mckee(RCM) algorithm[4] so that patches which share the same edges are numbered together. Then the interior edges are reordered according to the new patch ordering. If processor k owns the submatrix $Z(i_1 : i_n, j_1 : j_n)$, the list of source patches corresponding to unknowns j_1 to j_n and the list of field patches corresponding to unknowns i_1 to i_n are determined. Then the computation loops through these lists. This scheme avoids message passing and minimizes the amount of redundant arithmetic thus providing a satisfactory solution for Problem (2). It also puts the weighty elements close to the diagonal and thus improves the condition of the impedance matrix .

All robust MOM codes perform singularity extractions when the source and field patches are close together. Therefore the computation time for the near diagonal terms can be 30 times as much as the other terms. To load balance the matrix generation, we compute all the diagonal node sections in parallel before computing the other terms.

In summary, our parallel MOM codes differs from their corresponding sequential versions in the following aspects:

1. It is separated into three modules.
2. It uses an RCM ordering.
3. It generates the diagonal node sections first.

3 Usage of BESLIB

Using BESLIB to parallelize a MOM code, one needs to provide three subroutines:

1. MATRIX, which generates a block of the impedance matrix,
2. RHS , which generates a block of the RHS corresponding to the excitation vectors.
3. MULTSCA, which generates a block of the matrix corresponding to the scattering vectors.

The subsections of this section describe the specifics in the parallelization of each of the MOM codes, FERM, IBC3D, CARLOS-3D and SIG2D. The validation for the migrated codes includes:

1. comparing output with that of the original codes,
2. comparing with available analytical results, e.g., the Mie series,
3. comparing with measured data.

In all cases, the parallelization process preserves the integrity of the original codes.

3.1 Parallelizing FERM

FERM was originally written in 1987 by Lee and Schnidman from the Lincoln Laboratory [8] for the VAX. It admits perfectly conducting and resistive boundary conditions and uses the Rao-Wilton-Glisson basis functions[9]. Since the Intel solvers use double precision arithmetic, we converted the matrix generation into double precision arithmetic. We parallelized this code twice to run on the iPSC/860. The first parallelization [11] was based on the predecessor of ProSolver$^{(TM)}$-DES called LOOCS (Large Out-Of-Core Solver)[12]. LOOCS combined the matrix generation and factorization into one subroutine and did not allow the user the flexibility to address the issues stated in §2. Therefore the performance of the solver in the application is worse than that of the certification program which solves a matrix of random numbers. The second parallelization is based on ProSolver$^{(TM)}$-DES[1]. Besides the solver, ProSolver$^{(TM)}$-DES contains versatile I/O subroutines that allow the user to optimize his codes. Table 1 shows the timing results of FERM using 64 processors with 16 Mbytes of memory on each processor. All the targets have one plane of symmetry.

Note that in each of the above cases, two systems of equations are solved. Each system has size approximately equal to half of the number of unknowns.

No. of Unknowns	Fill Time(hrs)	Factor Time(hrs)	Total Time
6,816	0.244	0.139	0.421
10,200	0.379	0.282	0.724
10,680	0.498	0.298	0.866
15,408	0.910	0.663	1.695
21,000	1.462	1.389	3.003

Table 1: Timing Results for FERM

3.2 Parallelizing IBC3D

IBC3D was originally developed by Falco et al. at Riverside Research Institute for the VAX[3]. It admits anisotropic boundary conditions. It also uses the RWG basis functions. IBC3D was very much like FERM. In the parallelization of IBC3D, we retraced most of the steps we went through in the parallelization of FERM. As stated in the introduction, we reused a lot of the subroutines used in the parallelization of FERM to parallelize IBC3D. We grouped these subroutines together into a 'toolbox' called BESLIB. Table 2 shows the timing results of a series of perfectly conducting spheres. IBC3D does not take advantage of the symmetry planes of the targets.

No. of Unknowns	Fill Time(hrs)	Factor Time(hrs)	Total Time
5,000	0.1	0.15	0.2
10,000	0.35	0.8	1.2
15,000	0.85	2.2	3.1
25,000	2.80	6.8	9.5

Table 2: Timing Results for IBC3D

Isotropic and anisotropic treatments require a significantly longer time to generate the matrix as shown in Figure 1.

3.3 Parallelizing CARLOS-3D

CARLOS-3D distributed by the Electricmagnetic Code Consortium was developed by Putman et al. [7] at McDonnell Douglas Aerospace. It has full material modeling capability and uses the roof top basis functions.

The CARLOS-3D parallelization was started by converting the entire code to double precision arithmetic. Next the matrix generation was placed in the form required by subroutine MATRIX in BESLIB. This was fairly straight forward, since CARLOS-3D was already set up to do block fills of the matrix.

The parallelization of the computation of the incident vectors and the RCS was slightly more tricky. CARLOS-3D was originally set up to compute one right hand side (RHS), then solve for the corresponding solution, compute the corresponding scattering direction and the RCS, then compute another RHS, etc. BESLIB requires all the RHS to be computed before the solve subroutine in ProSolver$^{(TM)}$-DES is called. ProSolver$^{(TM)}$-DES also computes the solution of all the RHS simultaneouly. We rearranged the computation in the original CARLOS-3D to generate

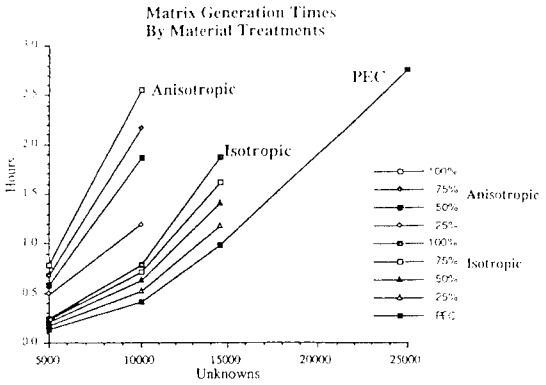


Figure 1: Timing Results for the Matrix Generation of a Range of Isotropic and Anisotropic Treatment

the RHS and the scattering vectors in a block format as required by subroutines GENRHS and MULTSCA.

The performance of CARLOS-3D is slightly worse than FERM and IBC3D because the node section size used is 260×260 instead of the optimal node section size used in FERM and IBC3D, which is 330×330.

Table 3 below shows a few timing results for various job sizes and cube sizes.

No. of Nodes	No. of Unknowns	Fill Time(hrs)	Factor Time(hrs)	Total Time
4	2,832	0.99	0.28	1.36
16	5,712	0.11	0.02	0.13
64	16,200	6.67	3.43	11.21

Table 3: Timing Results for CARLOS-3D

3.4 Parallelizing SIG2D

SIG2D was originally developed by the Science Application International Corporation (SAIC)[10]. It is a 2D moment method code using roof top basis functions. We started by converting the code to double precision arithmetic. Our version of the ProSolver$^{(TM)}$-DES does not handle symmetric matrices. Therefore we excluded the symmetry consideration in the original code. In the impedance matrix generation of the original code, the inner-most loop generates 16 elements that are not in consecutive storage. We restructured the loop structure to avoid unnecessary computation. We also scaled the rows of the impedance matrix with one of the BESLIB subroutines. Table 4 below shows the timing results of a few test cases.

No. of Unknowns	Fill Time(hrs)	Factor Time(hrs)	Total Time
1,848	0.038	0.064	0.127
6,692	0.580	0.803	1.626
10,716	1.926	2.358	4.867
12,342	2.151	3.434	6.375
13,954	2.928	4.716	8.342

Table 4: Timing Results for SIG2D

4 Conclusion and Future Improvement

We have demonstrated that a toolbox for parallelzation of moment method codes is useful and conserves time in the parallelization of MOM codes. However BESLIB still needs a lot of improvement. The following tasks would enhance the usefulness and efficiency of BESLIB.

1. Simplify and streamline the programmer interface.
2. Make the code even more modular.
3. Add a general out-of-core matrix multiply routine.
4. Add flags to turn scaling and RCM ordering on or off.

We also want to implement another load balancing scheme for the matrix generation. In this scheme, each processor looks at a token to determine the next node section to be created and the processor can create any node section, not just the ones it will be associated with during the solve.

References

[1] E. Castro-Leon and E.L. Yip, *Performance of a Dense, Complex Solver in an Electromagnetic Scattering Code* Proceedings: Intel Supercomputer Users' Group, 1992 Annual Users' Conference, pp 451-465

[2] C.C. Cha, B.M. Chiesa, R.L. Cravey, D.W. Hill and S.A. Roth, *Nonmetallic Radar Cross Section Analysis*, Final Technical Report RADC TR-88-63, Vol.I, Syracuse Research Corporation, May, 1988

[3] F. Falco, D. Koppel, N. Erlback and M. Orman *Anisotropic Impedance Boundary Condition 3D Scattering Code (IBC3D)*, Vol. I, Users' Manual and Programmers' Guide, Riverside Research Institute., November, 1991

[4] A. George and J.W. Liu, *Computer Solution of Large Sparse Positive Definite Systems*, Prentice-Hall, Inc., Englewood Cliffs, NJ., 1981

[5] G.H. Golub and C.F. Van Loan, *Matrix Computations*, John Hopkins University Press, 1989

[6] D. Jurgens and E.L. Yip, *Anisotropic Impedance Boundary Condition 3D Scattering Code, Parallel Version for the Intel Hypercube*, The Boeing Company, Defense and Space Group, April 1993

[7] J.M.Putman, L.N. Medgyesi-Mitschang, M.B. Gedera, *CARLOS-3D, Three Dimensional Method of Moments Code* McDonnell Douglas Aerospace – East, December, 1992

[8] S. Lee, D.A. Schnidman, F.A. Lichano, *Numerical Modeling of RCS and Antenna Problems*, Lincoln Laboratory, December, 1987

[9] S.M. Rao, D.R. Wilton and A.W. Glisson, *Electromagnetic Scattering by Surfaces of Arbitrary Shape*, IEEE Trans. Antennas and Propogation, Vol. AP-3g, pp.409-418, May, 1982

[10] *SAIC/SIG2D, Version 2.0, User Manual* Science Application International Corporation, December, 1990

[11] E.L. Yip *A 3D Electromagnetics Scattering Code on the iPSC/2 & iPSC/860*, Proceedings: Intel Supercomputer Users' Group, 1991 Annual Users' Conference, pp. 143-155

[12] *Boeing LOOCS External Product Specifications*, Intel Corporation, April 1990.

[13] *iPSC/860 ProSolver*$^{(TM)}$*-DES Manual*, Intel Corporation, March 1992, Order Number 312143-001

SESSION 13:

RECENT DEVELOPMENTS IN FDTD ANALYSIS

Chairs: M. Piket-May, D. Katz

Simulation of Microwave Circuits by FDTD Method

Chien-Nan Kuo, †Bijan Houshmand, and Tatsuo Itoh

Department of Electrical Engineering
University of California
Los Angeles, CA 90024-1595

†Jet Propulsion Laboratory
Pasadena, CA 91109

Abstract

This paper presents the application of the Finite-Difference Time-Domain (FDTD) method to microwave circuits. The FDTD method is extended to model the interaction of three-terminal active devices and electromagnetic fields by replacing the active device with equivalent current sources. The implementation of the current sources is investigated to show the effect on the results. A typical microwave amplifier is also simulated and the results are compared with measured data with good agreement.

1 Introduction

With the advent of powerful computing machines, the Finite-Difference Time-Domain (FDTD) method has been a popular tool to analyze electromagnetic phenomena. The FDTD method provides accurate full wave three-dimensional simulation of Maxwell's equations. Moreover, all the transient behavior of wave propagation can be observed during the simulation.

Reports have shown the FDTD method being applied to the analysis of microwave circuits. The frequency-dependent characteristics of microstrip circuits are studied, and the scattering parameters are calculated from the observed time response [1, 2]. Recently, it is extended to include lumped devices and active devices such that microwave active circuits are simulated with full wave analysis [3]. In [4], a Gunn diode in an active antenna is modeled as an equivalent active region and incorporated into the FDTD algorithm. In [5], the FDTD method is combined with SPICE to analyze an amplifier. The active device is the core kernel of the active circuit. The interaction between the active device and electromagnetic field has important effect on the characteristics of the entire circuit. In this paper, the FDTD method is extended to model the interaction of three-terminal active devices and electromagnetic fields. It is also applied to analyze a microwave amplifier.

2 Equivalent Current Sources of the Active Device

Fig. 1 shows the layout of a typical amplifier to analyze in this paper. The entire system contains distributed passive structures, lumped passive devices, and a GaAs MESFET. The distributed passive structures and the lumped passive devices could be simulated with FDTD method as in [1, 2, 3]. Besides, the analysis of this circuit lies on the modeling of the interaction between the three-terminal active device and electromagnetic fields.

The small signal feature of an active device is fully represented by its S parameters, or its lumped equivalent circuit. If the voltage-current relationships at the input ports of the device agree with the S parameters, the interaction of the active device and electromagnetic fields is accounted for. Thus, the active device can be substituted with equivalent current sources if the voltage-current relationships are maintained. Actually, these current sources stand for the current flowing into the active device. Because of the physical current flow direction, these current sources are placed in the longitudinal direction. Consequently, the placement of the equivalent current sources is illustrated in Fig. 2. One end of the sources is connected with the microstrips at the device gate and the drain ports. The other end is connected to the ground plane using vias, which provide a voltage reference as well as the modeling of the physical vias from source pads to the ground. Since the device region of this packaged MESFET covers many FDTD cells, all the FDTD cells at the gate and the drain ports are placed with the sources. Thus, the signal gain and the signal loss due to the active device are described by the equivalent current sources.

3 Extended FDTD method

The implementation of the extended FDTD lies on the integral form of the Maxwell's equations. As time evolves, the H field at half time scale is determined by Faraday's voltage law, which is the same as the conventional FDTD. Then Ampere's current law is applied to determine E field at integer time scale as in [5],

$$\nabla \times H = \epsilon \frac{\partial E}{\partial t} + J_{Device} \tag{1}$$

where J_{Device} represents the equivalent current source of the active device. This term J_{Device} is determined from the device lumped equivalent circuit such that one extra step is necessary to evaluate the E field in the cells of the active device region.

By integrating (1) over the FDTD cell, it follows the integral form,

$$I_{Total} = C \frac{dV}{dt} + I_{Device} \tag{2}$$

where I_{Total} is the total current flowing through the FDTD cell, I_{Device} is the current contributed from the active device, V is the voltage drop across the FDTD cell, and C represents the space equivalent capacitance of the FDTD cell. If the active device occupies many FDTD

cells, the integration should include all the FDTD cells at the gate and the drain ports, and the terms I_{Total} and C should include the contribution from all the cells. The voltage in (2) is calculated with its equivalent circuit, as shown in Fig. 3. The equivalent lumped circuit of the active device is coupled with the circuit model of the FDTD cells in the active region. Applying circuit theory, the state variable method is used to solve the voltage V at integer time scale and the value is then fed back into FDTD algorithm.

4 Results

The active device used in the amplifier is a packaged GaAs MESFET, NEC72084, which is biased at $V_D = 3$ V and $I_{DS} = 30$ mA. The amplifier is designed to have 9 dB gain at 6 GHz. The equivalent lumped circuit of the MESFET is depicted in Fig. 4. The element values are optimized to match the measured device S parameters. The simulations are performed with uniform grids. For the radial stubs in the DC bias circuit, the staircase approximation is used.

Fig. 5 shows the results of the calculated S parameters and the trends of the variation as reducing the number of the equivalent current sources. Since the equivalent current sources represent the signal reflection and the transmission characteristics of the active device, they should distribute over all the cells across the microstrip line to avoid additional current mismatching of the microstrip line and the equivalent sources at the connection. In Fig. 5, the total equivalent currents remain the same for each case, yet the frequency of the matching point shifts from 5.7 GHz to 5.19 GHz as the number of the sources decreases. This shift is due to the current mismatching.

The comparisons of simulation results with measured data are shown in Fig. 6. The gain at 6 GHz and the matching point of FDTD simulation are 9.3 dB and 5.7 GHz, respectively, and those of measured results are 9.23 dB and 5.6 GHz. The simulations have good agreement with measured data. Above all, those out-of-band dips near 1 GHz and 11 GHz in the measured curves are also predicted in the FDTD simulations.

5 Conclusion

The FDTD method is extended to provide a full vector electromagnetic analysis of wave interaction with microwave circuits. It is critical that the equivalent current sources should be implemented to agree with the physical current situations. This equivalent current source approach is used to analyze a typical microwave amplifier. The results show good agreement with measured data. Generally, this approach could be applied to nonlinear circuits, and performs accurate electromagnetic field simulations of microwave and millimeter wave circuits.

6 Acknowledgement

This work was supported by Hughes Micro, JSEP contract F49620-92-C-0055, and Army Research Office contract DAAH04-93-G-0068.

References

[1] X. Zhang and K. K. Mei, "Time-domain finite difference approach to the calculation of the frequency-dependent characteristics of microstrip discontinuities," *IEEE Trans. Microwave Theory and Tech.*, vol. 36, no. 12, pp 1775-1787, Dec. 1988.

[2] D. M. Sheen, S. M. Ali, M. D. Abouzahra, J. A. Kong, "Application of the three-dimensional finite-difference time-domain method to the analysis of planar microstrip circuits," *IEEE Trans. Microwave Theory and Tech.*, vol. 38, no. 7, pp 849-857, July 1990.

[3] W. Sui, D. A. Christensen and C. H. Durney, "Extending the two- dimensional FD-TD method to hybrid electromagnetic systems with active and passive lumped elements," *IEEE Trans. Microwave Theory Tech.*, vol. 40, pp. 724-730, Apr. 1992.

[4] B. Toland, J. Lin, B. Houshmand, and T. Itoh, "FDTD analysis of an active antenna," *IEEE Microwave and Guided Wave Lett.*, vol. 3, no. 11, pp. 423-425, Nov. 1993.

[5] V. A. Thomas, M. E. Jones, M. Piket-May, A. Taflove, and E. Harrigan, "The use of SPICE lumped circuits as sub-grid models for FDTD analysis," *IEEE Microwave and Guided Wave Lett.*, vol. 4, no. 5, pp. 141-143, May 1994.

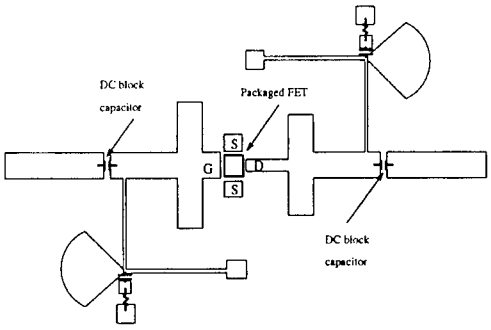


Figure 1: The layout of the microwave amplifier.

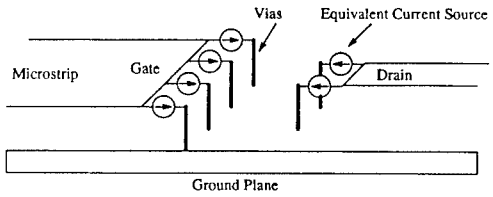


Figure 2: The equivalent current sources substituting for the active device are placed at the gate and drain ports, with one end connected to the microstrip line and the other end to the ground plane using vias.

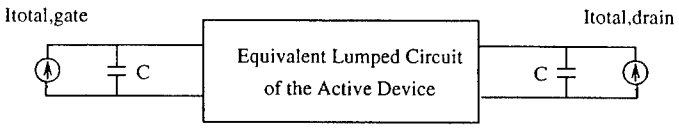


Figure 3: The equivalent lumped circuit of the integral form of Ampere's law.

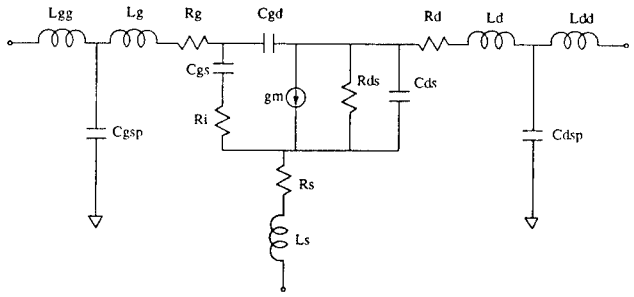


Figure 4: The small signal equivalent circuits of the packaged GaAs MESFET, NEC72084.

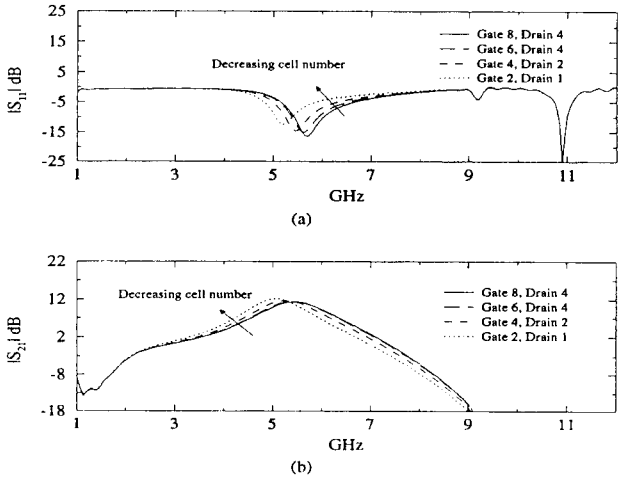


Figure 5: The calculated S parameters of FDTD simulations. The figures shows the trends as the number of equivalent current sources decrease, but with the same total current. The number of the sources at the gate and the drain port are shown in the legend.

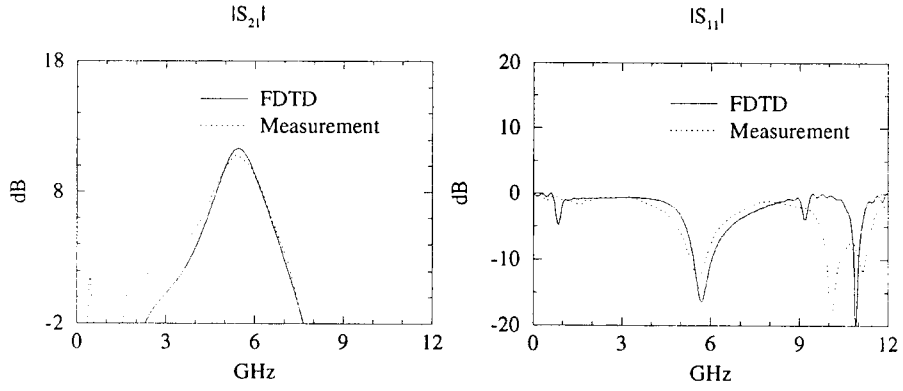


Figure 6: The results of FDTD simulations and the measurement. The simulation have good agreement with the measurement.

Adaptation of FDTD Techniques to Acoustic Modeling

James G. Maloney[1] and **Kathleen E. Cummings**[2]

[1]Signature Technology Lab, Georgia Tech Research Institute
[2]School of Electrical and Computer Engineering
Georgia Institute of Technology
Atlanta, Georgia 30332

I. INTRODUCTION

The Finite-Difference Time-Domain (FDTD) method has been used with great success to model various electromagnetics configurations, ranging from electromagnetic scattering (RCS) to driven antenna problems. The method has been extended over the years to allow frequency dispersive materials, surface impedance boundary conditions, sub-cell models of electrically thin material, etc. The quality of the absorbing boundary conditions used to truncate the computational domain has also continued to improve.

In this presentation, we will discuss the adaptation of a large part of the FDTD body of knowledge to the problem of acoustics. At a basic level, there are a number of parallels between Maxwell's equations and the coupled acoustic equations derived from the equations of continuity and momentum (assuming negligible viscosity and small perturbations from rest). It is natural to adapt the FDTD models which have found such great success in EM to the modeling of a variety of acoustics problems. This paper will present the many issues involved in the development of such an acoustic model including: discretization of the pressure and velocity equation (using Yee-like cells), derivation of the grid dispersion and stability relations, adaptation of absorbing boundary conditions, modeling of lossy walls, excitation of the model, etc. The well-known acoustics problem of the open-ended pipe was used to validate the model. The comparison of the numerical results and the analytical solution was excellent. As time permits, the application of the developed methodology to a variety of acoustics problems will also be presented.

This adaption of a popular EM modeling technique to another field, acoustics, is a prime example of the new multi-disciplinary nature of scientific research. This presentation will demonstrate how EM researchers can extend their techniques to a large variety of problems.

II. DISCRETIZATION OF ACOUSTIC EQUATIONS

If one assumes small perturbations from rest and negligible viscocity then the acoustic equations reduce to a form that is very similar to Maxwell's equations,[1]

Maxwell's equations	Acoustic equations	
$\epsilon_o \frac{\partial \vec{\mathcal{E}}}{\partial t} = \nabla \times \vec{\mathcal{H}}$	$\delta_o \frac{\partial \vec{u}}{\partial t} = -\nabla p$	(1)
$\mu_o \frac{\partial \vec{\mathcal{H}}}{\partial t} = \nabla \times \vec{\mathcal{E}}$	$\frac{\partial p}{\partial t} = -\delta_o c^2 \nabla \cdot \vec{u}$	(2)

[1]This small perturbation from rest and negligible viscocity assumption is in general valid for sound levels below 110 dB [1]. For reference, speech is from +30 to +80 dB, 120 dB is discomfort, and 140 dB is the pain threshold [2].

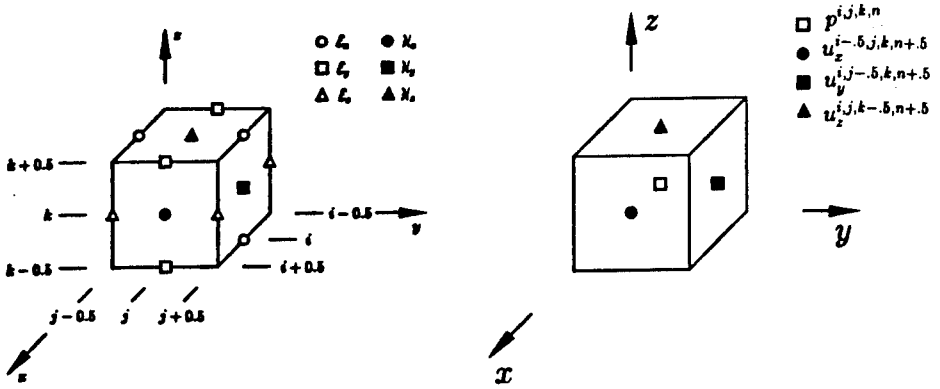


Figure 1: (a) Yee cell for Electromagnetics, (b) Yee-like cell for Acoustics. Both cells are displayed for the rectangular coordinates case.

where $\vec{u}$ is the gas particle velocity, comprised of velocity components in each coordinate direction, p is the deviation from ambient pressure, c is the speed of sound in the medium, and δ_o is the density of the gas at rest. [3]. In rectangular coordinates, these coupled acoustic equations can be expanded to yield

$$\delta_0 \frac{\partial \vec{u}}{\partial t} = -\frac{\partial p}{\partial x}\hat{x} - \frac{\partial p}{\partial y}\hat{y} - \frac{\partial p}{\partial z}\hat{z} \quad \text{and} \quad \frac{\partial p}{\partial t} = -\delta_0 c^2 \left[\frac{\partial u_x}{\partial x} + \frac{\partial u_y}{\partial y} + \frac{\partial u_z}{\partial z}\right]. \tag{3}$$

In FDTD modeling of Maxwell's equations, the solution space is discretized using the Yee cell, see Figure 1(a). The vector components of the electric and magnetic field are distributed around the unit-cell to allow the differential operators to be approximated by centered finite differences which yields a second order accurate formulation. In a similar fashion, we distribute the scalar pressure and 3 vector components of the velocity around an acoustic Yee-like unit-cell, see Figure 1(b). In rectangular coordinates, the discretized update equations thus become

$$u_x^{i-.5,j,k,n+.5} = u_x^{i-.5,j,k,n-.5} - \left(\frac{c\Delta t}{\Delta x}\right)\left(\frac{1}{c\delta_0}\right)\left(p^{i,j,k,n} - p^{i-1,j,k,n}\right), \tag{4}$$

$$u_y^{i,j-.5,k,n+.5} = u_y^{i,j-.5,k,n-.5} - \left(\frac{c\Delta t}{\Delta y}\right)\left(\frac{1}{c\delta_0}\right)\left(p^{i,j,k,n} - p^{i,j-1,k,n}\right), \tag{5}$$

$$u_z^{i,j,k-.5,n+.5} = u_z^{i,j,k-.5,n-.5} - \left(\frac{c\Delta t}{\Delta z}\right)\left(\frac{1}{c\delta_0}\right)\left(p^{i,j,k,n} - p^{i,j,k-1,n}\right), \tag{6}$$

and

$$\begin{aligned} p^{i,j,k,n+1} = p^{i,j,k,n} &- \left(\frac{c\Delta t}{\Delta x}\right)(c\delta_0)\left(u_x^{i+.5,j,k,n+.5} - u_x^{i-.5,j,k,n+.5}\right) \\ &- \left(\frac{c\Delta t}{\Delta y}\right)(c\delta_0)\left(u_y^{i,j+.5,k,n+.5} - u_y^{i,j-.5,k,n+.5}\right) \\ &- \left(\frac{c\Delta t}{\Delta z}\right)(c\delta_0)\left(u_z^{i,j,k+.5,n+.5} - u_z^{i,j,k-.5,n+.5}\right), \end{aligned} \tag{7}$$

where the notation $p(x,y,z,t) = p(i\Delta x, j\Delta y, k\Delta z, n\Delta t) = p^{i,j,k,n}$ is utilized.

These equations are updated in time using a leap-frog scheme. First, the u's at time level $n+.5$ are computed from p's at time level n and previous u's at time level $n-.5$. Then, the p's at time level $n+1$ are computed from u's at time level $n+.5$ and previous p's at time level n. This process repeats until the temporal simulation is complete.

II.1 GRID DISPERSION

With any discretized solution to wave type equations, one should be concerned about grid dispersion. Grid dispersion is the fact that waves in the numerical grid travel at speeds slightly different than in real space. Futhermore, this grid dispersion tends to be frequency and angle of propagation dependent. Therefore, it is difficult to calibrate for, and the best strategy is to try to minimize the amount of grid dispersion.

To solve for the dispersion relation, we assume a general plane wave is propagating throughout the grid, i.e.,

$$p, u_x, u_y, u_z \propto e^{j(\omega t - k_x x - k_y y - k_z z)} \tag{8}$$

where k_x, k_y, and k_z are the x, y, and z components of the numerical grid k. Using (8) to eliminate half of the field components in (4)-(7) yields

$$\left[1 - e^{-j\omega\Delta t}\right] u_x^{i-.5,j,k,n+.5} = -\left(\frac{c\Delta t}{\Delta x}\right)\left(\frac{1}{c\delta_o}\right)\left[1 - e^{-jk_x\Delta x}\right] p^{i,j,k,n}, \tag{9}$$

$$\left[1 - e^{-j\omega\Delta t}\right] u_y^{i,j-.5,k,n+.5} = -\left(\frac{c\Delta t}{\Delta y}\right)\left(\frac{1}{c\delta_o}\right)\left[1 - e^{-jk_y\Delta y}\right] p^{i,j,k,n}, \tag{10}$$

$$\left[1 - e^{-j\omega\Delta t}\right] u_z^{i,j,k-.5,n+.5} = -\left(\frac{c\Delta t}{\Delta z}\right)\left(\frac{1}{c\delta_o}\right)\left[1 - e^{-jk_z\Delta z}\right] p^{i,j,k,n}, \tag{11}$$

and

$$\begin{aligned}\left[e^{j\omega\Delta t} - 1\right] p^{i,j,k,n} = -(c\delta_o)\Bigg(& \left(\frac{c\Delta t}{\Delta x}\right)\left[e^{jk_x\Delta x} - 1\right] u_x^{i-.5,j,k,n+.5} \\ + & \left(\frac{c\Delta t}{\Delta y}\right)\left[e^{jk_y\Delta y} - 1\right] u_y^{i,j-.5,k,n+.5} \\ + & \left(\frac{c\Delta t}{\Delta z}\right)\left[e^{jk_z\Delta z} - 1\right] u_z^{i,j,k-.5,n+.5}\Bigg)\end{aligned} \tag{12}$$

Then, substituting (9)-(11) into (12) yields after some algebraic manipulation

$$\left[\sin^2(\omega\Delta t) - \left(\frac{c\Delta t}{\Delta x}\right)^2 \sin^2\left(\frac{k_x\Delta x}{2}\right) - \left(\frac{c\Delta t}{\Delta y}\right)^2 \sin^2\left(\frac{k_y\Delta x}{2}\right) - \left(\frac{c\Delta t}{\Delta z}\right)^2 \sin^2\left(\frac{k_z\Delta z}{2}\right)\right] p^{i,j,k,n} = 0. \tag{13}$$

In general $p^{i,j,k,n}$ is not zero and thus

$$\sin^2(\omega\Delta t) = \left(\frac{c\Delta t}{\Delta x}\right)^2 \sin^2\left(\frac{k_x\Delta x}{2}\right) + \left(\frac{c\Delta t}{\Delta y}\right)^2 \sin^2\left(\frac{k_y\Delta x}{2}\right) + \left(\frac{c\Delta t}{\Delta z}\right)^2 \sin^2\left(\frac{k_z\Delta z}{2}\right). \tag{14}$$

This is the dispersion relation for the discretized solution; it is identical to the dispersion relation for the FDTD technique applied to Maxwell's equations. For a uniform grid ($\Delta s{=}\Delta x{=}\Delta y{=}\Delta z$), it is commonly re-written in the form

$$\sin\left(\frac{\pi}{2}\frac{\Delta s}{\lambda_o}\right) = \left(\frac{c\Delta t}{\Delta s}\right)\sqrt{\sin^2\left(\pi\cos\alpha\frac{\Delta s}{\lambda_n}\right) + \sin^2\left(\pi\cos\beta\frac{\Delta s}{\lambda_n}\right) + \sin^2\left(\pi\cos\gamma\frac{\Delta s}{\lambda_n}\right)} \tag{15}$$

where λ_o is the wavelength in real space, λ_n is the numerical wavelength, and $\cos\alpha$, $\cos\beta$, $\cos\gamma$ are the direction cosines of the propagating plane wave. Then the phase error per cell is

$$\Theta_{\text{err}} = 360^\circ\left(\frac{\Delta s}{\lambda_n} - \frac{\Delta s}{\lambda_o}\right). \tag{16}$$

II.2 STABILITY

Another important criteria is the stability of the algorithm. The stability relation is derived in a similiar fashion. Again, we assume a general plane wave is propagating throughout the grid, i.e.,

$$p, u_x, u_y, u_z \propto \xi^n e^{-j(k_x x + k_y y + k_z z)} \tag{17}$$

but now we have not constrained ourselves only to time-harmonic plane waves. Thus, we have

$$\left[1-\xi^{-1}\right]u_x^{i-.5,j,k,n+.5} = -\left(\frac{c\Delta t}{\Delta x}\right)\left(\frac{1}{c\delta_o}\right)\left[1-e^{-jk_x\Delta x}\right]p^{i,j,k,n}, \tag{18}$$

$$\left[1-\xi^{-1}\right]u_y^{i,j-.5,k,n+.5} = -\left(\frac{c\Delta t}{\Delta y}\right)\left(\frac{1}{c\delta_o}\right)\left[1-e^{-jk_y\Delta y}\right]p^{i,j,k,n}, \tag{19}$$

$$\left[1-\xi^{-1}\right]u_z^{i,j,k-.5,n+.5} = -\left(\frac{c\Delta t}{\Delta z}\right)\left(\frac{1}{c\delta_o}\right)\left[1-e^{-jk_z\Delta z}\right]p^{i,j,k,n}, \tag{20}$$

and

$$\begin{aligned}[\xi-1]\,p^{i,j,k,n} = -(c\delta_o)\Big(&\left(\frac{c\Delta t}{\Delta x}\right)\left[e^{jk_x\Delta x}-1\right]u_x^{i-.5,j,k,n+.5} \\ &+ \left(\frac{c\Delta t}{\Delta y}\right)\left[e^{jk_y\Delta y}-1\right]u_y^{i,j-.5,k,n+.5} \\ &+ \left(\frac{c\Delta t}{\Delta z}\right)\left[e^{jk_z\Delta z}-1\right]u_z^{i,j,k-.5,n+.5}\Big)\end{aligned} \tag{21}$$

Again, substituting (18)-(20) into (21) yields after some manipulation

$$\xi^2 - 2A\xi + 1 = 0 \tag{22}$$

where

$$A = 1 - 2\left(\frac{c\Delta t}{\Delta x}\right)^2\sin^2\left(\frac{k_x\Delta x}{2}\right) - 2\left(\frac{c\Delta t}{\Delta y}\right)^2\sin^2\left(\frac{k_y\Delta x}{2}\right) - 2\left(\frac{c\Delta t}{\Delta z}\right)^2\sin^2\left(\frac{k_z\Delta z}{2}\right). \tag{23}$$

The solutions of (22) are

$$\xi = A \pm \sqrt{A^2 - 1}. \tag{24}$$

A growing (unstable) solution will occur if $|\xi| > 1$ This only occurs when $|A| > 1$; thus,

$$(c\Delta t) > \frac{1}{\sqrt{\left(\frac{1}{\Delta x}\right)^2 + \left(\frac{1}{\Delta y}\right)^2 + \left(\frac{1}{\Delta z}\right)^2}} \quad \textbf{unstable}. \tag{25}$$

However, when $|A| \leq 1$, then $|\xi| = 1$ and the grid is stable; thus,

$$(c\Delta t) \leq \frac{1}{\sqrt{\left(\frac{1}{\Delta x}\right)^2 + \left(\frac{1}{\Delta y}\right)^2 + \left(\frac{1}{\Delta z}\right)^2}} \quad \text{is } \textbf{stable}. \tag{26}$$

This stability criteria is the same as for the FDTD solution of Maxwell's equations.

III. ADAPTATION OF PML FOR ACOUSTICS

The most important recent advance in FDTD modeling is the introduction of the perfectly matched layer (PML) absorbing boundary condition [4]. Basically, the PML ABC is a region of fictitious lossy material that surrounds the computational space. This fictitious material has the desired property that waves at any angle and any frequency are not reflected upon entering the lossy region. Then the loss is adjusted to sufficiently attenuate the energy that entered the PML region. This material is called fictitious because fields within the PML layer are artificially split and obey a special set of equations that can not be cast in the form of the usual equations with some effective material properties.

The special equations, cast for use in acoustics, are

$$\frac{\partial u_x}{\partial t} + \sigma_x u_x = -\left(\frac{1}{\delta_o}\right) \frac{\partial}{\partial x}(p_x + p_y + p_z), \tag{27}$$

$$\frac{\partial u_y}{\partial t} + \sigma_y u_y = -\left(\frac{1}{\delta_o}\right) \frac{\partial}{\partial y}(p_x + p_y + p_z), \tag{28}$$

$$\frac{\partial u_z}{\partial t} + \sigma_z u_z = -\left(\frac{1}{\delta_o}\right) \frac{\partial}{\partial z}(p_x + p_y + p_z) \tag{29}$$

and

$$\frac{\partial p_x}{\partial t} + \sigma_x^* p_x = -\left(c^2 \delta_o\right) \frac{\partial u_x}{\partial x}, \tag{30}$$

$$\frac{\partial p_y}{\partial t} + \sigma_y^* p_y = -\left(c^2 \delta_o\right) \frac{\partial u_y}{\partial y}, \tag{31}$$

$$\frac{\partial p_z}{\partial t} + \sigma_z^* p_z = -\left(c^2 \delta_o\right) \frac{\partial u_z}{\partial z} \tag{32}$$

where the scalar pressure p has been broken into 3 fictitious components p_x, p_y, p_z and loss terms σ_x, σ_y, σ_z, σ_x^*, σ_y^*, σ_z^* have been introduced.

For example, if this material is placed at the positive x end of the solution space, then set $\sigma_x = \sigma_x^*$, $\sigma_y = \sigma_y^* = 0$, $\sigma_z = \sigma_z^* = 0$. The wave will not be reflected upon encountering the PML region,

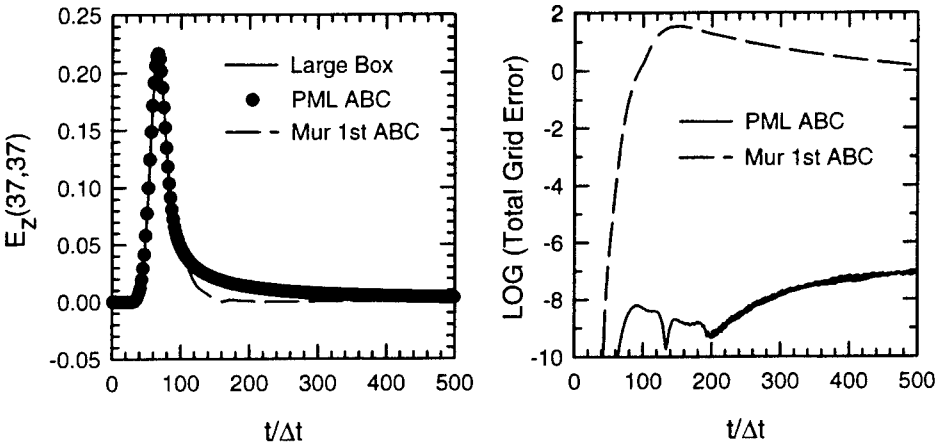


Figure 2: (a) Comparison of Ez(37,37) for PML and Mur 1st order type ABC, (b) Comparison of total energy error in the solution space.

and the wave will be attenuated as it propagates in the PML region. A similiar treatment is placed on the other faces of the solution space. The edges and corners however require some special attention, and the reader is refered to [4] for the details.

In order to verify the accuracy of the PML ABC, consider a simple 2D problem in which the computational space is defined to be 50 by 50 cells, with the pressure in the middle set equal to a gaussian pulse. Figure 2(a) compares the exact results (solid line) computed using a 500 by 500 box, the PML-surrounded box results (solid dots), and the simple Mur 1st order type ABC (Dashed line). Clearly, the PML-surrounded box solution and the exact solution are in good agreement, while the simple ABC is in error. The total energy error in the computational grid is compared in Figure 2(b). The PML results (solid line) are nearly 10 orders of magnitude better than the simple Mur 1st order type ABC (dashed line).

IV. VERIFICATION

The traditional method of verifying the accuracy of a numerical model is to select a problem with a well-known theoretical solution and to compare the results of using the numerical model to the theoretically expected results. For this paper, a three-dimensional unflanged, open-ended circular cylinder was modelled using the previously described acoustics formulation of FDTD. The model was excited with a Gaussian pulse. The reflection coefficient was calculated from the numerical solution of the propagation of the Gaussian pulse in the cylinder over time and compared to the theoretically derived reflection coefficent [5]. The comparison of the experimentally calculated and the theoretically expected values $|R|$ and l/a versus ka (where k is the wave number, $2\pi/\lambda$, and a is the radius of the cylinder) are shown in Figure 3. As can be seen, the agreement between the FDTD and the theoretical results is excellent. The accuracy of this finite-difference time-domain model is therefore verified.

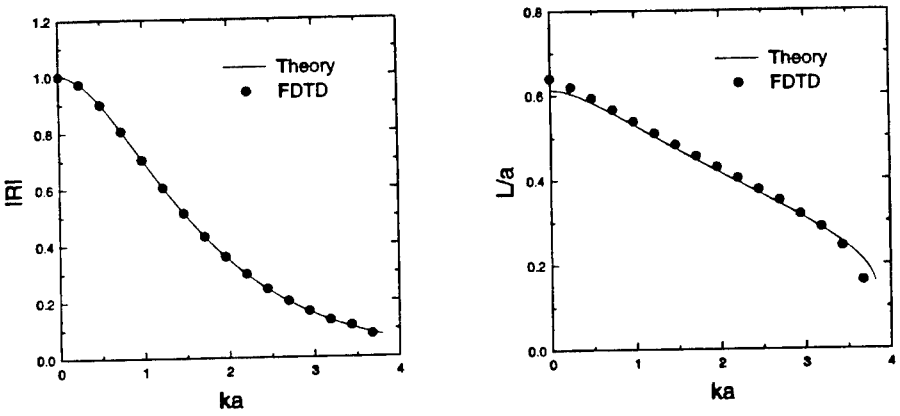


Figure 3: Comparison of $|R|$ and l/a, finite-difference time-domain solution and theoretical solution.

V. APPLICATION TO SPEECH MODELING

One important application of this new acoustics FDTD modelling technique is the problem of modelling speech production. Most current methods of modelling speech production involve either directly analyzing the acoustic speech waveform, which assumes a simplified linear model, or solving the acoustic wave equation in a series of cylindrical tubes, which assumes a simplified geometry. Although these classes of models have been successful for speech coding, recognition, synthesis. and analysis for many years, recent advances have proceeded at a very slow pace. Many researchers believe that the simplified models of speech production have been pushed as far as they will go, and that, in order to continue to advance the field of digital speech processing, improved models of speech production must be developed. This FDTD model of acoustics can provide a mechanism for accurately modeling acoustic wave propagation in the speech production process.

We are currently applying the FDTD model of acoustics discussed above to the problem of accurately modeling speech production. In this new model, acoustic wave propagation is solved for directly, in a geometry that accurately represents the vocal tract.

We believe that the FDTD approach has several distinct advantages over both traditional speech modeling techniques and finite element and boundary element models. First, a FDTD solution provides full knowledge of the acoustic flow at every point in the vocal tract for every time. Second, the finite-difference time-domain method makes no assumption of linearity between the input and the output (note that this is not true for frequency-domain finite-difference methods). Third, a FDTD model allows many parameters such as the geometry of the vocal tract and the excitation source to be altered easily. Finally, finite-different solutions are highly parallelizable, allowing for the efficient use of computing resources.

Several experiments have been performed using FDTD models of the vocal tract during vowel production. This has been accomplished in two dimensions using published X-ray data. Recently, MRI data of the vocal tract during vowel production has been obtained and is being used to

develop a three-dimensional model of speech production. Results from these experiments will be presented at the conference, as time permits.

VI. CONCLUSIONS

This paper has presented an adaptation of a propular EM modeling technique, FDTD, to the field of acoustics. The parallels between the EM and acoustic coupled equations were discussed, and the discretization of a three-dimensional acoustic cell and of the coupled acoustic equations were presented. The dispersion relation and stability criteria were derived for the acoustic FDTD model and were shown to be parallel to the FDTD formulation for EM. The perfectly matched layer (PML) ABC that has recently been introduced for EM was also adapted to this FDTD acoustic model, and it was shown that the PML solution is 10 orders of magnitude better than a simple Mur 1st order type ABC. The accuracy of the acoustic FDTD model was verified by modeling a well-known acoustics problem, the unflanged, open-ended circular cylinder, and comparing the numerical and analytic solutions for the magnitude and phase of the reflection coefficient. Finally, the application of this FDTD acoustic model to an important problem, modeling speech production, was discussed briefly.

ACKNOWLEDGEMENT

This material is based upon work supported under National Science Foundation Grant # CDA-9211129 and a grant from the American Speech-Language-Hearing Association.

References

[1] L. L. Beranek, *Acoustics.* Woodbury, NY: Acoustical Society of America, American Institute of Physics, 1993.

[2] L. L. Beranek, *Acoustical Measurements.* Woodbury, NY: Acoustical Society of America, American Institute of Physics, 1988.

[3] J. J. Bowman, T. B. A. Senior, and P. L. E. Uslenghi, Electromagnetic and Acoustical Scattering by Simple Shapes. New York: Hemisphere Pub., 1987.

[4] J. P. Berenger, "A Perfectly Matched Layer for the Absorption of electromagnetic waves," *J. Computational Physics*, Oct. 1994.

[5] H. Levine and J. Schwinger "On the Radiation of Sound from an Unflanged Circular Pipe," *Physical Review*, Vol 3, No 4, pp 383-406, 1948.

FDTD Investigation of the Antenna–Tissue Interaction for Cellular and Satellite Systems

Yahya Rahmat-Samii[†] and Michael A. Jensen[‡]

[†]Department of Electrical Engineering
University of California, Los Angeles
Los Angeles, CA 90024-1594
Tel. (310) 206-3847
Fax. (310) 206-8495

[‡]Department of Electrical Engineering
Brigham Young University
Provo, UT 84602
Tel. (801) 378-5736
Fax. (801) 378-6586

I. Introduction

The geometrical modeling flexibility of the finite-difference time-domain (FDTD) method [1] makes it a very powerful simulation methodology for analyzing and designing antenna structures for modern defense and commercial related products. An example of such an arena where the FDTD technique can be used to great advantage involves the design of antennas for transceiver handsets used in personal wireless communications networks. New devices demand antenna structures which can be efficiently and conveniently integrated with small, portable hand-held units. Figure 1 illustrates two such handset/antenna configurations: a back-mounted planar inverted F antenna (PIFA) designed for cellular applications and a circularly polarized patch antenna for use in satellite communications. The FDTD algorithm allows these antennas to be modeled in their true operating environment with the handset chassis and plastic casing and even the operator's biological tissue included in the simulation [2, 3].

The fact that the FDTD methodology allows modeling of the human tissue becomes particularly important when considering the performance requirements dictated by modern systems. For example, most hand-held transceivers are designed to maximize transmission efficiency in order to conserve power. However, high mismatch losses induced by the antenna/tissue coupling as well as gain loss due to absorption in the tissues can reduce the transmission efficiency. Additionally, for systems where a handset must link to a low-earth orbit satellite, the antennas must provide circularly polarized radiation with a reasonably isotropic pattern. Because the presence of the head can significantly alter the radiation pattern, it is essential to include its effect in the antenna analysis.

The goal of this paper is to illustrate the use of the FDTD methodology in conjunction with detailed models of human tissue and handset-mounted antennas in predicting the effect of the human body on the performance of small antennas. The study will address the computational issues involved in using the FDTD technique for this application, such as computational time and storage requirements, transient response duration of high-permittivity, low-Q dielectrics, and considerations for dispersive dielectrics. Simulation results will be provided for representative handset/antenna configurations designed for cellular and satellite communication networks.

II. FDTD Modeling

In performing the FDTD simulations of handset-mounted antennas, care must be exercised in modeling the antenna, handset, and biological tissue. In determining appropriate models, it is important to consider not only their geometrical accuracy but also the computational implications associated with their use. In this section, the models for the antennas, handsets, and biological tissue are discussed. Additionally, the computational storage and time requirements are presented.

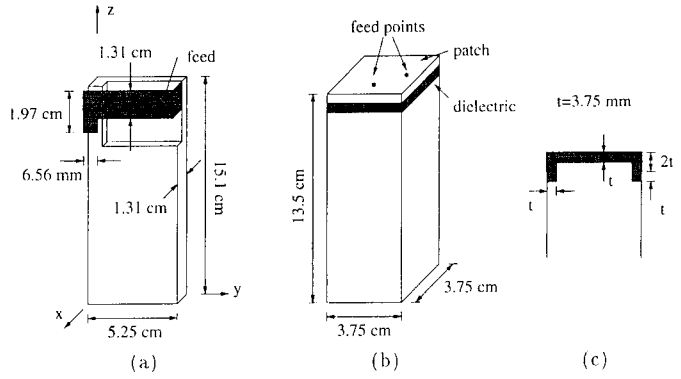


Figure 1: Geometry for (a) the back-mounted PIFA on the handset, (b) the circularly polarized patch antenna on the handset, and (c) cross-sectional view of the patch with dimensions.

A. Antenna/Handset Models

The basic modeling of the antenna and handset is accomplished by enforcing appropriate boundary conditions in the FDTD method on the conducting surfaces. Wires which may form part of the antenna itself or exist in the antenna feeding network are modeled by using a special wire subcell method which accounts for the finite wire diameter [4]. This practice is particularly important for obtaining accurate input impedance and gain values for the radiators [2]. If a plastic casing is used which surrounds the hand-held unit, it can be modeled by assigning the appropriate permittivity values to the cells immediately adjacent to the handset conductor. In this paper, the plastic casing is a dielectric with a relative permittivity of $\epsilon_r = 2$.

One interesting aspect involved with the FDTD simulation of antenna systems is the choice of excitation models used. Typically, a gap-voltage model is used in which the electric field is specified at the antenna feed point [5]. In this work, the coaxial feed model illustrated in Figure 2(a) is used [2]. With this model, the radii of the coaxial inner and outer conductors, r_a and r_b, are chosen to represent the proper input impedance of the actual antenna feed line. Special difference equations are then used at the interface between the coax and the antenna to account for the known field behavior within the coaxial line as well as the difference between the radius r_b and the FDTD discretization size [2]. Numerical simulations performed by the authors have demonstrated that the two approaches typically provide the same results. However, the advantage of the coaxial feed model is that it can reduce the amount of computational time required to obtain the antenna transient response. This is illustrated in Figure 2(b) which plots the normalized current versus the normalized time (η_o and c_o are the free-space impedance and speed of light respectively) for a 8.5 cm long wire (r_a = 0.46 mm) monopole centered on a 13 cm $\times$ 13 cm ground plane excited using the gap and coaxial feed models. A 320 ps wide Gaussian shaped voltage pulse has been used as the excitation for both plots. As can be seen, use of the coaxial feed model noticeably reduces the duration of the transient response.

B. Tissue Models

In order to obtain insight into the performance of antennas near a human operator, considerable care has been taken to develop tissue models which closely resemble true human anatomy [3]. These inhomogeneous models are formed within the FDTD framework by assigning the appropriate permittivity

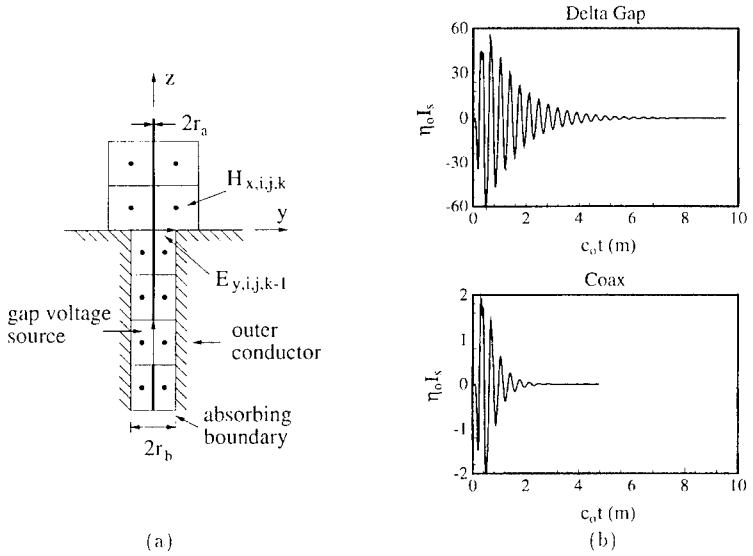


Figure 2: (a) Cross-sectional view of the simulated coax. (b) Normalized terminal antennna current versus time for the gap voltage and simulated coaxial source models.

and conductivity to different cells in the grid. The human hand is modeled as a 6.56 mm layer of bone completely surrounded by a 6.56 mm layer of muscle, as implied in Figure 3. The human head model, a cross section of which appears in Figure 4(a), consists of the tissues listed in Table 1. The permittivity, conductivity, and density of these tissues at 900 MHz and 2 GHz have been obtained from published data [6]. Figure 4(b) illustrates the full head, hand, and handset model which is used in the FDTD simulations.

One important issue relating to the time-domain modeling of high-permittivity dielectrics involves the slow rate at which energy is dissipated from the system. In order to demonstrate this phenomenon, consider a dipole antenna placed near a homogeneous sphere of dielectric, as shown in the inset of Figure 5. A 320 ps Gaussian voltage pulse is introduced at the antenna terminals and the input current is monitored as a function of time in Figure 5. The first plot, in which the dielectric sphere has a relative permittivity of $\epsilon_r = 1$, corresponds to the dipole in free-space. In the second frame, the sphere has $\epsilon_r = 73$, corresponding to the permittivity of the humour in the eye at 915 MHz. As can be seen, the introduction of the high-permittivity dielectric noticeably extends the transient response duration. However, addition of the tissue losses reduces the antenna transient response duration, as shown in the third frame of Figure 5. The final frame illustrates the response when the dipole is placed next to the full inhomogeneous head model, where again it is seen that the losses noticeably reduce the ringing duration.

A second issue involved in the modeling of biological tissue involves the dispersive nature of the tissue electrical parameters. An accurate way to accommodate such media in a time-domain simulation approach is to use a methodology which takes into account the dispersive nature [7]. This is particularly important for systems in which the wide-band response is desired. For this work, however, the bandwidth of interest is relatively narrow. Therefore, in order to maintain computational simplicity and speed, it will be assumed that the constitutive parameters are constant over the bandwidth.

Table 1: Relative permittivity (ϵ_r), conductivity (σ), and density (ρ) of the tissues in the head and hand at 900 MHz and 2 GHz.

Tissue	ϵ_r		σ (S/m)		ρ ($\times 10^3$ kg/m^3)
	915 MHz	2.0 GHz	915 MHz	2.0 GHz	
Bone	8.0	8.0	0.11	0.16	1.85
Skin	34.5	32.0	0.60	0.52	1.10
Muscle	58.5	55.0	1.21	1.90	1.04
Brain	55.0	53.0	1.23	1.70	1.03
Humour	73.0	75.0	1.97	2.40	1.01
Lens	44.5	41.0	0.80	1.29	1.05
Cornea	52.0	50.0	1.85	2.32	1.02

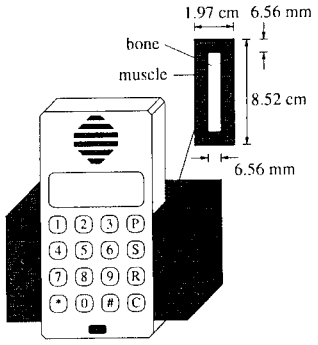


Figure 3: FDTD model of the human hand which surrounds three sides of the transceiver handset.

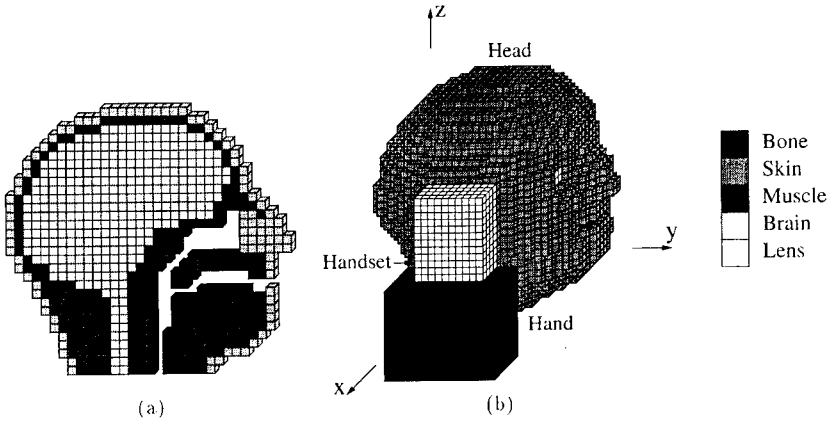


Figure 4: (a) Sagittal cut of the discrete head model at the head center and (b) entire head model with the hand and plastic-covered handset present.

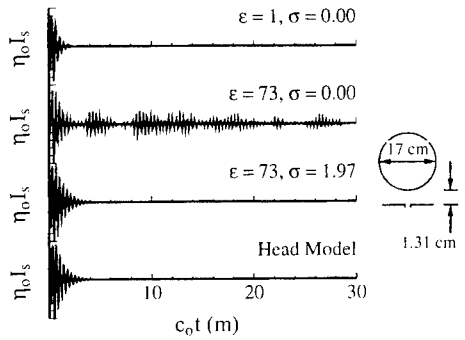


Figure 5: Normalized terminal antenna current versus time for the dipole near three different dielectric spheres and near the human head model.

C. Computational Requirements

Depending upon the physical quantity under investigation, two different computational grids are used. For example, for input impedance calculations, numerical convergence tests have proven that a cell size of 3.28 mm is adequate (for antennas operating around 915 MHz). For pattern computations, a 6.56 mm cell size appears to give converged results. The computer platform used in the simulations is an IBM RISC/6000 530H workstation. For the model with the larger cells, 1800 time steps are typically used, resulting in overall requirements of 2-3 hours of execution time and 17 MB of storage. For the model with the smaller cells, 3600 time steps are used, requiring 10-12 hours of run time and 35 MB of storage. For computations at 2 GHz, the models must be scaled appropriately to account for the reduction in wavelength.

III. Representative Results

The computational capabilities developed based on the FDTD methodology are of great utility in determining the effect of the operator tissue on the antenna performance. In this section, computational examples are provided to illustrate the use of the technique in determining the performance of the two handsets depicted in Figure 1.

A. Back-Mounted Planar Inverted F Antenna

As a first example, consider the back-mounted planar inverted F antenna (PIFA) shown in Figure 1(a). This handset/antenna structure is designed for use at 915 MHz in a cellular or other similar terrestrial-based communications system. The antenna geometry is chosen to minimize antenna size for the desired resonant frequency. Furthermore, because the plastic case which surrounds the handset will influence the antenna resonance, the antenna dimensions have been chosen such that the best match occurs at 915 MHz with the casing present.

An examination of the operator's influence on the antenna impedance behavior appears in Figure 6. In this plot, the magnitude of $|S_{11}|$ (assuming a 50Ω feeding coax) is plotted as a function of frequency for three different handset/tissue configurations. The first curve represents the behavior when no operator

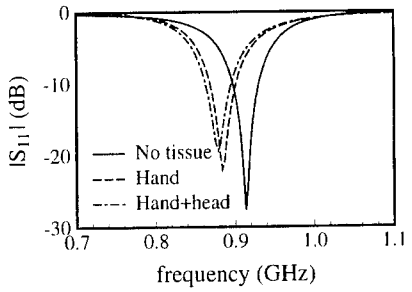


Figure 6: Computed $|S_{11}|$ versus frequency for the back-mounted PIFA on the plastic covered handset with no tissue present, with the top of the hand located 4.26 cm from the handset top, and with the hand and the head located 6.56 mm from the handset front.

is present. In the second curve, the hand is included and is placed such that its top is 4.26 cm below the top of the handset. In the third curve, the hand maintains its position and the head is placed 6.56 mm from the edge of the handset. As can be seen, the influence of the tissue can noticeably alter the match between the antenna and feed line. Such effects must be fully investigated in a given design to ensure that excessive mismatch losses will not occur as the user moves his hand along the handset.

The presence of the tissue can also significantly change the antenna gain pattern. This is demonstrated in Figure 7 which presents the gain pattern magnitude in the principal planes both with and without the tissue. In this computation, the handset it held upright with respect to the head although it is possible to investigate other handset orientations [3]. As can be seen, the tissue influences the pattern shape, polarization, and gain. One noticeable feature is that the hand and head absorb 48% of the power delivered to the antenna.

B. Circularly-Polarized Patch Antenna

Figure 1(b) illustrates the geometry for a transceiver handset with a dual-probe fed patch antenna. The patch construction, detailed more carefully in Figure 1(c), consists of a 3.75 mm thick conductor-clad dielectric ($\epsilon_r = 2.54$) which "caps" the conducting handset chassis. This design allows reduction of the antenna lateral dimensions for a given operating frequency. By exciting the two probes in phase quadrature, this antenna can be made to provide circular polarization. While the configuration of Figure 1(b) is to be investigated in this paper, other embodiments of this antenna are also being considered.

Figures 8 and 9 compare the radiation performance of the patch antenna when the handset is isolated and when it is held 3.75 mm from the operator's head. Figure 8(a) illustrates the magnitude of the radiation pattern in the principal coordinate planes at 2 GHz for this antenna when no tissue is included in the computation. As can be seen, the magnitudes of the $\hat{\theta}$ and $\hat{\phi}$ polarizations are approximately equal for $\theta < 60°$. Figure 8(b) compares the phase difference $\Delta\xi = \arg\{E_\theta\} - \arg\{E_\phi\}$ when the tissue is absent and present. Here, it is apparent that the phase difference is near $\pm 90°$ over a broad range of angles when no tissue is included. However, when the operator influence is accounted for in the computation, the phase difference deviates noticeably from the desired $\pm 90°$ value. This deviation will result in a degradation of the circularly polarized radiation.

This degradation of the circular polarization is further aggravated somewhat by the influence of the tissue on the antenna magnitude patterns. This is illustrated in Figure 9 which presents the patterns in the two principal planes. As can be seen, the magnitudes of the two polarizations deviate noticeably away from the $\theta = 0°$ direction, particularly in the x-z plane. It is also noteworthy that 53% of the

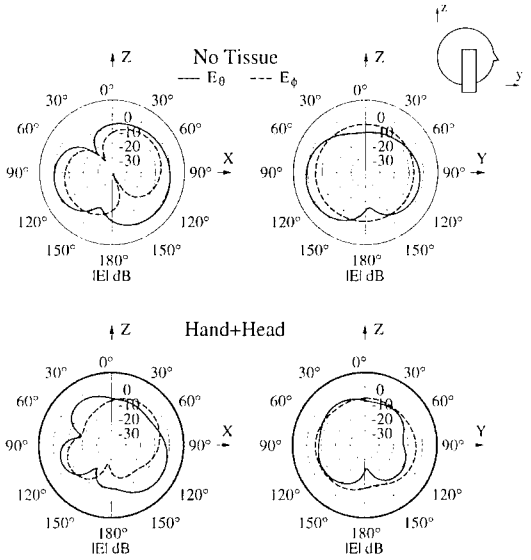


Figure 7: Computed gain patterns at 915 MHz for the back-mounted PIFA on the handset with and without the tissue present.

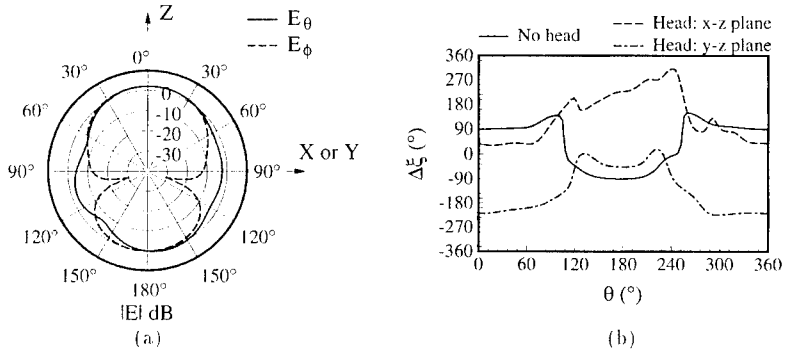


Figure 8: (a) Magnitude of the radiation pattern in the principal planes for the antenna of Figure 1(b) with no tissue present. (b) Phase difference between the $\hat{\theta}$ and $\hat{\phi}$ polarizations for the handset of Figure 1(b) alone and with the head and hand.

power delivered to the antenna is absorbed by the tissues. This loss coupled with the change in the pattern shape result in a gain reduction at $\theta = 0°$ from 2.11 dB to -3.3 dB. Note that if desired, the data presented here could be plotted in terms of left-hand and right-hand circularly polarized radiation modes.

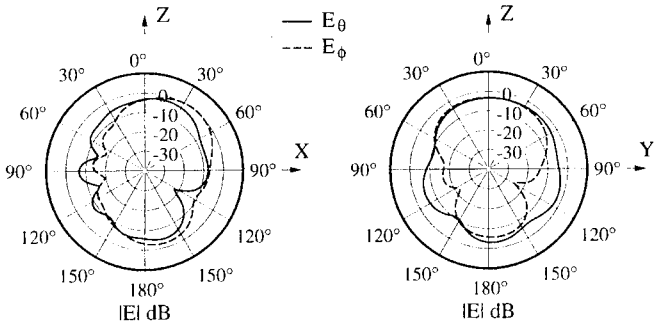


Figure 9: Radiation patterns for the geometry in Figure 1(a) with the head present as in Figure 4(b).

IV. Conclusions

This paper has demonstrated the use of the FDTD simulation methodology to investigate the performance of handset-mounted antennas operating near a human. Computational issues such as computational time and storage requirements, transient response duration of high-permittivity dielectrics, and considerations for dispersive dielectrics have been discussed. Representative examples have been presented to illustrate the influence of biological tissue on antennas for cellular and satellite communication systems.

Acknowledgements This work was sponsored in part by ARPA Contract # DAAB07-93-C-C501.

References

[1] K. S. Yee, *IEEE Trans. Antennas Propag.*, AP-14:302–307, May 1966.

[2] M. A. Jensen and Y. Rahmat-Samii, *IEEE Trans. Antennas Propag.*, 42:1106–1113, Aug. 1994.

[3] M. A. Jensen and Y. Rahmat-Samii, *Proc. of the IEEE*, 83:7–17, Jan. 1995.

[4] A. Taflove, K. R. Umashankar, B. Beker, F. Harfoush, and K. S. Yee, *IEEE Trans. Antennas Propag.*, 36:247–257, Feb. 1988.

[5] R. Luebbers, L. Chen, T. Uno, and S. Adachi, *IEEE Trans. Antennas Propag.*, 40:1577–1583, Dec. 1992.

[6] P. J. Dimbylow, *Phys. Med. Biol.*, 38:361–368, Feb. 1993.

[7] D. M. Sullivan, *IEEE Trans. Microwave Theory Tech.*, 40:532–539, Mar. 1992.

FDTD Modeling of Ground-Penetrating Radar Antennas

Brian J. Zook
Southwest Research Institute
P.O. Drawer 28510
San Antonio, TX 77228-0510

Introduction

Ground-penetrating radar (GPR) is a common technique in the detection of buried objects. The effectiveness of any GPR system is strongly affected by the antenna design, soil parameters, and target characteristics. In the past, optimal GPR designs required extensive measurements and design iterations. Modeling offers the promise of finding quality designs before the expensive construction of prototypes.

We are using the finite-difference time-domain (FDTD) method to model GPR. Of key importance is FDTD's capability of modeling the fields inside a penetrable medium, namely the ground. There are several advantages of this method for GPR modeling. First, the general and flexible nature of the FDTD method allows us to model complex antennas, complex targets, and possible soil inhomogeneities in a straightforward manner. Second, the method can model the soil, which is a dispersive (and dissipative) dielectric. We are modeling the dispersive soil as a Debye medium, using the recursive FDTD formulation [1]. A third advantage of the FDTD method is that we can find the broadband response of a system by using pulsed excitation, that is, find results over a broad frequency band with a single FDTD calculation. Thus we can model pulsed systems directly, as well as stepped-frequency and swept-frequency systems through postprocessing. Finally, we are using the damped Higdon's outer radiation boundary condition (ORBC) [2]. This ORBC is able to model dispersive media at the computational boundary, including the air/soil interface.

In this paper we present a few examples of using the FDTD method to model GPR antennas and applications. The method has previously been used for 2.5D simulations (3D source, 2D geometry) [3]. Our examples are all 3D models, although we have also used the method for 2D modeling.

Bowtie Antenna

Figure 1 shows a 3D FDTD bowtie antenna model. This is a top view, showing the FDTD cell edges that are modeled as perfect electrical conductors (PEC). We are using two symmetry planes in this example, reducing the FDTD model (in memory and runtime) by a factor of four. The left face has a PEC plane, creating mirror symmetry along that plane, while we use planar symmetry along the lower edge. The antenna is driven along the single center element at the lower left by setting the E_x field at that point after every timestep. This method of driving the antenna models the system as if the transmitter has infinite impedance; we are modeling only the antenna here, not the antenna feed, although that is possible. The FDTD cell resolution is 1 cm in all directions and the bowtie is located

1 cm above the surface of the earth. The earth extends completely to the edges of the simulation volume, except at the left face (where the PEC plane is located).

We can use the FDTD bowtie model to find the antenna input impedance as well as the field pattern in the soil. The input impedance is an important antenna characteristic, indicating the antenna bandwidth, among other things. Observing how the impedance varies with frequency, antenna configuration, geometry, and soil conditions aids the designer in producing an optimum GPR antenna. We are also interested in the pattern and amplitudes of the fields in the soil. Using FDTD, we can sample the fields at any number of locations within the ground, for example, at a constant depth.

Figure 2 shows the input impedance of the bowtie antenna suspended in free space; the results agree with measurements by Brown and Woodward [4]. Figure 3 shows the input impedance when the antenna is 1 cm above the ground. As expected, the soil clearly has a significant effect on the antenna characteristics. The magnitude of the impedance is dramatically reduced and the broadband characteristics are shifted to lower frequencies. For this calculation, we modeled the soil as a double-Debye medium, with Debye resonances of 7 MHz and 3 GHz. The soil has a complex relative dielectric constant of the form in Equation 1 and the parameters in Table I.

$$\tilde{\epsilon} = \epsilon_\infty - \frac{j\sigma}{2\pi f \epsilon_0} + \frac{a_1}{1 + f/f_1} + \frac{a_2}{1 + f/f_2} \tag{1}$$

Table I - Soil Parameters for Bowtie Model

$\epsilon_\infty = 1$
$\sigma = 0.020$ S/m
$a_1 = 100$
$f_1 = 7$ MHz
$a_2 = 11$
$f_2 = 3$ GHz

The pattern of radiation, both in the air and in the ground, is an important operating characteristic of a GPR antenna. Antenna radiation patterns are typically reported as far-field quantities. But in GPR applications, especially those detecting shallow buried objects, the near-zone fields are of utmost importance. Furthermore, the field patterns change significantly with distance in the ground, due to the dissipative and dispersive nature of the soil. Thus the traditional concept of (far-field) radiation pattern is not as meaningful in GPR antenna analysis. Instead, we are usually interested in the pattern of field strengths at a constant depth. This, for example, is meaningful when scanning a GPR over a buried object.

FDTD models all the fields in the computational volume. By saving these values at each timestep, we can examine the fields during postprocessing. Instead of saving all fields, we save all the components

at a series of locations, such as at a constant depth. After converting to the frequency domain, we find the fields as a function of position and frequency.

Figures 4 through 6 show the field strengths for the bowtie antenna model shown above. Each figure shows the electric field component at a depth of 15 cm. Figure 4 shows a scan of E_x along the X-axis (of the bowtie), which is the direction of orientation and polarization of the antenna, while Figure 5 shows the E_z (vertical) component. The excitation used in the model produced broadband results (to over 800 MHz), but only three discrete frequencies have been shown in the figures. Figure 6 shows the E_x field for a scan along the Y-axis perpendicular to the bowtie.

UHF Balanced-Bridge Detector

Lastly, we present 3D FDTD calculations showing the scattering from a buried target. Figure 7 shows a side view (cross section) of a UHF balanced-bridge detector, used in buried mine detection [5]. It consists of three equally-spaced dipoles; the outer two are driven out-of-phase and the center dipole is the receiver. When the detector is placed above a homogeneous half-space (no target), the received signal is zero. An off-center target upsets the balance, generating a signal at the receiver. As the detector is scanned across a target, we see a characteristic double-hump signature. The antenna is typically driven at a single frequency near 400 MHz.

We are modeling the UHF balanced-bridge using a pulsed excitation and an FDTD cell size of 1 cm. We use mirror symmetry to reduce the problem size by a factor of two. The antenna liftoff is 10 cm, the target is a 10 cm PEC cube, and the target is buried 5 cm deep. Figure 8 shows the received amplitude for a scan of the target, at two frequencies. It shows the double-hump characteristic of this type of detector.

Conclusions

We have shown a few examples of how the FDTD method can be used to model GPR antennas. While other computational methods can model the simple antennas shown here, the FDTD method is flexible enough to model more complex antennas, such as horns and cavity-backed antennas. The FDTD method also accounts automatically for any antenna-antenna interactions, important because many GPR systems use bi-static configurations. The inherent near-zone nature of the target and antenna interactions and the broadband bandwidth of many GPR systems makes the FDTD method particularly attractive. In addition, we have written an FDTD code that displays the fields as an animation; viewing the evolution of the fields often gives insight into antenna operation, as well as visual simulation diagnostics. We can use an FDTD model to generate synthetic data, useful for antenna optimization, system characterization, and signal-processing development. In summary, we find the FDTD method to be a useful tool for GPR antenna and system engineering.

References

1. Raymond Luebbers, Forrest P. Hunsberger, Karl S. Kunz, Ronald B. Standler, and Michael Schneider, "A Frequency-Dependent Finite-Difference Time-Domain Formulation for Dispersive Materials," *IEEE Trans. Electromagnetic Compat.*, vol. 32, no. 3, 222 227, August 1990.

2. Brian J. Zook, "A Dispersive Outer Radiation Boundary Condition for FDTD Calculations," *Proc. of the Tenth Annual Review of Progress in Applied Computational Electromagnetics*, Volume I, March 22 25, 1994, Monterey, CA, pp. 240 247.

3. M. Moghaddam, E.J. Yannakakis, W.C. Chew, and C. Randall, "Modeling of the Subsurface Interface Radar," *J. Electromagnetic Waves and Applications*, vol. 5, no. 1, 17 39, 1991.

4. G.H. Brown and O.M. Woodward, "Experimentally Determined Radiation Characteristics of Conical and Triangular Antennas," *RCA Rev.*, vol. 13, 425 452, December 1952.

5. David A. Hill, "Near-Field Detection of Buried Dielectric Objects," *IEEE Trans. Geoscience and Remote Sensing*, vol. 27, no. 4, 364 368, July 1989.

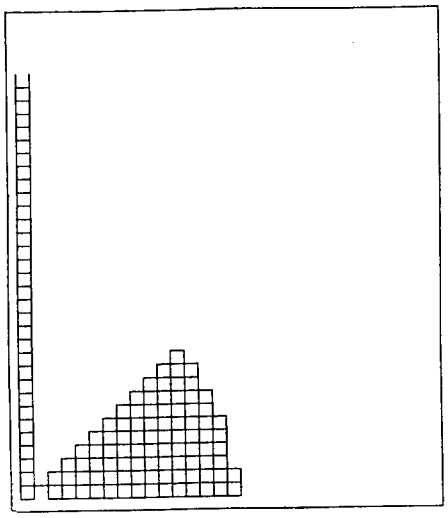


Figure 1. FDTD Model of Bowtie Antenna. Top view showing the FDTD cell edges that are set to be perfect electrical conductors.

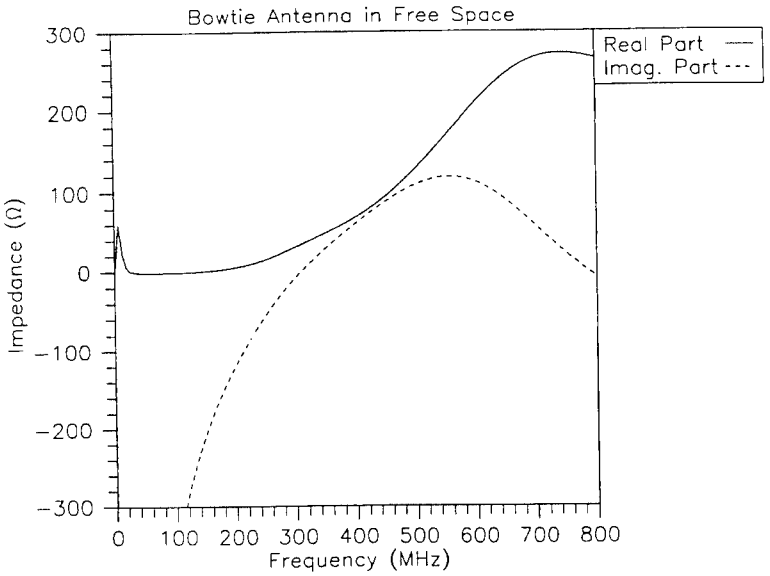


Figure 2. Impedance of Bowtie Antenna in Free Space. Shows both the resistance and the reactance.

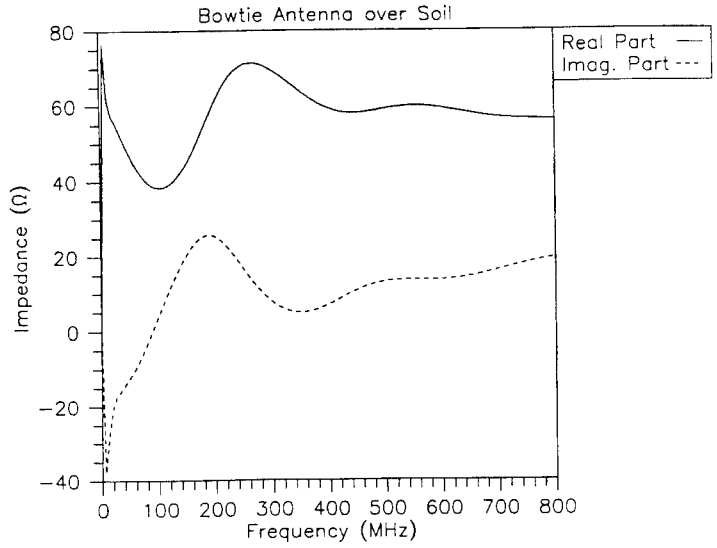


Figure 3. Impedance of Bowtie Antenna over Soil. Suspended 1 cm over soil, which is modeled as a double-Debye medium with parameters in Table I.

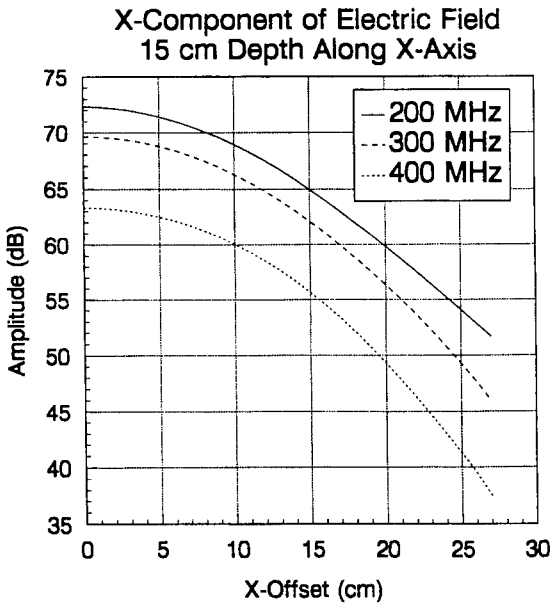


Figure 4. Bowtie Field Pattern at Depth of 15 cm. Shows E_x along axis of antenna.

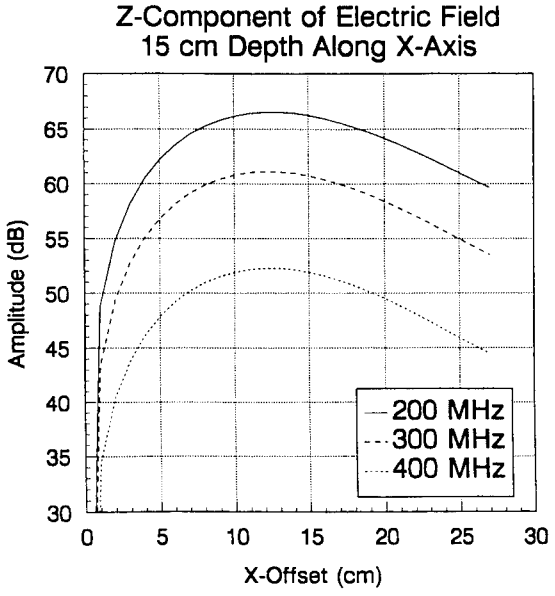


Figure 5. Bowtie Field Pattern at Depth of 15 cm. Shows E_z along axis of antenna.

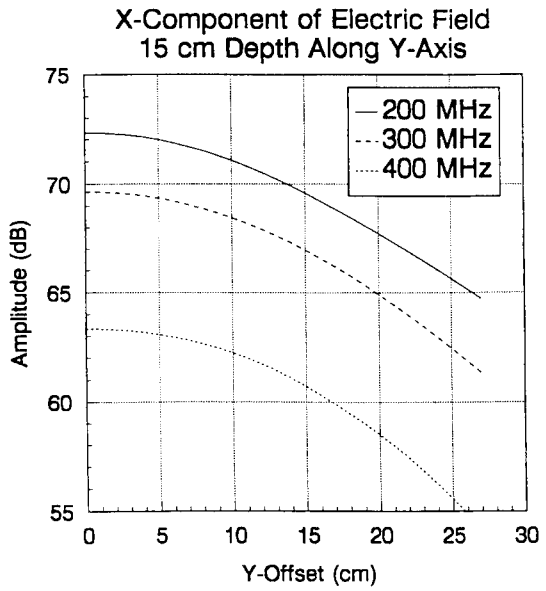


Figure 6. Bowtie Field Pattern at Depth of 15 cm. Shows E_x along perpendicular axis of antenna.

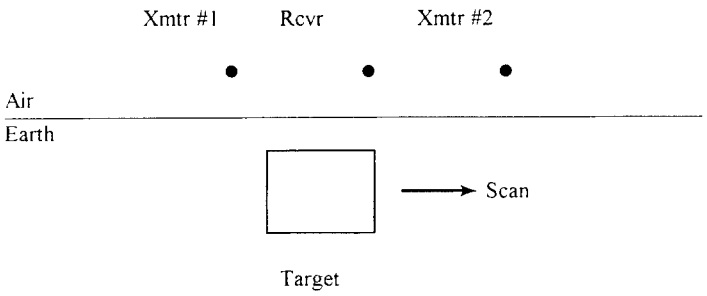


Figure 7. Side View (Cross Section) of 3D FDTD Model for UHF Balanced-Bridge Detector

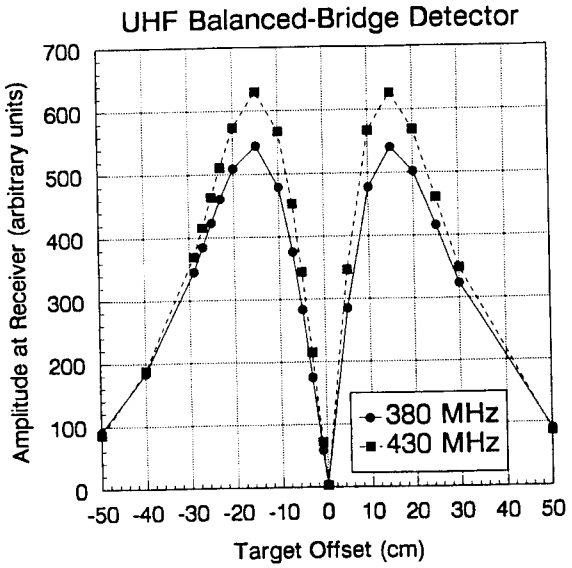


Figure 8. Simulated Response of UHF Balanced-Bridge Detector. The target is scanned in the direction indicated in Figure 7.

FDTD MODELING OF ULTRASHORT OPTICAL PULSE INTERACTIONS WITH NONRESONANT AND RESONANT MATERIALS AND STRUCTURES

Richard W. Ziolkowski
Electromagnetics Laboratory
Department of Electrical and Computer Engineering
The University of Arizona, Tucson, AZ 85721 USA
(602) 621-6173 (office) (602) 621-8076 (fax)
ziolkowski@ece.arizona.edu

Laser pulses are continuing to be utilized in a variety of advanced commerical, civilian, and military systems. Their bandwidth and intensity have been increasing, to the point at which the materials they interact with no longer respond in a linear fashion. The material response is nonlinear and the properties of the materials depend on the shape of the pulse propagating in them. Moreover, the materials have memory effects so that trains of multiple pulses can produce effects similar to those occuring from one large pulse. Despite the increase in complexity of the associated physical properties, these nonlinear effects offer the potential for a variety of novel device and systems applications.

Nonlinear optical (NLO) devices are currently being explored for their applications in various systems associated with communications, remote sensing, optical computing, etc. However, as the size of optical devices such as microcavity lasers is pushed to the size of an optical wavelength and less, the need for more exact materials and response models is tantamount to the successful design and fabrication of those devices. Most current simulation models are based on known macroscopic, phenomenological models that avoid issues dealing with specific microscopic behavior of the materials in such NLO devices. Inaccuracies in the simulation results are then exaccerbated as the device sizes shrink to subwavelength sizes and the response times of the excitation signals surpass the response times of the material. There are laser sources currently under development with sub-micron wavelengths that are pushing the boundaries of the sub-femtosecond regime. Phenomenological non-resonant models lose their ability to describe the physics in this parameter regime; hence, they lose their accuracy there. Quantum mechanical effects begin to manifest themselves; the simulation models must incorporate this behavior to be relevant.

Until recently, the modeling of pulse propagation in and scattering from complex nonlinear media has generally been accomplished with one-dimensional, scalar models. These models have become quite sophisticated; they have predicted and explained many of the

nonlinear as well as linear effects in present devices and systems. Unfortunately, they can not be used to explain many observed phenomena, and expectations are that they are not adequately modeling multi-dimensional nonlinear phenomena. It is felt that vector and higher dimensional properties of Maxwell's equations that are not currently included in existing scalar models in addition to more detailed material and device structure models may significantly impact the scientific and engineering results. The associated propagation and scattering issues have a direct impact on a variety of applications, particularly on the design and engineering of integrated photonic components that have immediate utility to nonlinear soliton fiber optical communications systems currently under development. It is believed that the successful development of semi-classical simulators that combine numerical quantum mechanical models of materials and macroscopic Maxwell's equations solvers will significantly affect the concept and design stages associated with novel nonlinear optics phenomena.

The problem of accurate numerical modeling of the propagation of ultrafast pulses in nonlinear media and their use in NLO optical devices has been subject to increasing interest in recent years. Since the most interesting nonlinear phenomena are transient and superposition is not available, it is natural to try to carry out this modelling directly in the time-domain. For this reason the finite-difference time-domain (FDTD) method is receiving intensive study for modeling linear and nonlinear optical phenomena. In contrast to the case for frequency-domain linear analysis, a single value of permittivity ϵ is completely inadequate to describe nonlinear time-dependent phenomena, and it is essential to model the interaction of the electromagnetic field with the material medium.

Initial simulations of these ultrafast optical pulse interactions have been based upon several well-known phenomenological material models[1-7]. They included the linear Lorentz dispersion model, the nonlinear Debye model, the nonlinear Raman model, and the instantaneous nonlinear Kerr model. This approach has allowed an investigation of the usually neglected longitudinal field component and polarization effects when optical beams self-focus in bulk materials and of the physics underlying the design of optical beam steerers and output couplers constructed from corrugated linear and nonlinear waveguides. Nonetheless, while they have been adequate for the applications considered, these phenomenological material models do not handle well fully resonant interactions. To understand the physics underlying the small-distance scale and short-time scale interactions, particularly in the resonance regime of the materials and the associated device structures, a first principles approach is desirable. This in turn requires quantum-mechanical descriptions of the electronic states available in the medium. Accurate physical models must incorporate all propagation effects such as dispersion and nonlinearity, with the proper physical linkages between them.

We have developed a simulator that utilizes the Maxwell-Bloch system for multi-level atoms for our material models in Maxwell's equations. This effort is novel in that it combines a realistic material model that is quantum mechanically based with a full-wave, vector

Maxwell's equations solver. The FDTD implementations of the Maxwell-Bloch modeling system in one space dimension and time has been accomplished[8] and has yielded some interesting physical consequences. In particular, in a density matrix approach to arrive at the Bloch equations describing a two-level atom medium we introduce the terms ρ_1, ρ_2, and ρ_3, which satisfy the relationship $\rho_1^2 + \rho_2^2 + \rho_3^2 = 1$, and represent, respectively, the dispersive or in-phase component of the polarization, the absorptive or in-quadrature component of the polarization, and the fractional difference in the populations for the two energy levels. The near-resonant behaviour of nonlinear systems cannot be meaningfully discussed unless dissipative effects are taken into account. The usual method of achieving this in simple systems is to include in the Liouville equations for these terms, phenomenologically obtained diagonal terms consisting of characteristic decay rates. If we take the incident electromagnetic field to be a uniform plane wave that is propagating along the z-axis and is polarized along the x-axis; i.e., $\vec{E}(\vec{r},t) = E_x(z,t)\,\hat{x}$ and $\vec{H}(\vec{r},t) = H_y(z,t)\,\hat{y}$ and set the spatial orientation of the dipole to be $\hat{x}$, the polarization takes the form $\vec{P} = P_x\,\hat{x}$, where

$$P_x(t) = -N_{atom}\,\gamma\,\rho_1(t)\,, \tag{1}$$

N_{atom} being the number density of atoms and γ the dipole coupling coefficient. The following one-dimensional Maxwell-Bloch system results from this reduction:

Maxwell equations

$$\partial_t\,H_y = -\frac{1}{\mu_0}\,\partial_z\,E_x \tag{2a}$$

$$\begin{aligned}\partial_t\,E_x &= -\frac{1}{\epsilon_0}\,\partial_z\,H_y - \frac{1}{\epsilon_0}\,\partial_t P_x \\ &= -\frac{1}{\epsilon_0}\,\partial_z\,H_y - \frac{N_{atom}\,\gamma}{\epsilon_0\,T_2}\,\rho_1 + \frac{N_{atom}\,\gamma\,\omega_0}{\epsilon_0}\,\rho_2\end{aligned} \tag{2b}$$

Bloch equations

$$\partial_t\,\rho_1 = -\frac{1}{T_2}\,\rho_1 + \omega_0\,\rho_2 \tag{3a}$$

$$\partial_t\,\rho_2 = -\omega_0\,\rho_1 - \frac{1}{T_2}\,\rho_2 + 2\,\frac{\gamma}{\hbar}\,E_x\,\rho_3 \tag{3b}$$

$$\partial_t\,\rho_3 = -2\,\frac{\gamma}{\hbar}\,E_x\,\rho_2 - \frac{1}{T_1}\,(\rho_3 - \rho_{30}) \tag{3c}$$

where T_1 is the excited state lifetime, T_2 is the dephasing time, and ρ_{30} is the initial population difference in the system. Note that the specification that $\rho_{30} = -1$ $(+1)$ represents all the atoms initially being in their ground (excited) states. This system of

equations can be discretized using finite differences in several different ways. We have characterized the performance of several of these discrete approaches and feel that we know how to extend this semi-classical model to higher space dimensions and to more complex media such as a three-level atom medium. Our best approach obtained to date will be highlighted in the presentation.

Using this FDTD approach to solving the semiclassical Maxwell-Bloch system, we have studied in a more exact manner (without removing the carrier wave) self-induced transparency effects in a two-level atom medium. Standard self-induced transparency (SIT) , the so-called π, 2π, 4π, ... results have been reproduced with this model. A SIT solution represents the nonlinear wave propagation dynamics in which a particular pulse shape, a carrier at the transition frequency with a hyperbolic secant envelope, having the appropriate high intensity completely loses its energy to a two-level atom medium by stimulating it from its ground state into its excited state, and then is completely reconstructed in a coherent manner via stimulated emission by having the excited medium completely decay back into its ground state. This SIT pulse thus propagates through the highly nonlinear two-level atom medium with no change in its shape; i.e., as though the medium is transparent; it is a soliton solution of the semiclassical Maxwell-Bloch system. The SIT effect is normally described with a rotating wave approximation of the Maxwell-Bloch system. As will be demostrated, we have recovered these SIT pulse dynamics with our FDTD Maxwell-Bloch simulator. However, we have also found[8] novel features that appear at points where the electric field is null and have been identified as being associated with the maximums of the time derivative of the electric field. These features are not present is standard approximate solutions to this problem.

These nonlinear time-derivative effects have been emphasized further[8] by considering a variety of ultrafast pulse cases. It have been demonstrated that during ultrafast pulse interactions with a two-level atom medium that a single cycle pulse can be designed that completely inverts the two-level atom medium. A multiple ultrafast pulse train has been given that can completely invert the medium from the ground to the excited state and then completely reverse the process. These results confirm that the time-derivative-driven nonlinear properties of the two-level atom medium have a significant impact on the time evolution of this system in the limit of ultrafast pulses.

We have also used[8] the FDTD Maxwell-Bloch simulator to recover expected small-signal gain results for sinusoidal input signals. The designed ultrafast inversion pulse has been combined with a sinusoid input signal to form a pump-probe signal set. It will be illustrated that a two-level atom medium could be inverted by the leading ultrafast pulse to yield a gain medium for the trailing sinusoidal probe pulse.

Several examples of the SIT and the time-derivative pulse propagation effects will be shown in the presentation. Full device and system integration complexities are presently being introduced into our model by considering multi-dimensional (spatial) extensions. We are investigating several different amplifier and microcavity laser configurations with the

resulting multi-dimensional FDTD Maxwell-Bloch simulator. Progress to date in higher dimensions will also be reported.

REFERENCES

1. Ziolkowski, R. W., and J. B. Judkins, "Full-wave vector Maxwell equation modeling of the self-focusing of ultrashort optical pulses in a nonlinear Kerr medium exhibiting a finite response time", *J. Opt. Soc. Am. B*, vol. 10(2), 186-198, 1993.

2. Ziolkowski, R. W., and J. B. Judkins, "Applications of Discrete Methods to Pulse Propagation in Nonlinear Media: Self-Focusing and Linear-Nonlinear Interfaces", invited paper, Special issue of Radio Science for the 1992 URSI EM Theory Symposium, Radio Sci., vol. 28(5), 901-911, 1993.

3. R. W. Ziolkowski and J. B. Judkins, "NL-FDTD Modeling of Linear and Nonlinear Corrugated Waveguides", J. Opt. Soc. Am. B, vol. 11(9), 1565-1575, 1994.

4. J. B. Judkins and R. W. Ziolkowski, "FDTD Modeling of nonperfect metallic thin film gratings", submitted to J. Opt. Soc. Am. A, 1994.

5. Goorjian, P. M., and A. Taflove, "Direct time integration of Maxwell's equations in nonlinear dispersive media for propagation and scattering of femtosecond electromagnetic solitons", *Opt. Lett.*, vol. 17(3), 180-182, 1992.

6. Goorjian, P. M., A. Taflove, R. M. Joseph, and S. C. Hagness, "Computational modeling of femtosecond optical solitons from Maxwell's equations", *IEEE J. Quan. Electr.*, vol. QE-28(10), 2416-2422, 1992.

7. R. M. Joseph, Goorjian, P. M., and A. Taflove, "Direct time integration of Maxwell's equations in two-dimensional dielectric waveguides for propagation and scattering of femtosecond electromagnetic solitons" *Opt. Lett.*, vol. 18(7), 491-493,1993.

8. Richard W. Ziolkowski, John M. Arnold, and Daniel M. Gogny, "Ultrafast pulse interactions with two-level atoms", submitted to Phys. Rev. A, 1995.

Time Domain Analysis of Electromagnetic Wave Propagation in Nonlinear Dielectric Slab

G. Miano, C. Serpico, L. Verolino, F. Villone
Dipartimento di Ingegneria Elettrica
Università degli Studi di Napoli "Federico II"
Via Claudio 21 I-80125 Napoli Italy

1. Introduction

In recent years the growing interest in nonlinear electromagnetic problems, usually related to electronic devices and systems, has resulted in several studies on nonlinear propagation phenomena [1]. These phenomena typically correspond to mathematical models constituted by a set of nonlinear hyperbolic partial differential equations. Indeed, the main feature of this kind of initial-boundary value problems is that perturbations propagate with finite speed. Often these problems are solved in the "weakly" nonlinear limit [2]; in this way the difficulties related to the resolution of nonlinear hyperbolic problems are overcome. On the contrary, in this paper the electromagnetic wave propagation in a "strongly" nonlinear dielectric is studied in the time domain, directly solving the set of the Maxwell equations using two complementary formulations [3] and the Galerkin method [4].

It is well known that nonlinear hyperbolic equations can generate discontinuous solutions, like shock-waves, even if the initial and the boundary conditions are regular [5]. Indeed, in contrast with diffusion processes, the propagation of waves does not lead to an increase of smoothness of the solution for increasing times. Consequently, it is not possible, in general, to prove the existence of smooth solutions of nonlinear wave equations for all times. Roughly speaking, the collisions of different parts of the wave, propagating with different speeds because of the nonlinearity, gives rise to the appearance of shock waves (discontinuous solutions). Such shock waves play a crucial role in gas dynamics, where they correspond to discontinuities of physical quantities (density, pressure, velocity). It has been shown that these discontinuities may appear also in the propagation of an electromagnetic wave through a nonlinear dielectric slab exhibiting the Kerr effect [6].

Because of this feature, classical numerical methods, like finite differences and Galerkin methods, may yield unsatisfactory results. We have already shown that, under particular conditions, the Galerkin equations describing the nonlinear propagation may exhibit bifurcation and chaotic phenomena [7]; thus, the numerical analysis has to be carried out with care. Our aim is to investigate how well complementary formulations and Galerkin methods can model the Maxwell equations describing the propagation in a dielectric slab exhibiting the Kerr effect [8]. Although the numerical methods presented in this paper hold for three-dimensional problems, for the sake of simplicity their performance has been evaluated by solving a canonical one-dimensional case. This choice has been made because the formation of sharp discontinuities of the front wave can be seen also in this "simple" case.

In addition to the Galerkin method we have developed two scheme based on the central finite differences [4] and on the characteristic formulation [9]. The characteristic method promises, with little modification, to be able to describe the discontinuous solutions. The results of the Galerkin method are then compared with the ones of the last two schemes.

2. Problem formulation

Let's consider an electromagnetic plane wave and suppose that it is incident from the left on a nonlinear, isotropic, homogeneous, nondispersive, time-invariant dielectric slab of width z_0 (Fig.1), whose constitutive property links the electric field to the electric displacement at the same time.

We suppose that the fields **E** and **D** are directed in the x direction, while the fields **H** and **B** are directed in the y direction, so that the plane wave propagates in the z direction:

$$\begin{cases} \mathbf{E} = E(z,t)\mathbf{i}_x \\ \mathbf{D} = D(z,t)\mathbf{i}_x \end{cases} \qquad \begin{cases} \mathbf{H} = H(z,t)\mathbf{i}_y \\ \mathbf{B} = B(z,t)\mathbf{i}_y \end{cases}$$

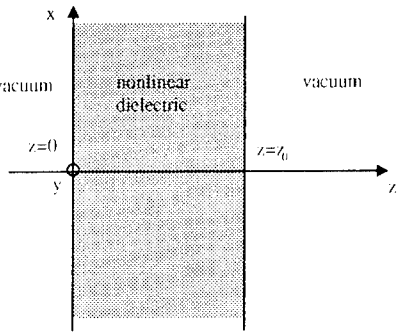


Fig. 1

We want to study the propagation of the electromagnetic field in the slab. Maxwell equations can be written, for $z\in[0,z_0]$ and $t>0$, in the following form:

$$\begin{cases} \dfrac{\partial E}{\partial z} + \dfrac{\partial B}{\partial t} = 0 \\ \dfrac{\partial H}{\partial z} + \dfrac{\partial D}{\partial t} = 0 \end{cases} \tag{1}$$

To solve the electromagnetic problem, we add to (1) the following constitutive relations, representing a dielectric slab exhibiting the *Kerr effect*

$$\begin{cases} B = \mu_0 H \\ E = E(D) = \left(1 + \eta D^2\right)\dfrac{D}{\varepsilon_0 \varepsilon_r} \end{cases} \qquad 0<z<z_0 \tag{2}$$

homogeneous initial conditions, and the following boundary conditions

$$\begin{cases} Z_0 H\left(z = 0^+, t\right) + E\left(z = 0^+, t\right) = 2E_i(-ct) \\ Z_0 H\left(z = z_0^-, t\right) - E\left(z = z_0^-, t\right) = 0 \end{cases} \tag{3}$$

where ε_0, μ_0 are respectively the permittivity and the permeability of vacuum, ε_r and η are two positive quantities describing the nonlinear dielectric, Z_0 is the characteristic impedance of the medium surrounding the slab (vacuum), z_0 is the slab width, and E_i is the incident wave, which is supposed to be:

$$E_i(-ct) = \begin{cases} E_m \sin(2\pi f_c t) & 0 < t < T \\ 0 & t < 0, t > T \end{cases} \tag{4}$$

where E_m, f_c and T are the amplitude, the frequency and the duration of the incident wave, respectively. The boundary conditions (3) have been obtained by imposing the continuity of E(z,t) and H(z,t) for $z=0$ and $z=z_0$, and taking into account the propagation phenomena in the vacuum.

It is interesting to note that while in the case of an infinitely long slab we can claim that there is an instantaneous link between H and D, now this is not possible any more. This happens because of the presence of a second dielectric/vacuum interface, on which the propagating wave partially reflects: as a consequence, H and D in any point of the slab and at any time depend on the whole history of H and D themselves.

It is convenient to put (1) - (4) in an dimensionless form. To do this, we write:

$E=E_0e$; $B=B_0b$; $H=H_0h$; $D=D_0d$; $t=T_0\tau$; $z=z_0\zeta$

where small and greek letters represent dimensionless quantities, while the "$_0$" denotes reference quantities. Note that the latter can be arbitrarily chosen, except for the last one, which is assumed to be equal to the slab width.

Now (1) - (4) become, for $\zeta\in[0,1]$ and $\tau>0$:

$$\begin{cases}\alpha_1\dfrac{\partial e}{\partial\zeta}+\dfrac{\partial b}{\partial\tau}=0\\ \alpha_2\dfrac{\partial h}{\partial\zeta}+\dfrac{\partial d}{\partial\tau}=0\end{cases}\qquad \begin{cases}\alpha_1=\dfrac{E_0T_0}{B_0z_0}\\ \alpha_2=\dfrac{H_0T_0}{D_0z_0}\end{cases}$$

$$\begin{cases}b=\alpha_3 h\\ e=\alpha_4\left(1+\alpha_5 d^2\right)d\end{cases}\qquad \begin{cases}\alpha_3=\dfrac{\mu_0H_0}{B_0}\\ \alpha_4=\dfrac{D_0}{\varepsilon_0\varepsilon_r E_0}\\ \alpha_5=\eta D_0^2\end{cases}$$

$$\begin{cases}\alpha_6 h\left(\zeta=0^+,\tau\right)+e\left(\zeta=0^+,\tau\right)=2e_i(\tau)\\ \alpha_6 h\left(\zeta=1^-,\tau\right)-e\left(\zeta=1^-,\tau\right)=0\end{cases}\qquad \alpha_6=\frac{Z_0H_0}{E_0}$$

$$e_i(\tau)=\begin{cases}\alpha_7\sin(2\pi\alpha_8\tau) & 0<\tau<T/T_0\\ 0 & \tau<0,\tau>T/T_0\end{cases}\qquad \begin{cases}\alpha_7=\dfrac{E_m}{E_0}\\ \alpha_8=T_0f_c\end{cases}$$

Since we can arbitrarily choose the values of five reference quantities, we can make the first five dimensionless constants α_i equal to 1. The last three will obviously be different from 1; thus, posing $\gamma=\alpha_6$, $G_0=\alpha_7$, $\nu=\alpha_8$, we can write, for $\zeta\in[0,1]$ and $\tau>0$:

$$\begin{cases}\dfrac{\partial e}{\partial\zeta}+\dfrac{\partial h}{\partial\tau}=0\\ \dfrac{\partial h}{\partial\zeta}+\dfrac{\partial d}{\partial\tau}=0\end{cases}\tag{5}$$

$$e=e(d)=(1+d^2)d\tag{6}$$

$$\begin{cases}\gamma h\left(\zeta=0^+,\tau\right)+e\left(\zeta=0^+,\tau\right)=2e_i(\tau)\\ \gamma h\left(\zeta=1^-,\tau\right)-e\left(\zeta=1^-,\tau\right)=0\end{cases}\tag{7}$$

$$e_i(\tau)=\begin{cases}G_0\sin(2\pi\nu\tau) & 0<\tau<T/T_0\\ 0 & \tau<0,\tau>T/T_0\end{cases}\tag{8}$$

In this form, the underlying parameters of the system are the damping constant γ, the driving amplitude G_0 and the driving frequency ν.

Note that we have got rid of the dimensionless magnetic induction b, because it is identical to h, since $\alpha_3=1$.

3. *Two different potential formulations and Galerkin schemes*

A physically well posed statement of the problem includes the relevant equations, the initial and the boundary conditions. It is useful practice to enforce some of them explicitly. The solution formulation is then, essentially, a procedure for imposing the remaining equations.

In this paper a new technique, based on complementary formulations, first used for magnetostatic problems [3], is proposed for solving the system of equations (5) - (8) and for estimating the errors due to the numerical approximation.

Two complementary formulations of the equations (5) - (8) are considered; each of them enforces one of the Maxwell equations. In the **F**-formulation the unknowns d and h are expressed in terms of the *electric potential* $f(\zeta,\tau)$ as

$$\begin{cases} d = \dfrac{\partial f}{\partial \zeta} \\ h = -\dfrac{\partial f}{\partial \tau} \end{cases}$$

whereas in the **A**-formulation they are expressed in terms of the *magnetic potential* $a(\zeta,\tau)$ as

$$\begin{cases} h = \dfrac{\partial a}{\partial \zeta} \\ e = -\dfrac{\partial a}{\partial \tau} \end{cases}$$

In 3D problems we would introduce the electric (magnetic) vector potential **F** (**A**) such that $\nabla\times\mathbf{F}=\mathbf{D}$, $\mathbf{H}=+\partial\mathbf{F}/\partial t$ ($\nabla\times\mathbf{A}=\mathbf{B}$, $\mathbf{E}=-\partial\mathbf{A}/\partial t$).

In each formulation, the remaining Maxwell equation has to be enforced explicitly. To do this, it is rewritten in a *weak form* first: then, it is discretized in the space by means of the *Galerkin method*. The boundary conditions (7) are imposed as natural boundary conditions. Finally, the ordinary differential equations obtained in this way are solved in time by a fourth-order Runge-Kutta method.

As far as the error introduced by the Galerkin method is concerned, it may be estimated by solving the same problem using both the formulations [3]. In this way, taking the difference between the solutions coming from the **F**-formulation and the **A**-formulation, a measure of the numerical error is obtained. This means that we are making the following assumption: the smaller is the difference between the solutions of the two formulations, the closer we are to the exact solution. This assumption allows an estimation of the global error and provides a useful indication for spatial discretization refinements.

3.1 Electric vector potential

Introducing the electric potential $f=f(\zeta,\tau)$ the second equation of system (5) is automatically satisfied, while the first can be written in the following form:

$$\begin{cases} \dfrac{\partial h}{\partial \tau} + \dfrac{\partial}{\partial \zeta}\left(c \left(\dfrac{\partial f}{\partial \zeta} \right) \right) = 0 \\ \dfrac{\partial f}{\partial \tau} + h = 0 \end{cases} \qquad (9)$$

to which we must add initial and boundary conditions.

Now we give a weak form of (9); to do this, we define the scalar product of two functions $u(\zeta)$ e $v(\zeta)$ as:

$$\langle u(\zeta), v(\zeta) \rangle = \int_0^1 u(\zeta) v(\zeta)\, d\zeta$$

Giving a weak form of (9) means projecting the residuals of (9) on a suitable set W of test functions $w(\zeta)$ and to vanish these projections:

$$\begin{cases} \left\langle w, \dfrac{\partial h}{\partial \tau} \right\rangle + \left\langle w, \dfrac{\partial}{\partial \zeta}\left(c\left(\dfrac{\partial f}{\partial \zeta} \right) \right) \right\rangle = 0 \\ \left\langle w, \dfrac{\partial f}{\partial \tau} \right\rangle + \langle w, h \rangle = 0 \end{cases} \qquad \forall w(\zeta) \in W$$

Integrating by parts and using boundary conditions (7) we get

$$\begin{cases} \dfrac{d}{d\tau}\langle w, h \rangle = \left\langle \dfrac{\partial w}{\partial \zeta}, c\left(\dfrac{\partial f}{\partial \zeta} \right) \right\rangle + \gamma w(0) \left. \dfrac{\partial f}{\partial \tau} \right|_{\zeta=0} + \gamma w(1) \left. \dfrac{\partial f}{\partial \tau} \right|_{\zeta=1} + 2w(0) c_i(\tau) \\ \dfrac{d}{d\tau}\langle w, f \rangle = -\langle w, h \rangle \end{cases} \qquad \forall w(\zeta) \in W \qquad (10)$$

Note that using this approach the boundary conditions are automatically taken into account in (10).

To solve (10) numerically, we divide the [0,1] interval in N subintervals (one-dimensional finite element mesh); then, we approximate the unknown fields h and f as linear combinations of a finite number N of basis functions $w_i(\zeta)$:

$$h(\zeta) = \sum_{i=1}^{N} h_i(\tau) w_i(\zeta) \qquad f(\zeta) = \sum_{i=1}^{N} f_i(\tau) w_i(\zeta)$$

Choosing as w_i the usual finite element basis functions, h_i and f_i are exactly the nodal values of the fields h and f. Then, we follow the Galerkin method: the basis functions w_i just introduced are chosen also as the test functions on which we project the residuals. Doing so, from the weak form (10) we get the following system of ordinary differential equations, in which the unknowns are the vectors $\mathbf{f} = \{ f_i \}$ and $\mathbf{h} = \{ h_i \}$:

$$\begin{cases} L\dot{\mathbf{h}} = \mathbf{g}(\mathbf{f}) - R\mathbf{h} + s(\tau) \\ L\dot{\mathbf{f}} = -L\mathbf{h} \end{cases} \qquad (11)$$

where $L_{ij} = \langle w_i, w_j \rangle$ i,j=1,N , $R = \mathrm{diag}(\gamma, 0, \ldots, 0, \gamma)$, $s(\tau) = (2c_i(\tau), 0, \ldots, 0)$ and $g_i(\mathbf{f}) = \left\langle \dfrac{dw_i}{d\zeta}, c\left(\sum_{j=1}^{N} f_j \dfrac{dw_j}{d\zeta} \right) \right\rangle$ i=1,N.

Note that $\det(L) \neq 0$, since $w_1, \ldots, w_N$ are linearly independent. Consequently, (11) can be solved for **f** and **h**.

3.2 Magnetic vector potential

Introducing the magnetic potential $a = a(\zeta, \tau)$ the first of (5) is automatically satisfied, while the second one can be written in the following form:

$$\begin{cases} \dfrac{\partial d}{\partial \tau} + \dfrac{\partial^2 a}{\partial \zeta^2} = 0 \\ \dfrac{\partial a}{\partial \tau} + c(d) = 0 \end{cases}$$

Performing the same calculations as before, we get the following equations

$$\begin{cases} \dfrac{d}{d\tau}\langle w, d \rangle = -\left\langle \dfrac{\partial w}{\partial \zeta}, \dfrac{\partial a}{\partial \zeta} \right\rangle + \dfrac{1}{\gamma} w(0) \left. \dfrac{\partial a}{\partial \tau} \right|_{\zeta=0} + \dfrac{1}{\gamma} w(1) \left. \dfrac{\partial a}{\partial \tau} \right|_{\zeta=1} + \dfrac{2}{\gamma} w(0) c_i(\tau) \\ \dfrac{d}{d\tau}\langle w, a \rangle = -\langle w, c(d) \rangle \end{cases} \qquad \forall w(\zeta) \in W \qquad (12)$$

Starting from (12), and introducing $\mathbf{d} = \{ d_i \}$ and $\mathbf{a} = \{ a_i \}$, we get:

$$\begin{cases} \mathbf{L}\dot{\mathbf{d}} = -\dfrac{1}{\gamma^2}\mathbf{R}\mathbf{L}^{-1}\mathbf{q}(\mathbf{d}) + \mathbf{S}\mathbf{a} + \dfrac{1}{\gamma}\mathbf{s}(\tau) \\ \mathbf{L}\dot{\mathbf{a}} = -\mathbf{q}(\mathbf{d}) \end{cases} \tag{13}$$

where $q_i(\mathbf{d}) = \left\langle w_i, c\left\{\left(\sum_{j=1}^{N} d_j w_i\right)\right\}\right\rangle$ i=1,N and $S_{ij} = \left\langle \frac{dw_i}{d\zeta}, \frac{dw_j}{d\zeta} \right\rangle$ i,j=1,N.

4. *Numerical experiments and discussion*

We have studied the propagation of an electromagnetic pulse through the nonlinear dielectric slab. All the numerical simulations proposed in this paper have been performed considering γ=1, v=10 (the thickness of the slab is ten times the wavelength of the incident field), and T/T_0=1/20 (the pulse duration of the incident field is equal to 1/2 wavelength).

In the following, we indicate with (d_A, h_A) and (d_F, h_F) the d, h fields obtained with the **A**-formulation and the **F**-formulation respectively.

Figure 2 refers to a "weakly" nonlinear case (the dimensionless amplitude of the incident wave is G_0=0.1): the waveform is not strongly deformed. Figure 2a shows the field d_A, while Fig. 2b shows the error of the Galerkin method (normalized difference of d_A and d_F), which demonstrates that d_F is very similar to d_A. The results obtained with the finite difference scheme (FDS) and the characteristic scheme (CS) (see Appendix A and B) are very close to d_A, with the exception that the CS scheme does not shows oscillations, while the FDS shows oscillations at the end of the pulse. Thus, we can state that all the proposed schemes are able to study such a situation, in which the nonlinearity doesn't play any significant role.

Figure 3 refers to a "strongly" nonlinear case (G_0=0.4), with N=1000: the results of all schemes are shown. The CS (Fig. 3c) shows the formation of a shock; note that continuously changing the parameter G_0 turns into an abrupt qualitative change in the properties of the solution. This is probably related to the appearance of bifurcations and chaotic phenomena [7]. The CS solution is taken in this case as the reference solution, because this scheme is naturally able to capture the discontinuous solution exactly [9], while the other schemes don't. It is straightforward that the FDS (Fig. 3d) is completely unsuitable to study such a situation, since its solution is both quantitatively and qualitatively wrong. On the other hand, the Galerkin scheme (Fig. 3a) gives a qualitatively good solution, which oscillates before the arrival of the shock. Anyway, the error (Fig. 3b) (defined as before) shows that the d_F solution strongly oscillates after the pulse has passed. We have verified that the oscillations saturate after a suitable period of time. This oscillation is certainly due to the different order of approximation of d_A and d_F: while d_A is piecewise linear, d_F is only piecewise constant, since it is the spatial derivative of f, which is piecewise linear. This conclusion is confirmed by the perfect duality of the behavior of the magnetic fields h_A and h_F. Moreover, we want to stress the fact that a discontinuous function (as the solution in this case) has an infinite Fourier spectrum, with significant very high frequency components. If either the equations or the scheme were dissipative (e.g. viscous processes or schemes), these high frequency components would be attenuated; since both the equations are lossless hyperbolic and the Galerkin scheme coupled with a Runge-Kutta scheme does not introduce numerical viscosity, these components are not attenuated and contribute to undesired oscillations.

These conclusions are confirmed by Fig. 4, in which the Galerkin scheme solution for N=5000 is presented. It is clear that while the d_A solution (Fig. 4a) seems quite better than the previous one, the error is asymptotically much greater, indicating a severe oscillation of the d_F solution. In normal conditions, increasing the number of subintervals N would lead to an improvement of the solution, as in the weakly nonlinear case. In this case, since the discontinuity is much sharper (the solution is closer to the ideal discontinuous one) the excitation of high frequency components is more relevant than before. This in turn causes a stronger undesired oscillation; in addition, the frequency of this oscillation is higher than previously.

Finally, in Table I the r.m.s. error $\varepsilon = \sqrt{\langle d_A - d_F, d_A - d_F \rangle}\,/G_0$ is given for different values of N and G_0.

When G_0=0.1 (weak nonlinearity), ε decreases when N increases: this means that we are converging to the exact solution. On the other hand, for G_0=0.4 (strong nonlinearity) this is not true any more: increasing N results in a global worsening of the solution, even if it gets closer to the ideal one in the region in which the pulse is present.

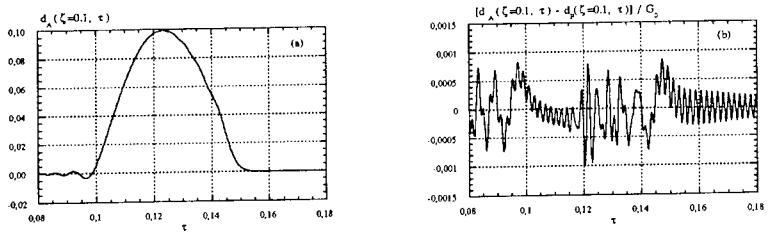


Fig. 2: Galerkin methods with N=1000 (G_0=0.1).

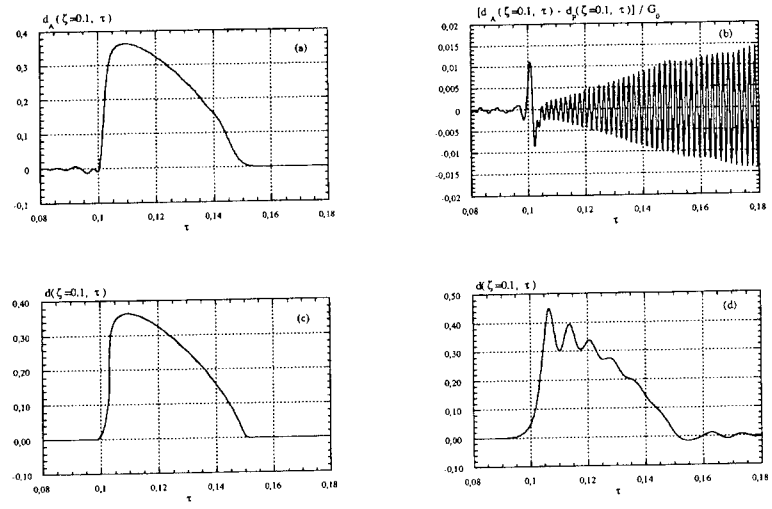


Fig. 3 (N=1000, G_0=0.4): (a), (b) Galerkin methods; (c) characteristic method; (d) finite differences.

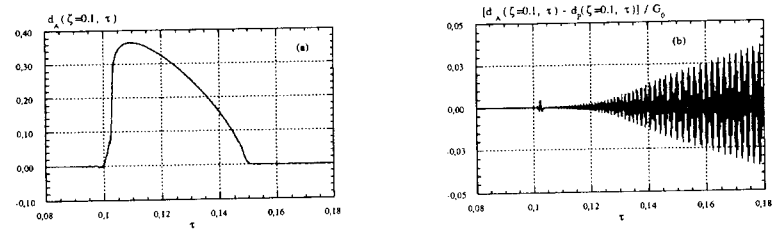


Figure 4: Galerkin methods with N=5000 (G_0=0.4).

	N=100	N=500	N=1000	N=5000
G_0=0.1	$\varepsilon=7.79\cdot10^{-4}$	$\varepsilon=6.08\cdot10^{-5}$	$\varepsilon=2.13\cdot10^{-5}$	$\varepsilon=1.85\cdot10^{-6}$
G_0=0.4	$\varepsilon=7.84\cdot10^{-3}$	$\varepsilon=5.45\cdot10^{-3}$	$\varepsilon=7.21\cdot10^{-3}$	$\varepsilon=1.77\cdot10^{-2}$

Table I

All these remarks demonstrate that studying the convergence of a Galerkin scheme even in a simple nonlinear propagation problem is still an open question.

References

[1] Uslenghi P.L.E., Editor: *Nonlinear Electromagnetics*, Academic Press, New York, 1980; *Special Issue on Advances in Nonlinear Electromagnetism*, Electromagnetics, Vol. 11, no. 3-4, 1991.

[2] Newel A.C., Moloney J.V., *Nonlinear Optics*, Addison-Wesley, New York, 1992.

[3] Rikabi J., Bryant C.F., Freeman E.M., "An error-based approach to complementary formulations of static field solutions", *Int. J. Num. Methods Eng.* 26, 1963 (1988).

[4] Ames W.F., *Numerical Methods for partial differential equations*, Academic Press, 1977

[5] Witham G.B., *Linear and Nonlinear waves*, John Wiley & Sons, New York, 1974

[6] Landau L.D., Lifsits E.M., *Electrodynamics of continuous media*, MIR, Moscow, 1986

[7] De Magistris M., Miano G., Verolino L., Visone C., Zamparelli E., "A Numerical Analysis of the Behaviour of the Galerkin Equations Relevant to Electromagnetic Wave Propagation in Nonlinear Media", IEEE Trans. on Magnetics, MAG-30 (1994).

[8] Albanese R., Fresa R., Miano G., Rubinacci G., Verolino L., "Finite Element Solution of Nonlinear Equations in the Time Domain", *COMPEL*, Vol. 13, 1994

[9] Ralston A., Wilf H.S., *Mathematical Methods for Digital Computers*, John Wiley & Sons, New York, 1960

Appendix A: finite difference scheme

Now we will describe how to solve (5) - (8) with a finite difference scheme. We divide the whole slab ($0\le\zeta\le1$) with N points ζ_i spaced of Δ, and we approximate the spatial derivative with a second order finite difference scheme (central finite differences):

$$x'(\zeta_i) \cong \frac{x(\zeta_{i+1}) - x(\zeta_{i-1})}{2\Delta} \qquad \varepsilon = o(\Delta^2)$$

Thus, we can write:

$$\begin{cases} \dfrac{\partial h_j}{\partial \tau} = \dfrac{e(d_{j-1}) - e(d_{j+1})}{2\Delta} \\ \dfrac{\partial d_j}{\partial \tau} = \dfrac{h_{j-1} - h_{j+1}}{2\Delta} \end{cases} \tag{A.1}$$

where h_j e d_j are the unknowns (nodal values of the fields). So, we get a system of ordinary differential equations, which can be solved with one of the available methods; in particular, we used a fourth-order Runge-Kutta algorithm.

Obviously, we must add to (A.1) initial and boundary conditions; moreover, (A.1) can be written only for j=2,...,N. Indeed, on the boundaries (j=1 and j=N), we can use only one-sided finite differences, since we can use only internal points; as a consequence, we must use at least three points to obtain second order schemes.

In particular, we used the following second order schemes:

$$x'(\zeta_1) \cong \frac{-x(\zeta_3) + 4x(\zeta_2) - 3x(\zeta_1)}{2\Delta} \qquad \varepsilon = o(\Delta^2)$$

$$x'(\zeta_N) \cong \frac{3x(\zeta_N) - 4x(\zeta_{N-1}) + x(\zeta_{N-2})}{2\Delta} \qquad \varepsilon = o(\Delta^2)$$

Appendix B: characteristic formulation and numerical scheme

Using the equation (6), the system (5) can be written in the following form:

$$\begin{cases} \dfrac{\partial h}{\partial \tau} + v^2(d)\dfrac{\partial d}{\partial \zeta} = 0 \\ \dfrac{\partial d}{\partial \tau} + \dfrac{\partial h}{\partial \zeta} = 0 \end{cases} \tag{B.1}$$

where $v^2 = \dfrac{\partial e}{\partial d} = 1 + 3d^2$. Let's consider the following ordinary differential equations:

$$\begin{cases} \dfrac{d\zeta}{d\tau} = \sigma_+ = +v \\ \dfrac{d\zeta}{d\tau} = \sigma_- = -v \end{cases} \tag{B.2}$$

The integral curves of (B.2) are called the *characteristic curves* C_+ and C_- of problem (B.1). Assuming that σ_+ and σ_- are smooth enough, the characteristic curves of the same family do not intersect: in this case, we can introduce a couple of curvilinear coordinates $\alpha(\zeta,\tau)$ and $\beta(\zeta,\tau)$ such that α (β) is constant over C_+ (C_-) curves.

It can be demonstrated [5, 9] that with these positions (B.1) become:

$$\begin{cases} \dfrac{\partial h}{\partial \alpha} + \sigma_+ \dfrac{\partial d}{\partial \alpha} = 0 \\ \dfrac{\partial h}{\partial \beta} + \sigma_- \dfrac{\partial d}{\partial \beta} = 0 \\ \dfrac{\partial \zeta}{\partial \alpha} = \sigma_+ \dfrac{\partial \tau}{\partial \alpha} \\ \dfrac{\partial \zeta}{\partial \beta} = \sigma_- \dfrac{\partial \tau}{\partial \beta} \end{cases} \tag{B.3}$$

which is called *characteristic system*, in which the unknowns are ζ, τ, h, d as functions of α and β.

Now we describe how to solve (B.3) numerically [9]. Let's suppose that the values of h and d are known in every point of a curve I (Fig. B.1) in the (ζ,τ) plane and let's consider two points, say A and B, on I. The C_+ characteristic starting from A and the C_- characteristic starting from B will meet on E. Integrating the first two of (B.3) along C_- and C_+ respectively we will get two expressions for the value $h(\zeta_E,\tau_E)$; equating these two values we get a nonlinear equation for $d(\zeta_E,\tau_E)$. Solving this nonlinear equation and integrating the last two of (B.3) we obtain the values on E of all the unknowns.

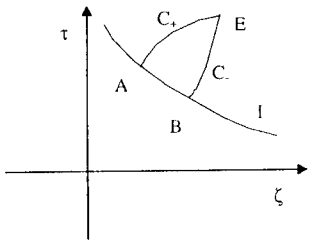


Fig. B.1

An Efficient Sub-gridding Algorithm for FDTD.

D.T.Shimizu, M.Okoniewski M.A.Stuchly

Department of Electrical and Computer Engineering
University of Victoria.
Victoria, B.C., Canada

Many electromagnetic problems which can be effectively modeled using FDTD techniques, have structures comprising large regions where fields vary slowly, and a few small areas where dramatic changes of the field components in space are expected and a fine discretization is required. In a straightforward approach a dense grid is used throughout the computational space. This frequently is not feasible due to the computer resources constraints. Therefore, a few schemes have been previously developed for a dynamic change of the discretization density in the FDTD algorithm. They include mesh refinement in both time and space [2, 3, 4], and mesh refinement in space only [5]

While the latter approach is much simpler to implement, the time and space sub-gridding yields a much more efficient code. This results from the fact that in the second approach the stability condition has to be computed in the smallest cell used, and thus a small time step utilized in the whole problem space.

We have developed an algorithm that provides mesh refinement in space and time. The previously developed algorithms [3, 4] were not described in sufficient details to allow us the comparison between their and our method. We have placed the greatest emphasis on providing a smooth transition between the coarse and fine meshes. To achieve this, extrapolation in time and interpolation in space are used, both accurate to the second order. Since the boundary of the two grids is usually positioned in a homogeneous region of the structure where the field components and its derivatives have smooth behaviour, the second order interpolation and extrapolation is expected to provide sufficient accuracy.

The following guidelines were set before developing the actual algorithm:

- the same stability condition should be used throughout the problem space to keep the numerical dispersion constant [2]

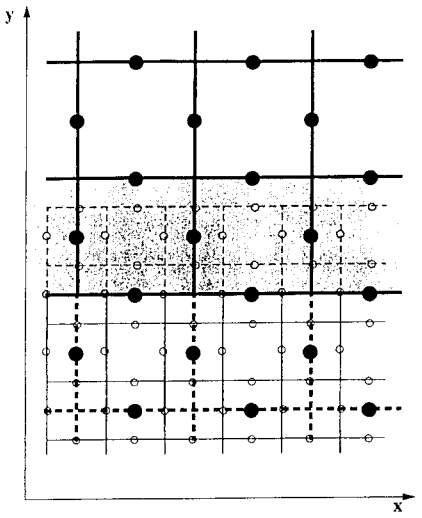


Figure 1: The overlapping meshes adopted in the sub-gridding algorithm

- to minimize the reflections from the fine mesh, small scaling factors, and a sequence of sub-grids rather than an abrupt transition into much finer mesh should be used.

As a main sub-gridding scheme an algorithm with a scaling factor of 2 was adopted (Fig.1). The two meshes are offset in space so that magnetic fields of coarse and corresponding magnetic field of dense mesh are aligned. Figure 1 schematically presents the alignment of the two meshes at their boundary.

Since the frequency of field updates is twice as fast in the fine mesh than in the coarse one, there is not enough information to keep the updates of the most external nodes of the fine mesh computed via FDTD scheme. The pulsing overlapping scheme was developed, where the external-most layer of the fine mesh is dropped in each time sub-step of the refined mesh. At the and of the cycle, the mesh is expanded back to its original size, and the missing field components are computed using interpolation and extrapolation. The gray region in the Fig.1 indicates the pulsing region.

In brief the algorithm can be described as follows (Capital letters denote field quantities of the coarse mesh):

1. Time t=n: Interpolate e^n at the overlapping strip of meshes from E^n
2. Time t=n+1/4: find $h^{n+1/4}$ within the sub-gridded mesh, using FDTD
3. Time t=n+1/2:

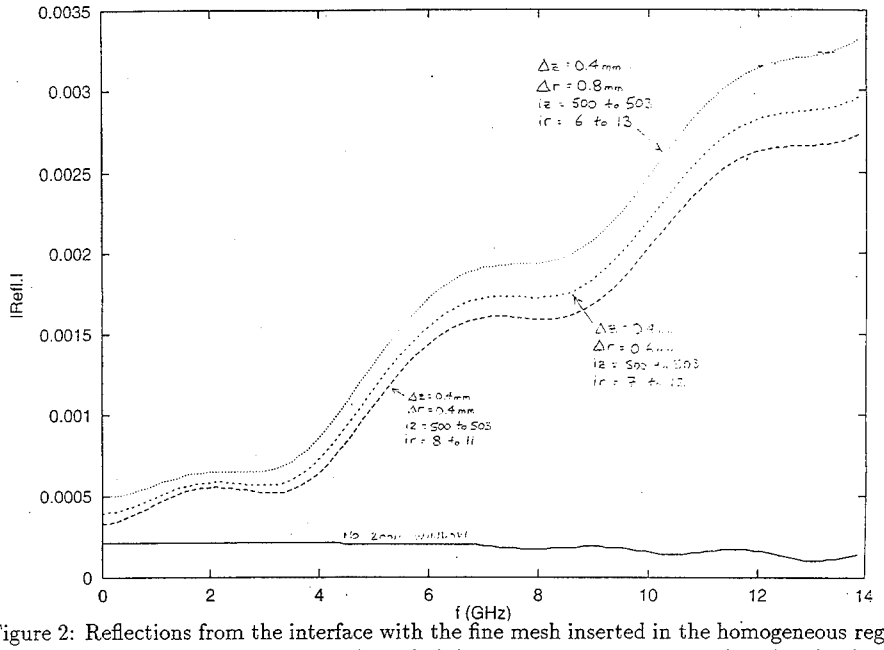


Figure 2: Reflections from the interface with the fine mesh inserted in the homogeneous region of a coaxial line. The fine mesh size in the radial direction is a parameter within the plot family.

- collapse the fine mesh and find $e^{n+1/2}$ using FDTD
- find $H^{n+1/2}$ in a coarse mesh using FDTD

4. Time t=n+3/4:
   - collapse the fine mesh and find $h^{n+3/4}$ using FDTD
   - interpolate $h^{n+1/4}$ and $h^{n+3/4}$ to refine $H^{n+1/2}$
   - expand mesh, use extrapolation in time and interpolation in space to obtain missing $h^{n+3/4}$ values.
5. Time t=n+1: obtain e^{n+1} and E^{n+1} using FDTD
6. cycle

This sub-gridding was implemented in a 2D cylindrical TM mode FDTD code (only E_r, E_z and H_φ field components are allowed). A number of test were carried out, using a homogeneous coaxial line and a coaxial line with discontinuities. Figure 2 illustrates some of the results obtained, namely the reflections generated by the sub-gridding scheme in a homogeneous coaxial line. The computations have been performed for a Teflon coaxial line of 0.456 and 1.49 mm inner and outer conductor radius, respectively. The density of the coarse mesh is 0.1mm, and the fine mesh dimension is shown as a parameter in the figure. It is worth noticing, that the reflections introduced by the

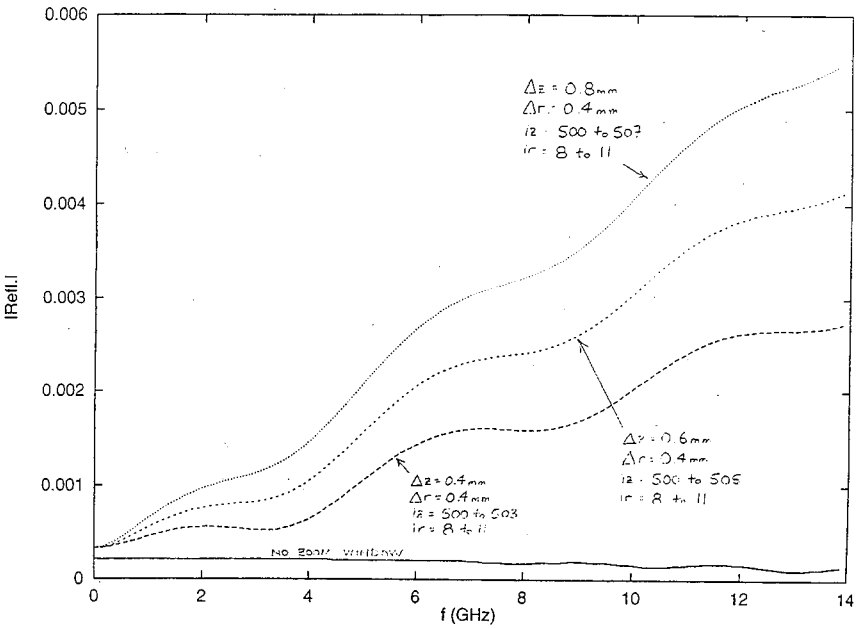


Figure 3: Reflections from the interface with the fine mesh inserted in the homogeneous region of a coaxial line. The fine mesh size in the longitudinal direction is a parameter within the plot family.

refined mesh do not exceed .35%. The developed scheme of sub-gridding satisfies the criteria of the stability and low reflections. Its main limitation is a small factor of mesh subdivision and as a consequence a need for a recursive sub-gridding if a large mesh size reduction is required. To the best of our knowledge, there is no efficient algorithm presently available that satisfies all three requirements.

1 Acknowledgment

Grants from the Natural Sciences and Engineering Research Council of Canada, B.C.Hydro, TransAlta Util., and TR Labs are greatfully acknowledged.

References

[1] K.S. Kunz, R.J. Luebbers, *"Finite Difference Time Domain Method for Electromagnetics"*, CRC Press Inc., 1993.

[2] I.S. Kim, W.J.R. Hoefer, "A local mesh refinement for the time-domain finite-difference method using Maxwell's curl equations," *IEEE Trans. Microwave Theory Tech.*, vol.38 pp.812-815, June 1990.

[3] S.S. Zivanovic, K.S. Yee, K.K. Mei, "A sub gridding method for the time-domain finite difference method to solve Maxwell's equations," *IEEE Trans. Microwave Theory Tech.*, vol.39 pp.471-479, March 1991.

[4] D.T. Prescott, N.V. Shuley, "A method for incorporating different sized cells into the finite-difference time-domain analysis technique," *IEEE Microwave and guided Wave Letters*, vol.2 pp.434-436, Nov.1992.

[5] S.Xiao, R.Valhdieck, H.Jin, "A Fast Two Dimensional FDTD Full-Wave Analyser with Adaptive Mesh Size", *1992 IEEE MTT-S Digest*, pp783-786, 1992

Using the Integral Forms of Maxwell's Equations to Modify and Improve the FDTD (2,4) Scheme

Mohammed F. Hadi
Prof. Melinda Piket-May
Department of Electrical Engineering
University of Colorado at Boulder

INTRODUCTION

One serious flaw of the finite-difference time-domain method which received little attention so far is the excessive phase error that accumulates in the field calculations as the EM waves advance in the numeric grid. In the standard (2,2) scheme (second-order differences in time and space) this phase error changes as a function of the propagation angle, α, with maximum error when propagation is along the principal numeric grid axes and minimum error when the propagation angle is at 45° off the principal grid axes.

To illustrate the above statement, a two-dimensional example is chosen; radiation from an infinite line source. To model this problem the 2–D space is divided following the example of Yee [1] and the TM Maxwell's equations are discretized as follows

$$\begin{aligned}
\frac{E_z|_{i,j}^{n+1} - E_z|_{i,j}^{n}}{\Delta t} &= \frac{1}{\epsilon \Delta x}\left[H_y|_{i+\frac{1}{2},j}^{n+\frac{1}{2}} - H_y|_{i-\frac{1}{2},j}^{n+\frac{1}{2}}\right] - \frac{1}{\epsilon \Delta y}\left[H_x|_{i,j+\frac{1}{2}}^{n+\frac{1}{2}} - H_x|_{i,j-\frac{1}{2}}^{n+\frac{1}{2}}\right] \\
\frac{H_y|_{i,j}^{n+\frac{1}{2}} - H_y|_{i,j}^{n-\frac{1}{2}}}{\Delta t} &= \frac{1}{\mu \Delta x}\left[E_z|_{i+\frac{1}{2},j}^{n} - E_z|_{i-\frac{1}{2},j}^{n}\right] \\
\frac{H_x|_{i,j}^{n+\frac{1}{2}} - H_x|_{i,j}^{n-\frac{1}{2}}}{\Delta t} &= -\frac{1}{\mu \Delta y}\left[E_z|_{i,j+\frac{1}{2}}^{n} - E_z|_{i,j-\frac{1}{2}}^{n}\right]
\end{aligned}$$

where $\Delta x = \Delta y = h = \lambda/R$ (with $R = 20$ typical). The stability criterion [2] forces a maximum limit on the time step that can be chosen for the algorithm

$$\Delta t \leq \frac{h}{c\sqrt{2}}$$

or

$$\Delta t = \frac{h}{c\nu\sqrt{2}} \quad , \qquad \nu \geq 1$$

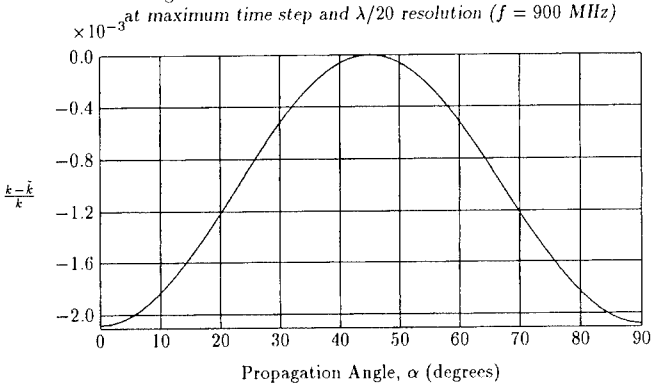
where ν is the courant number. The courant number is defined this way ($\nu = \Delta t/\Delta t_{\max}$) to provide a universal definition that is independent of the FDTD scheme used.

The dispersion relation which is given by [3]

$$\left(\frac{h}{c\Delta t}\right)^2 = \sin^2\left(\frac{\tilde{k}h\cos\alpha}{2}\right) + \sin^2\left(\frac{\tilde{k}h\sin\alpha}{2}\right)$$

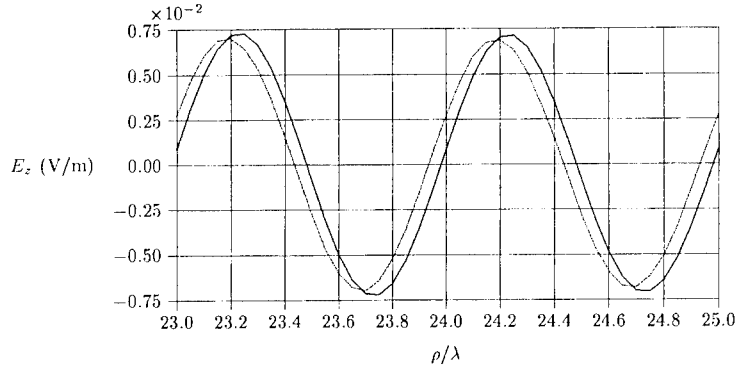
can be used to find the expected phase error in the algorithm as a function of the propagation angle, α, by solving it for the numeric wave number $\tilde{k}$ and comparing this $\tilde{k}$ with the physical wave number, k. Fig. 1 shows the normalized error in the numeric wave number versus the propagation angle for a resolution factor of $R = 20$.

Fig. 1 Normalized error in the numeric wave number at maximum time step and $\lambda/20$ resolution (f = 900 MHz)



When the propagation angle (α) and resolution factor (R) are fixed and the dispersion relation is solved for $\tilde{k}$ at different time steps, i.e., at different values of ν within the limits set by the stability criterion, it was found that decreasing the time step will cause the error in $\tilde{k}$ (which controls the phase error) to increase. Fig. 2 shows how the error in $\tilde{k}$ can translate into a phase error in the FDTD algorithm.

Fig. 2 Electric field radiated by an infinitely thin line source: Exact (solid line) vs. FDTD (dotted line). Phase error is approximately 18° at $\rho = 25\lambda$



The plot in this figure represents a snapshot in time of the electric field at a distance range of 23–25 wavelengths away from the line source. The solid line represents the exact solution given by

$$\tilde{E}(\bar{\rho},t) = \Re\left\{-\bar{a}_z \frac{\omega\mu I_o}{4} H_o^{(2)}(k\rho)e^{j\omega t}\right\} \quad , \qquad \rho > 0$$

and the dashed line represents the FDTD solution. The line current is chosen as a 900 MHz sinusoid. What Fig. 2 is saying is that the standard (2,2) scheme exhibits a phase error of approximately 18° when the wave has travelled 25 wavelengths with a resolution factor of $R = 20$. Please note that the error in the wave amplitude is due to the inaccurate modeling the singularity at $\rho = 0$, the location of the "infinitely" thin line source.

THE STANDARD (2,4) SCHEME

The standard (2,4) scheme refers to FDTD with second-order differences in time and fourth-order differences in space. The corresponding updating equations for the TM Maxwell's equations are given by [4]

$$\begin{aligned}
\frac{E_z|_{i,j}^{n+1} - E_z|_{i,j}^{n}}{\Delta t} &= \frac{1}{24\epsilon\Delta x}\left[H_y|_{i-\frac{3}{2},j}^{n+\frac{1}{2}} - 27H_y|_{i-\frac{1}{2},j}^{n+\frac{1}{2}} + 27H_y|_{i+\frac{1}{2},j}^{n+\frac{1}{2}} - H_y|_{i+\frac{3}{2},j}^{n+\frac{1}{2}}\right] \\
&\quad - \frac{1}{24\epsilon\Delta y}\left[H_x|_{i,j-\frac{3}{2}}^{n+\frac{1}{2}} - 27H_x|_{i,j-\frac{1}{2}}^{n+\frac{1}{2}} + 27H_x|_{i,j+\frac{1}{2}}^{n+\frac{1}{2}} - H_x|_{i,j+\frac{3}{2}}^{n+\frac{1}{2}}\right] \\
\frac{H_y|_{i,j}^{n+\frac{1}{2}} - H_y|_{i,j}^{n-\frac{1}{2}}}{\Delta t} &= \frac{1}{24\mu\Delta x}\left[E_z|_{i-\frac{3}{2},j}^{n} - 27E_z|_{i-\frac{1}{2},j}^{n} + 27E_z|_{i+\frac{1}{2},j}^{n} - E_z|_{i+\frac{3}{2},j}^{n}\right] \\
\frac{H_x|_{i,j}^{n+\frac{1}{2}} - H_x|_{i,j}^{n-\frac{1}{2}}}{\Delta t} &= -\frac{1}{24\mu\Delta y}\left[E_z|_{i,j-\frac{3}{2}}^{n} - 27E_z|_{i,j-\frac{1}{2}}^{n} + 27E_z|_{i,j+\frac{1}{2}}^{n} - E_z|_{i,j+\frac{3}{2}}^{n}\right]
\end{aligned}$$

Using the same technique as for the (2,2) scheme the stability criterion can be derived as

$$\Delta t = \frac{(6/7)h}{\sqrt{2}c\nu} \qquad \nu \geq 1$$

where ν is again defined as $\nu = \frac{\Delta t_{\max}}{\Delta t}$ and the dispersion relation as

$$\left(\frac{24h}{c\Delta t}\right)^2 \sin^2\left(\frac{\omega\Delta t}{2}\right) = \left[27\sin\left(\frac{\tilde{k}h\cos\alpha}{2}\right) - \sin\left(\frac{3\tilde{k}h\cos\alpha}{2}\right)\right]^2 + \left[27\sin\left(\frac{\tilde{k}h\sin\alpha}{2}\right) - \sin\left(\frac{3\tilde{k}h\sin\alpha}{2}\right)\right]^2$$

The results obtained from solving this dispersion relation will be explained in the next section.

THE MODIFIED (2,4) SCHEME

Starting with one of the updating equations from the Standard (2,4) scheme and with the help of Fig. 3 a different form of this equation can be derived that will direct the attention to a way of improving the algorithm. For example

$$\begin{aligned}
\epsilon\frac{\partial E_z}{\partial t} &= \frac{\partial H_y}{\partial x} - \frac{\partial H_x}{\partial y} \\
&= \frac{H_y|_{i-\frac{3}{2},j}^{n+\frac{1}{2}} - 27H_y|_{i-\frac{1}{2},j}^{n+\frac{1}{2}} + 27H_y|_{i+\frac{1}{2},j}^{n+\frac{1}{2}} - H_y|_{i+\frac{3}{2},j}^{n+\frac{1}{2}}}{24\Delta x} \\
&\quad - \frac{H_x|_{i,j-\frac{3}{2}}^{n+\frac{1}{2}} - 27H_x|_{i,j-\frac{1}{2}}^{n+\frac{1}{2}} + 27H_x|_{i,j+\frac{1}{2}}^{n+\frac{1}{2}} - H_x|_{i,j+\frac{3}{2}}^{n+\frac{1}{2}}}{24\Delta y} \\
&= \frac{H_y|_{i-\frac{3}{2},j}^{n+\frac{1}{2}} - H_y|_{i+\frac{3}{2},j}^{n+\frac{1}{2}}}{24\Delta x} - \frac{H_x|_{i,j-\frac{3}{2}}^{n+\frac{1}{2}} - H_x|_{i,j+\frac{3}{2}}^{n+\frac{1}{2}}}{\Delta y} \\
&\quad + \frac{H_y|_{i+\frac{1}{2},j}^{n+\frac{1}{2}} - H_y|_{i-\frac{1}{2},j}^{n+\frac{1}{2}}}{\frac{8}{9}\Delta x} - \frac{H_x|_{i,j+\frac{1}{2}}^{n+\frac{1}{2}} - H_x|_{i,j-\frac{1}{2}}^{n+\frac{1}{2}}}{\frac{8}{9}\Delta y} \\
&= -\frac{1}{8}\left\{\frac{3H_y|_{i+\frac{3}{2},j}^{n+\frac{1}{2}} - 3H_y|_{i-\frac{3}{2},j}^{n+\frac{1}{2}}}{9\Delta x} - \frac{3H_x|_{i,j+\frac{3}{2}}^{n+\frac{1}{2}} - 3H_x|_{i,j-\frac{3}{2}}^{n+\frac{1}{2}}}{9\Delta y}\right\}
\end{aligned}$$

$$
\begin{aligned}
&+\frac{9}{8}\left\{\frac{H_y|_{i+\frac{1}{2},j}^{n+\frac{1}{2}}-H_y|_{i-\frac{1}{2},j}^{n+\frac{1}{2}}}{\Delta x}-\frac{H_x|_{i,j+\frac{1}{2}}^{n+\frac{1}{2}}-H_x|_{i,j-\frac{1}{2}}^{n+\frac{1}{2}}}{\Delta y}\right\}\\
&=-\frac{1}{72\Delta x\Delta y}\left\{3\Delta yH_y|_{i+\frac{3}{2},j}^{n+\frac{1}{2}}-3\Delta yH_y|_{i-\frac{3}{2},j}^{n+\frac{1}{2}}-3\Delta xH_x|_{i,j+\frac{3}{2}}^{n+\frac{1}{2}}+3\Delta xH_x|_{i,j-\frac{3}{2}}^{n+\frac{1}{2}}\right\}\\
&\quad+\frac{9}{8\Delta x\Delta y}\left\{\Delta yH_y|_{i+\frac{1}{2},j}^{n+\frac{1}{2}}-\Delta yH_y|_{i-\frac{1}{2},j}^{n+\frac{1}{2}}-\Delta xH_x|_{i,j+\frac{1}{2}}^{n+\frac{1}{2}}+\Delta xH_x|_{i,j-\frac{1}{2}}^{n+\frac{1}{2}}\right\}\\
&=-\frac{1}{72\Delta x\Delta y}\oint_{c_2}\bar{H}\cdot d\bar{\ell}+\frac{9}{8\Delta x\Delta y}\oint_{c_1}\bar{H}\cdot d\bar{\ell}
\end{aligned}
$$

Knowing that

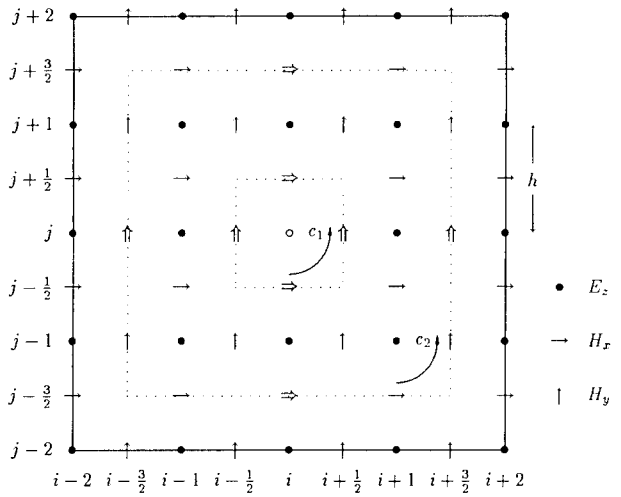
$$
\begin{aligned}
\oint_{c_1}\bar{H}\cdot d\bar{\ell} &= \frac{\partial}{\partial t}\int_{s_1}\bar{D}\cdot d\bar{s}=\epsilon\frac{\partial E_z}{\partial t}\,\Delta x\Delta y\\
\oint_{c_2}\bar{H}\cdot d\bar{\ell} &= \frac{\partial}{\partial t}\int_{s_2}\bar{D}\cdot d\bar{s}=\epsilon\frac{\partial E_z}{\partial t}\,9\Delta x\Delta y
\end{aligned}
$$

the original updating equation can now be written as

$$
\left[\epsilon\frac{\partial E_z}{\partial t}\right]_{\text{FDTD}}=-\frac{1}{8}\left[\epsilon\frac{\partial E_z}{\partial t}\right]_{c_2}+\frac{9}{8}\left[\epsilon\frac{\partial E_z}{\partial t}\right]_{c_1}
$$

This relation shows that the standard (2,4) updating equation is nothing but a weighted sum of the results from applying the modified Ampere's law on two different loops, c_1 and c_2 as shown in Fig. 3 (the bigger hollow arrows and white circle represent the fields used by the standard (2,4) scheme). Note that the two coefficients at the right hand side add up to unity to preserve the integrity of Maxwell's equations.

Fig. 3 The modified Ampere's law applied on Yee's TM Grid

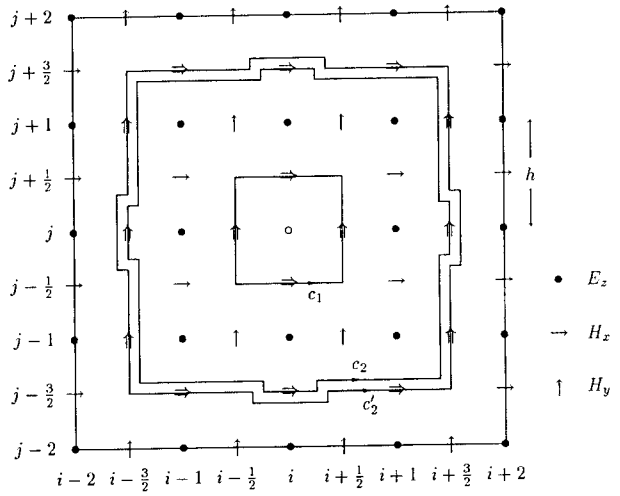


This new form of the standard (2,4) updating equation shows a straightforward way to include all twelve field values along the outer loop. However, this will force a change in the values of the two right hand side

coefficients whose sum must remain unity. Also, splitting the outer loop into two distinct loops (Fig. 4) allows more flexibility in minimizing the phase error and yields a more robust updating equation, as given below

$$\left[\epsilon \frac{\partial E_z}{\partial t}\right]_{\text{FDTD}} = K\left[\epsilon \frac{\partial E_z}{\partial t}\right]_{c_2} + K''\left[\epsilon \frac{\partial E_z}{\partial t}\right]_{c_2'} + (1-K-K'')\left[\epsilon \frac{\partial E_z}{\partial t}\right]_{c_1}$$

Fig. 4 Splitting the outer loop to allow flexibility in minimizing the phase error



The updating equations for the TM Maxwell's equations are now

$$\begin{aligned}
\epsilon \frac{\partial E_z}{\partial t} &= \frac{K}{9\Delta x\Delta y}\oint_{c_2} \bar{H}\cdot d\bar{\ell} + \frac{K''}{9\Delta x\Delta y}\oint_{c_2'} \bar{H}\cdot d\bar{\ell} + \frac{1-K-K''}{\Delta x\Delta y}\oint_{c_1} \bar{H}\cdot d\bar{\ell} \\
&= \frac{K}{3\Delta x\Delta y}\left\{\Delta x\left[H_x|_{i,j-\frac{3}{2}} - H_x|_{i,j+\frac{3}{2}}\right] + \Delta y\left[H_y|_{i+\frac{3}{2},j} - H_y|_{i-\frac{3}{2},j}\right]\right\} \\
&\quad + \frac{K''}{6\Delta x\Delta y}\left\{\Delta x\left[H_x|_{i-1,j-\frac{3}{2}} + H_x|_{i+1,j-\frac{3}{2}} - H_x|_{i-1,j+\frac{3}{2}} - H_x|_{i+1,j+\frac{3}{2}}\right]\right. \\
&\quad \left. + \Delta y\left[H_y|_{i+\frac{3}{2},j-1} + H_y|_{i+\frac{3}{2},j+1} - H_y|_{i-\frac{3}{2},j-1} - H_y|_{i-\frac{3}{2},j+1}\right]\right\} \\
&\quad + \frac{1-K-K''}{\Delta x\Delta y}\left\{\Delta x\left[H_x|_{i,j-\frac{1}{2}} - H_x|_{i,j+\frac{1}{2}}\right] + \Delta y\left[H_y|_{i+\frac{1}{2},j} - H_y|_{i-\frac{1}{2},j}\right]\right\} \\
-\mu \frac{\partial H_x}{\partial t} &= \frac{K}{3\Delta y}\left[E_z|_{i,j+\frac{3}{2}} - E_z|_{i,j-\frac{3}{2}}\right] + \frac{1-K}{\Delta y}\left[E_z|_{i,j+\frac{1}{2}} - E_z|_{i,j-\frac{1}{2}}\right] \\
\mu \frac{\partial H_y}{\partial t} &= \frac{K}{3\Delta x}\left[E_z|_{i+\frac{3}{2},j} - E_z|_{i-\frac{3}{2},j}\right] + \frac{1-K}{\Delta x}\left[E_z|_{i+\frac{1}{2},j} - E_z|_{i-\frac{1}{2},j}\right]
\end{aligned}$$

Again, the stability criterion can be derived as

$$\Delta t = \frac{3h}{c\nu\sqrt{2(3-4K)(3-4K-2K'')}} \qquad \nu \geq 1$$

and the dispersion relation as

$$\left(\frac{3h}{c\Delta t}\right)^2 \sin^2\left(\frac{\omega\Delta t}{2}\right) = \left[K\sin\left(\frac{3\tilde{k}h\sin\alpha}{2}\right) + 3(1-K)\sin\left(\frac{\tilde{k}h\sin\alpha}{2}\right)\right]$$
$$\cdot\left[\sin\left(\frac{3\tilde{k}h\sin\alpha}{2}\right)\left[K + K''\cos(\tilde{k}h\cos\alpha)\right] + 3(1-K-K'')\sin\left(\frac{\tilde{k}h\sin\alpha}{2}\right)\right]$$
$$+\left[K\sin\left(\frac{3\tilde{k}h\cos\alpha}{2}\right) + 3(1-K)\sin\left(\frac{\tilde{k}h\cos\alpha}{2}\right)\right]$$
$$\cdot\left[\sin\left(\frac{3\tilde{k}h\cos\alpha}{2}\right)\left[K + K''\cos(\tilde{k}h\sin\alpha)\right] + 3(1-K-K'')\sin\left(\frac{\tilde{k}h\cos\alpha}{2}\right)\right]$$

To find the optimum values for K and K'' the dispersion relation is again solved for the numeric wave number in terms of K and K'' at all propagation angles and the results are plugged into the following error function

$$\text{Error}_2 = \frac{2}{\pi}\int_0^{\pi/2}\left[\frac{k-\tilde{k}(\alpha)}{k}\right]^2 d\alpha$$

This error function is in turn minimized using an optimization routine in terms of K and K'' to find the optimum values that will give the least global phase error. Table 1 shows the optimum coefficients at $f = 900$ MHz for several resolution factors along with the corresponding error values. It is important to resolve the coefficients to 9 significant digits since these coefficients control the EM fields' phases which are more sensitive to small variations than the fields' magnitudes. Fig. 5 shows an error comparison among the three schemes discussed so far; the standard (2,2), the standard (2,4) and the modified (2,4) schemes.

Table 1. Optimum values for K and K'' at 900 MHz

R	K	K''	Error_2
5	−0.144931712	0.102068902	5.426×10^{-10}
10	−0.116192765	0.0734445091	8.979×10^{-14}
15	−0.111802038	0.0692811040	6.444×10^{-16}
20	−0.110322272	0.0678920244	1.963×10^{-17}
25	−0.109646972	0.0672605236	1.264×10^{-18}
30	−0.109282656	0.0669204694	1.208×10^{-19}
35	−0.109063833	0.0667164343	1.283×10^{-20}

When it comes to actual simulations the modified (2,4) scheme demonstrates an important advantage over the standard (2,4) scheme. The modified (2,4) scheme can be used in a hybrid algorithm along with the standard (2,2) scheme without any adverse effects on the stability of the overall algorithm. This is not the case with the standard (2,4) scheme [5]. Going back to the original example of an infinite line source and solving it using the modified (2,4) scheme yields a clean and phase error-free wave solution as shown in Fig. 6.

Fig. 5 Error$_2$ comparison among the different schemes at 900 MHz

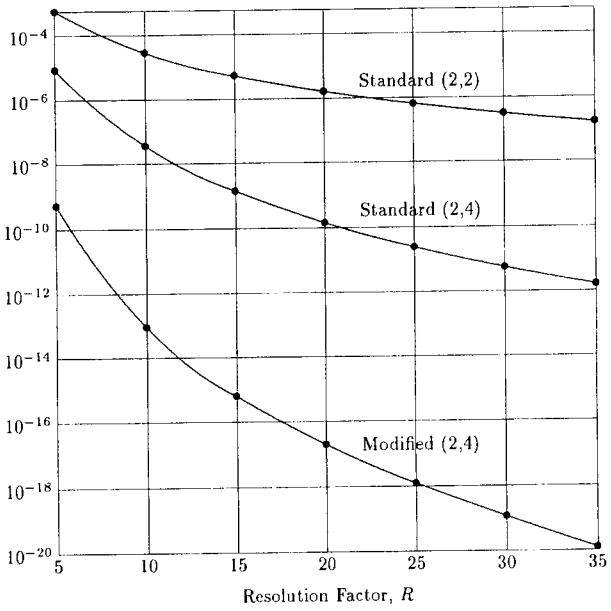
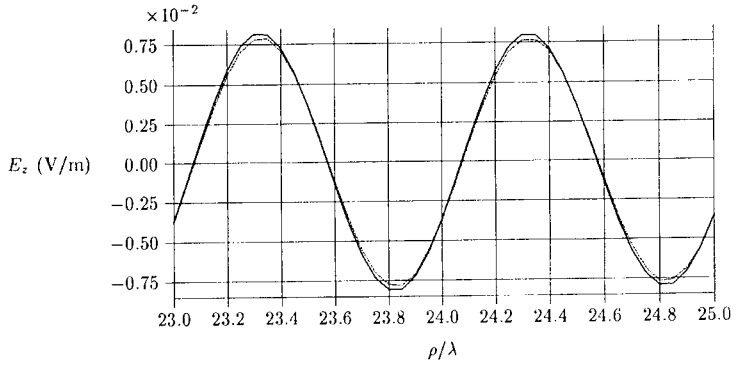


Fig. 6 Electric field radiated by an infinitely thin line source: exact (solid line) vs. modified (2,4) scheme (dotted line)



CONCLUSION

When used to model electrically large structures the modified (2,4) scheme is capable of providing huge savings in both computer time and memory. For example, to confine the FDTD algorithm within $\left|\frac{k-\tilde{k}}{k}\right| \leq 40$ parts per million the modified (2,4) scheme will require a resolution factor of $R = 5$ compared to a resolution factor of $R = 142$ for the standard (2,2) scheme. In 3-D simulations this 142/5 ratio needs to be raised to the fourth power to realize the computer time ratio and to the third power to realize the computer memory ratio between the two schemes. Even when the extra overhead generated within the modified (2,4) scheme is taken into account the rations are still huge; over 5 orders of magnitude for the computer time ratio and over 4 orders of magnitude for the computer memory ratio.

REFERENCES

1. Yee, K.S, *Numerical Solution of Initial Boundary Value Problems Involving Maxwell's Equations in Isotropic Media,* IEEE Trans. Antennas Propagation, Vol. AP-14, pp. 302-306, 1966.

2. Taflove, Allen and Brodwin, Morris E., *Numerical Solution of the Steady-State Electromagnetic Scattering Problems Using the Time-Dependent Maxwell's Equations,* IEEE Trans. Microwave Theory and Techniques, Vol. MTT-23, No. 8, pp. 623-630, 1975.

3. Taflove, Allen, *Basis and Application of Finite-Difference Time-Domain (FD-TD) Techniques for Modeling Electromagnetic Wave Interactions,* Evanston, IL: Northwestern University, 1992.

4. Deveze, T., Beaulieu, L. and Tabbara, W., *A Fourth Order Scheme for the FDTD Algorithm Applied to Maxwell's Equations,* IEEE APS Inter. Symp. Proc., Chicago, IL, 1992, pp. 346-349.

5. Deveze, T., Beaulieu, L. and Tabbara, W., *An Absorbing Boundary Condition for the Fourth Order FDTD Scheme,* IEEE APS Inter. Symp. Proc., Chicago, IL, 1992, pp. 342-345.

From the Berenger PML ABC to Micro-Lasers: Recent Advances in FD-TD Modeling Techniques[1]

Allen Taflove

Department of Electrical Engineering and Computer Science
McCormick School of Engineering
Northwestern University, Evanston, IL 60208

1. INTRODUCTION

Since 1990, there has been an explosion of interest in the engineering electromagnetic wave community in direct solutions of the Maxwell's curl equations on space grids in either the time or frequency domain. The finite-difference time-domain (FD-TD) method, introduced by Yee in 1966 [1], has received perhaps the most attention during this period because of its simplicity and robustness. Recent advances in FD-TD modeling techniques have further improved its modeling accuracy and expanded its range of applications. These advances are succinctly summarized in this review paper:

1. Berenger PML absorbing boundary condition;
2. Dispersive, nonlinear, and gain material models;
3. Active circuit device models;
4. Planar unstructured meshes; and
5. Software development for massively parallel computers.

2. BERENGER PML ABSORBING BOUNDARY CONDITION

2.1 Unbounded-Region Scattering Problems

As RCS measurements have become more sophisticated and attained dynamic ranges than 70 dB, it has become important to extend the accuracy range of FD-TD numerical modeling to balance theory and measurements. However, attainment of 70 dB dynamic range requires suppression of computational noise to amplitudes less than 10^{-4} times the incident wave. This has been a very difficult challenge, especially in the area of absorbing boundary conditions (ABC's) that simulate the non-reflective action of the walls of an anechoic chamber.

Until late 1994, the principal ABC's used in FD-TD codes were published originally by Mur [2] and Liao [3]. These ABC's provided effective outer-boundary reflection coefficients in the range of 0.5% - 5.0% for most FD-TD simulations. To obtain simulations having dynamic ranges comparable to those of recent anechoic chambers, a reduction of >40-dB (>100:1) has been needed in these reflectivities. After more than a decade of only incremental progress in ABC theory, it was becoming clear that this would require a fundamental advance.

---

[1]This paper is a condensation of the invited paper, "Advances in Finite-Difference Time-Domain (FD-TD) Numerical Modeling Techniques for Maxwell's Equations," presented at the Ninth International Conference on Antennas and Propagation (ICAP'95), Eindhoven University of Technology, The Netherlands, April, 1995.

Such an advance appears to be at hand with Berenger's recent publication of the novel "perfectly matched layer" (PML) ABC for 2-D FD-TD meshes [4], which provides *orders-of-magnitude* improved performance relative to earlier techniques. PML is based upon a splitting of E or H components in the absorbing boundary region with the possibility of assigning losses to the individual split field components. The net effect of this is to create a non-physical absorbing medium adjacent to the outer FD-TD mesh boundary that has a wave impedance independent of the angle of incidence and frequency of outgoing scattered waves. Berenger reported reflection coefficients for the PML ABC as low as 1/3000th that of the Mur or Liao ABC's when using a quadratically-graded PML loss profile. Katz et al [5] confirmed these remarkable claims and extended Berenger's ABC to 3-D open-region FD-TD simulations.

2.2 Effect of PML Grading Order

Reuter and Taflove [6] reported how the grading of the electric and magnetic loss with depth in the PML affects its performance. Their numerical procedure was identical to that of [4, 5] with the exception that the grading of the PML loss was specified to be either order-1 (linear), order-2 (quadratic, Berenger's baseline), order-3 (cubic), order-4, or order-5 for any desired PML thickness and normal-incidence reflectivity parameter, R(0).

It was found that the optimum grading of the PML loss is generally not quadratic and depends upon the PML thickness. For example, for a thickness of 16 cells, fourth-order PML loss grading yields local reflections at -55 dB relative to quadratic PML grading in 2-D, and -48 dB relative to quadratic grading in 3-D. The resulting optimized PML ABC is locally *300,000 times less reflective* than the second-order Mur ABC, and *30,000 times less reflective* than the third-order Liao ABC.

2.3 Waveguide Problems

FD-TD is increasingly being used to model the propagation of waves in microwave and optical circuits. A key problem here is the accurate termination of guided-wave structures extending beyond the FD-TD grid boundaries. The difficulty arises because propagation in a waveguide can be multimodal and dispersive, and the ABC utilized to terminate the waveguide must be able to absorb energy having widely varying transverse distributions and group velocities, v_g.

When applied to terminate guided wave structures, typical ABC's developed for free-space problems perform best for narrowband energy propagation where v_g is well defined. Recently, these ABC's have been specialized to account for variations of the waveguide modal v_g with frequency, for example, Bi et al [7] and Moglie et al [8]. However, these methods are not completely satisfactory, being either approximate or computationally intensive.

Reuter et al [9] applied Berenger's PML ABC to terminate FD-TD models of general 2-D waveguiding structures for transverse magnetic (TM) modes. The first application was an air-filled perfectly conducting (PEC) parallel-plate waveguide excited by a wideband carrier pulse which launched a TM_1 mode towards the PML termination. The group velocity of the pulse spectral components ranged from zero at f_{cutoff} to $\approx 0.98c$ at $5f_{\text{cutoff}}$. Using a 16-cell quadratically-graded PML, reflections between -70 dB and -95 dB were calculated at all frequencies between these two points.

Reuter et al [9] then applied the PML ABC to terminate the FD-TD model of a 2-D micron-scale dielectric film optical waveguide. A femtosecond-regime pulse modulating an optical carrier was used to launch three distinct modes having widely-varying frequency-dependent

propagation factors. The system was terminated by extending the air, film, and substrate layers into matching 16-cell thick, quadratically-graded PML absorbers. FD-TD calculations showed a composite reflectivity below -80 dB for the PML ABC across the entire incident spectrum.

These results showed that the PML ABC has a broadband effectiveness, robustness, and computational efficiency unmatched by previous ABC's for FD-TD waveguide models. PML is local in space/time and requires no knowledge of modal field distributions, multimoding, or dispersion characteristics of the guided wave. Extension to 3-D PEC and dielectric waveguide models is straightforward. Another useful application is for FD-TD modeling of problems involving the earth-air interface, in fact a subset of the three-layer dielectric geometry of [9].

3. DISPERSIVE, NONLINEAR, AND GAIN MATERIAL MODELS

The usage of short electromagnetic pulses, whether in radar applications or in lasers/nonlinear optics, requires understanding of the nature of pulse interactions with materials over wide bandwidths. In the case of high-power microwave or laser engineering, the pulses are likely to have a sufficiently high intensity such that material nonlinearity can also play an important role. Overall, the key factors in short-pulse physics are material dispersion, nonlinearity, and gain.

Two recent advances in FD-TD computational technology permit effective modeling of these material properties at the macroscopic (phenomenological) level. The first is the recursive convolution (RC) method, a highly efficient approach to model complicated linear dispersions consisting of an arbitrary number of Debye and Lorentzian relaxations. The second is the auxiliary differential equation (ADE) method, which permits modeling of nonlinearities and dispersive nonlinearities in addition to linear dispersions at the cost of an increase in computational complexity relative to the RC approach. The ADE method can also model linear and nonlinear dispersive gain media, such as those found in lasers.

3.1 Recursive Convolution Method

Luebbers et al [10] reported an efficient, "on-the-fly" recursive convolution (RC) approach to model electromagnetic wave interactions with linear dielectric materials having combinations of multiple Debye and Lorentzian dispersions. Here, a basic assumption is that the variation of the electric susceptibility, $\chi_e(\omega)$, with frequency is given by a general rational function expression. After a partial-fraction expansion, the corresponding time-domain susceptibility function, $\chi_e(t)$, is obtained by inverse Fourier transformation, yielding a finite sum of exponentially decaying sinusoids and simple exponentials. Upon substitution into the differential form of Ampere's Law, the resulting displacement current term is represented by a corresponding sum of convolutions of the decaying exponential functions with E.

Luebbers et al [10] made the key observation that, in a numerical realization of each of the convolutions as a discrete summation, all but the last term of the sum could be written in terms of the previous time step's evaluation of the sum multiplied by a constant exponential decay factor. Therefore, the summation over past E values could be evaluated *recursively* without having to store the past fields and without having to redo the complete sum every time step.

This procedure leads to great efficiency in computer resources. For each term used in $\chi_e(t)$, only one additional storage variable is required for each electric field component at each grid cell. This variable is real if the corresponding frequency-domain pole is first-order, and complex if the pole is second-order. On the arithmetic side, the addition of a pole requires only the extension of each of the summations by a single term. Because an arbitrary susceptibility

function can be expanded in a series of complex exponentials using Prony's or similar methods (yielding a set of real and complex poles), a material having a complicated dispersion can be modeled simply and efficiently from both a computer storage and algorithm viewpoint.

There are two problems, however, with the RC approach of [10]. First, the discrete convolutions are only first-order accurate in the space / time discretization due to their rectangular-rule realization of the underlying continuous integrals. Second, the RC approach cannot be used for materials that are simultaneously dispersive and nonlinear because convolution is based upon the a linear superposition integral. This prevents the application of the RC method to model the important class of nonlinear electro-optical materials.

3.2 Auxiliary Differential Equation Method

Kashiwa and Fukai [11] and Joseph et al [12] described an auxiliary differential equation (ADE) method for FD-TD modeling of material dispersions based upon applying the inverse Fourier transform to the constitutive relation between $D(\omega)$ and $E(\omega)$. This provided a time-domain ordinary differential equation (ODE) relating $D(t)$ and $E(t)$ that could be time-marched in parallel with the Yee algorithm. While useful and accurate for a single Lorentzian dispersion, this approach proved difficult to systematically extend to multiple relaxations. However, as discussed by Taflove [13], it is possible to refine this approach for a material having an arbitrary number of relaxations to yield a system of low-order ODE's. No inverse Fourier transformation is needed, and only one ODE is generated per dielectric relaxation.

Consider a material dispersion characterized by M Lorentzian responses. As noted earlier, the polarization of the E components can be expressed as a sum of M convolution integrals. However, the key property that drives the ADE formulation is that each convolution kernel function, $\chi_e(t)$, satisfies a linear, second-order ODE. This property makes it possible to treat each of the M convolution integrals as a new dependent variable which satisfies a second-order ODE in time. In turn, this yields a system of M coupled second-order ODE's that evolves the time response of the M convolution integrals. Central-difference time integration of this system provides a second-order accurate calculation of the composite polarization, which is then used to time-advance E.

As shown in [13], the ADE approach provides superior convergence and accuracy relative to the RC method of [10] for materials with multiple Lorentzian relaxations. However, the computational burden of the ADE method is substantially greater than that of the RC technique because of the need to solve a system of M equations rather merely sum M terms.

3.3 Application of the ADE Method to Nonlinear Dispersive Media (Nonlinear Optics)

The ADE method maintains unique capabilities relative to the RC approach in FD-TD modeling of electromagnetic fields in nonlinear dispersive dielectrics. As discussed in Goorjian and Taflove [14], the ADE method can model a dielectric having multiple frequency-dependent nonlinear as well as linear relaxations. The key is again the treatment of the convolution integrals. Because each kernel function satisfies a second-order ODE, the convolution integrals can again be treated as dependent variables which in this case satisfy a system of coupled, nonlinear, second-order ODE's. Using central-differencing in time, this system is evolved to provide the linear and nonlinear components of the dielectric polarization.

The ADE approach has permitted the initial FD-TD modeling of temporal optical soliton formation and propagation in 1-D half-spaces (Goorjian and Taflove [14]) and in 2-D dielectric waveguides (Joseph et al [15]). Joseph and Taflove also reported spatial optical soliton formation, propagation, and mutual deflection in 2-D homogeneous media [16], and Ziolkowski and Judkins reported self-focusing of short optical pulses [17] and wide-angle scattering of optical pulses propagating within nonlinear corrugated structures [18].

3.4 Application of the ADE Method to Dispersive Gain Media (Active Lasing Media)

Hagness and Taflove [19] reported a new approach based upon the ADE method that permits wideband modeling of the Lorentzian frequency-dispersive gain found in a homogeneously broadened two-level lasing system. This method provided second-order accuracy and numerical stability extending over hundreds of thousands of time steps. Relative to exact solutions for optical wave propagation in 1-D, the frequency-dependent gain calculated by this method had worst-case magnitude/ phase errors of only 0.01% -1% for FD-TD grid resolutions between $\lambda_o / 400$ and $\lambda_o / 40$, respectively.

It is believed possible to expand the range of physics modeled by the ADE formulation of FD-TD to include multiple Lorentzian resonances of the gain, frequency-dependent nonlinear gain saturation effects, and simultaneous multiple Lorentzian relaxations of the linear / nonlinear dielectric susceptibility. Success in this research would mean a comprehensive phenomenological modeling tool for the full-wave pulse dynamics of micron-scale semiconductor lasers.

3.5 The First FD-TD Laser Oscillator Model

Following the above theme, Hagness and Taflove [19] also reported what they believe to be the first FD-TD model of a laser oscillation originating from low-level Gaussian noise in the laser cavity. Here, their Lorentzian gain model was modified to include a typical gain saturation function. This was applied to a 1-D microcavity laser model spanning about 5 microns.

In the steady state, their computed laser output waveform was a pure sinusoid having a frequency corresponding to the cavity mode located at the peak of the Lorentzian gain spectrum of the lasing medium. The FD-TD model properly rejected multimode oscillations at other above-threshold cavity resonances having frequencies off the peak of the gain curve. The proper lasing mode was selected preferentially by the FD-TD simulation due to the action of the assumed gain-saturation nonlinearity.

Two other agreements with accepted results reinforced the validity of the FD-TD numerical laser model of [19]: (a) The calculated turn-on delay of the numerical laser from the Gaussian noise seed increased properly as the peak magnitude of the Lorentzian gain function was reduced to the lasing threshold of the primary cavity mode; (b) The FD-TD model properly calculated a linear increase in the output intensity of the laser as the peak value of the Lorenztian gain function increased beyond the lasing threshold of the primary cavity mode.

3.6 Comment

It should be noted that the use of the full-wave FD-TD Maxwell's equations approach to model the pulse dynamics of dispersive, nonlinear, and gain media is novel. The optics community

has routinely made paraxial and slowly-varying envelope approximations that result in the class of generalized nonlinear Schrödinger equations (GNLSE), as in Agrawal [20]. The least approximate methods for GNLSE solve nonlinear scalar equations for the envelope of a propagating optical pulse, discarding the sinusoidal carrier. Examples include the split-step Fourier method (used to simulate propagation of optical pulses in low-loss fibers over very long optical distances), and the propagating beam method (used to model directional couplers).

Relative to such approaches, FD-TD achieves robustness by directly solving Maxwell's equations for fundamental quantities (the *E* and *H* fields in space and time), rather than using asymptotic and paraxial approximations and calculating nonphysical envelope functions. FD-TD permits a rigorous treatment of optical structures having features comparable in size to the wavelength, a key advantage relative to previous modeling tools in the optics community.

4. ACTIVE CIRCUIT DEVICE MODELS

Thomas et al [21] reported that the lumped-circuit behavior of linear and nonlinear active devices can be directly incorporated into a generalized 3-D FD-TD Maxwell's equations solution. Here, the circuit simulator, SPICE, was linked to FD-TD so that SPICE would time-step Ampere's Law at grid locations where a lumped-circuit element was specified. In this way, the lumped element could be an arbitrarily large circuit having a description contained in a standard SPICE file. Thus, all of the extensive device models in SPICE could be used directly in the FD-TD simulation without the need to duplicate the model development. Further, the efficient circuit integration methods used in SPICE would be directly available without any need for user-implemented integration schemes.

Thomas et al [21, 22] reported successful applications of the hybrid FD-TD/SPICE modeling approach. In [21], the model involved a stripline-mounted VHF tuned amplifier consisting of a single NPN bipolar junction transistor provided with inductor-capacitor networks for base and collector impedance matching. In [22], the model involved a coupled pair of patch antennas excited by locally-mounted Gunn diodes. Very good agreement was obtained relative to benchmark data for voltages, currents, and fields in both cases.

The hybrid FD-TD/SPICE tool will be optimally applied when the speed of a circuit is so high and its physical embedding is so complex that it is crucial to model electromagnetic wave "artifacts." A wide range of digital applications is expected as clock speeds approach microwave frequencies. Analog applications will include analysis of linearity, intermodulation, harmonic generation, and conversion efficiency of microwave and millimeter wave integrated circuits. Another category of applications will include radiation, especially by arrays of patch antennas excited by semiconductor devices located directly at the antenna [22]. FD-TD/SPICE should also be useful in modeling circuit upset due to external electromagnetic fields generated by lightning, electromagnetic pulse, and high-power microwaves.

5. PLANAR UNSTRUCTURED MESHES

The computational requirements of a general unstructured 3-D FD-TD algorithm can be greatly reduced by exploiting symmetries in the model. As discussed by Gedney and Lansing [23], an important opportunity of this type arises for digital and microwave printed circuits which have planar symmetry. Such circuits can be uniquely described by a projection onto a 2-D plane. Here, the FD-TD grid used to analyze the 3-D problem can be described by an unstructured 2-D grid in a transverse plane and as a regular grid in the third-dimension. Only the 2-D grid

locations need be stored. This greatly relaxes the memory requirements of the algorithm to the extent that it is actually as memory efficient as basic FD-TD.

Conceptually, the grid of Gedney's and Lansing's "planar generalized Yee algorithm" [23] can be generated by extruding an x-y plane (horizontal) 2-D unstructured grid in the z (vertical) direction and segmenting it at discrete z intervals. A secondary grid is staggered within this primary grid such that its vertices lie at the centroids of the primary grid cells. Further, the edges of the secondary grid connect the centroids by passing through the faces of the primary grid. The E and H fields are then decomposed into orthogonal components. Subsequently, the transverse E and H fields are mapped onto the horizontal edges of the primary and secondary grids, respectively. Likewise, the vertical E and H fields are mapped onto the vertical edges of the primary and secondary grids, respectively. The fields are assumed to be constant along their respective edge lengths as well as over the dual faces through which they pass.

Based on this discretization, Faraday's and Ampère's Laws are approximated by choosing the surfaces of integration to be the faces of the secondary and primary grids, respectively. This leads to explicit time-stepping expressions for D_t and B_t flux densities in the transverse plane and field intensities, E_z and H_z. Note that the D_t and B_t fluxes are normal to the faces. However, the corresponding field intensities on the dual edges passing through these faces are not necessarily normal to the faces. As a result, the flux densities must be projected onto the edges before the dual fields can be updated. An auxiliary operator must be introduced to perform this projection. Madsen's general 3-D projection scheme [24] is useful since the flux projected onto the edges has zero divergence in a charge-free medium, and the time-stepping algorithm maintains numerical stability. With the assumed planar symmetry and the resulting orthogonality of the vertical and transverse fields, only fields within the transverse plane are needed for the interpolation. This results in a simplified projection of the D_t and B_t fluxes relative to the most general 3-D case.

Gedney and Lansing [23] (see also their Chapter 11 in [13]) reported a number of application examples of the planar generalized Yee algorithm including 32-GHz Wilkinson and Gysel power dividers, and signal lines and vias within the IBM 3090 thermal conduction module. Excellent computational accuracy and efficiency was indicated, complementing the high level of geometrical modeling flexibility afforded by the unstructuring of the FD-TD mesh in two coordinate dimensions. This approach has substantial promise for modeling microwave and digital circuit boards of great complexity.

6. SOFTWARE DEVELOPMENT FOR MASSIVELY PARALLEL COMPUTERS

In Chapter 16 of [13], Gedney and Barnard provided detailed descriptions of their recent highly efficient ports of unstructured- and structured-grid FD-TD algorithms to the INTEL Delta and CRAY T3D massively parallel computers. Barnard also addressed the issue of how fast the T3D can run the largest possible 3-D FD-TD model. His procedure involved measuring T3D performance while continually scaling the grid size upwards to keep each processing element (PE) fully involved. He found that the performance scaled nearly linearly, reaching a projected steady rate of 50 GFLOPS on 2,048 PE's for the most optimized code. Since a 2,048-PE T3D with 64 MBytes/PE has a total memory of 16.384 GWords, it would be possible to run in-core a two-billion grid-cell problem containing 12-billion unknown fields. This unprecedented combination of speed and memory capacity provides large opportunities for each of the emerging FD-TD models reviewed in this paper, as well as for traditional FD-TD simulations.

REFERENCES

1. Yee, K., "Numerical solution of initial boundary value problems involving Maxwell's equations in isotropic media," *IEEE Trans. AP*, vol. 14, pp. 302-307, 1966.
2. Mur, G., "Absorbing boundary conditions for the finite-difference approximation of the time-domain electromagnetic field equations," *IEEE Trans. EMC*, vol. 23, pp. 377-382, 1981.
3. Liao, Z., Wong, H., Yang, B. and Yuan, Y., "A transmitting boundary for transient wave analyses," *Sci. Sinica* (series A), vol. XXVII, pp. 1063-1076, 1984.
4. Berenger, J., "A perfectly matched layer for the absorption of electromagnetic waves," *J. Comp. Phys.*, vol. 114, 185-200, 1994.
5. Katz, D., Thiele, E. and Taflove, A., "Validation and extension to three dimensions of the Berenger PML absorbing boundary condition for FD-TD meshes," *IEEE MGW Lett.*, vol. 4, pp. 268-270, 1994.
6. Reuter, C. and Taflove, A., 1995, "Improvement of the performance of the Berenger PML ABC by use of non-quadratic loss grading," *IEEE MGW Lett.*, submitted.
7. Bi, Z., Wu, K., Wu, C. and Litva, J., "A dispersive boundary condition for microstrip component analysis using the FD-TD method," *IEEE Trans. MTT*, vol. 40, pp. 774-777, 1992.
8. Moglie, F., Rozzi, T., Marcozzi, P. and Schiavoni, A., "A new termination condition for the application of FDTD techniques to discontinuity problems in close homogeneous waveguide," *IEEE MGW Lett.*, vol. 2, pp. 475-477, 1992.
9. Reuter, C., Joseph, R., Thiele, E., Katz, D. and Taflove, A., "Ultrawideband absorbing boundary condition for termination of waveguiding structures in FD-TD simulations," *IEEE MGW Lett.*, vol. 4, pp. 344-346, 1994.
10. Luebbers, R., Steich, D. and Kunz, K., "FDTD calculation of scattering from frequency-dependent materials," *IEEE Trans. AP*, vol. 41, pp. 1249-1257, 1993.
11. Kashiwa, T. and Fukai, I., "A treatment by FDTD method of dispersive characteristics associated with electronic polarization," *MAOT Lett.*, vol. 3, pp. 203-205, 1990.
12. Joseph, R., Hagness, S. and Taflove, A., "Direct time integration of Maxwell's equations in linear dispersive media with absorption for scattering and propagation of femtosecond electromagnetic pulses," Optics Lett., vol. 16, pp. 1412-1414, 1991.
13. Taflove, A., *Computational Electrodynamics: The Finite-Difference Time-Domain Method.* Boston: Artech House. 1995.
14. Goorjian, P. and Taflove, A., "Direct time integration of Maxwell's equations in nonlinear dispersive media for propagation and scattering of femtosecond electromagnetic solitons," *Optics Lett.*, vol. 17, pp. 180-182, 1992.
15. Joseph, R., Goorjian, P. and Taflove, A., "Direct time integration of Maxwell's equations in 2-D dielectric waveguides for propagation and scattering of femtosecond electromagnetic solitons," *Optics Lett.*, vol. 18, pp. 491-493, 1993.
16. Joseph, R. and Taflove, A., "Spatial soliton deflection mechanism indicated by FD-TD Maxwell's equations modeling," *IEEE Photonics Tech. Lett.*, vol. 6, pp. 1251-1254, 1994.
17. Ziolkowski, R. and Judkins, J., "Full-wave vector Maxwell equations modeling of self-focusing of ultra-short optical pulses in a nonlinear Kerr medium exhibiting a finite response time," *JOSA B*, vol. 10, pp. 186-198, 1993.
18. Ziolkowski, R., "Numerical modeling of the interactions of continuous wave and ultrashort optical pulses with resonant materials and structures," invited paper, Sess. B/D-3, Nat. Radio Sci. Mtng., Boulder, CO, 1995.
19. Hagness, S. and Taflove, A., "A nonlinear full-wave electromagnetic model of semiconductor laser cavities," Opt. Soc. of Amer. Ann. Mtng, Dallas, TX, 1994.
20. Agrawal, G., Nonlinear Fiber Optics. New York: Academic Press, 1989.
21. Thomas, V., Jones, M., Piket-May, M., Taflove, A. and Harrigan, E., "The use of SPICE lumped circuits as sub-grid models for FD-TD high-speed electronic circuit design," *IEEE MGW Lett.*, vol. 4, pp. 141-143, 1994.
22. Thomas, V., Ling, K., Jones, M., Toland, B., Lin, J. and Itoh, T., "FDTD analysis of an active antenna," *IEEE MGW Lett.*, vol. 4, pp. 296-298, 1994.
23. Gedney, S. and Lansing, F., "A generalized Yee algorithm for the analysis of three-dimensional microwave circuit devices with planar symmetry," *IEEE Trans. MTT*, submitted.
24. Madsen, N., "Divergence preserving discrete surface integral methods for Maxwell's equations using nonorthogonal unstructured grids," Tech. Rpt. UCRL-JC-109787, LLNL, Livermore, CA, 1992.

SESSION 14:

PROPAGATION

Chair: K. Chamberlin

Terrain and Refractivity Effects in a Coastal Environment: Results From the VOCAR Experiment

Amalia E. Barrios
Ocean and Atmospheric Sciences Division
NCCOSC RDTE DIV 543
53170 WOODWARD ROAD
SAN DIEGO, CA 92152-7385

SUMMARY
Results from the VOCAR (variability of coastal atmospheric refractivity) experiment, performed in the southern California coastal area, are presented and compared with a terrain parabolic equation model called TPEM. Both homogeneous and range dependent refractivity environments are considered.

1. INTRODUCTION

Much emphasis has been given lately to radio field prediction in coastal environments. Currently, well established propagation models exist that have been shown to predict, fairly accurately, radio signals over water [1, 2, 3]. However, in a coastal environment, when one or both terminals are located a short distance inland, the smooth earth assumption that these models employ fails to account for terrain effects on these propagation paths.

An experiment was performed recently along the southern California coast in which RF signals from military and civilian Automatic Terminal Information Service (ATIS) transmitters were received at two locations on the southern California coastline. Some of the propagation paths were entirely over water while others were partially over land. Many of the inland transmitters were obstructed by very high cliffs and/or mountainous terrain typical of the California coastline. Even when the propagation path was more than 90% over water, predictions based on a smooth earth assumption fail to agree with measured data.

A split-step parabolic equation model that can account for terrain effects, called TPEM, has been previously described [4, 5] and is used here to investigate the signals that were measured from transmitters located several kilometers inland.

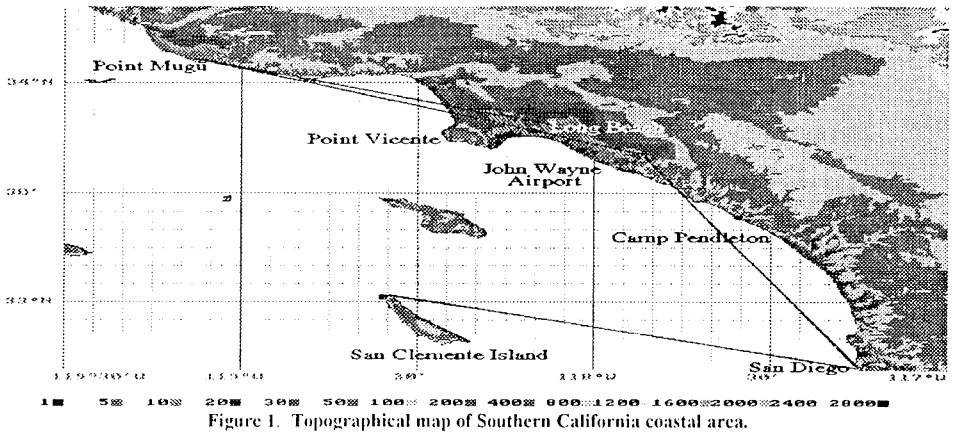


Figure 1. Topographical map of Southern California coastal area.

2. EXPERIMENT

In 1993, an experiment to characterize the variability of coastal atmospheric refractivity (VOCAR) was performed in the southern California coastal area. Signals from 14 military and civilian transmitters located along the coastline between San Diego and Santa Barbara were constantly being measured by receivers on the coast at the Naval Command, Control and Ocean Surveillance Center, Research Development Test and Evaluation Division in San Diego (NRaD) and at the Naval Air Warfare Center Weapons Division in Point Mugu (NAWCWPNS). Additional transmitters were placed on San Clemente Island and were also received at San Diego and Point Mugu.

During an intense measurement period between August 23 and September 3, 1993, signals were constantly being received over these land/water propagation paths. Observations taken over a few of the paths will be presented. The propagation paths and the surrounding area are shown in Figure 1. The topography information shown in this figure, and the terrain elevation information used by TPEM for all paths discussed in this paper, is from the Digital Terrain Elevation Data (DTED) database provided by the Defense Mapping Agency. Both receivers at NRaD and at NAWCWPNS were located at 30.5 m above mean sea level. Below is a table of the operating frequencies and antenna heights (above mean sea level) of the transmitters located inland.

Location	Frequency (MHz)	Antenna Height (m)
Long Beach Airport	127.75	17.1
John Wayne Airport	126.0	24.4
San Clemente Island	268.6	66.7

Table 1. Location, frequency, and antenna heights of ATIS transmitters shown in Fig. 1.

Radiosondes were launched approximately 4 to 5 times daily at North Island in San Diego, Point Mugu, San Clemente Island, Camp Pendleton and Point Vicente.

3. RESULTS

The first path considered is that from San Clemente Island to San Diego. Signals were received from a transmitter located at the Naval Auxilary Landing Field (NALF) on the island approximately two kilometers inland. A small mountain peak, roughly 137 m high and located between NALF and the shore, lay in direct line from the transmitter to the receiver at NRaD. The propagation path is 127 km long and although most of the path is over water, the presence of this peak created a substantial reduction in signal received at San Diego.

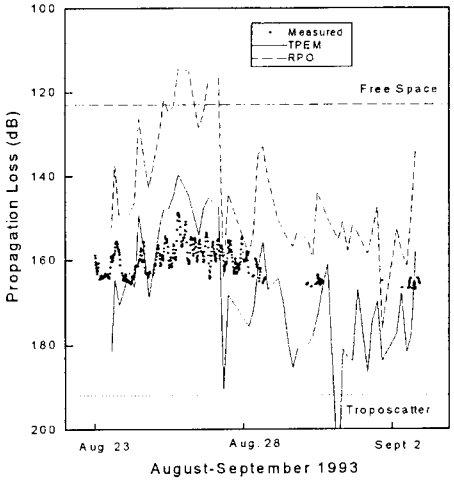


Figure 2. TPEM and RPO results vs. measurements for San Clemente Island to San Diego path using North Island soundings.

Radiosondes taken at North Island were used as refractivity inputs to RPO [3] and TPEM. RPO is a hybrid ray optics/PE model that assumes smooth earth and does not account for terrain. The results, along with observations for the ten day period in August and September, are shown in Figure 2. RPO underestimated the propagation loss by roughly 20 dB and in some instances, by as much as 40 dB, whereas, TPEM showed very good agreement. The free space and troposcatter thresholds are shown for reference. The troposcatter threshold was determined based on the model by Yeh[6]. Between August 29 and September 3 signal levels were generally too low to be detected, and during this time period TPEM predicted very low signal levels.

For the John Wayne Airport to San Diego propagation path there is a substantial mountain range, roughly 300 m at its peak, from 3 km out to 15 km away from the transmitting antenna. The remainder of the path is over water with the entire path being 123 km long. Refractivity profiles measured throughout the ten day period at Camp Pendleton were used as environmental inputs to RPO and TPEM. A comparison of their predictions against measured data is shown in Figure 3.

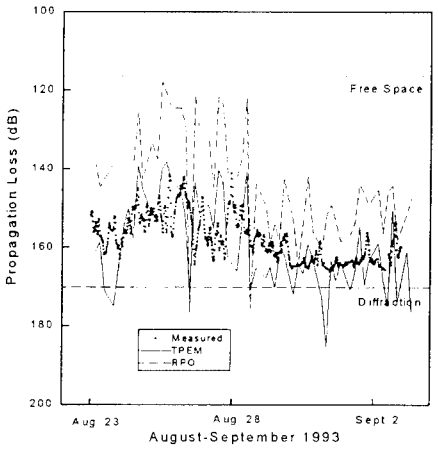


Figure 3. TPEM and RPO results vs. measurements for John Wayne to San Diego path using Camp Pendleton soundings.

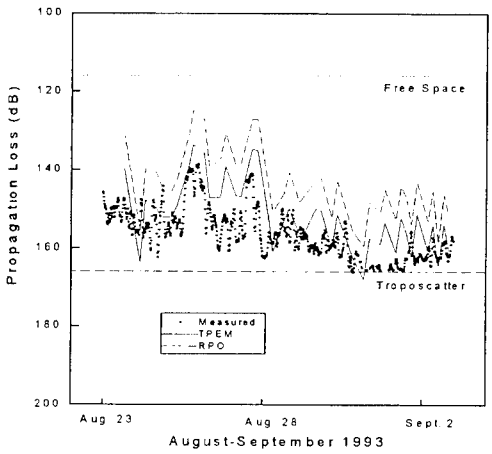


Figure 4 TPEM and RPO results vs. measurements for John Wayne Airport to Point Mugu path using Point Mugu soundings.

A substantial reduction in signal level due to the mountain range is apparent. Again, RPO underestimates the losses by approximately 10 to 20 dB while TPEM shows very good agreement. The diffraction threshold in this case was determined based on a standard atmosphere environment over the same terrain path.

Refractivity profiles measured at Point Mugu were used for the two propagation paths from John Wayne Airport to Point Mugu and Long Beach to Point Mugu. The terrain path from John Wayne Airport to Point Mugu is roughly 129 km. The path begins over the Los Angeles basin area and the remainder of the path is over water with some small mountain peaks near the receiving end at Point Mugu. Figure 4 shows RPO and TPEM results, along with observations, for this path. The terrain profile did not consist of very large obstructions and was relatively smooth, with most terrain elevation features having a height of 50 m or less. One would expect that a smooth earth assumption in this case would be adequate and that results from RPO would be in close agreement with observations. In fact, RPO and TPEM results differ by only 5 to 10 dB. However, in comparison with measurements, TPEM still gives a much better match to the data.

The path from Long Beach Airport to Point Mugu, a distance of 100 km, starts with fairly smooth terrain but contains some high coastal mountain peaks near the receiving end at Point Mugu. Results are shown in Figure 5. Here again, the presence of these peaks causes a significant reduction in received signal. TPEM shows very good agreement with observations, while RPO differs by as much as 20 to 30 dB.

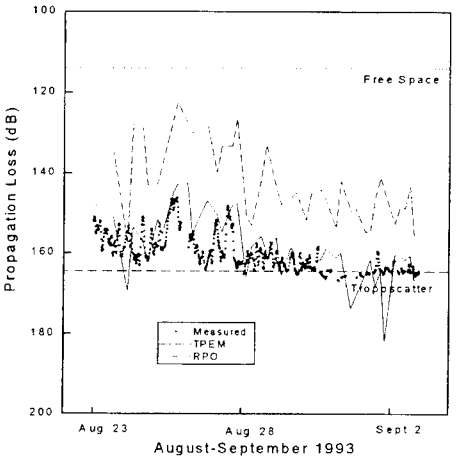


Figure 5. TPEM and RPO results vs. measurements for Long Beach to Point Mugu path using Point Mugu soundings.

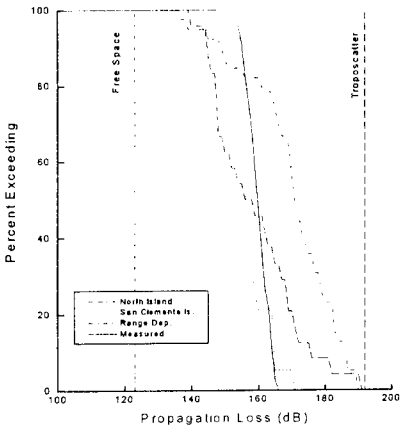


Figure 6. Distribution for San Clemente Island to San Diego path for homogeneous and range dependent refractivities.

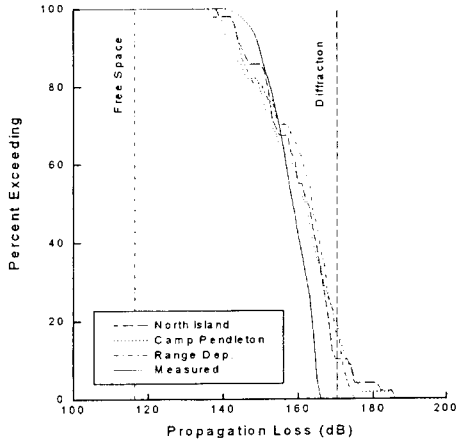


Figure 7. Distribution for John Wayne Airport to San Diego path for homogeneous and range dependent refractivities.

Clearly, for all of the propagation paths discussed in Figs. 2-5, the terrain had a significant effect on the field. The smooth earth assumption results, given by RPO, did not adequately model what was observed. Also, since the signal levels measured were usually well above troposcatter and diffraction levels, this indicates the refractivity had a major effect on the field as well. The refractivity profiles used in Figs. 2-5 were taken from one site only and were either at the receiving end of, or midway along, the path; and the atmospheric environment for these cases was assumed to be homogeneous. Refractivity measurements were taken at more than one location along each path. The atmosphere can change drastically at land/sea boundaries where anamolous conditions are attributable to very different mechanisms over land than over water. How much improvement, if any, would there be between predicted and measured fields if range dependent refractivity environments were considered?

Results from TPEM for the San Clemente Island to San Diego path for homogeneous and range dependent environments are shown in Figure 6. Only measurements and predictions for the first six days were included in this distribution due to the fact that data over the last half of the measurement period were spurious or nonexistent. The measured data is shown as a solid line and all information is given in terms of the percentage of time in which the propagation loss exceeds the abscissa value. The North Island curve represents results from TPEM assuming homogeneous environments based on soundings at North Island (this corresponds to Fig. 2). Similarly, the San Clemente Island curve represents results from TPEM assuming homogenous environments based on soundings measured at San Clemente Island. Lastly, soundings from both of these locations taken at roughly the same time of day (no further than 30 minutes apart) were used for the range dependent result. The results given by the San Clemente Island soundings produced the best agreement with observations, particularly at the higher loss values. In fact, the range dependent curve gives the worst agreement overall. This is a puzzling result and this case will be looked at in more detail in the next section.

For the path from John Wayne Airport to San Diego, results from homogeneous environments based on North Island and Camp Pendleton soundings agreed with measurements just as well as those using the range dependent environments, as shown by Figure 7. The range dependent environment for this path assumed horizontal homogeneity between John Wayne Airport and Camp Pendleton based on Camp Pendleton soundings, and then range dependent refractivity between Camp Pendleton and San Diego based on Camp Pendleton and North Island soundings.

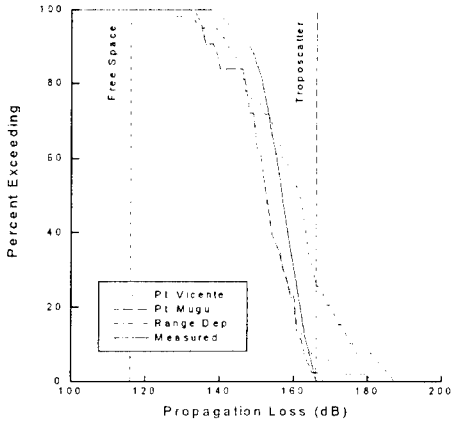


Figure 8. Distribution for John Wayne Airport to Point Mugu path for homogeneous and range dependent refractivities.

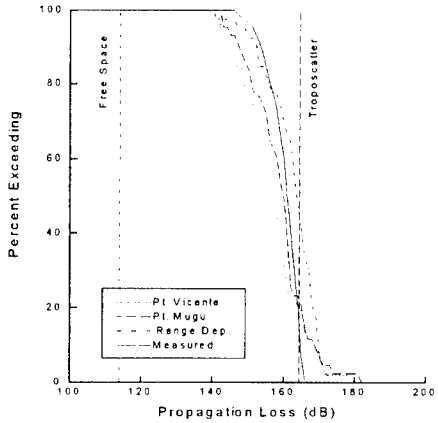


Figure 9. Distribution for Long Beach to Point Mugu path for homogeneous and range dependent refractivities.

In Figure 8, results using range dependent environments gave slightly better agreement at the lower loss values for the John Wayne Airport to Point Mugu path. The two curves representing homogeneous refractivity based on Point Vicente and Point Mugu soundings performed equally well, though they do not match the measured data very closely at the lower loss values. Here, the range dependent results assumed horizontal homogeneity from John Wayne Airport to Point Vicente based on Point Vicente soundings, then range dependent refractivity from Point Vicente to Point Mugu based on their respective soundings.

Figure 9 shows the distribution curves for the Long Beach to Point Mugu path. As in Fig. 8, the range dependent result assumed horizontal homogeneity from Long Beach to Point Vicente, then treated the environment as range dependent from Point Vicente to Point Mugu. The range dependent curve shows excellent agreement at the lower loss values.

4. DISCUSSION

In Figs. 6-9, the assumption of a homogeneous refractivity environment, using whatever soundings were available, gave fairly good agreement with observations. For three of the four propagation paths, little difference is seen in the distribution results when using a sounding midway or at one end of the path. A slight improvement occurred in only two of the paths, Figs. 8 and 9, when using range dependent refractivity environments. The most puzzling result was in the San Clemente Island to San Diego path (Fig. 6) where there was much better agreement with data when using soundings from San Clemente Island than from North Island. Also, applying range dependent environments showed the worst match. This leads one to assume that other mechanisms may be involved. Therefore, it is worth taking a second look at this case.

On the San Clemente Island to San Diego path there were refractivity measurements available at both terminal locations (although technically the radiosonde measurement site at North Island is located roughly 3 km from the receiver site, for most practical purposes, the refractivity measured can be considered representative of that at the receiving antenna). Also, this is the only path in which one of the terminal antennas was located away from the mainland. It was found that, over the ocean, the assumption of a horizontally stratified troposphere led to valid propagation assessments 86% of the time [7]. While the troposphere over the sea does exhibit horizontal homogeneity over relatively long distances in most cases, meteorological conditions occur occasionally in which the environment may change drastically in just a few kilometers, such as at air-mass boundaries associated with land/ocean interfaces. To test this theory, the predictions based on the range dependent environments will be repeated, however, the environments will be "weighted" in such a way as to make the refractivity homogeneous from San Clemente Island to 2 kilometers off-shore of San Diego (or from

the receiving antenna). From 2 kilometers off-shore to the receiving antenna the refractivity then becomes range dependent based on the San Clemente Island and North Island radiosonde measurements. The result is shown in Figure 10. Clearly, the predictions given by the "weighted" range dependent environment now show much better agreement with observations than the predictions given by the two homogeneous environments.

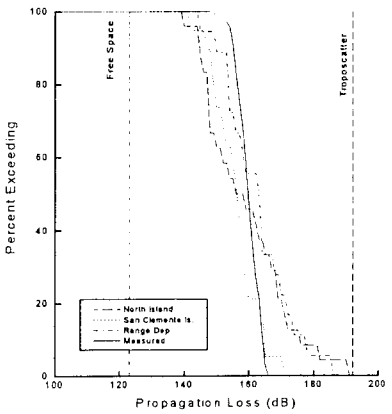


Figure 10. Distribution for San Clemente Island to San Diego path for homogeneous and "weighted" range dependent refractivities.

5. CONCLUSIONS

It has been shown that in a coastal environment, fields are greatly affected by the presence of terrain even when propagation paths are primarily over water. Another major effect on the field is, of course, the refractivity environment. Horizontally homogeneous refractivity environments based on soundings taken at midway and at either end of the path showed good agreement with measured data. Attempting to describe the atmosphere as accurately as possible by modeling a range dependent environment gave only slight improvement of comparisons with observations. An important result arose from one propagation path in which one of the terminal antennas was located far away from the mainland. In this case, a range dependent evironment based equally on the refractivity measured at both terminal antenna locations did not produce better agreement with data, but in fact showed the worst agreement overall. This was most likely due to the horizontally stratified refractivity in the surrounding ocean environment which changes abruptly very near large land masses. Therefore, more thought has to be given when applying a range dependent environment in coastal areas.

ACKNOWLEDGEMENT

This work was sponsored by the Office of Naval Research.

REFERENCES

1. Craig, K.H., "Propagation modeling in the troposphere: Parabolic equation method", Electron. Lett., 24, 1989, pp. 1136-1139.

2. Kuttler, J.G. and Dockery, G.D., "Theoretical description of the parabolic approximation/Fourier split-step method of representing electromagnetic propagation in the troposphere", Radio Sci., Mar-Apr. 1991, pp. 381-393.

3. Hitney, H.V., "Hybrid ray optics and parabolic equation methods for radar propagation modeling", "Radar 92", IEE Conf. Pub. 365, Oct. 1992, pp. 58-61.

4. Barrios, A.E., "Terrain modeling using the split-step parabolic equation method", "Radar 92", IEE Conf. Pub. 365, Oct. 1992, pp.66-69.

5. Barrios, A.E., "A Terrain Parabolic Equation Model for Propagation in the Troposphere", IEEE Trans. on Ant. and Prop., 42, 1, Jan. 1994, pp. 90-98.

6. Yeh, L.P., "Simple Methods for Designing Troposcatter Circuits", IRE Trans. on Comm. Systems, CS-8, 3, Sept. 1960, pp. 193-198.

7. Hitney, H.V., Richter, J.H., Pappert, R.A., Anderson, K.D., Baumgartner, G.B., "Tropospheric Radio Propagation Assessment", *Proc. of the IEEE*, Vol. 73, No. 2, Feb. 1985.

Capabilities and Limitations Associated with Using GTD to Model Propagation Path Loss in the Presence of Irregular Terrain

Kent Chamberlin
Dept. of Electrical and Computer Engineering
University of New Hampshire
Durham, NH 03824-3591
Kent.Chamberlin@UNH.EDU

Abstract

The Geometrical Theory of Diffraction has been used to model propagation path loss in the presence of irregular terrain over a wide range of frequencies, path lengths, and terrain types. The objective of this paper is to describe the fundamentals of this modeling approach and to reveal its known capabilities and limitations in light of recent work. Some comparisons of modeled and measured data are given to demonstrate the type of accuracy that can be achieved using the technique.

Introduction and Background

Since the late 1970's, the Geometrical Theory of Diffraction (GTD) has been used to model the effects of irregular terrain on radiowave propagation for a variety of applications and frequency ranges. For certain applications, GTD has provided results in very close agreement with measured data, while for other applications it does not produce close agreement. The primary purpose of this paper is to provide insights into the types of conditions where a GTD propagation model would be appropriate to use, and the degree of accuracy that can be expected. A brief history of the technique, along with pertinent references, is given below, followed by an overview of how the technique is implemented in a contemporary model. Finally, some validation data are shown to demonstrate the types of accuracy that are achievable.

The earliest known use of GTD for terrain-effect modeling involved the Instrument Landing System (ILS) glide slope [1]. One of the reasons that GTD worked well for this application is that for the geometry and frequency of interest (the receiving antenna at a 3° elevation angle for a 300 MHz signal and horizontal polarization), terrain without tree cover appears to be a good conductor, and terrain features are large with respect to a wavelength. Subsequent work with GTD proved it capable of providing good results for the ILS localizer (100 MHz) as well.

In the early 1980's [2], GTD was implemented in a general-purpose, point-to-point propagation model. This model was named GELTI, which stands for **G**TD **E**stimated **L**oss due to **T**errain **I**nteraction.

Validation of that model with respect to measured data shows it to be very accurate for paths where the number of rays in the model is sufficient to account for the significant propagation mechanisms, and for paths where the troposphere can be assumed to be homogeneous. While it is recognized that other GTD-based propagation models exist [3,4,5] the GELTI model is used as an example here because of its proven accuracy and because of the author's familiarity with it.

The original GTD diffraction coefficients were developed assuming that the scatterer was smooth and perfectly conducting. To more realistically model terrain interactions, those diffraction coefficients were modified to account for finite conductivity and local surface roughness. Validation work with GELTI, which implements those modified diffraction coefficients, has shown that those modified diffraction coefficients do provide greater prediction accuracy in some cases [6]. At this point in time, the range of frequencies and distances over which GTD terrain-effect modeling remains accurate is not fully known. However, close agreement between measured and modeled data has been observed from as low as 8 MHz [7] to as high as 9 Hz. Accuracy has also been seen for propagation paths up to roughly 50 miles, although accuracy appears to diminish for longer distances, likely due to the fact that other propagation mechanisms become more dominant.

To generate estimates of path loss due to irregular terrain, all GTD models use a piecewise-linear approximation to the actual terrain profile. Until fairly recently, this linearization process was performed manually, which made model accuracy dependent upon the expertise of the user and made the modeling process quite time consuming. However, an automated approach has been developed [8] that enables a piecewise-linear profile to be extracted from raw terrain data, which greatly simplifies the modeling process and makes model results user-independent. The automated terrain linearization approach is described briefly below.

Most GTD terrain-effect models are 2-dimensional in that only the terrain directly between the transmitting and receiving antennas is considered in estimating path loss. Experience has shown that for most paths, this simplification does not represent a major deficiency in the modeling process, and is considerably less computationally intensive than 3-dimensional approaches. Further, an extension of the terrain linearization process can be implemented to identify multipath-causing regions on the 3-dimensional terrain that can be taken into account when calculating path loss.

Overview of the GELTI Model

The GELTI model was a spin-off of earlier work modeling ILS performance in the presence of irregular terrain. Having undergone extensive modifications since its initial implementation, GELTI currently estimates propagation path loss by summing the contribution of ray and ray combinations listed below:

1) direct
2) reflected
3) diffracted
4) doubly-reflected
5) reflected-diffracted
6) doubly-diffracted
9) reflected-reflected diffracted
10) diffracted-reflected-reflected
11) diffracted-diffracted-reflected
12) diffracted-reflected-diffracted
13) reflected-diffracted-diffracted
14) reflected-reflected-reflected

7) diffracted-reflected
8) reflected-diffracted-reflected
15) diffracted-diffracted-diffracted
16) adjacent-edge diffracted

The contribution of the direct ray will be calculated if there is no blockage between the transmitting and receiving antennas. The magnitude and phase of that contribution is determined by free space loss, and both transmitting and receiving antennas are assumed to be isotropic. To model applications involving high-gain antennas, good results have been obtained by adjusting model results by the antenna gain at the observation angle of interest [9]. This approach to modeling high-gain antennas should be accurate for most propagation paths, since departure angles from the transmitting antenna for the various rays tend to be nearly equal. However, GELTI can readily be modified to apply an antenna pattern weighting to individual rays corresponding to different departure angles if the application warranted.

Reflected ray(s) will exist (there may be more than one) if there are points on the terrain profile where the angle of incidence is equal to the angle of reflection. The amplitude and phase of the reflected ray is determined by the complex-valued reflection coefficient, computed using the angle of incidence, electrical constants of the ground plane, and a roughness factor representing height variability in local terrain such as variability caused by vegetation, uneven ground, or waves, if propagation is over water. This roughness factor does not account for gross terrain variations, such as hills or ridges, since those effects are computed using GTD. The roughness factor is used to modify the reflection coefficient to account for imperfect reflection caused by local terrain roughness.

Using conventional GTD, the amount of diffracted energy re-radiated from an edge is determined by the diffraction coefficient, which is a function of the wedge angle, and the incident and diffracted ray geometries. The original formulation of the GTD diffraction coefficient was performed by Keller [10] in 1962. This formulation did exhibit singular behavior near the shadow boundary (where the direct ray contribution is discontinuous) and reflection boundary (where the reflected ray contribution is discontinuous), however, which hindered its utility as a modeling tool. This problem was later resolved by Kouyoumjian and Pathak [11] in their development of the Uniform Theory of Diffraction (UTD). As stated above, the terms GTD and UTD are often used synonymously, and GELTI employs UTD diffraction coefficients.

Higher order rays, such as the reflected-diffracted ray, are combinations of the fundamental rays. Although higher-order rays tend to be smaller in magnitude than the first-order rays (i.e., the direct, reflected, and diffracted rays), comparisons with measured data show that these rays can be important to model accuracy. Calculation of the magnitude and phase of the higher-order rays is accomplished by accounting for cumulative losses and phase shifts due to free-space propagation, reflection, and diffraction.

GELTI computes the total field at the receiver by taking the complex sum of all possible ray combinations. The contribution of each ray is determined explicitly within the code, enabling individual rays to be modified for antenna pattern or vegetation effects [12]

Earth curvature is presently accounted for by adjusting the terrain elevation, and hence will not properly model a stratified troposphere. However, the possibility of modifying GELTI to model such effects is being investigated [13].

In order to investigate all possible combinations of each ray type for a complex terrain profile, a large amount of computation time is required. To reduce execution time, it is assumed that some ray types can be ignored without significantly affecting the estimated signal strength. In GELTI, it is assumed that all back-scattering rays can be ignored. Because of this, GELTI is a forward-scatter model, and cannot be used to estimate backscatter from terrain or other obstacles without modification.

Automated Terrain Linearization

A problem common to most terrain-sensitive propagation models is establishing the parameters defining the terrain profile [14]. For GELTI, it is defining a piecewise-linear terrain profile to represent the actual terrain. Experience has shown that identifying the appropriate linear profile is the most significant factor affecting model accuracy. However, because of limited validation work with the model and the complexity of the problem, the linearization process has remained somewhat of an art, requiring considerable insight on the part of the user. Consequently, a significant effort has been dedicated to establishing and automating a methodology for creating linear profiles from raw terrain data to be used as input to GELTI. The result of that effort is the Automated Terrain Linearization Model (ATLM), that reads raw terrain data, and generates a linearized profile that can be used as input to the GELTI model. The development of the terrain linearization process outlined below uses examples relating to the Microwave Landing System (MLS), which operates at a frequency of around 5 GHz. However, the approach scales for frequency, and has been shown to work well over at least the same range of frequencies for which GELTI has been validated.

Representing an actual terrain profile by straight line segments assumes that some of the information contained in that profile can be ignored in the modeling process. Thus, the objective in linearizing a profile is to assess which parts of the profile will or will not affect propagation, and then to approximate the parts that will affect propagation by linear segments of appropriate slope and height. As a general rule, terrain will affect propagation if it: 1) blocks a ray trajectory, 2) supports reflection, or 3) contains an edge that will reradiate significant diffracted signal energy. These criteria are dependent upon antenna-terrain geometry and frequency, and hence the optimal linearized profile will be dependent upon those parameters as well.

Another goal in linearizing a profile is to keep the number of linear segments representing a terrain profile to a minimum. Including too many edges in a linear profile degrades model accuracy for essentially three reasons: 1) the model will not be capable of representing some ray trajectories with the sixteen available ray types, 2) some high-frequency assumptions fundamental to GTD will be violated as edges become closer together, and 3) computational errors resulting from the inclusion of multiple complex number calculations will become significant.

The approach used here to determine what segments of the actual terrain affect propagation was inspired by Fermat's principle for edge diffraction [15,]where the stationary phase points on the terrain profile are used to identify points of reflection or diffraction that need to be represented in the linearized profile. When dealing with actual terrain, there are often multiple stationary phase points clustered together, which may be caused by roughness in the terrain surface. To distinguish which of the stationary phase points are caused by roughness, the linearizing algorithm looks at the nearest neighboring stationary phase points; if both are within an empirically-determined phase value of the candidate point, that point is rejected. That phase value is the only empirical variable in the modeling process, and experience has shown that a value of $3\pi/8$ radians, which cor-

responds to ¾ Fresnel zones, produces good results. Further, results are relatively insensitive to variations in that variable.

Once the stationary phase points have been identified, linear regression is used to determine the slope and intercept of the actual terrain on either side of the stationary phase points. Linear regression is begun at the stationary phase point, and continues until the phase exceeds the empirical value described above. Thus, using a value of $3\pi/8$ radians for that variable will mean that linear regression will take place over 1.5 Fresnel zones to determine the slope and intercept of a reflection point on the terrain. The linear profile is built by piecing together the slopes and intercepts determined by linear regression.

Model Validation

As stated, early work with GTD terrain-effect modeling involved the ILS, and validation work for that application was oriented towards predicting navigation system performance, rather than in predicting absolute signal strength. The first major validation study for the GELTI propagation model was funded by ECAC [16], in which model results were compared against measured data collected by the Institute for Telecommunication Sciences. A conclusion reached in that study was that the GELTI model was generally more accurate than other contemporary models for paths less than 50 km in length. However, no attempt was made to define an RMS error for the model due to uncertainty about the terrain linearization process, which was performed manually for the study, as well as uncertainty about the quality of the comparison data (the measured signal strength data and the terrain profile data).

Follow-on validation and improvements were performed by Luebbers [17,18] with the results showing GELTI to be a viable means for predicting absolute signal strength for short-range propagation paths.

In 1989, a study was undertaken to predict signal strength for the microwave landing system (MLS) operating in the presence of humped runways [19]. One of the byproducts of this effort was the development of the automated terrain linearization process. Further, validation was performed using carefully collected terrain and measured signal strength data at five different sites. The results of that validation show that when accurate terrain and antenna data are entered in to GELTI, agreement between measured and modeled data can be within several dB.

Figure 1 shows plots of both the terrain profile and one comparison of measured versus modeled data. The measured data were collected using a van with a mast that would vary the receiving antenna over a range of heights from 3 to 40 feet above the ground; the signal strength plot of Figure 1 is for the receiver at the location farthest from the transmitting antenna. As seen in the plot of the profile, part of the path is below line of sight, and three diffractive edges are illuminated. As seen in the plot, the agreement between measured and modeled data is excellent. The discontinuity in the modeled data at a receiver height of around 25' is caused by the fact that the model does not calculate the ray that is reflected after being adjacent-edge diffracted.

While the path shown is relatively short, 11,500', it does represent over 58,000 wavelengths at 5 GHz. Hence these data can be used to infer model performance on longer paths at lower frequencies assuming that other tropospheric propagation mechanisms, such as ducting, do not become significant.

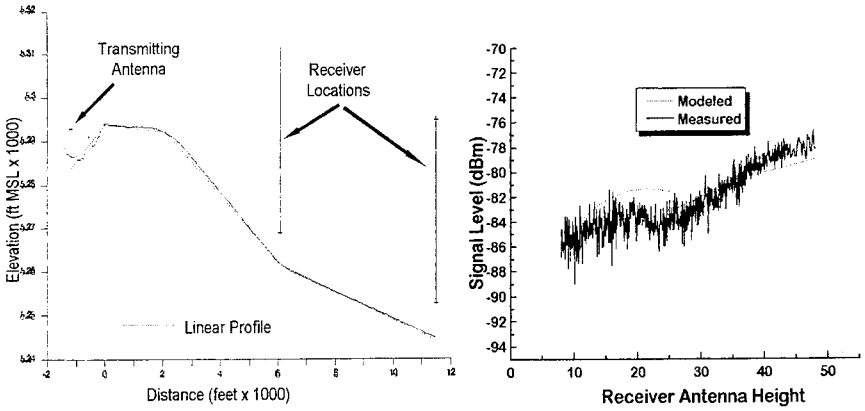


Figure 1 Terrain Profile and Measured-Modeled Data Comparison for the Denver Stapleton Runway 09 MLS Azimuth Transmitter.

Figure 2 plots both the profile and a comparison of measured and modeled signal strength for another site. The comparison data shown in the plot were collected at the location marked "Threshold RWY09", and the transmitting antenna was at the lower of the heights shown. Again, good agreement between measured and modeled data is evident.

Conclusions

Validation data provide strong evidence that GTD can be used to accurately predict signal behavior in the presence of irregular terrain over a wide range of frequencies. GTD models are theoretically correct, in that no empirical assumptions are made about the behavior of signal behavior. Consequently, GTD models are realistically responsive to frequency variations, which enables them to provide broadband propagation path information. Further, because ray trajectories are calculated, signals can be reconstructed in the time domain, a capability not offered by other modeling techniques.

The major limitations are that GTD models do not, at this point in time, account for an inhomogeneous troposphere, and that its results become inaccurate when the model implemented does not have a sufficient number of rays or ray types to account for the significant propagation mechanisms for a particular path. Experience has shown that these limitations cause the useful accurate range for GTD terrain-effect modeling to be around 50 miles, depending upon path specifics.

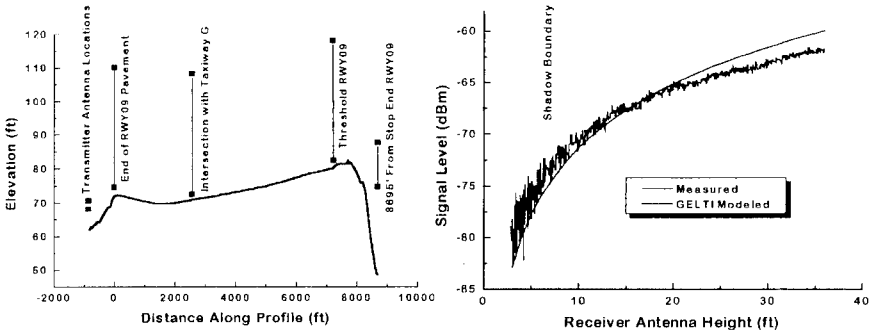


Figure 2 Terrain Profile and Measured-Modeled Data Comparison for Wilmington, Deleware Airport Runway 09 MLS Azimuth Antenna

To get accurate long-range prediction capability, it has been suggested that a GTD propagation model be coupled with a parabolic wave equation model, which is sensitive to an inhomogeneous troposphere. In such a hybrid model, the GTD model would generate initial-condition signal strength values for a region around a transmitting antenna, and the parabolic wave equation model would use those initial conditions in determining how the wave propagates through the troposphere. This would likely provide an improvement in prediction accuracy because of GTD's greater sensitivity to terrain variations.

References

[1] R. Luebbers, V. Ungvichian, and L. Mitchell, "GTD Terrain Reflection Model Applied to ILS Glide Slope," *IEEE Trans. Aerosp. Electron. Syst.*, p. 11, Jan., 1982.

[2] Kent Chamberlin and Raymond Luebbers,"An Evaluation of Longley-Rice and GTD Propagation Models," *IEEE Trans. on Ant. and Prop.*, Vol. AP-30, No. 6, Nov. 1982, p. 1093.

[3] Al-Nuaimi, M. O., and M. S. Ding [1991], "Estimation Models of Radio Path Diffraction Loss Experienced by Microwave Signals in Hilly Terrain," Proc. Int. Microwave Conf. SBM091, Rio de Janeiro, July 1991, 276-281.

[4] Frullone, M., P. Grazioso, G. Riva, and A. M. Pezza [1991], "Evaluation of Diffraction Losses over Multiple Obstacles for Field Strength Prediction," Proc. ISBT'91, Int. Symp. Broadcasting Techn. Zhuhai, China, 311-316.

[5] Bruno Bisceglia , *et. al.* [1988], "Symbolic Code Approach to GTD Ray Tracing," *IEEE Trans. on Ant. and Prop.*, Vol 36, No. 10, Oct. 1988.

[6] R. Luebbers, "Comparison of Lossy Wedge Diffraction Coefficients with Application to Mixed Path Propagation Loss Prediction", *IEEE Transactions on Antennas and Propagation*, July 1988.

[7] J.K. Breakall, J.S. Young, G.H. Hagn, R.W. Adler, D.L. Faust, and D.H. Werner, "The Modeling and Measurement of HF Antenna Skywave Radiation Patterns in Irregular Terrain" , *IEEE Trans. on Ant. and Prop.*, July 1994

[8] Kent Chamberlin, "An Automated Approach For Implementing GTD To Model 2-Dimensional Terrain Effects at Microwave Frequencies," *IEEE Trans. on EMC*, Publication date not set yet.

[9] Chamberlin, Kent,"Computer Modeling Of MLS Signal Strength in The Presence Of Runway Hump Shadowing," Invited Paper, presented at, and in the Proceedings of ANTEM'92, Symposium on Antenna Technology and Applied Electromagnetics, Winnipeg, Manitoba, Canada, August, 1992.

[10] J. B. Keller, "Geometrical Theory of Diffraction," Journal of the Optical Society of America, p. 116-130, 1962.

[11] R.G. Kouyoumjian and P. H. Pathak," A Uniform Geometrical Theory of Diffraction for an Edge in a Perfectly Conducting Surface," Proc. IEEE, P. 1448-1461, Nov. 1974.

[12] Chamberlin, Kent A.,"The Effect of Tree Cover on Air-Ground, VHF, Propagation Path Loss", *IEEE Transactions on Communications*, September, 1986.

[13] Bianchi, C., Chamberlin, K., and Sivaprasad, K.,"A Hybrid Geometrical Theory of Diffraction Model for Estimating Line-of-Sight Propagation Path Loss", Presented at and in the Proceedings of the Progress in Electromagnetics Research Symposium, July, 1991, Cambridge, MA.

[14] Andersson, K. [1992], "Required Resolution in Terrain Databases for Use with Propagation Prediction Models," Proc. NRS 92, Aalborg, Denmark, June 1-4,35-38, (Available from NRS 92, AUC-Servicecenter, Niels Jernes Vej 10, DK-9220 Aalborg, Denmark).

[15] Graeme L. James, *Geometrical Theory of Diffraction for Electromagnetic Waves*, 2nd Edition, IEE Electromagnetic Wave Series 1, 1980.

[16] Chamberlin, Kent A. and Luebbers, Raymond J.,"Evaluation of a Terrain Sensitive, Propagation Path Loss Model Based Upon the Geometrical Theory of Diffraction, Modified for Finite Conductivity and Local Surface Roughness", Final Report, Electromagnetic Compatibility Analysis Center, September, 1982.

17 R. Luebbers, "Propagation Prediction for Hilly Terrain Using GTD Wedge Diffraction", *IEEE Trans on Ants and Prop*, pp. 951-955, September 1984.

18 R. Luebbers, "A Semi-blind Test of the GTD Propagation Model for Reflective Rolling Terrain", *IEEE Trans on Ants and Prop*, March 1990

[19] Chamberlin, Kent,"Computer Modeling Of MLS Signal Strength in The Presence Of Runway Hump Shadowing", Final Report, prepared for the FAA Technical Center under contract No. 3400-02, Sept. 1990.

COMPARISON OF ELECTROMAGNETIC WAVE PROPAGATION COMPUTER PROGRAMS

Stephen A. Fast
Applied Research Laboratories University of Texas at Austin
10000 Burnet Road
Austin, Tx 78758

Thomas H. Koschmieder
Applied Research Laboratories University of Texas at Austin
10000 Burnet Road
Austin, Tx 78758

Background

Many propagation programs have been used to model radio wave propagation over terrain. Terrain is modelled by specifying elevations at various ranges from the transmitter. The terrain can be thought of as a series of half planes (or knife edges) or as a series of wedges generated by connecting the terrain elevation points. Various knife edge diffraction methods, the uniform geometrical theory of diffraction, Fresnel-Kirchhoff theory, and the parabolic equation approximation are applied in the propagation programs. Programs that apply diffraction techniques must calculate rays that diffract off intervening terrain features. In addition some programs calculate rays that combine diffractions with reflections.

The programs tested here that use knife edge diffraction reduce the number of knife edges to those which are most significant. When multiple half planes interact with the wave along the path, the interaction is approximated using various strategies combining a few single half plane diffractions.

For programs modelling the terrain as wedges, phase map techniques are applied to determine the significant wedges thus reducing the effort required to find the rays. When modelling terrain as a series of wedges, geometric theory of diffraction can be applied to model the interaction with each wedge. When multiple wedges interact with the ray, single wedge diffractions are combined.

The two other techniques avoid the problems of diffraction. When using Fresnel-Kirchhoff theory, the field is modelled by a series of Huygen sources that are stepped along the path. At each step the field is calculated from the previous step using Fresnel-Kirchhoff theory while accounting for reflection.

The second method is to step the field along the path and approximate the scalar wave equation with a parabolic equation. Either the Fourier split step method or the finite difference technique are applied to solve the parabolic equation. Since the parabolic equation method was originally developed to find the field passing through atmospheric irregularities, a change of variables transforms the terrain variations into atmospheric refractive index variations.

The purpose of the effort is to develop a standard set of terrain feature to test using the pro-

grams and compare the programs using the standard set of terrain features. Graphics presented show the terrain features and the comparisons of the programs.

Models

The following programs are compared: GTD Estimated Loss due to Terrain Interaction (GELTI) developed by R. Luebbers and K. Chamberlin [1], the Communications Research Centre (CRC) program developed by J. Whitteker [2], Smooth Earth Knife Edge (SEKE) as described by S. Ayasli [3], Terrain Integrated Rough Earth Model (TIREM) developed by the Electromagnetic Compatibility Analysis Center [4], Institute for Telecommunication Sciences' Irregular Terrain Model (ITM) [5], and Variable Terrain Radio Parabolic Equation (VTRPE) developed by F. Ryan [6].

GELTI searches for up to sixteen different ray types. A ray type consists of reflection and diffraction paths off terrain features. As many as three ground reflections, three diffractions, or combinations of diffractions and reflections can form a ray type. Geometric Theory of Diffraction, GTD, is used to calculate the diffraction losses [7]. The terrain profiles used by GELTI are preprocessed by the Automated Terrain Linearization Model (ATLM). ATLM locates the significant terrain features for a given radio link, and reduces the terrain profile to a simpler version that preserves the significant features.

The CRC model advances the field as an array of Huygen's principle sources along the path. The terrain is modelled by a series of knife edges and at each knife edge Fresnel-Kirchhoff theory is used to generate the field from the previous knife edge. The reflected wave is included by connecting each knife edge with a reflecting plane.

SEKE, TIREM, and ITM identify the terrain obstacles along the path and model them using knife edges. The diffracted field from multiple knife edges is found using the Epstein-Peterson method in TIREM and ITM and with a modified Deygout method in SEKE. SEKE also accounts for the reflected wave.

VTRPE uses the parabolic equation approximation to calculate the field. Because the parabolic equation method does not treat terrain directly, VTRPE linearly interpolates between terrain points and transforms the terrain variations into atmospheric irregularities. VTRPE steps the field in range dynamically adjusting the range step to minimize the error.

Conclusions

By developing a standard set of terrain features, propagation program results can be easily compared with expected phenomena and each other. In summary, a diversity of propagation modeling programs show both similarities and differences in their predictions. Generally, if different programs make similar assumptions, the more likely the losses and loss contours agree. The differences between results indicate that more interesting work can be accomplised by examining the differences induced by the terrain features and classifying terrain features accordingly. Continued work will lead to better predictions by all propagation prediction programs.

The data sets used for the comparisons are available to propagation prediction program developers. Programs to view data are also available.

References

1. R. Luebbers, and K. Chamberlin, "GELTI Propagation Model: Theory of Operation and User's Manual", Waveware, 1994.

2. J. H. Whitteker, "Fresnel-Kirchhoff Theory Applied to Terrain Diffraction Problems", Radio Science, Vol. 25, pp. 837-851, September-October 1990.

3. S. Ayasli, "SEKE: A Computer Model for Low Altitude Radar Propagation Over Irregular Terrain", IEEE Trans. Antennas and Propagation, Vol. AP-34, pp. 101-123, August 1986.

4. D. Eppink and W. Kuebler, "TIREM/SEM Handbook", ECAC-HDBK-93-076, ECAC, 1993.

5. G. Hufford, A. Longley, and W. Kissick, "A Guide to the Use of the ITS Irregular Terrain Model in the Area Prediction Mode", NTIA Report 82-100, 1982.

6. F. Ryan, "User's Guide for the VTRPE (Variable Terrain Radio Parabolic Equation) Computer Model", NOSC Technical Report 1456, October 1991.

7. K. Chamberlin, "Overview of Terrain-Effect Modeling Using the Geometrical Theory of Diffraction", Proceedings of the Beyond Line of Sight Conference, August 1994.

A MODEL FOR ESTIMATING ELECTROMAGNETIC WAVE ATTENUATION IN A FOREST (EWAF) ENVIRONMENT

Conrad Welch and Catherine Lemak
Computer Sciences Corporation, Systems Engineering Division
3160 Fairview Park Drive, Falls Church, VA 22042

Lee Corrington
The Electronic Proving Ground
Fort Huachuca, AZ 85613-7110

Abstract

This paper describes an elementary foliage propagation path loss model which represents a forest as a dissipative dielectric slab lying in a more lossy half-space represented by the ground. This physical concept was originally proposed by D.J. Pounds and A.H. LaGrone[1] and further investigated by Theodor Tamir[2]. Our Electromagnetic Wave Attenuation in a Forest (EWAF) model uses empirical foliage path loss information as a basis and therefore is closely tied to actual path losses encountered in real-world situations.

The EWAF model includes several features: the effects of antennas within the forest, outside the forest, and above the forest; wave polarization; forest density; canopy, trunk, and undergrowth losses; antenna beamwidth; wet foliage; lush foliage; and many other physical/forest conditions. It is implemented on a Sun/SPARC network and provides a good estimator for foliage losses anywhere in the world.

A. Introduction

For over a half-century, communicators have been concerned with radio frequency (RF) propagation path loss through foliage. Over the past 30 years, measurements and analyses have shown that actual losses encountered within forests are considerably less than had been estimated for propagation paths straight through foliage. Pounds and LaGrone[1] hypothesized in 1963 that propagation loss through foliage could be represented by propagation through a dielectric slab, where the antennas are submerged in the dielectric media.

Tamir[2,3] expanded this concept by developing the mathematics describing the dielectric slab propagation phenomenon. The literature contains much measured data for propagation losses through, around, and in the vicinity of foliage. Although mathematical models have been prepared that describe this propagation, very little has been done to provide communicators with a computerized tool for predicting foliage losses.

This paper describes a first step in the development of the EWAF computer model, which uses plausible inputs to estimate foliage losses. The model can be used by communications engineers to obtain an estimate of propagation losses through a forest or other foliage situations expected for a given set of operating conditions. The estimates will be useful for communications planners in situations where transmitter and receiver antennas (or perhaps only one) will be immersed in foliage. Representing the foliage by a dielectric slab will provide an estimate of foliage losses which could be expected in situations where meager information is available regarding the wood density.

The information available on propagation loss through foliage sometimes refers to the area in square feet of wood per acre of forest and assumes a uniform density throughout the forested region. In most instances, it is not possible to measure the wood density per acre. Furthermore, for large forested areas, the forest density is quite variable.

The EWAF model is not a rigorous mathematical treatment of a forest represented by a dielectric slab. It is actually based upon previously measured data for sparse and dense forests in the United States as well as very dense forests in India, as described by Tewari et al.[4], where the average annual rainfall ranges to 3000 millimeters. The model was implemented using Ada programming language and is part of a larger graphic user interface interactive engineering tool, the Analysis Software Environment. The model is resident on a Sun network at the Electronic Proving Ground, Fort Huachuca, Arizona, of the White Sands Missile Range.

B. Propagation of Radio Waves Through a Dielectric Slab

Radio (or electromagnetic) waves passing through foliage represented by a lossy dielectric slab commonly incur path loss rates of perhaps 0.25 decibels per meter (dB/m) in excess of free space [referred to as excess path loss (EPL)]. For path lengths of 1 kilometer, for example, the attenuation of a wave due to foliage would be 250 dB. Communication over radio links having such losses would usually be impossible or very difficult. However, experimental results indicate that the EPL due to foliage is actually much less, more like 40 or 50 dB at 400 megahertz (MHz).

These differences between expected and actual results led Pounds, LaGrone, and Tamir to the dielectric slab theory, where the wave travels up through the medium (incurring high losses) and then travels laterally along the boundary region at a much lower loss rate. Figure 1 depicts the propagation path geometry. This propagation in the boundary region is called the lateral wave and allows communication over much greater distances than would be possible otherwise.

When the RF propagation is compared to optics and the refraction encountered when a wave passes from a more dense medium to a less dense medium, the geometry becomes equivalent to Figure 2. (The more dense medium is the forest, the less dense medium is the air.) A large portion of the wave escapes through the boundary into space for high angles of incidence with the boundary region. As the angle of incidence decreases, the refracted wave at the surface becomes more nearly parallel to the boundary. At a critical angle of incidence, the wave travels parallel to the air-forest boundary and forms the lateral wave, which incurs fairly low loss and permits communication over extended distances. Associated with the lateral wave is a lossy wave, called the leakage field, that travels back down into the dielectric slab. The leakage field provides the route down to the receiving antenna, which may be submerged in the forest at some distance from the transmitting antenna. The leakage

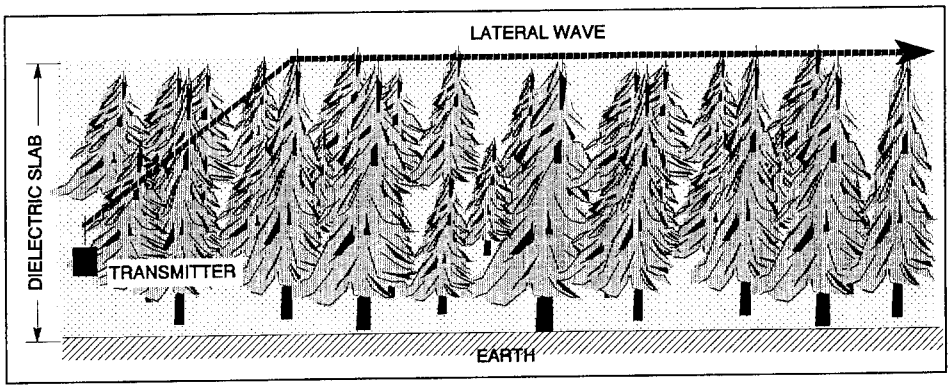


Figure 1. Propagation path along a dielectric slab

field is mostly attenuated by the forest and the underlying ground and, for practical purposes, does not reflect back out of the forest. The receiving antenna may be within the forest, above the forest, or beyond the forest. The model handles these cases when the distance from the forest is not more than two or three forest heights (see para H). Below the critical angle of refraction, the wave is reflected back into the lossy dielectric and is highly attenuated by the foliage and earth beneath.

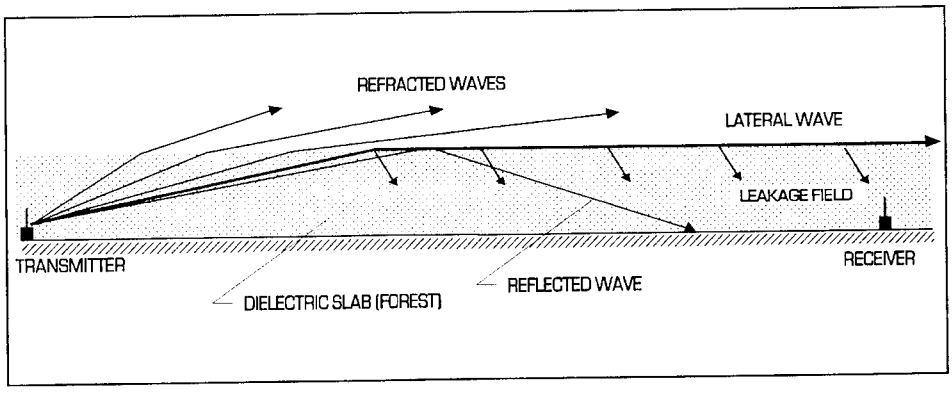


Figure 2. Refraction, reflection, and lateral waves and leakage field due to differences in medium density

C. Establishing Foliage Loss Rate

The relationship between the conductivity of the forest slab and the through-foliage loss for various frequencies is represented by the equation:

$$L_b = -20 \log e^{-2\sqrt{\sigma f}} \quad (1)$$

where

L_b = loss rate in dB/m (in the forest)
e = 2.71828
σ = conductivity in siemens
f = frequency in MHz.

This is the theoretical rate of attenuation of radio waves passing through a thin screen of trees as derived from Tamir's work by F.A. Losee[5] and further evaluated by Kivett and Diederichs[6]. This represents the propagation losses experienced by a direct wave through foliage and has close agreement with empirically collected data. The family of curves for various conductivities representing this loss is shown in Figure 3. The conductivities are directly related to the densities of the forested region. The top curve represents a very dense forest and the bottom curve represents sparse forest conditions. In the EWAF model, the engineer can select the forest density (represented by the conductivity) of the area for which estimates are desired.

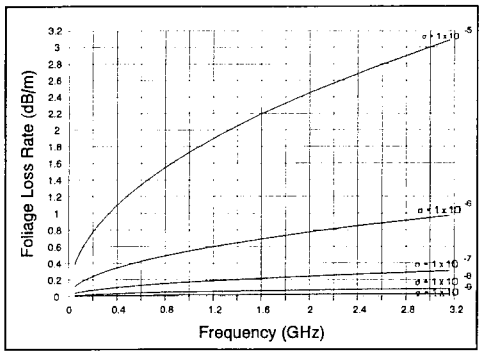


Figure 3. Frequency versus loss rate for several conductivities

Data are not available for all effects at all frequencies. Most effects are known at certain frequencies; for example, recent rain on a certain forest at 437 MHz was known to cause 3-dB increase in path loss over a known path. This can be equated to a specific increase in the conductivity of the forested region. Solving Equation 1 for conductivity yields:

$$\sigma = \frac{.0033136 L_b^2}{f} \quad (2)$$

where

L_b = loss rate in dB/m
σ = conductivity in siemens
f = frequency in MHz.

Equations 1 and 2 can be used to calculate conductivity at a certain frequency from a known path loss under particular foliage conditions and, from this value, determine the path loss at other frequencies for these same conditions. The EWAF model makes extensive use of this technique to evaluate the effect of the density of the undergrowth, leaf moisture content, rain-wet foliage, and other conditions of the forested region which change the conductivity of the dielectric slab. The lateral wave loss rate, typically one-tenth to one-fifteenth of the foliage loss rate, is similarly adjusted.

While Equation 1 fits most of the empirical data, some empirical data may show greater or lesser changes with respect to frequency. Some are not hard data and may have been taken at a limited number of frequencies (as little as two). Such a small sample may not be representative of the true variation of foliage loss rate with change in frequency. Often, an author will have a limited amount of data and will draw a foliage loss curve through the data without considering the normal signal strength variations. Such a curve cannot be satisfactorily extrapolated to other frequencies.

D. The Effect of Wave Polarization

Most of the available empirical data show an increase in foliage loss for vertically polarized electromagnetic waves. The Consultive Committee on International Radio (CCIR) has issued a recommendation[7] which includes the added losses encountered when using vertical polarization. The recommendation covers the propagation losses for "an approximate average for all types of woodland." The CCIR data are plotted in Figure 4.

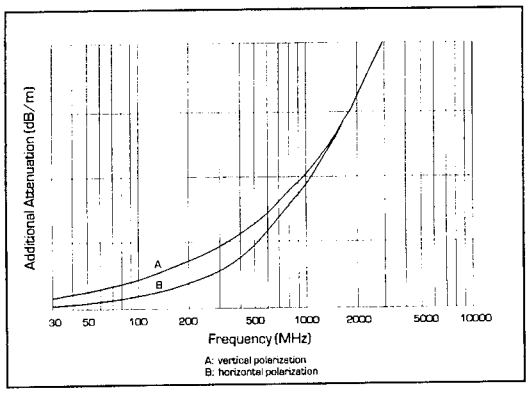


Figure 4. Specific attenuation of woodland (CCIR 1992)

The CCIR recommendation regarding polarization was incorporated into the foliage loss model for frequencies below 1.3 gigahertz (GHz). The EWAF model improves somewhat on the CCIR recommendation by allowing for differences in vegetation through changes in conductivity of the dielectric forest slab.

E. Antenna Beamwidth Effects

The beamwidths of the transmitting and receiving antennas play a significant role in the additional losses experienced due to propagation through foliage. This is particularly true for microwave links or tropospheric scattering links. When microwave or tropospheric scattering links are established within a forest, planners must take into account that the maximum range will be considerably reduced from operation not in a forest. The increased path attenuation calculation in the EWAF model is based upon the antenna response characteristics off-boresight for narrow beamwidth antennas.

F. Foliage Water Content

Most researchers who collect empirical data in the field conclude that the attenuation in a forested region is primarily due to the amount of moisture on or within the vegetation. To quantify this effect, most data collectors accompany the data with comments regarding the lushness of the vegetation and the presence or absence of moisture on the foliage. The preparers of the EWAF model gave special attention to these parameters. Within the model, the conductivity of the dielectric slab is adjusted to reflect comments regarding moisture on the foliage, lushness of the canopy, and lushness of the undergrowth to accurately reflect the effect of the estimated overall water content.

G. Effect of Forest Canopy, Exposed Tree Trunks, and Undergrowth

The density of the forest canopy, the volume of the wooded trunks, and the density of the undergrowth all affect the propagation path losses within a forest. Forests with relatively light canopies will transmit sunlight to the trunks and to the ground. The additional sunlight penetration into the forest tends to increase the foliage on the lower parts of the trees and increase the undergrowth. For example, Germany's Black Forest has a dense canopy, trunks that are not foliated, and no undergrowth. The result is a dark cavern carpeted with pine needles fallen from the high canopy. Other forests, like those in the panhandle of Florida, have such lush undergrowth that it is difficult to simply walk through.

The EWAF model allows the engineer to specify the density of the canopy, the tree trunk exposure, and the height and density of the undergrowth. The treatment of these layers within the dielectric slab, while not rigorous, does allow some consideration of these factors. In the future, the EWAF model will allow a rigorous treatment of these forest layers.

H. Propagation Outside the Forest

The EWAF model is intended primarily to provide an estimate of the electromagnetic propagation path losses through a forested region when both the transmitting and receiving antennas lie within the forest. Occasionally, however, either one or the other of the antennas is above the forest or beyond the forest. Empirical data are available to assist in the estimation of path losses extending out of the forest. In the case of antennas above the tops of the trees, data are available relating the slope angle of the path from the top of the trees to the antenna as related to the lateral wave loss rate. These slope angles are very small in most cases and involve propagation in the lateral wave mode for an appreciable portion of path.

Transmission beyond the edge of the forest, on the other hand, requires a transition from the lateral-wave mode to a free-space mode which resembles wave diffraction over an obstacle. Transmission beyond the edge of the forest is highly dependent upon the diffraction angle from the lateral wave (parallel to the ground) to the receiving antenna near the ground. Figure 5 shows the transition from the lateral-wave mode to the free-space mode at a diffraction angle.

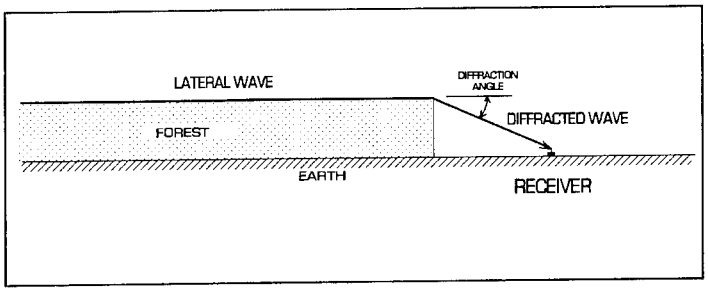


Figure 5. Lateral-wave transition to free-space propagation

I. Model Input Variables

The model accepts a wide variety of input parameters which describe the physical conditions under analysis. These parameters allow the model to ascribe physical constraints to the simulation and provide estimates of propagation loss through foliage commensurate with the scenario. These parameters are:

- Carrier Frequency
- Forest Density
- Link Length
- Type of Foliage (conifer/deciduous)
- Height of Transmitting Antenna
- Height of Receiving Antenna
- Height of Exposed Trunks
- Receiver Distance to Forest (or in forest)
- Transmitter Distance to Forest (or in forest)
- Presence of Moisture on Foliage
- Density of Undergrowth
- Polarization of Electromagnetic Wave
- Lushness of Forest
- Height of Undergrowth

The term "forest density" is used in the EWAF model as the input to establish propagation parameters. This parameter is stated in terms of visual observation of the forest as light, medium, dense, very dense, jungle, and heavy jungle. These values are then equated to the conductivity of the forest.

J. Concluding Remarks

The EWAF model provides the design engineer or communicator with a tool which can be used to estimate probable propagation path losses through vegetation. The model is not mathematically rigorous but instead is based upon empirical data which produce results surprisingly similar to losses which are experienced in the field. It requires input parameters which are available or can be obtained without field measurement. Constants and factors are contained in tables easily changeable for fine tuning the model as more empirical data are analyzed. The prediction of electromagnetic wave propagation path losses through layers of the forest could be improved with additional analyses.

K. Acknowledgements

The authors wish to thank Dr. Joseph Whalen at Computer Sciences Corporation for his support and many informative discussions on electromagnetic propagation; Dr. Stephen Fast of the University of Texas for his help, support, and interest in the project; Mr. Daniel Searls of the Electronic Proving Ground for his help, encouragement, and support; and Mr. Jerry Burchard and Ms. Lora Langworthy for their diligent efforts in preparation of the manuscript.

L. References

1. D.J. Pounds and A.H. LaGrone, "Considering Forest Vegetation as an Imperfect Dielectric Slab," Electric Engineering Research Laboratory, University of Texas, Austin, Report 6-53, May 1963.

2. Theodor Tamir, "On Radio-Wave Propagation in Forest Environments," IEEE Transactions on Antennas and Propagation, Vol. AP-15, No. 6, November 1967.

3. Theodor Tamir, "Radio Wave Propagation Along Mixed Paths in Forest Environments," IEEE Transactions on Antennas and Propagation, Vol. AP-25, No. 4, July 1977.

4. R.K. Tewari, S. Swarup, and M.N. Roy, "Radio Wave Propagation Through Rain Forests of India," IEEE Transactions on Antennas and Propagation, Vol. 38, No. 4, April 1990.

5. F.A. Losee, "The Influence of Trees on PLRS Communication Capability," Hughes Aircraft Company, July 1978.

6. J.A. Kivett and P.J. Diederichs, "PLRS Ground-to-Ground Propagation Test Technical Report (Draft)," Hughes Aircraft Company, January 1980.

7. Consultive Committee on International Radio, Recommendation 833, "Attenuation in Vegetation" (Question 9/5), International Telecommunications Union, Geneva, Switzerland, 1992.

VALIDATION OF THE RADIO PHYSICAL OPTICS PROPAGATION MODEL

Richard A. Paulus
Ocean & Atmospheric Sciences Division
NCCOSC RDTE DIV 543
53170 WOODWARD ROAD
SAN DIEGO CA 92152-7385

Abstract. The Radio Physical Optics (RPO) model is a hybrid electromagnetic propagation model composed of ray-optics and parabolic equation techniques to account for propagation effects over the ocean. The ray-optics sub-models provide computer efficient solutions in their regions of applicability; the parabolic equation sub-model provides the solution in the lower elevation angle regions and accommodates range-dependent refractive conditions. The model has been fully documented and a U.S. patent has been allowed on the hybrid techniques. RPO is considered applicable to the nominal frequency range of 100 MHz to 20 GHz and has been shown to be more computationally efficient, in both speed and memory usage, than conventional split-step parabolic equation models.

The scientific validation of RPO has consisted of 3 types of comparisons: (1) model to data, (2) model to model, and (3) internal consistency. Model to data comparisons have been made for normal and anomalous propagation conditions, including homogeneous and range-varying surface-based, elevated, and evaporation ducts. Model to model comparisons consist of comparing RPO outputs with the outputs of other high-fidelity models for the same input data. For this purpose, diverse propagation modeling techniques like waveguide and split-step parabolic equation methods were used as standards of comparison. Model consistency comparisons examined the ability of the numerical implementation of RPO to reproduce reciprocity for range-varying refractive conditions in accordance with the Lorentz Reciprocity Theorem. This paper shows example results for the three types of validation conducted on RPO.

I. BACKGROUND

The Radio Physical Optics (RPO) electromagnetic propagation model is a hybrid model composed of ray-optics and parabolic equation (PE) techniques developed by H. V. Hitney [1] to account for propagation effects over the ocean. The impetus for this development was the requirement in the Navy for a propagation assessment model that would extend the existing capability that assumes horizontal homogeneity of the refractive structure to accommodate range-varying refractive structure. Split-step PE models had become widely accepted for this purpose in the lower atmosphere but had the disadvantage of requiring increasing computational resources with increasing frequency, higher elevation angles, and higher altitudes to the point of being impractical for a full range of operational applications. Ray-optics techniques are very computer efficient for assessing propagation within the radio horizon but become intractable beyond that range. The concept of combining these two techniques into a computer efficient model is simple, but the implementation of such a model was a significant achievement and U.S. Patent No. 5,301,127 was awarded for the hybrid techniques.

The successful development of an entirely new model then raises the question of how good the model is. It must be as accurate as the existing models and it must correlate with radio/radar observations in order to be accepted. The scientific validation RPO has consisted of 3 types of

comparisons: model to data, model to model, and internal consistency. Validation of RPO is the combined work of a number of people resulting in several work-years of effort.

It is also necessary to distinguish what is meant by validation. By scientific validation, I mean the measurement of the physical and numerical credibility of the model. In terms familiar to the software engineer, independent verification and validation (IV&V) deals more with the numerical credibility of the model and how well that model addresses the requirements that drove its development. A final term I also define is tactical validation which is a measure of the physical credibility of an assessment system. An assessment system is not only the propagation model and the models that characterize the refractive environment, but also the system performance models that characterize detection, intercept, or communications criteria. Tactical validation may depend upon the application. For example, assessments of radar coverage for aircraft penetration of air defenses require only depicting the relative detection capability; whereas an assessment of detection ranges for a ship's search radar against cruise missiles must depict absolute detection range with high fidelity.

II. MODEL TO DATA COMPARISONS

One can not absolutely validate a propagation model by comparison to radio data because the propagation model is dependent upon an accurate characterization of the meteorological conditions and its output is compared to radio data that are measured by systems that have limits in their accuracies. The latter can be quite tightly controlled, but obtaining the meteorological data on a sufficient temporal and spatial scale to fully characterize the propagation environment is not likely [2]. Thus, there will always be differences between the model predictions and the measured data and the tradeoff is accuracy versus cost [3].

A convenient measure of effectiveness is whether or not the model provides improvement over either free space or standard atmosphere propagation. Comparisons of RPO predictions have been made to data for normal and anomalous propagation conditions and documented in technical reports and refereed journal articles [4-9].

An example of model to data comparisons for a range-varying elevated trapping layer utilizes radio and meteorological data collected by an aircraft flying a sawtooth pattern between San Diego, CA and Guadalupe Island [5]. Figure 1 shows the refractivity profiles on one day that is characterized by a surface-based duct in the vicinity of the transmitter that lifts downrange to become an elevated duct. Figure 2 shows coverage for a 520 MHz transmitter located at 30.5 m overlooking the ocean under the measured refractive conditions. At ranges greater than 100 km, energy that was trapped in the duct near the transmitter tends to follow the rise of the duct with increasing range. The RPO output at a range of 148 km for these refractive conditions is compared to the measured data in Figure 3. The comparison between predicted signal, in terms of propagation factor, and observed signal is considered good, particularly when compared

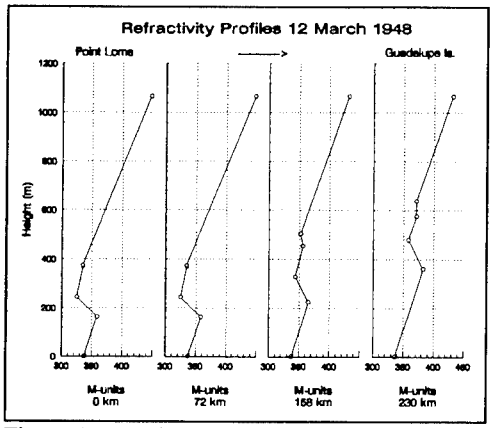


Figure 1. Modified refractivity profiles vs range from Point Loma in San Diego.

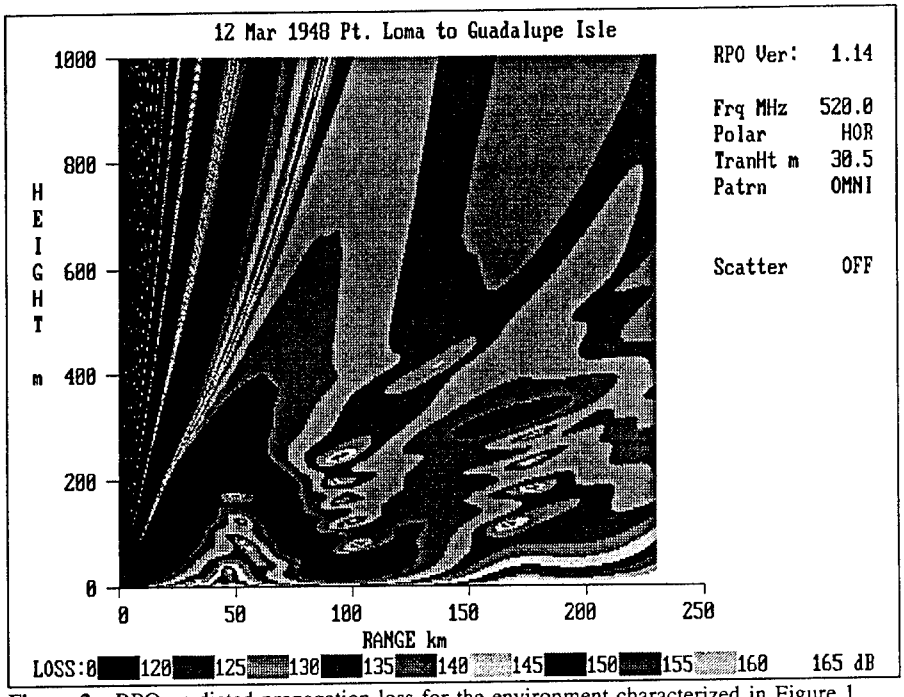


Figure 2. RPO predicted propagation loss for the environment characterized in Figure 1.

to the standard atmosphere case. The effects of ducting are readily apparent in comparison to the predicted propagation factor for a standard atmosphere. (Barrios [5] obtained qualitatively better comparisons for these data by using the predicted propagation factor along the aircraft slant path; for simplicity, this was not done here.)

A second example [9] comes from an evaporation duct experiment in a littoral area in the Aegean in which radio propagation measurements were made in the 1 to 40 GHz frequency range. Figure 4 shows data at 9624 MHz (dots) compared to range dependent RPO predictions (solid line) for low-sited antennas (transmitter at 4.5 m and receiver at 4.9 m). Surface meteorological measurements on the two islands of Naxos and Mykonos, 35.2 km apart, were used to characterize the evaporation

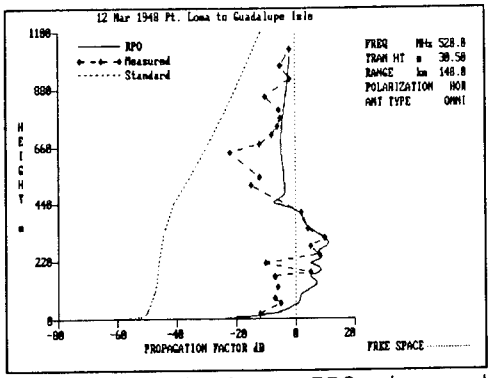


Figure 3. Comparison between RPO and measured radio data at a nominal range of 148 km.

duct structure (any influences from elevated refractive structures are thus not accounted for). Signals varied nearly 77 dB, from above free space to less than standard diffraction, over this 15 day period. Even though quite crude meteorological data were used to depict range-varying refractive structure, RPO is considered to follow the trends quite well and, with regards to absolute accuracy, is within 10 dB of the observed signal nearly 70% of the time. In particular, propagation loss predictions for 19 through 22 November are improved using range-dependent refractive structure to drive RPO [9].

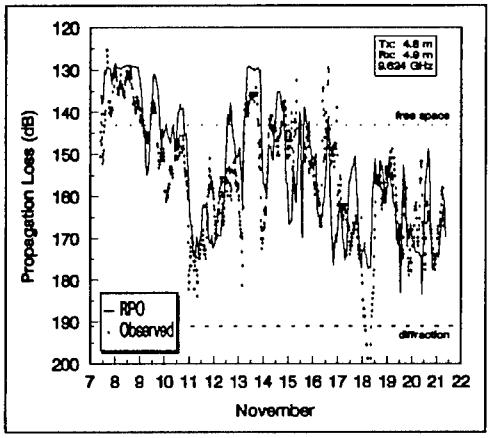


Figure 4. Comparison of observed and RPO predicted propagation loss vs time.

A third example comes from [7] and shows a comparison of RPO's troposcatter model to data. The troposcatter model is a semiempirical scatter model that adds a random refractive-index fluctuation to the mean refractive-index value at each height for which the parabolic equation submodel computes propagation loss. Without a troposcatter model, RPO would calculate diffraction losses that could far exceed what is observed. Although insignificant for radar applications, excessive losses could result in erroneous assessments of communications or electronic warfare intercept capabilities. Figure 5 shows propagation loss versus range for a 220 MHz transmitter at 23.5 m above sea level as derived from measurements by an aircraft flying at an altitude of 152 m between Scituate, MA and Sable Island. RPO without scatter overestimates propagation losses by up to 50 dB at ranges beyond about 150 km. RPO with scatter predicts propagation losses consistent with the measured data. Also shown in Figure 5 is the propagation loss predicted by EREPS (Engineer's Refractive Effects Prediction System), which will be amplified in the next section.

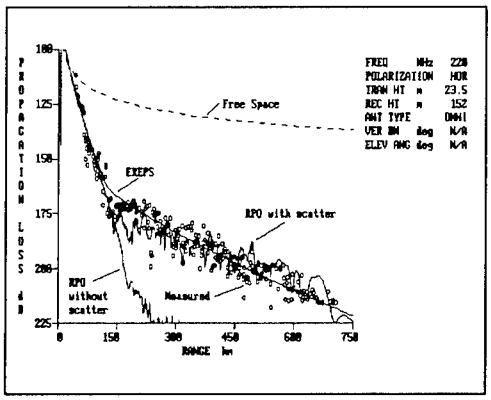


Figure 5. Comparison of observed and predicted (RPO with scatter, RPO without scatter, and EREPS) propagation loss vs range.

Additional comparisons to data, including the effects of elevated trapping layers and evaporation ducts short ranges, are shown in references [4-9].

III. MODEL TO MODEL COMPARISONS

Discrepancies between data and propagation model predictions can occur for several reasons including inadequacies in the propagation model, the meteorological characterizations, and radio-meteorological measurement errors. Thus RPO was also compared to other high-fidelity

propagation models, including waveguide and PE models [1]. Figure 6 is an example of propagation factor vs. height at a range of 185 km for a 3000 MHz transmitter at 30.5 m and a homogeneous 465 m surface-based duct. The RPO output is indistinguishable from waveguide and PE model results. The boundaries between the RPO submodels are shown by the horizontal dashed lines: PE (parabolic equation), XO (extended optics), and RO (ray optics). The geometry is such that the FE (flat earth) model region is higher than the ordinate scale. For reference, the standard atmosphere case is indicated by the dash-dot curve.

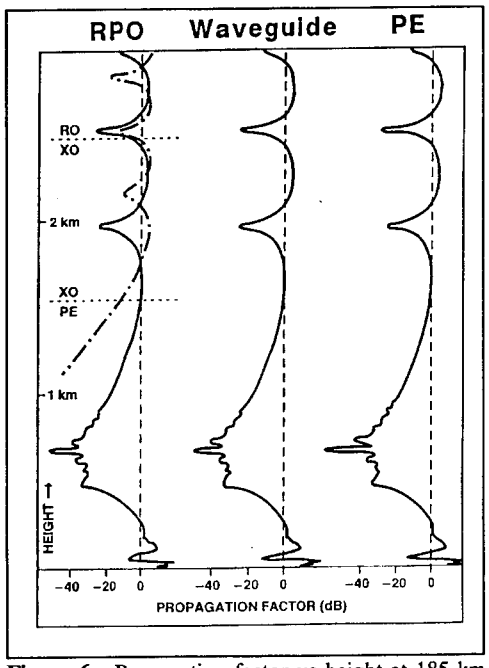


Figure 6. Propagation factor vs height at 185 km downrange as predicted by RPO, a waveguide model, and a PE model for a homogeneous surface-based duct.

The RPO troposcatter model [7] was compared to the empirical troposcatter model currently used in EREPS. EREPS is a PC-based set of software programs based on the propagation models that are currently in operational use in the U.S. Navy [10]. Figure 5 shows that RPO agrees with the EREPS model; numerous other comparisons resulted in differences between the two models of no more than a few decibels. Differences between the two models may occur for some frequencies in the more poleward regions of the world's oceans. The empirical EREPS troposcatter model is a function of N_s, surface refractivity, which decreases poleward. RPO uses an effective median structure parameter (C_n^2) profile to generate small refractive index fluctuations that are added to the refractive index value at each vertical point in the PE submodel. The effective median structure parameter profile is applied worldwide. A more meteorologically rigorous method would use observed C_n^2 profiles or profiles that vary with air mass. However, neither method is feasible in an operational model because of lack of data.

IV. MODEL CONSISTENCY

The numerical implementation of RPO was tested for physical consistency in parametric studies that showed RPO demonstrated reciprocity in range-dependent evaporation ducting and surface/elevated ducting environments [11-12]. Reciprocity requires signal levels at the terminals to be equal for both directions of propagation no matter what the intervening media. Possible reciprocity-breaking mechanisms in RPO include the differing split-step PE range step for opposing directions of propagation and sub-model boundary crossings.

Figure 7 shows coverage along a radial reciprocal to Figure 2 to a range of 230 km for a 520 MHz transmitter at 50 m above mean sea level. The coverage patterns between the two figures are considerably different downrange. Figure 8 shows propagation loss vs range (extracted from Figure

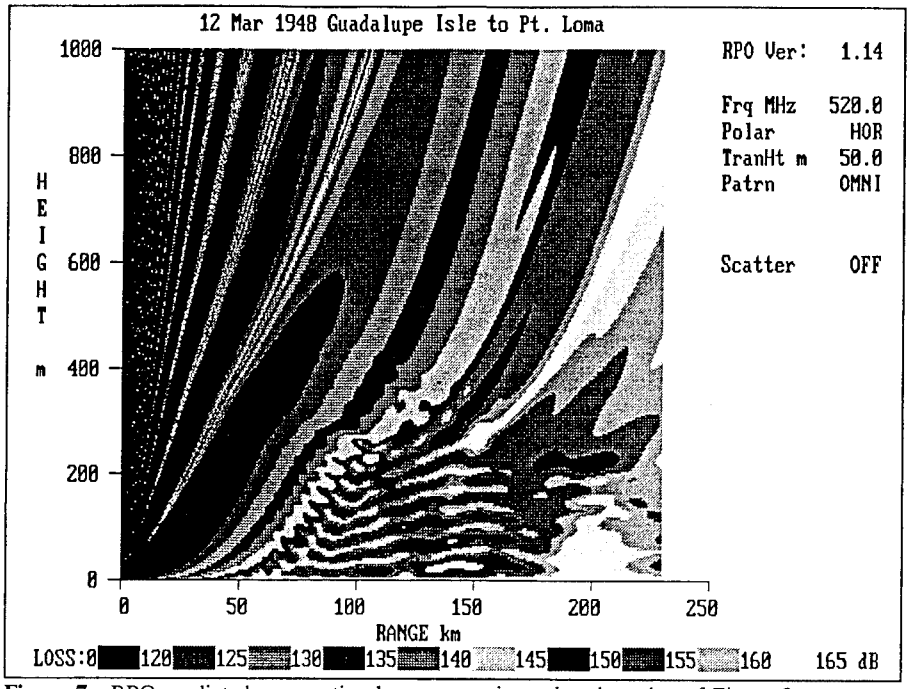


Figure 7. RPO predicted propagation loss on a reciprocal path to that of Figure 2.

2) at an altitude of 50 m for a 30.5 m transmitter at Point Loma radiating towards Guadalupe Isle. Also shown is propagation loss vs range (extracted from Figure 7) at an altitude of 30.5 m for a 50 m transmitter on a reciprocal path. Propagation loss varied by up to 40 dB. Reciprocity is demonstrated by the nearly equal propagation loss values at the 230 km terminal ranges.

V. CONCLUSIONS

RPO has been scientifically validated by comparison to experimental data and other high-fidelity models. In addition, the numerical implementation has been tested for internal consistency. RPO has been shown to be far faster than pure PE techniques for typical radar coverage assessments required by the U.S.

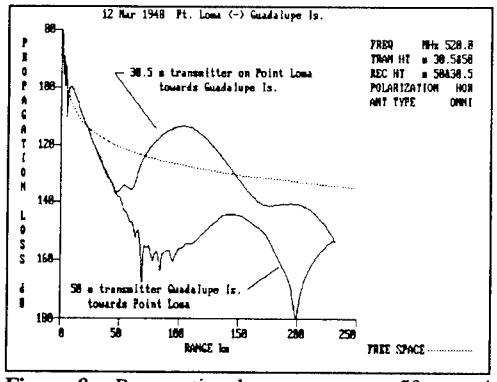


Figure 8. Propagation loss vs range at 50 m and 30.5 m altitude for a 30.5 m transmitter and a 50 m transmitter respectively.

Navy (*e.g.*, 3000 MHz, 50,000 feet in altitude, and 300 nmi in range).

ACKNOWLEDGEMENT

The validation of RPO was the work of several people as cited in the text. Their efforts were funded by the Office of Naval Research, ONR 322. Appreciation is also due to the Meteorological and Oceanographic Systems Project Office (PMW-175) of the Space and Naval Warfare Systems Command who have funded the transition of RPO to operational use by the U.S. Navy.

REFERENCES

[1] H.V. Hitney, "Hybrid ray optics and parabolic equation methods for radar propagation modeling," in *Radar 92*, IEE Conference Publication No. 365, pp. 58-61, Brighton, UK, 12-13 Oct. 92.

[2] J.H. Richter, "Structure, variability, and sensing of the coastal environment," AGARD CP-567, pp. 1-1 to 1-13, 1995.

[3] L.T. Rogers, "Effects of spatial and temporal variability of atmospheric refractivity on the accuracy of propagation assessments," AGARD CP-567, pp. 31-1 to 31-7, 1995.

[4] A.E. Barrios, "Radio wave propagation in horizontally inhomogeneous environments by using the parabolic equation model," Naval Ocean Systems Center Technical Report 1430, May 1991.

[5] A.E. Barrios, "Parabolic equation modeling in horizontally inhomogeneous environments," *IEEE Trans. Antennas Propagat.*, vol. 40, no. 7, pp. 791-797, Jul. 1992.

[6] H.V. Hitney, "Whispering gallery effects in the troposphere," *Radio Sci.*, vol. 27, no. 6, pp. 893-898, Nov. 1993.

[7] H.V. Hitney, "A practical tropospheric scatter model using the parabolic equation," *IEEE Trans. Antennas Propagat.*, vol. 41, no. 7, pp. 905-909, Jul. 1993.

[8] K.D. Anderson, "Radar detection of low-altitude targets in a maritime environment," NRaD TR 1630, Nov. 93.

[9] R.A. Paulus, "Propagation in the evaporation duct: model predictions and comparisons to data," NRaD TR 1644, Mar. 1994.

[10] W.L. Patterson, C.P. Hattan, G.E. Lindem, R.A. Paulus, H.V. Hitney, K.D. Anderson, and A.E. Barrios, "Engineer's Refractive Effects Prediction System (EREPS), Version 3," NRaD TR 2648, May 1994.

[11] R.A. Paulus, "The Lorentz reciprocity theorem as a consistency test for propagation models," AGARD CP-543, pp. 17-1 to 17-7, 1993.

[12] R.A. Paulus, "The Lorentz reciprocity theorem and range-dependent propagation modeling," *IEEE Trans. Antennas Propagat.*, vol. 42, no. 3, pp. 270-272, Feb. 1994.

VTRPE: A VARIABLE TERRAIN ELECTROMAGNETIC PARABOLIC EQUATION MODEL

FRANK J. RYAN

Naval Command Control and Ocean Surveillance Center
RDT&E Division, CODE 712
San Diego, CA. 92152-5000
e-mail: ryan@nosc.mil

§1.0 INTRODUCTION

In practice, the actual performance of a communication or radar system operating in the VHF–EHF band (30MHz–100GHz) and having propagation paths beyond-the-line-of-sight is often quite different from the characteristics predicted based upon free-space propagation physics. The free-space detection ranges are often several orders of magnitude different from those observed in the atmosphere. Some of the reasons for this discrepancy are: 1)The earth's surface is irregular and a finite conductor; scattering and reflecting incident energy in various directions. This leads to depolarization of the scattered field and creates complicated spatial interference patterns due to multi-pathing. 2)The curved earth casts a shadow, creating a "hole" for low altitude transhorizon propagation and irregular surface terrain gives rise to diffraction phenomena. 3) Spatial and temporal inhomogeneities in the atmospheric index of refraction cause significant ducting and refraction of radio wave energy. 4) Rough surface attenuation and volume absorption mechanisms attenuate the wave fields. These "anomalous" propagation effects are usually associated with all practical or real-world electromagnetic problems. To adequately address anomalous propagation, a model must incorporate full-wave propagation physics and range-dependent environmental inputs.

Various methods have been adopted to deal with anomalous propagation and they may loosely be grouped into three categories: empirical, analytical and numerical. Empirical techniques rely on direct measurements which limits their region of extrapolation. Analytical methods for solving the wave equation, such as separation of variables or the geometrical theory of diffraction, while often exact, suffer from being restricted to certain geometries or boundary conditions. Numerical methods, which attempt solution of the exact Maxwell field equations or equations derived from them, are particularly useful for solving complicated three-dimensional problems using a computer. The down side of numerical methods is the often unacceptable computational burden associated with them, particularly for full elliptic wave solvers. However, for tropospheric propagation, it is often correct that the electromagnetic energy flux is dominated by forward angle multiple scattering physics in which case the elliptic wave equations for the electromagnetic fields may be approximated by simpler parabolic wave equations.

In 1946 Leontovich and Fock[1] applied the parabolic wave equation (PE) to the problem of transhorizon radio wave propagation above a spherical earth, thereby making a breakthrough in electromagnetic wave propagation modeling. Approximately 30 years passed before a practical algorithm for solving the Leontovich–Fock parabolic wave equation was developed. In 1973, Hardin and Tappert[2] developed the split-step Fourier PE (SSFPE) algorithm. The SSFPE algorithm exploited advances in computer hardware and the development of the fast Fourier transform (FFT) algorithm to yield an efficient numerical solution to the Leontovich–Fock parabolic wave equation.[3] In the 80's, the SSFPE method was applied to tropospheric radar propagation by several researchers.[4–7] These treatments modeled the earth's surface as smooth.

For propagation over irregular surfaces, an integral equation method had been developed by Hufford[8] and later extended by Ott.[9] In 1991 the SSFPE algorithm was extended to include irregular, inhomogeneous terrain by Ryan[10] and forms the basis of the VTRPE (*V*ariable *T*errain *R*adio *P*arabolic *E*quation) model. The remainder of the paper reviews the electromagnetic SSFPE algorithm and covers the propagation physics in the VTRPE model.

§2.0 Parabolic Wave Equation

A quick review will now be given of the variable terrain electromagnetic parabolic wave equation derivation. Further details are available in Ryan.[10] For monochromatic radiation (implicit time-dependence $\exp(-i\omega t)$, with ω the radian frequency) the electric $\mathbf{E}$ and magnetic $\mathbf{H}$ radiation fields are solutions to second order vector equations obtained from Maxwell's equations. In rationalized mks units, the magnetic field vector $\mathbf{H}$ solves

$$\nabla^2\mathbf{H}(\mathbf{r}) + \frac{\nabla\varepsilon(\mathbf{r})}{\varepsilon(\mathbf{r})} \times \nabla \times \mathbf{H}(\mathbf{r}) + k_0^2\varepsilon(\mathbf{r})\mathbf{H}(\mathbf{r}) = 0\,, \tag{1}$$

with $k_0 = \omega/c$ the vacuum wave number, while the electric field vector $\mathbf{E}(\mathbf{r})$ is a solution of:

$$\nabla^2\mathbf{E}(\mathbf{r}) + \nabla\left(\mathbf{E}(\mathbf{r}) \cdot \frac{\nabla\varepsilon(\mathbf{r})}{\varepsilon(\mathbf{r})}\right) + k_0^2\varepsilon(\mathbf{r})\mathbf{E}(\mathbf{r}) = 0\,. \tag{2}$$

The propagation medium electrical properties are specified via the complex relative dielectric constant $\varepsilon(\mathbf{r})$. For nonionized media, the dielectric constant is $\varepsilon(\mathbf{r}) = \varepsilon'(\mathbf{r}) + i\sigma(\mathbf{r})/(\omega\epsilon_0)$, where ϵ_0 is the vacuum dielectric constant, σ is the medium conductivity, and ε' is the usual permittivity of the medium. Choose a spherical, earth-centered coordinate system $\mathbf{r} = (r, \theta, \phi)$, with respective unit vectors $(\hat{e}_r, \hat{e}_\theta, \hat{e}_\phi)$, and let $\phi = 0$ be the meridian plane containing the source and observation point.

Now Eqs. (1–2) are vector equations, the components of which are coupled together due to the presence of the $\nabla\varepsilon(\mathbf{r})$ term. However, these vector equations can be replaced by simpler scalar equations for the azimuthal fields if two conditions are met. First, the transmitter emits radiation that is linearly polarized— i.e., the electric field vector has nonzero components lying either wholly within (vertical polarization) or perpendicular to (horizontal polarization) the meridian plane containing the source and observation point. Second, the transverse gradients in ε are small: $\hat{e}_\phi \cdot \nabla\varepsilon(\mathbf{r}) \approx 0$. Fortunately, this is the case for tropospheric propagation involving many types of communication and radar systems. If these two approximations are made, then the vector wave equations for the full $\mathbf{E}$ or $\mathbf{H}$ fields can be replaced by simpler *scalar* equations for the non-zero azimuthal ϕ-component. The other field components can then be determined by straight forward application of the Maxwell curl relations. For vertical polarization, the azimuthal magnetic field component $\mathbf{H}(\mathbf{r}) = H_\phi(\mathbf{r})\hat{e}_\phi$ will then satisfy

$$\frac{\varepsilon}{r}\frac{\partial}{\partial r}\frac{1}{\varepsilon}\frac{\partial(rH_\phi)}{\partial r} + \frac{\varepsilon}{r^2\sin\theta}\frac{\partial}{\partial\theta}\frac{\sin\theta}{\varepsilon}\frac{\partial H_\phi}{\partial\theta} + \left[k_0^2\varepsilon - \frac{1}{r^2\sin^2\theta} - \frac{\cot\theta}{r^2\varepsilon}\frac{\partial\varepsilon}{\partial\theta}\right]H_\phi = 0, \tag{3}$$

while for horizontal polarization, the azimuthal electric field component $\mathbf{E}(\mathbf{r}) = E_\phi(\mathbf{r})\hat{e}_\phi$ satisfies

$$\frac{1}{r}\frac{\partial^2(rE_\phi)}{\partial r^2} + \frac{1}{r^2\sin\theta}\frac{\partial}{\partial\theta}\sin\theta\frac{\partial E_\phi}{\partial\theta} + \left[k_0^2\varepsilon - \frac{1}{r^2\sin^2\theta}\right]E_\phi = 0. \tag{4}$$

For numerical calculations, it is beneficial to transform Eqs. (3-4) to a cartesian coordinate system $\mathbf{x} = (x, z)$ by means of the earth flattening transformation: $x = a\theta, \quad z = a\ln(1 + h/a)$, where a is the effective earth radius, and $h = r - a$ is the local altitude. Applying this earth flattening transformation to Eqs. (3-4) yields a cartesian Helmholtz equation suitable for numerical work

$$\left[\frac{\partial^2}{\partial x^2} + \frac{\partial^2}{\partial z^2} + k^2(x, z)\right]w(x, z) = 0. \tag{5}$$

The new dependent variable w is defined as (subscripts $\{h, v\}$ denote horizontal and vertical polarization respectively)

$$\begin{aligned} w_h &\equiv \sqrt{r\sin\theta}\,E_\phi(\mathbf{r}) = \sqrt{a\sin(x/a)}e^{+z/(2a)}E_\phi(\mathbf{x}), \\ w_v &\equiv \frac{\sqrt{r\sin\theta}}{n}H_\phi(\mathbf{r}) = \frac{\sqrt{a\sin(x/a)}}{m(x,z)}e^{+3z/(2a)}H_\phi(\mathbf{x}), \end{aligned} \tag{6}$$

and m is the modified index of refraction $m(x,z) \equiv n(\mathbf{r})(1+h/a)$. An "effective" wave number $k(x,z)$ is also defined by

$$k_h^2 = k_0^2 m^2 - \frac{3\sec^2(x/a)}{4a^2} \quad \text{and} \quad k_v^2 = k_h^2 - \frac{\cot(x/a)}{an}\frac{\partial n}{\partial x} - n\left(\frac{\partial^2 n^{-1}}{\partial x^2} - \frac{\partial^2 n^{-1}}{\partial z^2} - \frac{\partial n^{-1}}{a\partial z}\right).$$

To solve Eq. (5) requires an initial condition plus boundary conditions to be met. The initial condition is taken to be a unit strength point dipole. The boundary conditions are: 1) a Sommerfeld radiation-type boundary condition at infinity $\lim_{r\to\infty} r\left(\frac{A}{r} - ik_0 A\right)$, where A denotes H_ϕ or E_ϕ; and 2) continuity of the tangential electric and magnetic fields at the earth's surface $r = a$. Continuity of tangential field components is achieved by modeling the earth as a locally homogeneous dielectric with finite conductivity and specifying a surface boundary condition:[11]

$$\left.\frac{\partial w_h(x,z)}{\partial z}\right|_{z=0} = -\left(\frac{1}{2a} + ik_0\sqrt{\varepsilon_s - 1}\right) w_h(x,0),$$
$$\left.\frac{\partial w_v(x,z)}{\partial z}\right|_{z=0} = -\left(-\frac{1}{2a} + \frac{1}{m(x,0)}\left.\frac{\partial m(x,z)}{\partial z}\right|_{z=0} + ik_0\frac{\sqrt{\varepsilon_s - 1}}{\varepsilon_s}\right) w_v(x,0), \tag{7}$$

with ε_s the complex dielectric constant of the earth's surface.

In practical system applications, the actual electric or magnetic fields are not directly used. Instead, to systematically incorporate propagation effects and antenna characteristics in system performance calculations, the generalized radar transmission equation is often employed.[12] The radar transmission equation relates the received power P_r (for a receiver with antenna gain G_r) to the transmitted power P_t (with transmitter antenna gain G_t) by $P_r(\mathbf{r}) = P_t G_r G_t \left[\frac{F}{2k_0 R}\right]^2$, where R is the transmitter-to-receiver distance, and F is the pattern propagation factor. By convention, F is normalized to the field of a unit-strength point dipole source: $F_h(\mathbf{r}) \equiv \left|\frac{E_\phi(\mathbf{r})}{E_{md}(\mathbf{r})}\right|$, and $F_v(\mathbf{r}) \equiv \left|\frac{H_\phi(\mathbf{r})}{H_{ed}(\mathbf{r})}\right|$, where E_{md} is the electric field from a vertical magnetic dipole, and H_{ed} is the magnetic field of a vertical electric dipole. Employing the dipole fields, the propagation factor for horizontal polarization F_h is computed as[13]

$$F_h(\mathbf{r}) = \frac{4\pi}{k_0\omega\mu_0}\frac{|w_h(\mathbf{r})|R^2}{(r\sin\theta)^{3/2}}\left[1 + (k_0 R)^{-2}\right]^{-\frac{1}{2}} \approx \frac{4\pi\sqrt{x}}{k_0\omega\mu_0}|w_h(\mathbf{x})|\left(1 + (z-z_0)^2/x^2\right).$$

Similarly, the propagation factor for vertical polarization F_v is

$$F_v(\mathbf{r}) = \frac{4\pi}{k_0\omega}\frac{|n(\mathbf{r})w_v(\mathbf{r})|R^2}{(r\sin\theta)^{3/2}}\left[1 + (k_0 R)^{-2}\right]^{-\frac{1}{2}} \approx \frac{4\pi\sqrt{x}}{k_0\omega}|m(\mathbf{x})w_v(\mathbf{x})|\left(1 + (z-z_0)^2/x^2\right).$$

If we define the general PE (GPE) operator $Q(\mathbf{x})$ by $Q(\mathbf{x}) = \sqrt{\frac{\partial^2}{\partial z^2} + k^2(\mathbf{x})}$, then Eq. (5) can be expressed in the equivalent factored form

$$\left(\frac{\partial}{\partial x} + iQ\right)\left(\frac{\partial}{\partial x} - iQ\right)w(\mathbf{x}) + i\left[\frac{\partial}{\partial x}, Q\right]w(\mathbf{x}) = 0.$$

(The notation $[F,G] \equiv FG - GF$ is called the commutator of the operators F and G)

Now for range-independent propagation the commutator $\left[\frac{\partial}{\partial x}, Q\right] = 0$, and the equation satisfied by the outwardly propagating waves is just

$$\frac{\partial w(\mathbf{x})}{\partial x} = iQ(\mathbf{x})w(\mathbf{x}). \tag{8}$$

Solving Eq. (8) is equivalent to solving range-independent Helmholtz equation Eq. (5), and is the most general PE that is exact for range independent media. Following Tappert,[3] a parabolic wave equation with Q defined above will be denoted as the general PE (GPE) and the Q operator will be denoted as the GPE propagator. GPE is the most complete PE that is evolutionary in range and neglects back scattering. For range-independent environments, it is exact within the limits of the far-field approximation, and is the starting point for all numerical PE algorithms. In following sections, the computational techniques used to solve the PE will be derived.

§3.0 Split-Step PE

The outgoing wave solution of Eq. (8) is now obtained using the split-step PE algorithm. First, for numerical stability, a rapidly varying phasor component is first removed from w via the envelope transformation $w(\mathbf{x}) = e^{ixk_{ref}}\psi(\mathbf{x})$, with k_{ref} the reference wave number. The complex PE envelope function ψ then solves

$$\frac{\partial\psi(\mathbf{x})}{\partial x} = iQ(\mathbf{x})\psi(\mathbf{x}), \tag{9}$$

where the pseudo-differential operator Q is now $Q(\mathbf{x}) = \sqrt{\partial^2/\partial z^2 + k^2(\mathbf{x})} - k_{ref}$. Next, the wide-angle PE (WAPE) approximation to Q is made by decomposing it into the sum of simpler local operators $Q(\mathbf{x}) \approx A(z) + B(\mathbf{x})$, where $A(z) = \sqrt{k_{ref}^2 + \partial^2/\partial z^2} - k_{ref}$ and $B(\mathbf{x}) = k(x_0 + \Delta x/2, z) - k_{ref}$. Given an initial condition $\psi(x_0, z)$, a formal solution to Eq. (9) can now be written in exponential operator form as

$$\psi(x_0 + \Delta x, z) \approx e^{+i\Delta x[A(z) + B(\mathbf{x})]}\,\psi(x_0, z), \tag{10}$$

Finally, the Trotter product formula is used to symmetrically factor the exponential operator in Eq. (10) into the product of simpler operators: a "kinetic energy" propagator $K(\Delta x) = e^{+i\Delta x A(z)}$, and a "potential energy" phase correction $U(\Delta x) = e^{+i\Delta x B(\mathbf{x})}$, yielding the split-step PE (SSPE) algorithm:

$$\psi(x + \Delta x, z) = K(\tfrac{\Delta x}{2})\,U(\Delta x)\,K(\tfrac{\Delta x}{2})\,\psi(x, z) + O(\Delta x^3). \tag{11}$$

The error term in Eq. (11) arises from the non commutation of A and B as well as from any x-dependence of the refraction operator B. Once a starting field is specified, the above expression is suitable for generating a numerical solution by repeated application of Eq. (11). This numerical solution is unconditionally stable due to the unitary nature of the operators K and U.

Now the operation $e^{+i\Delta x[A(z) + k_{ref}]}\,\psi(x_0, z) = e^{+i\Delta x\sqrt{k_{ref}^2 + \frac{\partial^2}{\partial z^2}}}\,w(x_0, z)$ is equivalent to solving the free-space Helmholtz equation $\left[\dfrac{\partial^2}{\partial x^2} + \dfrac{\partial^2}{\partial z^2} + k_{ref}^2\right] w(x, z) = 0$, with $w(x_0, z)$ as an initial condition. Thus the SSPE algorithm amounts to: a half-step of free-space propagation with the kinetic energy operator, $K(\Delta x/2)$; a phase correction operation, $U(\Delta x)$, to account for potential refractive effects not included in K; and finally another half-step of free-space propagation, $K(\Delta x/2)$.

The potential energy phase correction operator U is simply a multiplicative operation on the PE wave function and is easily implemented numerically. The kinetic energy propagator K, however, is more complex, due to the pseudo-differential nature of A. To implement the SSPE algorithm requires working in a basis which diagonalizes A. One such basis is the vertical wave number Fourier basis, in which A is just a c-number: $A(p) = \mathcal{F}[A(z)] = \sqrt{k_{ref}^2 - p^2} - k_{ref}$, where $\mathcal{F}$ is the z-space Fourier transform. The transform variable p may be associated with a vertical wave number via $p = k_0 \sin\theta$, where θ is the local propagation angle with respect to the horizontal. Thus, the kinetic energy operator $K\psi$ is evaluated as

$$K(\Delta x)\psi(x, z) \equiv e^{i\Delta x A(z)}\,\psi(x, z) = \mathcal{F}^{-1}\left\{e^{i\Delta x A(p)}\,\mathcal{F}\left[\psi(x, z)\right]\right\}. \tag{12}$$

To accommodate a perfect conductor surface boundary condition at $z = 0$, image techniques may be used in the SSFPE algorithm and odd parity (horizontal polarization) or even parity (vertical polarization) solutions obtained. The kinetic energy operator remains unchanged in this case, allowing the exponential Fourier transforms to be replaced by Fourier sine or cosine transforms over the half-line. For mixed surface boundary conditions such as Eq. (7) however, the kinetic energy operator K in Eq. (12) must be modified.

To determine the form of K appropriate for a surface impedance boundary condition of the form $\dfrac{\partial w(x, 0)}{\partial z} = \beta w(x, 0)$, the Helmholtz-Kirchoff formula is used to solve for the field $w(\mathbf{x})$ for $x > x_0$ in terms of an aperture field $w(\mathbf{x_0})$ and the normal derivative of Green's function G

$$w(x, z) = \int_0^\infty w(x_0, z_0)\frac{\partial G(x, z|x_0, z_0)}{\partial x_0}\,dz_0. \tag{13}$$

The appropriate half-space Green's function G which solves $\left[\frac{\partial^2}{\partial x^2} + \frac{\partial^2}{\partial z^2} + k^2\right] G(\mathbf{x}, \mathbf{x}_0) = -\delta(\mathbf{x} - \mathbf{x}_0)$, and satisfies the surface impedance boundary condition $\frac{\partial G}{\partial z} = \beta G$ at $z = 0$ is[14]

$$G(\mathbf{x}, \mathbf{x}_0) = \frac{2i\beta}{\sqrt{k^2 + \beta^2}} e^{i|x - x_0|\sqrt{k^2 + \beta^2}} - \beta(z + z_0)\, \theta(\Re\beta)$$
$$+ \frac{i}{2\pi} \int_{-\infty}^{+\infty} e^{i|x - x_0|\sqrt{k^2 - p^2}} + ipz_0 \left\{ e^{-ipz} + \frac{ip - \beta}{ip + \beta} e^{+ipz} \right\} \frac{dp}{\sqrt{k^2 - p^2}}, \quad (14)$$

where θ is the Heaviside step function: $\theta(x) = 1, x > 0\,; \theta(x) = 0, x < 0$. Substituting Eq. (14) in the Helmholtz–Kirchoff formula Eq. (13) and replacing w by the PE wave function ψ yields[15]

$$\psi(x_0 + \Delta x, z) = 2\beta e^{i\Delta x(\sqrt{k^2 + \beta^2} - k) - \beta z} \int_0^\infty \psi(x_0, t) e^{-\beta t}\, dt\, \theta(\Re\beta)$$
$$+ \frac{2}{\pi} \int_0^\infty dp\, e^{i\Delta x(\sqrt{k^2 - p^2} - k)} \frac{p \cos pz + \beta \sin pz}{p^2 + \beta^2} \int_0^\infty \psi(x_0, t)[p \cos pt + \beta \sin pt]\, dt. \quad (15)$$

The term in Eq. (15) containing the Heaviside step function (which is present only for vertical polarization) represents a surface wave (i.e., the discrete spectrum) traveling in the x direction and decaying exponentially away from the interface, while the integral term represents the continuous spectrum of incident and reflected waves from the surface.

If the modified Fourier transform $\mathcal{F}_\beta$ and the corresponding inverse transform $\mathcal{F}_\beta^{-1}$ are defined by[16]

$$\mathcal{F}_\beta[\psi] = \int_0^\infty \psi(z)[p \cos pz + \beta \sin pz]\, dz\,, \quad \mathcal{F}_\beta^{-1}[\Psi] = \frac{2}{\pi} \int_0^\infty \Psi(p) \frac{p \cos pz + \beta \sin pz}{p^2 + \beta^2}\, dp\,,$$

then the kinetic energy propagator K for a mixed (Robin) type surface boundary condition, that is the extension of Eq. (12), can be written compactly as

$$K(\Delta x)\psi(x_0, z) = e^{i\Delta x A(z)}\, \psi(x_0, z) = \mathcal{F}_\beta^{-1} \left\{ e^{i\Delta x A(p)}\, \mathcal{F}_\beta [\psi(x_0, z)] \right\}$$
$$+ 2\beta e^{i\Delta x(\sqrt{k^2 + \beta^2} - k) - \beta z} \int_0^\infty \psi(x_0, t) e^{-\beta t}\, dt\, \theta(\Re\beta)\,. \quad (16)$$

Note that the potential propagator U remains the same.

Since the SSFPE method is a marching algorithm, a starting field is required. Very close to the source, the propagation medium is assumed to be approximated as plane-stratified and is modeled by two semi infinite dielectric half-spaces having complex dielectric constants $\varepsilon_1, z > 0$ and $\varepsilon_2, z < 0$. The initial PE field $\psi_0(z)$ is assumed to be due to a finite aperture source distribution $s(z)$ located at the origin $x = 0$ in the half-space $z > 0$. The starter field $w(x, z)$ due to this aperture is computed using a scalar Green's function $G(x, z, z')$ as

$$w(x, z) = \int s(z') G(x, z, z')\, dz'\,. \quad (17)$$

The Green's function G has a spectral representation[14]

$$G_{h,v}(x, z, z') = \frac{i}{2\pi} \int_{\infty e^{i\pi}}^\infty \frac{\xi H_0^{(1)}(\xi x)}{\kappa_1} \left\{ e^{+i\kappa_1 |z - z'|} + \Gamma_{h,v}(\xi) e^{-i\kappa_1 (z + z')} \right\} d\xi,$$

where $\Gamma_{h,v}$ is the plane-wave surface reflection coefficient (including surface roughness), and $\kappa_1 = \sqrt{k^2 - \xi^2}$. If the source aperture distribution has the form

$$s(t) = s(t - z_0) e^{i(t - z_0)p_0}$$

corresponding to an antenna located at height z_0 and vertically steered to $p_0 = k_0 \sin\theta_0$, then the initial PE field $\psi_0(z)$ is

$$\psi_0(z) = \frac{1}{2\pi} \int_{-\infty}^\infty \{ e^{-ipz_0} f(p - p_0) + \Gamma_{h,v}(p) e^{+ipz_0} f(-p - p_0) \} (k^2 - p^2)^{-1/4}\, dp\,, \quad (18)$$

where $f(p)$ is the antenna pattern corresponding to s. This PE starting field displays the correct singular behavior as $p \to k$.

§4.0 Numerical Implementation

To implement the SSFPE algorithm, the infinite Fourier transforms in Eq. (12) or Eq. (16) are replaced by discrete sine or cosine transforms over the finite interval $0 \le z \le Z_{\max}$. These are evaluated numerically using fast Fourier sine and cosine transform algorithms. This requires the PE wave function ψ have compact support and be band limited in vertical wave number space. The band limiting in p-space is accomplished by applying a low-pass filter as part of the kinetic energy propagator step to remove high momentum components of $\Psi(0,p)$ before transforming back to z-space. This wave number filtering is critical, particularly when propagating over variable terrain, since propagating energy can be slope converted to steeper angles (i.e., higher p values) by the sloping terrain.

Another potential source of numerical difficulty in using the SSFPE method arises in treatment of the Sommerfeld outgoing wave radiation boundary condition. Since the SSFPE algorithm employs a FFT, the implementation of a radiation-type boundary condition is complicated. Truncation of the infinite z-domain down to a finite interval will introduce spurious discrete standing wave solutions (modes) in the vertical. In effect, the terminal impedance at the end of the transform grid $z = Z_{\max}$ is not properly matched to the radiation boundary condition.

To circumvent this problem and attenuate these spurious modes introduced by the finite Fourier transforms and also to prevent FFT "wrap around", a complex absorber potential or sponge, $V_{abs}(z)$, is added to the split-step B operator: $B(x,z) \Rightarrow B(x,z) + iV_{abs}(z)$. The specific functional form chosen for the complex absorber is

$$V_{abs}(z) = V_0 \operatorname{sech}^2[(z - Z_{\max})/w_0]\,. \tag{19}$$

For each PE step, this will lead to an effective z-space low-pass filter of the form $e^{-k_0 \Delta x V_{abs}}$ that is applied to the upper part of the PE grid. The sponge parameters $\{V_0, w_0\}$ are determined parametrically by minimizing the transmissivity and reflectivity from an equivalent quantum mechanical problem of free-particle scattering off a complex potential barrier having the form Eq. (19) and are function of frequency.[17] The "physical" propagation region in the VTRPE model thus extends to an altitude $z = H_{\max} < Z_{\max}$ to allow room for the complex absorber.

Once the FFT grid is defined, the vertical mesh spacing is set, but the PE range step Δx remains unspecified. Each application of the SSFPE algorithm, Eq. (11), leads to a local truncation error in the solution ψ that is proportional to the cube of the PE range step Δx. Since many range steps are typically taken, these can accumulate and produce unacceptable errors in the final solution. To prevent this from happening, the VTRPE code performs a global error estimate based upon a detailed analysis of the local SSFPE truncation error. To bound the total global error in the solution ψ, the PE range step Δx is chosen so that $\Delta x^2 \le \epsilon_{rel} \dfrac{\|\delta^{(1)}\psi\|}{\|\delta^{(3)}\psi\|}$, where ϵ_{rel} is a specified local relative error tolerance in ψ, and the PE wavefunction error norms are defined as

$$\|\delta^{(1)}\psi\| = \int \psi^* \left[\frac{\partial^2}{\partial z^2} - k_0^2 V\right] \psi \, dz\,,$$

$$\|\delta^{(3)}\psi\| = \int \left[k_0^2 \left(\frac{\partial V}{\partial z}\right)^2 |\psi|^2 - \frac{\partial^2 V}{\partial z^2}\left|\frac{\partial \psi}{\partial z}\right|^2 + \tfrac{1}{4}\frac{\partial^4 V}{\partial z^4}|\psi|^2\right] dz + \psi^* \frac{\partial \psi}{\partial z}\frac{\partial^2 V}{\partial z^2}\bigg|_{z=0}\,.$$

Here $V(z) = m^2(z) - 1$ is the "effective potential" related to the modified index of refraction m. As the VTRPE code advances the field, the local error budget is monitored and the range step-size Δx is dynamically adjusted to keep the local error below a preset threshold.

§5.0 Examples

An examples of VTRPE model output is shown in Figure 1. This is a screen dump from the PC version of the model and depicts a coverage diagram of path loss $PL = 20\log(2k_0R) - 20\log|F|$ in decibels. Figure-1 represents a 250m elevated transmitter over a 240m slope with three ridges down range. The transmitter frequency is 2.5GHz, with a 2-deg vertical beamwidth antenna pattern. The polarization is horizontal. Surface dielectric properties are characteristic of dry ground, and the solid dark line is the terrain profile. The atmospheric refractivity profile is a 300m surface based duct.

§6.0 Summary

This paper describes the basic physics and numerical techniques used in implementing a variable terrain electromagnetic parabolic wave equation propagation model. This propagation model allows for both finite surface conductivity and variable (i.e., highly irregular) surface terrain. The model is based a novel implementation of the split-step Fourier PE algorithm to efficiently compute the electromagnetic radiation fields for surface impedance boundary conditions.

The propagation model is implemented as the VTRPE (variable terrain radio parabolic equation) computer code and is used in the prediction of microwave propagation in complex real world environments. The VTRPE code has the following characteristics:

(1) full-wave propagation physics (i.e., field amplitude and phase are computed);
(2) direct solution of electromagnetic fields;
(3) exact treatment of refraction and diffraction phenomena;
(4) exact treatment of multipath phenomena;
(5) range-dependent atmospheric refractivity inputs, $N(z, r)$;
(6) infinite or finite conductivity surface boundary conditions;
(7) linear transmitter field polarization (vertical or horizontal);
(8) variable surface terrain elevation and surface dielectric properties;
(9) frequency dependent atmospheric attenuation;
(10) frequency range: $\approx 0.01 \rightarrow 100$ GHz;
(11) generalized transmitter radiation patterns;
(12) arbitrary transmitter/receiver geometry;
(13) automatic selection of the range step-size and FFT transform size; and
(14) automatic monitoring of solution global error.

The VTRPE model properly accounts for the dominant mechanisms governing tropospheric microwave propagation, including the effects of anomalous propagation arising from spatial changes in atmospheric refractivity and variable terrain features.

This work was supported under the NRaD Independent Research program.

References

1. M. A. Leontovich and V. A. Fock, "Solution of the problem of propagation of electromagnetic waves along the earth's surface by the method of parabolic equations," J. Phys. of the USSR **10**, 13–24 (1946).
2. R. H. Hardin and F. D. Tappert, "Application of the split-step Fourier method to the numerical solution of nonlinear and variable coefficient wave equations," SIAM Rev. **15**, 423 (1973).
3. Fred D. Tappert, "The parabolic approximation method," in *Wave Propagation and Underwater Acoustics*, edited by Joseph B. Keller and John S. Papadakis, (Springer-Verlag, New York, 1977, Lecture Notes in Physics, Vol. 70), pp. 224–287.
4. H. W. Ko, J. W. Sari, and J. P. Skura, "Anomalous microwave propagation through atmospheric ducts," Johns Hopkins APL Tech. Dig. **4**, 12–16 (1983).
5. G. D. Dockery and G. C. Konstanzer, "Recent advances in prediction of tropospheric propagation using the parabolic equation," Johns Hopkins APL Tech. Dig. **8**, 404–412 (1987).
6. F. J. Ryan, "RPE: A parabolic equation radio assessment model," in *Operational Decision Aids for Exploiting or Mitigating Electromagnetic Propagation Effects* (presented at NATO AGARD Electromagnetic Wave Propagation Panel Symposium, San Diego, CA, 15-19 May 1989).
7. K. H. Craig, "Propagation modeling in the troposphere: parabolic equation method," Elec. Lett. **24**, 1136-1139 (1989).
8. G. A. Hufford, "An integral equation approach to the problem of wave propagation over an irregular surface," Quart. J. Appl. Math. **9**, 391–404 (1952).
9. R. H. Ott, "RING: An integral equation algorithm for HF-VHF radio wave propagation over irregular, inhomogeneous terrain," Radio Sci. **27**, 867–882 (1992).

10. Frank J. Ryan, "Analysis of electromagnetic propagation over variable terrain using the parabolic wave equation," NOSC **TR-1453**, Naval Ocean Systems Center, San Diego, CA (1991).
11. V.A. Fock, *Electromagnetic Diffraction and Propagation Problems*, (Pergamon Press Ltd., Oxford, 1965), Chap. 14, pp. 276–307.
12. J.E. Freehafer, W.T. Fishback, W.H. Furry, and D.E. Kerr, "Theory of propagation in a horizontally stratified atmosphere," in *Propagation of Short Radio Waves*, edited by D. E. Kerr, (McGraw-Hill, 1951), pp. 27–41.
13. Charles Herach Papas, *Theory of Electromagnetic Wave Propagation*, (Dover Publications, New York, 1988), Chap. 4, pp. 81–97.
14. L.B. Felsen and N. Marcuvitz, *Radiation and Scattering of Waves*, (Prentice-Hall, Inc., Englewood Cliffs, N.J., 1973), Chap. 5.
15. F. J. Ryan, "Implementation of surface impedance boundary conditions in the split-step parabolic equation," J. Acoust. Soc. Am. **92**, 2432 (1992).
16. Ruel V. Churchill, *Operational Mathematics*, (McGraw-Hill, New York, 1972), Third Ed., Chap. 13, pp. 414–416.
17. F. J. Ryan and C. D. Rees, "Optimal absorber potentials in PE modeling," J. Acoust. Soc. Am. **86**, S53 (1989).

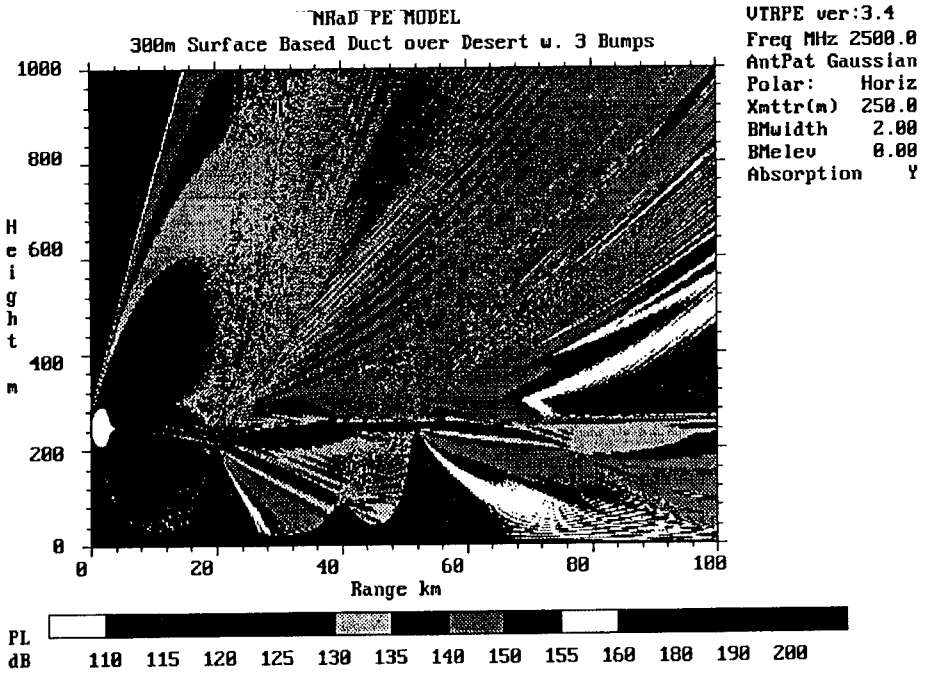


FIG. 1. Multiple ridge line propagation with 300m surface based duct

Estimating Tropospheric Refractivity Fields Using a Nonlinear Gauss-Markov Procedure and the PE Model

DONALD D. BOYER
Naval Surface Warfare Center
Dahlgren Division, CODE N24
Dahlgren, VA 22448

and

FRANK J. RYAN
Naval Command, Control and Ocean Surveillance Center
RDT&E Division, CODE 712
San Diego, CA 92152-5000

18 Jan 1995

1. Introduction

Shipboard radar and communication systems in a coastal marine environment are very sensitive to vertical and horizontal variations in the tropospheric refractivity conditions. These systems frequently experience extended or reduced detection ranges, inaccurate altitude estimates, and increased surface clutter due to the presence of nonstandard atmospheric refractivity conditions (e.g., surface or elevated ducts) and their concomitant impact on radio wave propagation. If synoptic range dependent refractivity fields were available in a timely manner aboard a ship, an automated decision aid could be designed to adjust the radar output to account for these anomalous propagation effects. In fact, a decision aid has been developed by The Applied Physics Laboratory for use on AEGIS ships, but its use is limited by the inadequacy of synoptic refractivity measurements.

In most Naval battle scenarios a cruiser or destroyer is usually in communication with other friendly ships and planes or helicopters, whose positions and velocities are known very accurately. This paper will describe a technique for supplementing available refractivity data in situ, by letting the on board microwave sensors receive a set of known signals transmitted at multiple frequencies from one or more of these friendly vehicles. The refractivity profile estimation, or remote sensing, is accomplished using matched field processing methods whereby a modeled signal waveform (replica) is cross correlated with measured sensor data to yield a tomographic reconstruction of the medium.

The proposed remote sensing algorithm uses a nonlinear Gauss-Markov estimation technique, implemented numerically with a finite difference Levenberg-Marquardt procedure. At each step of the iteration, a parabolic wave equation (PE) model is used to compute the forward solution or replica used in the matched field processor. The advantage of this proposed technique is that it offers the possibility of rapid sensing of atmospheric refractivity fields using readily available hardware assets.

This paper addresses the initial phase of the work, namely formulating the procedure and establishing the feasibility of the method. The next phase of the work will involve using measured coastal data from experiments at Wallops Island, and The Naval Surface Warfare Center at Dahlgren, Virginia.

2. Atmospheric Refractivity

In the troposphere, radio waves travel along curved ray paths and the amount of bending or refraction is proportional to the gradient of the refractive index n transverse to the ray path. At high altitudes, the index of refraction n will approach unity as the density decreases and, therefore, will tend to decrease with height in the atmosphere. Since n is very close to unity, it proves more convenient to work with the refractivity N defined by $N = (n - 1) \times 10^6$. For radio wavelengths removed from gaseous absorption

lines, the refractivity is found to be empirically related to the pressure p, temperature T and humidity (water vapor pressure) e [1]

$$N = 77.6\frac{P}{T} - 5.6\frac{e}{T} + 3.75 \times 10^5 \frac{e}{T^2}$$

where the pressure is measured in mbar and temperature in °K.

The variation of N with altitude will cause radio waves to propagate along curved paths, and it proves useful to analyze this ray curvature via a coordinate transformation which maps the curved earth's surface into a flat one. This is accomplished by replacing the radio refractive index n by the *modified* refractive index $m = n(1 + z/a)$, where a is the effective earth radius. In similar fashion, the modified refractivity M is defined by

$$M = (m - 1) \times 10^6 \quad \approx N + 0.157z$$

where z is height in meters. Variations of N with height caused by humidity and temperature gradients cause energy to be trapped when the vertical gradient of M is non-positive.

In the atmospheric boundary layer (the lower kilometer of the atmosphere), the vertical profiles of temperature and humidity are often approximately logarithmic.[2] Thus, over water where evaporation occurs and the humidity profile decreases with height, M will have a local minimum at some height $z = d$ above the water surface. If this height is sufficiently high in terms of wavelengths, then radio energy will be trapped and propagation to long ranges is possible. Over water, this phenomena is known as an evaporation duct. Similar situations can occur over land due to increases of temperature with height in nocturnal radiation inversions.

A convenient analytic representation of evaporation duct type refractivity profiles is provided by the log-linear form:

$$M(z) = M_0 + g[z - (d + z_0)\ln(1 + z/z_0)], \tag{1}$$

where M_0 is the surface refractivity value, g is the asymptotic gradient in M at large heights, d is the duct height (i.e., the height of local profile minimum), and z_0 is known as the roughness parameter. For the ocean surface, a typical value for z_0 is $z_0 \approx 10^{-4}$meters. The advantage of an analytic profile representation, such as the log-linear form, over a discrete form is the fewer number of parameters needed to specify the profile. This is important when numerical inversion methods are attempted as will be discussed later.

3. Inverse Medium Problem for Electromagnetic Waves

In the last few years Colton and Kress[4] have extended the theory of inverse scattering of acoustic and electromagnetic waves to include the inverse medium problem for electromagnetic waves. They define the inverse medium problem for electromagnetic waves to be the determination of the index of refraction $n(\mathbf{x})$ from a knowledge of the far field radiation pattern $\mathbf{E}_\infty$, of a time harmonic solution $\mathbf{E}(x, t)$ to Maxwell's equations in an isotropic inhomogeneous medium. These ideas are developed rigorously using classical and functional analysis in the above cited book by Colton and Kress. These techniques are applied to the detection and monitoring of leukemia in two papers, soon to be published by Colton and Monk.[5]

The refractivity estimation problem which the present paper addresses is an inverse medium problem, but it is much more complex than those defined by Colton and Kress. In order to obtain classical solutions to the forward scattering problems, Colton and Kress insist that the incident wave must be a homogeneous plane wave, there are no boundary conditions and they insist that the refractive index be spherically stratified. Even under these very restrictive assumptions classical solutions to inverse scattering problems for acoustic and electromagnetic waves are not available, and it is necessary to resort to numerical techniques. Some of these numerical techniques applicable to inversion problems for acoustic waves are described in detail in the book by Colton and Kress[4]. A powerful numerical technique for the inverse medium problem is developed by Colton and Monk[6], and applied to a medical imaging problem,

but the restrictive assumptions mentioned above are still necessary. The solution to the inverse medium problem proposed in this paper uses a numerical solution to the forward scattering problem as well as the inverse problem, which simplifies the mathematical formulation of entire procedure, as will be seen in the next section.

Inversion problems involving acoustic and electromagnetic waves arise in a variety of important applications ranging from medical imaging to geophysics to the non destructive testing of materials . Since these problems involve the inversion of a partial differential operator they generally fall into the class of problems which are called ill posed. A problem in mathematical physics is called *well posed* provided:

1. a solution should exist
2. the solution should be unique
3. the solution should depend continuously on the data

otherwise the problem is called *ill posed.* The third requirement is motivated by the fact that in all applications the data will be measured quantities, and it is desirable that small errors in the data will cause small errors in the solutions. It has been established that most all of the physically motivated classical initial-boundary value problems in partial differential equations, with the exception of the backwards heat conduction equation are well posed, see any book on partial differential equations such as [7]. Such problems in scattering theory are usually referred to as forward or direct problems. However most inverse scattering problems are ill posed. Though "illposedness" may be an undesirable adjective to a classical mathematician, in order to determine refractivity parameters from the far field measurements of electromagnetic path loss over the surface of the earth, it is necessary that the problem be substantially over determined; so no solution can actually exist.

To place the refractivity estimation problem in the context of a general inversion problem, consider a nonlinear function F which maps a Hilbert space X into a Hilbert space Y . An inversion problem for the operator F can be defined as follows: given an arbitrary y in Y, find a x in X such that

$$F(x) = y \tag{2}$$

In order to solve the nonlinear equation (2), it is customary to linearize about an approximate solution x_0 to the operator equation

$$F(x_0 + s) = F(x_0) + F'(x_0)s + o(\|s\|) \tag{3}$$

and apply a Newton-type iteration scheme. Given $x_0 \in X$, then for $k = 0, 1, \cdots$, set

$$x_{k+1} = x_k + s_k \tag{4}$$

where $s_k \in X$ is a solution to

$$F'(x_k)s_k = y - F(x_k) \tag{5}$$

If x_0 is a good approximate solution to Eq. (2), and Eq. (5) has a solution s_k for each k, then $\{x_1, x_2, \cdots, x_k\}$ will be a sequence of increasingly better approximate solutions to Eq. (2). If F is a partial differential operator on a Hilbert space of vector valued square integrable functions, then the differential operator is converted into an integral operator, and hopefully the solution to the direct problem may be expressible in terms of a Fredholm-type integral equation. In some cases classical solutions to the direct scattering problem are available and straightforward numerical solutions the inverse problem Eq. (2), without resorting to linearization and Newton-type methods. These cases are thoroughly explored in Colton and Kress' book [4]. They also have developed a new technique, called a *dual space method,* which does not require classical closed form solutions to the direct problem, but it does require that the direct problem be expressible in terms of an integral equation. Unfortunately propagation problems around the surface of the earth with range and height dependent refractivity do not lend themselves to Fredholm-type integral equation formulations. However, in recent years the parabolic approximation to the Helmholtz equation has been shown to be a very accurate and efficient procedure for solving the direct medium problem — even under very complex initial, boundary and refractivity conditions. The mathematical formulation

presented in the next section of this paper uses the PE approximation to solve the direct problem and a very robust numerical technique, based on the theory of nonlinear least squares, to solve the inverse medium problem and obtain estimates of range varying refractivity parameters based on measured far field propagation path losses.

The general inversion problem was stated in equation Eq. (2), with an iterative Newton-type solution technique given by equations Eq. (4) and Eq. (5). Now in most applied problems y is not in the range of F, because of measurement and modeling errors, so no solution to Eq. (2) exits. Thus it is desirable to design an approximate solution method which solves iteratively a sequence of well posed subproblems, rather than the ill posed inversion problem. The subproblems should satisfy each of the following characteristics:

1. Each subproblem is well posed.
2. Each subproblem lends itself to an efficient computational solution technique
3. Since the measured quantity y is not likely to be in the range of any of the subproblem operators, there must be simple criteria for determining when the solution to a subproblem is sufficiently close to y.

In the functional analysis literature, the construction of subproblems for an ill posed problem is referred to as *regularization*; see Colton and Kress [4] for a very thorough treatment of all of these topics. An algorithm commonly used to solve the general inversion problem Eq. (2), called the Levenberg-Marquardt algorithm, is based on a "linearize and regularize" approach, and was originally derived to solve the nonlinear least-squares problem.[8] The resulting subproblems after linearization are: given an approximate initial solution x_0 to Eq. (2), $x_0 \in X$, then for $k = 0, 1, \cdots$, set

$$x_{k+1} = x_k + s_k$$

where the parameter $\mu_k \geq 0$ and $s_k \in X$ together solve the subproblem

$$\left[F'(x_k)^* F'(x_k) + \mu_k I\right] s = F'(x_k)^* \left(y - F(x_k)\right) \tag{6}$$

In a Hilbert space setting $F'(x_k)^*$ is the adjoint of the Frechet derivative of the operator F, and the Levenberg-Marquardt procedure is an example of a Tikhonov regularization technique.

The refractivity estimation problem presented in this paper is an ill posed inversion problem in the general theory of the scattering of electromagnetic waves. Since the problem allows for very general initial and boundary conditions as well as height and range dependent refractivity, it is not possible to obtain classical solutions in terms of integral equations, even for the direct problem. The solution method proposed for the problem involves solving the direct problem with a PE model, which results from approximating the azimuth independent Helmholtz equation, ignoring the backscatter. The domain, which is the refractivity parameter space, will be discretized into a finite number of refractivity profiles, each characterized by a finite number of parameters. The output space, which is the far field path loss, will be discretized by transmitter height, receiver height, range and frequency. In this formulation the function F is a nonlinear vector-valued function, whose domain and range are both finite dimensional Euclidean spaces, and the derivative operators appearing in Eq. (6) are the Jacobian matrices of partial derivatives. Each column of $F'(x_k)$ consists of the partial derivatives of a given path loss with respect to each of the refractivity parameters. Correspondingly each row of $F'(x_k)$ consists the partial derivatives of a each path loss with respect to a given refractivity parameter. These partial derivatives are computed using finite difference approximations, and the finite differences are computed with the PE model. The Levenberg-Marquardt technique Eq. (6) is used to generate the subproblems after linearization. Each subproblem corresponds to minimizing the sum of the Euclidean norms of the residuals between each modeled path loss and each correspondingly discretized measured path. A new subproblem is generated by linearizing Eq. (3) about the solution to the previous subproblem. This technique results in a very robust numerical scheme, because the singular value decomposition of the Jacobian matrix can be used to eliminate redundant refractivity parameters. Then the solutions to the subproblems are being projected

into the subspace spanned by the significant parameters for the given range, transmitter height, receiver height and frequency diversity.

The measured data set to which the technique is being applied has transmitter and receiver height diversity as well as frequency diversity. Another set of data which will soon be available also exhibits range diversity, as well as transmitter and receiver height variations, but it has limited frequency diversity. The range diversity in the propagation measurements will add some interest since the procedure will estimate range dependent refractivity parameters. More details on the mathematical formulation and the data sets will be given in the next section.

4. Refractivity Estimation from Path Loss Measurements

It is well known in the radar community that if synoptic refractivity data were readily available, tactical decision aids could be developed to compensate for the effects of anomalous propagation on the sensors and weapon systems. The question that this paper addresses is how to obtain tropospheric refractivity data, given that measurements of the one-way path loss between a transmitter and a receiver are available. The question as to whether propagation measurements are easy to obtain over a wide frequency band is being addressed at The Naval Surface Warfare Center by Stapleton and Kang.[9] Also considerable effort has been devoted to the modeling of EM wave propagation over a broad frequency band with the PE model, see the two previous papers in these proceedings [10],[11]. The numerical procedure to be outlined in this section uses a PE model to solve the direct EM medium scattering problem, and the path loss measurements with a Levenberg-Marquardt procedure to perform the inversion.

Assume that there are l_1 transmitters locations and l_2 receivers locations. Though we can assume range diversity, to simplify the notation, assume a fixed range between antennae. Also assume that there are k distinct frequencies. The tropospheric refractivity environment is parameterized by a set of l profiles $\{P_1, P_2, \cdots, P_l\}$, with the i-th profile P_i defined by n_i parameters. Thus a parameter vector would be $\mathbf{x} = \{p_1^1, p_2^1, \cdots, p_{n_1}^1, \cdots, p_1^l, p_2^l, \cdots, p_{n_l}^l\}$. So when we say $\mathbf{x} \in \mathbf{R^n}$ we mean $n = n_1 + n_2 + \cdots + n_l$. We can either use an analytical representation for each profile, for example the log-linear formEq. (1), or a piecewise linear or spline characterization. The advantage of the former approach is the greatly reduced size of the parameter space that must be searched. Now since a PE model outputs a path loss at a discrete set of receiver heights, for a given transmitter height and frequency, the PE model must be executed $k \cdot l_1$times to obtain the $m = k \cdot l_1 \cdot l_2$ modeled path losses. Thus the direct medium scattering equation

$$\mathbf{y} = \mathbf{F}(\mathbf{x}) \tag{7}$$

denotes a nonlinear vector valued function, with the PE model mapping the refractivity parameter space in R^n into the modeled path loss space in R^m. Now we are not actually invertingEq. (7), since the measured path loss vector $\hat{\mathbf{y}}$ is not in the range of PE model so we must find a $\hat{\mathbf{x}}$ in the refractivity parameter space which minimizes the Euclidean norm of residual between modeled and measured path loss:

$$R(\mathbf{x}) = \frac{1}{2}(\mathbf{F}(\mathbf{x}) - \hat{\mathbf{y}})^T(\mathbf{F}(\mathbf{x}) - \hat{\mathbf{y}}) \tag{8}$$

The Levenberg-Marquardt technique Eq. (6) can now be written as find a $\mu_k \geq 0$ and an $\mathbf{x}$ such that

$$\left(\mathbf{J}_k^T\mathbf{J}_k + \mu_k\mathbf{I}\right)\mathbf{x} = \mathbf{J}_k^T(\hat{\mathbf{y}} - \mathbf{F}_k) \tag{9}$$

where $\mathbf{J}_k = \mathbf{J}(\mathbf{x}^k)$ is the Jacobian matrix of partial derivatives, approximated by finite differences, using PE for the function evaluations. A singular value decomposition will be performed on the Jacobian matrix to remove the redundant parameters. Then μ_k can be set equal to 0 in Eq. (9) and the much simpler Gauss-Newton method results, involving only positive definite Hessian approximations $\mathbf{H}_k = \mathbf{J}_k^T\mathbf{J}_k$. In this case a QR decomposition of the Hessians results in a very efficient, robust implementation. In the

computer implementation the modeled and the measured path losses are each divided by the path loss modeled for standard propagation, this also should reduce the residuals in Eq. (8) and force μ_k equal to zero.

The data set described in [9] has sufficient frequency and antennae height diversity to accurately estimate 50 to 100 refractivity parameters. And considering that the maximum antenna height is under 30 meters, and the antennae separation is 15 kilometers, it may be possible to obtain a good PE match to measured path loss with as few as 20 parameters.

One final note is that if a measurement covariance matrix $\mathbf{R}$ is available, then $\mathbf{R}^{-1}$ can be inserted into Eq. (8), and the resulting solution to Eq. (9) is the nonlinear Gauss-Markov or minimum variance statistical estimate of the refractivity parameters.

References

[1] Bean, B.R. and Dutton, E.J.: 1968, *Radio Meteorology*, Dover Books, New York.

[2] Gossard,E.E. and Strauch, R.G.: 1983, *Radar Observations of Clear Air and Clouds*, Elsevier Science Pub., Amsterdam.

[3] Sorbjan, Z.: 1989, *Structure of the Atmospheric Boundary Layer*, Prentice Hall, Englewood Cliffs.

[4] Colton, D. and Kress, R.: 1993, *Inverse Acoustic and Electromagnetic Scattering Theory*, Springer-Verlag, .

[5] Colton, D. and Monk, D.: in press, 'The Detection and Monitoring of Leukemia Using Electromagnetic Waves: Mathematical Theory'.

[6] Colton, D. and Monk, D.: in press, 'The Detection and Monitoring of Leukemia Using Electromagnetic Waves: Numerical Analysis'.

[7] Colton, D.: 1988, *Partial Differential Equations*, Random House, .

[8] Dennis, J.E. and Schnabel, R.B.: 1983, *Numerical Methods for Unconstrained Optimization and Nonlinear Equations*, Prentice Hall, .

[9] Stapleton, J. and Kang, S.: 1995, 'Direct Measurement of RF Propagation in the Low Elevation Regions for 2–18GHz', *Proc. URSI Conf.*, Boulder CO.

[10] Ryan, F.J.: 1995, 'VTRPE: A Variable Terrain Electromagnetic Parabolic Equation Model', ACES Conf. these proceedings.

[11] Paulus, R. : 1995, 'Validation of the Radio Physical Optics Model', ACES Conf., these proceedings.

MODELING OF RADIO WAVE DUCTING OVER REGULAR BOUNDARY

I.P. Zolotarev
Institute of Terrestrial Magnetism, Ionosphere and Radio Wave Propagation (IZMIRAN), Troitsk, Moscow reg., 142092 RUSSIA.

1. Introduction.

Many of essential features of UHF/VHF radio wave propagation in the atmosphere are closely related with the structure of radio refractive index. If the vertical gradient of radio refractive index negative and less then -157 N units/km the rays bend downward to the earth so that ducting is possible [10]. By statistics the percent incidence of ducting conditions over wide area is 40%- 80% [2], [5]. Due to presence of ducts it is possible beyond line-of-site radio wave propagation and radio communication at distances of about 2000 - 3000 km. The paths losses of radio waves in ducts usually are connected with dumping of waves in the atmosphere, reflection conditions and geometric factors.

The appearance of ducts is very well predictable. Very frequently the parameters of ducts can be modified by different acoustic and gravity waves creating periodic structure of radio refractive index along path. Atmospheric gravity waves producing wavelike disturbances of duct layers were detected by pressure sensors on the ground [2]. The behavior of rays in ducts is similar to that of nonlinear dynamical system and periodic space disturbances of ducts can cause catastrophic changes in behavior of rays. These effects can be very strong and more essential for assessments of communication link range than other paths losses. The another factor affecting on radio wave propagation is the shape of terrain [1], [7]. Very often the shape of boundary in atmospheric ducts contains quasi periodical components: waves on the sea surface, buildings, hills. In some cases influence of the boundary conditions on rays in ducts is similar to the effects caused by processes that periodically modulate refractivity index profile.

2. Refractive index profile.

Radio refractive index profiles in atmospheric ducts measured by radiosondes or lidars [8], [9] can have very complicated structure. Very often ducts have thin multiple layers structure [2]. For ray tracing in ducts can be used simple analytical or semi-empirical models of duct profile. Because of rapid divergence of rays in modulated ducts for assessments of ray propagation more preferable are synthesized models giving more close approach of altitude behavior of radio refractive index. An example of output for such model is shown in Figure 1, containing radio refractivity profile in N units and its altitude gradient. To fit in input points there were used special extrapolation procedure with trigonometric smoothing that gives better results than usually used spline methods. The profile in Figure 1 is a kind of elevated duct and is typical for many situations [7], [8].

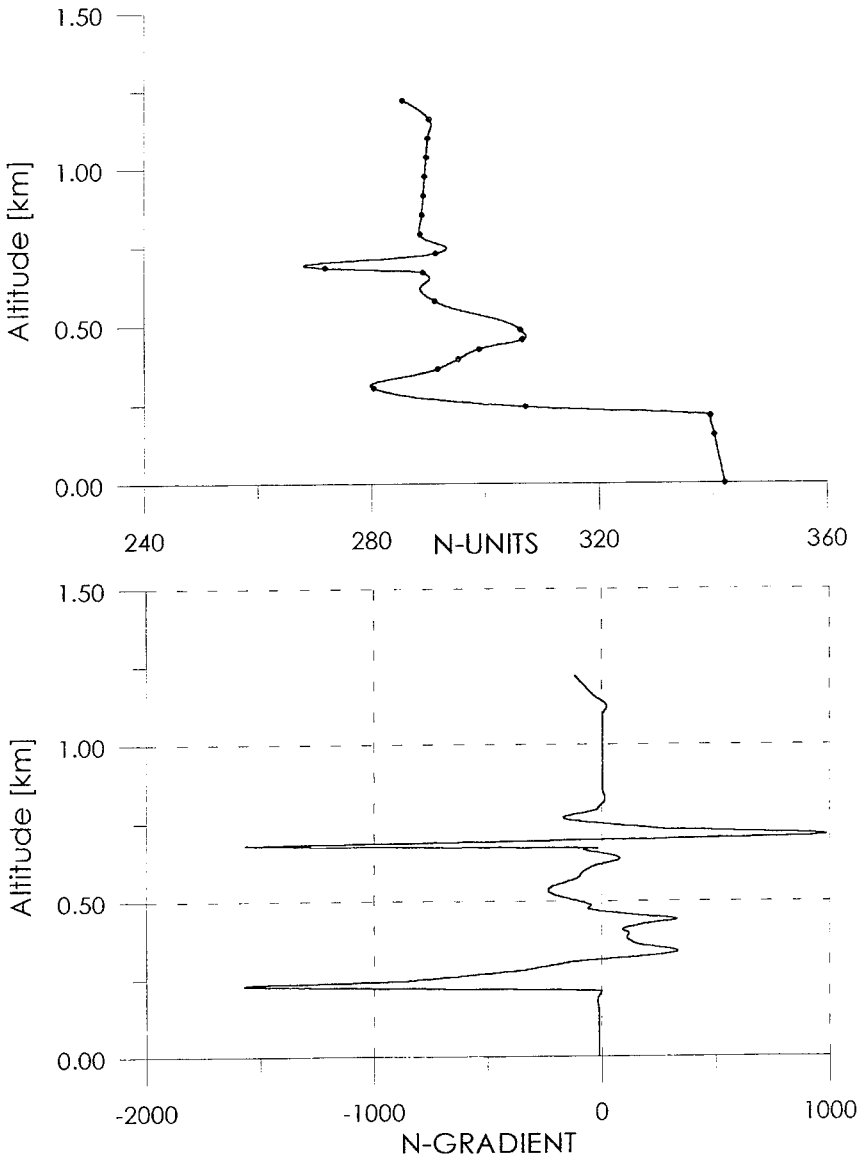


Fig. 1. Refractivity Profile for Elevated Duct and Altitude Gragient of Refractive Index.

3. Ray approximation.

For ray tracing in ducts can be used approximation of geometric optics. Instead of usually used length-altitude variables it is more convenient for ray tracing in modulated ducts to use altitude-impulse variables $(x_1,\ x_2)$ [6], [11], [12].

$$x_1 = r - R_E \tag{3.1}$$

$$x_2 = \frac{n\,\dot{r}}{\sqrt{\dot{r}^2 + \left(\frac{r}{R_E}\right)^2}} \tag{3.2}$$

where x_1 - altitude above the earth, r - radius of point on the ray path, R_E - radius of the Earth, n - radio refractive index, x_2 - impulse, $x_2 \equiv p_r = n\sin\alpha$, α - angle of ray inclination to the Earth. Impulse x_2 is proportional to the vertical component of wave vector. When x_2 is negative the ray bends downward to the earth, when x_2 equals to zero the ray is parallel to the earth and when x_2 is negative the ray propagates outward from the earth. Refractive index n is connected with refractivity N by relation [3], [10]

$$n = 1 + 10^{-6}N \tag{3.3}$$

In variables $(x_1,\ x_2)$ the ray paths satisfy to equations [6], [11], [12]

$$\dot{x}_1 = \frac{x_2\,(1 + x_1/R_E)}{\sqrt{n^2 - x_2^2}} \tag{3.4}$$

$$\dot{x}_2 = \frac{1}{R_E}\sqrt{n^2 - x_2^2} + \left(1 + \frac{x_1}{R_E}\right)\frac{n\partial n/\partial x_1}{\sqrt{n^2 - x_2^2}} \tag{3.5}$$

where $\dot{x}_{1,2} \equiv \partial x_{1,2}/\partial t$, $t = R_E\varphi$, φ - polar angle in the plane of ray trace.

Equations (3.4), (3.5) are nonlinear Hamilton system. It was solved numerically and results were represented as phase portrait figures.

4. Ducting in quiet atmosphere.

In the absence of disturbances the results of calculations for refractivity profile shown in Figure 1, are represented as corresponding phase portrait in Figure 2. Total phase space consist of non intersecting separate curves. Each curve corresponds to the separate ray path. Continuous curves correspond to rays trapped in elevated ducts. It is seen that the duct has complex thin structure. It consists of two elevated duct subsystems - lower subsystem (curves 3 and 2) and upper subsystem (curves 5, 6, 7). Curve 3 corresponds to the ray that propagates in the atmosphere not touching the surface of the earth. Curve 2 corresponds to the ray trapped in the duct that periodically reflects from the surface of the earth. Altitude gradient of refractivity index near the earth surface is small (Figure 1). So the rays starting near the earth at zero elevation angle bend outward. Upper duct subsystem consists of embracing duct (curve 5) and two nested separate subducts (curves 6 and 7) inside. Curves 1, 4, 8 correspond to untrapped rays that reflect from

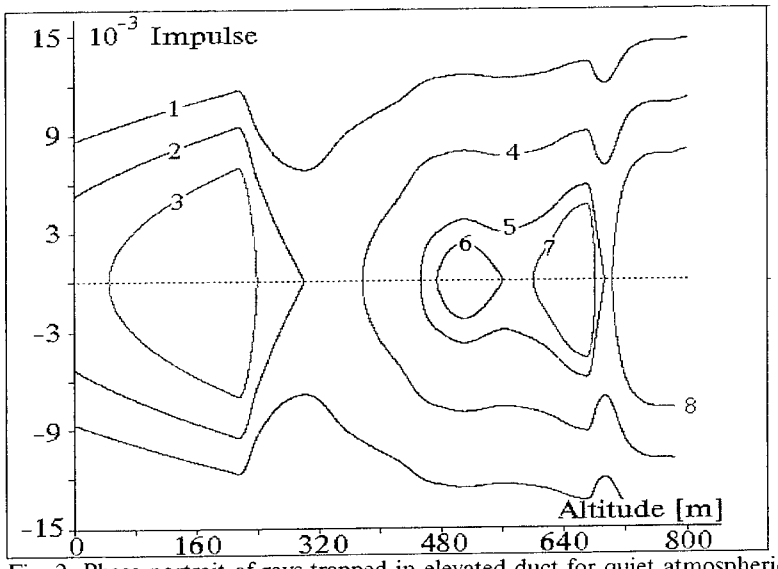


Fig. 2. Phase portrait of rays trapped in elevated duct for quiet atmospheric conditions.

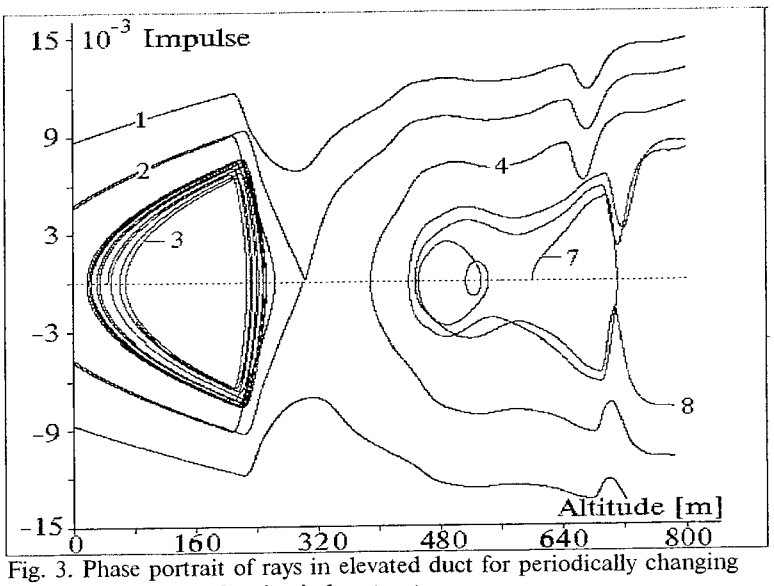


Fig. 3. Phase portrait of rays in elevated duct for periodically changing along path refractive index structure.

the earth or propagate between lower and upper duct subsystems and over upper duct subsystem. Topologically areas between curves 2 (6, 5) and 4 (7, 8) are separated by separatrix.

For rays trapped in duct the area under corresponding curve in the phase portrait is adiabatic invariant.

$$I = \oint x_2 dx_1 \tag{4.1}$$

Knowledge of the ray adiabatic invariant (4.1) at the site of transmitter allows to recalculate and obtain ray characteristics at the site of receiver and vice versa [4]. The method of ray adiabatic invariant can be used for slowly non periodically changing ducts. Usage of the method of ray adiabatic invariant for periodically modulated ducts is very restricted. Ray adiabatic invariant is constant only for disturbances that uniformly modify the structure of refractivity index profile.

5. Ducting in modulated atmosphere.

Periodical modulation of duct parameters destroys ray adiabatic invariant. Separate curves on phase portrait transform into phase layers. The width of phase layers depends on parameters of duct modulation. Very often ducting becomes impossible at all. Under 4% modulation of duct altitude with space wavelength of 160 km the phase portrait represented in Figure 2 has been transformed into phase portrait in Figure 3. The ducting area is significantly reduced although altitude gradients of refractivity index are almost the same. For former upper duct subsystem the ducting becomes impossible. Rays can be trapped in this structure for a very restricted time. They can penetrate from one subduct to another but then they go off duct subsystem. The similar is the behavior of rays near separatrix in lower duct subsystem. Ducting is possible only in internal region of lower elevated duct (curve 3 in Figure 2 and Figure 3). For another wavelengths of modulation or larger amplitudes the leakage of radio waves from ducts can be far more.

6. Ducting over periodical boundary.

To investigate ray tracing over periodical boundary the shape of lower boundary of duct was chosen in the form

$$r = R_E + a(1 + \sin(\frac{2\pi}{\lambda}t + \psi)) \tag{6.1}$$

where λ is space wavelength, a - amplitude, $t = R_E\varphi$, ψ - arbitrary phase shift. After mirror reflection the ray turns on angle β. For small amplitudes and wavelengths $a \ll R_E$, $\lambda \ll R_E$ and $2\pi a/\lambda \ll 1$ the angle β approximately equals

$$\beta \approx \beta_{\max} \cos(\frac{2\pi}{\lambda}t + \psi) \tag{6.2}$$

where $\beta_{\max} = 4\pi a/\lambda$. Behavior of rays over periodical boundary depends on numerical value of parameter ε that equals to the ratio of $\beta_{\max}$ to critical trapping angle α_c of rays in duct with smooth boundary, $\varepsilon = \beta_{\max}/\alpha_c$. For $\varepsilon \sim 0.04$ the results of calculation are shown in Figure 4. Parameter $\varepsilon \ll 1$ and influence of such boundary on rays is not very large. Only a part of rays near

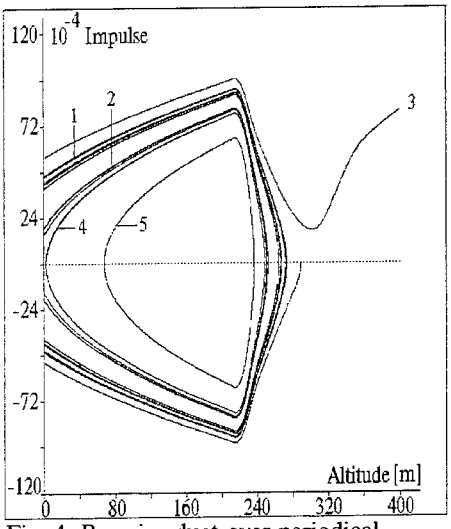


Fig. 4. Rays in duct over periodical boundary, ε≈0,04.

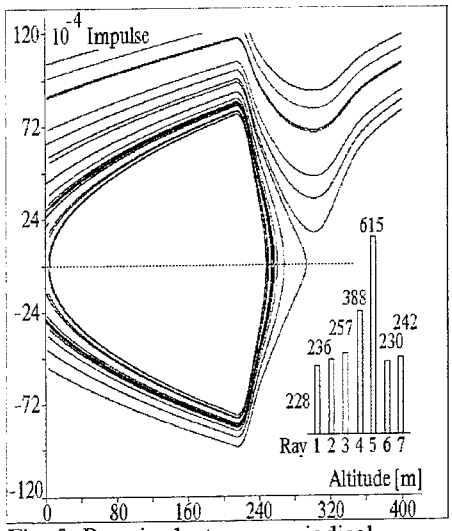


Fig. 5. Rays in duct over periodical boundary, ε≈7.

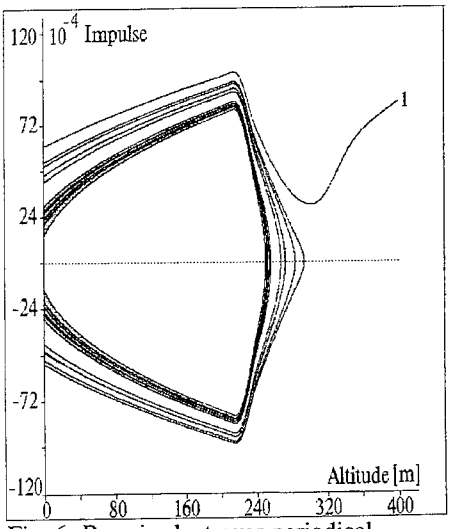


Fig. 6. Rays in duct over periodical boundary, ε≈0,34, ψ=π/2.

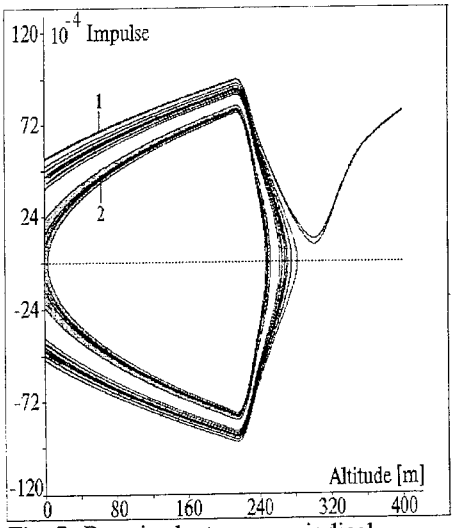


Fig. 7. Rays in duct over periodical boundary, ε≈0,34, ψ=0.

separatrix can not be trapped in duct. Periodical boundary can influence on ducting only through rays that can be reflected from the surface. For these rays curves in phase portrait can become multiperiodical. In Figure 4 curve 1 is three periodical and curve 2 is two periodical. For such boundary conditions can be used modified method of ray adiabatic invariant, where integrating in (4.1) is over several periods of ray oscillation in duct. For surface based ducts a share of rays reflecting from the boundary is larger than for elevated ducts and the effects are stronger. When parameter ε increases the curves in phase portrait similar to situation of periodically modulated refractive index begin to fill in separate layers. For large values of parameter ε the trapping of rays reflecting from the boundary becomes impossible. The only exception is situation, when space period T of ray oscillations in duct is multiple of wavelength $T = n\lambda$, $n = 1, 2, 3...$ and $\beta = 0$. In real situations it is possible to expect that only a narrow beam of rays can propagates in duct over periodical boundary for enough long distance for the case of large values of parameter ε. The most favorable is situation when rays reflect from the self focusing regions of boundary where the curvature is positive. For $\varepsilon \sim 7$ the results of ray tracing are shown in Figure 5. There were tracked 7 rays and the distribution of maximal length (in km) of ray paths in duct is represented as histogram in lower right corner in Figure 5. Knowledge of similar distribution allows to make estimations of expected field strength in ducts. The difference in elevation angles $\Delta\alpha$ of tracked rays was only 1% of critical trapping angle $\Delta\alpha/\alpha_c \leq 0.01$. But the lengths of ray paths differs approximately in 2.7 times. Parameter ε grows with shortening of λ. It is the case of large ε when propagation over periodical boundary differs from propagation in periodically modulated atmosphere. Modulation of atmosphere with wavelength far less than the period T of ray oscillations in duct have no large effect on ducting. For values $\varepsilon < 1$ behavior of rays depends on initial condition. In Figure 6 and Figure 7 are represented results of ray tracing for $\varepsilon \approx 0.34$. For Figure 6 phase shift was $\psi = \pi/2$, for Figure 7 phase shift $\psi = 0$. In both figures phase space is subdivided into two zones. It is zones of stability, where ducting for a long distance is possible. Ray corresponding to curve 1 in Figure 6 propagates in duct for a very long distance (more than 1000km), jumping from one zone into another. The same ray in Figure 7 leaves duct after 3 reflections from boundary. Another ray in Figure 7 propagates for a long distance in the same manner as first ray in Figure 6. So for values of ε near or less than 1 the behavior of rays is very sensitive to the conditions of ray reflection from the earth. Stability zones in Figures 6, 7 are separated by the gap. It is zone of instability. It determines the range of elevated angles at the reflection point for given phase shift ψ where ducting is impossible.

7. Summary.

Propagation of UHF/VHF waves is determined for many cases by the shape of terrain. Distance of radio communication and characteristics of received signals depend strongly on many processes connected with reflection from different areas of terrain, diffraction at sharp edges and scattering, produced by atmospheric turbulent fluctuations [1], [7]. For ducting conditions the distance of radio link can increase significantly but the structure of received signals can be very complicated. Periodicity in boundary conditions causes leakage of radio waves from ducts and determines the upper limit of radio link distance. From other side periodicity in the structure of duct parameters leads to mixing and coupling of rays and is responsible for additional phase delays of received signals. These effects can be very significant for assessment of the field strength. When maximal

inclination angle of tangent to the boundary surface is more than critical trapping angle the ducting in general situation becomes impossible. Reflection from periodical boundary can increase the distance of radio link only for the case of periodically modulated refractive index structure. After reflection the rays can be trapped in periodically modulated elevated duct and propagate for longer distance than for unmodulated case over periodical boundary.

Acknowledgment. The author is indebted to V.A.Popov for his numerical algorithm for fit method.

References

[1] Chamberlin, K. (1994), Overview of Terrain-Effect Modeling Using the Geometrical Theory of Diffraction, Beyond Line-Of-Sight Conference, session 9, 2-4 august, Austin, Texas, 1-17.

[2] Crane, R.K. (1981), A review of transhorizon propagation phenomena, *Radio Sci.*, **16**, N5, 649-669.

[3] Gossard, E.E. (1981), Clear weather meteorological effects on propagation at frequencies above 1 GHz, *Radio Sci.*, **16**, N5, 589-608.

[4] Gurevich, A.V., Tsedilina, E.E. (1979), Long distance propagation of short radio waves, M.: Nauka, 248.

[5] Helvey, R.A. (1994), Diurnal Variation in Oceanic Elevated Ducting, Beyond Line-Of-Sight Conference, session 5, 2-4 august, Austin, Texas, 1-7.

[6] Popov, A.V., Freizon, I.A., Zolotarev, I.P. (1990), Interaction of radio waves with the ionosphere, Moscow: Nauka, 89-96.

[7] Kukushkin, A.V., Freulicker, V.D. (1987), Beyond horizon propagation of UHF radio waves over the sea, *Radiophysics*, XXX, N7, 811-839.

[8] Patterson, W.L. (1994), Overview of the Electromagnetic Propagation Program at the Naval Command, Control, and Ocean Surveillance Center, RDT&E Division, Beyond Line-Of-Sight Conference, session 6, 2-4 august, Austin, Texas.

[9] Philbrick, C.R., Blood, D.W. (1994), Refractive Propagation Effects measured by Lidars, Beyond Line-Of-Sight Conference, session 4, 2-4 august, Austin, Texas, 1-21.

[10] Stephansen, E.T. (1981), Clear-air propagation on line-of-sight paths: A review, *Radio Sci.*, **16**, N5, 609-629.

[11] Zolotarev I.P. (1994), Effects of periodical modulation of atmospheric ducts on propagation of UHF/VHF waves, Beyond Line-Of-Sight Conference, session 8, 2-4 august, Austin, Texas.

[12] Zolotarev I.P. (1994), Propagation of UHF Waves in Periodically Modulated Ducts, *Turkish Journal of Physics*, **18**, N11, 1235-1239.

SESSION 15:

PARALLELIZATION OF EM CODES

Chairs: J. Volakis, A. Chatterjee

ADVANCES IN TIME-DOMAIN CEM USING MASSIVELY PARALLEL ARCHITECTURES

Chris Rowell, Vijaya Shankar, William F. Hall, and Alireza Mohammadian
Rockwell Science Center

Abstract

Accurate and rapid evaluation of radar signature for alternative aircraft/store configurations would be of substantial benefit in the evolution of integrated designs that meet RCS requirements across the threat spectrum. Finite-volume time domain methods offer the possibility of modeling the whole aircraft, including penetrable regions and stores, at longer wavelengths on today's supercomputers and at typical airborne radar wavelengths on the massively parallel teraflop computers of tomorrow. To realize this potential, practical means are being developed for the rapid generation of grids on and around the aircraft, and numerical algorithms that maintain high order accuracy on such grids are being constructed.

A structured grid and an unstructured grid-based finite-volume, time-domain Maxwell's equation solver has been developed incorporating modeling techniques for general radar absorbing materials. Using this work as a base, the goal of the CEM effort is to define, implement, and evaluate rapid prototype signature prediction, addressing many issues related to 1) physics of electromagnetics, 2) efficient and higher-order accurate algorithms, 3) boundary condition procedures, 4) geometry and gridding (structured and unstructured), 5) computer architecture (SIMD and MMD), and 6) validation.

Introduction

The ability to predict radar return from complex structures with layered material media over a wide frequency range (100 MHz to 20 GHz) is a critical technology need for the development of stealth aerospace configurations. Traditionally, radar cross section (RCS) calculations have employed one of two methods: high frequency asymptotics, which treats scattering and diffraction as local phenomena; or solution of an integral equation (in the frequency domain) for radiating sources on (or inside) the scattering body, which couples all parts of the body through a multiple scattering process. A third approach is the direct integration of the differential or integral form of Maxwell's equations in the time-domain.

The time-domain Maxwell's equations represent a more general form than the frequency-domain vector Helmholtz equations, which are usually employed in solving scattering problems. A time-domain approach can, for instance, handle continuous wave (single frequency) as well as a single pulse (broadband frequency) transient response. Frequency-domain-based methods usually provide the RCS response for all angles of incidence at a single frequency, while time-domain based methods provide solutions for many frequencies from a single transient calculation. Also, in a time-domain approach, one can consider time-varying material properties for treatment of active surfaces. By using Fourier transforms, the time-domain transient solutions can be processed to provide the

frequency-domain response. Frequency-dependent (dispersive) and anisotropic material properties can also be included within the time-domain formulation.

CEM is a critical technology in the advancement of future aerospace development through supercomputing. As we transition from the present Gigaflops to the next generation Teraflops computing, CEM will become integral to aerospace design not only as a stand alone technology but also as part of the multidisciplinary coupling that leads to well optimized designs.

Objectives

Toward establishing a computational environment for performing multidisciplinary studies, the initial goal is to advance the state-of-the-art in CEM with the following specific objectives.

1) Apply algorithmic advances in Computational Fluid Dynamics (CFD) to solve Maxwell's equations in general form to study scattering (radar cross section), radiation (antenna), and a variety of eletromagnetic environmental (electromagnetic compatibility, shielding, and interference) problems of interest to both the defense and commercial community.
2) Establish the viability of MIMD massively parallel architectures for tackling large scale problems not amenable to present day supercomputers.
3) Mature the CEM technology to the point of being able to perform coupled CFD/CEM optimization design studies.

CEM Issues

Proper development of a CEM capability appropriate for all aspects of aerospace design must consider various issues associated with electromagnetics. Some of them are:

1) Maxwell's Equations

In order to apply conservation principles (for example, in fluid dynamics mass, momentum, and energy are conserved), many of the governing equations representing appropriate physical processes are written in conservation form. The general form of a differential conservation equation can be written as

$$Q_t + E_x + F_y + G_z = \text{Source} \tag{1}$$

where Q is the solution vector and E, F, and G are the fluxes in x, y, and z coordinate directions, respectively. The conservation form readily admits weak solutions such as shock waves.

The integral form of the conservation laws which can easily be derived from the differential form by integrating Eq. (1) with respect to x, y, z over any conservation cell whose volume is V.

$$\begin{aligned} \int\int\int_V \left(\frac{\partial Q}{\partial t} + \frac{\partial E}{\partial x} + \frac{\partial F}{\partial y} + \frac{\partial G}{\partial z} \right) dx\, dy\, dz \\ = \int\int\int_V S\, dx\, dy\, dz = \widetilde{S} \quad . \end{aligned} \tag{2}$$

This can be rewritten in vector notation as

$$\frac{\partial}{\partial t}\int\int\int_V Q\,dx\,dy\,dz + \int\int\int_V \left(\vec{\nabla}\cdot\vec{\mathcal{F}}\right) dx\,dy\,dz = \widetilde{S} \quad . \tag{3}$$

In the above,

$$\vec{\mathcal{F}} = E\hat{j} + F\hat{k} + G\hat{l} \quad . \tag{4}$$

Applying the Gauss divergence theorem, we can convert the volume integral into a surface integral.

$$\frac{\partial}{\partial t}\left(\widetilde{Q}V\right) + \int\int_s \left(\vec{\mathcal{F}}\cdot\hat{n}\right) ds = \widetilde{S} \quad . \tag{5}$$

In the above equation, the cell average of the dependent variables are denoted by $\widetilde{Q}$. The outward unit normal at any point of the boundary surface of a cell has been denoted by $\hat{n} = \hat{n}_x\hat{j} + \hat{n}_y\hat{k} + \hat{n}_z\hat{l}$.

$$\widetilde{Q} = \frac{\int\int\int_V Q dV}{\int\int\int_V dV} \quad . \tag{6}$$

The integral form of the conservation laws given by Eq. (5) defines a system of equations for the cell average values of the dependent variables.

Maxwell's equations in their vector form are

$$\frac{\partial B}{\partial t} = -\nabla\times\mathcal{E} \tag{7}$$

and

$$\frac{\partial D}{\partial t} = \nabla\times\mathcal{H} - J \quad . \tag{8}$$

The divergence conditions $\nabla\cdot D = \rho$ and $\nabla\cdot B = 0$ are derived directly from Maxwell's equations, where $\nabla\cdot J = -\frac{\partial\rho}{\partial t}$. The vector quantities $\mathcal{E} = (\mathcal{E}_x, \mathcal{E}_y, \mathcal{E}_z)$ and $\mathcal{H} = (\mathcal{H}_x, \mathcal{H}_y, \mathcal{H}_z)$ are the electric and magnetic field intensities, $D = (D_x, D_y, D_z)$ is the electric displacement, $B = (B_x, B_y, B_z)$ is the magnetic induction, and $J = (J_x, J_y, J_z)$ is the current density and ρ is the charge density. The subscripts x, y, z in the vector representation of $\mathcal{E}$, $\mathcal{H}$, B, and D refer to components in respective directions.

Maxwell's equations can also be cast in integral conservation form as

$$\frac{\partial}{\partial t}\int\int_V\int\begin{pmatrix}\vec{B}\\ \vec{D}\end{pmatrix} dV + \int_S\int\begin{pmatrix}\hat{n}\times\vec{E}\\ -\hat{n}\times\vec{H}\end{pmatrix} dS = 0 \quad , \tag{9}$$

where the six components of $\vec{\mathcal{F}}\cdot\hat{n}$ in Eq. (5) are $(\hat{n}\times E, -\hat{n}\times H)$.

2.0 Finite–Volume Treatment

The major feature of the present discretization approach that distinguishes it from other finite–volume and finite–difference procedures is that the electric and magnetic field

unknowns are co-located in both space and time, rather than being assigned to two interpenetrating spatial grids and separated a half-step in time. These field unknowns are the volume averages of E and H within each cell in the space-filling grid.

An algorithm that maintains second-order accuracy in both space and time can be constructed as follows (advancing from time level m to $m+1$):

$$\langle Q\rangle_\alpha^{m+1/2} = \langle Q\rangle_\alpha^m - \frac{\Delta t}{2V_\alpha}\int_{\partial\alpha} \hat{n}\cdot F\left(Q_\alpha^{*m}\right) dS$$

$$K_\alpha^m = \frac{1}{V_\alpha}\int_{\partial\alpha} \hat{n} Q_\alpha^{*m} dS = \frac{1}{V_\alpha}\int_{\partial\alpha} \hat{n}\left(\hat{n}\times\left\{\hat{n}\times\left[\langle Q\rangle_\alpha^m - Q_\alpha^{*m}\right]\right\}\right) dS$$

$$Q_\alpha^{m+1/2}(\vec{r}\,) = \langle Q\rangle_\alpha^{m+1/2} + (\vec{r}-\vec{r}_\alpha)\cdot K_\alpha^m \quad \text{for } \vec{r} \text{ in cell } \alpha$$

$$\langle Q\rangle_\alpha^{m+1} = \langle Q\rangle_\alpha^m - \frac{\Delta t}{V_\alpha}\int_{\partial\alpha} \hat{n}\cdot F\left(Q_\alpha^{*(m+1/2)}\right) dS \quad .$$

Here we have written Maxwell's equations symbolically as

$$\frac{\partial Q}{\partial t} + \nabla\cdot F(Q) = 0 \quad , \quad Q = \left(\vec{D},\vec{B}\right) \quad .$$

and the solution of the Riemann problem just inside a cell interface is denoted Q^* (Ref. 1).

3) Geometry/Gridding

Problems in CEM involve arbitrarily shaped three-dimensional geometries that need to be represented properly in the computer simulation. In addition to the external shape, CEM also requires modeling the interior of the penetrable structure. Depending on the formulation (differential or integral), one may choose either a structured grid or an unstructured grid setup.

. Two gridding issues that need to be addressed in EM computations are: 1) number of grid points per wavelength to properly represent the fields in and around a scatterer; and 2) how far should the outer boundary be placed from the scattering object to adequately simulate the nonreflecting boundary condition. In general, the number of points/wavelength is not determined by wavelength alone, and involves the body dimensions (characteristic body size with respect to wavelength) also. The outer boundary location, theoretically, can be right on the body surface itself; however, the computational implementation of nonreflecting boundary conditions requires the outer boundary at a few (2 to 5) wavelengths away from the surface. Again, if one can construct higher order accurate implementations of nonreflecting boundary conditions, the outer boundary can be brought very close to the scattering surface. In general, the necessary grid resolution is provided only around and near the body surface. Between the body and the outer boundary, the mesh is allowed to stretch resulting in very crude (3 to 5 points per wavelength) meshes near the outer boundary regions.

The free space wavelength is reduced to smaller values inside a material (as ϵ and μ become large, the speed of propagation, $c = \frac{1}{\sqrt{\epsilon\mu}}$, goes down, causing the wavelength to scale accordingly). Thus, the grid resolution must take into account material properties to adequately resolve the fields inside material zones.

The number of grid points per wavelength required depends on the order of accuracy of the numerical scheme. A second-order accurate scheme usually requires at least ten grid points per local wavelength. One may be able to use a higher order scheme and minimize the number of grid points. However, as the order of accuracy goes up, the scheme will also require more computations per grid point, which may offset the execution savings with fewer grid points.

The requirement that the fields are resolved accurately with proper grid resolution makes CEM problems computationally intensive, requiring large scale supercomputing. For example, to compute the radar cross section of a typical aircraft at 1 GHz, even if one used 10 grid cells per wavelength, it will require tens of millions of grid points.

4.0) Massively Parallel Computing

4.1 Parallel Implementation

With the emergence of massively parallel computing architectures with potential for teraflops performance, any code development activity must effectively utilize the computer architecture in achieving the proper load balance with minimum internodal data communication.

The structured finite-volume code was originally developed and optimized for vector computer architectures. The implementation of the code on a distributed memory parallel architecture was accomplished by re-using much of the original vector code. Additional coding was added for handling inter-processor communication and other functions unique to the parallel implementation.

4.2 Parallelization Strategy

For the structured formulation of the finite-volume code the computational domain surrounding the target geometry is composed of 3-dimensional 6 sided volumes of grid points called zones or blocks. Each side or face of a zone either connects to another zone or has a boundary condition defined on that face (perfect conducting surface, outer boundary, etc.). The parallel algorithm takes advantage of this multi-zonal gridding capability in order to divide work among processors. The various zones are grouped onto processors, with each processor obtaining a solution for the cells within its own local set of zones.

4.3 Communication Requirements

The solution procedure does not allow for processors to proceed completely asynchronously. Solving for cells on zone faces that are connected to other zones requires information from within the adjacent zone. This information may be available locally if the adjacent zone resides on the same processor, or message passing may be required if the adjacent zone resides on another processor. This boundary update message passing or flux transfer message passing is done twice per solution time step and forms the bulk of the parallel code's message passing requirements.

4.4 Load Balancing

Load balancing is achieved by mapping zones onto processors. Perfect load balancing requires that each processor have the same number of zones, each containing the same number of grid points and equal numbers and types of boundary condition cells. Simple geometries may usually be zoned in such a manner as to obtain perfect load balancing. For complex geometries perfect load balancing is much more difficult, but adequate load balancing may usually be obtained by mapping a close to equal number of grid points onto each processor.

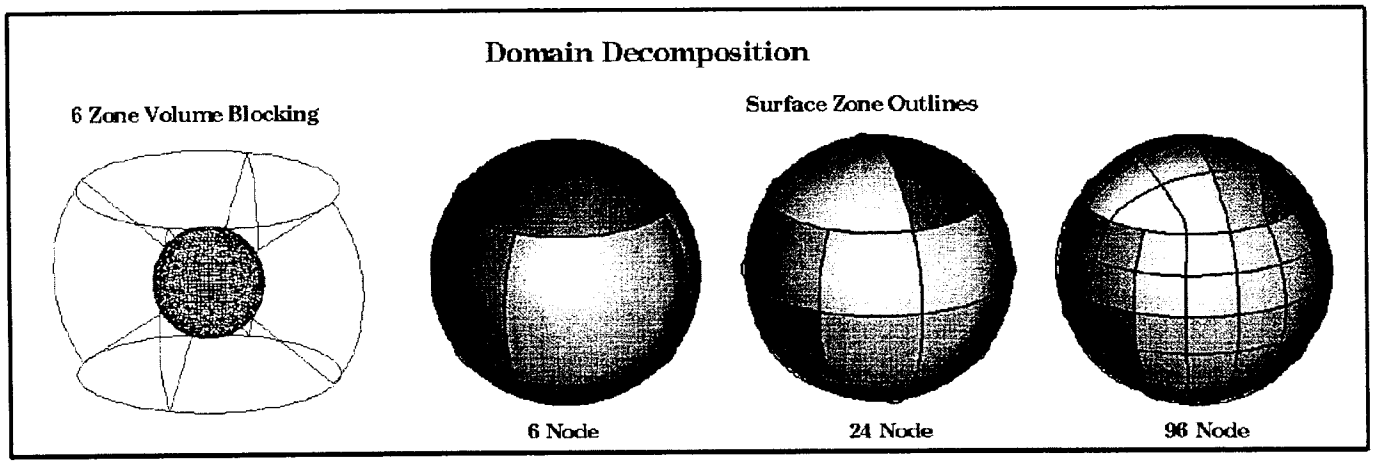
4.5 Scalability Results

Validation and timing studies have been performed on a 512-node nCUBE and a 208-node Intel Paragon. Currently the code shows good scalability on evenly balanced test cases. These cases typically had simple gridding requirements and a straight forward domain decomposition. The results show that inter-processor communication due to flux transfer never becomes a dominant time factor even on problems with large numbers of grid points run on many processors. The sphere test case illustrated in Fig. 1 shows how problem size and number of processors can be increased while solution time remains level. Perfectly conducting sphere grids were run on 6, 24, and 96 processors of the Intel Paragon. The number of grid points per processor remained constant at approximately 60,000 resulting in total grid sizes of approximately 0.35, 1.4, and 5.7 million grid points for the three cases. Since increasing the number of processors results in an increased number of zonal interfaces, flux message passing requirements increase throughout the system. Despite this increase in required message passing, communication times did not change appreciably.

Complex problems such as full scale fighter geometries also show encouraging results. Figure 2 shows timing results and zoning for the VFY218 fighter gridded for a frequency of 500MHz with a 10 point per wavelength resolution. A total of 58 zones and 2.2 million grid points were required. The grid was run on an Intel Paragon using 28, 61, and 128 processors. Preliminary timing data reveals that communication overhead remains at between 1 and 2.5 percent of the total solve time and that solution speedup occurs as the problem is distributed over more processors. Speedup may be improved by addressing load balancing issues arising from complex zoning arrangements.

References

1. A.H. Mohammadian, V. Shankar, and W.F. Hall, "Computation of Electromagnetic Scattering and Radiation using a Time-Domain Finite-Volume Discretization Procedure," Computer Phys. Comm., Vol 68, p.175, 1991.

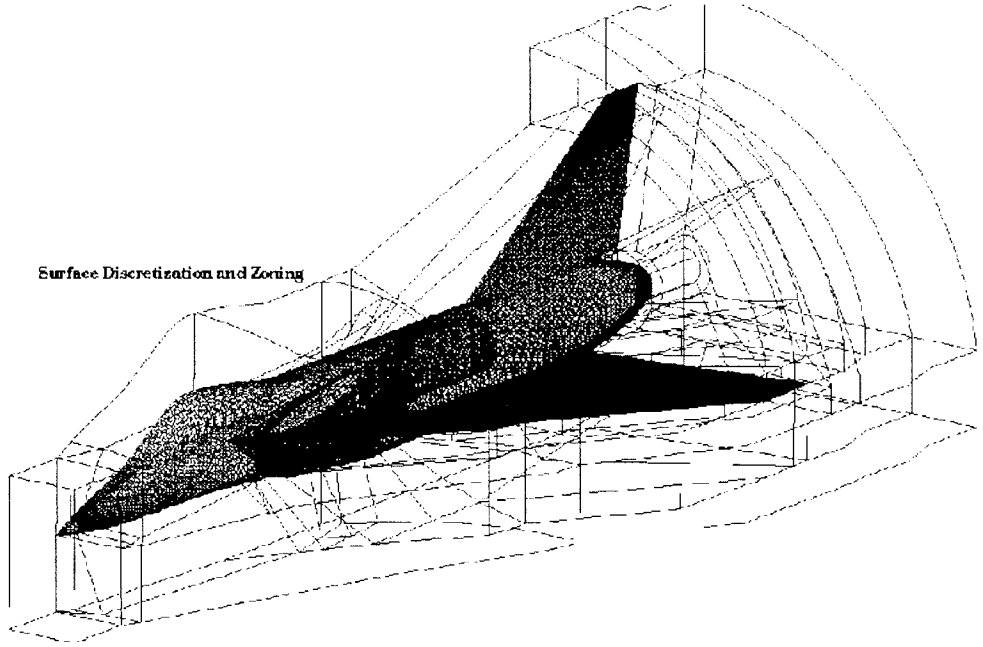


Timing Results

Nodes	6	24	96
Grid Pts/Node	59,049	59,049	59,059
Total Grid Pts	354,294	1,417,176	5,668,704
Flux Time	0.044	0.052	0.0349
Solve Time	4.515	4.518	4.509

(Time - seconds per time step)

Figure 1. Parallel CEM for a sphere



Preliminary Timing Results

Nodes	28	61	128
Grid Pts/Node	79,047	40,860	20,620
Flux Time	0.106	0.065	0.063
Solve Time	8.324	4.433	2.605

(Time - seconds per time step)

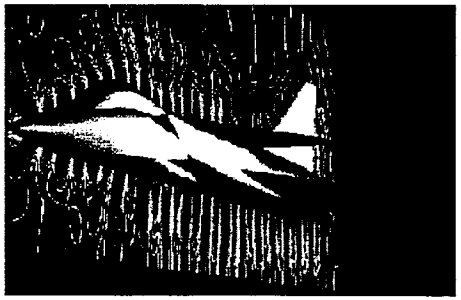


Figure 2. Parallel CEM for a fighter

Parallel Solutions of Maxwell's Equations on the Meiko CS-2

Niel Madsen, Bill Eme, David Steich, Grant Cook

Lawrence Livermore National Laboratory
Livermore, CA 94550

Abstract

The efficient numerical solution of Maxwell's equations in the time-domain on parallel computers is a non-trivial task. It is even more challenging when the numerical solution method involves the use of unstructured non-orthogonal and multi-element type grids.

This paper describes some efforts and experiences in utilizing distributed memory parallel computers like the Meiko CS-2 together with the DSI3D algorithm. Grid generation remains the most difficult part of accurate numerical EM simulation. However, this process will not be discussed as it is largely independent of the parallel computation issues.

The parallel solution paradigm chosen is that a single large problem will be solved through the use of multiple processors. This is in contrast to the "embarrassingly parallel" approach of solving many independent problems simultaneously (one per processor). The choice of this paradigm necessitates the partitioning of the single large problem among the available processors. In order for this to be efficient, two conditions must be met: 1) each processor should have an equal workload, and 2) the amount of inter-processor communication should be minimized. Several approaches are presented and discussed.

Once the problem has been partitioned, the inter-processor communication issues must be addressed. It is assumed that at problem startup time, a given processor knows only about its local part of the grid and knows nothing about any of the other processors' data. A definitive strategy for each processor to use to discover its neighbors and related required communication is presented. This, of course, requires significant inter-processor communication. As some variables which exist on the grid partition boundaries may be shared between two or more processors, questions of "ownership" arise and simple techniques for resolving asynchronous communication conflicts are established.

As some of the newer parallel computer processors are capable of processing vector data more efficiently, performance optimization through vector processing methods are used. Performance improvements of factors up to 20 have been noted. Specific performance figures for the Meiko CS-2 are presented.

Overall performance speedup data will be presented for the geometry preprocessor and the time-stepping processor. High efficiencies are achieved provided that there is a sufficient workload (problem size) maintained on each processor.

Finally, performance issues related to outer absorbing radiation boundary conditions and near-to-far field transformations are discussed.

Parallelization of the CARLOS-3D Method of Moments Code

J.M. Putnam and D.D. Car
McDonnell Douglas Corporation
J.D. Kotulski
Sandia National Laboratories

Abstract
Flat triangular patches and linear roof-top basis functions (S. M. Rao, D. R. Wilton, and A. W. Glisson, IEEE AP Trans., 30, 409-418, May 1982) have been used extensively over the past few years to model the scattering and radiation from complex three-dimensional objects. CARLOS-3D is a three-dimensional scattering code based on a Galerkin method of moments formulation employing roof-top basis functions to model fully arbitrary geometries composed of multiple conducting and homogeneous dielectric regions. The code was developed under the sponsorship of the Electromagnetic Code Consortium (EMCC) and is available to qualified users. Various boundary conditions including conducting, dielectric, resistive, and impedance can be specified on selected surfaces composing the target. Current continuity between connected surfaces is rigorously enforced using a general indexing scheme in the code to implement all of the boundary and junction conditions. The code is based on a Galerkin matrix operator notation which makes the main structure of the code independent of the geometry representation and basis functions used. Matrix symmetry is exploited during the system matrix fill procedure to reduce run times, and the symmetric system matrix is stored in packed form to reduce memory requirements. Geometric symmetry is also used to further reduce both the computational and memory requirements for large symmetric targets. The code has been validated against measured data and other codes for a large number of targets and is currently used by over 50 aerospace companies and government agencies.

This paper describes how the serial code was ported to the Intel Paragon. Details are given outlining the key steps in the parallelization process, along with special features in the code which facilitated the effort. The focus will be primarily on the parallel implementation of the matrix fill, right-hand-side fill, and the far-field computation. The solution for the current coefficients relies upon existing parallel solver packages. The code has been adapted to both the Intel Pro-Solver-DES package for out-of-core solutions and an in-core solver developed at Sandia.

Results are presented showing the performance of the code for some large scattering problems. Scaling of the computational resources with problem size is also addressed, along with other issues related to the parallel implementation.

Introduction

CARLOS-3D is a general-purpose method of moments (MM) code for computing the scattering from complex three-dimensional targets. It is based on a McDonnell Douglas Aerospace proprietary code

CARLOS, which models antenna and scattering problems for 2D and 3D geometries. CARLOS-3D was developed under the sponsorship of the Electromagnetics Code Consortium (EMCC), and is available to qualified organizations through them, subject to US export control laws. The code uses the MM technique, with Galerkin testing to solve the Stratton-Chu surface integral equations for a user specified geometry. All of the surfaces describing the scatterer, consisting of conducting surfaces and boundaries between different dielectric regions are replaced with equivalent electric (J) and magnetic (M) currents. The code solves for these induced equivalent currents, which are then used to compute the scattered far-fields.

Code Description

Arbitrary 3D surfaces are modeled using flat triangular facets, with the electric and magnetic currents expanded in terms of the Rao, Wilton, Glisson roof-top functions [1]. A roof-top function spans the two facets forming each interior edge of a surface. At junction edges, which are formed by the intersection of two or more surfaces, half roof-top expansion functions are used to expand the currents. Current continuity across a junction is enforced by equating the unknowns associated with each of the half roof-top functions for the edge. Junction edges are determined automatically for surfaces which have common node points along a line of intersection between surfaces.

Complex geometries, which are composed of multiple conducting and bulk dielectric regions can be modeled. Various boundary conditions can be imposed separately on each of the surfaces comprising the target. For a given geometry, each dielectric region is given a number, and every surface which forms a boundary between different regions must be entered as a faceted surface. Infinitesimally-thin conducting, resistive, and impedance sheets must also be defined. The user must specify both the interior and exterior regions for each surface, along with the boundary condition to impose. Resistive and magnetically-conducting boundaries can be either embedded in a region, or be defined on the interface between different regions. Tapered resistive and impedance surfaces are modeled by specifying values for each facet forming the surface. Impedance (Leontovich) boundary conditions are modeled as an equivalent combination resistive/magnetically-conducting boundary.

The Stratton-Chu integral equations can be solved using several different formulations. For conducting surfaces, either the electric field integral equation (EFIE), the magnetic field integral equation (MFIE), or the combined field integral equation (CFIE) can be used. The coupling parameter in the CFIE formulation is specified separately on each surface, allowing the formulation to be used for geometries with both open and closed surfaces. For dielectric boundaries, the PMCHW formulation (after Poggio, Miller, Chu, Harrington, and Wu) is used. Galerkin testing, in conjunction with the form of the current expansions, results in a symmetric system of equations whenever the PMCHW/EFIE formulation is used. In addition, the formulations implemented for treated surfaces also result in symmetric matrices which require only half of the matrix elements to be computed and stored.

Scattering from apertures, cavities, and gaps in a conducting surface can be modeled using an infinite ground plane option. Image theory is used to model both the source and the induced currents on all of the surfaces which are either conducting, dielectric or treated. The resulting system of equations is again symmetric.

Features

The CARLOS-3D code has a flexible and modular structure which facilitates the incorporation of new features. The major components of the code are independent of the surface representation (i.e., flat facets, quadrilaterals, curved surfaces, etc.), and of the basis functions which are used to approximate the surface currents, permitting the code to be easily adapted to advanced basis functions. The section of code which generates the system matrix for an arbitrary geometry is written in terms of a generalized Galerkin matrix operator notation [2]. These operators result from testing either the integral operators in the Stratton-Chu equations, the equivalent currents directly, or the incident fields. The subroutines which assemble the system matrix and right-hand-side vector refer to these generic operators. The generic operators then reference routines which are specifically written for a given basis function type. Only the geometry input routine, and these specialized Galerkin operator routines depend upon the surface representation and basis functions used. Symmetry relations, which can be established for the Galerkin matrix operators, are used to efficiently fill the system matrix by eliminating redundant calculations.

A systematic approach [3] is used to generate the matrix equation, $\mathbf{ZI}=\mathbf{V}$, for an arbitrary geometry with various boundary conditions imposed on the surfaces. This approach is based on a simple indexing scheme, which assigns an index number to each edge (roof-top or half roof-top function) defining the entire geometry. The index number for a particular edge specifies the location within the column vector, $\mathbf{I}$, of either the $\mathbf{J}$ or $\mathbf{M}$ current coefficient associated with that edge. This indexing is performed in the geometry input routine, and is based on the boundary condition which is imposed on each surface. The boundary condition is used to define the equivalent currents which reside on the surface, and the relationship between the interior and the exterior current coefficients. Current continuity across junction edges connecting separate surfaces is enforced by equating the indices associated with the half roof-top functions for the edge. The matrix assembly routine is based on the index associated with each basis function (edge), and not on the explicit form of the basis function or the surface representation. The matrix assembly routine in CARLOS-3D has been used to model 2D, body-of-revolution (BOR), and wire geometries with overlapping triangle function expansions. It has also been used for 3D geometries modeled with quadrilateral patches and higher order parametric basis functions.

CARLOS-3D can efficiently model arbitrary geometries with right/left and/or top/bottom symmetry, using only a half or quarter of the geometry. The Galerkin matrix operators defining the interactions between symmetric parts of the target are related, allowing the matrix equation to be decoupled into either two of four smaller systems. Each of the smaller systems of equations contains either approximately a half or quarter of the unknowns from the original system, and this decoupling is independent of the source excitation. These decoupled equations are filled and solved sequentially, reducing the memory required to store the matrix by a factor of either four or sixteen. By filling each system separately, memory requirements are reduced, but the matrix fill time is equivalent to that of the original system assuming no symmetry.

Matrix elements in CARLOS-3D are computed using a combination of analytic and numerical procedures. The algorithm is facet-based in order to eliminate redundant calculations. The matrix elements are evaluated using adjustable quadrature formulas to compute the double surface integrals over pairs of triangular facets. Normalized area coordinates, for flat triangular regions, are used to

compute generic double surface integrals between a pair of triangles which are then used to compute the interactions between all edge combinations. Self-term computations are based on an analytic procedure which reduces the four-fold integral to a double integral which is integrated numerically, with the singular part evaluated analytically. Near terms are evaluated using standard singularity-extraction methods, with the adjustable quadratures depending upon the test and source facet separation distance. This allows the matrix fill procedure to be optimized for both speed and accuracy.

The parallelization of CARLOS-3D was facilitated by an option in the code which can be used to specify an arbitrary sub-block of the **Z** matrix to fill. This block-fill option is implemented in a manner which minimizes the number of redundant matrix element evaluations, and only requires memory to store the sub-block being generated. The entire system matrix can be generated by partitioning the matrix into sub-blocks, and then filling each sub-block separately, with only a modest increase in execution time. This block-fill option has been used to adapt the code to out-of-core solver packages for solving large problems on a workstation. It is also the key feature which is used in the parallelization of the code which is described below.

Validation

CARLOS-3D has been extensively validated against both measured data and other numerical methods. Conducting and coated sphere results have been compared with Mie series solutions. Flat plate calculations have been compared with the measured data for all five of the EMCC benchmark targets [4], and for some large kite-shaped plates at MDA. Typically, converged results are obtained using 75 to 100 triangular facets per square wavelength of surface area. Additionally, the MM/BOR code CICERO [5] has been used to validate the modeling of junctions and dielectric materials for circular cylinders and cones. A circular cylinder which is half conducting and half Plexiglas [4, 6] was used to validate the modeling of junctions in CARLOS-3D. This case validates the junction modeling of the edges which form the intersection between the three surfaces (i.e., outer conductor, dielectric, and inner conductor). Other test geometries, including an air-coated plate and a conducting cube with either one or two attached air cubes were also used to ensure that junctions between intersecting surfaces with different boundary conditions are modeled correctly.

The formulations contained in CARLOS-3D for resistive, magnetically-conducting, and impedance surfaces have been tested against the results from other codes, and for special limiting cases. These limiting cases have been used extensively as a way for checking for self-consistency of the formulations. As an example, the boundary conditions at a dielectric boundary can be modeled as a resistive boundary between the two dielectrics, as the resistance becomes large. Similarly, as the resistance approaches zero, the surface becomes conducting, and the magnetic currents and interior electric currents should vanish. Both of these cases take a simple boundary condition and model it as the limit of a more complicated boundary condition involving additional unknowns. Additionally, thin-sheet formulations have been shown to be consistent with the equivalent formulation involving two distinct regions with the same material properties.

Parallelization

The parallel version of CARLOS-3D is structured so that it can be run either on a workstation, or on an Intel Paragon machine. All of the parallel logic is embedded in just a few routines which are only

executed on the parallel machine. The workstation version of the code can be easily ported to the Intel by following a list of conversion steps. This allows most of the code development to be performed on a workstation, with final testing done on the parallel machine. Also, the input data for both the serial and parallel versions is identical. In the parallel version, all of the input geometry data is read and processed on a single node (node zero). The geometry data is then sent to all of the other nodes. Parallel logic is used to generate the MM system matrix and right-hand-side (RHS) excitation vectors on all of the nodes. A parallel solver is then called to perform the matrix factorization and solution of the surface current coefficients. The scattered far-fields are computed in parallel, with the final results sent to node zero for output.

The strategy in the parallelization effort was to rely on existing parallel solver technology for the Paragon, and to simply adapt the code to the solver software. The conversion was basically performed in three steps. The first step was actually done for the purpose of implementing an out-of-core solution package into the serial code, and is now used extensively in the parallel code. The matrix fill procedure was modified so that an arbitrary sub-block of the MM system matrix could be generated. Logic was included to skip over any matrix element calculations which do not contribute to the selected sub-block. Since each triangular facet can have three unknowns associated with it, the ordering of the facets and edges (unknowns) can adversely affect the efficiency of the block-fill procedure. A Reverse Cuthill-McKee algorithm was included to reorder the facets and edges. Second, the serial code was moved to the parallel machine, and logic was included to perform the reading and sending of the geometry data. Finally, specific routines were written which interface CARLOS-3D to each solver package which is used. The parallel solver-specific routines generate the matrix and excitation vectors, call the solver, and compute the far-fields. Therefore, the code can be easily interfaced to other future solver packages by simply writing a new routine specific to that solver. For this work, we interfaced CARLOS-3D to both the Intel Paragon ProSolver-DES package for large out-of-core solutions, and to an in-core solver developed at Sandia National Laboratories.

For the ProSolver-DES interface, the MM system matrix is partitioned into sub-blocks. Care is taken to balance the workload between the nodes during the generation of the RHS vectors and the matrix sub-blocks. Since the RHS vector generation is much faster than the matrix generation, only selected nodes are used to perform the former task in order to reduce contention for the I/O channels to the out-of-core file system. Additionally, for symmetric targets, disk space is reused for storage of the system matrix and RHS files during the solution of the decoupled systems of equations.

For the Sandia solver interface, the matrix is partitioned so that each node is responsible for both a part of the system matrix and matrix of RHS vectors. The block-matrix fill option is used to generate the part of the matrix for which the node is responsible. The appropriate RHS vectors are also computed for each node, and then the solver is called. The parts of the permuted solution vectors which reside on each node are then used to compute the far-fields.

Results and Performance

The computation of the RCS for the VFY 218 aircraft and a one meter almond will now be discussed. These problems were run on the Sandia Paragon installation which has a normal configuration of 1840 compute nodes that are distributed in a 16 x 115 mesh. CARLOS-3D was interfaced to the Sandia in-core solver and the results are collected below.

The first problem geometry is the VFY 218 aircraft. This model contains 38,922 triangular patches and 19,840 nodes, and at 300 MHz the spatial resolution is 204 facets per wavelength squared. Using one symmetry plane two systems are solved, one with 29,381 and the second with 29,002. The run times for this problem with 1 and 181 RHS vectors are given in Table 1 and the monostatic RCS is shown in Figure 1.

Table 1: VFY 218 Job Statistics

Operation	Time(sec) (1 RHS)	Time(sec) (181 RHS)
I/O and Pre-processing	34.9	34.9
matrix assembly	846.0	846.0
system solve	965.0	1254.0
post-processing	20.1	20.1
Total	1866.0	2155.0

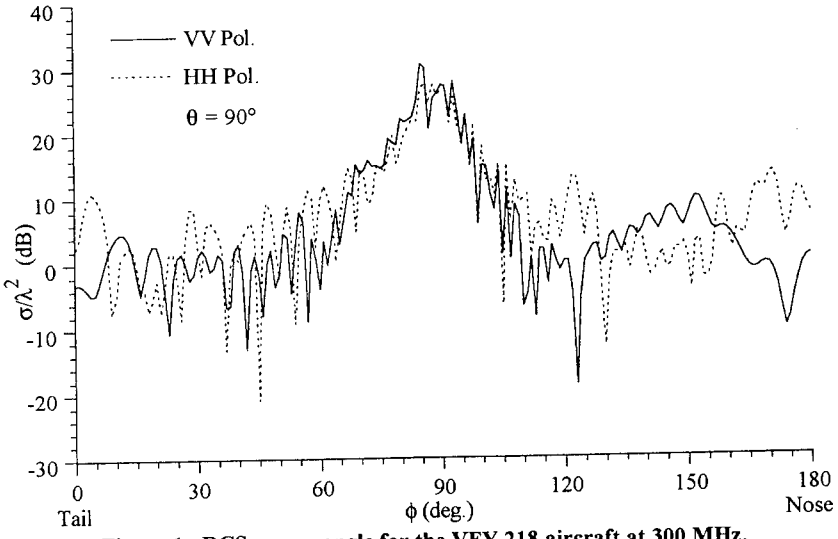


Figure 1. RCS versus angle for the VFY 218 aircraft at 300 MHz.

It is pointed out that the solver performance for 1 RHS is 137 Gflops/s. This was obtained by optimizing the solver to the machine topology, including the additional I/O nodes on the machine, and using the second processor on each node for computation. Normally, it is used for communication. The effect on performance of mapping the matrix to a square mesh is also given in Table 2.

Table 2: Solver Performance, 29381 unknowns

Paragon Mesh (matrix map)	RHS	Solve Time (sec)	Gflops/s	Mflops/s (node)
43 x 44	1	899.6(*)	75.19	37.9
16 x 115	181	637.3	106.1	57.7
16 x 119	1	490.8	137.8	72.4

(*) only one processor used for computation

The performance in Table 2 shows the effect of multiple RHS vectors using only one processor for computation and using a matrix mapping that does not match the machine topology.

The next problem considered is the 1 meter almond at 6 GHz. This model contains two planes of symmetry resulting in solving four systems of equations. These consist of 9984, 9828, 9828, and 9672 unknowns. The solver performance is shown for this problem in Table 3 for 9984 unknowns and 181 RHS vectors. The monostatic RCS is shown in Figure 2.

Table 3: Almond with 9984 unknowns and 181 RHS

Paragon Mesh (matrix map)	Solve Time (sec)	Gflops/s	Mflops/s (node)
16 x 16	273.1	9.7	37.9
16 x 32	163.9	16.2	31.6
16 x 115	57.2	49.4	26.8

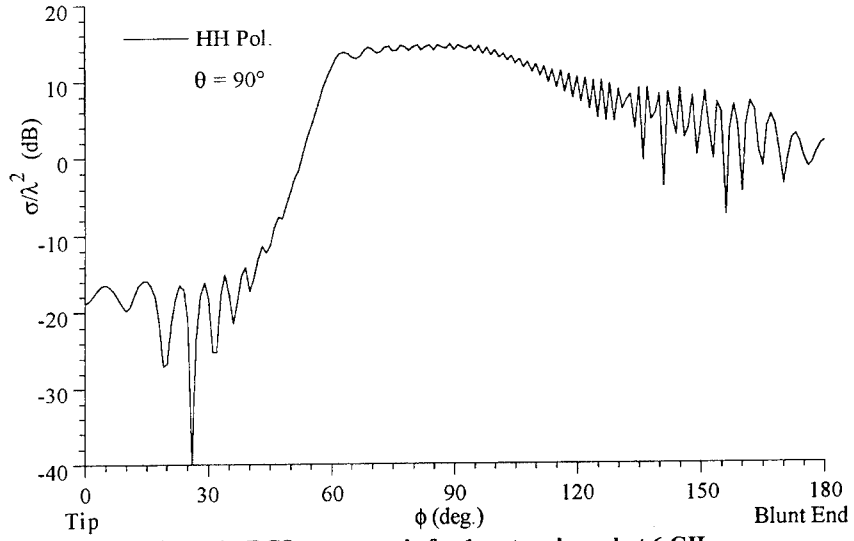


Figure 2. RCS versus angle for 1 meter almond at 6 GHz.

The overall timing for the almond is collected in Table 4. The total time also includes the pre-and post- processing that is necessary for the geometry and RCS calculation.

Table 4: Overall timing for almond

Paragon Mesh (matrix map)	Matrix Fill (sec)	Solve Time (sec(	Total Time (sec)
16 x 16	1216.6	1004.	2642.4
16 x 32	734.4	633.6	1634.4
16 x 115	397.8	222.7	766.8

Conclusion

The process of parallelizing a complex applications-oriented method-of-moments code CARLOS-3D has been described. This effort has resulted in a code which has the flexibility to run on both workstations, Intel iPSC/860 machines, and Paragon machines. The result is a code which is more easily extended, and permits most new features to be validated independent of the parallel implementation. The parallel implementation relies heavily upon features which were validated in the serial version. In addition, the structure of the code allows for the easy incorporation of advanced solvers and modeling techniques in the future.

References

[1] S.M. Rao, D.R. Wilton, and A.W. Glisson, "Electromagnetic Scattering by Surfaces of Arbitrary Shape", IEEE Trans. Ant. Prop., AP-30, 3, pp. 409-418, 1982.

[2] J.M. Putnam and L.N. Medgyesi-Mitschang, "Combined Field Integral Equation Formulation for Inhomogeneous Two- and Three-Dimensional Bodies: The Junction Problem", IEEE Trans. Ant. Prop. AP-39, 5, PP. 667-672, 1991.

[3] J.M. Putnam, "General Approach for Treating Boundary Conditions on Multi-Region Scatterers Using the Method of Moments", Proceedings of the 7th Annual Review of Progress in Applied Computational Electromagnetics, Monterey, CA, March 1991, pp. 304-319.

[4] A.C. Woo, H.T.G. Wang, M.J. Schuh, and M.L. Sanders, "Benchmark Plate Radar Targets for the Validation of Computational Electromagnetics Programs", IEEE Antennas & Propagation Magazine, December, 1992.

[5] J.M. Putnam and L.N. Medgyesi-Mitschang, "Combined Field Integral Equation Formulation for Inhomogeneous Bodies of Revolution (Combined Field Formulation of CICERO)", MDC Report No. QA003 for Sandia National Laboratories Contract No. 33-4257, December 1987.

[6] J.M. Putnam and M.B. Gedera, "CARLOS-3D: A General-Purpose Three-Dimensional Method-of-Moments Scattering Code," IEEE Antennas & Propagation Magazine April, 1993.

Parallel computing for electromagnetism at ONERA

A. de La Bourdonnaye, A. Cosnuau, X. Ferrières, P. Leca and F.-X. Roux
ONERA, Division Calcul Parallèle, Châtillon, France

Abstract. In this paper, on one hand, we present the development of a coupled volumic-surfacic finite element code for R.C.S. computations in frequency domain.
We have realized a parallel solver for the surfacic finite element part in the case of axi-symmetric bodies with multi-level meshes which avoid singular elements at the poles.
Yet, in the case of one level mesh, this solver reaches a performance of 3 Gflops on an 128-processor iPSC-860. Furthermore, we have studied parallel algorithms for the coupled solver which rely on an adaption of a substructuring method which is used for elliptic problems.

On the other hand we present the parallelization of a FDTD code based on a finite difference scheme in collaboration with the Department of Physics of ONERA. The parallelization is made through partitioning the grid into subdomains. The interface coherency is managed through message passing between processors allocated to neighboring subdomains. This approach has been demonstrated to be very efficient and scalable for distributed memory machines. The performance of this code for real industrial applications is 700 Mflops on a 64-processor Paragon.

1. Introduction. This paper mainly addresses two topics. The first one is the description of a coupled volumic-surfacic method for R.C.S. computations and the state of its implementation on a distributed memory iNTEL computer. The second topic is the parallelization of a FDTD code in collaboration with the Department of Physics.

In the first topic we aim at solving a frequency domain scattering problem with an heterogeneous spatially bounded obstacle. We choose to warp this body into a surface on which we will use exact (and thus non local) boundary conditions. It will allow us to use a volumic finite element method inside the surface and a discretized integral equation on the surface. Such mathematical formulations have yet been studied in many places, for instance in [4], [8], [9] or [6]. We make the choice of an axisymmetric warping surface as in [5], since it allows us to fasten part of the computation and to save memory. Here we focus on two points, first the solution algorithm of the coupled problem, which relies on a subdomain point of view and second, the actual implementation of the surfacic solver for the axisymmetric case. In this paper, we will first describe the physical situation we address, set some notations, and recall which mathematical formulation we use. After that we will present and analyze a solution scheme for the coupled system. Finally we will focus on the numerical solution of the integral equation part of the scheme.

For the second topic, we will briefly settle the background and present some computer performances.

2. Frequency Domain computations.

2.1. Position of the problem. Let Ω be a bounded domain of $\mathbb{R}^3$ and Γ its boundary which is supposed to be regular. Let $\epsilon(x), \mu(x)$ be the relative electric permitivity and magnetic permeabilty. They are supposed to be at least piecewise continuous. Moreover, we assume that outside Ω, $\epsilon = \mu = 1$. We want to find E, H the electromagnetic field satisfying the Maxwell system :

$$i\omega B = -rotE + J \tag{1}$$

$$i\omega D = rotH \tag{2}$$

$$divD = \rho \tag{3}$$

$$divB = 0 \tag{4}$$

and an outgoing wave condition where

$$D = \epsilon(x)E \tag{5}$$

$$B = \mu(x)H \tag{6}$$

and J is a source of electric current and ρ is the corresponding charge density.

2.2. Mathematical formulation of the coupled problem. For all that part, we will use the work of M. Cessenat [2], V. Levillain [8] and our own [6], as a mathematical background (see also Colton, Kress, [3]). For the sake of clearness in the formulas, we first define some operators.

$$P_1 : H_{div}^{-1/2}(\Gamma) \to H_{div}^{1/2}(\Gamma) \tag{7}$$

$$j \to n \wedge \int_\Gamma \nabla_y G(|x-y|) \wedge j dy \tag{8}$$

and (9)

$$P_2 : H_{div}^{-1/2}(\Gamma) \to H_{div}^{-1/2}(\Gamma) \tag{10}$$

$$j \to n \wedge \left(\int_\Gamma G(|x-y|) \wedge j dy + \frac{\nabla_\Gamma}{k^2} \int_\Gamma G(|x-y|) div_\Gamma j dy \right) \tag{11}$$

The Sobolev spaces H_{div}^s need not to be defined here since we shall not speak about regularity. We also denote $F = \frac{E}{i\omega}$. Then following [8] in the use of integral representation of electric and magnetic field, we obtain the following formulation of the Maxwell system where $<\ ,\ >$ denotes the hermitian product on Γ and $(\ ,\ )$ denote the hermitian product in Ω.

$$(\frac{1}{\mu} curl F,\ curl F') - k^2(\epsilon F,\ F') - (J_s,\ F') = < (\frac{I}{2} - P_1)(j) - k^2 P_2(n \wedge F),\ F' > \tag{12}$$

$$0 = < (\frac{I}{2} + P_1)(n \wedge F) + P_2(j),\ n \wedge j' > \tag{13}$$

where $j = H \wedge n$, and j' and F' are test functions.

2.3. General solution algorithm. Here we use an algorithm which comes from the substructuring method for elliptic problems. In our case, we suppose that we have two domains, one is Ω and the other its exterior. Of course, the equations modeling the exterior are the integral equations in (12-13). After having discretized these two equations with a finite element technique, we obtain the following linear system :

$$[F'_\Omega,\ F'_\Gamma,\ n \wedge j'] \cdot \left(\begin{bmatrix} A & B & 0 \\ B^* & C - k^2 P_2 & 1/2 - P_1 \\ 0 & 1/2 + P_1 & P_2 \end{bmatrix} \begin{bmatrix} F_\Omega \\ n \wedge F_\Gamma \\ j \end{bmatrix} - \begin{bmatrix} J_S \\ 0 \\ 0 \end{bmatrix} \right) = 0 \tag{14}$$

where the matrices A, B C represent the volumic part of equation (12) and the matrices P_1 and P_2 represent the integral operators denoted by the same symbols. Then the method consist in eliminating the unknowns F_Ω and j leading to the following system :

$$(S_i + S_e) n \wedge F = B^* A^{-1} B J_S \tag{15}$$

where $S_i = C - B^* A^{-1} B$ and $S_e = -k^2 P_2 - (1/2 - P_1) P_2^{-1} (1/2 + P_1) = -P_2^{-1} (1/2 + P_1)$ are usually called the *Schur complements* associated respectively with the inside and the outside of Ω. In order not to fill the resulting matrix, one commonly uses an iterative method (generally a conjugate gradient like method) for the linear system (15). We have only to factorize A and P_2. Here, with just two subdomains, the gain is the following. If the global system is well-conditioned, then the "Schur" method can efficiently use the best solvers for the sparse system inside Ω and the dense system on Γ.

2.4. A fast solver for an axisymmetric integral equation. In this part, we present the direct solver we are developing for axisymmetric integral equations. The interest of embedding the heterogeneous body in an axisymmetric surface is the following. Because of the symmetry, one can mesh Γ in a meridian-parallel way (see fig 1). Then, numbering the degrees of freedom

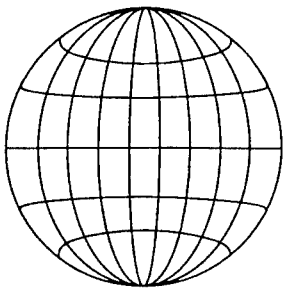


FIG. 1. *A meridian-parallel mesh*

by following the meridian lines, one obtains a block-circulant matrix, each block corresponding to the interaction between two meridians. First we see that we can save memory, and time for the computation of the matrix. Furthermore, this kind of matrix can be block-diagonalized using Fourier transforms. One can then factorize the blocks. All this machinery can be efficiently parallelized. Nevertheless, a meridian-parallel mesh as one main drawback : the triangles of the poles are degenerated. In order to treat this point, we developped a meshing technique which keeps the main advantages of the axisymmetric surfaces without the degenerated elements. Furthermore, this technique leads to algorithms which are still parallelizable.

Let us first develop the simplest algorithm. In order to obtain a full optimization, we impose the number of meridian slices to be a power of 2. With the numbering previously presented, the matrix $\mathcal{M}$ writes $\mathcal{M} =$

A_0	A_1	...	A_{n-1}
A_{n-1}	A_0	...	A_{n-2}
...	...	...	...
A_1	A_2	...	A_0

In order to maintain consistency between the element size in meridian and parallel directions, one must keep $n_s = \mathcal{O}(k)$, and $n = \mathcal{O}(k)$ where k is the wave number, n_s is the number of parallels and n is the number of meridians. The total number of degrees of freedom is then $N = n_s \times n = \mathcal{O}(k^2)$.

It is a well-known fact that this kind of matrix can be block-diagonalized with a FFT-type algorithm (cf. [5]). Let U be a vector of degrees of freedom. We decompose U in $(U_0, U_1, ..., U_{n-1})$, U_i being the components of U on the $(i-1)^{th}$ slice. We want to solve $V = \mathcal{M}U$ and we also decompose V as $V = (V_0, V_1, ..., V_{n-1})$.
We state a few more definitions. We call ω the primitive n^{th} root of unity and $\bar{\omega}$ its complex conjugate. Then we set $\mathcal{F}(W)_i = \sum_{j=0,n-1} \omega^{ij} W_j$ and $\bar{\mathcal{F}}(W)_i = \sum_{j=0,n-1} \bar{\omega}^{ij} W_j$ to be the discrete and discrete inverse Fourier transforms of $(W_0, W_1, ..., W_{n-1})$. We have $V = \frac{1}{n}\mathcal{F}(\mathcal{F}(A).\bar{\mathcal{F}}(U))$. Hence, for each k, $U_k = \frac{1}{n}\mathcal{F}(\mathcal{F}(A)_k^{-1}\bar{\mathcal{F}}(V)_k)_k$. Then the direct solver algorithm is as follows.

- Compute the inverse Fourier transform $\bar{\mathcal{F}}$ of V.
- Compute the Fourier transform $\mathcal{F}$ of A.
- Compute the LU factorisations of $\mathcal{F}(\mathcal{A})_k$ for each k.
- Perform inversions $U'_k = \mathcal{F}(A)_k^{-1}\bar{\mathcal{F}}(V)_k$.
- Compute the Fourier transform $\mathcal{F}$ of U' divided by n.

We evaluate the complexity. For the factorisation, we have n LU factorisations of size n_s, it makes $\mathcal{O}(N^2)$ operations. For the solution, we have 2 FFT's and n inversions of size n_s. It makes $\mathcal{O}(N^{3/2})$ operations.

Now we present the parallelization of the Direct Solver Algorithm. Let's first recall that iPSC860 is a distributed MIMD supercomputer with an hypercube network. In [5] we presented a parallel implementation of FFT's. In this paper we give another one which is more efficient for our purpose (details may be found in [7]).

Let's say for simplicity that we want to perform a block Fourier transform on n processors. Here, a block is either a vector subpart V_i or a block submatrix A_i. Our algorithm needs the size m of a block to be a multiple of the number of processors : $m = p.n$. So we have to perform m FFT's. We want to transfer data in order to have p FFT's to do on each processor. The situation at the beginning is that we have one block on each processor. Each block V_i will be divided into n sub-blocks V_i^j of size p. Now, processor i has to send V_i^j to processor j for all j. At the end of this communication phase, we have on processor i, the V_j^i sub-blocks for all j. Each processor can now perform local FFT's on the sub-blocks. Then we perform the inverse transposition algorithm to obtain the blocks $\mathcal{F}(V)_i$ to be each on one processor.

We are now going to explain how this algorithm is implemented on an hypercube network in order to reach maximum efficiency. First, we recall how is determined the path from processor i to processor j in the hypercube network. We write i and j in base 2 : $i = a_d a_{d-1}...a_1$ and $j = b_d b_{d-1}...b_1$. Let $c = c_d c_{d-1}...c_1$ be a "bitwise exclusive or" b. Then we construct a sequence (a_i) from a to b where a_i differs from a_{i-1} from only one bit. To construct this sequence we simply change a bit to the current term each time we encounter a 1 bit in the decomposition of c when we go from c_1 to c_d.
To perform the transposition algorithm, for each processor, we order the rest of the nodes of the hypercube in the following way. First, we put in a same class all the nodes which have the same distance from the reference one. Then, in each class we order the nodes with a lexicographical order (in fact a reverse one). Let's give an example for an hypercube with 8 processors. for node 0, "distance 1" nodes are nodes 1, 2 and 4, "distance 2" nodes are nodes 3, 5 and 6 and "distance

3" node is node 7. Then for processor 0 nodes are ordered in the following way : 1 2 4 3 5 6 7. For processor 1 it is an exercise to verify that nodes are ordered that way : 0 3 5 2 4 7 6.
Now for each processor, we begin to communicate with the first, then the second, then the next ..., according to the previously defined order. One can verify that a link is used atmost one time in each direction at each step. Hence, this communication scheme does not create any contention problem on the network. In the following tables we give some performances we have reached

TABLE 1
Block Circulant System on 64 nodes

Performances in Mflops (64 bits) with 1 rhs				
Block dimension	128	256	384	512
Mflops	585	997	1275	1433

TABLE 2
Block Circulant System on 64 nodes

Performances in Mflops (64 bits) with 128 rhs				
Block dimension	128	256	384	512
Mflops	825	1173	1395	1515

TABLE 3
Block Circulant System on 128 nodes

Performances in Mflops (64 bits) with 1 rhs				
Block dimension	128	256	384	512
Mflops	970	1917	2479	2846

TABLE 4
Block Circulant System on 128 nodes

Performances in Mflops (64 bit) with 128 rhs				
Block dimension	128	256	384	512
Mflops	1530	2308	2743	**3012**

on iPSC860. We measured CPU time for diagonalization, factorization and solution of linear systems. We vary the cube dimension, the block size and the number of right hand sides.

The next point is to show how to avoid sharp triangles at the poles. This method is developed in great details in [5]. We start at the poles with a finite number of triangles. Then until the width of the parallels is not greater than a criterion based on the wavelength, we carry on meshing each parallel as before. Once the criterion is reached, we divided each parallel band into two parallel sub-bands and we carry on dividing or regrouping according to the length of the parallels. Without going into very intricated details, we can just say that still using FFT we can obtain a sparse matrix, with the same complexity as we had for the previous algorithm. The matrix has a filling pattern looking like the one in figure (2). In that case we began with four elements at the poles, and we divided twice the parallels. We can see on this picture that the filling pattern is sky-line. Hence, a factorization will not modify the memory requirements. Furthermore, distributing the diagonal blocks among the processors, we still can design a parallel factorisation. In the next

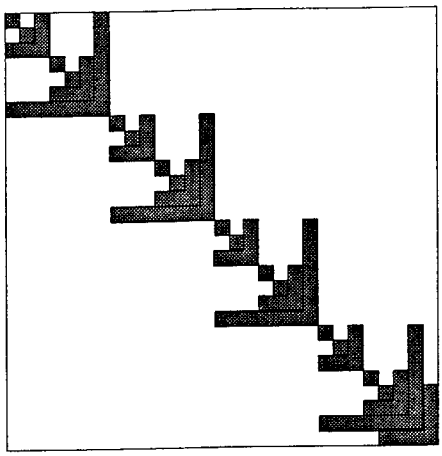


FIG. 2. *Pattern of the matrix with two divisions.*

table, we give some results of implementation of the solver on the iPSC860[1].

TABLE 5
Performances of the multilevel solver

Performances in Mflops (64 bits)				
Number of processors	8	16	32	64
Number of degrees of freedom	1960	3870	5215	16575
Mflops	170	316	546	-
Mflops with pivoting	140	271	454	1155

3. Parallelization of the code ALICE. ALICE is a 3D Maxwell equation solver, developped by the Department of Physics of ONERA. This code is mainly used for structures struck by lightning but its application domain could be extended. It uses a FDTD approach, based on an explicit finite differences Leap-Frog type scheme in space and time. The domain of computation contains both object structures and wires [10].
The parallelization of this code has been carried out by splitting the structured mesh into pencils. Each pencil is allocated into a processor. This code is scalable on any grid of processors. It is written in Fortran and runs with 32 bits arithmetics.
Some performances on industrial cases are given:

- A metallic box ($40 \times 40 \times 40$) embedded in a $80 \times 80 \times 80$ volume.
- Launcher1 on its launch pad : $205 \times 136 \times 112$.
- Launcher2 on its launch pad : $98 \times 104 \times 112$.
- A satellite : $96 \times 152 \times 168$.

[1] We are indebted for these results to F. Choukhroun

TABLE 6
Performances of ALICE on PARAGON and CRAY-YMP for 1000 time steps

Machine	PARAGON 64PE	CRAY-YMP 1PE	$T_{Cray}/T_{Paragon}$
80^3 Box	52s	184s	3.5
Launcher1	267s	771.87s	2.9
Launcher2	84.4s	286.175s	3.4
Satellite	173.33s	950s	5.48

Paragon execution times are very attractive compared to one-processor CRAY-YMP. Furthermore, the larger memory of the PARAGON machine makes some very big industrial applications exploitable: for instance, the case Launcher2 runs in 12 hours with a ($200 \times 400 \times 400$) domain (1.2 Gbyte) for 25000 time steps. Such a problem could not be treated with the CRAY-YMP machine

4. Conclusion. The parallel computing division of ONERA has two kinds of activity in the field of computational electromagnetism.
The first kind of activity is research of new numerical methods which perform well, both from the numerical and parallel computing point of view. That lead us first to the coupling between integral equations and volumic ones, and secondly, to the concept of multilevel meshes and solvers. Then, we try to adapt the method to obtain an algorithm which is as parallel as possible without spoiling the performances in terms of speed of computation. In our case, we reached for the one-level solver 3 GFlops on 128 processors of an iPSC860 and 1.1 GFlops for the multi-level one on 64 processors.
The second kind of activity consists of development of parallel versions of existing codes, in collaboration with other departments of ONERA or with industrial partners. We have given an example of such a development for the code ALICE, that is nowadays routinely exploited on the 66-processor PARAGON machine at ONERA. This development allows engineers of the department of Physics to use finer numerical models for predicting the electromagnetic beheaviour of structures struck by lightnings.

REFERENCES

[1] Workshop JINA90. *RCS of perfectly conducting or coated bodies*, Nice, France, November 1990.

[2] M. CESSENAT. *Resolution de problèmes de Maxwell en régime harmonique par des méthodes intégrales*, Tech. Rep., CEA, juin 1987.

[3] P. COLTON AND R. KRESS. *Integral equation method in scattering theory*, Pure and Applied Mathematics, (1983).

[4] M. COSTABEL. *Symmetric methods for the coupling of finite elements and boundary elements*, in Boundary elements IX. Brebbia, Wendland, and Kuhn, eds., 1987, pp. 411 -420.

[5] A. DE LA BOURDONNAYE. *Accélération du traitement numérique de l'équation de Helmholtz par équations intégrales et parallélisation.*. PhD thesis, Ecole polytechnique, Palaiseau, France, 1991.

[6] ——. *Some formulations coupling volumic and integral equation methods for Helmholtz equation and electromagnetism*, Num. Math. (accepted).

[7] P. LECA AND L. MANE. *Implementation of a 3d adi algorithm on distributed memory multiprocessors. application to the design of a parallel navier-stockes solver*, in CFD'PAR conference, Indianapolis, May 1990.

[8] V. LEVILLAIN, *Couplage élément finis-équations intégrales pour la résolution des équations de Maxwell en milieu hétérogene.*, PhD thesis, Ecole polytechnique, 1991.

[9] J. NEDELEC AND C. JOHNSON, *On the coupling of boundary integral and finite element methods*, Mathematics of computation, 35 (1980), pp. 1063–1079.

[10] J. GRANDO, F. ISSAC, M. LEMISTRE AND J.-C. ALLIOT, *Stability analysis including wires of arbitrary radius*, IEE APS Symposium, URSI Radio Science Meeting, Ann Harbor Michigan 1993.

The Performance of the Parallel Solution of the Quasi-Minimal Residual (QMR) Method on 2D Mesh Architectures

Lama Hamandi, Füsun Özgüner and Robert Lee
lama@ee.eng.ohio-state.edu, ozguner@ee.eng.ohio-state.edu
and lee@ee.eng.ohio-state.edu
Department of Electrical Engineering
The Ohio State University
2015 Neil Avenue
Columbus, OH 43210

I. Introduction

The edge-based finite element method[1] is an important numerical method for the electromagnetic modeling of complex geometries. The computation domain is discretized into tetrahedra where the unknowns are associated with the edges of the tetrahedra. This gives rise to a system of equations with potentially millions of unknowns, for large three-dimensional (3D) geometries. The solution of the resulting matrix equation is computationally intensive and requires parallelization in order to be solved practically.

In this paper, we address the parallelization of an iterative matrix solver, the Quasi-Minimal Residual (QMR) algorithm [2, 3], on distributed memory multiprocessors such as the Intel Delta[4], where the processors are interconnected in a 2D mesh topology with wormhole routing. The QMR is a recently introduced method for the solution of general non-Hermitian linear systems $Ax = b$. During the parallel solution of this system of equations, the rows of A and corresponding entries of the vectors are distributed to the processors of the mesh. The processors need to communicate to exchange the required data available on other processors.

The most time-consuming operation in the QMR algorithm is the matrix-vector multiplication, which requires extensive interprocessor communication. If the partitioning algorithm yields a banded matrix A, then only nearest neighbor communication is required. However, our matrices may not be banded and each processor may need to communicate with several other processors that are not necessarily adjacent to it, depending on the domain to be decomposed and the decomposition method. We have implemented this communication pattern with an algorithm which we call the "Most Messages First" (MMF) algorithm, and we use it in the parallel solution of the QMR method on the Intel Touchstone Delta.

In this paper, Section II lists the QMR algorithm. Section III describes the computation and communication requirements of this algorithm and provides the details of the MMF algorithm. Finally, Section IV shows the results and speedups obtained for the problem of electromagnetic scattering from a conducting sphere.

II. The Quasi-Minimal Residual (QMR) method

The QMR algorithm is an iterative method for solving linear systems of equations $Ax = b$ [2, 3]. Although the QMR method can solve general non-Hermitian linear systems, we will only use the simplest form of the QMR algorithm in this paper to illustrate its parallelization and communication requirements. We will use upper case letters (A, A^T) to refer to matrices, lower case letters (p, q, v, w, d, x) to refer to vectors and Greek letters $(\rho, \alpha, \epsilon, \vartheta, \eta, \xi, \delta, \beta, \omega)$ to refer to scalars. The subscript n refers to the iteration number of the QMR algorithm.

Algorithm 1 (The QMR algorithm) :

0) Choose $x_0 \in \mathcal{C}^{\mathcal{N}}$ *and set* $r_0 = b - Ax_0$.
Compute $\rho_1 = ||r_0||$ *and set* $v_1 = r_0/\rho_1$.
Choose $w_1 \in \mathcal{C}^{\mathcal{N}}$ *with* $||w_1|| = 1$.
Set $p_0 = q_0 = d_0 = 0, \alpha_0 = \epsilon_0 = \xi_1 = 1, \vartheta_0 = 0, \eta_0 = -1$.

For $n = 1, 2, \cdots$, *do:*

1) If $\epsilon_{n-1} = 0$, *then stop.*
Compute $\delta_n = w_n^T v_n$. *If* $\delta_n = 0$, *then stop.*

2) Compute

$$\begin{aligned} p_n &= v_n - p_{n-1}(\xi_n \delta_n / \epsilon_{n-1}), \\ q_n &= w_n - q_{n-1}(\rho_n \delta_n / \epsilon_{n-1}), \end{aligned}$$

3) Compute $\epsilon_n = q_n^T A p_n, \beta_n = \epsilon_n / \delta_n$, *and set*

$$\begin{aligned} \tilde{v}_{n+1} &= Ap_n - v_n \beta_n, \qquad \rho_{n+1} = ||\tilde{v}_{n+1}||, \\ \tilde{w}_{n+1} &= A^T q_n - w_n \beta_n, \qquad \xi_{n+1} = ||\tilde{w}_{n+1}||, \end{aligned}$$

4) Compute

$$\vartheta_n = \frac{\omega_{n+1}\rho_{n+1}}{\omega_n \alpha_{n-1}|\beta_n|}, \qquad \alpha_n = \frac{1}{\sqrt{1+\vartheta_n^2}}, \qquad \eta_n = -\eta_{n-1}\frac{\rho_n \alpha_n^2}{\beta_n \alpha_{n-1}^2},$$

$$d_n = p_n \eta_n + d_{n-1}(\vartheta_{n-1}\alpha_n)^2, \qquad x_n = x_{n-1} + d_n.$$

5) If $\rho_{n+1} = 0$ *or* $\xi_{n+1} = 0$, *then stop.*
Otherwise, set

$$v_{n+1} = \tilde{v}_{n+1}/\rho_{n+1}, \qquad w_{n+1} = \tilde{w}_{n+1}/\xi_{n+1}.$$

III. Computational Requirements of the QMR algorithm

The computational requirements of the QMR algorithm can be classified into three types.

1. The first type involves the product of a matrix and a vector, such as the product of A and vector p_n, and the product of A^T and vector q_n. We will refer to this type as the Matrix-Vector (MV) type.

2. The second type is characterized by the product of two vectors, such as the calculation of dot products ($w_n^T v_n$), and vector norms ($||\tilde{w}_{n+1}||$). We will refer to this type as the Dot-Product (DPr) type.

3. The third type involves the addition of two vectors scaled each by a scalar constant, such as $d_n = p_n \eta_n + d_{n-1}(\vartheta_{n-1}\alpha_n)^2$. This type will be referred to as Scalar-Alpha-X-Plus-Beta-Y (SAXPBY) [2, 3] type.

The matrix A and the vectors are distributed to the processors of the mesh using a partitioning scheme that load balances the data in the processors and minimizes processor interactions. The processors should be load balanced so that they finish computation at approximately the same time. Communication time should be minimized since it increases the total execution time of the parallel QMR. We used the Adaptive Jumps (AJ) method [5] to decompose the matrix and vectors among the processors, and decrease the total volume of communication required for the parallel execution of QMR.

A. Parallelizing the MV type

1. The product $A.p_n$

During the parallel calculation of $A.p_n$, the processors need to communicate to exchange the required entries of the p_n vector that are mapped to other processors. Figure 1 shows an example of the distribution of the matrix A and vector p_n to 4 processors P_0, P_1, P_2, and P_3. Each processor may need to communicate with several other processors that are not necessarily adjacent to it. The resulting communication pattern is very irregular. It depends on the sparsity of A, and on the way it is partitioned. This pattern of communication is referred to as the "All-To-Many Personalized Communication" (ATMPC) [6]. The "*all-to-many*" pattern implies that each processor needs to communicate with only a few other processors.

One way to implement the ATMPC is to use All-To-All Personalized Communication (ATAPC) algorithms [7, 8, 9, 10, 11]. The ATAPC pattern is a regular pattern in which each processor needs to send a personalized message to every other processor. The ATMPC can be implemented using the ATAPC pattern by sending zero-length messages between two processors that do not actually need to communicate. However, this scheme is not optimal; particularly if each processor needs to communicate with only few other processors. It will leave most of the processors and links of the multiprocessor idle. On the other hand, if each processor randomly sends its messages, deadlock can occur. During deadlock, the processors wait on each other, and no one can actually receive the messages that are destined to it.

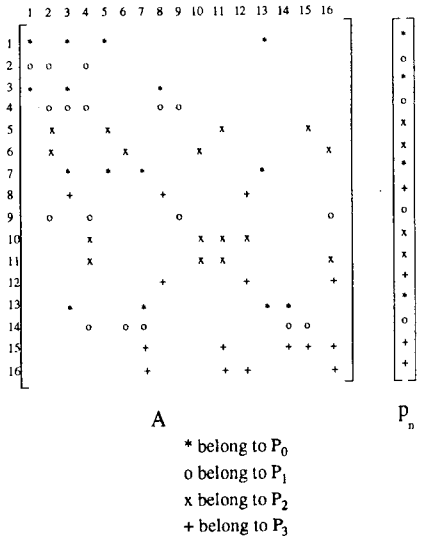


Figure 1: The distribution of matrix A and vector p_n to 4 processors P_0, P_1, P_2, and P_3.

The Most Messages First algorithm

Our approach to implement the ATMPC pattern of communication on the 2D mesh is a greedy approach. We schedule the processor that has the most messages first. We group the messages into several groups. Messages within the same group are sent simultaneously, and form one step of the ATMPC algorithm. We attempt to schedule as many messages as possible during each step of the ATMPC in order to decrease the maximum number of steps (MNS) of this irregular communication. We call our scheduling algorithm, the "Most Messages First" (MMF) algorithm. This algorithm specifies which processors should communicate at each step, as well as the total number of steps of the ATMPC algorithm. It is run only once for a given distribution. The MMF algorithm is based on the assumption that each processor can send and receive at most one message. Therefore, multiple messages from (to) a processor should be sent (received) sequentially. The minimum number of steps of the ATMPC algorithm is therefore the maximum number of messages that any processor has to send.

The scheduling procedure is based on a communication array C $(p \times p)$ that is available for the given distribution of A to the processors (p = number of processors). C is set such that entry (i, j) gives the length of the message that processor i needs to send to processor j. If C is not sparse, then an ATAPC algorithm should be used. When C is sparse, the null entries are removed from it, and its rows are compressed to the left. The compressed C matrix is distributed among the processors. Each processor stores only the compressed row that indicates the messages it should send. The compressed row of C on each processor P_i is stored as two linear arrays $ML(j)$

(Message Length) and $DP(j)$ (Destination Processor). $ML(j)$ is the length of the message that processor P_i has to send to processor $DP(j)$. We use the notation $(ML(j), DP(j))$ to represent this message. Furthermore, NS_i is the number of steps processor P_i requires to send its messages, and RM_i is the number of remaining messages that processor P_i has to schedule. NS_i and RM_i are initialized to the number of nonzero messages P_i has to send. The MMF algorithm rearranges the entries in the DP and ML arrays, such that at the end of this algorithm, entries $DP(j)$ and $ML(j)$ on all the processors represent a group of messages to be sent simultaneously at step j of the ATMPC. Furthermore, MNS, the maximum number of steps of the ATMPC algorithm, is set to be equal to the largest NS_i over all processors ($i = 0, \cdots, p-1$).

Let us choose processor P_0 to coordinate the scheduling process. At each step j, processor P_0 sorts the processors by the number of unscheduled messages they need to send. Processor P_0, then, goes over this list in a descending order, and allows each processor to schedule a message at the current step j. This technique gives the processor with the largest number of messages a better chance to schedule a message; therefore, it keeps MNS as close to the minimum as possible.

When a processor P_i is ready to schedule a message for step j of the ATMPC, it checks the j^{th} entry of its arrays DP and ML. If $DP(j)$ is not receiving any messages at step j, the message $(ML(j), DP(j))$ is scheduled at this step, and processor $DP(j)$ is masked. The number of remaining messages RM_i in P_i is decremented. However, if $DP(j)$ is masked, the MMF algorithm goes to the end of the DP array, that is, it considers entry $DP(NS_i)$. If $DP(NS_i)$ is also masked, the algorithm considers $DP(NS_i - 1)$, $DP(NS_i - 2)$, $\cdots$, until it either finds a processor $DP(NS_i - k)$ that is not masked or it gets to $DP(j)$ again. In the former case, the entries $DP(NS_i - k)$ and $DP(j)$ are exchanged. Similarly, the entries $ML(NS_i - k)$ and $ML(j)$ are exchanged. Therefore, the message $(ML(NS_i - k), DP(NS_i - k))$ is scheduled at the j^{th} step, and RM_i is decremented. The message $(ML(j), DP(j))$ is moved temporarily to the $(NS_i - k)^{th}$ step. In the latter case, if $DP(j)$ is reached again, then there is no messages in processor P_i that can be sent at step j. The message $(ML(j), DP(j))$ is moved to the end of the DP and ML arrays, hence it is stored at location $NS_i + 1$. As a result, NS_i is incremented, but RM_i is not changed. Entries $DP(j)$ and $ML(j)$ are replaced by -1 to indicate that processor P_i is not sending any message at step j of the ATMPC. Moreover, processor P_i informs processor 0, of the remaining number of messages it has to send.

Processor P_0 updates the mask array, and sends it to the next processor in the sorted list. This is repeated until all the processors had a chance to schedule a message for step j of the ATMPC. Once step j is scheduled, j is incremented, processor P_0 sorts the processors by the number of remaining messages they need to send and the above algorithm is repeated again to schedule the messages of a new step of the ATMPC. When all the messages on every processor are scheduled, the maximum number of steps of the ATMPC (MNS) is set to be equal to the largest NS_i, $i = 0, \cdots p-1$. After scheduling the steps of the ATMPC by the MMF algorithm, they are used repeatedly each time $A.p_n$ is computed or each time an ATMPC pattern is invoked.

2. The product $A^T.q_n$

Since each processor stores some rows of A and not its columns, A^T is not readily available on the processors. In order to calculate $t = A^T.q_n$ efficiently without affecting the speedup, its

computation and communication times should not be more expensive than those of $A.p_n$.

We compute the product $A^T.q_n$ using the results of the MMF algorithm. No additional preprocessing time is required. Each processor calculates its contribution to the nonzero values of vector t. Those values correspond to the column indices of the nonzero values of A stored in that processor. Then each processor collects only the nonzero entries of the t vector corresponding to the rows it is storing. The communication pattern required to collect vector t after calculating it ($t = A^T.q_n$) in each processor is the same as the one used to collect vector p_n prior to multiplying it by A. The steps of the ATMPC scheduled by the MMF algorithm in the preprocessing phase, are used again for multiplying A^T by q_n.

B. Parallelizing the DPr type

The type DPr includes the computation of dot products ($w_n.v_n$) and vector norms ($||\tilde{v}_{n+1}||$). Since the vectors are distributed among the processors, each processor computes the partial dot product or partial norm on the portion of the vectors that it has. Then a **Global Combine** operation [12] is needed to collect the partial results from all the processors, compute the final dot product or norm, and then distribute the result back to all the processors.

C. Parallelizing the SAXPBY type

Parallelizing the SAXPBY operations is the simplest among the three types. Each processor scales and adds the portions of the vectors it is storing. No communication is needed among the processors.

IV. Results and Speedup

The parallel algorithm was tested for several examples on the Delta multiprocessor [4]. At this point, the most extensive testing of the parallel code has been for the canonical problem of electromagnetic scattering from a perfectly conducting sphere of radius 1.2 wavelengths where a simple first order absorbing boundary condition (ABC) is used. The number of unknowns used for this example is 197,574. The radar cross section result is compared against the Mie series solution in Figure 2. The results are good, given that the truncation boundary is 0.3 wavelengths from the sphere. The corresponding speedup results are shown in Figure 3. The memory per processor was not enough to run these examples with less than 8 processors, so the entries in Figure 3 are normalized with respect to the results obtained with 8 processors. The speedup obtained while running the QMR on 16 processors is 1.96 as compared with QMR running on 8 processors. This is a very good result that approaches the ideal value of two. As the number of processors increases, the deviation of the speedup from the ideal becomes more obvious. This behavior is expected since the communication time becomes more significant as the amount of computation on each processor is reduced.

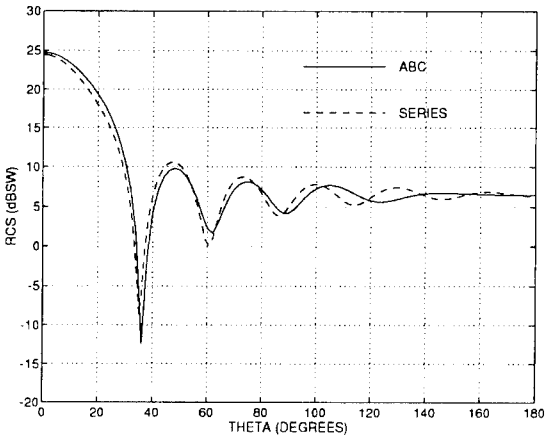


Figure 2: RCS for a 1.2 wavelength sphere. Comparison of the FEM solution terminated by an ABC to a series solution

# of processors	time (secs)	Speedup	Ideal Speedup
8	2621.0	1.0	1.0
16	1339.7	1.96	2.0
32	794.8	3.3	4.0
64	489.6	5.35	8.0
128	334.6	7.83	16.0

Figure 3: Execution time and speedup for the sphere example (197,574 variables) when run on the Intel Touchstone Delta.

V. References

[1] J. F. Lee and R. Mittra, "A note on the application of edge-elements for modeling three-dimensional inhomogeneously-filled cavities," *IEEE Transactions on Microwave Theory and Techniques*, vol. 40, pp. 1767–1773, September 1992.

[2] R. W. Freund and N. M. Nachtigal, "An implementation of the QMR method based on coupled two-term recurrences," Numerical Analysis Manuscript 92-06, AT&T Bell Laboratories, 1992.

[3] R. W. Freund and N. M. Nachtigal, "Implementation details of the coupled QMR algorithm," Numerical Analysis Manuscript 92-12, AT&T Bell Laboratories, October 1992.

[4] Intel Corporation, "A Touchstone DELTA system description," February 1991.

[5] L. Hamandi, R. Lee, and F. Özgüner, "A domain decomposition technique for the parallel solution of linear systems of equations resulting from finite element discretization," in *The First International Conference on Electronics, Circuits, and Systems*, (Cairo, Egypt), pp. 978–983, December 1994.

[6] S. Ranka, J. C. Wang, and M. Kumar, "Personalized communication avoiding node contention on distributed memory systems," in *1993 International Conference on Parallel Processing*, pp. I241–I244, 1993.

[7] D. S. Scott, "Efficient all-to-all communication patterns in hypercube and mesh topologies," in *Proceedings of the* 6^{th} *Distributed Memory Concurrent Computers*, pp. 398–403, 1991.

[8] S. H. Bokhari and H. Berriman, "Complete exchange on a circuit switched mesh," in *Scalable High Performance Computing Conference*, pp. 300–306, April 1992.

[9] S. Gupta, S. Hawkinson, and B. Baxter, "A binary interleaved algorithm for complete exchange on a mesh architecture," tech. rep., Intel Corporation, Supercomputer Systems Division, Beaverton, OR, 1993.

[10] S. Takkela and S. Seidel, "Broadcast and complete exchange algorithms for mesh topologies," Tech. Rep. 93-04, Department of Computer Science, Michigan Technological University, Houghton, Michigan, November 1993.

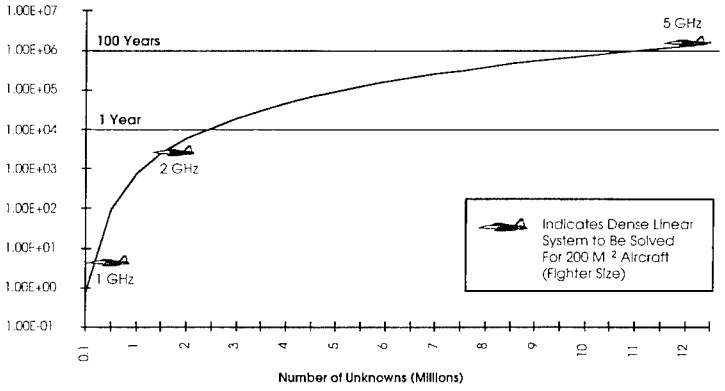
[11] R. Thakur and A. Choudhary, "All-to-all communication on meshes with wormhole routing," in *Proceedings of the* 8^{th} *International Parallel Processing Symposium*, April 1994.

[12] M. Barnett, R. Littlefield, D. G. Payne, and R. van de Geijn, "Global combine on mesh architectures with wormhole routing," in *Proceedings of the 7th International Parallel Processing Symposium*, IEEE Computer Society Press, April 1993.

Advanced Parallel Solver Techniques

Adrian S. King
Intel Supercomputer System Division
CO6-10, Zone 8
14924 NW Greenbrier Pkwy
Beaverton, OR 97006

A key element to the future of Computational Electromagnetics (CEM) is the development of advanced solver algorithms for a variety of systems of equation types such as sparse/dense, symmetric/unsymmetric, and real/complex. Success here will require major advances in mathematics in order to solve important electromagnetics problems. The magnitude of the problem at hand is demonstrated by looking at the time required today to solve large complex dense linear systems of various sizes utilizing current LU decomposition techniques at a sustained TeraFLOP rate.



TeraFLOPS solution time today versus linear system size utilizing current LU decomposition techniques

Clearly, alternatives to such "brute-force" solutions must be pursued. This presentation will describe advanced solver development efforts and their parallel implementations. Both iterative and direct solution techniques will be addressed.

Parallelized FDTD for Antenna Radiation Pattern Calculations

Z M Liu*, Ananda S Mohan, T A Aubrey, and W R Belcher
School of Electrical Engineering, University of Technology, Sydney,
P O Box 123, Broadway, NSW 2007, Australia Fax: + 61 2 330 2435
*Email: johnliu@ee.uts.edu.au Phone:+ 61 2 330 1259 (work) + 61 2 399 3082 (home)

Abstract - Development of code for solving radiation problems using the Finite Difference Time Domain (FDTD) method requires consideration of three major aspects. These are 1) the core FDTD algorithm, 2) the absorbing boundary condition (ABC) and 3) the near to far zone transformation. In this paper, methods of parallelizing each of these aspects are discussed. The computer used is a CM-5 (connection machine) with 32 processors, each with four vector units (VU). The programming language used is CM Fortran. Performance of the parallelized code for the various parts of the FDTD approach is compared with existing serial code. The results of this comparison are encouraging. The parallel core FDTD algorithm run on the CM-5 is found to run approximately 100 times faster than the Fortran 77 code on a SUN SPARC-2 workstation. The parallel code determines radiation patterns about 27 times faster than the serial code.

Introduction

The Finite Difference Time Domain method (FDTD) has been extensively studied and successfully applied to many electromagnetic problems, for example [1]. The technique is relatively simple to implement and can be applied to problems with complicated geometries and inhomogeneous, anisotropic materials. However, its computer intensive nature can limit its usefulness as a design tool. Large problems can take several hours to run on a high performance workstation. The development in parallel computing techniques, especially the development of MPC (massively parallel computers) provides a way to reduce computer run time. Such techniques have attracted the attention of the electromagnetic community [2-4].

Parallelizing the FDTD for a variety of computer architectures has been reported. A HP-735 workstation cluster is used in [2], the ASP (Associative String Processor) which is a SIMD (single instruction, multiple data) machine is used in [3], and a HP400, a 486-based PC and a 386-based PC with transputer arrays are used in [4]. As different parallel computer systems have different structures, the programming strategies, and even the programming languages, are also different. In these references a method for parallelizing the near to far zone transformation has not been described.

In this paper a method of parallelizing the FDTD approach for antenna analysis is discussed. The computer used is a CM-5 (connection machine) which has 32 processors. The programming language used is CM Fortran. The three major steps involved in solving radiation problems by the FDTD method, that is the FDTD algorithm, the absorbing boundary condition (here Mur's ABCs are used), and the near to far zone transformation are discussed in detail. The development of the code using CM Fortran and the results obtained are presented.

CM-5 and CM Fortran

The CM-5 is the connection machine produced by Thinking Machines Corporation, USA. A CM-5 has a number of processors with each processor having four vector units (VU). Each VU has its own memory. The CM-5 has a scalable architecture which allows the number of processors to be increased. The CM-5 used here has 32 processors and a total of 128 VUs. Each VU has 8 Mbit memory and so the computer has 1024 Mbit memory. Users can choose to use either 16 or 32 processors.

The programming language used in the present work is CM Fortran which is Thinking Machine's version of the Fortran language. It is very similar to, and in the future will incorporate, the High Performance Fortran (HPF) subset standard. It is a subset of Fortran 90, with two important extensions. The first is a set of compiler directives (which appear to other compilers as comments) that specify how data is to be distributed over the processor, the second is the FORALL statement, (which was originally proposed for but then dropped from the Fortran 90 standard). In particular, parallelism is explicitly

represented by the programmer using Fortran 90 array operations. No attempt is made to parallelize DO loops.

Normally, the bottleneck for the CM Fortran is the time consuming communications between processors. The main programming issue is to avoid such communications, and if they are unavoidable make them most efficient.
The CM-5 can be viewed as consisting of a number of virtual processors, each with its own memory. If no axis of an array is specified as serial, every element of the array is stored in a separate virtual processor's memory. In this case, if two arrays have the same shape and size, then elements having the same subscripts will be stored in the same virtual processor's memory and so the operations on them can be performed without any communications. If the program operates on two elements which have different subscripts then the compiler will generate communication code even when the elements are stored in the same VU, (memory allocation for the distributed memory is a run time property).

Another important consideration when using the CM-5 is the array size. In conventional serial code run time is directly related to array size. In the CM-5 there exist optimum array dimensions. For example 16×16 element arrays can be processed as quickly and with the same memory requirements as 9×9 element arrays. The consequence of this is that larger problems can be tackled or the absorbing boundaries can be moved further away from the radiating structure without penalty in many cases. Detailed description of this feature can be found in the CM Fortran handbook for CM-5 [5].

Parallelizing FDTD Algorithm

The FDTD method is a direct solution of Maxwell's time-dependent curl equation. In an isotropic medium, Maxwell's equation can be written as

$$\nabla\times\mathbf{E}=-\mu\frac{\partial\mathbf{H}}{\partial t},\qquad \nabla\times\mathbf{H}=\sigma\mathbf{E}+\varepsilon\frac{\partial\mathbf{E}}{\partial t} \tag{1}$$

In a Cartesian coordinate system (x,y,z), vector fields $\mathbf{E}$ and $\mathbf{H}$ can be expressed as $\mathbf{E}=\hat{x}E_x+\hat{y}E_y+\hat{z}E_z$ and $\mathbf{H}=\hat{x}H_x+\hat{y}H_y+\hat{z}H_z$, and so the above two vector equations can be decomposed into six scalar equations, which can be discretized by central finite-difference approximation, and the six commonly used FDTD equations, (2), can be obtained, [6].

$$H_x^{n+1}(i,j,k)=H_x^n(i,j,k)+R_h\left[E_y^n(i,j,k+1)-E_y^n(i,j,k)+E_z^n(i,j,k)-E_z^n(i,j+1,k)\right] \tag{2a}$$

$$H_y^{n+1}(i,j,k)=H_y^n(i,j,k)+R_h\left[E_z^n(i+1,j,k)-E_z^n(i,j,k)+E_x^n(i,j,k)-E_x^n(i,j,k+1)\right] \tag{2b}$$

$$H_z^{n+1}(i,j,k)=H_z^n(i,j,k)+R_h\left[E_x^n(i,j+1,k)-E_x^n(i,j,k)+E_y^n(i,j,k)-E_y^n(i+1,j,k)\right] \tag{2c}$$

$$E_x^{n+1}(i,j,k)=C_a E_x^n(i,j,k)+C_h\left[H_z^{n+1}(i,j,k)-H_z^{n+1}(i,j-1,k)+H_y^{n+1}(i,j,k-1)-H_y^{n+1}(i,j,k)\right] \tag{2d}$$

$$E_y^{n+1}(i,j,k)=C_a E_y^n(i,j,k)+C_h\left[H_x^{n+1}(i,j,k)-H_x^{n+1}(i,j,k-1)+H_z^{n+1}(i-1,j,k)-H_z^{n+1}(i,j,k)\right] \tag{2e}$$

$$E_z^{n+1}(i,j,k)=C_a E_z^n(i,j,k)+C_h\left[H_y^{n+1}(i,j,k)-H_y^{n+1}(i-1,j,k)+H_x^{n+1}(i,j-1,k)-H_x^{n+1}(i,j,k)\right] \tag{2f}$$

where
$$R_h=\delta t/\mu(i,j,k)\delta\qquad C_a=1-\sigma(i,j,k)\delta t/\varepsilon(i,j,k)\qquad C_h=\delta t/\varepsilon(i,j,k)\delta \tag{3}$$

Also $\delta=\delta x=\delta y=\delta z$ (because cubic cell is used here), and δt is the time increment. The above six FDTD equations form the largest computational part in FDTD method. Parallelization of these equation involves several steps which are now described.

Step 1. Define arrays. There are 24 different terms in (2), we define each term as a separate array. Let `na1` and `n` represent superscripts $n+1$ and n respectively. Also let `ia1`, `is1`, `ja1`, `js1`, `ka1` and `ks1` represent subscripts $i+1$, $i-1$, $j+1$, $j-1$, $k+1$ and $k-1$ respectively. The FDTD space domain is bounded by a rectangular box $x=(0,\delta I_{max})$, $y=(0,\delta J_{max})$ and $z=(0,\delta K_{max})$, In the following `Imax`, `Jmax` and `Kmax` are the upper bound for i, j and k respectively. The 24 arrays may be defined as

```
      REAL, ARRAY (0:Imax, 0:Jmax, 0:Kmax)::
     & Ex_na1, Ex_n, Ex_n_ja1, Ex_n_ka1, Hx_na1, Hx_n, Hx_na1_js1, Hx_na1_ks1,
     & Ey_na1, Ey_n, Ey_n_ia1, Ey_n_ka1, Hy_na1, Hy_n, Hy_na1_is1, Hy_na1_ks1,
     & Ez_na1, Ez_n, Ez_n_ia1, Ez_n_ja1, Hz_na1, Hz_n, Hz_na1_is1, Hz_na1_js1
```

Here each term is defined as a separate array to improve the readability of this paper. However by reusing names, the number of the arrays may be reduced to eight to reduce memory requirements.

To implement (2) in parallel, the size and shape of all of the arrays should be the same as defined above, so that elements

having the same subscripts will be stored in the same location of the virtual processor's memory. This helps to make the communications simple thus improving the efficiency of the code.

Step 2. Update the field component values, using the information at current time step is n+1, that is

```
Ex_n = Ex_na1
Ey_n = Ey_na1
Ez_n = Ez_na1
Hx_n = Hx_na1
Hy_n = Hy_na1
Hz_n = Hz_na1
```

Step 3. Move the data. The six FDTD equations involve large amount of communications. For example, in (2a) six elements are involved; the $H_x^{n+1}(i,j,k)$, $H_z^n(i,j,k)$, $E_y^n(i,j,k)$, $E_z^n(i,j,k)$, $E_y^n(i,j,k+1)$ and $E_z^n(i,j+1,k)$ components. The first four elements have the same subscripts, while the other two have different subscripts and so communications are unavoidable. The calculation can be performed only after $E_y^n(i,j,k+1)$ and $E_z^n(i,j+1,k)$ are moved to the virtual processor's memory where $H_x^{n+1}(i,j,k)$ is stored. An efficient method to move the elements of arrays is to use the circular shift command, CSHIFT, an intrinsic function in CM Fortran (also in HPF), as shown below.

```
Ex_n_ja1 = CSHIFT (Ex_n, dim=2, shift=1)                                    (4a)
Ex_n_ka1 = CSHIFT (Ex_n, dim=3, shift=1)                                    (4b)
Ey_n_ia1 = CSHIFT (Ey_n, dim=1, shift=1)                                    (4c)
Ey_n_ka1 = CSHIFT (Ey_n, dim=3, shift=1)                                    (4d)
Ez_n_ia1 = CSHIFT (Ez_n, dim=1, shift=1)                                    (4e)
Ez_n_ja1 = CSHIFT (Ez_n, dim=2, shift=1)                                    (4f)

Hx_na1 = Hx_n + Rb*(Ey_n_ka1 - Ey_n + Ez_n - Ez_n_ja1)                      (5a)
Hy_na1 = Hy_n + Rb*(Ez_n_ia1 - Ez_n + Ex_n - Ex_n_ka1)                      (5b)
Hz_na1 = Hz_n + Rb*(Ex_n_ja1 - Ex_n + Ey_n - Ey_n_ia1)                      (5c)

Hx_na1_js1 = CSHIFT (Hx_na1, dim=2, shift=-1)                               (6a)
Hx_na1_ks1 = CSHIFT (Hx_na1, dim=3, shift=-1)                               (6b)
Hy_na1_is1 = CSHIFT (Hy_na1, dim=1, shift=-1)                               (6c)
Hy_na1_ks1 = CSHIFT (Hy_na1, dim=3, shift=-1)                               (6d)
Hz_na1_is1 = CSHIFT (Hz_na1, dim=1, shift=-1)                               (6e)
Hz_na1_js1 = CSHIFT (Hz_na1, dim=2, shift=-1)                               (6f)

Ex_na1 = Ca*Ex_n + Cb*(Hz_na1 - Hz_na1_js1 + Hy_na1_ks1 - Hy_na1)           (7a)
Ey_na1 = Ca*Ey_n + Cb*(Hx_na1 - Hx_na1_ks1 + Hz_na1_is1 - Hz_na1)           (7b)
Ez_na1 = Ca*Ez_n + Cb*(Hy_na1 - Hy_na1_is1 + Hx_na1_js1 - Hx_na1)           (7c)
```

Step 4. Perform calculations. After shifting the arrays, all terms in (2) will be located in the same virtual processor's memory. Thus all virtual processors will perform the calculations simultaneously. The code for this step is shown in equations (5) and (7) above, where Rb, Ca and Cb are as given in equation (3).

Parallelizing Mur's ABCs

Only the implementation of Mur's ABC for the E_z field component on the plane $x = 0$ is shown here. Other cases can be done similarly. Eliminating the half integer values by replacing $k-1/2$, $k+1/2$ and $k+3/2$ with $k-1$, k and $k+1$ respectively, equations (15) and (16) in [7], the first and second order Mur ABCs, become

$$E_z^{n+1}(0,j,k) = E_z^n(1,j,k) + C_1\left(E_z^{n+1}(1,j,k) - E_z^n(0,j,k)\right), \tag{8}$$

$$
\begin{aligned}
E_z^{n+1}(0,j,k) = & -E_z^{n-1}(1,j,k) \\
& + C_1(E_z^{n+1}(1,j,k) + E_z^{n-1}(0,j,k)) + C_2(E_z^n(0,j,k) + E_z^n(1,j,k)) \\
& + C_3(E_z^n(0,j+1,k) + E_z^n(0,j-1,k) + E_z^n(1,j+1,k) + E_z^n(1,j-1,k) \\
& + E_z^n(0,j,k+1) + E_z^n(0,j,k+1) + E_z^n(1,j,k+1) + E_z^n(1,j,k+1))
\end{aligned} \tag{9}
$$

where $C_1 = (c_0\delta t - \delta)/(c_0\delta t + \delta)$, $C_2 = 2(1 - c_0\delta t/\delta)$ and $C_3 = (c_0\delta t)^2 / \left(2\delta(c_0\delta t + \delta)\right)$. (10)

Mur's second order ABC can not be applied in the corner regions as it uses information from points tangential to the boundary. In corner regions Mur's first order ABC is used instead.

While E_z is a three dimensional array and lies across the nodes, operations in (8,9) involve the elements of E_z on two surfaces ($i = 0$and $i = 1$) only. The steps involved in implementing the ABCs (8,9) are now described.

Step 1. Define array. There are 14 different terms in equations (8) and (9); we define each term as a separate array. As in step 1 of the last section, let `na1`, `n` and `ns1` represent superscripts $n+1$, n and $n-1$ respectively. Also let `0` represent $i = 0$ and `1` represent $i = 1$. Let `ja1`, `js1`, `ka1` and `ks1` represent subscripts $j+1$, $j-1$, $k+1$ and $k-1$ respectively. The 14 terms are defined as

```
      REAL, ARRAY (0:Imax,0:Kmax)::
     & Ez_na1_0,    Ez_na1_1,    Ez_n_0,      Ez_n_1,      Ez_ns1_0, Ez_ns1_1,
     & Ez_n_0_js1, Ez_n_0_ja1, Ez_n_0_ks1, Ez_n_0_ka1,
     & Ez_n_1_js1, Ez_n_1_ja1, Ez_n_1_ks1, Ez_n_1_ka1
```

Step 2. Find the field values at times n and n−1. This is similar to step 2 in last section.

```
Ez_ns1_0 = Ez_n_0
Ez_ns1_1 = Ez_n_1
Ez_n_0   = Ez_na1_0
Ez_n_1   = Ez_na1_1
```

Step 3. Move the data. There are 8 terms in (9) whose subscripts are not `(0,j,k)` or `(1,j,k)`. As in step 3 of the last section, they are shifted using CSHIFT.

```
Ez_n_0_js1 = CSHIFT (Ez_n_0, dim=1, shift=-1)
Ez_n_0_ja1 = CSHIFT (Ez_n_0, dim=1, shift= 1)
Ez_n_0_ks1 = CSHIFT (Ez_n_0, dim=2, shift=-1)
Ez_n_0_ka1 = CSHIFT (Ez_n_0, dim=2, shift= 1)
Ez_n_1_js1 = CSHIFT (Ez_n_1, dim=1, shift=-1)
Ez_n_1_ja1 = CSHIFT (Ez_n_1, dim=1, shift= 1)
Ez_n_1_ks1 = CSHIFT (Ez_n_1, dim=2, shift=-1)
Ez_n_1_ka1 = CSHIFT (Ez_n_1, dim=2, shift= 1)
```

Step 4. Extract `Ez_na1` on the surface `i=1` and pass them to `Ez_na1_1`, that is

```
Ez_na1_1 = Ez_na1(1,:,:)
```
(11)

This is efficiently achieved by using a communication compiler in CMSSL library as below

```
call comm_get(Ez_na1_1,trace_extract,Ez_na1,ier)
```
(12)

Detailed explanation of `comm_get` (and the associated `comm_setup` and `comm_send`) may be found in the handbook for CMSSL of CM Fortran, [5].

Step 5. Apply Mur's first order ABC using the following operation. This is for obtaining the boundary values of corner regions. Note that this operation is performed on the whole surface i=0. The boundary values of the inner region are overwritten by the second order Mur's ABC in a subsequent operation (see step 6 of this section).

```
Ez_na1_0 = Ez_n_1 + C1*(Ez_na1_1 - Ez_n_0)
```

where `C1` is as shown in (10).

Step 6. Apply Mur's second order ABC for the inner region using the following operations. Here `C1`, `C2` and `C3` are as shown in (10). Also `Jms1=Jmax-1` and `Kms2=Kmax-2`.

```
                Ez_na1_0(1:Jms1, 1:Kms2, :) = - Ez_ns1_1(1:Jms1, 1:Kms2, :)
& + C1 * (  Ez_na1_1(1:Jms1, 1:Kms2, :) +   Ez_ns1_0(1:Jms1, 1:Kms2, :))
& + C2 * (    Ez_n_0(1:Jms1, 1:Kms2, :) +     Ez_n_1(1:Jms1, 1:Kms2, :))
& + C3 * (Ez_n_0_ja1(1:Jms1, 1:Kms2, :) + Ez_n_0_js1(1:Jms1, 1:Kms2, :)
&       + Ez_n_1_ja1(1:Jms1, 1:Kms2, :) + Ez_n_1_js1(1:Jms1, 1:Kms2, :)
&       + Ez_n_0_ka1(1:Jms1, 1:Kms2, :) + Ez_n_0_ks1(1:Jms1, 1:Kms2, :)
&       + Ez_n_1_ka1(1:Jms1, 1:Kms2, :) + Ez_n_1_ks1(1:Jms1, 1:Kms2, :))
```

Step 7. Replace `Ez_na1(0,:,:)` by `Ez_na1_0`, i.e. do the operation

```
Ez_na1(0,:,:) = Ez_na1_0
```
(13)

This is achieved efficiently by using a communication compiler from the CMSSL library. That is

```
call comm_send(Ez_na1,trace_replace,Ez_na1_0,ier)
```
(14)

The extraction and replacement operations in step 4 and step 7 of this section can be performed by directly incorporating equations (11) and (13) into the code. Such an approach is less efficient than using the communication compiler instructions of equations (12) and (14), this strategy being about four times faster. (Even so, steps 4 and 7 still use the majority of the computer time. If the total time from step 2 to step 7 is 1 second, then step 4 will use about 0.64 second and step 7 will use 0.23 second.)

Another technique used in our program is to obtain `Ez_na1(0,:,:)` and `Ez_na1(Imax,:,:)` simultaneously. This can be done by slightly changing the above steps.

Parallelizing Near Zone to Far Zone Transformation

The far zone transformation method used here follows from [1,8]. Let S' be a closed surface which is wholly within the FDTD space domain and encloses all antennas and scatters (if any). As Cartesian coordinates are used here, S' is a rectangular box. By integrating the contributions from the tangential electromagnetic fields on all cell surfaces on S', the far zone electrical field E_θ and E_ϕ can be obtained as,

$$E_\theta = -\eta W_\theta - U_\phi, \quad E_\phi = -\eta W_\phi + U_\theta \tag{15}$$

where η is the impedance of free space, $W_{\theta,\phi}$ and $U_{\theta,\phi}$ are found from [6] as

$$\mathbf{W}(\vec{r},t) = \frac{1}{4\pi rc}\frac{\partial}{\partial t}\left\{\int_{S'} \mathbf{J}_s\left(t+(\vec{r}'\cdot\hat{r})/c - r/c\right)ds'\right\}, \qquad \mathbf{U}(\vec{r},t) = \frac{1}{4\pi rc}\frac{\partial}{\partial t}\left\{\int_{S'} \mathbf{M}_s\left(t+(\vec{r}'\cdot\hat{r})/c - r/c\right)ds'\right\} \tag{16}$$

and

$$\mathbf{J}_s = \hat{n}\times\mathbf{H}, \qquad \mathbf{M}_s = -\hat{n}\times\mathbf{E}. \tag{17}$$

In this paper, we only consider the contribution to the far zone field from E_x on the face of S' which has an outward unit normal vector $\hat{y}$. We denote this potion of S' by the subscript yh. The contributions from other tangential fields on this surface, as well as tangential fields on other five surfaces, can be obtained in a similar way.

A sinusoidal excitation is used for the radiation pattern calculation. The source is switched on at $t = 0$ (In the code at `n=0` ; `n` is the time step). After computing for `n = Nmin` time steps (`Nmin` should be large enough to ensure that the steady state has been reached), the tangential electromagnetic fields at the centre of each cell surface on the surface S' are calculated and stored in the memory until `n = Nmax` is reached. (`Nmax` should be large enough to let the relation (24) hold, see below). The tangential E-fields at the centre of a cell surface are obtained by averaging the two E-fields adjacent to the cell surface centre. The tangential H-fields are obtained by averaging the four H-fields adjacent to the cell surface centre. The process of obtaining tangential E- and H-fields is similar to obtaining boundary values by Mur's ABCs. E_x at cell surface centres on the face S'_{yh} is obtained in this process. The field components are three dimensional arrays with the third axis being time and may be expressed as, for example, $E_{xyh}(i,k,n)$. After E_{xyh} and the other tangential field components on S' are obtained between time steps `Nmin` and `Nmax` and stored in the memory, they are used to calculate the far zone field.

As seen in [8], E_x on S'_{yh} contributes to U_z only. Averaging the left hand side of two equations (13)-(14) in [8], we may

find the contribution of E_{xyh} on a single cell surface (denoted by subscripts i, k) to U_z as

$$U_{z,i,k}(\hat{r}) = \frac{\delta x \delta z}{8\pi c \delta t}\left(E_{xyh}(i,k,m+1) - E_{xyh}(i,k,m-1)\right) \tag{18}$$

where

$$m = NINT(m_0 + (\vec{r}' \cdot \hat{r})/(c\,\delta t)) \tag{19}$$

$$m_0 = NINT((t - r/c)/\delta t) \tag{20}$$

$$\hat{r} = \sin\theta\cos\phi\hat{x} + \sin\theta\sin\phi\hat{y} + \cos\theta\hat{z} \tag{21}$$

$$\vec{r}' = (i+1/2)\delta x\hat{x} + j_{yh}\delta y\hat{y} + (k+1/2)\delta z\hat{z} \tag{22}$$

Here the operator *NINT* is as for the FORTRAN generic function which rounds a real number to the nearest whole number. Note that, r does not appear in (18) as it can be chosen arbitrarily as only relative values of far fields are required. Using (21)-(22) in (19) leads to

$$m = NINT\left(m_0 + \left((i+1/2)\sin\theta\cos\phi + j_{yh}\sin\theta\sin\phi + (k+1/2)\cos\theta\right)/(\delta c\delta t)\right) \tag{23}$$

We can see that m can be constructed as a four dimensional array, expressed `M(i,k,θ,ϕ)`. Again note that, we don't have to know the values of t and r in (20). Instead, we may just choose m_0 properly ensuring that the relation

$$\mathtt{Nmin} < m < \mathtt{Nmax} \tag{24}$$

holds for all six faces of S'.

By summing $U_{z,i,k}$ over i and k and replacing $\hat{r}$ with its θ and ϕ components in (18), U_z due to E_x on S'_{yh} is

$$U_z(\theta,\phi) = \frac{\delta x \delta z}{8\pi c \delta t}\sum_{i,k}\left(E_{xyh}(i,k,m+1) - E_{xyh}(i,k,m-1)\right) \tag{25}$$

The main steps needed to implement this equation in CM Fortran are shown below. For the sake of improved readability the symbols θ, ϕ and δ are retained in the code list although they are illegal in CM Fortran.

Step 1. Define arrays. In the following definitions, `mi` and `ma` represent the lower and upper bound respectively for relevant variables except for `Nmin` and `Nmax`. The variables `Exyh_cshift` and `Temp` are explained in steps 3 and 5 below.

```
real,    array(Imi:Ima,Kmi:kma,Nmin:Nmax)::Exyh,Exyh_cshift
integer,array(Imi:Ima,Kmi:kma,θmi:θma,ϕmi:ϕma)::M
real,    array(Imi:Ima,Kmi:kma,θmi:θma,ϕmi:ϕma)::Temp
real,    array(θmi:θma,ϕmi:ϕma)::Uz
```

Step 2. Use compiler directive to control the layout of arrays, i.e. control how the arrays are placed in the distributed memory. It will become clear in step 5 why the third and fourth axes should be distributed on a single node rather than across the nodes. (Compiler directive must start from column 1.)

```
CMF$ LAYOUT         Exyh(:news,:news,:serial)
CMF$ LAYOUT Exyh_cshift(:news,:news,:serial)
CMF$ LAYOUT            M(:news,:news,:serial,serial)
CMF$ LAYOUT         Temp(:news,:news,:serial,serial)
```

Step 3. For all `i,k` and `m`, perform the operation `Exyh(i,k,m+1)-Exyh(i,k,m-1)` and assign the results to array `Exyh_cshift`. That is

```
Exyh_cshift = CSHIFT( Exyh, 3, 1 ) - CSHIFT( Exyh, 3, -1 )
```

Step 4. Obtain the array `M`. In this step, the 'distances' from far field point (θ,ϕ) to cell surface centres on face S'_{yh} are calculated in parallel.

```
forall (i=Imi:Ima,k=Kmi:Kma,θ=θmi:θma,ϕ=ϕmi:ϕma)
& M(i,k,θ,ϕ)=NINT(M0 + ((i+0.5)*sin(θ)*cos(ϕ)
&          + Jyh*sin(θ)*sin(ϕ) + (k+0.5)*cos(ϕ))/(δcδt))
```

Step 5. Sum $U_{z,i,k}$ over i and k. In this step, a gather operation along the 3rd axis of `Exyh_cshift` is performed. The CM Fortran utility library has an efficient gather/scatter algorithm along a serial axis, which is why the third and fourth axes must be declared `:serial` in step 2.

```
forall(i=Imi:Ima,k=Kmi:Kma,θ=θmi:θma,ϕ=ϕmi:ϕma)
&   Temp(i,k,θ,ϕ)=Exyh_cshift(i,k,M(i,k,θ,ϕ))
 Uz = A*SUM(SUM(Temp,DIM=2),DIM=1)
```

where $A = (\delta x \delta z)/(8\pi c \delta t)$

Results

The parallel FDTD code that has been described was applied to the problem of references [9,10], that is, a $\lambda/4$ monopole on a conducting box in the presence of a simple hand-head model. Thr results obtained were similar to the reported results. Table 1 shows the comparison of CPU time for a serial code run on a SUN SPARC-2 workstation and CM busy time for the parallel code run on a CM-5 for the core FDTD algorithm. The parallel code is about 60 times faster when 16 processors are used compared with the serial code, and about 100 times faster when 32 processors are used.

Far field patterns on two planes normal to each other were also calculated (as in [9] and [10]). In our calculations, the angle increment for far field points is three degrees, and the integration surfaces S' for far zone transformation are 2 cells distant from the objects being studied, in all directions. Compared with computer times in [9] and [10] for far field pattern calculations, the parallel code is approximately 16 times faster for 16 processors and approximately 27 times faster for 32 processors. Note that this time comparison may be misleading due to: 1) different ABCs are used, 2) some parameters, such as the angle increment for far field points, are not stated in the references, 3) different sources are used and 4) the method used to obtain the far field patterns is not explicitly described in the references. Even so the time comparison is offered as an indicator of code performance.

The parallel code was also used to obtain the radiation pattern of a $\lambda/2$ dipole. Table 2 shows CM busy time for different parts of the program for these calculations. The integration surface S' for far zone transformation is 8 cells inside the FDTD space boundary in all directions. Radiation patterns are calculated on two normal planes, and the angle increment for far field points is three degrees. The FDTD space size has been carefully chosen to maximise efficiency.

By comparing the results in this table and the results in [9] and [10] it can be seen that the percentage of the computer time used by different parts of the program in serial case and in parallel case are significantly different. While FDTD algorithm takes 57% and 81% of the CPU time in [9] and [10] respectively, it takes only 16% of computer time for the parallel code. For ABCs, which take only 3.8% and 5.5% CPU time in [9] and [10] respectively (note, Mur's ABCs are not used in [9,10]), Mur's ABCs take about 30-35% computer time in the parallel code.

Table 1 The comparison of CPU time on SUN SPARC-2 and CM busy time on CM-5 for FDTD algorithm for a monopole on a conducting box in the presence of head and hand model. (time steps = 1500.)

FDTD space size	SUN SPARC-2	CM-5 16 Processors(64 VUs)	CM-5 32 Processors(128 VUs)
55×46×56	3059 s[7]	47 s	28 s
96×86×102	11478 s[8]	194 s	113 s

Table 2. CM busy time for different parts of the program for a $\lambda/2$ dipole radiation pattern calculations, f = 1.875 GHz, cell size = $5mm^3$, time steps = 1000.

CM-5 configuration	16 Processors(64 VUs)		32 Processors(128 VUs)	
FDTD space size	64×80×48	64×144×48	64×80×80	64×144×80
Total CM busy time	237 s	408 s	209 s	345 s
FDTD algorithm	15.49 %	15.33 %	15.68 %	16.60 %
Mur's ABCs	34.71 %	31.06 %	34.81 %	29.50 %
Equivalent currents	9.35 %	15.54 %	10.81%	18.03 %
Near to far field	37.45 %	34.99 %	35.77 %	32.70 %
Others	2.99 %	3.08 %	2.92 %	3.17 %
Total	100 %	100 %	100 %	100 %

Conclusion

In this paper, methods of parallelizing FDTD algorithm, Mur's ABCs, and near zone to far zone transformation are discussed. On a 32 processor CM-5, the core FDTD algorithm is 100 times faster than an existing serial code run on a SUN SPARC-2 workstation, and the calculation of the radiation patterns on two planes normal to each other is approximately 27 times faster. The code is transportable in that it can be run unmodified on other CM-5 machines irrespective of the number of processors.

Acknowledgment - The CM-5 facility is at the Sydney Regional Centre for Parallel Computing (SRCPC). The authors thank Dr Russell Standish, the parallel programming consultant in SRCPC for numerous useful suggestions and discussions. His help was invaluable. The second and third authors also thank Ericsson, Australia for their financial support.

References

[1] K. S. Kunz and R. J. Luebers, *The Finite Difference Time Domain Method for Electromagnetics,* CRC Press, USA, 1993.

[2] V. Varadarajan, and R. Mittra, "Finite-difference time-domain (FDTD) analysis using distributed computing," *IEEE Microwave and Guided Wave Letters.*, vol. 4, pp. 144-145, May 1994.

[3] D. P. Rodohan, and S. D. Saunders, "Rapid solution of the finite difference time domain method using parallel associative techniques," *Eight International Conference on Antennas and Propagation.*, London, UK, vol. 1, pp. 596-599, 1993.

[4] W. J. Buchanan, N. K. Gupta, and J. M. Arnold, "Simulation of radiation from a microstrip antenna using three-dimensional finite-difference time-domain (FDTD) method,"

[5] *CM Fortran Document Set: Preliminary Documentation for Version 2.0 Beta,* Thinking Machines Corporation, Cambridge, MA, 1993.

[6] M. N. O. Sadiku, *Numerical Techniques in Electromagnetics,* CRC Press, USA, 1992, Section 3.8.

[7] G. Mur, "Absorbing boundary conditions for finite-difference approximation of the time-domain electromagnetic-field equations," *IEEE Trans. Electromagn. Compat.*, vol. EMC-23, pp. 1073-1077, 1981

[8] R. Luebbers, K. Kunz, M. Schneider, and F. Hunsberger, "A finite difference time domain near-zone to far-zone transformation," *IEEE Trans. Antennas Propagat.*, vol. AP-39, pp 429-933, April 1991.

[9] J. Toftgard, S. N. Hornsleth, and J. B. Andersen, "Effects on portable antennas of the presence of a person," *IEEE Trans. Antennas Propagat.*, vol. AP-41, pp. 739-746, June 1993.

[10] J. Toftgard, S. N. Hornsleth, and J. B. Andersen, "Effects on portable antennas by the presence of a person," *ACES/TEAM international workshop on applied computational electromagnetics: directions for the nineties*, Telecom Australia Research Labs, 14th August 1992.

Calculation of Electromagnetic Fields with the Multiple Multipole Method (MMP Method) on Parallel Computers

C. Tudziers, H. Singer
Technical University Hamburg-Harburg

Abstract

The MMP Method extended by line sources is well suited for the analysis of electromagnetic field problems in electrodynamics. To handle large-scale problems, an existing MMP program package was modified for implementation on a parallel computer (MIMD system with distributed memory). The program package has been divided into three parts which have been parallelized individually. Tests have been performed on several systems including a machine containing 128 processors, with satisfactory results.

Introduction

The MMP Method is used for the numerical computation of 3D electromagnetic fields. Large scale problems involve long computation times and large equation systems. Parallel computers are designed to handle such problems. As shown later, the MMP code can be divided into three nearly independent parts. An effective parallelization requires parallel algorithms for all of them. We developed such algorithms in order to implement them in an existing MMP code which has already been successfully run on sequential computer systems. In this paper we present these algorithms and show the results of some tests performed on different parallel systems.

The MMP Method

The MMP Method is based on the Helmholtz equations for time harmonic fields.

$$\Delta\vec{H} + k^2\vec{H} = 0\,, \qquad \Delta\vec{E} + k^2\vec{E} = 0 \qquad \text{with } k = \omega\sqrt{\varepsilon\mu}\,.$$

They can be solved by Debye potentials and separation in spherical coordinates (r,θ,ψ). The results are series which include spherical Bessel j_ℓ, Hankel $h_\ell^{(2)}$ and Legendre functions $Y_{\ell m}$:

$$\vec{E} = \vec{r} \times \operatorname{grad} v + \frac{1}{j\omega\varepsilon}\operatorname{rot}(\vec{r} \times \operatorname{grad} u)\,,$$

$$\vec{H} = -\frac{1}{j\omega\mu}\operatorname{rot}(\vec{r} \times \operatorname{grad} v) + \vec{r} \times \operatorname{grad} u\,,$$

$$u(r,\theta,\psi) = \sum_{\ell=1}^{\infty}\sum_{m=-\ell}^{\ell}\left[a_{\ell m}\cdot h_\ell^{(2)}(kr) + b_{\ell m}\cdot j_\ell(kr)\right]\cdot Y_{\ell m}(\theta,\psi)\,,$$

$$v(r,\theta,\psi) = \sum_{\ell=1}^{\infty}\sum_{m=-\ell}^{\ell}\left[c_{\ell m}\cdot h_\ell^{(2)}(kr) + d_{\ell m}\cdot j_\ell(kr)\right]\cdot Y_{\ell m}(\theta,\psi)\,.$$

For $b_{\ell m}$=$d_{\ell m}$=0 these equations represent the fields of radiating dipoles (ℓ=1), quadrupoles (ℓ=2) and higher-order multipoles. In numerical calculations the electromagnetic field is divided into a known incident part $<E^{(i)},H^{(i)}>$ and the scattered field $<E^{(s)},H^{(s)}>$.

$$\vec{E} = \vec{E}^{(i)} + \vec{E}^{(s)} \qquad \vec{H} = \vec{H}^{(i)} + \vec{H}^{(s)}$$

The latter is approximated by several expansions of the described form.

An important extension of the MMP method consists in joining a large number of aligned multipole expansions to one segment. A source density is defined which is modulated by certain basis functions along the segment length. The electromagnetic field of such segments is calculated by numerical integration. This procedure can reduce the total number of unknown coefficients and thereby save storage. This technique is fully described in [1] for straight lines. It can also be applied to rings or arbitrary curves [2].

To determine the unknown coefficients, the boundary conditions of the electromagnetic field at surfaces have to be considered (Fig. 1).

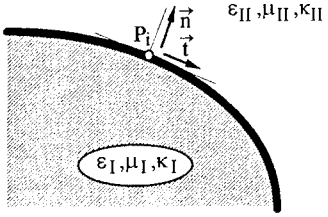


Fig. 1: Boundary conditions

$$\vec{t}\cdot(\vec{E}^{(II)} - \vec{E}^{(I)}) = 0\,,$$
$$\vec{t}\cdot(\vec{H}^{(II)} - \vec{H}^{(I)}) = C_t\,,$$
$$\vec{n}\cdot(\underline{\varepsilon}^{(II)}\,\vec{E}^{(II)} - \underline{\varepsilon}^{(I)}\,\vec{E}^{(I)}) = 0\,,$$
$$\vec{n}\cdot(\mu^{(II)}\vec{H}^{(II)} - \mu^{(I)}\vec{H}^{(I)}) = 0$$

where $\underline{\varepsilon}^{(i)} = \varepsilon_o\cdot(\varepsilon_r^{(i)} - j\dfrac{\kappa^{(i)}}{\omega\cdot\varepsilon_o})$.

For $\kappa_{II}\to\infty$:

$$\vec{t}\cdot\vec{E}^{(II)} = 0\,,$$
$$\vec{n}\cdot\vec{H}^{(II)} = 0\,.$$

Usually, these equations are evaluated successively at a number of surface points in order to obtain a system of linear independent equations for the unknown sources in the following form:

$$\text{surface points}\downarrow \begin{bmatrix} a_{11} & \cdots & a_{1n} \\ \vdots & & \vdots \\ a_{m1} & \cdots & a_{mn} \end{bmatrix} \cdot \begin{bmatrix} q_1 \\ \vdots \\ q_n \end{bmatrix} = \begin{bmatrix} b_1 \\ \vdots \\ b_m \end{bmatrix} \qquad \text{sources} \rightarrow$$

$$\Leftrightarrow \quad \underline{A}\cdot\underline{q} = \underline{b}$$

The elements of the matrix $\underline{A}$ hold the frequency-dependent geometrical and material data of the configuration, while the vector $\underline{b}$ contains the information on the known incident field. $\underline{q}$ is the vector of the unknown sources. In the case of m=n (point matching) this system has a unique solution. But the solution vector obtained in this way often yields large deviations of the boundary conditions outside the matching points. Better results are achieved if the number of surface points is increased (m > 2n) and the overdetermined equation system is evaluated [3]. The sought solution must minimise the square product of the residuum $\underline{r}$:

$$\underline{r}^{*} \cdot \underline{r} \rightarrow \text{minimum} \qquad \text{with } \underline{r} = \underline{A} \cdot \underline{q} - \underline{b}.$$

Therefore the following equation system must be solved [4]:

$$\Rightarrow \underbrace{\underline{A}^{H} \cdot \underline{A}}_{\underline{Z}} \cdot \underline{q} - \underbrace{\underline{A}^{H} \cdot \underline{b}}_{\underline{y}} = 0 \qquad \Leftrightarrow \qquad \underline{Z} \cdot \underline{q} = \underline{y}$$

where $\underline{A}^{H}$ is the Hermitian transpose of $\underline{A}$. This so-called Least Squares Method (LSM) implies a matrix multiplication of $\underline{A}$ before the quadratic matrix $\underline{Z}$ can be decomposed in order to determine the solution vector $\underline{q}$. Usually, the QR-Decomposition (Householder) is applied to the overdetermined equation system in such problems. The first way, however, allows the required amount of memory to be reduced, as shall be shown later.

After this stage, the electromagnetic field can be computed at arbitrary space points. For the analysis of the result, a graphic output is useful. In general, this implies the computation of the field at a large number of space points.

Consequently, the MMP code can be summed up by the three most time-consuming parts:

- Computation of the matrix elements in order to compose an equation system
- Solution of the equation system
- Field computations

The Parallel Computer

All parallel computers used in our investigations are based on the MIMD type (MIMD = Multiple Instruction stream, Multiple Data stream, Fig. 2). This means that every processor has its own local memory. The data transfer must be performed by communication (Message Passing). The development of the parallel algorithms has been made on a transputer system containing 128 transputers (Parsytec SC128) with 4 MByte of local memory. Each of them has four links for communication with a transfer rate of 1 MByte/s. The transputers can be connected via the links to different types of networks (e.g. rings, trees or lattices). The second parallel system mentioned in this paper is a cluster of six HP735 workstations connected via FDDI (100 MBit/s) under PVM.

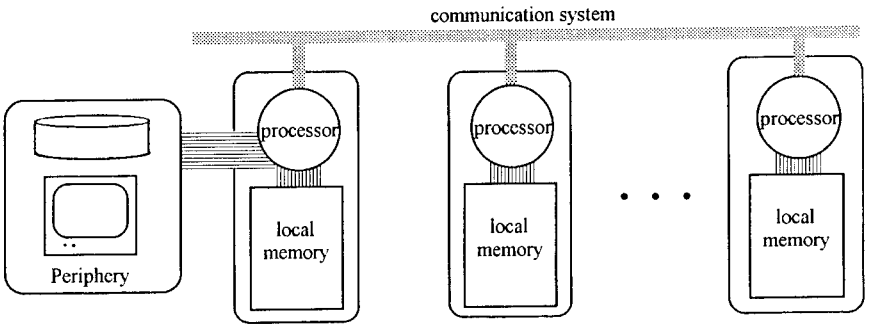


Fig. 2: Model of a MIMD system

Parallelization

In order to achieve an effective usage of the parallel systems, the three parts of the MMP code mentioned above have to be parallelized. The aim is to solve large-scale problems in acceptable computation times. Such problems with several thousand unknowns lead to a large requirement of storage for the matrix. Therefore the equation system has to be distributed among the local memories of the processors. The largest computable problem size is thus limited by the sum of the local memories. The parallel algorithms for the computation of the matrix elements and for the solution of the equation system have to deal with this kind of distribution.

Several examples are proposed in order to test the effectiveness of the parallel algorithms. One of them is a series of perfectly conducting bars in a plane-wave field depicted in Fig. 3. This configuration was used purely to examine the efficiency of the parallel algorithm. The tests were performed on the transputer system. Since each transputer had 4 MByte of memory, the maximum number of unknowns was around 500 in these first examples.

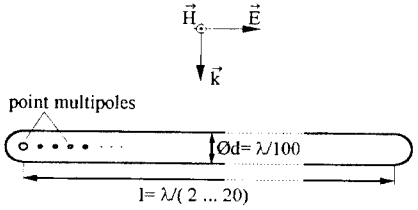
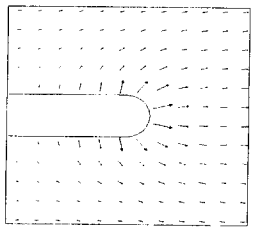


Fig. 3: Test configuration and plot of the electric field for $l = \lambda / 10$

$\omega \cdot t = 0$

$E_{max} = 3.8 \cdot \hat{E}^{(i)}$



Parallelization of the matrix computation

Firstly, the algorithm for point matching is regarded. In this case, there is principally no difference if the rows or columns of the matrix are distributed among the local memories. But the structure of the already existing sequential program makes it easier to choose the row-oriented technique. On every processor a process p_A is started which is able to compute one row of the matrix (Fig. 4).

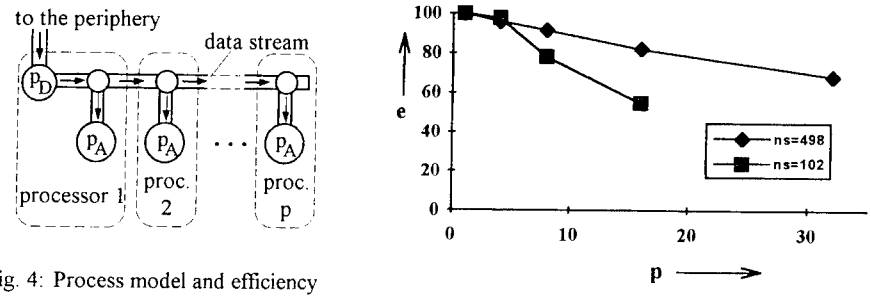


Fig. 4: Process model and efficiency

The first processor holds an additional process p_D which is responsible for the connection to the periphery and the load balancing. Initially, this process sends data as regards geometry, material constants, frequency and topology to each processor. Subsequently, it combines a certain number of surface points to packages and sends them successively to the computation processes. These processes

calculate the corresponding rows of the equation system and store them in their local memories. Afterwards, each process can order a new data package by sending a signal to the distribution process. At the end, after all surface points have been distributed, each processor holds a certain number of rows of the equation system in its local memory. In general, this number varies, because the computation times of the matrix elements are different. To achieve equal loads for all processors in the following matrix decomposition, the processors with too many rows have to send the excess rows to the ones with less rows. The graph in Fig. 4 shows the behaviour of this algorithm at several processor numbers p by means of two simple test examples with 102 and 498 unknowns. The efficiency e is defined as

$$e = \frac{1}{p} \cdot \frac{T_s}{T_p} \cdot 100\%.$$

T_s and T_p are the computation times of the sequential and parallel program, respectively. The curve decreases at higher processor numbers, because the central distribution process is not able to provide the data packets fast enough to keep the processors permanently busy, especially at lower loads. This can be avoided by increasing the package size or by adopting an alternative load balancing strategy discussed later.

The parallelization of the least squares technique is more complicated, due to the matrix product:

$$\underline{Z} = \underline{A}^{H} \cdot \underline{A} = \begin{pmatrix} a^{*}_{11} & \cdots & a^{*}_{m1} \\ \vdots & & \vdots \\ a^{*}_{1n} & \cdots & a^{*}_{mn} \end{pmatrix} \cdot \begin{pmatrix} a_{11} & \cdots & a_{1n} \\ \cdot & & \cdot \\ \cdot & & \cdot \\ \cdot & & \cdot \\ a_{m1} & \cdots & a_{mn} \end{pmatrix} \quad \Rightarrow \quad z_{ij} = \sum_{k=1}^{m} a^{*}_{ki} \cdot a_{kj}.$$

The analysis of the matrix elements z_{ij} shows that they can be written as the sum of products containing only elements of one row of $\underline{A}$. Thus, it is not necessary to store the whole matrix $\underline{A}$. After one or more rows have been computed and stored in a buffer, the corresponding products can be calculated and added to the already known parts of the elements z_{ij}. In the following these rows are no longer needed and the buffer can be overwritten.

The data structure consuming most of the storage is the matrix $\underline{Z}$. Therefore $\underline{Z}$ has to be distributed among the local memories of the processors. On the other hand, the computation of the rows of $\underline{A}$ is performed by the different processors. Since each row of $\underline{A}$ contains portions of each element of $\underline{Z}$, these portions must be delivered to the corresponding processors via the communication system. Fig. 5 shows the parallel algorithm schematically. The processes p_A receive packets of surface points and compute the corresponding rows of $\underline{A}$. Afterwards, they calculate the products of the row elements and send them to the right processors. The processes p_Z receive them and summarise the arriving portions to the already collected parts of the elements z_{ij}. Of course, the portions are not sent element by element. Prior to this, a buffer is filled before being sent as a whole to the corresponding processor.

Fig. 5 also shows the efficiency obtained with the described algorithm for several test configurations. Both curves of the already known configuration-type lie below the curves of the point matching algorithm because of the additional communication quantity. The third curve belongs to another test configuration where segment sources have been used, which entail a numerical integration for the corresponding matrix elements. As a result, the computation of the matrix elements takes considerably more

time than the matrix multiplication. Due to this fact, the ratio of communication to computation time gets better and the efficiency rises.

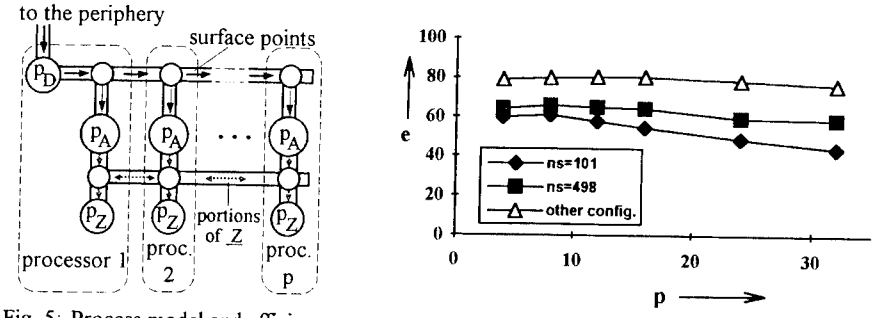


Fig. 5: Process model and efficiency

Parallelization of the matrix decomposition

After the equation system has been established, it remains in the local memories of the processors in order to activate the solution process immediately. In the case of the point-matching technique, Gaussian elimination with partial pivoting is employed. The matrix obtained by the LSM is symmetric and Cholesky decomposition can be applied. In literature a lot of algorithms are suggested for the parallel solution of equation systems considering different methods and distribution schemes. Therefore we refer at this place to the work of other scientists [5,6].

Parallelization of the field computation

Essentially, the parallelization of this last section in the MMP code can be easily performed by means of the so-called farming method. Similar to the point matching algorithm explained in the first subsection, a central process (master) sends out data packets containing space points to computation processes (worker) placed on each processor. After one worker process has determined the results, it sends them back to the central process. The master must receive the results, do some further work (e. g. storing to memory or disk, analysing) and send out a new data package to the waiting worker.

One disadvantage of this method often occurs in the case of massively parallel systems or short computation times. Since every working process sends its results to the central master, the collection of the results by the master may not always be achieved rapidly enough. Consequently, an interruption in sending out new data packets to the idle workers may ensue. Due to this idle time, the efficiency of the parallel program decreases rapidly in the case of higher processor numbers.

This behaviour can be improved by several approaches. One of them consists in sending out large packages of tasks in order to reduce the number of communications. If possible, the results should be stored in the local memories of the processors until completion of task distribution and be sent to the master all together. Since the matrix of the equation system is no longer needed, almost the entire memory is available. Thus, the same behaviour as in the parallel point matching can be observed.

Another improvement often successfully applied, is to store a certain number of tasks in the local memories. After the result of the actual task has been sent to the master, the worker process can begin to compute the new data immediately. New jobs received from the master are appended to the queue.

Additional tests

In order to test the parallel program in the case of higher computation amounts and higher processor numbers, two further examples are considered. The first one is the perfectly conducting object shown in Fig. 6a. The scattered field is approximated by five multipole expansions with $\ell = 8$ inside the body, which results in 960 unknown sources. The short tube in Fig. 6b was computed exclusively with ring segments (810 unknowns). The plots in Fig. 6c have been made with 100x100 points.

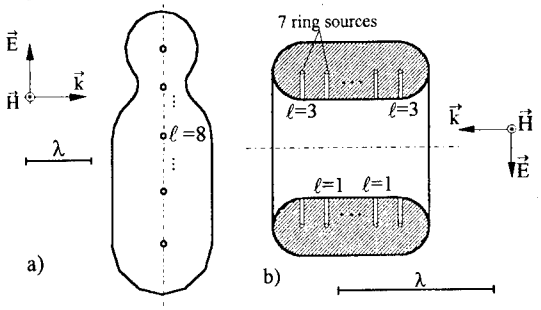
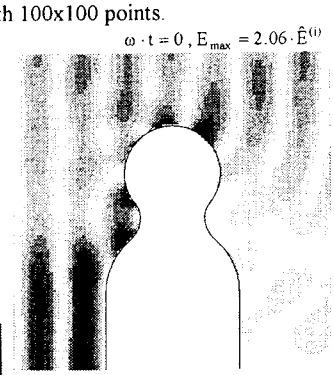
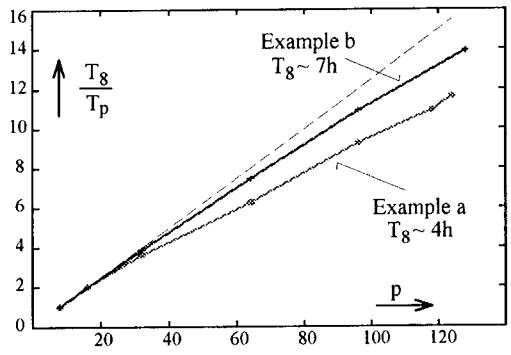


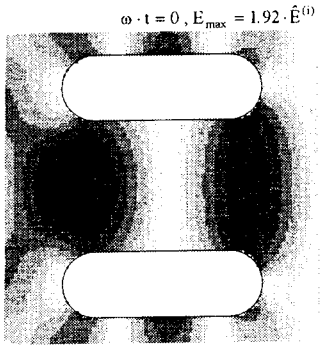
Fig. 6: Further examples



c) Plots of the electric field



d) Computation times of the whole program



The computation times related to the one with eight processors have been plotted in Fig. 6d. As expected the distance to the ideal curve rises with increasing processor number but no stoppage can be observed. Thus, even with large processor numbers the parallel code provides a sufficient effect. The difference between the two examples is again explained by the distinct kind of source used in both configurations.

As mentioned earlier, the parallel MMP code has also been run on a workstation cluster. Our experience shows the computation power of each workstation to correspond to 32 transputers. Since these machines have been permanently used by other people, exact measurements were impossible. A qualitative analysis showed results similar to those of the transputer system.

Conclusions

The previous sections demonstrate the application of the MMP Method on parallel computers. The parallel algorithms developed for the three parts of the MMP code fulfil the following criteria.

- Scalability, they can be run on an arbitrary number of processors.
- They are effective at crucial problem sizes.
- They are applicable to different types of parallelization architectures based on the MIMD model.

References

[1] D. Hoyer, H. Singer: "Solution of EMC Problems Using the Multiple Multipole Method", EMC Zürich 1991 paper 90M5

[2] P. Leuchtmann, M. Gnos: "Curved Line Multipoles for the MMP-Code", Applied Computational Electromagnetics (Conference Proceedings p. 46-53), Monterey 1994

[3] Ch. Hafner: "The Generalized Multipole Technique for Computational Electromagnetics", Artech Boston • London, 1990

[4] B. Noble, J. W. Daniel: "Applied Linear Algebra", Prentice-Hall, 1988

[5] E. Chu, A. George: "Gaussian elimination with partial pivoting and load balancing on a multiprocessor", Parallel Computing 5 (1987) 65-74, North-Holland

[6] W. Rönsch, H. Strauss: "A linear algebra package for a local memory multiprocessor: Problems, proposals and solutions", Parallel Computing 7 (1988) 413-418, North-Holland

Implementation of the finite-difference time-domain method on parallel computers.

R. S. David and L. T. Wille, Department of Physics, Florida Atlantic University, Boca Raton, FL 33431, USA.

Abstract: We discuss the application of massively parallel computers to the Finite-Difference Time-Domain (FDTD) method in electromagnetics. With regard to this technique we compare and contrast machines based on the Single Instruction Multiple Data (SIMD) paradigm to those employing a Multiple Instruction Multiple Data (MIMD) approach, notably distributed systems. Although these methodologies are quite different they both yield excellent performance and demonstrate the applicability of parallel processing to FDTD methods. A specific application to the FDTD solution of the scattering of a plane wave off a dielectric sphere is implemented on the MasPar family of SIMD computers. Parallel versus sequential implementations of this problem are compared. While sequential programs result in a near linear increase in computation time as the problems size increases, parallel programs exhibit discontinuous plateau-like jumps. Scaling studies were carried out by increasing the problem size while increasing the number of processors and demonstrate the method's excellent scalability properties.

1. Introduction.

Computational electromagnetic problems are increasingly requiring calculations that are generally very computer intensive. Large amounts of computer time may be needed to reach steady state or to provide for adequate spatial and temporal resolution. Parallel computation is now being considered by researchers in this and many other areas to obtain results more quickly. The increased speed combined with the enhanced memory capacity of parallel machines provides higher accuracy and better resolution than would be possible on a sequential machine for the same amount of computer time. Three main approaches exist for the computational solution of electromagnetic problems. They are the Method of Moments (MOM) [1,2], the Finite-Difference Time-Domain (FDTD) method [1,3,4], and the Finite Element Method (FEM) [1,3]. The MOM is based on the integral formulation of Maxwell's equations with appropriate boundary conditions. In contrast, the FDTD method and the FEM are formulated from the differential form of Maxwell's equations. These approaches have also been combined, resulting in hybrid formulations [1,3]. Parallel implementations of all of these methods have been developed for selected problem instances [5-10]. Recently Varadarajan and Mittra [10] implemented a parallel version of the FDTD method on a distributed system. These authors used a cluster of workstations with the Parallel Virtual Machine (PVM) networking software to form a multiple-instruction multiple-data (MIMD) environment. In contrast, the present authors [9] implemented the FDTD method on a two-dimensional mesh computer (MasPar MP-1 and MP-2) which operates in a single-instruction multiple-data (SIMD) setting. Although these two approaches are quite dissimilar, both yield very efficient performance and, in different ways, demonstrate the computational improvements available from parallel processing.

The FDTD method is particularly well suited for massively parallel implementation because it has a regular grid based structure with field updates occurring simultaneously at every grid point. To produce a parallel formulation the field space may be divided into disjoint regions (geometrical decomposition) each of which is assigned to a dedicated processor called a processing element (PE). As time proceeds each PE affects its field variables using information from neighboring PE's according to the FDTD equations. Field coordinates are updated simultaneously, *i. e.* in parallel, in contrast to a loop over the field dimension as would be used on a sequential computer. Excluding the boundary region, only nearest neighbor information is used for field updates which implies only short-range communications between PE's, a requirement that parallel machines are characteristically designed for. Parallel machines typically work optimally when communication between distant PE's is kept to a minimum as is the case for nearest neighbor connections used in the FDTD method. For an absorbing boundary as described by Taflove [11] the field coordinates along the boundary require information from nearest and next-nearest

neighbors resulting in a slight, but acceptable, increase in computation time. Of more critical importance, the boundary field points must be updated separately from the interior field points. Thus the PE's assigned to the interior grid points remain idle while the boundary is being updated. As will be discussed below, this can be circumvented by redistributing the boundary calculations to other PE's - a form of load balancing. However the overhead associated with this redistribution can prove detrimental to any gains made.

For the PVM distributed system implementation advocated by Varadarajan and Mittra [10] the problem domain was divided into N regions of equal size by partitioning the physical space along the z-direction. This was mapped to the processors which were configured in a linear array that was connected through an Ethernet LAN segment. Thus the computational task was divided up into N subtasks with care taken to minimize idle time and interprocessor communication. Here N was taken to be relatively small (N = 4-8). Thus the system operates in a MIMD fashion because different instructions may be simultaneously executed on different PE's and synchronization is not specifically enforced at each clock cycle. Each PE has its own instruction stream that operates on its own data. A MIMD approach works well for coarse grained problems and is able to handle a higher degree of irregularity compared to SIMD processing. Thus it is well suited for problems that generally require greater processing flexibility. However, this flexibility of MIMD machines can also be a hindrance due to synchronization issues. Typically synchronization must be forced by software directives which for systems with very many PE's can become quite a formidable task. Also the different subtasks assigned to the various PE's implies that different PE's have different computational burdens at a particular time. To minimize the time caused by processors waiting for other processors to finish their tasks (idle time), great care must be taken that the problem formulation is properly load balanced. Data management for MIMD computers either uses private memory associated with each PE with all communication and synchronization done through message passing (multicomputers) or through shared memory space (multiprocessors). Clusters of workstations (a 'farm') can also be organized into a MIMD system using networking software such as PVM or Linda [12].

An alternative parallel approach for solving the FDTD problem works on a much finer scale and assigns a PE to each point in the discretized field using a massively parallel computer containing several thousands of PE's. Being of SIMD architecture, the massively parallel computers utilize a control unit that broadcasts the same instruction to all PE's. Different data specific to each PE and therefore each field point are operated on by the same instruction simultaneously. Typically SIMD machines are used for problems containing fine grain parallelism where the problem space is for the most part regular. By their very design SIMD machines operate synchronously allowing them to avoid synchronization problems but with the cost of loosing flexibility. It is very important to formulate a SIMD based problem such that the data is mapped in a regular fashion to take advantage of synchronization. In principle it is possible for a shared global memory to be accessed by PE's in a SIMD machine. This is impractical to build however so that what is typically available are machines with private memory associated with each PE. Data is exchanged between PE's via an interconnection network. The most common networks used are simple two- and three-dimensional meshes as well as hypercubes. Using embedding theory [13, 14] a parallel algorithm implemented on one type of network may be ported to another network, although there may be a loss of efficiency associated with such a mapping.

This paper focuses on the application of massively parallel computers to the FDTD method with particular emphasis on identifying and utilizing the parallel structure of a problem to maximize computational efficiency. As an example a computer code modeling the scattering of a plane wave off a dielectric sphere as implemented using the FDTD method is parallelized. Data mapping strategies are investigated to conform the FDTD method to the two-dimensional mesh massively parallel computer used. Comparison of computational results is made to a sequential machine to provide a measure for parallel computation usefulness in the FDTD method.

2. Parallel Implementation.

To exploit a problem's parallelism its structure must be carefully investigated to determine the extent of its natural parallelism. This is not necessarily obvious and quite often is hidden, particularly

when the starting point is an algorithm written for a sequential computer. There is the notion of trivial parallelization which involves dividing a problem into separate parts that do not need to know anything about the other parts. The separate parts are solved simultaneously yet independently. An electromagnetic example of this would be the calculation of results over a range of frequencies, angles of incidence, polarizations, etc. A different PE is assigned to each computational task without any of the PE's needing to communicate information to any other PE. This approach works well for coarse grained problems where the number of PE's is of the same order as the number of tasks and where each PE has enough memory to carry out its job. Many problems however do not fall in this category and have a different grade of parallelism which involves communications between different subtasks. The modeling of an electromagnetic wave propagating through a region is an example of this. Here the problem space may be divided up into disjoint regions with each region being assigned to a PE. As time progresses each part of space as assigned to a specific PE is updated in relation to all other regions. Synchronous communication between PE's is clearly necessary at this point. What the communication pathways actually are determines the extent of the natural parallelism. If these pathways propagate throughout the problem space in a replicated fashion then the problem generally has a high degree of parallel structure and excellent speed-up will be possible on a parallel computer. If on the other hand no reoccurring communication pathways are present then the problem possesses little parallel structure and will most likely not benefit from parallel computation. Most problems typically lie somewhere in between these extremes, with portions of the problem space exhibiting a repeated communication pathway network while other parts have no connectivity at all. Additionally the distance between nodes in the algorithm graph plays an important role in determining how fast the parallel computations are carried out. For instance, a problem may have long range highly regular connectivities but this can not be exploited if the computer on which the problem is being implemented does not have an efficient long range communication capability.

An inspection of the underlying equations shows that there is considerable natural parallelism built into the structure of the FDTD method. To demonstrate this the specific example of a plane wave incident on a lossless dielectric sphere is considered, although the discussion is by no means limited to this case. The FDTD method can be employed to determine the scattered fields and the results may be compared to the exact solution to this problem as provided by Mie [1]. Owing to its regular geometric form this problem provides clear insight into how the FDTD method is mapped into a parallel regime. A numerically solved sequential FDTD solution to this problem is provided by Sadiku [1]. To approximate the spatial and temporal derivatives Yee's second-order central-difference approximations were used [1, 4, 15]. The electromagnetic fields in the interior region are given by six FDTD equations that are all quite similar. For example, using standard notation [1], the electric field component in the x direction at a time n and a field point (i, j, k) is given by:

$$E_x^n(i,j,k) = E_x^{n-1}(i,j,k) + H_z^n(i,j,k) - H_z^n(i,j-1,k) + H_y^n(i,j,k-1) - H_y^n(i,j,k). \quad (1)$$

Note that only terms from nearest neighbor grid points are used and that only temporal information from the same or previous time step is needed. The other equations at interior grid points are very similar. To terminate the physical domain absorbing boundary conditions as developed by Taflove *et al.* [11] are typically used. These come in several types. For example, the electric field in the z-direction at time n and at boundary points (i,0,k) is given by:

$$E_z^n(i,0,k) = E_z^{n-2}(i,1,k). \quad (2)$$

Thus, this boundary condition (and others similar to it) only involves communication of nearest neighbor magnitude, although it does invoke temporal information two time steps away. Another type of boundary condition involves two or three components and contains fields at points two lattice jumps away. An example of such a condition gives the x-component of the magnetic field on the x = 0 boundary and takes the form:

$$H_z^n(0,j,k) = (H_z^{n-2}(1,j,k-1) + H_z^{n-2}(1,j,k) + H_z^{n-2}(1,j,k+1))/3. \quad (3)$$

Again this and similar boundary conditions involves temporal information two steps away in addition to field variables residing on PE's that are next-nearest neighbors. Thus, just like the interior grid points, the boundary conditions all involve short-range communications. However the boundary must be computed separately from the interior, an intrinsically serial operation that could impose a limitation on the parallel nature of the FDTD. While on a sequential computer the time spent on boundary sites is negligible compared to that consumed in calculating fields at interior grid points this is no longer true on a parallel

machine and the computation of the boundary information may well become the time-determining factor in the calculations. Thus, special care needs to be taken to ensure that this part of the program is performed efficiently.

Starting from a sequential FDTD implementation as given by Sadiku [1] a parallelized program was developed in two parallel computer languages, MPF and MPL, both of which run on the MasPar class of massively parallel computers [12, 16]. MPF and MPL are parallel extensions of the Fortran 90 and C languages respectively. The MasPar MP-1 (DECmpp 12000) parallel computer utilizes 1,024 - 16,384 PE's in a two-dimensional SIMD mesh architecture with toroidal wrap-around at the boundaries. Short-range PE communication of nearest neighbor magnitude is provided by a fast X-net network while for long-range PE communication a somewhat slower global router is used. Each PE is equipped with forty 32-bit registers and has 16 or 64 kByte of private RAM memory. An array control unit (ACU) is used to control the PE array, *i. e.* it fetches, decodes, and broadcasts the instructions among the PE's. All parallel operations are run on the data parallel unit (DPU) which is collectively made up of the communication network, the PE array, and the ACU. Serial computations, data I/O, and the user interface are run on a UNIX frontend workstation (DECstation 5000). MasPar also makes the MP-2, a computer that is faster than the MP-1 but still binary compatible with it. All computations reported in this paper were performed on a 4,096-node (64x64 PE-array) MP-1 with 16 kBytes of memory. The MasPar software provides facilities to employ only a 1,024-node (32x32) or 2,048-node (64x32) portion of the PE-array. Thus results will be presented for code executed on the 1 k, 2 k, and 4 k processor boards.

MPF and MPL provide for different approaches to parallel implementation. The former is a version of Fortran 90 [17, 18] with extensions. The MPF compiler puts variables defined according to the Fortran 77 standard on the front-end, while those adhering to the Fortran 90 standard are placed onto the PE array. In the latter case, for a three-dimensional spatial array as used in the FDTD method, unless special mapping directives are used, the first dimension is mapped along the x-direction of the PE-array, the second dimension along the y-direction, with further dimensions going into memory. A layering into memory is used if the actual dimension exceeds that of the processor grid in the corresponding direction. The compiler assigns operations it considers parallel to reside on the DPU. All other operations reside on the front-end. Because the compiler decides what is parallel and what is not the programmer must be very careful to structure the program so that data is not continually traveling between the DPU and the front-end. Called 'sloshing', if it occurs this effect can greatly diminish parallel gains made. In contrast, MPL, based on Kernighan and Ritchie C, allows for specific placement of data on and manipulation of the PE array. Variables are defined as either singular or plural with the singular variables residing on the front-end and the plural variables being defined on every PE residing on the DPU. This flexibility provides the programmer with an explicit way to avoid sloshing as well as implementing an algorithm requiring software control at the PE level. The price to be paid for this is that the amount of programming effort and careful algorithm design is much greater than in MPF. Also, the ensuing code tends to be not very portable since it is designed for a specific configuration of the parallel machine. For example, running an MPF code on a different partition of the PE-array can be done by a simple compiler directive in MPF, while a more thorough re-write may be necessary in MPL.

The MPF implementation of the problem under study basically involved conforming the sequential FDTD code into a more parallel form, *i. e.* rewriting the code to a Fortran 90 standard. Despite the fact that the FDTD method has much parallel structure the actual code written to implement it on a sequential computer was by definition not parallel. For the compiler to properly map the code onto the PE array careful attention was used to eliminate as much as possible any remnants of sequential code. The field coordinates were mapped onto the two-dimensional PE-array using the default compiler assignments along the x- and y-directions with the z-direction and time assigned to memory. As a consequence computations became parallel in two dimensions. The third dimension over z however must be carried through sequentially with an iterative loop construct for each PE. Only X-net nearest and next-nearest neighbor magnitude computations are used to update the fields both in the interior and along the boundary. For the interior grid points N sequential operations go to one parallel operation. Along the boundary in a number of cases only one edge of the PE grid is being used causing the interior PE's to remain idle while the boundary field is being updated. Data redistribution from memory to the PE array is a possible remedy to this (as will be discussed below) but is difficult to implement using MPF. Specific implemen-

tation details regarding MPF were given in our previous paper [9] although there the boundary conditions were not yet parallelized, a shortcoming that has now been circumvented.

MPL can be used to re-map data along a boundary from memory to the PE array using a coordinate 'rotation' (see Fig. 1). Due to its ability to explicitly place, define, and change data on the PE grid a coordinate 'rotation' can be accomplished by taking data along the boundary that runs into memory. and redistributing it amongst all PE's. Suppose, for example, that the $x = 0$ boundary condition given by equation (3) needs to be implemented. If the data is stored according to the default only the processors in the first column of the PE-array will be active and a loop over memory locations (z-direction) needs to be performed (left-hand side of Fig. 1). This constitutes a very inefficient use of the parallel array since the vast majority of processors is idle. It is possible to perform a coordinate 'rotation' and to map the $x = 0$ boundary onto a temporary two-dimensional array which is completely stored on the PE-array (right-hand side of Fig. 1). Now these boundary sites may be updated in a single cycle, a much more efficient use of the processors. However, the price to be paid for this parallelism is that data needs to be broadcast from memory on processors in the first column to all other processors. While there are efficient software directives to speed up this broadcast, this is still a time consuming step and it may outweigh any speed-up gained from having all processors active. Whether or not the coordinate 'rotation' leads to a gain in speed depends on the speed of communication of the parallel machine used and on the amount of computation involving boundary sites. In the case under study it was found that the redistribution led to a longer execution time compared to a code in which no such 'rotation' was performed. However, the stratagem is a valuable one and may be useful in more complex situations or on parallel computers that have a faster broadcast mechanism than the MasPar MP-1. In particular, it might be very well suited for hypercubes since a one-to-all broadcast can be performed very efficiently on this interconnection network [13].

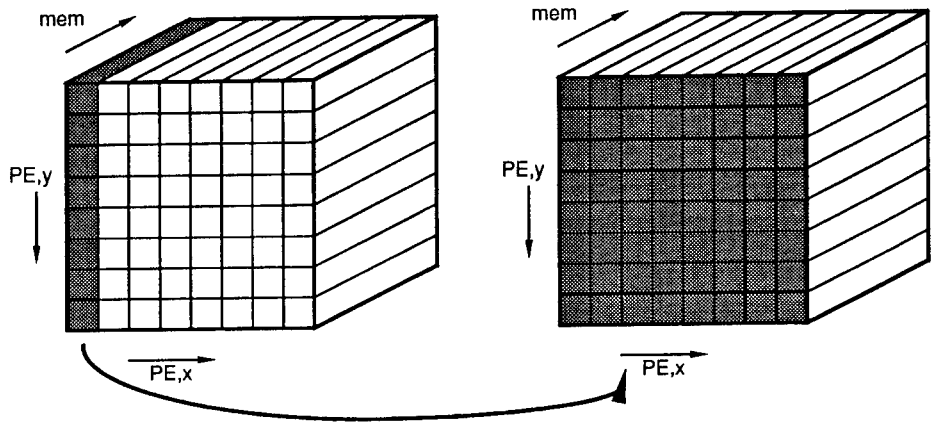


Fig. 1: Rotation from memory (mem) to two-dimensional PE-array in order to ensure load balancing during updates of boundary sites (see text).

The MPL code without boundary rotation turned out to be marginally faster than the corresponding MPF code, which is hardly surprising considering the explicit programmer control over data placement. However, the gains in execution time were only on the order of 10 % and hardly justify the amount of programmer effort involved. They illustrate the effectiveness of the MPF compiler in generating efficient parallel code for this kind of problems. In the remainder of this paper only results obtained by the MPF code will be shown, since the general trends for the MPL code were identical, apart from its slightly higher speed.

3. Results and discussion.

For the model problem considered here calculations were performed for a range of grid sizes, with the total number of grid points equal to $I_x x I_y x I_z$, where I_x, I_y, and I_z are the number of grid points in the x-, y-, and z-direction, respectively. Thus all field variables were taken to be matrices of the form $A(I_x,I_y,I_z)$. To investigate scaling properties, in all calculations I_y and I_z were kept fixed, but I_x was allowed to vary. Not surprisingly the execution time for the sequential program (executed on a DECstation 5000) showed a perfect linear dependence on I_x. In stark contrast, Fig. 2 shows the execution time for 500 time steps on various partitions of the parallel machine. To be noted is that this time remains constant over a range of problem sizes and exhibits discontinuous jumps whenever a wrap-around at the PE-boundary occurs leading to a layering in memory. The various symbols indicate that computations were performed on a 32x32 PE-array (open squares), a 64x32 PE-array (solid circles), and a 64x64 PE-array (solid squares). On the 32x32 array the jumps occur whenever I_x exceeds a multiple of 32, while on the other arrays this happens at multiples of 64, commensurate with the dimension of the PE-array in the x-direction. The ratio between the execution time for various plateaus is always very close to an integer, reflecting that the calculations are essentially completely parallel. It is to be noted however that there tends to be a slight increase in computation time near the middle of the plateaus. This is because for such I_x values the communication between boundary sites is long-range and thus involves a router call. On the other hand, for I_x close to a multiple of the PE-dimension in the x-direction a short-range (and faster) X-net call will be sufficient.

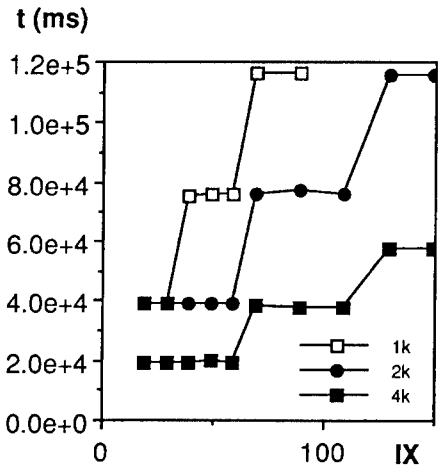


Fig. 2: Execution time (in ms) as a function of number of points in x-direction, I_x, for various PE-array sizes.

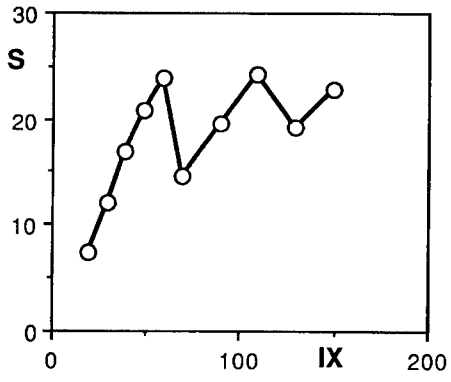


Fig. 3: Speed-up of parallel program relative to sequential program on DECstation 5000 as a function of problem size, I_x.

A useful measure of parallel program performance is the speed-up, S. This is defined as the ratio of the execution time, T_1, for the best sequential algorithm running on a single processor divided by the execution time, T_p, for the parallel algorithm on p processors. Efficient parallel programs typically show a linear increase in speed-up as the number of processors is increased. However, if the problem size is fixed speed-ups tend to level off or even collapse as p is increased since it may not be possible to take

full advantage of all available processors or the communication overhead may become burdensome. This is a consequence of a very important result in parallel computing known as Amdahl's law [13]. As observed by Gustafson, the way out of this dilemma is to increase the problem size as the number of processors is increased. Algorithms that are able to maintain efficiency under this operation are known as 'scalable' and are considered optimal.

On a SIMD system it may not be possible to run the program on a single processor. Instead in the definition of speed-up one may use the time taken by the sequential program on another computer as the reference point. In the present work we have taken the serial time T_1 to be that needed to execute the original sequential program on a DECstation 5000. The ensuing speed-up (on a 64x64 array) as a function of problem size is shown in Fig. 3. To be noted is that the speed-up peaks near multiples of 64 (where full use of the PE-array is made) and then abruptly drops off when a layering in memory occurs (corresponding to the jumps between plateaus in Fig. 2). The size of the drops diminishes as I_x increases, with speed-up converging to a peak-value of about 25. Moreover, by taking the values listed in Fig. 2 and plotting scaled speed-up versus number of processors one finds nearly perfect scalability illustrating that the algorithm has essentially been completely parallelized.

These results form a satisfying complement to the work by Varadarajan and Mittra [10] on a very similar problem in a MIMD environment. These authors found that to maintain speed-up at an optimal value they had to scale the problem in such a way that computation-to-communication ratios were kept much larger than unity. Moreover, in addition to this consideration, problem sizes had to be increased with increasing number of processors to maintain efficiency. Thus, although the details of the implementation differ, the essential factors necessary to guarantee an optimal use of resources are the same in their work as in the present one. A number of other authors (see [5] and references therein) have also quoted excellent speed-ups on scaled problems. It should be pointed out that SIMD architectures may be less suited for more complex problems involving irregular grids or adaptive meshes. In those cases MIMD computers hold the edge, although load balancing and synchronization may be cumbersome. Also, once the decision is made to invest development effort on a MIMD platform one should additionally consider using MOM or FEM techniques rather than exclusively the simpler FDTD method.

In summary, the FDTD method is very well suited for implementation on parallel computers, be it within a SIMD or a MIMD framework. This is a consequence of this technique's regular structure, simultaneous updating, and short-range communication. The main loss of efficiency is due to the boundary conditions: all processors containing only interior grid points are idle while boundary sites are being updated. On a two-dimensional mesh a redistribution of the load may be accomplished through a rotation from PE-memory to the PE-array, but this in itself incurs considerable overhead which may offset the gains obtained by having all processors active. Nevertheless, in more complex situations such a step is justifiable in order to attain complete parallelism in the calculations. The resulting code shows excellent scalability demonstrating a perfect match between problem formulation and parallel architecture. The speed-up that can be attained over a single processor workstation is already considerable. Thus, it is only to be expected that further improvements will be possible as faster parallel computers with more processors enter the market place.

Acknowledgements: Robert S. David is the recipient of a Motorola Partnerships in Research Grant.

References.

[1] M. N. O. Sadiku, 'Numerical Techniques in Electromagnetics', CRC Press, Boca Raton (1992).
[2] R. F. Harrington, 'Field Computation by Moment Methods', Macmillan, New York (1968).
[3] M. A. Morgan (ed.), 'Finite Element and Finite Difference Methods in Electromagnetic Scattering', Elsevier, New York (1990).
[4] K.S. Kunz and R. J. Luebbers, 'The Finite Difference Time Domain Method for Electromagnetics', CRC Press, Boca Raton, 1993.
[5] K. D. Tatalias and J. M. Bornholdt, IEEE Trans. Magnetics, **25**, 2901 (1989).
[6] D. B. Davidson, IEEE Antennas Propagation Magazine, **32**, 6 (1990).
[7] D. B. Davidson, IEEE Antennas Propagation Magazine, **34**, 9 (1992).

[8] Y. Lu, A. G. Mohamed, G. Fox, and R. F. Harrington, in 'Parallel Processing for Scientific Computing', eds. R. F. Sincovec, D. E. Keyes, M. R. Leuze, L. R. Petzold, and D. A. Reed, SIAM, Philadelphia, 1993, pp. 216-220.
[9] R. S. David and L. T. Wille, in '10th Annual Review of Progress in Applied Computational Electromagnetics', vol. 1, ed. A. Terzuoli, Applied Computational Electromagnetics Society, 1994, pp. 495-502.
[10] V. Varadarajan and Raj Mittra, IEEE Microwave and Guided Wave Letters, **4**, 144 (1994).
[11] A. Taflove and K. R. Umashankar, in 'Finite Element and Finite Difference Methods in Electromagnetic Scattering', ed. M. A. Morgan, Elsevier, New York (1990).
[12] K. Hwang, 'Advanced Computer Architecture - Parallelism, Scalability, Programmability', McGraw-Hill, New York (1993).
[13] V. Kumar, A. Grama, A. Gupta, and G. Krypis, 'Introduction to Parallel Computing', Benjamin/Cummings, Redwood City (1994).
[14] F. T. Leighton, 'Introduction to parallel algorithms and architectures: arrays • trees • hypercubes', Morgan Kaufmann, San Mateo (1992).
[15] K. S. Yee, IEEE Trans. Ant. Prop., **AP-14**, 302 (1966).
[16] A. Trew and G. Wilson (eds.), 'Past, Present, Parallel - A Survey of Available Parallel Computing Systems', Springer-Verlag, Berlin (1991).
[17] W. S. Brainerd, C. H. Goldberg, and J. C. Adams, 'Programmer's Guide to Fortran 90', McGraw-Hill, New York (1990).
[18] M. Metcalf and J. Reid, 'Fortran 90 Explained', Oxford University Press, Oxford (1990).

SESSION 16:

EM THEORY II

Chairs: K. Yee, R. Gordon

FDTD INVESTIGATION OF THE ABILITY TO INCREASE ELECTROMAGNETIC FIELDS AROUND HEAD TUMORS [1]

D. B. Dunn, A. J. Terzuoli, Jr, G. C. Gerace • Air Force Institute of Technology
C. M. Rappaport • Northeastern University

INTRODUCTION

Cancer has been a leading cause of death in the United States for several decades and remains so today; therefore, it is a leading topic of research. Current researchers employ several methods to destroy and limit the growth of cancerous tissue. However, all methods contain a similar characteristic; they destroy the healthy tissue as well as the tumor. One promising option in the treatment of cancer, involves concentration of microwave energy at the tumor site. For this, electromagnetic waves are launched into the tissue from many different locations. The waves pass through the tissue and cross at one point where constructive interference occurs. At this location, the wave form amplitude is significantly higher than at any other point in the tissue. This area of higher molecular vibration results in hyperthermia. In addition, the increased microwave levels have been shown to aid in chemotherapy.

The current drawback to this technique in treatment is achieving the optimal solution of resolution and deep penetration. Electromagnetic waves can penetrate bone and muscle structures with little reflection, but high frequencies have not been able to penetrate deeply into high water-content tissue such as muscle. This has made resolution at depth difficult in the past.

Using a computer model, this paper deals with focusing high-frequency electromagnetic waves within a human head. Although deep penetration through the muscular tissue of the brain is difficult, this study shows that with the combination of high frequencies and constructive interference, microwave concentration is possible even for tumors deep in the center of the brain.

Rappaport and Morgenthaler [1] derived an optimal field distribution for radiating a tumor within a homogeneous sphere of muscle tissue. To apply this theory to the inhomogeneous structure of a human head, the Finite Difference Time Domain (FDTD) technique for electromagnetics is used [2], which approximates Maxwell's differential equations as finite differences and directly solves them across time and space.

METHODOLOGY

This research entails setting up three distinct simulations. The first duplicates the analytical results using FDTD on a homogeneous sphere using the Penn State University FDTD code [3]. A series of FDTD simulations on laminated spheres comprise the second set of simulations. This set provides insight into the effects of inhomogeneities on the propagation of the ideal source radiation. A series of FDTD simulations on an actual model of a human head developed from an MRI scan comprise the final set of simulations. The incident field is specified in the FDTD code by setting up an electric shell, with a radius of 9.45 cm, around the sphere and specifying the E-field values at every cube along this shell. This distribution then radiates, and the field propagates through the FDTD grid, producing the same results as the analytic version. This verifies the use of FDTD to simulate a constant E-field around a sphere.

---

[1] This work was supported by the U. S. Air Force Wright, Armstrong, and Phillips Laboratories.

CODE MODIFICATIONS

Two main modifications are made on the Penn State FDTD code. The design of the code is for use in antenna calculations; thus, it is set up to have a small number of feeds, one for each antenna. Forcing an E-field around the surface requires approximately 50,000 feeds. Specifying each one individually proves to be both time consuming and memory intensive. To avoid this pitfall, the FEED subroutine is modified to calculate each value using the analytic field equations. To reduce the computational time at each time step, the subroutine approximates the source by computing the analytical value the components would have at the center of the cube and gives all six components their value based on this result rather than recalculating the field for every component.

The second major modification is the addition of a peak E-field storage array. This allows the user to specify an area over which the peak E-field value will be recorded. This is only useful because the FDTD simulations are using one frequency. By recording the peak value of the E-field, the power deposited can be easily calculated using $P = \sigma|E|^2/2$, where σ represents the conductivity of the material. Thus a simple conversion into the frequency domain has been made for comparison to the analytical results.

These two modifications allow the source distribution to be specified, and the resultant field to be recorded and analyzed. The first modification allows the FDTD code to implement the source distribution around any geometry specified in the FDTD space. The code propagates the field through the space and the second modification allows the frequency response to be recorded for analysis in MATLAB.

FDTD SIMULATIONS AND RESULTS

Three basic forms of FDTD simulations are done. All three forms are set up with identical FDTD space parameters, but the geometry is changed for each simulation. For these simulations, a 92 x 92 x 95 grid is set up with cubic cells 2.55 millimeters on a side. The Courant stability [2] condition indicates a 49.19 picosecond time step. The outer sphere in each simulation has a radius of 37 cells, or 9.45 cm. The analytical solution sets the spherical source distribution at the radius of 37 cells.

The first simulation is on a simple homogeneous sphere. This simulation serves as a verification of the code. It is to demonstrate the ability to use the FDTD code with the entire incident field specified. The results of this simulation are then compared with the analytic results.

A four layer model comprises the next simulation. This contains an outer shell of bone to simulate a bone-like fluid bolus, a thin layer of muscle tissue simulating the skin layer, a bone sphere to simulate the skull, and finally an inner shell of muscle simulating the brain. For this simulation the radius of the inner sphere is 32 cells. The outer radius of the bone layer is 34 cells, and the radius of the skin shell is 35 cells.

An FDTD model of an actual human head provides the basis for the final simulations. This model is made by converting an MRI scan of a human head into a head mesh to be read in by the FDTD code. This is a four tissue model of the head created by David Steich of Penn State University. To create it, the actual permeabilities, permittivities, conductivities and magnetic conductivities are never directly measured; instead typical values are inserted for each material type. This provides a first order approximation to the human head. The addition of a basic neck extension was added to the head to simulate the inability to place a source in the neck region. The addition of a neck is a simple extension of the final layer in the head, down to the edge of the FDTD grid.

A liquid bolus surrounds this head approximation. This bolus allows the use of the spherical source distribution on the edge of the bolus, providing a closer match in material parameters as the field propagates into the head. Although it is about 9.45 cm to the center of the head, it is not spherical; therefore, the full size head cannot fit within the 9.45 cm bolus and has to be shrunk for the initial tests. To do accomplish this, the original head mesh cell size of 3.2 mm is reduced to 2.55 millimeters.

The material characteristics of the bolus are chosen as close as possible to those of muscle. For the next simulation, the cell size increases from 2.55 millimeters to 3.2 millimeters on each side of the FDTD cubes. This simulation provides an opportunity to determine if it is possible to increase the penetration depth in the actual head. Brain tissue is less lossy than muscle tissue; therefore, it is conceivable that greater penetration may be possible in the presence of the inhomogeneities of the human head.

HOMOGENEOUS SPHERE

The simulation on the homogeneous sphere illustrates FDTD can be used in this manner described. The difference from the analytic results shows only a 6% error with a standard deviation of 8.29%. The majority of this error comes from incomplete source coupling. An analysis of the power profile demonstrates spikes along the top and bottom of the sphere. This effect is pronounced at the top and bottom of the sphere because of the polarization. Since the tangential component of the E-field is always continuous and the field is essentially vertically *(z)* polarized, the field along the equator is tangential and couples completely. The field near the poles is normal to the sphere's surface. Because the normal E-field is discontinuous by a factor of the difference in the permittivities, the field at the poles does not completely couple into the muscle tissue, thus forming the spikes. It is believed that this could be reduced by defining the sphere to extend beyond the source distribution, thereby eliminating this discrepancy in material parameters.

LAMINATED SPHERE

The next simulation is on a four-layer sphere. The material properties of the outer sphere model bone-like material, the next layer patterns muscle material, the third layer is defined as bone material, and finally, the properties of the inner sphere imitate muscle tissue. Therefore, this simulation is attempting to recreate a liquid bolus with bone-like electrical characteristics around a head. This simulation models the head as a muscle-like brain core surrounded by a spherical *skull* of bone and finally a thin *skin* layer of muscle tissue.

Figure 1 shows the E-field distribution across the central *xy* cut of the laminated sphere normalized to one at the center. The field along the equator of the sphere is predominately directed in the *z* direction. Thus, along this equatorial cut, the field will be tangent to the surface of each sphere. Because the tangential E-field has to be continuous across a dielectric boundary, along this cut the field should be continuous everywhere. Figure 1 shows this is not the case. There are E-field spikes along the edges of the inner spheres. The stair stepped edges of the spheres cause this phenomenon. Instead of having a smooth surface, small cubes form the edge. This edge produces a locally horizontal rather than vertical surface. At this point the E-field becomes normal rather than tangential. The amount of the discontinuity of the normal E-fields is proportional to the difference in relative permittivities of the two materials; therefore, the field spikes in the cube.

Figures 1 and 2 illustrate the effect of the staircase errors. Figure 1 shows the E-field distribution across the sphere in a two-dimensional image. The spikes appear as single pixels slightly darker or lighter than those around them. Figure 2 is plot of the changes in the IDTHRE components from level $z = 39$ to level $z = 40$, where IDTHRE is an array containing the material ID's for the *z* directed geometry components. Wherever the IDTHRE, or *z* directed component, changes from one level to the next, there is a locally horizontal surface where it should be vertical; therefore, Figure 2 shows only the location of each stair step. Investigation of Figures 1 and 2 reveals that every spike corresponds to the edge of a stair step. These spikes are numerical artifacts which will not actually occur.

After investigating the effects of the simple inhomogeneities, the remaining two simulations again use the model of the head developed from an MRI scan. The material characteristics define three different materials, with muscle-like properties, representing skin and white and gray matter, and one material with the low-water content properties of bone. The first of these uses a head that is

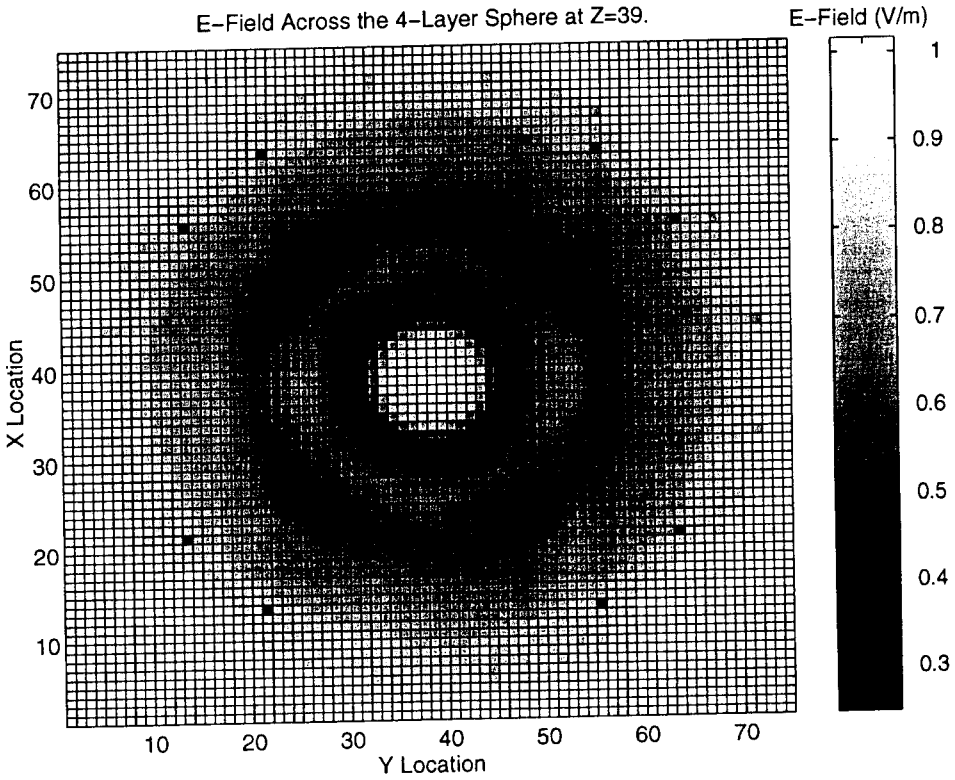


Figure 1. 2-D image of the E-field distribution across the z = 39 cut of the 4-layer laminated sphere.

reduced to fit within the 9.45 cm source shell. The second uses a full size head, with an enlarged source shell to fit around the enlarged head.

Table 1 shows a comparison of the analysis statistics on each of the simulations. *Center Mean (CM)* is a measure of the mean power in the center three-cell cube of the head. Because the power is normalized to 1 at the center, this will always be near 1; a narrow spike near the center indicates accurate focusing. *Total Mean (TM)* is a measure of the mean power everywhere else in the head. This does not include the power in the bolus because circulation of the bolus liquid can prevent overheating in the bolus. The lower this value, the smaller the risk will be of over-heating undesirable locations. The third value in the table is the ratio of the mean power at the center to the total mean power *(CM/TM)*. The higher this value, the easier it will be to heat the tumor without affecting healthy tissue. The final three numbers are percentages of the cells over various thresholds. The first gives the percent of cells with power > 1. Each of these points will reach temperatures higher than the central tumor, thus destroying the healthy tissue at that location. Ideally this number will be zero. The final two columns give the percentages of cells with a value > 0.9 and > 0.8 respectively. Although these points would not be raised to fatal temperatures, the high temperature levels may be dangerous to the healthy tissue.

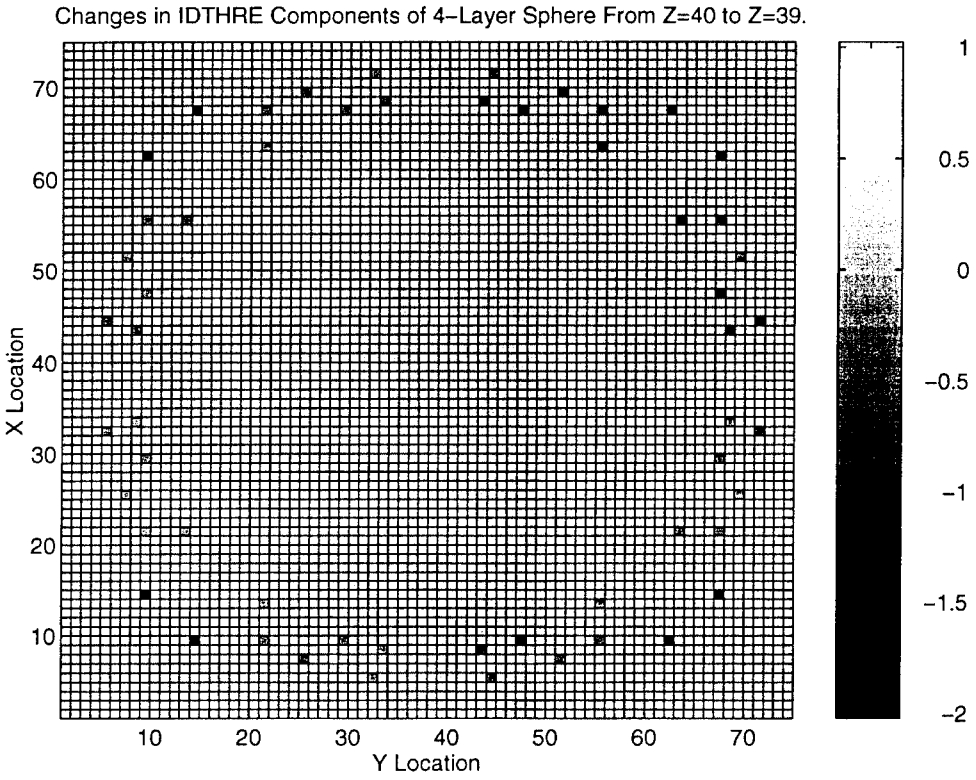


Figure 2. A plot of the location of the stair stepped edges in layer 39 of the four-layer sphere.

The spikes exist predominately in the neck region. Because there is an discontinuity in the source distribution from outside and inside the neck region, the field diffracts along the edge of the source distribution introducing the large spikes proportional to this discontinuity. In the larger head, the higher source power makes the stepped edge of the source the larger contributor to the diffracted field. In addition, some areas along the outside skin could reach an unhealthy temperature.

CONCLUSION

This research demonstrates that FDTD is an effective tool in evaluating several vital aspects of microwave hyperthermia as a treatment method. Specifically, the initial simulations confirming the optimal analytical solution, derived by Rappaport and Morgenthaler, demonstrated the utility of the FDTD numerical approach for analyzing this treatment scenario. The Laminated sphere simulations demonstrated the problem of stair step spiking. Finally, the head simulations demonstrated that in theory, microwave hyperthermia is a possible treatment option.

Simulation	*Center Mean (CM)*	*Total Mean (TM)*	*CM/TM*	% of cells > 1	% of cells > 0.9	% of cells > 0.8
Small Head	.8795 (W/m^2)	.1142 (W/m^2)	7.701	.01%	.05%	.08%
Full Head	.8436 (W/m^2)	.2389 (W/m^2)	3.531	1.33%	2.0%	2.89%

Table 1. Statistics on the FDTD Head Model Simulations

The simulation on the inhomogeneous laminated sphere demonstrates the effects inherent in an FDTD approach. The stair step approximation of a spherical surface introduced stair step spikes due to a locally horizontal surface along an otherwise vertical interface. In addition to these spikes, the FDTD approach proved to be difficult in obtaining complete coupling from the source to the sphere of treatment. These drawbacks not only demonstrate the effects of FDTD approximations, but also introduce an area to be considered in microwave treatment. Because the head is not spherical, there will be horizontal sections of interface along an otherwise vertical interface. For example, along the base of the mandible, there is a long vertical interface; along the inside of the occipital cavity there are vertical interfaces. All of these areas will be candidates for a true spiking phenomenon.

The simulations on the actual head models proved very encouraging. The source distribution placed around a small head within a spherical water bolus produced excellent focusing. There were only 20 cells above that at the center, all of which were confined to the neck region. This is due to the stepped edge of the source distribution near the neck. There was no taper down as the source neared the edge of the neck, thus launching a diffracted field near the edge of the source distribution, creating several small but strong spikes in the neck region.

These spikes are troubling, although not discouraging. In addition to the fact that there was no attempt made to taper the edge of the field distribution, the neck region itself was extremely approximate. The MRI scan produced no neck region, therefore the head was simply continued down from the base to the edge of the FDTD space. There was no spinal chord, esophagus, or trachea modeled. In addition, the head itself was approximated from an MRI scan. Although serving to produce an example of what could be possible in this area, it still needs further research and refinement.

The simulations done on a full size head demonstrated two important issues. First, these are the first simulations to show FDTD can be used on a complete 3-D model of a human head in a treatment scenario. Second, and most important, these simulations show that even without any form of optimization to account for the inhomogeneous structure of the human head, it is possible to radiate a deep-set tumor with reasonable precision.

ACKNOWLEDGMENT: The authors express their gratitude to the following people for their help, assistance, comments, and support: Dick Albanese, Alan Fenn, Ray Luebbers, Carl Baum, Leo Felsen, Dennis Andersh, Russ Burleson, Matt Kabrisky, Joe Sacchini, Paul Skinner.

REFERENCES

[1] C. Rappaport, and F. Morgenthaler, "Optimal Source Distribution for Hyperthermia at the Center of a Sphere of Muscle Tissue," *IEEE Trans. Microwave Th. and Tech.*, December 1987, pp. 1322-1327.

[2] K. Kunz and R. Luebbers, *The Finite Difference Time Domain Method for Electromagnetics.* Ann Arbor: CRC Press, Inc., 1993.

[3] J. H. Beggs, R. J. Luebbers, and H. S. Langdon. *User's Manual for TEC: PSU FDTD Code Version C for Two-Dimensional Transverse Electric Transient Scattering from Frequency-Independent Dielectric and Magnetic Materials.* Electrical and Computer Engineering Department, The Pennsylvania State University, University Park, PA, June 1993.

FDTD AND PMM BASED DESIGN OF A TEM HORN ANTENNA WITH REDUCED OFF-BORESIGHT FIELDS [1]

D. J. Wolstenholme, A. J. Terzuoli, Jr, G. C. Gerace
Air Force Institute of Technology

INTRODUCTION

There are many potential applications for Ultra-Wideband (UWB), short pulse radiating systems; target recognition, collision avoidance, and detection through lossy materials (such as concrete) are some examples. These systems require broadband antennas with low dispersion characteristics; the transverse electromagnetic (TEM) horn [1] is one such antenna.

A TEM horn antenna, shown in Figure 1, is a two-conductor, end-fire, traveling wave structure. With proper selection of the flare angle and plate widths, the TEM horn maintains a constant impedance and radiates only the TEM mode. Unfortunately, the abrupt transition from the conductors to free space causes diffraction, which increases the off boresight electric field strength. Applying a Tapered Periodic Surface (TPS) [2] to the ends of an antenna eases the transition from conductive elements to free space. A TPS is a lattice of wire or slot elements with progressively shorter lengths from one edge of the surface to the other. A wire TPS is shown in Figure 2. The TPS gradually tapers from a low reactance *($Z = 0$)* to a high reactance *($Z = \pm j\infty$)* thereby reducing diffraction.

This work has two main purposes: *first,* to reduce the off-boresight electric field levels for a TEM horn antenna, and *second,* to maximize the on-boresight peak-to-peak electric fields over a bandwidth of 20:1. These goals are met by applying a TPS to the ends of the horn. Designs are presented for a TEM horn antenna and for a TPS. The two can be designed separately keeping in mind that the goal is to reduce the off-boresight fields for bandwidth of 300 MHz to 6 GHz. In general, the design of a TEM horn requires selecting the length and width at the aperture, and selecting the flare angle between the plates. The parameters are adjusted to meet the four design criteria for an ultra-wideband, short pulse radiating system, namely: *1)* constant amplitude response, *2)* linear phase response, *3)* no reflections or resonances along the conductors, and *4)* wide bandwidth.

In the process of designing a TPS, a Periodic Moment Method (PMM) computer code [3] models each of the TPS elements and computes the reflection coefficient for each element versus frequency. From the reflection coefficient, a transmission line model determines the sheet impedance for each element. The final TPS geometry is then determined by approximating a known impedance function. After the proper geometry is determined, a two-dimensional Finite Difference Time Domain (FDTD) code [4] models the TPS. This model predicts the reduction of field levels in the shadow region of the model. After both the TEM horn and TPS designs are validated, the testing begins. Testing of the TEM horn and TPS attachments is performed at the High Energy Research and Test Facility of the USAF Phillips Laboratory.

METHODOLOGY AND RESULTS

TEM HORN DESIGN

There are three main aspects to the design of a TEM horn [5, 6]: the low frequency cutoff, the high frequency cutoff, and the characteristic impedance. The cutoff frequencies determine the limits of the horn's performance; the characteristic impedance provides the details necessary to designing the feed to the antenna. The length of the conductors determines the lowest frequency that propagates in a TEM horn. The low frequency cutoff (6 dB) is given by [5]:

[1] This work was supported by the U. S. Air Force Wright and Phillips Laboratories.

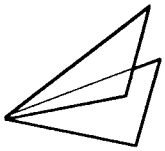


Figure 1. TEM Horn Antenna

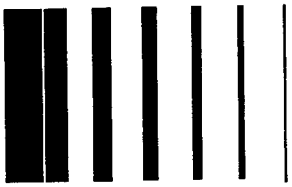


Figure 2. Wire Type of Tapered Periodic Surface

$$f_{low} = \frac{c}{2L} \tag{1}$$

where L is the length of the horn and c is the speed of light. Therefore, the length must be at least 19.69" to propagate a signal with 300 MHz components. The high frequency cutoff is determined by the flare angle between the plates, and consequently, the height of the TEM horn at the aperture. Therefore, the upper cutoff frequency (6 dB) is given by [6]:

$$f_{high} = \frac{(.604)c}{2L\sin^2(\beta/2)} \tag{2}$$

where the β is the flare angle between the plate and the ground plane. The highest desired frequency is 6 GHz; the flare angle between the plate of the TEM horn and the ground plane is 20°; the height of the horn at the aperture is 6.732".

The height and width of the TEM horn at the aperture defines the characteristic impedance of the TEM horn. For a TEM horn mounted above a ground plane, the characteristic impedance is [6]:

$$Z_{char} = \begin{cases} \frac{2}{\sqrt{K}}(59.95)\ln\left(\frac{8h}{w} + \frac{w}{4h}\right) & 0 \le \frac{w}{h} \le 1 \\ \frac{2}{\sqrt{K}}(376.69)\left[\frac{w}{h} + 2.42 - \frac{.44h}{w} + \left(1 - \frac{h}{w}\right)^6\right]^{-1} & 1 < \frac{w}{h} < 10 \end{cases} \tag{3}$$

where K is the antenna sensitivity, w is the width of the horn at the aperture, and h is the height above the ground plane. In order to keep the phase difference less than 30°, the width must be less than 5.078"; a width of 4.921" was chosen. The corresponding characteristic impedance is 288 Ω, assuming the sensitivity K = 1.

TPS DESIGN

The purpose of a TPS is to gradually change the impedance along the length of the surface. Layers of conductive strips with a dielectric substrate between are capacitive in nature [7]; as the amount of overlap in the strips decreases, the capacitance decreases, and the impedance approaches $-j\infty$. The PMM code [3] models the geometry of the TPS elements as a double layer. The top layer consists of copper conductive strips separated by gaps; the bottom layer has an identical pattern of conductive strips shifted back by 0.44". A slab of glass epoxy 0.01" thick with $e_r = 4.5$ separates the layers. Fifty-nine elements are designed with starting with strip width = 0.87" (gap width = 0.01") and decreasing to strip width = 0.29" (gap width = 0.59") in increments of 0.01". Each element has a

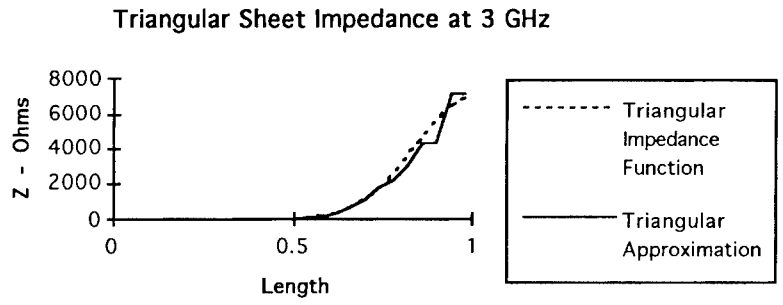


Figure 3. Approximate vs. Desired Triangular Sheet Impedance Function at 3 GHz

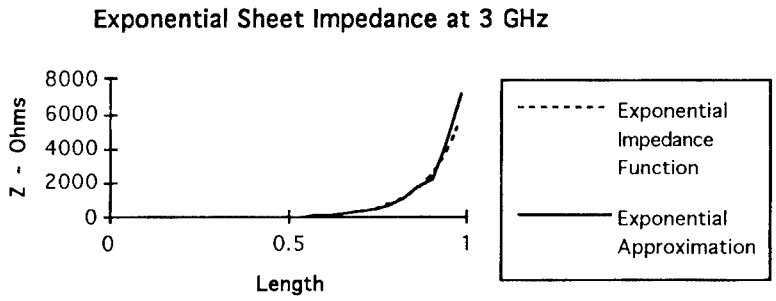


Figure 4. Approximate vs. Desired Exponential Sheet Impedance Function at 3 GHz

different reflection coefficient, and therefore, a different impedance. From this pool of fifty-nine elements, twenty-five elements are chosen to approximate specific impedance functions.

Using a transmission line model the sheet impedance of each element is determined from the reflection coefficient by:

$$Z_s = \frac{-Z_c(1+R)}{2R} \quad \text{where } Z_c = Z_o \cos\eta \tag{4}$$

where Z_O is the characteristic of free space (377 Ω), and η is the angle of the normal (80°). Two taper functions are designed, an exponential taper and a triangular taper, with impedences given by [8]:

$$Z_{exp}(d) = Z_o e^{d \ln(7000/Z_o)} \quad \text{where } 0 \le d \le 1 \tag{5}$$

$$Z_{dri}(d) = \begin{cases} Z_o e^{2d^2 \ln(7000/Z_o)} & \text{for } 0 \le d \le \frac{1}{2} \\ Z_o e^{(4d-2d^2-1)\ln(7000/Z_o)} & \text{for } \frac{1}{2} \le d \le 1 \end{cases}. \quad (6)$$

The desired impedance taper is a function of length; the taper element impedances are functions of gap width. Matching the impedances determines the gap width as a function of length. Synthesizing a taper function from the gap width versus length provides an approximate impedance function. The approximate taper function fits 25 impedance points to the desired taper function using a smallest difference method. Figures 3 and 4 depict just how well the approximate function fits the desired function.

FDTD MODELING

A two-dimensional FDTD code [4] models the tapered periodic structures. The simulations predict the ability of the TPS design to reduce the off-boresight fields. There are four different geometries: a triangular taper, a exponential taper, a short reference metal plate, and a long metal plate. The short plate is 19.69" long and represents the original reference TEM horn. The long plate is 41.69" long and represents a TEM horn as long as both the original horn plus the TPS attachment.

Figure 5 shows the diffracted fields from the exponential taper, triangular taper, and long plate relative to the field diffracted from the short reference plate. The long plate provides better reduction at the shallow angles, but the tapers decrease the fields far off boresight. The exponential taper outperforms the triangular taper in almost all cases. At the 90° test location, the exponential taper reduces the diffraction by 7.839 dB. The triangular taper reduced the fields 4.213 dB. The long plate decreases the diffraction by only 0.04 dB.

TESTING PROCEDURE

The High Energy Research and Technology Facility of Phillips Laboratory at Kirtland AFB, New Mexico provides the facilities and equipment to test the three designs. Table 1 displays the peak values of the fields at each location and the amount of reduction performed by each taper. The first column, *Test Pt.,* gives the test location for each measurement; the second row, *pulse,* is the main radiated pulse. The other measurements are the diffracted field levels, the signal level is measured in millivolts, and the *Reduction* (dB), is calculated as follows:

$$\text{Reduction (dB)} = 20 \log\left(\frac{V_{\text{peak, taper}}}{V_{\text{peak, ref}}}\right). \quad (7)$$

The exponential taper outperforms the triangular taper at all locations except the 20° off-boresight test point. Even for the on-boresight maximization that did not behave as expected, the exponential taper approached the goal more closely than the triangular taper. The 20° off-boresight mark is a confusing point. Since that is the angle of elevation of the TEM horn, the location corresponds to grazing incidence for the radiating pulse and any diffraction occurring at the edge. Diffraction is very weak near grazing and is difficult to predict accurately. The discrepancy at this location is due to slight shifts in the probe location.

CONCLUSIONS

This research involved the design, modeling, and testing of both a TPS and a TEM horn. The goal was to reduce the off-boresight fields for a TEM horn and increase the peak-to-peak field levels on boresight. This was accomplished by applying a TPS to the free space end. The TPS reduced the

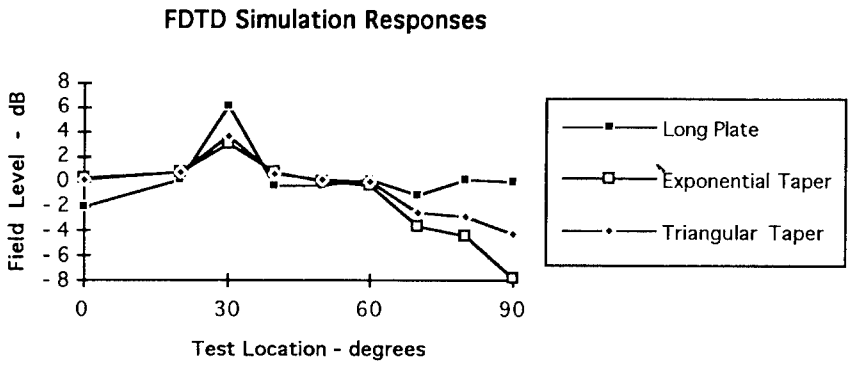


Figure 5. Two-dimensional FDTD Field Levels Relative to the Field Diffracted from the Reference Plate

Test Pt.	*Ref. Horn*	*Exp. Taper*	*Reduction*	*Tri. Taper*	*Reduction*
pulse	*13.1700*	*9.86849*	*-2.507*	*9.11670*	*-3.195*
0	*-8.87810*	*-6.03380*	*-3.354*	*-6.69750*	*-2.448*
20	*5.34938*	*6.12187*	*+1.172*	*5.22781*	*-0.200*
30	*9.63531*	*8.82187*	*-1.381*	*8.65000*	*-0.937*
40	*8.78906*	*5.79719*	*-3.614*	*7.08406*	*-1.873*
50	*6.59125*	*3.67563*	*-5.073*	*4.54060*	*-3.237*
60	*5.31500*	*2.58125*	*-6.273*	*2.82281*	*-5.496*
70	*4.61313*	*1.77188*	*-8.311*	*2.28313*	*-6.109*
80	*3.94125*	*1.36625*	*-9.202*	*1.64688*	*-7.591*
90	*3.57531*	*1.12438*	*-10.048*	*1.37875*	*-8.277*

Table 1. Test Results for Diffracted Field Level

diffraction from the free space end by providing a gradual transition from the conductive plates of the TEM horn to free space.

Two TPSs were designed — one that approximated an exponential impedance function and one that approximated a triangular impedance function. Both reduced the off-boresight fields of the TEM horn. In most cases the exponential taper reduced the field levels further than the triangular taper. For example at 90° off boresight, the exponential taper reduced the edge diffracted field by 10 dB. The triangular taper reduced the fields by 8.2 dB.

Therefore, this research illustrates that a TPS is an effective method of reducing diffraction. A procedure for designing a TPS to fit a specific impedance function was presented. A two-dimensional FDTD model predicted the tapers would reduce the diffraction, and experimentation verified the TPS's ability to reduce the peak off-boresight field levels for a TEM horn.

ACKNOWLEDGMENT

The authors wish to express their gratitude to the following people for their help, assistance, comments, and support: Ray Luebbers, Carl Baum, Leo Felsen, Dennis Andersh, Russ Burleson, Joe

Sacchini, Paul Skinner, Gerald Buchenaur, Raley Marek, Errol English, Steve Miller, the Mission Research Corp.

REFERENCES

[1] S. Evans and F. Kong, "TEM Horn Antenna: Input Reflection Characteristics in Transmission," *IEE Proc.*, Vol. 130, Pt. H, No. 6, pp. 403-409, Oct. 1983.

[2] E. K. English, "Tapered Periodic Surfaces: A Basic Building Block for Broad Band Antenna Design," to appear in *Ultra Wide Band, Short Pulse Electromagnetics, vol. II,* L. Carin, L. B. Felsen, and S. U. Pillai, Eds. New York: Plenum, 1995.

[3] L. W. Henderson, *Introduction to PMM*, Technical Report 715582-5, The Ohio State University ElectroScience Laboratory, Department of Electrical Engineering; prepared under Contract F33615-83-C-1013 for Avionics Laboratory (AFWAL/AAWP-3), Air Force Wright Aeronautical Systems Command, Wright-Patterson Air Force Base, OH, Feb. 1986.

[4] J. H. Beggs, R. J. Luebbers, and H. S. Langdon. *User's Manual for TEC: PSU FDTD Code Version C for Two-Dimensional Transverse Electric Transient Scattering from Frequency-Independent Dielectric and Magnetic Materials*. Electrical and Computer Engineering Department, The Pennsylvania State University, University Park, PA, June 1993.

[5] M. Kanda, "The Effects of Resistive Loading of "TEM" Horns," *IEEE Trans. Electromag. Compat.*, Vol. EMC-24, No. 2, pp. 245-255, May 1992.

[6] A. R. Ondrejka, J. M. Ladbury, and H. W. Medley, "TEM Horn Antenna Design Guide," National Institute of Standards and Technology, Boulder, CO, unpublished report.

[7] R. A. Burleson, A. J. Terzuoli, Jr, E. K. English, "Two Dimensional Tapered Periodic Edge Treatments for Broadband Diffraction Reduction," to appear in *Ultra Wide Band, Short Pulse Electromagnetics, vol. II,* L. Carin, L. B. Felsen, and S. U. Pillai, Eds. New York: Plenum, 1995.

[8] D. M. Pozar. *Microwave Engineering*. Reading, Mass: Addison-Wesley Publishing Company, 1990.

Determination of the Complex Aperture Distribution of a Planar Spiral Antenna from 3-D Far-Field Radiation Pattern Data

Michael Kluskens, Wendy Lippincott, and Mark Kragalott

Naval Research Laboratory
Washington, D.C. 20375

Abstract

A technique to approximate the complex aperture distribution of an antenna by a set of discrete sources has been developed. The locations for a set of sources are found from the far-field radiation pattern using an imaging technique. The far-field electric field equations for this set of electric and magnetic sources are transformed into a set of matrix equations, which are then solved for the source magnitudes and phases. These sources can then be used to solve for the antenna's radiation pattern performance in a complex structural environment. This distributed source technique was applied to the case of a planar spiral antenna on the edge of a small ground plane.

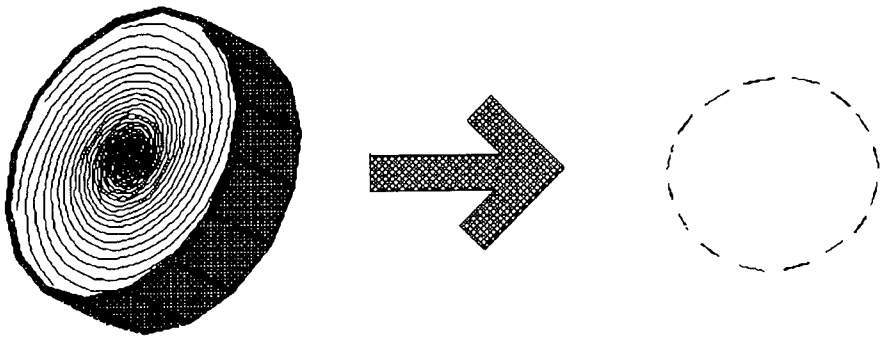
I. Introduction

Placing a planar spiral antenna on a complex platform can require considerable effort to ensure that the surrounding structures do not unduly affect the radiation pattern. Decisions regarding antenna placement can be made through anechoic chamber studies or computational electromagnetic simulations. This study was designed to validate the use of the Ohio State Basic Scattering Code (NECBSC)[1,2] for modeling this antenna on a simple ground plane.

NECBSC is a high frequency ray tracing/diffraction code based on the Uniform Geometrical Theory of Diffraction (UTD). In general, NECBSC is suited for structures many wavelengths in dimension. Other codes using techniques such as the Method of Moments (MoM) or the finite difference time-domain (FDTD) method provide more exact modeling of the antenna, but become computationally impractical when other large structures must be modeled near the antenna. NECBSC can be used in a timely manner to provide mechanical designers information on the effects of their designs on antenna performance.

NECBSC models antennas as a set of infinitely small electric and magnetic current elements. It can also approximate an antenna using linear interpolation on the far-field radiation pattern (the interpolated source technique). With this technique the fields radiate from a single point weighted by the pattern function interpolated from the measured horizontally and vertically polarized patterns.

For NECBSC modeling of a spiral antenna mounted on the edge of a small (4λ x 4λ) ground plane, the interpolated source technique is not accurate because of the point source approximation. This paper presents a distributed source technique to reduce the spiral antenna to a set of sources located at the radiating regions of the spiral, thereby approximating the near-zone fields of the antenna more accurately than is possible using the interpolated source technique. This improved approximation to the near-zone fields on the antenna is important when calculating the radiation pattern of the antenna in the presence of other large structures. The technique presented in this paper is two-fold. First, the locations for a set of sources is found from the far-field radiation pattern using an imaging technique. Next, the far-field electric field equations for this set of electric and magnetic sources are transformed into a set of matrix equations. These are then solved for the source magnitudes and phases. Figure 1 shows a schematic of this procedure.



Cavity Backed Spiral

Set of sources with computed amplitudes and phases that generate the spiral far-field pattern

Fig. 1 Distributed Source Technique.

The far-field transformation technique was first developed by Mautz and Harrington[3] and Pelton, Marhefka, and Burnside[4] for 2-D radiation patterns. This paper expands their technique to 3-D patterns using an imaging technique to determine the placement of the sources. This technique is then applied to a planar cavity spiral antenna with the results compared to measurements and the NECBSC interpolated source technique.

II. Planar Spiral Antenna

The antenna used for all the modeling work is an 8-arm right-hand-circular (RHC) log-periodic spiral. Each arm has six full turns, starting at a radius of 0.125 inches and ending at a radius of 11.0 inches. The operational frequency is from 0.5 to 1 GHz. Figure 1 shows a wire model of the spiral antenna.

The antenna is placed at the top of an absorber filled cavity that is 6.3" in depth. The spiral produces radiation in both forward and backward directions. The downward radiation is absorbed by the cavity, reducing the total output power by half. One advantage of the spiral is its wide bandwidth. This eliminates the need for using more than one antenna to cover a wide range of frequencies. The spiral also has the advantage of being conformal to a surface, thereby not blocking the radiation of other emitters.

III. Antenna Imaging

Imaging the antenna current distribution, $J_{x,y,z}(x,y,z)$, from the far-field radiation pattern is necessary to determine optimum placement for the sources to be used with NECBSC. The imaging technique used in this paper is based on work by Cook, Anderson, Whitaker, and Bennett[5] and reduces to an integration of the radiation pattern (E_θ, E_ϕ) over one hemisphere given by

$$J_{x,y,z}(x,y,z) \approx \frac{1}{C}\iint E_{x,y,z}(\phi,\theta)\, e^{-jk[(x\cos\phi + y\sin\phi)+z\cos\theta]}\cos\theta\sin\theta\, d\phi\, d\theta \tag{1}$$

where

$$E_x(\phi,\theta) = E_\theta(\phi,\theta)\cos\phi\ \cos\theta - E_\phi(\phi,\theta)\sin\phi \tag{2a}$$

$$E_y(\phi,\theta) = E_\theta(\phi,\theta)\sin\phi\cos\theta + E_\phi(\phi,\theta)\cos\phi \tag{2b}$$

$$E_z(\phi,\theta) = -E_\theta(\phi,\theta)\sin\theta \tag{2c}$$

and $k = 2\pi/\lambda$ is the free space wavenumber and C is a constant. Equation (1) can be integrated directly or evaluated using FFT techniques. Figure 2 shows a 3-D view of the far-field of the spiral. Figure 3 shows the normalized magnitude of the electric current distribution calculated over the top surface of the antenna using Equation (1). Figure 4 represents a slice through the center of the image.

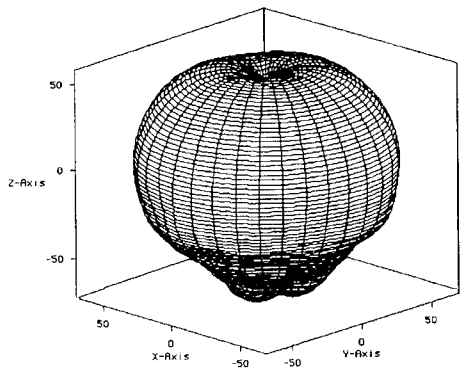


Fig. 2 Far-field radiation pattern of the spiral antenna at 0.7 GHz.

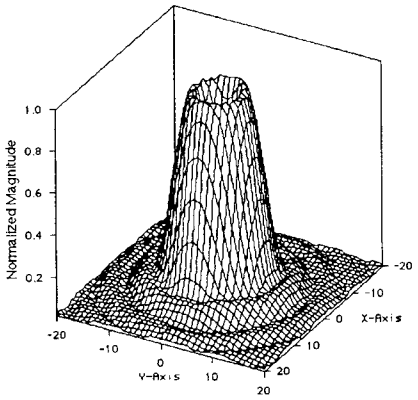


Fig. 3 Normalized magnitude of the electric current distribution on the top surface of the planar spiral at 0.7 GHz.

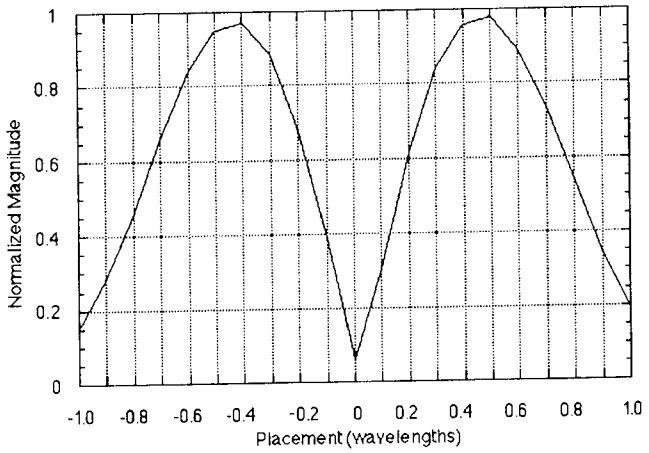


Fig. 4 Normalized magnitude of the electric current distribution on the top surface of the planar spiral at 0.7 GHz (cut through center of antenna).

Equation (1) was used at three frequencies to determine the optimum placement of the sources. In each case, the optimum placement was at a radius of approximately 0.45 wavelengths. This is 40% greater than the placement that would be used if it was assumed that the spiral radiates most of its energy in mode 2 at a circumference of two wavelengths, i.e. a radius of $1/\pi$ wavelengths. Evidently,

the cavity around the spiral and the shape of this eight arm spiral influence the current distribution enough to invalidate generic assumptions about the current distribution on the surface of this spiral antenna. When a radius of 0.45 wavelengths is not used for the source locations, the calculation of the sources, described in the next section, produces large magnitude sources which produce the specified far-field pattern through cancellation only if sufficient numerical precision is used in the calculations. Using these incorrectly placed sources in NECBSC calculations for the spiral over the ground plane produces inaccurate results, probably indicating that the near-zone fields are less accurate approximations to the actual near-zone fields.

IV. Calculation of the Sources

Once the appropriate locations for the sources are determined, the magnitude and phase of sources are obtained using a 3-D extension to the technique developed by Mautz and Harrington[3] and Pelton, Marhefka, and Burnside[4] for 2-D patterns. The magnitude and phase of the sources are given by the solution to the following matrix equation

$$\begin{bmatrix} E_\theta \\ E_\phi \end{bmatrix} = \begin{bmatrix} T_{11} & T_{12} & T_{13} & T_{14} & T_{15} & T_{16} \\ T_{21} & T_{22} & T_{23} & T_{24} & T_{25} & T_{26} \end{bmatrix} \begin{bmatrix} J_x \\ J_y \\ J_z \\ M_x \\ M_y \\ M_z \end{bmatrix} \tag{3}$$

where the T submatrices are the far-field radiation patterns of the respective sources and are given by

$$T_{11(n,m)} = -T_{24(n,m)} = \cos\phi_m \cos\theta_m \, e^{jk\left[(x_n \cos\phi_m + y_n \sin\phi_m)\sin\theta_m + z_n \cos\theta_m\right]} \tag{4a}$$

$$T_{21(n,m)} = \; T_{14(n,m)} = -\sin\phi_m \, e^{jk\left[(x_n \cos\phi_m + y_n \sin\phi_m)\sin\theta_m + z_n \cos\theta_m\right]} \tag{4b}$$

$$T_{12(n,m)} = -T_{25(n,m)} = \sin\phi_m \cos\theta_m \, e^{jk\left[(x_n \cos\phi_m + y_n \sin\phi_m)\sin\theta_m + z_n \cos\theta_m\right]} \tag{4c}$$

$$T_{22(n,m)} = \; T_{15(n,m)} = \cos\phi_m \, e^{jk\left[(x_n \cos\phi_m + y_n \sin\phi_m)\sin\theta_m + z_n \cos\theta_m\right]} \tag{4d}$$

$$T_{13(n,m)} = -T_{26(n,m)} = -\sin\theta_m \, e^{jk\left[(x_n \cos\phi_m + y_n \sin\phi_m)\sin\theta_m + z_n \cos\theta_m\right]} \tag{4e}$$

$$T_{23(n,m)} = \; T_{16(n,m)} = 0 \tag{4f}$$

and the vector $(J_x, J_y, J_z, M_x, M_y, M_z)$ contains the unknown complex coefficients of the N electric and magnetic point sources located at (x_n, y_n, z_n), for $n = 1 \ldots N$. The vector (E_θ, E_ϕ) contains the complex coefficients of the M known far-field points located at (ϕ_m, θ_m), for $m = 1 \ldots M$. The elements of the T submatrices can be modified to take into account sources other than point sources, including one-sided sources such as those available in NECBSC. This is inherently a least squares problem since we are approximating a function by a sum of other functions, i.e. the far-field pattern by the sum of the far-field patterns of the point sources. As a consequence, the number of point sources, N, must be significantly less than the number of far-field points, M, to avoid the problems typically encountered with an over specified least squares problem. One typical problem is that the resulting far-field pattern could vary greatly between the specified far-field points rather than exhibiting a smooth transition from one known far-field point to another. The particular problem we observed when using either excessive or incorrectly placed sources is that the resulting source magnitudes will exceed reasonable magnitudes and only achieve the least squares fit to the far-field points through severe cancellation which requires that all calculations be done using excessive numerical precision. Every case with excessive source magnitudes gave very poor results when incorporated into a NECBSC model. In addition, the number of point sources, N, should be minimized since the computational complexity increases as order MN^2.[6]

The antenna could be represented by electric currents alone; however, by Mayes theorem, electric and magnetic sources generate the same fields outside the region containing the sources if [7,8]

$$\mathbf{J} = \frac{\nabla \times \mathbf{M}}{j\omega\mu} \tag{5a}$$

$$\mathbf{M} = -\frac{\nabla \times \mathbf{J}}{j\omega\varepsilon} \tag{5b}$$

i.e. for a given electric source there is an equivalent magnetic source and vice versa. Since Mayes theorem involves the derivative of the spatial distribution of the currents, one of the representations for a given source will be more spatially concentrated than the other. For this reason, both electric and magnetic sources are used in this paper.

In the initial modeling, eight source locations were used spaced 45° apart at a radius of 0.45 wavelengths. Each location had three electric and three magnetic x-, y-, and z-directed sources. This was found to give good results but had 1-2 dB too much ripple in the azimuth patterns near the horizon. To produce a more uniform ring of currents sixteen source locations with a spacing of 22.5° were tried next. This over specified the least squares problem creating the problems discussed previously. As an alternative, the 48 sources from the first solution were linearly interpolated around the ring into a total of 96 sources spaced 22.5° apart. This gave a stable solution and matched the measurements well.

V. Antenna Alone: Distributed Source Technique Versus Measurements

Figures 5 through 12 compare the distributed source calculations and measurements for the spiral antenna without a ground plane. The results presented here were computed using a far-field pattern consisting of elevation cuts with $\Delta\theta$=2° and $\Delta\phi$=10° at 0.5 GHz. Elevation cuts at 0° and 60° degrees and azimuth cuts at 60° and 80° from boresight are shown for both horizontal and vertical polarizations. No scaling factor was used in any of these calculations. In general, both polarizations have good matches to the measurements; however, the calculated horizontal polarization does not have as deep a dip at 130° in the elevation patterns as the measurements.

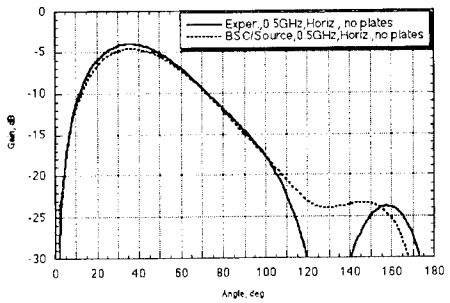


Fig. 5 Experimental versus NECBSC with 96 sources interpolated from 48 sources, 0.5 GHz, no plates, horizontal polarization, elevation cut at 0 degrees.

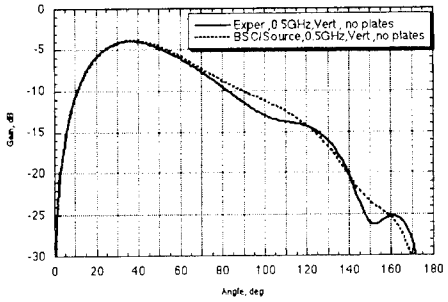


Fig. 6 Experimental versus NECBSC with 96 sources interpolated from 48 sources, 0.5 GHz, no plates, vertical polarization, elevation cut at 0 degrees.

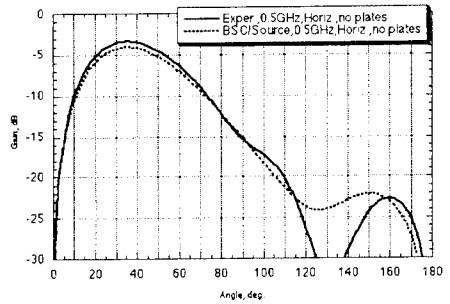


Fig. 7 Experimental versus NECBSC with 96 sources interpolated from 48 sources, 0.5 GHz, no plates, horizontal polarization, elevation cut at 60 degrees.

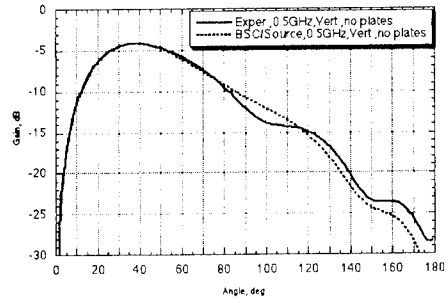


Fig. 8 Experimental versus NECBSC with 96 sources interpolated from 48 sources, 0.5 GHz, no plates, vertical polarization, elevation cut at 60 degrees.

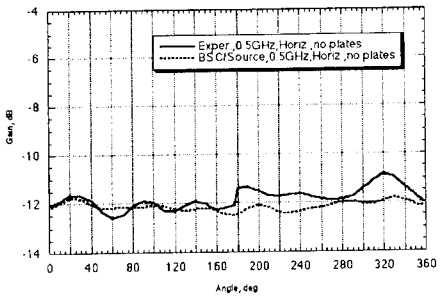


Fig. 9 Experimental versus NECBSC with 96 sources interpolated from 48 sources, 0.5 GHz, no plates, horizontal polarization, azimuth cut at 80 degrees.

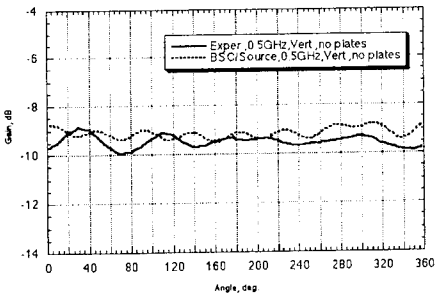


Fig. 10 Experimental versus NECBSC with 96 sources interpolated from 48 sources, 0.5 GHz, no plates, vertical polarization, azimuth cut at 80 degrees.

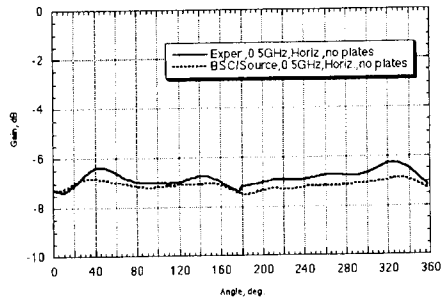


Fig. 11 Experimental versus NECBSC with 96 sources interpolated from 48 sources, 0.5 GHz, no plates, horizontal polarization, azimuth cut at 60 degrees.

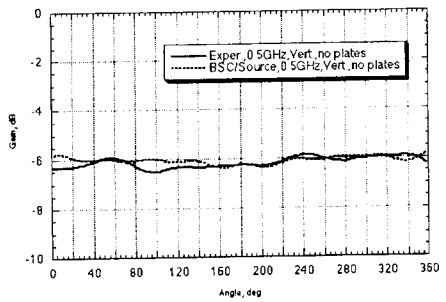


Fig. 12 Experimental versus NECBSC with 96 sources interpolated from 48 sources, 0.5 GHz, no plates, vertical polarization, azimuth cut at 60 degrees.

VI. Antenna on Edge of Small Ground Plane: Distributed Source Technique Versus Measurements

The distributed source calculations and measured far-field azimuth patterns of the spiral on the edge of a small ground plane are compared next. The geometry is shown in Figure 13. The ground plane is a square 66 inches on a side. The spiral was set at heights of 0.3, 2.2, and 6.3 inches above the ground plane and the radiation pattern was measured at the frequencies 0.5, 0.7, and 0.9 GHz.

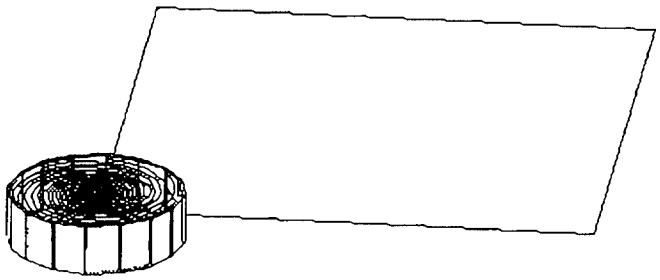


Fig. 13 Spiral antenna on the edge of a square plate 66 inches on a side.

The ground plane was modeled as a six-sided plate, with the three points closest to the spiral set at a distance of 12.2" from the center of the spiral. Figures 14 through 19 show the results for 0.5 GHz. The plots are azimuth cuts taken 60 degrees from boresight. Figures 14, 16, and 18 are the horizontal polarizations and Figures 15, 17, and 19 are the vertical polarizations. Horizontal and vertical polarizations for 0.7 GHz and 0.9 GHz are shown in Figures 20 through 25 and Figures 26 through 31, respectively. No scaling factor was used in any of these calculations. As can be seen, good agreement is obtained between the distributed source calculations and the measurements.

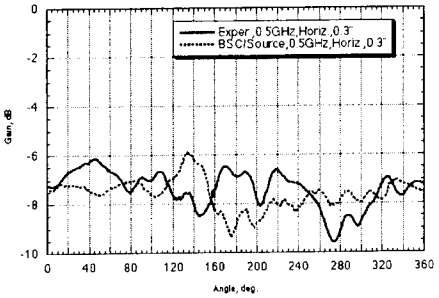


Fig. 14 Experimental versus NECBSC with 96 sources interpolated from 48 sources, 0.5 GHz, plate 0.3" below spiral, horizontal polarization, azimuth cut at 60 degrees.

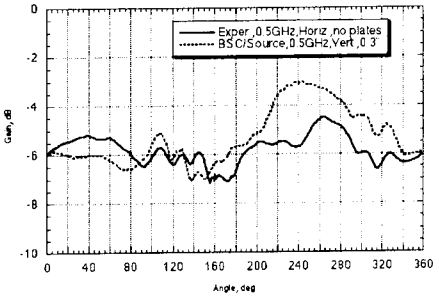


Fig. 15 Experimental versus NECBSC with 96 sources interpolated from 48 sources, 0.5 GHz, plate 0.3" below spiral, vertical polarization, azimuth cut at 60 degrees.

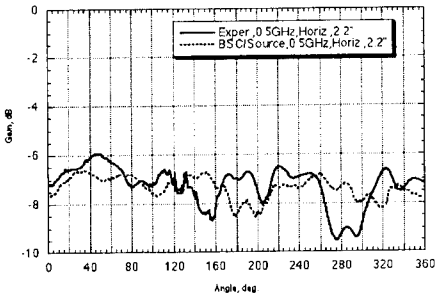


Fig. 16 Experimental versus NECBSC with 96 sources interpolated from 48 sources, 0.5 GHz, plate 2.2" below spiral, horizontal polarization, azimuth cut at 60 degrees.

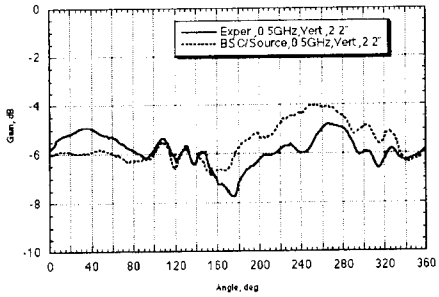


Fig. 17 Experimental versus NECBSC with 96 sources interpolated from 48 sources, 0.5 GHz, plate 2.2" below spiral, vertical polarization, azimuth cut at 60 degrees.

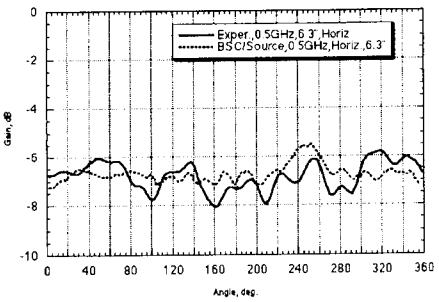


Fig. 18 Experimental versus NECBSC with 96 sources interpolated from 48 sources, 0.5 GHz, plate 6.3" below spiral, horizontal polarization, azimuth cut at 60 degrees.

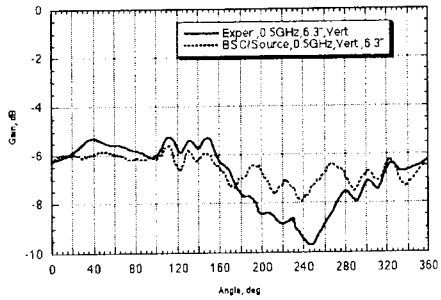


Fig. 19 Experimental versus NECBSC with 96 sources interpolated from 48 sources, 0.5 GHz, plate 6.3" below spiral, vertical polarization, azimuth cut at 60 degrees.

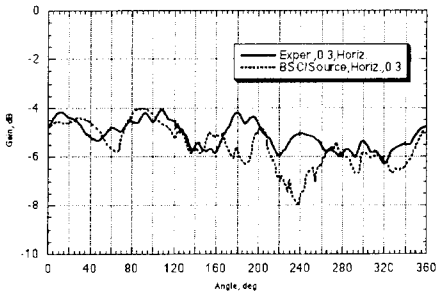


Fig. 20 Experimental versus NECBSC with 96 sources interpolated from 48 sources, 0.7 GHz, plate 0.3" below spiral, horizontal polarization, azimuth cut at 60 degrees.

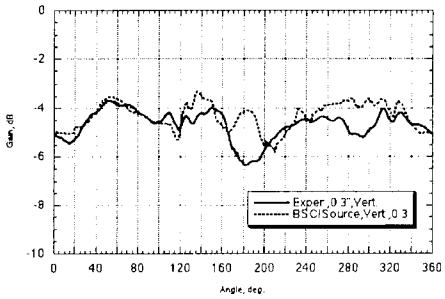


Fig. 21 Experimental versus NECBSC with 96 sources interpolated from 48 sources, 0.7 GHz, plate 0.3" below spiral, vertical polarization, azimuth cut at 60 degrees.

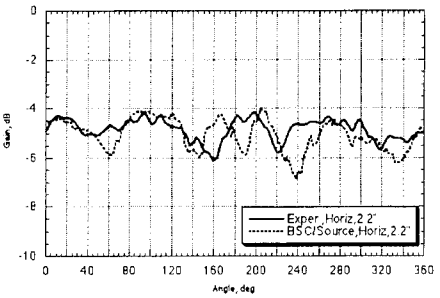


Fig. 22 Experimental versus NECBSC with 96 sources interpolated from 48 sources, 0.7 GHz, plate 2.2" below spiral, horizontal polarization, azimuth cut at 60 degrees.

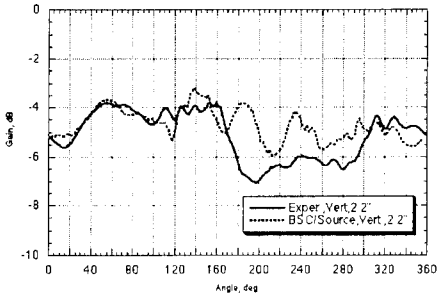


Fig. 23 Experimental versus NECBSC with 96 sources interpolated from 48 sources, 0.7 GHz, plate 2.2" below spiral, vertical polarization, azimuth cut at 60 degrees.

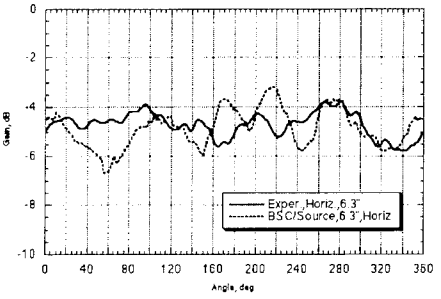


Fig. 24 Experimental versus NECBSC with 96 sources interpolated from 48 sources, 0.7 GHz, plate 6.3" below spiral, horizontal polarization, azimuth cut at 60 degrees.

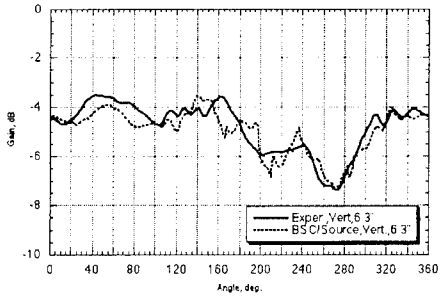


Fig. 25 Experimental versus NECBSC with 96 sources interpolated from 48 sources, 0.7 GHz, plate 6.3" below spiral, vertical polarization, azimuth cut at 60 degrees.

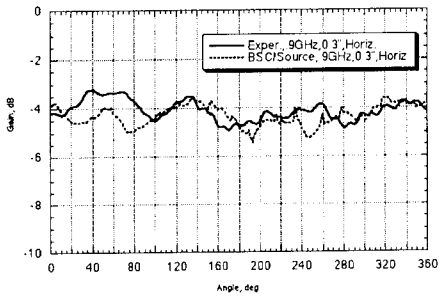


Fig. 26 Experimental versus NECBSC with 96 sources interpolated from 48 sources, 0.9 GHz, plate 0.3" below spiral, horizontal polarization, azimuth cut at 60 degrees.

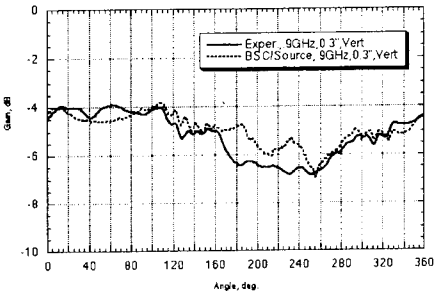


Fig. 27 Experimental versus NECBSC with 96 sources interpolated from 48 sources, 0.9 GHz, plate 0.3" below spiral, vertical polarization, azimuth cut at 60 degrees.

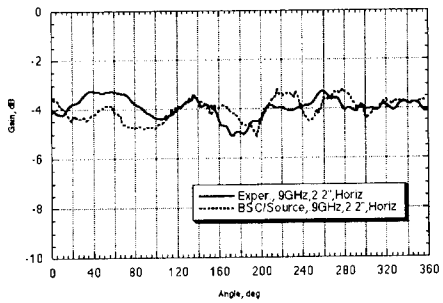


Fig. 28 Experimental versus NECBSC with 96 sources interpolated from 48 sources, 0.9 GHz, plate 2.2" below spiral, horizontal polarization, azimuth cut at 60 degrees.

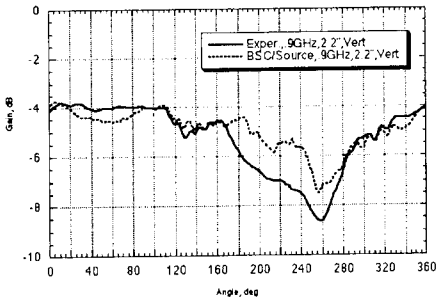


Fig. 29 Experimental versus NECBSC with 96 sources interpolated from 48 sources, 0.9 GHz, plate 2.2" below spiral, vertical polarization, azimuth cut at 60 degrees.

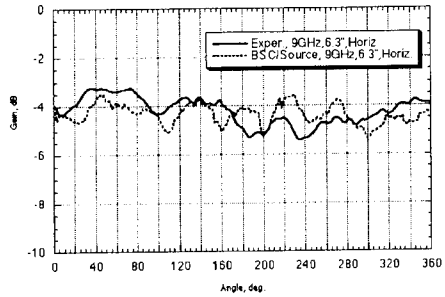


Fig. 30 Experimental versus NECBSC with 96 sources interpolated from 48 sources, 0.9 GHz, plate 6.3" below spiral, horizontal polarization, azimuth cut at 60 degrees.

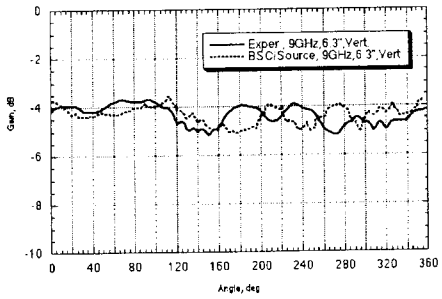


Fig. 31 Experimental versus NECBSC with 96 sources interpolated from 48 sources, 0.9 GHz, plate 6.3" below spiral, vertical polarization, azimuth cut at 60 degrees.

The match between calculations and measurements is better at the higher frequencies, as would be expected with any UTD code. It should be noted that no scaling factor was used in the calculations.

VII. Antenna on Edge of Small Ground Plane: Interpolated Source Technique Versus Measurements

Figures 32 to 37 show the results of NECBSC calculations using the interpolated source technique with the spiral on a ground plane at varying heights. With this technique, the measured far-field pattern of the antenna is input into the NECBSC code and is used as the pattern function for a point source. The ground plane plate was input as a square plate with one corner near the source. This was found to give a better match to the data than using a six- or eight-sided plate with the edge rounded near the point source. A constant scale factor was used. As can be seen, sometimes a very good match to the data is achieved and sometimes it appears to be offset by a few dB. The results deteriorated as the spacing between the spiral antenna and the plate increased. The worst results occurred with vertical polarization at the maximum spacing of 6.3 inches, which is shown in Figure 37. These calculations were all done at 0.7 GHz and should be compared to the distributed source calculations shown in Figures 20 through 25. The results at 0.5 and 0.9 GHz were similar, with some good matches and some poor matches.

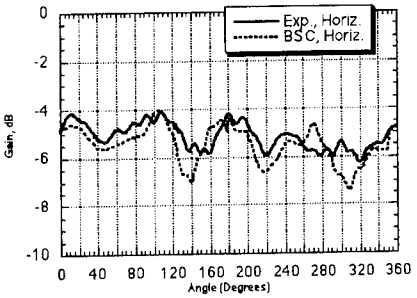


Fig. 32 Experimental versus NECBSC with interpolated source, 0.7 GHz, plate 0.3 inches below spiral, horizontal polarization, azimuth cut at 60 degrees.

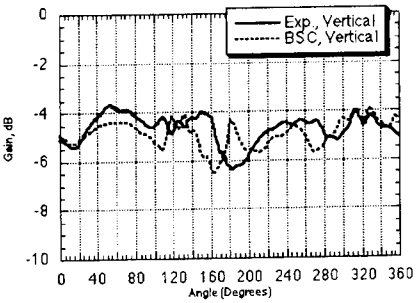


Fig. 33 Experimental versus NECBSC with interpolated source, 0.7 GHz, plate 0.3 inches below the spiral, vertical polarization, azimuth cut at 60 degrees.

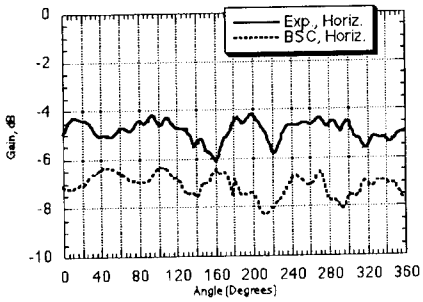


Fig. 34 Experimental versus NECBSC with interpolated source, 0.7 GHz, plate 2.2 inches below the spiral, horizontal polarization, azimuth cut at 60 degrees.

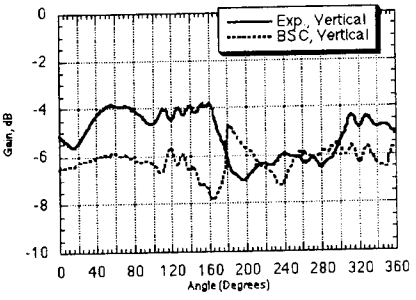


Fig. 35 Experimental versus NECBSC with interpolated source, 0.7 GHz, plate 2.2 inches below the spiral, vertical polarization, azimuth cut at 60 degrees.

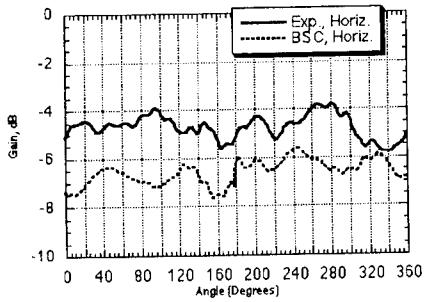


Fig. 36 Experimental versus NECBSC with interpolated source, 0.7 GHz, plate 6.3 inches below the spiral, horizontal polarization, azimuth cut at 60 degrees.

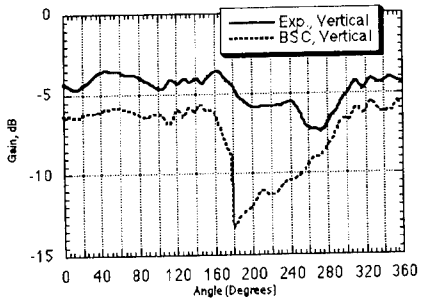


Fig. 37 Experimental versus NECBSC with interpolated source, 0.7 GHz, plate 6.3 inches below the spiral, vertical polarization, azimuth cut at 60 degrees.

VIII. Conclusions

The distributed source technique did a reasonably good job modeling the planar spiral antenna on a small ground plane. Results were better at the higher frequencies. It is a significant improvement over the interpolated source technique which uses a single point source. This technique has proven useful for the problem of modeling antennas on large complex structures. It can easily be applied to other antenna types.

IX. References

[1] R. J. Marhefka and W. D. Burnside, "Antennas on complex platforms", *Proc. IEEE*, vol. 80, pp. 204-208, Jan. 1992.

[2] R. J. Marhefka and J. W. Silvestro, "Near zone - basic scattering code," Tech. Rep. 716199-13, ElectroScience Laboratory, The Ohio-State University, Columbus, Mar. 1989.

[3] J. R. Mautz and R. F. Harrington, "Computational methods for antenna pattern synthesis," *IEEE Trans. Antennas Propagat.*, vol. 23, pp. 507-512, July 1975.

[4] E. L. Pelton, R. J. Marhefka, and W. D. Burnside, "An iterative approach for computing an antenna aperture distribution from given radiation pattern data," Tech. Rep. (78)4583-6, ElectroScience Laboratory, The Ohio State University, Columbus, June 1978.

[5] G. G. Cook, A. P. Anderson, A. J. T. Whitaker, and J. C. Bennett, "High resolution three-dimensional microwave imaging of antennas," *IEEE Trans. Antennas Propagat.*, vol. 37, pp. 768-779, June 1989.

[6] E. Anderson, J. Dongarra, and S. Ostrouchov, "Installation guide for LAPACK," LAPACK Working Note 41, University of Tennessee, Knoxville, March 1993.

[7] P. E. Mayes, "The equivalence of electric and magnetic sources," *IRE Trans. Antennas Propagat.*, vol. 6, pp. 295-296, July 1958.

[8] E. H. Newman, "TM and TE scattering by a dielectric/ferrite cylinder in the presence of a half-plane," *IEEE Trans. Antennas Propagat.*, vol. 34, pp. 804-813, June 1986.

ANALYSIS OF MICRO-CONTAMINATION OF SILICON WAFERS BASED ON DISCRETE SOURCES METHOD (DSM)

Yu.A. Eremin* and N.V. Orlov*

*Faculty of Applied Mathematics & Computer Science,
Moscow State University,
Vorobyov's Hills, 119899 Moscow, Russia
Fax: +7(095)939-2596; Tel: +7(095)939-1776;
E-mail: EREMIN@cs.msu.su

Abstract. Generalized Multipole Technique has been adjusted for analysis of wafer contaminations inspecting systems. This technique has enabled to investigate such complete mathematical models as particles deposited on a smooth substrate surface and pits. Some computer simulation results were discussed.

Advance inspection technologies should have reliable detectors of micro-contaminations down to 0.1 microns. To establish morphology of micro-contamination it is essential not only particles detection but recognition a particle from a pit and reconstruction both particle size and material also. During last decade much effort has been directed to improve wafer surface scanners, which generally make use of laser light (wavelength is either 633 nm or 488 nm) scattering to detect contaminants.

Solution of the similar problems impossible without of the complete mathematical model analysis of and computer simulation. The other reason consists of improvement resolution ability of existing technology equipment to provide high signal to noise ratio. To increase resolution ability of existing technology equipment or to extract contaminant's material it is necessary to have efficient mathematic and computer tools for simulation.

Therefore calculation of light scattering from particles deposited on surfaces or pits is of great interest in the simulation, development and calibration of contamination-inspection scanner. A member of studies has addressed this problem with the use of widely differing methods. The most general methods such as finite-difference or boundary integral equation technique are very consume and demand to use super computers. The main difficulty of this techniques consists of the necessity to take into account unbounded substrate surface presence. In this report we suggest Generalized Multipole Technique (GMT) for a light scattering analysis by a particle or pit on a smooth surface. GMT has

been originally used to compute EM waves scattering from axi-symmetric body buried underground [1].

Complete mathematical model for EM scattering of laser beam consists of Maxwell system inside and outside of the particle, Silver-Muller radiation conditions at the infinity and conjunction conditions on the boundaries of media discontinuous. In the frame of GMT a scattered field is represented as superposition of multipoles' fields. It satisfies to Maxwell equations, radiation conditions and conjunction conditions on the smooth unbounded substrate surface analytically.

We should represent exciting field - P/S plane wave in the same manner, satisfying these conjunction conditions also. Multipole amplitudes need to be determined from the boundary condition at the local obstacle surface only. Under investigation axi-symmetric obstacles to simplify the boundary-value scattering problem we employ Fourier-series expansion both for scattering and exiting fields for reduction space scattering problem to the set of the ones at the azimuthal half-plane.

We use the special construction for EM fields of multipoles taking into account Sommerfeld integrals also. Multipoles are located in the complex plane joining to axis of symmetry.

The singular part of fields can be represented as finite linear combination of a primary functions. Multipole' amplitudes for each harmonic should be determined as a pseudo solution of overdetermined linear system received from point-matching approach at the meridian of the obstacle (particle or pit). This allows to get a minimum of mean square norm for Fourier harmonics of boundary values of the EM fields at the meridian of the obstacle and provides the results stability [2].

The efficiency of the GMT allows to employ code created for PCs. One is able to investigate arbitrary shaped obstacle having arbitrary refractive index and diameter up to 3 incident wavelengths. Furthermore, calculation has been realized to examine any angular incidence and for P/S polarization simultaneously. A possibility to estimate the error of the result obtained has been realized as well.

We carried out analysis of light scattering by particles of different size and matter deposited on the smooth surface of bare silicon. We used Tencor Surfscan -4000 and 5500 as the models of inspecting system [3].

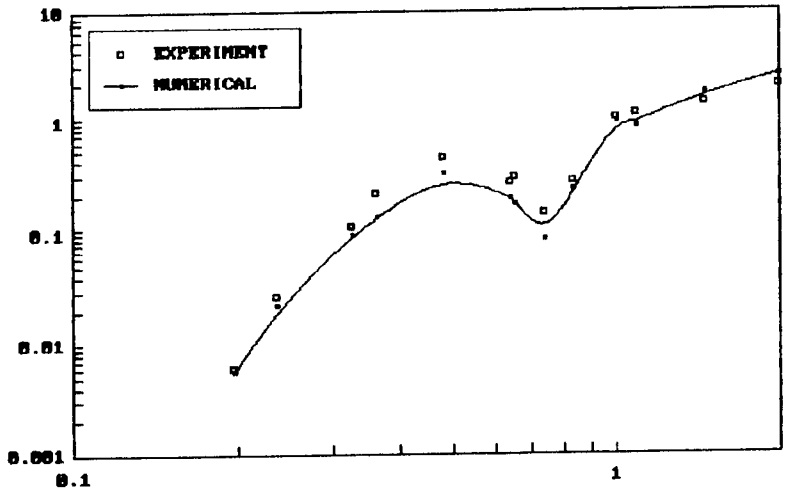


Fig. 1

We investigated many kinds of particles both metallic and dielectric. We compared our results with the calibrate data for polistirol particles and with the experimental results especially for a small ones.

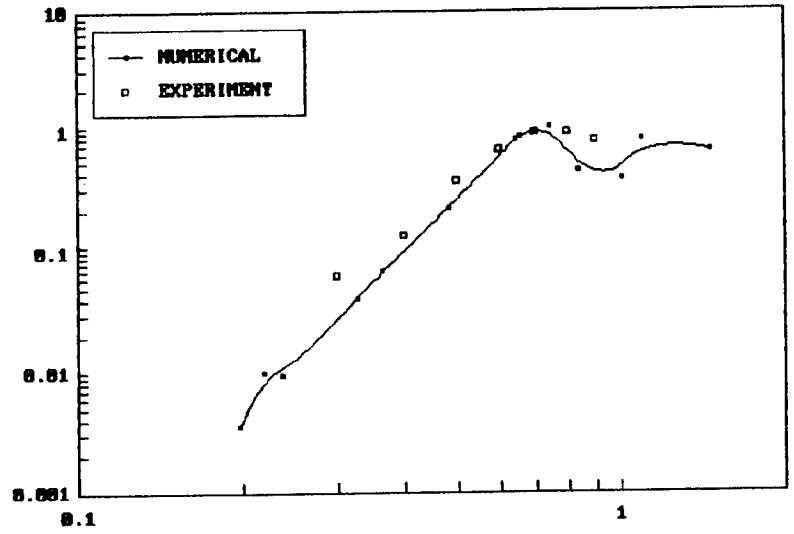


Fig. 2

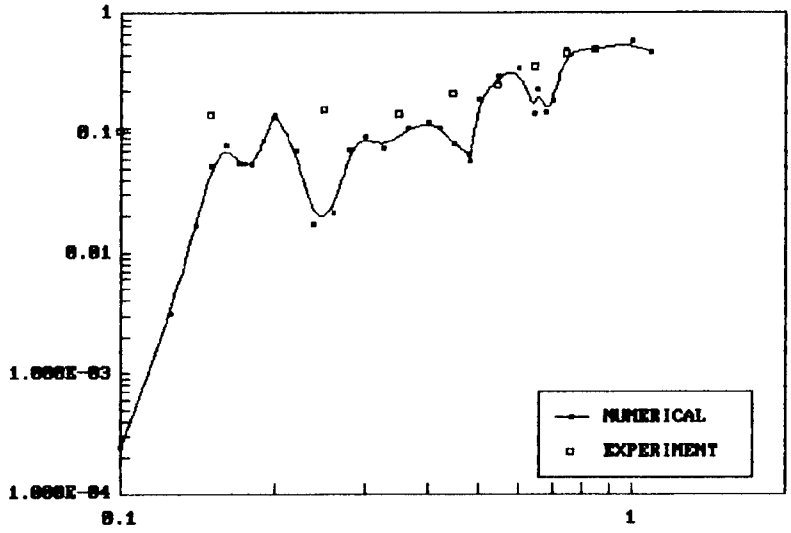


Fig.3

We carried out investigation of light scattering by particles and pits locating on a layer deposited on the smooth surface also. Our results seem to be useful to establish differences between scattering pattern of a particle and pit. In Figs 1-3 the experimental data obtained from system Tencor Surfscan-5500 are shown as compared with the numerical ones. Vertical axis denotes the scattering cross section (μm^2) and horizontal one is the particle diameter (μm). Fig. 1 demonstrates case of polistirol particle, Figs 2,3 correspond to Silicon and SiO_2 particles.

Conclusion. GMT [2] seemed to be effective tool to improve resolution ability of contaminations inspecting system by computer simulation. Code created allows to investigate complete mathematical models by PC using only. Results obtained enable to distinguish a particle from a pit.

References

[1] Yu. Eremin and N. Orlov. *Sov. J. Comm. Techn. Electronics.* 1989, **34**, No.8, p.15.
[2] Yu. Eremin and A. Sveshnikov. *Electromagnetics.* 1993, No.2.
[3] B. Lui, S. Chae and G. Bae. *Proc. Symp. Contaminant Control and Defects Reduction in Semiconductor Manufacturing.* 1992, **92-21**, p.57.

Analysis of Convergence Properties of Projection Methods for Solving CEM Applications

Ivakhnenko V. I., Kukk A. V.,
Tyrtyshnikov E. E., Yeremin A. Yu., Zamarashkin N. L.
Russian Academy of Sciences and Elegant Mathematics, Inc.(USA)
E-mail: tee@post.inm.ras.ru and badger@sms.ccas.msk.su

Boundary integral methods provide a promising approach to solution of challenging industrial CEM problems. In particular, the electric field integral equations are often in use since they can be applied both to closed and open perfectly conducting scatters with and without (multilayered) dielectric coverings. Unfortunately, this approach mostly based on the Rao-Wilton-Glisson method (in its current state of the art) possesses two principal drawbacks:

(A) it is necessary to solve very large dense complex simultaneous equations which requires enormous memory and arithmetic costs (even taking into account recent advances in iterative algorithms for solving dense linear systems);

(B) the Rao-Wilton-Glisson possesses the very slow convergence especially when solving CEM problems with GHz frequencies for very large electric sizes, it is commonly adopted that the size of the linear systems encountered is strictly linearly dependent on the frequency.

Besides these two well recognized drawbacks we would like to mention another very negative disadvantage of the Rao-Wilton-Glisson method:

(C) it is very hard to believe that in the framework of the current state of the art of the Rao-Wilton-Glisson method it is possible to prove a constructive convergence rate theorem providing a reliable and computable aposteriori integral solution error estimates.

Therefore, we need an alternative to the Rao-Wilton-Glisson method which is free of drawbacks (A) – (C). Our results are related to construction of such an alternative.

We begin with some model 2D CEM problems including E- and H- polarization problems for perfect conducting bodies with and without dielectric coverings. Following the Galerkin approach

in order to solve an operator equation $Au = f$ we use the linear system in the form

$$\sum_{j=1}^{N}(A\phi_j, \phi_i)x_j = (f, \phi_i),\ i = 1, \cdots, N,$$

with a suitable choice of the test functions and the scalar product. We propose to construct the hierarchical test functions from a family of basic functions $\Psi = \{\psi_i\}$, defined on a reference support. In this case the functions ϕ_i can be defined from ψ_i via a natural change of variables in order to translate the basic function to a prescribed local support. Thus, we construct a hierarchical family of supports $\Omega = \{\omega_i\}$. Any test function ϕ_i is supplied with two indices l (referring to the set of basic functions) and m (referring to the set of supports). In general Ψ and Ω can be obtained by hierarchical rules.

When using the segment $[0, 2\pi]$ as a reference support we define the family of basic functions as follows

Level 0:

$$f_0(t) = \begin{cases} \frac{1-\cos t}{2}, & t \in [0, 2\pi], \\ 0, & t \notin [0, 2\pi]; \end{cases}$$

Level 1:

$$f_1^{(1)}(t) = \cos t \cdot f_0(t),$$
$$f_1^{(2)}(t) = \sin t \cdot f_0(t),$$

...

Level l:

$$f_l^{(1)}(t) = \cos lt \cdot f_0(t),$$
$$f_l^{(2)}(t) = \sin lt \cdot f_0(t),$$

The approximate solution $\tilde{u}$ to u on the reference support is sought then in the following form

$$\tilde{u} = \sum_{i=1}^{2}\sum_{l=1}^{n} c_l^{(i)} f_l^{(i)} + c_0 f_0$$

which can be considered as a truncated Fourier series multiplied by the cut-off function. The equation

$$f_{l;a,b}^{(i)}(t) = f_l^{(i)}\left(2\pi\frac{t-a}{b-a}\right).$$

specifies the translation of the basic functions to an arbitrary support $[a, b]$.

To give a flavor of what kind of the numerical results were obtained we present numerical results for the E-polarized wave scattering problem for a perfectly conducting cylinder. In this case the electric field integral equation takes the form

$$i\omega\mu \int_S \frac{1}{4\pi}\frac{e^{ikr}}{r}\vec{j}^{\,*}\, ds = -\vec{E}_z^{\,i},$$

describing the fact that the tangential component of the total electric field must vanish on the scatterer S.

Table 1 presents the sizes of linear systems produced by the hierarchical approximation method and the RWG method in order to guarantee a prescribed accuracy (AC) of the computed solution with respect to the analytical solution for sampled values of the electrical size (ES). By definition, $ES = ka$, where k is the wave number and a is the cylinder radius. The error of the computed current is measured in the C-norm. We are usually interested in the relative error $AC = \frac{\|x - x_*\|_C}{\|x_*\|_C} \cdot 100\%$, where x is the computed solution while x_* is the analytical solution. It should be emphasized that for both methods we tried to get least size linear systems which provide the desired accuracy (in the RWG method we vary only the number of supports per wavelength, while in the hierarchical method we vary both the number of supports per wavelength and the number of levels taken up for each support).

Table 1: Comparison of Sizes of Linear Systems for the Rao-Wilton-Glisson method and the Hierarchical Approximation Method when Solving the E-polarization Problem for the Perfect Conductor

The Rao-Wilton-Glisson method			
	ES		
AC	50	100	200
$\approx 5\%$	600 (5%)	2000 (5.2%)	2500 (6%)
$\approx 1\%$	1000 (1.2%)	5000 (1.3%)	10000 (2.8%)
$\approx 0.1\%$	10000 (0.3%)	>40000	> 60000
The hierarchical method			
	ES		
AC	50	100	200
$\approx 5\%$	120	300	560
$\approx 1\%$	150	500	630
$\approx 0.1\%$	208	720	810

The results presented show that the hierarchical approximation method allows us to reduce substantially the size of linear systems (in contrast to the RWG method) especially for large electric sizes (high frequencies) and high accuracies. In the hierarchical approximation method we need to use about 3-5 unknowns per wavelength to obtain an accuracy AC less than 1% while the RWG method requires about 20-40 supports (unknowns) per wavelength to get the same accuracy.

The hierarchical approximation method has some other important advantages. Our results show that the accuracy of the RWG method with the constant number of supports per wavelength can vary dramatically depending upon the electrical size. To the contrary, the hierarchical approximation method is practically insensitive to the resonant frequencies. Figure 1 shows the relative errors corresponding to the first and to the second levels of the hierarchical test functions. The relative error for the first level is quite similar to that of the RWG method , the latter is shown on Fig. 2. However, the relative error for the second level is almost constant and is almost

independent of the electrical size. The detailed description of the numerical comparison of the hierarchical method with the RWG method can be found in [2].

The primary observation that follows from our numerical experiments consists in the justification of the cost-effectiveness and robustness of the hierarchical approach. Even for smooth bodies and moderate accuracy, our method significantly outperforms the RWG method, not to say about cases when a high accuracy is needed. The hierarchical approach generally has the exponential convergence rate with respect to levels. Moreover, this method seems to manifest the exponential convergence with respect to the number of unknowns, i.e. the linear system size. We can thus conclude that the hierarchical approach enables us to reach very high accuracy on small linear systems. We have also shown that the hierarchical approach can be successfully applied to stretched out and nonsmooth scatterers.

One should appreciate it that the $3D$ vector boundary integral equations are much harder to analyze than the scalar equations of the $2D$ case. All the theory necessary for work with the $2D$ case was well-known for years whereas a general theory of the $3D$ electric field integral equations has been developed just recently.

For the $2D$ case we are mainly interested to prove the quasiexponential convergence rate of our hierarchical schemes. Let a sequence u_n converge to u. Then the convergence rate is called quasiexponential if for any $s > 0$ there exists $c_s > 0$ such that

$$|| u_n - u || \leq \frac{c_s}{n^s}.$$

We show that the quasiexponential convergence rate is guaranteed whenever the solution possesses some regularity properties.

Consider a closed continuous piecewise smooth curve L with corner points x_i and and introduce a class of functions

$$\Phi^\alpha = \{f = \sum_{i=1}^{m} f_i \rho_i^{\alpha_i},\ f_i \in C^\infty\},$$

where $\alpha_i \geq \alpha$ are prescribed exponents.

Definition. A set of functions $\{\xi_i\}_{i=1}^m$ associated with a covering $U = \{U_i\}_{i=1}^m$ of L is called a pseudopartition of unity if it satisfies the following requirements:

(a) ξ_i is infinitely smooth on the closed interval which is mapped onto the closure of U_i;

(b) ξ_i is nonzero in U_i;

(c) ξ_i is allowed to take the zero value of a finite multiplicity at the end points of U_i;

(d) ξ_i is equal to zero outside the closure of U_i.

Define the approximation space $\mathcal{T}_n$ as the set of all functions v of the form

$$v = \sum_{i=1}^{m} \rho_i^{\alpha_i} \xi_i T_{i,n},$$

where $T_{i,n}$ is a trigonometric polynomial of degree n.

Theorem. Let $u \in \Phi^\alpha$ and $\xi_i \in C^k$ for all i. If $\alpha < k + \frac{1}{2}$ then for any $s \geq 0$ there exists $c_s > 0$ such that for all $n \geq 1$

$$\inf_{v_n \in \mathcal{T}_n} ||u - v_n||_\alpha \leq \frac{c_s}{n^s},$$

i.e., the Galerkin method converges quasiexponentially.

Corollary. For any smooth closed and for any smooth open screen the Galerkin method with the approximation spaces $\mathcal{T}_n$ converges quasiexponentially.

The Galerkin schemes for $3D$ problems can be introduced quite similarly to the formulations of the $2D$ case. The only but principal difficulty arises that the operator we now deal with is no longer strongly elliptic. As a consequence, for $3D$ electromagnetic diffraction problems the approximation property of test functions is still necessary but no longer sufficient to provide the convergence. It now comes no surprise that some Galerkin algorithms useful for many industrial applications (in particular, the Rao-Wilton-Glisson method) have got no rigorous proof of convergence yet.

A relevant theory of the electric field integral equation has been proposed just recently in [1]. It makes it possible to propose some projection methods and present a proof that these methods are guaranteed to converge.

The Diagonal Galerkin Method. Let the test functions v_i^1 and v_i^2 are chosen such that

$$\text{div } v_i^1 = 0, v_i^2 = \text{grad } h_i$$

for some scalar function h_i.

Let

$$u_n^1 \in \text{span } \{v_1^1, \ldots, v_n^1\},$$
$$u_n^2 \in \text{span } \{v_1^2, \ldots, v_n^2\}.$$

Then the diagonal Galerkin method is defined by the following equations

$$\begin{cases} (Au_n^1, v_i^1) = (f, v_i^1), \ i = 1, \ldots, n, \\ (Au_n^2, v_i^2) = (f, v_i^2), \ i = 1, \ldots, n. \end{cases}$$

Theorem. If the electric field integral equation has a unique solution then the diagonal Galerkin method is guaranteed to converge.

Corollary. For a smooth closed screen the convergence rate for the hierarchical p–version is quasiexponential.

Actually the theorem states that there exists a Galerkin method which is convergent in the cases of closed and open screens. Such a Galerkin method requires the choice of specific test functions with above described properties. Moreover, this theoretical study provides a principal key to an analysis of convergence properties for other sets of test functions (and ultimately to choose "optimal" test functions) which appear to be similar in a sense to the above described functions.

To the best of our knowledge a rigorous mathematical proof of convergence of a Galerkin method for the 3D EFIE was not published so far. The detailed description of such a proof can be found in [3].

It should be noted that in spite of the lack of rigorous proofs there are some well-designed Galerkin schemes which usually behave as convergent in industrial applications. We propose a method which allows one to explain why these methods converge in practice. We propose in fact a new pseudoprojection method which we call the τ-projection method. Under rather general hypotheses we prove that the τ-projection method is guaranteed to converge for a continuously

invertible operator A provided that $0 < \tau < 1/||A^{-1}||$. We believe this result opens up a way to produce some convergence rate estimates for the Galerkin method applied to $3D$ vector equations.

Shortly we a going to present some numerical results for the 3D case. Consider the diffraction problem on the metal plate of the rectangular form $[-\pi, \pi] \times [-\pi, \pi]$ on the plane of coordinates x and y. Let the incident field be $\vec{E} = E_x\vec{e_x} + E_y\vec{e_y}$, where $|\vec{E}| = 1$ and $\text{arctg}\frac{E_x}{E_y} = 20^o$. The wave number is equal to 5. For each vector component of the unknown current we use 4 supports along the vector direction and 20 supports on the transverse direction, the trigonometric polynomials being employed only for one direction. Totally we have 160 supports. What is interesting to look at is the following convergence history of the hierarchical method:

The Convergence History of the Hierarchical Method

Level	0	1	2	3
System Size	160	480	800	1120
Error (%)	—	118	12	8

The RWG-like method (which exploits quadrilateral supports) for the same problem demonstrated the following convergence history:

The Convergence History of the RWG-like Method

System Size	420	760	924	1104	1300	1512	1740
Error (%)	—	16	21	29	49	28	15

We thus see that in contrast to the RWG method the hierarchical method exercises the monotone decrease of the error estimate and allows one to deal with smaller linear systems.

References

[1] Yu. G. Smirnov. On the solvability of vector integro-differential equations in electromagnetic diffraction problem on arbitrary screens. *Ž. Vychisl. Math. Fiz, N11*, 1994. (in russian).

[2] V. I. Ivakhnenko, A. V. Kukk, E. E. Tyrtyshnikov, A. Y. Yeremin. Hierarchical Approximations of Boundary Integral Formulations for Electromagnetic Wave Scattering Problems.I: The Galerkin Formulation with a Hierarchical Set of test Functions and Curvilinear Supports. Research Report EM-RR-8/93, Elegant Mathematics, Inc.(USA), 1993.

[3] Ivakhnenko V. I., Tyrtyshnikov E. E., Yeremin A. Y., Zamarashkin N. L. Hierarchical Approximations of Boundary Integral Formulations for Electromagnetic Wave Scattering Problems. II. Theoretical Foundations of the Galerkin Method Versions for 2D and 3D Electric Field Integral Equations. Research Report EM-RR-15/94, Elegant Mathematics, Inc.(USA), 1994.

Figure 1: Accuracy of the Hierarchical Approximation Method with the Fixed Number of Supports per Wavelength versus the Electrical Size when Solving the E-polarization Problem for the Perfectly Conducting Circular Cylinder.

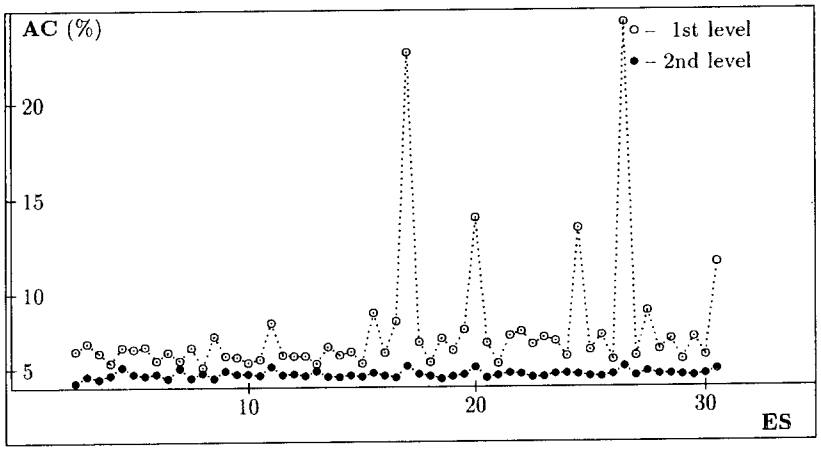
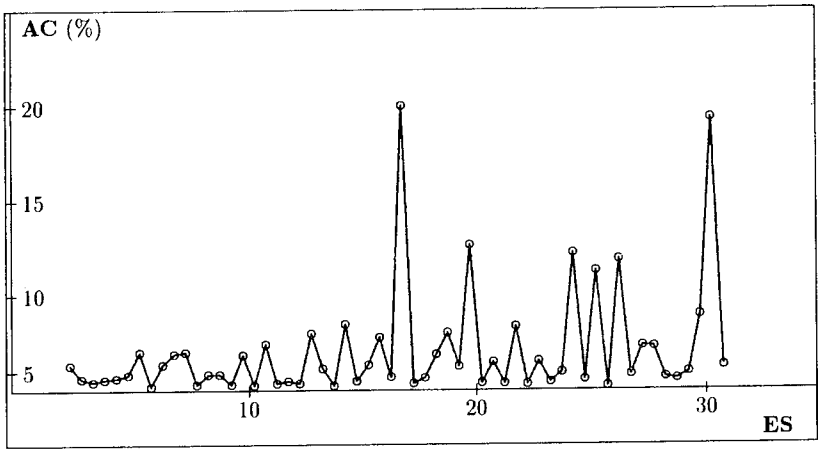


Figure 2: Accuracy of the RWG Method with the Fixed Number of Supports per Wavelength versus the Electrical Size when Solving the E-polarization Problem for the Perfectly Conducting Circular Cylinder.



SESSION 17:

ELECTROMAGNETIC MODELING TECHNIQUES FOR INTEGRATED OPTICS

Chair: A. Cangellaris

Analysis and Design of Guided-wave Optical Devices Using Finite-Difference Time-Domain Method

S. K. Chaudhuri and **S. T. Chu**

Department of Electrical and Computer Engineering
University of Waterloo
Waterloo, Ontario
Canada, N2L 3G1
Email: sujeet@maxwell.uwaterloo.ca

Abstract

In this paper we discuss research trends on the finite-difference time-domain (FDTD) algorithm in optics and present the types of devices whose design and analysis can benefit from the use of this method. The FDTD method is a versatile and powerful method for the analysis of electromagnetic wave interactions. It is well suited for the analysis of compact geometries having strong wave interactions or having weak but extended interactions that can add up coherently. Although the method offers many advantages over the existing optical guided wave theories, the optical size of most optical devices requires enormous computational resources that makes the FDTD analysis impractical. This paper discusses current efforts on the improvement in the efficiency of the method through modifications to the full vector formulation and on the extension of the FDTD algorithm to more complex media with dispersive and nonlinear propagation properties.

1. Introduction

As the physical size of optical devices becomes more compact and with increasing computational power of new workstations, the FDTD method appears to be an attractive solution to the analysis of these devices. However, most current optical devices and structures are hundreds and even thousands of wavelengths long, which makes it impractical to analyzed them by FDTD. The large size requirement for optical structure is due mainly to the weakly guiding nature of the optical waveguides and the relatively weak dispersion of most optical waveguides. In the design of optical devices, it is necessary to limit the total loss to satisfy the power budget requirement for the optical system to be practical. Excess loss in coupling between the devices and waveguide, at bends and interfaces within the devices cannot be tolerated. The reduction of the total loss usually requires the devices to be made adiabatic, with very slow transitions. For example, at the

branching section of devices such as directional couplers and power splitters, the typical branching angle is less than 1°. Since the fields of the optical waveguides are associated with surface waves having fields extending outside of the core, waveguides must be separated sufficiently apart for them to be isolated from each other. These factors can make the branching section of the device alone to be hundreds of wavelengths long.

Another reason for the large size requirement is because of the relatively weak dispersion relationship found in optical structures. For example, within the wavelength band of operation of a wavelength division multiplexer, typically a fraction of 1 μm, the relative change of the coupling length is typically less than a percentage. In order to increase the wavelength sensitivity of the devices, such as to reduce the linewidth of a directional coupler type optical wavelength filter, will require an increase in the optical length of the device. These factors make the optical length of the common devices to be in the orders of thousands of wavelengths.

Despite the fact that the FDTD method seems computer intensive in the analysis of optical devices, the method draws attention in optical waveguide research because it solves certain problems that are difficult to be solved by the other guided-wave theories. In the following section we will review some of the more popular analysis methods in guided-wave optics and discuss on problems that are well suited for FDTD analysis. In Section 3, we will present alternative FDTD algorithms for optics which demand less computational resources. We will also discuss the role of the extended FDTD algorithms such as for dispersive, time-varying and weak nonlinear media in guided-wave optics.

2. Optical Guided-Wave Analysis and Devices for FDTD

In order to show how FDTD method fits into the rest of the analysis tools in guided-wave optics, it is necessary to have an understanding of the characteristics of optical waveguides, the fabrication limits, and a knowledge of the existing numerical analysis used in the field. The previous section has introduced some of the characteristics of optical waveguide, here we will start by briefly discussing some of the existing methods that are commonly used in the analysis of guided-wave optical problems.

There exists a number of methods and approaches in the analysis of optical guided-wave problems. Two of the most common approaches are the coupled-mode theory (CMT) [1] and beam-propagation method (BPM) [2]. The CMT usually considers the propagation of only the two dominant guided modes while neglecting the coupling of the radiation modes. The theory is very effective in most adiabatic situations where radiation is small and it is traditionally the most preferable method by designers and experimentalists in guided-wave optics. Another method that has gained its acceptance in guided-wave optics during the last few years is the beam-propagation method. The BPM is a numerical method that solves the one-way wave equation in the spatial domain, the simulation is for the propagation of the optical signal in the forward direction. Although the method assumes that the reflection effects are weak and can be neglected, it does account for the

forward radiation fields. It is a good approximation for many optical structures and the method has been efficiently applied to many geometries. It is important to realize that the analysis of adiabatical structures will be more economical using these approaches than the FDTD method.

The FDTD method can be implemented in guided-wave analysis in a straight forward manner [3] except the input to the optical devices are in the form of a guided mode, and at the truncation plane the medium is no longer homogeneous. In the rest of this section, we will discuss the recent research trends of FDTD algorithm in guided-wave optics. One of the current research trends concentrates on areas where the FDTD method has a degree of superiority over the existing methods in guided-wave optics. Some of the areas are: 1) Study of structures having strong wave interaction and can cause strong reflections, some of these are sharp bends, corner reflectors and mirrors [4]. The dimension of these problems are typically within a few tens of wavelengths, however, because the junction is very close to the boundaries, good absorbing boundary conditions are needed to absorb both the guided modes and the radiation fields generated; 2) Extended FDTD algorithms for complex media with dispersive and nonlinear propagation properties [5-6]. The recent development on the dispersive FDTD algorithms can be applied directly to guided-wave optics in the study of pulse propagation. In applying these algorithms a good understanding of the optical materials used in optics is required. Algorithms have been developed for propagation in nonlinear materials, from solitons propagation to weak nonlinear propagations. A report on some of these algorithms will be presented; 3) Study of the dynamic behaviours of optical devices. These require FDTD algorithm for time varying media for the study of optical modulators, photodetectors and sensors [7-8]; 4) Study of optical micro-cavities and resonators. A new research area in optics is on synthetic process of optical material such as the photonic band gap structures [9]. The dispersive characteristics of the bulk optical materials are altered by embedding micron size micro-cavities into them. The small size of the cavities makes it feasible to be analyzed by the FDTD method.

3. Alternate FDTD algorithms

In guided-wave optical analysis, most of the propagating modes are linearly polarized. This is because of the weak refractive index differences Δn found at the core-cladding interfaces in the waveguides of the optical devices. It is more efficient to develop algorithms that deal with the propagation of only the dominant field component for these devices. The semi-vectorial FDTD algorithm [10] is one of these algorithms.

The **E** formulation of the semi-vectorial FDTD algorithm starts with the vector wave equations of the electric field **E** in a sourceless medium,

$$\mu\epsilon\frac{\partial^2\mathbf{E}}{\partial t^2} = \nabla^2\mathbf{E} - \nabla\left[\left(\nabla\frac{1}{\epsilon}\right)\cdot(\epsilon\mathbf{E})\right]. \quad (1)$$

Let E_y be the dominant field component and from the y-component of (1) we have

$$\mu\epsilon\frac{\partial^2 E_y}{\partial t^2} = \frac{\partial^2 E_y}{\partial x^2} + \frac{\partial^2 E_y}{\partial z^2} - \frac{\partial}{\partial y}\left[\frac{1}{\epsilon}\frac{\partial}{\partial y}(\epsilon E_y)\right] - \frac{\partial}{\partial y}\left[\frac{1}{\epsilon}\left(\frac{\partial \epsilon}{\partial x}E_x + \frac{\partial \epsilon}{\partial z}E_z\right)\right]. \quad (2)$$

The last term in (2) corresponds to the polarization coupling between the dominant E_y field with the minor E_x and E_z fields, the significance of this coupling depends on the magnitudes of the minor fields and the derivatives of $\partial\epsilon/\partial x$ and $\partial\epsilon/\partial z$. In most optical guided-wave analyses, the polarization coupling is weak and one can apply the semi-vectorial approximation, which neglects the polarization coupling. After eliminating the polarization coupling term from (2) we have the governing equation of the semi-vectorial FDTD algorithm for the E_y field,

$$\mu\epsilon\frac{\partial^2 E_y}{\partial t^2} = \frac{\partial^2 E_y}{\partial x^2} + \frac{\partial^2 E_y}{\partial z^2} - \frac{\partial}{\partial y}\left[\frac{1}{\epsilon}\frac{\partial}{\partial y}(\epsilon E_y)\right]. \quad (3)$$

Although in (3) the polarization coupling is neglected, it does not eliminate all of the vectorial behaviours of the wave propagation. The last term of (3) properly models the boundary condition at the dielectric interfaces parallel to the xz-plane, normal to the polarization direction. The semi-vectorial FDTD algorithm can be derived by finite-differencing (3), and the usual source excitation and absorbing boundary conditions similar to the full-vector FDTD algorithm can be applied directly. It can be shown that the semi-vectorial FDTD algorithm is stable if

$$v_{max}\Delta t < \frac{1}{\sqrt{\frac{1}{\Delta x^2} + \frac{T_{max}}{\Delta y^2} + \frac{1}{\Delta z^2}}} \quad (4)$$

where

$$T_{j\pm1} = \frac{2\epsilon_r(i, j \pm 1, k)}{\epsilon_r(i, j, k) + \epsilon_r(i, j \pm 1, k)},$$

and T_{max} is the maximum $T_{j\pm1}$ in the region, v_{max} is the maximum possible phase velocity in the region. Since the semi-vectorial FDTD algorithm deals only with a single field component, both the computation time and memory requirements are drastically reduced. It is important to point out that in the two-dimensional case, with $\partial/\partial y \equiv 0$, the electric and magnetic fields are decoupled and the semi-vectorial formulations for the E_y and H_y are exact. Using the semi-vectorial FDTD algorithm for two-dimensional analyses, a 50% reduction on computational time and a 30% reduction on memory requirement can be achieved without any lost of accuracy as compared with the full-vector FDTD algorithm.

An important development of the FDTD algorithms in optics is on the extension of the FDTD algorithm for wave propagation in complex media such as for dispersive, nonlinear and time varying media. These extended algorithms are generally more rigorous than those in the current optical waveguide research. If the algorithms can be made efficient,

they will have an impact on the research in these areas. One of the areas where the FDTD method has successfully implemented is in nonlinear optics. Goorjian and Taflove modelled the propagation of femtosecond electromagnetic solitons using a direct time integration approach [6], their approach is very general and can be used to study solitons collision. If the material nonlinearity is weak, the nonlinearity can be incorporated into the FDTD analysis directly. Following [11], the forms of the nonlinear permittivity is

$$\epsilon_r = \epsilon_r{}^0 + f(\alpha|E|^2) \tag{5}$$

where in the Kerr law media,

$$f(\eta) = \eta$$

and in saturable two-level media,

$$f(\eta) = \frac{\eta}{1 + \frac{\eta}{\Delta\epsilon_{r,sat}{}^2}}.$$

The coefficient of nonlinearity α is generally many orders of magnitude less than unity but it does scale with power. It is convenience to set α to unity, resulting in nonlinear effect at low power levels. If the features being studied involve only the field patterns at steady-state, then the nonlinearity can be incorporated directly. Assuming the magnitude of the electric field is changing very slowly, and approximate the magnitude from the field values at the two previous time-steps. Then ϵ_r can be updated for the next time-step using (5). Using this method, the turn-on time of the nonlinearity is $3\Delta t/2$; this is acceptable for many application. The above approach was found to be very effective in modelling self-guiding structures, nonlinear directional couplers and solitons emission and capture. Some of these results will be reported in the meeting.

4) Conclusion

We have reported on the current research trends on the FDTD algorithm in optics. Due to the size of most optical devices, research efforts have been concentrated on the development of more efficient FDTD algorithms. We have presented the governing formulation of the semi-vectorial FDTD algorithms for optics. For two-dimensional analyses, it requires 50% less computational time and 30% less storage than the full-vector FDTD without any lost of accuracy. We have also presented a summary on areas where the FDTD method has a degree of superiority over the existing methods in guided-wave optics.

References

[1] D. Marcuse, "Theory of dielectric optical waveguides," *Academic Press*, New York, 1974.

[2] M. D. Feit and J. A. Fleck, Jr. "Light propagation in graded-index optical fibers", *Appl. Opt.*, **17**, no. 24, pp. 3990-3998, 1978.

[3] S. T. Chu and S. K. Chaudhuri, "A Finite-Difference Time-Domain Method for the Design and Analysis of Guided-Wave Optical Structures", *IEEE J. Lightwave Technol.*, **LT-5**, pp. 2033-2038, 1989.

[4] S. M. Lee *et al* "Modeling of Rough-Surface Effects in an Optical Turning Mirror Using the Finite-Difference Time-Domain Method", *IEEE J. Lightwave Technol.*, **LT-9**, pp. 1471-1480, 1991.

[5] R. M. Joseph *et. al.*, "Direct Time integration of Maxwell's equations in Linear Dispersive media with Absorption for Scattering and Propagation of Femtosecond Electromagnetic Pulses", *Opt. Lett.*, **16**, pp. 1412-1414, 1991.

[6] P. M. Goorjian and A. Taflove, "Direct Time integration of Maxwell's equations in nonlinear dispersive media for propagation of femtosecond electromagnetic solitons", *Opt. Lett.*, **17**, pp. 180-182, 1992.

[7] E. Sano and T. Shibata, "Fullwave Analysis of Picosecond Photoconductive Switches", *IEEE J. Quantim Electron.*, **QE-26**, pp. 372-377, 1990.

[8] J. S. Kimmel and D. A. Christensen, "Finite-Difference Time-Domain Modelling and Experimental Characterization of Planar Waveguide Fluorescence Sensors", *SPIE Chemical, Biochemical, and Environmental Fiber Sensors III*, **1587**, pp. 136-146, 1991.

[9] E. Yablonovitch, "Photonic Band Structure" in *Analogies in Optics and Micro Electronics* W. van Haeringen and D. Lenstr *ed.*, Kluwer Academic, The Netherlands, 1990.

[10] W. P. Huang *et al.*, "A Semi-Vectorial Finite-Difference Time-Domain Approach for Guided-Wave Optics", *IEEE Photon. Tech. Lett.*, **PTL-3**, pp. 803-806, 1991.

[11] R. A. Sammut and C. Pask, "Gaussian and Equivalent-Step-Index Approximation for Nonlinear Waveguides", *JOSA Part B*, **8**, pp. 395-402, 1991.

Vectorial Analysis of Optical Waveguides by the Method of Lines

Reinhold Pregla, Wilfrid W. Pascher
Allgemeine und Theoretische Elektrotechnik,
FernUniversität, D-58084 Hagen
E-mail: R.Pregla@FernUni-Hagen.de , W.Pascher@FernUni-Hagen.de

Abstract

Waveguides in integrated optical circuits can be described as multilayered structures. The refractive index is varying in lateral direction and is different from one layer to the other. The analysis of such structures by the method of lines is demonstrated using an alternative unified approach. This semi-analytical finite difference technique is both highly accurate and efficient for multilayered optical waveguides. Loss can be taken into account by using complex refractive indices. Numerical results are given for a rib waveguide and compared with results of other papers.

1 Introduction

Waveguides in integrated optical circuits consist of a number of composite layers. Two typical structures are sketched in Fig. 1 and a general model for a multilayered structure is given in Fig. 2. The method of lines (MoL) is very efficient for the analysis of these types of optical waveguides. The MoL takes advantage of the layered structure and uses discretization only as far as necessary. Finite differences are used, but only in one direction for waveguides, whereas an analytical solution is retained for the other coordinate. This semi-analytical approach yields accurate results with less computational effort than other techniques. The MoL was introduced by Russian mathematicians for the solution of partial differential equations and developed in the first author's group for the analysis of multilayered waveguide structures in the microwave and optical regions [1]-[7]. Strip-loaded optical and dielectric waveguides [3]-[5] as well as diffused and groove guides [6] have been analysed with high accuracy. A comprehensive description of the MoL is given in [1].

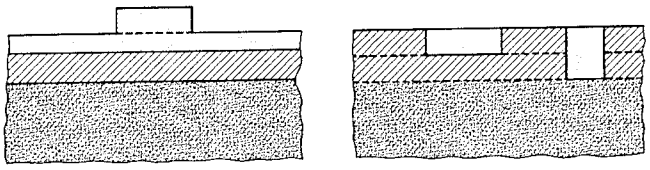


Fig. 1: Waveguides in integrated optics
(a) Rib (or strip loaded film) guide (b) two coupled channel guides

In this paper a unified approach is presented. We use a single Hertz potential with two components instead of two potentials with one component each as in [1] and [3]-[6]. This enables us to use a more

concise mathematical formulation with less algebraic manipulations than in the conventional approach. Thus the analysis is easier to follow and the computer algorithms are readily programmed.

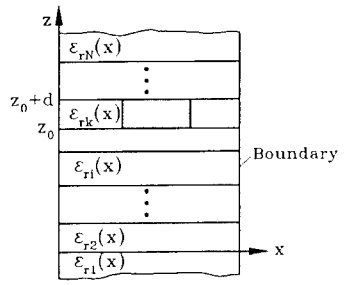


Fig. 2:
General analysis model for
multilayered waveguide structures

In some optical structures metallizations are important, too (e.g. electro-optic modulators). The metallization may have a finite thickness and should be assumed as dielectric with complex or imaginary permittivity. In $\pm z$ direction the structure is either infinite or closed by a metallic or magnetic wall. In x direction metallic or magnetic walls are used. For modelling of open structures absorbing boundary conditions have been introduced [8] [9].

2 Theory

The following steps are essential in the MoL analysis of optical waveguides:

- partitioning of the cross section into suitable layers according to the model in Fig. 2
- discretization of the wave equation in one coordinate direction
- transformation to obtain decoupled ordinary differential equations for the Hertz potential
- solution of the equations and determination of the tangential electromagnetic fields in each single layer
- transfer of the fields through the multilayered structure after transformation back to spatial domain
- determination of the propagation constant and the field distribution as the solution of an indirect eigenvalue problem

2.1 Basic equations

For the analysis we use the Hertz potential $\vec{\Pi}_e$ defined in [10]. In our case $\vec{\Pi}_e$ should have the two components Π_x and Π_y in the two coordinate directions x and y, respectively. This is analogous to the case in Cartesian coordinate system described in [7] [11] [12]. The permittivity may depend on the x coordinate too. The general case with dependence on three coordinates is described in [13]. The Hertz potential $\vec{\Pi}_e$ has to fulfill the vector wave equation [10].

$$\nabla^2\vec{\Pi}_e - \varepsilon_r^{-1}(\nabla\varepsilon)\nabla\cdot\vec{\Pi}_e + \varepsilon_r\vec{\Pi}_e = 0 \tag{2.1}$$

$$\eta_0\vec{H} = j\nabla\times\vec{\Pi}_e \qquad \vec{E} = \varepsilon_r^{-1}\nabla\times\nabla\times\vec{\Pi}_e \tag{2.2}$$

The detailed formulae are given in the Appendix A.
The permittivity for this problem may be only a function of x: $\varepsilon_r = \varepsilon_r(\overline{x})$. We assume propagation in y direction according to $\exp(-j\sqrt{\varepsilon_{re}}\overline{y})$ Therefore we have $\dfrac{\partial}{\partial\overline{y}} = -j\sqrt{\varepsilon_{re}}$.

We have to solve two coupled wave equations

$$\varepsilon_r \frac{\partial}{\partial \bar{x}} \left(\frac{1}{\varepsilon_r} \frac{\partial}{\partial \bar{x}} \Pi_x \right) + \frac{\partial^2 \Pi_x}{\partial \bar{z}^2} + (\varepsilon_r - \varepsilon_{re}) \Pi_x - j\sqrt{\varepsilon_{re}} \left(\varepsilon_r \frac{\partial}{\partial \bar{x}} \left(\frac{1}{\varepsilon_r} \Pi_y \right) - \frac{\partial}{\partial \bar{x}} \Pi_y \right) = 0 \tag{2.3}$$

$$\frac{\partial^2 \Pi_y}{\partial \bar{x}^2} + \frac{\partial^2 \Pi_y}{\partial \bar{z}^2} + (\varepsilon_r - \varepsilon_{re}) \Pi_y = 0 \tag{2.4}$$

in which $\bar{x}$, $\bar{y}$ and $\bar{z}$ are the coordinates x, y and z, respectively, normalized with the free space wave number k_o. We obtain the field components by

$$\eta_o H_x = -j \frac{\partial \Pi_y}{\partial \bar{z}} \qquad \varepsilon_r E_x = -j\sqrt{\varepsilon_{re}} \left[\frac{\partial \Pi_y}{\partial \bar{x}} + j\sqrt{\varepsilon_{re}} \Pi_x \right] - \frac{\partial^2 \Pi_x}{\partial \bar{z}^2} \tag{2.5}$$

$$\eta_o H_y = j \frac{\partial \Pi_x}{\partial \bar{z}} \qquad \varepsilon_r E_y = -\frac{\partial}{\partial \bar{x}} \left[\frac{\partial \Pi_y}{\partial \bar{x}} + j\sqrt{\varepsilon_{re}} \Pi_x \right] - \frac{\partial^2 \Pi_y}{\partial \bar{z}^2} \tag{2.6}$$

$$\eta_o H_z = j \left[\frac{\partial}{\partial \bar{x}} \Pi_y + j\sqrt{\varepsilon_{re}} \Pi_x \right] \qquad \varepsilon_r E_z = \frac{\partial^2 \Pi_x}{\partial \bar{x} \partial \bar{z}} - j\sqrt{\varepsilon_{re}} \frac{\partial \Pi_y}{\partial \bar{z}} \tag{2.7}$$

These equations can be transformed to the equation for TE_z and TM_z for ε_r constant. The potential components Π_y and Π_x are connected in an identical way with the field components H_x and H_y, respectively.

3 Discretization

For inhomogeneous layers not only the potentials but also the permittivities have to be discretized. The discretization has to be done on two different discretization line systems and yields

$$\begin{aligned}
\Pi_x &\longrightarrow \boldsymbol{\Pi}_x \text{ (vector)} & \Pi_y &\longrightarrow \boldsymbol{\Pi}_y \text{ (vector)} \\
\varepsilon_r &\longrightarrow \boldsymbol{\epsilon}_x \text{ (diagonal matrix)} & \varepsilon_r &\longrightarrow \boldsymbol{\epsilon}_y \text{ (diagonal matrix)} \\
\frac{\partial}{\partial \bar{x}} &\longrightarrow \bar{h}^{-1} \boldsymbol{D}_x = \overline{\boldsymbol{D}}_x & \frac{\partial}{\partial \bar{x}} &\longrightarrow \bar{h}^{-1} \boldsymbol{D}_y = \overline{\boldsymbol{D}}_y \\
\frac{\partial}{\partial \bar{x}} \Pi_x &\longrightarrow \overline{\boldsymbol{D}}_x \boldsymbol{\Pi}_x & \frac{\partial}{\partial \bar{x}} \Pi_y &\longrightarrow \overline{\boldsymbol{D}}_y \boldsymbol{\Pi}_y
\end{aligned} \tag{3.1}$$

The subscripts on the difference operators $\boldsymbol{D}$ indicate for which potential the difference operator has to be used. $\boldsymbol{\epsilon}_x$ and $\boldsymbol{\epsilon}_y$ are diagonal matrices. The subscripts indicate the discretization line system to which the quantities belong. The discretized wave equations run

$$\frac{\mathrm{d}^2}{\mathrm{d}\bar{z}^2} \boldsymbol{\Pi}_x + \left[-\boldsymbol{\epsilon}_x \overline{\boldsymbol{D}}_x^t \boldsymbol{\epsilon}_y^{-1} \overline{\boldsymbol{D}}_x - \varepsilon_{re} \boldsymbol{I} + \boldsymbol{\epsilon}_x \right] \boldsymbol{\Pi}_x + j\sqrt{\varepsilon_{re}} \left[\overline{\boldsymbol{D}}_y - \boldsymbol{\epsilon}_x \overline{\boldsymbol{D}}_y \boldsymbol{\epsilon}_y^{-1} \right] \boldsymbol{\Pi}_y = \boldsymbol{0} \tag{3.2}$$

$$\frac{\mathrm{d}^2}{\mathrm{d}\bar{z}^2} \boldsymbol{\Pi}_y + \left[-\overline{\boldsymbol{D}}_y^t \overline{\boldsymbol{D}}_y - \varepsilon_{re} \boldsymbol{I} + \boldsymbol{\epsilon}_y \right] \boldsymbol{\Pi}_y = \boldsymbol{0} \tag{3.3}$$

The two potentials $\boldsymbol{\Pi}_x$ and $\boldsymbol{\Pi}_y$ are coupled with each other for inhomogeneous layers and the potentials on different discretization lines are coupled as well. Using an adequate notation the decoupling procedure is nearly the same as for the conventional approach [1]. We would like to combine the last two equations in matrix form. Therefore we define the matrix $\widehat{\boldsymbol{Q}}$

$$\widehat{\boldsymbol{Q}} = \begin{bmatrix} \boldsymbol{\epsilon}_x \overline{\boldsymbol{D}}_x^t \boldsymbol{\epsilon}_y^{-1} \overline{\boldsymbol{D}}_x + \varepsilon_{re} \boldsymbol{I} - \boldsymbol{\epsilon}_x & \sqrt{\varepsilon_{re}} \left(\overline{\boldsymbol{D}}_y - \boldsymbol{\epsilon}_x \overline{\boldsymbol{D}}_y \boldsymbol{\epsilon}_y^{-1} \right) \\ \boldsymbol{0} & \overline{\boldsymbol{D}}_y^t \overline{\boldsymbol{D}}_y + \varepsilon_{re} \boldsymbol{I} - \boldsymbol{\epsilon}_y \end{bmatrix} = \begin{bmatrix} \boldsymbol{Q}_x & \boldsymbol{Q}_{xy} \\ \boldsymbol{0} & \boldsymbol{Q}_y \end{bmatrix} \tag{3.4}$$

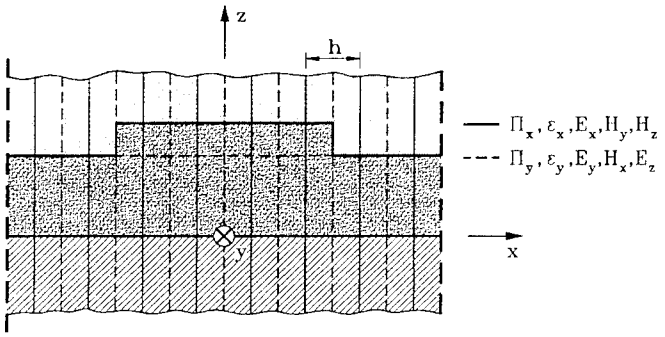


Fig. 3: Discretization of a rib guide

and the supervector

$$\widehat{\Pi} = [\Pi_x^t, \; -j\Pi_y^t]^t \tag{3.5}$$

The hat (^) on the quantities indicates supervectors and supermatrices. Now the equations (3.2) and (3.3) can be written in a shorter form

$$\frac{\mathrm{d}^2}{\mathrm{d}\overline{z}^2}\widehat{\Pi} - \widehat{Q}\widehat{\Pi} = \mathbf{0} \tag{3.6}$$

By transformation to the principle axes (diagonalization)

$$\widehat{T}^{-1}\widehat{Q}\widehat{T} = \widehat{\Gamma}^2 \quad \widehat{\Pi} = \widehat{T}\widehat{\Pi} \quad \widehat{\Gamma} = \mathrm{Diag}\,(\Gamma_x, \; \Gamma_y) \quad \widehat{T} = \begin{bmatrix} T_x & T_{xy} \\ \mathbf{0} & T_y \end{bmatrix} \tag{3.7}$$

we obtain uncoupled equations

$$\frac{\mathrm{d}}{\mathrm{d}\overline{z}^2}\widehat{\overline{\Pi}} - \widehat{\Gamma}^2\widehat{\overline{\Pi}} = \mathbf{0} \tag{3.8}$$

where Γ_x, T_x and Γ_y, T_y are the eigensolutions of Q_x and Q_y, respectively. The eigenvector submatrix T_{xy} is obtained from these as the solution of a system of equations.
The general solution of (3.8) is

$$\widehat{\overline{\Pi}} = \cosh\left(\widehat{\Gamma}(\overline{z} - \overline{z}_o)\right)\widehat{A} + \sinh\left(\widehat{\Gamma}(\overline{z} - \overline{z}_o)\right)\widehat{B} \tag{3.9}$$

We obtain for the relation between the potentials and derivates in the planes A ($z = z_o$) and B ($z = z_o + d$):

$$\frac{\mathrm{d}}{\mathrm{d}\overline{z}}\begin{bmatrix} \widehat{\overline{\Pi}}_A \\ \widehat{\overline{\Pi}}_B \end{bmatrix} = \widehat{\widehat{\Gamma}}^2 \begin{bmatrix} -\widehat{\gamma} & \widehat{\alpha} \\ -\widehat{\alpha} & \widehat{\gamma} \end{bmatrix} \begin{bmatrix} \widehat{\overline{\Pi}}_A \\ \widehat{\overline{\Pi}}_B \end{bmatrix} \tag{3.10}$$

with

$$\widehat{\gamma} = (\widehat{\Gamma}\tanh\widehat{\Gamma}\overline{d})^{-1} \qquad \widehat{\alpha} = (\widehat{\Gamma}\sinh\widehat{\Gamma}\overline{d})^{-1} \qquad \widehat{\widehat{\Gamma}} = \mathrm{Diag}(\widehat{\Gamma}, \widehat{\Gamma}) \tag{3.11}$$

With the definitions for the fields (analogous to eq. (3.5))

$$\widehat{\overline{H}} = \eta_o \begin{bmatrix} -j\overline{H}_y \\ \overline{H}_x \end{bmatrix} \qquad \widehat{\overline{E}} = \begin{bmatrix} \overline{E}_x \\ -j\overline{E}_y \end{bmatrix} \tag{3.12}$$

and

$$\begin{aligned}\hat{\varepsilon} &= \mathrm{Diag}(\epsilon_x,\ \epsilon_y)\\ \hat{R} &= \hat{\varepsilon}^{-1}\left\{\begin{bmatrix}-\varepsilon_{re}\boldsymbol{I}_x & -\sqrt{\varepsilon_{re}}\overline{\boldsymbol{D}}_y\\ \sqrt{\varepsilon_{re}}\overline{\boldsymbol{D}}_x & -\overline{\boldsymbol{D}}_y^t\overline{\boldsymbol{D}}_y\end{bmatrix}+\hat{\boldsymbol{Q}}\right\}=\begin{bmatrix}\overline{\boldsymbol{D}}_x^t\epsilon_y^{-1}\overline{\boldsymbol{D}}_x-\boldsymbol{I}_x & -\sqrt{\varepsilon_{re}}\overline{\boldsymbol{D}}_y\epsilon_y^{-1}\\ \sqrt{\varepsilon_{re}}\epsilon_y^{-1}\overline{\boldsymbol{D}}_x & \varepsilon_{re}\epsilon_y^{-1}-\boldsymbol{I}_y\end{bmatrix}\end{aligned} \tag{3.13}$$

the solutions for the fields transverse to the z direction can be written as

$$\hat{\boldsymbol{E}} = -\hat{\boldsymbol{R}}\hat{\boldsymbol{\Pi}} \qquad \hat{\boldsymbol{H}} = \frac{\mathrm{d}}{\mathrm{d}\overline{z}}\hat{\boldsymbol{\Pi}} \tag{3.14}$$

or in the transform domain

$$\hat{\overline{\boldsymbol{E}}} = -\hat{\overline{\boldsymbol{R}}}\,\hat{\overline{\boldsymbol{\Pi}}} \qquad \hat{\overline{\boldsymbol{H}}} = \frac{\mathrm{d}}{\mathrm{d}\overline{z}}\hat{\overline{\boldsymbol{\Pi}}} \qquad \hat{\overline{\boldsymbol{R}}} = \hat{\boldsymbol{T}}^{-1}\hat{\boldsymbol{R}}\hat{\boldsymbol{T}} \tag{3.15}$$

The relation between the electric and magnetic field of the two planes can be described by the equation

$$\begin{bmatrix}\hat{\overline{\boldsymbol{H}}}_A\\ \hat{\overline{\boldsymbol{H}}}_B\end{bmatrix} = \hat{\overline{\Gamma}}^2\begin{bmatrix}-\hat{\gamma} & \hat{\alpha}\\ -\hat{\alpha} & \hat{\gamma}\end{bmatrix}\begin{bmatrix}\hat{\overline{\boldsymbol{\Pi}}}_A\\ \hat{\overline{\boldsymbol{\Pi}}}_B\end{bmatrix} = -\hat{\overline{\Gamma}}^2\begin{bmatrix}-\hat{\gamma} & \hat{\alpha}\\ -\hat{\alpha} & \hat{\gamma}\end{bmatrix}\begin{bmatrix}\hat{\overline{\boldsymbol{R}}}^{-1} & \\ & \hat{\overline{\boldsymbol{R}}}^{-1}\end{bmatrix}\begin{bmatrix}\hat{\overline{\boldsymbol{E}}}_A\\ \hat{\overline{\boldsymbol{E}}}_B\end{bmatrix} \tag{3.16}$$

In analogy to [1] we may write

$$\begin{bmatrix}\hat{\overline{\boldsymbol{H}}}_A\\ \hat{\overline{\boldsymbol{H}}}_B\end{bmatrix} = \begin{bmatrix}\overline{\boldsymbol{y}}_1 & \overline{\boldsymbol{y}}_2\\ \overline{\boldsymbol{y}}_2 & \overline{\boldsymbol{y}}_1\end{bmatrix}\begin{bmatrix}\hat{\overline{\boldsymbol{E}}}_A\\ -\hat{\overline{\boldsymbol{E}}}_B\end{bmatrix} \tag{3.17}$$

with

$$\overline{\boldsymbol{y}}_1 = \hat{\overline{\Gamma}}^2\hat{\overline{\gamma}}\hat{\overline{\boldsymbol{R}}}^{-1} \qquad \overline{\boldsymbol{y}}_2 = \hat{\overline{\Gamma}}^2\hat{\overline{\alpha}}\hat{\overline{\boldsymbol{R}}}^{-1}\ . \tag{3.18}$$

Now we can completely use the algorithm developed there for transfer from one layer to the other [1][6]. This is only possible without modifications if the layers are homogeneous because for this case the transformation matrices are equal for each layer. Otherwise the admittances and fields have to be transformed back to the original domain and the algorithm should be used for these quantities in the original domain.
For homogeneous layers we obtain the simplified equations

$$\hat{\overline{\boldsymbol{R}}} = \frac{1}{\varepsilon_r}\begin{bmatrix}\overline{\boldsymbol{\lambda}}_x^2-\varepsilon_r\boldsymbol{I}_x & \sqrt{\varepsilon_{re}}\boldsymbol{\delta}^t\\ \sqrt{\varepsilon_{re}}\boldsymbol{\delta} & -\varepsilon_d\boldsymbol{I}_y\end{bmatrix} \qquad \hat{\overline{\boldsymbol{R}}}^{-1} = \hat{\Gamma}^{-2}\begin{bmatrix}\varepsilon_d\boldsymbol{I}_x & \sqrt{\varepsilon_{re}}\boldsymbol{\delta}^t\\ \sqrt{\varepsilon_{re}}\boldsymbol{\delta} & \varepsilon_r\boldsymbol{I}_y-\overline{\boldsymbol{\lambda}}_y^2\end{bmatrix} \tag{3.19}$$

from eqs. (3.13) and (3.15), where $\varepsilon_d = \varepsilon_r - \varepsilon_{re}$, $\boldsymbol{\delta} = \boldsymbol{T}_y^t\boldsymbol{D}_x\boldsymbol{T}_x$. For $\overline{\boldsymbol{y}}_1$ and $\overline{\boldsymbol{y}}_2$ we have

$$\overline{\boldsymbol{y}}_1 = \hat{\overline{\gamma}}\boldsymbol{\Lambda} \qquad \overline{\boldsymbol{y}}_2 = \hat{\overline{\alpha}}\boldsymbol{\Lambda} \qquad \boldsymbol{\Lambda} = \begin{bmatrix}\varepsilon_d\boldsymbol{I}_x & \sqrt{\varepsilon_{re}}\boldsymbol{\delta}^t\\ \sqrt{\varepsilon_{re}}\boldsymbol{\delta} & \varepsilon_r\boldsymbol{I}_y-\overline{\boldsymbol{\lambda}}_y^2\end{bmatrix} \tag{3.20}$$

For an infinitely thick layer we obtain

$$\overline{\boldsymbol{y}}_1 = \hat{\overline{\Gamma}}^{-1}\boldsymbol{\Lambda} \qquad \overline{\boldsymbol{y}}_2 = \hat{\mathbf{0}} \tag{3.21}$$

Nonequidistant Discretization

It should be mentioned that a nonequidistant discretization can be introduced, too. In this case the potential and the difference operators are normalized with the diagonal matrices resulting from the discretization distances h_{xi} and h_{yi}. We define

$$\boldsymbol{s}_x = \mathrm{diag}(\sqrt{h/h_{xi}}) \quad \boldsymbol{s}_y = \mathrm{diag}(\sqrt{h/h_{yi}}) \quad \hat{\boldsymbol{s}} = \mathrm{diag}\,(\boldsymbol{s}_x,\ \boldsymbol{s}_y) \tag{3.22}$$

according to [14] and normalize

$$\widehat{\boldsymbol{\Pi}}_n = \hat{\boldsymbol{s}}^{-1}\widehat{\boldsymbol{\Pi}} \qquad \widehat{\boldsymbol{H}}_n = \hat{\boldsymbol{s}}^{-1}\widehat{\boldsymbol{H}} \qquad \hat{\boldsymbol{E}}_n = \hat{\boldsymbol{s}}^{-1}\hat{\boldsymbol{E}} \tag{3.23}$$

$$\boldsymbol{D}_{xn} = \boldsymbol{s}_y\boldsymbol{D}_x\boldsymbol{s}_x \qquad \boldsymbol{D}_{yn} = \boldsymbol{s}_x\boldsymbol{D}_y\boldsymbol{s}_y \tag{3.24}$$

The whole analysis presented in section 3 formally remains the same for nonequidistant discretization if these normalized quantities are used instead of the original ones.

4 Results

To give an example for the validity of the new approach a strip-loaded slab guide as given in [15][5] has been analysed. The convergence curve is exactly the same as for the conventional MoL approach [5]. The field distribution given in Fig. 4 clearly exhibits the vectorial nature of the fundamental HE_{00} mode (quasi TE-mode). The main magnetic component H_z must be negative with respect to the main electric component E_x because the Poynting vector S_y must be positive. The total number of discretization lines used in the compentation is 120 for each line system for the half structure. For a clear representation the field is depicted within the range $-80 \le x/h \le +80$ only in Fig. 4.

As a second example the microwave electric field distribution in the cross section of an electro optic modulator is presented in Fig. 5. This multilayered structure contains metallic electrodes (black in Fig. 5) and semiconductor layers (shaded). Both are modelled by a suitable complex permittivity $\varepsilon_r = \varepsilon_r' - j\varepsilon_r''$, where $\varepsilon_r' = 12.4$ for semiconductors, ε_r'' is $1.015 \cdot 10^5$ and $1.015 \cdot 10^4$ for top and bottom layers, respectively. $\varepsilon_r = -j7.193 \cdot 10^8$ for the electrodes. The optical field can be calculated with the same computer program. Again the computational window is wider on the lateral sides, but it has been cut at the half electrode width for better representation.

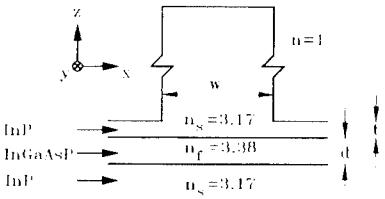


Fig. 4: Integrated optical waveguide on InP according to [15] operating at $\lambda = 1.55\mu$m: $w = 2.4\mu$m, $t = 0\mu$m.

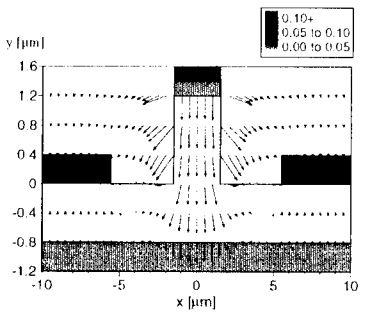


Fig. 5: Microwave electric field distribution in the cross section of an electro-optic modulator on InP at $f = 10$GHz.

5 Summary

An alternative approach for the vectorial analysis of multilayered optical waveguides has been presented. The

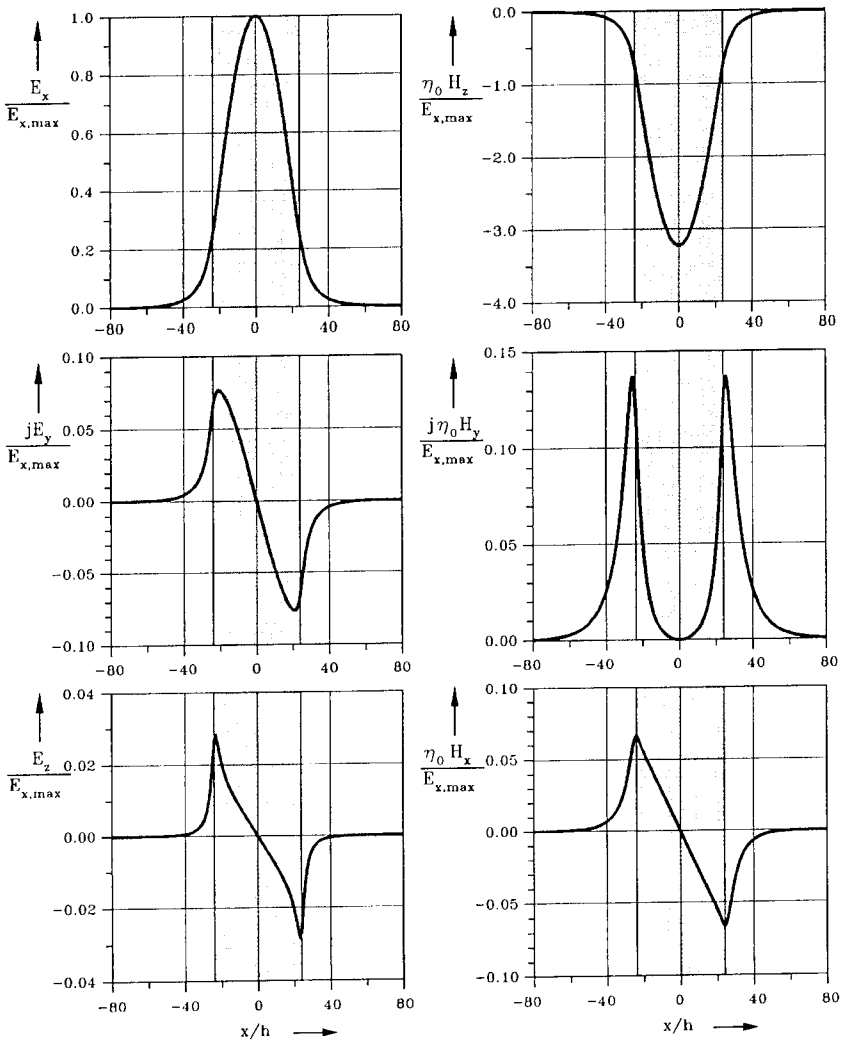


Fig. 6: Field distribution of HE_{00} mode at the half height of the slab layer, normalized on the maximum of E_x. The shaded area corresponds to the strip width w.

formulation uses a different Hertz potential than the conventional approach and is clearer and easier to program. Results for a rib waveguide are in excellent agreement with other vectorial approaches. The microwave field distribution of an electro-optic modulator has been given, too.

References

[1] R. Pregla and W. Pascher, "The Method of Lines", in T. Itoh, (editor), *Numerical Techniques for Microwave and Millimeter Wave Passive Structures*, pp. 381-446, J. Wiley Publ., New York, 1989

[2] U. Schulz, R. Pregla, "A New Technique for the Analysis of the Dispersion Characteristics of Planar Waveguides and its Application to Microstrips with Tuning Septums", *Radio Science*, vol. 16, no. 6, pp. 1173–1178, 1981

[3] H. Diestel, "A Method for Calculating the Guided Modes of Strip-Loaded Optical Waveguides with Arbitrary Index Profile", *IEEE J. Quantum Electron.*, vol. QE–20, no. 11, pp. 1288–1293, 1984

[4] R. Pregla, M. Koch, and W. Pascher, "Analysis of hybrid waveguide structures consisting of microstrips and dielectric waveguides", *Proc. 17th Eur. Microwave Conf.*, 1987, pp. 927-932.

[5] U. Rogge and R. Pregla, "Method of lines for the analysis of strip-loaded optical waveguides", *J. Opt. Soc. Am. B*, Vol. 8, No. 2, February, 1991, pp. 459-463.

[6] U. Rogge and R. Pregla, "Method of lines for the analysis of dielectric waveguides", *J. Lightwave Technol.*, Vol. 11, No. 12, December, 1993, pp. 2015-2020.

[7] R. Pregla, "Method of Lines Based Beam Propagation Method" in *Methods for Modeling and Simulation of Optical Guided-Wave Devices* in the book series *Progress in Electromagnetics Research* (Chief editor: J. A. Kong, Publisher: Elsevier), in print.

[8] Dreher, A., and R. Pregla, "Analysis of Planar Waveguides with the Method of Lines and Absorbing Boundary Conditions," *IEEE Microwave Guided Wave Lett.*, Vol. 1, No. 6, 138-140, 1991.

[9] Pregla, R., and D. Kremer, "Method of Lines with Special Absorbing Boundary Conditions — Analysis of Weakly Guiding Optical Structures," *IEEE Microwave Guided Wave Lett.*, Vol. 2, No. 6, 239-241, 1992.

[10] R. E. Collin, *Field Theory of Guided Waves*, McGraw-Hill, 1960.

[11] R. Pregla, J. Gerdes, E. Ahlers, S. Helfert, "MoL-BPM Algorithms for Waveguide Bends and Vectorial Fields", *Digest Integrated Photonics Research*, April 13-16, 1992, Vol. 10, pp. 32-33, New Orleans, Louisiana

[12] J. Gerdes, S. Helfert and R. Pregla, "Three - Dimensional Vectorial Eigenmode Algorithm for Nonparaxial Propagation in Reflecting Optical Waveguide Structures," *El. Letters*, 1995.

[13] R. Pregla, E. Ahlers, "New vector-BPM in cylindrical coordinates based on the Method of Lines", *Digest Integrated Photonics Research*, Febr. 23-25,1995, Dana Point, California, USA

[14] H. Diestel and S. B. Worm, "Analysis of Hybrid Field Problems by the Method of Lines with Nonequidistant Discretization", *IEEE Trans. Microwave Theory Tech.*, vol. MTT-24, No. 6, June 1984, pp. 633-638.

[15] Working Group I, European Cooperation in the Field of Scientific and Technical Research Project COST-216, "Comparison of different modelling techniques for longitudinal invariant integrated optical waveguides", *IEE Proc. 136J(5)*, 1989, pp. 273-280.

Appendix

The complete system of coupled equations reads as follows

$$\varepsilon_r \frac{\partial}{\partial \overline{x}} \left(\frac{1}{\varepsilon_r} \frac{\partial \Pi_x}{\partial \overline{x}} \right) + \frac{\partial^2 \Pi_x}{\partial \overline{y}^2} + \frac{\partial^2 \Pi_x}{\partial \overline{z}^2} + \varepsilon_r \Pi_x + \varepsilon_r \frac{\partial}{\partial \overline{x}} \left[\frac{1}{\varepsilon_r} \left(\frac{\partial \Pi_z}{\partial \overline{z}} + \frac{\partial \Pi_y}{\partial \overline{y}} \right) \right] - \frac{\partial}{\partial \overline{x}} \left[\frac{\partial \Pi_z}{\partial \overline{z}} + \frac{\partial \Pi_y}{\partial \overline{y}} \right] = 0 \quad \text{(A1)}$$

$$\frac{\partial^2 \Pi_y}{\partial \overline{x}^2} + \varepsilon_r \frac{\partial}{\partial \overline{y}} \left(\frac{1}{\varepsilon_r} \frac{\partial \Pi_y}{\partial \overline{y}} \right) + \frac{\partial^2 \Pi_y}{\partial \overline{z}^2} + \varepsilon_r \Pi_y + \varepsilon_r \frac{\partial}{\partial \overline{y}} \left[\frac{1}{\varepsilon_r} \left(\frac{\partial \Pi_z}{\partial \overline{z}} + \frac{\partial \Pi_x}{\partial \overline{x}} \right) \right] - \frac{\partial}{\partial \overline{y}} \left[\frac{\partial \Pi_z}{\partial \overline{z}} + \frac{\partial \Pi_x}{\partial \overline{x}} \right] = 0 \quad \text{(A2)}$$

$$\frac{\partial^2 \Pi_z}{\partial \overline{x}^2} + \frac{\partial^2 \Pi_z}{\partial \overline{y}^2} + \varepsilon_r \frac{\partial}{\partial \overline{z}} \left(\varepsilon_r^{-1} \frac{\partial \Pi_z}{\partial \overline{z}} \right) + \varepsilon_r \Pi_z + \varepsilon_r \frac{\partial}{\partial \overline{z}} \left[\frac{1}{\varepsilon_r} \left(\frac{\partial \Pi_x}{\partial \overline{x}} + \frac{\partial \Pi_y}{\partial \overline{y}} \right) \right] - \frac{\partial}{\partial \overline{z}} \left[\frac{\partial \Pi_x}{\partial \overline{x}} + \frac{\partial \Pi_y}{\partial \overline{y}} \right] = 0 \quad \text{(A3)}$$

$$\begin{aligned}
\eta_o H_x &= j \left[\frac{\partial \Pi_z}{\partial \overline{y}} - \frac{\partial \Pi_y}{\partial \overline{z}} \right] \qquad \varepsilon_r E_x = \frac{\partial}{\partial \overline{y}} \left[\frac{\partial \Pi_y}{\partial \overline{x}} - \frac{\partial \Pi_x}{\partial \overline{y}} \right] - \frac{\partial}{\partial \overline{z}} \left[\frac{\partial \Pi_x}{\partial \overline{z}} - \frac{\partial \Pi_z}{\partial \overline{x}} \right] \\
\eta_o H_y &= j \left[\frac{\partial \Pi_x}{\partial \overline{z}} - \frac{\partial \Pi_z}{\partial \overline{x}} \right] \qquad \varepsilon_r E_y = \frac{\partial}{\partial \overline{z}} \left[\frac{\partial \Pi_z}{\partial \overline{y}} - \frac{\partial \Pi_y}{\partial \overline{z}} \right] - \frac{\partial}{\partial \overline{x}} \left[\frac{\partial \Pi_y}{\partial \overline{x}} - \frac{\partial \Pi_x}{\partial \overline{y}} \right] \qquad \text{(A4)} \\
\eta_0 H_z &= j \left[\frac{\partial \Pi_y}{\partial \overline{x}} - \frac{\partial \Pi_x}{\partial \overline{y}} \right] \qquad \varepsilon_r E_z = \frac{\partial}{\partial \overline{x}} \left[\frac{\partial \Pi_x}{\partial \overline{z}} - \frac{\partial \Pi_z}{\partial \overline{x}} \right] - \frac{\partial}{\partial \overline{y}} \left[\frac{\partial \Pi_z}{\partial \overline{y}} - \frac{\partial \Pi_y}{\partial \overline{z}} \right]
\end{aligned}$$

Vector Finite Element Analysis of Lossless and Lossy Dielectric Waveguides.

by

P. Cheung and †A. Gopinath.

Dept. of Elec. and Comp. Eng., U. of Minnesota, Duluth, MN 55812, USA.
†Dept. of Elec. Eng., U. of Minnesota, Minneapolis, MN 55455, USA.

Abstract- Recently a transverse magnetic field formulation of the finite element method for solving lightwave propagation in lossless optical waveguides was demonstrated using only two components of the magnetic field. We extend this formulation to include loss in the waveguide, and compare the results from this formulation with those of other formulation for a lossless and a lossy channel waveguide. Our results from this new approach agree well with those from previously published data. The advantage of this new formulation is that it does not require the use of the perturbation technique to solve for the loss in the waveguide, and the eigenvalue matrix formulation directly solves for the complex propagation constant.

I. Introduction

In the finite element method analysis of lossy dielectric, the approach is to use the variational formulation to solve for the lossless propagation modes of the guide [1-4] or the frequency [4] with a perturbation approach involving 2 or all 3 components of the fields for the complex propagation constant. Recently, Abid et al demonstrated a unique approach to solve for the propagation constant of lossless dielectric waveguides using two components (H_x and H_y) of the transverse magnetic field with no spurious modes. In this formulation ε (dielectric constant) is assume to be piecewise constant and the coupling between H_x and H_y components of the field is imposed through the interface continuity of the tangential components E_z and H_z. In this paper we extend this formulation to solve for the complex propagation constant of lossy dielectric waveguides. The advantage of using this method is that it does not require the use of the perturbation method and the eigenvalue matrix formulation directly solves for the complex propagation constant. We compare the results of this approach to published results for a lossless and lossy channel waveguide. The results obtained agree very well with those from other techniques.

This paper is divided into three parts. For the purpose of completeness, the formulation is presented with extension to complex case in the first part. In the second part we discussed the numerical implementation of the formulation using the FEM. In the third section we present results for a lossless and lossy waveguide with comparison to published results.

II. Formulation

We first consider a harmonic wave propagating in the z-direction of the dielectric waveguide, the fields are given by:

$$\mathbf{E}(x,y,z) = \mathbf{E}(x,y)\exp(-\gamma z) \tag{1}$$

$$\mathbf{H}(x,y,z) = \mathbf{H}(x,y)\exp(-\gamma z) \tag{2}$$

III. Numerical Implemenation

To implement the finite element solution of the above formulation, the dielectric waveguide is discretized into 2*N*M right angle first order triangle elements. The functional of equations (7a and 7b) is:

$$F(H_i) = \int\left\{\sum\left[-\nabla H_i \bullet \nabla H_i + k^2 \varepsilon H_i H_i + \gamma^2 H_i H_i\right]\right\} dxdy \qquad (10)$$

where i = x, y. By minimizing the functional $F(H_{x,y})$ with respect to the nodal values of H_x and the H_y, a set of linear equations is obtained, the problem is reduced to an eigevalue matrix equation of the form:

$$[S][H] = -\gamma^2[T][H] \qquad (11)$$

The dimension of the square matrices [S] and [T] are 2[(N+1)(M+1)-(N+M+2)]. This is because H_x and H_y are set to zero at the 2(N+M) external boundary nodes. The coefficients of the [S] matrix are complex and each column of [H] is the eigenvector representing the values of H_x and H_y at the nodes.

The matrix equation (11) is to be solved in a subspace of vectors which satisfy the inner interface boundary conditions, namely the condition of E_z and H_z across the common side of any two adjacent triangles having two different dielectrics. The continuity of E_z and H_z is first transformed into another set of equations, each is associated with one side of a triangle along the interface:

$$\left[\frac{1}{\varepsilon_a}\left(\frac{\partial H_{ya}}{\partial x} - \frac{\partial H_{xa}}{\partial y}\right)\right] = \left[\frac{1}{\varepsilon_b}\left(\frac{\partial H_{yb}}{\partial x} - \frac{\partial H_{xb}}{\partial y}\right)\right] \qquad (12a)$$

$$\left(\frac{\partial H_{ya}}{\partial x} - \frac{\partial H_{xa}}{\partial y}\right) = \left(\frac{\partial H_{yb}}{\partial x} - \frac{\partial H_{xb}}{\partial y}\right) \qquad (12b)$$

Both equations are normalized by a multiplication factor equal to the length of the common interface side. The subscripts"a" and "b" represent the adjacent triangles with different dielectric constants, and this results in a total of "r" equations of type (12). This set can be written in matrix form:

$$[R][H] = \lambda\,[I][H] \qquad (13)$$

where [I] is an identity matrix. The eigenvectors of (13) associated with the zero eigenvalues are the set of vectors that defines the subspace, in which (10) is to be solved. The matrices [R] and [H] have the same dimensions as [S]. The matrix [R] is singular since it has only "r" non-zero rquations, and we solve (13) by Singular Value Decomposition. The solutions sought are for λ=0, and its associated eigenvectors constitute the null space of this equation. An alternative approach is to use Gaussian elimination to obtain the null set of eigenvectors. The dimension of the null space is (n-r), and the vectors of the new basis are in a rectangular matrix [Z], of the dimension n X (n-

r). Since the solutions are now sought in the null space of (13) , the new vectors [C] are related to the old vectors [H] by:

$$[H]=[Z][C] \tag{14}$$

Substituting (14) into (11), then multiplying both sides by $[Z^t]$ results in:

$$[S^n][C[= -\gamma^2 [T^n][C] \tag{15}$$

where:

$$[S^n] = [Z^t][S][Z] \tag{16}$$

and

$$[T^n] = [Z^t][T][Z] \tag{17}$$

Equation (15) is solved for γ and [C], then [C] is mapped to the original space through the relations in (14).

VI. Results

We apply the above method to find the propagation modes of a lossy channel waveguide. Fig. 1 shows the dimension of the a channel waveguide used for the simulation, the gain curve for the TE(1,1) mode of the guide is given in Fig. 2. The results are compared to those from reference [1] and shows good agreement over the range of the dimensions of the guide simulated. In our simulation, the gain region is 0.2 μm thick with a width of 1.0 μm. This region has a refractive index of $n_1 = 3.5 + j0.001$. These dimensions corresponds to the case of d = 5w in reference [1, 4]. The cladding layers has a refractive index of $n_2 = 3.2 - j0.001$" and is 2.0μm thick and 5μm wide. An overview of the magnitude of the magnetic field distribution overlaid with the contour plot is given in Fig. 3 for the case of $k_o d = 3$. The contours are set at levels of 0.0 to 1.0 with intervals of 0.1. The contour plots shows that the mode is well confined within the gain region of the guide and a stable solution for the natural mode of the guide is obtained using the present approach.

V. Conclusion

We have extended the new transverse H-field FEM formulation to obtain the complex propagation constant of a lossy dielectric waveguides to include loss or gain with no spurious modes. The results shows good agreement with published data for a lossy channel waveguide.

Acknowledgments:
This work was supported in part by the U. of Minnesota, Minneapolis and Duluth campus, and the U. of Minnesota Supercomputer Institute.

References:
[1] K. Hayata, K. Miura, M. Koshiba,"Finite Element Formulation for Lossy Waveguides", IEEE Trans. Microwave Theory Tech., Vol. 36, No. 2, pp. 268-76, Feb. 1988.

Since the solutions are now sought in the null space of (13) , the new vectors [C] are related to the old vectors [H] by:

$$[H]=[Z][C] \tag{14}$$

Substituting (14) into (11), then multiplying both sides by $[Z^t]$ results in:

$$[S^n][C] = -\gamma^2 [T^n][C] \tag{15}$$

where:

$$[S^n] = [Z^t][S][Z] \tag{16}$$

and

$$[T^n] = [Z^t][T][Z] \tag{17}$$

Equation (15) is solved for γ and [C], then [C] is mapped to the original space through the relations in (14).

VI. Results

We apply the above method to find the propagation modes of a lossy channel waveguide. Fig. 1 shows the dimension of the a channel waveguide used for the simulation, the gain curve for the TE(1,1) mode of the guide is given in Fig. 2. The results are compared to those from reference [1] and shows good agreement over the range of the dimensions of the guide simulated. In our simulation, the gain region is 0.2 μm thick with a width of 1.0 μm. This region has a refractive index of $n_1 = 3.5 + j0.001$. These dimensions corresponds to the case of d = 5w in reference [1, 4]. The cladding layers has a refractive index of $n_2 = 3.2 - j0.001$" and is 2.0μm thick and 5μm wide. An overview of the magnitude of the magnetic field distribution overlaid with the contour plot is given in Fig. 3 for the case of $k_0 d = 3$. The contours are set at levels of 0.0 to 1.0 with intervals of 0.1. The contour plots shows that the mode is well confined within the gain region of the guide and a stable solution for the natural mode of the guide is obtained using the present approach.

V. Conclusion

We have extended the new transverse H-field FEM formulation to obtain the complex propagation constant of a lossy dielectric waveguides to include loss or gain with no spurious modes. The results shows good agreement with published data for a lossy channel waveguide.

Acknowledgments:
This work was supported in part by the U. of Minnesota, Minneapolis and Duluth campus, and the U. of Minnesota Supercomputer Institute.

References:
[1] K. Hayata, K. Miura, M. Koshiba,"Finite Element Formulation for Lossy Waveguides", IEEE Trans. Microwave Theory Tech., Vol. 36, No. 2, pp. 268-76, Feb. 1988.

[2] Jia-Fa Lee, Din-Kow Sun, and Z. J. Cendes, "Full-Wave Analysis of Dielectric Waveguides Using Tangential Vector Finite Elements", IEEE Trans. Microwave Theory Tech., Vol. 39, No. 8, pp. 1262-71, Aug. 1991.
[3] B. M. Dillion, and J. P. Webb, "A Comparision of Formulations for the Vector Finite Element Analysis of Waveguides", IEEE Trans. Microwave Theory Tech., Vol. 42, pp. 308-316, 1994.
[4] C. Themistos, B. M. A. Rahman, and K. T. V. Grattan, "Finite Element Analysis for Lossy Optical Waveguides by using Perturbation Techniques", IEEE Photonics Technology Letters, Vol. 6, No. 4, pp. 537-539, 1994.
[5] Zine-Eddine Abid, K. L. Johnson, and A. Gopinath, "Analysis Dielectric Guides by Vector Transverse Magnetics Fields Finite Elements", Journal of Lightwave Technology, Vol. 11, No. 10, pp. 1545-1549, Oct. 1993.

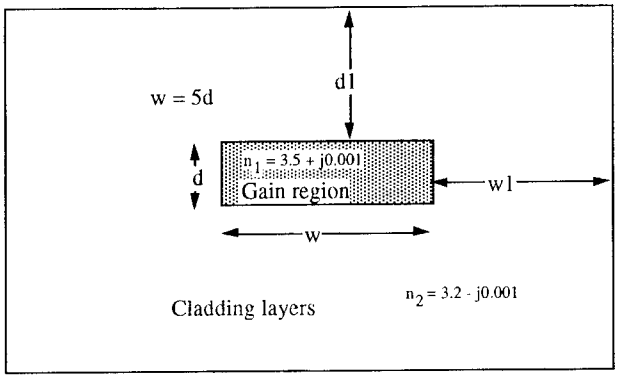


Fig. 1: Channel waveguide with dimensions w = 1.0 μm, d = 2.0 μm for the gain region and w1 = 5.0 μm and d1 = 1.0 μm for the cladding.

Fig. 2: Gain curve of the TE(1,1) mode of the channel waveguide.

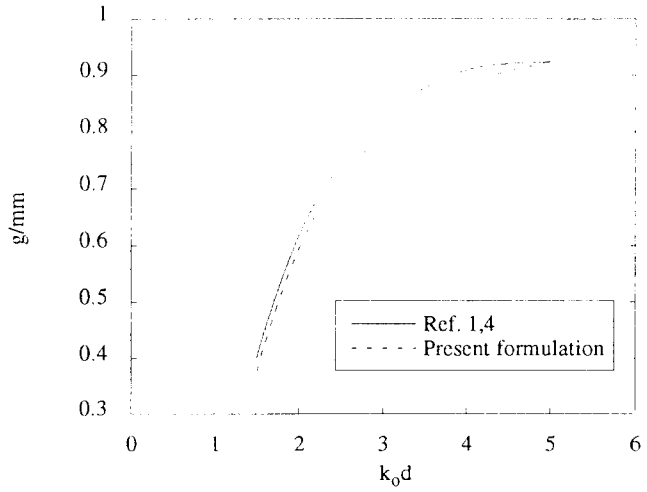
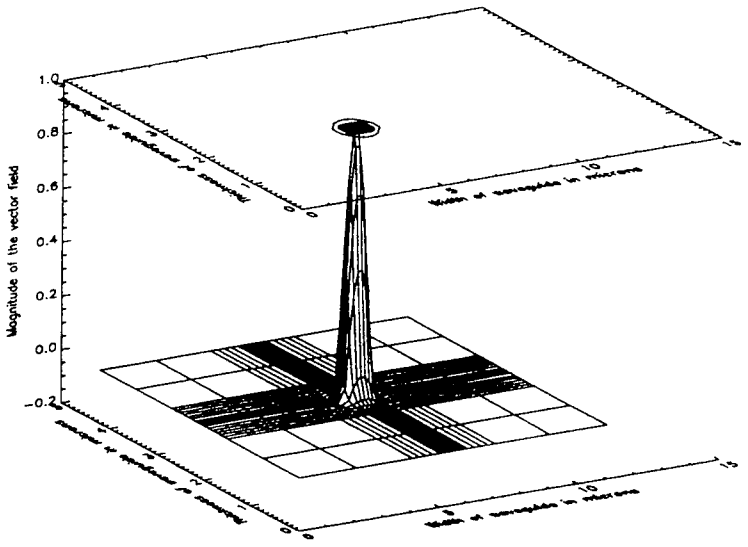


Fig. 3: Magnetic field distribution of the TE(1,1) mode of the channel waveguide.



NL-FDTD MODELING OF LINEAR AND NONLINEAR CORRUGATED WAVEGUIDING SYSTEMS FOR INTEGRATED OPTICS APPLICATIONS

Richard W. Ziolkowski and Justin B. Judkins*
Electromagnetics Laboratory
Department of Electrical and Computer Engineering
The University of Arizona, Tucson, AZ 85721 USA
(602) 621-6173 (office); (602) 621-8076 (fax)
ziolkowski@ece.arizona.edu

With the continuing and heightened interest in linear and nonlinear optically integrated devices, more accurate and realistic numerical simulations of these devices and systems are in demand. Such calculations provide an integrated optics/photonics testbed in which one can investigate new basic and engineering concepts, materials, and device configurations before they are fabricated. The time from device conceptualization to fabrication and testing should therefore be enormously improved with numerical simulations that incorporate more realistic models of the linear and nonlinear material responses and the actual device geometries. It is felt that vector and higher dimensional properties of Maxwell's equations that are not currently included in existing scalar models, in addition to more detailed materials models, may significantly impact the scientific and engineering results.

We have been simulating a variety of linear and nonlinear corrugated waveguiding systems for their applications to integrated optics systems. Corrugated waveguide structures have many potential uses as beam steerers and grating assisted couplers. We are developing a simulation toolbox that eventually will be used to design these and many other integrated optical devices. To meet self-imposed design goals that specify integrated optical devices that are only a few wavelengths or pulse lengths in size, we require a thorough understanding of the basic physics that we are modeling without the typical approximations generally used for this class of problems. This in turn has required our simulations to be based upon numerically solving the full-wave, vector Maxwell's equations. We have shown that this approach leads to a superior understanding of the underlying physics and to improved engineering designs[1-4]. These numerical solutions have been obtained in two space dimensions and time with a nonlinear finite difference time domain (NL-FDTD) method which combines a generalization of a standard, FDTD, full-wave, vector, linear Maxwell's equations solver with a Lorentz linear dispersion model, a nonlinear Raman model, and an instantaneous Kerr nonlinear model. In particular, we are solving in a self-consistent manner the system of equations:

$$\frac{\partial}{\partial t}\left[\mu_0 \vec{H}\right] = -\nabla \times \vec{E} \tag{1}$$

$$\frac{\partial}{\partial t}\left[\epsilon_L \vec{E}\right] = \nabla \times \vec{H} - \frac{\partial}{\partial t}\vec{P} \tag{2}$$

$$\frac{\partial^2}{\partial t^2}\vec{P}^L + \Gamma_L \frac{\partial}{\partial t}\vec{P}^L + \omega_L^2 \vec{P}^L = \epsilon_0 \chi_0 \omega_L^2 \vec{E} \qquad \text{Lorentz Model} \tag{3}$$

$$\frac{\partial^2}{\partial t^2}\chi^{NL} + \Gamma_R \frac{\partial}{\partial t}\chi^{NL} + \omega_R^2 \chi^{NL} = \epsilon_R \omega_R^2 |\vec{E}|^2 \qquad \text{Raman Model}\,, \tag{4}$$

where $\vec{P} = \vec{P}^L + \vec{P}^{NL}$ and

$$\vec{P}^{NL} = \epsilon_0 \chi^{NL} \vec{E} + \epsilon_0 \chi^{Kerr} |\vec{E}|^2 \vec{E}\,, \tag{5}$$

the last term representing the instantaneous Kerr nonlinearity, χ^{Kerr} being the instantaneous Kerr susceptibility. The resulting NL-FDTD simulator can model pulse propagation in complex environments under the influence of linear and nonlinear dispersive, linear and nonlinear diffractive, and time retardation effects of the materials in and surrounding the electromagnetic structures. By coupling the linear and nonlinear dispersion models together simultaneously with the natural boundary conditions arising from dielectric and metallic discontinuities, we are able to handle the gratings and corrugated interfaces readily. Moreover, both the TE and TM polarization cases can be simulated. Consequently, more complex, realistic integrated optical structures are straightforwardly modeled with the NL-FDTD approach.

The NL-FDTD approach can handle ultrafast single-cycle cases as readily as multiple-cycle cases having an intrinsic carrier wave. Since most current optical systems deal directly with a carrier-wave type signal, the NL-FDTD approach can simulate the propagation and scattering effects associated with those narrow bandwidth systems. However, it can also simulate the behaviors of the interactions of ultrafast pulses. Ultrafast pulses are single-cycle or multiple-cycle envelopes containing fewer than 15 cycles. Sources in the laboratory have produced pulses compressed to as fast as 4 fs and the optics community is already investigating the *attosecond* regime. By using these ultrafast sources we illustrate two advantages of the time domain approach: (1) the ability to carry phase information over a wide spectrum, and (2) the ability to model transient effects which occur either quickly or slowly relative to the time scale of the pulse. The evolution of the pulse in the medium can be dependent on both the material's resonances in the presence of the beam as well as the initial shape of the exciting pulse. Switching or steering of this type of pulsed beam requires one to make advantage of interference effects and the material's transient response.

The complex waveguiding structures under consideration are filled with either linear or nonlinear dispersive materials that have finite response times. The corrugations themselves can be modeled as dielectric teeth (an extension of the dielectric waveguide) or metallic teeth (deposited into or on top of the dielectric waveguide). A corrugated waveguide with these dielectric or metallic teeth can be viewed as a leaky-wave antenna. The corrugation section is a slow-wave structure whose impedance properties determine the properties of its radiated fields. The field radiated by an infinite linear or nonlinear corrugated structure can be modeled with a Floquet mode representation. The resulting fields have to satisfy a phase matching or Bragg condition resulting from the electromagnetic boundary conditions. Physically this means that because of the regular placement of the teeth in the corrugation section, the individual scattered fields will interfer constructively only along certain perferred directions and the "leaked" energy will appear in the form of pulsed beams that radiate at angles specified by the Bragg condition both into the air and into the substrate regions.

In particular, let θ_t be the angle that the radiated beam subtends with respect to the normal of the waveguide, n_0 be the index of refraction above the corrugations, and $n_G = n_B + n_2\, I$ be the index of refraction in the waveguide, which includes the effective waveguide index n_B (which varies slightly from the TE and TM cases to achieve the desired TE_0 and TM_0 initial spatial amplitude distributions) and the intensity induced index change $n_2\, I$. This Bragg condition then takes the form

$$\frac{\omega}{c}\, n_0\, sin\theta_t = \frac{\omega}{c}\, n_B + m\, \frac{2\,\pi}{\Lambda} \qquad \text{where} \quad m = 0, \pm 1, \pm 2, ...$$

or

$$\theta_t = \sin^{-1}\left[\, \frac{n_B}{n_0} + \frac{n_2}{n_0}\, I + m\, \frac{\lambda}{n_0\, \Lambda}\, \right] \qquad \text{where} \quad m = 0, \pm 1, \pm 2, ... \qquad (6)$$

This immediately translates into a practical device: the output-beam from the corrugation section can be steered away from the normal by the strength of the intensity of the input waveguide pulsed-beam, the size of the unit cell or the strength of the nonlinearity.

A special case of this relationship suggests a useful output coupler design. If we specify that the corrugation spacing be $\Lambda = \lambda / n_B$, then the first-order ($m = -1$) output-beam from the corrugation section of the waveguide has the transmission angle:

$$\theta_t = \sin^{-1}\left(\, \frac{n_2}{n_0}\, I\, \right) \approx \frac{n_2}{n_0}\, I\,. \qquad (7)$$

Thus, the output-beam from the corrugation section can be steered away from the normal simply by adjusting the strength of the intensity of the input waveguide pulsed-beam or the nonlinear index. Our simulations have confirmed this effect.

The multi-dimensional NL-FDTD model has been applied to the modeling of the extraction of energy from a variety of linear and nonlinear waveguiding structures using corrugated waveguide sections. Expected conversion efficiencies from the guided mode energy to the radiated field energy have been observed in the linear case. The nonlinear waveguiding structures are presenting interesting challenges in their analysis and interpretation. A variety of TE and TM cases with metallic corrugations will be presented to illustrate the desired linear and nonlinear output coupler and beam steering effects. Typical simulation geometries are shown in the figures below. Since the electric field behavior near the edges of these metallic corrugations is significantly different between the two polarizations, the resulting radiated field structures reflect this difference. Output beam characteristics depending on the medium response time, the polarization, and the material parameters, have been studied and will be reported. Near field simulations obtained with the NL-FDTD approach are translated into far field information with near-to-far-field transforms tailored to the Fresnel and Fraunhofer regimes. Particular emphasis will be given to ultrafast pulses whose time-record length is approximately the same size as the corrugation region. It is found that even pulses that are short in comparison with the corrugation region can be effectively used to beam steer and couple energy through a grating-assisted coupler from one corrugated waveguide to another.

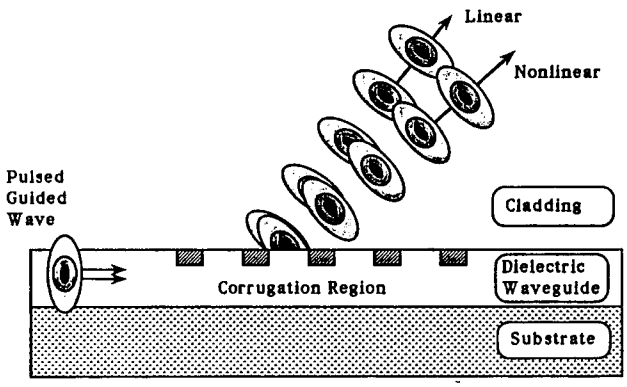
REFERENCES

1. Ziolkowski, R. W., and J. B. Judkins, "Full-wave vector Maxwell equation modeling of the self-focusing of ultrashort optical pulses in a nonlinear Kerr medium exhibiting a finite response time", *J. Opt. Soc. Am. B*, vol. 10(2), 186-198, 1993.

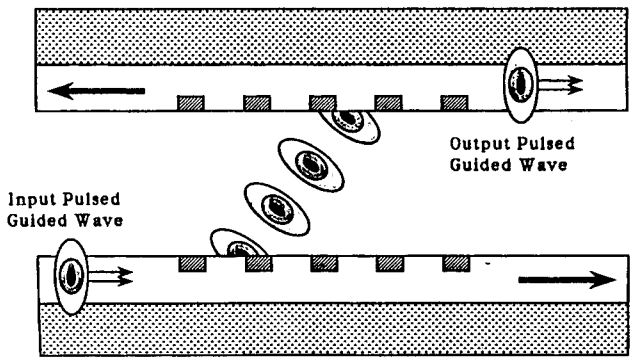
2. Ziolkowski, R. W., and J. B. Judkins, "Applications of Discrete Methods to Pulse Propagation in Nonlinear Media: Self-Focusing and Linear-Nonlinear Interfaces", invited paper, Special issue of Radio Science for the 1992 URSI EM Theory Symposium, Radio Sci., vol. 28(5), 901-911, 1993.

3. R. W. Ziolkowski and J. B. Judkins, "NL-FDTD Modeling of Linear and Nonlinear Corrugated Waveguides", J. Opt. Soc. Am. B, vol. 11(9), 1565-1575, 1994.

4. J. B. Judkins and R. W. Ziolkowski, "FDTD Modeling of nonperfect metallic thin film gratings", submitted to J. Opt. Soc. Am. A, 1994.



1. The output direction of nonlinear grating-assisted beam steering, integrated optics devices can be controlled by the intensity of the incident pulse.



2. The S-parameters of nonlinear grating-assisted, waveguide output couplers can be controlled by the intensity of the incident pulse.

Analysis of Coupled Nonlinear Optical Waveguides by Matrix Method

Vijai Tripathi and Andreas Weisshaar
Department of Electrical and Computer Engineering
Oregon State University
Corvallis, Oregon 97331

H.S. Chang
Hanyang University
Seoul, Korea

An improved matrix method for the analysis and design of nonlinear directional couplers (NLDC) with saturable coupling media is presented. The method represents an extension of the original matrix method which has been used to study linear waveguides with homogeneous or inhomogeneous refractive index profiles and three-layer nonlinear waveguides with Kerr-like or non-Kerr-like medium. The original matrix approach becomes inaccurate for a structure where a nonlinear medium is bounded by two linear films of finite thickness. The extended method is based on an iterative averaging algorithm which calculates the average values of the dielectric constant and the field amplitude in each stratified nonlinear layer. The values obtained in the averaging process converge very fast and the method requires only two or three iterations for each layer. This numerical method is applied to compute the optical intensity dependent output power distributions of symmetric and asymmetric multiple quantum well (MQW) nonlinear directional couplers. A two-level saturation model is incorporated with the matrix method to consider saturation of the refractive index in the MQW coupling medium. The optical intensity dependent dispersion characteristics for individual guided modes of a symmetric structure are compared with the exact solutions expressed in terms of Jacobian elliptic functions. To analyze output power distributions of the couplers, the matrix method utilizes the mode combination method which expresses the total field as a combination of symmetric and antisymmetric modes that are perturbed by the change of the refractive index profile due to the presence of the other mode. For a symmetrical structure, the numerical results are shown to be in agreement with published experimental data. Typical simulation results and applications of coupled structures are presented.

SESSION 18:

TOPICS IN FRACTAL AND WAVELET ELECTRODYNAMICS

Chairs: D.H. Werner, P.L. Werner

AN OVERVIEW OF FRACTAL ELECTRODYNAMICS RESEARCH

D. H. Werner
The Applied Research Laboratory
The Pennsylvania State University
P.O. Box 30
State College, PA 16804

Abstract

Mandelbrot [1] observed that many natural objects possess an inherent self-similarity in their geometrical structure. In order to quantify this behavior, Mandelbrot coined the term fractal and introduced the concept of fractal geometry. Since the pioneering work of Mandelbrot and others, fractals have been finding increasing applications in the fields of engineering and science. Of particular interest in this paper is the research area known as fractal electrodynamics. The term fractal electrodynamics was first suggested by Jaggard in 1990 to identify the newly emerging branch of research which combines fractal geometry with Maxwell's theory of electromagnetism [2]. This paper is intended to present a brief introduction to the subject of fractal electrodynamics followed by an overview of significant research in the field.

1. Introduction

Modeling of man-made objects has benefitted from the simplicity of the objects and a reliance upon classical Euclidean geometry and the well developed mathematics of polynomials. Modeling of natural or complex objects have proved to be much more difficult. The traditional approach to modeling natural structures has been to approximate them with a collection of elementary Euclidean objects such as circles, squares, triangles, cubes, spheres, disks, cylinders, cones and ellipsoids. However, naturally occurring objects typically possess structure of several scale lengths which is very difficult to accurately describe in terms of Euclidean geometric approximations. Fractal geometry is an extension or generalization of classical Euclidean geometry, and it is well suited for use in constructing precise models of physical structures. Among the items which have been successfully modeled using fractals are profiles of forest tops (vegetation canopies), trees, leaves, ferns, edges of clouds, snowflakes, coastline and sea-floor topography.

One of the important attributes of many fractals is that they possess a self-similar structure on all scales [1]. This designation means that any small portion of a fractal under high magnification looks like some larger portion under low magnification. In other words, these fractals have the property that they are scale invariant. For any fractal resulting from a physical system, scale invariance exists only over a finite range of scales. Under these conditions, the fractal behavior is bounded from both above and below. Physical fractals which have characteristic inner and outer scale lengths are known as bandlimited fractals [2]. The occurrence of bandlimitation can be attributed to the fact that natural

fractals are often the result of regular but nonperiodic forces which give rise to complex structures through repetitive actions.

Fractals can be quantified and compared by using certain numbers which are associated with their behavior. These numbers are commonly called fractal dimensions. Fractal dimensions provide a measure of the degree to which a fractal fills the metric space it is contained in. There are several definitions of fractal dimension in use. The two most frequently used are the Hausdorff-Besicovitch and the box-counting fractal dimensions [3,4]. However, the box-counting definition is usually used for the computational or experimental determination of fractal dimensions of physical sets.

The connection between the box-counting fractal dimension and our intuitive concept of dimension can be established by considering the following example [2,5]. Let F be the one-dimensional line segment of length L. This line segment can be divided into N_ε identical smaller segments of length ε which are self-similar to L with a scale factor of L/N_ε. Hence, the number of segments of length ε that are contained in the line segment of length L is

$$N_\varepsilon(L^1) = \left(\frac{L}{\varepsilon}\right)^1 \tag{1}$$

The line segment of length ε can be considered as a one-dimensional yardstick for measuring the line segment of length L. Similarly, let F be the two-dimensional area $A=L^2$. This area can be divided into N_ε identical to smaller areas of length ε on a side which are self-similar to A with a scale-factor of $L/(N_\varepsilon)^{1/2}$. The number of squares of area ε^2 that are contained in the square of area L^2 is

$$N_\varepsilon(L^2) = \left(\frac{L}{\varepsilon}\right)^2 \tag{2}$$

The yardstick in this instance is the square with sides of length ε. Next, suppose that F is the three-dimensional volume $V=L^3$. This volume can be divided into N_ε identical smaller volumes of length ε on a side which are self-similar to V with a scale factor of $L/(N_\varepsilon)^{1/3}$. The number of cubes of volume ε^3 that will fit inside the cube of volume L^3 is

$$N_\varepsilon(L^3) = \left(\frac{L}{\varepsilon}\right)^3 \tag{3}$$

The cube with sides of length ε represents the yardstick. Finally, it is recognized that the above three results represent special cases of the measurement of an n-dimensional cube with volume L^n using an n-dimensional cube with sides of length ε as the yardstick. The number of cubes of volume ε^n required to fill a cube of volume L^n is then

$$N_\varepsilon(L^n) = \left(\frac{L}{\varepsilon}\right)^n \tag{4}$$

The above treatment of self-similar objects which have Euclidean or integer dimension n can be generalized to include self-similar objects which have fractional dimension D. The relationship between yardstick size ε and number of yardsticks N_ε for a D-dimensional self-similar object is assumed to be

$$N_\varepsilon(F) = C\left(\frac{1}{\varepsilon}\right)^D \tag{5}$$

for some positive constant C. Taking the natural logarithm of both sides and solving for D results in

$$D = \frac{\ell n\, N_\varepsilon(F) - \ell n\, C}{\ell n\,(1/\varepsilon)} \tag{6}$$

The box-counting fractal dimension of F is defined as the value of D to which the right hand side of (6) converges when ε tends to zero. Hence

$$\dim_B(F) = \lim_{\varepsilon \to 0} \frac{\ell n\, N_\varepsilon(F)}{\ell n\,(1/\varepsilon)} \tag{7}$$

where use has been made of the fact that

$$\lim_{\varepsilon \to 0} \frac{\ell n\, C}{\ell n\,(1/\varepsilon)} = 0 \tag{8}$$

A brief introduction to the underlying geometric properties of fractals has been presented in this section. For the interested reader, a more in-depth treatment of the subject may be found in the excellent review by Jaggard [2]. The following section contains a summary of significant research in the relatively new field of fractal electrodynamics.

2. Literature Review

The intent of this section is to present a brief summary of research, complete with references, in the discipline of fractal electrodynamics. Every effort has been made to provide a review which is comprehensive in scope as well as up to data. The information contained in this section may be used to provide a starting point for the serious researcher or as background material for the reader with merely a casual interest in the subject.

A special section devoted to fractals in electrical engineering was featured in a recent issue of the *Proceedings of the IEEE* [6]. The first paper in this special section makes use of the multiple scale nature of wavelets to represent the 1/f family of self-similar fractal signals. This paper provides an illustration of the connection that exists between wavelets and fractals. Another paper in this special section discusses how fractional derivative operators in electromagnetic theory and superconductivity may be linked to fractals. This theory is applied to several fractal electrodynamics problems including electrochemical, dielectric and magnetic relaxations. Other papers in this special section of interest include the use of "Fractal Brownian Motion Models for Synthetic Aperture Radar Imagery Scene Segmentation" and "Ultrasonic Characterization of Fractal Media."

The scattering of electromagnetic waves from corrugated random surfaces with fractal slopes was considered by Jakeman [7,8]. A generalized Rayleigh solution [9] as well as a Kirchhoff solution [10] have been obtained for scattering from fractally rough surfaces. The AC response of fractally rough interfaces has been investigated by Liu and Kaplan [11]. Also, the important question of whether there is a radar clutter attractor has been addressed by Leung and Haykin [12]. Other areas of research include the study of diffraction by bandlimited fractal screens [13,14], optical beam propagation in a bandlimited fractal medium [15], wave transmission through a one-dimensional Cantor-like fractal medium [16], reflection from fractal multilayer media [17,18], scattering from bandlimited fractal fibers [19], and fractal models of atmospheric refractivity fluctuation [20].

In addition to the fractal electrodynamics research noted above, there has also been some work done in the area of fractal antennas, arrays and apertures. The application of fractals to the discipline of antenna array theory was first reported by Kim and Jaggard [21]. They made use of the underlying order in fractal geometry to develop a procedure for the design of low sidelobe random arrays. This procedure combines the virtues of periodic subarray generators with those of random array initiators to form a quasi-random linear array composed of self-similar subarrays. Allain and Cloitre [22] discuss properties associated with the spatial spectrum of a general family of self-similar deterministic arrays which are constructed recursively by a certain inflation method. The problems of diffraction by fractally serrated apertures and triadic Cantor targets have also been investigated [23,24]. The radiation of electromagnetic waves by fractal structures, known as fractal radiators, is explored in [25]. In particular, the theory of frequency independent antennas is considered from the fractal geometric point of view. Several examples of self-similar antennas are presented including logarithmic spirals, conical logarithmic spirals, and log-periodics. The properties of fractal arrays are also briefly discussed. The fundamental relationship between self-similar fractal arrays and their ability to generate radiation patterns which possess fractal features is examined in [26]. The theoretical foundation and design procedures are developed in this paper for using fractal arrays to synthesize fractal radiation patterns having certain desired characteristics (see second paper of this section). Finally, a fractal approach to lightning radiation on a tortuous channel is studied in [27]. This paper demonstrates that the lightning return stroke radiation is fractal and has the same fractal dimension as the channel path.

A review of fractal electrodynamics research conducted by researchers at Xidian University, Xian, Shaanxi, China, was included in the *Proceedings of the 1993 International Symposium on Radio Propagation (ISRP '93)* [28]. Among the topics addressed are wave propagation and scattering in fractal media, electromagnetic scattering from a one-dimensional fractal surface, multiple backscattering

of millimeter waves from a random fractal atmosphere, and the electromagnetic scattering from a fractal multilayered cylinder at normal incidence.

REFERENCES

[1] B. B. Mandelbrot, *The Fractal Geometry of Nature*, W. H. Freeman, New York, 1983.

[2] D. L. Jaggard, "On fractal electrodynamics," in *Recent Advances in Electromagnetic Theory*, H. N. Kritikos and D. L. Jaggard, eds., pp. 183-224, Springer-Verlag, New York, 1990.

[3] M. F. Barnsley, *Fractals Everywhere*, Academic Press, New York, 1988.

[4] K. Falconer, *Fractal Geometry*, Wiley, New York, 1988.

[5] R. F. Voss, "Fractals in nature: from characterization to simulation," in *The Science of Fractal Images*, H. Peitgen and D. Saupe, eds., Springer-Verlag, New York, 1988.

[6] D. L. Jaggard, Guest Editor, "Special Section on Fractals in Electrical Engineering," *Proceedings of the IEEE*, vol. 81, No. 10, p. 1423, Oct. 1993.

[7] E. Jakeman, "Scattering by a corrugated random surface with fractal slope," *J. Phys. A.*, vol. 15, pp. L55-L59, 1982.

[8] E. Jakeman, "Fresnel scattering by a corrugated random surface with fractal slope," *J. Opt. Soc. Amer.*, vol. 72, pp. 1034-1041, 1982.

[9] D. L. Jaggard and X. Sun, "Rough surface scattering: A generalized Rayleigh solution," *J. Appl. Phys.*, vol. 68, pp. 5456-5462, Dec. 1990.

[10] D. L. Jaggard and X. Sun, "Scattering from fractally corrugated surfaces," *J. Opt. Soc. Am. A.*, vol. 7, No. 6, pp. 1131-1139, June 1990.

[11] S. H. Liu and T. Kaplan, "Theory of AC response of rough interfaces," in *Fractals in Physics*, L. Pietronero and E. Tosatti, eds., North-Holland, New York, pp. 383-389, 1988.

[12] H. Leung and S. Haykin, "Is there a radar clutter attractor?" *Appl. Phys. Lett.*, vol. 56, No. 6, pp. 593-595, Feb. 1990.

[13] D. L. Jaggard and Y. Kim, "Diffraction by bandlimited fractal screens," *J. Opt. Soc. Amer.*, vol. A4, pp. 1055-1062, 1987.

[14] A. Lakhtakia, N. S. Holter, V. K. Varadan and V. V. Varadan, "Self-similarity in diffraction by a self-similar fractal screen," *IEEE Trans. Antennas Propagat.*, vol. AP-35, No. 2, pp. 236-239, Feb. 1987.

[15] Y. Kim and D. L. Jaggard, "Optical beam propagation in a bandlimited fractal medium," *J. Opt. Soc. Amer.*, vol. A5, pp. 1419-1426, 1988.

[16] V. V. Konotop, O. I. Yordanov and I. V. Yurkevich, "Wave transmission through a one-dimensional Cantor-like fractal medium," *Europhys. Lett.*, vol. 12, pp. 481-485, 1990.

[17] D. L. Jaggard and X. Sun, "Reflection from fractal multilayers," *Opt. Lett.*, vol. 15, pp. 1428-1430, 1990.

[18] X. Sun and D. L. Jaggard, "Wave interactions with generalized Cantor bar fractal multi-layers," *J. Appl. Phys.*, vol. 70, pp. 2500-2507, Sept. 1991.

[19] D. L. Jaggard and X. Sun, "Scattering from bandlimited fractal fibers," *IEEE Trans. Antennas Propagat.*, vol. 37, No. 12, pp. 1591-1597, Dec. 1989.

[20] Y. Kim and D. L. Jaggard, "Band-limited fractal model of atmospheric refractivity fluctuation," *J. Opt. Soc. Am. A*, vol. 5, No. 4, pp. 475-480, April 1988.

[21] Y. Kim and D. L. Jaggard, "The fractal random array," *Proc. IEEE*, vol. 74, No. 9, pp. 1278-1280, 1986.

[22] C. Allain and M. Cloitre, "Spatial spectrum of a general family of self-similar arrays," *Phys. Rev. A*, vol. 36, pp. 5751-5757, Dec. 1987.

[23] Y. Kim, H. Grebel and D. L. Jaggard, "Diffraction by fractally serrated apertures," *J. Opt. Soc. Amer.*, vol. A8, pp. 20-26, 1991.

[24] D. L. Jaggard and T. Spielman, "Triadic Cantor target diffraction," *Microwave Opt. Technol. Lett.*, vol. 5, pp. 460-466, Aug. 1992.

[25] D. H. Werner, "Fractal radiators," Proceedings of the IEEE Dual-Use Technologies & Applications Conference, SUNY Institute of Technology at Utica/Rome, New York, 23-26 May 1994, vol. I, pp. 478-482.

[26] D. H. Werner and P. L. Werner, "On the synthesis of fractal radiation patterns," Accepted for publication in *Radio Science*, Jan.-Feb. 1995.

[27] G. Vecchi, D. Lebate and F. Canavero, "Fractal approach to lightning radiation on a tortuous channel," *Radio Science*, vol. 29, No.4, July-Aug. 1994, pp. 691-704.

[28] Proceedings of the 1993 International Symposium on Radio Propagation (ISRP '93), Beijing, China, 18-21 August 1993, pp. 559-1401.

FRACTAL ARRAYS AND FRACTAL RADIATION PATTERNS

P. L. Werner
College of Engineering
The Pennsylvania State University
DuBois, PA 15801

D. H. Werner
Applied Research Laboratory
The Pennsylvania State University
P.O. Box 30
State College, PA 16804

A. J. Ferraro
Department of Electrical Engineering
The Pennsylvania State University
University Park, PA 16802

1. INTRODUCTION

This paper investigates using fractal arrays to synthesize fractal radiation patterns with certain desired features. The theoretical foundation and design procedures for fractal radiation pattern synthesis are developed. Generalized Weierstrass functions, which possess fractal characteristics, play a fundamental role in the theory of fractal radiation pattern synthesis. With the appropriate choice of array element spacings and excitations, bandlimited Weierstrass functions may be used to express the array factor for a nonuniformly but symmetrically spaced linear array. The structure of resulting fractal radiation patterns can be controlled over a finite range of scales by the number of elements in the array. The fractal dimension of the radiation pattern for a fixed array geometry may be varied by changing the array current distribution. A unique synthesis technique is developed which is based on Fourier-Weierstrass expansions. This technique allows the selection of an appropriate generating function, in addition to the dimension, for a desired fractal radiation pattern. The fractal arrays which result from this procedure are composed of a sequence of self-similar uniformly spaced linear subarrays.

2. WEIERSTRASS FRACTAL ARRAYS

Fractals can be quantified and compared by using certain numbers which are related to their behavior. These numbers are commonly called fractal dimensions. Fractal dimensions provide a measure of the degree to which a fractal fills the metric space it is contained in. The box-counting or box definition is usually used for the computational or empirical determination of fractal dimensions. For a given fractal F, the box-counting fractal dimension, denoted by $\dim_B(F)$, is defined as [1]

$$\dim_B(F) = \lim_{\delta \to 0} \frac{\ln N_\delta(F)}{\ln(1/\delta)} \tag{1}$$

where N_δ represents the smallest number of sets of diameter at most δ required to cover the fractal F. The class of functions known as generalized Weierstrass functions are represented by

$$f(x) = \sum_{n=1}^{\infty} \eta^{(D-2)n}\, g(\eta^n x) \tag{2}$$

where $1<D<2$, $\eta>1$, and g is a suitable bounded periodic function [1,2]. These generalized Weierstrass functions have the property that they are everywhere continuous but nowhere differentiable and exhibit fractal behavior at all scales. The fractal dimension D, in this case, is a fractional dimension which lies between the integer dimensions of one and two. Generalized Weierstrass functions are the foundation on which the theory of fractal radiation pattern synthesis is based.

The array factor for a nonuniformly but symmetrically spaced linear array of 2N elements may be expressed in terms of a bandlimited Weierstrass function as

$$f_N(u) = 2 \sum_{n=1}^{N} I_n \cos(kd_n u + \alpha_n) \tag{3}$$

provided the current amplitudes and element spacings are chosen according to

$$I_n = \eta^{(D-2)n} \tag{4a}$$

$$kd_n = a\eta^n \tag{4b}$$

with $\eta>1$, $1<D<2$, $u = \cos\theta$, $k = 2\pi/\lambda$ and λ is the free-space wavelength. The Weierstrass partial sum of (3) may be classified as bandlimited since the resulting radiation pattern only exhibits fractal behavior over a finite range of scales. The structure of the radiation pattern becomes finer and more detailed as the number of array elements is increased.

A normalized form of the Weierstrass array factor can be obtained by dividing (3) by its maximum value. The expression for this normalized array factor is

$$g_N(u) = \left\{\frac{1 - \eta^{(D-2)}}{1 - \eta^{(D-2)N}}\right\} \sum_{n=1}^{N} i_n \cos(a\eta^n u + \alpha_n) \tag{5}$$

where

$$i_n = \eta^{(D-2)(n-1)} \tag{6}$$

represent the normalized excitation current amplitudes. Let τ be a constraint which is imposed on the minimum separation between any two consecutive elements in the array. There are two possible cases in which the minimum spacing constraint may be satisfied. These cases are as follows:

$$1)\quad d_2 - d_1 = \tau \quad \text{and} \quad d_1 \geq \frac{\tau}{2} \tag{7a}$$

$$2)\quad d_1 = \frac{\tau}{2} \quad \text{and} \quad d_2 - d_1 \geq \tau \tag{7b}$$

which may be used to derive an expression for a as a function of τ and η

$$a = \begin{cases} \dfrac{k\tau}{\eta(\eta-1)}, & 1 < \eta \leq 3 \\ \dfrac{k\tau}{2\eta}, & \eta \geq 3 \end{cases} \tag{8}$$

3. FRACTAL LINE SOURCES

For a line source of infinite length, the radiation pattern F(u) and the current distribution I(s) are related by the following Fourier transform pair [3]:

$$F(u) = \int_{-\infty}^{\infty} I(s)\, e^{j2\pi us}\, ds \tag{9a}$$

$$I(s) = \int_{-\infty}^{\infty} F(u)\, e^{-j2\pi su}\, du \tag{9b}$$

where

$$u = \cos\theta \tag{10a}$$

$$s = z/\lambda \tag{10b}$$

In particular, suppose that the radiation pattern of an infinite line source may be represented as a bandlimited generalized Weierstrass function of the form

$$F(u) = \sum_{n=0}^{N-1} \eta^{(D-2)n}\, g(\eta^n u) \tag{11}$$

where D is the fractal dimension and g(u) is a generating function. Here we assume that the generating function g(u) is periodic and even, i.e. $g(u+2)=g(u)$ and $g(-u)=g(u)$. Hence, g(u) may be expanded in a Fourier cosine series as

$$g(u) = \frac{a_0}{2} + \sum_{m=1}^{\infty} a_m \cos(m\pi u) \tag{12}$$

where the Fourier coefficients are determined from

$$a_m = 2 \int_0^1 g(u) \cos(m\pi u)\, du \tag{13}$$

Substituting (12) into (11) and replacing u by u+1 maps the interval [-1,1] to the interval [0,2]. This results in

$$F(u) = \frac{a_0}{2} \frac{\eta^{(D-2)N} - 1}{\eta^{(D-2)} - 1} + \sum_{m=1}^{\infty} a_m \left\{ \sum_{n=0}^{N-1} \eta^{(D-2)n} \cos[m\pi\eta^n(u+1)] \right\} \tag{14}$$

where

$$a_m = 2 \int_0^1 g(u-1)\cos(m\pi u)\, du \tag{15}$$

with the requirements that $\eta > 1$ and $1 < D < 2$. We call such a representation a Fourier-Weierstrass expansion.

The line source current distribution required in order to produce the desired fractal radiation patterns may be obtained by evaluating the Fourier integral (9b). Performing the necessary integration results in an expression for the current distribution given by

$$\begin{aligned} I(s) &= a_0 \frac{\eta^{(D-2)N} - 1}{\eta^{(D-2)} - 1} \operatorname{sinc}(2\pi s) \\ &+ \sum_{m=1}^{\infty} \sum_{n=0}^{N-1} a_m \eta^{(D-2)n} \left\{ e^{jm\pi\eta^n} \operatorname{sinc}[2\pi s - m\pi\eta^n] \right. \\ &\left. + e^{-jm\pi\eta^n} \operatorname{sinc}[2\pi s + m\pi\eta^n] \right\} \end{aligned} \tag{16}$$

An approximation may be obtained for the current distribution on a finite length line source by truncating (16) in the following way:

$$\tilde{I}(s) = \begin{cases} I(s), & |s| \le \dfrac{L}{2\lambda} \\ 0, & |s| > \dfrac{L}{2\lambda} \end{cases} \tag{17}$$

Following this procedure yields

$$\tilde{F}(u) = \frac{a_0}{2\pi}\,\frac{\eta^{(D-2)N}-1}{\eta^{(D-2)}-1}\,\{Si[\pi(L/\lambda)\,(1+u)] + Si[\pi(L/\lambda)\,(1-u)]\}$$
$$+ \frac{1}{2\pi}\sum_{m=1}^{\infty}\sum_{n=0}^{N-1} a_m \eta^{(D-2)n}\,\{\cos[m\pi\eta^n(u+1)]\;S_{mn}(u) \qquad (18)$$
$$+ \sin[m\pi\eta^n(u+1)]\;C_{mn}(u)\}$$

where

$$S_{mn}(u) = Si[\pi(L/\lambda - m\eta^n)\,(1+u)]$$
$$+ Si[\pi(L/\lambda + m\eta^n)\,(1+u)] \qquad (19a)$$
$$+ Si[\pi(L/\lambda - m\eta^n)\,(1-u)]$$
$$+ Si[\pi(L/\lambda + m\eta^n)\,(1-u)] \quad \text{for } -1 \le u \le 1$$

$$C_{mn}(u) = Ci[\pi|L/\lambda - m\eta^n|\,(1+u)]$$
$$- Ci[\pi(L/\lambda + m\eta^n)\,(1+u)]$$
$$- Ci[\pi|L/\lambda - m\eta^n|\,(1-u)] \qquad (19b)$$
$$+ Ci[\pi(L/\lambda + m\eta^n)\,(1-u)] \quad \text{for } -1 < u < 1$$
$$\text{and } m\eta^n \neq L/\lambda$$

$$C_{mn}(u) = \ell n\left[\frac{1+u}{1-u}\right] - Ci[2\pi(L/\lambda)\,(1+u)]$$
$$+ Ci[2\pi(L/\lambda)\,(1-u)] \quad \text{for } -1 < u < 1 \qquad (19c)$$
$$\text{and } m\eta^n = L/\lambda$$

$$C_{mn}(\pm 1) = \pm\left\{Ci[2\pi|L/\lambda - m\eta^n|\,]\right.$$
$$- Ci[2\pi(L/\lambda + m\eta^n)] \qquad (19d)$$
$$\left. - \ell n\left|\frac{L/\lambda - m\eta^n}{L/\lambda + m\eta^n}\right|\right\} \text{ for } m\eta^n \neq L/\lambda$$

$$C_{mn}(\pm 1) = \pm \left\{ \gamma + \ln[4\pi(L/\lambda)] - \mathrm{Ci}[4\pi(L/\lambda)] \right\} \text{ for } m\eta^n = L/\lambda \tag{19e}$$

in which

$$\mathrm{Si}(x) = \int_0^x \frac{\sin t}{t}\, dt \tag{20a}$$

$$\mathrm{Ci}(x) = -\int_x^\infty \frac{\cos t}{t}\, dt = \gamma + \ln(x) + \int_0^x \frac{\cos t - 1}{t}\, dt \tag{20b}$$

and the parameter $\gamma = 0.57721\ldots$ is Euler's constant.

4. FOURIER-WEIERSTRASS FRACTAL ARRAYS

We begin our study of bandlimited Fourier-Weierstrass fractal arrays by expressing (14) in the following convenient form:

$$F(u) = I_0 + 2 \sum_{m=1}^{\infty} \sum_{n=0}^{N-1} I_{mn} \cos(kd_{mn} u + \alpha_{mn}) \tag{21}$$

where

$$I_0 = \frac{a_0}{2} \frac{1 - \eta^{(D-2)N}}{1 - \eta^{(D-2)}} \tag{22a}$$

$$I_{mn} = \frac{a_m}{2} \eta^{(D-2)n} \tag{22b}$$

$$kd_{mn} = m\pi\eta^n \tag{22c}$$

$$\alpha_{mn} = m\pi\eta^n \tag{22d}$$

and the Fourier coefficients a_m corresponding to a particular generating function may be obtained through the use of (15). A useful representation of the array factor for a Fourier-Weierstrass array with a finite number of elements may be obtained by simply truncating the outer summation in (21) and interchanging

the order of summation. This leads to an approximate expression for the desired fractal radiation pattern given by

$$\bar{F}(u) = I_0 + 2 \sum_{n=0}^{N-1} \sum_{m=1}^{M} I_{mn} \cos(k d_{mn} u + \alpha_{mn}) \tag{23}$$

The double summation appearing in (23) may be interpreted as representing the superposition of radiation produced by a sequence of N uniformly spaced M-element linear arrays. The recurrence relation of the element spacings for each of the M-element subarrays is

$$\Delta_{n+1} = \eta \, \Delta_n \quad \text{with} \quad \Delta_0 = \frac{\lambda}{2} \tag{24}$$

This unique property of Fourier-Weierstrass arrays reveals their underlying fractal structure by suggesting that they are composed of a sequence of self-similar uniformly spaced linear subarrays. Recurrence relations for the excitation current amplitudes and phases may be found in a similar way

$$I_{m\,n+1} = \eta^{(D-2)} \, I_{mn} \quad \text{with} \quad I_{m0} = \frac{a_m}{2} \tag{25a}$$

$$\alpha_{m\,n+1} = \eta \, \alpha_{mn} \quad \text{with} \quad \alpha_{m0} = m\pi \tag{25b}$$

Finally, an expression for the normalized array current excitation amplitudes may be obtained by dividing (22b) by (22a), which yields

$$i_0 = 1 \tag{26a}$$

$$i_{mn} = \left(\frac{a_m}{a_0}\right) \left(\frac{1 - \eta^{(D-2)}}{1 - \eta^{(D-2)N}}\right) \eta^{(D-2)n} \tag{26b}$$

Figure 1 shows a synthesized radiation pattern formed by a triangular generating function with $\eta=2$ and a desired fractal dimension of $D=1.1$. A Fourier-Weierstrass array with $M=4$ and $N=8$ was used to synthesize this radiation pattern. Various stages in the construction of the Fourier-Weierstrass array with $\eta=2$ and a triangular generating function are illustrated in Figure 2. The self-similarity property of the subarrays is also clearly identifiable in Figure 2.

REFERENCES

[1] K. Falconer, *Fractal Geometry*, Wiley, New York, 1990.

[2] M. V. Berry, Z. V. Lewis, On the Weierstrass-Mandelbrot fractal function, *Proc. R. Soc. Lond. A, 370*, pp. 459-484, 1980.

[3] W. L. Stutzman, G. A. Thiele, *Antenna Theory and Design*, John Wiley & Sons, New York, 1981.

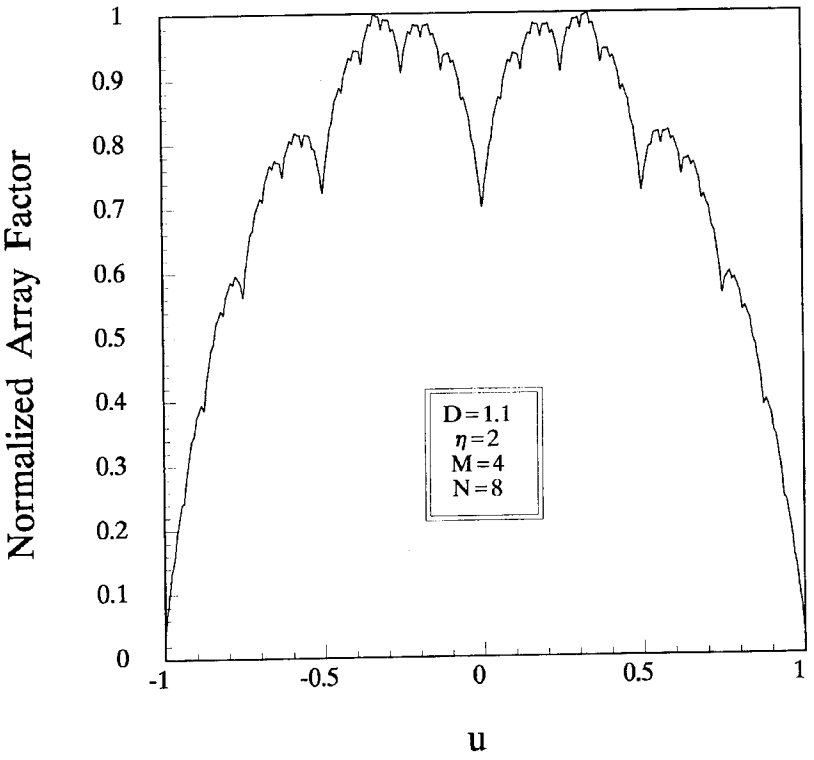

Normalized Array Factor
1
0.9
0.8
0.7
0.6
0.5
0.4
0.3
0.2
0.1
0
-1
-0.5
0
0.5
1
u
D=1.1
η=2
M=4
N=8

Figure 1

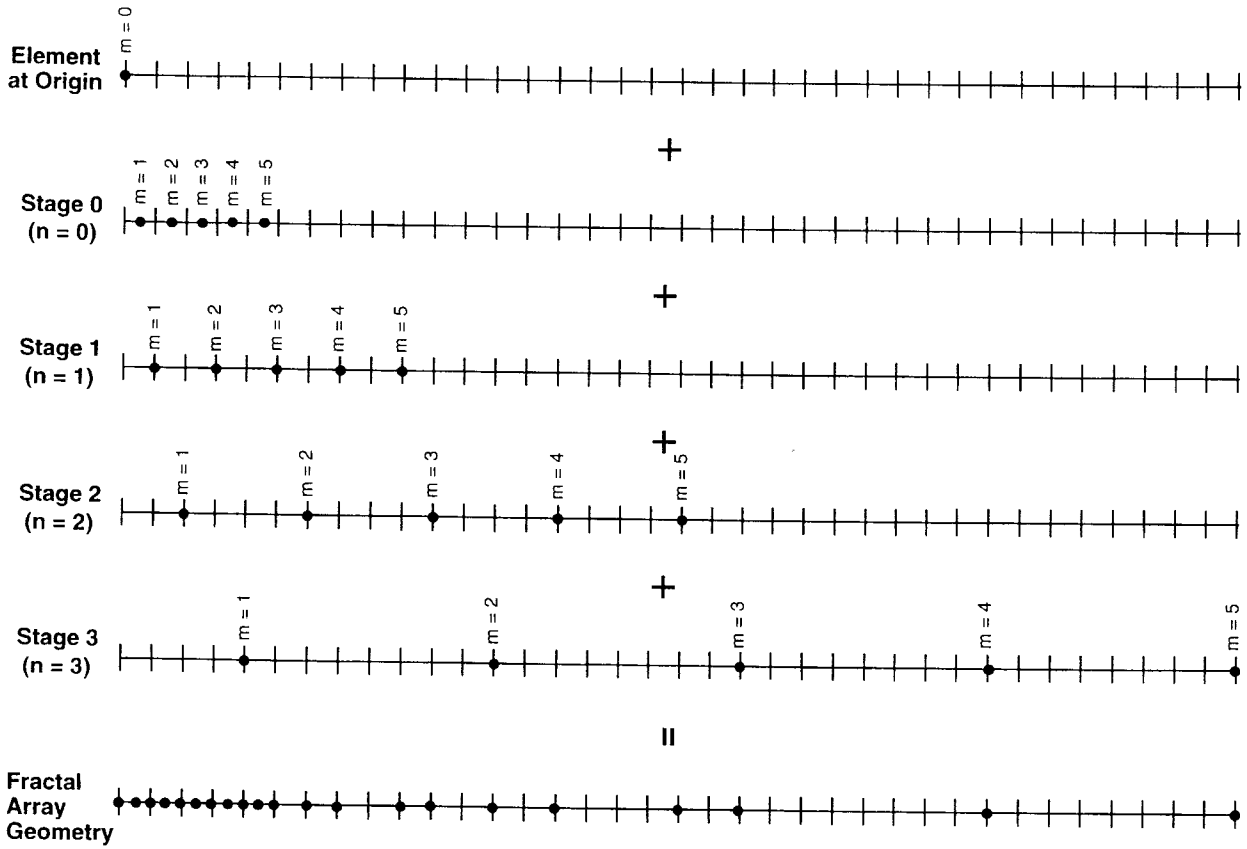

Element at Origin
m = 0
+
Stage 0 (n = 0)
m = 1
m = 2
m = 3
m = 4
m = 5
+
Stage 1 (n = 1)
m = 1
m = 2
m = 3
m = 4
m = 5
+
Stage 2 (n = 2)
m = 1
m = 2
m = 3
m = 4
m = 5
+
Stage 3 (n = 3)
m = 1
m = 2
m = 3
m = 4
m = 5
=
Fractal Array Geometry

Figure 2

Wavelet Transforms and Time/Time-scale Analysis

(Tutorial Session)

Randy K. Young, PhD
Applied Research Laboratory, The Pennsylvania State University
P. O. Box 30, State College, PA 16804-0030
(814) 863-4499 Fax: (814) 863-784
E-mail: rky@arl.psu.edu

Tommy G. Golsberry
Office of Naval Research
Code 321
800 N. Quincy St., Arlington, VA 22217-5660
(703) 696-0805

Fractal theories exploit the multi-scale self-similarity properties that nearly define wavelet transforms. However, a critical component of fractal analysis is that the self-similar "pattern" may not be apriori known; e.g., the underlying pattern may need to be extracted from the observed phenomenon, as in image compression. This "kernel" function or underlying pattern is analogous to wavelet analysis's "analyzing or mother wavelet;" these analyzing functions may not be apriori known, could be arbitrarily chosen, or may be extracted from the signal being analyzed as well. In addition, similar to fractal analysis, very fine scale steps or scale resolution can be employed. Although much of orthogonal wavelet theory concentrates on very coarse scale steps (powers of 2), general continous wavelet transform theory allows arbitrarily fine scaling. For these more general wavelet transforms, the properties of the resulting representation depend intimately upon the properties of the analyzing or mother wavelets. Thus, the wavelet analysis applied in fractal analysis should include very general wavelet transforms and not be limited to the often-used orthogonal transforms.

This introduction and tutorial on wavelet and time/time-scale (space and time in general) analysis will provide a framework for understanding these theories and intertwining them with established analysis techniques. The general class of wavelet transforms will be divided into orthogonal and nonorthogonal wavelet transforms and these will examined and compared to conventional Fourier transform techniques. The broad utility of wavelet transforms has been initially thrust by the *efficiency* of orthogonal (or nearly orthogonal) wavelet transforms. Image/video processing has been substantially impacted.

Although space-time-varying systems theory can also be naturally formulated with wavelet transforms, this brief introduction can not adequately over this topic. However, it should be noted that the scaling operator of the wavelet transform can warp either the space or time coordinates or both; this scaling action can account for relativistic effects and reference frame motion. For space-time-varying systems, the wavelet transform is the "natural transform," analogous to the Fourier transform being the "natural transform" for linear time (space) *invariant* systems (LTI systems); however, unlike the LTI systems having exponential functions as eigenfunctions, the space-time-varying systems do not have analogous eigenfunctions.

These relationships and analogies will be detailed to provide the interconnections between transform techniques and to establish the limitations of these analogies. The impact of these techniques in computational electromagnetics is already significant and the potential for further, more diversified impacts, is also considerable.

INTRODUCTION/BACKGROUND

Wavelet theory is the mathematics associated with building a model for a signal, system, or process with a set of "special signals." The special signals are just little waves or "*wavelets*." They must be oscillatory (waves) and have amplitudes which quickly decay to zero in both the positive and negative directions (little). See Figure 1.1 for an example of a wavelet (this is a classical wavelet, termed the "Morlet mother wavelet," after its inventor). The required oscillatory condition leads to sinusoids as the building blocks (see Figure 1.2). The quick decay condition is a tapering or windowing operation. These two conditions must be simultaneously satisfied for the function to be a little wave or wavelet. Forming the product of the oscillatory and decay functions yields the wavelet of Figure 1.1.

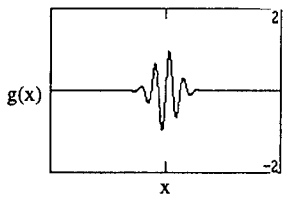


Figure 1.1: Morlet Mother Wavelet

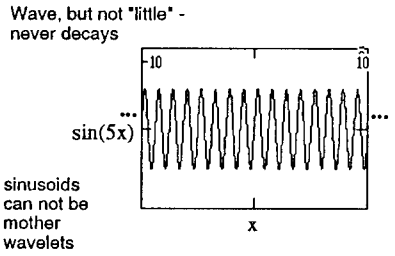


Figure 1.2: Oscillatory or Wave Requirement

Sets of "wavelets" are employed to approximate a signal (or process, or system, etc.) and each element in the wavelet set is constructed from the same function, the original wavelet, appropriately called the *mother wavelet*. Each element of the wavelet set is a scaled (dilated or compressed) and translated (shifted) mother wavelet. Wavelet theory is a mathematical tool that can be applied almost anywhere and like most tools, its primary purpose is to improve the efficiency (analogous to a wrench turning a bolt rather than using your fingers). When wavelet representations are more efficient than alternative representations for a particular application, wavelet transform should be employed there. In some applications wavelet theory may produce undesirable inefficiencies and, thus, wavelet theory should not be blindly forced upon an application. But, for "fractal/chaotic" problems where the multiscale self-similarity exists, wavelet transform are naturally efficient.

The Wavelet Transform

Before defining the wavelet transform, admissible functions are defined. For a function to be a mother wavelet it must be admissible. Recall, from earlier discussion that for a function to be a wavelet or mother wavelet it must be oscillatory and have fast decay toward zero. If these conditions are combined with the condition that the wavelet must also integrate to zero (its "d.c." or zero frequency component is zero), then these three conditions are the "non-rigorous" admissibility condition that must be satisfied for a function to be a mother wavelet. Essentially, admissible functions are bandpass signals - these signals cannot have zero frequency components and they must decay, so they will not have infinite frequency components either. Note that most signals that travel through a medium or in free-space are finite duration, bandpass waves, so this requirement is not very restrictive. Although a Laplace transform also includes a kernel function (a decaying exponential) that both decays and oscillates, the decay is always centered around zero (unlike these wavelets), frequency shifts are used (instead of time scaling), and the kernel of the Laplace transform is an exponential (exclusively). As will be emphasized throughout this book, the mother wavelet (kernel of the wavelet transform) can be almost any function.

More rigorously, an $L^2(\mathbb{R})$ function (a finite energy function - square integrable over the range of its independent variable), g, which can be either real or complex, is an **admissible function** if:

$$c_g = \int_{-\infty}^{\infty} \frac{|G(\omega)|^2}{|\omega|} d\omega < \infty \qquad (1.1)$$

where $G(\omega)$ is the Fourier transform of g. Note that the lower limit of integration is minus infinity instead of 0. This is required if the mother wavelet is complex and has a spectrum that is nonsymmetric about zero frequency. This admissibility condition is sufficient (may be more restrictive than required) but is not necessary (some functions are

admissible but do not satisfy this condition). A more general necessary and sufficient condition (the complete definition of admissibility) for functions to be admissible is defined with group theoretic concepts in [Gro2, Hei]. In summary, admissible functions (and mother wavelets) are those that cycle (oscillate), have finite energy, and have an average value of zero. Most natural signals satisfy these properties; energy usually travels as wave packets (oscillates and has an average value of zero - its average square value is the energy). Thus, most natural signals would classify as admissible functions.

The **wavelet transform** operator, W_g, maps a finite energy or $L^2(\mathbb{R})$ signal that is real or complex valued as follows: $W_g: L^2(\mathbb{R}) \rightarrow L^2(\mathbf{R} \setminus \{0\} \times \mathbf{R})$. Stated less mathematically, any finite energy signal is mapped from the time or space domain to a finite energy two-dimensional distribution in the scale-translation or *wavelet domain*. The **continuous wavelet transform** of a function, f, with respect to a given admissible mother wavelet, g, is defined as:

wavelet domain coeff at scale a and translation b

$$= W_g f(a,b) = |a|^{-\frac{1}{2}} \int f(x) g^*\left(\frac{x-b}{a}\right) dx \qquad (1.2)$$

$$= \left\langle f, \frac{1}{\sqrt{|a|}} g\left(\frac{x-b}{a}\right) \right\rangle = \langle f, g_{a,b} \rangle = \langle f, U(a,b)g \rangle$$

where superscript "*" denotes complex conjugate and $\langle , \rangle$ is an inner product (shorthand notation for the correlation integral defined in this equation). Note that this definition requires $g(x)$ to be an admissible function. The wavelet element, $g_{a,b}$, is defined by a **unitary affine mapping** $U(a,b): g(x) \mapsto \frac{1}{\sqrt{|a|}} g\left(\frac{x-b}{a}\right)$ or, less mathematically, $g_{a,b}$ is a version of the mother wavelet, $g(x)$, that has been scaled by the scale parameter, a, and translated by the translation parameter, b. Note that for continuous wavelet transforms the choice of the mother wavelet is only constrained by the admissibility condition. ***One is free to choose the mother wavelet for optimal behavior in the particular application of interest.***

Wavelet Transform Mapping

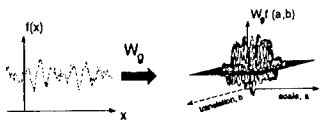


Figure 1.3: Wavelet Transform of f with respect to g

The wavelet transform can be related to the more commonly used Fourier transform or Fourier series. The Fourier models represent functions as weighted sum of exponentials at different frequencies. The weight at each different frequency is the Fourier coefficients. Wavelet models analogously represent functions as a weighted sum of scaled and translated mother wavelets. The wavelet transform has a mother wavelet replace the exponential, scaling and translation replace frequency shifting, and a two-dimensional surface of wavelet coefficients replace the one dimensional Fourier

coefficients. As a special case where the mother wavelet is $g(x)=e^{jx}$, $a=\frac{1}{\omega}$, and $b=0$, then the wavelet transform in equation (1.2) becomes:

$$W_g f(a,b) = W_{e^{jx}} f\left(\frac{1}{\omega},0\right)$$

$$= \int f(x)\, e^{-j\omega x}\, dx = F(\omega)$$

which is a Fourier transform. Rigorously, several mathematical difficulties arise with this substitution, but the intuitive interpretation and inverse relationship between frequency and scale are the desired results.

Wavelet Transform Examples

The wavelet transforms of several elementary functions are presented in the next four figures to display the characteristics of the wavelet domain representation. Note the increase in dimensionality of the wavelet representation; the dimensionality increases by a factor of two. For the first three wavelet transforms the mother wavelet was a complex Morlet mother wavelet (or a Gaussian weighted tone) with about six significant cycles in it (the imaginary part of this complex mother wavelet was shown in **Figure 1.1, Figure 1.1**). For these figures a 30 dB range of magnitude is displayed - if the magnitude was less than 30 dB below the peak, it was set to zero along with its corresponding phase. These figures are not studied in detail until the wavelet transform properties are examined; however, note the time localization property of the wavelet transform for the impulse (or delta function) and the edges of the rectangle. Frequency or scale localization can also be observed from the wavelet transform of a tone (sinusoid).

Several important conclusions can be made from these figures. First, note that both the magnitude and the phase localize in both time and scale (frequency). The localization in phase is observed from the converging phase ridges (not the zeroing due to small magnitudes). The simultaneous localization is due to the entire envelope being moved; the mother wavelet is translated. For the impulse or delta function, the wavelet transform will simply be the mother wavelet with translation replacing the time parameter (look at equation (1.1) with the input being an impulse - $W_g[\delta(x)](a,b) = g\left(\frac{-b}{a}\right)/\sqrt{|a|}$). At each different scale the wavelet distribution is a scaled mother wavelet.

Note that the phase of the wavelet transform and the real part of the wavelet transform are essentially redundant information (and, thus, look alike). To be consistent with matched filter or correlation processing, the phase will be chosen over the real part for the representations in this book.

For all of these cases the mother wavelet was complex. For both the impulse and the rectangle, the input was real. If a real mother wavelet was used (the real part of the complex mother wavelet), then only the real part of the wavelet transform would be obtained. The real part of the wavelet transform can be very poor for identification/detection. If the wavelet transform is only evaluated at points that are near the nulls of the real part of the transform, then those evaluated points can be sensitive to noise or might suggest a particular feature of the signal is not present when it really is present. These nulls in the real part can lead to incorrect results and invalid conclusions. This is similar to matched filter processing with real signals as opposed to complex signals; processing with a real signal produces nulls in the matched filter's output and leads to sensitivities and a less robust filter. Usually, for general signal processing it will be desirable to have complex mother wavelets to avoid the possibility of a null (this can be interpreted as a constraint on the density of the wavelet domain "hypothesis grid").

As mentioned previously, and emphasized throughout this paper, the wavelet transform representation and its properties are dictated by the mother wavelet. Because the set of mother wavelets is so large (essentially any bandpass signal) the freedom of choosing a mother wavelet makes general wavelet transform characterizations of a

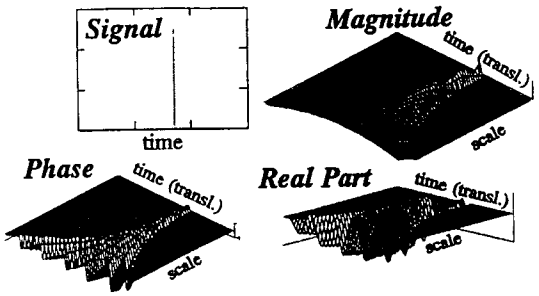


Figure E.1: Wavelet Transform of Impulse

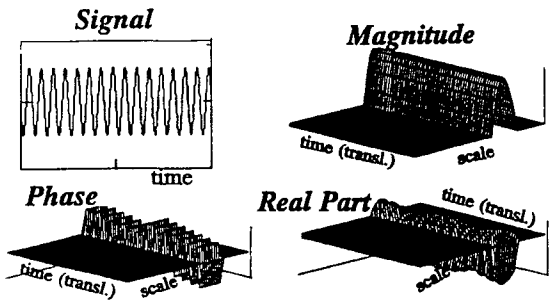


Figure E.3: Wavelet Transform of a Tone

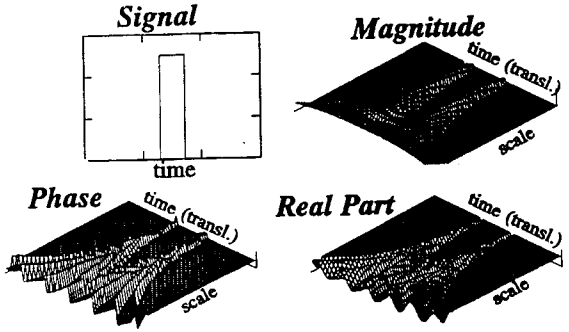


Figure E.2: Wavelet Transform of Rectangle

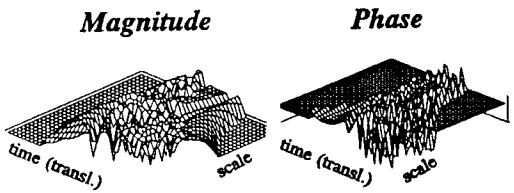


Figure E.4: Wavelet Transform of Rectangle with Respect to a New Mother Wavelet

particular function nearly impossible. **A valid statement for one mother wavelet can be completely invalid for another mother wavelet.** As an example consider the wavelet transform of the same rectangular signal as in Figure E.2, but now with respect to a FM signal with both quadratic and linear modulation (a sophisticated mother wavelet). This new wavelet transform's magnitude and phase are displayed in Figure E.4. Both Figure E.2 and E.4 are wavelet transforms of the rectangle signal; however, the qualities of the signal in the transform domain are more distinguishable in Figure E.2 (such as edges of the signal). For general signal qualities represented in the wavelet transform domain, a simple mother wavelet should be employed. For many other applications where gain and resolution are important more complicated or sophisticated mother wavelets might be used.

The characterization of mother wavelets being "bandpass" can be deceiving. A mother wavelet can be wideband and have multiple simultaneous frequencies that are at significantly different frequencies; the mother wavelet itself can be multi-modal, etc. The Fourier spectrum of a mother wavelet can have many "holes" or frequencies with very little energy in between frequencies that have a lot of energy. The admissible constraint is not a very restrictive condition and the bandpass interpretation should not be accepted too literally. For a further tutorial discussion with more wavelet transform examples and properties refer to the references [Com, Rio, Wei, You].

Discrete Time Wavelet Series - A Specific Structure

The discrete time wavelet series is discrete in both the time domain and the scale-translation (wavelet) domain. Since **time dilation by a factor of 2** can be efficiently implemented simply by dropping every other sample of a discrete signal (decimating or subsampling by a factor of 2), the transform to be presented here only considers time scaling by powers of 2. The structure of this particular wavelet decomposition is presented in Figures 1.4 and 1.5. This structure can be valid for multiresolution, orthogonal, biorthogonal, or PR-QMFs, with each case specifying the requirements for the filter coefficients. The filters are simply denoted as low pass, g(k), and high pass, h(k), filters to present a general form, but these filters are intimately related to the mother wavelet of the wavelet transforms [Com, Dau, Mal, Mey, Rio, Vet]. The high pass filter, h(k), is usually considered as the "mother wavelet" (the order of the coefficients changes in some cases) and the outputs of the high pass filters are thus the wavelet coefficients (the high pass filter convolves its impulse response (mother wavelet) with the incoming signal to create an output (a sequence of wavelet coefficients)).

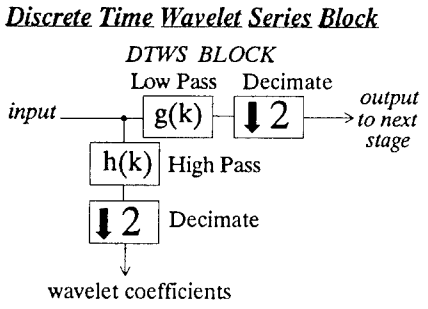


Figure 1.4: DTWS Processing Block

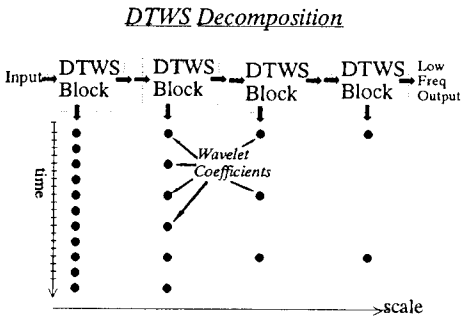


Figure 1.5: DTWS Structure

The decomposition process is demonstrated in Figure 1.4. The entire DTWS decomposition consists of passing the signal through identically structured processing "blocks." Each block is defined to have both a low pass filter (the "scaling function" discussed in wavelet literature) and a high pass filter (the "wavelet function"). The output of each filter is decimated by a factor of 2. The outputs of the lowpass filter are forwarded to the next DTWS block. The outputs of the high pass filters are the wavelet coefficients. These coefficients are the new representation of the signal.

Multiple "band splitting" blocks are cascaded to form a DTWS. The input signal goes in from the left, a series of wavelet coefficients comes out the bottom, and a final low frequency time series exits out the right. The low frequency signal and the wavelet coefficients together represent the time domain signal. This is one example of the DTWS. The "forward" transform is often termed the analysis filter or analysis stage. The pyramidal structure of this DTWS results because fewer and fewer coefficients are output from each successive stage until the last, single coefficient is output at the end of the filter stages (or the peak of the pyramid). The pyramidal decomposition is more easily viewed in the frequency domain and is the multiresolution wavelet transforms (refer to Figure 1.6 to see the pyramidal decomposition in the frequency domain).

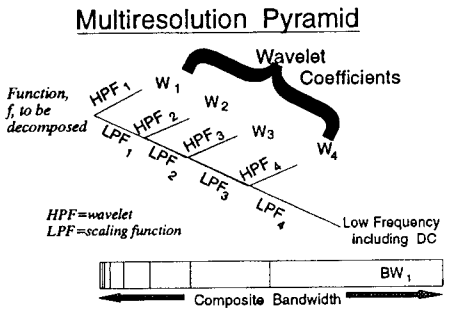


Figure 1.6: Multiresolution Wavelet Transform Structure

From the list of special wavelet transforms, the multiresolution wavelet transforms are the most general [Mal, Mey]. Multiresolution wavelet transforms allow the mother wavelets to be nonorthogonal and have many other properties. The primary constraint on the mother wavelet (or high pass filter) is really formulated on a different function, the *scaling function* (or low pass filter). Multiresolution transforms "build-in" a pyramidal structure that is not required for general wavelet transforms. The pyramidal structure requires a repetitive application of the same (but scaled) scaling and wavelet functions, or lowpass and highpass filters, respectively. This pyramidal structure forces the scaling function to satisfy a constraint termed the two-scale equation (originally [Mal] and detailed in [Chu]). In addition, the multiresolution wavelet transforms often begin with a scaling function that is derived from a **spline** function (splines are usually simple functions, such as polynomials that can be efficiently represented). Many desirable advantages exist for using splines to derive mother wavelets (and these are detailed by Chui [Chu]) but the constraints imposed on the mother wavelet (the filters) limits the set of possible mother wavelets. Further details of the mathematics are deferred to the many references on multiresolution wavelet transforms [Chu, Com, Dau, Mal, Mey, Vet].

However, the standard application of the multiresolution wavelet transform is to form a series of half-band filters that divide a spectrum into a high frequency band and a low frequency band. These filters initially act on the entire signal bandwidth and, thus, act at the high frequencies (small scale values) first and gradually reduce the signal bandwidth with each stage (smaller bandwidths correspond to larger scales). See Figure 1.6. The high frequency band output is taken as the wavelet transform coefficients for a "fine" scale, and the low frequency band output is *decimated* by a factor of 2 (every other sample is discarded). This low frequency band is then split into a high and low band; this band splitting and decimation process continues and produces an octave band representation of the signal. The wavelet coefficients for a particular scale are the output samples of a particular high pass filter. Each different output sample corresponds to a different translation at that particular scale. The output rate of each of these filters is decimated by a factor of two as the scale value steps in the coarse direction. The pyramidal structure in **Figure 1.1** results from the recursive structure of the multiresolution wavelet transform. The high pass filter outputs (wavelet coefficients) represent

the signal's characteristics and energy at a particular scale. The output of the final lowpass filter is the residual or "d.c." portion of the signal - the most blurred (most coarse) signal.

For this interpretation of the multiresolution wavelet transform it would be confusing if the mother wavelet was sophisticated (a large bandwidth or quickly changing characteristics); a frequency "band" may not make sense. If a sophisticated mother wavelet was used, the filters may have very sharp peaks or have multi-modal shapes; these are not acceptable in the standard multiresolution analysis. Thus, as with the other constrained wavelet transforms, the mother wavelets are assumed to be "bandpass" and not be sophisticated. The "sophisticated" mother wavelets to be examined later, are not necessarily characterized as bandpass. Subsequent ambiguity analysis will provide insight into the characteristics of these sophisticated mother wavelets. In some practical applications (especially images) the signal information does appear to follow an octave band distribution, in many other applications the information does not.

CONCLUSIONS

Because fractal techniques exploit: 1) apriori unknown signals/functions, and 2) the self-similarity property to eliminate redundancy at, possibly unknown "scale steps;" the utilization of wavelet techniques may require the more general nonorthogonal wavelet transforms that 1) do not highly constrain the mother or analyzing wavelet, and 2) allow the scale resolution to be nearly arbitrary as well. These features are not nessarily offered by the orthogonal wavelet transform or multiresolution wavelet transform techniques.

REFERENCES

[Bur] Burt, P. J., and Adelson, E. H., "The Laplacian Pyramid as a Compact Image Code," IEEE Trans. on Com., vol. 31, no. 4, 1983, pp. 532-540

[Chu] Chui, C. K., *An Introduction to Wavelets*, Academic Press, Inc., San Diego, 1992

[Coi] Coifman, R. R., "Wavelet Analysis and Signal Processing," in Signal Processing, Part I: Signal Processing Theory, L. Auslander et al. eds., IMA, vol. 22, Springer, New York, 1990

[Com] Combes, J. M., Grossman, A., and Tchamitchian, Ph., *Wavelets: Time-Frequency Methods and Phase Space*, Springer-Verlag, New York, NY, 1989

[Dau1] Daubechies, I., "Orthonormal bases of compactly supported wavelets," *Comm. Pure Appl. Math.*, vol. 41, 1988

[Dau2] Daubechies, I., "Time-frequency localization operators: a geometric phase space approach," *IEEE Trans. Inform. Theory*, vol. 34, 1988, pp. 605-612

[Dau3] Daubechies, I., "The wavelet transform, time/frequency localization and signal analysis," *IEEE Trans. Inform. Theory*, vol. 36, Sept. 1990, pp. 961-1005

[Fla] Flandrin, P., "Wavelets and related time-frequency transforms," *Proc. SPIE* 1348, 1990, pp. 2-13

[Hei] Heil, C. E., and Walnut, D. F., "Continuous and Discrete Wavelet Transforms," *SIAM Review*, vol. 31, no. 4, Dec. 1989, pp. 628-666

[Mal1] Mallat, S. G., "A theory for multiresolution signal decomposition: the wavelet representation," *IEEE Trans. Pattern Anal. Machine Intel.*, vol. 31, 1989, pp. 674-693

[Mal2] Mallat, S. G., "Multifrequency channel decompositions of images and wavelet models," *IEEE Trans. Acoust. Speech Signal Processing*, vol. 37, 1989, pp. 2091-2110

[Mey] Meyer, Y., Ondelettes, Hermann, Paris, 1990

[Rio] Rioul, O., and Vetterli, M., "Wavelets and Signal Processing," *Signal Processing Magazine*, vol. 8, no. 4, October, 1991, pp. 14-38

[Vai1] Vaidyanathan, P. P., "Multirate Digital Filters, Filter Banks, Polyphase Networks, and Applications: A Tutorial," *Proc. IEEE*, vol. 78, no. 1, 1990, pp. 56-93

[Vai2] Vaidyanathan, P. P., "Quadrature Mirror Filter Banks, M-band Extensions and Perfect-Reconstruction Techniques," *IEEE ASSP Magazine*, vol. 4, no. 3, pp. 4-20, July 1987

[Vet1] Vetterli, M., "A theory of multirate filter banks," *IEEE Trans. Acoust., Speech, Signal Proc.* 35, 1987

[Vet2] Vetterli, M., "Filter Banks Allowing Perfect Reconstruction," *Signal Processing*, vol. 10, no. 3, April 1986

[Wei] Weiss, L. G., Wavelets and Wideband Correlation Processing," IEEE Signal Processing Magazine, Jan., 1994, pp. 13-32

[You1] Young, R. K., *Wavelet Theory and Its Applications*, Kluwer Academic Publishers, 1993

[You2] Young, R. K., "Wideband Space-Time Processing and Wavelet Theory," Ph. D. Dissertation, Dept. Elect. Engr.

Wavelet-based Processing to Efficiently Achieve Broadband Monostatic and/or Passive Cross-sensor Processing

Randy K. Young, PhD and Prof. Leon H. Sibul
Applied Research Laboratory, The Pennsylvania State University
P. O. Box 30, State College, PA 16804-0030
(814) 863-4499 Fax: (814) 863-7841
E-mail: rky@arl.psu.edu

ABSTRACT

In many newer communications and sensing systems the utilization of broadband, high time-bandwidth product signals mandates the more general time-scaling to be utilized in the place of Doppler shifting. CDMA and spread spectrum techniques are becoming common place in wireless communications. This paper demonstrates the added value of nonorthogonal wavelet transforms, employed to efficiently formulate the computations in both active monostatic and passive multisensor processing (applicable to communications and remote sensing systems). The primary motivation is to provide efficient transform (wavelet) domain processing for wideband (high time-bandwidth product or spread spectrum) signals, analogous to the efficient Fourier transform domain processing for narrowband/stationary (small time-bandwidth product) signals.

RECEIVER PROCESSING

Typical receivers in communications and remote sensing systems employ simple correlators as their core processor. The correlation receiver compares a "reference signal" to "modified versions" of a second signal. The standard correlation receiver, referred to as the narrowband receiver in this paper, correlates a received signal with a time delayed and Doppler frequency shifted version of either the transmitted signal (in the active case) or a second received signal (in the multi-sensor passive case). This receiver performs:

$$NB\,Rec_{out}(\tau,\omega_D) = \int r(t)\; o^*(t-\tau)\; e^{-j\omega_D t}\,dt$$

on r(t) and o(t) which are the two signals being processed, and hypothesizes many time delays and many Doppler shifts on o(t). At the correctly hypothesized delay and Doppler, the geometry and motion are properly accounted for, and the receiver has a high response or achieves a "peak" in its output.

For the high time-bandwidth product signals, an alternative receiver accounts for time scaling rather than just Doppler shift. This "wideband" correlation receiver performs:

$$WBRec_{out}(a, b) = \int r(t)\ o^{*}\left(\frac{t-b}{a}\right)\ dt$$

where the time-scale hypthesis is "a" and the time translation parameter is "b." This is the receiver that is primarily addressed in this paper.

WAVELET-BASED PROCESSING TO EFFICIENTLY ACHIEVE BROADBAND MONOSTATIC AND/OR PASSIVE CROSS-SENSOR PROCESSING

For many current applications involving satillite assets, the combination of rapid motion (of this sensor/emitter/transciever) and high time-bandwidth product signals leads to conditions that require **signals to be time scaled, rather than simply Doppler shifted,** to achieve high processing gains. If the combination of both the signal characteristics (high time-bandwidth product signals) and the sensor/source geometry (sensor separation and sensor and/or emitter/reflector motion) is such that different Doppler shifts must be used on different frequency bands to maintain coherence across the entire signal spectrum, then the signal processing could utilize time scaling to maintain coherence across the duration of signal (essentially accounting for the rapid motion of the sensor/emitter/transceiver with the processing). These conditions are mathematically stated by the "narrowband condition;" this condition places the limits on the parameter to determine when a single Doppler shift can account for the motion over the entire duration, T, of the signal with bandwidth BW (and a maximum relative speed of v and a speed of light of c). If this condition is satisfied, a single Doppler shift will sufficiently account for the relative sensor motions ([Van] and many other references, refer to [You] or [Wei] for other references):

$$\frac{2v}{c} < \frac{1}{T \times BW} \quad or \quad T < \frac{c}{2v \times BW}$$

By accounting for the true time-scaling of the signal due to the relative motions, the interval over which coherent processing can be achieved is significantly increased. The relative speeds can be completely accounted for by applying the proper time-scaling to the signals; thus, the limitations on the processing are imposed by the relative accelerations, acc, instead (note that linear velocities will cause relative acceleration if sensors/emitters/transcievers are not moving directly at one another). The "first order time-varying" condtion, typically applied to high time-bandwidth product signals, identifies the duration over which an applied time-scale will account for the relative motion and maintain the coherence of the entire signal. This condition is:

$$T < \frac{2c}{\sqrt{acc} \times BW}$$

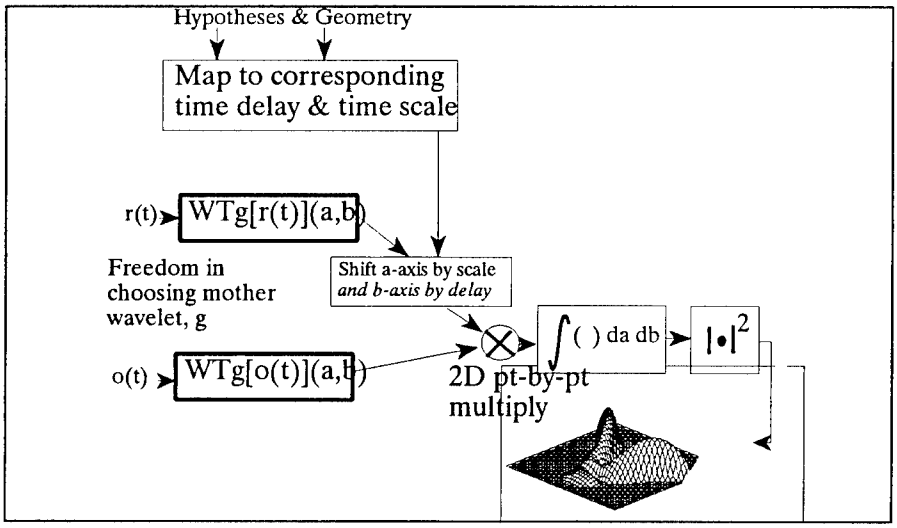
Note that the valid processing duration will be significantly larger when the time-scaling is applied to the signals rather than a single Doppler shift.

The time scaling operation that is required in the broadband processing is an extremely computationally intensive operation when performed with the standard multirate filtering [Vai]. When geometries are not precisely known or remote sensing is being performed, many time-scale hypotheses are necessary. Massive computational demands result from the required fine-grained time scaling; the fine time-scaling is necessary because of the fine time-scale resolution inherent in these high time-bandwidth signals. In multirate filters a fine time scale change or resampling of the digital signal is accomplished by upsampling and lowpass filtering (or interpolating) and then downsampling (decimating); the upsampling and decimation rates are integer numbers but are different integers (if they were the same integer, the time scale would be one and the signal would be unchanged). For example, assume that a time scale accuracy of 0.0001 was required to achieve a desired resolution. With a multirate filter the resampling would require a ratio of 10001 to 10000 which is 1.0001 in time scale. Although this is possible, it is very inefficient for many fine scales, especially if the possible time scales cover a broad and continuous range. The multirate filters achieve efficiency by using several stages of filters at different sampling rates; however, to achieve their efficiency one integer in the upsample/downsample ratio must remain fixed and the other integer must have simple factors (preferably several factors all being less than about 10). For a fine time-scale grid, without any hypothesis gaps, these constraints on the integers (that define the time scale itself) are not practical. An alternative processor formulates the time scaling a simple/efficient operation "in the wavelet domain;" it operates on the signals wavelet transforms rather than directly on the time signals or on the spectrums of the signals.

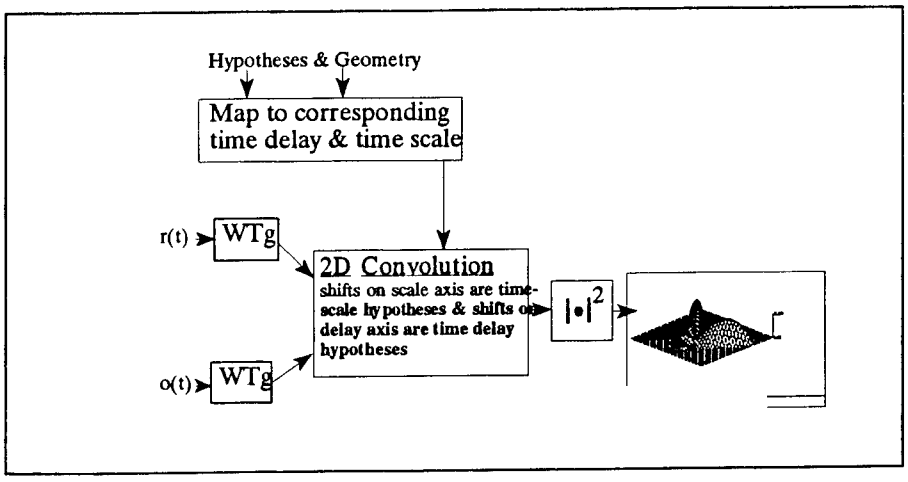
WAVELET DOMAIN TIME-SCALING

The primary theoretical concept is to map the inefficient time-scaling operation from the time domain (as done with multirate filters) to the wavelet domain. **In the wavelet domain the operation of time-scaling a signal becomes simply shifting the signal along the scale-axis; however, orthogonal wavelet transforms cannot be utilized for this operation, only nonorthogonal wavelet transforms can be employed.** Since shifts are simple or efficient operations, this method of time-scaling is preferable in many (but possibly not all) processing architectures. Thus, the time-scaling operation is achieved by a shift of the wavelet transform of the signal along the scale axis. For both active and passive processing a time delay must also be applied to one of the signals besides the time scaling operation. Again, this time delay operation can be accomplished in the wavelet domain as well. Time delay is accomplished by a shift along the time/translation/delay-axis in the wavelet domain. Thus the two operations of time delay and time-scaling can be accomplished by shifts along each axis in the wavelet

domain representation of the signal. See Figure 1 where the received signal is r(t) and, depending on whether multisensor passive or monostatic active processing is being performed, o(t) is the "other" signal (another received signal or the transmitted replica).



Where WTg is the wavelet transform operator (transform) with respect to the "mother" or analyzing wavelet function, g(t), and the "a" and "b" parameters are the time-scale and time-translation parameters, respectively . If, under special circumstances, the time delay and time-scale grid of hypotheses are "uniform" (equal grid spacing between each delay hypothesis and similarly for the time-scale hypothesis), the operations of shifting the wavelet domain representation and performing the multiplications and sums can all be combined. **The combination of these operations acting on the two wavelet domain representations (both 2D signal representations) is 2D convolution.** Under this restrictive assumption many fine time delay and time-scale hypotheses can be simultaneously and **efficiently** evaluated - utilizing efficient 2D convolutional techniques. See Figure 2.



A significant additional feature of this wavelet domain processing is that the signals have this intermediate wavelet domain representation. As discussed in [You], the wavelet domain representation is sensitive to the chosen mother wavelet. If the mother wavelet is chosen properly, it could provide significant classification features regarding the environment being sensed. So, this intermediate wavelet transform representation could be a significant byproduct for the classification process.

The mathematics that justify and formulate this concept follow. Several more detailed derivations are in [You, You1, You2]. The wavelet domain wideband receiver is formulated as:

$$WBRec_{out}(a, b) = \int WT_g[\, r(t)\,](a', b') \times WT_g[\, o(t)\,]\left(\frac{a'}{a}, \frac{b'-b}{a}\right) \frac{da'\,db'}{(a')^2}$$

where Wtg[r(t)] is the two-dimensional function (the wavelet transform of r(t)) and the arguments or the independent variables of are in the brackets [ ]. The intuitive effects of these equations are more easily interpretted by the earlier figures. The presentation will provide examples of these computations and quantify the computational savings for those particular examples on a praticular architecture.

CONCLUSIONS

In many newer communications and sensing systems the utilization of broadband, high time-bandwidth product signals mandates the more general time-scaling to be utilized in the place of Doppler shifting. Nonorthogonal wavelet transforms are utilized to efficiently formulate the computations in both active monostatic and passive multisensor processing (applicable to communications and sensing systems). The efficiency gains are very significant but are also architecture dependent. The presentation will provide examples of these computations and quantify the computational savings for those particular examples on a praticular architecture.

REFERENCES

[Bur] Burt, P. J., and Adelson, E. H., "The Laplacian Pyramid as a Compact Image Code," IEEE Trans. on Com., vol. 31, no. 4, 1983, pp. 532-540

[Chu] Chui, C. K., *An Introduction to Wavelets*, Academic Press, Inc., San Diego, 1992

[Coi] Coifman, R. R., "Wavelet Analysis and Signal Processing," in Signal Processing, Part I: Signal Processing Theory, L. Auslander et al. eds., IMA, vol. 22, Springer, New York, 1990

[Com] Combes, J. M., Grossman, A., and Tchamitchian, Ph., *Wavelets: Time-Frequency Methods and Phase Space*, Springer-Verlag, New York, NY, 1989

[Dau1] Daubechies, I., "Orthonormal bases of compactly supported wavelets," *Comm. Pure Appl. Math.*, vol. 41, 1988

[Dau2] Daubechies, I., "Time-frequency localization operators: a geometric phase space approach," *IEEE Trans. Inform. Theory*, vol. 34, 1988, pp. 605-612

[Dau3] Daubechies, I., "The wavelet transform, time/frequency localization and signal analysis," *IEEE Trans. Inform. Theory*, vol. 36, Sept. 1990, pp. 961-1005

[Fla] Flandrin, P., "Wavelets and related time-frequency transforms," *Proc. SPIE* 1348, 1990, pp. 2-13

[Hei] Heil, C. E., and Walnut, D. F., "Continuous and Discrete Wavelet Transforms," *SIAM Review*, vol. 31, no. 4, Dec. 1989, pp. 628-666

[Mal1] Mallat, S. G., "A theory for multiresolution signal decomposition: the wavelet representation," *IEEE Trans. Pattern Anal. Machine Intel.*, vol. 31, 1989, pp. 674-693

[Mal2] Mallat, S. G., "Multifrequency channel decompositions of images and wavelet models," *IEEE Trans. Acoust. Speech Signal Processing*, vol. 37, 1989, pp. 2091-2110

[Mey] Meyer, Y., Ondelettes, Hermann, Paris, 1990

[Rio] Rioul, O., and Vetterli, M., "Wavelets and Signal Processing," *Signal Processing Magazine*, vol. 8, no. 4, October, 1991, pp. 14-38

[Vai1] Vaidyanathan, P. P., "Multirate Digital Filters, Filter Banks, Polyphase Networks, and Applications: A Tutorial," *Proc. IEEE*, vol. 78, no. 1, 1990, pp. 56-93

[Vai2] Vaidyanathan, P. P., "Quadrature Mirror Filter Banks, M-band Extensions and Perfect-Reconstruction Techniques," *IEEE ASSP Magazine*, vol. 4, no. 3, pp. 4-20, July 1987

[Vet1] Vetterli, M., "A theory of multirate filter banks," *IEEE Trans. Acoust., Speech, Signal Proc.* 35, 1987

[Vet2] Vetterli, M., "Filter Banks Allowing Perfect Reconstruction," *Signal Processing*, vol. 10, no. 3, April 1986

[Wei] Weiss, L. G., Wavelets and Wideband Correlation Processing," IEEE Signal Processing Magazine, Jan., 1994, pp. 13-32

[You1] Young, R. K., *Wavelet Theory and Its Applications*, Kluwer Academic Publishers, 1993

[You2] Young, R. K., "Wideband Space-Time Processing and Wavelet Theory," Ph. D. Dissertation, Dept. Elect. Engr.

The Intervallic Wavelets with Applications in the Surface Integral Equations

G.W. Pan and J. Y. Du
Department of Electrical Engineering and Computer Science
University of Wisconsin-Milwaukee

Abstract— **Orthonormal wavelets have been successfully used as basis and testing functions in the integral equations to replace the pulse, triangular, and PWS (picewise sinusoidal) functions. Very sparse coefficient matrices have been obtained due to the vanishing moments, localization, MRA (multiresolution analysis), of the wavelets. However, in many practical problems, the solution domain is confined in a bounded interval, while the wavelets are defined on the entire real line. To overcome this problem, periodic wavelets are introduced. Nonetheless, the unknown functions must take on equal values at the endpoints of the bounded interval, in order to apply periodic wavelets as the basis functions. This requirement has limited the applicability of the periodic wavelets. In particular, when three dimensional problems are considered, the unknown must have a constant value at its contour boundary, which is too restrictive. In this paper we present a new approach, employing the intervallic wavelets. The intervallic wavelets form an orthonormal basis and preserve the same MRA of other usual unbounded wavelets. No requirement for the endpoints values are imposed if the unknown function is expanded in terms of intervallic wavelets. No biorthogonal basis is needed. Hence, the intervallic wavelets are very versatile to apply to the surface integral equations where the unknowns are defined on spatial surfaces, which are bounded by line contours. There is no need for the unknowns to take a constant value on the boundary contour. The construction of the intervallic wavelets is presented. Numerical examples of scattering and guided wave problems are discussed.**

I. INTRODUCTION

Recently, a new category of orthogonal systems, namely orthogonal wavelets, has emerged [1],[2]. In computer vision and signal processing, wavelets have become a hot topic [3] mainly due to the multiresolution analysis (MRA) and the localization properties in both space and frequency domains. Orthogonal wavelets also have many fascinating properties for electromagnetic field computations. First, wavelets are sets of orthonormal bases of $\mathbf{L}^2(\mathbf{R})$. They are problem-independent orthogonal bases and thus are suitable for numerical computations for general cases. Second, the trade-off between the orthogonality and continuity is well balanced in orthogonal wavelet systems because now the orthogonality always holds whether the supporting regions are overlapped or not. One can build an orthogonal wavelet system with any order of continuity, expecting larger supporting regions as higher order of continuity is selected. Third, in addition to the advantages of the traditional orthogonal basis systems, orthogonal wavelets have zero moments such that there is much more certainty to yield sparse systems of linear algebraic equations [4]. Furthermore, orthogonal wavelets have localization properties in both the space and frequency domains. Therefore, the decorrelation of the expansion coefficients occurs both in the space and Fourier domains. Nevertheless, according to the theory of multigrid processing [5], one can improve convergence by operating on both fine and coarse grids to reduce both the high-frequency and low-frequency component errors between the approximate and exact solutions in contrast to the traditional way of operating only on fine grids to reduce the high-frequency component. The expansion with subsectional bases actually is equivalent to the expansion on the finest scale only. On the contrary, the multiresolution analysis implemented by wavelet expansion provides a multigrid method. Finally, the pyramid scheme employed in the wavelet analysis provides fast algorithms [4].

Wevelets have been successfully used in electromagnetics to solve resonance and interference problems using compactly supported Daubechies wavelets [6]. To extend the domain of the 1D wavelets from the real line to curves and closed contours, the boundary element method has been combined with wavelets [7]. The Fast wavelet algorithm was proposed [4], and applied to EM problems [8] to reduce the computational effort of the inner product computations for the coefficient matrix. For more effective treatment of the end points of an interval, on which the unknown is defined, periodic wavelets and biorthogonal wavelets have been employed [8],[9]. Although these two approaches have improved the efficiency, each has its limitations. For instance, in order to use periodic wavelets, the unknown must have equal values at the two endpoints of the interval. This constraint becomes more restrictive when the unknown is defined on a surface. In this case the unknown must take equal values on the contour on which the surface is spanned.

In this article we introduce the intervallic wavelets which have released the above constraint.

II. BASIC WAVELET THEORY

2.1 Scaling Function

A multiresolution analysis of $L^2(R)$ is defined as a sequence of closed subspaces V_j of $L^2(R)$, $j \in Z$, with the following properties:

$$V_j \subset V_{j+1}$$

$$v(x) \in V_j \Leftrightarrow v(2x) \in V_{j+1}$$

$$v(x) \in V_0 \Leftrightarrow v(x+1) \in V_0$$

$$\bigcap_j V_j = \{0\}, \bigcup_j V_j = L^2(R)$$

A scaling function $\varphi(x) \in V_0$, with a non-vanishing integral, exists such that the collection $\{\varphi(t-l) \mid l \in Z\}$ is a Riesz basis of V_0.
Since $\varphi \in V_0 \subset V_1$, a sequence $(h_k) \in l^2(Z)$ exists such that the scaling function satisfies

$$\varphi(x) = \sqrt{2}\sum_k h_k \varphi(2x-k)$$

This functional equation is referred to the dilation equation, where $\{h_k\}$ are the coefficients of the lowpass filter and

$$\sum_k h_k = 1$$

It is immediate that the collection of functions $\{\varphi_{j,l} \mid l \in Z\}$, with

$$\varphi_{j,l}(x) = 2^{j/2}\varphi(2^j x - l)$$

is a Riesz basis of V_j

2.2 Wavelets

We will use W_j to denote a space complementing V_j in V_{j+1}, i.e. a space that satisfies

$$V_{j+1} = V_j \oplus W_j$$

and

$$\bigoplus_j W_j = L^2(R)$$

A function ψ is a wavelet if the collection of functions $\{\psi(x-l) \mid l \in Z\}$ is a Riesz basis of W_0. The collection of wavelet functions $\{\psi_{j,l} \mid l, j \in Z\}$ is then a Riesz basis of $L^2(R)$. The definition of $\psi_{j,l}$ is similar to that of $\varphi_{j,l}$. Since the wavelet ψ is an element of V_1, a sequence $(g_k) \in l^2(Z)$ exists such that

$$\psi(x) = \sqrt{2}\sum_k g_k \varphi(2x-k)$$

When

$$W_0 \perp V_0$$

the wavelets are orthogonal wavelets, satisfying

$$g_k = (-1)^{k-1} h_{-(k-1)}$$

III. PERIODIC WAVELETS

So far we have been discussing wavelet theory on the real line. For many applications, the functions involved are only defined on a compact set, such as an interval or surface. In order to apply wavelets, some modifications are required. Consider a periodic function with period 1, i.e., $f(x+1) = f(x)$, then the wavelet coefficients on a given scale satisfy $< f, \psi_{j,k} > = < f, \psi_{j,k+2^j} >$, $k \in Z$, and $j \geq 0$. A periodic MRA on the interval $[0,1]$ can be constructed by periodizing the basis functions as follows

$$\varphi_{j,k}^{per} = \sum_{l \in Z} \varphi_{j,k}(x+l) \text{ for } 0 \leq l < 2^j \text{ and } j \geq 0$$

$$\psi_{j,k}^{per} = \sum_{l \in Z} \psi_{j,k}(x+l) \text{ for } 0 \leq l < 2^j \text{ and } j \geq 0$$

If the support of $\varphi_{j,k}$ is a subset of $[0,1]$, then $\varphi_{j,k}^{per}(x) = \varphi_{j,k}(x)$. Otherwise, $\varphi_{j,k}(x)$ is chopped into pieces of length 1, which are shifted onto $[0,1]$ and added up, yielding $\varphi_{j,k}^{per}(x)$. This "wrap around" procedure is satisfactory in many situations. However, unless the behavior of the function f at 0 matches that at 1, the periodic version of f has a singularity there.

IV. INTERVALLIC WAVELET

Standard wavelet analysis involves constructing basis for collections of functions on the real line R such as the square integrable functions on real line, $L^2(R)$. For many applications it is necessary, or at least more natural, to work on a subset of the real line.

4.1 Scaling Functions

Let us sketch the construction of orthogonal wavelets on $[0,1]$, which was proposed by B. Jawerth[10,11]. Start from an orthogonal Coifman scaling function with $6N$ non-zero coefficients, and assume the scale is fine enough so that the endpoints are independent. All polynomials of degree $< 2N$ can be written as linear combinations of the $\varphi_{j,k}$ for $k \in Z$, with coefficients are polynomials of degree $< 2N$. Hence, confined the windowed parts of polynomials on $[0,1]$ are in $V_j^{[0,1]}$. Since the $\{\varphi_{j,k}\}$ is an orthonormal basis for V_j, any monomial x^α, $\alpha \leq 2N-1$, has the representation

$$x^\alpha = \sum_k < x^\alpha, \varphi_{j,k} > \varphi_{j,k}(x)$$

The restriction to $[0,1]$ can then be written

$$x^\alpha \mid_{[0,1]} = \Big(\sum_{k=-4N+2}^{2N} + \sum_{k=2N+1}^{2^j-4N} + \sum_{k=2^j-4N+1}^{2^j+2N} \Big) < x^\alpha, \varphi_{j,k} > \varphi_{j,k}(x) \mid_{[0,1]}$$

Let

$$x_{j,L}^\alpha = 2^{j(\alpha+1/2)} \sum_{k=-4N+2}^{2N} < x^\alpha, \varphi_{j,k} > \varphi_{j,k}(x) \mid_{[0,1]}$$

and

$$x_{j,R}^\alpha = 2^{j(\alpha+1/2)} \sum_{k=2^j-4N+1}^{2^j+2N} < x^\alpha, \varphi_{j,k} > \varphi_{j,k}(x) \mid_{[0,1]}$$

where subscript L and R represent left and right.
Hence

$$2^{j/2}(2^j x)^\alpha = x_{j,L}^\alpha + 2^{j(\alpha+1/2)} \sum_{k=2N+1}^{2^j-4N} < x^\alpha, \varphi_{j,k} > \varphi_{j,k}(x) \mid_{[0,1]} + x_{j,R}^\alpha$$

Define the spaces $\overline{V_j}$, $j \geq j_0$, to be the linear span of the functions $\{x_{j,L}^\alpha\}_{\alpha \leq 2N-1}$, $\{x_{j,R}^\alpha\}_{\alpha \leq 2N-1}$, $\{\varphi_{j,k} \mid_{[0,1]}\}_{k=2N+1}^{2^j-4N}$, namely

$$\overline{V_j} = \overline{\{x_{j,L}^\alpha\}_{\alpha \leq 2N-1}} \cup \overline{\{\varphi_{j,k} \mid_{[0,1]}\}_{k=2N+1}^{2^j-4N}} \cup \overline{\{x_{j,R}^\alpha\}_{\alpha \leq 2N-1}}$$

The collections $\{x^{\alpha}_{j,L}\}_{\alpha\leq 2N-1}$, $\{x^{\alpha}_{j,R}\}_{\alpha\leq 2N-1}$, and $\{\varphi_{j,k}\,|_{[0,1]}\}_{k=2N+1}^{2^j-4N}$ are mutually orthogonal, from previews construction, all polynomials of degree $\leq 2N-1$ are in $\overline{V_j}$, and

$$\overline{V_j} \subset \overline{V}_{j+1}$$

it can be proved that $\overline{V}_j$ form an MRA of $L^2([0,1])$.
All of the functions in collections are linearly independent, and can be used as basis function. In order to form an orthonormal basis, we only have to orthogonalize the functions $x^{\alpha}_{j,L}$ and $x^{\alpha}_{j,R}$.

4.2 Orthogonalization

More specifically, let us consider the left endpoint and set

$$\varphi^{\alpha}_{j,L} = \sum_{\beta=0}^{2N-1} a^{\alpha\beta} x^{\beta}_{j,L}$$

The $2N \times 2N$ matrix $A = \{a^{\alpha\beta}\}$.
For a symmetric matrix X with each element

$$X^{\alpha\beta} = < x^{\alpha}_{j,L}, x^{\beta}_{j,L} >$$

the orthonormality condition is

$$I = AXA^*$$

Now note that X is positive definite and symmetric, hence, the Cholesky decomposition holds, namely $X = CC^*$. The choice of

$$A = C^{-1}$$

that is, we have proven that the functions in $\{\varphi^{\alpha}_{j,L}\}_{\alpha=0}^{2N-1}$ are orthonormal. Similarly, we perform the orthogonalization of $x^{\alpha}_{j,R}$.

4.3 Wavelets

To obtain to the corresponding wavelets we let $\overline{W_j}$ be the orthogonal complement of $\overline{V_j}$ in $\overline{V}_{j+1}$. the wavelet $\psi_{j,k}$ with $3N \leq k \leq 2^j - 3N$ are all in $\overline{V}_{j+1}$ and confine entirely inside $[0,1]$. The remaining $6N$ functions required for an orthonormal basis of $\overline{W_j}$, can be found by using

$$\varphi_{j+1,l} = \sum_k < \varphi_{j+1,l}, \varphi_{j,k} > \varphi_{j,k} +$$

$$\sum_k < \varphi_{j+1,l}, \psi_{j,k} > \psi_{j,k}$$

V. SOLVING INTEGRAL EQUATION

In this section we apply the intervallic scaling functions and wavelets in solving the integral equation

$$\int f(x')K(x,x')dx' = g(x)$$

5.1 Expansion in Terms of Intervallic Wavelets

With the domain of integration being $[0,1]$, let us expand the unknown function f in the integral equation in terms of the scaling functions and wavelets on the bounded interval as

$$f(x) = \sum_k \overline{f}_{J,k}\varphi^I_{J,k}(x)$$

$$= \sum_k \overline{f}_{j_0,k}\varphi^I_{j_0,k}(x) + \sum_{j\geq j_0}^{J-1}\sum_k \tilde{f}_{j,k}\psi^I_{j,k}(x)$$

Here $\{\psi^I_{j,k}\}$ term represents bandpass filter characteristics, and extract successively lower and lower frequency components of the unknown function with decreasing values of the scale parameter j , while $\{\varphi^I_{j_0,k}\}$ term indicates lowpass filter characteristics, and retains the lowest frequency components or the coarsest approximation of the original function.
The second expansion of f is substituted in the integral equation, the resultant equation is tested with the same set expansion functions. As a result, a set of linear equations is formed

$$A = \begin{pmatrix} A_{\varphi,\varphi} A_{\varphi,\psi} \\ A_{\psi,\varphi} A_{\psi,\psi} \end{pmatrix}$$

$$X = \begin{pmatrix} \overline{X}_{\varphi} \\ \tilde{X}_{\psi} \end{pmatrix}$$

$$B = \begin{pmatrix} < g, \varphi^I_{j_0,k'} >_{k'} \\ < g, \psi^I_{j',k'} >_{j',k'} \end{pmatrix}$$

where

$$A_{\varphi,\varphi} := < \varphi^I_{j_0,k'}, (L_K\varphi^I_{j_0,k}) >_{k\,k'}$$

$$A_{\varphi,\psi} := < \varphi^I_{j_0,k'}, (L_K\psi^I_{j,k}) >_{j,k.k'}$$

$$A_{\psi,\varphi} := < \psi^I_{j',k'}, (L_K\varphi^I_{j_0,k}) >_{k\,j',k'}$$

$$A_{\psi,\psi} := < \psi^I_{j',k'}, (L_K\psi^I_{j,k}) >_{j,k\,j',k'}$$

$$< f, g > = \int_0^1 f(x)g(x)dx$$

$$(L_K f)(x) = \int_0^1 f(x')K(x,x')dx'$$

$\overline{X}_{\varphi}$ and $\tilde{X}_{\psi}$ are vector.

5.2 Numerical Integration

The evaluation of the coefficient matrix entries involves numerical integrations, which are time consuming. However, by taking the advantage of the vanishing moments and compact support of the wavelets, many entries can directly identified or calculated without performing the quadrature procedures. Away from the singular points of the kernel, the integrand behaves as a polynomial locally. Consequently, the integral that contains at least one wavelet function, as the basis or the testing function, will result in zero. In the mean while the integral, that contains scaling functions as basis and testing functions, will take the zero order moment of the kernel. For those integrals in which the basis and testing functions overlaps, and therefore the kernel singular point lies within the integration interval, the numerical integration has to be conducted. Even though

the integration limits range from 0 to 1, the intervals of actual integrations are much smaller because of the compact support of the intervallic father and mother wavelets.

VI. NUMERICAL EXAMPLES

Shown in Fig. 1. is a perfectly conducting cylinder, which excited by an impressed electric field E_z^i. The induced current J_z on the conducting cylinder produce a scattered field E_z^s. The boundary condition is

$$E_z = E_z^i + E_z^s = 0 \text{ on C}$$

that is, the tangential electric field vanishes on C, the contour of the ellipse, Hence, we have the Integral equation

$$E_z^i = \frac{\kappa\eta}{4}\int_C J_z(\rho')H_0^{(2)}(\kappa \mid \rho - \rho' \mid)dl' \ \rho \text{ on C}$$

where $E_z^i(\rho)$ is known and J_z is the unknown, $H_0^{(2)}$ is Hankel function of the second kind, zero order, $\kappa = \frac{2\pi}{\lambda}$, $\eta \approx 120\pi$.
If incident field from the direction ϕ_i. E_z^i is given by

$$E_z^i = e^{j\kappa(x\cos(\phi_i)+y\sin(\phi_i))}$$

A parameter of interest is the scattering cross section σ, defined as the width for which the incident wave carries sufficient power to produce, by omnidirectinal radiation, the same scattered power density in a given direction. Mathematically, this is

$$\sigma(\phi) = 2\pi\rho \mid \frac{E^s(\phi)}{E^i} \mid^2$$

where $E^s(\phi)$ is the distant field from J_z, It can be found by using the asymptotic expression for $H_0^{(2)}$. The result is

$$E^s(\phi) = \eta\kappa K\int_C J_z(x',y')e^{j\kappa(x'\cos\phi+y'\sin(\phi))}dl'$$

where

$$K(\rho) = \frac{1}{\sqrt{8\pi\kappa\rho}}e^{-j(\kappa\rho+3\pi/4)}$$

and

$$\sigma(\phi) = \frac{\kappa\eta^2}{4} \mid \int_C J_z(x',y')e^{j\kappa(x'\cos(\phi)+y'\sin(\phi))}dl' \mid^2$$

This can be evaluated numerically once J_z is found.
Using the procedures described in section V,corresponding matrix equations are solved for a elliptic cylindrical surface. Fig. 2, 3, 4 and 5 show the surface current distribution and radar cross section by conventional MoM and this method. The results of the conventional MoM and this method agree very well.

VII. CONCLUSIONS

In this paper, the intervallic wavelets are constructed and applied to the solution of boundary integral equations for electromagnetic problems, in which the unknown functions are defined on a finite interval. Numerical examples are provided. The results agree well with the moment method solutions.

REFERENCES

[1] I. Daubechies, *Ten lectures on Wavelets*, SIAM, Philadephia, 1992.
[2] C. K. Chui, *An Introduction to Wavelets*, Academic Press, 1991.
[3] S. G. Mallat,"A theory for multiresolution signal decomposition: the wavelet representation," *IEEE Trans. Pattern Anal. Machine Intell.*, vol.PAMI-11, pp. 674-693, July 1990.
[4] G. Beylkin, R. Coifman, and V. Roklin, *Fast wavelet transforms and numerical algorithm I* , Commun. pure Appl. Math., vol. 44, pp. 141-183.
[5] W. Hackbusch, *Multi-grid methods and applications*, Spring-Verlag, 1985.
[6] G. Wang, J. Zhang, and G. Pan,"Solution of inverse problems in image processing by wavelet expansion," submitted to *IEEE Trans. Image Processing*.
[7] G. Wang and G. Pan, *A Hybrid Wavelet Expansion and Boundary Element Analysis for Multiconductor Transmission Line in Multilayered Dielectric Media*, IEEE Microwave Theory Tech. to appear in Feb. 1995.
[8] X. Zhu and G. Pan, *A Fast Adaptive Algorithm Using Periodic Lemarie-Meyer Wavelets to Solve Boundary Integral Equations*, University of Wisconsin-Milwaukee.
[9] J. C. Goswami, A. K. Chan, C. K. Chui, *On Solving First-Kind Integral Equations using Wavelets on a Bounded Interval*, Texas A&M University.
[10] B. Jawerth, Wim Sweldens, *An Overview of Wavelet Based Multiresolution Analyses*, University of South Carolina.
[11] L. Andersson, N. Hall, B. Jawerth, G. Peters, *Wavelets on Closed Subsets of the Real Line*, University of South Carolina.
[12] C. K. Chui (ed.), *Wavelets - A tutorial in theory and applications*, Academic Press, 1992.
[13] I. Daubechies,"Orthonormal bases of compactly supported wavelets," *Commun. Pure Appl. Math.*, vol.41, pp. 909-996, Nov. 1988.
[14] B. K. Alpert,"Wavelets and other bases for fast numerical linear algebra," in *Wavelets: a tutorial in theory and applications*, C. K. Chui, Ed., New York: Academic Press, 1992.

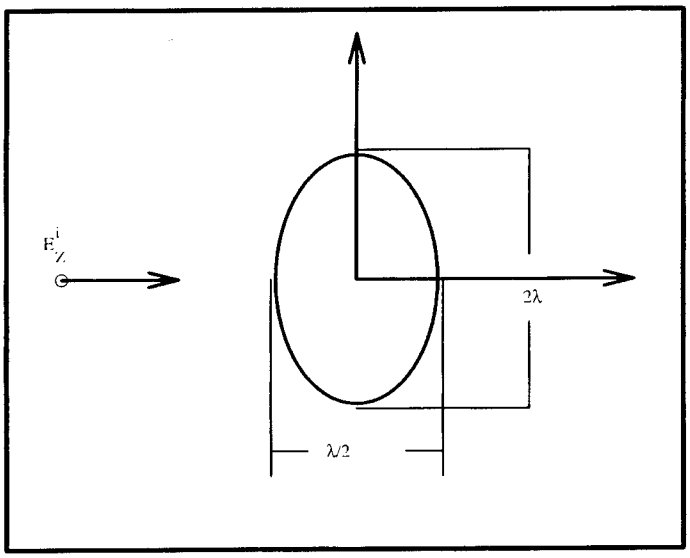


Fig.1 Cross section of an infinitely long metallic cylinder illuminated by TM plane wave

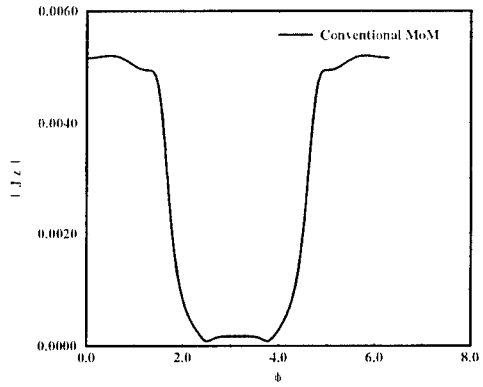


Fig.2 Current density computed using Conventional MoM

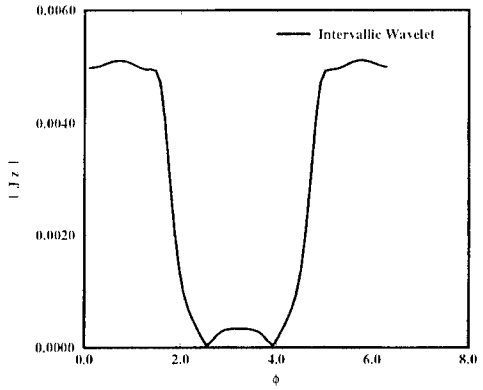


Fig.3 Current density computed using Intervallic Wavelet

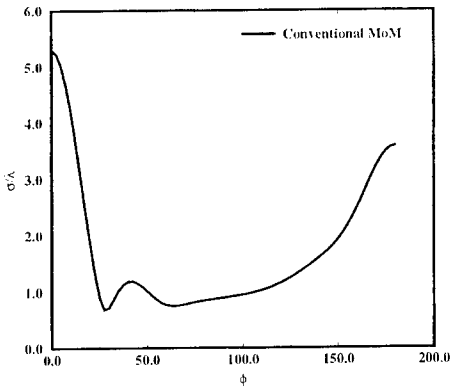


Fig.4 Radar cross section computed using Conventional MoM

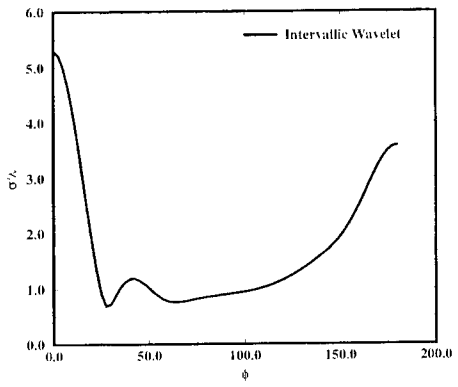


Fig. 5 Radar cross section computed using Intervallic Wavelet

Radar Cross Section Data Reduction Using Wavelets

Azar S. Ali, Serge E. Duval, Randy L. Haupt

Department of Electrical Engineering
2354 Fairchild Dr Suite 2F6
US Air Force Academy, CO 80840

Abstract

To help reduce the data processing burden during target identification from radar cross section data, many time-frequency transforms were investigated. It is found that some transforms show more potential than others. The Daubechies-6, Daubechies-20, and Mallat transforms yielded coefficients which clustered in a useful manner, while the STFT, FFT, Choi-Williams, and Wigner-Ville transforms did not perform as well.

Introduction

There is currently an increased interest in using radar cross section (RCS) data for target identification. To make a correct identification from the early time response, a large amount of radar data has to be analyzed. The processing of such a large amount of data makes the target identification process both costly and slow. Consequently, there is much ongoing work on ways to reduce the amount of data that needs to be processed. Recently Rothwell et al [1], proposed using the Discrete Wavelet Transform to reduce the data storage requirement for target discrimination. In this paper, we investigate various other time-frequency transforms for their potential use in the data reduction process.

Data Acquisition

The data to be processed consist of the measured RCS from two model aircraft: an F-14 and an A-10. The measurements were taken in a direct illumination tapered anechoic chamber at the US Air Force Academy. Measurements were made with a vertically polarized incident wave in a stepped frequency CW mode. Each target was measured at a single elevation in a 360° azimuth scan at 0.5° increments (giving 721 observation angles). For each 0.5° increment, 801 frequency samples were taken equally spaced over a 6-18 GHz band. Each target measurement produced a 801 X 721 (577,521 element) matrix of complex RCS values. This huge data set was then transformed to the time domain via a Chirp-Z IFFT and time gated between ± 2.5 nsecs. Gating was used to better isolate the targets from their surroundings. It also reduced the data set to a 512 X 721 matrix of complex values for each target. The gating window was dimensioned so that it had negligible effect on the data.

Transform Applications

The time domain measurements were analyzed using time-frequency transform tools in order to find characteristic features and to reduce the data size. It is important to notice that in an identification problem, the primary goal is not to reconstruct the original signal using a smaller set of data, but to find proper parameters for each target in order to differentiate them. Most of the information that is kept for reconstruction is irrelevant for identification, since the problem to be solved is a classification problem, which is less demanding than a matching problem. Consequently, we can discard information during the identification process, but cannot do so during signal reconstruction.

Furthermore the larger the data set, the more susceptible it is to environmental disturbances. The ability of each element of the data set to discriminate between targets decreases as the size of the data set increases, since then the identification process is spread over a larger number of parameters. Thus each parameter makes a small contribution towards target identification. This is in contrast to smaller data sets in which the parameters are more robust and not as sensitive to environmental disturbances such as noise and variations in the observation angle.

From this point of view, the data analysis can be done using various transforms, in order to find a few relevant coefficients which can be combined in the decision process. The observation angle is unknown when the identification has to be made, but the radar which is used provides information (speed vector, acceleration, speed vector rotation, etc.) that allows us to define an angle range in which it is located. It is then important to find features that are maintained for several consecutive observation angles. In other words, clustered coefficients must be found.

In the following part of this paper, several transforms are illustrated. Considering the data size, we can classify the transforms into two families. The first one includes the transforms that do not increase the data size: for each 512 X 1 input vector, the output is a 512 X 1 coefficient matrix. The FFT and the Wavelet Transforms belong to this family. With our data, they yield a 512 X 721 output matrix. The second family increases the amount of data: with a 512 X 1 input vector, the output is a 512 X N matrix, with N greater than 1. STFT, Wigner-Ville and Choi-Williams transforms belong to this family, and were applied to selected vectors (512 X 1) that represent the time domain RCS at particular observation angles. All three transforms used a 32-point sliding window. The Wigner-Ville and the Choi-Williams yielded a 512 X 32 matrix of coefficients, while the STFT yielded a 512 X 512 matrix of coefficients for each 512 X 1 input vector.

The Wavelet Transforms were evaluated using the Rice University Toolbox [2]. For an input vector f, the result is stored in a vector W as:

$$W = [H^k f; GH^{k-1}f; GH^{k-2}f; ...; GHf; Gf]$$

where H is a vector containing the low pass filter coefficients which determine the dilation equation. G is a vector containing the band pass quadrature mirror filter coefficients constructed from H, and establishes the wavelet equation $\psi(x)$ in terms of the scale function $\varphi(x)$. The dilation equation is given by:

$$\varphi(x) = \sqrt{2}\sum_{i\in Z} H(i)\varphi(2x-i)$$

and

$$G(i) = (-1)^i H(1-i)$$

$$\psi(x) = \sqrt{2}\sum_{i\in Z} G(i)\varphi(2x-i)$$

Results

In the discussions that follow, we use the word order to describe coefficients. By "order" we mean the rank of the coefficient, i.e. we take the coefficients and rank them in descending order of magnitude, so the 1st order coefficient means the largest coefficient.

Figures 1 shows the azimuth-frequency plane plots for the magnitude of the 1st order FFT coefficients. When the entire azimuth-frequency plane plots of all the coefficients for the FFT were examined simultaneously, no real clustering occurred. The FFT coefficients representing the F-14 did not form a cluster which was distinct from that formed by the coefficients representing the A-10. Actually, the FFT coefficients were randomly scattered all over the azimuth-frequency plane for both targets and so were not very useful for a target identification application. Various other order FFT coefficients were then examined for clustering. For example, we looked at the 2nd, 3rd, and 512th order FFT coefficients. These provided no useful clustering for the magnitude nor the phase of the FFT coefficients.

The Daubechies-6 coefficients were evaluated next. The Daubechies-6 transform was applied separately to the amplitude and the phase of the time domain RCS. The amplitude of the RCS yielded coefficients of some specific orders which clustered in a useful way as shown in Figures 2 through 4. For example, Figures 2 through 4 show the clustering for the amplitudes of the 2nd, 3rd, and 4th order Daubechies-6 coefficients. Since the amplitudes of the above coefficients cluster so distinctly for various angle indices (which correspond to certain observation angle to the aircraft), these coefficients can be used to distinguish between the F-14 and the A-10.

As shown by Figure 2(a), the F-14 has a large number of coefficients clustered around the frequency index 2 for the angle index ranging between 600 and 720 (120 to 180 degrees). Figure 2(b) on the other hand, shows that the A-10 has a large number of coefficients clustered around the frequency index 4 for the same angle index range.

In Figure 3(a), the Daubechies-6 amplitude coefficients of 3rd order clustered around the frequency index 4 for the F-14 for an angle index range of 325 to 425. For this same angle range and coefficient, Figure 3(b) for the A-10 shows clustering around the frequency index 6 and no clustering around 4.

Similar arguments can be made for the 4th order Daubechies-6 amplitude coefficients as shown in Figures 4(a) and 4(b). In Figure 4(b), the A-10 shows good clustering around the frequency index 3 for angle ranges between 500-550, and 650-700. The F-14 in Figure 4(a) shows clustering

around the frequency index 6 for the same angle range. So, when you're in the appropriate observation sector, you can easily distinguish the F-14 from the A-10 by using coefficients of order 2, 3, or 4. There were no distinct clusters for the coefficients obtained with the phase of the RCS.

Azimuth-frequency plots of the Daubechies-20 coefficients for the amplitude of the RCS are shown in Figures 5 and 6. For the 3rd order coefficients of the F-14 as shown in Figure 5(a), there is no clustering around the frequency index 3 for an angle range between 0 and 175. For the A-10 shown in Figure 5(b), the 3rd order coefficient clusters around the frequency index 3 for the same angle range. For the 4th order coefficients, there is distinct clustering for the angle index range between 225 and 325 (-68 to -18 degrees). In this angle range, the 4th order coefficients for the F-14 are clustered around the frequency index 3 while the A-10 coefficients are clustered around 9. The Daubechies-20 coefficients for the phase of the time domain RCS did not cluster in any useful way.

Figures 7 and 8 show the azimuth-frequency plots for the Mallat coefficients of orders 5 and 6 calculated from the amplitude of the RCS. The 5th order Mallat coefficients for the F-14 are clustered around the frequency index 7 for an angle index range between 300 to 400 (approximately -30 to 20 degrees), while those for the A-10 are clustered around the frequency index 5. There is also good clustering for the 6th order coefficients as shown in Figure 8. Consequently, the Mallat coefficients of order 5 and 6 can be used to distinguish between the F-14 and the A-10. There were no distinct clusters for the Mallat coefficients calculated from the phase of the RCS.

Using a 32-point window for the STFT, the Wigner-Ville, and the Choi-Williams transforms, we looked at coefficients for observation angles between -10 and +10 degrees. We found no useful clusters when using any of these three transforms. These transforms are more difficult to use because they increase the data set. Further investigation must be done in order to explore all observation angles, coefficient orders, and other window sizes.

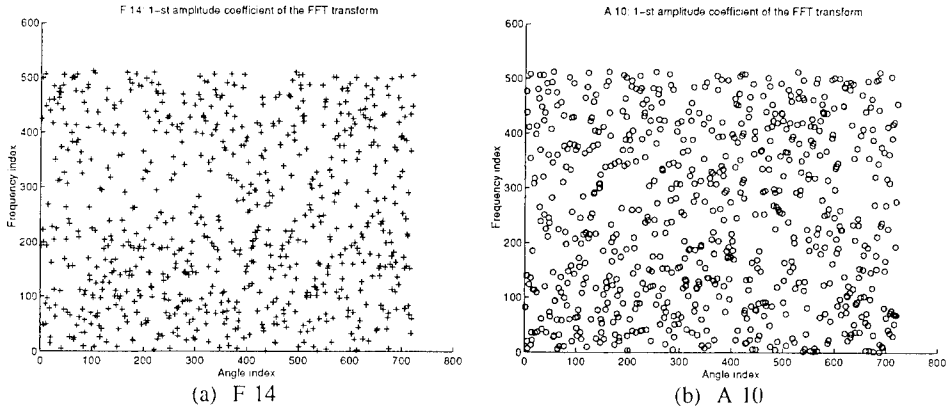
Conclusion

The study made on RCS measurements in order to discriminate two aircraft shows good clustering for some of the transforms used. For that purpose, the Wavelet Transforms seem to be the most promising, but further investigation has to be made on the STFT, Wigner-Ville and Choi-Williams transforms. In addition, the clustered coefficients extend in approximately 50 degree sectors. Therefore the segmentation of the observation angle is compatible with the ambiguity of the target orientation relative to the radar.

References

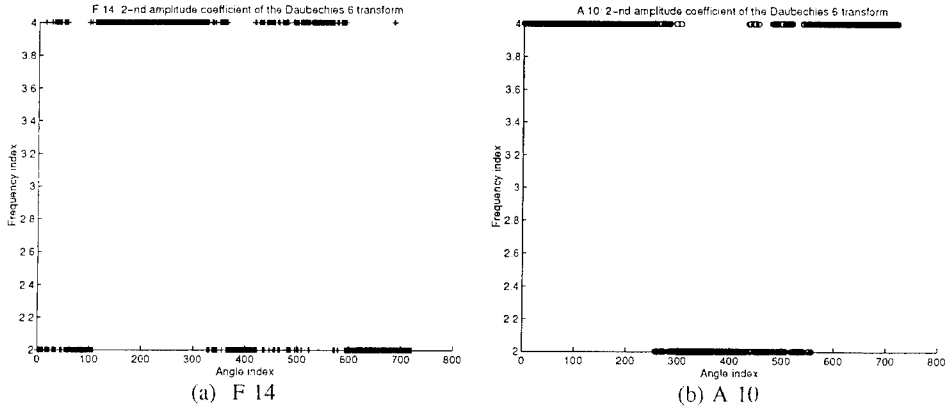
1. Rothwell, E. J., K. M. Chen, D. P. Nyquis, J. E. Ross, and R. Bebermeyer, "A Radar Target Discrimination Scheme Using the Wavelet Transform for Reduced Data Storage", *IEEE Trans. on Antennas and Propagation*, Vol. 42, No. 7, 1033-1037, Jul 1994.

2. J. E. Odegard, Rice University, 1994, ftp from cml.rice.edu in directory /pub/dsp/software.



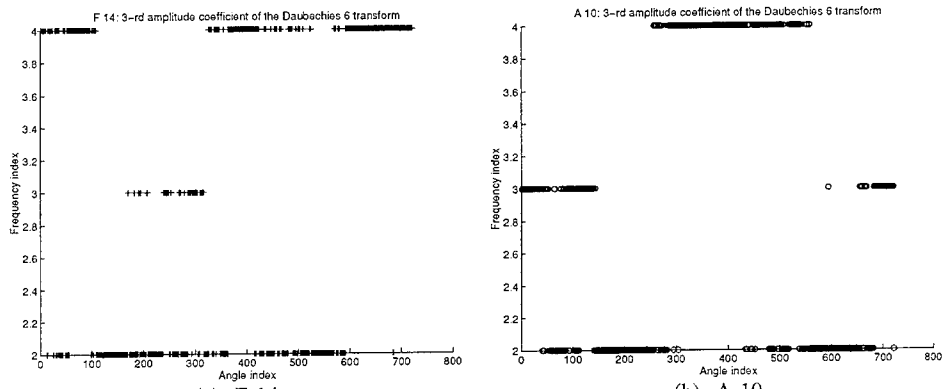
(a) F 14 (b) A 10

FIGURE 1: 1-st amplitude coefficient for the FFT



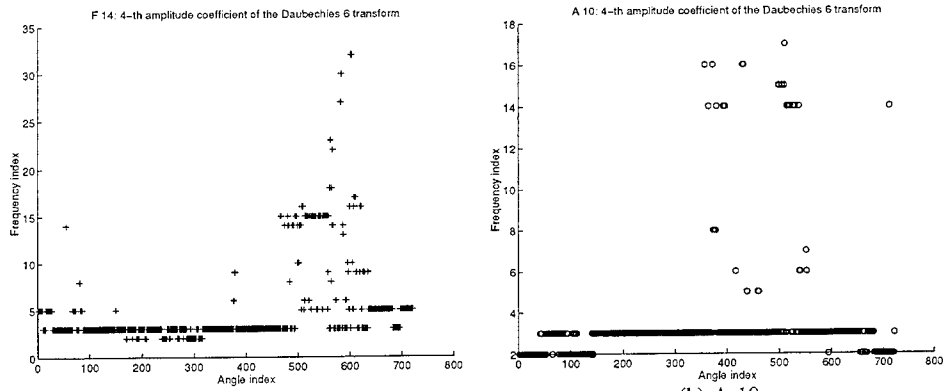
(a) F 14 (b) A 10

FIGURE 2: 2-nd amplitude coefficient for the Daubechies 6 transform



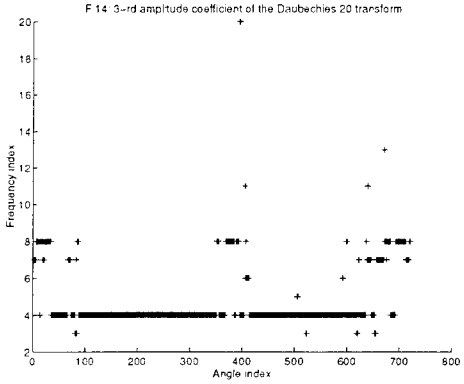
(a) F 14 (b) A 10

FIGURE 3: 3-rd amplitude coefficient for the Daubechies 6 transform

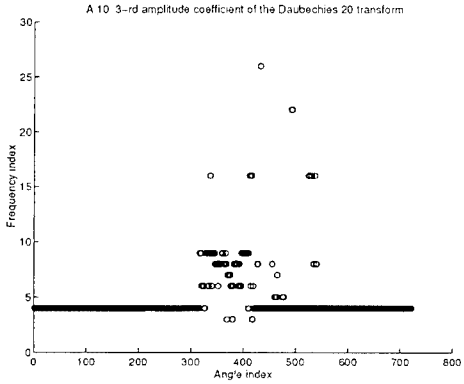


(a) F 14 (b) A 10

FIGURE 4: 4-th amplitude coefficient for the Daubechies 6 transform

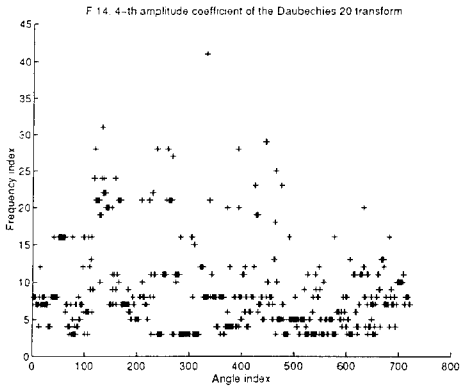


(a) F 14

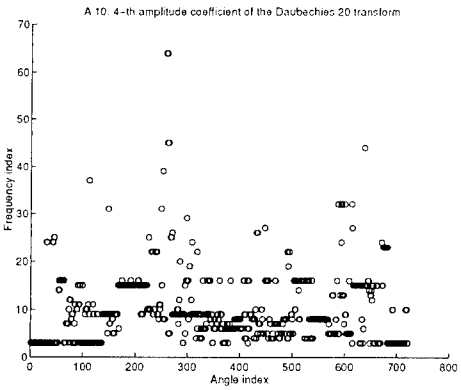


(b) A 10

FIGURE 5: 3-rd amplitude coefficient for the Daubechies 20 transform

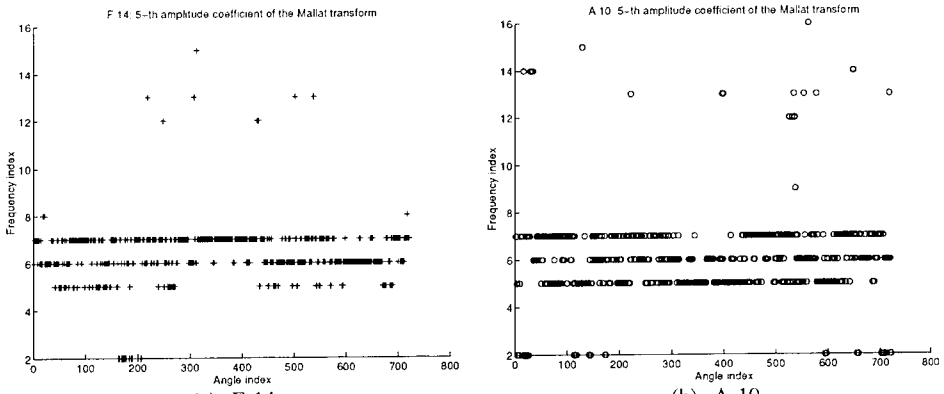


(a) F 14



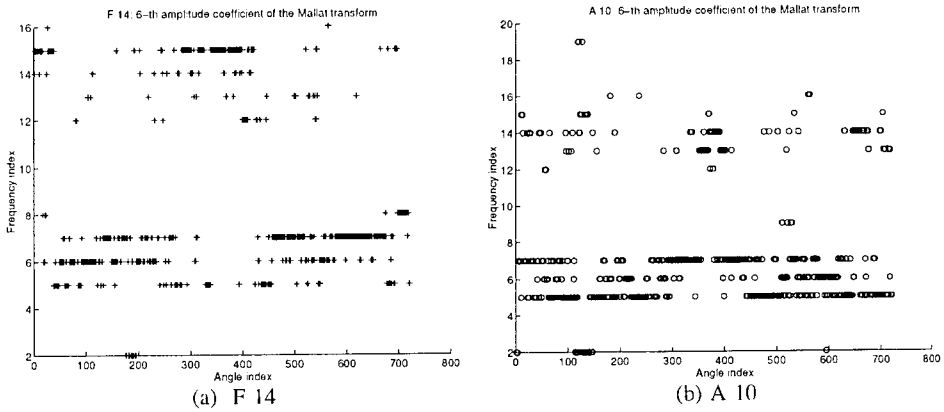
(b) A 10

FIGURE 6: 4-th amplitude coefficient for the Daubechies 20 transform



(a) F 14 (b) A 10

FIGURE 7: 5-th amplitude coefficient for the Mallat transform



(a) F 14 (b) A 10

FIGURE 8: 6-th amplitude coefficient for the Mallat transform

SESSION 19:

NEC APPLICATIONS

Chair: J. Breakall

COMPUTATIONALLY EFFICIENT AND ACCURATE APPROXIMATIONS FOR IMPEDANCE MATRIX ELEMENTS OF NEC-TYPE METHOD OF MOMENTS FORMULATIONS

D. H. Werner
The Applied Research Laboratory
The Pennsylvania State University
P.O. Box 30
State College, PA 16804

S. E. Metker and J. A. Huffman
Department of Electrical Engineering
The Pennsylvania State University
University Park, PA 16802

1. Introduction

The method of moments formulation has proven a powerful tool in the antenna modeling community. The proliferation of low end PC platforms has brought this modeling capability to the average user. With this continuing availability, however, comes the need for faster, less computationally intensive calculations. With only subtle losses in precision, the matrix fill times for many small problems can be drastically decreased.

Several widely used codes which are available to the antenna modeling community, such as NEC and GEMACS, are based on a Method of Moments (MoM) formulation which combines three-term trigonometric basis functions with point matching. The particular form used in this technique to represent the current on segment n is [1]

$$I_n(z) = A_n + B_n \sin \beta (z-z_n) + C_n \cos \beta (z-z_n) \tag{1}$$

such that $|z-z_n| \le \Delta/2$ where z_n denotes the midpoint coordinate of the segment and Δ is the segment length. When computing the elements of the impedance matrix, certain integrals must be evaluated which are related to the constant term, the sine term and the cosine term. The integrals associated with the sine and cosine terms have closed form solutions. On the other hand, because of the presence of the constant term, it is necessary to evaluate generalized exponential integrals of the form

$$E_0^0(\rho,z) = \int_{-\Delta/2}^{\Delta/2} \frac{e^{-j\beta R}}{R} dz' \tag{2}$$

where

$$R = \sqrt{(z-z')^2 + \rho^2} \tag{3}$$

Several methods have been used in the past to compute this integral including numerical integration and some series representations. However, a rigorous evaluation of the generalized exponential integral, the

only non-analytic term in the MoM formulation, takes up a significant portion of the impedance matrix fill time. Fortunately, many of the impedance elements have only a small effect on the moment method solution and, therefore, a high degree of accuracy is not required in their evaluation. This paper presents approximations to the generalized exponential integral which can greatly reduce the computational time while maintaining a high degree of accuracy in the MoM solution. It is shown that the self-impedance terms as well as the adjacent terms, i.e., the terms separated by one segment length, can be accurately and efficiently computed using the first two terms of a recently found thin-wire asymptotic expansion for the generalized exponential integral [2]. All other matrix elements are computed using the far field approximation for the generalized exponential integral. Comparisons of input impedances for various thin-wire antenna configurations are made with a MoM formulation in which a more robust evaluation of the generalized exponential integral is made. Also presented are the corresponding matrix fill times for the approximate and robust MoM codes. In addition to this, comparisons are made of accuracy and efficiency between these codes and the NEC3D code.

2. Impedance Matrix Element Approximations

Numerical integration schemes may be employed to evaluate (2). However, this integral is difficult to evaluate directly using numerical techniques because its integrand is sharply peaked. One common procedure for avoiding this problem is to extract the "singularity" from this integral, which leads to [2]

$$E_0^0(\rho,z) = F_{-1} + \int_{-\Delta/2}^{\Delta/2} \frac{e^{-j\beta R} - 1}{R}\, dz' \tag{4}$$

where

$$F_{-1} = \begin{cases} \ell n\left[\dfrac{\zeta_2 + R_2}{\zeta_1 + R_1}\right], & \zeta_1 > 0 \\ \ell n\left[\dfrac{R_1 - \zeta_1}{R_2 - \zeta_2}\right], & \zeta_1 \le 0 \end{cases} \tag{5}$$

and

$$R_1 = \sqrt{\zeta_1^2 + \rho^2} \tag{6}$$

$$R_2 = \sqrt{\zeta_2^2 + \rho^2} \tag{7}$$

Evaluation of the generalized exponential integral (2) is often accomplished numerically using (4) and can take a significant portion of the total computational time required for a matrix fill operation. Exact series

expansions offer an alternative approach for the efficient as well as accurate evaluation of (2). One form of an exact expression for (2) may be derived by using a Maclaurin series expansion of the complex exponential function contained in the integrand and integrating term by term [2]. The result is

$$E_0^0(\rho,z) = e^{-j\beta R_0} \sum_{n=0}^{\infty} \sum_{k=0}^{n} \frac{(-j\beta)^k (j\beta R_0)^{n-k}}{k!\,(n-k)!} F_{k-1} \tag{8}$$

where

$$F_m = \int_{\zeta_1}^{\zeta_2} R^m \, d\zeta \tag{9}$$

in which $\zeta_1 = -\Delta/2 - z$, $\zeta_2 = \Delta/2 - z$, and $R_0 = \sqrt{z^2 + \rho^2}$. Closed form solutions can be obtained for the integrals F_{-1} and F_0 while a recurrence relation can be used to determine the higher order integrals F_m for $m \geq 1$. The solution to F_{-1} is given in (5), while $F_0 = \Delta$ and

$$F_m = \frac{1}{(m+1)} \left[\zeta_2 R_2^m - \zeta_1 R_1^m + m\rho^2 F_{m-2} \right] , \quad m \geq 1 \tag{10}$$

Another exact representation of (2) was recently derived in [2]. This expansion is simplified in [3] and takes the form

$$E_0^0(\rho,z) = J_0(\beta\rho) \ln(\gamma_1/\gamma_2) + \sum_{m=1}^{\infty} \frac{(-j)^m}{m!} J_m(\beta\rho) \left[\gamma_1^m - \gamma_2^m - \gamma_1^{-m} + \gamma_2^{-m} \right] , \quad |z| \geq \Delta/2 \tag{11}$$

and

$$E_0^0(\rho,z) = J_0(\beta\rho) \ln(\gamma_1 \gamma_2) + \sum_{m=1}^{\infty} \frac{(-j)^m}{m!} J_m(\beta\rho) \left[\gamma_1^m + \gamma_2^m - \gamma_1^{-m} - \gamma_2^{-m} \right] , \quad |z| \leq \Delta/2 \tag{12}$$

where

$$\gamma_1 = \eta_1 + \sqrt{\eta_1^2 - 1} \tag{13}$$

$$\gamma_2 = \eta_2 + \sqrt{\eta_2^2 - 1} \tag{14}$$

$$\eta_1 = \frac{\sqrt{(|z| + \Delta/2)^2 + \rho^2}}{\rho} \tag{15}$$

$$\eta_2 = \frac{\sqrt{(|z| - \Delta/2)^2 + \rho^2}}{\rho} \tag{16}$$

For thin wires, a small argument approximation for Bessel functions can be used to find asymptotic representations of (11) and (12) [4]. The resulting asymptotic expansions are

$$E_0^0(\rho,z) \sim a_0 + \sum_{m=1}^{\infty} \frac{(-j)^m}{m\, m!}\, c_m \quad \text{as} \quad \beta\rho \to 0 \quad \text{and} \quad z = 0 \tag{17}$$

and

$$E_0^0(\rho,z) \sim b_0 + \sum_{m=1}^{\infty} \frac{(-j)^m}{m\, m!}\, d_m \quad \text{as} \quad \beta\rho \to 0 \quad \text{and} \quad |z| \geq \Delta/2 \tag{18}$$

The quantities found in (17) and (18) are given by

$$a_0 = 2\,\ell n\,(\sigma) \tag{19}$$

$$b_0 = \ell n\,(\gamma_+/\gamma_-) \tag{20}$$

$$c_m = 2\left(\frac{\beta\rho}{2}\,\sigma\right)^m \tag{21}$$

$$d_m = \left(\frac{\beta\rho}{2}\gamma_-\right)^m - \left(\frac{\beta\rho}{2}\gamma_+\right)^m \tag{22}$$

and

$$\sigma = \frac{\sqrt{(\Delta/2)^2 + \rho^2} + \Delta/2}{\rho} \tag{23}$$

$$\gamma_\pm = \frac{\sqrt{(|z| \pm \Delta/2)^2 + \rho^2} + ||z| \pm \Delta/2|}{\rho} \tag{24}$$

A MoM code was developed using the trigonometric basis functions of (1) with extrapolated continuity and point matching. The code results were compared using several methods for evaluating the generalized exponential integral (2) required for the calculation of impedance matrix elements. The first option in the code, which will be called the robust option, evaluates E_0^0 using (8) for the self-impedance cases. All other cases use a three point Gaussian quadrature numerical procedure to compute E_0^0 as expressed in (4). This technique results in extremely accurate values for the generalized exponential integral and the corresponding impedance matrix elements.

A second option in the code, the approximate option, evaluates E_0^0 using (17) and (18). In particular, for self-impedance cases ($z = 0$), the approximate option computes the first two terms in (17) and for the adjacent mutual impedances ($|z| = \Delta$), the approximate option computes the first two terms in (18) such that

$$E_0^0 \approx 2\ln(\sigma) - j\beta a\sigma \,, \quad z = 0 \quad \text{and} \quad \rho = a \tag{25}$$

$$E_0^0 \approx \ln(\gamma_+/\gamma_-) + j\frac{\beta a}{2}(\gamma_- - \gamma_+) \,, \quad |z| = \Delta \quad \text{and} \quad \rho = a \tag{26}$$

All other mutual impedance terms are computed by using the far field approximation to evaluate E_0^0 [5]

$$E_0^0 \approx \Delta \frac{e^{-j\beta R_0}}{R_0} \tag{27}$$

Both thin-wire options are valid for computing the impedance matrix in the MoM formulation for wires with radii $a \leq 1\times10^{-3}\lambda$ and a segment length-to-radius ratio $\Delta/a \geq 8$. The approximate thin-wire option offers increased efficiency in filling the impedance matrix because only analytic expressions are used in the formulation while the robust thin-wire option uses a more rigorous and, consequently, more accurate

calculation of E_0^0.

Table 1 shows a comparison of the input impedance of a half-wave dipole for various radii computed using the two options available in the code. The dipole was divided into 21 segments. Relative percent errors for the input impedance, Z_{in}, input resistance, R_{in}, and input reactance, X_{in} were computed using the results from the robust and approximate options such that

$$\% \text{ error} = \left| \frac{\text{robust} - \text{approximate}}{\text{robust}} \right| \times 100 \qquad (28)$$

Errors remain small for all cases, indicating that reasonable accuracy can be obtained with the approximate thin-wire option.

Table 1. Input Impedance of a 21 Segment Half-Wave Dipole for Various Wire Radii

Radius (λ)	Z_{in} (Ω) (robust) (approximate)	% error, Z_{in}	% error, R_{in}	% error, X_{in}
1×10^{-7}	75.8527 + j41.4588 75.8574 + j41.4958	4.318×10^{-2}	6.281×10^{-3}	8.930×10^{-2}
1×10^{-6}	76.5108 + j41.7338 76.5170 + j41.7802	5.374×10^{-2}	8.097×10^{-3}	1.112×10^{-1}
1×10^{-5}	77.5600 + j42.1846 77.5688 + j42.2468	7.112×10^{-2}	1.134×10^{-2}	1.474×10^{-1}
1×10^{-4}	79.5047 + j43.0631 79.5194 + j43.1569	1.050×10^{-1}	1.854×10^{-2}	2.178×10^{-1}
1×10^{-3}	84.4198 + j45.4769 84.4571 + j45.6634	1.984×10^{-1}	4.418×10^{-2}	4.102×10^{-1}
1×10^{-2}*	97.8659 + j45.1660 96.3048 + j44.4417	1.597	1.595	1.604

* Segmentation of half-wave dipole reduced to seven in order to satisfy Δ/a ratio for thin-wires.

For most of the non-adjacent mutual impedance calculations, the approximate technique for evaluating E_0^0 discussed above works very well. However, for separate wires which lie close together, i.e. within a segment length Δ, a more accurate form is used. For these cases, the MoM code uses the first two terms of the Maclaurin series expansion given in (8). That is,

$$E_0^0 \approx e^{-j\beta R_0} \left[F_{-1}(1 + j\beta R_0) - j\beta \Delta \right] \qquad (29)$$

Accuracy of the robust and approximate thin-wire options is illustrated in Table 2 where input impedance results are shown for a half-wave dipole, a three element Yagi-Uda and a simple tee antenna. The geometry of the multiple wire antennas are illustrated in Figure 1 where the wire radii are $a=1x10^{-6}\lambda$ in all cases. The results are compared with NEC3D which is known to be a reliable thin-wire antenna modeling code.

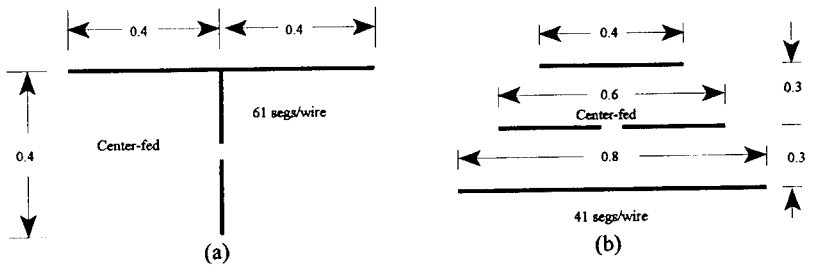


Figure 1 - a) Tee Antenna ; b) Yagi-Uda Antenna. Note that the figures are not drawn to scale and all distances are in wavelengths.

The difference between the PSU MoM code and NEC3D is primarily due to the extrapolated current continuity method used by the PSU code. NEC3D relies on a more mathematically intensive current and charge continuity method to enforce boundary conditions between segments. However, the differences between the two PSU code options shows that using the approximate method for calculation of the generalized exponential integral results in a negligible loss in precision.

The advantages of the approximate method are revealed, however, in terms of matrix fill time. As an indication of the efficiency obtained using the options within the PSU MoM code, execution times in filling the impedance matrix for the three antenna configurations were measured and compared to the fill time associated with NEC3D. NEC3D uses a time-consuming adaptive Romberg technique to numerically evaluate E_0^0 using the form given in (4). As shown in Table 3, the approximate integral calculation has decreased the matrix fill time by about 25% from the robust formulation with no significant change in the input impedance. It is expected that larger and more complex structures will show similar results since the approximations are more accurate when the source point and field point are separated by a greater distance.

In method of moments, a critical analysis of where computational time is spent can be educational. Isolating problem areas and potential bottlenecks are essential to increasing computational speed. Here, we see that certain MoM codes may potentially spend a majority of time calculating the generalized exponential integral to a needless precision. As expected, only the self and nearby adjacent terms contribute significantly to the impedance matrix thereby rendering many highly precise calculations unnecessary.

Table 2. Input Impedance Results

	NEC3D	PSU MoM (robust) (approx.)	% Error (robust vs. approx.)
Half Wave Dipole	77.775 + j44.501	76.830 + j43.581 76.837 + j43.601	1.860×10^{-2}
Yagi-Uda (3 element)	162.44 + j569.52	164.93 + j572.17 164.91 + j 571.63	8.663×10^{-2}
Tee Antenna	311.68 - j2848.6	301.43 - j2807.7 301.67 - j2805.0	9.523×10^{-2}

Table 3. Matrix Fill Times

	NEC3D	PSU MoM (robust)	PSU MoM (approx.)	% Improvement (robust vs. approx.)
Half Wave Dipole	3.84 sec	1.05 sec	0.77 sec	26.6
Yagi-Uda (3 element)	5.60 sec	1.59 sec	1.15 sec	27.7
Tee Antenna	12.25 sec	3.46 sec	2.64 sec	23.7

References

[1] Y. S. Yeh and K. K. Mei, "Theory of conical equiangular-spiral antennas Part I - Numerical techniques," *IEEE Trans. Antennas Propagat.*, vol. AP-15, pp. 634-639, Sept. 1967.

[2] D. H. Werner, "An exact formulation for the vector potential of a cylindrical antenna with uniformly distributed current and arbitrary radius," *IEEE Trans. Antennas Propagat.*, vol. 41, pp. 1009-1018, Aug. 1993.

[3] D. H. Werner, "Author's reply to the comments of A. E. Gera," *IEEE Trans. Antennas Propagat.*, vol. 42, pp. 1201-1202, Aug. 1994.

[4] D. H. Werner, P. L. Werner, J. A. Huffman, A. J. Ferraro and J. K. Breakall, "An exact solution of the generalized exponential integral and its application to moment method formulations," *IEEE Trans. Antennas Propagat.*, vol. 41, pp. 1716-1719, Dec. 1993.

[5] R. F. Harrington, *Field Computation by Moment Methods*, New York, MacMillan, 1968.

Development of the Coupled-Resonator Antenna Principle

A Computer Modeling Case History

Gary A. Breed
Crestone Engineering
7318 S. Birch Street
Littleton, Colorado 80122

Introduction

This paper describes the role of a commercial antenna modeling program in the development of a patent-pending method for the design and construction of multiple-frequency antennas. Without a reliable computer model, characterization of the principle that underlies this design method would have required extensive experimentation which, in this case, would have been impractical to conduct. Modeling not only made it possible to obtain data from which design equations could be derived, but various nuances and subtleties of the principle have been identified which would likely have remained undiscovered from purely empirical data.

The Coupled-Resonator Principle

It is well known that conductors in proximity to one another exhibit strong mutual coupling. A design technique called the Coupled-Resonator (C-R) principle [1] has been developed which uses this coupling to advantage. The C-R principle defines the conditions for optimum coupling, creating a system with multiple resonant frequencies, driven at a single feedpoint. Such a multiple-resonant structure consists of a driven dipole or monopole at the lowest frequency of operation, with additional resonant conductors surrounding it, placed at the appropriate distances.

Figure 1 demonstrates the C-R principle in its simplest form, a two-frequency system. A half-wavelength driven dipole is resonant at some frequency, F_1, and driven at the center. A typical return loss sweep for such a dipole is depicted in Figure 1(a). In Figure 1(b), an additional conductor, half-wavelength resonant at an arbitrarily-chosen higher frequency, F_2, is placed nearby. Coupling between this conductor and the driven dipole creates a return loss sweep, observed at the dipole feedpoint, which shows a "bump" at the resonant frequency of the second conductor.

The main premise of the Coupled-Resonator principle is that there is an optimum spacing between conductors where the coupling results in a matched condition at F_2, as sketched in Figure 1(c). The effect at F_1 is minimal, and the system is matched at both frequencies.

The above description also applies to systems where the driven element is a monopole fed against ground, given the equivalence of a monopole and dipole. In this case, the feedpoint impedance of a monopole will be one-half that of an equivalent dipole.

This two-frequency example can be expanded to three, four, five or more frequencies by adding additional resonators and placing them radially around the fed dipole or monopole, as shown in Figure 2. A practical upper limit on the number of frequencies this structure will support is reached when the complexity of multiple interactions

obscures the desired coupling. Systems up to seven frequencies have been successfully modeled. Five-frequency systems have been constructed and readily tuned and matched at the desired resonant frequencies.

Design Equations

The variables involved in the design of antennas using the C-R principle are: conductor diameter, conductor spacing, feedpoint impedance, and the ratio of frequencies. These are all defined from the point of reference of the additional frequency under consideration, F_n.

Conductor spacing follows this general relationship:

$$\frac{\text{Log (d)}}{\text{Log (D/4)}} = .54$$

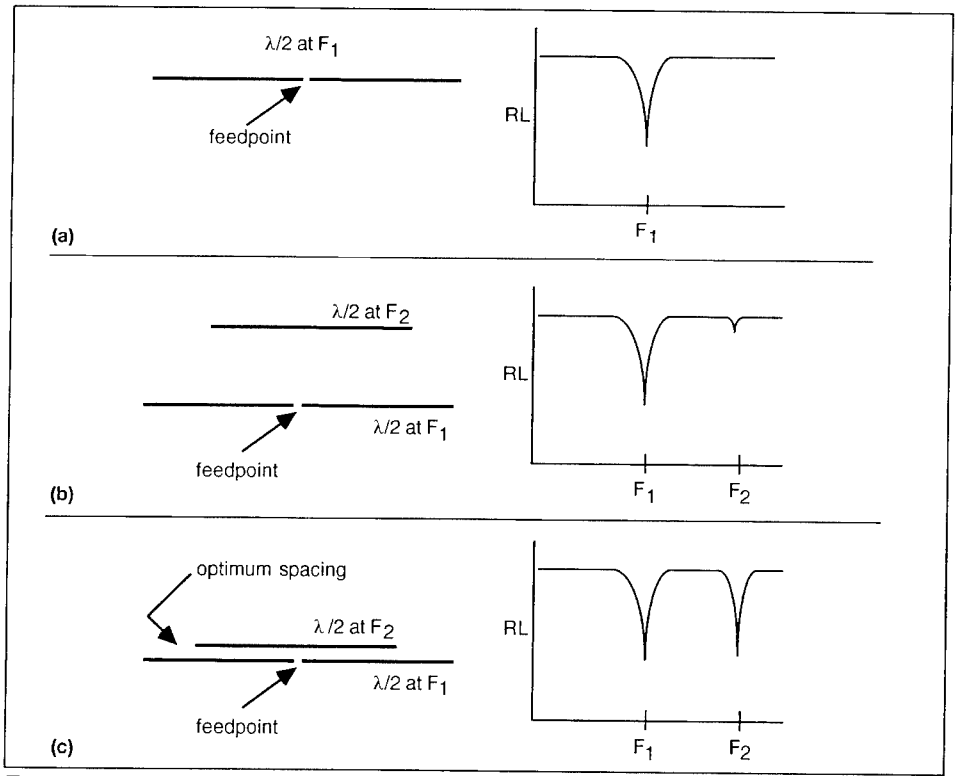


Figure 1. Coupled-resonator behavior: (a) shows a simple dipole and its return loss sweep through resonance at F_1; (b) illustrates the effect of an additional conductor, resonant at F_2, placed in the vicinity of the first dipole, and; (c) shows how a two-frequency system appears when the spacing between the conductors is optimum.

where d is the distance between conductors and D is the diameter of the conductors, both expressed in wavelengths at F_n. This approximation is normalized for a feedpoint impedance at F_n equal to that of the dipole in free space (72 ohms) or a monopole over perfect ground (36 ohms), and for an F_n/F_1 ratio of 1.3 or greater.

The equation can be modified to allow for a wider range of impedances and lower F_n/F_1 ratios. Using a straight-line approximation for impedance and a first-order $1/e^{-x}$ curve-fit for frequency ratio correction, the original equation then becomes:

$$d_{1n} = 10^{[0.54\mathrm{Log}(D/4)]} \times \frac{Z_0 + 35.5}{109} \times [1 + e^{-[(((F_n/F_1)-1.1)\times 11.3)+0.1]}]$$

where,

Z_0 is the desired feedpoint impedance at F_n, within the range of 25 to 125 ohms.
F_1 is the resonant frequency of the driven dipole
F_n is the resonant frequency of the additional resonator
F_n/F_1 frequency ratio is greater than 1.1:1
d is in the range of 0.01 to 0.00001 wavelength

A significant characteristic is independently control of impedance at each frequency, F_2, F_3 ... F_n. Adjustment of the spacing, combined with the reactance change as antenna length is altered, allows a wide range of adjustment.

There are two additional characteristics that can be explained by the simplified equivalent circuit shown in Figure 3. At F_n, the feedpoint impedance is the combination of Z_1, the impedance of the driven dipole or monopole, and Z_n, the coupled-resonator impedance, plus Z_x, which is the total effect of any other resonators in the system (predominantly capacitance). Compensation for Z_x is readily achieved by simply lengthening the F_n resonator (typically 0.25 to 0.5 percent) to add inductance.

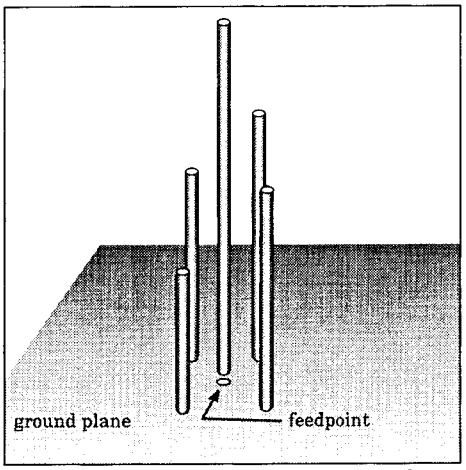


Figure 2. Pictorial of a five-frequency C-R antenna in monopole configuration.

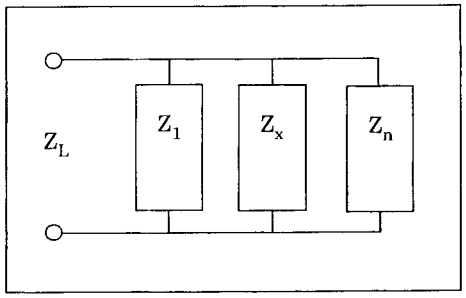


Figure 3. Simplified equivalent circuit of a C-R antenna system at F_n.

Another effect is an apparent anomaly that occurs when the ratio of F_n/F_1 is approximately 3, where a significant increase in the spacing is required to achieve the desired impedance. This is readily explained by noting that the driven dipole has a relatively low impedance at 3/2 wavelength (3/4 wavelength for a monopole). In this case, Z_n must be higher than normal to achieve the desired parallel combination of Z_1 and Z_n, which corresponds to a greater spacing distance.

Radiation Characteristics

Antennas designed according to the C-R principle are accurately modeled using method-of-moments analysis, including software based on either the Numerical Electromagnetics Code (NEC) or MININEC3. The program used for development of this antenna technique was ELNEC [2]. in most configurations, the directivity (gain) is very close to that of a simple dipole at all frequencies, suggesting that radiation is primarily from the resonant conductor. Some frequencies exhibit a slight gain over a dipole, suggesting that in-phase current is present in the portion of the driven dipole which extends beyond the active region. Analysis of the currents verifies these conclusions. A later section details the role of modeling in determining antenna behavior.

Advantages and Limitations

The principal advantage of this antenna design is the absence of reactive components, such as tuned circuits or capacitively-loaded coaxial stubs, which are often used to achieve multi-frequency operation. These components may introduce losses, or require time-consuming tuning adjustment. The C-R antenna design achieves its performance by controlling the physical dimensions of conductor length, diameter and spacing.

Another significant advantage is that the feedpoint impedance at each additional frequency can be controlled by adjustment of resonator spacing and length. For example, when a C-R antenna element is placed in an array, the driving point impedances can be significantly different at each operating frequency. The C-R principle allows each frequency's resonator to be adjusted over a useful range of resistance and reactance.

Two limitations should be noted. First, the tradeoff for electrical simplicity is a relatively complex mechanical assembly. The structure must support a central dipole or monopole and maintain spacing with the additional resonators with insulators or other means. However, it should be noted that other multi-frequency configurations also have special construction requirements. The other limitation of the C-R method is a reduction in VSWR bandwidth at F_2, F_3 and higher frequencies of operation, compared to a simple dipole or monopole. This shortcoming can be mitigated by the use of large-diameter conductors, or in extreme cases, additional resonators with overlapping coverage. Again, other common multi-frequency antenna designs also exhibit reduced bandwidth.

The Role of Computer Modeling in Development

While investigating various configurations of multiband antennas for possible amateur radio use, the open-sleeve antenna was evaluated. The open-sleeve is a derivative of the coaxial dipole, in which a simple dipole or monopole is enclosed by a coaxial sleeve that is approximately one-half the length of the driven element, and resonant at about twice the frequency. The open sleeve reduces the configuration to two conductors that represent a "skeleton" of the original coaxial sleeve. This antenna is well known, having been developed in the 1940s and included in several major reference texts [3].

Descriptions of these antennas referred to the coaxial or open-sleeve section as a transmission line transformer. An intuitive conclusion was made that the current distri-

bution and radiation patterns calculated by ELNEC were not consistent with a transformer model. Once this conclusion was reached, it was a logical step to assume that two conductors were unnecessary, since the simulation of a coaxial line was not required, hence, the concept of a single additional conductor for each new frequency of coverage (see the sequence illustrated in Figure 4).

Without the restrictions of a simulated coaxial line, the structure of a antenna using a coupled resonator element becomes much simpler. The first expansion of the concept was to evaluate an antenna with more than one additional resonator. A three-frequency design was modeled successfully, with current distribution and radiation pattern analyzed at each frequency. This model confirmed that each additional resonator operated independently — maximum current occurred in whichever conductor was resonant, and the radiation pattern was dipole-like at each frequency. More complex models of four, five, six and seven frequency antennas further reinforced the original concept, while uncovering new performance characteristics.

Construction of Trial Antennas

Before continuing, validation of the accuracy of the model was deemed highly desirable. At this point, all work on the C-R concept had been performed on the computer. It was time to build some antennas.

The first antenna was constructed one step at a time. A dipole for the 14 MHz amateur band was built from aluminum tubing, tapering from 1-1/4" to 5/8" diameter. An average uniform diameter of approximately 1" was assumed for the computer model. Next, a conductor resonant in the 21 MHz band was placed in parallel with the 14 MHz dipole, at a distance of 7" o.c. Plastic spacers were used to maintain uniform spacing. As predicted, the 21 MHz resonance was seen at the feedpoint, and the resonance (nonreactive feedpoint impedance) of the 14 MHz moved slightly higher in frequency. The capacitance introduced by the new conductor explains the frequency shift. Finally, a third conductor resonant in the 28 MHz band was added in the same manner, placed on the opposite side of the 14 MHz fed dipole for maximum isolation from the 21 MHz res-

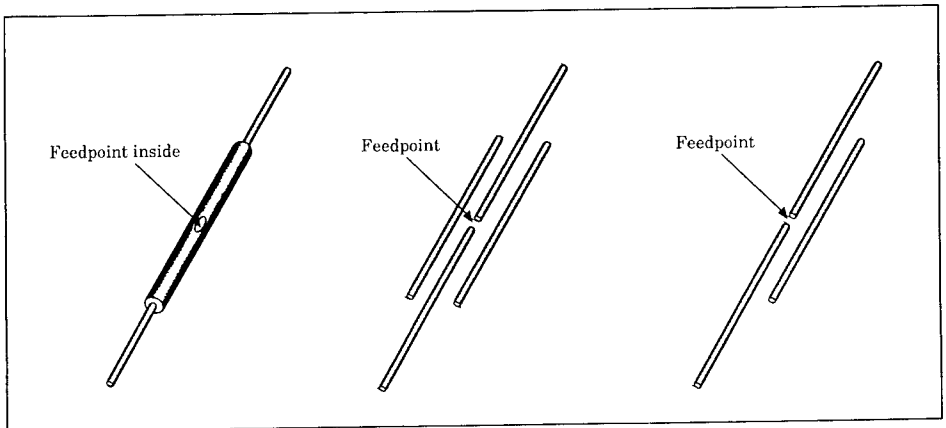


Figure 4. Evolution of the coupled-resonator principle. (left) The coaxial sleeve dipole; (center) the coaxial sleeve reduced to two parallel lines in the open-sleeve dipole; and (right) the C-R antenna with a single additional conductor. All are equivalent structures.

onator. The new resonance appeared at the feedpoint as expected, with another small shift in the resonant frequency at 14 MHz.

An additional characteristic was evaluated at this time — VSWR bandwidth. The model had predicted that this system would have a narrower bandwidth between 2:1 VSWR points at both 21 and 28 MHz, compared to a simple dipole at each frequency. the highest frequency would have the most pronounced narrowing. The measured bandwidth at 28 MHz was 400 kHz, about 10-15 percent greater than predicted, a reasonable accuracy for a modest experiment.

On-the-air amateur radio contacts were made using this antenna, and although a calibrated comparison antenna was not available, based on the author's experience, performance was within the expected range for a dipole.

An additional antenna completed the early tests to confirm the validity of the models. A dipole for the 18 MHz and 24 MHz amateur bands was constructed from #12 copper wire, with a series of plastic spaces used to maintain the computer-modeled 2" spacing. Performance was obtained as predicted, with one behavior of note. The VSWR at 24 MHz varied over a wide range versus the height above ground. Although this is a well-known phenomenon, the degree of variation was greater than expected, and greater than observed with the earlier antenna. Evaluating this characteristic using the computer model, the variation was confirmed. Apparently, the combination of closer spacing and tighter physical tolerances required for the small-diameter wire conductors is the cause. The lower Q of the aluminum tubing construction minimized these effects.

Development of Design Equations

Having confirmed the validity of the ELNEC model for antennas using the Coupled-Resonator principle, a methodical search was undertaken to establish design equations. After some very preliminary calculations to establish the likely nature of the equation, the following parameters were evaluated for the simplest two-frequency case:

- Required spacing versus conductor diameter, with a fixed 2:1 frequency ratio.
- Spacing versus frequency ratio, with fixed conductor diameter
- Spacing versus resistive component of impedance, with fixed conductor diameter
- Determine appropriate frame of reference

First, models were created and iterations performed to gather data to tabulate the required spacing for element diameters of 0.00001, 0.0001, 0.001 and 0.01 wavelength diameters. The dimensions for both diameter and spacing were referenced to the additional frequency, F_n, and for an impedance equal to a dipole in free space, or 72 ohms. The data were only collected for the case where both the driven dipole/monopole and the additional resonator were the same diameter. When plotted, the data made a nearly straight-line fit on a log-log scale. Weighting the data in favor of the spacing distance resulted in a a more accurate log-log curve fit, resulting in the basic equation:

$$\frac{\text{Log d}}{\text{Log (D/4)}} = .54 \qquad (1)$$

where, d is the center-to-center spacing distance and D is the element diameter, both expressed in wavelengths at F_n.

Next, data were collected to determine the deviation from the above equation for fre-

quency ratios other than 2:1. Diameters were held constant while the frequency (and element length, of course) was varied from a ratio F_n/F_1 of 1.1 to 5.0. The data were collected using both 0.01 and 0.0001 wavelength diameters. Above a ratio of 1.4, the spacing was essentially the same as required for the 2:1 ratio of (1). From a ratio of 1.4 down to 1.1, the required spacing increased in a curve that appeared to be classic $1/e^{-x}$ function. A first-order fit to this curve provides the following correction factor for (1):

$$1 + e^{-[(((Fn/F1) - 1.1) \times 11.3) + 0.1]} \qquad (2)$$

At this point, a special case should be noted. The required spacing deviates from a regular function at a F_n/F_1 ratio of 3. At this point, the impedance of the driven dipole is relatively low, being 3/2 λ. The impedance of the coupled-resonator element must be higher than usual for the parallel combination to equal the desired 72 ohms. This is an anomalous situation and is not reflected in the design equations, which are believed to accurately describe the impedance contributed by the additional resonator.

Finally, holding the frequency ratio constant at 2, the variation in spacing required to obtain a resistive component of impedance other than 72 ohms was determined. This data was plotted, resulting in a shallow curve on a linear scale. Over the range of 25 to beyond 120 ohms, the following linear expression is accurate to within 5 to 10 percent:

$$\frac{Z_0 + 35.5}{109} \qquad (3)$$

Applying the corrections of (2) and (3) to equation (1) gives the basic design equation for a Coupled-Resonator element:

$$d_{1n} = 10^{[0.54 \text{ Log } (D/4)]} \times \frac{Z_0 + 35.5}{109} \times [1 + e^{-[(((Fn/F1) - 1.1) \times 11.3) + 0.1]}] \qquad (4)$$

This equation is not presented as a rigorous description, rather it serves as a basis for design and optimization. In general, the spacings determined using this equation are accurate within 5 to 10 percent, even in systems of five or more frequencies. Also, (4) does not describe systems with unequal diameter elements. An approximation using the mean diameter of the driven and additional elements is an adequate starting point if the variation in diameters is modest. Optimization will then complete the task of determining the proper spacing.

The design equation of (4) also does not include element length. In general, lengths are similar to those required for half-wavelength dipoles of the same diameter, as noted in all major antenna reference texts. However, the exact length involves two additional variables — the effects of all additional conductors (capacitance), and the parallel combination of the driven dipole impedance and the Coupled-Resonator impedance. In practice, the variation in length is less than one percent from a normal dipole length in the majority of configurations. Greatest variations have been found with extreme F_I/F_n ratios (e.g. greater than 5), and in systems with large numbers of additional resonators and a relatively small maximum F_I/F_n (2.5 or less).

Additional refinement of the design equation would be desirable, and suggestions have been made at a few engineering schools that this might be a good project for a

graduate-level student. The main conclusion that can be drawn from the work done so far is this — It appears clear that the derivation of an accurate and complete design equation is a straightforward task. What remains to be done is the characterization of the interactions of the driven, resonant and non-resonant conductors (primarily capacitance) and the inclusion of the impedance of the driven element, which is seen in parallel with the impedance of the resonant coupled element.

Conclusions

The ability to simulate this antenna configuration on a computer was essential to its development. The MININEC-based ELNEC program was used, and its accuracy was verified by the construction of several test antennas using various numbers and sizes of conductors. Once validity of the model was established, a large number of iterations could then be performed to collect data to establish the basic relationships among physical dimensions, resulting in a useful design equation which has a minimum of constraints.

References

1. G. Breed, "A Method of Constructing Multiple-Frequency Dipole or Monopole Antenna Elements Using Closely-Coupled Resonators," Application for Patent, July 1994.

2. ELNEC, available from Roy Lewallen, P.O. Box 6658, Beaverton, OR 97007.

3. e.g., R. Johnson, *Antenna Engineering Handbook*, Mc-Graw-Hill, Third Ed., 1993.

Appendix

Notes on the Patent Application and Prior Art

Like all "discoveries," the Coupled-Resonator principle described in this paper is based in part on the work of others, having been initiated by an examination of the open-sleeve antenna. In addition, several specific antenna configurations are known which incorporate some characteristics described here and in the referenced patent application.

The intended contribution of this discussion is that the Coupled-Resonator concept be recognized as a *basic antenna design principle* that can be widely applied. In this light, all parasitic antennas, such as Yagi-Uda arrays and the coaxial and open-sleeve antennas, are specific applications of this fundamental principle. The scope of the patent application is the use of this principle to create dipole and monopole antenna elements which cover up to seven, and possibly more, frequencies.

It is hoped that further development of the work begun here will result in improved understanding of the behavior of conductors in proximity. The analysis tools are in place to accurately model the behavior of various configurations, but work remains to be done to develop complete synthesis tools that implement specific designs using the C-R relationships.

ANTENNA DESIGN AND DEVELOPMENT USING NEC-WIN

Todd A. Erdley, Jeffrey J. Shapiro, Joel S. Young
Paragon Technology, Inc.
200 Innovation Blvd., Suite 240
State College, PA 16803

James K. Breakall
Department of Electrical Engineering
The Pennsylvania State University
University Park, PA 16802

NEC-WIN is a graphically oriented antenna design and optimization program based on the Numerical Electromagnetics Code core. NEC-WIN provides a wide range of powerful features which significantly enhance the ability of the antenna designer to quickly and efficiently analyze even the most complex antenna structures. The program is based in Windows and it has taken advantage of the graphical nature of Windows to provide an enhanced interface for the NEC commands. While users will still be able to enter NEC commands as they have done previously, they will also be able to access graphical assisted commands which prompt the user for the required data.

User's efficiency is further enhanced using the three dimensional viewing capability of the program. Using NEC-VU, the designer has instant access to a graphical representation of the structure during the data entry process. NEC-VU can be used to visualize the antenna using rotate, zoom and pan features. Furthermore, the designer has the ability to analyze the structure in order to verify wire connections and placement. This process is further enhanced by using NEC-VU's configuration capability to highlight non-connected wires. Once a wire without a connection is found, the user can access the edit mode and use a cursor to highlight the wire. NEC-VU indicates which wire number is highlighted and where the wire was created in the input file.

After successfully creating the input file, the user can process the file within NEC-WIN as a standard NEC file or with optimization capability, depending on the functions that were selected in the input file. NEC-WIN provides a comprehensive plotting capability for visualizing the results. The user can select line type, line width and line color for various sets of data to be plotted. In addition, the user can overlay various results on a single plot and incorporate and overlay results from a previous antenna file. Full control of legends, titles, line types and widths for the plot are provided.

This paper will show how NEC-WIN enables the user to enter data using graphical assistance and the viewing capabilities of NECVU. Following data entry, the paper will detail how to run NEC and gain the results of the analysis using the plotting ability of NEC-WIN.

NEC-WIN DATA ENTRY:

One of the most difficult problems related to NEC based codes has been the user interface. The typical manner a user directs NEC to process an input file is for that user to create an input file using a specific set of commands and syntax with a DOS text editor. This is a cumbersome technique and it has lead to significant frustrations by many users. NEC-WIN is designed to provide users with a graphical interface in the Windows environment such that they do not have to experience the typical frustration when creating a NEC input file.

NEC-WIN's editor has been optimized for different experience levels that an antenna designer may have. In the "expert" mode, NEW-WIN provides a text editor where users familiar with the NEC commands can enter the information directly. NEC-WIN includes commands such as cut, copy, paste, undo, redo, find and replace with the text editor to support data entry. These commands become very useful when working with large input files or during the editing process of multiple input files which are simultaneously open on the screen.

The second mode for data entry with NEC-WIN is designed for users that have some knowledge of NEC commands, but are not familiar enough with the commands to know all of the data that must be entered for a particular command. Figure 1 is a display of a typical screen for NEC-WIN in this mode. Under the NEC-WIN main menu bar on the left side of the screen is the editor box that contains the text for an input file. On the right side of the screen is a scrollable menu that provides a list of the NEC commands along with a short statement as to each commands use. As an example, if the user wants to command NEC to create a radiation pattern, the user would scroll through the card list until he reached RP: Radiation Pattern Request. By selecting this card, the user will automatically have an "RP" placed in the text file and he will be vectored to the Radiation Pattern input screen as seen in Figure 1.

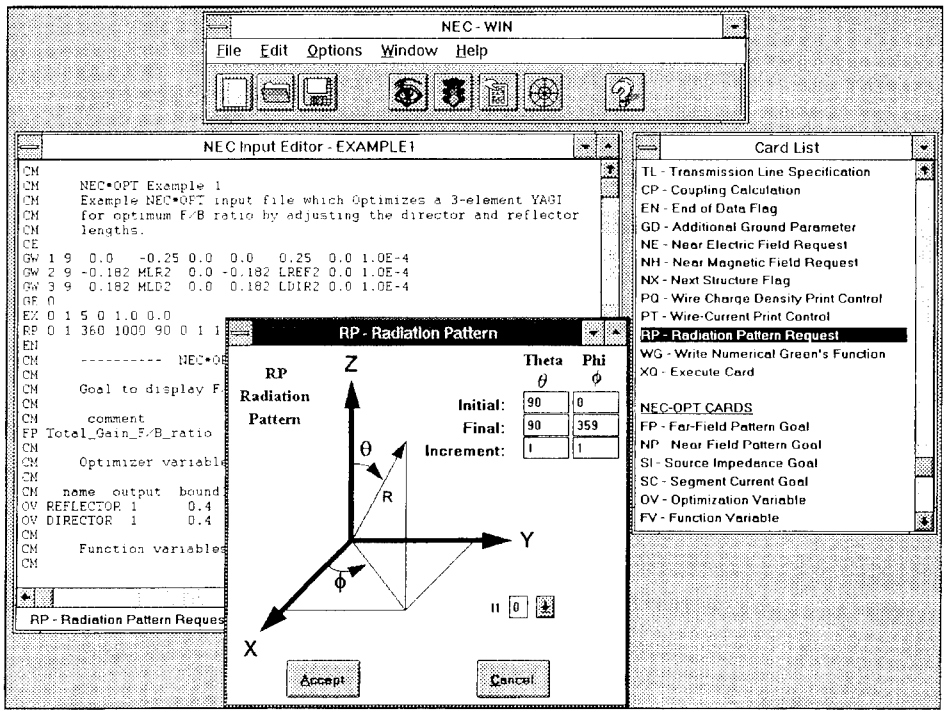


Figure 1: NEC-WIN Data Input Screen

The Radiation Pattern screen in Figure 1 typifies the graphical nature of the displays used for data entry. These screens are based on providing a consolidated list of inputs that are required for NEC to create the appropriate text line. For the RP card, the user will enter the start and stop points for theta and phi along with the number of steps used for processing. The remaining inputs associated with the RP card are set to a default condition. The user can enter the basic data and accept the default information to quickly create the card or one can access the defaults and change these to the appropriate settings. By creating defaults, the input of data is more intuitive and the process is significantly faster.

The other mode for data entry with NEC-WIN is the "novice mode". This mode is designed for users that have no knowledge of NEC, but they understand how to create a wire model of an antenna. When the user enters the novice mode, three buttons (Comments, Geometry, Output) are available for the user to enter data. The key area for the novice is the geometry entry section. In this area, the user will enter the start and stop points of the wire in an "Excel-like" worksheet. In addition to entering the wire end-point information, NEC-WIN has graphical-based screens for scaling, rotation, or translation of a particular wire. The user can add sources and loads to wires within the geometry input screen. The key to the data entry process in the novice mode is that it can be done in any order and the user does not need to be aware of how a NEC input file is constructed.

VIEWING AN ANTENNA USING NEC-VU:

NEC-VU provides a fast, easy, efficient way to view the segment geometry of a NEC antenna structure. The program is accessed from the main control panel of NEC-WIN by clicking on the "eye" icon. NEC-VU analyzes the NEC input file that the user is developing in order to provide a three-dimensional representation of the antenna geometry on the screen. A sample of a NEC-VU display screen for a very complex structure is shown in Figure 2. After the object is displayed on the screen, the user can analyze the structure using the mouse to perform rotation, panning and zooming. The ability to perform these operations in a continuous real-time mode with no "flicker" is where the power of NEC-VU is evident.

NEC-VU was developed in Assembly language in order to maximize the rotation speed of the antenna. By paying close attention to the vertical refresh rate of the screen and optimizing the code such that all of the updates can be done in a compressed time frame, NEC-VU has the ability to rotate the antenna structure in a manner that is typically seen only on workstations. Furthermore, NEC-VU maintains the same ability to provide continuous rotation on input files that contain over 4000 segments.

The key application of NEC-VU is for the visualization of the antenna structure and analysis of the structure to ensure that the input file has been generated correctly. NEC-WIN enables the user to access a configuration file where one can define different line types, such as free ends, segments, and junctions to have different colors. This makes visual verification of the antenna much easier in that free ends, for example, can be defined as a different color than the rest of the segments such that they will be easy to identify during the analysis. NECVU also supports an editing mode whereby the user can move the cursor to a segment on the display and have NECVU indicate what wire number corresponds to this point as well as the location in the input file where that wire was created.

Figure 2: NEC-VU Display Example

PROCESSING THE ANTENNA STRUCTURE:

NEW-WIN processes antenna files using NEC-OPT, which is based on the NEC2 core. NEC-OPT consists of a quasi-Newton optimizer integrated with a double precision version of NEC2 and the required interfaces to provide the necessary communication between the two sections. Both constrained and unconstrained optimization is provided by the optimizer. The user can provide the necessary commands to control the design goals, variables and optimization parameters. In addition to optimization, the NEC-OPT package has the ability to sequence any variable defined in the NEC input file over a specified range of values. This is useful for developing design curves or performing a worst case analysis.

NEC-WIN contains an extended command set beyond the standard NEC commands in order to support users that desire optimization. The power of using the NEC-OPT core is apparent when one establishes goals for certain parameters that the user wants to optimize. Four different NEC output types may be sampled and processed as one changes the geometry in an effort to reach these goals. The specific outputs that can be optimized are far-field patterns, near-field patterns, source impedance, and segment currents. For each goal there are many options which select specific parts of the desired NEC output data or define the processing to be performed on it. The many options provide a generic and versatile interface to nearly every type of NEC output data. High level characteristics such as gain, pattern beamwidht, VSWR, front-to-back ratio and many others may be chosen for optimization and output processing.

Multiple goals may be specified for the same run of NEC-OPT. Each goal may be separately weighted to allow the user to balance the significance of each goal to meet the specific needs of the problem. At the conclusion of the processing, NEC-OPT creates a file which contains the results of the optimization. The user can view this information and alter the input data set to correspond to the optimized structure.

VIEWING RESULTS WITH NEC-WIN:

While many of the problems associated with NEC based codes have been the user interface, another glaring weakness of the codes is the ability to look at the results without having to export data to alternate packages for processing and plotting. NEC-WIN has been developed with an extensive plotting package that provides unmatched flexibility for creating plots of the results obtained after running NEC-OPT. The package provides the user with a wide variety of commands that enables one to customize the output for their particular requirements and save these settings as a series of macros for later usage.

Access to pattern plots is available from the main NEC-WIN menu by clicking on the "pattern" icon. This commands NEC-WIN to examine the current file and determine what pattern plots are available. Following the processing, NEC-WIN presents a display as seen in Figure 3. On the left side of the screen is a summary of the available patterns. The table contains each patterns type (azimuth or elevation), the range of theta and phi, along with the frequency and the file name where the pattern is contained. On the right side of the screen are controls for defining the horizontal gain, vertical gain and total gain. For each gain type, one can define the type of line, line color and line width corresponding to the selected pattern in the table. In addition the user the ability look at the output files from previous processing runs and combine the available patterns such that one can do overlays.

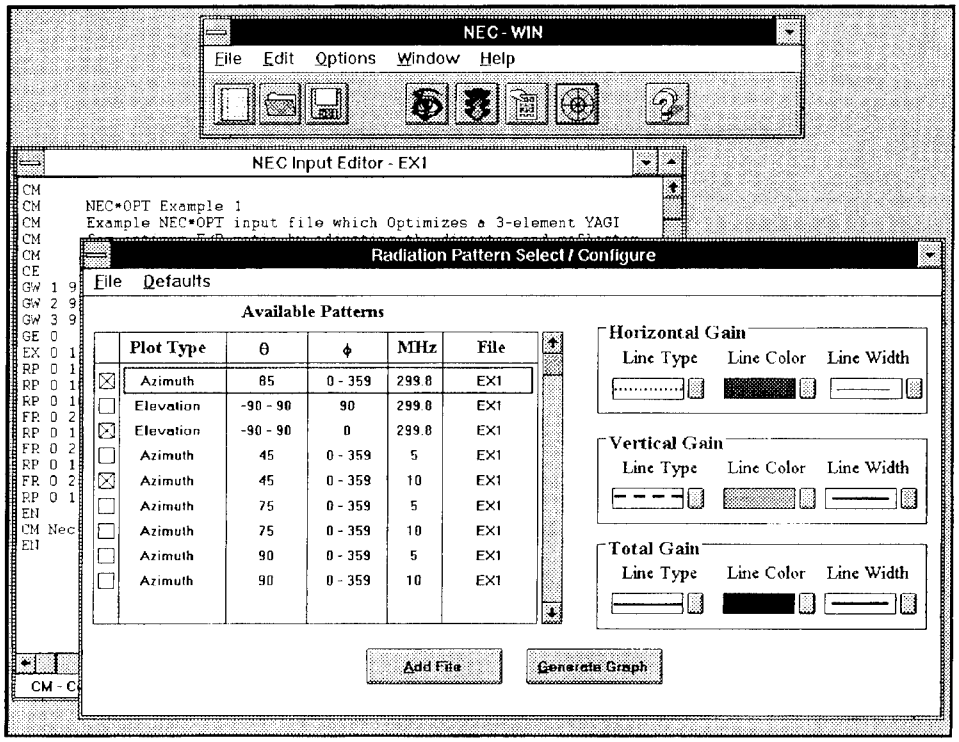


Figure 3: Radiation Pattern Configuration Screen

After the plots have been configured, the user can generate a graph after adjusting plot parameters in the azimuth and elevation plot control screens. When this is complete, a graph as seen in Figure 4 is generated. The user has complete control over the look and feel of this graph in that one can change the font style, size, and type for all labels, titles and markings on the graph. In addition, a title of an arbitrary length can be added and the program will automatically scale the graph to fit on the screen or the output plot. In addition, the user can add a legend with customized information on each line of the legend along with the ability to add a title and a footer. Furthermore, the position of the legend and title can be adjusted to a variety of locations.

Plots are available to the screen as well as to a printer. The user can also output tabular data corresponding to the graph. One of the most interesting features of NEC-WIN is the ability to copy the entire plot or a section of the plot to a clipboard and move to a word processor where the information can be pasted into a document. NEC-WIN also allows the user to create a three dimensional surface plot of the output as seen in Figure 5. This pattern can be examined in the same way that a user would manipulate the antenna using NEC-VU. Using NEC-SURF, the user can access rotate, pan and zoom functions to gain a better understanding of the antennas performance.

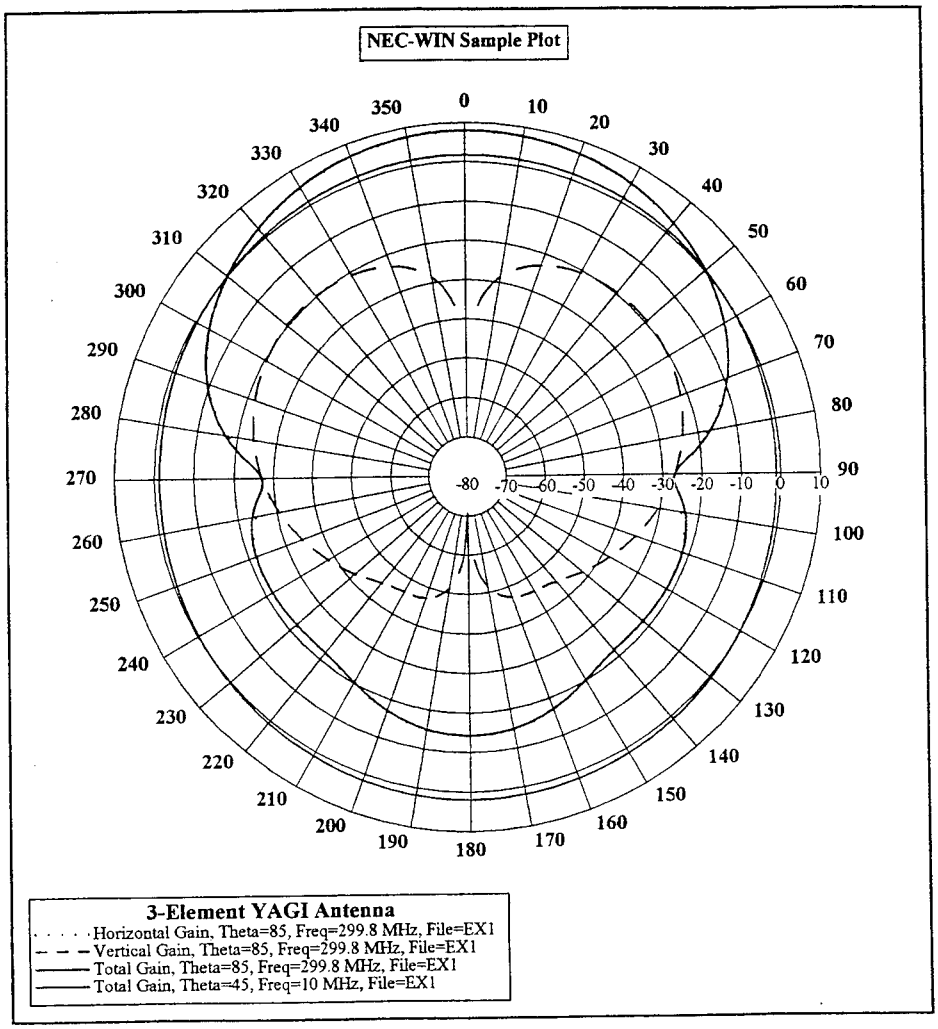


Figure 4: Sample Output of NEC-WIN Plot Program

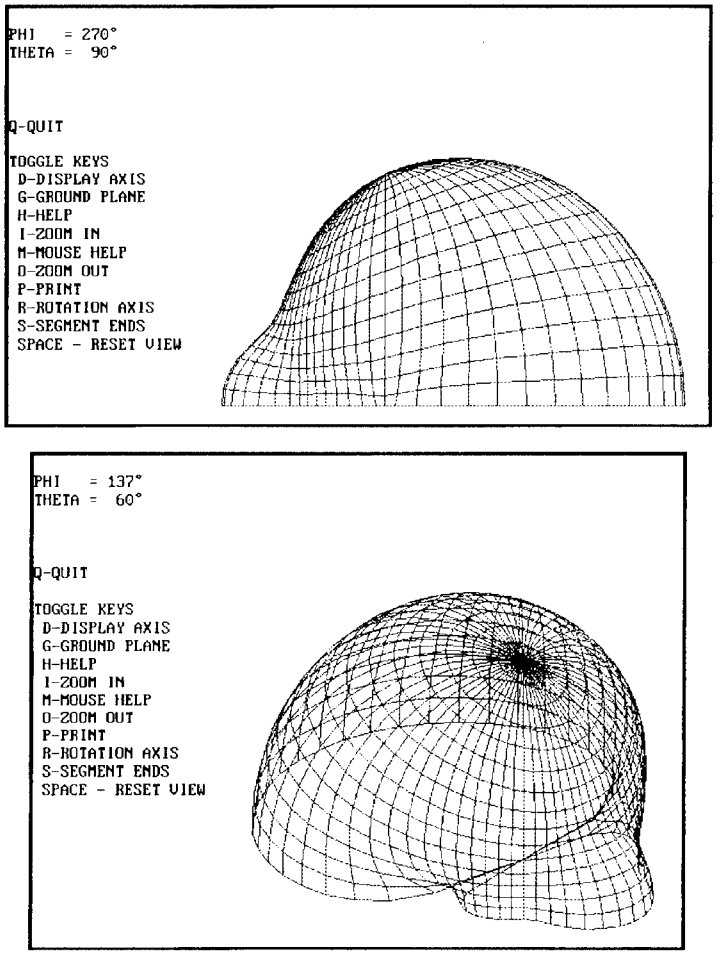


Figure 5: NEC-SURF Output of Antenna Pattern

CONCLUSION:

NEC-WIN is a powerful antenna design and analysis program that provides users with an unmatched level of performance and options. The program uses a modified version of NEC2 to include optimization capabilities as part of the core processing. Using NEC-WIN, the antenna designer has graphical based input and three-dimensional viewing of the structure to assist in developing the input geometry. After the file has been processed, the user can plot various patterns, obtain a tabular output of the data or view that antenna pattern in a three-dimensional surface plot.

THE "PAINT" SYSTEM
A UTD/NEC HYBRID PACKAGE FOR SIMULATING ANTENNA PATTERNS OVER 3-DIMENSIONAL IRREGULAR TERRAIN

Joel S. Young and **James K. Breakall**
Department of Electrical Engineering
The Pennsylvania State University
University Park, PA 16802

Abstract

This paper describes a software package (PAINT) which utilizes the uniform theory of diffraction (UTD) in conjunction with the numerical electromagnetics code (NEC) to predict radiation patterns of antennas situated in 3-dimensional (3D) irregular terrain at high frequencies (HF). The PAINT system is a user friendly integrated software package which performs all the tasks necessary to predict antenna patterns over 3D irregular terrain. The software package is self contained and runs on a personal computer (PC) platform. The package can utilize existing terrain databases to generate 3D terrain models. The models are analyzed with an existing UTD program, and the results can be processed and displayed by other routines in the integrated software package. The 3D modeling capability allows azimuth as well as elevation patterns to be simulated. Primary validation is accomplished by comparing to field measurements of elevation patterns. In addition, the antenna performance of an existing HF receiving facility is analyzed, and the results are compared to predictions from NEC utilizing a flat earth model.

1. Introduction

The presents of an irregular foreground can have a significant effect on the performance of HF antennas [1]. It is desirable to be able to simulate these effects as part of the evaluation process before going through the expense of constructing and measuring the antenna. This work is part of an on-going research effort sponsored by the Navy and conducted at the Applied Research Laboratory of the Pennsylvania State University to study HF communications[2].

PAINT is an acronym that stands for Performance of Antennas In Non-ideal Terrain. As the name implies the system is designed to simulate the perturbations to antenna patterns caused by locating the antenna over 3D irregular terrain. The PAINT modeling system is an integrated collection of software programs written in Fortran to run on a PC platform using the MS-DOS operating system. The PAINT system is designed to isolate the user from unnecessary details of the simulation process. The PAINT system makes extensive use of menus and graphical displays which allows an unfamiliar user to generate and analyze complex models with only minimal training.

The PAINT system can directly access various sources of terrain data such as the United States Geological Survey (USGS) Digital Elevation Model (DEM) terrain data, and the Defense Mapping Agency's (DMA) Digital Terrain Elevation Data (DTED). Graphical data displays enable the user to quickly select and process millions of points of terrain data into a usable terrain model. Complex antennas used in the model may be defined by the user, or they may be taken directly from the output of the NEC program. The UTD analysis of the model is performed by the NECBSC program developed for the Navy by Ohio State University[3]. The output patterns may be displayed in polar form on the screen or sent to a hard copy device.

2. The Modeling Process

The PAINT modeling system is an integrated environment that provides all the routines necessary to simulate the pattern of an antenna situated in irregular terrain. The initial simulation process consists of a sequence of steps from site selection through simulated output plotting. Each step may consist of executing one or more PAINT commands. This section provides a basic overview of the modeling process from start to finish. Figure 1 shows the basic steps of the modeling process and the two letter commands of the PAINT modeling system that perform each function.

The first step in the modeling process is site selection. The goal of site selection is to select a small region of terrain around the area where the antenna is to be located. The region should be as small as possible while still containing all major structures which effect the antenna's performance. For instance, if the antenna is located in a valley between

two hills the selected terrain site should be large enough to contain the two hills nearest the antenna. Three different sources of terrain data may be accessed by the PAINT system. USGS DEM data, Level 1 DMA DTED data on CD-ROM, and X,Y,Z triplets contained in a text file may all serve as terrain data inputs for the PAINT system. Each of the USGS and DTED data sets may contain over 1.4 million points of terrain data. To effectively handle the enormous amount of terrain data, the user performs a 2-stage graphical selection process to determine a smaller region of interest. After the site terrain data has been chosen it can be further simplified, if desired, and converted to the flat plate structure which is used in the NECBSC model. The plates used in the model may be given lossy dielectric parameters to more accurately simulate real ground.

The next step is to define the antennas used in the simulation. The user may define multiple wire antennas with various orientations, or if complex antennas have been previously modeled with NEC, they may be taken directly from the NEC output file. By using the currents from NEC to define the source, ground losses may be included in the final output patterns. The frequency may be set manually, or if a NEC source is used, the frequency is set to that used in the NEC analysis. Next, the user may define azimuth and elevation patterns as well as a totally arbitrary pattern cut if so desired.

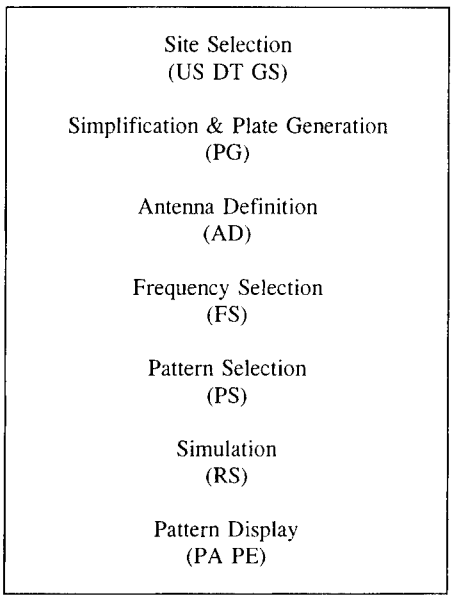


Figure 1 Steps in the PAINT Modeling Process.

At this point the model is complete and ready to be analyzed. All of the parts of the model generated by the previous operations are combined in an input file, and the simulation is analyzed by the NECBSC program. Azimuth an Elevation plotting routines are included in the package to display the simulated results.

Once the model is complete the user does not have to go through all the steps from start to finish every time. He may go back and alter one or more of the model creation steps by running the command again with different inputs and then rerun the simulation and examine the resulting patterns.

As an aid to the modeling process a 3D wire-frame viewer was developed to display the 3D plate and antenna structures. 3D visualization is necessary for complex models to verify proper orientation and placement of the antennas.

3. Validation Results

The PAINT system has been validated by comparing simulated results to accurately measured elevation patterns taken over irregular terrain located near Cedar Valley Utah [4]. The terrain data is shown in Figure 2 and a simplified plate model is shown in Figure 3. The antennas in Figure 3 have been exaggerated to increase there visibility. There are actually 6 antennas at the site, a monopole and a dipole at each of 3 locations. Only one antenna was active during each measurement. The relative elevation patterns for an 8 MHz analysis are shown in Figure 4. The antenna locations labeled front top and back in Figure 4 correspond to the antenna locations shown in Figure 3 going from right to left respectively. Figure 4 indicates good agreement between the measured and simulated data for nearly all cases. For the front location the hill is located on the left side of the antenna. The blockage caused by the hill causes the front location patterns to be reduced on the left side at low elevation angles. The top location is not obstructed on either side. The back location is obstructed by the hill on the right side, but less so than the front location.

Figure 5 shows a terrain model of an existing HF receiver site located at Rock Springs, PA. This site was modeled by the PAINT system using DTED terrain data on CD-ROM. No measured data of the site was available to compare to the simulated data, so the PAINT results are compared to NEC results for a flat lossy earth model ($\epsilon_r = 12$, $\sigma = 6.5$ mS/m). The antenna used for the simulation is an 8-element log-periodic dipole array (LPDA) shown in Figure 6. The antenna was simulated at an appropriate height over flat lossy ground using NEC. The PAINT system utilized

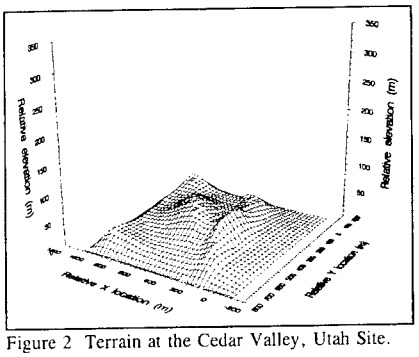


Figure 2 Terrain at the Cedar Valley, Utah Site.

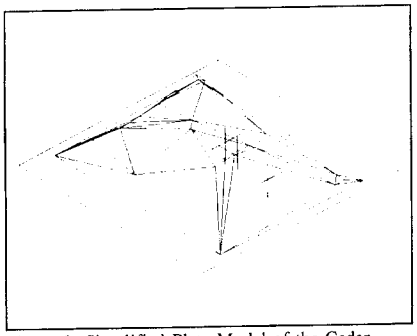


Figure 3 Simplified Plate Model of the Cedar Valley, Utah Site with Antennas.

the currents from NEC to define the source and calculated the additional effects caused by the irregular terrain. It would be very difficult to simulate this antenna with the NECBSC program without the NEC hybrid interface used by the PAINT system. The NEC currents include the effects of ground losses so the output patterns from the PAINT system represent an actual gain in dBi. The simulated results are compared in Figure 7. This example demonstrates the ability of the 3D PAINT model to simulate azimuth as well as elevation patterns. The LPDA is pointed down the terrain slope shown in Figure 5. This corresponds to the left side of the elevation plot and straight up on the azimuth plot shown in Figure 7. The azimuth pattern was taken at an elevation of 10 degrees which is near the peak of the pattern. As shown in both plots of Figure 7, the hill in the background significantly corrupts the back-lobe pattern of the antenna. The hill also provides some additional gain in the forward direction at low elevation angles. The front-lobe of the azimuth pattern and the majority of the elevation pattern are in good agreement with the NEC flat earth result.

4. Conclusions and Future Work

The PAINT system is a very powerful tool for simulating irregular terrain effects on antenna patterns. It provides access to the vast amount of existing terrain database information, and it provides the tools to quickly convert the raw terrain information into a useable model. The PAINT system provides the ability for an unfamiliar user to begin studying the effects of irregular terrain quickly without spending a long time learning how to use complex and unfriendly software. By using a 3D model, the PAINT system can produce azimuth as well as elevation patterns.

The results of the PAINT system compared favorably with accurately measured elevation data taken at the Cedar Valley, Utah test site. The PAINT results also compared favorably with NEC simulations of the Rock Springs, PA receiver site. While no measured data was available for this site the simulations provide insight on the antenna's performance in the presents of irregular terrain.

The PAINT system has been validated primarily at HF. At lower frequencies, it is expected that the simulation accuracy will suffer due to the lack of a surface wave in the simulation. At higher frequencies the simulation is limited by the ability to accurately define the terrain. As the frequency increases, more plates are required to accurately define the terrain. This causes the simulation run time to increase drastically, because the simulation time increases exponentially with the number of plates in the model. Another limitation of the simulation is that currently only single order diffraction effects are considered in the simulation. This prevents pattern predictions into regions where the path to the source is shadowed by more than one obstacle. A future update to the NECBSC program which includes higher order diffraction effects may correct this situation. For most cases these limitations do not prevent the PAINT system from making accurate simulations at HF frequencies.

One topic of current research is to determine the best method of terrain simplification. The terrain databases currently available contain millions of points of elevation data. Currently on the PC, models are limited to a few hundred plates or less due to the time required to run the simulation. The PAINT system contains several different methods of

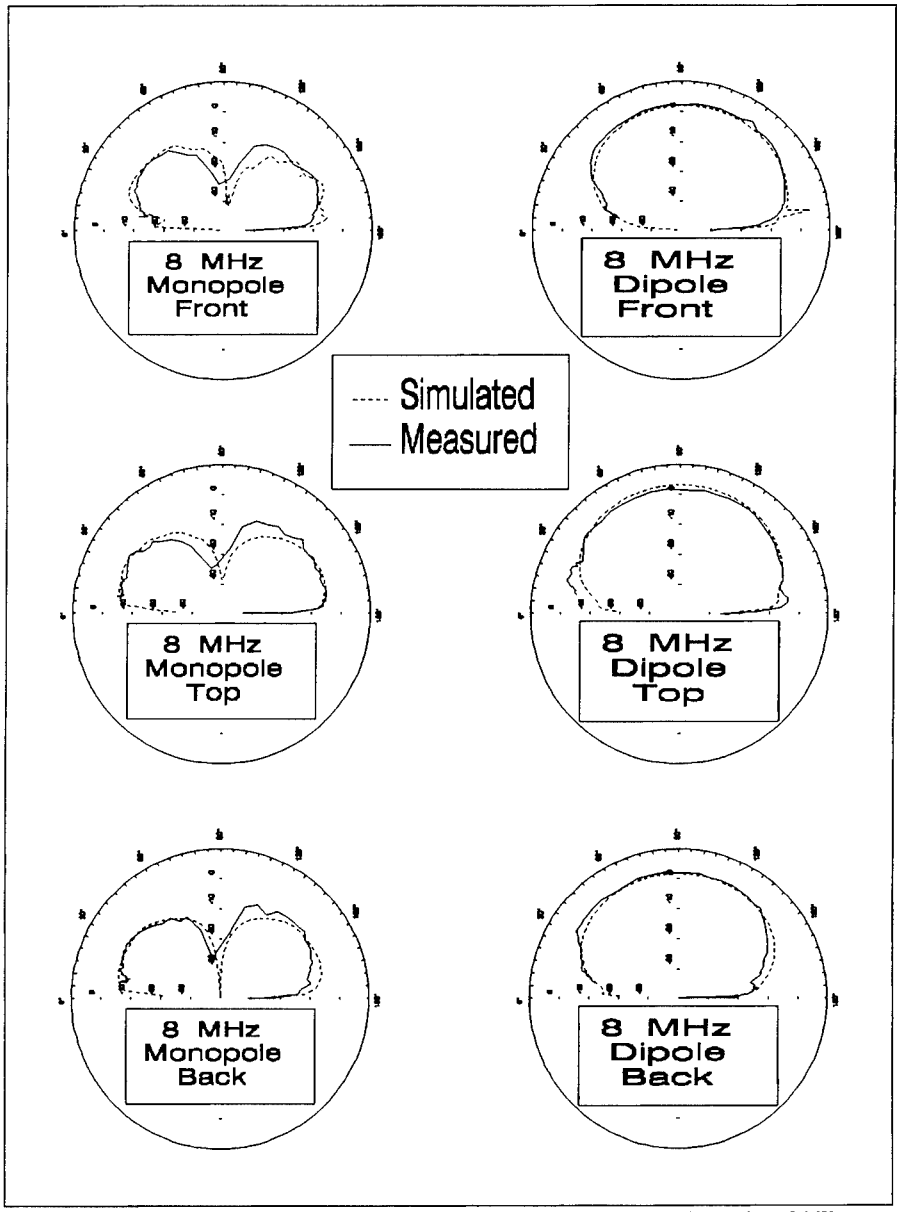


Figure 4 Measured and Simulated Relative Elevation Patterns Over Cedar Valley, Utah Terrain at 8 MHz.

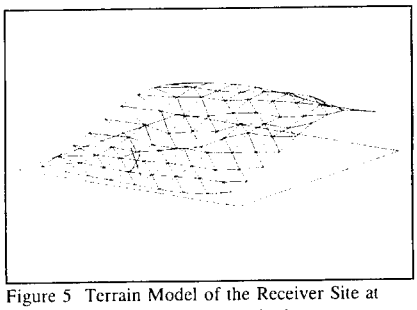


Figure 5 Terrain Model of the Receiver Site at Rock Springs, PA. The source is shown as an exaggerated X and the elevation is scaled by a factor of 2.

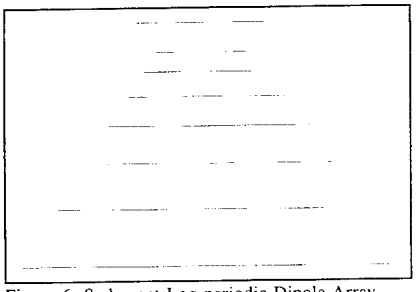


Figure 6 8-element Log-periodic Dipole Array Antenna Used at the Rock Springs, PA Receiver Site.

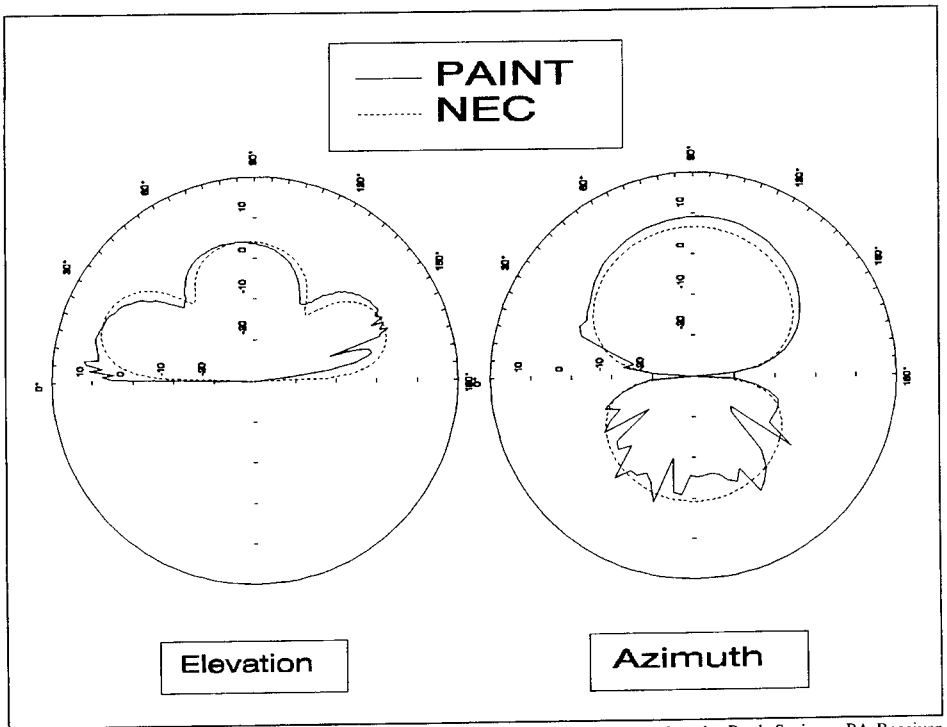


Figure 7 Elevation and Azimuth patterns of the LPDA Antenna at 11 MHz Located at the Rock Springs, PA Receiver Site Showing Absolute Gain in dBi.

terrain simplification, and work is being done to determine the tradeoffs between the amount of simplification and the simulation accuracy for the various methods.

The PAINT system is flexible enough to allow the use of synthetic user-generated terrain data as a source of terrain information for model creation. This allows a wide range of canonical problems such as gaussian hills, semi-circular bosses, or any analytic terrain surface to be modeled. Future work may be directed toward analyzing some of these synthetic shapes and comparing the PAINT models to the results of other simulation techniques.

5. References

1. Baily, S. T., K. L. Beeke, and R. G. Manton, "The Performance of HF Curtain Antennas with Irregular Foregrounds," *HF Radio System and Techniques, Proceedings of 4th International Conference*, London, United Kingdom, 11-14 April 1988, pp. 132-136.

2. Young, J. S. ,"Simulation of Antenna Patterns over 3-Dimensional Irregular Terrain Using the Uniform Geometrical Theory of Diffraction (UTD) [Development of the PAINT System]," Ph.D. Thesis, The Pennsylvania State University, University Park, PA, December 1994.

3. Marhefka, R. J., W. D. Burnside, "Numerical Electromagnetic Code - Basic Scattering Code (Version 2), Part I: User's Manual," The Ohio State University, ElectroScience Laboratory, Technical Report 712242-14, July 1982.

4. Hagn. G. H., D. L. Faust, "Cedar Valley Antenna Tests, Covering Period 10-24 May 1990," SRI International, Arlington, Virginia, 28 May 1990.

SESSION 20:

FEM

Chairs: R. Burkholder, J. Karty

Numerically Characterizing Electromagnetic Fields Local to the Edge of a Conducting Strip Using a Matched Asymptotic Technique and the Finite Element Method

Azar S. Ali
Department of Electrical Engineering
US Air Force Academy
USAFA CO 80840

Christopher L. Holloway
US Department of Commerce
Institute for Telecommunication Sciences
Boulder, CO 80303

Abstract

For a conducting strip, a precise closed form characterization of the field distribution for arbitrary shaped edges and any conductor thickness is not possible. A matched asymptotic expansion and a finite element code are used to study the electromagnetic fields local to the edge of a conducting strip. This formulation is shown to be valid for any edge shape and strip thickness versus skin depth. In this paper, this formulation is discussed and results for the 90 degree edge are presented.

Introduction

Planar circuits are made by laying strips of conductor (microstrip, coplanar waveguides, etc.) on a grounded substrate as shown in Figure 1. As signals propagate along these microstrip

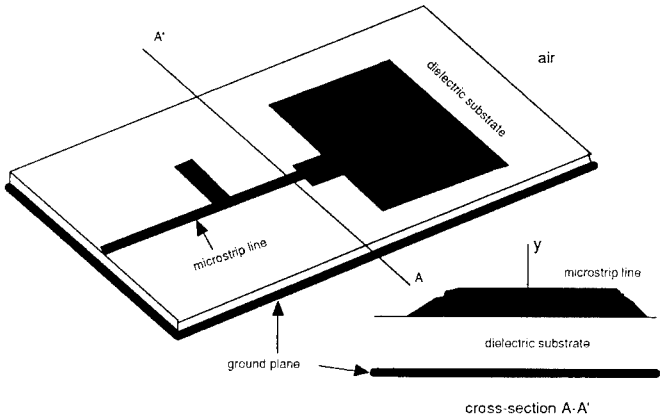


Figure 1. Planar circuit example showing layout of microstrip lines

lines, power is lost. The power loss is proportional to a number of factors such as conductor thickness t, skin depth δ, and the edge shape as shown in Figure 2. While the conductor power loss is in general a small effect, it increases as the operating frequency increases. Consequently, considerable effort has been expended in trying to characterize it [1-6].

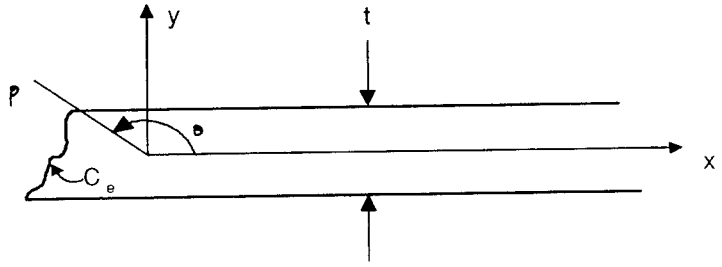


Figure 2. Cross section of the isolated edge.

Recently, Holloway and Kuester [7] used the method of matched asymptotics to propose quasi closed form expressions for the conductor loss for planar structures as a function of t, δ, and the edge shape. They studied losses from an isolated conducting edge. Their expressions yielded excellent results which agreed well with that of Heinreich [2], Goldfarb [3], and Wheeler [4]. In [7], the distribution of the electromagnetic fields around the edge of the conductor was not studied explicitly. The emphasis was on computing the power loss. In this paper, we use the method of matched asymptotics to explicitly study the field distribution around the isolated edge of a conducting strip. The field distribution for a 90° edge will be investigated for various t/δ ratios.

Formulation

We're interested in finding the fields inside the strip conductor local to the edge (see Figure 2). Assuming a dominant current along the z-axis we have the TM polarized field components E_z, H_x, and H_y. Maxwell's equations then reduce to

$$\overline{a}_z \times \nabla E_z = j\omega\mu_{d,c}\overline{H}$$

and

$$\nabla \times \overline{H} = j\omega\varepsilon_{d,c}\overline{a}_z E_z$$

in which the subscripts d,c refer to dielectric (air in this case) and conductor, respectively. The boundary conditions on the electric and magnetic fields are given by

$$E_z^c \Big|_c = E_z^d \Big|_c$$

and

$$\overline{H}_t^c \Big|_c = \overline{H}_t^d \Big|_c$$

where the subscript t refers to tangential components. Next the electromagnetic fields can be written in terms of the magnetic vector potential $\overline{A} = \overline{a}_z A_z$ as

$$\overline{H} = \frac{1}{\mu} \nabla \times \left(\overline{a}_z \, A \right)$$

and

$$E_z = - j\omega A$$

The magnetic vector potential must then satisfy the modified Helmholtz equation

$$\left(\nabla^2 + \omega^2 \mu \varepsilon_{d,c} \right) \overline{A} = 0$$

with the following boundary conditions

$$A^c \Big|_c = A^d \Big|_c$$

and

$$\frac{1}{\mu_c} \frac{\partial}{\partial n} A^c \Big|_c = \frac{1}{\mu_d} \frac{\partial}{\partial n} A^d \Big|_c$$

In [7], the method of matched asymptotics is used to expand the fields in terms of the small parameter $\nu = k_d t / 2$, where k_d is the wave number in the dielectric, and t the strip thickness. In the outer region, far from the edge, and in the dielectric, they expanded the potential as

$$A^d \sim T^0(x,y) + \nu T^1(x,y) + \nu^2 T^2(x,y) + O(\nu^3) \qquad (1)$$

and far from the edge, inside the conductor, they expanded the potential as

$$A^c \sim U^0(x,\tilde{y}) + \nu U^1(x,\tilde{y}) + \nu^2 U^2(x,\tilde{y}) + O(\nu^3) \qquad (2)$$

where the scaled variable, $\tilde{y} = \frac{y}{\nu}$, was used to account for the possible rapid field variations in the y-direction. T and U must then satisfy the following modified Helmholtz equations:

$$\frac{\partial^2}{\partial x^2} T + \frac{\partial^2}{\partial y^2} T + k_d^2 T = 0 \qquad (3)$$

$$\frac{\partial^2}{\partial x^2} U + \frac{1}{\nu^2} \left[\frac{\partial^2}{\partial \tilde{y}^2} U + \omega^2 \varepsilon_0 G U \right] = 0$$

and boundary conditions

$$T(x,2t) = U\left(x, \pm \frac{1}{k_d} \right) \qquad (3a)$$

and

$$\frac{1}{\mu_d} \frac{\partial T(x,y)}{\partial y} \Big|_{y=2t} = \frac{1}{\mu_c \nu} \frac{\partial U(x,\tilde{y})}{\partial \tilde{y}} \Big|_{\tilde{y} = \pm \frac{1}{k_d}}$$

where G represents the relative permittivity in the conductor.

Similarly, in the inner region close to the edge, the potential was expanded in an asymptotic series. As pointed out in [7], the fields in the inner region must be expanded in half powers of ν as

$$A^d \sim V_0(\tilde{x},\tilde{y}) + \nu^{1/2} V_1(\tilde{x},\tilde{y}) + \nu V_2(\tilde{x},\tilde{y}) + O(\nu^{3/2}) \tag{4}$$

in the dielectric and as

$$A^c \sim W_0(\tilde{x},\tilde{y}) + \nu^{1/2} W_1(\tilde{x},\tilde{y}) + \nu W_2(\tilde{x},\tilde{y}) + O(\nu^{3/2}) \tag{5}$$

in the conductor. The second scaled variable, $\tilde{x} = \frac{x}{\nu}$, was introduced to account for the rapid field variations along x. V and W must satisfy the following modified Helmholtz equations

$$\left(\tilde{\nabla}^2 + k_d^2 \nu^2\right) V = 0 \tag{6}$$

$$\left(\tilde{\nabla}^2 + k_G^2\right) W = 0$$

and corresponding boundary conditions

$$V\big|_C = W\big|_C \tag{6a}$$

$$\left.\frac{\partial W}{\partial \tilde{n}}\right|_C = \mu_{cr} \left.\frac{\partial V}{\partial \tilde{n}}\right|_C$$

where $\frac{\partial}{\partial \tilde{n}}$ refers to the normal derivative along the conductor dielectric interface, and

$$\tilde{\nabla} = \bar{a}_x \frac{\partial}{\partial \tilde{x}} + \bar{a}_y \frac{\partial}{\partial \tilde{y}}.$$

Zeroth and first order solutions

Substituting the expansions for $T(x,y)$ and $U(x,\tilde{y})$ given by (1) and (2) into the modified Helmholtz equation (3), it can be shown that $U^0 \equiv 0$, and $U^1 = A_1(x)e^{-jk_d\tilde{y}} + B_1(x)e^{jk_d\tilde{y}}$. For the fields in the dielectric, $T^0 \to f_m \sin\left(\frac{m\varphi}{2}\right) J_{\frac{m}{2}}(k_d\rho)$ and T^1 must satisfy $\left(\nabla^2 + k_d^2\right) T^1 = 0$. $A_1(x), B_1(x)$, and f_m are determined from the boundary conditions given in (3a).

A similar process using Equations (4) through (6) for the zeroth order fields in the inner expansions yields $V_0 \equiv 0$ and $W_0 \equiv 0$. The first order fields must satisfy the Laplace and Helmholtz equations

$$\tilde{\nabla}^2 Q_1 = 0 \tag{7}$$

$$\left(\tilde{\nabla}^2 + k_G^2\right) P_1 = 0$$

where

$$Q_1(\tilde{x},\tilde{y}) \equiv \frac{1}{f_1}\sqrt{\frac{\pi}{2k_a}}\, V_1(\tilde{x},\tilde{y}) - \tilde{\rho}^{1/2}\sin\left(\frac{\varphi}{2}\right) \tag{7a}$$

$$P_1(\tilde{x},\tilde{y}) \equiv \frac{1}{f_1}\sqrt{\frac{\pi}{2k_a}}\, W_1(\tilde{x},\tilde{y})$$

are subject to the boundary conditions

$$P_1\big|_C - Q_1\big|_C = \tilde{\rho}^{1/2}\sin\left(\frac{\varphi}{2}\right) = V(x,y) \tag{7b}$$

$$\left.\frac{\partial P_1}{\partial \tilde{n}}\right|_C - \mu_{cr}\left.\frac{\partial Q_1}{\partial \tilde{n}}\right|_C = \mu_{cr}\,\bar{a}_n \bullet \tilde{\nabla}\left(\tilde{\rho}^{1/2}\sin\left(\frac{\varphi}{2}\right)\right)\Bigg|_C = D(x,y)$$

Numerical Results

The solution to the system of equations in (7) present some unusual features. These features were treated by Holloway in [8] where the general class of Eddy current problems was addressed. The solution shown in [8] utilized a variational technique and developed a functional for the system in (7). The functional as given in [8] and [9] is

$$\begin{aligned} W(P_1) = {} & \int_V \left(\nabla P_1^{tr}\right)^2 dV - k^2 \int_V \left(P_1^{tr}\right)^2 dV + \int_V \left(\nabla Q_1^{tr}\right)^2 dV \\ & - \int_S \left(P_1^{tr} + Q_1^{tr}\right) D\, dS + \int_S \left(\frac{\partial P_1^{tr}}{\partial n} + \frac{\partial Q_1^{tr}}{\partial n}\right) V\, dS \\ & - \int_S \left(P_1^{tr} - Q_1^{tr}\right)\frac{\partial P_1^{tr}}{\partial n}\, dS - \int_S \left(P_1^{tr} - Q_1^{tr}\right)\frac{\partial Q_1^{tr}}{\partial n}\, dS \end{aligned} \tag{8}$$

where the 'tr' superscript denotes trial, and V and D are the jumps in the potential and its derivative as given in equation 7(b).

A finite element code was then written to implement the solution of (8). Results for the fields within the conductor close to the edge are shown in Figures 3 and 4 for the 90°. In

Figures 3 and 4, we see the fields decay slowly for the thickness $t \sim \delta$. As the thickness increased to $t \sim 2\delta$, 4δ , and $10\ \delta$, we see that the fields appear to drop off in a somewhat exponential manner along y as expected. Similar results can be obtained for the 45° edge but are not included here.

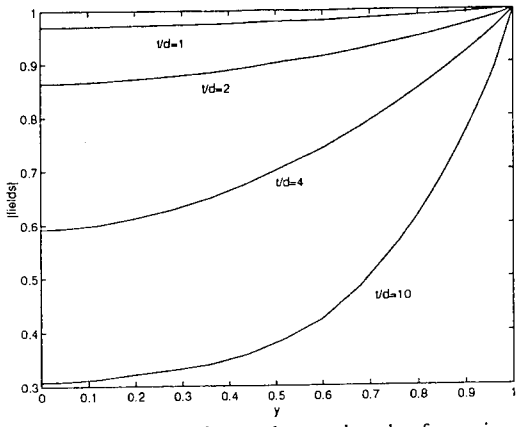


Figure 3. Fields within the conductor close to the edge for various t/δ ratios.

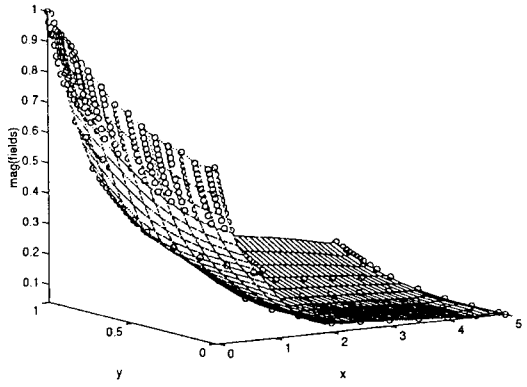


Figure 4. 3-D view of the fields for the 90° edge for t/δ=4.

Conclusion

The electromagnetic fields local to the edge of a conducting strip cannot be characterized in a closed form. The matched asymptotic technique with the use of finite elements allow these local fields to be approximated in a very reasonable manner.

References

1. Pucel, R. A., D. J. Masse and C. P. Hartwing, "Losses in Microstrip", *IEEE Trans., Microwave Theory and Tech.*, 12(6), 342-350, 1968.
2. Heinrich, W., "Full-wave Analysis of Conductor Losses on MIMIC Transmission Lines", *IEEE Trans., Microwave Theory and Tech.*, 38(10), 1468-1472, 1990
3. Goldfarb, M. E. and A. Platzker, "Losses in GaAs Microstrip", *IEEE Trans., Microwave Theory and Tech.*, 38(12), 1957-1963, 1990.
4. Wheeler, H. A., "Formulas for the Skin Effect", *Proc. IRE*, 30, 412-424, 1942.
5. Vakanas, L. P., A. C. Cangellaris, and J. L. Prince, "A Parametric Study of the Attenuation Constant of Lossy Microstrip Lines", *IEEE Trans., Microwave Theory and Tech.*, 38(8), 1136-1139, 1990.
6. Paleczny, E., D. Kinowski, J. F. Legier, P. Pribetich and P. Kennis, "Comparison of Full Wave Approaches for Determination of Microstrip Conductor Losses for MIMIC Applications", *Electron. Lett.*, 26(25), 2076-2077, 1990
7. Holloway, C. H., and E. F. Kuester, "Edge Shape Effects and Quasi-Closed Form Expressions for the Conductor Loss of Microstrip Lines", *Radio Science*, Vol 29, No. 3, 539-559, Jun 1994.
8. Holloway, C. H., " A Variational Formulation for a General Class of an Eddy Current Problem", manuscript in preparation.
9. Holloway, C. H.., "Edge and Surface Shape Effects on Conductor Loss Associated with Planar Circuits", *MIMICAD Tech. Report No. 12*, Department of Electrical Engineering, University of Colorado, Boulder, CO, April 1992.

AN ENHANCED "A POSTERIORI" REMESHING ALGORITHM FOR ADAPTIVE MESHING OF 2D FINITE ELEMENT PROBLEMS

P. Girdinio[*], *A. Manella*[+], *G. Molinari*[*]

[*]Dipartimento di Ingegneria Elettrica, Università di Genova 11a, Via Opera Pia I-16145 Genova, Italy
[+]TechnoSoft s.a.s. 7, Via S. Ilario I-16167 Genova, Italy

Abstract

A procedure for the adaptive definition of a Finite Element mesh matching an user-defined error level, on the basis of an error estimate on a first Finite Element solution, is presented. The proposed procedure sets up a tentative mesh defining an initial distribution of nodes on the boundary on the basis of the estimated error and refines the mesh until an error-based criterion in the bulk of the domain is satisfied. The implementation of the procedure in a 2D Finite Element development environment is presented and obtained results are discussed.

1. INTRODUCTION

Finite Element solutions of electromagnetic problems are becoming widely available and used to deal with a variety of problems, ranging from electrostatic and magnetostatic ones to those relevant to high frequency devices, also including nonlinear media.

One of the problems that still hinders the diffusion of Finite Element applications for complex, real-life design problems, now more and more affordable in term of computer resources, is certainly the need to discretize the problem domain. This phase of the solution process, crucial to obtain an adequate accuracy, is often rather involved, particularly with the complex and multi-material domains frequently found in real electromagnetic devices, and generally requires significant user skills to provide an adequate solution.

A possible approach to tackle this problem is to perform a first initial solution on a rough, automatic mesh, to estimate the error of the solution with an "a posteriori" estimation algorithm, to "adapt" the mesh, refining it where the error estimate is higher, to compute a new solution and to iterate the procedure until the error estimate falls below a user-defined level. Because of the significant potential advantages of this approach, the research on error estimation and adaptive meshing techniques is very active since many years, in a series of directions [1-7].

The most followed strategies for mesh adaption in Finite Element codes generally build successive improved meshes by refining the previous one under the guidance of an error estimation algorithm. The refinement can be obtained by adding new elements *(h refinement)*, by raising the order of the involved elements *(p refinement)*, by moving the position of the existing nodes *(r refinement)* or by combinations of the above approaches. A number of different algorithms for error estimation and mesh adaption in computational electromagnetics have been proposed, as mentioned above, including some developed and tested by the group of the authors [8-11].

2. MOTIVATIONS AND STRUCTURE OF THE PROPOSED PROCEDURE

In this paper, on the basis of the previous experience in error estimation and adaptive meshing by the research group of the authors, a rather innovative approach to the adaption problem is proposed. In this approach, after the first solution, instead of refining the initial mesh, a complete remeshing of the domain is performed, on the basis of the error estimation on the first mesh.

A major disadvantage of remeshing algorithms, that is probably at the basis of their limited current diffusion in engineering adaption procedures, is that they "forget" the previous node placement information, and have then to face each time a meshing from scratch, using geometrical and error estimation data only. This implies, to allow an efficient usage in "general purpose" computational electromagnetic codes, that a very sound and reliable automatic meshing algorithm must be available, and that also the exploitation of error estimation data must be reliable and robust, to allow a proper handling of the wide variety of multi-region, intricate domains of practical interest. However, if the above requirements can be satisfied, there are, in the opinion of the authors, some significant potential advantages over more "traditional" refinement techniques:

i) a remeshing procedure can also reduce the density of nodes, correcting possible "meshing overkills" performed by the initial mesh;
ii) in an efficient remeshing procedure a single iteration is frequently enough to satisfy the error level required by the user, and in general a lower number of iteration can be expected;
iii) in time-varying problems involving time discretization, where areas requiring high accuracy can vary with time, the feature of "forgetting" previous meshings can turn into an advantage.

On the basis of previous experience of their research group in the area of error estimation and h-refinement, and of some initial encouraging results obtained with a first remeshing algorithm [12], the authors have devised the two-dimensional enhanced remeshing procedure presented in this paper. In order to assess carefully its potential under conditions easy to evaluate, the current version of the procedure is relevant to magnetostatic and electrostatic problems only, and is implemented with first order triangular elements in a single material domain.

The procedure starts with an initial solution obtained on a mesh generated by means of an automatic meshing routine and with a subsequent element-by-element error estimation over the whole domain [13-16]. On the basis of the error estimate on each element, a "sizing function" on the problem domain is defined. This function depends also on a desired error level defined by the user and indicates an "optimal" local size of triangle for the given error level. For elements abutting on the boundary, the estimated error is averaged and assigned to boundary and interface nodes; the values of nodal error evaluated in this way are then used to define along the boundaries of the geometry a "spacing function", also depending on the user-specified error previously mentioned.

The generation of the new mesh is then started, defining firstly, by means of the spacing function, the number of nodes along each side of the problem boundary and their non-uniform distribution. Once the position of nodes along all boundary sides has been selected, a first triangulation is performed by means of the usual Delaunay criterion. Then a loop is started to define the triangles in which a node should be added; the criterion for node addition is based on the sizing function previously defined. For each new node a local reshaping of the mesh is performed to minimize badly shaped triangles; the loop is completed when all triangles in the mesh are marked as small enough on the basis of the sizing function. The mesh obtained in this way is then subjected to a final "smoothing" with geometrical criteria, to complete the procedure.

To allow a deeper evaluation of the procedure, the algorithms used to perform the various steps of mesh definition are described in detail in the following section.

3. MESH DEFINITION ALGORITHM

The mesh definition algorithm is launched when a first solution on an initial mesh has been performed, and an estimation of the error of the obtained solution has been computed. The error estimation is assumed to be available separately on each element of the domain as a constant value e_k as provided by the error estimators previously mentioned [14-16].

3.1 Evaluation of the sizing function

To define the sizing function on the problem domain, an "error weighted element size" is defined over each element k as:

$$f_k = \Omega_k \frac{e_{ref}}{e_k} \tag{1}$$

where Ω_k is the area of the element, e_{ref} is the reference error level defined by the user and e_k is the error estimate on the element. These quantities are then used to assign a "weighted nodal size" value F_i to each mesh node as:

$$F_i = \frac{\sum_{k=1}^{m} f_k \Omega_k}{\frac{1}{N}\sum_{k=1}^{N} \Omega_k} \tag{2}$$

where i is the generic node, the upper summation is performed over the m elements of the region of support of the node and the lower one over the N elements of the whole problem domain.

Once the F_i values have been computed for every mesh node, the "sizing function" $S(x, y)$ can be computed in every point of the problem domain using the element shape functions.

3.2 Evaluation of the spacing function

To evaluate the spacing function, the averaged nodal error on the boundary nodes, E_i is first defined as:

$$E_i = \frac{\sum_{k=1}^{m} e_k \Omega_k}{\frac{1}{N}\sum_{k=1}^{N} \Omega_k} \tag{3}$$

with the same meaning of symbols as in eqs. (1) and (2).

On each boundary side having P nodes in the initial mesh, and defining s_1 and s_P as the one dimensional coordinates of the initial and final nodes of the boundary side, nodal values of the spacing function are evaluated as:

$$D(s_i) = \frac{2(s_P - s_1)}{(P-1)\left(1 - \frac{E_i}{e_{ref}}\right)} \tag{4}$$

The spacing function $d(s)$ is then defined over the boundary side as a piecewise linear function assuming the values of eq. (4) at the nodes.

3.3 Boundary node definition

The first step to define the boundary nodes of the new mesh along a boundary side is to compute the required number of nodes along that side, T, on the basis of the spacing function. This number is computed for each boundary side Γ as:

$$T = \int_{\Gamma} \frac{1}{d(s)} ds \tag{5}$$

The one-dimensional coordinates s_i of the generic node i along the boundary side of the new mesh is then defined by the relation :

$$s_i = \frac{1}{2}(s_{i+1} + s_{i-1}) + \frac{1}{2}(s_{i+1} - s_{i-1})\left(\frac{d(m_i) - d(m_{i+1})}{d(m_i) + d(m_{i+1})}\right) \tag{6}$$

where d is the spacing function defined above and m_i is the midnode one dimensional coordinate of node i defined as:

$$m_i = \frac{1}{2}(s_i - s_{i-1}) \tag{7}$$

The values of s_i along each side of the boundary are then computed solving the set of nonlinear equations defined by eq. (6), as proposed by Frey [17]. Once the boundary node definition has been completed, an initial triangulation using these node only is performed and optimized using a standard Delaunay algorithm.

3.4 Bulk node definition

To define the position of internal nodes, on every element of the intermediate mesh built up as outlined in the previous subsection a test is performed to check if the circumcentre is internal to the element. If not, the triangle is not considered a suitable candidate for a node placement since it is likely to be disrupted by the Watson algorithm applied to the surrounding ones [17,18].

If the triangle passes this test, a tentative new node is placed along the segment between incentre and circumcentre, and a series of steps are taken to check if the tentative node should be maintained or removed.

The first step is the definition of a region of support of the new node, using the classic Watson algorithm [18], and building j "virtual triangles" centred on the new node.

For each triangle k, the sizing function $S(x, y)$ defined in subsection 3.1 is computed at the nodes and assumed to vary over the area of the triangle Ω_k according to the element shape function. An "optimal local size" based on the error information contained in the function $S(x,y)$ is then computed as:

$$\Omega_k^{opt} = \frac{1}{\Omega_k} \int_{\Omega_k} S(x, y) d\Omega_k \tag{8}$$

For each of the above virtual triangles the ratio λ between the optimal and the real local size is computed as:

$$\lambda_k = \frac{\Omega_k^{opt}}{\Omega_k} \tag{9}$$

If for every virtual triangle of the area of support λ is smaller than one, the tentative node is deleted and the original triangle labelled as permanent; if not, the node and the virtual triangles are inserted in the mesh. The process is completed when all triangles are labelled as permanent.

The mesh originated by the above procedure is then subjected to a final "smoothing", using a rubber banding technique,to improve the aspect ratio of triangles if required.

4. TEST CASES

Two test cases are presented:

- L-shaped problem, often used for error estimate validation since it presents a singular point and it has a known solution;
- a geometry which has singular points, null field zones and homogeneous field zones distributed on it.

For each test case the initial mesh and the final mesh are shown.

In both cases the error requested on the solution was the 1% and the value was reached with a single remeshing loop.

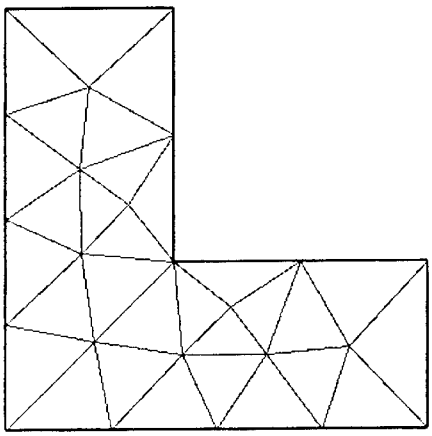


Fig 1: L-shaped problem initial mesh (23 nodes, 30 elements)

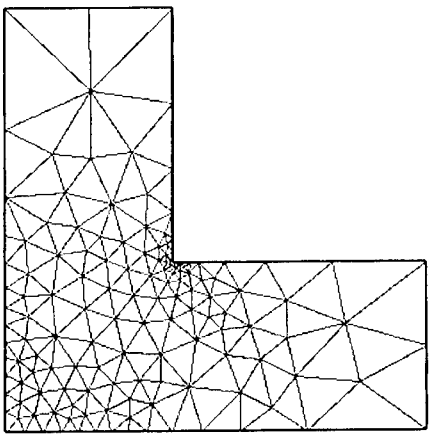


Fig 2: L-shaped problem final mesh (143 nodes, 240 elements)

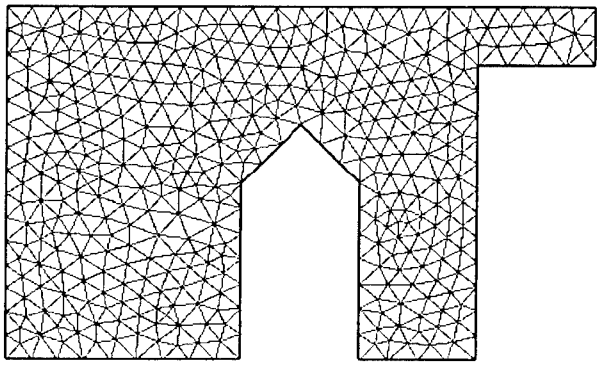


Fig. 3: Test case 2 initial mesh (435 nodes, 778 elements)

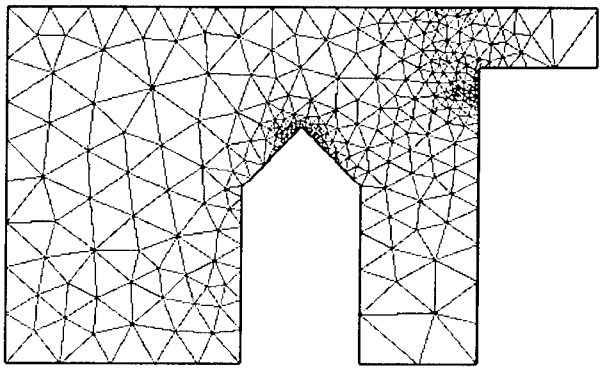


Fig. 4: Test case 2 final mesh (344 nodes, 561 elements)

5. CONCLUSIONS

The remeshing algorithm presented in this paper has proven, in the test cases performed so far, rather reliable and efficient, providing good quality results also with rather coarse initial meshes. With accuracy requirements adequate for many initial design purposes, the procedure has provided in most cases a mesh matching the requirements in a single iteration. Even if a remeshing iteration is somewhat computationally heavier than an usual h- or p-type adaption one, this seems to indicate a high likehood of computational savings for the remeshing approach, since more "classical" adaption procedures usually require three to five iterations or more in similar cases.

If coupled with reliable and efficient automatic meshing routines and with accurate and robust error estimation algorithms, the remeshing procedure here described appears promising to set up an efficient "accuracy driven problem solution" requiring to the user only the setting of accuracy levels desired and

no other intervention to define the mesh. However, further tests are necessary in more realistic design structures and in a larger variety of cases to test the ability of the procedure to reach this ambitious goal.

Further activity is also required to extend the coverage beyond the electrostatic and magnetostatic cases tested so far, particularly to problems involving time discretization, for whose solution, if reliable error estimators are available, the features of the proposed algorithm appear particularly promising.

6. REFERENCES

[1] I. Babuska, W.C. Rheinboldt: "A-posteriori error estimates for the Finite Element method" Int. J. for Num. Methods in Eng., Vol. 12, 1978, pp. 1597-1615.

[2] Z.J. Cendes, D.N. Shenton: "Adaptive mesh refinements in finite element computation of magnetic fields" IEEE Trans. on Magnetics, Vol. 21, Sept. 1985, pp. 1811-1816.

[3] C.S. Biddlecombe, J. Simkin, C.W. Trowbridge:"Error analysis in finite element models in electromagnetic fields" IEEE Trans. on Magnetics, Vol. 22, Sept. 1986, pp. 811-813.

[4] S. Hahn, C. Calmels, G. Meunier, J.L. Coulomb:"A posteriori error estimate for adaptive finite element mesh generation" IEEE Trans. on Magnetics, Vol. 24, Jan. 1988, pp. 315-317.

[5] M.G. Vanti, A. Raizer, and J.P.A. Bastos: "A magnetostatic 2D comparison of local error estimators in FEM". IEEE Trans. on Magn., Vol. 2, n. 2, March 1993, pp. 1902-1905.

[6] F.A. Fernandez, Y.C. Yong, and R.D. Ettinger: "A simple adaptive mesh generator for 2-D finite element calculations". IEEE Trans. on Magn. March 1993, Vol. 2, n. 2, 1882-1885.

[7] S. McFee and J.P. Webb: "Automatic mesh generation for h-p adaption". IEEE Trans. on Magn. Vol. 2, n. 2, March 1993, pp.1894-1897.

[8] P. Fernandes, P. Girdinio, P. Molfino, G. Molinari, M. Repetto: "A comparison of adaptive strategies for mesh refinement based on 'a posteriori' local error estimation procedures", IEEE Trans. on Mag., Vol. 26, n. 2, March 1990, pp. 795-798.

[9] P. Fernandes, P. Girdinio, G. Molinari: "Local error estimation in 2D magnetostatic problems with inhomogeneous materials and surface currents" (invited) Proc. of International Conference on Electromagnetic Field Problem and Applications, 14-16 Oct. 1992, Hangzhou, Cina.

[10] P. Fernandes, P. Girdinio, M. Repetto, G. Secondo: "Refinement strategies in adaptive meshing", IEEE Trans. on Mag., Vol. 28, n. 2, March 1992, pp. 1739-1742.

[11] P. Fernandes, P. Girdinio, G. Molinari: "Techniques of h-refinement in adaptive meshing algorithms", COMPEL, Vol. 13, Supplement A, May 1994, pp. 329-334.

[12] P. Girdinio, A. Kost, T. Kowalski, A. Manella, G. Molinari: "An automatic remeshing procedure for 2D electromagnetic FE codes" Proceedings of VI IGTE Symposium on Numerical Field Calculation in Electrical Engineering, Graz, Austria, 26-28 Sept. 1994, pp.144-149.

[13] P. Fernandes, P. Girdinio, P. Molfino, M. Repetto: "An enhanced error estimator procedure for finite element field computation with adaptive mesh refinement", IEEE Trans. on Mag., Vol. 26, no. 5, September 1990, pp. 2187-2189.

[14] P. Fernandes, P. Girdinio, G. Molinari, M. Repetto: "Locar error estimation procedures as refinement indicators in adaptive meshing", IEEE Trans. on Mag., Vol. 27, no. 5, September 1991, pp. 4189-4192.

[15] G. Drago, P. Molfino, M. Nervi, M. Repetto: "A Local Field Error problem approach for error estimation in Finite Element analysis" - IEEE Trans. on Mag. Vol. 28 n. 2, 1992, pp. 1743-1746.

[16] P. Girdinio, A. Manella, P. Molfino, M. Nervi: "A Facet Element error estimate for adaptive meshing in electrostatic FEM solutions", Proceedings of VI International IGTE Symposium on Numerical Field Calculation in Electrical Engineering, Graz, Austria, 26-28 Sept. 1994, pp.138-143.

[17] H. Frey - "Selective refinement: a new strategy for automatic node placement in graded triangular meshes" - Int. Jou. for Num. Meth. in Eng. vol. 24, 1987, pp. 2183-2200.

[18] D.F. Watson: "Computing the n-dimensional Delaunay tessellation with applications to Voronoi polytopes" Comp. J., Vol. 24, n. 2, 1981, pp. 167-172 .

FINITE ELEMENT ANALYSIS OF WAVEGUIDES USING EDGE–BASED MAGNETIC VECTOR POTENTIAL AND NODAL–BASED ELECTRIC SCALAR POTENTIAL

Jin–Fa Lee
Dept. of Electrical & Computer Engrg.
Worcester Polytechnic Institute
Worcester, MA 01609 USA

Gary Lizalek and John Brauer
The MacNeal–Schwendler Corporation
4300 W. Brown Deer Road
Milwaukee, WI 53223 USA

Email: j_brauer@macsch.com

Abstract

This paper presents and applies a new formulation for finite element computation of propagation constants and mode shapes in a wide variety of waveguiding structures. The formulation is novel in that its solution variables are the two components of the magnetic vector potential in the cross–sectional waveguide plane and the electric scalar potential. These variables form the eigenvectors of an eigenvalue problem in which the eigenvalues are related to propagation constants at the frequency of interest. The new finite elements are applied to inhomogeneous waveguide problems, including isotropic and anisotropic microstrip lines, and the computed high frequency propagation constants are shown to agree closely with those of previous papers. The new formulation also obtains correct *low frequency* propagation constants and mode shapes.

INTRODUCTION

Computation of waveguide dispersion, i.e., propagation constant versus frequency, has been carried out using finite elements for several years. A good summary of the various existing techniques has been recently presented in [1], where a total of six different formulations are examined and compared. Included are formulations by Lee et al [2], by Hano [3], and by Koshiba et al [4]. All six examined formulations use components of either the electric field or the magnetic field as their primary solution variables, as do more recent formulations [5], [6].

This paper presents a new formulation that for the first time uses *potentials* as the primary solution variables, not the fields themselves. The potentials used are the two components of the magnetic vector potential $\overline{A}$ and the electric scalar potential ϕ. The vector potential is used as an edge or tangential variable in edge–based finite elements, while the scalar potential is nodal–based. Use of the edge–based vector potential eliminates spurious modes in the desired solution spectrum and allows accurate analysis of waveguides with sharp interior conducting corners.

The first part of this paper uses Galerkin techniques to derive the eigenvalue equation in terms of the vector and scalar potentials. Next, the inhomogeneous rectangular waveguide of Hano [3] is analyzed by the new method. Finally, the two microstrip lines of Koshiba et al [4] are analyzed. The isotropic microstrip line is analyzed over an extremely broad frequency range, and the anisotropic microstrip line is also analyzed. High frequency propagation constants computed here are compared with those of others. Also, low frequency propagation constants are computed for the isotropic microstrip line.

THEORY

The new formulation is implemented in MSC/EMAS^{TM}, an electromagnetic analysis software package with 3D, 2D, 1D, and 0D finite elements [7], [8]. Its solution variables in 3D are the three components of magnetic vector potential $\vec{A}$ and the time−integrated electric scalar potential. To compute propagation constants for 2D waveguide cross−sections, we choose the transverse components of the magnetic vector potential $\vec{A}$ and the electric scalar potential ϕ (volts). Electric field is then:

$$\vec{E} \equiv -j\omega\vec{A}_\tau - \nabla\phi \tag{1}$$

We transform the potentials as follows, where c_0 is the speed of light in vacuum:

$$\vec{A}'_\tau \equiv j\vec{A}_\tau \qquad \phi' \equiv \frac{\phi}{c_0} \tag{2}$$

Substituting (2) in (1), and denoting transverse components by τ and the complex propagation constant in the longitudinal z direction by $\gamma = \alpha + j\beta$:

$$\vec{E} = -\omega\vec{A}'_\tau - c_0\nabla_\tau\phi' + \gamma c_0\phi'\,\hat{z} \tag{3}$$

$$\vec{E}_\tau = -\omega\vec{A}'_\tau - c_0\nabla_\tau\phi' \qquad E_z = \gamma c_0\phi' \tag{4}$$

The magnetic flux density is defined by Faraday's Law:

$$\vec{B} = -j\left\{\left(\nabla_\tau - \gamma\,\hat{z}\right) \times \vec{A}'_\tau\right\} = -j\left(\nabla_\tau \times \vec{A}'_\tau - \gamma\,\hat{z} \times \vec{A}'_\tau\right) \tag{5}$$

$$\vec{B}_\tau = j\,\gamma\left(\hat{z} \times \vec{A}'_\tau\right) \qquad B_z = -j\left(\nabla_\tau \times \vec{A}'_\tau\right) \tag{6}$$

$$\frac{1}{c_0} = \sqrt{\mu_0\,\varepsilon_0} \qquad \eta = \sqrt{\frac{\mu_0}{\varepsilon_0}} = \frac{1}{\varepsilon_0 c_0} \qquad k_0 = \frac{\omega}{c_0} \tag{7}$$

Using the above relations, Ampere's Law gives (where reluctivity is ν):

$$-j\,\nabla \times [\nu_r]\left(\nabla \times \vec{A}'\right) + \omega\mu_0[\sigma]\vec{A}'_\tau + \eta[\sigma](\nabla\phi') + jk_0^2[\varepsilon_r]\vec{A}'_\tau + jk_0[\varepsilon_r](\nabla\phi') = 0 \tag{8}$$

The continuity equation gives:

$$\left.\begin{aligned} j\omega c_0\varepsilon_0\,\nabla_\tau \cdot [\varepsilon_r]\nabla_\tau\phi' + j\omega^2\varepsilon_0\,\nabla_\tau \cdot [\varepsilon_r]\vec{A}'_\tau + c_0\nabla_\tau \cdot [\sigma]\nabla_\tau\phi' + \omega\nabla_\tau \cdot [\sigma]\vec{A}'_\tau \\ + \gamma^2\left(\, j\omega c_0\varepsilon_0\varepsilon_{zz_r}\,\phi' + c_0\sigma_{zz}\,\phi'\right) \end{aligned}\right\} = 0 \tag{9}$$

Galerkin's method is now used. Testing with $j\,\delta\vec{A}'_\tau$ and with $\frac{-j}{\omega\varepsilon_0 c_0}\,\delta\phi'$ can be shown to yield an equation in terms of the square of the propagation constant:

$$[K]\begin{Bmatrix}\vec{A}'_\tau \\ \phi'\end{Bmatrix} = \gamma^2\,[M]\begin{Bmatrix}\vec{A}'_\tau \\ \phi'\end{Bmatrix} \tag{10}$$

where [K] and [M] are symmetric indefinite matrices. The eigenvalues of (10) are the propagation constants and the eigenvectors define the modal fields. The matrices of (10) have been derived

for first order and second order quadrilateral and triangular finite elements in MSC/EMAS for the case of propagating modes, where $\gamma = j\beta$. In this case the eigenvalues of (10) are real.

APPLICATION TO INHOMOGENEOUS RECTANGULAR WAVEGUIDE

Here we present the results of the above formulation for the inhomogeneous rectangular waveguide of Hano [3]. It is modeled using quadrilateral finite elements and analyzed by MSC/EMAS.

Fig. 1 shows the model made up of 40 first order quadrilaterals. Hano's dimension h is here set to 0.1 meter. Note that half of the guide is filled with air. The other half is filled with a dielectric material ε that has permittivity 4 times air. Figure 1 shows the computed E and H fields for the first two modes at 1.91 GHz, which corresponds to Hano's $k_0 h = 4$.

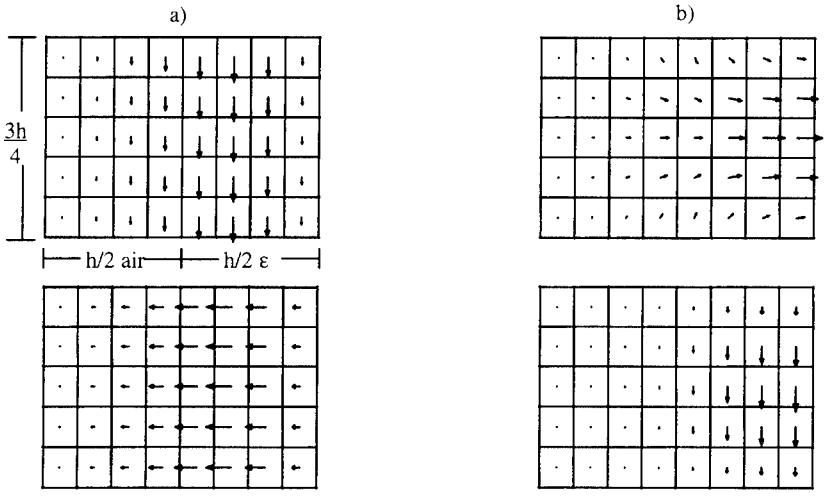


Fig. 1. Finite element model of inhomogeneous rectangular waveguide and E (upper), H (lower) fields computed at 1.91 GHz. a). mode 1, b). mode 2.

Table 1 lists the propagation constants computed at three different frequencies. Note that at $k_0 h = 2.5$, only the fundamental mode exists. At $k_0 h = 4$, three modes propagate, and six modes propagate at $k_0 h = 5$. The propagation constants of Table 1 agree very closely with those of Hano's graph [3]. Unlike Hano's paper, no spurious modes were observed using the formulation of this paper.

Table 1. MSC/EMAS computations of inhomogeneous rectangular waveguide

f (GHz)	$k_o h$	Propagation constants β (1/meter)
1.19	2.5	27.365
1.91	4.0	63.702, 61.196, 47.381
2.38	5.0	85.499, 85.200, 74.142, 36.959, 33.045, 29.665

APPLICATION TO MICROSTRIP LINE

Here we present the results of the above formulation for the inhomogeneous microstrip transmission line of Koshiba [4]. It is modeled using quadrilateral finite elements and analyzed by MSC/EMAS.

Fig. 2 shows the microstrip model made up of 80 first order quadrilaterals. As specified by Koshiba, the width w of the strip is 1.27 mm, and the dielectric height h has the same dimension. Note that the model is very coarse in that the strip is only two elements wide.

Fig. 2 also shows the E and H fields computed for the first two modes at 30 GHz. These are for Koshiba's first case where the substrate has an isotropic relative permittivity of 8.875. Table 2 lists the computed propagation constants at this frequency and at lower frequencies. Note that at the low frequencies, only the fundamental quasi−TEM mode exists. Table 2 also lists the propagation constants computed here for Koshiba's second case, which is anisotropic. The permittivity tensor is assumed to be diagonal, with a relative permittivity of 9.4 in the x and z directions, and 11.6 in the vertical y direction.

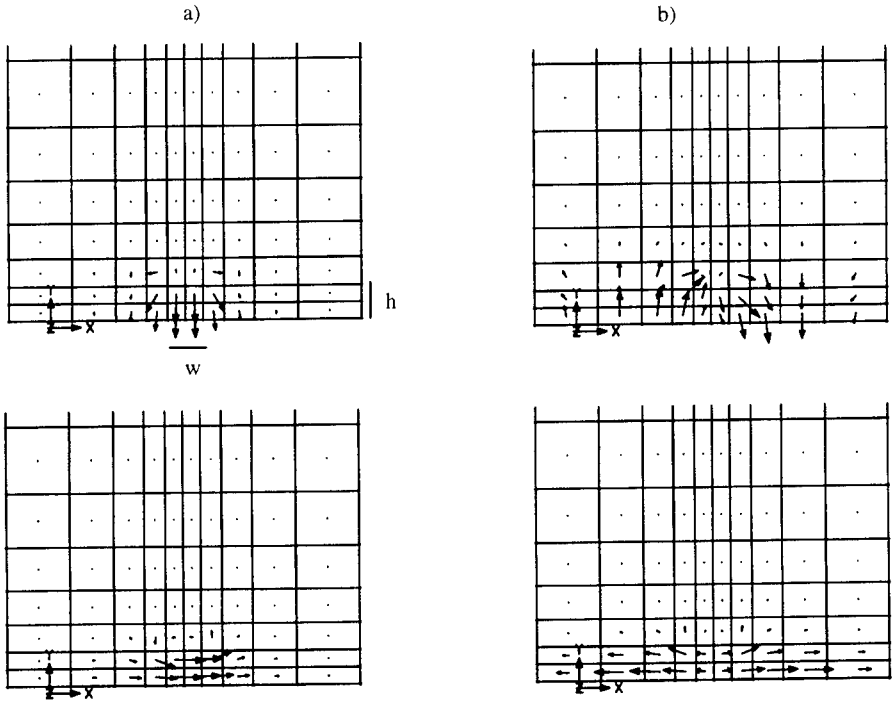


Fig. 2. Finite element model of microstrip and computed
E (upper), H (lower) fields for isotropic dielectric at 30 GHz. a). mode 1, b). mode 2.

Table 2. MSC/EMAS computations of microstrip line, where + = additional mode(s)

f (Hz)	Isotropic β(1/m)	Anisotropic β (1/m)
1 k	5.18E−5	not analyzed
10 k	5.11E−4	not analyzed
1 M	5.11E−2	not analyzed
5 G	263	294
10 G	545	615
15 G	840, 238, 224	954, 244, +
20 G	1144, 580, +	1304, 724, +
25 G	1454, 1014, +	1661, 1204, +
30 G	1767, 1315, +	2021, 1652, +

The propagation constants of Table 2 can be compared to those computed by Koshiba. Both the results of his original method [4] and his recently improved method [9] will be compared to the Table 2 propagation constants for the first two modes.

Fig. 3 shows the results for the first isotropic mode over frequencies up to 30 GHz. Note that the results here appear to be identical to those of Koshiba. However, Fig. 4 is a detail near the origin. Note that the MSC/EMAS results are a straight line, whereas Koshiba's results are not. Because the first mode is TEM, the slope should be constant at these frequencies. Hence the MSC/EMAS formulation is more accurate than Koshiba's at low frequencies.

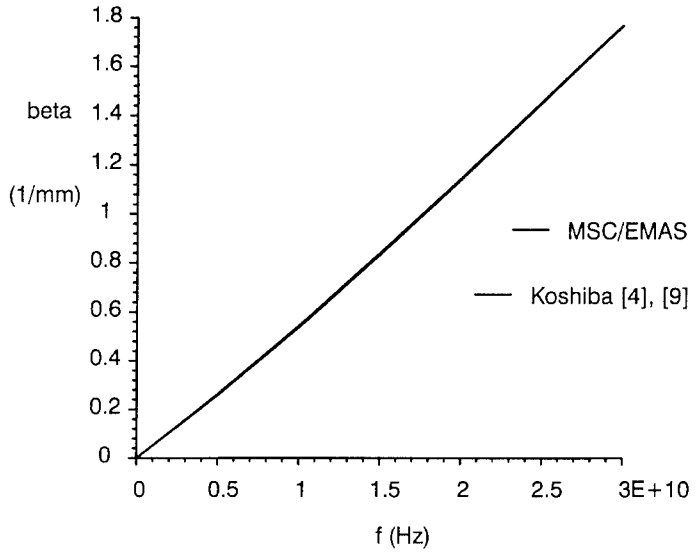


Fig. 3. Isotropic microstrip, mode 1

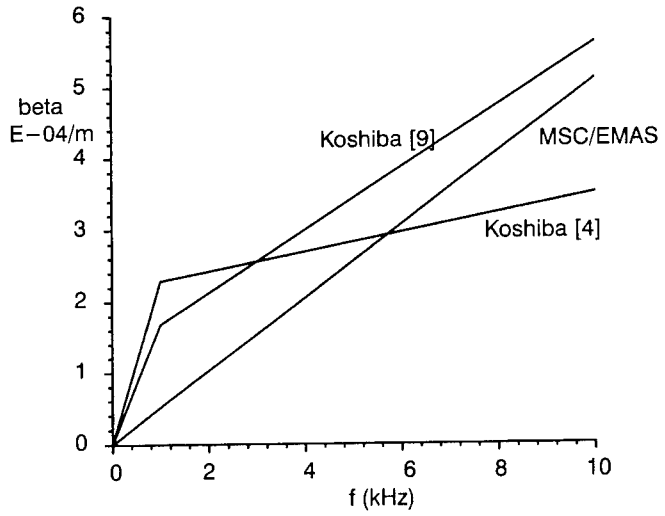


Fig. 4. Isotropic microstrip mode 1, low frequency

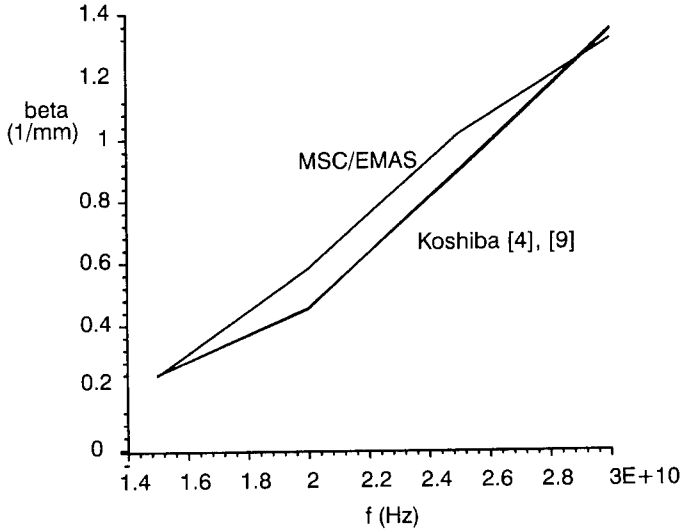


Fig. 5. Isotropic microstrip, 2nd mode

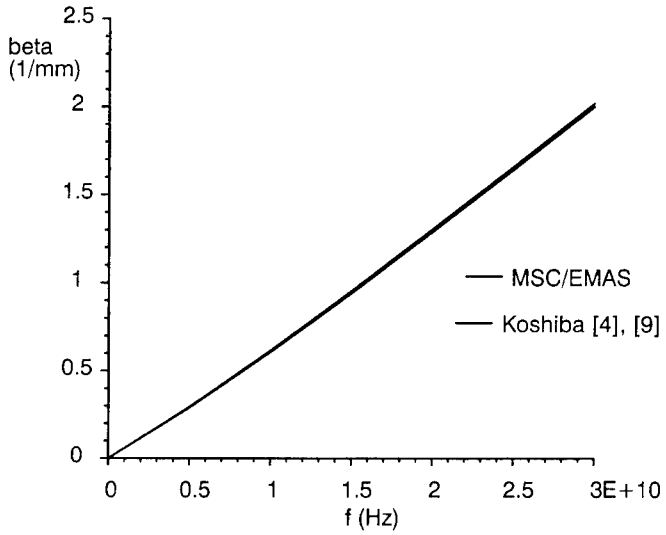


Fig. 6. Anisotropic microstrip, mode 1

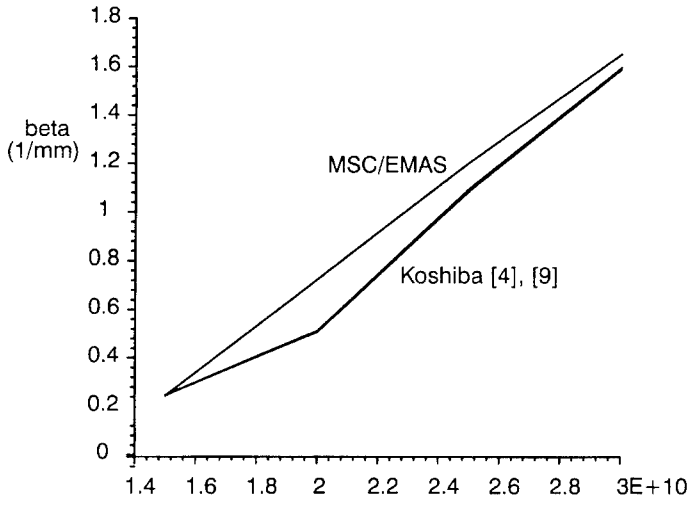


Fig. 7. Anisotropic microstrip, mode 2

Fig.5 compares propagation constants computed for the second mode in the isotropic case. Note that the MSC/EMAS results disagree somewhat from Koshiba's results for this mode.

Figs. 6 and 7 compare propagation constants computed for the two modes in the anisotropic case. Note again that the MSC/EMAS results agree closely with Koshiba's results for the first mode, but disagree somewhat from Koshiba's results for the second mode.

CONCLUSIONS

New finite elements have been developed for computation of propagation constants and modal fields in waveguiding structures. The use of edge–based magnetic vector potential and nodal–based electric scalar potential appears to be advantageous in that low frequency results for microstrip are more accurate than those reported by others. The high frequency propagation constants are also accurately computed, as demonstrated by the microstrip with isotropic or anisotropic materials, and by a rectangular inhomogeneous waveguide.

ACKNOWLEDGMENT

The authors thank Dr. Masanori Koshiba for sending us his detailed numerical results for microstrip propagation constants using the methods of his two papers [4], [9].

REFERENCES

[1] Bernice M. Dillon and Jon P. Webb, "A comparison of formulations for the vector finite element analysis of waveguides," *IEEE Trans. Microwave Theory & Techniques*, v. 42, Feb. 1994, pp. 308–316.

[2] J. Lee, D. Sun, and Z. Cendes, "Full–wave analysis of dielectric waveguides using tangential vector finite elements," *IEEE Trans. Microwave Theory & Techniques*, v. 39, Aug. 1991, pp. 1262–1271.

[3] Mitsuo Hano, "Finite element analysis of dielectric–loaded waveguides," *IEEE Trans. Microwave Theory & Techniques*, v. 32, Feb. 1984, pp. 1275–1279.

[4] Masanori Koshiba and Kazuhiro Inoue, "Simple and efficient finite element analysis of microwave and optical waveguides," *IEEE Trans. Microwave Theory & Techniques*, v. 40, Feb. 1992, pp. 371–377.

[5] Jin–Fa Lee, "Finite element analysis of lossy dielectric waveguides," *IEEE Trans. Microwave Theory & Techniques*, v. 42, June 1994, pp. 1025–1031.

[6] M. S. Alam, K. Hirayama, Y. Hayashi, and M. Koshiba, "Analysis of shielded microstrip lines with arbitrary metallization cross secton using a vector finite element method," *IEEE Trans. Microwave Theory & Techniques*, v. 42, Nov. 1994, pp. 2112–2117.

[7] John R. Brauer (ed.), *What Every Engineer Should Know About Finite Element Analysis (2nd ed.)*, New York: Marcel Dekker, Inc., 1993.

[8] J. R. Brauer, B. S. Brown, and M. M. Jenich, "ABC finite elements for open boundary electromagnetic problems of frequencies from dc to GHz,", *Proc. of ACES Symposium*, 1993, pp. 830–837.

[9] Masanori Koshiba, Shiji Maruyama, and Koichi Hirayama, "A vector finite element method with the high–order mixed–interpolation–type triangular elements for optical waveguiding problems," *J. of Lightwave Technology*, v. 12, March 1994, pp. 495–502.

A Scattering Analysis of Laser Beam Wave by Groove Pits on Optical Memory Disk by Using FEM with BEM

Yasumitsu MIYAZAKI and Keiji TANAKA

Department of Information and Computer Sciences, Toyohashi University of Technology, 1-1, Hibarigaoka, Tempaku-cho, Toyohashi-shi, Aichi, 441 Japan

Abstract — Numerical solutions of electromagnetic fields are presented for scattering by guide-grooves and recording marks on re-writable type phase-change optical disks with multi-layered structure. The finite element method with boundary element method can be applied to scattering analysis of various groove forms and inhomogeneous recording marks under different conditions of the incident beam. Near and scattered far fields characteristics from guide-grooves having trapezoidal shapes in cross section are studied for different polarization of incident beam wave. Characteristics of read-out signals are also calculated as functions of groove height and film-thickness of multi-layer. As a result of numerical analysis, the groove height to obtain maximum tracking sensitivity and optimum film-thickness of multi-layer are found.

1 Introduction

Recently, optical memory disks able to store a large information have been used as video disks, digital audio disks, CD-ROM and so on. Memory signals are recorded on disk substrate in the form of pits or recording marks, which have dimensions of the order of optical wavelength λ_0. Exact evaluation of the scattering characteristics is important to optimize the shape of pits, guide-grooves and recording marks, in order to increase the memory density and capacity.

The optical disks are classified into several categories of read-only type, write-once type, and re-writable type. Scattering characteristics of read-only disk pits and guide-grooves have been studied using the diffraction theory in a scalar field[1], the diffraction theory in a vector field[2], and precise electromagnetic field analysis[3]. According to diffraction theory in a scalar field, where the size of a scattering body is of the same order or less than the wavelength λ_0, an exact solution cannot be obtained. In the diffraction theory of vector field or the precise field analysis, on the other hand, the analysis is more complicated and imposes restrictions on the shapes of pits and guide-grooves and the incident beam. We used the boundary element method (BEM) to apply several conditions and obtained satisfactory results[4]-[6].

In the scattering analysis of laser beam wave from pits and grooves on the optical disks of write-once type and re-writable type, it is necessary to analyze the optical scattering characteristics of pits and grooves on the boundaries of multi-layered dielectric medium. For re-writable type of phase-change optical disk, memory signals are recorded on the recording layer. The recording layer changes from crystalized form before recording into non-crystalized one after recording, and it yields inhomogeneous region of refractive index, called the "Recording mark". The scattering field analysis by the finite element method (FEM) with BEM yields exact characteristics.

In the case of the re-writable type optical disk, the FEM can be applied to the analysis of the inhomogeneous region of the multi-layer, and the BEM can be applied to the homogeneous region of the poly-carbonate (PC) substrate, which is an open region. The fields represented by BEM and FEM are matched on the boundary between the PC substrate and multi-layer. The fields on the boundary between multi-layer and reflection layer satisfy the surface impedance boundary condition. In this paper, scattering characteristics by re-writable type groove pits are discussed for TE-wave and TM-wave. In this paper, we have presented the formulation using the FEM with BEM in section 2 and shown some results in section 3.

2 Formulation

Figure 1 shows sectional view across the radius of phase-change optical disk. There are recording marks in the recording layer over the guide-groove. Memory signals are detected by photo detectors as a change of

Table 1: Analysis parameter of phase-change optical disk (λ_0=0.83[μm])

Region	Structure of Film		Refractive Index	Film-thickness
S_1	Substrate	PC	$n_1 = 1.58$	Infinity
S_2	Upper protective Layer	ZnS-SiO_2	$n_{21} = 2.1$	d_1=140nm
	Memory Layer	GeSbTeSe	$\hat{n}_{22} = 5.6 - j2.4$ $\hat{n}_r = 4.5 - j1.0$	d_2=40nm
	Lower protective Layer	ZnS-SiO_2	$n_{23} = 2.1$	d_3=200nm
S_3	Reflection Layer	Au	$\hat{n}_3 = 0.2 - j5.0$	Infinity

scattered field intensities. Actual phase- change optical disks have three dimensional structure. However, for simplification, the scattering analysis model regards a two-dimensional structure. Figure 2 shows the scattering analysis model for phase-change optical disk with coordinates for the trapezoidal guide-grooves and the incident beam. Let the coordinate system for the guide-grooves be (x, y, z) with an origin O and that for incident beam be (x, y', z') with an origin O'. The phase-change optical disk is consist of a reflection layer region S_3, a multi-layer region S_2 and a substrate region S_1 formed poly-carbonate. The multi-layer region S_2 consists of protective and recording layers. There is a boundary Γ_1 between the region S_1 and S_2, and a boundary Γ_2 between the region S_2 and S_3. The boundaries Γ_1 and Γ_2 have the shape of trapezoidal guide-groove. The shape of trapezoidal guide-groove on the reflection layer has an upper width $2w_U$, lower width $2w_L$, recording mark width $2w_r$, height h and track pitch b. The shape of guide groove is similar to the boundary Γ_1 and Γ_2. A recording layer of GeSbTeSe film[7] is formed between dielectric layers made of ZnS-SiO_2, and an Au reflective layer is set below them. The values of refractive index and the film thickness in each layers used for the analysis are shown in Table 1. The refractive index in recording mark changes $\hat{n}_{22}$ into n_{rm}. In our formulation, the region S_1 which is homogeneous and unclosed region applies to the BEM. And inhomogeneous region S_2 applies to the FEM. Then the region S_3 which is a good conductor applies to surface impedance approximation method.

The incident beam ϕ_x^{in} is two-dimensional Gaussian beam of TE-wave (having only the x component of electric field $\mathbf{E}$) or TM-wave (having only the x component of magnetic field $\mathbf{H}$). The beam waist w_0 is located on y' axis; y_0 represents the tracking error; and θ_{in} represents the angle of incidence. The focus point (y_0, z_0) of the incident beam sets a point O_f on the recording layer.

The incident beam ϕ_x^{in} for TE-wave and TM-wave

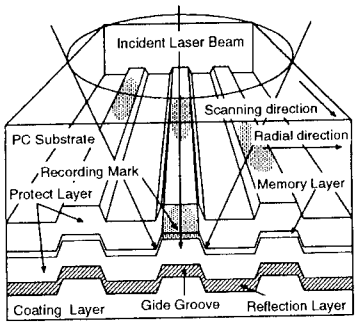


Figure 1: A radial section of phase-change optical disk

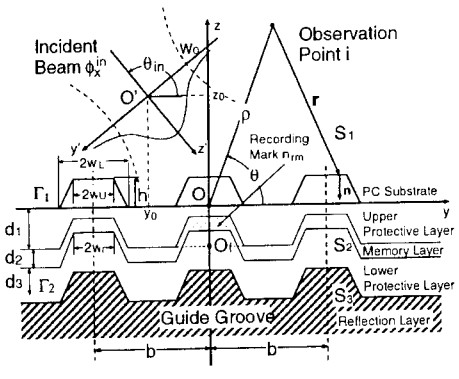


Figure 2: Analysis model for phase-change optical disk.

can be represented by

$$\phi_x^{in} = \begin{pmatrix} E_0 \\ H_0 \end{pmatrix} u(y', z'), \tag{1}$$

where

$$u(y', z') = \sqrt{\frac{w_0}{w(z')}} \cdot \exp\left[-j(k_1 z' - \psi(z')) - \left(j\frac{2z'}{k_1 w_0^2} + 1 \right) \frac{y'^2}{w^2(z')} \right], \tag{2a}$$

$$w^2(z') = w_0^2 \left\{ 1 + \left(\frac{2z'}{k_1 w_0^2} \right) \right\}, \tag{2b}$$

$$\psi(z') = \frac{1}{2} \tan^{-1} \left(\frac{2z'}{k_1 w_0^2} \right), \tag{2c}$$

w_0 is the spot size at the beam waist and $k_1 = \omega\sqrt{\varepsilon_1 \mu_1}$ is propagation constant in the region S_1. The time factor $\exp(j\omega t)$ is omitted from our formulations.

The field ϕ_1 in the region S_1 and the field ϕ_2 in the region S_2 satisfy the following Helmholz's equations, respectively;

$$\nabla^2 \phi_1 + k_1^2 \phi_1 = -g_1 \qquad \text{in } S_1, \tag{3}$$

$$\nabla \cdot \left(\frac{1}{p_2} \nabla \phi_2 \right) + q_2 k_0^2 \phi_2 = 0 \qquad \text{in } S_2, \tag{4}$$

where g_1 is a wave source in the region S_1. p and q are given by

$$p_n = \begin{cases} 1 \\ \varepsilon_n/\varepsilon_0 \end{cases}, q_n = \begin{cases} \varepsilon_n/\varepsilon_0 & \text{(TE-wave)} \\ 1 & \text{(TM-wave)} \end{cases}, \tag{5}$$

where $\varepsilon_n/\varepsilon_0 (n = 1, 2, 3)$ is ratio of permittivity in each region and $k_0 = \omega/c$ is the free space propagation constant with c the light velocity.

The boundary conditions on Γ_1 are given by

$$\phi_1 = \phi_2, \tag{6a}$$

$$\frac{1}{p_1} \frac{\partial \phi_1}{\partial n} = \frac{1}{p_2} \frac{\partial \phi_2}{\partial n}, \tag{6b}$$

where $\partial/\partial n$ represents the differential of the inward normal direction to the region S_2.

The boundary condition on Γ_2 for TE-wave and TM-wave can be represented by the surface impedance boundary condition;

$$\frac{1}{p_2} \frac{\partial \phi_2}{\partial n} = \begin{pmatrix} j\omega\mu_0/Z_m \\ j\omega\varepsilon_0 Z_m \end{pmatrix} \phi_2, \tag{7}$$

where

$$Z_m = \sqrt{\frac{\mu_0}{\varepsilon_3}} \tag{8}$$

is the surface impedance of the region S_3, because S_3 is good conductor.

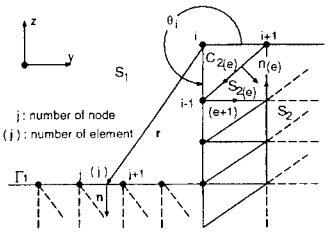


Figure 3: Integral of each element

2.1 Boundary element analysis in the region S_1

For the boundary element analysis, the weight function is the Green function in the two-dimensional free space as follows;

$$\phi^* = -\frac{j}{4} H_0^{(2)}(k_1 r), \tag{9}$$

where $H_0^{(2)}$ is the zero-th order Hankel function of the second kind. When the boundary element method with weighted residual procedure is applied to Eq.(3), the following equation is obtained:-

$$\int_{\Gamma_1} (\phi_1 \frac{\partial \phi^*}{\partial n} - \phi^* \frac{\partial \phi_1}{\partial n}) d\Gamma = \phi_{xi}^{in} - \phi_{1i}. \tag{10}$$

When point i is on the boundary Γ_1, the following boundary integral equation is obtained:-

$$C_i \phi_{1i} + \oint_{\Gamma_1} \frac{\partial \phi^*}{\partial n} \phi_1 d\Gamma - \oint_{\Gamma_1} \phi^* \frac{\partial \phi_1}{\partial n} d\Gamma = \phi_{xi}^{in}, \tag{11}$$

where C_i is determined by the angle θ_i which is defined in figure 3, and $C_i = \theta_i/2\pi$ is obtained. $\oint$ represents the Cauchy principal value integration. By dividing Eq.(11) into N_{elt} boundary elements and expanding the field ϕ_1 and $\partial\phi_1/\partial n$ using the interpolation functions $f_j (j = 1, 2, \ldots, N_{nbl})$, the discrete equation with respect to point i on the boundary Γ_1 is obtained. ϕ_1 and $\partial\phi/\partial n$ at all the nodal points are given by the matrix representation,

$$[H] \{\phi_1\} - [G] \left\{ \frac{\partial \phi_1}{\partial n} \right\} = \left\{ \phi_x^{in} \right\}, \tag{12}$$

where matrices $[H]$ and $[G]$ represent square matrices of $N_{nbl} \times N_{nbl}$. $\{\phi_1\}$, $\{\partial\phi_1/\partial n\}$ and $\left\{\phi_x^{in}\right\}$represent vectors of $N_{nbl} \times 1$.

2.2 Finite element method in the region S_2

For the finite element analysis, the region S_2 is divided into N_{ef} triangular elements. We apply the

Galerkin method to obtain the equation about an element '(e)', by multiplying Eq.(4) by the weight function $f_j (j = 1, 2, \ldots, N_{nf})$, and integrating over the area $S_{2(e)}$of a triangular element '(e)' as shown in figure 3. The following equation is obtained by summation of all elements:

$$\sum_e \int_{S_{2(e)}} (q_2 k_0^2 f_j \phi_2 - \frac{1}{p_2} \nabla f_j \cdot \nabla \phi_2) dS - \sum_e \int_{C_{(e)}} f_j \frac{1}{p_2} \frac{\partial \phi_2}{\partial n_{(e)}} d\Gamma = 0, \quad (13)$$

where $\int_{C_{2(e)}}$ represents an integration along the contour $C_{(e)}$ and $n_{(e)}$ represents a unit vector of inward normal direction to the region $S_{2(e)}$ as shown in figure 3 Eq.(13) reduces to the following equation due to the boundary and continuity conditions between neighboring elements:

$$\int_{S_2} (q_2 k_0^2 f_j \phi_2 - \frac{1}{p_2} \nabla f_j \cdot \nabla \phi_2) dS - \int_{\Gamma_1 + \Gamma_2} f_j \frac{1}{p_2} \frac{\partial \phi_2}{\partial n} d\Gamma = 0. \quad (14)$$

The field ϕ_2 in the region S_2 is represented by expanding using the interpolation function f_k, which is similar to weight function f_j. The differential $\partial\phi_2/\partial n$ along normal direction on the boundary Γ_1 and Γ_2,is also represented similarly. Therefore ϕ_2 and $\partial\phi_2/\partial n$ at all the nodal points in the region S_2 are given by the matrix representation,

$$[K]\{\phi_2\} - [M]\left\{\frac{\partial \phi_2}{\partial n}\right\} = \{0\}, \quad (15)$$

where $[K]$ represents a square matrix of $N_{nf} \times N_{nf}$, $[M]$ represents a matrix of $N_{nf} \times (N_{nb1} + N_{nb2})$. Also $\{\phi_2\}$ and $\{\partial\phi_2/\partial n\}$ represents vectors of $N_{nf} \times 1$ and $(N_{nb1} + N_{nb2}) \times 1$, respectively.

2.3 Combination of FEM and BEM

By substituting the boundary conditions Eq.(6a) and Eq.(6b) at the boundary Γ_1. and the boundary condition Eq.(7) at the boundary Γ_2 into Eq.(15), the field represented by BEM and FEM are matched on the boundary Γ_1. ϕ_2 and $\partial\phi_2/\partial n$ at each nodal point are obtained by solving matrix equations of the FEM and BEM. The scattered field ϕ_{1i}^{sc} at an arbitrary point i in the region S_1 is given by

$$\phi_{1i}^{sc} = \sum_{j=1}^{N_{nb1}} G_{i,j} \frac{\partial \phi_{1j}}{\partial n} - \sum_{j=1}^{N_{nb1}} H_{i,j} \phi_{1j}, \quad (16)$$

where $H_{i,j}$ is the element in the matrix $[H]$ when the value C_i for its diagonal element is put to zero. The scattered field intensity $P_s(\theta)$ is defined by

$$P_S(\theta) = 20 \cdot \log_{10}\left(\frac{|\phi_1^{sc}(\rho,\theta)|}{max|\phi_0^{sc}(\rho,\theta)|}\right), \quad (17)$$

where $\phi_0^{sc}(\rho,\theta)$ represents the scattered far field from the perfectly conducting plane in the PC substrate ($n_1 = 1.58$).

If both the incident beam and the groove shape in figure 2 are symmetrical to z-axis, the analysis region can be reduced to half that of each region. Although the region S_2 is an infinite one, this is truncated at a point where equivalent surface current is sufficiently attenuated. We have confirmed that numerical solutions obtained by the present formulation agree well with another method[8].

3 Numerical Results

The constant parameters used in the calculations are; incident wavelength $\lambda_0 = 0.83\mu$m. NA (Numerical Aperture of objective lens) = 0.5, $w_0 = 0.41\lambda_0/NA$, $\rho = 1000\lambda_0/n_1$, $w_U = w_r = w_0$, $w_L = 1.2w_U$, $b = 1.6\mu$m. The refractive index and film-thickness of each layer show in Table 1. These parameters are used in the calculations for the following numerical examples unless we pay attention to the parameter. There are three guide-grooves in the analysis region. The recording layer is homogeneous before recording, but that changes to inhomogeneous after recording. This is because the recording signal is marked on recording layer over center guide-groove after recording by the writing laser beam. We call the part of marking 'Recording Mark'.

Figure 4 shows allocation of triangular element in region S_2 with symmetry about z-axis. The region S_2 is divided into N_{ef} structured triangular elements. The boundary Γ_1 and Γ_2 are divided into N_{eb1} and N_{eb2} linear elements, respectively. The length of linear element and the edge of triangular element are less than 1/10 of the wavelength λ_n (n=1,2,3) in each region. As a result of dividing the elements in each region, the finite element mesh consist of 2520($=N_{ef}$) triangular elements with 1377($=N_{nf}$) nodes. There are 81($=N_{nb1}$) nodes on the boundary Γ_1 and 97($=N_{nb2}$) nodes on the boundary Γ_2. Taking advantage of the property of band and sparse of $[K]$ matrix, the memory size of the computer can be small.

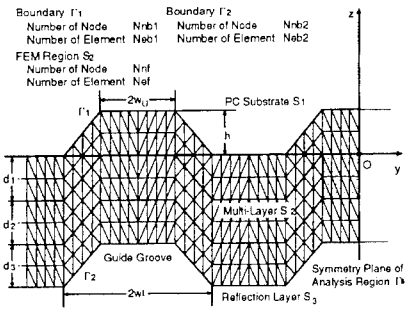


Figure 4: Allocation of triangular elements

3.1 Characteristics of Scattered Far Fields

Figure 5 shows the changes of the scattering far field patterns before and after recording for TE-wave and TM-wave, where BEF-REC and AFT-REC in the figure represent the state before recording and after recording, respectively. The scattered far field patterns change widely in the range $\theta = 60 \sim 90°$. The main lobes fall to a low value after recording both polarizations. The scattered far field at $\theta = 90°$ after recording is lower by about 6dB than that before recording. The side lobe at about 70° appears after recording. The dip between main and side lobes for TM-wave is larger than that for TE-wave. So the difference before and after recording for TM-wave is larger than that for TE-wave.

Figure 6 shows the changes of the scattered far field patterns as a function of tracking error y_0 for TE-wave and TM-wave before recording. As the tracking error y_0 is large, the scattered far field in the range of $\theta = 0 \sim 90°$ is large in comparison with $\theta = 90 \sim 180°$. When y_0 is 0.4μm, there is a deep dip at about 100°. Then the difference of scattered field between right and left half planes is maximum. When y_0 is greater than 0.4μm, the scattered far field intensity at $\theta = 90°$ becomes much larger and the scattering far field patterns become symmetric.

3.2 Characteristics of Near Fields

The scattered far field and the field in the multi-layer are relative to each other. Therefore, we have analyzed fields near the center guide-groove. Fields are composed of scattered fields and incident fields. First figure 7 and figure 8 show distributions of electric fields

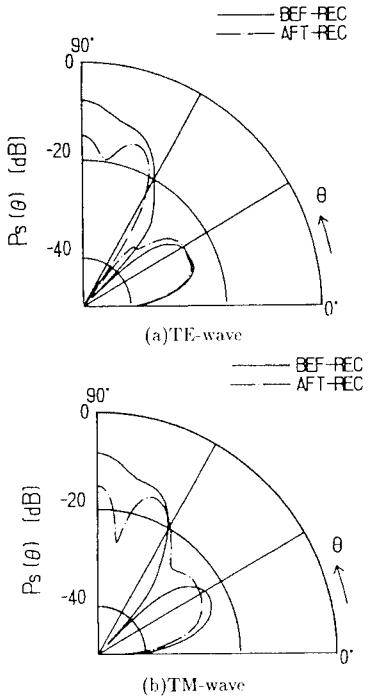


Figure 5: Scattered field patterns by phase-change optical disk, for $w_U = w_r = w_0$, $w_L = 1.2w_U$, $h = \lambda_0/8n_1$, $b = 1.6\mu$m, $y_0 = 0$, $\rho = 1000\lambda_0/n_1$.

and magnetic fields for TE-wave and TM-wave, where figure (a) and (b) represent it before recording and after recording, respectively. For both the polarization, there are standing waves over the boundary Γ_1, and the standing waves ratio before recording are bigger than that after recording. In the multi-layer region S_2, the electric fields in lower protective layer after recording for TE-wave are greater than that before recording. Also the magnetic fields for TM-wave are similar, except that the magnetic fields are great on the conductive medium. These phenomena are considered resonant in lower protective layer between recording and reflection layers. The difference of scattered field before and after recording is that the film-thickness for resonance is changed by the refractive index of recording layer. This difference affects scattered far fields. The

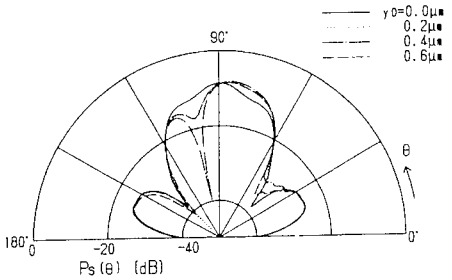


Figure 6: Scattered field patterns with tracking errors (TE-wave), for $w_U = w_r = w_0$, $w_L = 1.2w_U$, $h = \lambda_0/8n_1$, $b = 1.6\mu$m, $\rho = 1000\lambda_0/n_1$.

main lobes of scattered far field patterns largely depend on the film-thickness of lower protective layer. And read-out signal I_s is maximum when the film-thickness d_3 in lower protective layer is a suitable value.

Near field intensity and corresponding equivalent induced currents are important for evaluation of scattering by inhomogencities and index changes. Figure 9 shows equivalent induced currents corresponding to field intensities at the boundary discontinuities ϕ_i and $J_i = \partial\phi_i/\partial n$.

3.3 Characteristics of Read-Out Signals

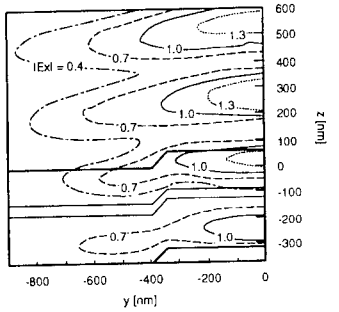
The wave to be scattered by the recording mark and guide-grooves on the optical disk are detected by two split photo detector through an objective lens. Here we define the read-out signal I_s and the tracking error signal I_d. I_s is sum of output signal of both two detectors. I_d is difference output signal of two detectors. The read-out signal and tracking signal are given by

$$I_s = \frac{1}{I_0}\int_{-\alpha}^{\alpha} |\phi_1^{sc}|^2 d\theta, \tag{18}$$

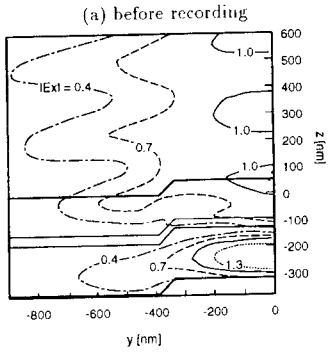
$$I_d = \frac{1}{I_0}\left\{\int_{0}^{\alpha} |\phi_1^{sc}|^2 d\theta - \int_{-\alpha}^{0} |\phi_1^{sc}|^2 d\theta\right\}, \tag{19}$$

respectively. Where ϕ_1^{sc} is the distribution of scattered far fields, $\alpha = \sin^{-1}(NA/n_1)$ is the angle of aperture, I_0 represents read-out signal by the perfectly conductive plane in the PC substrate ($n_1 = 1.58$). Now we define read-out signal $I_{s(BEF)}$ before recording and $I_{s(AFT)}$ after recording and amplitude of read-out signal $\Delta I_s = I_{s(BEF)} - I_{s(AFT)}$.

Figure 10 shows read-out signal I_s and maximum tracking error signal I_{dmax} versus the guide-groove



(a) before recording

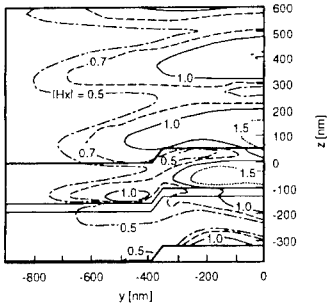


(b) after recording

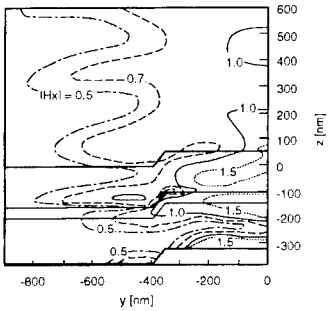
Figure 7: Distributions of electric fields near a center guide-groove (TE-wave), for $w_U = w_r = w_0$, $w_L = 1.2w_U$, $h = \lambda_0/8n_1$, $b = 1.6\mu$m, $y_0 = 0$.

height h before recording. Read-out signal I_s represents a value in the case of $y_0 = 0$, and maximum tracking error signal I_{dmax} represents a value in the case of $y_0 = 0.4\mu$m. In the case of $h = 0$, I_s is maximum and I_{dmax} is about zero. For TE-wave, I_{dmax} is maximum at a height of $h = 70$nm. For TM-wave, I_{dmax} is maximum at a height of $h = 60$nm. These value of h are about $\lambda_0/8n_1$. Then h is an optimum height to obtain maximum tracking sensitivity for each polarizations. When h is lower than $\lambda_0/8n_1$, read-out signal I_s keeps half intensity in comparison with read-out signal of $h = 0$.

Figure 11 shows read-out signal I_s versus the upper width w_U/w_0 of guide-groove for TE-wave before recording, where lower width $w_L = 0.2w_0 + w_U$. As the upper width w_U/w_0 approaches 0.5, I_s decreases.



(a) before recording



(b) after recording

Figure 8: Distribution of magnetic fields near a center guide groove(TM-wave), for $w_U = w_r = w_0$, $w_L = 1.2w_U$, $h = \lambda_0/8n_1$, $b = 1.6\mu$m, $y_0 = 0$.

When h is lower than $\lambda_0/8n_1$, there is not very much change of I_s by w_U/w_0.

Figure 12 shows read-out signal I_s and amplitude of read-out signal ΔI_s versus the film-thickness in each layer for TE-wave, where figures (a), (b) and (c) show the dependences on film-thickness of upper protective layer, recording layer and lower protective layer. For upper protective layer, the film-thickness doesn't affect read-out signal I_s. The skin depth of recording layer is $0.043\lambda_0$ before recording and $0.075\lambda_0$ after recording. Hence, when the film-thickness d_2 of recording layer is thinner than the skin depth, read-out signal I_s changes very much. For resonance, I_s depends on the film-thickness d_3 of lower protective layer. When the amplitude of read-out signal ΔI_s is maximum, the film-thicknesses in each layer are $d_1 = 180$nm, $d_2 = 40$nm and $d_3 = 200$nm. Now the maximum amplitude of read-out signal changes by about 21 %.

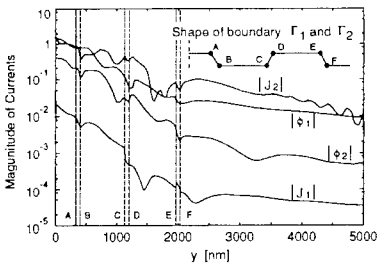


Figure 9: Magnitude of equivalent induced currents intensity on the boundary Γ_1 and Γ_2 (TE-wave), for $w_U = w_r = w_0$, $w_L = 1.2w_U$, $h = \lambda_0/8n_1$, $b = 1.6\mu$m, $y_0 = 0$.

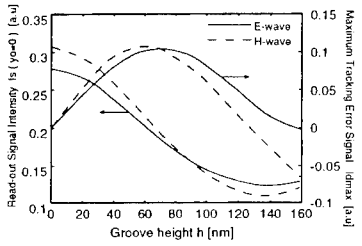


Figure 10: Dependence of read-out signal I_s and tracking error signalI_d on the groove height h, for $w_U = w_r = w_0$, $w_L = 1.2w_U$, $b = 1.6\mu$m, $y_0 = 0$, $\rho = 1000\lambda_0/n_1$.

4 Conclusion

The scattering characteristics of laser-beam waves on a phase-change optical disk memory were numerically analyzed by using the finite element method with boundary element method which can be applied to various conditions. We obtained some results as follows:

(1) The main lobes of the scattering patterns fall to a low value after recording both polarizations. The scattering far field at $\theta = 90°$ after recording is lower by about 6dB in comparison with that before recording. The side lobes at about 70° appear after recording.

(2) The scattering far fields largely depend on resonance in lower protective layer.

(3) For TE-wave, I_{dmax} is maximum at a height of $h = 70$nm. For TM-wave, I_{dmax} is maximum at a height of $h = 60$nm. These values are about

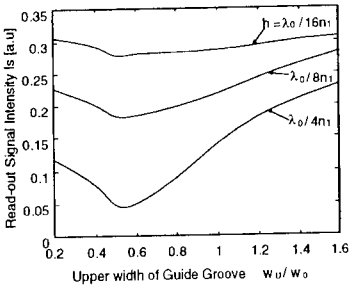


Figure 11: Dependence of read-out signal I_s on the upper width of guide-groove w_U/w_0 , for $w_L = 0.2w_0 + w_U$, $b = 1.6\mu$m, $y_0 = 0$, $\rho = 1000\lambda_0/n_1$.

$\lambda_0/8n_1$. When h is lower than $\lambda_0/8n_1$, read-out signal I_s keeps half intensity in comparison with read-out signal of at a height of $h = 0$nm.

(4) As the upper width w_U/w_0 approaches 0.5, I_s decreases. When h is lower than $\lambda_0/8n_1$, there is not very much change of I_s with w_U/w_0.

(5) When the film-thicknesses in each layer are $d_1 = 180$nm, $d_2 = 40$nm and $d_3 = 200$nm, the maximum amplitude of read-out signal ΔI_s changes by about 21 %.

These results give important field characteristics to obtain optimum design of phase-change optical disk.

References

[1] H. H. Hopkins: "Diffraction theory of laser read-out systems for optical video discs", J. Opt. Soc. Am.,**69**, pp.4 (1979).

[2] J. H. T. Pasman, H. F. Olijhoek and B. Verkaik: "Developments in optical disk mastering", SPIE Proc., **529**, pp.62 (1985).

[3] Y. Miyazaki: "Scattering of Beam Wave by Surface Pits on Videodisks" Tech. Rep., IECE, Japan, **A.P81**-131 (1981). [in Japanese]

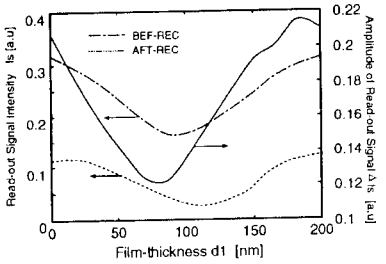
[4] K. Manabe, Y.Miyazaki: "An Analysis of Scattering characteristics of a Beam Wave from Pits with Arbitrary Shapes on Optical Disks", Proc. Int. Sym. on Optical Memory, Jpn. J. Appl. Phys. **26**, Suppl. pp.109 (1989).

[5] Y.Yamakawa, Y.Miyazaki : "Beam scattering analysis of two dimensional dielectric pits by finite element method", IEE of Japan Technical report(OFSET'90), **EMT–90**–32, pp.147 (1990).

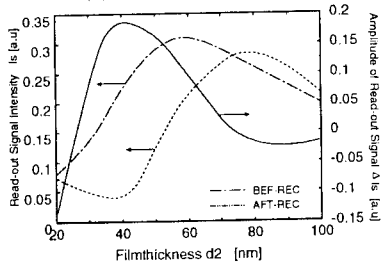
[6] Y.Miyazaki, K.Manabe : "Scattered near-field and induced current of a beam wave by pits on optical disks using boundary element analysis", Radio Science, **26**, 1, pp.281 (1991)

[7] E. Okuno, K. Nishiuchi, K. Ishibashi, N. Yamada and N. Akahira: "Multiple recording method for pulse-width modulation recording on an erasable phase change optical disk" Jpn. J. Appl. Phys. **30**, 4, pp.677 (1991).

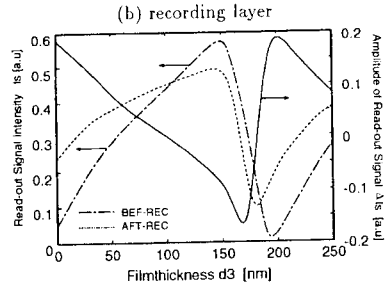
[8] K. Tanaka, Y. Miyazaki: "A Combination Analysis of FEM and BEM for Beam Scattering by Guide Grooves of an Phase Change Type Optical Disk" IEE of Japan Technical report, **EMT–94**–36 (1994). [in Japanese]



(a) upper protective layer



(b) recording layer



(c) lower protective layer

Figure 12: Dependence of read-out signal I_s on each film-thickness, for $w_U = w_r = w_0$, $w_L = 1.2w_U$, $h = \lambda_0/8n_1$, $b = 1.6\mu$m,$y_0 = 0$.

3D NODAL- AND MIXED-BASED ELEMENTS FOR UNBOUNDED MICROWAVE PROBLEMS

A. Nicolas, L. Nicolas, J.L. Yao-bi
CEGELY - URA CNRS 829
Ecole Centrale de Lyon
BP163 - 69131 Ecully cedex - France

ABSTRACT

We present 3D finite element formulations for the modeling of unbounded microwave problems. Formulations are directly written in terms of vector fields. The open boundary is modeled using Engquist-Majda absorbing boundary condition. Two types of finite elements are compared: nodal-based and mixed-based.

INTRODUCTION

The finite element (F.E.) method is an efficient way for solving open boundary frequency domain microwave problems, such as scattering or antenna radiation. The coupling with absorbing boundary condition (A.B.C.) allows to truncate the F.E. domain to finite size by absorbing the outgoing wave. If global A.B.C. are exact by nature, they however cannot be used in a 3D context, because they generate a full matrix on the boundary. On an other hand, local A.B.C. are based on an approximation, but they preserve the sparsity of the F.E. matrix. That is the reason why we have chosen a local A.B.C. for our formulations. Furthermore, we prefer to work with a rectangular outer boundary, so we use the Engquist-Majda A.B.C.
This paper deals with the modeling of unbounded microwave problems (computation of near and far field) and compares two types of finite elements used for the numerical discretization: nodal-based elements and H(curl) mixed elements. We first give the Galerkin form of the vector wave equation. We show then how the Engquist-Majda A.B.C. is written, and how the numerical discretization is performed using both types of finite elements. Finally, we compare both finite elements on two examples: radiation from an infinitesimal dipole and scattering by a perfect electric conducting cylinder.

FINITE ELEMENT FORMS OF THE VECTOR WAVE EQUATION

By crossing both curl Maxwell's equations written in the frequency domain, we get the vector wave equation (for the magnetic field **H** for example):

$$\nabla \times \left(\frac{1}{\varepsilon_r} \nabla \times \mathbf{H} \right) - k_0^2 \mu_r \mathbf{H} = -j\omega\varepsilon_0 \mathbf{J} \qquad (1)$$

Galerkin forms.

Applying the Galerkin method with a vector weighting function **W**, we obtain:

$$\int_\Omega (\varepsilon_r^{-1} \nabla \times \mathbf{H}) \cdot (\nabla \times \mathbf{W}) d\Omega - k_0^2 \int_\Omega \mu_r \mathbf{H} \cdot \mathbf{W} d\Omega + \oint_\Gamma \varepsilon_r^{-1} (\mathbf{n} \times \nabla \times \mathbf{H}) \cdot \mathbf{W} d\Gamma = -j\omega\varepsilon_0 \int_\Omega \mathbf{J} \cdot \mathbf{W} d\Omega \qquad (2)$$

In the previous expression, the surface integral is used for the implementation of the local absorbing boundary condition, through the approximate tangential operator $\boldsymbol{T}$:

$$\mathbf{n}\times\nabla\times\mathbf{H}\approx\boldsymbol{T}(\mathbf{H}) \text{ on the external boundary} \tag{3}$$

The current density $\mathbf{J}$ is the source used for the computation of the radiation of an antenna, such as an open ended waveguide [1]. For scattering problems, there is no localized source $\mathbf{J}$, and the vector wave equation becomes homogeneous (the right hand side in (1) is zero). The total field $\mathbf{H}$ is separated into incident field $\mathbf{H^i}$ and scattered field $\mathbf{H^d}$, and the A.B.C. is written only for the scattered field. This leads then to the formulation (called total field formulation):

$$\begin{aligned}\int_\Omega(\varepsilon_r^{-1}\nabla\times\mathbf{H})\cdot(\nabla\times\mathbf{W})d\Omega-k_0^2\int_\Omega\mu_r\mathbf{H}\cdot\mathbf{W}d\Omega+\oint_\Gamma\varepsilon_r^{-1}\boldsymbol{T}(\mathbf{H})\cdot\mathbf{W}d\Gamma=\\ \oint_\Gamma\varepsilon_r^{-1}\{\boldsymbol{T}(\mathbf{H^i})-\mathbf{n}\times\nabla\times\mathbf{H^i}\}\cdot\mathbf{W}d\Gamma\end{aligned} \tag{4}$$

Both expressions (2) and (4) are for an numerical implementation of mixed elements. If a scalar weighting function N is used now to get the Galerkin form (case of nodal-based elements), these expressions become:

- for an antenna problem:

$$\int_\Omega(\nabla N\times\varepsilon_r^{-1}\nabla\times\mathbf{H})d\Omega+k_0^2\int_\Omega\mu_rN\mathbf{H}d\Omega-\oint_\Gamma\varepsilon_r^{-1}N(\mathbf{n}\times\nabla\times\mathbf{H})d\Gamma=-j\omega\varepsilon_0\int_\Omega N\mathbf{J}d\Omega \tag{5}$$

- for a scattering problem:

$$\int_\Omega(\nabla N\times\varepsilon_r^{-1}\nabla\times\mathbf{H})d\Omega+k_0^2\int_\Omega\mu_rN\mathbf{H}d\Omega-\oint_\Gamma\varepsilon_r^{-1}N\boldsymbol{T}(\mathbf{H})d\Gamma=-\oint_\Gamma\varepsilon_r^{-1}N\{\boldsymbol{T}(\mathbf{H^i})-\mathbf{n}\times\nabla\times\mathbf{H^i}\}d\Gamma \tag{6}$$

Similar expressions to (2), (4), (5) and (6) may be obtained for the electric field $\mathbf{E}$, by just replacing $\mathbf{H}$ by $\mathbf{E}$ and crossing ε_r and μ_r. For scattering problems -(4) and (6)-, incident field has to evaluated only on the external boundary Γ.

Boundary conditions.

In microwave engineering, good conductors are supposed to be lossless, because of the value of the frequency (at 1 GHz, the skin depth inside the aluminium is about 2.6 μm). There is no field inside and they are assumed to be perfect: they are not meshed and the boundary Γ in (2), (4), (5) and (6) is made of the external boundary and of the boundaries of the conductors. On the conductors, we have the boundary condition for the electric field:

$$\mathbf{n}\times\mathbf{E}=\mathbf{n}\times(j\omega\varepsilon)^{-1}\nabla\times\mathbf{H}=0 \tag{7}$$

In the $\mathbf{H}$-formulations, the surface term in (2), (4), (5) and (6) cancels then out on the boundaries of the conductors, and the boundary condition is implicit. When these expressions are written for the electric field $\mathbf{E}$, the boundary condition can no longer be implicit and has to be explicitly enforced in the global system matrix.

NUMERICAL IMPLEMENTATION

Nodal-based finite elements.

Although they seem more suitable for potential problems, nodal elements may be used for the discretization of vector field problems: they are easy to implement, they conform exactly to curved surfaces and they minimize the time of computation. Furthermore, spurious modes may be eliminated using the penalty function $-\nabla(\nabla.\mu_r\mathbf{H})$: this makes the formulation equivalent to a laplacian one, and decouples the coordinates of the nodes inside the media. Including this penalty function, (5) becomes [1]:

$$\int_\Omega (\nabla N \times \varepsilon_r^{-1} \nabla \times \mathbf{H}) d\Omega + k_0^2 \int_\Omega \mu_r N \mathbf{H} d\Omega - \int_\Omega (\nabla . \mu_r \mathbf{H})(\nabla N) d\Omega - \oint_\Gamma \varepsilon_r^{-1} N(\mathbf{n} \times \nabla \times \mathbf{H}) d\Gamma + \oint_\Gamma N(\nabla . \mu_r \mathbf{H}) d\Gamma = -j\omega\varepsilon_0 \int_\Omega N \mathbf{J} d\Omega \quad (8)$$

There are 3 complex unknowns per node, corresponding to the three components of the vector field. Because of the penalty surface integral, the resulting matrix is not symmetric.

According to the classical finite element analysis, we use first order hexahedrals and each component of the field **H** is interpolated by:

$$H^{x,y,z} = \sum_{i=1}^{nodes} N_i H_i^{x,y,z}, \text{ with } N_i = \frac{1}{8} \prod_{j=1}^{3} (1 \pm u_j) \quad (9)$$

Note that, with nodal elements, taking into account the normal discontinuity of the fields at material interfaces is not easy. But it is possible to do it: the nodes at interfaces have first to be decoupled, and the boundary condition has then to be explicitely enforced inside the system matrix.

Mixed-based finite elements.

Mixed elements seem more physical and more suitable for the modeling of fields: they only enforce the tangential continuity of the fields and allow the normal discontinuity at materials interfaces. Furthermore, this floating of normal continuity allows these elements to handle objects with sharp edges.

Numerical discretization is performed using mixed elements conforming in space *H*(curl) [2]: in particular, 1st order R1 elements on hexahedral have been implemented. There is only one unknown per edge and the unknown vector field **H** is expanded as:

$$\mathbf{H} = \sum_{i=1}^{N} H_i \mathbf{W}_i, \text{ with } H_i = \sigma_i(\mathbf{H}) \quad (10)$$

where N is the total number of degrees of freedom associated with the mesh. The vector shape function $\mathbf{W}_i$ associated with the edge $C=\{a_m,a_n\}$ is given by [3]:

$$\mathbf{W}_i = N_m \nabla L_n - N_n \nabla L_m \quad (11)$$

and has the degree of freedom σ_i:

$$\sigma_i(\mathbf{p}) = \int_C \mathbf{p} \cdot \tau_{mn} ds \tag{12}$$

where: - L_m and L_n are first order nodal-based functions associated with the edge $C=\{a_m,a_n\}$,
- N_i are Lagrange shape functions of first order within hexahedral,
- τ_{mn} is a unit tangent vector to the edge C and orientates it.

In this form, these elements appear clearly to be an extansion of Whitney edge elements in hexahedral.

3D ENGQUIST-MAJDA A.B.C.

Because each component of **H** is solution of the scalar Helmholtz equation and satisfies the Sommerfeld condition, it follows that each component of **H** may be approximated by the 2D Engquist-Majda A.B.C. on the rectangular outer boundary. Hence we can derivate this following 3D vector A.B.C.:

$$\mathbf{n} \times \nabla \times \mathbf{H} = \boldsymbol{T}(\mathbf{H}) = jk_0 \mathbf{H}_t + \frac{j}{2k_0} \nabla_t^2 \mathbf{H}_t + \nabla_t (\mathbf{n} \cdot \mathbf{H}) \tag{13}$$

This A.B.C. leads to a non-symmetric linear system matrix, due to the last term in (13): this is not important when using nodal-based elements, because the matrix is already non-symmetric. However, when using mixed-based elements, an alternative symmetric version may be obtained using some simple approximations [3]: we just state that, because (**n**.**H**) is a scalar radiation field, it can be approximated by a first order Engquist-Majda A.B.C., which means (because the divergence of **H** is null):

$$\nabla \cdot \mathbf{H}_t = jk_0 (\mathbf{n} \cdot \mathbf{H}), \text{ implying that } \nabla_t (\nabla \cdot \mathbf{H}_t) \approx jk_0 \nabla_t (\mathbf{n} \cdot \mathbf{H}) \tag{14}$$

The "symmetric" 3D vector Engquist-Majda condition is then:

$$\mathbf{n} \times \nabla \times \mathbf{H} = \boldsymbol{T}(\mathbf{H}) = jk_0 \mathbf{H}_t + \frac{j}{2k_0} \nabla_t^2 \mathbf{H}_t - \frac{j}{k_0} \nabla_t (\nabla \cdot \mathbf{H}) \tag{15}$$

Rigorously, one should evaluate line integrals comming from the implementation of the A.B.C. in the Galerkin form: they do not vanish on the edges of the external rectangular boundary, and adequate edge and corner conditions should be prescribed. We make however the approximation that parasite waves generated by these geometrical singularities are essentially local (this is justified), and that a small amount of them propagates toward the interior of the domain.

VALIDATION

Radiation by an infinitesimal dipole.

This example has already been presented in [1] and [3]: it validates the F.E. forms coupled with the symmetric and non-symmetric Engquist-Majda A.B.C. A very thin current element of short length

and with a constant current is positioned symmetrically at the origin and oriented along the z axis. The problem has been modeled with two symmetries (yz and zx planes). The size of the computational domain is 1λ x 1λ x 2.1λ. Each finite element is a 0.1λ x 0.1λ x 0.1λ brick. This leads to a mesh made of 2662 nodes. The frequency is 3GHz.

Fig.1 shows that the computed solution removes from the analytical one when we are close to the edges and corners of the F.E. domain. In the interior of the domain, both solutions are close.

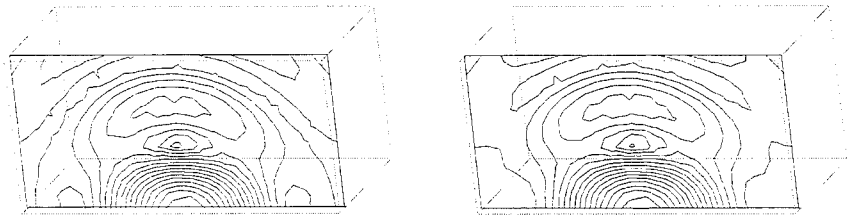


Fig.1: instantaneous magnetic field in the yz plane at x = 0.1λ
Left: analytical solution - right: mixed finite elements with symmetric A.B.C.

This is confirmed by Fig.2, which shows also that the accuracy of the symmetric Engquist-Majda condition coupled to mixed-based F.E. is approximately the same as the non-symmetric one coupled to either nodal- or mixed-based F.E.

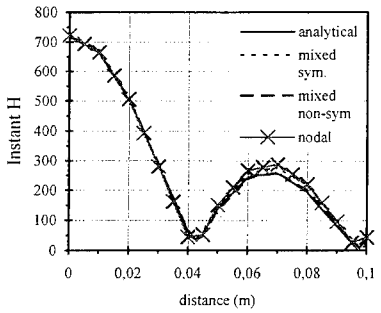


Fig. 2: instantaneous magnetic field along a line perpendicular to the dipole, going from the dipole to the external boundary.
Comparison of nodal F.E. formulation with mixed F.E. formulation.

Tab.1 compares the number of unknowns and computation time for both formulations. Note that, for the nodal-based F.E. formulation, the A.B.C. leads to a non-symmetric system matrix. This one is however approximately symmetrized by adding the transposed matrix, and solved using a symmetric solver: results seem quite good.

From tab. 1, it can be seen that the number of unknowns for both first order nodal and R1 mixed bricks is quite the same. On the other hand, the number of non-zero terms is really different (nodal and mixed symmetric have to be compared): mixed elements generate much less non-zero terms (in a 1.6 ratio). However CPU time is more important with mixed elements, which means that our solver is really not adapted to this type of elements.

formulation	A.B.C.	unknowns	non-zero terms	CPU time (in s)	solver
nodal	non-symmetric	7986	176919	498	conjugate gradient
mixed	symmetric	7381	111301	1028	conjugate gradient
mixed	non-symmetric	7381	215221	18779	gmres

Tab. 1: comparison of nodal- and mixed-based F.E. formulations
for the modeling of the infinitesimal dipole (2662 nodes).
NB: the system matrix resulting from the nodal formulation is approximately
symmetrized and solved with a symmetric solver (conjugate gradient)

Scattering by a perfect electric conducting cylinder.

Both formulations (nodal-based and mixed-based with symmetric A.B.C.) are now compared for the case of the scattering by a perfect electric conducting cylinder of various length (fig.3): the radius of the cylinder is 0.6λ and its length (along the z axis) goes from 0.6λ to 5λ. The incident magnetic field has only one component along the z axis, and propagates in the direction of the positive y. Frequency is 3GHz.

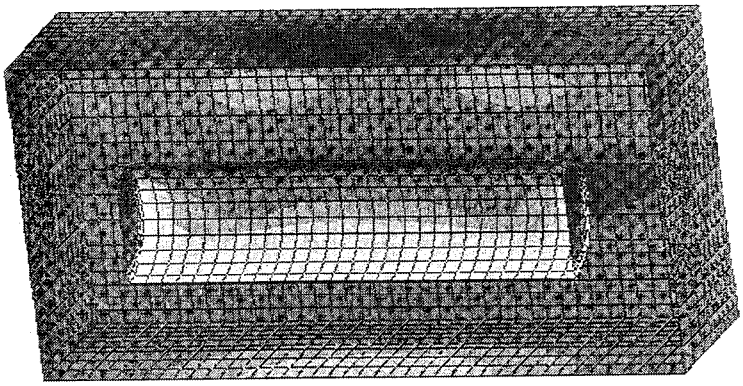


Fig. 3: scattering by a p.e.c. cylinder - 3GHZ - $\mathbf{H}^i=H^i\mathbf{z}$ and $\mathbf{k}^i=k^i\mathbf{y}$
Instantaneous magnetic field on the cylinder and on the external box.

Tab. 2 summarizes the results in term of unknowns, number of non-zero terms and CPU time. Again, for a given problem, the number of unknowns generated is identical for both types of F.E., while the number of non-zero terms is 1.6 time smaller with R1 mixed elements. We compare also in Fig. 4 the CPU times for the assembling of the F.E. system matrix (because the solver is not adapted to mixed elements, we do not take into account the CPU time for the solving of the system matrix).

		first order nodal			R1 mixed		
length	nodes	unknowns	non-zero	assembling (in s)	unknowns	non-zero	assembling (in s)
0.6	5109	15327	369354	477	14311	218785	472
1.2	6821	20463	485010	685	19167	294345	766
1.8	8319	24957	586209	886	23416	360460	1078
2.3	9817	29451	687408	1106	27665	426575	1430
2.8	11101	33303	774150	1308	31307	483245	1778
3.3	12599	37797	875349	1572	35556	549360	2291
4.3	15167	45501	1048833	2035	42840	662700	3129
5.0	17093	51279	1178946	2427	48303	747705	3890

Tab. 2: comparison of nodal- and mixed-based F.E. formulations for the modeling of p.e.c. cylinders. length is given in wavelength - assembling is the CPU time to build the F.E. system matrix

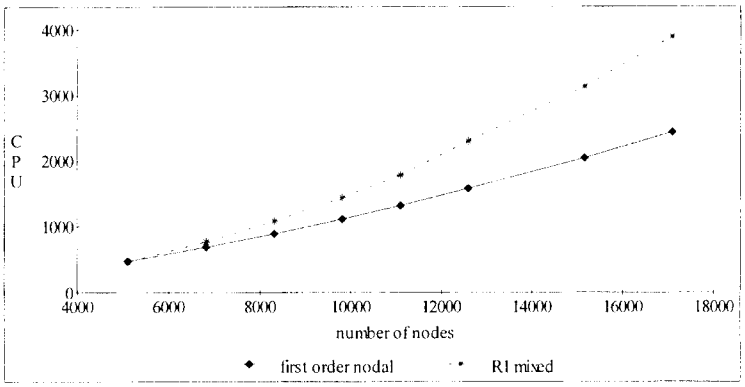


Fig. 4: comparison of CPU times for the assembling of the F.E. system matrix, depending on the number of nodes of the mesh.

CONCLUSION

We have compared in this paper two types of finite elements used for the modeling of open boundary microwave problems. If the accuracy of both types of elements is comparable, R1 mixed finite elements seem more suitable for field problems, because the discontinuities of the fields are easy to handle. Next step will be to work on the solver itself, in order to get acceptable CPU times.

REFERENCES

[1] L. Nicolas, K.A. Connor, S.J. Salon, B.G. Ruth, L.F. Libelo, "Three dimensional finite element analysis of high power microwave devices", IEEE Trans. on Mag., vol.29, pp.1642-1645, mar. 93.
[2] J.C. Nédélec, "A new family of mixed elements in R^3", Numer. Math. 50, pp.57-81, 1986.
[3] J.L. Yao Bi, L. Nicolas, A. Nicolas, "H(curl) elements on hexahedral and vector A.B.C.'s for unbounded microwave problems", accepted for IEEE Trans. on Mag., may 1995.
[4] L. Nicolas, "An integral-type approach for the computation of the far field radiated by microwave devices", IEEE Trans. on Mag., vol.30, pp.3124-3127, sept. 94.

A rationale for the use of mixed-order basis functions within finite element solutions of the vector Helmholtz equation

Andrew F. Peterson
School of Electrical and Computer Engineering
Georgia Institute of Technology
Atlanta, GA 30332-0250

Donald R. Wilton
Department of Electrical Engineering
University of Houston
Houston, TX 77204-4793

Abstract: The curl-curl form of the vector Helmholtz equation can be used to describe the behavior of three-dimensional time-harmonic electromagnetic fields. Finite element discretizations of this equation encounter difficulties related to the presence of numerous eigenfunctions belonging to the nullspace of the operator, in addition to the desired eigensolutions. Spurious numerical solutions arising in waveguide and cavity formulations appear to be caused by the inability of the basis functions to properly model the nullspace eigenfunctions, and can be alleviated by using a complete polynomial basis that only imposes tangential continuity from cell to cell. However, such an expansion tends to capture many eigenfunctions from the nullspace, and produces a relatively large number of zero eigenvalues. A reduction in the number of zero eigenvalues can be obtained through the use of special mixed-order functions, such as the "edge elements" proposed by Nedelec in 1980. Although the lowest-order edge elements are in widespread use in the electromagnetics community, their extension to higher polynomial orders has been inhibited by an incomplete understanding of their properties. In this paper, we demonstrate that polynomial-complete basis functions can be separated into two subsets, one of which has zero curl and can only represent eigenfunctions in the nullspace of the operator. Members of this set can be discarded to improve the efficiency of solution, leaving mixed-order basis functions. Specific examples of linear, quadratic, and cubic order basis functions will be presented. Numerical results will be used for illustration.

1. Introduction

The curl-curl form of the vector Helmholtz equation can be used to describe the behavior of time-harmonic three-dimensional electromagnetic fields. Finite element discretizations of this equation encounter difficulties related to the presence of numerous eigenfunctions belonging to the nullspace of the operator, in addition to the desired eigensolutions [1]. For example, waveguide and cavity formulations based on Lagrangian interpolation polynomials produce spurious nonzero eigenvalues, believed to be grossly inaccurate approximations of the zero eigenvalues associated with the nullspace of the operator. In recent years, certain types of mixed-order vector basis functions ("edge elements") have been shown to eliminate the spurious eigenvalues, or at least to

approximate those eigenfunctions accurately enough to produce the proper eigenvalues of zero. However, the process by which they accomplish this is not widely understood. In addition, several different families of vector basis functions have been proposed [1-6]. Only a few of these higher-order basis functions have been subjected to systematic numerical tests to evaluate their performance. As an additional point of confusion, the functions proposed for triangular and tetrahedral cells differ from those used with quadrilateral and hexahedral cells, both in the available number of degrees of freedom and in the mathematical form of the representation. Finally, the merits of mixed-order edge elements versus polynomial-complete edge elements remains in question [7].

The purpose of this paper is to attempt to provide a rationale for the use of mixed-order vector basis functions with the curl-curl equation. We first consider the nature of the eigensolution families, then demonstrate that polynomial-complete functions that do not impose normal continuity from cell to cell properly model the nullspace of the operator. Complete polynomial expansions can be separated into two subsets, one of which has zero curl and will only contribute to additional eigenfunctions in the nullspace. Members of this set can be discarded to improve the efficiency of solution, leaving a mixed-order representation of the Nedelec type [2]. Specific examples of linear, quadratic, and cubic order basis functions for triangular cells will be presented. Numerical results will be used for illustration.

2. Properties of the vector Helmholtz eigensolutions

Consider the vector Helmholtz equation

$$\nabla \times \nabla \times \bar{E} = k^2 \bar{E} \qquad (1)$$

for the electric field in a homogeneous source-free region. Eigenfunctions of this equation can generally be separated into two families, one of which is a valid electromagnetic field of the form $\{\bar{E} = \nabla \times \bar{V}\}$, and the other of which has the form $\{\bar{E} = \nabla\Phi\}$. The gradient $\nabla\Phi$ is a mathematical solution to (1) but does not represent an electromagnetic field in a source-free region. Since $\nabla \times \nabla\Phi = 0$, these solutions only satisfy (1) for $k = 0$. Such eigenfunctions are said to form the "nullspace" of the curl-curl operator. Both eigenfamilies satisfy the boundary conditions as well as the Helmholtz equation. An example of one family of continuous eigenfunctions from the nullspace for a 2D cavity is provided in an earlier article [1].

The solution family $\{\nabla\Phi\}$ is of interest, even when k is not zero, because a general discretization of the Helmholtz operator will capture eigenfunctions from both families. In other words, unless the basis functions are orthogonal to all functions in the nullspace, a matrix representing the curl-curl operator will have some eigenvectors that approximate those functions. Both eigensolution families must maintain tangential continuity across any mathematical boundary, and in the absence of medium discontinuities the electromagnetic fields $\{\bar{E} = \nabla \times \bar{V}\}$ must also exhibit normal continuity. However, members of the family $\{\nabla\Phi\}$ may exhibit jump discontinuities in their normal component while still maintaining the property that $\nabla \times \nabla\Phi = 0$. In fact, experience suggests that numerical solutions of the form $\{\nabla\Phi\}$ tend to be highly discontinuous functions. It appears that the spurious nonzero eigenvalues obtained when

discretizing (1) with traditional Lagrangian functions are a consequence of the use of continuous basis functions to approximate the highly discontinuous eigenfunctions. It is easy to show that the projection of a discontinuous function with zero curl onto a continuous basis set results in a function having nonzero curl, and thus a "spurious" nonzero eigenvalue.

Actual solutions of the more general vector Helmholtz equation

$$\nabla \times (\mu_r^{-1} \nabla \times \bar{E}) = k^2 \varepsilon_r \bar{E} \tag{2}$$

exhibit jump discontinuities in the field components normal to material interfaces (which typically coincide with cell boundaries in a finite element solution). Therefore, it appears that discretizations of (1) and (2) should employ a basis set that imposes tangential continuity but not normal continuity. Such basis functions are known as "curl conforming" [2].

3. Polynomial-complete expansions for triangular cells

Polynomial-complete curl-conforming basis functions have been used by Nedelec [3], Mur [7], and others for triangular and tetrahedral cells. Six linear-order basis functions overlap a triangular cell. Within a cell, they have the obvious Cartesian representation

$$\bar{B}(x,y) = \hat{x} (A + Bx + Cy) + \hat{y} (D + Ex + Fy) \tag{3}$$

containing six degrees of freedom. From this representation, specific basis functions can be obtained that interpolate to the tangential component at the ends of each edge of the cell. These functions maintain tangential continuity by sharing that coefficient with the analogous function defined in the adjacent cell but do not impose normal continuity from cell to cell. There are a total of two basis functions per edge throughout the model. Table 1 shows the simplex-coordinate representation of these basis functions. Table 2 shows numerical eigenvalues produced when these basis functions are used to discretize (1) for a circular, homogeneous cavity. The results contain a large number of zero eigenvalues that presumably represent the nullspace, and nonzero eigenvalues that appear to have a one-to-one correlation with analytical results for the electromagnetic cavity modes.

Analogous basis functions can be created that provide a complete quadratic representation. An expansion of the form

$$\begin{aligned} \bar{B}(x,y) = {} & \hat{x} (A + B\,x + C\,y + D\,x^2 + E\,xy + F\,y^2) \\ & + \hat{y} (G + H\,x + I\,y + J\,x^2 + K\,xy + L\,y^2) \end{aligned} \tag{4}$$

contains twelve degrees of freedom, and basis functions can be defined (for instance) that interpolate to three tangential components along each edge of a triangular cell and one normal component at the middle of each edge. Their expression in simplex coordinates appears in Table 1. The nine quadratic basis functions that interpolate to tangential components share a coefficient with the analogous function in the neighboring cell in order to maintain tangential continuity. The three

basis functions per cell that interpolate to the normal component are entirely local and thus the normal component is not constrained to be continuous from cell to cell. The resulting representation requires three unknowns per edge and three unknowns per cell. Table 2 shows numerical eigenvalues produced using these basis functions to model fields within a circular cavity. The results contain a large number of zero eigenvalues, and nonzero eigenvalues that appear to have a one-to-one correspondence with analytical results for the cavity modes.

Table 1

Simplex-coordinate definition of polynomial-complete basis functions throughout a triangular cell.

Linear (LT/LN)	Quadratic (QT/QN)
$\xi_1\nabla\xi_2$	$\xi_2(2\xi_2-1)\nabla\xi_1$
$\xi_2\nabla\xi_1$	$\xi_3(2\xi_3-1)\nabla\xi_1$
$\xi_1\nabla\xi_3$	$\xi_1(2\xi_1-1)\nabla\xi_2$
$\xi_3\nabla\xi_1$	$\xi_3(2\xi_3-1)\nabla\xi_2$
$\xi_2\nabla\xi_3$	$\xi_1(2\xi_1-1)\nabla\xi_3$
$\xi_3\nabla\xi_2$	$\xi_2(2\xi_2-1)\nabla\xi_3$
	$\xi_2\xi_3(\nabla\xi_2 - \nabla\xi_3)$
	$\xi_1\xi_3(\nabla\xi_3 - \nabla\xi_1)$
	$\xi_1\xi_2(\nabla\xi_1 - \nabla\xi_2)$
	$\xi_2\xi_3\nabla\xi_1$
	$\xi_1\xi_3\nabla\xi_2$
	$\xi_1\xi_2\nabla\xi_3$

Table 2

Lowest eigenvalues produced by a discretization of a circular cavity with ε_r=1, μ_r=1, and unit radius using polynomial-complete linear (LT/LN) and quadratic (QT/QN) basis functions, for the TE polarization. The model consisted of 42 triangular cells and resulted in a matrix of order 108 for the LT/LN functions and 288 for the QT/QN functions.

LT/LN	QT/QN	exact
0.0 (67)	0.0 (163)	
1.87 (2)	1.84 (2)	1.841 (2)
3.20 (2)	3.06 (2)	3.054 (2)
4.13 (1)	3.84 (1)	3.832 (1)
4.6 (2)	4.21 (2)	4.201 (2)
6.0 (2)	5.35 (2)	5.318 (2)
6.1 (2)	5.37 (2)	5.331 (2)

4. Mixed-order expansions for triangular cells

The data in Table 2 suggest that polynomial-complete functions are sufficient for eliminating spurious nonzero eigenvalues, as long as they impose only tangential continuity from cell to cell. However, it appears that a large fraction of the available degrees of freedom in the expansions of (3) and (4) are used to capture eigensolutions in the nullspace of the curl-curl operator. To reduce wasted computational effort, some of the degrees of freedom associated with the nullspace can be eliminated. Nedelec appears to be the first to (a) observe that the degrees of freedom associated with the gradient of an order-(n+1) polynomial belong to the nullspace of an order-n representation, and (b) develop basis functions with reduced degrees of freedom [2].

The linear vector basis function in (3) can be projected onto two subspaces to obtain

$$\bar{B}(x,y) = \hat{x}\,\{A + (C-E)/2\ y\} + \hat{y}\,\{D + (E-C)/2\ x\} \tag{5}$$

and a complementary representation

$$\bar{B}_{grad}(x,y) = \hat{x}\,\{Bx + (C+E)/2\ y\} + \hat{y}\,\{(E+C)/2\ x + Fy\} \tag{6}$$

Equations (5) and (6) each contain three degrees of freedom. The functions in (6) have identically zero curl within the cell. Since these functions are constrained to have tangential continuity from cell to cell, their curl is identically zero over the entire problem domain. Under these conditions, (6) is the general form of the gradient of a quadratic polynomial, and basis functions with this form can only represent functions in the nullspace of the curl-curl operator. Thus, it should be possible to restrict the basis set to the functions in (5). The reduced expansion defined by (5) consists of mixed-order polynomial functions that provide a constant tangential component and a linear normal (CT/LN) component along any cut through the cell. Simplex coordinate descriptions of the CT/LN functions are provided in Table 3. Table 4 shows numerical eigenvalues produced by the CT/LN basis set when used to discretize (1) for a circular, homogeneous cavity of unit radius. As compared to the complete linear (LT/LN) data in Table 2, the results contain the same number of nonzero eigenvalues but far fewer zero eigenvalues (the number of zero eigenvalues is reduced by exactly the number of basis functions excluded, which is half the original matrix order).

The quadratic representation in (4) can be modified in an analogous manner. The complete expansion can be projected onto two subspaces, to produce a representation of the form

$$\begin{aligned}\bar{B}(x,y) = {} & \hat{x}\,\{A + B\,x + C\,y\ + (E-2J)/3\ xy + (2F-K)/3\ y^2\} \\ & + \hat{y}\,\{G + H\,x + I\,y + (2J-E)/3\ x^2 + (K-2F)/3\ xy\}\end{aligned} \tag{7}$$

containing eight degrees of freedom and a complementary representation

$$\begin{aligned}\bar{B}_{grad}(x,y) = {} & \hat{x}\,\{D\,x^2 + 2(E+J)/3\ xy + (F+K)/3\ y^2\} \\ & + \hat{y}\,\{(E+J)/3\ x^2 + 2(K+F)/3\ xy + L\,y^2\}\end{aligned} \tag{8}$$

containing four degrees of freedom. It can be seen that (8) has identically zero curl, and thus those degrees of freedom only represent functions in the nullspace of the curl-curl operator. Therefore, it

Table 3

Simplex-coordinate definition of mixed-order basis functions within a triangular cell. The last two LT/QN and last six QT/CuN functions are entirely local.

CT/LN	LT/QN	QT/CuN
$\xi_1\nabla\xi_2 - \xi_2\nabla\xi_1$	$\xi_1\nabla\xi_2$	$\xi_2(2\xi_2-1)\nabla\xi_1$
$\xi_1\nabla\xi_3 - \xi_3\nabla\xi_1$	$\xi_2\nabla\xi_1$	$\xi_3(2\xi_3-1)\nabla\xi_1$
$\xi_2\nabla\xi_3 - \xi_3\nabla\xi_2$	$\xi_1\nabla\xi_3$	$\xi_1(2\xi_1-1)\nabla\xi_2$
	$\xi_3\nabla\xi_1$	$\xi_3(2\xi_3-1)\nabla\xi_2$
	$\xi_2\nabla\xi_3$	$\xi_1(2\xi_1-1)\nabla\xi_3$
	$\xi_3\nabla\xi_2$	$\xi_2(2\xi_2-1)\nabla\xi_3$
	$\xi_2\xi_3\nabla\xi_1 - \xi_1\xi_2\nabla\xi_3$	$\xi_2\xi_3(\nabla\xi_2 - \nabla\xi_3)$
	$\xi_1\xi_3\nabla\xi_2 - \xi_1\xi_2\nabla\xi_3$	$\xi_1\xi_3(\nabla\xi_3 - \nabla\xi_1)$
		$\xi_1\xi_2(\nabla\xi_1 - \nabla\xi_2)$
		$\xi_1(2\xi_1-1)(\xi_2\nabla\xi_3 - \xi_3\nabla\xi_2)$
		$\xi_2(2\xi_2-1)(\xi_3\nabla\xi_1 - \xi_1\nabla\xi_3)$
		$\xi_3(2\xi_3-1)(\xi_1\nabla\xi_2 - \xi_2\nabla\xi_1)$
		$\xi_1^2(\xi_2\nabla\xi_3 - \xi_3\nabla\xi_2)$
		$\xi_2^2(\xi_3\nabla\xi_1 - \xi_1\nabla\xi_3)$
		$\xi_3^2(\xi_1\nabla\xi_2 - \xi_2\nabla\xi_1)$

Table 4

Lowest eigenvalues produced by a discretization of a circular cavity with ε_r=1, μ_r=1, and unit radius using mixed-order basis functions, for the TE polarization. The 42-cell model produced a matrix with order 54 for the CT/LN functions and 192 for the LT/QN functions.

CT/LN	LT/QN	exact
0.0 (13)	0.0 (67)	
1.86 (2)	1.84 (2)	1.841 (2)
3.10 (2)	3.05 (2)	3.054 (2)
3.82 (1)	3.84 (1)	3.832 (1)
4.28 (2)	4.20 (2)	4.201 (2)
5.27 (2)	5.32 (2)	5.318 (2)
5.39 (2)	5.35 (2)	5.331 (2)

should be possible to restrict the expansion to the eight degrees of freedom in (7). These happen to produce a linear-tangential, quadratic-normal (LT/QN) representation, and basis functions can be defined that interpolate to the tangential and normal components in several ways. One specific form of the basis functions is given in simplex coordinates in Table 3. Table 4 shows numerical eigenvalues produced by the LT/QN functions when used to discretize (1) for a circular, homogeneous cavity of unit radius. As compared to the complete quadratic case, the results contain the same number of nonzero eigenvalues but far fewer zero eigenvalues; the number of zero eigenvalues is reduced by exactly the number of basis functions excluded.

It is noteworthy that the six linear basis functions in Table 1 form a subset of the LT/QN functions defined in Table 3. By comparing Tables 2 and 4 we observe that the LT/QN expansion produces exactly the same number of zero eigenvalues as the complete linear expansion. This suggests that the additional basis functions used to build up the set of 8 LT/QN functions do not contribute to eigenfunctions in the nullspace. However, their addition to the set of six LT/LN functions in Table 1 clearly improves the accuracy of the nonzero eigenvalues.

A general cubic polynomial representation of a vector function in 2D contains 20 degrees of freedom. There are five degrees of freedom associated with the gradient of a fourth-order polynomial, which can be excluded to reduce the Cartesian form of the basis functions to

$$\begin{aligned}\tilde{B}(x,y) = \hat{x}\,\{&A + B\,x + C\,y + D\,x^2 + E\,xy + F\,y^2 + G\,x^2y + H\,xy^2 + 3I\,y^3\} \\ + \hat{y}\,\{&J + K\,x + L\,y + M\,x^2 + N\,xy + O\,y^2 - 3G\,x^3 - H\,x^2y - I\,xy^2\}\end{aligned} \qquad (9)$$

Within a cell, one possible form of the 15 basis functions is given in simplex coordinates in Table 3. Nine of these functions interpolate to the tangential vector component along cell edges, while six functions build up the normal component. Together, these 15 basis functions provide a representation with quadratic tangential and cubic normal components (QT/CuN).

The CT/LN, LT/QN and QT/CuN basis functions in Table 3 are consistent with Nedelec's spaces [2]. Cendes [5] proposed functions with the same number of degrees of freedom per cell as the Nedelec functions, but with a different mathematical form than the LT/QN and QT/CuN functions in Table 3. Webb and Forghani have proposed hierarchal vector basis functions for tetrahedral cells [6]. Their functions appear to incorporate those of Cendes [5], and therefore are not consistent with the Nedelec spaces in [2].

5. Mixed-order expansions for quadrilateral cells

Nedelec also originally proposed mixed-order basis functions for quadrilateral and hexahedral cells [2]. These functions have a different number of degrees of freedom than those used on triangles and tetrahedral cells, and a different mathematical expression in Cartesian coordinates than the mixed-order functions developed in the preceding section. The relationship between these basis functions can be seen as follows.

The mixed-order functions for triangular cells are somewhat optimal in that they discard all the obvious degrees of freedom associated with the nullspace. There is no reason why some of

these degrees of freedom cannot be kept in the representation, however. For instance, as an alternative to the subspaces defined by (7) and (8), we could employ the projection

$$\bar{B}(x,y) = \hat{x}\,\{A + B\,x + C\,y + D\,xy + E\,y^2\} + \hat{y}\,\{F + G\,x + H\,y + I\,x^2 + J\,xy\} \qquad (10)$$

omitting the subspace

$$\bar{B}_{grad}(x,y) = \hat{x}\,K\,x^2 + \hat{y}\,L\,y^2 \qquad (11)$$

which has zero curl. This way of separating the subspaces eliminates two degrees of freedom, leaving 10. However, 12 degrees of freedom are required to build up a linear tangential and quadratic normal (LT/QN) component along the sides of a rectangular cell. The polynomial components in (11) do not contribute to an LT/QN expansion, and instead it is convenient to add two cubic-order degrees

$$\hat{x}\,K\,x\,y^2 + \hat{y}\,L\,x^2\,y \qquad (12)$$

The resulting expansion provides an LT/QN representation along the cell edges. (The expansion for quadrilaterals differs from that used with triangles in that it is not purely LT/QN along any cut within a cell.) Crowley confirmed that these functions properly represent the nullspace and therefore eliminate spurious modes [4], when only tangential continuity is imposed.

6. Summary

Spurious eigenvalues arising with discretizations of the curl-curl form of the vector Helmholtz equation appear to be caused by the inability of a continuous basis expansion to properly model the discontinuous nullspace eigenfunctions, and can be alleviated by using an expansion that only imposes tangential continuity. Thus, a wide variety of basis functions can be used successfully, as long as they do not impose normal continuity. Mixed-order basis functions of the Nedelec variety [2] help to reduce the computational requirements of a vector finite element implementation by eliminating some of the degrees of freedom associated with the nullspace. Linear, quadratic, and cubic order basis functions of this type have been discussed.

References

[1] A. F. Peterson, "Vector finite element formulation for scattering from two-dimensional heterogeneous bodies," *IEEE Trans. Antennas Propagat.*, vol. 43, pp. 357-365, 1994.

[2] J. C. Nedelec, "Mixed finite elements in R3," *Num. Math.*, vol. 35, pp. 315-341, 1980.

[3] J. C. Nedelec, "A new family of mixed finite elements in R3," *Num. Math.*, vol. 50, pp. 57-81, 1986.

[4] C. W. Crowley, *Mixed Order Covariant Projection Finite Elements for Vector Fields.* Ph.D. Dissertation, McGill University, 1988.

[5] Z. J. Cendes, "Vector finite elements for electromagnetic field computation," *IEEE Trans. Magnetics*, vol. 27, pp. 3958-3966, Sept. 1991.

[6] J. P. Webb and B. Forghani, "Hierarchal scalar and vector tetrahedra," *IEEE Trans. Magnetics*, vol. 29, pp. 1495-1498, 1993.

[7] G. Mur, "Edge elements, their advantages and their disadvantages," *IEEE Trans. Magnetics*, vol. 30, pp. 3552-3557, 1994.

Finite Element Waveguide Simulator Techniques

J. R. Sanford and N. M. Johansson
Chalmers University of Technology, Gothenburg, Sweden

Introduction: Periodic arrays find applications as frequency selective surfaces, spatial filters, array antennas and in corrugated horns. Here we illustrate how to compute the electromagnetic characteristics of such structures using widely accessible finite element models and extended waveguide simulator concepts. We apply the method to three distinct examples and verify the solutions by other means. The results indicate the accuracy and many useful applications of the method. The first example is the calculation of the transmission coefficient of a dichroic surface. In the second we determine the surface impedance of a corrugated surface. Finally, we consider the return loss of waveguide type elements in large arrays. The generality of the technique and the accessibility of commercial finite element method (FEM) codes make the procedure extremely useful for verifying other numerical models[1].

Waveguide simulators are used extensively for the characterisation of elements in large planar phased array antennas[2]. In a properly designed simulator the element has the reception characteristics of an element in an infinite array environment. Hence, a physically bound experimental model simulates an unbound scattering problem. The method has limited usefulness for a number of reasons. First, the periodic element needs a symmetry plane since waveguide modes are equivalent to pairs of symmetric plane waves and each plane wave in the pair must see the identical element with the same orientation. Additionally, the incidence angle of the simulated plane wave is a function of frequency. Further, the dominant mode of the waveguide (*TE* or *TM*) dictates the polarisation. Therefore, each frequency and incidence angle under consideration requires the construction of a separate waveguide simulator. Measurements using the simulators requires construction of adapters to standard size transmission line.

With the advent of sophisticated finite element models, some of the shortcomings of the experimental model can be overcome. FEM was first applied to waveguide problems in the late sixties[3,4] but because the method is so numerically intensive it was not very useful until the development of adequate computers. Now a variety of user friendly FEM analysis packages are commercially available[5,5a]. Finite element techniques are particularly applicable to physically bound problems. We take advantage of this by using a bound simulator model for the unbound array. Rather than building a new simulator for every frequency or incident angle, we model the simulator using the finite element technique. The computational model overcomes many limitations of the experimental model. Lossless walls are introduced to consider frequencies near the waveguide cut-off frequency. Additionally, the use of magnetic boundaries permit new waveguide modes to propagate. These utilities allow us to consider orthogonal polarisations and hence circular polarisation. A number of symmetries reduce the computation time significantly.

Generalised Simulator Theory: The described procedure is applicable to a wide variety of periodic geometries. The guidelines of conventional waveguide simulation are well documented[2,6]. One can conceive a variety of simulator geometries, each corresponding to different planes of incidence or polarisation. Let us first consider only rectangular waveguide TE_{mn} and the dual TM_{mn} simulator types. All *TE* modes in rectangular waveguide consist of *H*-polarised waves, and all *TM* modes in the waveguide consist of *E*-polarised waves. Hence, each waveguide mode defines a specific scattering situation (i.e. incidence angle, incidence plane, *E* or *H* polarisation). Figure 1 depicts a simulator containing three elements of a periodic structure. We use this to calculate the electrical characteristics

of an infinite periodic structure when excited by an *E*-polarised plane wave.

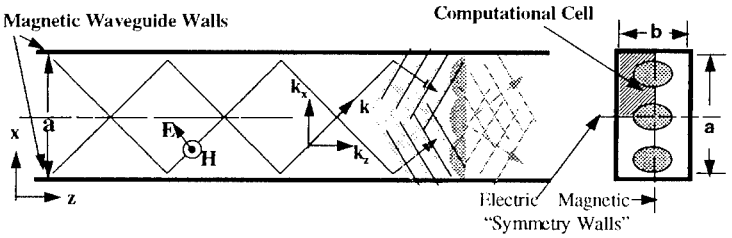


Figure 1 - Magnetic Walled TM_{10} Waveguide Simulator

In a two dimensional periodic array there are several directions in which planes of symmetry reside. Additionally, the simulator can hold a number of the structure unit cells. Hence, the dimensions of the simulator are chosen by

$$a = p\tau_x \qquad b = q\tau_y \tag{1}$$

where τ_x and τ_y are the periodicities in each of their respective directions and p and q are integers corresponding to the number of unit cells in the simulator.

In general, the direction of plane wave propagation may be represented by the propagation vector $\vec{k} = k_x\hat{x} + k_y\hat{y} + k_z\hat{z}$. In waveguide, $\vec{k}$ is established from the waveguide mode indices. The waveguide propagation constants in the various directions are given by,

$$k_x = \frac{m\pi}{a}, \quad k_y = \frac{n\pi}{b}, \quad k_z^2 = k_0^{\,2} - k_x^2 - k_y^2 \qquad m,n = \ldots -2,-1,0,1,2,\ldots \tag{2}$$

where m and n are integers corresponding to the waveguide mode and $k_0 = 2\pi / \lambda$. Clearly, the values of m and n are limited if k_z is to have a real value. The incidence angle for higher order mode propagation is given by

$$\sin\theta_i = \frac{k_\rho}{k_0}, \quad \tan\phi_i = \frac{k_y}{k_x} \qquad \text{where } k_\rho^2 = k_x^2 + k_y^2 \tag{3}$$

An interesting consequence of these formulas is that a waveguide array element with thin walls and dimensions *a, b*, it is perfectly matched at the scan angle dictated by the above equation. This is obvious since the waveguide element and the waveguide simulator have the same dimensions.

We now state the grating lobe condition in terms of propagation vectors. Assuming a rectangular lattice, the scattered beam positions are given by

$$k_x^s(l_x) = k_x^i - k_0\frac{l_x\lambda}{\tau_x}, \quad k_y^s(l_y) = k_y^i - k_0\frac{l_y\lambda}{\tau_y} \qquad l_x, l_y = \ldots -2,-1,0,1,2,\ldots \tag{4}$$

where l_x and l_y are the indices of the grating lobe and s and i denote respectively scattered and incident field. Combining this with relations (1) and (2),

$$k_x^s(l_x) = \frac{m\pi}{p\tau_x} - k_0\frac{l_x\lambda}{\tau_x} = \left[m - 2l_x p\right]\frac{\pi}{a}, \quad k_y^s(l_y) = \frac{n\pi}{q\tau_y} - k_0\frac{l_y\lambda}{\tau_y} = \left[n - 2l_y q\right]\frac{\pi}{b} \tag{5}$$

Figure 2 depicts equation (5) in *k*-space, showing only the positive m and n values. A grating lobe occurs at each $|k_{gl}(l)|<k_0$. The bracketed term in (5) is an integer and for each positive value of this integer there is a corresponding negative value. Hence, for every grating lobe there are three symmetric grating lobes. This applies to the evanescent fields as well ($|k_{gl}(l)|>k_0$). This conforms with our supposition that waveguide modes are equivalent to combinations of symmetric plane waves. The $(m\text{-}2l_x p,\ n\text{-}2l_y q)$ waveguide simulator modes correspond to grating lobes. It may turn out that the

newly excited waveguide mode is the degenerate (-*m*,-*n*) mode. In this case the grating lobe is the mirror image of the transmitted (incident) field and no new mode is excited in the waveguide simulator. Hence, one may have a grating lobe without exciting a new waveguide mode but not the converse. There is always grating lobe when a new waveguide mode is excited.

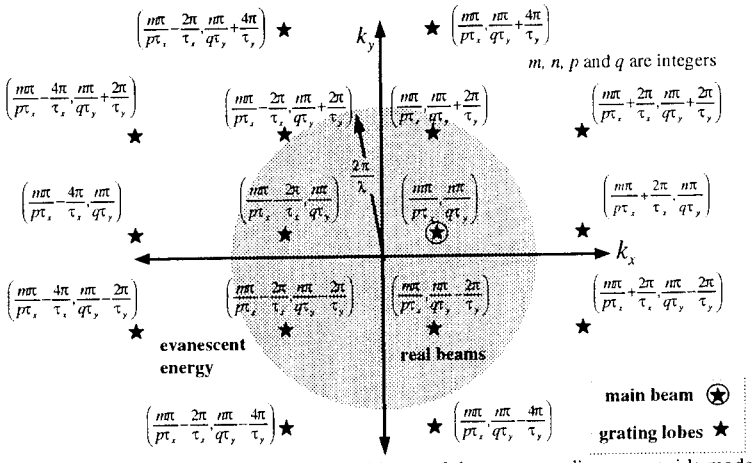


Figure 2 - Incident beam and grating lobe positions and the corresponding waveguide modes

FEM Simulator Models: We now turn our attention to the capabilities of the finite element numerical simulator model relative to conventional waveguide simulators. The simulator shown in figure 1 is not physically realisable because of its "magnetic walls". The "magnetic walls" are composed of perfect magnetic conductors (PMC) and have tangential *H*-fields equal to zero. Although such materials are not known to exist in nature, we can construct a FEM numerical model of the simulator and hence determine the *E*-polarised scattering characteristics of the periodic structure. For an *H*-polarised plane wave we apply duality and exchange the electric walls with magnetic walls.

The simulator geometries used in experimental models are not necessarily the best for numerical models. If the simulator is large enough, higher order modes also propagate. Measurement using these higher order modes poses many problems. That is not the case using FEM computations. In total, there are three useful simulator geometries, as shown in figure 3.

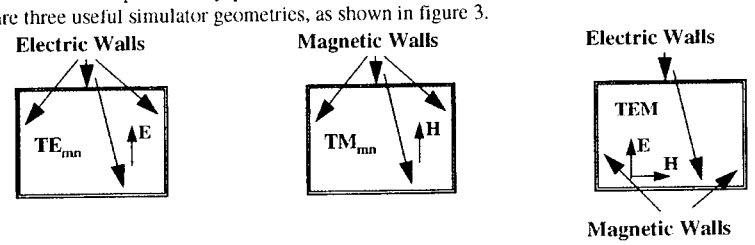


Figure 3 - Simulator Geometries

The left most simulator geometry is the conventional experimental type and the middle is as discussed above. The simulator geometry on the right uses both electric and magnetic walls. The fundamental TEM mode propagating in this "waveguide" is a uniform plane wave over the bounds of the guide.

Image theory dictates that the unit cells in this guide see what is equivalent to normal incidence on the infinite periodic structure. Normal incidence can not be considered using conventional waveguide simulators. We obtain horizontal polarisation by simply exchanging the magnetic and electric walls. In all cases, we obtain circular (elliptic) polarised reflection by taking the complex sum of the E and H polarised reflection coefficients with the appropriate phase delay (and amplitude weighting).

From (5) we recognise a restriction on the observation angles. We can compute only a discrete set of k_x and k_y corresponding to the integers m, n, p and q. The range of observation points increases with larger p and q as does the computer processing time. After a single computation using finite element technique, the resulting matrix allows us to determine the coupling between all the propagating modes. Hence, if the simulator supports NxM modes, then we know the reflection coefficient for NxM incident angles. Normally we are interested in results over a frequency band. In such cases we set p and q to some nominal value and compute results for $m=1,2,...,M$ and $n=1,2,...,N$ and a set of frequencies $f=f_1 f_2,...,f_R$. This gives us a total of MxNxR point over which we interpolate.

The required computational time is proportional to the square of the volume of the simulator. We reduce this time by 75% by placing a perfectly conducting electric wall along the centreline of the structure. This is permitted since the symmetry dictates that the electric field is zero along this plane. For doubly periodic structures a similar symmetry plane allows an additional reduction in the volume, making the computation time about 1/16 of the original for the same numerical accuracy. Instead of the FEM, the simulator geometry can be considered using FDTD. In this case we are able to process multiple frequencies in a single run but only with a single mode. Therefore we trade multiple incident angles for multiple frequencies.

Reviewing the general formulation, the angle of incidence is equivalent to knowing the progressive phase change of the currents on each array element and is dictated by the waveguide simulator mode and the unit cell dimensions (m, n, p, q, τ_x, τ_y). Even if we excite the structure with a single waveguide mode, other modes may be reflected. These other modes correspond to symmetric pairs of grating lobes. The relative amplitudes of these grating lobes are the same as the relative power of the newly excited modes. Here we consider only rectangular lattices but the observations are equally valid for triangular lattices.

Case Studies: The usefulness of the method is best illustrated by a few examples. For each of the cases we develop or duplicate an alternate analysis method. The results of each example are corroborated by the alternate method and the accuracy is examined. The examples also give some insight into the functioning of the periodic structures.

a. Reflection From a Dichroic Surface

In this section, we calculate the reflection through the crossed-dipole surface shown in figure 4 using the FEM simulator model and a spectral moment method. This periodic geometry is considered in a number of papers[7,8]. We investigate normal incidence and hence use a simulator with two electric walls and two magnetic walls. Figure 5 shows the cross section of the simulator unit cell with the magnitude of the E-field as calculated by FEM. The left and right walls are PMC while the top and bottom are PEC. As expected, the E-field over the conductor is small since the tangential component of E-field is zero.

For comparison purposes we use the full-wave moment method analysis for an illuminating field that is applicable for any arbitrary incident angle. The method is described in detail by Tsao and Mittra[7] and outlined as follows. An integral equation is developed for the fields due to a set of currents on the free-standing crosses. We assume the current on each cross to be identical except for a progressive phase term. This assumption corresponds to plane wave incidence. The problem is formulated in the

spectral domain. This reduces the convolution form of the integral equation for the induced current into an algebraic one. We use Galerkin's procedure in order to solve the spectral domain equation. To account for the discontinuous nature of the induced current at the junction of the cross we use a set of entire domain "junction basis functions".

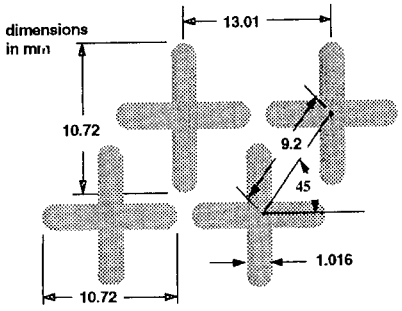


Figure 4 - Dichroic surface geometry printed on 0.127mm kapton (ε_r=4.25)

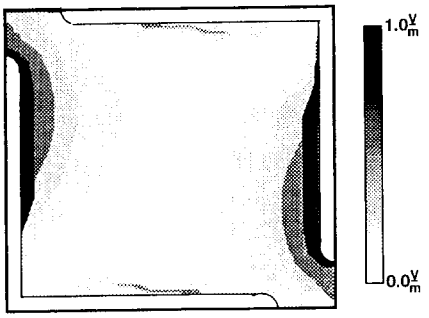


Figure 5 - Simulator unit cell and the *E*-field magnitude

Figure 6 shows the computed power transmission coefficients for the free standing cross frequency selective surface. The left curve is for free standing crosses and the right is for crosses on a sheet of kapton. As one would expect, the dichroic is a good microwave reflector when the elements are roughly one half wavelength in the *E*-plane.

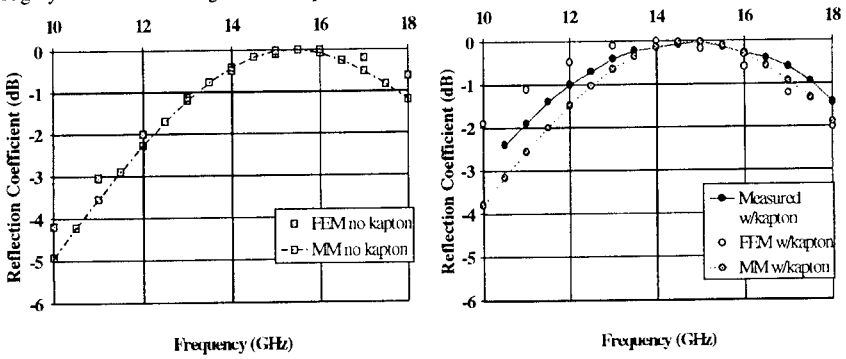


Figure 6 - Dichroic Reflection Coefficient

The FEM results match the measured results except for a 0.8GHz shift in frequency. The FEM simulator results compare adequately with those of the spectral Galerkin moment method. The moment method routine considers the crosses to have squared ends rather than rounded. This may account for the disparity. Validation of this case is particularly useful since the documented methods do show some discrepancies[7,8].

b. Surface Impedance: We now direct our attention to the computation of the surface impedance of an infinite impenetrable planar surface. Knowledge of the surface impedance allows boundary value problems to be solved[9]. If the surface can be characterised by a surface impedance, the surface has a periodicity smaller than a wavelength. The surface impedance of a periodic structure is a function of the plane of incidence. A distinction must be made between the macroscopic and microscopic viewpoints. From a microscopic view the surface has drastically varying field magnitudes and hence a nonuniform surface impedance. However, the aggregate effect of these fields may be represented in the large by a parameter such as Z_s. In general, this surface impedance will be a function of the orientation and incidence angle. The surface impedance seen by the incident wave is found from

$$Z_s = C\int_0^{mb}\int_0^{na} \frac{E_{\tan}}{H_{\tan}}\,dxdy = \frac{1+\Gamma e^{j\beta z_{ref}}}{1-\Gamma e^{j\beta z_{ref}}} \tag{6}$$

where a and b describe a unit cell, m and n are integers and C is a normalisation constant. Evanescent fields exist near the surface but integrate to zero over the unit cell. Hence, we obtain the same surface impedance magnitude regardless of the calculation plane ($z=z_{ref}$).

For demonstration purposes we consider a perfectly conducting corrugated surface with a dielectric in the corrugations. Corrugated surfaces are widely used in the design of electromagnetic structures. Consider an obliquely incident TM (*E*-polarised) plane wave as shown in figure 7. We determine the surface admittance over a range of incidence angles and frequencies for a plane wave with a path of travel transverse to the corrugations.

We choose the corrugation depth in such a way as to have the transverse magnetic fields cancel at the top of the corrugations. This results in a large reactance (small susceptance), as shown in figure 8, where η_0 is the free space impedance.

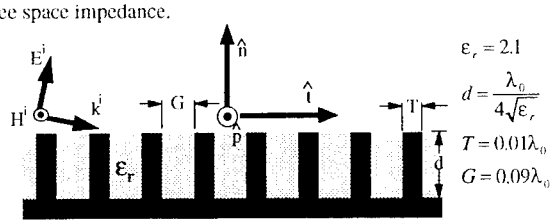
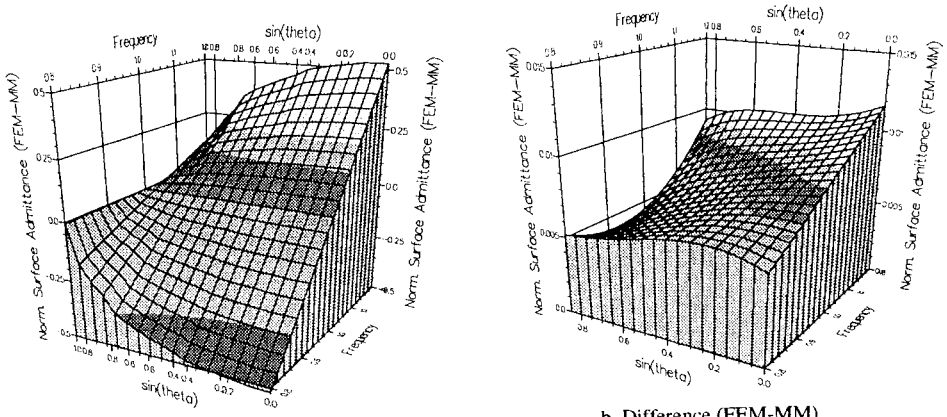


Figure 7 - Transverse Propagating TM Incidence

Extensive documentation of the infinite corrugated surface and the infinite periodic array is available[10]. Previous studies use, among other techniques, mode matching, moment method and direct analytical solutions. Here we use the mode matching technique as described by Wang[11, pp 365-376] to verify the FEM simulator results for a dielectric filled corrugated surface. A brief description of the procedure is as follows. We first divide the space into two regions. Integral equations are formulated by enforcing boundary conditions at the interface. We use parallel plate cavity modes to represent the field inside the corrugation. These modes fulfil the boundary conditions of the cavity formed by the corrugation. We equate the tangential electric and magnetic fields of the two regions in the aperture. This gives the unknown coefficients of the free space Floquet modes. Assuming the corrugations are spaced close together, there is a single specular reflection. Its amplitude corresponds to that of the zeroth order Floquet mode. The coefficient of this propagating mode gives the surface impedance of the structure.

The FEM simulator and the mode matching results are shown in figure 8. Also shown is the difference between the results. The FEM simulator approach yields results within about 2% of the mode matching solution.



a. Surface Admittance

b. Difference (FEM-MM)

Figure 8 - Corrugated Structure Surface Admittance

c. Return Loss of Waveguide Elements with Dielectric Loaded Walls

Waveguide simulators are most often used for the design of phased array elements. We calculate the reflection of the array shown in figure 9. It consists of perfectly conducting parallel plate waveguides with homogeneous dielectric slabs on the side walls. If the dielectric slabs are chosen using,

$$\text{slab thickness} = \frac{\lambda}{4\sqrt{\varepsilon_r - 1}} \tag{7}$$

the geometry provides a relatively uniform aperture distribution. Therefore it gives a higher directivity than conventional waveguide elements with the same aperture dimensions. Results for a thick-walled waveguide element with dielectric loaded walls are not available in open literature. Mailloux and Steyskal[12] reported a similar technique for a less general case.

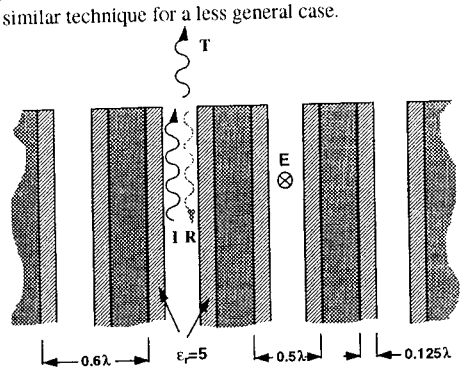
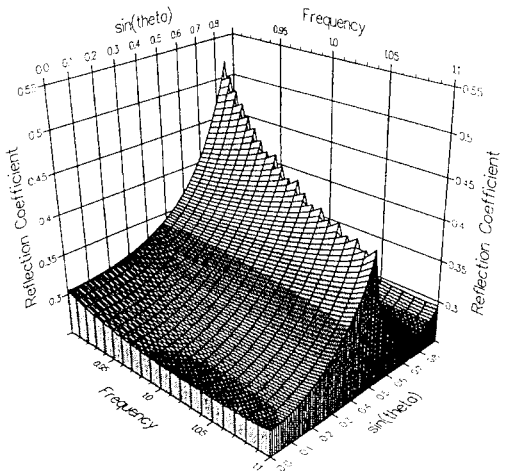
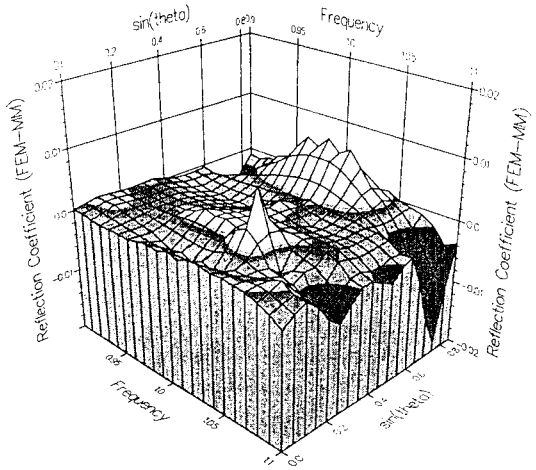


Figure 9 - Inhomogeneously Loaded Waveguide Array

We again determine the return loss of the array elements by applying the mode matching technique. A superposition of parallel plate modes represents the fields in the inhomogeneous dielectric filled waveguide. The field radiated into free space is a sum of Floquet modes with unknown amplitudes. Matching the tangential components of the fields at the aperture reduces the problem to a system of linearly algebraic equations for the amplitudes of each waveguide mode and Floquet harmonic. We solve the system by Gauss-Jordan elimination and extract the reflection coefficient. The technique includes all mutual coupling effects.



a. Loaded Waveguide Element Reflection Coefficient



b. Difference between FEM and moment method results

Figure 10 - Inhomogeneously Loaded Waveguide Results

The reflection coefficient of the defined array is shown in figure 10 along with the difference between the approaches. The FEM simulator and the mode matching reflection coefficient differ by less than 2%. At higher frequencies and large incident angles we notice a ridge corresponding to a grating lobe. The techniques are both valid for this case as well as when only a single plane wave is excited.

The effective element pattern radiated from the infinite array is given by

$$f(\theta) = \left(1 - \left|\Gamma(\theta)\right|^2\right)\cos\theta \tag{11}$$

where Γ is the infinite array reflection coefficient when no grating lobe radiates[12]. Figure 11 shows the effective element pattern computed using the waveguide simulator technique (shown with points) and the mode matching method described above (shown with lines). The dimensions of the array are in figure 9, where the wavelength corresponds to f_0.

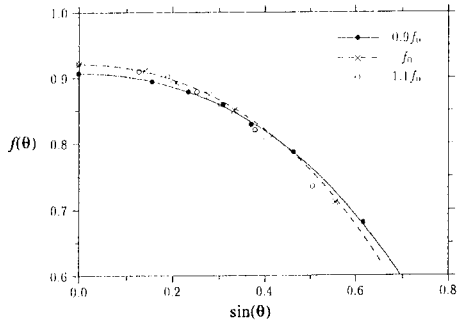


Figure 11 - Effective Element Pattern of Dielectric Slab Array

Conclusions and Future Work: We combine the finite element modelling technique with waveguide simulator concept to determine the electrical properties of periodic structures and then apply the method to a number of interesting antenna and scattering geometries. Comparisons with results obtained by other methods validate the analysis procedure. The method proves useful for predicting the electromagnetic properties of complex periodic structures.

The method is not numerically efficient since the entire waveguide simulator is modelled using the finite element technique. The alternative methods outlined in the paper were normally a few orders of magnitude faster than the FEM simulator technique. Still, it is very useful for validating other analysis techniques or for testing design ideas and no time is spent on computer programming. Further, it is a tool presently accessible to engineers in most high tech firms. We presently use this FEM simulator technique to verify all our numerical models for periodic structures and normally obtain accuracy far beyond that achievable by measurement.

References:

[1] P.P. Silvester & R.L. Ferrari, Finite Elements for Electrical Engineers, Cambridge University Press 1990.

[2] P. W. Hannan, M. A. Balfour, "Simulation of a Phased-Array Antenna in Waveguide," IEEE AP Trans., Vol. 1, January 1964.

[3] S. Ahmed and P. Daly, "Waveguide solutions by the finite element method," Radio and Electronic Engineering, 38, 217-223, 1969.

[4] P. Silvester, A general high order finite element waveguide analysis program," IEEE Transactions on Microwave Theory and Techniques, Vol 21, 538-42, 1969.

[5] HP 85180 High-Frequency Structure Simulator User Guide, Hewlett Packard, June 1991.

[5a] MSC/EMAS Users Guide, MacNeal-Schwendler Inc., May 1991.

[6] F. S. Johansson, "Periodic arrays of thin conducting elements for frequency filtering and scanning," Technical Report No. 178, Chalmers U. of Tech., 1987.

[7] R. Mittra, "Spectral-Domain Analysis of Frequency Selective Surfaces Comprised of Periodic Arrays of Cross Dipoles and Jerusalem Crosses," Trans. AP, Vol 32, No 5, May 84.

[8] E. L. Pelton and B. A. Munk, "Scattering from periodic arrays of crossed dipoles," IEEE Trans. on Antennas and Propagation, vol 27, pp. 323-330, May 1979.

[9] R. E. Collin, Field Theory of Guided Waves, pp. 605-636, pp. 247-322, IEEE Press 1991.

[10] R. S. Elliott, "On the Theory of Corrugated Plane Surfaces," IRE Trans. on Antennas and Propagation, 1954.

[11] J. J. H. Wang, Generalized Moment Methods in Electromagnetics, Wiley 1991.

[12] R. J. Mailloux and H. Steyskal, "Analysis of Dual-Frequency Array Technique," IEEE Trans. on Antennas and Propagation, Vol. AP-27,, pp. 130-136, March 1979.

[13] R. J. Mailloux, Phased Array Antenna Handbook, pp. 331-339, Artech House, Norwood MA, 1994.

A SOLUTION FOR OPEN BOUNDARY ELECTROMAGNETIC FIELD PROBLEMS BY MAPPED INFINITE AND VIRTUAL ELEMENTS

L.H.A. de Medeiros and A. Raizer
Departamento de Engenharia Elétrica - Universidade Federal de Santa Catarina
Caixa Postal 476 - CEP 88040-900 - Florianópolis - S.C. - Brazil.
Phone: 55.48.2319649 - Fax: 55.48.2343790 - E-mail: raizer@grucad.ufsc.br

Abstract - Mapped infinite elements technique is described to solve electromagnetic field unbounded problems. The method is based on the mapping of a semi-infinite strip onto finite local element using singular mapping functions. The infinite element is used like a boundary condition, therefore without increasing the final matrix dimension, with less calculation time and lower computation costs. Tests have been done in 2-dimensional electromagnetic problems and results have shown to be quite good. Virtual elements are described and used to explore the entire domain. Results are presented based on the solution of two different electromagnetic structures.

INTRODUCTION

Finite element method (FEM) is a general technique for solving boundary value problems [1,4,6,13]. Several electromagnetic devices are studied in free space, or in unbounded domains. The most used technique is placing the boundary 'far enought' of the studied device, but with computation costs [2-4,13]. Several techniques for modelling unbounded problems have been studied [3,9,10,14]. These methods are classified in global methods, in which the exterior domain is considered as one, such as truncation and ballooning [2,3], and elementary methods, in which the exterior domain is divided into a finite number of elements, or infinite elements [8,11].

In this paper, mapped infinite elements technique is described and some results in two dimensional electromagnetic problems are show. To the visualisation of the exterior field the virtual element technique is described [8].

MATHEMATICAL FORMULATION AND APPLICATION OF FINITE ELEMENT METHOD

The governing equations of electromagnetic problems are the Maxwell's equations [1,4]

$$curl\,\mathbf{E} + \partial\mathbf{B}/\partial t = 0 \tag{1}$$

$$curl\,\mathbf{H} - \partial\mathbf{D}/\partial t = \mathbf{J} \tag{2}$$

$$div\,\mathbf{B} = 0 \tag{3}$$

$$div\,\mathbf{D} = \rho \tag{4}$$

With the constitutive relations of the form

$$\mathbf{D} = \varepsilon\,\mathbf{E} \tag{5}$$

$$\mathbf{B} = \mu\,\mathbf{H} + \mathbf{Br} \tag{6}$$

$$\mathbf{J} = \sigma\,\mathbf{E} \tag{7}$$

Where, E is the electric field, B the magnetic flux density, H the magnetic field, D the electric flux density, J the current density, ρ the charge density, ε the electric permittivity, μ the magnetic permeability, σ the electric condutivity, **Br** the remanent magnetic flux density.

In this paper, only linear magnetostatic problems in low frequences are treated, so, using equations 2,3,6 and defining a magnetic vector potential **A** as follows [4]:

$$\mathbf{B} = \text{curl } \mathbf{A} \tag{8}$$

The following equation has to be solved

$$\text{curl } \nu \text{ curl } \mathbf{A} = \mathbf{J} + \text{curl } \nu \mathbf{Br} \tag{9}$$

Where, ν is the magnetic reluctivity ($1/\mu$).

Applying Galerkin's and finite element methods to the equation above, the matrix system is obtined as follows [1,4],

$$\sum_{i=1}^{n} K_{ji} A_i = F_j \tag{10}$$

Where

$$K_{ji} = \int_{\Omega} \nu \left[curl\, \mathbf{N}_j\right]^T \left[curl\, \mathbf{N}_i\right] d\Omega \tag{11}$$

$$F_j = \int_{\Omega} \left\{ \left[\mathbf{N}_j\right]^T \mathbf{J} + \nu \left[curl\, \mathbf{N}_j\right]^T \mathbf{Br} \right\} d\Omega \tag{12}$$

Where, N is the shape function [1,4,13], Ω is the domain of study and n the number of nodes.

MAPPED INFINITE ELEMENT

Coordinate mapping between local and global systems is commonly used in FEM. In mapped infinite element technique a singular mapping function M_i, based on $1/(1-\xi)$, is used. With these functions some nodes from local system are mapped into nodes at infinity in global system, and when $\xi \to 1 \Rightarrow M_i \to \infty$.

A one dimensional element in global coordinate with node 3 at infinity that is mapped onto a parent element in local system $-1 \le \xi \le +1$, is considered in figure 1.

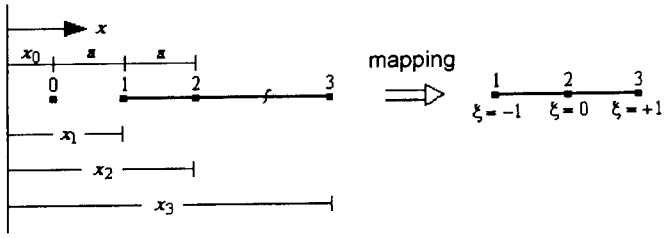


Figure 1. One dimensional infinite element mapping

In one dimensional element the mapping (from global x to local ξ coordinate) can be defined as

$$x = M_1(\xi)x_1 + M_2(\xi)x_2 \tag{13}$$

Where

$$M_1(\xi) = \frac{-2\xi}{1-\xi} \quad \text{and} \quad M_2(\xi) = \frac{1+\xi}{1-\xi} \tag{14}$$

Three points can be identified in this mapping, $x=x_1$ for $\xi=-1$, $x=x_2$ for $\xi=0$ and for $x=x_3$

$$x = \lim_{\xi \to +1} \frac{-2\xi x_1 + (1+\xi)x_2}{1-\xi} = \infty \tag{15}$$

which places node 3 automatically at infinity, and node 3 do not be explicity in equantion (13).

The mapping above is applied to the geometry of the problem and a standard shape function N_i is applied to the state variable A as follows:

$$A = \sum_{i=1}^{n} N_i A_i = \left(\frac{-\xi+\xi^2}{2}\right)A_1 + (1-\xi^2)A_2 + \left(\frac{\xi+\xi^2}{2}\right)A_3 \tag{16}$$

Where n extends to the finite nodes only and A_3 is usually imposed equal zero as the infinite boundary condition [6,8].

It is important verify that $\sum_{i=1}^{n} M_i \equiv 1$, to assure that the mapping is not affected by any change in the origin coordinate system [10,11].

The Jacobian defines the mapping between global and local systems. With equation (13), it is defined as [2,6]:

$$J = \frac{\partial M_1(\xi)}{\partial \xi} x_1 + \frac{\partial M_2(\xi)}{\partial \xi} x_2 \tag{17}$$

The transformation from global derivatives to local ones can be defined as:

$$\frac{\partial N}{\partial x} = \frac{\partial N}{\partial \xi}\frac{\partial \xi}{\partial x} \tag{18}$$

The method can be extended to two dimensional problems by introducing finite mapped functions in the η direction and keeping the ε direction infinite (figure 2).

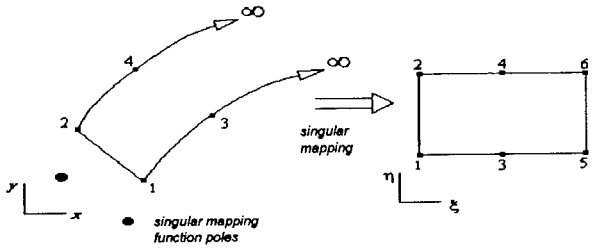


Figure 2. Singular mapping of a global element with nodes placed at infinity in local reference element.

The coupling of finite element method with infinte element method is made with the increasing of a boundary condition that defines an infinite boundary (figure 3).

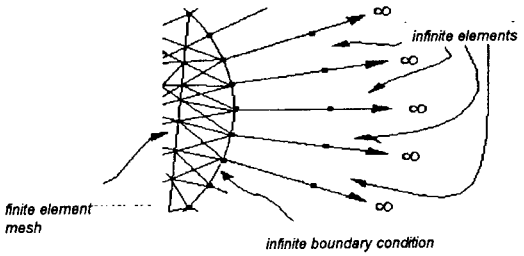


Figure 3. Infinite elements coupled with finite element mesh

The final element matrix is defined as:

$$k_{ji} = \int\int_{\Omega} \nu \left[\left(\frac{\partial N_j}{\partial \xi}\frac{\partial \xi}{\partial x} + \frac{\partial N_j}{\partial \eta}\frac{\partial \eta}{\partial x} \right)\left(\frac{\partial N_i}{\partial \xi}\frac{\partial \xi}{\partial x} + \frac{\partial N_i}{\partial \eta}\frac{\partial \eta}{\partial x} \right) + \left(\frac{\partial N_j}{\partial \xi}\frac{\partial \xi}{\partial y} + \frac{\partial N_j}{\partial \eta}\frac{\partial \eta}{\partial y} \right)\left(\frac{\partial N_i}{\partial \xi}\frac{\partial \xi}{\partial y} + \frac{\partial N_i}{\partial \eta}\frac{\partial \eta}{\partial y} \right) \right] |J| d\xi d\eta \quad (19)$$

Where |J| is the determinant of the Jacobian, defined as:

$$|J| = \det [J] = \frac{\partial x}{\partial \xi}\frac{\partial y}{\partial \eta} - \frac{\partial x}{\partial \eta}\frac{\partial y}{\partial \xi} \quad (20)$$

The field variable at nodes 5 and 6 (figure 2) are specified as zero as boundary condition of the infinite element and do not appear at matrix Kji (equation 19) [6,9].

THE VIRTUAL FINITE ELEMENTS

A good accuracy of solution is obtained with the mapped infinite element technique coupled with the finite element method explained above. But the external field is not obtained by the use of this technique. To solve this problem, a mesh with C^0 Lagrange's elements [13] is created in the external region (called virtual elements) shown in figure 4 [8].

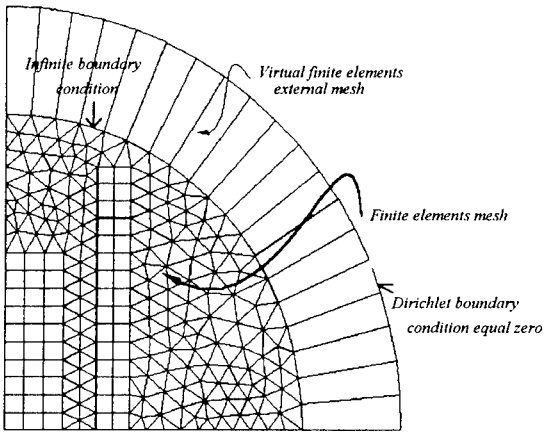


Figure 4. Virtual elements applied at the finite element mesh coupled with the mapped infinite element technique.

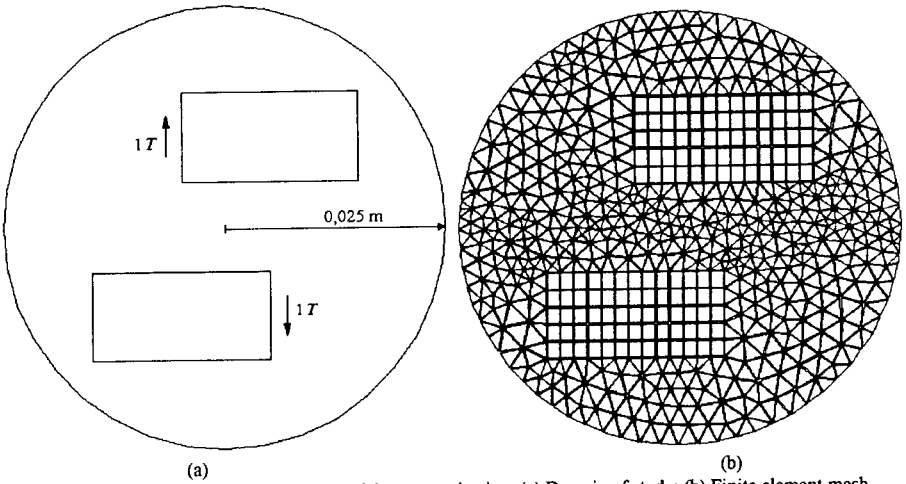
In the virtual mesh, a Dirichlet boundary condition is imposed, and the values of the state variable in the finite element mesh calculated with mapped infinite elements is manteined.

APPLICATION

The method has been succesfully applied in several 2D electromagnetic field problems. Two examples are presented. In figure 5(a) and figure 7(a) the studied domains are presented.

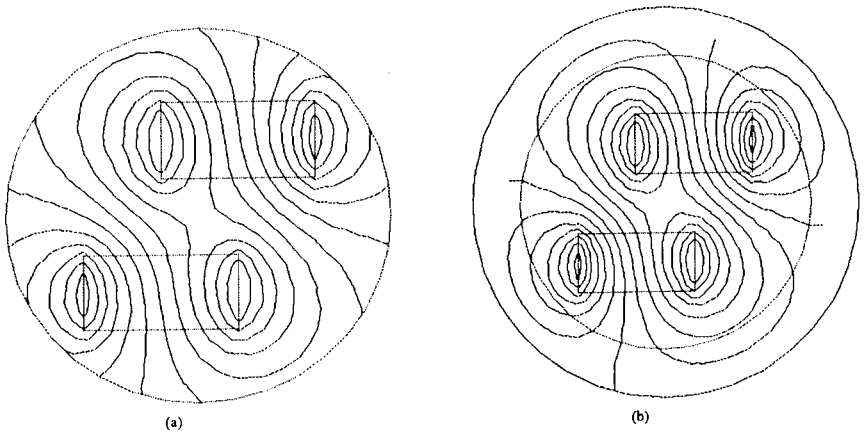
The mesh of the domains are presented in figures 5(b) and 7(b). Mapped infinite elements are used in all the boundary of figure 5 and in the arc of circunference of figure 7.

In figure 6 and figure 8, the equipotentials are presented. Figures 6.(a) and 8.(a) present the equipotential field with infinite elements only. A new region is created and discretized in virtual elements and a Dirichlet boundary condition equal zero is imposed (figure 4). In figures 6.(b) and 8.(b), infinite elements with virtual elements are used at the infinite boundary to show the whole field.



(a) (b)

Figure 5. Permanent magnetics with repulsive magnetization. (a) Domain of study; (b) Finite element mesh



(a) (b)

Figure 6..(a) Infinite elements only. (b) Infinite elements with virtual elements

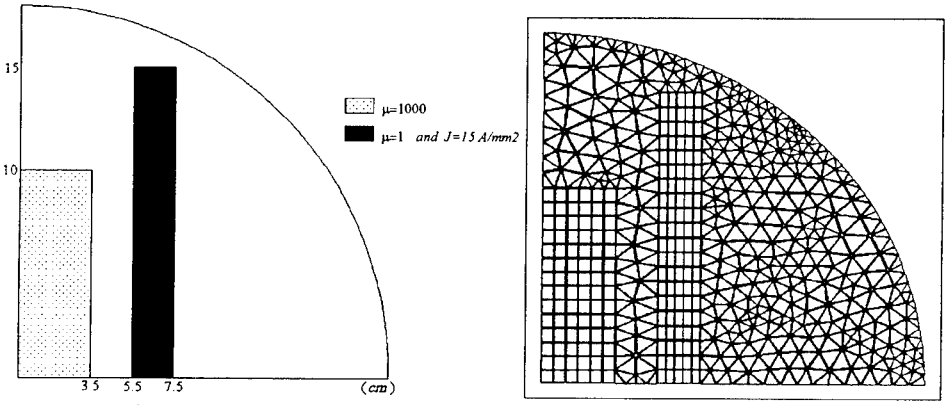


Figure 7. Field winding with an iron core.(a) Domain of study;.(b) Finite element mesh

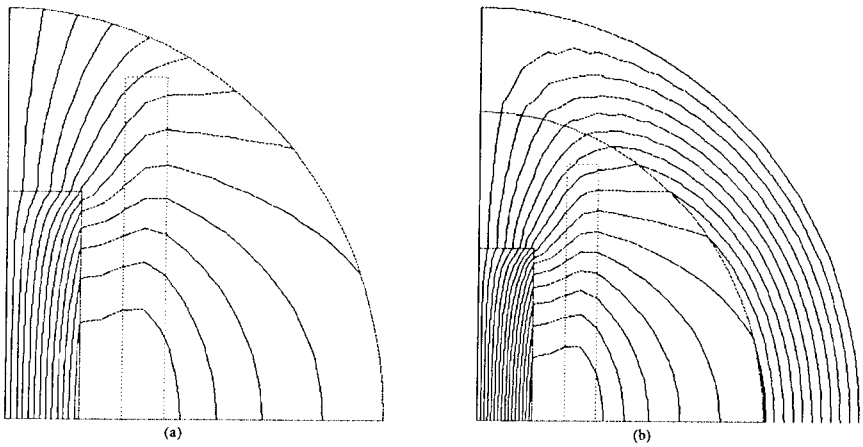


Figure 8.(a) Infinite elements only. (b) Infinite elements with virtual elements

CONCLUSION

The method described, with mapped infinite element used as a boundary condition does not increase the final matrix dimension. The number of elements and nodes of the domain mesh are not altered. The results obtained show that Finite Element Method coupled with Mapped Infinite Elements technique gives better results than with FEM only. In electromagnetic problem where the field tends to zero at infinity, the use of a technique like mapped infinite element becomes very importante. Virtual elements is a good solution to obtain the external field and to explore the entire domain. The results show that mapped infinite element technique can solve unbounded problems with good accuracy.

REFERENCES

[1] N. Ida, J. P. A. Bastos "Electromagnetics and Calculus of Fields", Springer-Verlag, New York, 1992.

[2] A. Bossavit, C. Emson, I. D. Mayergoyz "Methodes Numeriques en Electromagnetisme, Geometrie Differencielle, Elements Finis, Modeles d'Hysteresis", Eyrolles, Paris, 1991.

[3] J. F. Imhoff, G. Meunier, J. C. Sabonnadiere "Finite Element Modeling of Open Boundary Problems", IEEE Transactions on Magnetics, vol. 26, no. 2, pp 588-591, March 1990.

[4] S.R.H. Hoole "Computer-aided analysis and design of electromagnetic devices, Elsevier, 1989.

[5] P. Bettess "Finite Element Modelling of Exterior Eletromagnetic Problems", IEEE Transactions on Magnetics, vol. 24, no. 1, pp 238-243, January 1988.

[6] R. D. Cook, D. S. Malkus, M. E. Plesha "Concepts and Applications of Finite Element Analysis", Third Edition, J. Wiley and Sons, New York, 1989.

[7] O. C. Zienkiewicz, C. Emson, P. Bettess "A Novel Boundary Infinite Element", International Journal for Numerical Methods in Engineering, vol. 19, pp 393-404, 1983.

[8] L. H. A. Medeiros "Elemetos Infinitos Mapeados e Elementos Virtuais no Calculo de Campos Eletromagneticos em Problemas de Fronteiras Abertas pelo Metodo de Elementos Finitos", MSc. Dissertation, UFSC, Florianopolis-Brazil, 1994.

[9] O. C. Zienkiwicz, K. Bando, P. Bettess, C. Emson, T. C. Chiam "Mapped Infinite Elements for Exterior Wave Problems", International Journal for Numerical Methods in Engineering,, vol. 21, pp 1229-1251, 1985.

[10] P. Bettess "Infinite Elements", International Journal for Numerical Methods in Engineering, vol. 11, pp 53-64, 1977.

[11] G. Beer, J. L. Meek "Infinite Domain Elements", International Journal for Numerical Methods in Engineering, vol. 17, pp 13-52, 1981.

[12] D. A. Lowther, E. M. Freeman, B. Forghani "A sparse matrix open boundary method for finite element analysis", Third Biennial IEEE Conference on Eletromagnetic Field Computation, 1988.

[13] G. Dhatt, G. Touzot "Une Presentation de la Methode des Elements Finis", Maloine, Paris, 1984.

[14] S. Subramaniam, M. Feliziane, S. R. Hoole "Open Boundary Eddy-current Problems using Edge Elementd", IEEE Transactions on Magnetics, vol. 29, no. 2, pp 1499-1503, March 1993.

SESSION 21:

EM ANALYSIS TECHNIQUES FOR ELECTRICALLY LARGE CAVITIES

Chair: D. Pflug

Application of Modal and Plane Wave Expansions to Modeling Large Jet Engine Cavities

by
Janice L. Karty and James M. Roedder
McDonnell Douglas Corporation
P. O. Box 516, MC 0642263
St. Louis, MO 63166

Abstract

The electromagnetic modeling of large cavities has been an active research topic for several years. Recently, efforts at McDonnell Douglas Aerospace (MDA) have focused on upgrades to the CAVERN (Cavity Electromagnetic Analysis) code. Our approach separates the scattering from jet engine cavities into two principal physical mechanisms. One involves the initialization and propagation of energy down the duct. The other is the scattering from complicated engine face configurations.

An important benefit of this approach is that the exterior moldline or the duct configuration can change, but the engine analysis need not be recomputed. Demonstrably, this is more efficient than using the same technique for the external airframe, for propagation down the duct, and for the engine face. For complex large inlets CAVERN uses the shooting and bouncing ray (SBR) technique to trace rays to an area near the engine face where the geometrical cross section typically becomes uniform and cylindrical in nature. A termination aperture is defined, and the rays across this plane are decomposed into equivalent modes. A Fast Fourier Bessel Transform (FFBT) is incorporated in CAVERN for optimal efficiency for the ray-modal conversion.

A modal reflection coefficient matrix is used to characterize the engine face region and provide outgoing modal functions at the termination aperture. Application of the reciprocity theorem allows computation of the radar cross section using an integral evaluated across this plane without requiring tracking the rays to the physical aperture. For a given frequency, this modal methodology is two times faster than using the standard SBR approach for propagation both into and out of an inlet. The solution with FFBT modal decompositon for conversion of rays into modes is several orders of magnitude faster than direct integration.

More accurate analyses capturing higher order mechanisms can be used when separately characterizing the termination region of the duct at the engine face. The methods of choice in the termination scattering region are exact low frequency methods such as finite element. However, these methods are limited to electrical lengths much smaller than typically required for full sized air vehicles at X-band in terms of storage and computational times. Presently, physical optics/physical theory of diffraction (PO/PTD) is used for the termination matrix, along with plane wave decomposition of the ray optic field in the termination area. This is a cooperative effort with Ohio State University. Conceptually, calculation of a plane wave reflection coefficient matrix is much simpler than the creation of the modal matrix. A physical optics code such as CADDSCAT is used to generate a plane wave matrix for modeling the engine face. This matrix is then converted to a modal matrix and stored for subsequent use in CAVERN when scattering from a specified engine is required. The termination matrix methodology streamlines calculations for large jet engine inlets. This technique has been utilized on a variety of geometries. Future work will examine the range of validity of the PO/PTD solution for the generation of the termination matrix.

I. Introduction

Engine inlets in aircraft are a primary contributor to the radio-frequency signature for certain aspect ranges, and it is imperative to provide not only the most accurate but also the most efficient methods for computing the radar cross section (RCS). It is attractive to separate the exterior and interior scattering for generation of RCS . With this approach, the engine face problem can be analyzed and results accessed separately. Furthermore, more accurate analyses capturing higher order scattering mechanisms are used when separately characterizing the engine region. Figure 1 summarizes the separation of the jet engine scattering problem into three areas of major focus. The first involves physical aperture coupling to external features. This includes multiple bounce and shadowing effects of the external features with respect to the aperture. This could be accomplished with Generalized Ray Expansion (GRE) or SBR. SBR was used for the hybrid termination analysis included here. The second area is the termination aperture, involving modal decomposition or plane wave expansions. The third area is the termination scattering region. The methods of choice here involve exact low frequency methods such as finite element. These methods are not quite ready for complex terminations of 40 wavelength diameter in terms of storage or computational times, and physical optics/ physical theory of diffraction (PO/PTD) can also be used for the termination matrix.

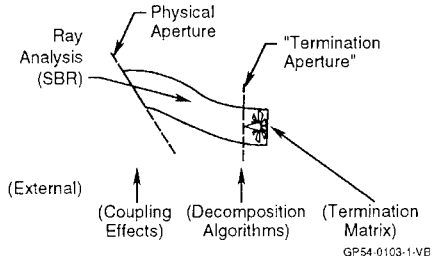


Figure 1. Areas of Major Focus

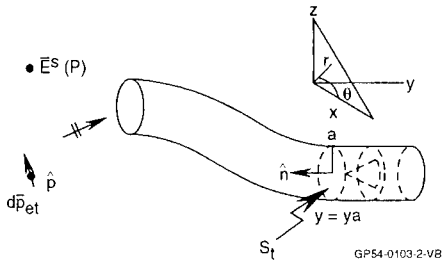


Figure 2. Geometry of the Inlet Scattering Problem

CADDSCAT analysis is used to generate a plane wave termination matrix using PO/PTD for modeling engine face complexity (Section II). This matrix is then converted to a modal termination matrix (Section III), and stored off for usage when scattering from a specified engine must be added to external aircraft effects. Calculations using the new technique are compared with available data for cylindrical cavities terminated with flat plates, hemispherical hubs and curved blade geometries (Section IV).

II. Modal Decomposition and Plane Wave Termination Reflection Matrix

CAVERN uses standard ray analysis combined with a modal analysis near the termination region to calculate RCS. Rays are initiated in the aperture plane and traced to an area near the back of the cavity where the geometrical cross section becomes uniformly cylindrical. The ray representation of the electric field is expanded in terms of the known modal functions. An application of the reciprocity theorem of electromagnetics allows computation of RCS using a reaction integral. (Ref. 1)

Tracking rays both into and out of the cavity is subject to errors associated with the geometrical optics approximation. For realistic sized ducts with length to diameter ratios of >3:1, the validity of standard ray approaches may break down completely. CAVERN's solution to this problem has been the use of both ray and modal analyses with a reflection coefficient matrix representing the engine face. The reciprocity algorithm is used for both efficiency and accuracy so that rays do not have to be traced back to the entrance of the cavity. For a variety of ducts, MDA's CAVERN code provides more fidelity than is possible with other methods.

The unique features of CAVERN, combining the ray and modal solutions and the calculation of RCS in conjunction with the reaction integral based on the reciprocity theorem were discussed in Ref. 2. The termination reflection coefficients matrix can be found with finite element methods under development. (Ref. 3) In this section, we focus on the modal decomposition, as well as plane wave decomposition and PO/PTD termination matrices, which are being pursued cooperatively with OSU (Ref. 4) and are discussed in the next sections.

Figure 2 shows the geometry definitions necessary for an application of the reciprocity theorem. As discussed in Ref. 2, we note that the equations governing the conversion of rays to modes can be compactly formulated. The radial integral can be written as linear combinations of

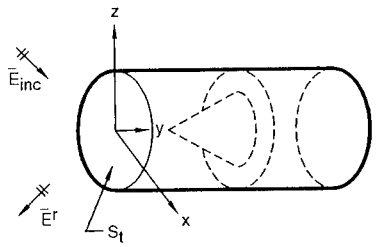
$$F(\theta) = \rho\, g(\rho, \theta) = 2\pi\rho \int_0^\infty rf(r, \theta) J_n(2\pi\rho\, r) dr \qquad (1)$$

where $\rho = p_q/2\pi a$

with p_q equal to the roots of the Bessel function or its derivative, and where $J_n(x)$ is the Bessel function.

Applying the FFBT to this integral , we use the technique discussed in Ref. 5. The non-uniform ray information must be transformed to an exponential grid in order to use the procedures. The FFBT method translates the problem into three simple FFTs, resulting in more than an order of magnitude improvement in runtime. Performing the theta integral first with FFTs provides all the modal information for n at once and is a more efficient way to evaluate the integral of Equation 1. The generation of the grid is not very expensive and the problem is simply reduced to the calculation of many FFTs.

In the plane wave decomposition technique, rays are transformed into discrete plane waves. There are both incoming and outgoing plane waves. These outgoing plane waves are related to the incoming plane waves through a plane wave termination reflection matrix. Figure 3 illustrates the plane wave expansion. The geometry of the engine area from the termination aperture to the back of the blade area is modeled with incident plane waves. The plane wave matrix is generated bistatically. Each incident angle has associated with it an entire spectrum of observation angles. Thus, a plane wave matrix is generated. For large bodies, it is expected that a plane wave matrix generated with PO/PTD will capture essential scattering mechanisms for the termination area. The plane wave termination matrix is easily generated with CADDSCAT, using the equation shown in Figure 4. Here j represents the incident plane wave, i is the reflected plane wave, and a is the radius of the circular area of the termination aperture.

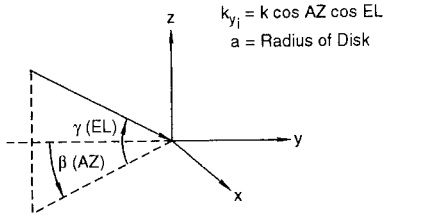


- Define Set of Plane Waves
- Have Each Plane Wave Illuminate Termination

GP54-0103-3-VB

Figure 3. Plane Wave Expansion

$$\Gamma^{PW}_{ij} = \frac{\pi}{j\,2\,k_{y_i}\,a^2} \cdot \left\{ \begin{array}{l} \text{CADDSCAT} \\ \text{Bistatic Scattered Field Results} \end{array} \right\}$$



Coordinate System for Plane Wave Scattering by the Termination.

GP54-0103-4-VB

Figure 4. Generation of Plane Wave Matrix
Equation 51 of Ref 7

To accurately analyze a complex engine face, exact methods are attractive. The authors of Ref. 4 used a modified MDA code (CICERO) utilizing method of moments (MM) for bodies of revolution to calculate a plane wave scattering matrix. This scattering matrix for the termination region is then used with either a modal, SBR, or GRE solution in the front section. Detailed results on these methods are included in Ref 4. Exact methods will work well for rotationally symmetric terminations of diameters less than $\sim 10\lambda$. However, these methods presently remain a computational challenge, and are being investigated at the University of Michigan (Ref. 3), and OSU. In this paper, we are using the method outlined in Refs. 6, 7 for calculating the plane wave termination matrix for an arbitrary engine face with PO/PTD.

An example for a flat plate termination is described below. For the case of a flat disk with the termination aperture coincident with the back plate, we expect the area (A) to be πa^2. Using the PO formula for a flat plate at normal incidence, we have:

$$\sigma = 4\pi \frac{A^2}{\lambda^2} = \frac{4\pi(\pi a^2)^2}{\lambda^2} \tag{2}$$

We know that

$$\sigma = \lim_{r\to\infty} 4\pi r^2 \, (E_{scat}/E_{inc})^2. \tag{3}$$

Combining these two equations, we find:

$$\text{(relative scattered field)} = \lim_{r\to\infty} r\,(E_{scat}/E_{inc}) = \frac{\pi a^2}{\lambda}. \tag{4}$$

Using the equation in Figure 4, we obtain:

$$\left|\Gamma_{ij}^{PW}\right| = \frac{\pi}{2\frac{2\pi}{\lambda}a^2}\left(\frac{\pi a^2}{\lambda}\right) = \frac{\pi}{4} \tag{5}$$

The maximum number of plane waves is determined by the inequality

$$m_q^2 + n_q^2 \le (ka \sin \delta_{max}/\pi)^2 \tag{6}$$

where δ_{max} is the maximum plane wave propagation angle, usually 80°, not to exceed 90° (Ref. 6). In the case of a two λ diameter disk, shown in Figure 5, we obtain nine plane waves (per each polarization) to satisfy the above relationship. The "-π/4" elements are the theoretically derived values, based on a scattered field of $\pi a^2/\lambda$ as discussed above (Equation 4). In Figure 6, we show a section of the matrix calculated by CADDSCAT corresponding to the idealized case. The plane wave angles were generated according to Ref. 7.

Table 1 lists the size of the matrices expected for various engine face radii. The matrices are large, increasing approximately as a^4. The numbers in the table do not reflect a factor of two to account for both vertical and horizontal polarizations. Typically, fighter inlets have a radius of approximately 20 wavelengths at X-band.

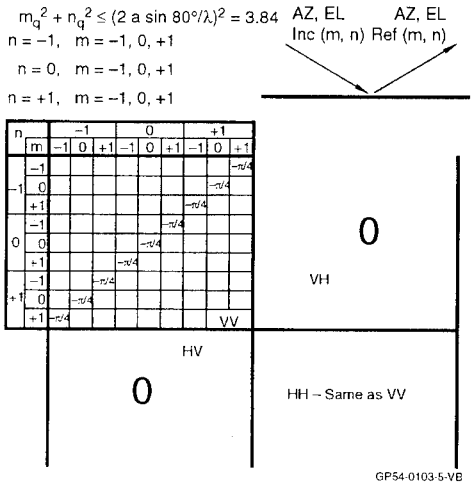


Figure 5. Plane Wave Matrix Example for 2λ Diameter Disk
Flat Plate Termination

Index	AZ, Inc (deg)	EL, Inc (deg)	AZ, Ref (deg)	EL, Ref (deg)	Γ^{PW}
1001	35.26	30.00	35.26	30.00	(Small)
2001	35.26	30.00	0	30.00	(Small)
3001	35.26	30.00	−35.26	30.00	(Small)
4001	35.26	30.00	30.00	0	(Small)
...					
...					
9001	35.26	30.00	−35.26	−30.00	−π/4
...					
...					
...					
1009	−35.26	−30.00	35.26	30.00	−π/4
2009	−35.26	−30.00	0	30.00	(Small)
3009	−35.26	−30.00	−35.26	30.00	(Small)
4009	−35.26	−30.00	30.00	0	(Small)
...					
...					
9009	−35.26	−30.00	−35.26	−30.00	(Small)

GP54-0103-6-VB

Figure 6. Plane Wave Format for 2λ Diameter Disk

TABLE 1. PLANE WAVE TERMINATION MATRIX SIZE

a(λ)	Number of Plane Waves (NPW)
1.0	9
2.5	69
5.0	301
8.3	853

(size of PW matrix) = (NPW) • (NPW)

III. Conversions Between Modes and Plane Waves

In this section, the conversion of plane wave matrices generated by CADDSCAT to modal matrices is discussed. The modal decomposition used in CAVERN subroutines is then interfaced to these matrices. Cooperative work is also ongoing to interface University of Michigan modal matrices directly with CAVERN.

The conversion of plane wave matrices to modal matrices is done using a modification of Ref. 7. This conversion is shown in Figure 7 using the transfer matrices of Ref. 7. Once the plane wave termination matrix (Γ^{PW}) is found, the modal matrix (Γ^{WG}) is calculated by matrix multiplication of the transfer matrices. Matrix [T+] translates coefficients of incident modal functions to coefficients of incident plane wave functions. The "+" refers to plane waves traveling in the +y direction, with incidence toward the complex termination and "-" refers to travel reflected from the complex termination.

Figure 8 shows the necessary process. Conversion between plane wave and modal termination matrices is directly accomplished with the PW2MODI program. With the MDA code structure, generation of the plane wave matrix could be accomplished with bistatic finite element results or test data.

For a simple flat plate disk with a two λ diameter, the plane wave matrix generated with CADDSCAT has dominant terms of $-\pi/4$ and the other terms are small as was shown in Figure 6. When the plane wave matrix is converted to modes with the PW2MODI code, the diagonal terms for the converted modal matrix are close to -1 for the most part, but they may not agree with more exact methods for this small-sized geometry. For the two λ diameter case, these matrices are in close agreement with results from the OSU subroutines discussed in Ref. 7.

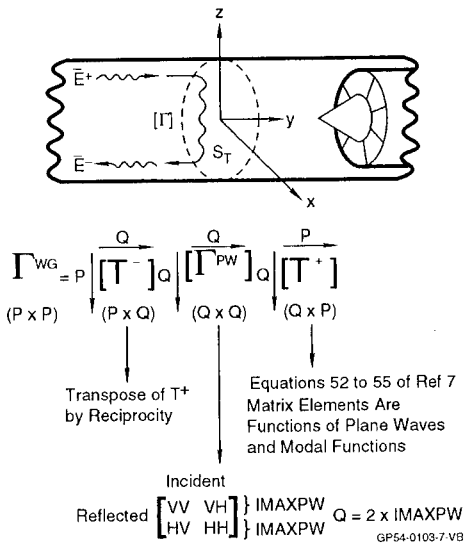


Figure 7. Conversion of Plane Wave to Modal Matrix

P = Maximum Number of Modes, Q = Maximum Number of Plane Waves

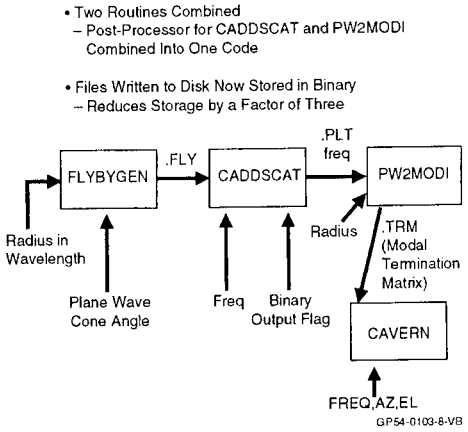


Figure 8. Engine Face Analysis Process

IV. CAVERN Results with Plane Wave Matrices and Modal Conversion

An initial validation case for CAVERN using the new method was for a cylinder with a flat plate termination having the same diameter as the F-15 engine. This 1m by 3m cylinder was analyzed at 3.0 GHz (equivalent to a 10 wavelength diameter). CADDSCAT PO was used to generate the plane wave matrix for the termination aperture plane, which coincided with the cavity back plate. PW2MODI was used to convert the plane wave matrix to a modal matrix, needed as input to CAVERN. We obtained very close agreement between CAVERN's CWTERM results (using -1's along the diagonal) and the new plane wave expansion/ modal conversion method.

Realistic geometries do not allow us to have the termination plane at the back plate. To validate the methods being used, we performed a comparison of our results with those of OSU. This comparison is shown in Figure 9 for a termination aperture placed 10" in front of the back plate. In the OSU results, SBR is used in the first section of the duct. The plane wave expansion is used to couple the duct to the termination, and the plane wave termination matrix was calculated using an SBR approach. The termination section is 10" in length as shown. In the CAVERN plot, SBR is used in the duct section and a plane wave termination was calculated using an SBR approach. PW2MODI was used to calculate a modal termination matrix which was then read into CAVERN. This plot provides a comparison of the RCS and allows us to evaluate the usage of the modal and plane wave decomposition techniques. The results are relatively insensitive to the placement of the termination aperture.

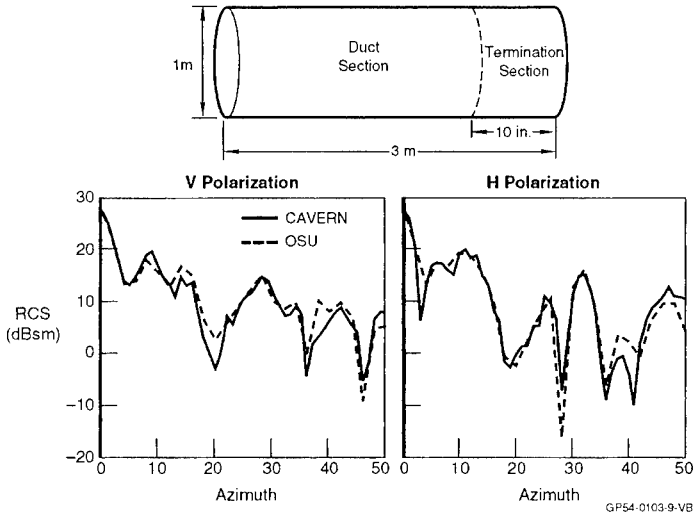


Figure 9. Comparison Between CAVERN and OSU Results for 10 Inch Section of Termination
Frequency = 3 GHz, Elevation = 0°

CAVERN results using the SBR/modes/SBR method are shown in Figure 10 for a duct with a hemispherical hub termination. Comparison results from OSU are shown labeled "modcic" and "sbrcic" in Figure 10. In the OSU result ("modcic"), an exact modal solution is used in the 2m duct section and the MDA MM code CICERO for the 0.5m termination region. (Ref. 4) In the OSU result ("sbrcic"), the 2m duct section is analyzed with SBR. Clearly, the results differ based on whether approximate ray or exact modal solutions are used in the front duct section. The SBR/plane wave/MM result (labelled sbrcic) is in fairly good agreement with the CAVERN result and is consistent with the level of agreement for OSU results using SBR/plane waves/MM and SBR/plane waves/SBR for flat plate 1m diameter by 2.5m length cylinders at 2.4 GHz. (Ref. 4)

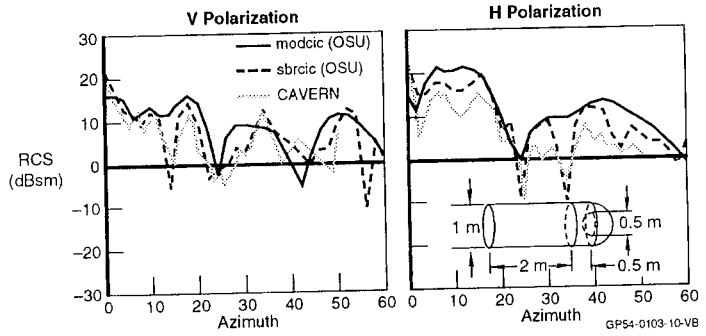


Figure 10. Co-Polarized RCS Patterns
Frequency = 2.4 GHz, Elevation = 0°

Results for the twisted blade configurations, similar to that shown in Figure 11, are being generated with University of Michigan's limited mode matching, transmission line, and finite element methods for a variety of frequencies. The modal matrix for the geometry of Figure 11 has been found using the methods outlined in the previous sections for the plane wave matrix and for conversion to a modal termination matrix for CAVERN for an outer diameter of 10 wavelengths. The included surfaces are the blade sections with the hub and also the cylindrical duct illustrated in Figure 11. The hub radius is 2.5λ. There are 17 twisted blades that are each 4° wide. The blades are terminated directly in a short. The CAVERN RCS for this case is shown in Figure 11. It will be compared to finite element results when available from the University of Michigan and OSU.

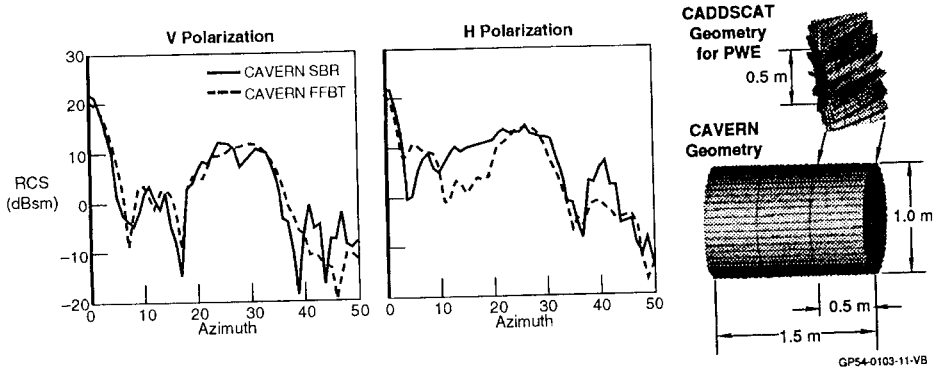


Figure 11. RCS Results
Frequency = 3 GHz, Elevation = 0°, 5λ Radius

V. Summary Discussion

The major thrusts of this effort are summarized below:

1. Fast Fourier Bessel Transform (FFBT) Techniques for the modal decomposition algorithm were incorporated into CAVERN

2. generation of the plane wave termination matrix using the PO/PTD approach of CADDSCAT has been accomplished,

3. codes to convert the plane wave matrix to a modal termination matrix were written, and

4. use of SBR for duct propagation, coupled with modal decomposition, and plane wave termination matrix generation has been compared to available data for both flat plate and complex hub/blade terminations.

VI. Acknowledgements

The authors thank Drs. Burkholder and Pathak of Ohio State University for many discussions and personal communications which made this work possible. We thank Drs. Louis Medgyesi-Mitschang and Ronald Pearlman of McDonnell Douglas Aerospace (MDA) in providing valuable insightful discussions. Interchanges with Major Dennis Andersh, Dr. Kueichien Hill, and Lt. Russ Burleson of Air Force Wright Laboratory, Dr. Cullen Lee of Sandia National Laboratories, Dr. Andy Lee of Demaco, Dr. John Volakis, Dan Ross, and Hristos Anastassiu of the University of Michigan, Dr. Rob Lee of Ohio State University, and Dr. Gary Thiele and Dan Reuster of the University of Dayton have also been enlightening.

References

[1] P. H. Pathak and R. J. Burkholder, "A Reciprocity Formulation for Calculating EM Scattering by an Obstacle within an Open-Ended Waveguide Cavity," IEEE Trans. Microwave Theory and Techniques, Vol. 41, No. 4, April 1993.

[2] J. L. Karty and S. D. Alspach, "Electromagnetic Modeling of Jet Engine Cavities with the CAVERN Code," ACES Meeting, March 1993.

[3] P. Ross, J. L. Volakis and T. Ozdemir, "A New Finite Element Formulation for Modeling Circular Inlets with Irregular Termination," University of Michigan Radiation Laboratory Report, May 1993.

[4] P. R. Rousseau, R. J. Burkholder, C. W. Chuang, R. C. Chou, and P. H. Pathak, "Computing the EM scattering from a Bifurcated Jet Inlet Cavity with a Body-of-Revolution Termination," Ohio State University, ElectroScience Lab Report, March 1993.

[5] A. E. Siegman, "Quasi Fast Hankel Transform," Optics Letters, Vol. 1, No. 1, pp.13-15, July 1977.

[6] P. R. Rousseau, P. M. Pathak, R. J. Burkholder and C. W. Chuang, "A study of Electromagnetic Scattering by Obstacles Placed within Open Cavities," Ohio State University, ElectroScience Lab Report, Sept. 1992.

[7] R. J. Burkholder and P. R. Rousseau, "Conventions for Modal and Plane Wave Basis Expansions for Characterizing the Reflection from a Complex Waveguide Termination," Ohio State University, Personal Communication, Jan. 1994.

Scattering from Dielectric Loaded Cavities Using Shooting and Bouncing Rays

M. C. Christensen and S. W. Lee
University of Illinois at Urbana-Champaign

D. J. Andersh
Wright Lab WPAFB OH

1. Abstract

Shooting and Bouncing Rays (SBR) is a high-frequency technique for attacking complex 3-D scattering problems. It has been implemented in a general-purpose radar signature computer code 'Xpatch' and the code is widely used in the RCS community [1-2]. SBR so far has been applied to scatterers made of conductor or conductor coated with thin material. In this paper, we extend SBR to bulk material, and present several test cases involving cavities loaded with bulk dielectric. Our SBR results generally are in good agreement with the exact solution calculated by method of moments (MoM).

2. Introduction

A difficult problem in performing electromagnetic scattering computations is predicting the scattering from electrically large, realistic objects with bulk materials. Low-frequency methods, such as MoM, Finite Element Method, and Finite Difference Time Domain, are well suited for handling problems involving materials, but are often limited by electrically large geometries. This is due to the large number of unknowns needed to accurately represent the problem. High-frequency methods, such as SBR, Geometrical Theory of Diffraction, and Physical Theory of Diffraction, are good for predicting the scattering from these geometries, but generally do not deal with bulk materials as well. A method for doing high-frequency calculations for a general geometry containing bulk materials and using SBR is presented in this paper.

3. Formulation

The method used by Xpatch to compute the scattered far-fields from a target consists of three steps: (1) Calculating the scattered far-fields for the first bounce response over the lit surfaces using physical optics (PO); (2) shooting a grid of parallel rays representing a plane wave towards the target, tracing each ray through the target, then performing a PO type integration at the ray's last hitpoint; and (3) adding the first-order edge-diffraction from all conducting edges. Our proposed method for using bulk materials expands on step (2) above.

At each ray hitpoint on a bulk material, Snell's Law is used to compute both the reflected and transmitted ray directions, and a new ray is spawned in that transmitted direction. The complex fields for each ray are computed using the incident fields and the Fresnel reflection and transmission coefficients for the given interface. These rays are then traced until the ray either exits

the target, or reaches a predetermined number of bounces. For those rays that do exit the target, a PO type integration is performed at that ray's last hitpoint to determine the backscattered far-fields.

This proposed method is versatile, because it can in theory handle geometries containing bulk materials, conducting surfaces, and thin material surfaces at the same time. Preliminary results indicate that the method works better for lossless cases than for lossy cases, due to the fact that the direction of constant phase in a lossy material is different from the direction of the energy flow.

4. Results

We have implemented the SBR bulk material method in Xpatch. We will now present a comparison of results using Xpatch and a 2-D MoM code [3] for some simple geometries. Since Xpatch is a 3-D code, the conversion

$$\mathrm{RCS}_{\mathrm{dBsm}} = \mathrm{REW}_{\mathrm{dBm}} + 10\log\frac{2l^2}{\lambda}$$

is used to convert from 2-D Radar Echo Width results to 3-D Radar Cross Section results. In the above, l represents the length of the object in the z-direction and λ is the wavelength in meters. All geometries used with Xpatch can then be created uniform in z, and the problem becomes 2-dimensional, with the backscattering only computed over an azimuthal sweep. In all cases, the E-field vector points out of the page.

4.1 Bulk Cube

The first geometry tested is a simple square cube of bulk material, using varying dielectric constants. The dimensions are 6.67λ on a side, and the backscattered fields are computed from 0 to 90 degrees due to symmetry. For this case, the bulk material used has a relative permittivity of 2.0 - j1.0 and a relative permeability of 1.0 + j0.0. The plot comparing the MoM results with the SBR results is shown in Figure 1.

4.2 Bulk Cube with Conducting Sides

The next set of geometries deal with the backscattering from lossless bulk materials with conducting walls. This represents a more general problem, incorporating both bulk materials and conductors. The first case is that of a lossless material with a dielectric constant of 9.0 + j0.0 and one conducting side, and the results comparing the MoM solution with that of the SBR are shown in Figure 2.

The next case is similar to the above, except that now we use conductor on two sides of the material, and a different dielectric. For this case, an azimuthal sweep from 0 to 360 degrees is performed, using a material with a relative permittivity of 4.0 + j0.0. The results are shown in Figure 3.

A case with three conducting sides is next, using a bulk dielectric with a relative permittivity of 2.0 + j0.0. The results of an azimuthal sweep from 0 to 360 degrees are shown in Figure 4.

In all three cases, good agreement is shown between the MoM and the SBR results for most points. This is encouraging, showing that the method is able to handle different lossless dielectrics and conducting surfaces simultaneously.

4.3 Bulk Material Inside a Cavity

The next step is to verify that the proposed method can work for a more complicated geometry, that of a cavity with a smaller bulk cube inside it. For this case, we use a 10λ x 10λ cavity loaded with a diagonally placed 2.36λ dielectric cube, centered within the cavity. The relative permittivity of the material is 2.0 + j0.0. This represents a significant difference in the geometry, due to the fact that there are now air gaps between the conductor and the bulk material, and direct interactions between rays entering, leaving, and re-entering the bulk material are present. Again we find good comparison between the MoM results and the Xpatch predicted results, as shown in Figure 5.

4.4 Bulk Loaded Jet Engine

For this case, range profiles are computed for two different aircraft inlet structures. The first is a jet engine inlet made of only conducting surfaces. The second is the same jet engine inlet, except that a large dielectric block has been placed inside the inlet near the engine blades. A side-view of the proposed geometry is shown in Figures 6 and 7. It should be noted that this is done for illustrative purposes only -- this would, of course, not be done in practice. The two range profiles are then compared in Figure 8, where the effects of the bulk dielectric material can be seen.

5. Conclusions

In this paper, we have demonstrated that SBR works well for some simple geometries involving bulk material. It remains to verify that similar accuracy can be obtained for more general 2-D and 3-D cases.

6. References

[1] S. W. Lee, D. J. Andersh, D. D. Reeves, S. K. Jeng, H. Ling, Y. Chu, D. P. Sullivan, C. L. Yu, "User Manual for Xpatch", DEMACO, Inc., 1993.

[2] D. J. Andersh, M. Hazlett, S. W. Lee, D. D. Reeves, D. P. Sullivan, and Y. Chu, "XPATCH: A high-frequency electromagnetic-scattering prediction code and environment for complex three-dimensional objects," *IEEE Antennas and Propagation Magazine*, Vol. 36, No. 1, Feb. 1994.

[3] S. K. Jeng and S. W. Lee, "McMoM2D - 2.0 User's Manual", DEMACO, Inc., July 1991.

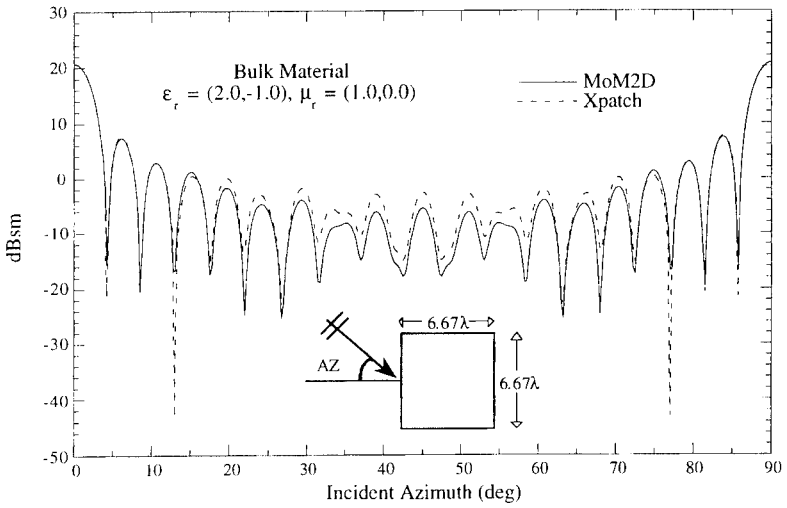


Figure 1. Scattering from a bulk material cube with ε_r = (2.0,-1.0), μ_r = (1.0,0.0). The E-field is directed out of the page.

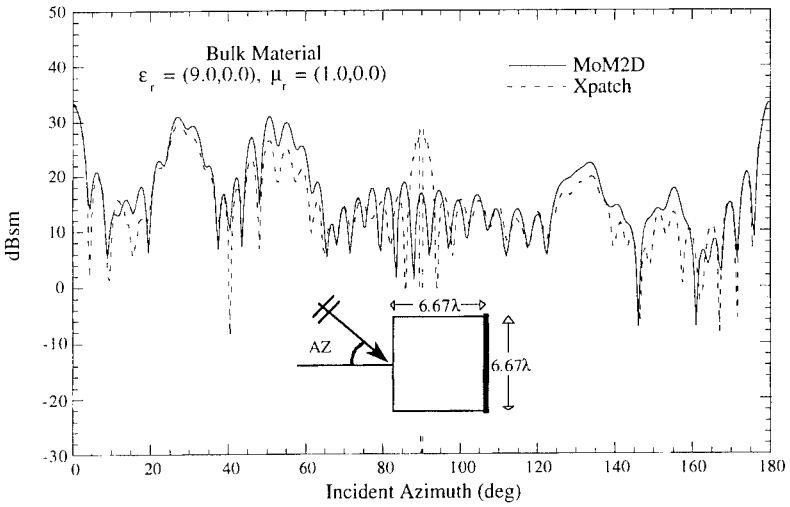


Figure 2. Scattering from a bulk cube with ε_r = (9.0,0.0), μ_r = (1.0,0.0) and conductor on one side. The E-field is directed out of the page.

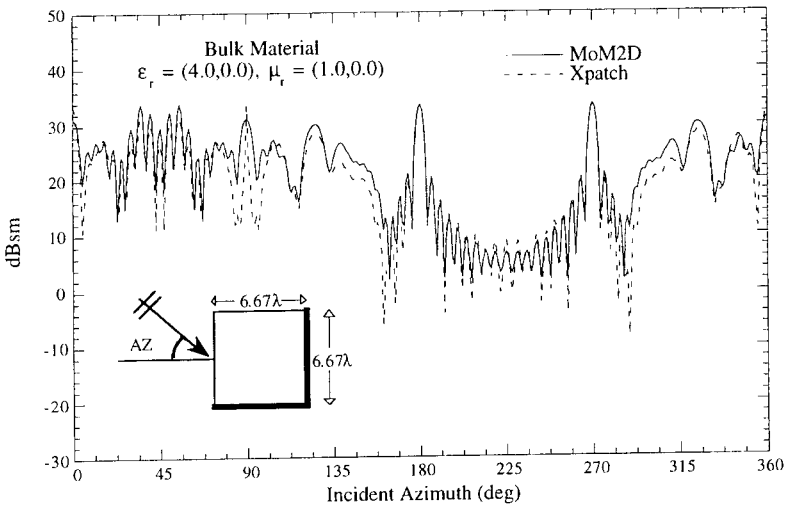


Figure 3. Scattering from a bulk cube with ε_r = (4.0,0.0), μ_r = (1.0,0.0) and conductor on two sides. The E-field is directed out of the page.

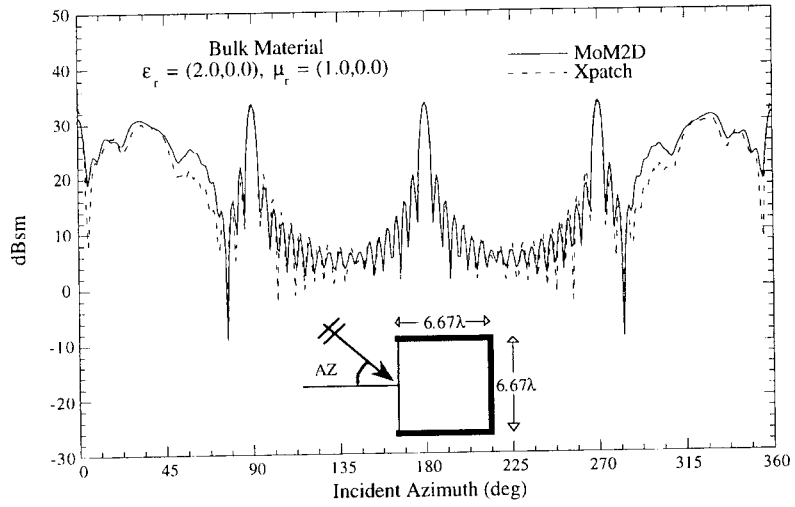


Figure 4. Scattering from a bulk cube with ε_r = (2.0,0.0), μ_r = (1.0,0.0) and conductor on three sides. The E-field is directed out of the page.

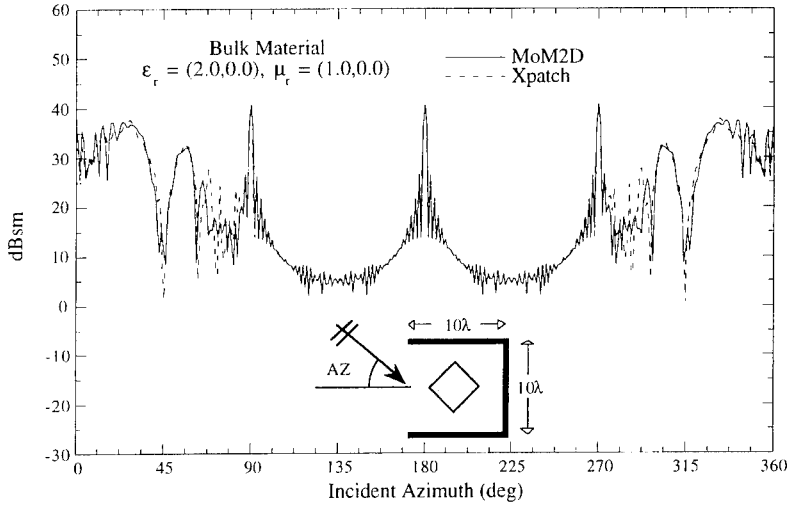


Figure 5. Scattering from a 2.36λ bulk cube inside a 10λ x 10λ conducting cavity. The bulk material has ε_r = (2.0,0.0), μ_r = (1.0,0.0). The E-field is directed out of the page.

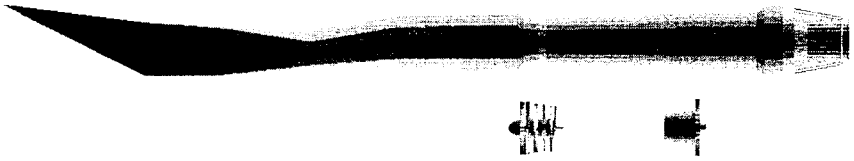


Figure 6: View of the complete jet inlet from Azimuth = -90°, Elevation = 0°. Both objects are to the same scale, and show the relative position of the blades and hubs inside the inlet.

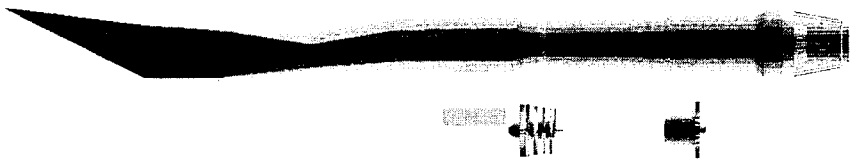


Figure 7: View of the same jet inlet from Azimuth = -90°, Elevation = 0°. The position of the bulk material is shown in the lower figure.

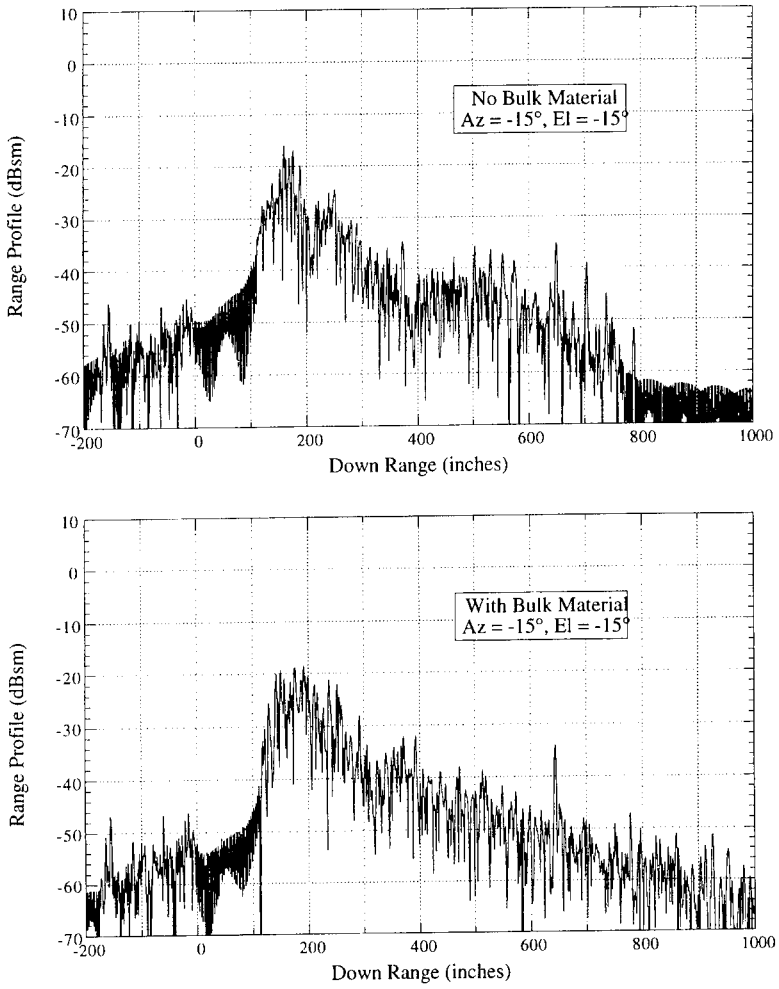


Figure 8. Range profiles for the two inlets, using only those rays entering the inlet mouth. The top figure shows a range profile for the empty inlet, and the bottom figure shows the range profile for the loaded inlet. The differences between the two can be seen in both magnitude and in the late-time response.

XPATCH SIMULATION OF LARGE INLET STRUCTURES

Rajan Bhalla and Hao Ling

Department of Electrical and Computer Engineering
The University of Texas at Austin
Austin, TX 78712-1084

1. INTRODUCTION

Xpatch is a general-purpose high-frequency radar signature prediction code based on the shooting and bouncing ray (SBR) technique [1]-[3]. In this work, we present the signature simulation results for large inlet structures using *Xpatch*. First, the accuracy of *Xpatch* is demonstrated through comparisons with the modal approach for canonical duct configurations. It is shown that the accuracy of *Xpatch* for typical engine intake structures (with 1 m opening and 8 m depth) remains valid from X-band down into the S-band regime. In addition, a fast scheme for generating the 2-D ISAR (inverse synthetic aperture radar) imageries of targets is described. This is achieved by deriving a closed form image-domain ray spread function and carrying out the image update using the fast ray summation scheme of Sullivan [4]. The utilization of the fast scheme reduces the signature prediction time to only the geometrical ray tracing time. Finally, we present the simulation methodology and prediction results for inlet structures containing rotating compressor blades based on *Xpatch* simulation. The jet engine modulation (JEM) phenomenon can be clearly identified in both the Doppler spectrum and ISAR imagery.

2. XPATCH1 AND XPATCH3

In the *Xpatch* package, there are two separate codes for radar signature computation, namely, *Xpatch1* and *Xpatch3*. Both codes contain the same ray tracer. However, the field calculations are carried out in the frequency domain in *Xpatch1* and in the time domain in *Xpatch3*. Below we describe an approximate but extremely fast method of generating the ISAR imageries of targets in *Xpatch3* that we have implemented recently. Contrary to the *Xpatch1* approach where the ISAR image is obtained by inverse Fourier transforming the predicted scattered field data over frequency and aspect, *Xpatch3* uses an image domain SBR formulation. We shall represent the *Xpatch1* ISAR image by the expression:

$$\text{Image}(x,z) = \text{F.T.}^{-1}\{ \sum_{i \text{ rays}} \mathbf{E}_i^s(\omega,\theta) \} \qquad (1)$$

where the quantity in the parentheses is the total scattered field at frequency ω and aspect θ and is obtained through the summation over all exit rays. The x and z variables represent respectively the cross range and down range coordinates. By interchanging the order of the inverse Fourier transform and the ray summation, this term can be determined in closed form under the small angle approximation [5], and the resulting image is explicitly expressed as:

$$\text{Image}(x,z) = \sum_{i \text{ rays}} \alpha_i \; h(x - x_i , z - z_i) \qquad (2)$$

where

$$h(x,z) = e^{-2\,jk_0 z}\ \mathrm{sinc}(\Delta k\, z)\ \mathrm{sinc}(k_0 \Delta\theta\, x)$$

is the "ray spread function," Δk and $\Delta\theta$ are the bandwidth and angular widths associated with the image.

To speed up the computation of the ray sum, a scheme proposed by T. D. Sullivan [4] can be utilized. The application of the fast scheme is based on the observation that we can recast (2) into a convolution between a weighted impulse train and the ray spread function:

$$\mathrm{Image}(x,z) = \Big[\sum_{i\ \mathrm{rays}} \alpha_i\, \delta(x - x_i)\, \delta(z - z_i) \Big] * h(x, z) \qquad (3)$$

Rather than performing the direct convolution, we take advantage of the FFT algorithm. The problem associated with taking the FFT of the weighted impulses which do not occur on a uniformly sampled grid is overcome by using an interpolation scheme [6]. The table below compares the breakdown of the computation time for ISAR image formation for a full-size aircraft at X-band using direct convolution and the Sullivan scheme. The timing is done on a Silicon Graphics Indigo R4000 workstation. The time to perform the convolution using the Sullivan scheme takes 1 min. as compared to 3.2 hrs. by direct convolution, a speed gain of a factor of 180. It is evident that the total image simulation time of 40 min. is just the ray-trace time. The time spent on the Sullivan scheme is essentially zero.

	Total Computation	Ray Tracing Time	Ray Summation
Direct Convolution	3.9 hrs.	40 min.	3.2 hrs.
Sullivan Scheme	41 min.	40 min.	1 min.

3. XPATCH VALIDATION FOR INLETS

Figs. 1-3 show the comparison of the ISAR imageries generated at various frequencies using *Xpatch1* and *Xpatch3* versus a benchmark modal result for an open-ended rectangular duct of dimensions 1 m x 1 m x 8 m. The angular span used to generate the modal and the *Xpatch1* data is ±3° about the central angle. The bandwidth used is 10% of the center frequency. The images under column (a) are for normal incidence and those under column (b) are for 45° incidence. From Fig. 1, we observe that the modal and the *Xpatch1* results are almost indistinguishable at 10 GHz (duct opening of 33.3 λ). The *Xpatch3* result adequately predicts the location of the termination contribution, but shows less spread in the ISAR plan. This is because the termination contribution is due to highly multiple bounce returns. Since *Xpatch3* uses the ray trace information at only one central angle, the actual ray path fluctuations at near-by angles is not predicted. Figs. 2 and 3 show the same set of comparisons at 5 GHz and 2 GHz, respectively. We observe that even at 2 GHz, where the duct opening is only 6.7 λ, the location of the return is still well predicted by *Xpatch*. The amplitude of the *Xpatch* return does, however, show more discrepancy in comparison to the modal benchmark at lower frequencies. Fig. 4 shows the ISAR images for a full-size airplane simulated using *Xpatch1* and *Xpatch3* at 10 GHz with a bandwidth of 1 GHz. The look angle is 30° from nose-on. The *Xpatch1* image is generated using an aspect sweep of ±3°. In addition to the obvious point scatterers on the target, we notice a large cloud in the image which is due to the returns from the left inlet duct. This identification is quite obvious if one refers back to the earlier examples on the canonical duct. The comparison between the *Xpatch1* image and *Xpatch3* image is good.

4. JET ENGINE MODULATION SIMULATION

Finally, dynamic ISAR simulation when moving parts such as rotating engine blades exist in the duct is presented. In range-Doppler imaging the Doppler frequency shifts from different parts of the target are linearly related to the cross-range location of the scatterers on the target. When moving engine blades are present, additional Doppler shifts are produced which strongly affect the ISAR image. This phenomenon is of particular importance since it can be exploited as an identification feature and, therefore, its effect on the ISAR imagery must be fully understood. Simulated ISAR imagery of an open-ended duct with rotating rotor blades is shown in Fig. 5. The dynamic simulation of the ISAR image was done by calculating the multi-frequency scattered field data at different time snapshots on the target with both the fan and the target rotating. The Doppler modulation caused by the moving part is clearly evident in the ISAR image. The periodic motion of the fan blades gives rise to harmonics in the Doppler spectra with a fundamental frequency f_p = (fan spin rate) x (# of blades) [7].

ACKNOWLEDGEMENT

This work was supported by NASA Grant NCC3-1589 and in part by the Joint Services Electronics Program under Contract No. AFOSR F49620-92-C-0027.

REFERENCES

[1] H. Ling, R. Chou and S. W. Lee, "Shooting and bouncing rays: calculating the RCS of an arbitrary shaped cavity," *IEEE Trans. Antennas Propagat.*, vol. AP-37, pp. 194-205, Feb. 1989.

[2] J. Baldauf, S. W. Lee, L. Lin, S. K. Jeng, S. M. Scarborough and C. L. Yu, "High frequency scattering from trihedral corner reflectors and other benchmark targets: SBR versus experiment," *IEEE Trans. Antennas Propagat.*, vol. AP-39, pp. 1345-1351, Sept. 1991.

[3] D. J. Andersh, M. Hazlett, S. W. Lee, D. D. Reeves, D. P. Sullivan and Y. Chu, "*Xpatch.* A high frequency electromagnetic-scattering prediction code and environment for complex three-dimensional objects," *IEEE Antennas Propagat. Mag.*, vol. 6, pp. 65-69, Feb. 1994.

[4] T. D. Sullivan, "A technique of convolving unequally spaced samples using fast Fourier transforms," Sandia National Laboratories, SAND89-0077, Jan. 1990.

[5] R. Bhalla and H. Ling, "Image-domain ray-tube integration formula for the shooting and bouncing ray technique," Tech. Rept., Univ. of Texas, April 1993. Also submitted for publication in *Radio Science*.

[6] R. Bhalla and H. Ling, "A fast algorithm for signature prediction and image formation using the shooting and bouncing ray technique," Tech. Rept., Univ. of Texas, January 1994. Also accepted for publication in *IEEE Trans. Antennas Propagat.*

[7] R. Bhalla, H. Ling, S. W. Lee and D. J. Andersh, "Dynamic simulation of Doppler spectra of targets with rotating parts," *Microwave Optical Tech. Lett.*, vol. 7, pp. 840-842, December 1994.

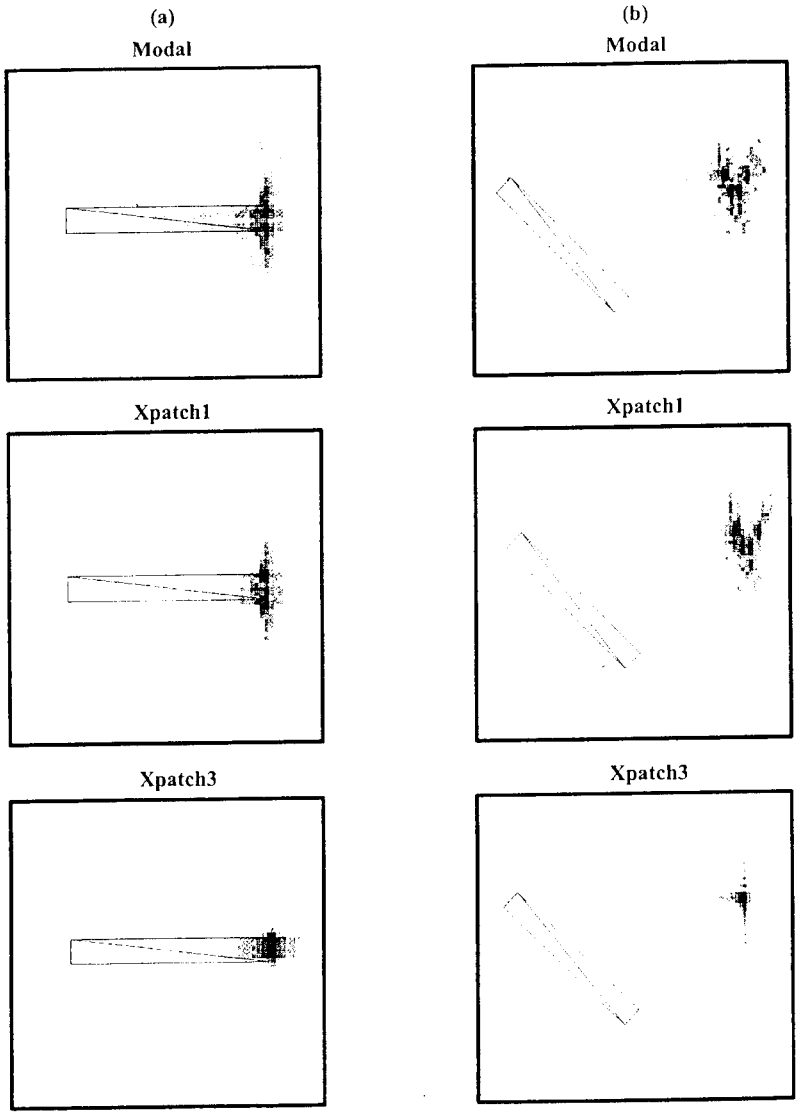


Fig. 1. Comparison between ISAR images generated using modal, Xpatch1 and Xpatch3 for (a) Normal incidence, (b) 45° incidence at center frequency of 10 GHz.

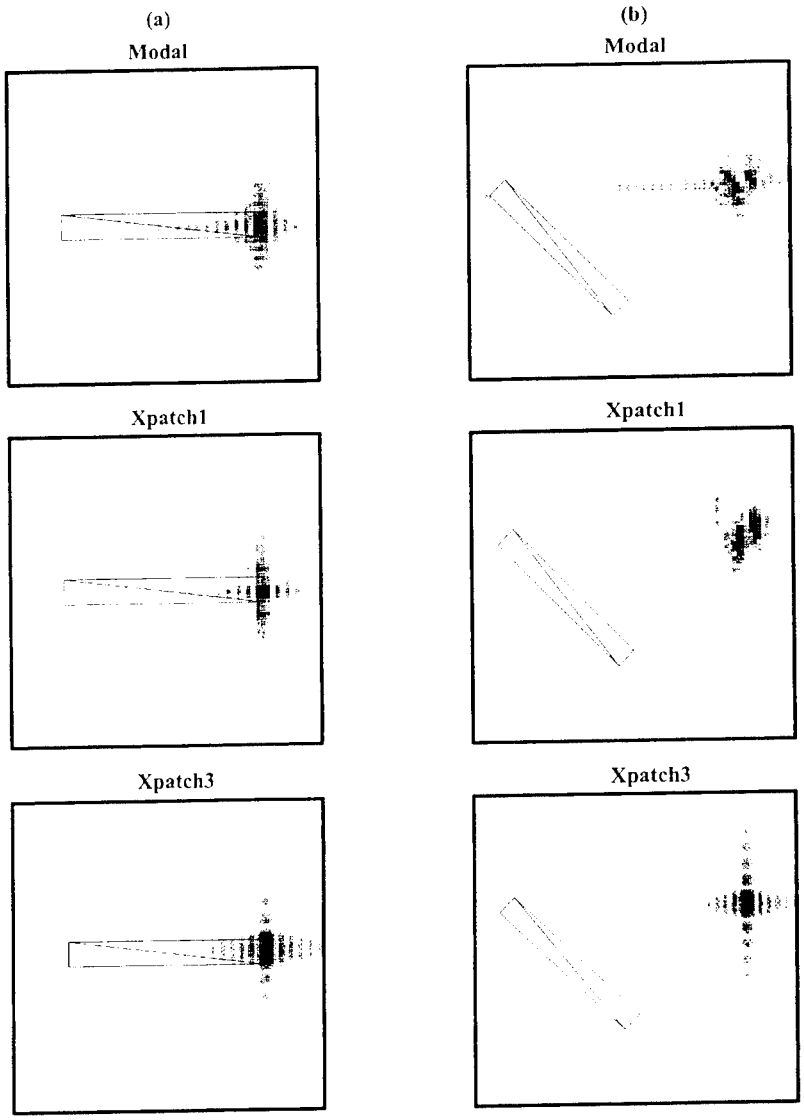


Fig. 2. Comparison between ISAR images generated using modal, Xpatch1 and Xpatch3 for (a) Normal incidence, (b) 45° incidence at center frequency of 5 GHz.

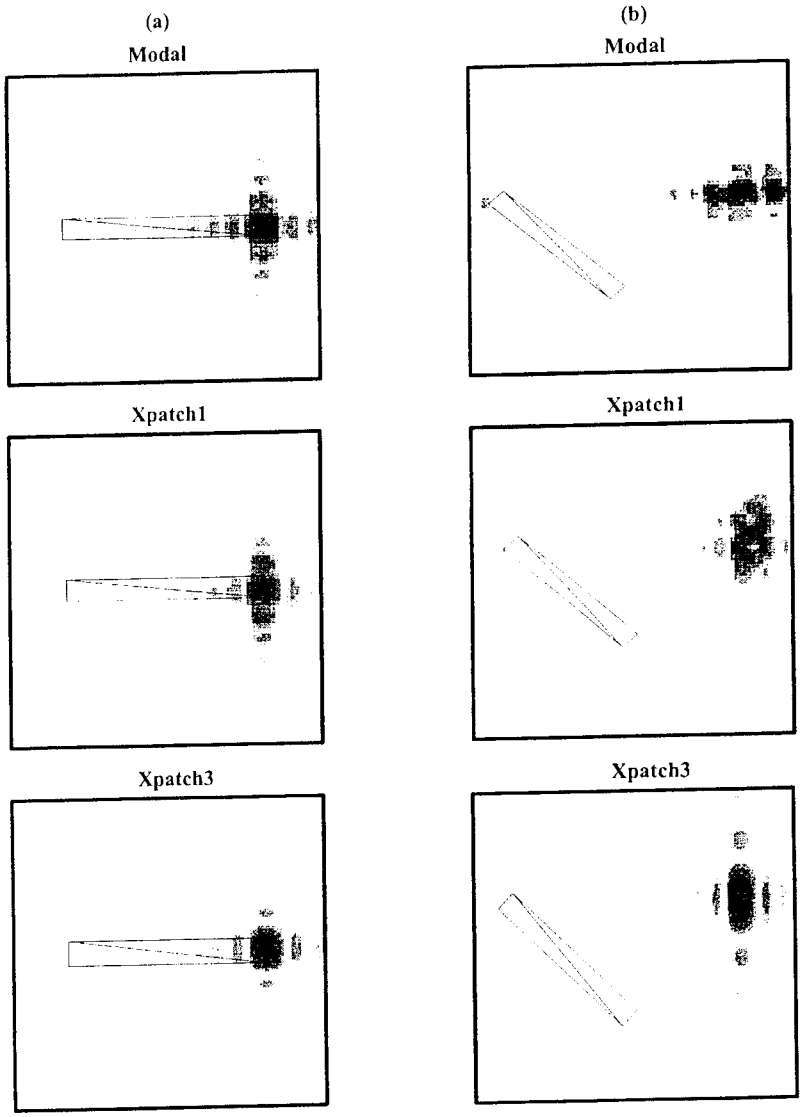
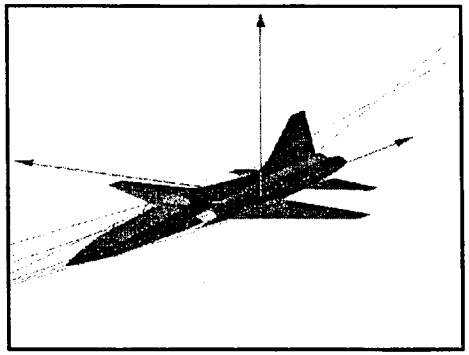
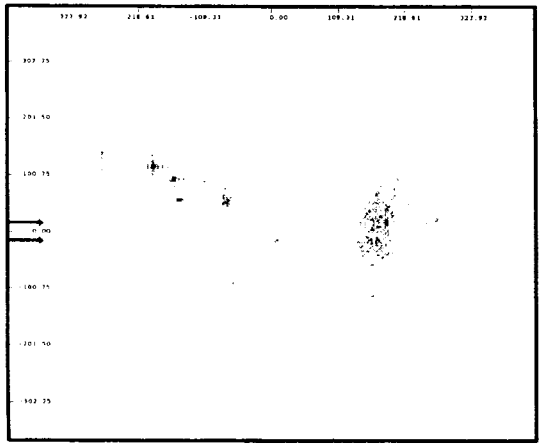


Fig. 3. Comparison between ISAR images generated using modal, Xpatch1 and Xpatch3 for (a) Normal incidence, (b) 45° incidence at center frequency of 2 GHz.

(a) Model aircraft



(b) Xpatch1



(c) Xpatch3

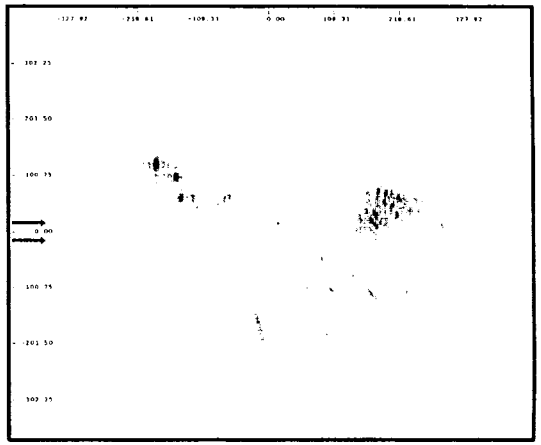


Fig. 4. ISAR image comparison between Xpatch1 and Xpatch3 for a model aircraft.

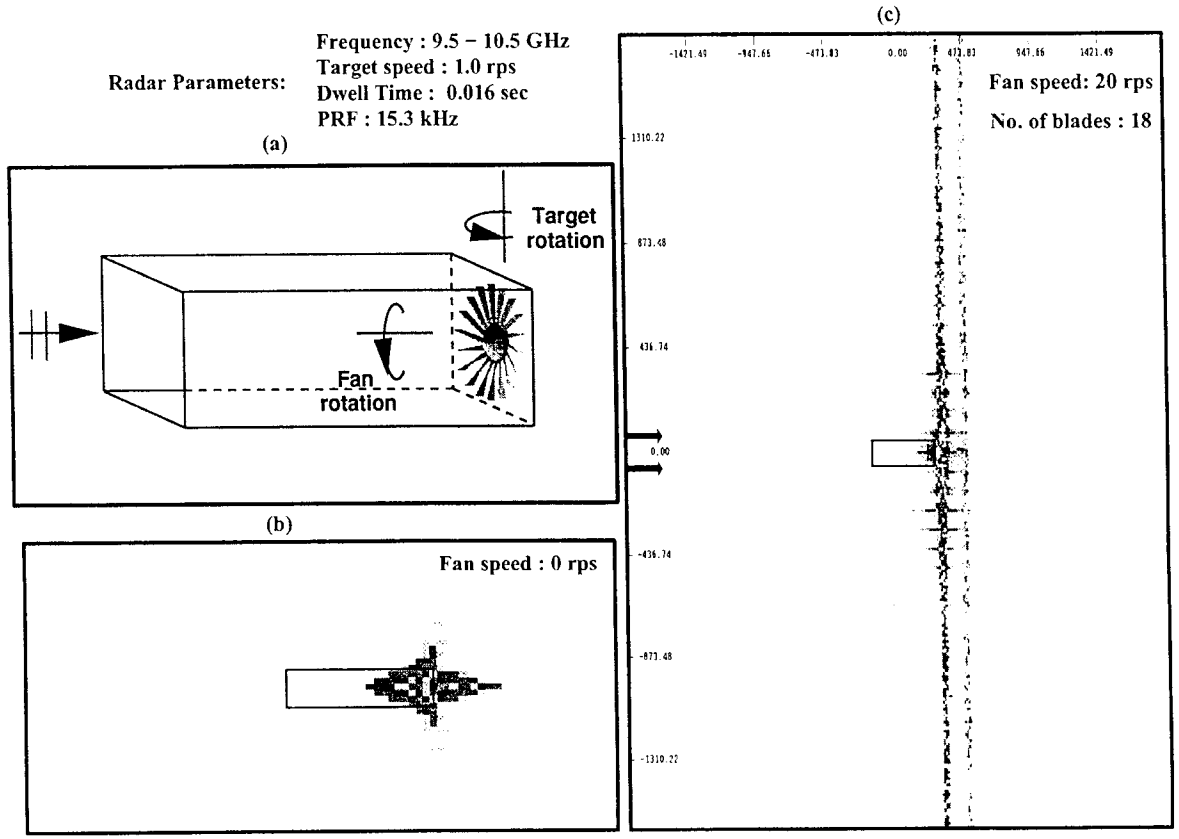


Fig. 5. Simulated ISAR imagery of an open–ended duct with rotating rotor blades. (a) Target geometry (b) ISAR image with fan stationary, (c) ISAR image with fan rotating at 20 rps.

AN ITERATIVE PHYSICAL OPTICS APPROACH FOR THE EM ANALYSIS OF CAVITIES AND OTHER MULTI-BOUNCE GEOMETRIES*[1]

Robert J. Burkholder
The Ohio State University ElectroScience Laboratory
1320 Kinnear Road, Columbus, Ohio 43212

Abstract—The iterative physical optics method has been shown to be very useful in the analysis of electromagnetic coupling and propagation in electrically large and smoothly varying ducts such as jet inlet cavities. In this approach the incident field excites the first order physical optics (PO) currents on the walls of the cavity, which are then allowed to re-radiate a finite number of times to account for multiple reflections. Each re-radiation, or iteration, essentially provides the next higher order interaction. Convergence is very rapid once all the important higher order multi-bounce effects have been included. The same method may be applied to external radiation and scattering problems where multiple reflections and diffractions are important; the iterations provide multiple reflections and diffractions, to within the accuracy of PO, without ray tracing. Numerical results are presented to demonstrate the accuracy and convergence of the method for 2-D and 3-D cavity and exterior multi-bounce problems.

1 Introduction

The analysis of electromagnetic (EM) penetration and propagation in electrically large cavities is important for predicting the scattering by jet inlets and exhausts, and for studying the EM field distributions inside microwave reverberation chambers. A variety of high-frequency asymptotic methods have been developed and applied to this problem [1-3]. In the hybrid modal method [1], the cavity is modeled with sections of uniform waveguides and the natural waveguide modes are used to describe the interior fields. This limits the method to canonical shapes, and materials and geometric perturbations are difficult to incorporate. However, it yields very accurate results and is often used to provide reference solutions for approximate methods which are more versatile. The shooting and bouncing ray (SBR) method [2] and the generalized ray expansion (GRE) [3] find the fields inside cavities by launching a dense grid of ray-tubes from a source (or sources) and tracking each ray-tube through multiple reflections from the inner cavity walls. These methods can handle much more arbitrary geometries with material coated walls, but have limited accuracy and may require a very large number of rays to be tracked. Furthermore, parameters associated with the ray launching, such as the ray-tube density and the discretization of sources, and the means of obtaining volumetric fields from discrete ray-tubes is generally not robustly defined.

The iterative physical optics (IPO) method has recently been applied to analyze the scattering by large open-ended cavities [4]. In this method, physical optics (PO) currents [5] excited

[1]*Sponsored by the Air Force Wright Laboratory Target Recognition Technology Branch, Wright-Patterson AFB, OH.

by an incident source distribution replace the inner walls of the cavity. The PO currents then re-radiate iteratively to excite higher-order PO currents which account for the multiple reflections inside the cavity – each iteration adds one more internal reflection. The method is very robust because it only involves the integration of equivalent surface currents existing over the walls and apertures. Material coated or impedance surfaces may be approximately modeled via an equivalent surface impedance.

The IPO method may be formulated as an iterative solution to the magnetic field integral equation (MFIE), but with some additional rules regarding shadowing effects associated with the high-frequency approximations of PO. The simple rules avoid the the problem of finding shadow boundaries because shadowing effects will automatically be included in the iteration process. They also make the iterative solution of the MFIE very rapidly convergent (to within the PO approximation) and resonances are avoided because the surface is usually not closed. The IPO method is much more efficient than an exact iterative solution to an integral equation because the number of iterations is related to the number of high-frequency interactions of importance (i.e., reflection, diffraction, and reflection-diffraction mechanisms), and does not depend on the minimization of a residual error. It is also more efficient than an exact integral equation solution because the discretization density may be only 4 to 16 samples per square wavelength instead of the usual 64 to 100.

The IPO method may also be applied to other multi-bounce problems, such as the propagation of communications signals in and around buildings in an urban environment. Each iteration adds another higher order reflection, diffraction, or reflection-diffraction mechanism until all the significant high-frequency interactions are included.

The IPO algorithm is presented in the next section using a formulation based only on the magnetic field and its associated equivalent electric surface currents (from which the electric field may subsequently be found). This greatly simplifies the implementation because singularities in the kernel of the integral equation are avoided. If material surfaces are present, the procedure requires a slightly more complicated combined field formulation using an equivalent surface impedance. Numerical results and conclusions are presented in the last section. An $e^{j\omega t}$ harmonic time dependence is assumed and suppressed throughout.

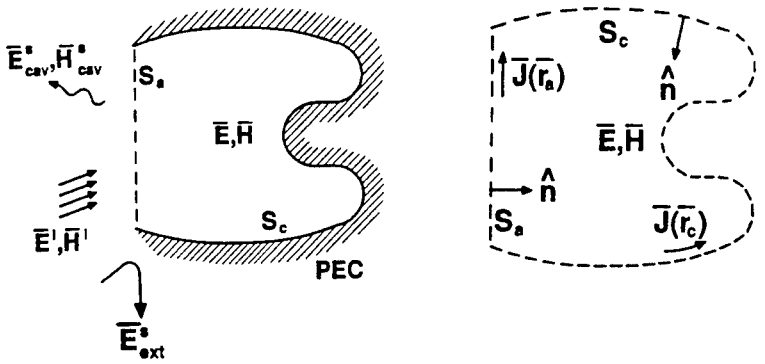
2 The IPO Algorithm

Figure 1(a) shows a typical cavity penetration/scattering geometry. An external plane wave $(\bar{E}^i, \bar{H}^i)$ is incident on the aperture of the cavity S_a. It is of interest to find the total fields in the cavity interior $(\bar{E}, \bar{H})$, and the external fields scattered by the cavity $(\bar{E}^s_{cav}, \bar{H}^s_{cav})$. The fields $(\bar{E}^s_{ext}, \bar{H}^s_{ext})$ scattered by external features of the geometry containing the cavity are not of interest here, but could also be computed using PO. Figure 1(b) shows the equivalent current problem formulated using only electric surface currents. The aperture current has an incident and scattered component,

$$\bar{J}(\bar{r}_a) = \bar{J}^i(\bar{r}_a) + \bar{J}^s(\bar{r}_a) \tag{1}$$

where the incident current is assumed from the Kirchhoff approximation to be

$$\bar{J}^i(\bar{r}_a) = 2\hat{n} \times \bar{H}^i(\bar{r}_a). \tag{2}$$



(a) Original geometry. (b) Equivalent current problem.

Figure 1: Open-ended cavity illuminated by an external plane wave.

It is assumed that $\bar{J}^i$ radiates into the cavity, exciting the PO wall currents $\bar{J}$. At any point $\bar{r}$ inside the cavity, the total magnetic field is then the sum of the incident field radiated by $\bar{J}^i$ plus the field radiated by $\bar{J}$:

$$\bar{H}(\bar{r}) = \bar{H}^i_c(\bar{r}) + \int_{S_c} \bar{J}(\bar{r}'_c) \times \nabla G_o(\bar{r} - \bar{r}'_c) dS' \tag{3}$$

where

$$\bar{H}^i_c(\bar{r}) = \int_{S_a} \bar{J}^i(\bar{r}'_a) \times \nabla G_o(\bar{r} - \bar{r}'_a) dS' \tag{4}$$

$$\nabla G_o(\bar{R}) = \hat{R}\left(jk + \frac{1}{R}\right)\frac{e^{-jkR}}{4\pi R}. \tag{5}$$

The wall current $\bar{J}$ is found approximately by applying the laws of PO iteratively. The initial value $\bar{J}_0$ is the first order PO current given by

$$\bar{J}_0(\bar{r}_c) = 2\hat{n} \times \bar{H}^i_c(\bar{r}_c). \tag{6}$$

The next value $\bar{J}_1$ is the sum of the first value $\bar{J}_0$ plus a principal value integral over $\bar{J}_0$:

$$\begin{aligned} \bar{J}_1(\bar{r}_c) &= \bar{J}_0(\bar{r}_c) + 2\hat{n} \times \oint_{S_c} \bar{J}_0(\bar{r}'_c) \times \nabla G_o(\bar{r}_c - \bar{r}'_c) dS' \\ &= 2\hat{n} \times \bar{H}^i_c(\bar{r}_c) + 2\hat{n} \times \oint_{S_c} \bar{J}_0(\bar{r}'_c) \times \nabla G_o(\bar{r}_c - \bar{r}'_c) dS'. \end{aligned} \tag{7}$$

As will be seen shortly, the principal value of the integral over S_c is used so that the iteration procedure leads directly to a form of the conventional magnetic field integral equation (MFIE).

The value for the current after two iterations is the sum of the first $\bar{J}_1$ plus an integration over the difference $\bar{J}_1 - \bar{J}_0$:

$$\begin{aligned} \bar{J}_2(\bar{r}_c) &= \bar{J}_1(\bar{r}_c) + 2\hat{n} \times \oint_{S_c} \left[\bar{J}_1(\bar{r}'_c) - \bar{J}_0(\bar{r}'_c)\right] \times \nabla G_o(\bar{r}_c - \bar{r}'_c) dS' \\ &= 2\hat{n} \times \bar{H}^i_c(\bar{r}_c) + 2\hat{n} \times \oint_{S_c} \bar{J}_1(\bar{r}'_c) \times \nabla G_o(\bar{r}_c - \bar{r}'_c) dS'. \end{aligned} \tag{8}$$

Each subsequent iteration reduces to the same result, i.e.,

$$\bar{J}_N(\bar{r}_c) = 2\hat{n} \times \bar{H}^i_c(\bar{r}_c) + 2\hat{n} \times \oint_{S_c} \bar{J}_{N-1}(\bar{r}'_c) \times \nabla G_o(\bar{r}_c - \bar{r}'_c) dS' \tag{9}$$

which has the conventional iterative form of the MFIE. However, it is important to keep in mind that this iteration procedure is not expected to converge to the exact solution because the surface S_c is not closed. Furthermore, a rule based on physical insight into the theory of PO is used when numerically evaluating the integral in (9). First, the surface is discretized into flat facets and the current is assumed to be constant over each facet. The integral in (9) over a facet at $\bar{r}'_c$ radiating to a facet at $\bar{r}_c$ is non-zero only if the facet at $\bar{r}_c$ "faces" the facet at $\bar{r}'_c$. Mathematically, this condition is defined by

$$\hat{n}(\bar{r}_c) \cdot (\bar{r}_c - \bar{r}'_c) < 0 \tag{10}$$

where $\hat{n}(\bar{r}_c)$ is the unit surface normal of the facet at $\bar{r}_c$, and is enforced regardless of any intervening wall facets. This definition helps the algorithm to handle shadowing effects caused by convex protrudances in the cavity walls, *without searching for shadow boundaries.* As the numerical results will show, it is very rapidly convergent even for fairly complex geometries. It is noted that the evaluation of $\bar{H}^i_c(\bar{r}_c)$ using (4) follows the same rule, with $\bar{r}'_a$ substituted for $\bar{r}'_c$.

Once a reasonable approximation for $\bar{J}$ has been reached, the scattered current in the aperture is then given by (again using the Kirchhoff approximation)

$$\bar{J}^s(\bar{r}_a) = -2\hat{n} \times \int_{S_c} \bar{J}(\bar{r}'_c) \times \nabla G_o(\bar{r}_a - \bar{r}'_c) dS' \tag{11}$$

which radiates the scattered fields $(\bar{E}^s_{cav}, \bar{H}^s_{cav})$ into the external region.

3 Numerical Results

In [4], results are shown which indicate that a discretization density of 9 facets per square wavelength gives very accurate results for smoothly varying inlet duct geometries larger than a few wavelengths in diameter. 4 facets per square wavelength has also been shown to give adequate results, especially for larger duct geometries. This rather coarse discretization is attainable because the fields may be sampled at the Nyquist rate over smooth surfaces which are slowly varying with respect to wavelength.

Figure 2 demonstrates the convergence of the algorithm in predicting the radar cross section (RCS) patterns of a cylindrical cavity, and compares the results with a modal reference solution. The N=0 case corresponds to simply using the first order PO currents given by (6) without

any iteration. Adding iterations gives more internal reflections which become significant for wider incidence angles. For a maximum incidence angle of 50°, 3 iterations is adequate for this geometry. Of course, a deeper cavity would require more iterations because there would be more internal reflections of importance.

Figure 3 shows the RCS patterns of a cylindrical cavity with a hub termination. The modal reference solution uses the mode-matching technique and was obtained from John Volakis and Hristos Anastassiu at the University of Michigan Radiation Laboratory, Ann Arbor. CICERO is a BOR moment method code developed by McDonnell-Douglas, St. Louis, MO. The results show that good accuracy is attainable for complex geometries at a low computational cost using the IPO algorithm.

Figure 4 shows a 2-D external multi-bounce problem consisting of a line source in the presence of three square blocks (buildings). The far-field radiation pattern is computed using the IPO algorithm and compared with a moment method solution (MoM). For more complex geometries such as this, a slightly modified form of (9) has been found to have better convergence properties:

$$\bar{J}_N(\bar{r}_c) \;=\; \hat{n} \times \bar{H}_c^i(\bar{r}_c) + \hat{n} \times \oint_{S_c} \bar{J}_{N-1}(\bar{r}_c') \times \nabla G_o(\bar{r}_c - \bar{r}_c') dS' + \frac{1}{2}\bar{J}_{N-1}. \qquad (12)$$

The initial value $\bar{J}_0$ is still given by (6). Figure4 shows a reasonably well-converged IPO result after only 4 iterations, and which after 10 iterations has converged to within graphical resolution. The agreement with the MoM solution is excellent, considering that the approximations of PO have been used according to the rule defined by Equation (10).

References

[1] P. H. Pathak and R. J. Burkholder, "Modal, Ray and Beam Techniques for Analyzing the EM Scattering by Open-ended Waveguide Cavities," *IEEE Trans. Antennas Propagat.*, vol. AP-37, pp. 635-647, May 1989.

[2] H. Ling, R.-C. Chou and S. W. Lee, "Shooting and Bouncing Rays: Calculating RCS of an Arbitrary Cavity," *IEEE Trans. Antennas Propagat.*, vol. AP-37, pp. 194-205, February 1989.

[3] P. H. Pathak and R. J. Burkholder, "High-frequency Electromagnetic Scattering by Open-ended Waveguide Cavities," *Radio Science*, vol. 26, pp. 211-218, Jan-Feb 1991.

[4] F. Obelleiro, J.L. Rodriguez, and R.J. Burkholder, "An Iterative Physical Optics Approach for Analyzing the Electromagnetic Scattering by Large Open-Ended Cavities," Accepted for publication in *IEEE Trans. Antennas Propagat.*

[5] R.F. Harrington, Time Harmonic Electromagnetic Fields, pp. 127-128, McGraw Hill, New York, 1961.

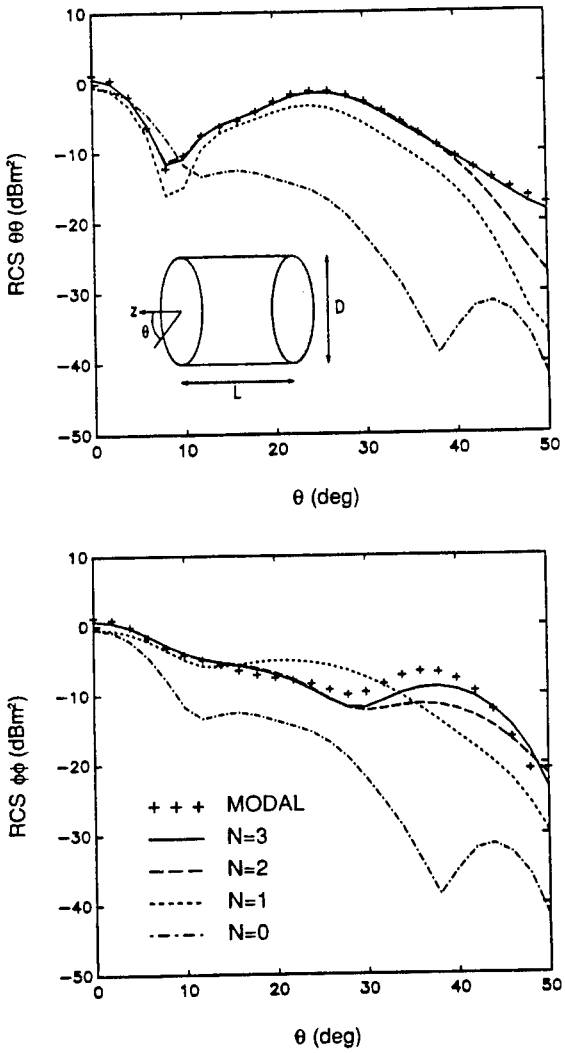
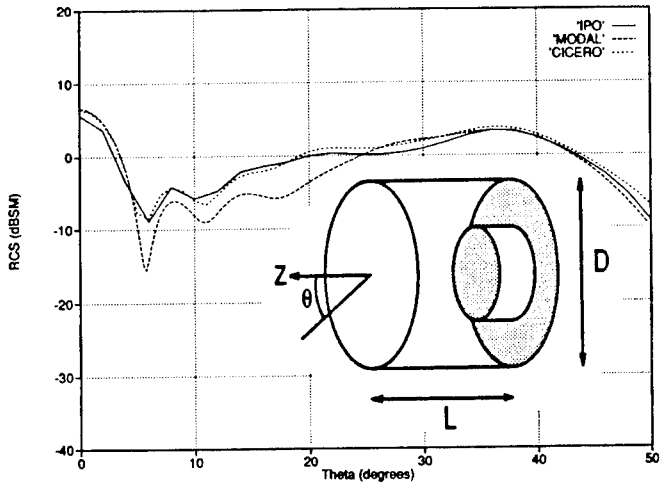
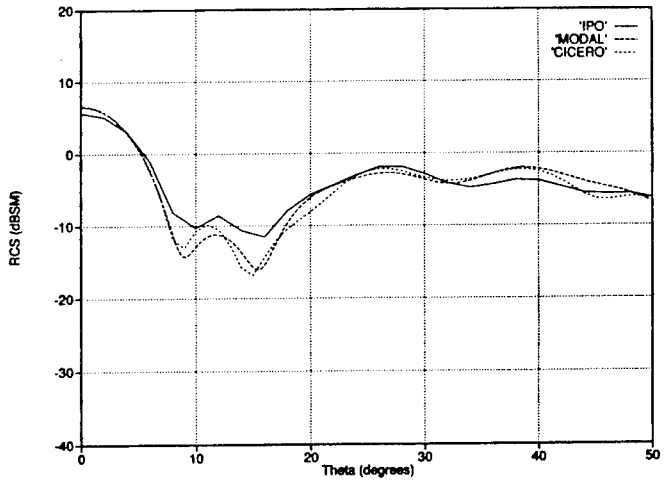


Figure 2: RCS patterns of a 4-by-4 wavelength cylindrical cavity with a flat termination. L=D=12 cm, Frequency=10 GHz. 9 facets per square wavelength used for IPO results.



(a) $\hat{\theta}$ polarization.



(b) $\hat{\phi}$ polarization.

Figure 3: RCS patterns of a 6-by-6 wavelength cylindrical cavity with a cylindrical hub termination. L=D=18 cm, hub diameter=9 cm, hub length= 4.5 cm, Frequency=10 GHz. 9 facets per square wavelength and N=4 iterations used for IPO results.

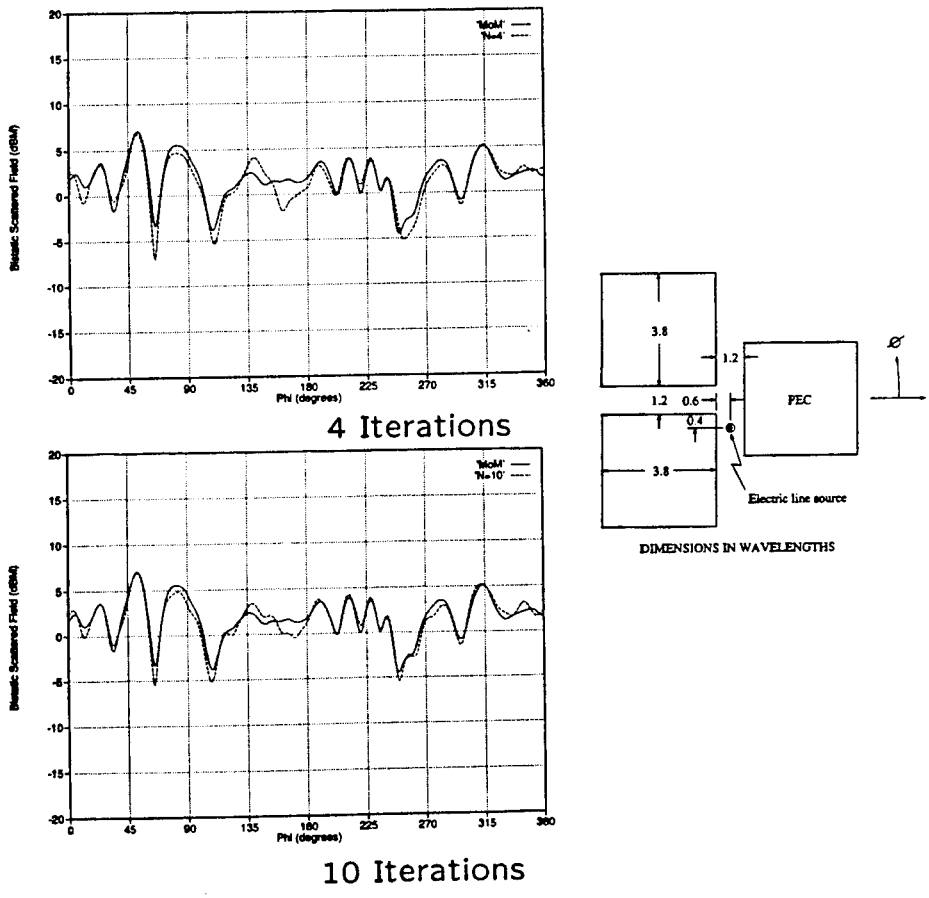


Figure 4: Far-field pattern of an electric line source radiating in the presence of 2-D buildings.

IMPROVED RAY BASIS IN THE HYBRID ANALYSIS OF EM SCATTERING BY LARGE OPEN CAVITIES

R.J. Burkholder, P.H. Pathak, & H.T. Chou
The Ohio State University ElectroScience Laboratory
1320 Kinnear Road, Columbus, Ohio 43212

D. Andersh & J. Fath
Wright Laboratory, Avionics Directorate, WPAFB, Ohio

Abstract

A hybrid analysis of the electromagnetic scattering by electrically large elongated open cavities containing a large interior termination is developed in this paper when the illumination is from the exterior region. The analysis is divided into three basic parts. One of these parts deals with the external scattering from the open end being illuminated, and also with the coupling of the rest of this illumination just inside the cavity via the aperture formed at the opening. The other two parts deal with the propagation of the latter cavity coupled field through its length to a region near the interior termination at the other end of the cavity, and with the scattering of these fields by the interior termination, respectively. The analysis of the three parts can be done separately by methods best suited for each one and then combined systematically via generalized reciprocity relations. The propagation region analysis is performed via ray methods, and in particular a highly efficient new ray tube basis set is employed which tends to track the shape of the ray tubes as they propagate within the cavity thereby reducing the number of ray tubes by an order of magnitude over that required when using conventional ray tubes. In this paper, special emphasis is given to the propagation region analysis.

I Introduction

The electromagnetic (EM) scattering from an externally illuminated electrically large open cavity of relatively arbitrary shape and containing a large interior termination is analyzed via a hybrid approach. Figure 1 illustrates the geometry of this problem. It is assumed that the

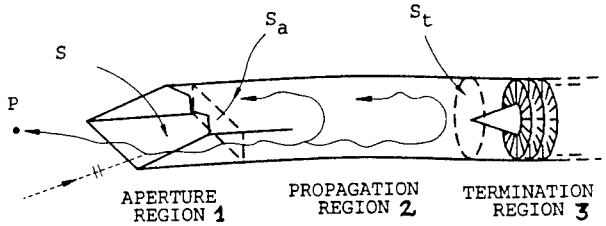


Figure 1: Cavity configuration.

medium surrounding the cavity is free space. The scattering from the external features of the cavity and its housing are not of interest here except for the scattering from the open end being illuminated; however, if desired, these other external effects can in general be included via the uniform geometrical theory of diffraction (UTD) and its modifications [1]. The scattering from the open end region being illuminated, henceforth referred to as region 1, can be done by UTD and its modifications, or by numerical methods, to provide not only the external fields scattered by the opening, but also the fields coupled just inside the cavity via the open end. The fields coupled into region 1 then propagate inside the elongated cavity region which is referred to as region 2. Region 1 analysis also provides the equivalent sources over the cavity cross section S_a just inside the opening to couple into region 2 via the generalized ray expansion (GRE) [2, 3]. The GRE launches a discrete set of ray tubes from an array of points over the sources in S_a and propagates them into region 2 via ray bounces at the interior cavity walls. The ray paths need to be found only once in the GRE for a given cavity geometry; only the strengths of the rays change with illumination but the ray paths do not. The cavity is assumed to be perfectly conducting, but the interior cavity walls may contain a thin lossy material coating. The ray tubes are initially assumed to have a circular cross-section which, upon reflection can become elliptical. The conventional GRE ray tubes are chosen to be sufficiently thin so that their cross-section can be approximated as being circular even after each bounce; however, the use of this approximation requires an extremely large number of ray tubes because they are thin. A new set of ray tubes with an elliptic cross-section are thus introduced into the GRE; these also start out with a circular cross-section but simple rules are developed to track their shape after each reflection. These new tubes are referred to as elliptic ray basis functions (ERBF's) and their propagation rules predict how their elliptic cross-section can rotate and change shape with propagation distance. The latter information allows the ERBF's to be much fatter than the conventional narrow tubes. Typically, an order of magnitude fewer ERBF's than conventional ray tubes may be used. Thus, the ERBF's make the GRE more efficient. The GRE fields are evaluated over a cavity cross-section S_t at the end of region 2 near the interior termination. The termination region beyond S_t is designated as region 3. The GRE fields at S_t illuminate the termination which then scatters fields back to S_t; the latter fields are found separately by numerical methods or by asymptotic high frequency approximations if applicable. An analysis of these three regions can be performed separately by methods best suited for each region and then combined systematically to arrive at a hybrid solution. This hybrid scheme is summarized next in Section II where the separate analyses of regions 1, 2 and 3 are briefly discussed in Parts A, B and C of Section II, and these analyses are then systematically combined in Section D via some generalized reciprocity relationships. Section III presents some numerical results. An $e^{+j\omega t}$ time dependence is assumed and suppressed.

II Summary of the Hybrid Procedure

The field scattered by the electrically large cavity to some external point P sufficiently far from it, when it is illuminated by an external source as in Figure 1, can be expressed as [2,3]

$$\bar{E}^s(P) \sim \bar{E}^s_{\text{rim}}(P) + \bar{E}^s_{\text{int}}(P) + \bar{E}^s_{\text{ext}}(P) \tag{1}$$

where $\bar{E}$ refers to the electric field and the superscript s refers to the scattered component of this field. Here $\bar{E}^s_{\text{rim}}(P)$ is the field directly scattered into the exterior region by the edge of the open end being illuminated, whereas $\bar{E}^s_{\text{int}}(P)$ in (1) is the field scattered into the exterior by the interior cavity effects such as the interior walls and the termination. The term $\bar{E}^s_{\text{ext}}(P)$ in (1) represents the contribution to $\bar{E}^s(P)$ which results from other external features of the cavity (e.g., the cavity housing) which is not of interest in the present work and will thus be neglected. However, $\bar{E}^s_{\text{ext}}(P)$ can generally be found via the UTD and its modifications [1]. It is important to note that $\bar{E}^s_{\text{int}}(P)$ is generally the dominant contributor to $\bar{E}^s(P)$ in (1) as compared to $\bar{E}^s_{\text{rim}}(P)$, this being the case due to the electrically large termination which is assumed to exist within the cavity.

A Analysis of Region 1 (Aperture Region)

The open end of the cavity being illuminated forms an aperture S. The analysis of this aperture region involves two parts. In one part, $\bar{E}^s_{\text{rim}}(P)$ scattered externally to P by the edge of S which is illuminated must be found; in the other, the remaining field $\bar{E}^a(P_a)$ that is coupled from the external illumination via S to any point P_a in an interior aperture S_a just inside the cavity as shown in Figure 1 must also be found. If the incident field $\bar{E}^i$ on S is ray optical, then $\bar{E}^s_{\text{rim}}(P)$ may be found via the UTD [1] or in a more general fashion via the equivalent current method (ECM) as indicated in [1, 3]. In the special but generally rare situations that ECM becomes inapplicable (e.g., if $\bar{E}^i$ is not ray-optical and if the relevant equivalent currents cannot be found) a numerical method of solution must be employed to find $\bar{E}^s_{\text{rim}}(P)$; such a method is currently under investigation. Likewise, the field $\bar{E}^a(P_a)$ at any point P_a in S_a may be found via the UTD and its modifications [1]. Again, if for any reason $\bar{E}^a(P_a)$ cannot be found via UTD or its appropriate modifications (such as ECM) then one must resort to numerical solution techniques.

B Analysis of Region 2 (Propagation Region)

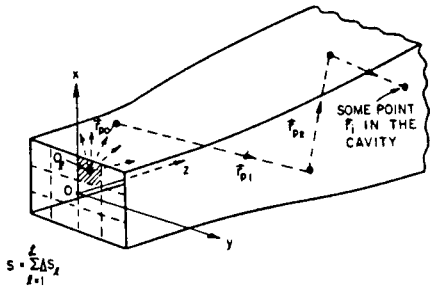
The electric and magnetic fields $(\bar{E}^a, \bar{H}^a)$ at any point P_a in S_a found in part A define a set of equivalent surface currents $(\bar{J}^a_s, \bar{M}^a_s)$ on S_a that launch the fields $(\bar{E}^{in}, \bar{H}^{in})$ into the cavity interior.

$$\bar{J}^a_s = \hat{n} \times \bar{H}^a\Big|_{S_a} \quad ; \quad \bar{M}^a_s = \bar{E}^a \times \hat{n}\Big|_{S_a} \tag{2;3}$$

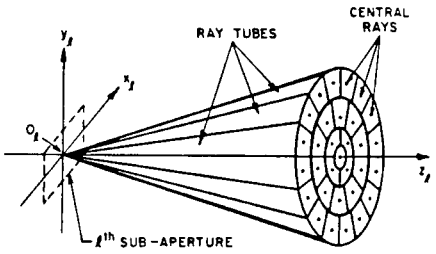
The generalized ray expansion (GRE) is employed to find $(\bar{E}^{in}, \bar{H}^{in})$ from $\bar{J}^a_s$ and $\bar{M}^a_s$ in S_a. Actually,

$$\bar{E}^{in} = \bar{E}^{ig}_+ + \bar{E}^{ig}_- \quad ; \quad \bar{H}^{in} = \bar{H}^{ig}_+ + \bar{H}^{ig}_- \tag{4;5}$$

where $(\bar{E}^{ig}_+, \bar{H}^{ig}_+)$ are the fields which propagate from S_a to a mathematical surface S_t chosen sufficiently near the termination; whereas, $(\bar{E}^{ig}_-, \bar{H}^{ig}_-)$ are part of the fields which after being launched from S_a return to S_a without reaching S_t. The $(\bar{E}^{ig}_-, \bar{H}^{ig}_-)$ generally exist if the interior cavity walls are tapered between S_a and S_t. According to the GRE, S_a is divided into $\mathcal{L}$ subapertures such that $S_a = \sum_{l=1}^{\mathcal{L}} \Delta S_l$, where the size of ΔS_l is dependent mostly on the overall length of the cavity L_c from S_a to S_t. In particular, the maximum linear dimension D_l of the largest ΔS_l should typically be smaller than $\sqrt{2L_c\lambda}$ where λ is the free space wavelength, and D_l should



(a) Ray field originating from the phase center O_l of the lth subaperture of area ΔS_l (shaded).



(b) Grid of ray tubes originating from O_l of any l^{th} subaperture of area ΔS_l.

Figure 2: Launching of GRE rays.

also be less than half the maximum transverse dimension of S_a. This choice of ΔS_l allows the fields radiated into the cavity by $(\bar{J}_s^a, \bar{M}_s^a)$ to be approximated by a superposition of the fields of spherical waves originating from the phase centers O_l, within ΔS_l, of each of the $\mathcal{L}$ subapertures. For example, the fields launched from O_l in ΔS_l of the lth subaperture ($l = 1, 2, \cdots \mathcal{L}$) can be expressed as a superposition of the fields of P non-overlapping ray tube fields emanating radially out from O_l as in Figure 2(a). The discrete number of P ray tubes; i.e., the size and hence the density of ray tubes is chosen to adequately represent the field within each ray tube via the rules of ray optics as each ray tube propagates via interior reflections along the entire length of the cavity. At present, any diffraction effects at the smooth interior cavity walls are neglected; this is generally reasonable since the interior wave effects are mostly dominated by multiple internal reflections. Thus,

$$\bar{E}_+^{ig}(S_t) \;=\; \sum_{l=1}^{\mathcal{L}} \sum_{p=1}^{P} \bar{E}_{pl}^{ig}(S_t) \quad ; \quad \bar{E}_-^{ig}(S_a) \;=\; \sum_{l=1}^{\mathcal{L}} \sum_{m=1}^{M} \bar{E}_{ml}^{ig}(S_a) \tag{6;7}$$

where $\bar{E}_{pl}^{ig}(S_t)$ is the field of the p^{th} ray tube launched from O_l in the lth subaperture ΔS_l that ultimately reaches some point in S_t after N bounces. The $\bar{E}_{ml}^{ig}(S_a)$ has an analogous interpretation. Even though the ray tube discretization shown in Figure 2(b) does not automatically produce ray tubes with circular cross-section, one can define an "effective" circular cross-section for each ray tube at launch. Thus, the radius "a" of the effective circular cross-section of the ray tube is given adequately by $a \approx \frac{d\Delta\psi}{\sqrt{\pi}}$, where d is the propagation distance along the axial ray in the tube measured from its launch point, and $\Delta\psi$ is the angle between any pair of adjacent ray tubes that emanate from that same launch point. The field $\bar{E}_{pl}^{ig}(S_t)$ at a point in S_t can be expressed in terms of its components $E_{pl}^{\parallel}$ and $E_{pl}^{\perp}$ which are respectively $\parallel$ and $\perp$ to the plane of incidence defined at the point of last (Nth) reflection before reaching a point in S_t. Thus, in matrix notation, $\bar{E}_{pl}^{ig}(S_t)$ becomes [3]:

$$\begin{bmatrix} E_{pl}^{\parallel}(S_t) \\ E_{pl}^{\perp}(S_t) \end{bmatrix} \;\sim\; \left(\prod_{q=1}^{N} e^{-jkr_{pq}} \sqrt{\frac{\det Q_q(r_{pq})}{\det Q_q(O)}} \cdot [R_{pq}]\,[T_{pq}] \right) \cdot [C_{pl}] \frac{e^{-jkr_{po}}}{r_{po}}$$

$$\cdot e^{-j\frac{k}{2}[x_{pN}]^T Q_N(r_{pN})[x_{pN}]} \cdot U\left(1-[x_{pN}]^T Q_N^a(r_{pN})[x_{pN}]\right). \quad (8)$$

where the notation $\prod_{q=1}^{N}\Omega_q \equiv \Omega_N\cdot\Omega_{N-1}\cdots\Omega_3\cdot\Omega_2\cdot\Omega_1$ is employed in (8). The field $\bar{E}_{pl}^{ig}$ reaches S_t from O_l via $q=1,2,3,\cdots N$ bounces as in Figure 2(a). Note that r_{po} is the distance from O_l to the point of first reflection ($q=1$) along the p^{th} ray. Also r_{pq} is the distance only from the $q-1$th reflection to the next, or q^{th}, reflection along the p^{th} ray; thus, r_{pN} is the distance along the p^{th} ray from the last (or Nth) reflection to a point in S_t. The $[R_{pq}]=\begin{bmatrix} R_{\|} & 0 \\ 0 & R_{\perp}\end{bmatrix}$ is the usual 2×2 Fresnel reflection coefficient matrix defined with respect to the plane of incidence fixed at the q^{th} reflection of the p^{th} ray. The 2×2 matrix $[\mathcal{T}_{pq}]$ transforms the field polarization of the p^{th} ray before the q^{th} reflection occurs to one fixed in the q^{th} plane of incidence from that fixed in the previous or the $(q-1)$th plane of incidence, because the plane of incidence can in general change at each reflection on an arbitrary curved interior cavity wall. The 1×2 column matrix $[C_{pl}]$ denotes the two orthogonal components of the vector radiation pattern $\bar{C}_{pl}$ of the electric field along the p^{th} ray launched from O_l with the cavity walls absent.

$$\bar{C}_{pl} = \frac{jkZ_0}{4\pi}\iint_{\Delta S_l}\left[\hat{r}_{po}\times\hat{r}_{po}\times\bar{J}_s^a(\bar{r}_l')+Y_0\hat{r}_{po}\times\bar{M}_s^a(\bar{r}_l')\right] \cdot e^{jk\hat{r}_{po}\cdot\bar{r}_l'}dS' \quad (9)$$

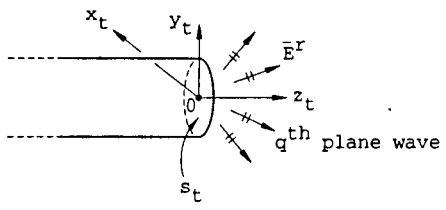
with $Y_0=Z_0^{-1}$ and Z_0 is the free space impedance. Also $\bar{r}_l'$ is any point in ΔS_l which is measured from O_l. It is noted that $\bar{C}_{pl}\frac{e^{-jkr_{po}}}{r_{po}}$ constitutes the p^{th} ray electric field incident at the first point of reflection ($q=1$). The $Q_q(\cdot)$ denotes the wavefront curvature matrix of the p^{th} ray after the q^{th} reflection; in particular, $Q_q(O)$ is the reflected wavefront curvature matrix of the p^{th} ray evaluated at the q^{th} point of reflection while $Q_q(r_{pq})$ is its value at the next point of reflection $q+1$ after this ray propagates a distance r_{pq}. The elements of the 1×2 matrix $[x_{pN}]$ are the coordinates along the $\|$ and $\perp$ directions fixed in the plane of incidence of the p^{th} ray at the last (Nth) point of reflection. The magnetic field associated with $\bar{E}_{pl}^{ig}$ is $\bar{H}_{pl}^{ig}\sim Y_0\hat{r}_{pN}\times\bar{E}_{pl}^{ig}$. The GRE field of the p^{th} ray from O_l is the same as the conventional one given previously in [2,3] except for the new modification contained in U of (8) which tracks the shape of the p^{th} tube as it propagates via reflections. The shape is an ellipse whose boundary changes (rotates and changes size) with propagation. Hence the GRE field in (8) is said to be given in terms of the ERBF's. The rules for this change in shape of the ray tube ellipse after each bounce is given by the matrix $Q_q^a(\cdot)$ in (8) as

$$\begin{bmatrix}1 & 0\\ 0 & -\cos\theta_q^i\end{bmatrix}^T Q_{q-1}^a(r_{pq-1})\begin{bmatrix}1 & 0\\ 0 & -\cos\theta_q^i\end{bmatrix} = \begin{bmatrix}1 & 0\\ 0 & \cos\theta_q^i\end{bmatrix}^T Q_q^a(O)\begin{bmatrix}1 & 0\\ 0 & \cos\theta_q^i\end{bmatrix} \quad (10)$$

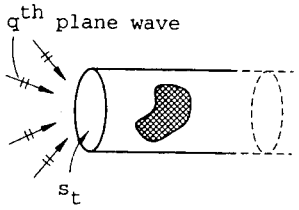
with

$$Q_0^a(r_{po}) = \begin{pmatrix}\frac{\pi}{\Delta\psi r_{po}} & 0\\ 0 & \frac{\pi}{\Delta\psi r_{po}}\end{pmatrix} \quad (11)$$

and $U(t)=\left\{\begin{array}{l}1, t>0\\ 0, t<0\end{array}\right\}$; also, θ_q^i is the angle of incidence (or reflection) that the incident (or reflected) ray makes with the normal to the interior cavity wall at the q^{th} reflection point.



(a) $\bar{E}^r$ of represented by discrete plane waves propagating out of S_t plane ($z_t = 0$) associated with the open waveguide cavity region.



(b) Plane waves shown in part (a) of this figure are now incident on S_t associated with the termination region.

Figure 3: Decomposition of original geometry at S_t.

C Analysis of Region 3 (Termination Region)

In this section, the contribution to the external scattered field produced by the interior cavity termination is considered and the analysis for incorporating the effects of scattering within the cavity by the termination when it is excited by the fields arriving at S_t from S_a is summarized. Let the fields arriving at S_t from S_a, which are defined as $(\bar{E}_+^{ig}, \bar{H}_+^{ig})$, be assumed to exist in the ABSENCE of the termination and with the region beyond S_t being assumed to be a smooth extension such that no waves are reflected back to S_t due to this extension. Usually, the cross-section at S_t is circular (as for example, a jet inlet cavity) and one may assume the infinite extension beyond S_t to be a smooth circular waveguide in such a situation. The fields $(\bar{E}_+^{ig}, \bar{H}_+^{ig})$ are thus the unperturbed fields (i.e., in the presence of the smooth extension of the cavity beyond S_t and with the termination absent). Next, let these unperturbed fields $(\bar{E}_+^{ig}, \bar{H}_+^{ig})$ radiate the fields $(\bar{E}^r, \bar{H}^r)$ from S_t if the region beyond S_t is now removed. These radiation fields $(\bar{E}^r, \bar{H}^r)$ constitute a Kirchhoff approximation because they are assumed to be produced outside S_t by the "unperturbed" fields $(\bar{E}_+^{ig}, \bar{H}_+^{ig})$. One may express $\bar{E}^r(x_t, y_t, z_t)$ at any point (x_t, y_t, z_t) external to S_t as a plane wave spectral (PWS) integral. The continuous PWS can be approximated by a sufficient number (Q) of discrete "propagating" plane waves, as shown in Figure 3(a):

$$\bar{E}^r(x_t, y_t, z_t) \approx \sum_{q=1}^{Q} \bar{E}_q^r. \tag{12}$$

Each of these Q plane waves are next made to illuminate the obstacle or termination region as shown in Figure 3(b). Each q^{th} plane wave when allowed to be incident on S_t of the termination region (see Figure 3(b)) produces the fields $(\bar{E}_q^{sg}, \bar{H}_q^{sg})$ which are scattered by the obstacle or termination region. The scattered fields $(\bar{E}_q^{sg}, \bar{H}_q^{sg})$ may be found numerically via an integral equation or finite element method, or via some approximate high frequency method such as the physical theory of diffraction (PTD) [1] if applicable, or by measurements if possible. In these analytical high frequency, numerical or experimental simulations to find $(\bar{E}_q^{sg}, \bar{H}_q^{sg})$, one illuminates the termination region geometry of Figure 3(b) with a field which is locally a unit amplitude plane wave over S_t, and which is incident in the q^{th} direction with the same polarization as $\bar{E}_q^r$. The far zone bistatic scattering would then be evaluated or measured in the half space

to the left of S_t in Figure 3(b). Next, this far field data would be weighted appropriately by the amplitude of $\bar{E}_q^r$ and transformed via a fast Fourier transform (FFT) to give the values of $(\bar{E}_q^{sg}, \bar{H}_q^{sg})$ back at the plane S_T. Alternatively, $(\bar{E}_q^{sg}, \bar{H}_q^{sg})$ could also be obtained directly on S_t if one employs analytical or numerical methods. The complete termination region scattered field at S_t due to all of the Q plane waves illuminating S_t is given by

$$\left(\bar{E}^{sg}, \bar{H}^{sg}\right)\Big|_{S_t} = \sum_{q=1}^{Q} \left(\bar{E}_q^{sg}, \bar{H}_q^{sg}\right)\Big|_{S_t}. \tag{13}$$

In realistic cases, the termination region must be truncated smoothly or with absorbers to minimize the external scattering effects arising from this isolated region. The edge diffraction effects arising from the rim of S_t in Figure 3(b) are unavoidable with the procedure which employs a physical breakup of the actual cavity into the isolated propagation and termination regions however, these edge effects are generally weak in $(\bar{E}^{sg}, \bar{H}^{sg})\Big|_{S_t}$ if S_t is electrically large. An alternative procedure to find $(\bar{E}^{sg}, \bar{H}^{sg})\Big|_{S_t}$ without a physical breakup at S_t is also possible but is not discussed here because it is not practical if an experimental approach is used to find these fields.

D Hybrid Procedure to find $\bar{E}^s_{int}(P)$

The results of parts B and C are next combined to find $\bar{E}^s_{int}(P)$. Let a test electric current source $\bar{J}_t$ be placed at the observation point P, where

$$\bar{J}_t = \hat{p}\delta(\bar{r} - \bar{r}_p). \tag{14}$$

Then it is convenient to write $\bar{E}^s_{int}(P)$ as the sum of two terms

$$\bar{E}^s_{\rm int}(P) = \bar{E}^{s1}_{\rm int}(P) + \bar{E}^{s2}_{\rm int}(P) \tag{15}$$

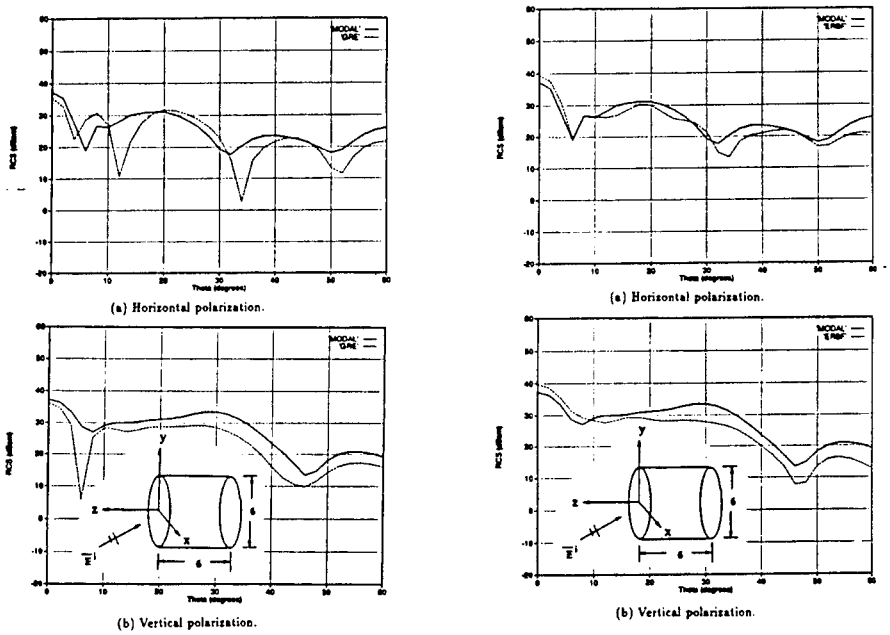
where the $\hat{p}$ component of each of these two terms with $\hat{p}$ being arbitrary is shown via a generalized reciprocity theorem [4] to be

$$\bar{E}^{s1}_{\rm int}(P)\cdot\hat{p} \approx \iint_{S_t} \left(\bar{E}^{sg} \times \bar{H}^{ig}_{t+} - \bar{E}^{ig}_{t+} \times \bar{H}^{sg}\right)\cdot d\bar{s} \tag{16}$$

and in an analogous fashion

$$\bar{E}^{s2}_{\rm int}(P)\cdot\hat{p} \approx \iint_{S_a} \left(\bar{E}^{ig}_{-} \times \bar{H}^{a}_{t} - \bar{E}^{a}_{t} \times \bar{H}^{ig}_{-}\right)\cdot ds. \tag{17}$$

In (16), the $(\bar{E}^{ig}_{t+}, \bar{H}^{ig}_{t+})$ are fields produced at S_t by $\bar{J}_t$ in the presence of the cavity but in the absence of the interior termination assuming that the region beyond S_t is assumed to extend smoothly to infinity [4]. This can be found via GRE exactly as discussed in part B of Section II to obtain $(\bar{E}^{ig}_{+}, \bar{H}^{ig}_{+})$ at S_t, and using the same ray paths. The $(\bar{E}^{a}_{t}, \bar{H}^{a}_{t})$ in (17) are the fields produced at S_a by $\bar{J}_t$ in the presence of the cavity which is assumed to extend smoothly to infinity beyond S_a with termination removed so that there are no interior reflections beyond S_a. These fields may be found in a manner analogous to that used to find $(\bar{E}^a, \bar{H}^a)$.



(a) GRE using 84,548 conventional ray tubes. (b) GRE using 17,436 ERBF's.

Figure 4: RCS patterns of a 6-by-6 wavelength cylindrical cavity. GRE used 32 subapertures.

III Numerical Results

Figure 4 shows the RCS patterns of 6-by-6 wavelength cylindrical cavity found using GRE with conventional ray tubes and GRE with ERBF's, and compared with a modal reference solution.

References

[1] P.H. Pathak, "Techniques for High-Frequency Problems," in *Antenna Handbook—Theory, Applications, and Design*, Chapter 4, Van Nostrand Reinhold, New York, 1988.

[2] R.J. Burkholder, "High-Frequency Asymptotic Methods for Analyzing the EM Scattering by Open-Ended Waveguide Cavities," Ph.D. dissertation, The Ohio State University, June 1989.

[3] P.H. Pathak, R.J. Burkholder, "High Frequency EM Scattering by Open-Ended Waveguide Cavities," *Radio Science*, Vol. 26, No. 1, pp. 211–218, Jan.-Feb. 1991.

[4] P.H. Pathak and R.J. Burkholder, "A Reciprocity Formulation for the EM Scattering by an Obstacle Within a Large Open Cavity," *IEEE Trans. Antennas and Propagat.*, Vol. 41, No. 4, pp. 702–707, April 1993.

Overlapping Modal and Geometric Symmetries for Computing Jet Engine Inlet Scattering

Daniel C. Ross[*], *John L. Volakis*[*], *Hristos T. Anastassiu*[*] *and Dennis Andersh*[+]

[*]Radiation Laboratory
Electrical Engineering and Computer Science Dept.
University of Michigan
1301 Beal Ave.
Ann Arbor MI 48109-2122
Phone: (313) 764-0500
FAX: (313) 747-2106
dross@engin.umich.edu
volakis@engin.umich.edu

[+]U.S. Air Force
WL/AARA
2010 Fifth Ave. Bldg. 23
WPAFB, OH 45433-7001
Phone: (513) 255-1115
FAX: (513) 476-4414

abstract -- By examining the scattering from inlets terminated by fan-like structures, possessing discrete angular symmetry, it is found that only a very limited amount of intermodal coupling is possible. This fact is exploited in a hybrid finite element/modal scheme to develop a very efficient solution, where only one slice of the geometry need be modeled. At this presentation, the method will be outlined and results will be presented for validation purposes. Specific attention will be given to the implementation of the phase boundary conditions which are essential in taking advantage of the engine's angular periodicity. The phase boundary condition must be extended to handle a domain which includes the axis of the inlet and a scheme for including degrees of freedom along the axis will be given. Alternatively, the overlapping modal and geometric symmetries can be exploited in other means to develop simplified analysis and characterization schemes which avoid volume meshing altogether without compromising the geometrical adaptability of the formulation. One such solution scheme, which employs the limited set of coupling modes as the basis of the solution, will be presented and validated with measured and reference data.

1.0 Introduction

The use of a hybrid finite element/modal technique to model the radar scattering from jet engine inlets is depicted in Figure 1 [1] [2]. Briefly, the finite element method (FEM) is employed to generate a modal scattering matrix for the engine face while some high frequency or modal technique is used to trace the fields in and out of the inlet. It is necessary to perform the FEM analysis once for each traveling mode in the circular inlet to generate the scattering matrix. That is, the incoming field is decomposed into waveguide modes prior to the application of the FEM and the FEM is used only to generate the modal scattering matrix.

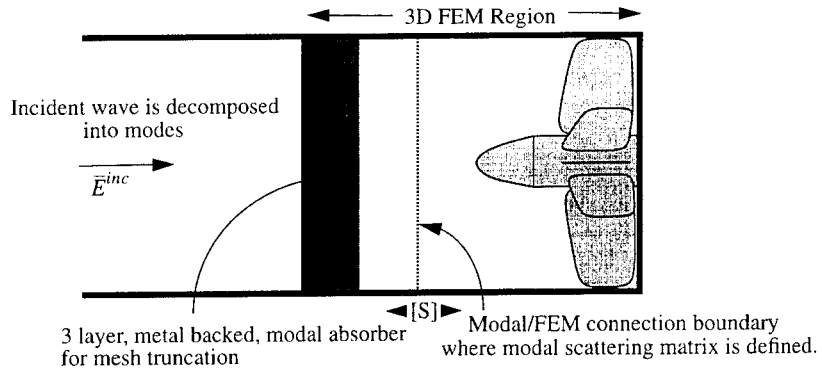


FIGURE 1. Hybrid FEM/Modal analysis.

While the hybrid finite element/modal technique was validated in [1] for an engine-like termination consisting of straight blades, the electrical sizes considered were small (approximately 1λ radius) where typically the inlet can have a radius of 10λ and greater. Because the number of degrees of freedom grows as the square of the radius, to apply the method directly to large structures would invoke computational costs that are indeed staggering. Also, the number of traveling modes (note that the analysis must be repeated for each mode) and the size of the scattering matrix, grow as the radius squared. For the inlet configurations considered in [1] approximately 50,000 elements were needed with about 20,000 degrees of freedom and the analysis was repeated approximately 10 times, once for each mode. Given this, an inlet which is 10λ in radius would require 100 times the computational resources (5,000,000 elements) and the analysis must be repeated 100 times over (2,000,000 degrees of freedom, 1,000 times) thus increasing the total computational cost by about 10,000. In effect, the computational cost increases as the radius to the fourth power.

Obviously, some physically derived simplification is needed to scale the problem to a workable size. By exploiting the cyclic, geometric symmetry which exists in an engine face, it is shown that the entire problem can be reduced down to a single unique slice of the geometry.

For example, if the engine face has 40 blades, it is sufficient to only model, and carry out the analysis for a single angular period of the geometry which encompasses (1/40)'th of the total computational volume. To achieve this computational scaling, it is necessary to work with modal field excitations and not plane wave excitations. The modal field excitations can be found by decomposing the incident plane wave, as is typically done for generating the scattering matrix of the termination. By exploiting the modal (excitation) and geometric symmetries, it can be shown that a very limited set of scattered modes is possible. It is also demonstrated that all of the scattered modes have a constant phase shift from one geometry slice to another. From a computational point of view, since all scattered modes have equal phase shift across the slice, a phase boundary condition can be imposed at the two interior faces of the FEM mesh to bound the problem. This technique has been used successfully in [3] and [4] and is extended to 3-dimensions in this paper, with considerations for applying the phase boundary condition along the axis.

We also introduce an alternative, integral equation formulation that fully exploits the limited mode phenomenon by making use of the modal dyadic Green's function within the guide. Preliminary results for this method will be shown and the major difficulty of extracting the singularity from the modal Green's function will be discussed.

2.0 Overlapping Modal and Geometric Symmetries

Consider a unique slice of an engine-like termination as shown in Figure 2. Let ϕ_s be the angular extent of the unique slice of the geometry. For any fan-like structure $\phi_s = 2\pi/N_s$ where N_s is the symmetry number (number of blades). Since the incident field will be a cylindrical mode with an angular dependance of the form $e^{\pm jn_{in}\phi}$, the FEM system resulting from a solution of the entire problem would take the form

$$\begin{bmatrix} K^1 & & & & \\ & K^2 & & & \\ & & K^3 & & \\ & & & \cdots & \\ & & & & K^{N_s} \end{bmatrix} \begin{pmatrix} E_s^1 \\ E_s^2 \\ E_s^3 \\ \cdots \\ E_s^{N_s} \end{pmatrix} = \begin{pmatrix} f \\ fe^{\pm jn_{in}\phi_s} \\ fe^{\pm 2jn_{in}\phi_s} \\ \cdots \\ fe^{\pm (N_s-1)jn_{in}\phi_s} \end{pmatrix} \tag{1}$$

where E_s^k is the unknown scattered electric field in slice k. Because the geometry is the same in each slice, $K^1 = K^2 = K^3 \ldots = K^{N_s}$ and by linearity, the unknown scattered fields must all be equal to within a phase factor. That is

$$E_s^2 = E_s^1 e^{\pm jn_{in}\phi_s} \qquad E_s^3 = E_s^1 e^{\pm j2n_{in}\phi_s} \qquad \ldots \qquad E_s^{N_s} = E_s^1 e^{\pm j(N_s-1)n_{in}\phi_s} \tag{2}$$

and consequently, the scattered field is a periodic function in ϕ with period ϕ_s and a progressive phase advance of $e^{\pm jn_{in}\phi_s}$ in each period (slice). This restricts the possible scattered modes, and it can be shown that these scattered modes must satisfy

$$n_{out} = n_{in} \pm mN_s \qquad m\text{: any integer} \tag{3}$$

From the above analysis it can be seen that coupling does not occur to modes having $n_{out} = n_{in} \pm 1$ since a symmetry number of 1 ($N_s = 1$) is not a possibility. This fact will turn out to be of great importance for establishing boundary conditions on the axis of the FEM solution. Also, note that all of the possible scattered modes share a common phase shift from symmetry face 1 to symmetry face 2. Thus, all scattered modes are related, on a cut of constant z, from face 2 to face 1 by

$$E_\rho^2 = E_\rho^1 e^{\pm jn_{in}\phi_s} \qquad E_\phi^2 = E_\phi^1 e^{\pm jn_{in}\phi_s} \qquad E_z^2 = E_z^1 e^{\pm jn_{in}\phi_s} \tag{4}$$

where E^2 is the scattered field on face 2 and E^1 is the scattered field on face 1. This fact was first exploited in [4] to efficiently compute eigenmodes within a cyclotron using FEM. For the jet engine scattering problem at hand, a phase boundary condition can be used to restrict the FEM computational region to a single slice of the original problem. The implementation of the phase boundary condition for three-dimensional FEM analysis of the engine face is discussed next.

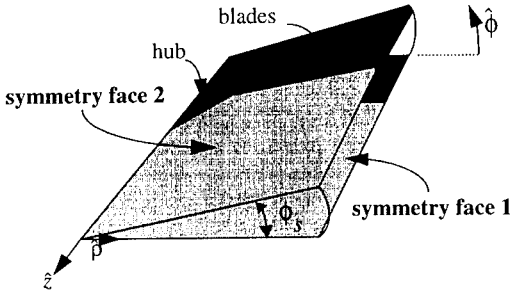


FIGURE 2. Computational domain of sliced engine section.

3.0 Phase Boundary Conditions for 3-D FEM

The implementation of the phase boundary condition involves relating the degrees of freedom on face 1 to face 2 by

$$\begin{aligned}
\hat{\rho}^2 \cdot (\hat{x}E_x^2 + \hat{y}E_y^2) &= \hat{\rho}^1 \cdot (\hat{x}E_x^1 + \hat{y}E_y^1)\, e^{\pm jn_{in}\phi_s} \\
\hat{\phi}^2 \cdot (\hat{x}E_x^2 + \hat{y}E_y^2) &= \hat{\phi}^1 \cdot (\hat{x}E_x^1 + \hat{y}E_y^1)\, e^{\pm jn_{in}\phi_s} \\
E_z^2 &= E_z^1 e^{\pm jn_{in}\phi_s}
\end{aligned} \tag{5}$$

After some algebra (5) becomes

$$E_x^2 = \frac{\left[\rho_x^1 - \rho_y^2\left(\frac{\phi_x^1}{\phi_y^2}\right)\right]e^{\pm jn_{in}\phi_s}E_x^1 + \left[\rho_y^1 - \rho_y^2\left(\frac{\phi_y^1}{\phi_y^2}\right)\right]e^{\pm jn_{in}\phi_s}E_y^1}{\rho_x^2 - \rho_y^2\left(\frac{\phi_x^2}{\phi_y^2}\right)}$$

$$E_y^2 = \frac{\left[\phi_x^1 - \phi_x^2\left(\frac{\rho_x^1}{\rho_x^2}\right)\right]e^{\pm jn_{in}\phi_s}E_x^1 + \left[\phi_y^1 - \phi_x^2\left(\frac{\rho_y^1}{\rho_x^2}\right)\right]e^{\pm jn_{in}\phi_s}E_y^1}{\phi_y^2 - \phi_x^2\left(\frac{\rho_y^2}{\rho_x^2}\right)} \qquad (6)$$

$$E_z^2 = e^{\pm jn_{in}\phi_s}E_z^1$$

where $\rho^1_{(x,y)}, \phi^1_{(x,y)}$ and $\rho^2_{(x,y)}, \phi^2_{(x,y)}$ are the components of the polar unit vectors at face 1 and 2, respectively. Expression (6) can be used directly to assemble degrees of freedom on face 1 in favor of degrees of freedom on face 2.

3.1 Boundary conditions along axis.

Since the hybrid FEM-Modal formulation as shown in Figure 1 makes use of an absorbing layer to truncate the mesh, the space between the engine face and the absorber must include the axis of the guide where the phase boundary condition cannot be defined. In practice, boundary conditions on the axis must be imposed differently for each modal excitation. First, consider the behavior of the modes on the axis as shown in Table 1. Since it was previously noted that mode coupling does not occur to modes having $n_{out} = n_{in} \pm 1$, there will never be a mode from column 1 and column 2 which exist concurrently. If a mode included in column 1 is present, i.e. n_{in} *modulo* $N_s = 0$, then the boundary conditions to be enforced on the axis are $E_x = E_y = 0$ which is consistent with all possible scattered modes. If a mode from column 2 is present, i.e. $(n_{in} \pm 1)$ *modulo* $N_s = 0$ then the boundary condition $E_z = 0$ is enforced. If all scattered modes are such that $n_{out} > 1$, then the conditions $E_x = E_y = E_z = 0$ are imposed.

4.0 Example

As an example, an inlet terminated in a short with radius of 0.66λ is analyzed by using only a 4 degree slice of the original problem. The absorber is placed 0.5λ from the short and the connectivity boundary (where the scattering matrix is calculated) is located 0.25λ from the short. The calculated scattered fields on the slice boundary for two modal excitations as depicted in Figure 3 are seen to have the correct behavior everywhere including the axis. When calculating the scattering matrix, this termination should simply generate a diagonal matrix with each mode having a reflection coefficient of -1. The errors in our calculations using a 4 degree slice are given in Table 2 for the first five modes. These errors are within acceptable ranges for

finite element implementations and are mainly attributable to the finite reflections from the absorber used to terminate the mesh.

MODE	n=0	n=1	n>1
TE E_x, E_y	$= 0$	$\neq 0$	$= 0$
TE E_z	$= 0$	$= 0$	$= 0$
TM E_x, E_y	$= 0$	$\neq 0$	$= 0$
TM E_z	$\neq 0$	$= 0$	$= 0$

TABLE 1. Behavior of modes on axis

Mode	TM_{01}	TM_{11}	TE_{01}	TE_{11}	TE_{21}
% error	-0.99%	-5.77%	+.12%	+2.35%	-.06

TABLE 2. Error in the calculated reflection coefficients for an inlet terminated in a short, using a 4 degree slice.

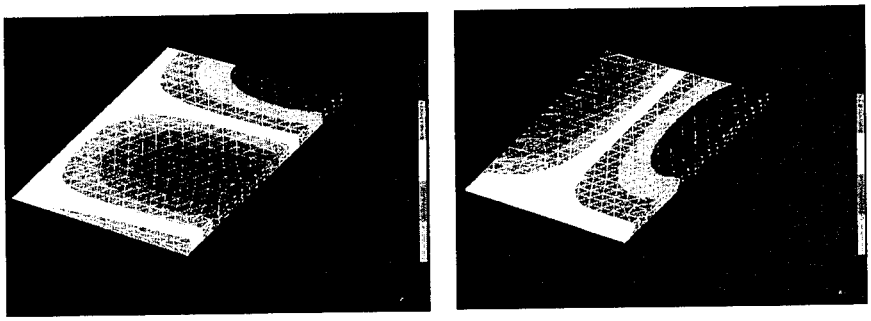


FIGURE 3. Calculated scattered field $Re\,(E_\theta)$ for TM_{01} (left) and TE_{11} (right) excitation of a shorted inlet using a four degree slice. Observe correct behavior of field along axis where phase boundary condition is not defined.

5.0 Limited Mode Model

The overlapping geometric and angular symmetry of the jet engine scattering problem can also be exploited within an integral equation approach termed, the Limited Mode Model (LMM).

At the heart of this method is a limited eigenfunction expansion of the dyadic Green's function for the interior of a cylindrical waveguide. Under single mode excitation, the dyadic Green's function becomes a singly (not doubly) infinite series, making its computation highly efficient.

To begin, consider the general case of a metal obstacle within a cylindrical waveguide aligned with the z axis. The unknown induced electric current $\bar{J}(\bar{r}')$ on the surface Ω of the obstacle due to the excitation $\bar{E}^{inc}$ can be found by

$$\oint_{\Omega} \bar{E}^{inc}(\bar{r})\, ds = -\oint_{\Omega} \bar{\bar{G}}(\bar{r}/\bar{r}') \cdot \bar{J}(\bar{r}')\, ds' \tag{7}$$

The dyadic Green's function for the cylindrical waveguide can be represented as an eigenfunction (modal) expansion[5] which includes all waveguide modes traveling in either direction away from the source, viz.

$$\bar{\bar{G}}(\bar{r}/\bar{r}') = -\frac{1}{2}\sum_{n=-\infty}^{\infty}\sum_{p=0}^{\infty}\{\bar{E}^{+/-}_{TE_{n,p}}(\bar{r})\,\bar{E}^{-/+}_{TE_{n,p}}(\bar{r}') + \bar{E}^{+/-}_{TM_{n,p}}(\bar{r})\,\bar{E}^{-/+}_{TM_{n,p}}(\bar{r}')\} - \frac{\hat{z}\hat{z}}{j\omega\varepsilon_0}\delta(\bar{r}-\bar{r}') \tag{8}$$

The superscript + indicates that a mode is traveling in the +z direction($\bar{E}^{+} \propto e^{-j\beta(z-z')}$), and the superscript - corresponds to a mode traveling in the -z direction ($\bar{E}^{+} \propto e^{+j\beta(z-z')}$). The upper signs are for the case $z > z'$ and the lower signs are for the case $z < z'$.

The performance of (8) is known to be poor due to the extremely slow convergence of the dyadic Green's function. However, if we specialize the solution to obstacles with discrete angular symmetry, the doubly infinite summation in (8) reduces to a singly infinite summation since only discrete values of n are present in the expansion of the scattered field as given by (3).

An additional simplification to the computation is introduced by expanding the current as

$$\bar{J}_{i,n}(\bar{r}') = \sum_{i=1}^{N_i} I_{i,n}\bar{J}_i(\bar{r}')\, e^{jn\phi} \tag{9}$$

and using testing functions of the form

$$\bar{J}_{j,m}(\bar{r}) = \overline{\bar{J}^{*}}_{i,n}(\bar{r}') = \bar{J}_j(\bar{r}')\, e^{-jm\phi} \tag{10}$$

where m and n each take on every possible limited mode index independently.

The most difficult aspect of the formulation is the singularity of the dyadic Green's function. Unlike the free space Green's function, this singularity is expressed as a divergent series. There are three techniques for handling the singularity of the dyadic Green's function: move the observation contour slightly, use a partial summation technique, or find an analytic function expressible as cylindrical waveguide modes that can be subtracted from the divergent series, numerically integrated and the added back in and analytically integrated. It will be demon-

strated that only the last technique will result in a viable method although this has not been accomplished to date.

It will be shown how the limited mode model requires far less computation than the FEM implementation even though a dense system of equation results (see Figure 4), does not require a phase boundary condition, and most importantly, requires only a surface mesh, not a volume mesh. These attractive points give some motive for finding an analytical extraction of the dyadic Green's function singularity.

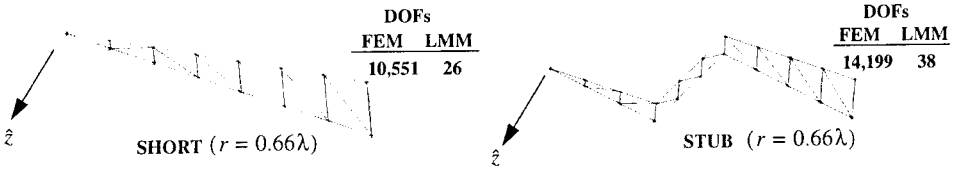


FIGURE 4. Domain of solution for LMM and comparison of numbers of degrees of freedom in FEM to LMM.

6.0 Conclusions

Phase boundary conditions can be used to exploit the symmetry within an FEM solution of a jet engine inlet cavity terminated by an angularly periodic structure (such as the front frame or a compressor section) provided that a special set of boundary conditions is applied along the axis where the phase boundary condition is not defined. The implementation of the phase boundary condition within a three-dimensional FEM solution has been validated and the scheme can now be used within a broader implementation with the goal of characterizing real engines. As a consequence of the limited mode phenomenon, an alternative scheme based on an integral equation, dyadic Green's function approach was introduced. This scheme has the desirable quality of requiring only a surface mesh (instead of a volume mesh) and requiring no phase boundary conditions since the angular variation of the solution is built directly into the method. However, to be complete, this method still requires the analytical extraction of the dyadic Green's function singularity.

REFERENCES

[1] D.C. Ross, J.L. Volakis and H.T. Anastassiu, "Hybrid Finite Element-Modal Analysis of Jet Engine Inlet Scattering", To appear in *IEEE Trans. Antennas and Propagation.*

[2] Robert Lee and Tse-Tong Chia, "Analysis of Electromagnetic Scattering from a Cavity with a Complex Termination by Means of a Hybrid ray-FDTD Method", *IEEE trans. Antennas and Propagation*, Vol. 41, No. 11, pp. 1560-1569, Nov. 1993

[3] E.M. Nelson, "A Finite Element Formulation for Multipole Modes in Axisymmetric Structures", *Proceedings of the 10th Annual ACES Conference*, 1994, pp. 152-158.

[4] A. Frenkel, J.R. Brauer and M.A. Gockel, "Complex Periodic Boundary Conditions for AC Finite Element Models", *Proceedings of the 10th Annual ACES Conference*, 1994, pp. 195-202.

[5] C.T. Tai, *Dyadic Green Functions in Electromagnetic Theory*, Second Edition, IEEE Press, Piscatawnay, NY. 1994.

SESSION 22:

ACCURACY ESTIMATION IN ELECTROMAGNETIC MODELING

Chair: S.M. Wandzura

ASSESSING THE INFLUENCE OF COEFFICIENT ACCURACY, MATRIX CONDITION NUMBER, SIZE AND TYPE, AND COMPUTER PRECISION ON MATRIX-SOLUTION ACCURACY

E. K. Miller, Stocker Visiting Professor
Ohio University, Athens, OH 45701, 614-593-1603

ABSTRACT
Matrices occupy a central role in most physical modeling. As the size of matrices being solved increases, it is becoming more important to quantify what factors influence the accuracy of the final result. The condition number (CN) of a matrix is an important controlling factor in limiting the solution accuracy, the effect of which can be circumvented by increasing the precision of the computations. This typically involves going from single to double precision, e.g., going from 64-bit to 128-bit word size. But the number of unknowns, the accuracy to which the original matrix coefficients are obtained, and the accuracy to which the right-hand-side is known also affect the final result.

This discussion reports results from some ongoing computer experiments that are being conducted with the goal of acquiring some insight into such questions. The computations are performed using a compiled BASIC language (Future Basic) that permits varying the computer precision up to 240 digits (or more) through a simple configuration command. By also varying the matrix size, the accuracy to which the original matrix coefficients are computed and the matrix type and condition number, some quantitative guidelines might be developed concerning the influences of these factors on solution accuracy. One result that is obtained, not new in this study but which is consistent with previous findings, is that with the solution accuracy, SA, the computation precision, P, and CN, all expressed in digits, their relationship can be expressed as $P - CN \leq SA$ where CN is one of the estimates commonly used, such as the ratio of maximum-to-minimum singular values, and when $CA \sim P$ is the coefficient accuracy. Thus, even for a condition number of 10^{100}, it is possible to obtain approximately X digits of solution accuracy if P and CA are increased to ~100 + X digits. When the coefficient accuracy of the original matrix is taken into account, possibly being less than P, the above result becomes, for the matrices studied, $CA - CN \leq SA \leq CA$, i.e., coefficient inaccuracy can counter any benefit otherwise derived from increasing the compute precision and vice-versa if CA is not commensurately increased. The results obtained thus far will be reviewed and their implications for computational electromagnetics (CEM) will be discussed.

INTRODUCTION
Matrices arise in myriad ways in mathematics, the physical sciences and many other areas of human activity such as economics, one example of the latter being financial applications where spreadsheets applications have become ubiquitous. Matrices are found useful because they provide a way of expressing multi-variable relationships, those where an outcome, or set of outputs, depends on a weighted combination of inputs. In the most general sense, these relationships might be compared to the state-transition matrices used in system analysis. Although that term is usually associated with time-dependent problems, any problem where a convolution relationship occurs can be described in an equivalent fashion. Such matrices comprise the connection between the state variables, which are the independent variables for a given problem, and the system state, or state vector, which is the set of outputs. In CEM problems, where the usual notation has $[Z]\cdot I] = V]$ and $I] = [Y]\cdot V]$, the input vector is (usually) the exciting field, the output vector is the set of induced sources, and the state variables are the spatial (and sometimes temporal) problem variables that determine the system matrix [Z] whose solution

(inverse) is [Y]. A CEM matrix represents, in a sampled, discretized, and approximated form, the electromagnetic physics of the problem being modeled, and as such must contain all the information needed for the subsequent solution if physically valid results are to be obtained.
It's worth noting that the CEM model could at best provide an exact solution to a rigorously described physical problem but most often introduces physical and numerical modeling errors. Even if an exact (or arbitrarily accurate) numerical solution were to be obtained to the CEM model, a physical modeling error arises because that model is an approximate representation of the physical problem. Beyond that, an exact numerical solution is rarely accessible adding a further numerical modeling error to the computed results. The "art" of numerical modeling involves reaching appropriate tradeoffs between the various factors that affect these modeling errors, foremost of which is the number of samples or unknowns, N, and the sampling dimensionality relative to the problem dimensionality.

In computational applications, the matrix is represented as a set of numerical coefficients, of which there are N^2 for an N'th-order matrix. When most of these coefficients are zero, as is the case for differential-equation (DE) models, the matrix is said to be sparse, whereas when all of the coefficients are nonzero, as happens for integral-equation (IE) models, the matrix is described as dense, or full. In the trivial case where the matrix has only nonzero's on the diagonal, interactions between the outputs is zero and the matrix is solvable algebraically in at most N operations as is the case for FDTD (Finite-Difference Time Domain). Otherwise, a general solution independent of the input, or right-hand side (RHS), generally requires an operation count (OC) that varies between N^2 and N^3 depending on the matrix structure and coefficient count. RHS-dependent solutions can similarly be achieved with OCs that vary from KN to KN^2, where K depends on a variety of factors including the matrix structure and can also depend on N.

A common ingredient to contend with whenever seeking a solution of a matrix is how well-conditioned, or conversely, how ill-conditioned that matrix may be. A well-conditioned matrix has, by convention, a CN that is near unity, whereas a matrix whose condition number is 10^{100} would be regarded as extremely ill conditioned. The CN indicates how sensitive the output vector will be to errors in the input vector or to errors in the matrix coefficients themselves. Other equivalent statements concerning matrix conditioning are the degree to which any errors or uncertainties are amplified in the solution process, or the degree to which information is lost between problem description and problem solution. A conventional numerical statement relating the CN(Z) for matrix [Z] and solution errors is that

$$\frac{\|\delta I\|}{\|I\|} \le CN(Z)\frac{\|\delta Z\|}{\|Z\|} \text{ or } \frac{\|\delta I\|}{\|I\|} \le CN(Z)\frac{\|\delta V\|}{\|V\|},$$

where ||--|| signifies some suitable norm. A larger CN implies that a more accurate problem description will be needed accompanied by higher computation precision in order to maintain a specified solution accuracy.

Clearly, the coefficients that comprise a matrix represent a collection of information that is transformed during the solution process to a different, but equivalent, collection of information to the extent that no information is lost during the solution process. The process of inverting a matrix can at best preserve, but not add, information to the problem. More often, information might be expected to be lost. In this article we explore some ramifications of solving matrix-based problems in terms of how solution accuracy might be related to the information content of the matrix being solved. In the following, we describe the experimental methodology and the error measures employed, summarize some matrices that might provide useful test cases, and present some preliminary results.

EXPERIMENTAL METHODOLOGY

It is generally very difficult to deduce analytically the numerical behavior of arbitrary matrices. Instead, aside from a few special cases some of which are cited below, it is necessary to perform computer "experiments" designed to elicit trends and patterns about the expected behavior of problems of interest.

The overall strategy used here is to "track" information flow from an original matrix to its solution. Several experimental matrices have been extracted for this purpose from *A Collection of Matrices for Testing Computational Algorithms* by Gregory and Karney (1969) which includes a collection of matrices having CN's whose solutions are analytically expressible and some of whose inverses are also available in analytical form . Others were created specifically as candidates whose CN's could be varied parametrically. First we discuss various accuracy metrics of matrix solution accuracy.

Assessing Solution Accuracy

There are numerous ways to quantitatively assess the accuracy of any numerical solution. When the specific problem involves solving matrices, some of the possibilities include:

1) Comparing true, $[Y_t]$, and computed (approximate), $[Y_a]$, inverses. When the inverse of a test matrix is known either analytically or can be computed to high accuracy compared with that expected in a given experiment, then this "true" inverse can be used to determine the accuracy of the computed inverse.

2) Comparing the product of $[Z_t]\cdot[Y_a]$ with [I], the identity matrix. Since the product of the original matrix and its inverse should equal the identity matrix, their difference provides a measure of the inaccuracy in $[Y_a]$.

3) Comparing solutions for specified RHS's. This test would involve comparing $[Y_t]\cdot R]$ with $[Y_a]\cdot R]$, where R] is a RHS test vector, where many different RHS's could be used. For the specific RHS's given by successive unit vectors, the test would become 1) above.

4) Comparing $[Z_t]$ with $[Y_a]^{-1}$. Inverting $[Y_a]^{-1}$ would produce $[Z_t]$ in the absence of error and so provides a measure of the solution accuracy that results from the two inversion operations.

5) Comparing the eigenvalue (EV) or singular value (SV) spectra of $[Z_t]$ and $[Z_a]$, where $[Z_a]$ is an approximate representation of $[Z_t]$ due to truncating the coefficients of the latter, or of $[Y_t]$ and $[Y_a]$, respectively.

For the results presented here, the SA and other metrics are presented as digits of agreement between a reference and a test result on a per-coefficient basis. For example, in using test (2), we compute $[D] = [Z_t]\cdot[Y_a] - [I]$ where [D] is a difference matrix, and then find $d_{ave} = \Sigma d_{ij}/N^2 = -[\Sigma \log_{10}(D_{ij})]/N^2$, i,j = 1,...,N for an NxN matrix and where, if $D_{ij} = 0$, d_{ij} is set to the compute precision P used for that computation. Using a digits measure, furthermore, is logical from the perspective of information theory as the "information content" represented by a specific outcome can be expressed as a logarithmic measure of the set of all possible outcomes in units of bits or digits. Thus, the quantitative results presented below for SA can be interpreted as the accessible information in Z_t that appears in a Y_a derived from it. Two SA metrics are employed here, one $SA_d = Y_t - Y_a$ (the "difference" metric) and the other $SA_p = Z_t Y_a - I$ (the "product" metric). When SA_d is less than the P or CA, the implication is that the actual information content of Z_t must be less than N^2P due to some degree of linear dependency among the equations which comprise it, or equivalently that information is lost as a result of roundoff in the solution process. It seems obvious to conclude that the information content of Y_a not only cannot exceed that of

Z_t but that the information finally obtained in Y_a actually defines the accessible information content of Z_t. Also observe that as equation linear dependence increases, the information-carrying digits move further to the right in each coefficient so that a given number of digits in the coefficients in Z_t then represents less actual information. Although there seems to be no obvious reason for SA_d to be much different from SA_p, the results obtained here show that substantial differences can exist with the latter generally exceeding the former.

Candidate Test Matrices

A variety of matrices that might be used for the kinds computer experiments reported here are listed below. Also included are their condition numbers and inverses, if analytically known. Unless otherwise stated, the coefficient indices are summed from 1 to N, where N denotes the matrix order. All analytic results for CN's and matrix inverses are from Gregory and Karney (1969).

—Hilbert matrix: $z_{i,j} = \dfrac{1}{(i+j-1)}$.

This matrix has a CN of order $10^{1.5N}$, and so represents a challenging problem for larger N for testing matrix-solution algorithms, but unfortunately the CN cannot be varied independent of N. The Hilbert matrix has an analytic inverse given by

$$y_{i,j} = \frac{(-1)^{i+j}(N+i-1)!(N+j-1)!}{(i+j-1)[(i-1)!(j-1)!]^2(N-i)!(N-j)!}.$$

—Lotkin matrix: $z_{1,j} = 1,\ j = 1,\ldots,N,$

$$z_{i,j} = \frac{1}{(i+j-1)},\ i = 2, 3, \ldots,N,\ j = 1,\ldots,N.$$

The Lotkin matrix CN is of order $10^{1.5N}\log(N)$, similar to that of the Hilbert matrix to which its coefficients are identical except for the first row. Its inverse is also known analytically and is given by

$$y_{i,1} = (-1)^{N-i}\binom{N+i-1}{i-1}\binom{N}{i},\ i = 1,2,\ldots,N,$$

$$y_{i,j-1} = (-1)^{i-j}\binom{i+j}{j}\binom{i+j-1}{j-1}\binom{N+i-1}{i+j}\binom{N+j}{i+j}i,\ i = 1,2,\ldots,N,\ j = 1,2,\ldots,N-1.$$

--Matrix of random numbers:

$z_{i,j} = x_r$, for $0 \le x_r \le 1$ or $-1 \le x_r \le 1$ with x_r uniformly distributed.

The CN of a random matrix evidently is not derivable analytically, but the geometric mean of the CN's of a large collection of real square matrices of normally distributed random numbers has been determined to be of order 4.65N [Edelman (1989)].

--Matrix of random numbers with last Nll equations nearly parallel:

$z_{i,j} = x_r,\ i = 1,2,\ldots,N\text{-}Nll;\ z_{i,j} = 10^{-y}x_r + (1\text{-}10^{-y})z_{i-1,j},\ i = N\text{-}Nll+1,\ldots,N.$

This matrix is generated to have Nll equations whose degree of linear dependence is determined by the parameter y, and produces a singular-value CN ~10^y, where the number of small singular values is Nll - 1. Varying Nll and y provides a way to tailor the eigenvalue spectrum and also to vary the CN.

--Unitary matrix of random numbers:

$z_{i,j} = 1. + x_r,\ i = 1,2,\ldots,N\text{-}Nll;\ z_{i,j} = 1. + 10^{-y}x_r,\ i = N\text{-}Nll+1,\ldots,N.$

We might anticipate that the CN of such a matrix would also be of order 10^y since information about coefficient differences is approximately y digits to the right of the decimal. The eigenvalue spectrum of this matrix can also be varied through the values chosen for N|| and y and letting y be a function of i.

--The Rump matrix:

A class of very ill-conditioned matrices, having CNs varying from 10^{30} to 10^{164}, and exactly representable in floating-point arithmetic is described by Rump (1991). The example used here has a CN ~ 10^{44} in a 6x6 matrix and is given by

$$z_{i,j} = \begin{bmatrix} 3257199\cdot 2^3 & 6746489\cdot 2^1 & -8816797\cdot 2^0 & 1247053\cdot 2^5 & 13508351\cdot 2^3 & -14061827\cdot 2^2 \\ 1247053\cdot 2^4 & 13508351\cdot 2^2 & -14061827\cdot 2^1 & 3527199\cdot 2^3 & 6746489\cdot 2^1 & -8816797\cdot 2^0 \\ 1 & -2^{24} & 0 & 0 & 0 & 0 \\ 0 & 1 & -2^{24} & 0 & 0 & 0 \\ 0 & 0 & 0 & 1 & -2^{24} & 0 \\ 0 & 0 & 0 & 0 & 1 & -2^{24} \end{bmatrix}$$

--Diagonal, unitary matrix: $z_{i,j} = 1.$ for $i \neq j$; $z_{i,i} = 1. + 10^{-y}$.

Again, this matrix could be expected to have a condition number of order 10^y and its eigenvalue spectrum varied by letting y be a function of i.

—Binomial, lower–triangular matrix: $z_{i,j} = (-1)^j \binom{i-1}{j-1}$ for $j \leq i$, $z_{i,j} = 0$ otherwise.

This matrix has a CN ~ exp(4Nlog2) and its inverse is equal to the original matrix.

--Circulant matrix of random numbers:
$c_{1,j} = x_j$, $c_{i,j} = c_{1,j'}$, where $j' = N-i+1+j$ (-N is $j' > N$)

--Toeplitz matrix of random numbers:
$c_{1,j} = x_r$, $c_{i,1} = x_r$; $c_{i,j} = c_{i-1,j-1}$, $i,j = 1, \ldots, N$

Condition-Number Estimates

A variety of CN measures have been employed to test matrix ill-conditioning. Gregory and Karney (1969) discuss several, some of which are summarized below. Perhaps the most widely used CN estimates employ the ratio of maximum to minimum EV's, λ, or singular values SV's, w, of the given matrix, as expressed by

$$CN_{ev} = \frac{\max_i |\lambda_i|}{\min_i |\lambda_i|} \text{ and } CN_{sv} = \frac{\max_i |w_i|}{\min_i |w_i|}.$$

Two other CN's discussed by Gregory and Karney are

$$CN_{max} = N \cdot \max_{i,j} |z_{i,j}| \cdot \max_{i,j} |y_{i,j}| \text{ and } CN_{norm} = \frac{1}{N} \|[Z]\|_E \cdot \|[Y]\|_E,$$

where $$\|[Z]\|_E = \left[\sum_{i=1}^{N} \sum_{j=1}^{N} z_{i,j}^2 \right]^{1/2}.$$

It is observed by Gregory and Karney that CN_{ev}, CN_{sv} and CN_{norm} do not differ much from CN_{max} and, in particular [Taussky and Todd (1952) and Westlake (1968)] that

$$\frac{1}{N^2}CN_{max} \le CN_{norm} \le CN_{max} \text{ and } CN_{ev} \le N \cdot CN_{max},$$

and where, for symmetric matrices,

$$\frac{1}{N}CN_{max} \le CN_{ev}.$$

They further mention that for random matrix elements from a normal population, $CN_{max} \sim [N]^{1/2}\log(N)$ and $CN_{norm} \sim [N]^{1/2}$. These values are more optimistic than the result obtained by Edelman from his computer experiments where $CN_{ev} \propto N$. Finally, they observe [see for example Golub and Van Loan 1983)] that the estimate

$$CN_{Kinf} = \| [Z] \| \cdot \| [Y] \| = Kinf$$

known as the K_{inf} CN is more often used where the norms for [Z] and [Y] are not necessarily the same. Here, we use [Golub and Van Loan (1983)]

$$Kinf = \max_i \sum_j | z_{i,j} | \cdot \max_i \sum_j | y_{i,j} | .$$

Among the vector norms that have been employed are the p-norm

$$\| I] \|_p = (|I_1|^p + |I_2|^p + \cdots + |I_N|^p)^{1/p}$$

which for p = 1 or 2 is called the l_1-norm and the Eucledian or l_2-norm, respectively, and the infinity-norm

$$\| I] \|_\infty = \max_j |I_j|.$$

Two other examples of matrix norms are given by

$$\| [Z] \| = \max \frac{\| [Z] \cdot x] \|}{\| x] \|} \text{ and } \| [Z] \| = \max_{\|x\|=1} \| [Z] \cdot x] \| .$$

Of the CNs above, CN_{Kinf} and CN_{sv}, CN_{ev} have been used in our experiments. A possibly more relevant *a posteriori* estimate of the effective CN of a matrix might be provided by determining the accuracy actually achieved in solving the matrix as compared with the "true" result as mentioned above. The difference between the computed and true results, from which SA is found, can also directly provide an estimate for CN by simply determining the difference between P and SA. This approach has also been employed in the following computations with the result denoted as CN_{eff}. Note that all results presented in units of digits are on a per-coefficient basis. For example, in comparing two values for a matrix, Y_t and Y_a, the total digits of agreement between their N^2 coefficients is divided by N^2 to obtain a normalized per-coefficient results. The SVInt was evaluated by assuming a "precision floor" exists P digits below the largest SV and summing the number of digits contributed by each SV relative to this floor.

NUMERICAL RESULTS

Experiments were conducted with many of the matrices outlined above, but results are presented here for just a few of these, the Hilbert matrix, the random matrix with Nll nearly parallel equations, and the Rump matrix.

The Hilbert Matrix (HM)

Because of the high condition number it yields for relatively few equations, the HM provides a useful test case for studying conditioning effects. Computations using the HM were performed as a function of P, N, and CA. Results for SA are presented SA in Fig. 1 as a function of CA with N a parameter and with P = 64 digits. It can be seen than the SA for each metric declines linearly with decreasing CA, but that the difference between them increases progressively as N gets larger. The curves in Fig. 2 exhibit the product metric and integral of the singular-value spectrum (SVInt) for the HM for CA = P as a function of N. The slope of SVInt is about one-half that of the SA product metric, with the former decreasing as 1/2N and the latter as 1/N, so that approximately

$$\text{SVInt} \sim P - N/2 \text{ digits and } SA_p \sim P - N = \text{SVIntx} - N/2 \text{ digits.}$$

Random Matrix (RM)

Similar computations were conducted for a matrix consisting of random numbers uniformly distributed between -1 and +1 with Nll and CA systematically varied and with P = 48 digits. Note that for this problem, increasing Nll plays the same role as increasing N for the HM in terms of increasing the CN. Results are presented in Fig. 3 for the difference and product metrics as a function of CA for Nll having the values 0, 6, 11, 16, 21, 26 and 30, and with y = 10. Results obtained here exhibit some distinct differences from the HM. Although the SA decreases linearly in proportion to the CA, the two metrics behave quite differently. For Nll = 0, where the CN is near unity, both metrics are close to the CA. However, when Nll has a non-zero value, the difference metrics are nearly equal independent of the specific value of Nll and are given by $SA_d \sim CA - CN$. The product metrics, on the other hand, are given by $SA_p \sim CA - (Nll/N)CN$. Results for SVInt and SA_p as a function of Nll are shown in Fig. 4 for P = CA = 24, where it can be seen that these metrics are nearly equal as Nll is increased, varying with N approximately as $SA_p \sim P - (Nll/N)y \sim$ SVInt digits. Thus, on the basis of these two quite different cases, we might tentatively conclude that SVInt and SA_p satisfy a relationship like $\text{SVInt} - N/2 \leq SA_p \leq \text{SVInt}$ which encompasses a very broad range of values.

Condition Numbers and Singular Values

It is instructive to examine the behavior of some of the CNs mentioned above for the HM and RM as the ill-conditioning of these matrices is increased, as included in Figs. 5 and 6. For both matrices the Kinf CN is the largest, while CN_{eff}, as determined by $P - SA_p$, is the smallest, with CN_{sv} lying in between. Most interesting is the fact that for the RM and with Nll = 2 and y = 10, which produces one small singular value, CN_{eff} is little different from that for Nll = 0 whereas Kinf and CN_{sv} are nearly equal to their maximum values for this case. As Nll is increased, CN_{eff} increases ~ (Nll/N)y.

Singular-Value Spectra for the Hilbert and Rump Matrices

If the SVs (or EVs) of a matrix are found to decrease monotonically out to some point and then to stabilize at a nearly constant value, this result may be indicative of reaching a computation "noise" or precision floor. An example of this is shown in Fig. 7 where the SVs of a Hilbert matrix of N = 30 are plotted with the CA a parameter which ranges from 8 to 40 digits and with P = 64 digits. The spectrum for each value of CA becomes essentially constant at the x'th SV and beyond when SV_{max}/SV_x (in digits) approximately equals CA.

A quite different result is shown in Fig. 8 where the SVs of the N = 6 Rump matrix and of two RMs,

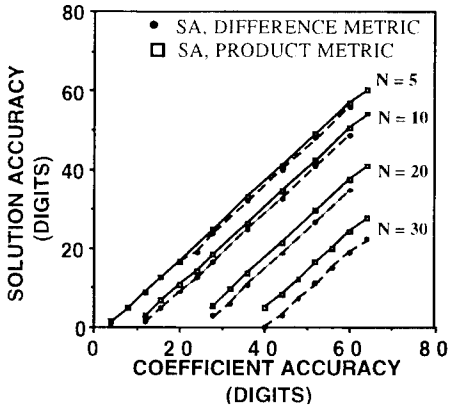


Fig. 1. Solution accuracy for Hilbert matrices of size N as a function of coefficient accuracy. Solid circles are for the difference metric and the open squares are for the product metric of SA.

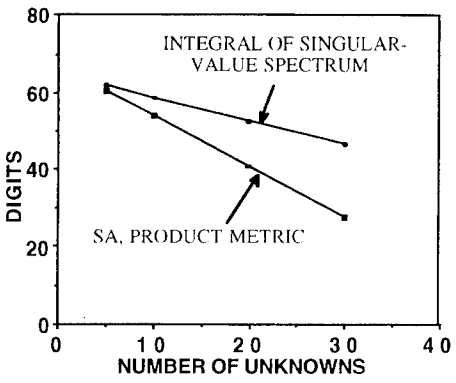


Fig. 2. Integral of the SV spectrum and SA product metric as a function of size for the Hilbert matrix for P = 64 digits. SA varies approximately as 1/N while SVInt varies as 1/2N.

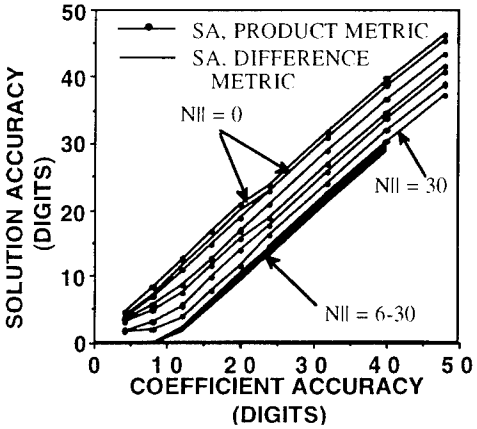


Fig. 3. Solution accuracy as a function of coefficient accuracy for matrix of random numbers with number of nearly parallel equations (first ten digits equal) a parameter.

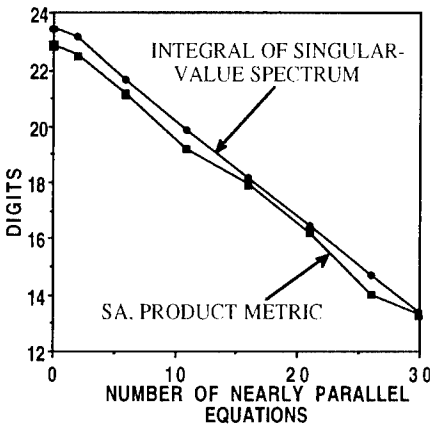


Fig. 4. Integral of SV spectrum and SA product metric as a function of Nll for a matrix of random numbers. Both the SA and SVInt vary approximately as 1/Nll.

also of N = 6, are plotted. The RMs each had Nll = 2 with y = 44, chosen to approximate the behavior of the Rump matrix whose CN is about 10^{44}. The first used normalized coefficients while the

coefficients of the second were multiplied by the magnitude of the largest coefficient of the Rump matrix to equilibrate their SV spectra. Although the SV spectra for the Rump matrix and the second RM are nearly identical, the behavior of their respective SA metrics were found to be much different. The RM exhibits a dependence on CA like that already shown in Figs. 3 and 4 whereas the Rump matrix seems much more sensitive to CA in a fashion similar to the HM as is shown in Fig. 9. Apparently matrix structure or coefficient pattern, which is much more organized in the case of the HM and Rump matrix than is the case for the RM, has an influence that is not revealed by CN or SV spectra alone.

Solution Accuracy and Singular-Value Integrals

The SVInt and SA were shown above to be related above for the HM and RM although in significantly different ways, where for the HM we found $SA_p \sim SVIntx - N/2$ digits while for the RM we had $SA_p \sim SVInt$ digits. It is informative to see how these SA metrics and SVInt's depend on CA for the HM and RM, some results for which are shown in Figs. 10 and 11 respectively. There we observe that the close correlation between the SVInt and SA is maintained for the RM with N = 30 for NII = 0 and NII = 30, where using y = 10 in the latter case produces a $CN_{eff} \sim 10^{10}$. For the HM, on the other hand, the SA and SVInt, while also showing a linear dependency on CA, are increasingly different from each other as N increases with the SVInt always being larger. Thus, the SVInt appears to provide a meaningful measure for the expected SA of a RM over a wide variation of CNs while for the HM the SVInt differ from the SA by an amount dependent on N, hence dependent on the CN. In both cases, the SA is less than the CA by an amount that defines the effective CN.

CONCLUDING COMMENTS

Perhaps the most significant result obtained in this study that is relevant to CEM applications is that coefficient accuracy, CA, must increase in proportion to the matrix condition number, CN, to maintain a desired solution accuracy, SA, all expressed in digits. If the CN of a CEM matrix increases as some function of the number of unknowns, say f(N), then this means that $CA \geq SA + CN = SA + f(N)$. Since N is invariably larger for differential-equation (DE) models except for problems that involve inhomogeneous media, this implies that CA would need to be proportionately larger for DE models, everything else being equal.

Another result worth noting is that the effective CN, i.e., the difference between compute precision, P, and SA may turn out be much less than the standard estimates for CN indicate. A related result is that the product metric for SA, given by $[Z_t]\cdot[Y_a] - [I]$, generally always exceeds that obtained from the difference metric, $[Y_t] - [Y_a]$, where the subscripts "a" and "t" denote the true and approximate values of the original (or [Z]) and inverse (or [Y]) matrices. This result might be explained by noting that each coefficient in the product metric $[Z_t]\cdot[Y_a]$ comes from N multiplies and additions with the possibility that errors in individual coefficients will cancel while those in the difference metric $[Y_t] - [Y_a]$ are individually accounted for.

Finally, we note that an integral of the singular-value (SV) spectrum, SVInt, for a matrix whose coefficients are random numbers, even one with two or more nearly parallel equations, yields a result that is close to the achieved SA, when both results are expressed in digits. This is in contrast to what is found for the Hilbert matrix, where the SVInt exceeds the SA by an amount apparently determined by the matrix CN. Even when the CN and SV spectra are essentially identical, as was found for the random matrix and Rump matrix, the dependence of their SA on the CA was found to be quite different. Apparently matrix structure, which is much more ordered for the Hilbert and Rump matrices than for the random matrix, also plays an important role in the SA achieved. Further study will be needed to test these tentative conclusions for a wider variety of matrices, most importantly including actual CEM examples.

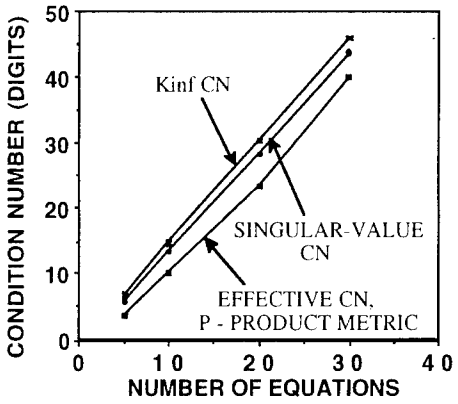


Fig. 5. CNs for Hilbert matrix as a function of matrix size. CN_{eff} is consistently found to be lowest while Kinf is highest, with all increasing with matrix size, as expected.

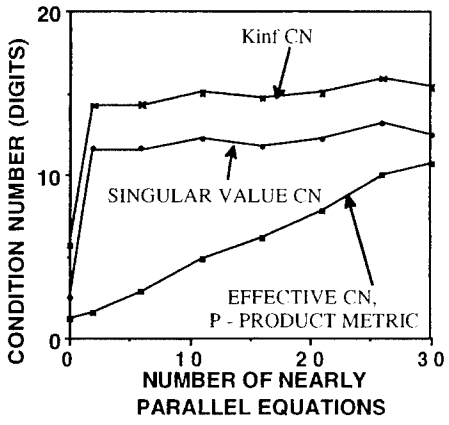


Fig. 6. CNs for random matrix as a function of Nll. While Kinf and CN_{sv} both become large with Nll= 2, CN_{eff} starts at a small value and increases monotonically with Nll.

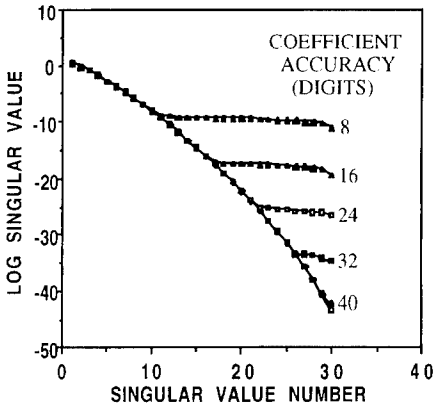


Fig. 7. SV spectra for N = 30 Hilbert matrix with coefficient accuracy a parameter with P = 64 digits. As the spectrum falls to the floor defined CA, it then stabilizes at a nearly constant value.

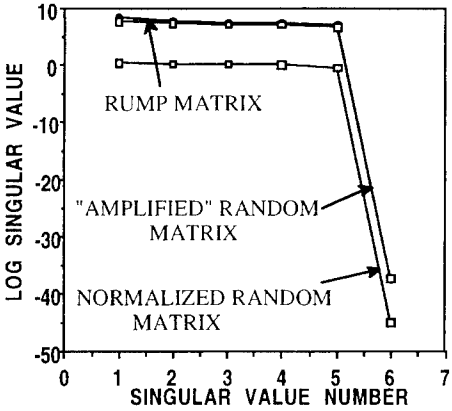


Fig. 8. SV spectra for the Rump matrix and for a random matrix having Nll = 2 with y = 44 digits with N = 6 for both. The coefficients of the "amplified" RM are multiplied by the magnitude of the Rump matrix largest coefficient to equalize their maximum SVs.

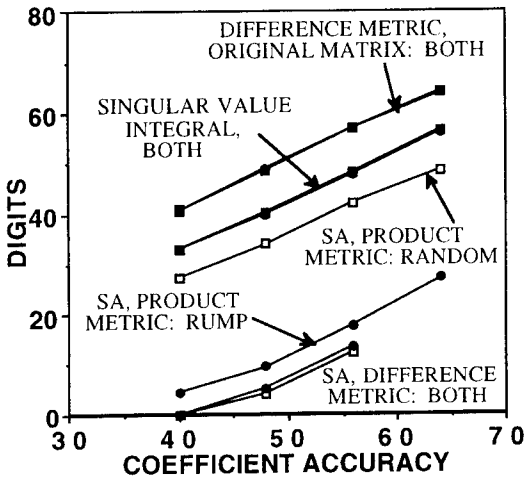


Fig. 9. SVInt and SA metrics for the N = 6 Rump and random matrices as a function of CA. The upper curves displays the difference metric for the true and approximate original matrices while the next shows the SVInt for both, with nearly identical results for each matrix. The difference metrics for SA of both matrices are very similar but their product metrics are very different.

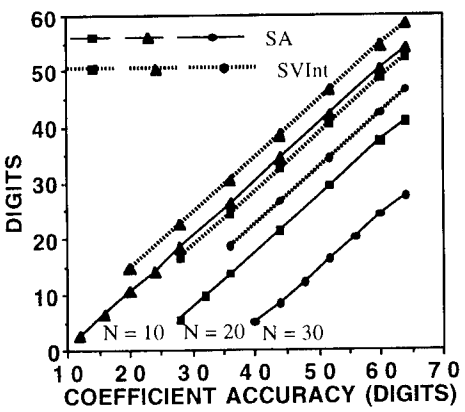


Fig. 10. SA_p and SVInt as a function of CA for Hilbert matrix of variable N. Triangles, squares and circles are for N = 10, 20 and 30 respectively, while dotted lines depict SVInt and solid lines depict SA_p.

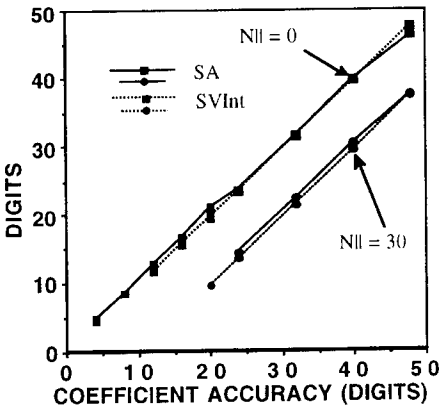


Fig. 11. SA_p and SVInt as a function of CA for an N = 30 random matrix of variable Nll. Solid squares are for Nll = 0 and solid circles are for Nll = 30, while dotted lines show SVInt and solid lines show SA_p.

REFERENCES

Edelman, Alan (1989), *Eigenvalues and Condition Numbers of Random Matrices*, PhD dissertation, Massachusetts of Technology, Numerical Analysis Report 89-7.

Golub, G. H. and C. F. Van Loan (1983), *Matrix Computations*, The Johns Hopkins University Press, Baltimore, ISBN 0-8018-3011-7 Pbk.

Gregory, R. T. and D. L. Karney (1969), *A Collection of Matrices for Testing Computational Algorithms*, Wiley-Interscience, New York, ISBN 471-32669-0.

Hamming, R. W. (1962), *Numerical Methods for Scientists and Engineers*, McGraw-Hill, Inc., New York, republished in 1986 by Dover Publications, New York, ISBN 0-486-56241-6.

Lanczos, Cornelius (1956), *Applied Analysis*, Prentice-Hall, Inc., Englewood Cliffs, NJ, republished in 1988 by Dover Publications, New York, ISBN 0-486-65656-X.

Rump, S. M. (1991), "A Class of Arbitrarily Ill-Conditioned Floating-Point Matrices," *SIAM J. Matrix Anal. Appl.*, Vol. 12, No. 4, pp. 645-653.

Taussky, O. and J. Todd (1952), "Systems of Equations, Matrices, and Determinants," Math. Mag., Vol. 26, pp. 71-88.

Westlake, J. R. (1968), *A Handbook of Numerical Matrix Inversion and Solution of Linear Equations*, John Wiley and Sons, Inc., New York.

Numerical Accuracy Issues in Finite Element Frequency Domain Solutions of Radar Scattering Problems

John D'Angelo
C+AES, Inc.

Abstract

This paper discuss issues regarding the numerical accuracy of finite element frequency domain methods for scattering problems. These issues are also pertinent to other partial differential equation (PDE) methods such as finite difference and finite volume. The areas discussed are dispersion error, the order of the approximation function, modeling the singular behavior of the field at sharp corners of perfect electric conductors (PECs), and the convergence criteria of the iterative solvers.

Introduction

Partial differential equation (PDE) methods (finite element, finite difference, and finite volume) are inherently suited for solving large, complex scattering problems. This characteristic is mainly due to their *local* nature, i.e. unknowns in a PDE discretized space are only coupled to neighboring unknowns. The converse is true for method of moment or boundary element techniques, which are *global* methods, where each discretized unknown is coupled to all others. Local techniques result in sparse systems of equations which are computationally efficient in terms of computer memory and floating point operations. This is especially true for problems containing numerous bulk material regions or if a material coating cannot be accurately modeled by a surface impedance approach.

However, with this local nature advantage of PDE's, challenges arise in their numerical accuracy. Dispersion error is a primary concern. PDE methods do not have the advantage of a Green's function, as do global methods, to help maintain phase accuracy in the solution. The wave behavior with a PDE technique is model by a volume discretization and the phase and group velocity of the electromagnetic field solution is numerically dependent on the mesh density, the direction of wave through the mesh, and the order of the approximation function used to model the field unknown. Also, as shown in [1,2], the dispersion error is also dependent on the wavelength size of the scatterer.

Also discussed in this paper is the need for accurate modeling of the singular field behavior at sharp metallic corners, and the level of convergence needed in the iterative solution of finite element frequency methods for RCS calculation.

Analysis

The following is a numerical study of the error in finite element solutions of RF scattering problems. The first numerical experiment will use a two-dimensional, field analysis of the scalar Helmholtz equation

$$\nabla^2\phi + k_0^2\phi = 0 \qquad (1)$$

Here, the finite element method will be used to model a free-space section with a plane wave traveling through it in the -X direction. The finite element solution will then be compared to the exact representation of the plane wave. In (1), ϕ is either the total H field for TE polarization or the total E field for TM polarization (H and E are both Z directed.)

Equation (1) is discretized in finite element form using both first, second and third order approximation functions for comparison. The finite element solutions will be truncated by a second

order Bayliss-Turkel absorbing boundary condition (ABC) [3]. Equation (1) is discretized by first using a weak Galerkin weighting method.

$$\int_V \psi\left(\nabla^2\phi + k_0^2\phi\right)dV = 0 \tag{2}$$

where ψ is the arbitrary weighting function and V is the solution domain. Equation (2) is then integrated by parts

$$\int_V\left[\nabla\psi\cdot\nabla\phi - k_0^2\psi\phi\right]dV - \int_S\left[\psi\frac{\partial\phi}{\partial n}\right]dS = 0 \tag{3}$$

In (3), S is the exterior surface of the finite element solution domain where the Bayliss-Turkel ABC is applied. Here, the forcing function of the plane wave is applied through the ABC - the Bayliss-Turkel ABC can be described by an operator on the scattered field unknown, i.e.

$$\frac{\partial\phi_s}{\partial n} = A\,\phi_s \tag{4}$$

In (4), ϕ_s is the scattered field, $\phi = \phi_s + \phi_i$. ϕ_i is the incident plane wave, i.e., $\phi_i = e^{-jk_0x}$. Using (4) in (3) results in

$$\int_V\left[\nabla\psi\cdot\nabla\phi - k_0^2\psi\phi\right]dV - \int_S\left[\psi A\phi\right]dS = \int_S\left[\psi\frac{\partial\phi_i}{\partial n} - \psi A\phi_i\right]dS \tag{5}$$

To examine the effect of electrical problem size, in this example, the free-space region will be examine for two problem sizes. The first has a length of four wavelengths from one end to the other, the second has a length of ten wavelengths. The model will be first meshed at a rate of approximately 10 nodes per wavelength. To examine the effect of the order of the approximation function, first to third order elements will be used. The element types consist of both triangular and quadrilateral shaped elements. The triangular elements are of the Lagrangian types whereas the quadrilateral are of the Serendipity type. The total number of nodes for each case will be kept nearly constant for the three approximation orders.

For the four wavelength size problem, the total number of nodes is approximately equal to 1300. Figures 1 (a-c) shows the error for the three types of elements. The error is defined here by

$$Error = \left|\phi - \phi_{exact}\right| \tag{6}$$

Table 1 shows the peak error for the three approximations function for this case.

As shown in Table 1, the error decreases dramatically by 6.23 times from first order to second order and 13.4 times from first to third order. This illustrates, as also described in [1,2], that dispersion error is large for first order approximation functions and should be avoided. Second and third order approximation functions prove to be better suited for wave equation problems. Table 2 shows the maximum error for approximately 20 nodes per wavelength (twice the number of elements) for the same problems. Table 2 shows that the error for the first to third approximation functions behaves as $O(h^2)$, $O(h^3)$, and $O(h^4)$, respectively, as theory predicts.

Approximation Function Order	$\max imum \lvert\phi - \phi_{exact}\rvert$
first	0.4439
second	7.1240×10^{-2}
third	3.3141×10^{-2}

Table 1
Maximum error versus Approximation function order for the four wavelength example with denser mesh - ~10 nodes per wavelength

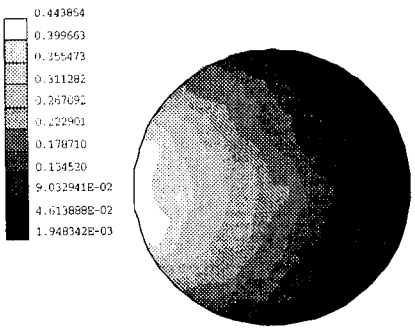


Figure 1 (a)
Error for the four wavelength case using first order approximation functions

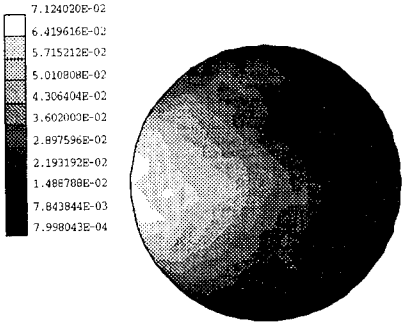


Figure 1 (b)
Error for the four wavelength case using second order approximation functions

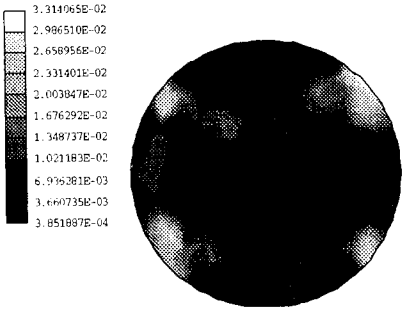


Figure 1 (c)
Error for the four wavelength case using third order approximation functions

Also shown in figures 1(a-b) is the dispersion error is larger in the far end of the solution domain, with respect to the incident field direction, and smaller at the near end. This occurs for the first order and

second order approximation functions, for the third order approximation function the error is evenly distributed. This was also observed in [1].

Approximation Function Order	$\max imum \lvert\phi - \phi_{exact}\rvert$
first	0.1167
second	5.3223×10^{-3}
third	2.3450×10^{-3}

Table 2
Maximum error versus Approximation function order for the four wavelength example with denser mesh - ~20 nodes per wavelength

Another aspect is the error versus problem size. Table 3 shows the maximum error for the ten wavelength case with a discretization rate of approximately 10 nodes per wavelength, showing a marked increase.

Approximation Function Order	$\max imum \lvert\phi - \phi_{exact}\rvert$
first	1.144
second	0.174
third	3.494×10^{-2}

Table 3
Maximum error versus Approximation function order for the ten wavelength example

In figures 2 (a-b) the error is shown for another four wavelength case. Here the outer boundary and mesh is rectangular. The ABC is an Engquist-Majda type [4] and a discretization rate of 10 nodes per wavelength is used with second order elements. Figure 2 (a) has an incident field in the -X direction (0 degrees) and Figure 2 (b) at 45 degrees incident.

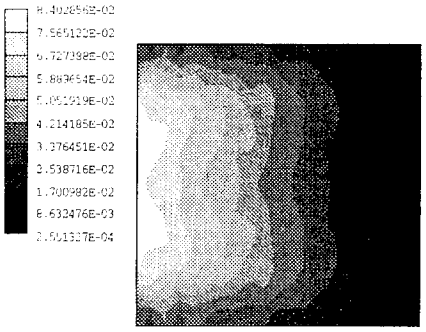


Figure 2 (a)
Error for the rectangular four wavelength case using with 0 degrees incidence.

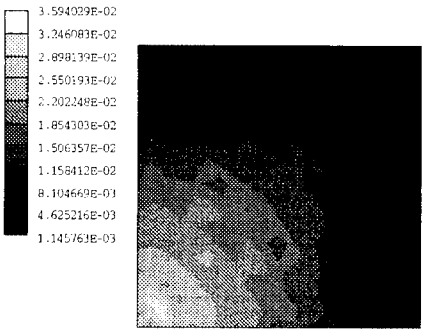


Figure 2 (b)
Error for the rectangular four wavelength case using with 45 degrees incidence.

Here, the error is less at 45 degrees incidence is less than zero degrees. This can be attributed to the increase in the effective order of the approximation function. At 45 degrees for this regular mesh, the fields traverse the elements along their diagonal. Along the diagonal, the approximation function is bi-quadratic whereas along the horizontal axis it is quadratic.

Another aspect is the convergence criteria of the iterative solver. Iterative solvers are used here for three-dimensional finite element problems because of their low demands on computer memory and operation count when compared to direct solvers. The solver used here is the Quasi-Minimal Residual (QMR) type [5]. It is shown here that the convergence criteria for the iterative solver need not be exceedingly strict for obtaining accurate values of RCS. The convergence criteria for solving a matrix equation, $Ax = b$, is called the residual. The residual is usually defined by:

$$\text{Residual} = \frac{|Ax - b|}{|b|} \tag{7}$$

The norms in (7) are either the L_2 or the L_∞ norms. Here, a square PEC plate will be used as an example. This plate is square with a dimension of five wavelengths per side and a monostatic solution for an elevation cut will be used. Figure 3 shows the RCS calculated with the L_2 norm residual set at 0.01 and 0.001. Figure 3 shows the typical result that the residual need not be a exceedingly low value to obtain correct RCS results. The relatively high residual of 0.01 produces nearly identical results while typically requiring a third to half the number of iterations as the 0.001 criterion. Figure 4 shows the comparison of the finite element method with a GTD technique [6].

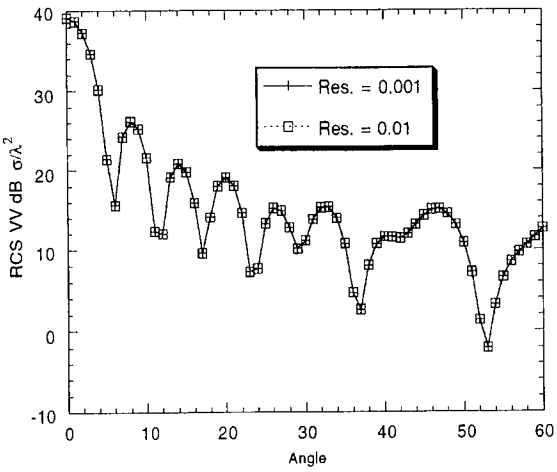


Figure 3
Monostatic RCS comparison for square five wavelength PEC plate, elevation cut. Comparing different convergence critereons.

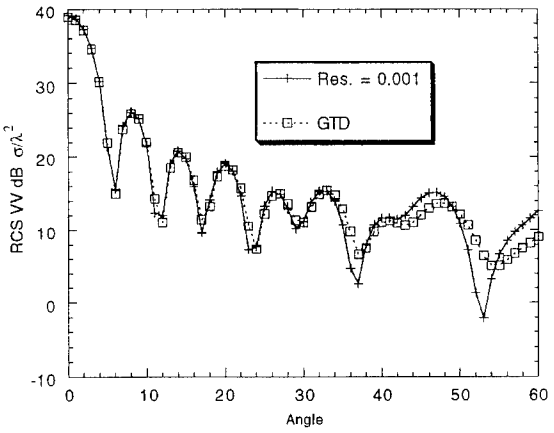


Figure 4
Monostatic RCS comparison for square five wavelength PEC plate, elevation cut. Comparing the finite element method with GTD.

Another aspect of RF scattering analysis is modeling the singular behavior of the electromagnetic field at sharp PEC corners. It is shown here that for a node based formulation, special handling of corners is required. Node based elements are used instead of "edge-based" elements because of they require much less computer resources and allow the solution of larger, more practical problem sizes [7,8].

However, although node-based element are efficient, difficulties arise when sharp corner are present. To improve the results for these cases, techniques to include edge-based functions at the corners with node-based everywhere else were developed. Edge-based elements have the advantage in modeling corners because they use tangential component of the field, thereby avoiding the ambiguous normal corner direction, and have more degrees of freedom to aid in modeling the rapidly changing field.

Figure 5 shows the monostatic RCS for a small PEC cube using a node-based formulation and a combined node/edge method. Using the node/edge method improves the overall solution.

Conclusion

Accurate modeling of scattering using finite element methods is an ongoing technology. Results show that using higher order basis functions dramatically improves the accuracy. Also, as problem sizes increase, denser meshes are required to maintain the same level of accuracy as smaller problems.

Also shown is that the convergence criteria of the iterative solvers need not be set to exceedingly small values to obtain accurate RCS results. L_2 residuals of 0.01 were shown to have comparable results to 0.001 thereby saving considerable computations.

Lastly, it was shown that special treatment of corner singularities is required when using a node-based finite element formulation.

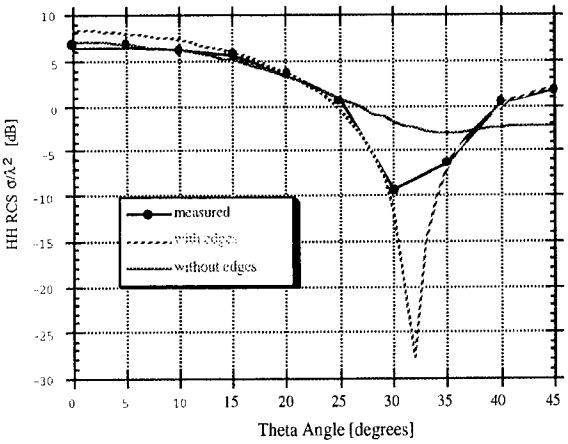


Figure 5
Monostatic scattering from a metallic cube,
length of cube = 2.46 cm, freq. = 10 Ghz, HH polarization.
Comparison of measured data, node only method and combined node/edge elements.

References

[1] Peterson, A.F., "Error in the finite element discretization of the scalar Helmholtz equation over electrcally large regions," IEEE Microwave and Guided Wave Letters, vol. 1, no. 8, pp. 219-222, August 1991.

[2] Lee, R., and Cangellaris, A.C., "A study of discretization error in the finite element approximation of wave solutions," IEEE Trans. Antennas Propagat., vol.1, no. 8, pp. 542-549.

[3] Bayliss, A., Turkel, E., "Radiation boundary conditions for wave-like equations," Comm. Pure Appl. Math., vol. 33, pp. 707-725, 1980.

[4] Engquist, B., Majda, A., "Absorbing boundary conditions for the numerical simulation of waves," Math. Comp., vol. 31, pp. 629-651, 1977.

[5] Freund, R.W., "Conjugate gradient type methods for linear systems with complex symmetric coefficient matrices," SIAM J. Sci. Stat. Comput., vol. 13, no. 1, Jan. 1992.

[6] Ruck, G.T., Barrick, D.E., Stuart, W.D, Krichbaum, C.K., Radar Cross Section Handbook, Plenum Press, 1970.

[7] Boyse, W.E, Lynch, D.R., Palusen, K.D., Minerbo, G.N., "Nodal-base finite element modeling of Maxwell's equations," IEEE Trans. Antennas and Propagation, vol. AP-40, pp. 642-651, June 1992.

[8] Mur, G., "The finite element modeling of three-dimensional electromagnetic fields using edge and nodal elements," IEEE Trans. Antennas and Propagation, vol. AP-41, pp. 948-953, July 1993.

Accuracy in Computation of Matrix Elements of Singular Kernels *

Stephen Wandzura
Hughes Research Labs

Abstract

Often a principal limiting factor in the accuracy of moment method (MoM) solutions of field integral equations is the technique of approximation used in the representation of near interactions. "Near", in this context, means interactions that are sensitive to singularities (typically logarithms or inverse powers) in the kernel or Green function at vanishing separation. The problem arises because high-order (e.g. Gaussian) numerical quadrature techniques are generally known only for nonsingular integrands. "High-order" means that one can obtain extra digits of precision at relatively modest cost; in practice, for sufficiently smooth integrands, the quadrature error vanishes exponentially in the sampling frequency. In the computation of near matrix elements, Gaussian quadrature is often employed in a way that destroys its high-order behavior, a practice often called "singularity subtraction". It is somewhat amusing that the problem may be attributed in part to a semantic difficulty: mathematically, a "singularity" is a point where a function *or any of its derivatives* is not defined, however, many consider only "infinities" to be singular. The trouble is that Gaussian quadrature loses its real advantage when confronted with an integrand that is singular *by the mathematical definition*; this is most easily seen by reference to the formula for the error in Gaussian quadrature.

The first part of the presentation will exhibit, by simple numerical example, the high-order behavior of Gaussian quadrature, and how it is destroyed by crude "singularity subtraction", even with functions that appear, visually, to be extrodinarily smooth. I will then exhibit two (very different) methods by which high-order computations with singular kernels can be accomplished. The first is the application of quadrature rules designed specifically for the type of singularity possessed by the kernel. For two dimensional scattering problems, such rules, accurate for functions of the form $f(x) + g(x) \log x$, where f and g are nonsingular, have only recently been discovered. In the case of three dimensions, an old technique know as the Duffy transformation accomplishes the same purpose. This method has the advantage that it strictly computes

*This research was supported by the Advanced Research Projects Agency of the Department of Defense and was monitored by the Air Force Office of Scientific Research under Contract No. F49620-91-C-0064. The United States Government is authorized to reproduce and distribute reprints for governmental purposes notwithstanding any copyright notation hereron.

the matrix elements of the MoM with the specified basis functions, and can be directly applied to geometries with edges and corners. The second high-order technique results from a modification of the kernel itself, in a way that removes the singularity, but leaves convolution of the kernel with sufficiently smooth functions unchanged. This method is similar to, and was inspired by, the way in which ultraviolet divergences are regulated in quantum field theory. It has the advantage that ordinary product-type Gaussian quadrature (of somewhat high order) can be used. Finally, I observe that the accurate computation of near interactions is not specific to a MoM formulation; the same issues arise, and in fact admit the same solution, in the computation of the "local corrections" necessary to apply the Nyström method to problems with singular kernels.

1 Accuracy of Quadrature for Singular Functions

1.1 The Problem

In the computation of Galerkin matrix elements of the integral kernel of, for example, the electric field integral equation, some ("near") elements involve integration over the singularity of the Green function at vanishing spatial separation. For smooth $2d$ (cylindrical) surface scatterers, the singular integration can be isolated to a one dimensional integration of the form

$$z = \int_0^a dr g(r) Y_0(kr)\,, \tag{1}$$

where Y is a Bessel function of the second kind and $g(r)$ is a regular function of the separation r between source and field points. (The second kind Bessel function is the imaginary part of a Hankel function, the real part of which is regular.) The Bessel function can be decomposed[1]

$$Y_0(x) = \frac{2}{\pi} \ln(x/2)\, J_0(x) + s(x)\,, \tag{2}$$

where J is the Bessel function of the first kind and s is a regular function. Since, for small x, $J_0(x) \approx 1 + \mathcal{O}(x^2)$, the function

$$\bar{Y}_0(x) \equiv Y_0(x) - \frac{2}{\pi} \ln(x/2) \tag{3}$$

is finite as $x \to 0$. Furthermore, as can be seen in Figure 1, $\bar{Y}_0(x)$, in spite of being singular in the sense that it is differentiable only once at $x = 0$, is quite smooth to the eye. Because of this, it is common to compute $z = \hat{z} + \bar{z}$, where

$$\hat{z} \equiv \frac{2}{\pi} \int_0^a dr g(r) \ln(kr/2) \tag{4}$$

[or even with $g(r) \to g(0)$] analytically, with the remainder $\bar{z}$ approximated by numerical quadrature. This procedure is called *singularity subtraction*. Its disadvantage is that it is an

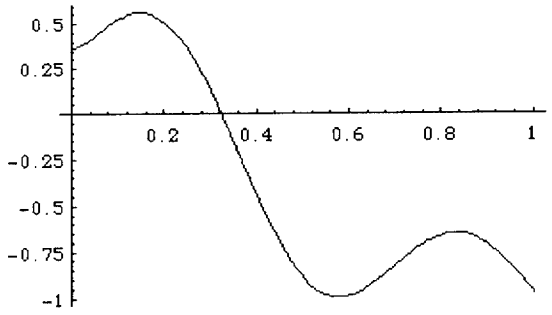


Figure 1: The function $\bar{Y}_0(x)$, a Bessel Function of the second kind with the $\log(x/2)$ term removed.

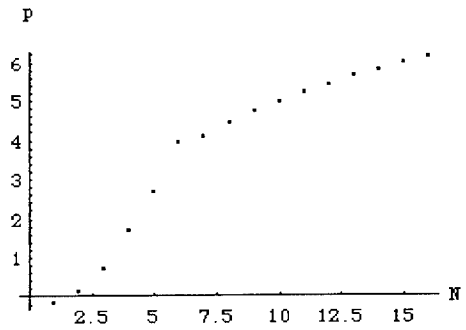


Figure 2: Digits of precision in $\bar{z}_N$ computed by Gaussian quadrature.

inherently low-order technique, in that high precision calculations are very expensive. As an illustration of this, consider the computation of a very simple case

$$\bar{z} = \int_0^1 dx \bar{Y}_0(10x) \approx -0.363851 \tag{5}$$

by $N-$point Gaussian quadrature[1]. Defining the precision as

$$p(N) \equiv -\log_{10} \left| \frac{\bar{z}_N - \bar{z}}{\bar{z}} \right| , \tag{6}$$

where $\bar{z}_N$ is the quadrature approximation, we see in Figure 2 that the precision increases very slowly. (The largest value of $N = 16$ corresponds to the rule of thumb "ten points per wavelength".) The behavior would be even worse if a more rapidly varying factor (from a curvilinear surface or a high-order basis function) were in the integrand of $\bar{z}$. Often heard statements by experienced practitioners of the method of moments like "everybody knows that one can't get more than three or four digits from numerical quadrature" stem from this kind of behavior.

1.2 A Solution for $2d$ Surface Scattering Problems

In searching for a high-order method of computation of quantities like z, it is helpful to consider how one can define $N-$point Gaussian quadrature. One approximates an integral by a weighted sum:

$$\int_0^1 dx\, f(x) \approx \sum_{n=1}^{N} w_n f(x_n) \tag{7}$$

such that the result is exact for the $2N$ functions $\left\{1, x, x^2, \ldots, x^{2N-1}\right\}$. The low accuracy of Gaussian quadrature is a reflection of the fact that a sequence of polynomials converges to $\bar{Y}(kx)$ (multiplied by any regular function) very slowly. This way of thinking led me to consider what would happen if one adjusted the weights w_n and abscissae x_n such that the quadrature were exact for a different set of $2N$ functions, namely

$$\left\{1, \ln x, x, x \ln x, \ldots, x^{N-1}, x^{N-1} \ln x\right\} .$$

I found (with some difficulty, as the equations to be solved for the x's and w's are quite ill conditioned) that the resulting rules are very well behaved; that is, all the weights are positive and all the abscissae are within the integration interval. Generalizations of these "linlog" quadrature rules are analyzed and tabulated in [2]. When $N-$point linlog rules are applied to the $\bar{z}$ defined above, excellent convergence is obtained, as illustrated in Figure 3. At Hughes Research Laboratories, we have used these quadrature rules to implement a very high-order $2d$ scattering code.

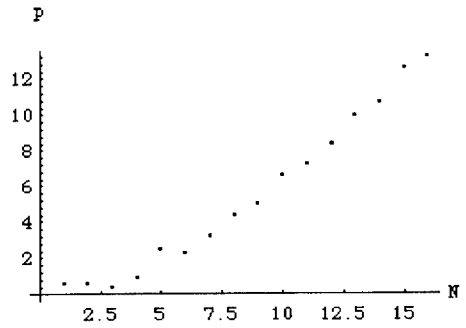


Figure 3: Digits of precision in $\tilde{z}_N$ computed by "linlog" quadrature.

1.3 Solutions for $3d$ Surface Scattering Problems

It is not easy to generalize the method described above to three dimensional surface scattering problems. An excellent and entertaining discussion of the difficulties is given by Lyness[3]. The basic trouble is that the rather obvious extension, construction of a quadrature rule that is exact for $g(r)/r$ for polynomial g where r is, for example, the distance to a vertex of a triangular patch, cannot be done in a way that is invariant to "stretching" of the patch. This means that one would have to compute weights and abscissae for each patch, an expensive procedure. (It is not altogether impractical, though; a good way to do it is discussed by Strain[4].)

There are a couple of feasible approaches that can be described briefly, although they can be clumsy in practice. Both involve changes of variables in the integral (for example)

$$z = \int_0^a dx \int_0^x dy f(x,y)/r(x,y)\,, \tag{8}$$

where f is a regular function. The first is to use a product rule on the integral as it stands, with Gauss-Legendre quadrature for the inner (dy) integration and "linlog" rule for the outer (dx) integration. Easier, perhaps, is the Duffy transformation[3, 5]:

$$z = \int_0^a dx \int_0^1 dt \frac{x}{r} f(x,tx)\,, \tag{9}$$

with Gauss-Legendre quadrature used for both integrations; this works because the Jacobian of the transformation exactly cancels the singularity.

2 Accuracy in Regulation of Singular Kernels

An alternative to using special quadratures to compute convolutions with singular kernels is the modification of the kernel itself to truly remove the singularity. "Truly" means here to

render the kernel *and all its derivatives* finite. Short-distance regulation of kernels is a time-honored technique in physics; it was the key to solving the problem of extracting predictions from higher-order computations in quantum electrodynamics[6, 7]. (The regulation methods cited were, however, in present terminology, "low-order" — the resultant kernels, although finite for vanishing separations, were still singular.)

The question of how to preserve accuracy control while regulating the kernel is illuminated by the observation that achieving high-order convergence by use of special quadratures still requires that the functions that are convolved with the kernel be regular. If one were to introduce singular basis functions, for example, to model sources near geometric singularities of the scatterer, the techniques described in the previous section would need to be modified. Thus the key is to require that the regulated kernel not only converge to the singular kernel as the regulation is removed, but that it gives *identical* results to the singular kernel when convolved with a suitable class of smooth functions.

I will show how this can be done to the kernel $1/(4\pi r)$ for the Laplace Equation in three dimensions for convolution with functions on smooth two dimensional manifolds (smooth surfaces of $3d$ objects). The first step is to Fourier transform to momentum space, giving $1/q^2$. We then regulate the short-distance (large q) with a factor $\exp -a^2q^2/4$. Fourier transforming back to real space gives the regulation prescription

$$\frac{1}{4\pi r} \to \frac{\mathrm{erf}(r/a)}{4\pi r}\,, \tag{10}$$

where the regulated kernel obviously is nonsingular (because erf is an odd function), approaches the unregulated kernel (for fixed r) as $a \to 0$, and has only local corrections. The last property means that the difference between the kernels vanishes as fast as a Gaussian for $r \gg a$. Because of this, we need not concern ourselves with kernel modification for sufficiently far interactions, allowing compatibility with the Fast Multipole Method[8].

The regulation so far is low order, in the sense that results computed with the regulated kernel will have regulation errors that are proportional to a low power of a. What we want to do, then, is to add a smooth local function that renders the regulation high order. A fairly obvious choice is thus

$$\bar{G}_B(r) = \frac{\mathrm{erf}\,(r/a)}{4\pi r} + \frac{1}{a} e^{-a^2r^2} F_B\left(\frac{r^2}{a^2}\right)\,, \tag{11}$$

where F_B is a Bth order polynomial with coefficients adjusted to enforce

$$\int_0^\infty dr\, r^{2m+1} \left[\bar{G}_B(r) - G(r)\right] = 0 \quad ; \quad m = 0, \ldots, B\,. \tag{12}$$

The application of this method to the wave equation in an arbitrary number of dimensions is straightforward. We have implemented and verified it for both $2d$ and $3d$ electromagnetic scattering problems.

3 Independence of Problem from Discretization Method

The question naturally arises whether the details that have to be treated in order to achieve high-order discretization of integral equations with singular kernels are specific to the method of moments (MoM). Can these issues be circumvented by use, say, of a Nyström discretization? The answer is no. The best way to apply the Nyström method to such problems[4] is to compute local corrections to quadrature rules that would be appropriate to nonsingular kernels. In fact, one of the questions that led to the high-order regulation method above was whether these local corrections could be transferred from the quadrature rules to the kernel. Since this can be done, it may even provide a more efficient method of correction computation (in the multidimensional case) than the adaptive quadrature rules use by Strain[4].

References

[1] M. Abramowitz and I. A. Stegun, *Handbook of Mathematical Functions*, Applied Mathematics Series, National Bureau of Standards, Cambridge, 1972.

[2] J.-H. Ma, V. Rokhlin, and S. Wandzura, "Generalized gaussian quadrature rules for systems of arbitrary functions," Technical Report YALEU/DCS/RR-990, Yale University, Department of Computer Science, October 1993, To be published in SIAM Journal of Numerical Analysis.

[3] J. N. Lyness, "On handling singularities in finite elements," In T. O. Espelid and A. Genz, editors, *Numerical Integration — Recent Developments, Software and Applications*, pages 219–233, Kluwer Academic Publishers, Dordrecht, 1992.

[4] J. Strain, "Locally-corrected multidimensional quadrature rules for singular functions," Technical report, Lawrence Berkeley Laboratory, 1994, To be published in *SIAM Journal of Scientific Computing*.

[5] M. G. Duffy, "Quadrature over a pyamid or cube of integrands with a singularity at a vertex," *Journal of Numerical Analysis*, 19:1260–1262, 1982.

[6] W. Pauli and F. Villars, "On the invariant regularization in relativistic quantum theory," *Reviews of Modern Physics*, 21:434–444, 1949.

[7] R. P. Feynman, "Space-time approach to quantum electrodynamics," *Physical Review*, 76:769–789, 1949.

[8] R. Coifman, V. Rokhlin, and S. Wandzura, "The fast multipole method: A pedestrian prescription," *IEEE Antennas and Propagation Society Magazine*, 35(3):7–12, June 1993.

Accuracy Estimation and High Order Methods[†]

Lisa R. Hamilton, John J. Ottusch*, Mark A. Stalzer,
R. Steven Turley, John L. Visher, and Stephen M. Wandzura

Hughes Research Laboratories
3011 Malibu Canyon Road, Malibu, CA 90265

Abstract

Accuracy estimates are a prerequisite for meaningful comparisons of calculated radar cross sections (RCS), especially performance comparisons. RCS codes incorporating high order methods have advantages over low order codes both for achieving accurate answers and for estimating solution accuracy. In this paper, we describe high order convergence and some high order methods used in RCS computations; we describe a straightforward method for estimating calculated RCS accuracy; and we discuss the tradeoffs between solution accuracy and cost (in terms of cpu time and memory) for high and low order RCS codes.

1. Introduction

In our experience at conferences dealing with radar scattering calculations, when the accuracy of a given RCS calculation is described at all, it is described in an imprecise, qualitative way that can be paraphrased as follows: "When my calculation and so-and-so's calculation (or so-and-so's experimental results) are plotted on the same scale, they appear to be similar." Similarities are nice indeed, but without quantification of the estimated accuracies of the various results, whether calculational or experimental, there is no way to determine which one should be given the most credence or what may be the underlying cause of observed differences. In addition, when it comes time to compare the efficiency of different codes in computing a particular RCS, the computed results must be of comparable accuracy for the comparison to have any meaning.

Differences between a calculated RCS and the actual RCS for a given body result from 1) deficiencies in the abstract model of the scatterer and 2) deficiencies in the way the RCS of the abstract model is calculated. The former category is modeling error. It includes such simplifications as modeling a surface as a perfect conductor, treating thin body parts as though they actually had zero thickness, etc. The latter category is solution error. When two codes agree on an abstract model, differences in their calculated RCS's are a reflection of the different ways they arrive at approximate numerical solutions to Maxwell's equations for the boundary conditions appropriate to that model of the scatterer.

The attitude of many workers in the field seems to be that there is no way to estimate the accuracy of a computed RCS for a given model, except in a qualitative way by comparing it to other calculated RCS's for the same model. For RCS codes that use the method-of-moments approximation, which, in principal, can generate solutions with arbitrary accuracy, this is not the case. In fact, there are straightforward ways to estimate the accuracy of an RCS calculation even when the correct answer is unknown. One such method is described below.

Another reason that calculated RCS's are infrequently accompanied by accuracy estimates is a widespread underappreciation of the tradeoff between the cost of a calculation (in terms of CPU time and memory) and the accuracy of the resultant solution. Accurate solutions require more computer resources than inaccurate ones.

[†] This research was supported in part by the Advanced Research Projects Agency of the Department of Defense and was monitored by the Air Force Office of Research under Contract Number F49620-91-C-0064. The United States Government is authorized to reproduce and distribute reprints for governmental purposes notwithstanding any copyright notation hereon.

This, coupled with the fact that the cost of a calculation increases as a moderate power of the size of the problem, means that as problem sizes grow, the resource requirements for obtaining acceptably accurate results using standard, low order RCS codes grow ever more quickly and can easily become exorbitant.

Incorporation of high order methods in an RCS code can improve the situation dramatically. High order numerical methods are distinguished by their ability to rapidly converge to the correct answer. A well-known example is Gaussian quadrature, the name of a class of high order methods used for numerically evaluating integrals. Numerical methods can be classified as high order only with respect to a certain class of problems. For problems within this class they converge rapidly to the correct answer. The rate of convergence is determined by order of the method, ρ, and it increases as the order of the method increases. For problems outside this class they converge to the correct answer, albeit at a slower rate. Rapid convergence to an incorrect answer almost always results from an implementation error. Intelligently applying high order methods in a method-of-moments RCS code can reduce the cost of calculating an acceptably accurate RCS to the extent that an otherwise impractically large problem may be done on a supercomputer or even a workstation and in less time.

The principal advantage of high order methods is that they reduce the power by which the cost grows as a function of accuracy for fixed problem size. Consequently, cost is a less sensitive function of accuracy for high order codes than it is for low order codes. Therefore, when comparing the performance of different codes, it is even more important to have a good estimate of the accuracy of a result computed by a low order code than it is for a result computed by a high order code.

The mathematical basis of these arguments is as follows. One can express the solution to Maxwell's equations for EM scattering from a surface as an integral equation, whose solution can be computed numerically by discretizing the surface into separate patches and expressing the surface current on each patch as a linear combination of elemental currents. The number N of independent elemental surface currents whose coefficients must be determined is proportional to (A / Δ), where A is the surface area of the scatterer and Δ is a discretization scale. The asymptotic cost of computing these coefficients increases as N^{α}. The exponent α is 3 for cpu time and 2 for memory for a direct / dense solver and is ≤ 2.5 for cpu time and ≤ 1.5 for memory for a single stage fast multipole method[1] iterative solver. In general, the process of discretizing an integral equation for purposes of numerical solution introduces errors in the computed result that scale as Δ^{ρ}, where the exponent ρ is the order of the numerical method used to solve the discretized equation. From these relations one can deduce that cost $\propto$ (1 / error) $^{\alpha / \rho}$; i.e. cost scales as (1 / error) to a certain power, but that power decreases in proportion to the order of the method.

This doesn't quite tell the whole story because we haven't described the coefficient of proportionality, which also depends on the order of the method. Calculations of impedance matrix elements using high order methods are more complicated, so they generally require more code and more time than a low order calculation does. The time requirement, in particular, generally grows as the order of the method increases. The effect this has on the total cost of a large calculation is small, however, when compared to the dramatic effect high order methods have on the rate at which the time and memory requirements grow with increasing accuracy. Experience has shown that low order methods are more efficient for relatively small problems and low accuracies, but for large problems or high accuracies, high order codes have a distinct, and ever-increasing advantage.

Let us now return to the topic of accuracy estimation. As Δ gets smaller and smaller, numerical solutions to Maxwell's equations calculated in the manner described previously will converge to the correct answer.* To put it another way, if a series of RCS computations were performed in which the discretization scale Δ decreased geometrically, the differences between the calculated RCS's and the exact RCS would decrease as a function of Δ (for sufficiently small values of Δ). Suppose the series starts with Δ_0 and ends with Δ_n. The most accurate of the calculations would be the one corresponding to the finest discretization scale, Δ_n. The accuracy of this solution can be estimated by using it as a stand-in for the exact solution and observing how fast the other solutions converge to it. If they converge monotonically, the error in the Δ_n solution can be conservatively esti-

* This holds true in the absence of errors implementing the method-of-moments algorithm and in the regime where round-off errors are insignificant.

mated to be of the order of the difference between the Δ_n and Δ_{n-1} solutions. The essential point here is that one RCS calculation is insufficient to provide any information about accuracy; in general, a series of calculations is required to corroborate convergence to a unique answer, and from the convergence rate to derive an accuracy estimate.

2. Discussion

In the rest of this paper, we will discuss some example problems that demonstrate the differences between high and low order codes, the tradeoffs between cost and accuracy in RCS computations, and how accuracy estimation is affected by method order. The first example, involving vector EM scattering from a 1λ-radius sphere, is a graphic demonstration of what we mean by high order convergence of RCS results. The second example, involving scalar scattering from a 1λ-radius circle in 2D, compares how the order of one's method(s) affects the rate at which a computed RCS converges to the correct answer. The third example, involving scalar scattering from a 2D object we call the "bat", demonstrates that high order methods have the upper hand where it really counts, namely on large problems in which the RCS has a large dynamic range as a function of angle and the computation is of little use unless it is accurate where the cross section is low.

The costs of the various calculations will be measured in terms of the number of unknowns, which for our purposes is equivalent to cpu memory since we used a dense / direct solver in all cases. We decided to focus on this one cost measure for simplicity and brevity of presentation.

2.1 Sphere

A good way to illustrate the difference between high and low order convergence is to compare how efficiently an RCS code using high order methods and one using low order methods compute cross sections for the same geometry. For the comparison here, we have chosen two method-of-moments codes, FastScat† and CARLOS-3D (date of release, Sept. 1992). CARLOS-3D[2] is the EMCC-distributed standard for computing vector EM scattering in 3 dimensions. It can be classified as a low order code because it is limited to using standard Rao-Wilton-Glisson (RWG)[3] current basis functions (CBF) and a surface representation consisting of flat patches. Its quadratures employ a mixture of high and low order methods.‡ FastScat is an RCS code being developed at Hughes Research Laboratories that employs high order methods§ in its current basis functions[4] (generalized RWG CBF's), quadratures[5], and geometry description[6] (exact surfaces).

We computed the monostatic RCS of a 1λ-radius sphere with both FastScat and CARLOS-3D. In both cases, the sphere was patched by approximately identical triangular patches, starting from an inscribed icosahedron. In the FastScat case, each patch was mapped exactly to the surface of the sphere. The patches were not further subdivided. Accuracy improvements were achieved by invoking progressively higher-order CBF's. In the CARLOS-3D case, only the lowest CBF order exists. To increase the accuracy of the computed RCS, we increased the density of unknowns by subdividing the patches into progressively smaller (nearly) identical triangular patches, each of whose vertices were on the surface of the sphere.

The cross section of a perfectly-conducting sphere can be determined to arbitrary precision by numerically summing the Mie series. For a 1λ-radius sphere the monostatic θθ-pol RCS is 5.03176 dB¨, independent of observation angle. Calculated RCS's do vary with angle, however, due to current discretization, quadrature errors, and in the case of CARLOS-3D, inaccurate realization of the surface using flat patches. Figure 1 shows two plots of RCS vs. latitude on the sphere, one for FastScat and one for CARLOS-3D. In each plot the calculated RCS is shown for about 275, 500, 750, and 1000 unknowns as indicated in the legend. In the FastScat case these curves correspond to CBF orders of 5, 7, 9, and 10; in the CARLOS-3D case, they correspond to subdividing the inscribed icosahedron into 180, 320, 500, and 720 nearly identical triangles. The least accurate computations are about equally bad in the two cases. As the surface density of unknowns increases,

† FastScat is a trademark of the Hughes Aircraft Company.

‡ CARLOS-3D's quadratures are high order for non-touching, flat patches; for touching or same patch quadratures, CARLOS-3D uses a singularity subtraction technique that is inherently low order.

§ FastScat's methods are high order for scatterers comprised of smooth surfaces, whether flat or curved.

¨ dB stands for dB-λ^2, an engineering unit of RCS measurement.

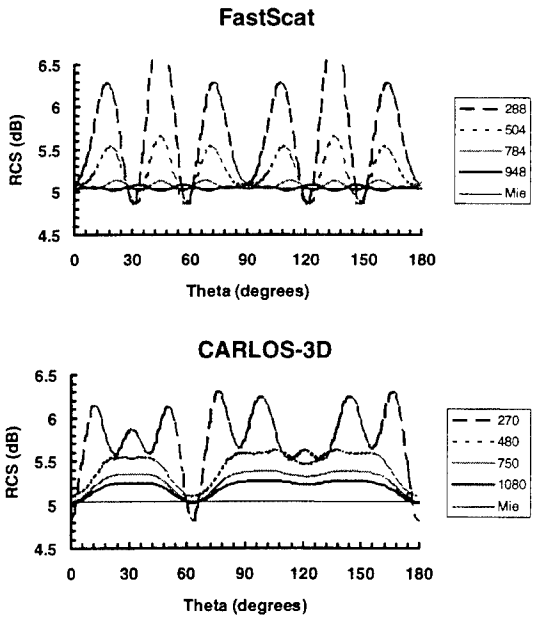


Figure 1

however, it is easy to see that the FastScat solutions converge to the correct answer more rapidly. This is the essence of high order convergence.

2.2 Circle

Next we consider the bistatic RCS for TM scattering from a perfectly-conducting 1λ-radius circle. It is a simple, but useful candidate for demonstrating how different aspects of the computation as well as the order of their numerical methods affect the rate of convergence to the correct answer. Like the sphere, there are Mie series solutions for the cross section, so there can be no dispute about what the correct answer is. However, for our purposes it is useful to characterize the differences between a given calculated solution and the correct solution over a range of angles as a single number, and there is some dispute about the best way to do this. Our standard error measures are maximum relative error, maximum error ÷ average RCS, and rms error.[††] It must be emphasized that for this problem the results are essentially independent of which error measure is used.

As we stated earlier, FastScat can employ high order methods in its current basis functions, quadratures, and surface representation. The user can control the order of the method used for each aspect of the computation. In general, the convergence rate of the calculation as a whole is determined by the lowest method order of the three. It's analogous to the strength of a chain being determined by its weakest link. To show how the method

[††] These error measures are defined as follows:
Maximum relative error ≡ $\max(|\sigma(\theta) / \sigma_{exact}(\theta) - 1|)$
Maximum error ÷ average RCS ≡ $\max(|\sigma(\theta) - \sigma_{exact}(\theta)|) / \text{ave}(\sigma_{exact}(\theta))$
RMS error ≡ $\text{rms}(\sigma(\theta) / \sigma_{exact}(\theta) - 1)$

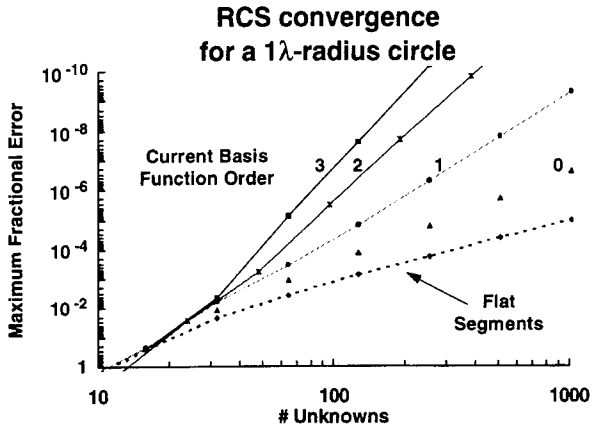


Figure 2

order of an individual component affects the rate of convergence of the full solution, we need to set the method order for each of the other two components high enough so that they don't contribute any noticeable error. Once this has been done, we can measure how quickly the solution converges as we vary Δ by making the patches smaller. For example, to investigate the effect of current basis function order (up to a high precision such as 10^{-10}), we could set the quadrature order high enough to guarantee that the integrals are accurate to at least 1 part in 10^{12} and use an exact surface representation. Then, for a fixed CBF order, we would compute the RCS for a series of 1λ-radius circles divided into 4, 8, 16, 32, and so on, identical circular arcs. We have plotted the errors for such a series of calculations in Figure 2 for CBF orders 0, 1, 2, and 3.[‡‡] On the same plot, we also show an example of how the surface model affects the convergence rate. The dashed curve connects points that were computed by replacing the circular arc patches with flat patches.[§§] The order of the quadratures was the same as in the previous case. For this case, however, only one CBF order is shown, namely zero. The reason is that the poor surface representation so limits the rate of convergence that increasing the CBF order has no noticeable effect on the accuracy of the solution. Curves for higher CBF orders are virtual copies of the zeroth-order CBF result, shifted to higher numbers of unknowns.

The most important feature to note is that, for enough unknowns, the data fits a linear trend line whose slope increase as the CBF order increases. Since the discretization scale, Δ, is inversely proportional to the number of unknowns, N, this simply reflects the fact that the error diminishes as Δ^x, where x increases with method order. And, since memory is proportional to N^2, it also shows how method order affects the relationship between accuracy and cost. For errors less than about 10^{-2}, not only are the errors in the RCS's calculated by higher order methods lower, but also the marginal cost of additional accuracy is lower. This makes assessment of the resource requirements corresponding to a given solution accuracy more reliable, which is the performance comparison benefit mentioned earlier.

Not many practical problems require that the RCS be calculated to anywhere near a precision of 1 part in 10^{10}. For example, if 1 part in 10 were deemed a "practical" accuracy requirement, then one can see from Figure 2 that using flat patches and zeroth order CBF's is about as efficient as using an exact surface and higher order CBF's. So, do these results have any relevance to more practical problems? The answer is yes. A small circle was chosen for reasons of expediency (particularly with regard to the low order calculations) and because it

‡‡ For TM scattering in 2D, the n^{th} order current basis function is essentially an n^{th} order Legendre polynomial.
§§ This is how RAM-2D works, for example.

is a geometry for which the relationship between method order and convergence rate can be demonstrated so clearly and easily.*** Truly interesting practical problems are generally much bigger. When the problems get bigger, the RCS as a function of angle often has a large dynamic range. It is in these situations that the advantages of high order methods become evident even at "practical" accuracies. This leads us to the final example problem.

2.3 Bat

Consider the fictitious 2D geometry shown in Figure 3 which we call the "bat". It is composed of straight faces connected smoothly by circular arcs of radius R. There are two long edges of length L and six short edges, each of length L / 3, at right angles to each other. All surfaces are perfect conductors. It is interesting from a practical point of view because it has three high RCS specular reflection regions (one of which is the 2D analog of a corner cube) and a low RCS everywhere else.

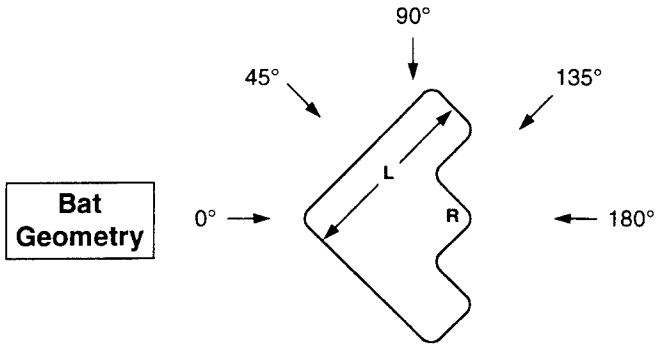


Figure 3

Let us focus on the monostatic RCS for TM scattering from a R = 1λ, L = 300λ bat. We don't have an exact solution to this problem so we followed the prescription described earlier to ascertain accuracy. A series of FastScat computations was performed with increasingly fine discretizations in order to look for convergence to a unique answer. For these calculations, we used an exact surface representation and quadratures good to at least 8 digits of accuracy. The discretization scale size was changed by changing the CBF order while keeping the size of the patches fixed at about one wavelength per patch. The result shown in Figure 4a used 4^{th}-order CBF's and required 6000 unknowns. It is estimated to have an accuracy comparable to the width of the plotted line. There are narrow peaks at 45° and 135° as expected and a broader peak centered at 180° resulting from the "corner square" effect. The oscillations evident in the cross section are the result of interference, not due to any solution error.

For comparison purposes, we also calculated the RCS of the bat in the standard low order way using zeroth-order CBF's. By increasing the patching density to about five patches per wavelength we kept the number of unknowns constant at 6000. This result is shown in Figure 4b. Whereas this calculation generally agrees with the high order calculation at angles where the cross section is high, in the low cross section regions the calculated RCS is clearly erroneous, the error exceeding 20dB at some angles.

*** Note: we have also observed similar behavior for scalar and vector EM scattering from 1λ-radius spheres.

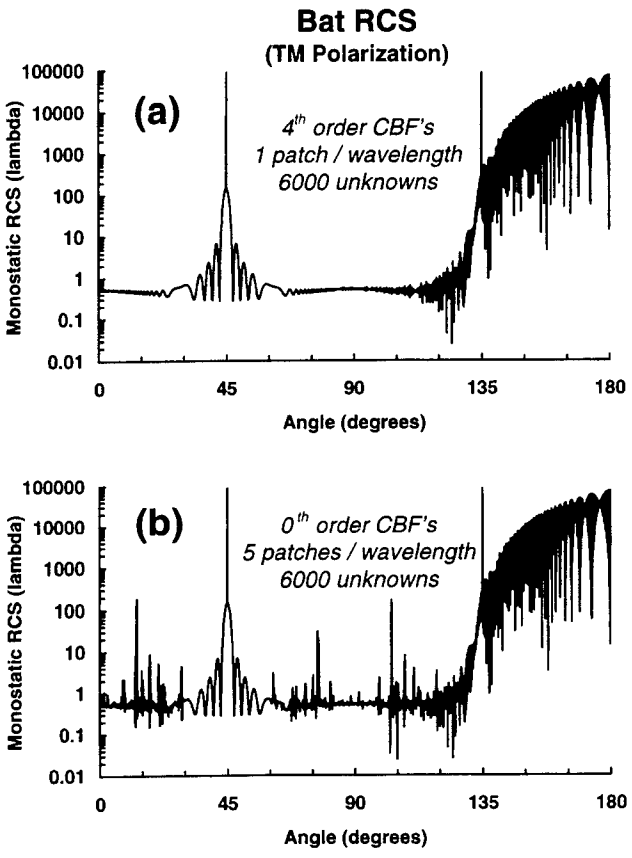


Figure 4

This problem dramatically illustrates the limitations of using low order methods for RCS computations. For someone interested in the low cross section regions of this body, the results of the low order calculation would be particularly misleading. If one were interested in improving (or for that matter, estimating) the accuracy of such a calculation, one could make the patches smaller still, knowing that the low order calculation would eventually reach the same accuracy as the high-order calculation. However, the additional cost would be significant.

3. Summary

Using high order methods to solve RCS problems pays significant dividends, particularly on large problems. The benefits that accrue are 1) lower cpu time and memory required to achieve a given accuracy, 2) lower

marginal cost for achieving additional digits of accuracy (which is a big advantage for accuracy estimation), and its corollary, 3) reduced sensitivity of the cost to any imprecision in the estimate of the solution accuracy (which makes it easier to make meaning performance comparisons).

References

1. R. Coifman, V. Rokhlin, and S. Wandzura, *The fast multipole method: A pedestrian prescription*, IEEE Antennas and Propagation Society Magazine, **35**, 7-12 (1993).

2. J. M. Putnam, L. N. Medgyesi-Mitschang, and M. B. Gedera, *CARLOS-3D™ Three-Dimensional Method of Moments Code*, Theory and User Manual, McDonnell Douglas Corporation, St. Louis, MO (10 December 1992).

3. S. M. Rao, D. R. Wilton, and A. W. Glisson, *Electromagnetic scattering by surfaces of arbitrary shape*, IEEE Transactions on Antennas and Propagation, **AP-30**, 409-418 (1982).

4. L. R. Hamilton, P. A. Macdonald, M. A, Stalzer, R. S. Turley, J. L. Visher, and S. M. Wandzura, *Electromagnetic scattering computations using high-order basis functions in the method of moments*, IEEE Antennas and Propagation Society International Symposium Digest , **Vol 1**, 435-438 (1994).

5. S. M. Wandzura, *Accuracy in computation of matrix elements of singular kernels*, to be published in Applied Computational Electromagnetics Society Symposium Digest (1995).

6. S. M. Wandzura, *Electric current basis functions for curved surfaces*, Electromagnetics, **12**, 77-91 (1992).

ACCURACY ISSUES IN TIME–DOMAIN CEM USING STRUCTURED/UNSTRUCTURED GRID FORMULATIONS

Vijaya Shankar, William F. Hall, and Sampath Palaniswamy
Rockwell Science Center

Abstract

A Computational Electromagnetics (CEM) capability for solving scattering, radiation, and other problems of interest such as microstrip circuit analysis, bioelectromagnetics and EMP/EMI has been developed by numerically solving the time-domain Maxwell's equations employing some of the algorithmic rigors of Computational Fluid Dynamics (CFD). The differential conservation form of Maxwell's equations is used for the structured grid option and the integral conservation form for the unstructured grid formulation. Application of the CEM code for computing the radar cross section (RCS) of a complete fighter involving tens of millions of grid points on a massively parallel architecture is demonstrated along with a number of other applications including the propagation of microwave energy through a complete human body.

Introduction

A structured grid and an unstructured grid–based finite–volume, time–domain Maxwell's equation solver has been developed incorporating modeling techniques for general radar absorbing materials. Using this work as a base, the goal of the CEM effort is to define, implement, and evaluate rapid prototype signature prediction, addressing many issues related to 1) physics of electromagnetics, 2) efficient and higher–order accurate algorithms, 3) boundary condition procedures, 4) geometry and gridding (structured and unstructured), 5) computer architecture (SIMD and MMD), and 6) validation.

Some of the accuracy issues associated with the time-domain CEM formulation are:

1) Stability and accuracy of finite-volume schemes applied to the discretized Maxwell's equations using von Neumann analysis
2) Demonstration of accuracy for various 1-D problems such as the wave propagation through material interfaces and the Salisbury screen, 2-D problems such as the perfectly conducting, clad and dielectric circular cylinders (comparison with Mie series), and 3-D problems such as the perfectly conductiong and coated spheres (comparison with Mie series).
3) Study on how many grid cells per wavelenth, accuracy of outer boundary condition treatment and convergence criteria for CW and pulse cases
4) Resource requirements to achieve (say within 1 dB) accurate solutions for general 3-D problems

1) Maxwell's Equations

In order to apply conservation principles (for example, in fluid dynamics mass, momentum, and energy are conserved), many of the governing equations representing appropriate

physical processes are written in conservation form. The general form of a differential conservation equation can be written as

$$Q_t + E_x + F_y + G_z = \text{Source} \tag{1}$$

where Q is the solution vector and E, F, and G are the fluxes in x, y, and z coordinate directions, respectively. The conservation form readily admits weak solutions such as shock waves.

The integral form of the conservation laws which can easily be derived from the differential form by integrating Eq. (1) with respect to x, y, z over any conservation cell whose volume is V.

$$\begin{aligned} &\int\int\int_V \left(\frac{\partial Q}{\partial t} + \frac{\partial E}{\partial x} + \frac{\partial F}{\partial y} + \frac{\partial G}{\partial z}\right) dx\, dy\, dz \\ &\quad = \int\int\int_V S\, dx\, dy\, dz = \widetilde{S} \quad . \end{aligned} \tag{2}$$

This can be rewritten in vector notation as

$$\begin{aligned} &\frac{\partial}{\partial t}\int\int\int_V Q\, dx\, dy\, dz \\ &\quad + \int\int\int_V \left(\vec{\nabla}\cdot\vec{\mathcal{F}}\right) dx\, dy\, dz = \widetilde{S} \quad . \end{aligned} \tag{3}$$

In the above,

$$\vec{\mathcal{F}} = E\hat{j} + F\hat{k} + G\hat{l} \quad . \tag{4}$$

Applying the Gauss divergence theorem, we can convert the volume integral into a surface integral.

$$\frac{\partial}{\partial t}\left(\widetilde{Q}V\right) + \int\int_s \left(\vec{\mathcal{F}}\cdot\hat{n}\right) ds = \widetilde{S} \quad . \tag{5}$$

In the above equation, the cell average of the dependent variables are denoted by $\widetilde{Q}$. The outward unit normal at any point of the boundary surface of a cell has been denoted by $\hat{n} = \hat{n}_x\hat{j} + \hat{n}_y\hat{k} + \hat{n}_z\hat{l}$.

$$\widetilde{Q} = \frac{\int\int\int_V Q dV}{\int\int\int_V dV} \quad . \tag{6}$$

The integral form of the conservation laws given by Eq. (5) defines a system of equations for the cell average values of the dependent variables.

Maxwell's equations in their vector form are

$$\frac{\partial B}{\partial t} = -\nabla\times\mathcal{E} \tag{7}$$

and

$$\frac{\partial D}{\partial t} = \nabla\times\mathcal{H} - J \quad . \tag{8}$$

The divergence conditions $\nabla \cdot D = \rho$ and $\nabla \cdot B = 0$ are derived directly from Maxwell's equations, where $\nabla \cdot J = -\frac{\partial \rho}{\partial t}$. The vector quantities $\mathcal{E} = (\mathcal{E}_x, \mathcal{E}_y, \mathcal{E}_z)$ and $\mathcal{H} = (\mathcal{H}_x, \mathcal{H}_y, \mathcal{H}_z)$ are the electric and magnetic field intensities, $D = (D_x, D_y, D_z)$ is the electric displacement, $B = (B_x, B_y, B_z)$ is the magnetic induction, and $J = (J_x, J_y, J_z)$ is the current density and ρ is the charge density. The subscripts x, y, z in the vector representation of $\mathcal{E}$, $\mathcal{H}$, B, and D refer to components in respective directions.

Under the transformation of coordinates implied by

$$\tau = t\,,\ \xi = \xi(t,x,y,z)\,,$$
$$\eta = \eta(t,x,y,z)\,,\ \zeta = \zeta(t,x,y,z)\,,$$

Eqs. (7) and (8) can be rewritten as

$$\overline{Q}_\tau + \overline{E}_\xi + \overline{F}_\eta + \overline{G}_\zeta = \overline{S} \tag{9}$$

where

$$\overline{Q} = \begin{pmatrix} \frac{\vec{B}}{J} \\ \frac{\vec{\mathcal{B}}}{J} \end{pmatrix},\ \overline{E} = \begin{pmatrix} \frac{-\vec{\xi}\times\vec{\mathcal{H}}}{J} \\ \frac{\vec{\xi}\times\vec{\mathcal{E}}}{J} \end{pmatrix},\ \overline{F} = \begin{pmatrix} \frac{-\vec{\eta}\times\vec{\mathcal{H}}}{J} \\ \frac{\vec{\eta}\times\vec{\mathcal{E}}}{J} \end{pmatrix},$$
$$\overline{G} = \begin{pmatrix} \frac{-\vec{\zeta}\times\vec{\mathcal{H}}}{J} \\ \frac{\vec{\zeta}\times\vec{\mathcal{E}}}{J} \end{pmatrix},\ \text{and}\ \overline{S} = \begin{pmatrix} \frac{-\vec{\mathcal{J}}}{J} \\ 0 \end{pmatrix} \tag{10}$$

where $J = |\partial(\xi,\eta,\zeta)/\partial(x,y,z)|$ is the Jacobian of the transformation and, *e.g.*, $\vec{\xi} = (\partial_x\xi, \partial_y\xi, \partial_z\xi)$. The quantities $\vec{\xi} \times \vec{H}$ and $\vec{\xi} \times \vec{E}$ in Eq. (11) represent tangential magnetic and electric fields at a constant ξ surface. Thus, the fluxes $\overline{E}$, $\overline{F}$, and $\overline{G}$ are nothing but the tangential fields.

Maxwell's equations can also be cast in integral form as

$$\frac{\partial}{\partial t}\int\int_V \int \begin{pmatrix} \vec{B} \\ \vec{D} \end{pmatrix} dV + \int_S \int \begin{pmatrix} \hat{n}\times\vec{E} \\ -\hat{n}\times\vec{H} \end{pmatrix} dS = 0 \quad , \tag{11}$$

where the six components of $\vec{\mathcal{F}} \cdot \hat{n}$ in Eq. (5) are $(\hat{n} \times E, -\hat{n} \times H)$.

In general, the differential form, Eq. (10), will be employed for finite–volume schemes using a structured grid arrangement, and the integral form, Eq. (11), will be used for unstructured grid cell arrangements using finite–element–like finite–volume schemes.

2.0 Finite–Volume Treatment

The major feature of the present discretization approach that distinguishes it from other finite–volume and finite–difference procedures is that the electric and magnetic field unknowns are co–located in both space and time, rather than being assigned to two interpenetrating spatial grids and separated a half–step in time. These field unknowns are the volume averages of E and H within each cell in the space–filling grid.

An algorithm that maintains second-order accuracy in both space and time can be constructed as follows (advancing from time level m to $m+1$):

$$\langle Q\rangle_\alpha^{m+1/2} = \langle Q\rangle_\alpha^m - \frac{\Delta t}{2V_\alpha}\int_{\partial\alpha} \hat{n}\cdot F\left(Q_\alpha^{*m}\right) dS$$

$$K_\alpha^m = \frac{1}{V_\alpha}\int_{\partial\alpha} \hat{n} Q_\alpha^{*m} dS = \frac{1}{V_\alpha}\int_{\partial\alpha} \hat{n}\left(\hat{n}\times\left\{\hat{n}\times\left[\langle Q\rangle_\alpha^m - Q_\alpha^{*m}\right]\right\}\right) dS$$

$$Q_\alpha^{m+1/2}(\vec{r}) = \langle Q\rangle_\alpha^{m+1/2} + (\vec{r}-\vec{r}_\alpha)\cdot K_\alpha^m \quad \text{for } \vec{r} \text{ in cell } \alpha$$

$$\langle Q\rangle_\alpha^{m+1} = \langle Q\rangle_\alpha^m - \frac{\Delta t}{V_\alpha}\int_{\partial\alpha} \hat{n}\cdot F\left(Q_\alpha^{*(m+1/2)}\right) dS \quad .$$

Here we have written Maxwell's equations symbolically as

$$\frac{\partial Q}{\partial t} + \nabla\cdot F(Q) = 0 \quad , \quad Q = \left(\vec{D},\vec{B}\right) \quad ,$$

and the solution of the Riemann problem gives the interface flux.

For Maxwell's equations, the different values of $\hat{n}\times\vec{E}$ and $\hat{n}\times\vec{H}$ on the two sides of an interface mix together in characteristic combinations to form the numerical interface fluxes $\hat{n}\times\vec{E}^*$ and $\hat{n}\times\vec{H}^*$. For two cells with different ϵ and μ, these fluxes take the form

$$\hat{n}\times E^* = \hat{n}\times\frac{\left\{\left[E^+(\epsilon c)^+ + \hat{n}\times H^+\right] + \left[E^-(\epsilon c)^- - \hat{n}\times H^-\right]\right\}}{(\epsilon c)^- + (\epsilon c)^+}$$

$$\hat{n}\times H^* = \hat{n}\times\frac{\left\{\left[H^+(\mu c)^+ - \hat{n}\times E^+\right] + \left[H^-(\mu c)^- + \hat{n}\times E^-\right]\right\}}{(\mu c)^- + (\mu c)^+}$$

where the normal points from the (-) cell into the (+), and $c = \frac{1}{\sqrt{\epsilon\mu}}$ is the speed of light inside each cell.

In order to understand the stability and accuracy, we apply this scheme to the simple scalar advection equation

$$\frac{\partial u}{\partial t} + c\frac{\partial u}{\partial x} = 0.$$

Advancing the solution u from time level n to $n+1$, the fully discrete operator takes the form

$$u_j^{n+1} = u_j^n + CFL(\frac{3u_j^n - 4u_{j-1}^n + u_{j-2}^n}{2} + CFL(\frac{u_j^n - 2u_{j-1}^n + u_{j-2}^n}{2}))$$

where $CFL = c\frac{\Delta t}{\Delta x}$. This operator is second order accurate in space and time, and can operate in a stable fashion up to a CFL number of 2. It has perfect shift at CFL of one and two. The spectral characteristics for the phase and amplitude variations are shown in Figures 1a and 1b.

3) Geometry/Gridding

Two gridding issues that need to be addressed in EM computations are: 1) number of grid points per wavelength to properly represent the fields in and around a scatterer; and 2) how far should the outer boundary be placed from the scattering object to adequately simulate the nonreflecting boundary condition. In general, the number of points/wavelength is not determined by wavelength alone, and involves the body dimensions (characteristic body size with respect to wavelength) also. The outer boundary location, theoretically, can be right on the body surface itself; however, the computational implementation of nonreflecting boundary conditions requires the outer boundary at a few (2 to 5) wavelengths away from the surface. Again, if one can construct higher order accurate implementations of nonreflecting boundary conditions, the outer boundary can be brought very close to the scattering surface. In general, the necessary grid resolution is provided only around and near the body surface. Between the body and the outer boundary, the mesh is allowed to stretch resulting in very crude (3 to 5 points per wavelength) meshes near the outer boundary regions.

The free space wavelength is reduced to smaller values inside a material (as ϵ and μ become large, the speed of propagation, $c = \frac{1}{\sqrt{\epsilon\mu}}$, goes down, causing the wavelength to scale accordingly). Thus, the grid resolution must take into account material properties to adequately resolve the fields inside material zones.

The number of grid points per wavelength required depends on the order of accuracy of the numerical scheme. A second-order accurate scheme usually requires at least ten grid points per local wavelength. One may be able to use a higher order scheme and minimize the number of grid points. However, as the order of accuracy goes up, the scheme will also require more computations per grid point, which may offset the execution savings with fewer grid points.

The requirement that the fields are resolved accurately with proper grid resolution makes CEM problems computationally intensive, requiring large scale supercomputing. For example, to compute the radar cross section of a typical aircraft at 1 GHz, even if one used 10 grid cells per wavelength, it will require tens of millions of grid points.

4) Validation

Once a CEM code is developed, the results must be validated against known exact solutions and carefully tailored experimental data. There are many computational issues such as grid resolution, location of the outer boundary, and accuracy of the boundary condition procedures that can only be addressed through a careful study of many validation cases. The Electromagnetic Code Consortium (EMCC) has a list of validation cases comprising many target shapes specifically designed for validating codes.

The CEM code has been extensively tested for the following geometries.

1) Canonical objects such as spheres, cylinders, ogives, thin rods, cones, airfoils, and a circular disc
2) Almond shaped target
3) Inlets of various shapes (square, circular, curved, $\cdots$) including the presence of infinite ground plane

4) Flat plates of various planforms
5) Double sphere
6) Complete wing geometries with layers
7) Finned projectiles and cone-cylinder combinations
8) Scattering from ship-like targets
9) Complete fighter targets

To demonstrate the accuracy the present scheme, results are shown in Figure 2 for a number of spheres having different Ka values, including the case of a coated sphere and a resistive shell cylinder. Using about 10 points per wavelength on the surface (expanding grid is used from the body to the outer boundary), results are shown to compare very well with series solutions.

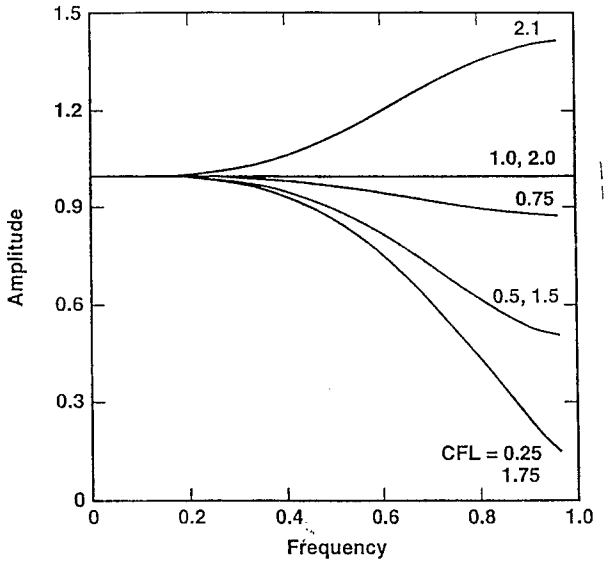


Figure 1a. Spectral amplitude variation as function of CFL number.

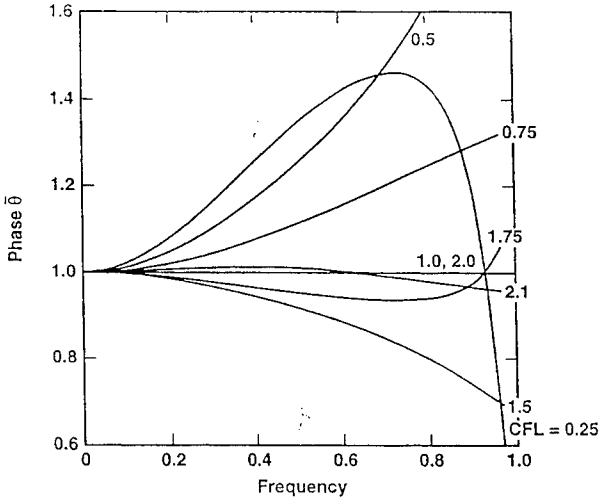


Figure 1b. Spectral phase variation as function of CFL number.

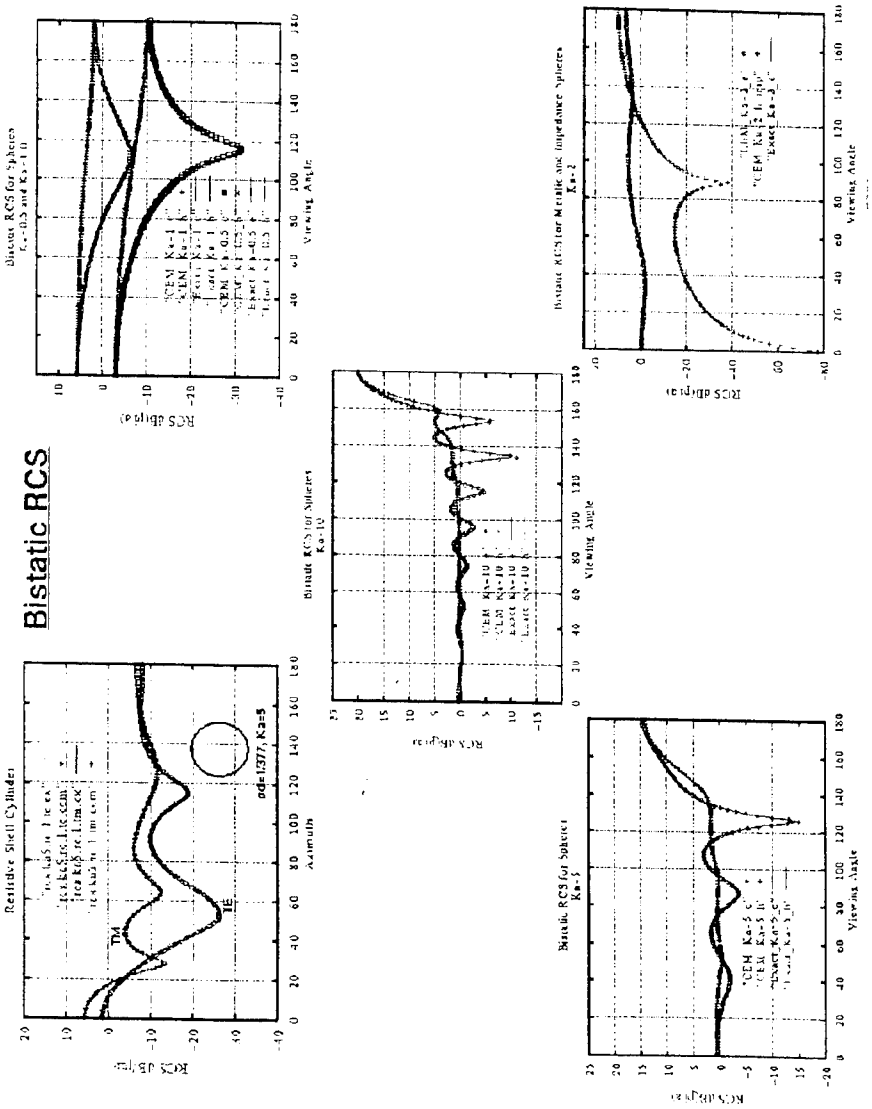


Figure 2. RCS results for spheres.

An Accuracy Study for the 3D Hybrid Finite Element Method of Moments SWITCH Code

G. E. Antilla and Y.C. Ma
Northrop Corporation
B-2 Division
Pico Rivera, CA. 90660-8068

This paper will focus on the accuracy of the SWITCH code, which is a 3D curvilinear hybrid finite element - method of moments code. An explicit scheme to estimate accuracy will be presented, and this method will then be applied to a variety of objects predicted by SWITCH. Specific test cases will include: dielectric and coated metal spheres, cavity backed patch antennas, and business card and conesphere EMCC benchmark targets. The trade off between accuracy and computer resources will be discussed for the hybrid approach used in SWITCH. The advantage of high accuracy with fewer unknowns through higher order basis functions will also be demonstrated.

A useful measure for assessing accuracy is the Pcum X measure, where x represents a percentage between 0 and 100. This quantity is the RCS in dB for which x% of the data in a region is below this level. The region of data considered is usually an angular sector of a pattern, but could be applied to any set of data. The Pcum 50 and Pcum 10 levels will be used to compare SWITCH predictions to either analytical solutions or measured data. The use of the Pcum 10 calculation for comparing data is helpful since it avoids a direct comparison point for point in deep pattern nulls where two patterns may be significantly different. For each data comparison, an overlay plot of the two patterns will also be presented along with the Pcum 50 and Pcum 10 comparisons. The overlay is also important for assessing accuracy because a visual check of the pattern structure may spot anomalies between patterns that may be smoothed out in the Pcum evaluation.

The trade off between accuracy and computer resources will be discussed for the SWITCH code. The first-order curvilinear roof-top basis functions used in SWITCH have been shown to be efficient basis functions, giving high accuracy with fewer unknowns than faceted basis functions resulting in reduced computer storage. Examples will be shown to demonstrate this efficiency. The SWITCH code also incorporates higher order basis functions which result in even fewer unknowns and reduced storage. These higher order basis functions usually result in longer running times when a Galerkin method of moments approach is used. The SWITCH code has encoded a subdomain testing procedure for the higher order basis functions resulting in a substantial speed up of run time compared to the Galerkin approach. Both approaches are encoded in SWITCH and the differences in run time will be shown.

Modeling Accuracy of Method of Moments

Michael B. Gedera
Louis N. Medgyesi-Mitschang
Ronald Pearlman
John M. Putnam
Dau-Sing Wang

McDonnell Douglas Corporation
P.O. Box 516
St. Louis MO 63166

Abstract

In this paper four MM-based codes are compared for a set of canonic and non-canonic scattering problems as a function of several parameters. These include the discretization density and uniformity required to achieve a convergent answer for various quantities such as the mono- or bi-static far fields, near fields, and surface fields or currents. Only the electric field integral equation (EFIE) formulation, restricted to perfectly conducting scatterers, will be discussed.

The four MM codes to be compared are the CARLOS-3D (vers. 3.0), CARLOS-Q, CARLOS-SW and CLOAK codes. These codes were developed at McDonnell Douglas and are based on the Galerkin implementation of the EFIE formulation using different surface discretizations such as flat triangular facets, curved quadrilateral patches, and combinations of the two. The following basis functions are considered: roof top, surface wave, Hermite, Chebyshev, and higher order polynomial expansions. For standardization the LINPACK LU decomposition is used to solve the resulting system of equations for all formulations.

1.0 Introduction

The method of moments (MM) technique for the solution of complex radiation and scattering problems has achieved universal acceptance as an extremely robust solution procedure for Maxwell's equations. Many codes have been developed for one-dimensional (wire), 2-D and 3-D problems, including specialized versions used interactively by designers. The accuracy of these codes has reached such a state of development that high value range measurements are calibrated with MM derived data.

The nature of the MM technique precludes proof of absolute convergence of the solutions for a given problem. Therefore, from the very beginning the MM results were compared to classical "exact" results such as the Mie solution for circular cylinders and spheres, experimental data and other numerical solutions for non-canonic geometries when available. Implicit in comparing these results was the assumption that the surface (geometry) of the object under analysis was accurately described mathematically when comparing different analysis techniques. Similarly, it was assumed that experimental data was taken with sufficient care with regards to calibration, sting interactions, and fabrication of the test object. Computational efficiency, loosely defined as the CPU time and memory resources required to achieve a given level of accuracy, was generally not considered.

In this paper we approach the issue of fidelity in a different manner. First we compare only MM techniques with each other. We restrict the discussion to the Galerkin form and assume that a given LU solver algorithm is used. The mathematical description of the scatterers is generated via a Unigraphics 10.0 package from which the inputs for the various codes are generated. All cases were run on an HP 9000/750 workstation. This allows consistent across-the-board comparisons to be made.

2.0 Description of Codes

As noted above, only the electric field integral equation (EFIE) implementation with the four codes is considered. This restricts the comparisons to perfectly electrically conducting bodies (PEC) only. A short description of the codes under consideration follows. The major differences are the surface representations and the basis functions used. The EFIE formulation is identical in each case; namely, it proceeds from an operator-based implementation that is invariant as to geometry or basis functions. Implementation of the specific forms of these operators varies with the foregoing geometry and basis function descriptions. This is outlined in some detail below.

2.1 CARLOS-3D (vers. 3.0)

CARLOS-3D is a general-purpose MM code for computing the scattering from complex 3-D objects. The code implements Galerkin testing to solve the Stratton-Chu surface integral equations. Complex geometries composed of multiple conducting and bulk dielectric regions can be modeled, although in this paper we focus on PEC cases only. (Refs. 1,2)

A major feature of the code is its modularity built on the generalized Galerkin operators which are geometry and surface-representation independent, permitting the code to be easily adapted to advanced basis functions and parametric surfaces. These operators result from testing either the integral operators in the Stratton-Chu equations, the equivalent currents, or the incident fields. CARLOS-3D vers. 3.0 implements this with the Rao-Wilton-Glisson roof-top basis functions. Matrix elements in the code are computed using a combination of analytic and numerical procedures with the algorithm being facet-based to eliminate redundancy. Self-terms are computed analytically. Near terms are evaluated using singularity extraction with adjustable quadrature formulas optimizing matrix fill times and accuracy.

2.2 CARLOS-Q

Due to the modular architecture of CARLOS-3D, it is straightforward to implement a variety of different surface representations and basis functions. A quadrilateral patch (Q-patch) formulation was implemented within the CARLOS-3D framework, which is denoted as CARLOS-Q in this paper (Ref. 3). A parametric surface geometry representation is employed in the Q-patch formulation to subdivide an arbitrary 3-D surface into quadrilateral patches. This parametric geometry representation permits the direct use of common geometry data formats, such as the CAD, AGM, and IGES files.

The code accepts a parametric bi-cubic geometry representation which substantially simplifies the preparation of the input data for CARLOS-Q in comparison to the original triangular facet approach. This feature is especially advantageous for multi-frequency calculations since the discretization density can be changed without having to re-mesh the surface, which is a costly and time-consuming part of the overall EM modeling process.

The Q-patch formulation is an efficient EM modeling technique for arbitrary 3-D surfaces which employs a set of roof-top basis functions to represent the unknown surface currents on each patch. These basis functions are edge-based and are similar to the Rao-Wilton-Glisson basis functions for

triangular facets. This feature, together with the modularity of CARLOS-3D, makes it possible to have a hybrid mesh representation of the surface geometry that combines triangular facets with quadrilateral patches, not discussed here. The combination of the parametric geometry representation and the edge-based basis functions substantially improves the modeling capability of complex geometries.

2.3 CARLOS-SW

CARLOS-SW incorporates a set of higher order basis functions that simulate the surface-wave effects on the boundary of a scatterer. The purpose of this code is to maximize the reduction of unknowns by employing a set of surface-wave (SW) basis functions that efficiently represents the unknown surface currents. These SW basis functions consist of a slowly-varying function multiplied by a phase factor that resembles the surface diffraction terms developed for high frequency approximations. The slowly-varying function is expressed in terms of Chebyshev functions. In addition a physical optics term is added to the current representation to further reduce the number of unknowns required in the calculation. Details of this analysis can be found in Ref. 4.

We have validated CARLOS-SW for both 2-D and 3-D geometries. Substantial reduction of the number of unknowns was observed. For example, the scattering from a 20 λ wide, 2-D curved surface required only 26 unknowns for CARLOS-SW, while 250 unknowns were required by a conventional MM code.

2.4 CLOAK

CLOAK is a general purpose MM code that operates on exact surface descriptions of the scatterer, represented by combinations of B-surfaces and parametric bi-cubic curvilinear patches. The basis functions are higher order polynomial expansions which map directly onto the surface isoparametric lines. With this higher order formulation, a typical discretization density is roughly four basis functions per wavelength. Of course, the double surface integrations required to calculate matrix elements result in greater matrix fill time than with simpler basis functions.

Although CLOAK was originally developed independently, the defining features of the code have recently been integrated into the CARLOS-3D framework. A major advantage of using an exact surface representation is that the geometry description is frequency independent, meaning that it only needs to be generated one time. Other techniques require re-discretization for each different frequency regime, which as noted previously, can be a costly step.

3.0 Measurands

Four principal measurands are chosen for comparison. They are: the density of basis functions required to span a given scatterer, the total number of unknowns (degrees of freedom) associated with this sampling, the matrix fill time, and the accuracy achieved for different classes of "observables" to be elucidated later. Note that the matrix storage requirements for all of these techniques is directly related to the total number of unknowns.

3.1 Sampling Density and Number of Unknowns

In discussing the sampling density required for a given technique, two issues are important. First, the shape of the surface must be discretized and represented in a fashion that will accurately represent the true shape of the scattering geometry. Second, this geometry sampling must be consistent with the accuracy achievable by the basis function used in order to capture the correct variations of the unknown surface currents. In general, the simpler the surface representation and associated basis

functions, the easier it is to compute the MM matrix elements. When more complicated surface representations and basis functions are used, more work must be done in computing the individual matrix elements. However, these more complicated techniques also result in a reduction of the total number of matrix elements which must be computed, and ultimately in the overall order of the MM system that needs to be solved.

Each of the four codes discussed in this paper uses a different surface representation and set of basis functions. Both the surface representations and basis functions can be characterized in two broad categories: flat facet-based representations versus curved discretizations, and linear basis functions versus higher order polynomial basis functions. The flat-facet surface representation essentially ignores any curvature and relies on higher sampling density to accurately capture this information, while the curved surface discretizations can capture the curvature to any desired degree of accuracy. Similarly, the linear basis functions require higher sampling density in order to capture rapid current oscillations, while the higher order basis functions have much of this built into the basis functions themselves and hence allow more coarse sampling.

CARLOS-3D uses the Rao-Wilton-Glisson roof-top basis functions applied to a triangularly-faceted surface description. With this method, a given triangle pair sharing a common edge forms the basis function with the unknown current coefficient being associated with the common edge. The basis function allows the current to vary linearly from zero, at the vertices opposite this common edge, to a maximum value at some point along the common edge. Since the surface representation and basis functions are both linear, typically this formulation requires a higher sampling density to achieve a given solution accuracy, usually on the order of 100 triangles distributed per square wavelength, or 8 - 10 basis functions in a linear dimension.

CARLOS-Q enhances the geometry modeling capability of CARLOS-3D. This technique employs the parametric bi-cubic surface representation to provide direct access to the geometry data from commonly used geometry software packages. In addition, the edge-based basis functions used in CARLOS-Q are similar to the roof-top functions in the triangular facet-based CARLOS-3D formulation which allows hybrid formulations of the two different techniques. The curvilinear (quadrilateral) patches used in the Q-patch formulation not only provide an accurate surface representation but also help to reduce the number of unknowns by eliminating the unnecessary ones.

CARLOS-SW utilizes entire domain basis functions which take advantage of asymptotic approximations of surface diffraction terms in order to reduce the number of unknowns. The surface of the scatterer is first subdivided into smooth, irregular regions, where the smooth surface is treated as one curved patch. The size of the patch determines the required number of basis functions. We have observed the solutions converges for as little as 5 basis functions per wavelength for surface dimensions less than 10 λ.

The CLOAK code utilizes curved bi-cubic patches or B-surfaces to represent the scatterer. Each of these curved surfaces is then partitioned into a quilt of curved quadrilateral sub-patches, about one-quarter wavelength on a side, and higher-order polynomial basis functions are applied. Thus, as the frequency changes, CLOAK automatically adjusts the density of basis functions applied to the geometry. The total number of basis functions is approximately twice the number of sub-patches. So, if the quilt is composed of sub-patches sampled at a linear density of 4 per wavelength (16 sub-patches per square wavelength), the total number of unknowns per square wavelength is approximately 32.

3.2 Matrix fill

Accurate numerical evaluation of the matrix elements arising in the MM technique is a key determinant of the resulting accuracy of the overall results of the computations. In the Galerkin MM technique, the mathematical expressions of the matrix elements for 3-D objects require in general a

four-fold surface integration to be carried out. This integration is obviously a function of the surface representation used for the object as well as the basis/testing functions used. Additionally, the particular type of quadrature used will strongly impact both the accuracy and fill time.

Extensive investigations have been carried out to achieve the highest accuracy possible, particularly for the self-term (diagonal) elements of the matrix. Various numerical and semi-analytical methods have been proposed including singularity extraction. The four codes being compared use different methods for this vital step of the numerical implementation of the MM technique. In principle, any degree of accuracy can be achieved via quadrature methods at the cost of much enhanced computation times. Since matrix fill is proportional to N^2, it is imperative to adopt the most accurate yet computationally efficient integration technique.

3.3 Accuracy

A single test case was chosen to provide a quantitative comparison of the accuracy of the four techniques. Although the "accuracy" achieved by a given code will depend on many factors, including the geometry itself, the comparison is intended to provide the reader with a feel for the convergence properties of the different numerical techniques which can be weighed against their relative computational costs. To that end, the geometry chosen is the well-known "business card," the EMCC test case number 4 (Ref. 5). This case is a thin metal plate, $3.5\lambda \times 2\lambda$, with an azimuthal cut at 10° elevation from the surface of the plate. Since the geometry is symmetric about the x and y axes, a monostatic cut from $\phi = 0°$ to $\phi = 90°$ suffices, where $\phi = 0°$ corresponds to incidence along the short side of the plate.

In the subsequent comparisons between the different codes, a baseline "exact" solution is used to quantify a measure of "accuracy." This "exact" solution is a numerical entire domain MM solution, which used 105 basis functions in the long direction of the plate and 30 in the short direction, a density which is well beyond the necessary limit for convergence. Figure 1 provides a comparison of this "exact" solution with measured data provided by the EMCC. Although the computed data differs from the measurements in some areas, the measured data is not without its own inaccuracies.

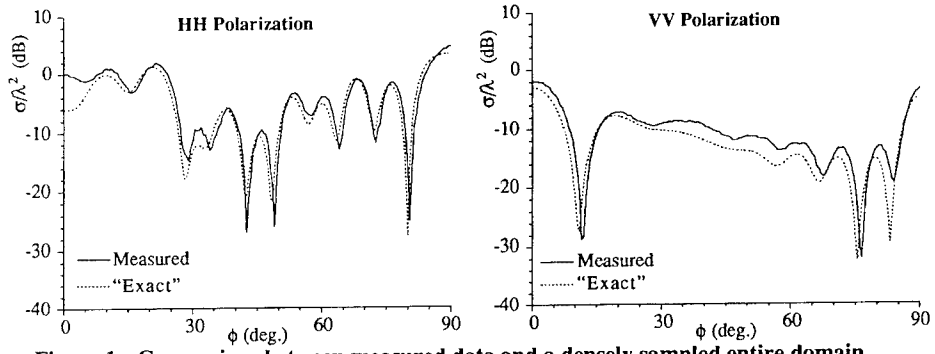


Figure 1: Comparison between measured data and a densely sampled entire domain solution for EMCC test case number 4.

Each of the four codes was used to generate a set of three different solutions for this test case, representing low, medium, and high density sampling in order to demonstrate the convergence properties for each method. These convergence results are shown in Figures 2 - 5.

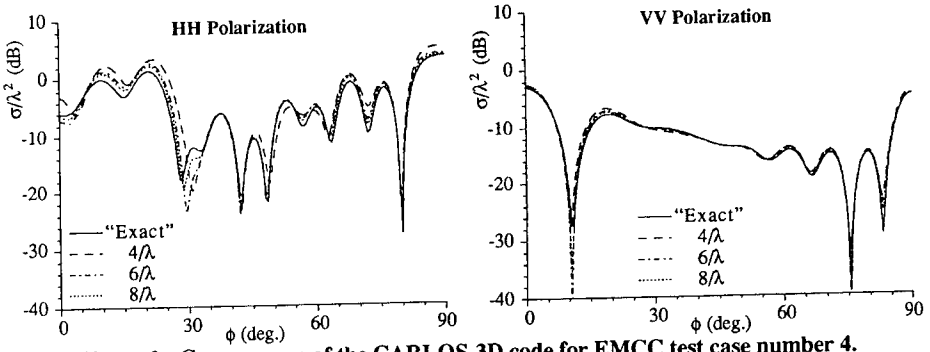


Figure 2: Convergence of the CARLOS-3D code for EMCC test case number 4.

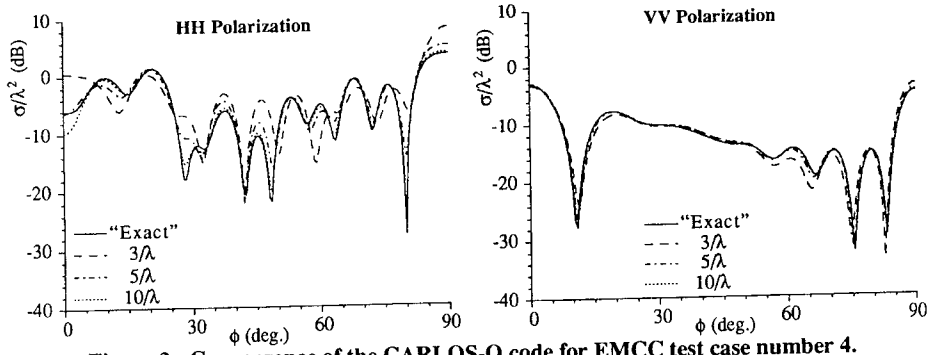


Figure 3: Convergence of the CARLOS-Q code for EMCC test case number 4.

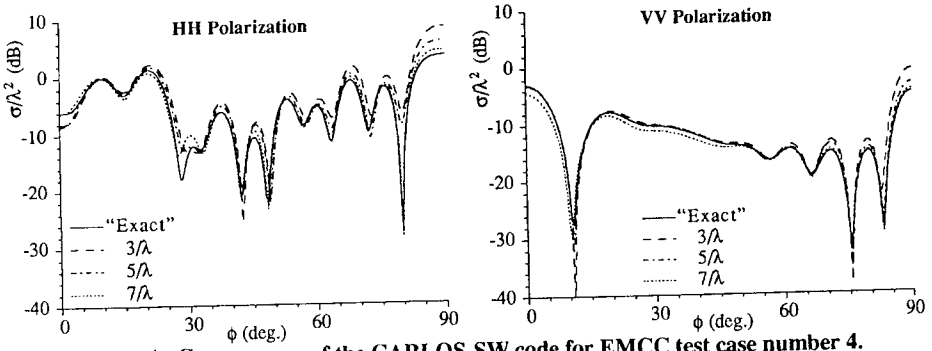


Figure 4: Convergence of the CARLOS-SW code for EMCC test case number 4.

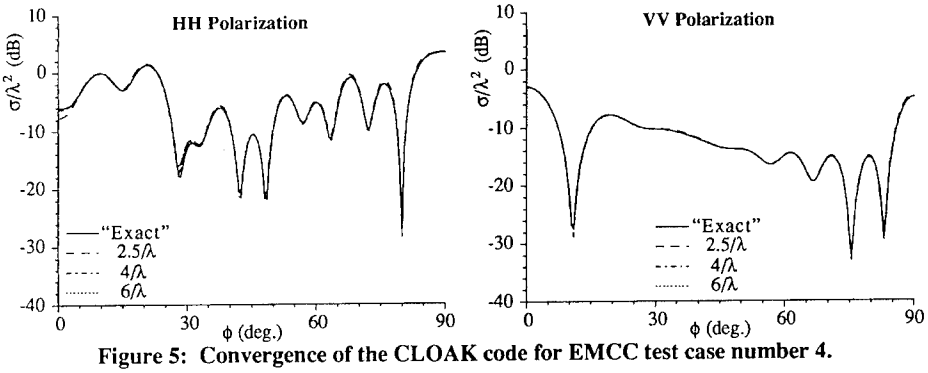


Figure 5: Convergence of the CLOAK code for EMCC test case number 4.

The accuracy results of these 12 different cases are summarized in Tables I - IV, where the accuracy measure is computed as the root-mean-square error between the given numerical simulation and the "exact" entire domain solution, normalized by the RMS value of the "exact" solution. Note that these calculations were performed on the normalized cross section values, not on a logarithmic (dB) scale. The column labeled "Basis Fcns/λ" represents the sampling density in a linear dimension and the column "Total Unknowns" gives the order of the overall MM matrix equation that was solved. Note that matrix fill time is not presented here due to the many factors which influence this measurand, such as the particular choice of quadrature formulas used for the numerical integration.

Table I
Summary of CARLOS-3D convergence.

Basis Fcns/λ	Total Unknowns	Error HH	Error VV
4	360	0.574	0.140
6	688	0.275	0.091
8	1300	0.173	0.062

Table II
Summary of CARLOS-Q convergence.

Basis Fcns/λ	Total Unknowns	Error HH	Error VV
3	126	1.151	0.165
5	313	0.319	0.068
10	1345	0.084	0.023

Table III
Summary of CARLOS-SW convergence.

Basis Fcns/λ	Total Unknowns	Error HH	Error VV
3	104	1.461	0.613
5	264	0.567	0.172
7	480	0.184	0.246

Table IV
Summary of CLOAK convergence.

Basis Fcns/λ	Total Unknowns	Error HH	Error VV
2.5	152	0.065	0.041
4	318	0.031	0.007
6	642	0.026	0.007

5.0 Summary

Four different Galerkin MM formulations for arbitrary 3-D geometries have been described. A comparison was made with respect to geometry modeling accuracy, matrix fill time, and far-field solution accuracy. It was noted that the use of a generalized operator notation in the MM solution permits the incorporation of different geometry representations and basis functions within a single code architecture. This also allows the incorporation of hybrid methods which use combinations of the different formulations discussed in this paper.

Although this paper has only presented results for the "business card" test case, additional quantitative comparisons have been made with the four codes. Some of these include far-field solutions for a sphere, a curved shell, the NASA almond and ogive, and a complex curved surface. These results provide further quantitative assessment of the relative performance of the codes compared in this paper.

References

[1] J.M. Putnam, L.N. Medgyesi-Mitschang, and M.B. Gedera, *CARLOS-3D™: Three Dimensional Method of Moments Code*, Vols. 1 & 2, 1992, Prepared for Dynetics, Inc., Huntsville, AL, under sponsorship of U.S. Govt. Electromagnetic Code Consortium.

[2] L.N. Medgyesi-Mitschang, J. M. Putnam, M.B. Gedera, "Generalized method of moments for three-dimensional penetrable scatterers," *J. Opt. Soc. Am. - A*, vol. 11, no. 4, (1994), pp. 1383-1398.

[3] R. Agarwal, D.S. Wang, and M.R. Axe, *A Hybrid Method of Moments and Computational Fluid Dynamics Method for Computational Electromagnetics*, Theory Report, NAS2-13891, NASA-Ames, Moffett Field, CA, 1994.

[4] D.S. Wang, "Current-based hybrid analysis for surface-wave effects on large scatterers," *IEEE Trans. on Antenna and Propagat.*, Vol. 39, No. 6, 1991.

[5] H.T.G. Wang, M.L. Sanders, A. Woo, and M. Schuh, *Radar Cross Section Measurement Data: EMCC Benchmark Targets (RAM Coated and Dielectric Targets)*, Naval Air Warfare Center Weapons Division, Technical Memorandum NAWCWPNS TM 7318, August, 1992.

REQUIRING QUANTITATIVE ACCURACY STATEMENTS IN EM DATA

E. K. Miller, Stocker Visiting Professor
Ohio University, Athens, OH 45701, 614-593-1603

ABSTRACT

Of all the activities associated with developing computer models for any application including computational electromagnetics (CEM), validation must be considered the most critical over the long term. Without quantitative assurance that the results produced by a model are commensurate with the needs of the intended application, there will always remain questions concerning whether analysis and design evaluations based on that model can be relied upon. Unfortunately, in contrast to the situation in years past when experimental measurements were the principle source of such data and error estimates were routinely expected to accompany them, the growth in computer-model results seems to be characterized by an almost complete lack of meaningful accuracy statements. As a means of correcting this problem, it is first proposed that some modest initial steps be taken, such as requiring error estimates to be included with all computed data published in the CEM literature. The rest of the paper provides additional background and considers aspects of model validation as a means of improving CEM overall model utility. Several of the author's papers on this topic are listed as references.

A PROPOSAL FOR QUALITY CONTROL OF PUBLISHED NUMERICAL RESULTS

With the proliferation of quantitative results in EM arising from ever more sophisticated experimental apparatus and from almost universal use of computer models, the need to accompany such data with accuracy (or error) estimates is becoming acute. It's not unusual to find published articles that contain numerical results having no independent confirmation of their accuracy or even lacking any discussion of how good the author considers the results to be. When accuracy is considered, it is becoming quite common to find results from another numerical computation, such as a "moment-method" model, referred to as the "exact" solution without any accompanying measured data. Furthermore, in such cases, the usual discussion finds only qualitative descriptors such as "good agreement" or "excellent results" being used. Even when accuracy is quantitatively addressed, the comments made about it are usually inconsistent and incomplete. For example, one author might consider only impedance errors important, another might view peak gain the primary quantity of interest, and still another shifts in pattern nulls the limiting factor.

Consequently, with few exceptions, the reader is left with only a fuzzy, qualitative interpretation of accuracy and error concerning the results actually presented in the publication, let alone the accuracy and error characteristics of the process (computational or experimental) by which that data has been generated if that process were to be used for substantially similar problems. The situation only gets more fuzzy when the reader wonders about the accuracy of that process and its error characteristics when used for substantially different problems. This paper addresses one approach to alleviating this problem. Basically, the idea is to implement a policy that requires an author to add a separate section following the introduction to any article in which computed results are presented. In that section, statements of the following general form, with whatever elaboration is appropriate, will be included:

> "The results presented here are estimated to be accurate to _____," where quantitative statements such as:
>
> "The error in peak gain is ≤ 0.5 dB; or
>
> "Nulls in the scattering pattern are located to within 2 deg; or
>
> "Input impedance is obtained to within 5 ohms; or

"Etc.
are made. This would be followed with the mandatory additional statements below.

"This estimate is based on using the following kind(s) of validation exercise(s) _____," where whatever experimental, analytical and/or computational validation that has used is summarized.

"The kinds of problems for which the above error/accuracy statement can be made include _____," where the problem geometry and electrical characteristics are summarized.

"Nominal sampling densities required to achieve these estimated accuracies are _____," where wavelength-dependent and/or geometry-dependent values are given.

"The operation count needed to exercise the model reported here is estimated nominally to be $Af^{\wedge}x, \ldots$ " or some equivalent statement, where numerical values for A and x are given. While providing computer running times is acceptable, that alone is not enough because there is such a variation in computer architectures that model-to-model comparisons based on running time are not very informative.

". . . and the variable storage need to exercise this model is estimated nominally to be $Bf^{\wedge}y$," where again numerical values for B and y are given.

In conclusion, we note that the above procedure is aimed at validating the results obtained from a given model when used for a specific application. This is much different from validating the model itself, which is a more general and open-ended problem and one to which the above procedures would contribute but not resolve. Both problems are discussed further below. Also note that simply including independent data obtained from measurement, analysis or computation would itself be sufficient to satisfy the above quantitative validation requirements so long as the check data itself has associated error estimates from which such inferences can be drawn or when error estimates are derived by the author(s) from comparing the independent data and the model results in question. The above proposal constitutes the main thesis of this presentation. In order to round out the discussion and provide further background, we now examine the problem of model validation in more detail .

BACKGROUND

In this section we consider the steps involved in developing a CEM model and the role of validation in that process and then examine the general requirement of verifying and validating the results obtained and the model itself. There being no uniformity of useage, the terms "model," "code," and "program" are used interchangably here as names for the software that's used for EM computations.

Developing a CEM Model

The process of developing a computer model involves a small number of basic steps whatever particular details are involved. Because these steps are universally encountered, it is worthwhile to summarize them as follows:

Conceptualization--Encapsulating observation and analysis in terms of elementary physical principles and their mathematical description (e.g., the idea that a Green's function can be used to represent the fields of arbitrary source distributions).

Formulation--"Fleshing out" of the elementary description into a more complete,

formally solved, mathematical representation (e.g., development of an integral equation from a source integral and required boundary conditions on field behavior).

Implementation--Transforming the formulation into a computer algorithm using various numerical techniques (e.g., using the method of moments).

Computation-- Defining the model and obtaining quantitative results (the "crank-turning" stage).

Approximation--Simplifying operations and assumptions that can arise at any step in the process of model development and application (e.g., reducing a surface integral to a line integral by using the "thin-wire" approximation or approximating a solid conductor with a wire mesh).

Validation--Determining the numerical and physical credibility of the computed results (using analytical, experimental, and/or other numerical results for comparison with the computer model being employed).

For any applications-oriented software, the most time-consuming and laborsome of these steps is the last, that of validation. This is becoming increasingly the case as growing computer power has expanded the size, complexity, and volume of problems that are routinely modeled. Whereas computer resources available in the 1960s limited the amount of data needed to describe problems and represent the results, there has been an explosive growth in the scope of applications as summarized in Table I.

Long after work on the model has been completed, questions will continue to arise about its performance. Such questions include:

- is a given result valid?
- can the model be used reliably for a given problem?
- what might be the numerical accuracy and physical relevancy of the results that are obtained?

These questions become especially important as modeling moves from a primarily research environment to one which involves an increasing emphasis on analysis and design applications. The difficulties caused by uncertainty over model performance also increase with the expanding proliferation of modeling codes and computational resources becoming available. The question of perceived model validity is of particular concern in that it can lead to correct results being rejected because of unwarranted skepticism or acceptance of incorrect results because of misplaced confidence. Either outcome is undesirable and both should be avoided by developing the validation procedures needed for an appropriate level of user confidence to be achieved.

Without essentially "exact" results to serve as benchmarks, there will always be some lingering doubts regarding the validity, let alone accuracy, of computer models. Unfortunately, as is well known, there are few closed-form, exact solutions available from classical electromagnetics. For a 3D computer model to match results for a spherical body is hardly convincing anymore that the same model will work as well for a more arbitrary body geometry. Checks of the kind provided by the sphere can be regarded only as necessary, but not sufficient, conditions for solution validity. But without reference solutions to provide benchmark results, quantification of computer-model accuracy and validity for the most part will continue to remain an open question.

Verification and Validation

The term "validation" as generally used actually covers two related, but distinctly different, aspects of computation, verification and validation and unless otherwise specified are both considered here to be

included under validation. Verification determines that a modeling code produces results consistent with its design while validation establishes how well its results conform to physical reality. Both are ingredients essential to performing reliable modeling computations. Verification is a necessary, but not sufficient, condition for achieving acceptable code performance, while validation determines how reliably a given code can be applied to physically meaningful problems. Clearly, the latter aspect of code performance cannot be reached without confirming the former which is why validation is the more general term.

Computational checks at various points in the computation would be advantageous in establishing quantitative measures of code performance with respect to both verification and validation. These checks would address such problems as:

1) moving codes between computers;
2) confirming the continued valid operation of the code over time on a given computer, and;
3) guiding the user concerning the validity of the computed results.

Computational models would ideally also include features that support "dialable" accuracy to permit an explicit tradeoff between the cost of the computation and the accuracy of the results.

The first step in assessing computational accuracy stems from the two sources of error in any modeling exercise. These are the physical modeling error (E_p) which arises from approximating the physical problem of interest with some idealized mathematical representation, and the numerical modeling error (E_n) which occurs because only an approximate numerical solution is obtained to that idealized mode. Determining E_p will require access to measured data because most problems require some physical approximation, such as representing a smoothly curved object by plane, triangular facets. Given adequate computational resources, E_n can always be made smaller than E_p. The essence of the verification and validation approach outlined is to develop a protocol for systematically and consistently estimating E_n in response to the three points above.

Several options could be considered for this purpose, but they are rarely utilized in current modeling codes. For items (1) and (2) above, for example, it would be advantageous to users if model developers were to include a set of precomputed test cases, including the model input; results at various stages of the computation; and the final observables such as radar cross sections and/or thermal emissions. Concerning item (3), including a user option to exercise various validation checks that might range from testing far-field reciprocity, to evaluating boundary errors, or even comparing results from two different numerical models would be extremely helpful. Finally, it would be especially valuable to more casual users if a code offered the modeler a quantitative "figure of merit" (FoM) to indicate the reliability of the computed results.

Clearly, verification and validation options range from being quite easily implemented to posing significant research challenges. As problem complexity and the associated total FLOP count continue to increase with faster computers, such options will become increasingly more essential to assisting users in achieving effective code useage in analysis and design. We now examine some specific approaches to realizing a validation ethic or protocol.

ONE APPROACH TO VALIDATION

It might be helpful at this point to clarify what validation should mean in a modeling context. Among the definitions given by the 1975 American Heritage Dictionary for "validate" are the following:

--to declare or make legally valid; to mark with an indication of official sanction; to substantiate or *verify*,

while under "verify" we find

--to confirm or substantiate in law by oath; to establish the truth, accuracy or reality of,

with the most relevant of both meanings provided by the last statement concerning the "truth, accuracy or reality of." Proceeding with the understanding that the inclusive term validation means to establish the truth, accuracy or reality of model performance, several key issues arise as are discussed briefly below.

What Problems and Solutions?--The first decision to be made in model validation is the selection of appropriate test problems. Although numerical validation can (and should) be performed within a model itself using internal checks as discussed below, a more logical starting point for model validation is the use of external data or checks. From an analytical viewpoint, we need to consider for which problems are answers, preferably of known accuracy, available to serve as independent sources of results? Alternatively, are there certain kinds of problems for which experimental data of needed accuracy can be obtained? Furthermore, from among that set of candidate analytical and/or experimental problems, which provide the most appropriate testing of model capabilities? For example, while one way of validating a wire code such as *NEC* can be to compare results for scattering from a wire-mesh model of a sphere with the MIE series, that would not be especially relevant for determining the code's performance when used for modeling wire antennas. As discussed further below, we suggest that the problems and solutions that are selected for validation purposes might be usefully assigned to one of two categories, described as primary and secondary benchmarks.

What Comparisons?--A second decision concerning model validation involves which quantities are to be used for this purpose. Most obviously, these quantities should include physical observables for which measured data, at least in principle, can be obtained. But mathematical quantities and relationships which might be essentially inaccessible using measurements might also be useful as sources of data for validation purposes. For example, the eigen values and eigen vectors of the moment-method impedance matrix might be candidates for use in model validation, but they are not directly measurable in general.

How Accomplished?--Finally, we must carefully consider how the quantities chosen for use in model validation are to be compared, and over what range of variables and parameters the comparisons should be performed? The spatial or temporal variation of a given field quantity might be appropriate for some applications. On the other hand, a result derived from integrated measures of such quantities, for example total scattered power, might be more relevant for other purposes. The former approach might be called microscopic in that the fine structure of the solution is being examined, while the latter could be described as macroscopic because it provides a less detailed but broader means of comparison.

These various issues are not easily settled and will require thoughtful consideration and, most likely, systematic refinement as procedures for model validation evolve. We are suggesting essentially that an experimental *protocol* be developed for this purpose. This *protocol* would set down clearly defined procedures for validating present and future models in an agreed-upon way that is both physically and numerically relevant to intended applications.

VALIDATING USING INTERNAL AND EXTERNAL CHECKS

We noted above that essentially two kinds of procedures can be used to establish some quantitative measure of code validity:

1) **Internal Validation**, a check that can be made concerning solution validity within the model itself; and

2) **External Validation**, a check that utilizes information from other sources which could be analytical, experimental or numerical.

Internal Checks--Existing computer models often do not perform internal checks on the results they produce, but instead leave that as an exercise for the user. For example, *NEC* could provide and indeed has been exercised to give various kinds of checks relating to power balance, reciprocity and boundary-condition matching. But the software to perform the wide range of internal checks that might be most useful for a given application is usually not completely implemented in a code, but instead may need to be "patched in" by the user for a particular problem and check. It would be extremely valuable if a variety of such checks were to be built into the code by the developer so they were available to be exercised as desired by the modeler.

As a particular example of the possible applications of internal checks, consider the case when a problem new to the modeler is encountered and the initial results are obtained. Present practice usually involves "eye-balling" the data to see if it "feels" right, perhaps having first run some documented test cases to verify code performance. Since these test cases would not likely resemble the new problem, their successful solution might not provide much insight concerning the new results. If, however, a series of checks built into the code could then be exercised at the modeler's discretion to verify that conditions necessary for a valid solution of Maxwell's Equations are satisfied, confidence in the model's numerical reliability could be more readily established. These checks might range from fairly exhaustive, such as computing boundary fields to determine how well boundary conditions are satisfied, to fairly simple, such as evaluating the degree to which reciprocity and power conservation are demonstrated. They could only be viewed as necessary but not sufficient conditions for solution validity, and could only involve such behavioral aspects as are not implicit in the model already (e.g., some formulations produce symmetric matrices so that bistatic scattering and transmit-receive reciprocity are assured analytically). Developing a figure-of-merit from the results of such checks that would provide a "quality factor" (or more if application-specific measures are useful) for the solution in a single number seems not only feasible but highly desirable.

External Checks--The second kind of check involves use of independent data from other sources. Perhaps the most convincing overall is experimental data, but analytical or numerical results should be comparably useful. Indeed, one of the most convenient computational checks would be provided by a code that permits two different numerical models to be developed for the same problem, for example by incorporating user-selectable basis and weight functions. For greatest utility, such checks ideally should not be microscopic or of single-point nature, e.g. a comparison of results for input impedance at a single frequency. This is because experience shows that computer models produce results that exhibit apparently slight frequency shifts, angle shifts or spatial shifts in field quantities with respect to "exact" solutions, or even other computer models. When the effects of such shifts are observed near maxima in the response of interest, they may appear relatively insignificant, but when examined near deep minima or even nulls, the differences can become unbounded. Consequently, macroscopic or global comparisons are usually more meaningful, but even they may not be straightforward to interpret. If the shifts mentioned are observed, it would seem more appropriate to develop a correlation measure such as computing the minimum squared difference between the two results as they are shifted along the axis of the common variable, rather than simply doing an absolute differencing. For other models and applications, the results may be even less directly comparable, as is the case for IE -and DE-based models. Some work is needed in the general area of how results from two different representations of the same problem can be most meaningfully compared.

KINDS OF MODELING ERRORS

Error types and error sources are discussed here since the type of error and its source dictate what kinds of validation metrics might be most appropriate.

Types of Errors--The error type refers to the general effect produced on the modeling process as:

Type 0 errors--Type-0 errors keep a program from running to conclusion, and are therefore the most obvious when they occur, but not necessarily the easiest to correct.

Type 1 errors--Type-1 errors occur when a program runs to conclusion to produce the requested output which contains obviously incorrect results. A fairly common example is that of obtaining a negative input resistance for an antenna.

Type 2 errors--Type-2 errors arise when the program runs and produces what appear to be physically plausible results, but which are invalid for the problem being modeled. This category of error is generally most insidious because it is generally the most difficult to identify and correct.

Type 3 errors--Type-3 errors are user dependent as they occur when the modeler misinterprets, mistrusts, or misuses the results produced in the computation. It is reasonably well accepted for example, that computer models produce results that are generally more accurate on a relative than on an absolute basis. For example, often the nulls and peaks of a radiation pattern or a transfer function are shifted between computation and measurement, although their overall structures may be essentially the same. A modeler unacquainted with such shifts might consequently not accept computed results which exhibit them, even though they are basically correct and useful for the problem under consideration.

Sources of Errors--The error source defines the cause of error as arising in at least four ways:

Software errors--These can originate from the operating-system software or programming errors in the modeling code.

Numerical modeling errors--A numerical modeling error arises from obtaining insufficiently accurate numerical results for the model that has been selected, one example being non-converged results. Another example is that of using word sizes of insufficient bit length which affect matrix-fill and matrix-solution accuracy due either to machine limitations or user preference.

Physical modeling errors--A physical modeling error arises from an inadequate "match" between the physical reality of interest and the numerical model that has been used. A common example in antenna modeling is that of improperly representing the source region in the numerical model, giving rise to an error which primarily affects the input susceptance.

User errors--Aside from such obvious sources as input-data errors, this category includes misapplication of the model by violating stated limitations intrinsic to the formulation or its numerical implementation. An example of the former is use of a model based on the magnetic-field integral equation for open or thin structures. Violation of the thin-wire approximation by using segment lengths shorter than the wire diameter is one example of the latter. User errors can occur because the model results are misinterpreted, mistrusted or misused due to unrealistic expectations, unwarranted skepticism or blind faith. The two extremes of user reaction that can

follow are rejection of correct results or acceptance of wrong results, either of which might be equally unfortunate.

Accuracy Metrics or Measures--Application-relevant, model-independent measures must be developed for quantitatively assessing the accuracy of computed results. As a starting point, we might consider the following categories of results:

1) Far-field quantities--For exterior problems, far-field quantities and results derived therefrom are often the primary goal of the model application. These include macroscopic or integral measures such as total far-field power as well as the microscopic or angle-dependent results from which these quantities are derived. In those cases where the far-field polarization properties are important, these quantities are needed separately for the appropriate field components. Because the E and H fields are related simply by the medium wave impedance, only one of them must be dealt with explicitly.

2) Near-field quantities--The near fields are generally thought to provide a more demanding measure of model performance than does the far field. Because the E and H fields are, in the near field, related by a position-dependent impedance, both are relevant quantities for validation purposes. We note that for interior problems, all fields, by definition, are near-field quantities in some sense.

3) Boundary quantities--These are quantities associated with steps in medium properties at surfaces on which boundary conditions are stated as part of the problem definition. Both the fields themselves, as well as their associated sources, are boundary quantities that are useful for validation. Derived quantities such as antenna input admittance also fall into this category.

4) Other quantities--There are other numerical quantities provided by many models for which no direct physical measurement can be made but which nonetheless are useful for assessing computation accuracy. For example, convergence of the eigen value (EV) spectrum as the number of unknowns is increased in an IE-based model serves as one measure of convergence and by inference, of accuracy. But the EV would not be directly measurable, although it might be obtained from computation based on the appropriate physical measurement.

5) Approximations--Affecting the accuracy of all the above measures are the approximations inherent in any model whether made in the formulation or subsequent numerical implementation. These approximations affect both the kinds of problems for which the code can be used and the level of accuracy that might reasonably be expected from it, and can also dictate how the code might be used for achieving increased accuracy for problems that stretch its capabilities. For example, a model that can be applied to geometries having edges or bends but which provides no special treatment for such features might yield better results when the sampling density is systematically increased in such regions.

CONCLUDING COMMENTS

The problem of establishing the accuracy of model results, or model validation, can only grow in importance as the size and complexity of the problems being modeled and the uses to which they are put continues to expand. Unfortunately, qunatitative validaiton of specific results or of the models used to

produce them has not kept pace with the evolving status of CEM as an EM susdiscipline. While admittedly a difficult problem, model validation is at present defficient and thus impedes all other aspects of model development and application. Rather than continuing the status quo it is proposed that a modest first step towards a validation ethic be taken by requiring uniform statements concerning the accuracy or errors of such results to be included in all future published material in the reviewed literature. It is essential to the continued development of CEM that developers and users alike are aware of the limitations of computed results and how they can be appropriately interpreted with respect to intended applications.

REFERENCES

Miller, E. K. and A. J. Poggio (1978), "Moment-Method Techniques in Electromagnetics from and Applications Viewpoint", in Electromagnetic Scattering, Academic Press, pp. 315-357.

Miller, E. K. and G. J. Burke (1984), "Error Measures for Numerical Modeling", USNC-URSI National Radio Science Meeting, University of Colorado, Boulder, CO, January 11-13.

Miller, E. K. (1986), "User Friendly Electromagnetics Software", 2nd Annual Review of Progress in Applied Computational Electromagnetics, US Naval Postgraduate School, Monterey, CA, March 20-22.

Miller, E. K. (1987), "Development of a Modeling Handbook for Use in Computational Electromagnetics", 3rd Annual Review of Progress in Applied Computational Electromagnetics, Naval Postgraduate School, Monterey, CA, March 24-26.

Miller, E. K. (1988), "Development of EM Modeling Software Performance Standards", 1988 IEEE AP-S International Symposium, Syracuse University, Syracuse, NY, June 6-10, pp. 1340-1343.

Miller, E. K. (1989), "Characterization, Comparison, and Validation of Electromagnetic Modeling Software," ACES Journal, special issue on Electromagnetics Computer Code Validation, pp. 8-24.

Miller, E. K. (1992), "Necessary and Sufficient Conditions for Portable, Reliable, and Useful CEM Software," Published in Proceedings of Allerton Antenna Conference, University of Illinois, Urbana, IL.

Miller, E. K. and R. P. Kruger (1993), "A Proposed Approach for Developing Next-Generation Computational Electromagnetics Software," in Proceedings of the Ninth Annual Review of Progress in Applied Computational Electromagnetics, Naval Postgraduate School, Monterey, CA, March 22-26, pp. 122-138.

SESSION 23:

PDE METHODS IN ELECTROMAGNETICS

Chairs: R. Lee, J.-F. Lee

Optimization issues in finite element codes for solving open domain 3D electromagnetic problems

A. Chatterjee and J. L. Volakis
Radiation Laboratory
Department of Electrical Engineering and Computer Science
University of Michigan
Ann Arbor MI 48109-2122

January 9, 1995

1 Introduction

The finite element method (FEM) is attractive for modeling three dimensional problems because of its $O(N)$ memory requirement and its flexibility in geometry design and modification. The $O(N)$ memory feature provides favorable scaling properties as the problem size increases. Its geometrical adaptability provides the versatility required for designing complex systems. Thus, FEM has become the method of choice for electromagnetics CAD software, and its applications continue to increase.

In spite of the obvious attractions of FEM for general purpose 3D electromagnetic field solvers, it has a few drawbacks. Since the method was initially used for solving bounded problems, its extension to open problems is not easy. In open problems, we are interested in the behavior of the fields infinitely far away from the structure of interest. However, it is impractical to extend the finite element mesh very far from the scattering or radiating structure. The normal practice is to extend the mesh a few element lengths from the body and apply boundary conditions on the mesh termination surface. These boundary conditions, which are local to the element and hence preserve system sparsity, are called absorbing boundary conditions(ABCs). Although, numerous ABCs exist for 2D problems [1, 2], ABCs for 3D vector problems are comparatively fewer. Peterson [3] derived vector ABCs for spherical mesh truncations; however, in most practical cases, the sphere is the least economical shape of mesh truncation in terms of computer resources. In an earlier paper [4], we derived ABCs which can be enforced on surfaces conformal to the structure of interest, thus optimizing computational cost. Since that time, we have implemented these ABCs in a general purpose, 3D

finite element solver with success [5]. In this paper, we present a few more results which demonstrate that these ABCs indeed optimize the usage of computational resources without significant degradation in accuracy.

Besides the optimization of the mesh truncation strategy, we carried out optimizations on the numerical aspects of the code. Since a finite element code involves operations on sparse matrices, indirect addressing is a necessary part of the programming task. This feature combined with very short vector lengths for the sparse matrix result in poor vectorization and parallelization. Essentially, this is the price paid for $O(N)$ storage and improved scalability of the technique. In an earlier paper [6], we had detailed our efforts in parallelizing such a code on various distributed memory, multiprocessor architectures. The parallelization strategies that we had used were extremely successful; the code, however, ran very slowly on vector machines. In this paper, we employ a novel data storage scheme for speeding up the computation on vector architectures and present a strategy for reducing inter-processor communication on multiprocessor machines.

2 Conformal ABCs

2.1 Theory

In this section, we will present a brief description of the conformal ABCs and examine their performance with respect to spherical ABCs. At first, we generalize the Wilcox expansion [7] for a vector field in the Dupin coordinate system. Next, we apply the $\hat{\mathbf{n}} \times \nabla\times$ operator to the electric field ($\mathbf{E}$) to arrive at the first order absorbing boundary condition

$$\hat{\mathbf{n}} \times \nabla\times\mathbf{E} - (jk_o + \kappa_m - \overline{\boldsymbol{\eta}}\cdot)\,\mathbf{E}_t \;=\; 0 \qquad (1)$$

for a conformal mesh termination boundary. In this expression, k_o is the free space wave number, the subscript t denotes the tangential component of a vector and

$$\begin{aligned} \kappa_m &= \frac{\kappa_1 + \kappa_2}{2} \\ \overline{\boldsymbol{\eta}} &= \kappa_1\hat{\mathbf{t}}_1\hat{\mathbf{t}}_1 + \kappa_2\hat{\mathbf{t}}_2\hat{\mathbf{t}}_2 \end{aligned}$$

where $\kappa_{1,2}$ are the two principal curvatures of the ABC surface.

The second order ABC is obtained by using the $\hat{\mathbf{n}} \times \nabla\times$ operator once more and subsequently simplifying the resulting expression to yield

$$\begin{aligned} -(D - 2\kappa_m)\,\hat{\mathbf{n}} \times \nabla\times\mathbf{E} + \left\{4\kappa_m^2 - \kappa_g + D\,(jk_o - \overline{\boldsymbol{\eta}}\cdot) + (\overline{\boldsymbol{\eta}})^2\cdot + \kappa_m\Delta\kappa\overline{\boldsymbol{\zeta}}\cdot\right\}\mathbf{E}_t \\ +\nabla\times\left\{\hat{\mathbf{n}}\,(\nabla\times\mathbf{E})_n\right\} + \left(jk_o + 3\kappa_m - \frac{\kappa_g}{\kappa_m} - 2\overline{\boldsymbol{\eta}}\cdot\right)\nabla_t E_n = 0 \quad (2) \end{aligned}$$

where $\kappa_g = \kappa_1\kappa_2$ is the Gaussian curvature, the subscript n denotes the normal component of a vector and

$$D \;=\; 2jk_o + 5\kappa_m - \frac{\kappa_g}{\kappa_m}$$

$$\begin{aligned} \Delta\kappa &= \kappa_1 - \kappa_2 \\ (\overline{\boldsymbol{\eta}})^2 \cdot \mathbf{E}_t &= \kappa_1^2 E_{t_1} \hat{\mathbf{t}}_1 + \kappa_2^2 E_{t_2} \hat{\mathbf{t}}_2 \\ \overline{\boldsymbol{\zeta}} &= \hat{\mathbf{t}}_1 \hat{\mathbf{t}}_1 - \hat{\mathbf{t}}_2 \hat{\mathbf{t}}_2 \end{aligned} \tag{3}$$

Also, $\hat{\mathbf{t}}_1, \hat{\mathbf{t}}_2$ are the orthogonal tangential unit vectors in the Dupin coordinate system. The finite element implementation becomes simpler, and in some cases symmetric, if the term - $\nabla_t E_n$ - can be replaced by a double derivative. Fortunately, on considering the series expansion of the term $\hat{\mathbf{n}} \times \nabla \times \nabla_t E_n$ and simplifying, we have

$$\nabla_t (\nabla \cdot \mathbf{E}_t) = jk_o \nabla_t E_n \tag{4}$$

Thus we can rewrite the second order conformal ABC as

$$\begin{aligned} (D - 2\kappa_m)\, \hat{\mathbf{n}} \times \nabla \times \mathbf{E} = \left\{ 4\kappa_m^2 - \kappa_g + D\,(jk_o - \overline{\boldsymbol{\eta}} \cdot) + (\overline{\boldsymbol{\eta}})^2 \cdot + \kappa_m \Delta\kappa \overline{\boldsymbol{\zeta}} \cdot \right\} \mathbf{E}_t + \\ \nabla \times \left\{ \hat{\mathbf{n}} \left(\nabla \times \mathbf{E} \right)_n \right\} + \frac{1}{jk_o} \left(jk_o + 3\kappa_m - \frac{\kappa_g}{\kappa_m} - 2\overline{\boldsymbol{\eta}} \cdot \right) \nabla_t \left(\nabla \cdot \mathbf{E}_t \right) \end{aligned} \tag{5}$$

To make (1) and (5) implementable in finite element systems, the results are simplified by taking the dot product of the expression with $\mathbf{E}$, using the divergence condition, the vector wave equation and some vector identities [5]. The first order conformal ABC in readily implementable form is given by

$$\int_{S_o} \mathbf{E} \cdot P_1(\mathbf{E})\, dS = (jk_o + \kappa_m) \int_{S_o} \left(E_{t_1}^2 + E_{t_2}^2 \right)\, dS - \int_{S_o} \left(\kappa_1 E_{t_1}^2 + \kappa_2 E_{t_2}^2 \right)\, dS \tag{6}$$

where S_o is the mesh truncation surface and $P_1(\mathbf{E}) = \hat{\mathbf{n}} \times \nabla \times \mathbf{E}$ with the subscript denoting the order of the ABC.

The second order ABC reduces to

$$\begin{aligned} \int_{S_o} \mathbf{E} \cdot P_2(\mathbf{E})\, dS &= \int_{S_o} \left(\alpha_1 E_{t_1}^2 + \alpha_2 E_{t_2}^2 \right)\, dS + \int_{S_o} \beta (\nabla \times \mathbf{E})_n^2\, dS \\ &\quad - \int_{S_o} (\nabla \cdot \mathbf{E}_t) \left\{ \nabla \cdot (\overline{\boldsymbol{\gamma}} \cdot \mathbf{E})_t \right\}\, dS \end{aligned} \tag{7}$$

where the tensors $\overline{\boldsymbol{\alpha}}, \overline{\boldsymbol{\gamma}}$ and the scalar β are given by

$$\begin{aligned} \overline{\boldsymbol{\alpha}} &= \frac{1}{D - 2\kappa_m} \left[\left\{ 4\kappa_m^2 - \kappa_g + D\,(jk_o - \kappa_1) + \kappa_1^2 \right\} \hat{\mathbf{t}}_1 \hat{\mathbf{t}}_1 \right. \\ &\quad \left. + \left\{ 4\kappa_m^2 - \kappa_g + D\,(jk_o - \kappa_2) + \kappa_2^2 \right\} \hat{\mathbf{t}}_2 \hat{\mathbf{t}}_2 \right] \\ \overline{\boldsymbol{\gamma}} &= \frac{1}{jk_o (D - 2\kappa_m)} \left[\left(jk_o + 3\kappa_m - \frac{\kappa_g}{\kappa_m} - 2\kappa_1 \right) \hat{\mathbf{t}}_1 \hat{\mathbf{t}}_1 \right. \\ &\quad \left. + \left(jk_o + 3\kappa_m - \frac{\kappa_g}{\kappa_m} - 2\kappa_2 \right) \hat{\mathbf{t}}_2 \hat{\mathbf{t}}_2 \right] \\ \beta &= \frac{1}{D - 2\kappa_m} \end{aligned} \tag{8}$$

It should be remarked that the normal component of each surface edge must be made continuous across inter-element boundaries (triangular patches in our case) for the contour integral associated with the third term in (7) to vanish. Moreover, it can be shown that the first order ABC (6) is always symmetric whereas the second order ABC (7) is symmetric only when $\kappa_1 = \kappa_2$ on the boundary surface or when the surface is cylindrical and linear edge bases are employed. For a detailed analysis of symmetry considerations, the reader is referred to [5].

2.2 Results

In this section, we present validations for the conformal ABCs derived in the previous section. A complete description of the numerous geometries that were validated using these ABCs can be found in [5].

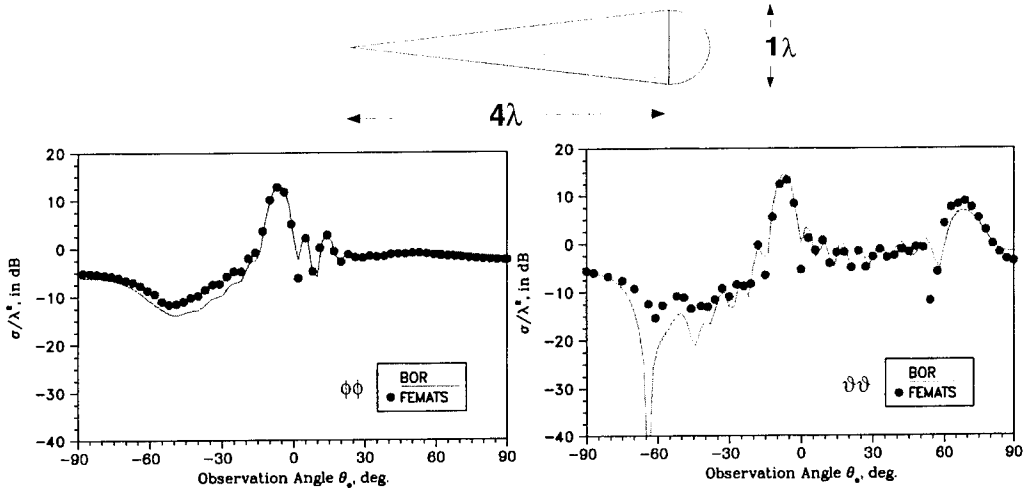


Figure 1: Backscatter pattern of a perfectly conducting conesphere (cone height=4λ ; radius = 0.5λ) for $\phi\phi$ and $\theta\theta$ polarizations. Black dots indicate computed values and the solid line represents data from a body of revolution code [11]. Mesh termination surface is a rectangular box.

The geometry for which the RCS results were computed is unique in its own way. A conesphere is basically a hemisphere attached to a cone. It is a difficult geometry to mesh since a surface singularity exists at the tip of the cone. The singularity can be removed in two ways: i) by creating a small region near the tip and detaching it from the surface or ii) by chopping off a small part near the tip of the cone. The second option inevitably leads to small inaccuracies for backscatter from the conical tip; however, we chose this option since the conical angle in our tested geometry was extremely

small (around 7°) and the mesh generator failed to mesh the first case on numerous occasions. In Figure 1, we plot the backscatter patterns of a 4.5λ long conesphere having a radius of 0.5λ for $\theta\theta$ and $\phi\phi$ polarizations. The mesh truncation surface is a rectangular box placed 0.4λ from the surface of the conesphere. The far-field results compare extremely well with computations from a body of revolution code [11].

3 Vectorization/parallelization strategies

Since our focus is on solving large problems, the code must be optimized to run fast on vector and parallel architectures. In [6], we detailed our parallelization strategy and presented results on speedup and inter-processor communication. However, the performance of the code on vector processors was not very encouraging. In the subsequent sections, we outline our optimization scheme for vector computers and present techniques for reducing inter-processor communication on distributed memory architectures.

3.1 Vector optimization

Since a sparse matrix has a very small number of non-zeros per row by definition and only the innermost loops are vectorizable, it is difficult to get good vector performance from such codes. Further, indirect addressing is an inherent part of sparse data structures - a feature which allows us to exploit the $O(N)$ storage characteristic but reduces speed on vector machines. Therefore, there are two main problems which limit the vectorizability of a sparse matrix code - short vector lengths and indirect addressing. The latter problem cannot be corrected but the first bottleneck can be removed. This is done by storing the matrix in a different format such that the vector lengths are approximately equal to the order of the system being solved. In the traditional storage system - Compressed Sparse Row (CSR) format - the non-zeros of the matrix and their corresponding column numbers are stored in a long complex and integer vector, respectively, with another short integer vector to store the number of non-zeros per row. However, this does not permit vectorizability since the average vector length is very small - 16 in our case. The ITPACK format [12] alleviates the short vector length problem by storing the entire matrix in a rectangular block. In this block, the number of rows equals the row count of the original matrix and the number of columns equals the maximum number of non-zeros in a row of the matrix; rows containing fewer non-zero elements are padded with zeros. This scheme works very well for matrices where the average non-zeros per row are approximately the same. In our case, this storage technique is not very beneficial since approximately 30% of the space is lost in zero padding.

The storage format that works best for our type of matrix is called the *jagged diagonal* format [13]. The rows are ordered in decreasing order of the number of non-zeros per row. The rows containing the maximum number of

non-zero entries are thus placed at the top of the matrix and the rows with the minimum non-zero entries are shuffled to the bottom. In the actual storage scheme, the leftmost elements of each row are stored as a dense vector with an additional vector indicating the column numbers of each element. The matrix is thus stored as a collection of vectors of decreasing length. The inner loop of the matrix-vector multiplication routine traverses the entire length of a jagged diagonal, which can be of the order of the system being solved. This feature greatly enhances vectorization. The storage requirement of the above format can be made to be the same as the previously mentioned CSR format through careful programming. The altered matrix-vector multiplication routine then runs at around 275 Mflops on a Cray C-90 whereas the older code with CSR storage peaked at 60 Mflops. The dot product reaches speeds of 550 Mflops and the vector updates execute at 600 Mflops. It must be mentioned that the CRAY C-90 is a substantially faster machine than the Cray YMP but the CSR formatted matrix-vector multiplication routine runs about 4 times slower on the C-90. Therefore, we can reliably state that the method of *jagged diagonals* is the best sparse matrix storage scheme in terms of computer storage and vectorizability. The still slower execution speeds of the matrix-vector multiply compared with the vector update is due to the indirect addressing in the inner loop which causes memory contention.

3.2 Reduction of processor communication

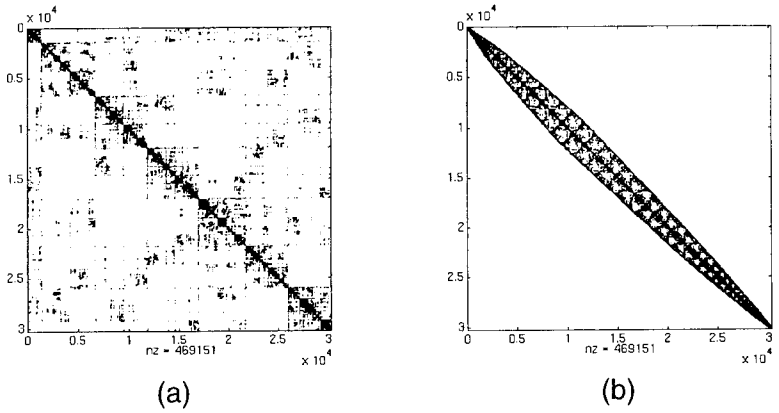


Figure 2: (a) Original sparse matrix (b) Re-ordered sparse matrix using a profile reduction algorithm.

In the previous section, we discussed optimization from the viewpoint of a vector processor. In this section, we propose a scheme for reducing interprocessor communication on multi-processor architectures. In [6], we out-

lined our success in parallelizing the computationally intensive portions of a finite element code on distributed memory architectures. It was also pointed out that further speedups could be achieved only through reducing data communication among the various processors.

The majority of processor time in a finite element code is spent in the equation solver. In our code, we employ an iterative solver since it preserves the sparsity of the finite element matrix, making minimal demands on computer storage. In the biconjugate gradient algorithm, there are principally two operations in which the most intensive communication takes place. The first is the sparse matrix-vector multiplication and the second is the search vector update at the end of each iteration.

In the matrix-vector multiply, each processor computes a block of the result vector by multiplying the corresponding block of rows of the sparse matrix with the operand vector. Since the operand vector is distributed among the processors, data communication is required. Each processor does two things: (i) it sends out a request for those matrix entries it does not own but needs for performing the multiplication and (ii) sends out those matrix entries it owns on request from other processors. The communication pattern is determined by the sparsity structure of the matrix, which in our case is derived from an unstructured mesh. Therefore the communication pattern is unstructured and irregular. However, on reordering the matrix using a standard profile reduction algorithm (part *b* of Figure 2), the matrix becomes banded and the only communication should occur between adjacent processors. In fact, by storing a few extra matrix entries in each processor, inter-processor communication can be removed altogether in the matrix-vector multiplication phase. However, the time taken for communication due to the vector update still remains the same.

4 Conclusion

In this paper, we have talked about the optimization strategies that were employed to improve our finite element code from the algorithmic and the numerical point of view. We have achieved notable success on both fronts.

The problem size was reduced by a significant amount owing to the use of conformal ABCs and the savings are only going to increase as the problem size gets larger. Higher order ABCs may enable us to bring the mesh termination surface even closer to the target, enabling us to do larger problems with the available computer resources. The numerical aspect is also important for addressing the utility and the feasibility issues for solving practical 3D problems in a reasonable amount of time. As processor speeds increase and parallel architectures mature, the speed and performance of the code will vastly improve. Therefore, issues concerning the performance of the finite element-ABC technique and its implementability in large scale computer simulations will continue to be important in the years to come.

References

[1] A. Bayliss and E. Turkel. Radiation boundary conditions for wave-like equations. *Comm. Pure Appl. Math.*, Vol. 33, pp. 707-725, 1980.

[2] B. Engquist and A. Majda. Absorbing boundary conditions for the numerical simulation of waves. *Math. Comp.*, Vol. 31,pp. 629–651, 1977.

[3] A.F. Peterson. Absorbing boundary conditions for the vector wave equation. *Microwave and Opt. Techn. Letters.*, vol. 1, pp. 62-64, Apr 1988.

[4] A. Chatterjee and J.L. Volakis. Conformal absorbing boundary conditions for the vector wave equation. *Microwave and Opt. Techn. Letters.*, Vol. 6, no. 16, pp. 886-889, Dec 1993.

[5] A. Chatterjee. *Investigation of finite element-ABC techniques for electromagnetic field simulation.* PhD thesis, University of Michigan, Ann Arbor, 1994.

[6] A. Chatterjee, J.L. Volakis, and D. Windheiser. Paralell computation of 3D electromagnetic scattering using finite elements. *Int. J. Num. Modeling*, 7:329–342, 1994.

[7] C.H. Wilcox. An expansion theorem for electromagnetic fields. *Comm. Pure Appl. Math.*, vol. 9, pp. 115-134, May 1956.

[8] M. Schuh, A. Woo, M. Sanders, and H.T.G. Wang. Radar cross-section measurement data of four small cavities. Technical Report 108782, NASA Ames, Nov 1993.

[9] A. Glisson and D.R. Wilton. Simple and efficient numerical techniques for treating bodies of revolution. Technical Report 105, Univ. of Mississippi, 1982.

[10] V. Shankar, W.F. Hall, A. Mohammedian, and C. Rowell. Development of a finite-volume, time-domain solver for Maxwell's equations. *Rockwell Technical Report prepared for NASA/NDC under contract N62269-90-C-0257*, May 1993.

[11] J.M. Putnam and L.N. Medgyesi-Mitschang. Combined field integral equation formulation for axially inhomogeneous bodies of revolution. Technical Report MDC QA003, McDonnell Douglas Research Labs, December 1987.

[12] D.R. Kincaid and T.C. Oppe. ITPACK on supercomputers. *Numerical Methods, Lecture Notes in Mathematics*, vol. 1005, pp. 151-161, 1982.

[13] E. Anderson and Y. Saad. Solving sparse triangular linear systems on parallel computers. *International Journal of High Speed Computing*, vol. 1, no. 1, pp. 73-95, 1989.

A Characteristic-Based 3D Time Domain Maxwell Equation Solver

Joseph J. S. Shang* & Kueichien C. Hill†
Wright Laboratory
Wright-Patterson Air Force Base, Ohio 45433-7602

Abstract

This paper discusses the fundamental formulations for solving the three dimensional Maxwell's equations using characteristic-based finite volume time domain method. The characteristic-based "non-reflection" boundary condition at the outer truncation boundary and the boundary condition on the surface of a scatterer are also presented. Numerical results calculated using this method for radiation from a dipole and scattering from a perfectly conducting sphere are compared to the theoretical solutions.

1 Introduction

Methods based on solving Maxwell's equations in the partial differential equation (PDE) form have emerged as viable techniques in recent years. The increased popularity of the PDE methods is due to their inherent capability in treating penetrable materials compared to other techniques based on the integral equation (IE) form and the asymptotic approximation. The PDE methods, especially those employing explicit schemes, also have an advantage over IE methods in terms of computer memory requirement. Of the PDE methods known to EM engineers and researchers, the finite difference time domain (FDTD) method developed by Yee in 1966 is the most widely used method due to its simplicity. However, Yee's FDTD suffers stair casing error if the boundary of the physical geometry deviates from the uniform computational grids. The other widely used PDE method is based on the finite element method (FEM) in which the geometry is discretized into elements that are conformal to the physical geometry. Unfortunately, finite element method requires much more computer memory for storing those unstructured grids. In addition, the accuracy of FEM solutions usually depends on the quality of the grids. This paper introduces the EM researchers to a structured grid characteristic-based finite volume time domain method [1,2,3] to solve the 3D time domain Maxwell equations. This characteristic-based technique has been

*Senior Scientist. Fellow AIAA
†Electronics Engineer, Signature Technology Office
This paper is declared a work of the U.S. Government and is not subject to copyright protection in the United States.

widely used in the computational fluid dynamics (CFD) community to solve hyperbolic partial differential equation systems. Recognizing that Maxwell's equations in time domain PDE form constitute a hyperbolic PDE system, most of the algorithms developed for the CFD applications can be readily applied to the computational electromagnetics (CEM) problems. This technique appears to offer certain advantages over the FDTD and FEM methods because it can solve the problem conformally like the FEM and yet efficiently like the FDTD due to the structured grid used. The characteristic "non-reflection" boundary condition has similar accuracy compared to the absorbing boundary condition such as Mür's, but is computationally more efficient to implement it. This paper will discuss the fundamental formulations of the characteristic-based finite volume time domain method, the "non-reflection" boundary condition at the outer truncation boundary, the boundary condition on the surface of the scatterer, and the field update and time-stepping procedure. Some numerical results will be presented to demonstrate the capability of this method.

2 Formulations

The time domain Maxwell's equations are given by

$$\frac{\partial B}{\partial t} + \nabla \times E = 0 ; \qquad \nabla \cdot B = 0 \tag{1}$$

$$\frac{\partial D}{\partial t} - \nabla \times H = -J ; \qquad \nabla \cdot D = q_v \tag{2}$$

where E is the electric intensity; H is the magnetic intensity; D is the electric flux density; B is the magnetic flux density; J is the electric current density; and q_v is the electric charge density. J and q_v are related through the continuity equation given by

$$\nabla \cdot J = -\frac{\partial q_v}{\partial t} . \tag{3}$$

In simple linear matter, B and D are related to E and H by the constitutive relationships:

$$D = \epsilon E ; \qquad B = \mu H \tag{4}$$

where ϵ and μ are the permittivity and permeability of the media, respectively. Maxwell's equations can be rewritten in flux-vector form given by

$$\frac{\partial \mathrm{U}}{\partial t} + \frac{\partial \mathrm{F}}{\partial x} + \frac{\partial \mathrm{G}}{\partial y} + \frac{\partial \mathrm{H}}{\partial z} = \mathrm{S} \tag{5}$$

where

$$\mathrm{U} = \left[\begin{array}{cccccc} B_x & B_y & B_z & D_x & D_y & D_z \end{array} \right]^{\mathrm{T}} ; \qquad \mathrm{S} = \left[\begin{array}{cccccc} 0 & 0 & 0 & -J_x & -J_y & -J_z \end{array} \right]^{\mathrm{T}} ; \tag{6}$$

$$\mathrm{F} = \left[\begin{array}{cccccc} 0 & -E_z & E_y & 0 & H_z & -H_y \end{array} \right]^{\mathrm{T}} ; \qquad \mathrm{G} = \left[\begin{array}{cccccc} E_z & 0 & -E_x & -H_z & 0 & H_x \end{array} \right]^{\mathrm{T}} ; \tag{7}$$

$$\mathrm{H} = \left[\begin{array}{cccccc} -E_y & E_x & 0 & H_y & -H_x & 0 \end{array} \right]^{\mathrm{T}} . \tag{8}$$

T stands for the transpose of a matrix. From the constitutive relationships, F, G, and H are related to U by

$$\mathrm{F} = \mathrm{AU}, \qquad \mathrm{G} = \mathrm{BU}, \qquad \text{and} \qquad \mathrm{H} = \mathrm{CU} \tag{9}$$

where

$$A = \begin{bmatrix} 0 & 0 & 0 & 0 & 0 & 0 \\ 0 & 0 & 0 & 0 & 0 & -\frac{1}{\epsilon} \\ 0 & 0 & 0 & 0 & \frac{1}{\epsilon} & 0 \\ 0 & 0 & 0 & 0 & 0 & 0 \\ 0 & 0 & \frac{1}{\mu} & 0 & 0 & 0 \\ 0 & -\frac{1}{\mu} & 0 & 0 & 0 & 0 \end{bmatrix}, B = \begin{bmatrix} 0 & 0 & 0 & 0 & 0 & \frac{1}{\epsilon} \\ 0 & 0 & 0 & 0 & 0 & 0 \\ 0 & 0 & 0 & -\frac{1}{\epsilon} & 0 & 0 \\ 0 & 0 & -\frac{1}{\mu} & 0 & 0 & 0 \\ 0 & 0 & 0 & 0 & 0 & 0 \\ \frac{1}{\mu} & 0 & 0 & 0 & 0 & 0 \end{bmatrix}, C = \begin{bmatrix} 0 & 0 & 0 & 0 & -\frac{1}{\epsilon} & 0 \\ 0 & 0 & 0 & \frac{1}{\epsilon} & 0 & 0 \\ 0 & 0 & 0 & 0 & 0 & 0 \\ 0 & \frac{1}{\mu} & 0 & 0 & 0 & 0 \\ -\frac{1}{\mu} & 0 & 0 & 0 & 0 & 0 \\ 0 & 0 & 0 & 0 & 0 & 0 \end{bmatrix}. \quad (10)$$

By solving for the eigenvalues and eigenvectors of A, A can be expressed as

$$A = S_x \lambda S_x^{-1} \quad (11)$$

where λ is the diagonal matrix given by

$$\lambda = \begin{bmatrix} \lambda_1 & 0 & 0 & 0 & 0 & 0 \\ 0 & \lambda_2 & 0 & 0 & 0 & 0 \\ 0 & 0 & \lambda_3 & 0 & 0 & 0 \\ 0 & 0 & 0 & \lambda_4 & 0 & 0 \\ 0 & 0 & 0 & 0 & \lambda_5 & 0 \\ 0 & 0 & 0 & 0 & 0 & \lambda_6 \end{bmatrix}. \quad (12)$$

λ_1, λ_2, λ_3, λ_4, λ_5, and λ_6 are the eigenvalues of A given by $\lambda = \left\{-\frac{1}{\sqrt{\epsilon\mu}}, -\frac{1}{\sqrt{\epsilon\mu}}, \frac{1}{\sqrt{\epsilon\mu}}, \frac{1}{\sqrt{\epsilon\mu}}, 0, 0\right\}$. S_x is the diagonalizing matrix given by

$$S_x = \begin{bmatrix} 0 & 0 & 0 & 0 & 0 & 1 \\ \sqrt{\frac{\mu}{\epsilon}} & 0 & -\sqrt{\frac{\mu}{\epsilon}} & 0 & 0 & 0 \\ 0 & -\sqrt{\frac{\mu}{\epsilon}} & 0 & \sqrt{\frac{\mu}{\epsilon}} & 0 & 0 \\ 0 & 0 & 0 & 0 & 1 & 0 \\ 0 & 1 & 0 & 1 & 0 & 0 \\ 1 & 0 & 1 & 0 & 0 & 0 \end{bmatrix}; \quad (13)$$

and S_x^{-1} is the inverse of S_x. Similarly, B and C can be expressed as $B = S_y \lambda S_y^{-1}$ and $C = S_z \lambda S_z^{-1}$ with

$$S_y = \begin{bmatrix} -\sqrt{\frac{\mu}{\epsilon}} & 0 & \sqrt{\frac{\mu}{\epsilon}} & 0 & 0 & 1 \\ 0 & 0 & 0 & 0 & 1 & 0 \\ 0 & \sqrt{\frac{\mu}{\epsilon}} & 0 & -\sqrt{\frac{\mu}{\epsilon}} & 0 & 0 \\ 0 & 1 & 0 & 1 & 0 & 0 \\ 0 & 0 & 0 & 0 & 0 & 1 \\ 1 & 0 & 1 & 0 & 0 & 0 \end{bmatrix} \quad \text{and} \quad S_z = \begin{bmatrix} \sqrt{\frac{\mu}{\epsilon}} & 0 & -\sqrt{\frac{\mu}{\epsilon}} & 0 & 0 & 0 \\ 0 & -\sqrt{\frac{\mu}{\epsilon}} & 0 & \sqrt{\frac{\mu}{\epsilon}} & 0 & 0 \\ 0 & 0 & 0 & 0 & 1 & 0 \\ 0 & 1 & 0 & 1 & 0 & 0 \\ 1 & 0 & 1 & 0 & 0 & 0 \\ 0 & 0 & 0 & 0 & 0 & 1 \end{bmatrix}. \quad (14)$$

In order to achieve the approximate Riemann solver and apply the non-reflection boundary condition at the truncation boundary, F needs to be split into F^+ and F^- [4] with F^+ and F^- corresponding to the outgoing and incoming waves, respectively. To accomplish this, λ will be split into λ^+ and λ^- with λ^+ containing only the positive eigenvalues $(\frac{1}{\sqrt{\epsilon\mu}}, \frac{1}{\sqrt{\epsilon\mu}})$ and λ^- containing only the negative eigenvalues $(-\frac{1}{\sqrt{\epsilon\mu}}, -\frac{1}{\sqrt{\epsilon\mu}})$. Thus, one has

$$F = F^+ + F^- = S_x \lambda^+ S_x^{-1} U + S_x \lambda^- S_x^{-1} U \quad (15)$$

where

$$\mathrm{F}^{+} = \frac{1}{2}\left[\begin{array}{ccccccc} 0 & \left(\frac{B_y}{\sqrt{\epsilon\mu}} - \frac{D_z}{\epsilon}\right) & \left(\frac{B_z}{\sqrt{\epsilon\mu}} + \frac{D_y}{\epsilon}\right) & 0 & \left(\frac{B_z}{\mu} + \frac{D_y}{\sqrt{\epsilon\mu}}\right) & \left(-\frac{B_y}{\mu} + \frac{D_z}{\sqrt{\epsilon\mu}}\right) \end{array}\right]^{\mathrm{T}} \quad (16)$$

$$\mathrm{F}^{-} = \frac{1}{2}\left[\begin{array}{ccccccc} 0 & -\left(\frac{B_y}{\sqrt{\epsilon\mu}} + \frac{D_z}{\epsilon}\right) & \left(-\frac{B_z}{\sqrt{\epsilon\mu}} + \frac{D_y}{\epsilon}\right) & 0 & \left(\frac{B_z}{\mu} - \frac{D_y}{\sqrt{\epsilon\mu}}\right) & -\left(\frac{B_y}{\mu} + \frac{D_z}{\sqrt{\epsilon\mu}}\right) \end{array}\right]^{\mathrm{T}}. \quad (17)$$

Similarly, G and H can be split into $\mathrm{G}^{+} + \mathrm{G}^{-}$ and $\mathrm{H}^{+} + \mathrm{H}^{-}$ with

$$\mathrm{G}^{+} = \frac{1}{2}\left[\begin{array}{ccccccc} \left(\frac{B_x}{\sqrt{\epsilon\mu}} + \frac{D_z}{\epsilon}\right) & 0 & \left(\frac{B_z}{\sqrt{\epsilon\mu}} - \frac{D_x}{\epsilon}\right) & \left(-\frac{B_z}{\mu} + \frac{D_x}{\sqrt{\epsilon\mu}}\right) & 0 & \left(\frac{B_x}{\mu} + \frac{D_z}{\sqrt{\epsilon\mu}}\right) \end{array}\right]^{\mathrm{T}} \quad (18)$$

$$\mathrm{G}^{-} = \frac{1}{2}\left[\begin{array}{ccccccc} \left(-\frac{B_x}{\sqrt{\epsilon\mu}} + \frac{D_z}{\epsilon}\right) & 0 & -\left(\frac{B_z}{\sqrt{\epsilon\mu}} + \frac{D_x}{\epsilon}\right) & -\left(\frac{B_z}{\mu} + \frac{D_x}{\sqrt{\epsilon\mu}}\right) & 0 & \left(\frac{B_x}{\mu} - \frac{D_z}{\sqrt{\epsilon\mu}}\right) \end{array}\right]^{\mathrm{T}} \quad (19)$$

$$\mathrm{H}^{+} = \frac{1}{2}\left[\begin{array}{ccccccc} \left(\frac{B_x}{\sqrt{\epsilon\mu}} - \frac{D_y}{\epsilon}\right) & \left(\frac{B_y}{\sqrt{\epsilon\mu}} + \frac{D_x}{\epsilon}\right) & 0 & \left(\frac{B_y}{\mu} + \frac{D_x}{\sqrt{\epsilon\mu}}\right) & \left(-\frac{B_x}{\mu} + \frac{D_y}{\sqrt{\epsilon\mu}}\right) & 0 \end{array}\right]^{\mathrm{T}} \quad (20)$$

$$\mathrm{H}^{-} = \frac{1}{2}\left[\begin{array}{ccccccc} -\left(\frac{B_x}{\sqrt{\epsilon\mu}} + \frac{D_y}{\epsilon}\right) & \left(-\frac{B_y}{\sqrt{\epsilon\mu}} + \frac{D_x}{\epsilon}\right) & 0 & \left(\frac{B_y}{\mu} - \frac{D_x}{\sqrt{\epsilon\mu}}\right) & -\left(\frac{B_x}{\mu} + \frac{D_y}{\sqrt{\epsilon\mu}}\right) & 0 \end{array}\right]^{\mathrm{T}} \quad (21)$$

Equation (5) can now be solved by approximating the continuous derivatives with discrete operators given by

$$\frac{\triangle \mathrm{U}}{\triangle t} + \frac{\triangle \mathrm{F}}{\triangle x} + \frac{\triangle \mathrm{G}}{\triangle y} + \frac{\triangle \mathrm{H}}{\triangle z} = \mathrm{S}. \quad (22)$$

Depending on the accuracy desired, equation (22) can be discretized in many different ways. Let $t = n\triangle t$ denote the nth time level and (i, j, k) denote the (x, y, x) coordinate of a point at $x = i\triangle x, y = j\triangle y$, and $z = k\triangle z$, U is defined at the centroid of the finite volume cell with index (i, j, k) while F, G, and H are defined on the surfaces of the cell with indices $(i + \frac{1}{2}, j, k)$, $(i, j + \frac{1}{2}, k)$, and $(i, j, k + \frac{1}{2})$, respectively. The field update procedure starts with calculating U at the cell surfaces by interpretating the values of U at the appropriate cell centroids. The following formulations give the values of $\mathrm{U}^{R}_{i+\frac{1}{2}}$ and $\mathrm{U}^{L}_{i+\frac{1}{2}}$ using the upwind biased algorithm [5]:

$$\mathrm{U}^{L}_{i+\frac{1}{2}} = \mathrm{U}_i + \frac{\phi}{4}\left[(1-\kappa)\bigtriangledown + (1+\kappa)\triangle\right]\mathrm{U}_i \quad (23)$$

$$\mathrm{U}^{R}_{i+\frac{1}{2}} = \mathrm{U}_{i+1} - \frac{\phi}{4}\left[(1+\kappa)\bigtriangledown + (1-\kappa)\triangle\right]\mathrm{U}_{i+1} \quad (24)$$

where $\bigtriangledown \mathrm{U}_i = \mathrm{U}_i - \mathrm{U}_{i-1}$ and $\triangle \mathrm{U}_i = \mathrm{U}_{i+1} - \mathrm{U}_i$; ϕ equals zero for first order accuracy scheme and one for higher order accuracy schemes. κ is set to a value to give the desired order of accuracy. For instance, when $\kappa = 0$, the above equations yield a second order accurate scheme which is used to give the results reported in this paper. From the values of $\mathrm{U}^{R}_{i+\frac{1}{2}}$ and $\mathrm{U}^{L}_{i+\frac{1}{2}}$, the fluxes can be reconstructed by

$$\mathrm{F}_{i+\frac{1}{2}} = \mathrm{F}^{+}(\mathrm{U}^{L}_{i+\frac{1}{2}}) + \mathrm{F}^{-}(\mathrm{U}^{R}_{i+\frac{1}{2}})\,; \quad \mathrm{G}_{j+\frac{1}{2}} = \mathrm{G}^{+}(\mathrm{U}^{L}_{j+\frac{1}{2}}) + \mathrm{G}^{-}(\mathrm{U}^{R}_{j+\frac{1}{2}})\,; \quad \mathrm{H}_{k+\frac{1}{2}} = \mathrm{H}^{+}(\mathrm{U}^{L}_{k+\frac{1}{2}}) + \mathrm{H}^{-}(\mathrm{U}^{R}_{k+\frac{1}{2}}). \quad (25)$$

Once F, G, and H are obtained on the cell surfaces, they are used to calculate $\triangle U$ in equation (22). To update U in time, a two-stage Runge-Kutta second order accurate scheme is used to produce the results reported here:

$$\begin{array}{c} \mathrm{U}_0 = \mathrm{U}_n \\ \mathrm{U}_1 = \mathrm{U}_0 - \triangle \mathrm{U}(\mathrm{U}_0) \\ \mathrm{U}_2 = \mathrm{U}_0 - 0.5(\triangle \mathrm{U}(\mathrm{U}_1) + \triangle \mathrm{U}(\mathrm{U}_0)) \\ \mathrm{U}_{n+1} = \mathrm{U}_2 \end{array} \quad (26)$$

The source function is applied as the initial boundary value at the location where the source exists. The non-reflection boundary condition is applied by setting F^-, G^-, and H^- equal to zero at the outer truncation boundary to suppress the wave coming into the computational domain. The non-reflection boundary condition is exact for one dimensional problems since the direction of the wave propagation is always aligned with the coordinate. However, it becomes approximate for two and three dimensional problems when the wave propagation direction is no longer aligned with the coordinates.

Equation (5) is useful when the scatterer in the computational domain can be discretized into uniform grids. But in most practical applications, a curvilinear grid which conforms to the surface of the scatterer is required. Equation (5) can be mapped to a curvilinear coordinate system defined by

$$\xi = \xi(x, y, z); \qquad \eta = \eta(x, y, z); \qquad \zeta = \zeta(x, y, z) \tag{27}$$

and rewritten as

$$\frac{\partial \tilde{U}}{\partial t} + \frac{\partial \tilde{F}}{\partial \xi} + \frac{\partial \tilde{G}}{\partial \eta} + \frac{\partial \tilde{H}}{\partial \zeta} = \tilde{S} \tag{28}$$

where

$$\begin{array}{lll} \tilde{U} = \frac{1}{|J|} U \ ; & \tilde{F} = \frac{1}{|J|} (\xi_x F + \xi_y G + \xi_z H) \ ; & \\ \tilde{G} = \frac{1}{|J|} (\eta_x F + \eta_y G + \eta_z H) \ ; & \tilde{H} = \frac{1}{|J|} (\zeta_x F + \zeta_y G + \zeta_z H) \ ; & \tilde{S} = \frac{1}{|J|} S \ . \end{array} \tag{29}$$

J is the Jacobian of the coordinate transform given by

$$J = \begin{bmatrix} \xi_x & \eta_x & \zeta_x \\ \xi_y & \eta_y & \zeta_y \\ \xi_z & \eta_z & \zeta_z \end{bmatrix} \tag{30}$$

and $|J|$ is its determinant.

Again, the continuous derivatives in Equation (28) can be approximated by discrete operators given by

$$\frac{\triangle \tilde{U}}{\triangle t} + \frac{\triangle \tilde{F}}{\triangle \xi} + \frac{\triangle \tilde{G}}{\triangle \eta} + \frac{\triangle \tilde{F}}{\triangle \zeta} = \tilde{S}. \tag{31}$$

However, if one attempts to find the split fluxes in the (ξ, η, ζ) coordinate system, one would need to rederive the eigenvalues and eigenvectors in the (ξ, η, ζ) coordinate system. Recognizing that all outward normal vectors on the surfaces of each structured grid cell are defined by $\frac{\nabla \xi}{|\nabla \xi|}$, $\frac{\nabla \eta}{|\nabla \eta|}$, and $\frac{\nabla \zeta}{|\nabla \zeta|}$, locally orthogonal coordinate systems can be generated on the constant ξ, η, and ζ surfaces, respectively. For instance, the locally orthogonal coordinate system for constant ξ can be found by defining its first unit vector as

$$\hat{n}_{\xi 1} = \frac{\nabla \xi}{|\nabla \xi|} \ . \tag{32}$$

The second unit vector can be found by defining an arbitrary vector $\bar{R}_\xi$ on the constant ξ surface and taking the cross product of $\bar{R}_\xi$ and $\hat{u}_{\xi 1}$ to give

$$\hat{u}_{\xi 2} = \frac{\bar{R}_\xi \times \hat{u}_{\xi 1}}{|\bar{R}_\xi \times \hat{u}_{\xi 1}|}. \tag{33}$$

The third unit vector is generated by

$$\hat{u}_{\xi 3} = \hat{u}_{\xi 1} \times \hat{u}_{\xi 2} \ . \tag{34}$$

Similarly, the locally orthogonal coordinate systems $(\hat{u}_{\eta 1}, \hat{u}_{\eta 2}, \hat{u}_{\eta 3})$ and $(\hat{u}_{\zeta 1}, \hat{u}_{\zeta 2}, \hat{u}_{\zeta 3})$ for constant η and ζ planes can be found by replacing the subscript ξ in equations (32) to (34) with η and ζ respectively. Because $(\hat{u}_{\xi 1}, \hat{u}_{\xi 2}, \hat{u}_{\xi 3})$ are orthogonal, $u_\xi^{-1} = u_\xi^{\mathrm{T}}$.

Transforming $\tilde{\mathrm{F}}$ to $(\hat{u}_{\xi 1}, \hat{u}_{\xi 2}, \hat{u}_{\xi 3})$ coordinate system, one has

$$\hat{\mathrm{F}} = \begin{bmatrix} u_\xi & 0 \\ 0 & u_\xi \end{bmatrix} \tilde{\mathrm{F}} = \frac{|\bigtriangledown \xi|}{|\mathrm{J}|} \begin{bmatrix} 0 & -\frac{\hat{D}_x}{\epsilon} & \frac{\hat{D}_y}{\epsilon} & 0 & \frac{\hat{B}_x}{\mu} & -\frac{\hat{B}_y}{\mu} \end{bmatrix}^{\mathrm{T}}. \tag{35}$$

Notice that $\hat{\mathrm{F}}$ has the same form as the F in Cartesian coordinate system. Thus, the eigenvalues and diagonalizing matrices for $\hat{\mathrm{F}}$ are the same as those of F. In other words, $\hat{\mathrm{F}}$ can be split into $\hat{\mathrm{F}}^+$ and $\hat{\mathrm{F}}^-$ in the same way as F in the Cartesian coordinate system. Similarly, $\tilde{\mathrm{G}}$ and $\tilde{\mathrm{H}}$ can be transformed to $(\hat{u}_{\eta 1}, \hat{u}_{\eta 2}, \hat{u}_{\eta 3})$ and $(\hat{u}_{\zeta 1}, \hat{u}_{\zeta 2}, \hat{u}_{\zeta 3})$ coordinate systems to split the fluxes. Thus, the field update procedure for the curvilinear coordinate system is done by first transforming $\tilde{\mathrm{U}}$ to the $(\hat{u}_{\xi 1}, \hat{u}_{\xi 2}, \hat{u}_{\xi 3})$ coordinate system to find $\hat{\mathrm{F}}^+$ and $\hat{\mathrm{F}}^-$, then transforming $\hat{\mathrm{F}}$ back to $\tilde{\mathrm{F}}$ to calculate $\triangle\tilde{\mathrm{F}}$. Similar procedure is repeated for the calculation of $\triangle\tilde{\mathrm{G}}$ and $\triangle\tilde{\mathrm{H}}$. Finally, $\triangle\tilde{\mathrm{U}}$ is found from equation (31). The time integration procedure and the interpretation procedure for finding $\tilde{\mathrm{U}}^L$ and $\tilde{\mathrm{U}}^R$ on the cell surfaces are the same as in equations (23) to (26).

3 Boundary Conditions on the Surface of the Scatterer

Maxwell's equations in integral form yield the following boundary conditions:

$$\begin{aligned} \hat{n} \times (E_1 - E_2) = 0 \ ; \qquad & \hat{n} \cdot (B_1 - B_2) = 0 \\ \hat{n} \times (H_1 - H_2) = J_s \ ; \qquad & \hat{n} \cdot (D_1 - D_2) = \rho_s \end{aligned} \tag{36}$$

Since there are a total of six field components for the electric and magnetic fields, equation (36) only provides three deterministic equations in relating the field components across the surface of the scatterer; namely, the two tangential components of the electric field and the normal component of the magnetic field are continuous across the surface of the scatterer. For a non-perfectly conducting scatterer, the surface current and charge densities, J_s and ρ_s, are finite and confined to the surface. Thus, one has

$$\hat{n} \cdot \bigtriangledown(\hat{n} \times (H_1 - H_2)) = 0 \ ; \qquad \hat{n} \cdot \bigtriangledown(\hat{n} \cdot (D_1 - D_2)) = 0 \tag{37}$$

which provides derivative conditions needed to completely describe the behavior of the electric and magnetic fields in the normal direction. In the case of a perfectly conducting scatterer, the surface current and charge densities approach infinity. However, they can be defined in a limiting sense such that equation (37) still applies.

4 Results

Two simple cases using the second order finite volume scheme discussed in this paper will be given. The first case is to find the radiated field from a short dipole in free space. The dipole has a current source equals to $sin(2\pi t)$. Figure 1 shows the calculated field components at the time when the initial pulse has propagated a distance of 2.248 wavelengths away from the dipole. A $(49 \times 48 \times 96)$ grid was used to generate the results. The fields shown are located on the constant $y = 20\triangle y$ and $z = 48\triangle z$ plane. The results agree very well with the theoretical solutions.

The second case is the plane wave scattering from a perfectly conducting sphere with $ka = 2.3$, where k is the free space wave number and a is the radius of the sphere. A $(49 \times 48 \times 96)$ grid was used to generate the results. The field solutions in the time domain were transformed to the frequency domain and integrated to yield the radar cross section. Two sets of results are shown in Figure 2, one after the plane wave has gone through one period and the other after two periods. Showing the results obtained at different time levels ensures the field has reached a time harmonic steady state. Both results agree well with those obtained using Mie series solutions.

5 Conclusions

The fundamental formulations for the characteristic-based finite volume time domain method has been presented. The boundary conditions at the outer truncation boundary and on the surface of the scatterer are also discussed. The numerical results for a radiating dipole and perfectly conducting sphere agree well with the theoretical solutions. Although the initial results show great potential for this method, continuing study is required to fully mature this technology.

References

1. Shang, J.S., "Characteristic-Based Algorithm for Solving 3D Time-Domain Maxwell Equations," AIAA paper 93-0461, January 1993.
2. Shang, J.S. and D. Gaitonde, "Scattered Electromagnetic Field of a Reentry Vehicle," AIAA paper 94-0231, January 1994.
3. Shang, J.S. and R.M. Fithen, "A Comparative Study of Numerical Algorithms for Computational Electromagnetics," AIAA paper 94-2410, January 1994.
4. Steger, J.L. and R.F. Warming, "Flux Vector Splitting of the Inviscid Gasdynamic Equations with Application to Finite Difference Methods," Journal of Computational Physics, 40(2):263-293, April 1981.
5. Anderson, W.K., J.L. Thomas, and B. van Leer, "A Comparison of Finite Volume Flux Vector Splittings for the Euler Equations," AIAA paper 85-0122, 1985.

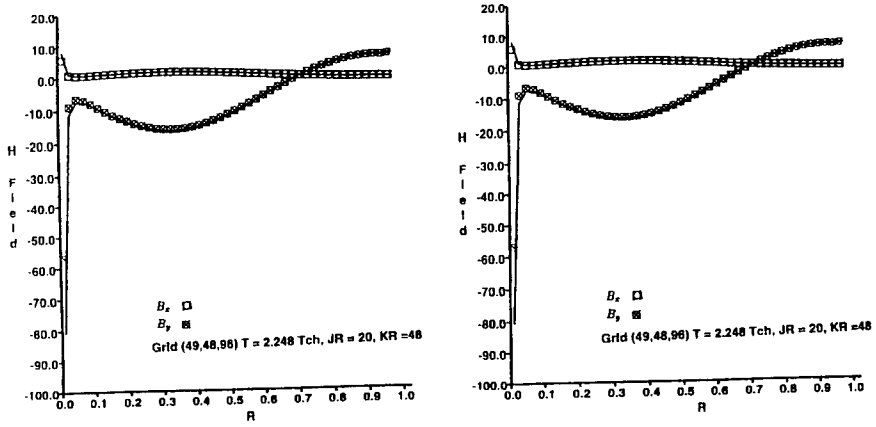


Figure 1. Fields radiated from a dipole

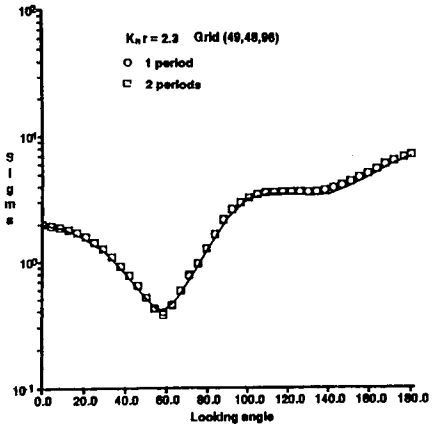


Figure 2. Radar cross section of a conducting sphere with $ka = 2.3$

FINITE ELEMENT SOLUTION OF EDDY CURRENT PROBLEMS IN ELECTROMAGNETICS

(Invited)

O. A. Mohammed and G. F. Üler
Department of Electrical & Computer Engineering
Florida International University
Miami, Florida 33199, USA

Abstract

This paper presents several computational techniques for handling the eddy current problems in electrical devices. Both sinusoidal as well as transient variations of excitation systems in linear and nonlinear cases are presented. The applications utilize the finite element method in three dimensions. Examples are shown using vector and/or scalar formulations. Finally a neural network model is suggested to implement the solution of the two dimensional eddy current problem in parallel with an implementation example.

Introduction

In dealing with eddy current problems involving sinusoidal variation, the idea of complex magnetic vector potential is used to formulate and solve the field problem. In treating the nonlinear transient eddy current problem, a method which utilize the magnetic vector potential (A) and electric scalar potential (ϕ) which is known as the (A-ϕ)[1-4] method is used to formulate and solve the field problem. The time derivative in this class of problems is treated using the Crank-Nicolson, State-Space techniques as well as other time marching schemes. Another method involving the electric vector potential (T) and the magnetic scalar potential (Ω) which is known as the (T-Ω) method is also used to formulate and solve the 3D transient eddy current problem. [5]

A technique for solving the electromagnetic field equations and calculating the eddy current density values is based on the Iterative Scalar Potential (ISP) formulation.[6] The procedure is simple and has a major advantage in that the numerical problem is solved in terms of electromagnetic field variables which has a physical meaning. Furthermore, in this method, there is only one degree of freedom per node which results in sizable savings in computation time. The numerical results of this new technique are obtained in less than 50% of the time consumed utilizing other methods.

A parallel architecture for eddy current calculations is formed with a neural network which is formed by nodes that are fully interconnected. Each node is modeled with a set of circuit elements as determined by the governing equation.[7] The interconnection between the nodes is produced through weights similar to dependent sources in an electrical circuit according to a specific rule. The directly connected nodes could interact directly with each other while indirectly connected nodes affect each other through the propagation effects of the continuous-time dynamic of the whole network. A preliminary implementation of this model in a parallel environment is presented.

The Transient Eddy Current Problem (A-ϕ Formulation)

In the numerical model, the magnetic vector potential and electric scalar potential (A-ϕ) method are used to formulate and solve the field problem. This method is defined by the following equations:

$$\nabla \times (\bar{\nu} \cdot \nabla \times A) = J_0 - \sigma \left(\frac{\partial A}{\partial t} + \nabla \phi \right) \tag{1}$$

$$\nabla \cdot \sigma \left(\frac{\partial A}{\partial t} + \nabla \phi \right) = 0 \tag{2}$$

where A and ϕ are the magnetic vector potential and the electric scalar potential, respectively. J_0 is the magnetizing current density, ν is the reluctivity tensor, and σ is the conductivity. The application of the Galerkin method to equations (1) and (2) gives the following integral equations:

$$-\int_V \nabla N_i \times (\bar{\nu} \cdot \nabla \times A)\, dv + \sigma \int_V N_i \left(\frac{\partial A}{\partial t} + \nabla \phi \right) dv = \int_V N_i \cdot J_0 \cdot dv - \int_{S1} N_i \cdot \hat{n} \cdot H \; ds \tag{3}$$

and

$$\sigma \int_V \left(\frac{\partial A}{\partial t} + \nabla \phi \right) \cdot \nabla N_i \cdot dv = \int_V J_0 \cdot \nabla N_i \cdot dv - \int_{S2} N_i \cdot \hat{n} \cdot J_e \cdot ds \tag{4}$$

where N_i are the interpolation functions, S1 is the boundary surface of the volume V, S2 is the conductor's surface, $\hat{n}$ is the unit vector normal to S1 and S2, and H is the magnetic field intensity.

The partial derivatives in equations (3) and (4) can be replaced by values of magnetic vector potential components at the nodes of a finite element grid, multiplied by an appropriate set of algebraic coefficients. For a node i, in this grid, the corresponding general equations governing the field and eddy currents are as follows after implementing the boundary conditions:

$$-\sum_{j=1}^{NN} \eta_{ji} A_{ju} + \sigma_i \left(\frac{\partial A}{\partial t} + \nabla \phi_i \right) = J_{0i} \tag{5}$$

$$\sigma_i \sum_{j=1}^{NN} \left[\eta_{ji} \left(\frac{\partial A_{iu}}{\partial t} + \nabla \phi_i \right) - \eta_{ji} J_{0i} \right] = 0 \tag{6}$$

where η_{ji} are the finite element coefficients, A_{iu} are the magnetic vector potential components, J_{oi} is the external (excitation) current density, NN is the total number of nodes, and u designates the x, y, and z components.

The Crank-Nicolson Technique

The time in equations (5) and (6) can be divided into increments. Each increment has a duration τ, which is the time between the n and $n+1$ time instants. Hence, equations (5) and (6) can be approximated as follows:

$$-\frac{1}{2} \sum_{j=1}^{NN} \eta_{ji} \left(A_{ju}^n + A_{ju}^{n+1} \right) + \sigma_j \left(\frac{A_{iu}^{n+1} + A_{iu}^n}{\tau} + \frac{\nabla \phi_i^{n+1} - \nabla \phi_i^n}{\tau} \right) = \frac{1}{2} \left(J_{0i}^n + J_{0i}^{n+1} \right) \tag{7}$$

and

$$\sigma_i \sum_{j=1}^{NN}\left[\eta_{ji}\left(\frac{A_{iu}^{n+1}+A_{iu}^{n}}{\tau}+\frac{\nabla\phi_i^{\,n+1}-\nabla\phi_i^{\,n}}{\tau}\right)-\frac{1}{2}\eta_{ji}\left(J_{0i}^{n}+J_{0i}^{n+1}\right)\right]=0 \tag{8}$$

After algebraic manipulations and rearrangement of the terms in equations (7) and (8), one has the following relationships:

$$-\frac{1}{2}\sum_{j=1}^{NN}\eta_{ji}A_{ju}^{n+1}+\frac{\sigma_i}{\tau}\left(A_{iu}^{n+1}+\nabla\phi_i^{n+1}\right)=\frac{1}{2}\sum_{j=1}^{NN}\eta_{ji}A_{ju}^{n}+\frac{\sigma_i}{\tau}\left(A_{iu}^{n}+\nabla\phi_i^{n}\right)+\frac{1}{2}\left(J_{0i}^{n}+J_{0i}^{n+1}\right) \tag{9}$$

and

$$\frac{\sigma_i}{\tau}\left[\sum_{j=1}^{NN}\eta_{ji}A_{iu}^{n+1}+\sum_{j=1}^{NN}\eta_{ji}\nabla\phi_i^{\,n+1}\right]-\frac{\sigma_i}{\tau}\left[\eta_{ji}A_{ju}^{n}+\sum_{j=1}^{NN}\eta_{ji}\nabla\phi_i^{\,n}\right]-\frac{1}{2}\sum_{j=1}^{NN}\eta_{ji}\left(J_{0i}^{n}+J_{0i}^{n+1}\right)=0 \tag{10}$$

The State-Space Technique

Another method, used for computing the time derivatives in equations (5) and (6), is the state-space approach. These equations can be written for a volume containing excitation coils, metallic structures and nonconducting media. It should be pointed out that the excitation winding cannot have eddy currents. If one designates the total number of nodes in nonconducting media to be l, the total number of nodes within the excitation winding to be m, and the total number of nodes in the metallic structure to be k, then the following can be written in a matrix form after proper node numbering and matrix row and column permutation operations:

$$\begin{bmatrix}\eta_{ji}(l\times l) & \eta_{ji}(l\times m) & \eta_{ji}(l\times k)\\ \eta_{ji}(m\times l) & \eta_{ji}(m\times m) & \eta_{ji}(m\times k)\\ \eta_{ji}(k\times l) & \eta_{ji}(k\times m) & \eta_{ji}(k\times k)\end{bmatrix}\begin{bmatrix}(A_{ul},\phi)\\ (A_{um},\phi)\\ (A_{uk},\phi)\end{bmatrix}=\begin{bmatrix}0\\ 0\\ (\sigma A_{uk},\phi)\end{bmatrix}-\begin{bmatrix}0\\ J_{0m}\\ 0\end{bmatrix} \tag{11}$$

By means of matrix manipulations one has:

$$\mathbf{A}_{ul}=\left[\mathbf{L}_1\right]^{-1}\mathbf{L}_2\cdot\left(\mathbf{A}_{uk},\nabla\phi\right)+\left[\mathbf{L}_1\right]^{-1}\cdot\mathbf{J}_{0m} \tag{12}$$

$$\mathbf{A}_{um}=\left[\mathbf{L}_3\right]^{-1}\mathbf{L}_4\cdot\left(\mathbf{A}_{uk},\nabla\phi\right)+\left[\mathbf{L}_3\right]^{-1}\cdot\mathbf{J}_{0m} \tag{13}$$

where the matrices $\mathbf{L}_1$ through $\mathbf{L}_4$ are definable in terms of the finite element coefficients. It also follows that $\mathbf{A}_{uk}$ is governed by the following system of ordinary differential equations:

$$\dot{\mathbf{A}}_{uk}=\mathbf{W}\cdot\left(\mathbf{A}_{uk},\nabla\phi\right)+\mathbf{Z}\cdot\mathbf{J}_{0m} \tag{14}$$

where $\mathbf{W}$ and $\mathbf{Z}$ are matrices defined in terms of the finite element coefficients.

Equations (12) and (13) are basically a set of algebraic relationships while equation (14) is a set of first order differential equations. This last equation is the main state-space equation. The solution of equation (14) followed by the application of equations (12) and (13), results in the magnetic vector potential (MVP) over the whole volume under consideration, and hence the other field variables can be obtained. The solution, however,

hinges upon the calculation of the associated *transition matrices*. These matrices allow the calculation of the instantaneous values of the state variables from their previous values. From equation (14), one can write a standard recursive relation giving the MVP vector, $\mathbf{A}_{uk}[(n+1)\tau]$, at the $(n+1)^{st}$ instant of time in terms of the vector of MVP at the n^{th} time instant $\mathbf{A}_{uk}(n)\tau$ as:

$$\mathbf{A}_{uk}[(n+1)\tau] = \mathbf{R}_1 \cdot \mathbf{A}_{uk}[n\tau] + \mathbf{R}_2 \cdot \mathbf{J}_{0m} \tag{15}$$

where τ is the time increment or the sampling time by which the time duration is divided into steps of length τ, and $\mathbf{R}_1$ is the first state transition matrix given as:

$$\mathbf{R}_1 = e^{\tau \mathbf{W}} = \mathbf{U} + \tau\ \mathbf{W} + \frac{\tau^2 \mathbf{W}^2}{2!} + \frac{\tau^3 \mathbf{W}^3}{3!} + \cdots \tag{16}$$

and $\mathbf{R}_2$ is the second state transition matrix which contributes the influence of the excitation forcing function into the solution. This matrix is calculated directly from a series expansion as:

$$\mathbf{R}_2 = \left(\tau\ \mathbf{U} + \frac{\tau^2 \mathbf{W}}{2!} + \frac{\tau^3 \mathbf{W}^2}{3!} + \frac{\tau^4 \mathbf{W}^3}{4!} + \cdots\right) \cdot \mathbf{Z} = \mathbf{W}^{-1}(\mathbf{R}_1 - \mathbf{U})\mathbf{Z} \tag{17}$$

It is assumed that material properties remain time invariant between two integration steps. In equations (16) and (17), $\mathbf{U}$ is the identity matrix. It should be mentioned that in a non-linear transient solution, the state transition matrices $\mathbf{R}_1$ and $\mathbf{R}_2$ are updated at every time step.

Time Marching Solution Procedure

In order to accomplish a solution of the instantaneous magnetic field governed by equations (12) through (14), in a volume, one would proceed according to the following steps.

STEP 1 : $n = 0$; set all initial conditions.

STEP 2 : Calculate the excitation vector $\mathbf{J}_{0m}(n\tau)$.

STEP 3 : Form the matrix equation (11) and equations (12), (13), and (14).

STEP 4 : Calculate $\mathbf{R}_1(n\tau)$ and $\mathbf{R}_2(n\tau)$ using equations (16) and (17).

STEP 5 : Calculate at the $(n+1)\tau$ instant of time the vector $\mathbf{A}_{uk}[(n+1)\tau]$ using equation (15).

STEP 6 : Calculate the remaining vectors $\mathbf{A}_{ul}[(n+1)\tau]$ and $\mathbf{A}_{um}[(n+1)\ \tau]$ using equations (12) and (13)

STEP 7 : Calculate the flux densities throughout the volume, as well as other field variables.

STEP 8 : Update the reluctivities for all elements in the magnetic material region.

STEP 9 : Set the increment on the time; set $n = n + 1$.

STEP 10 : If the transient duration has been reached, print results. If not, go to STEP 2.

Application and Results

The A-ϕ method is applied to a practical problem that comprises an exciting coil set between two steel channels, and a steel plate inserted between the channels as shown in Figure (1). The steel plates are made of nonlinear material, and the amplitude of the excitation current rises exponentially with time. Solving the problem following the Crank-Nicolson and State-Space methods, two sets of solutions were obtained. The results are compared with each other and also with measurements. This comparison is carried out for the magnetic flux density and eddy current density values at the specified test points in the model. The test points[18] for the comparison of the magnetic flux density values are designated as S1($0.0 \le x \le 1.6$ mm, $0.0 \le y \le 25.0$ mm, z=0.0 mm), S2 (x =41.8 mm, $0.0 \le y \le 25.0$ mm, $60.0 \le z \le 63.2$ mm), and S3 ($122.1 \le x \le 125.3$, $0.0 \le y \le 25.0$, z= 0.0 mm). Similarly, the test points for the comparison of the eddy current densities are identified as P1 (1.6,6.25,0.0mm), P2 (41.8,6.25,63.2 mm), and P3 (125.3, 6.25,0.0). In Figures (2) and (3), the measured magnetic flux density values are compared with Crank-Nicolson and State-Space results, respectively. The same comparison is displayed in Figures (4) and (5) for the eddy current density values.

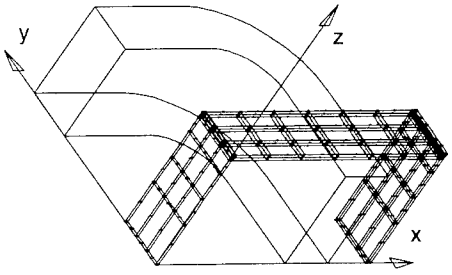


Figure 1. Example outline for the steel plates and coil

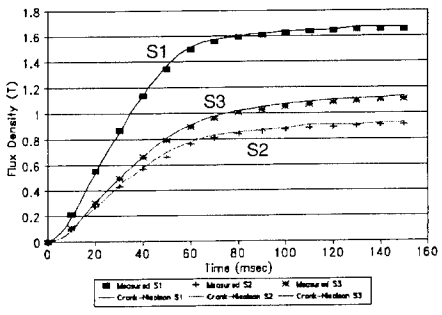


Figure 2. Comparison of measured flux density values and Crank-Nicolson results.

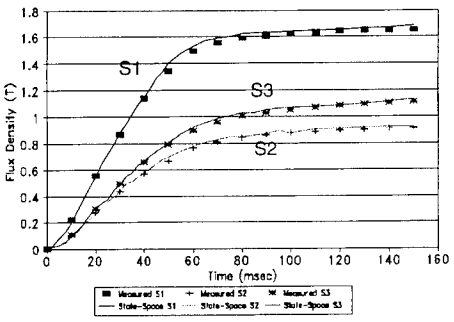


Figure 3. Comparison of measured flux density values and State-Space results.

T-Ω Method for Transient Eddy Current Problems

In this method, the electric vector potential (T) and magnetic scalar potential (Ω) are used as unknowns to solve the 3D nonlinear transient eddy current problem. Results of implementation using first and second order hexahedral finite elements are given. The same example utilized above with the A-ϕ method is used. In the steel plates, Figure (1), T and Ω are used. Outside the plates, only Ω is used. T and Ω are defined as follows:

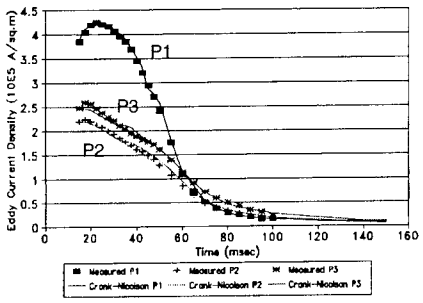


Figure 4. Comparison of measured eddy current density values and Crank-Nicolson results.

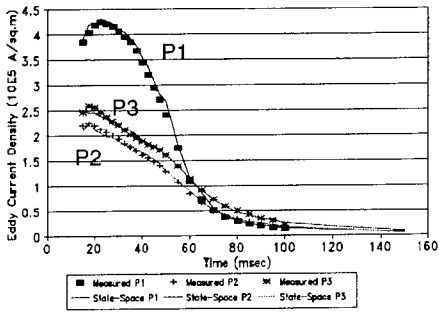


Figure 5. Comparison of measured eddy current density values and State-Space results.

$$\mathbf{H} = \mathbf{T} - \nabla\Omega + \mathbf{H}_s \qquad \text{in } V_e \tag{18}$$

$$\mathbf{J} = \nabla \times \mathbf{T} \qquad \text{in } V_e \tag{19}$$

$$\mathbf{H} = \mathbf{H}_s - \nabla\Omega \qquad \text{in } V_a \tag{20}$$

where V_e and V_a denotes eddy current regions and eddy current free regions respectively. The magnetic field intensity $\mathbf{H}_s$ due to the coil in free space is computed before solving the field equations by employing Biot-Savart law. The field equations are derived from the potentials as follows:

$$\nabla \times \rho\, \nabla \times \mathbf{T} - \nabla\, \rho\, \nabla \cdot \mathbf{T} + \frac{\partial \mu (\mathbf{T} - \nabla\Omega)}{\partial t} = -\frac{\partial \mu \mathbf{H}_s}{\partial t} \qquad \text{in } V_e \tag{21}$$

$$\nabla \cdot \frac{\partial \mu (\mathbf{T} - \nabla\Omega)}{\partial t} = -\nabla \cdot \frac{\partial \mu \mathbf{H}_s}{\partial t} \qquad \text{in } V_e \tag{22}$$

$$\nabla \cdot \frac{\partial \mu (-\nabla\Omega)}{\partial t} = -\nabla \cdot \frac{\partial \mu \mathbf{H}_s}{\partial t} \qquad \text{in } V_a \tag{23}$$

After using vector identities and Gauss' theorem, the weak form of the field equations are expressed as:

$$\int_{V_e} \left\{ \nabla \times \mathbf{N}_j \cdot \rho\, \nabla \times \mathbf{T} + \mathbf{N}_j \cdot \frac{\partial \mu (\mathbf{T} - \nabla\Omega)}{\partial t} \right\} dv = \int_{V_e} -\mathbf{N}_j \cdot \frac{\partial \mu \mathbf{H}_s}{\partial t} dv. \tag{24}$$

$$\int_{V_e} \nabla N_j \cdot \frac{\partial \mu (\mathbf{T} - \nabla\Omega)}{\partial t} dv = \int_{V_e} -\nabla N_j \cdot \frac{\partial \mu \mathbf{H}_s}{\partial t} dv \tag{25}$$

$$\int_{V_e} \nabla N_j \cdot \frac{\partial \mu (-\nabla\Omega)}{\partial t} dv = \int_{V_e} -\nabla N_j \cdot \frac{\partial \mu \mathbf{H}_s}{\partial t} dv \tag{26}$$

In a simplified way, equations (24) through (26) could be rewritten as:

$$\mathbf{M}(\mu)\frac{\partial \mathbf{u}}{\partial t} + \mathbf{K}\,\mathbf{u} = -\mathbf{M}(\mu)\frac{\partial \mathbf{H}_s}{\partial t} \qquad \text{in } V_e + V_a \tag{27}$$

where **u** is the solution vector.

For the time differential, the step by step method is employed. Discretizing the solution **u** with time as the independent variable, and using a weighted residual approach[10], we can express equation (27) approximately as:

$$\left(\frac{\mathbf{M}(\mu)_{n+1}}{\Delta t} + \mathbf{K}\,\theta\right)\mathbf{u}_{n+1} = \left(\frac{\mathbf{M}(\mu)_{n+1}}{\Delta t} - \mathbf{K}(1-\theta)\right)\mathbf{u}_n - \left(\frac{\mathbf{M}(\mu)_{n+1}}{\Delta t}\mathbf{H}_{s_{n+1}} - \frac{\mathbf{M}(\mu)_n}{\Delta t}\mathbf{H}_{s_n}\right) \tag{28}$$

where θ is a parameter relevant to weighting function. θ equals 1, 1/2 or 2/3 corresponding to the Backward difference, Crank-Nicolson or Galerkin difference schemes respectively. The subscripts $n+1$ and n stand for the adjacent two time steps, and $\Delta t = t_{n+1} - t_n$.

If Newton - Raphson iteration is chosen to treat the nonlinearity of equation (28), the Jacobian matrix will not be symmetric. Therefore, when ICCG method is used to solve the equation, the computation time for each ICCG iteration will be doubled compared with the case for a symmetric matrix. Therefore, In each time step, a relaxation method is adopted here. The values of element permeability μ are modified iteratively as follows:

$$\mu^{m+1} = \mu^m + \omega\left(\mu^{m+1} - \mu^m\right) \tag{29}$$

where ω is a relaxation factor, m+1 denotes the current iteration. From our experience, a variable relaxation factor was shown to be less time consuming. For lower saturation levels, a relatively high value for ω to start the nonlinear iteration, say $\omega = 1.0$, may be used. The value may be reduced after 5 or 6 iterations to , say $\omega = 0.5$. For higher saturation levels, choose a lower value for ω to start , say $\omega = 0.5$, then reduce the value gradually to, say $\omega = 0.1$. In general, the number of nonlinear iterations could be reduced in this manner.

Numerical Results

The computations were carried out using first and second order hexahedral elements. The time functions of the average flux density and the local eddy current density obtained from the computations are given in Figures (6), (7) and (8), compared with the measured values[4,8,9] and the above results using A-ϕ scheme. Section 1, S1 denotes the section of the plate at $0 \le x \le 1.6$, $0 \le y \le 25$, $z = 0$ (mm) as defined above. Positions 1 and 2 (P1 and P2 defined above) stand for the point (1.6, 6.25, 0.0) and (41.8,6.25,63.2) (mm) in the plates respectively. Figures (9) and (10) show the distribution of the flux densities and the eddy current densities on the part of the steel plate surface, respectively.

It can be seen that the calculated results agree with the measured results basically. However, the computation accuracy with T-Ω scheme is not as satisfactory as with A- ϕ scheme. The reason may lie in the treatment of the interface condition. To ensure the zero-normal components of the eddy current densities on the interface between the conductor and nonconductor regions, the tangential components of **T**, T_t, should be set to zero in the numerical procedure explicitly.

In the implemented example, the flux densities and eddy current densities change rapidly along the direction perpendicular to the main surface of the steel plate. The discretized errors with $T_t = 0$ are more sensitive to the mesh density. Thin plate structure with the skin effect limits the fining of the mesh density along the thickness of the plates. When the saturation level of the steel plates is low, the use of second order elements will improve the computation accuracy effectively. But the improvement is not so distinct when the

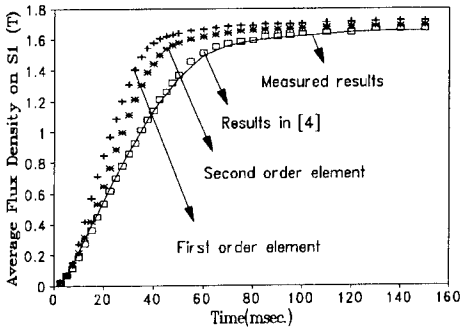


Figure 6 . Average flux densities on section S1.

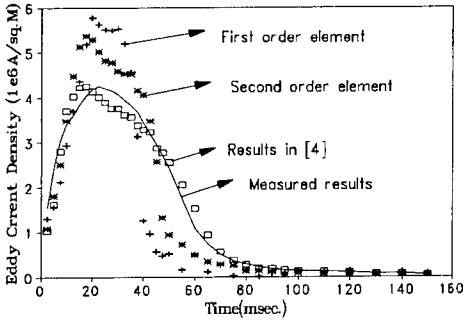


Figure 7. Eddy current at position P1.

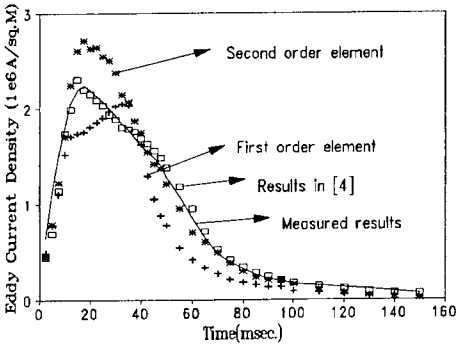


Figure 8. Eddy current densities at position P2.

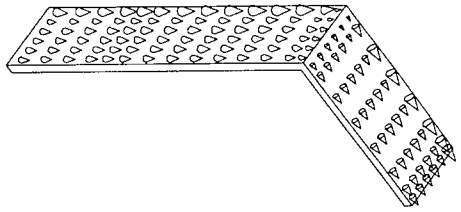


Figure 9. Flux densities on the plate surface

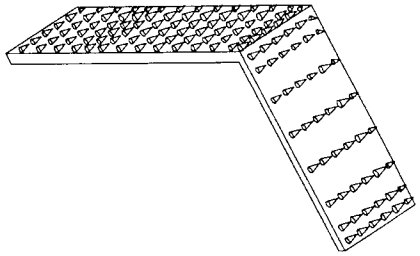


Figure 10. Flux densities on the plate surface

saturation level increases. The reason is that for the same node number with first order element mesh, the second order element mesh takes less number of elements. Therefore, the description of the material characteristics is less accurate with the second order element. The number of ICCG iterations with second order elements is larger than with first order elements. This is because not only the non-zero entries of the coefficient matrix increase, but also the distribution of the entries is more scattered. Therefore, the characteristic of the matrix gets worse. Taking the solution of the last iteration as the first guess for the current iteration could reduce the number of iterations greatly in the ICCG procedure.

ISP Method and Formulation for Eddy Current Problems

Another new technique for solving the electromagnetic field equations and calculating the eddy current density values is based on the Iterative Scalar Potential (ISP) formulation. The procedure is simple and is outlined as follows:

$$\nabla \times \mathbf{H} = \mathbf{J}_e \qquad \nabla \cdot \mathbf{B} = 0 \tag{30}$$

$$\nabla \times \mathbf{E} = \mathbf{J}_m \qquad \nabla \cdot \mathbf{D} = 0 \tag{31}$$

where $\mathbf{J}_e = \mathbf{J}_c + \sigma \mathbf{E} \qquad \mathbf{J}_m = -\dfrac{\partial \mathbf{B}}{\partial t}$

Here, $\mathbf{J}_e$ and $\mathbf{J}_m$ are unknowns, and $\mathbf{J}_c$ is the conduction current density. The magnetostatic field is described as:

$$\nabla \times \mathbf{H} = \mathbf{J}_c \qquad \nabla \cdot \mathbf{B} = 0 \tag{32}$$

A scalar potential can be used to solve equation (32) and the equivalent integral form is:

$$\sum_j \int_V \left(\nabla N_i\right)\left(\mu \nabla N_j\right) \Phi_j \, dv = \int_V \left(\nabla N_i\right) \cdot B_c \, dv - \int_S N_i \, B \cdot n \, ds \tag{33}$$

Bc in equation (33) can be determined based on $\mathbf{J}_c$ as:

$$B = -\mu \nabla \Phi + B_c \tag{34}$$

If $\mathbf{J}_e$ is assumed, then B can be solved using a scalar potential in a manner similar to equation (33). Hence, $\mathbf{J}_m$ can be determined and E is obtained using a scalar potential where the method of solving equation (31) is similar to the method of solving equation (32). The above equations can be written in an iterative form as follows:

$$\nabla \times H_r^{k+1} = J_c + \sigma \, E_r^k \tag{35}$$

$$\nabla \times E_r^{k+1} = -\omega \, \mu \, H_i^{k+1} \tag{36}$$

$$\nabla \times H_i^{k+1} = \sigma \, E_i^{k+1} \tag{37}$$

$$\nabla \times E_i^{k+1} = \omega \, \mu \, H_r^{k+1} \tag{38}$$

where the subscripts r and i indicate real and imaginary parts of complex field quantities and the superscript k designates the k^{th} step of iteration. For fast convergence of the iterative process, accelerating coefficients are used. These coefficients are determined from the calculation expressions used to obtain the $(k+1)^{st}$ step. When determining the $(k+1)^{st}$ step for H^{k+1}, E^{k+1}, H^{k+1}, and E^{k+1}, the required values of E^k, H^{k+1}, E^{k+1}, H^{k+1}, are calculated as follows, respectively:

$$E_r^k = \left(E_r^k + E_r^{k-1}\right) \cdot C1 \tag{39}$$

$$H_r^{k+1} = \left(H_r^{k-1} + H_r^k\right) \cdot C2 \tag{40}$$

$$E_i^{k+1} = \left(E_i^{k+1} + E_i^k\right) \cdot C3 \tag{41}$$

$$H_i^{k+1} = \left(H_i^{k+1} + H_i^k\right) \cdot C4 \tag{42}$$

where $C1$, $C2$, $C3$, and $C4$ are accelerating coefficients recalculated throughout the iterative process. This procedure is repeated for $k = 1, 2, ..., N$ and the final solutions are; $B = B_N$ and $E = E_N$.

Application and Results

The ISP method is applied to an aluminum bar example shown in Figure (11). This bar was surrounded by a coil containing 987 turns and was excited by various values of excitation current at 60 Hz and 120 Hz. Other geometrical details regarding this example are given in the following section. Table 1. show a comparison between the measured and calculated values of eddy current losses in the bar at 60 Hz. Table 1. also include a comparison with the numerical results obtained using the A-ϕ method explained above. As can be seen from the results in the Table 1. follow the expected patterns of the current squared law and are in good correlation with solutions from the A-ϕ method as well as with experimental data. From our experience with this method, the advantages of this method are; 1) The numerical problem is solved in terms of the field variables directly which has a physical meaning, and 2) sizable reduction in CPU time to obtain the solution in comparison to other methods. The numerical results of this new technique are obtained in less than 1/2 of the time consumed utilizing the A-ϕ method.

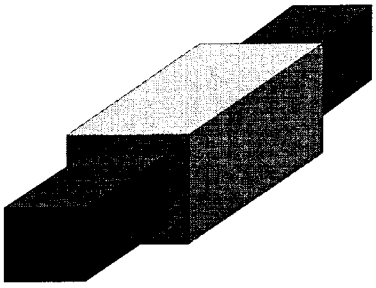


Figure 11. Aluminum bar example and surrounding coil

The solutions compared here are linear and the coil excitation is sinusoidal and this method is not attractive for nonlinear transient eddy current problems. Nonlinear solutions utilizing this ISP method was performed on a transformer problem and were reported in reference [6].

Table 1. Comparison between experimental an numerical values of eddy current losses (W) for the aluminum bar example

	1.0 A	1.5 A	2. 0 A
Laboratory Results (60 Hz)	0.5800	1.5600	3.5200
Numerical A-ϕ Method	0.7480	1.6730	2.9740
ISP Method (60 Hz)	0.6604	1.5379	2.9927
ISP Method (120 Hz)	1.1842	2.6525	5.4267

Neural Computation of the 2-D Eddy Current Problem

The above methods of solving electromagnetic field and eddy current problems involve computation procedures which utilizes the serial nature of computer systems. Recently some researchers are exploring neural network and parallel procedures to solve electromagnetic problems more efficiently and with a high degree of robustness.[11,12] These recent developments have followed the important work of Hopfield [13] in optimization in addition to several other works in optimizing electromagnetic devices. The developments here contributes to these continuing efforts by suggesting an architecture that provide a parallel computation alternative for a variety of problems in electromagnetics. This procedure is also applicable to any problem which can be modeled by partial differential or integro-differential equations or any sparse system of equations.

Description of the Method

The ability to preserve the parallel processing nature, the continuous-time dynamics, as well as global interaction of network elements is of great interest in solving eddy current problems. A parallel architecture for eddy current problems is formed with nodes which are fully interconnected as shown in Figure (12). Each node is modeled with a set of circuit elements as determined by the governing equation. The interconnection between the nodes is produced through weights similar to dependent sources in an electrical circuit according to a specific rule. The directly connected nodes could interact directly with each other while indirectly connected nodes affect each other through the propagation effects of the continuous-time dynamic of the whole network. In general, the interconnection can be of any dimension. A node of any row or column (i,j) process information through a function derived from the governing field equation. To determination the eddy currents in a two dimensional system, the governing equation is as follows:

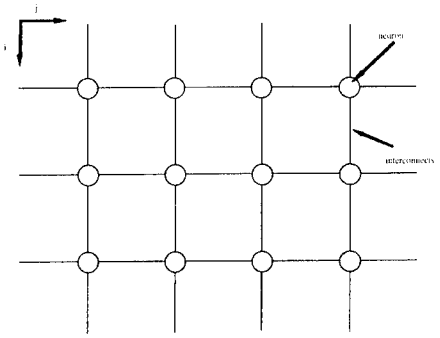


Figure 12. A 2-D neural system for eddy current calculations

$$\nabla \times (\nu \nabla \times \mathbf{A}) - \sigma \frac{\partial \mathbf{A}}{\partial t} + \frac{\sigma}{a} \int_S \frac{\partial \mathbf{A}}{\partial t} ds + \mathbf{J} = 0 \tag{43}$$

where ν is the material reluctivity, $\boldsymbol{A}$ is the magnetic vector potential, σ is the conductivity, a is the cross sectional area of the exciting conductor, S is the surface, and $\boldsymbol{J}$ is the measured current. If equation (43) is discretized using two dimensional finite differences, one obtains the following for each node.

$$\begin{aligned} &w_1 A_{i,j+1} + w_2 A_{i,j-1} + w_3 A_{i+1,j} + w_4 A_{i-1,j} - (w_1 + w_2 + w_3 + w_4) A_{ij} \\ &-\sigma_i \mu_{ii} \frac{\partial A_{ij}}{\partial t} + \frac{\sigma_{ij} \mu_{ij}}{a} \sum_k \frac{\partial A_{kl}}{\partial t} a_{kl} + \mu_{ij} J_{ij} = 0 \end{aligned} \tag{44}$$

where w's are obtained from the geometries and the summation over k relates to numbers over the coil area. Equation (44) discretizes the function in space with inter-connected nodes, and uses the continuous-time dynamics to simulate the behavior of the magnetic vector potential. Each node in Figure (12) is modeled by the cell circuit of Figure (13). The values of the circuit elements are given as follows:

$$\begin{aligned} &I_S = \frac{I_{ij}\mu_{ij}}{a} \quad I_1 = w_1 A_{i,j+1} \quad I_2 = w_2 A_{i,j-1} \quad I_3 = w_3 A_{i+1,j} \quad I_4 = w_4 A_{i-1,j} \quad I_{S_1} = \frac{\sigma_{ij}\mu_{ij}}{a} \quad I_{k,l} = \frac{\partial A_{k,l}}{\partial t} \\ &R_1 = \frac{1}{w_1 + w_2 + w_3 + w_4} \quad C_1 = \sigma_{ij}\mu_{ij} \quad V_1 = A_{ij} \quad C_2 = \frac{\sigma_{kl}\mu_{kl}}{a} a_{kl} \end{aligned} \tag{45}$$

This parallel interaction on the nodes make the process much faster than the sequential process. The above procedure is implemented on two examples. In these applications, we consider purely sinusoidal excitation and hence, complex representation of all field variables is possible. The *d/dt* term can be replaced by $j\omega$. If the eddy current in the exciting coil is considered, all the terms of equation (44) will be considered. The results are compared with solutions from standard finite element analysis.

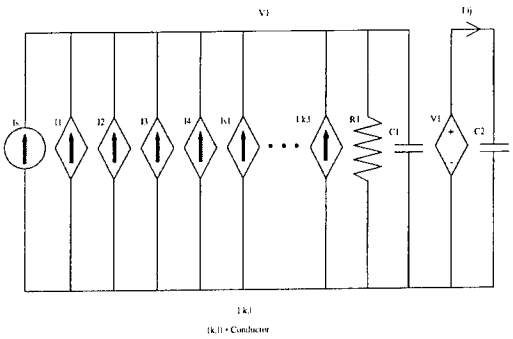


Figure 13. A cell circuit for each node

Example and preliminary Results:

The example described in Figure (11) is that of an aluminum bar (2.54 cm x 2.54 cm x 20.32 cm) inserted in a coil (8.128 cm long and 0.32 cm thick) as shown in Figure (3). The coil has 987 turns. We will compute this problem with 1.0 A, 1.5 A and 2.0 A rms currents at 60, 120 Hz frequency. Other frequencies of 200 Hz and 1000 Hz will also be tested. The eddy current losses in the coil is neglected.

Figures (14) and (15) show results of the aluminum bar example by using this neural parallel approach and by standard FE analysis for 2.0 A at 60 Hz. Table 2. show the results of eddy current loss at 1.0 A, 1.5 A and 2.0 A. The 2-D eddy current loss data at 60 Hz shown in Table 2. could be also compared with the 3-D finite element results obtained using the ISP and the A-ϕ methods above. These results are in good comparison with the results obtained in the previous section for the same example.

Table 2. Comparison of solutions at various currents for the aluminum bar

	Parameter	2-D Finite Element Solution	Neural Solution
I = 1.0 A, f=60 Hz	Eddy current loss (W)	0.6742	0.6731
I = 1.5 A, f=60 Hz	Eddy current loss (W)	1.5938	1.5914
I = 2.0 A, f=60 Hz	Eddy current loss (W)	2.8845	2.8862
I = 2.0 A, f=120 Hz	Eddy current loss (W)	5.3389	5.3415

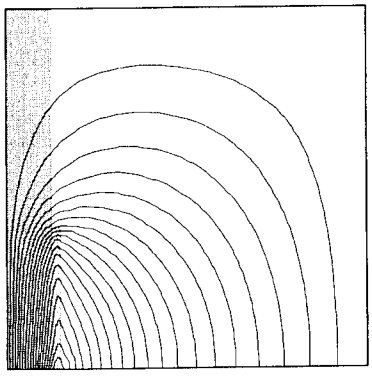


Figure14. MVP lines from FE solution at 60 Hz

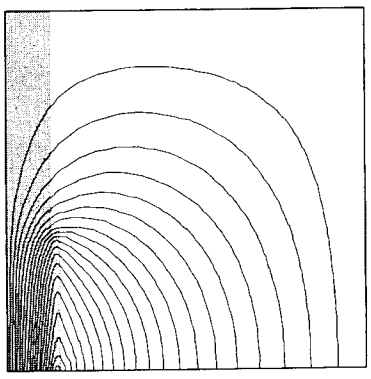


Figure15. MVP lines from Neural solution at 60 Hz

Conclusion

This paper presented an variety of formulations and computational techniques for eddy current problems in electrical devices. Techniques for two dimensional and three dimensional cases are presented utilizing vector and scalar formulations. Both sinusoidal and transient variations of excitation systems in both the linear and nonlinear cases were treated. The implemented examples showed how the various techniques are utilized. Due to the serial nature of current methods of eddy current analysis, a neural network model was suggested for implementation in a parallel environment with a simplified example in two dimensions.

References

1. Demerdash, N. A., Nehl, T. W., Mohammed, O. A., Fouad, F. A. and Miller, R.H. "Solution of Eddy Current Problems Using Three Dimensional Finite Element Complex Magnetic Vector Potential," *IEEE Transactions on Power Apparatus and Systems*, Vol. PAS-101, No. 11, November 1982, P.P. 4222-4229.
2. Mohammed, O. A., Uler, F. G. and Ming, Z., "3D Finite Element Transient Field and Eddy Current Computations in Nonlinear Thin Steel Plates Over A Coil;" *The International Journal For Computation and Mathematics in Electrical and Electronic Engineering*, COMPEL Vol. 9, No. 1, Sup. A., P.P. 269-271, March, 1990.
3. Mohammed, O. A. and Uler, F. G. " 3-D Finite Element Time-Varying Fields and Eddy Currents in Nonlinear Thin Steel Channels," *IEEE Transactions on Magnetics*, Vol. 27, September 1991, P.P. 4008-4011.
4. Mohammed, O. A. and Uler, F. G. " A State Space Approach and Formulation for the Solution of Nonlinear 3-D Transient fields and Eddy Current Problems," *IEEE Transactions on Magnetics*, Vol. 28, No. 2, March, 1992, P.P. 1111-1114
5. Dexin, X., Mohammed, O. A., Uler, F. G. and Koh, C. S." T-Ω Finite Element Analysis of 3D Nonlinear Transient Eddy Current Problems," *International Journal of Applied Electromagnetics in Materials*, Elsevier. (to appear 1995).
6. Mohammed, O. A., Uler, F. G. and Xiaodi, Z., "The ISP Technique for 3D Eddy Current in General Media," *IEEE Transactions on Magnetics*, Vol. MAG. 26, No. 5, p.p. 1668-1670, September, 1990.
7. Mohammed, O. A. and Uler, F. G. " Neural Computations of Eddy Currents in Metallic Structures," Proceedings of *the 6th International IGTE Symposium on Numerical Field Calculation in Electrical Engineering*, Graz, Austria, pp. 282-287, September 26-28, 1994.
8. Mohammed, O. A. and Uler, F. G., " Recent Results on Bench Mark Problem 10 - The Nonlinear Transient Eddy Current 3-D Model;" Proceedings of the *European TEAM Workshop and International Seminar on Electromagnetic Field Analysis*, p.p. 37-61, 1992.
9. T.Nakata, N.Takahashi and K.Fujiwara, Proceedings of *European TEAM Workshop and International Seminar on Electromagnetic Field Analysis*, pp.211-221, 1991.
10. Jackson H.Hwang and William Lord, *IEEE Transactions on Magnetics* 10(4), pp.1113-1118,1974.
11. Fakhraie, S. M., Konrad, A. and Smith K. C. "Neuro-Computation Technique in Sampled data Electromagnetic Field Problems," IEEE Transactions on Magnetics, Vol. 30, No. 5, pp. 3637-3640, September 1994.
12. Yamashita, H., Kowata, N., Cingoski, V. and Kaneda, K., "Direct Solution Method for Finite Element Analysis using Hopfield Neural Network," *IEEE CEFC*, Aix-les-Bains, France.
13. Hopfield, J. J. and Tank, D. W. " Computing with Neural Circuits: A Model," *Science*, Vol. 233, pp. 625-633, August, 1986.

Ten Years of Evolution of the FDTD-like Conformal Techniques

Kane S. Yee
Lockheed Palo Alto Research Laboratory

Abstract

FDTD has been criticized for its inability to model accurately curved boundary electromagnetic problems. This shortcoming has been addressed by the FDTD community for the last ten years or so. It is the purpose of this paper to give a connecting account of the FDTD-derived conformal techniques (time leapfrog and spatially staggered) and to supply some motivation leading to those techniques. The paths to these techniques improving the original rectangular FDTD have not been straight , however.

Introduction

The present author published the FDTD numerical algorithm to solve Maxwell's equation in rectangular coordinates in 1966 [1]. He did no further work on it until 1984 when he returned to the Lawrence Livermore National Laboratory to work on microwave coupling problems requiring the numerical solution of Maxwell's equations. Meanwhile (1970-1980) the workers on EMP (Kunz, Holland, Lee, and Merewether of Mission Research Corporation) have made use of FDTD and have introduced many necessary auxiliary results to make the FDTD algorithm a practical tool to analyze the EMP problems [2-5]. In 1975 Taflove introduced the name FD-TD and has since contributed greatly to the techniques and applications of FDTD [6-8]. In fact, the original application of FDTD to the RCS calculation was due to him and his coworkers. FDTD as a practical tool seems to be complete after the publication of the radiation boundary condition approximation by Mur in 1981 [9]. Since the mid 1980, the application of FDTD to solve electromagnetic problems has been explosive. The number of citations of the 1966 paper [1] by journal articles is now well over 600; and if we include citations of orally presented papers, the number can easily top 1000! But, practically all these applications are based on the stair-casing rectangular FDTD algorithm.

Meanwhile our colleagues in the method of moments (MOM) and in finite elements (FE) have been rightly pointing out the fact that the FDTD would have trouble modeling curved surfaces other than some special cases where a coordinate representation of the surface is possible; and even then the curvilinear FDTD would have problem. In order to enlarge the scope of applicability of the rectangular FDTD, Holland published the FDTD algorithm in general coordinate systems in 1983 [10]. The curvilinear algorithm was implemented by Fusco in 1990 [11a, 11b]. The main shortcoming of the Holland algorithm is that it requires a coordinate system. In 1984 Yee [12] and Weiland [13] noticed a generalization of the original FDTD through the surface-curve integral form of Maxwell's equations. In a series of technical notes in the Lawrence Livermore National Laboratory and through personal conversations with workers in time domain electromagnetics, Yee (among others) has urged them to use the Faraday's law and Ampere's law in the orginal experimental forms (surface-curve integral form) as he has found them to be fruitful in the microwave coupling problems. Taflove has adopted the integral form and derived many useful results [14-16]. The integral form of Maxwell's equations was used by Holland and colleagues in deriving thin wire and thin slot modifications of FDTD, but the wide use of the integral form to derive numerical approximations seems to have started in its earnest since 1984.

Presently, workers in the time domain FDTD routinely use the integral form to derive numerical discretization of the Maxwell's equations. With the help of the integral form, Yee was able to show that it was possible to generalize FDTD to an irregular grid (in 2-D and in special cases in 3-D) where a known coordinate system is not necessary (Figure 4A). But he encountered difficulties in 3-D generalization. This new approach was delivered in the first ACES meeting in March 1985 in Livermore. Among those present was T. Jurgen who later wrote a dissertation under Taflove on the application of the integral form to make adjustment of FDTD near the curved boundary [15,16]. A significant breakthrough in generalizing FDTD for a general unstructured irregular grid was introduced by Madsen and Ziolkowski [17,18] when they, in addition to using the surface-curve integral form, also employed the volume-surface integral form of Maxwell's equations. In their work the main tool is the surface-curve integral form and the auxiliary tool is the volume-surface integral form employed for "correction". The Madsen-Ziolkowski method works well when the grid is nearly orthogonal. The implementation is, however, very complicated for a general grid; and Madsen has since abandoned it in favor of the discrete surface integral (DSI) where he uses the surface-curve integral form and averaging [19]. Meanwhile Yee and his colleagues attempted to generalize the FDTD with overlapping grids generated by coordinated patches [20]. In theory this method would work, but in practice it is too complicated to implement for general problems. Nevertheless, the overlapping-grid FDTD was found effective for many special problems and it can be very general for 2-D scattering by smooth cylinders as in

this case a local tangent-normal orthogonal grid can be introduced. In the search for further generalization of the overlapping-grid FDTD and with the desire to make use of surface triangular grids such as employed by MOM analysts, Yee made use the volume-surface integral form of Maxwell's equations in addition to the surface-curve integral form. This is the FDTD/FVTD hybrid technique [21]. The FDTD/FVTD hybrid is now quite well developed and, to the opinion of the present author, it is rather easy to implement.

The Evolution of the FDTD-like Algorithm

Starting from the Maxwell's equations in partial differential equation form:

$$\nabla \times \vec{E} = -\mu \frac{\partial \vec{H}}{\partial t} \qquad \nabla \times \vec{H} = \varepsilon \frac{\partial \vec{E}}{\partial t} + \sigma \vec{E}$$

one can apply the standard central difference to derive the following finite difference equations (refer to Figure 7A and [1] for notations):

$$H_x^{n+1/2}(i, j+1/2, k+1/2) = H_x^n(i, j+1/2, k+1/2) + \frac{\Delta t}{\mu(i, j+1/2, k+1/2)\Delta x}[E_y^n(i, j+1/2, k+1) - E_y^n(i, j+1/2, k) + E_z^n(i, j, k+1/2) - E_z^n(i, j+1, k+1/2)]$$

and other equations.

In Figures 1a and 1b we show Maxwell's equations in surface-curve integral form, together with the verbal description of these laws. The verbal statements are copied directly from Schelkunoff's last book [22] where he urged the reader to consider Maxwell's equations in their integral forms. The original FDTD equations can be derived directly from these two sets of equations if one chooses the area to be the faces of the cubes (Fig. 7A). But the expression in Figures 1a and 1b are more general. In fact the area vector **A** is well defined even if the curve is not planar. The approximate discretized equations can be derived if one pays a little attention to the mean-value theorem of vector integrals. Roughly, the curve ∂A can not be too weird and the area enclosed by it should not be too odd. The data along ∂A should be sufficient to allow an accurate evaluation of the line integral. Knowing a little on the electromagnetic field behavior will help to ascertain the limitation of this approximation. In neighborhoods of thin wires and thin gaps these approximations need to be modified to reflect the singular behavior of the electromagnetic field. Depending on what curve is chosen and depending on where the field variables are located, these integral forms provide great flexibility to generate discretized equations. Maxwell's equations are very symmetric in **E** and **H**. The discretized equations to update **E** and **H** should be as similar as possible. Such symmetry has been attained in the original FDTD. In deriving discretized equations, one only needs to evaluate approximately a line integral and a surface integral. We will call the curve where the line integral involving the electric field **E** is evaluated the electric contour and similarly for a magnetic contour. The grid or grids chosen for the application of these integral forms should have the following essential property (Figure 2a, Figures 7 A, B,C):

Each edge associated with an electric field component ought to have a magnetic contour enclosing it (right hand rule) and each edge associated with a magnetic field component ought to have an electric contour enclosing it (left hand rule).

The rectangular FDTD grid, the Holland generalized FDTD grid, and the Madsen DSI grid all have the above property. For accurate approximation, one should "center" the variables with respect to the contours and the areas.

Equivalent to the surface-curve integral forms there is the volume-surface integral forms of the Faraday and Ampere laws (Figures 1c, 2b, 7D). The discretization involves no more than the evaluation of volume and surface vector integrals. Again accuracy depends on the locations of the field variables.

We shall from now on referred to the updating of the field variables by the surface-curve integral form of Maxwell's equations as FDTD (finite difference time domain, generalized) and the updating of the field variable by the volume-surface integral form of Maxwell's equations as FVTD (finite volume time domain).

To see how various schemes are related, we would like to introduce some terminology of the original FDTD grid (Figure 7A). The FDTD cubes will be referred to as electric cubes. The totality of electric cubes form an electric grid. The vertices (edges, faces) of these cubes will be referred to as electric vertices (edges, faces) The component of the electric field along an electric edge is located at the middle of the electric edge. If we connect the centers of two cubes having a common face, we obtain another grid known as the magnetic grid (Figure 1c, 10). The cubes of the magnetic grid are the magnetic cubes and so on. The component of the magnetic field along a magnetic edge is located at the middle of a magnetic edge. The boundary of a magnetic (electric) face forms a magnetic contour enclosing an electric (magnetic) edge. We observe that the area vector associated with a magnetic contour is along the same direction as the electric edge in an orthogonal coordinate system. Imagine now the rectangular electric grid is distorted in a non-orthogonal coordinate grid. We would have the same topology as the rectangular grid. This is

the grid Holland used (Figure 7B). There is a difference between a general non-orthogonal grid and the rectangular grid. The direction of the area vector enclosed by a magnetic (electric) contour may not be in the same direction as that of the electric (magnetic) edge this contour is associated with. To evaluate the electric contour integral we need the component of the electric field along the edges (which we assume we have). The component of an electric (magnetic) field associated with an electric (magnetic) edge is updated along the area vector associated with the magnetic (electric) contour. This area vector is not along the direction of the electric edge unless the coordinate is orthogonal. Thus, in order to obtain the component of the electric vector along an electric edge, Holland had to first calculate the electric vector at the middle of an electric edge. FDTD will yield the component along the area vector. Thus one relation of the three rectangular components at the middle of an electric edge is known; and the other two relations must come from interpolations (Figures 8B and 13b). This interpolation process is only possible if there is a smooth coordinate system and of course the computational elements are small compared to wavelength. When the coordinate system is nearly orthogonal, the direction of an electric edge and the area vector of the associated magnetic contour will be nearly the same. This is the basis of the Madsen-Ziolkowski method. They updated the component of the electric field along the magnetic area vector and, unlike Holland, they updated the other two relations (corrections) by FVTD. The process is very awkward. The latest Madsen DSI algorithm is shown in Figure 8C and Figure 13c. It is much simpler In this algorithm the FVTD is discarded and the component of the electric field along an electric edge by the updated FDTD data with an averaging. The DSI of Madsen is a generalization of the FDTD and Holland's FDTD in that one does not need a coordinate system for computation. In fact (referring to Figure 13c) it is only required that the magnetic area vectors associated with the edges a, b, and c respectively to be linearly independent. This algorithm is applicable in an unstructured grid. The FDTD updating and the averaging for the field variables seems to be more complicated, however, when compared with the overlapping FDTD/FVTD advanced by Yee. The composite FVTD grid consists of two grids--an electric grid and a magnetic grid. At the electric vertices are located the electric vector and at the magnetic vertices are located the magnetic vector. The magnetic vertices should be near the centers of the electric element (distorted cubes, prisms, or any other solid "elements") and the electric vertices should be near the centers of the magnetic elements (Figures 1c,10). The electric vector and the magnetic vector are updated by the FVTD algorithm (Figure 2b).

It is the present author's habit to assign electric edges or electric vertices at the boundary of a computational grid. The data at the boundary, whether it is a physical boundary or a computational boundary, can not be updated by either the FDTD or FVTD algorithm because the necessary magnetic contour or the magnetic surfave would not be contained in the computational volume. The data at the physical boundary is obtained with the help of the boundary condition and the data in the outer computational volume is obtained with the help of the radiation boundary condition simulation. These simulations will not be discussed here. Shown in Figure 3 are three possible grids. The stair-casing grid is for the rectangular FDTD, the locally distorted grid can be used by DSI and by FVTD, and the overlapping conformal grids can be used by the FDTD/FVTD hybrid. In the overlapping grid, the outer boundary is the computational boundary and it is also the outer boundary of the rectangular grid. The inner boundary of the rectangular grid is one to two "zones" away from the scattering object. The body conformal grid consists of several layers of prisms (Figure 10). In the interior field points of the rectangular grid we use the FDTD algorithm for updating, and in the interior vertices of the conformal grid we use the FVTD algorithm for updating. The data at the outer boundary of the rectangular grid is fixed with the help of radiation condition simulation and the data at the physical boundary (the scatterer) is fixed with the help of the physical boundary condition. The data at the interior boundary of the rectangular can be obtained through interpolation of the calculated data of the conformal grid (Figure 12), and the data at the outer boundary of the conformal grid can be obtained through interpolation of the calculated data of the rectangular grid (Figure 12). The overlapping allows a systematic interpolation. The price paid over a single distorted grid is the double interpolations at each time step. However, one can obtain a conformal 3-D grid for the overlapping-grid from a surface grid, whereas a distorted grid requires a full fledge 3-D grid which is more difficult to generate. One can use the FDTD/FVTD hybrid with a single distorted grid (the grid shown in Figure 5 is the electric grid, and there is a corresponding magnetic grid not shown). Holland uses the grids Fig. 5A and Fig. 5B to perform calculations with the Madsen-Ziolkowski scheme [23], whereas we use the grid shown in Figure 5C with our FDTD/FVTD for the scattering calculation by a circular cylinder [24]. For 2-D problems the FDTD/FVTD is very flexible as we showed with the possible grids used in Figure 6 [24].

The Madsen-Ziolkowski modified finite volume technique, the Madsen discrete surface integral technique, and our FDTD/FVTD overlapping grid technique sometime encounter late time growth. There exist two ways to remedy this instability. Riley and Turner [25] employ a time averaging of the magnetic vector **H** and have found stability. In our work with the FDTD/FVTD hybrid, we find stability by employing an averaging of the rectangular grid data and the conformal grid data for the magnetic field in the overlapping region [26]. Recently papers showing improvement of the FDTD and the FVTD have also been published by Vinokur and Yarrow [27] and by Liu [28a, 28b].

There also a exists locally modified rectangular grid of Jurgen-Taflove [14, 16], and Fang-Ren [29] as shown in Figure 9. In these grids the rectangular grid is retained; the locations of the rectangular field components are the same as that in the rectangular FDTD. The FDTD (generalized) is used to update some variables near the boundary. However, near the boundary, some field variables are obtained through extrapolation and/or interpolation. The present author tried this technique but gave up because of the bookkeeping complexity. The quoted authors apparently have overcome (at least partially if not completely) the bookkeeping nightmare and produced some calculations showing the improvement over the stair-casing grid.

Recently, an FDTD-like technique employing the Whitney elements has been suggested by Yee and exploited by Chan et. al. [30]. The idea is illustrated in Figure 14 for the 2-D TM waves. The explanation in 3-D is simple (in principle). Imagine the computational space to consist of tetrahedrals. We assign the electric field component at the middle of the edge of the tetrahedral, and the normal component of the magnetic field at the centers of the faces of the tetrahedral. The electric contours are the boundary of the faces of the tetrahedral. Knowing the electric field components at the middle of the edges, the normal component of the magnetic field at the centers of the faces can be updated by means of FDTD. The difficulty (this is the difficulty the present author did not know how to overcome for 3-D in 1984 to recently until he heard of the Whitney elements through J. F Lee in 1992) is how to make use of the normal component of the magnetic field on the faces of a tetrahedral. The Whitney "face" elements are the vector interpolates defining a vector field throughout the whole tetrahedral having the same normal components at the centers of the faces. For a given electric edge there are tetrahedrals sharing this edge. The magnetic vector is defined throughout these tetrahedral. For a given electric edge, one can construct a surrounding magnetic contour which lies inside the collection of tetrahedral, and which encloses an area with the area vector in the direction of the electric edge. The electric field component along this edge can now be updated. A variant of this method can be our FDTD/FVTD hybrid because the Whitney elements allow us to define a magnetic vector at the center of each tetrahedral.

Other Time Domain Methods

Our finite element colleagues have recently been very active in the time domain method of solving Maxwell's equations. In 1984 Cangellaris et. al. [31a,b] published the point matching finite element time domain method. Because they matched Maxwell's equations at the nodes, they obtained an explicit system of ordinary differential equations. But most of the recent time domain finite element numerical equations are derived from a Galerkin process. Also the Whitney elements seemed to be preferred. Mur [32,33] used the Whitney edge elements to represent the electric field and the Whitney face elements to represent the magnetic field. He then uses a Galerkin weighing procedure to generate a linear system of ordinary equations to solve for the time dependent expansion coefficients. Lee [34] uses the Whitney edge elements alone as expansion functions and uses the Galerkin method in the weak form of the vector wave equation satisfied by the electric vector to derive a system of ordinary different equations. Mahadevan and Mittra [35, 36], following the work of Mur, have obtained results with the Whitney edge and face elements. All these methods require an inversion of a matrix. However, they are able to give criteria for the numerical stability of their methods, whereas for the DSI and our FDTD/FVTD such stability analyses have not been obtained. So far we still rely on our knowledge of the stair-casing FDTD to guide us on the stability question. However, the big advantage of DSI and the FDTD/FVTD is that they are explicit, requiring no inversion of a large matrix.

There is a very successful time domain conformal technique introduce from computational fluid dynamics by Shankar and his associates in Rockwell [37, 38]. The Maxwell's equations are cast in conservative form and a finite volume discretization is employed. Grids used in hydrodynamic calculations are used for their calculations.

Conclusion

From the above exposition, it is seen that the conformal time domain numerical solution of Maxwell's equations is a very active field. Not only the FDTD-like algorithms have advanced, but also other similar methods as well. Furthermore, the division of finite difference and finite element methods seems to be artificial and is narrowing. If Cangellaris and Mei had made use of the finite volume time domain technique in 1984, they would have derived results very similar to our FVTD and their point matched finite element method would have been simplified; and if Yee had known the Whitney elements (they existed since Whitney published his book in 1957 [39]) in 1984, he would have obtained results very similar to those by Mur, Lee, Mittra, and others in an explicit manner.

Acknowledgement

Dr. Gordon Strate's assistance in editing the paper is greatly appreciated.

References

1. K. S. Yee, "Numerical solution of initial boundary value problems in isotropic media", *IEEE Trans. Antennas Propag.*, vol. AP-14, no. 3, pp.302-307, May, 1966.

2. Merewether, D. E., "Transient Currents Induced on a Metallic Body of Revolution by an Electromagnetic Pulse", *IEEE Trans. Electromagnetic Compatibility*, Vol. EMC-13, No. 2, May 1971.

3. Kunz, K. S. and K. M. Lee, "A three-dimensional finite-difference soloution of the external response of an aircraft to a complex transient EM enironment." I. The method of its implementation. II. Comparisons of predictions and measurements, *IEEE Trans. EMC*, 20,328, 1975.

4. Holland, R., THREDE: "A Free-Field EMP Coupling and Scattering Code", *IEEE Trans. Nuc. Sci.*, vol. NS-24, Dember 1977.

5. Holland, R., L. Simpson,. and K. S. Kunz, "Finite difference analysis of EMP coupling to lossy dielectric structures, *IEEE Trans.* EMC, 22(2), 203, 1980.

6. Taflove, A. and M.E. Bodwin, "Numerical solution of steady-state electromagnetic scattering problems using the time-dependent Maxwell's equations," *IEEE Trans. Microwave Theory Tech.*, 23, 623-630, 1975.

7. Taflove, A. and K. R. Umashankar, "Radar Cross Section of general three dimensional scatters," *IEEE Trans. on Electromagnetic Comp.* vol. EMC-25 pp.433-440, Nov. 1983.

8. Taflove, A., K. R. Umashankar, and T. G. Jurgen, "Validation of FD-TD modeling of radar cross section up to nine wavelengths," *IEEE Trans. on Antennas and Propagation*, vol. Ap-33, pp. 662-666, June 1985.

9. Mur, G. " Absorbing Boundary Conditions for Finite-Difference Approximations of the Time-Domain Electromagnetic Field Equations," *IEEE Trans Electromag. Compat.*, vol. EMC-23, pp. 1073-1077, Nov. 1981.

10. R. Holland, "Finite-difference solutions of Maxwell's equations in generalized non orthogonal coordinates", *IEEE Trans. Nuc. Sci.*, vol. NS-30, pp.4589-4591, 1983.

11a. Fusco, M. A."FDTD Algorithm in Curvilinear Coordinates," *IEEE Trans. Antennas and Propagation*, vol.-38 pp. 76-89, Jan. 1991

11b. Fusco, M. A., M. V. Smith, and L. W. Gordon, "A three-Dimensional FDTD Algorithm in Curvilinear Coordinates," *IEEE Trans. Antennas and Propagation*, vol-39 pp. 1463-1472, Oct.1991

12. Kane S. Yee, "Numerical Solution to Maxwell's Equations with Non-orthogonal Grids", *Proc. of 1st Review of Numerical Electromagnetic Codes*, March 19-21,1985. Also Lawrence Livermore Technical Report UCRL-93268, April 1987.

13. Weiland, T, "On the numerical solution of Maxwell's equations and applications in the field of accelerator physics. *Particle Accelerators*, 15:pp.245-292, 1984

14. Taflove, A. K.Umashankar, B. Beker, F. Harfoush, and K. S. Yee, "Detailed FD-TD Analysis of Electromagnetic Field Penetrating Narrow Slots and Lapped Joints in Thick Conducting Screens", *IEEE Trans. Ant. and Propagation*, Feb. 1988.

15. Jurgen, T. G., A. Taflove, and K. R. Umashankar, and T. G. Moore, " Finite difference time domain modeling of curved surfaces," *IEEE Trans. AntennasPropagation*, vol. 40, April 1992.

16. Jurgen, T. G., and A. Taflove, " Three-Dimensional Contour FDTD Modeling of Scattering from Single and Multiple Bodies," *IEEE Tran. AntennasPropag.* vol. 41, No. 12 ,pp.1703-1708.

17. Madsen, N. K. and R. W. Ziolkowski, " Numerical solution of Maxwell's equations using irregular nonorthogonal grid," *Wave Motion*, vol.10, pp. 583-596, March 1988.

18. N. K. Madsen and R. W. Ziolkowski, " A Three-dimensional Modified Finite Volume Technique for Maxwell's Equations", *Electromagnetics*, vol. 10, nos.1-2,pp.147-161, Jan. 1990.

19. K. N. Madsen, "Divergence Preserving Discrete Surface Integral Methods for Maxwell's Curl Equations Using Non-Orthogonal Unstructured Grids", Lawrence Livermore National Laboratory UCRL JC-109787, Feb. 1992.

20.. Kane S. Yee, J. S. Chen, and A. H. Chang, "Conformal Finite Difference Time Domain (FDTD) with Overlapping Grids", *IEEE Trans on Ant. and Propagation*, vol. 40, No. 9, pp.1068-1075, Sept., 1992.

21. Kane S. Yee and J. S. Chen, "Conformal Hybrid Finite Difference Time Domain and Finite Volume Time Domain ", *IEEE. Trans. Antennas Propag.* vol. 42. No. 10, Oct. 1994.

22. Schelkunoff, S. A., Electromagnetic Fields, Blaisdell Publishing Company, New York, 1963.

23. Holland, R., "Pitfalls of Staircase Meshing," *IEEE Trans. on Electromagnetic Compatibility*, vol.35, NO. 4, Nov. 1991.

24. Chen, J. S., J. V. Prodan, and K. S. Yee "An FDTD/FVTD 2D-algorithm to solve Maxwell's equations, " *ACES 1995 Conference Proceeding.*

25. Riley, D. and C. D. Turner, "Finite-Volume Hybrid-Grid (FVHG) Techique for the Solution of the Transint Maxwell's Equations," *ACES Newsletter*, July 1994.

26. Chen, J. S., A. H. Chang, and K. S. Yee. "Numerical Experiments on Late Time Growth Involving the FDTD/FVTD Hybrid Code," To be submitted to IEEE Trans. Antennas and Propagation.

27. Vinokur, M. and M. Yarrow, "Finite-Surface Method for the Maxwell Equations with Corner Singularities," Proc. of the 32nd Aerospace Sciences Meeting and Exhibit, AIAA-94-0233, January 10-13 1994 / Reno , NV.

28a. Liu, Y., "Fourier Analysis of Numerical Algorithms for the Maxwell Equations," Proc. of the 31st Aerospace Sciences Meeting and Exhibit, AIAA-94-0233, January 11-14 1994 / Reno , NV.

28b. Liu, Y., " A Generalized Finite-Volume Algorithm for Solving the Maxwell Equations on Arbitrary Grids," *Conference Proceeding vol. I, 10th Annual Review of Progress in Applied Computational Electromagnetics*, March21-26, 1994.

29. Fang, Jiayuan and Jishi Ren, "A Locally Conformal Finite-Difference Time-Domain Algorithm of Modeling Arbitrary Shape Planar Metal Strips," *IEEE Transactions on Microwave Theory and Techniques*, Vol. 41, No. 5, May 1993.

30. Chan, C. H., H. Sangani, K. S. Yee, and J. T. Elson, "A Finite-Difference Time-Domain Method Using Whitney Elements, " *Microwave and Optical Technology Letters*, Vol. 7, No. 14, Oct. 1994 pp. 673-676.

31a. Cangellaris, A. C.,. C. C. Lin, and K. K. Mei, "Point -matched time domain finite-element methods ", presented at Nat. Radio Sci. Meeting at Boston, MA, June 1984.

31b. Cangellaris, A. C.,. C. C. Lin, and K. K. Mei, "Point -Matched Time Domain Finite-Element Methods for Electromagnetic Radiation and Scattering " *IEEE Trans, Antennas Propagation*, Vol. AP-35, pp. 1160-1173, Oct. 1987.

32. Mur, G. and A. T. de Hoop, " A finite element method for computing three-dimensional electromagnetic fields in inhomogeneous media," *IEEE Trans. on Magnetics*, vol. MAG-21, pp.2188-2191, November 1985.

33. Mur, G. "A mixed finite element method for computing three-dimensional time-domain electromagnetic fields in strongly inhomogeneous media," IEEE Trans. on magnetics, vol. 26, no. 2 March 1990.

33. Mur, G. , "The finite-element modeling of three-dimensional time-domain electromagnetic fields in strongly inhomogeneous media," *IEEE Trans. on magnetics*, vol. 28, no. 2 March 1992.

34. Lee, J. F. , "Solving Maxwell's equations by finite element time domain methods," to be submitted.

35. Mahadevan, K. and R. Mittra, " Use of Whitney's edge and face elements for efficient finite element time domain solution of Maxwell's equations," to be submitted.

36. Mahadevan, K. and R. Mittra, " Radar crosssection computation of inhomogeous scatterers using edge based finite element method in frequency and time domain" to be submitted.

37. Shankar, V., M. V. Mohammadian, and W. F. Hall, "A time-domain differential solver for electromagnetic scattering problems," *IEEE Proc.*, vol. 77, pp.709-721, May 1989.

38. Shankar, V., M. V. Mohammadian, and W. F. Hall, "A time-domain finite-volume treatment for the Maxwell's equations," *electromagnetics.*, vol. 10, pp.127-145, Jan. 1990.

39. Whitney, H., Geometric Integration Theory, Princeton Univeristy Press, Princeton, 1957.

The magnetic displacement current (the time rate of change of magnetic flux) passing through a given surface equals the negative electromotive force or the "voltage" (the line integral of the electric intensity) round the edge of the surface

$$\oint_{\partial A} \vec{E} \bullet d\vec{l} = -\int_{A} \dot{\vec{B}} \bullet \hat{n} da$$
$$\approx -\dot{\vec{B}} \bullet \int_{A} \hat{n} da$$
$$= -\dot{\vec{B}} \bullet \vec{A}$$

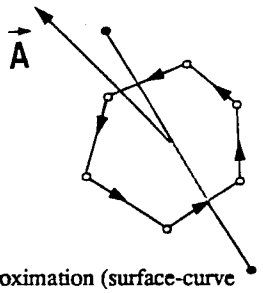


Fig. 1a Faraday-Maxwell's Law and Its Approximation (surface-curve integral form; FDTD)

The total electric current (the sum of convection, conduction and displacement currents) passing through a given surface equals the magnetomotive force (the line integral of the magnetic intensity) round the edge of the surface

$$\oint_{\partial A} \vec{H} \bullet d\vec{l} = \int_{A} (\dot{\vec{D}} + \sigma\vec{E} + \vec{J}) \bullet \hat{n} da$$
$$\approx (\dot{\vec{D}} + \sigma\vec{E} + \vec{J}) \bullet \int_{A} \hat{n} da$$
$$= (\dot{\vec{D}} + \sigma\vec{E} + \vec{J}) \bullet \vec{A}$$

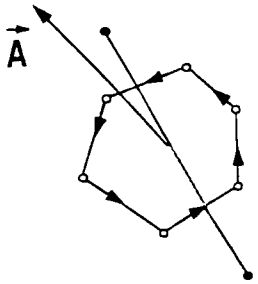


Fig. 1b Ampere-Maxwell's Law and Its Approximation (surface-curve integral form; FDTD)

Faraday's Law

$$\int_{\partial V} \hat{n} \times \vec{E}\, da = -\int_V \dot{\vec{B}}\, dv$$

$$\approx -\dot{\vec{B}} V$$

Ampere's Law

$$\int_{\partial V} \hat{n} \times \vec{H}\, da = \int_V (\dot{\vec{D}} + \sigma\vec{E} + \vec{J})\, dv$$

$$\approx (\dot{\vec{D}} + \sigma\vec{E} + \vec{J}) V$$

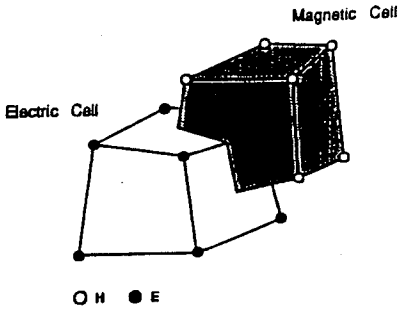


Fig. 1c Faraday-Maxwell's Law and Ampere-Maxwell's Law and Their Approximations (volume-surface integral form; FVTD)

- **Magnetic field update** (Faraday's law)

$$-\int_A \dot{\vec{B}} \bullet d\vec{a} = \int_{\partial A} \vec{E} \bullet d\vec{l}$$

Time discretized as

$$-\frac{1}{\Delta t}\int_A \left(\vec{B}^{n+1/2} - \vec{B}^{n-1/2}\right) \bullet \hat{n} ds = \int_{\partial A} \vec{E}^n \bullet d\vec{l}$$

- **Electric field update** (Ampere's law)

$$\int_A \dot{\vec{D}} \bullet \hat{n} ds = \int_{\partial A} \vec{H} \bullet d\vec{l}$$

Time discretized as

$$\frac{1}{\Delta t}\int_A \left(\vec{D}^{n+1} - \vec{D}^{n}\right) \bullet \hat{n} ds = \int_{\partial A} \vec{H}^{n+1/2} \bullet d\vec{l}$$

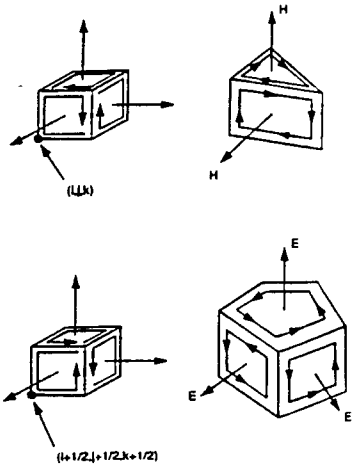


Fig. 2a The Leapfrog in Time Discretization of Maxwell's Equations (FDTD)

- **Magnetic field update** (Faraday's Law)

$$-\int_V \dot{\vec{B}}\,dv = \int_{\partial V} \hat{n}\times\vec{E}\,da$$

Time discretized as

$$-\frac{1}{\Delta t}\int_V \left(\vec{B}^{n+1/2}-\vec{B}^{n-1/2}\right)dv = \int_{\partial v}\hat{n}\times\vec{E}^{n}\,da$$

- **Electric field update** (Ampere's law)

$$\int_V \dot{\vec{D}}\,dv = \int_{\partial v}\hat{n}\times\vec{H}\,da$$

Time discretized as

$$\frac{1}{\Delta t}\int_V \left(\vec{D}^{n+1}-\vec{D}^{n}\right)dv = \int_{\partial v}\hat{n}\times\vec{H}^{n+1/2}\,da$$

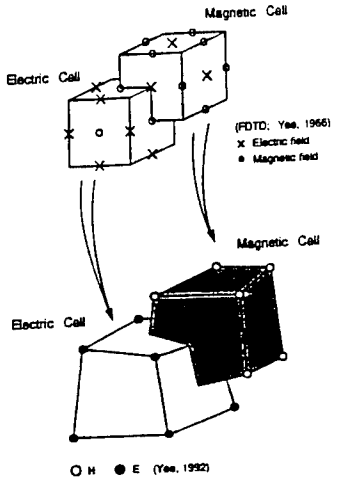
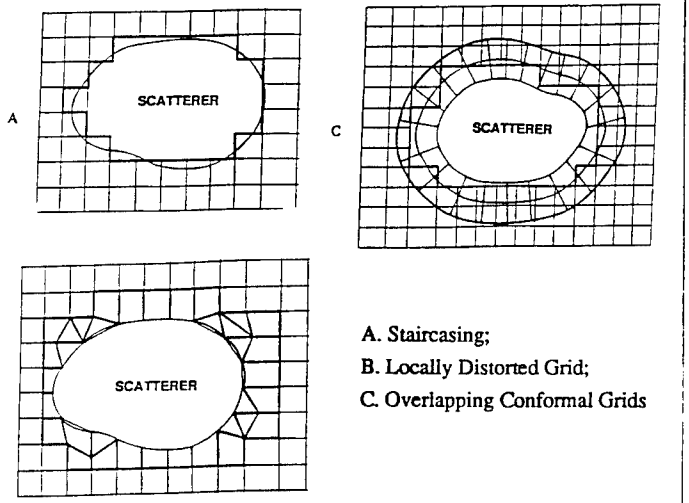


Fig. 2b The Leapfrog in Time Discretization of Maxwell's Equations (FVTD)



A. Staircasing;
B. Locally Distorted Grid;
C. Overlapping Conformal Grids

Fig. 3 Three Possible Ways of Gridding in the Neighborhood of the Scatterer.

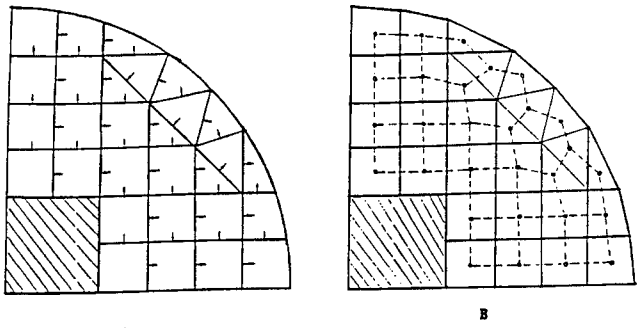


Fig. 4 Two Early 2-D Irregular Grids for Internal e/m Problems:
A. A Grid for the Interior of a Circular Cylinder (Yee, 1984);
B. The Madsen-Ziolkowski Grid of Grid A.

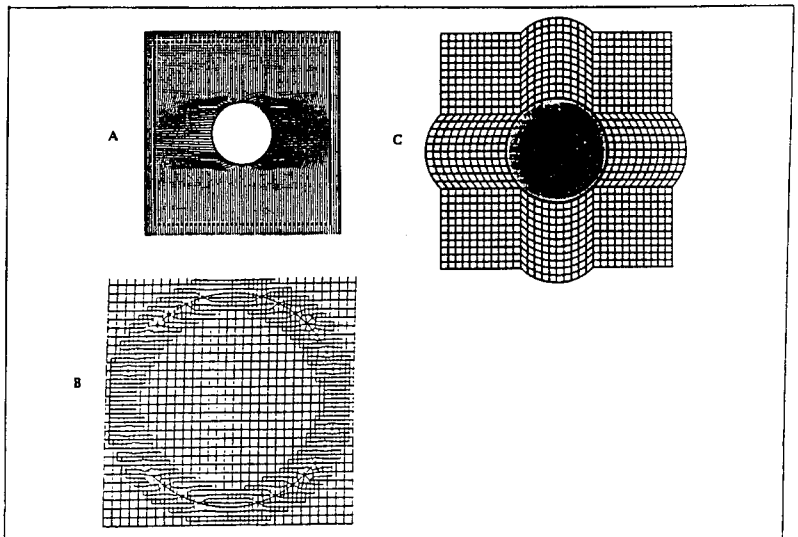


Fig. 5 Three Irregular Grids for a Circular Cylinder:
A. Locally distorted grid; the outer part of this grid is rectangular (Holland, 1992)
B. Unstructured locally distorted grid (Holland, 1992)
C. Structured non-orthogonal grid (Chen-Prodan-Yee, 1993)

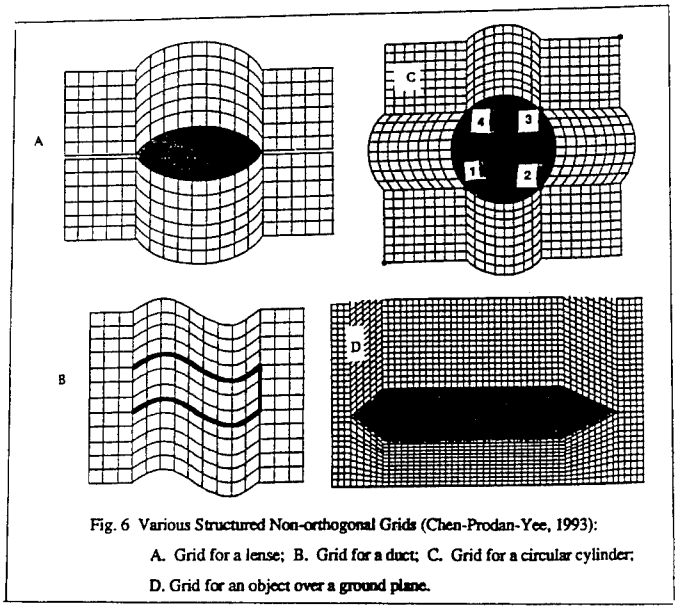


Fig. 6 Various Structured Non-orthogonal Grids (Chen-Prodan-Yee, 1993):
A. Grid for a lense; B. Grid for a duct; C. Grid for a circular cylinder;
D. Grid for an object over a ground plane.

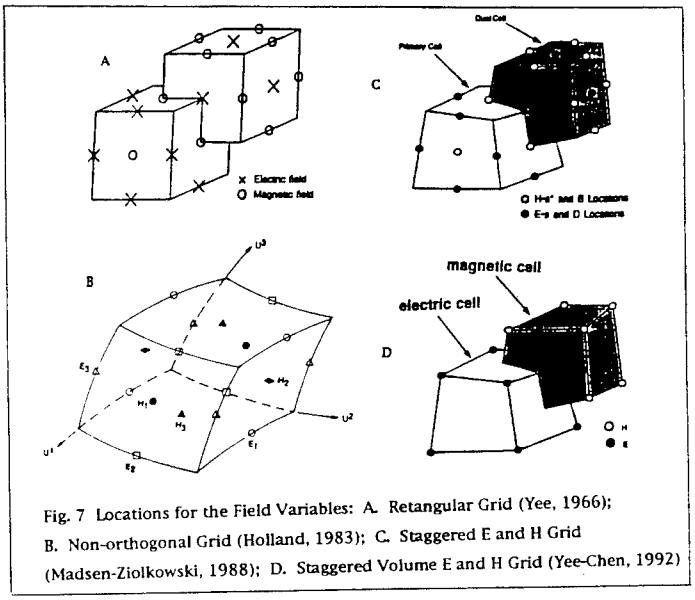


Fig. 7 Locations for the Field Variables: A. Retangular Grid (Yee, 1966);
B. Non-orthogonal Grid (Holland, 1983); C. Staggered E and H Grid
(Madsen-Ziolkowski, 1988); D. Staggered Volume E and H Grid (Yee-Chen, 1992)

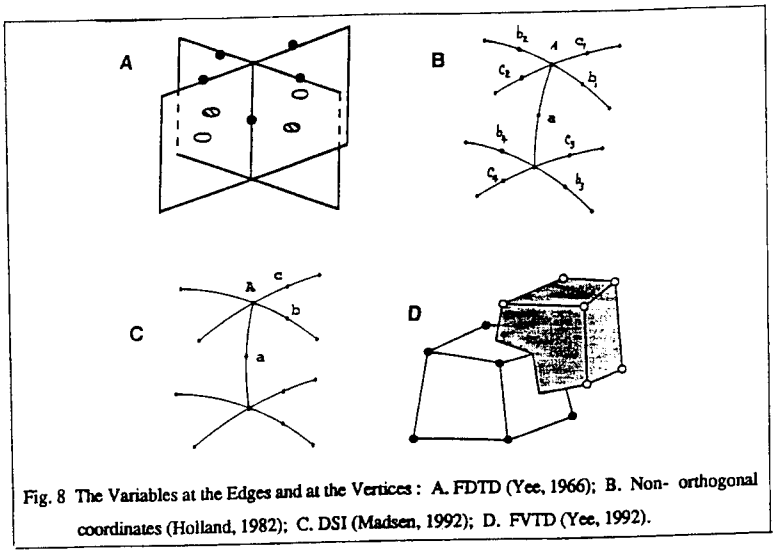


Fig. 8 The Variables at the Edges and at the Vertices : A. FDTD (Yee, 1966); B. Non- orthogonal coordinates (Holland, 1982); C. DSI (Madsen, 1992); D. FVTD (Yee, 1992).

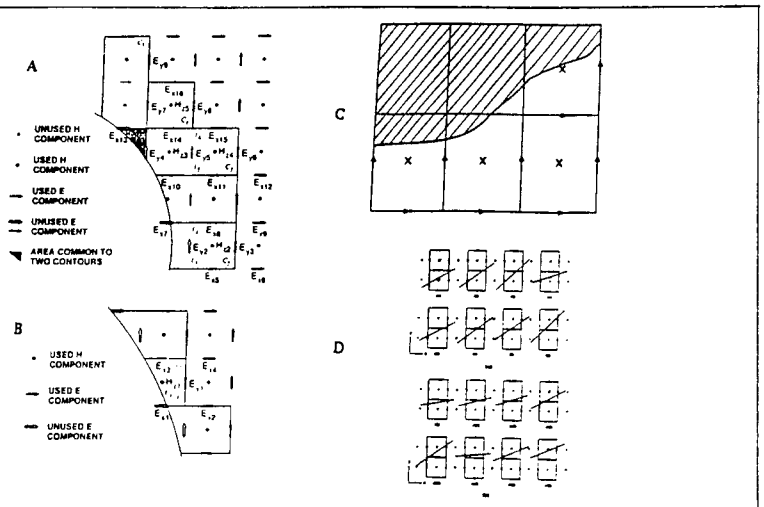


Fig. 9 Rectangular Grids with Special Adjustment at the Curved Boundary: A, B (Taflove,1987; Jurgen-Taflove, 1993); C, D (Fang-Ren, 1993 with 16 cases)

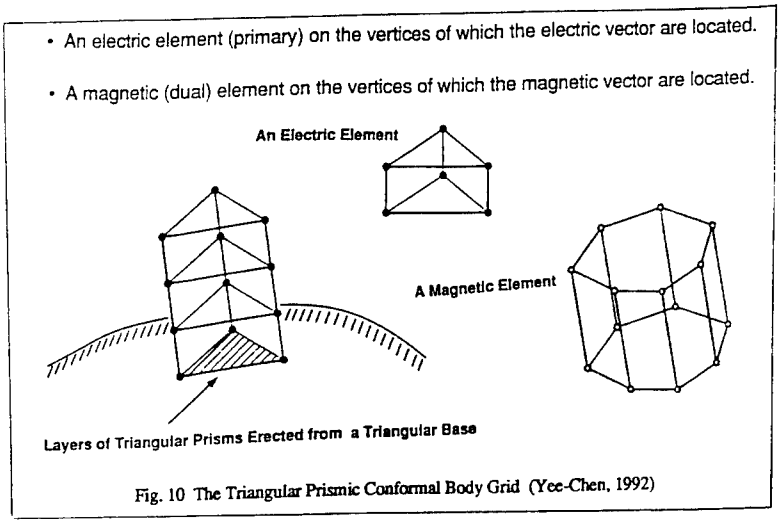


Fig. 10 The Triangular Prismic Conformal Body Grid (Yee-Chen, 1992)

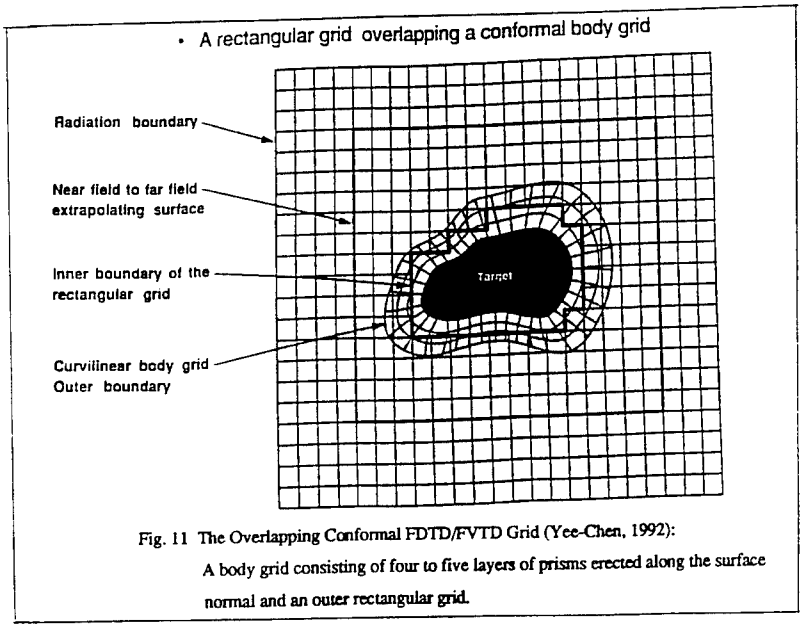
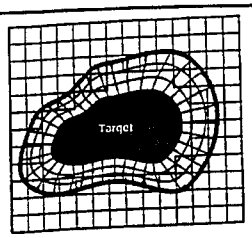


Fig. 11 The Overlapping Conformal FDTD/FVTD Grid (Yee-Chen, 1992):
A body grid consisting of four to five layers of prisms erected along the surface normal and an outer rectangular grid.

- **From rectangular to body grid**

Make use of the rectangular coordinates of an electric vertex in the body grid in order to interpolate from the rectangular components of the electric field in the rectangular grid.



- **From the body grid to the rectangular grid**

For a rectangular field point determine which electric element it belongs and where in that element it is located.

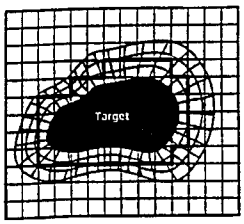


Fig. 12 The Outer Boundary of the Conformal Grid and Inner Boundary of the Rectangular Grid. The data at these boundaries are obtained through interpolations.

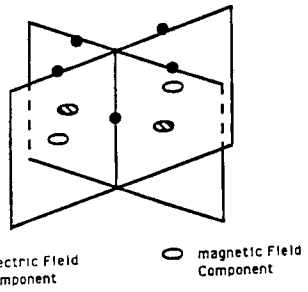


Fig. 13a FDTD Rectangular Field Components: The variables are updated with the FDTD algorithm.

- $\hat{a}, \hat{b}_1, \hat{b}_2, \hat{b}_3, \hat{b}_4, \hat{c}_1, ..., \hat{c}_4$ are the unit area vectors of the area vectors enclosed by the magnetic contours linking the various edges respectively.
- $\hat{a} \bullet \vec{E}(a), \hat{b}_i \bullet \vec{E}(b_i)$, *and* $\hat{c}_i \bullet \vec{E}(c_i)$ are calculated with FDTD
- Define

$$\hat{A} = \hat{a}; \hat{B} = \frac{b_1 + b_2 + b_3 + b_4}{|b_1 + b_2 + b_3 + b_4|}; \hat{C} = \frac{c_1 + c_2 + c_3 + c_4}{|c_1 + c_2 + c_3 + c_4|}$$

- Approximate

$$\hat{B} \bullet \vec{E}(a) = \frac{1}{4}\left\{\hat{b}_1 \bullet \vec{E}(b_1) + \hat{b}_2 \bullet \vec{E}(b_2) + \hat{b}_3 \bullet \vec{E}(b_3) + \hat{b}_4 \bullet \vec{E}(b_4)\right\}$$

$$\hat{C} \bullet \vec{E}(a) = \frac{1}{4}\left\{\hat{c}_1 \bullet \vec{E}(c_1) + \hat{c}_2 \bullet \vec{E}(c_2) + \hat{c}_3 \bullet \vec{E}(c_3) + \hat{c}_4 \bullet \vec{E}(c_4)\right\}$$

- Using $\hat{A} \bullet \vec{E}(a), \hat{B} \bullet \vec{E}(a), \hat{C} \bullet \vec{E}(a)$ to determine $\vec{E}(a)$

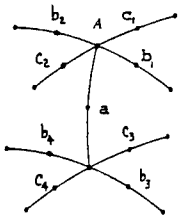


Fig. 13b Non-orthogonal FDTD Variable Locations: The variables are updated with FDTD and averaging.

- $\hat{a}, \hat{b}$, *and* $\hat{c}$, are the unit area vectors of the area vectors enclosed by the magnetic contours linking the edges a, b, and c respectively.
- $(\hat{a} \bullet \vec{E})(a), (\hat{b} \bullet \vec{E})(b)$, *and* $(\hat{c} \bullet \vec{E})(c)$ are calculated with FDTD.
- From the above three quantities, solve for an approximate value for $\vec{E}(a)$.
- Similarly find other approximate values for $\vec{E}(a)$ and average among them .

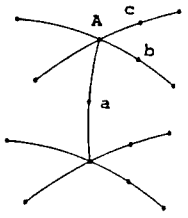


Fig. 13c DSI Variable Locations: The variables are updated with FDTD and averaging.

$$E_z^{n+1} = E_z^n + \frac{\Delta t}{A\varepsilon} \sum_{i=1}^{M} \frac{\vec{H}_i^{n+1/2} + \vec{H}_{i+1}^{n+1/2}}{2} \bullet \ell_i \hat{l}_i$$

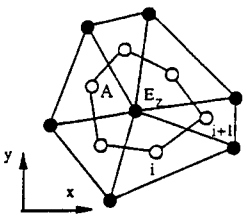
$$\vec{H}^{n+1/2}(x_c, y_c) = \vec{H}^{n-1/2}(x_c, y_c) - \sum_{i=1}^{3} h_i \vec{W}_{i,i+1}(x_c, y_c)$$

$$h_i = \frac{\Delta t}{\mu} \frac{(E_{z,i}^n - E_{z,i+1}^n)}{\ell_i}$$

$$(x_c, y_c) = \left(\frac{x_1 + x_2 + x_3}{3}, \frac{y_1 + y_2 + y_3}{3} \right)$$

$$\vec{W}_{i,i+1} = \hat{z}\xi_i \times \nabla \xi_{i+1} + \nabla \xi_i \times \hat{z}\xi_{i+1}$$

$$\xi_i(x,y) = \frac{(x_{i+1} - x)(y_{i+2} - y) - (x_{i+2} - x)(y_{i+1} - y)}{(x_{i+1} - x_i)(y_{i+2} - y_i) - (x_{i+2} - x_i)(y_{i+1} - y_i)}$$



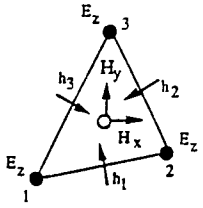


Fig. 14 The Leapfrog Updating Scheme with Whitney Elements for 2-D TM Waves: The Whitney "face" elements are used as interpolates for the magnetic vector from the normal "face" components.

Whitney Elements Time Domain (WETD) Methods for Solving Three-Dimensional Waveguide Discontinuities

Jin-Fa Lee
ECE Dept., WPI
Worcester, MA 01609

Abstract

In this paper, we present an unconditionally-stable finite element time domain (FETD) method using edge elements for modeling three-dimensional waveguide discontinuity problems. Unlike the FDTD methods, the current approach can be used in conjunction with unstructured meshes, particularly, tetrahedral finite elements. Furthermore, since it is unconditionally stable, it offers great advantages in handling EM problems with element sizes in the discretization vary several orders of magnitude across the problem domain. The time step is determined by the accuracy rather than by the stability as in the conditionally stable algorithms. Moreover, the computational complexity of the proposed FETD algorithm is analyzed and confirmed by numerical experiments.

1 Introduction

The finite difference time domain (FDTD) algorithm has been used widely in solving transient responses of electromagnetic problems. However, using FDTD in its original form, it is difficult to model complex EM problems with curved surfaces. Many variants have been proposed in the past with the aim to circumvent this difficulty with varying degrees of success [1]. Almost all of these approaches are based upon, one form or the other, the use of finite difference approximation in both spatial and temporal domains. It is the purpose of this paper to formulate, using Whitney elements for solving Maxwell's equations. In this way, the proposed FETD method can be used on a tetrahedral finite element mesh and consequently, they impose no geometric limitations.

The approach proposed herein is an unconditionally stable finite element time domain method, using only the edge elements or Whitney 1-forms in the spatial domain. Since it is unconditionally stable, it offers great advantages in handling EM problems with element sizes in the discretization vary several orders of magnitude across the problem domain. In those situations, the time steps are no longer limited by the smallest element size as in the conditionally stable algorithms. Consequently, a much bigger time step could be employed in the numerical simulation. However, the price paid for is the need for matrix inversion for each time step, and consequently, the computational complexity at worst case, could be proportional to $N^{1.5}$, where N is the number of unknowns.

The rest of this paper is organized as follow. Section 2 presents the formulation of the unconditionally stable FETD algorithm, its computational complexity is analyzed in section 3.

Numerical results of two examples, an T junction and a rectangular waveguide to coaxial cable converter, are shown in section 4.

2 Formulation

In this paper, we consider the solution of Maxwell's equations in space-time R^4

$$\begin{aligned} \nabla \times \vec{E} &= -\mu \frac{\partial \vec{H}}{\partial t} \\ \nabla \times \vec{H} &= \vec{J} + \epsilon \frac{\partial \vec{E}}{\partial t} \end{aligned} \tag{1}$$

We shall derive an implicit finite element time domain (FETD) approach which is unconditionally stable to solve (1) based on the use of edge elements.

Faedo-Galerkin Process

For the derivation of the implicit FETD algorithm, we start with an initial value problem (IVP) in terms of the electric field $\vec{E}$ as

$$\begin{aligned} \nabla \times \frac{1}{\mu_r} \nabla \times \vec{E} + \frac{\epsilon_r}{c^2} \frac{\partial^2 \vec{E}}{\partial t^2} = -\mu_0 \frac{\partial \vec{J}}{\partial t} \quad &\text{in} \quad \Omega \\ \hat{n} \times \vec{E} = 0 \quad &\text{on} \quad \Gamma_e \\ \hat{n} \times \nabla \times \vec{E} = 0 \quad &\text{on} \quad \Gamma_h \\ \nabla \times \vec{E} = \frac{1}{c} \frac{\partial \vec{E}}{\partial t} \quad &\text{on} \quad \Gamma_\infty \end{aligned} \tag{2}$$

where Γ_e, Γ_h are electric and magnetic walls, respectively, and Γ_∞ is the truncation boundary. For simplicity, we have adopted the first-order absorbing boundary condition (ABC) on Γ_∞ in order to truncate the infinite domain into a finite region.

To simplify the derivation, let us assume that $\vec{J} = 0$, although the inclusion of $\vec{J}$ in the derivation is rather straightforward. The *weak* or the *Galerkin* form of the IVP (2) can be stated as

$$\begin{aligned} &\int_\Omega \frac{1}{\mu_r} \nabla \times \vec{v} \bullet \nabla \times \vec{E} d\Omega + \oint_{\Gamma_\infty} \frac{1}{c} \vec{v} \bullet \left(\frac{\partial \vec{E}}{\partial t} \times \hat{n} \right) d\Gamma \\ &+ \frac{1}{c^2} \int_\Omega \epsilon_r \vec{v} \bullet \frac{\partial^2 \vec{E}}{\partial t^2} d\Omega = 0 \end{aligned} \tag{3}$$

for any test vector function $\vec{v}$. By choosing edge elements to span both the trial and test function spaces, the application of the Faedo-Galerkin process results in a system of ordinary differential equations (ODEs)

$$[T] \frac{d^2 \mathcal{E}}{c^2 dt^2} + [B] \frac{d\mathcal{E}}{cdt} + [S] \mathcal{E} = 0 \tag{4}$$

where $\mathcal{E}$ is the coefficient vector, and

$$\begin{aligned}
[T]_{ij} &= \int_{\Omega} \epsilon_r \vec{W}_i \bullet \vec{W}_j d\Omega \\
[B]_{ij} &= \oint_{\Gamma_\infty} \vec{W}_i \bullet \left(\vec{W}_j \times \hat{n}\right) d\Omega \\
[S]_{ij} &= \int_{\Omega} \frac{1}{\mu_r} \nabla \times \vec{W}_i \bullet \nabla \times \vec{W}_j d\Omega
\end{aligned} \tag{5}$$

The general three-point recurrence schemes for second order equations have been documented in [2]. Applying them to the ODEs (4), the result is

$$\begin{aligned}
& \left\{ \frac{1}{c^2}[T] + \frac{\gamma \Delta t}{c}[B] + \beta \Delta t^2 [S] \right\} \mathcal{E}^{n+1} \\
+ & \left\{ \frac{-2}{c^2}[T] + (1 - 2\Gamma)\frac{\Delta t}{c}[B] + (\frac{1}{2} - 2\beta + \gamma)\Delta t^2 [S] \right\} \mathcal{E}^{n} \\
+ & \left\{ \frac{1}{c^2}[T] - (1 - \gamma)\frac{\Delta t}{c}[B] + (\frac{1}{2} + \beta - \gamma)\Delta t^2 [S] \right\} \mathcal{E}^{n-1} \\
= & \ 0
\end{aligned} \tag{6}$$

In the present approach, we have chosen $\gamma = \frac{1}{2}$ and $\beta = \frac{1}{4}$, resulting in the following difference equation:

$$\mathcal{E}^{n+1} = 2\mathcal{E}^{n} - \mathcal{E}^{n-1} + \frac{[\mathcal{P}]\mathcal{E}^{n-1} - [\mathcal{Q}]\mathcal{E}^{n}}{[\mathcal{M}]} \tag{7}$$

where

$$\begin{aligned}
[\mathcal{P}] &= 4c\Delta t[B] \\
[\mathcal{Q}] &= 4c\Delta t[B] + 4c^2 \Delta t^2 [S] \\
[\mathcal{M}] &= 4[T] + 2c\Delta t[B] + c^2 \Delta t^2 [S]
\end{aligned} \tag{8}$$

The proof of the stability condition using the Z-transform technique can be found in Ref. [3].

3 Computational Complexity

In this section, we shall briefly discuss the computational complexity of the time-marching scheme proposed in (7). Assuming the physical time is fixed, the total CPU time can be expressed as

$$T_{cpu} = (\#\text{time steps}) \times T_{step} \tag{9}$$

where T_{step} is the average CPU time to update the electric field from time $n\Delta t$ to $(n+1)\Delta t$. It is clear from (7) that for each time step, a matrix equation of the form

$$[\mathcal{M}]x = y \tag{10}$$

needs to be solved. Fortunately, $[\mathcal{M}]$ is positive definite and (10) can be solved efficiently using the preconditioned conjugate gradient (PCCG) method. Subsequently, we write

$$T_{step} \propto n_{CG} \times N \tag{11}$$

where N is the dimension of the matrix $[\mathcal{M}]$. Equation (11) is obtained simply because each CG iteration involves nothing but matrix and vector multiplications. Moreover, it can be shown that with the diagonal preconditioner [4], we have

$$\kappa(\frac{[\mathcal{M}]}{[\mathcal{D}]}) \propto \frac{1}{h^m}; \qquad 0 \leq m \leq 1 \tag{12}$$

where $\kappa([\mathcal{A}])$ is the condition number of matrix $[\mathcal{A}]$. In Eq. (12), $[\mathcal{D}]$ is the diagonal portion of $[\mathcal{M}]$ and h is the element size.

Furthermore, in the application of the CG method, it has been shown that

$$\| x - x_n \| \leq \| x - x_0 \| \left(\frac{\sqrt{\kappa} - 1}{\sqrt{\kappa} + 1} \right)^n \tag{13}$$

with $\| x - x_n \|$ is the error for the nth iteration, and $\| x - x_0 \|$ the error for the initial guess x_0. Consequently, the number of iterations n_{CG} for PCCG to converge can be roughly estimated as

$$n_{CG} \geq \left(\frac{\sqrt{\kappa} + 1}{2} \right) \left(1 - \frac{\delta}{\| x - x_0 \|} \right) \tag{14}$$

where δ is the tolerance set for convergence. Therefore, we have

$$n_{CG} \propto \frac{1}{h^{m/2}} \tag{15}$$

Putting everything together and assuming that we choose $\Delta t \propto h$ results in

$$\begin{aligned} T_{cpu} &\propto (\#\text{time steps}) \times n_{CG} \times N \\ &\propto \frac{1}{h} \times \frac{1}{h^{m/2}} \times \frac{1}{h^3} \\ &\propto h^{-(8+m)/2} \propto N^{(8+m)/6} \end{aligned} \tag{16}$$

Compared to the FDTD, whose computational complexity is $N^{1.333}$, the current FETD is slightly less efficient. However, as mentioned earlier, the unconditionally stable nature of the current formulation makes it extremely appealing for modeling problems with very small features.

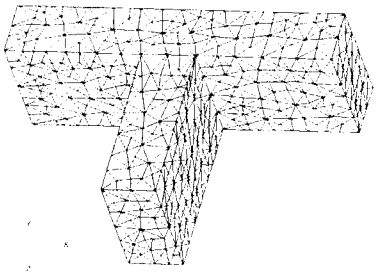


Figure 1: Finite element mesh for a T-junction.

4 Numerical Results

Two waveguide discontinuities are analyzed by using the current FETD approach. One is a T junction and the other is a rectangular waveguide to coaxial cable converter. To perform the FETD analysis, the tetrahedral meshes for both cases are generated using an automatic mesh generation program.

T Junction

Shown in Fig. 1 is a sample finite element mesh used for the FETD program to analyze a three-port T junction. Each of the port is a rectangular waveguide with dimensions of $1cm \times 2cm$. Several meshes were created and used for the analyses to characterize the performance of the FETD formulation. The characteristics of the meshes, the corresponding time steps used in the algorithm, and the total CPU times are shown in Table I. Figure 2 plots the CPU times versus the total number of unknowns. It is found that the computational complexity is approximately $T_{cpu} \approx N^n$ where $4/3 \leq n \leq 3/2$ which is consistent with Eq. (16). Furthermore, the steady-state field distribution of this T junction is shown in Fig. 3.

Table I: Statistics of FETD algorithm for a T junction.

N	h_{min}	$c\delta t$	T_{cpu}
1191	0.1199	0.52916	116.06
1685	0.1199	0.47481	216.53
1883	0.0846	0.45506	249.36
3640	0.0658	0.37289	649.0
6309	0.0591	0.31190	1425.12

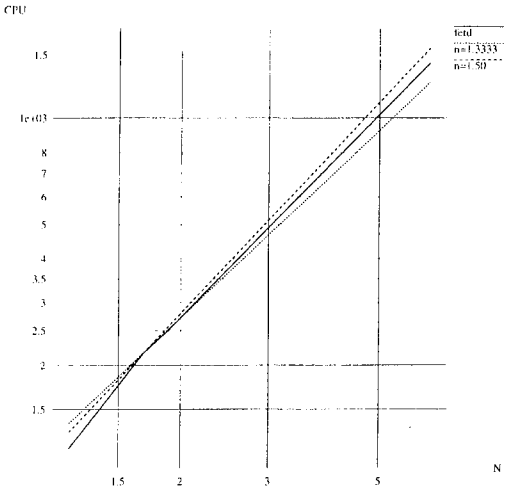


Figure 2: The computational complexity of the unconditionally stable FETD algorithm.

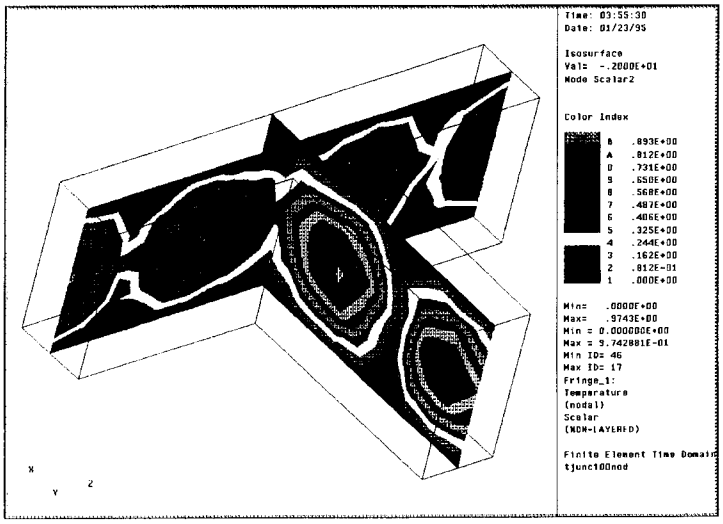


Figure 3: The field distribution at steady-state of the T junction obtained from the FETD algorithm.

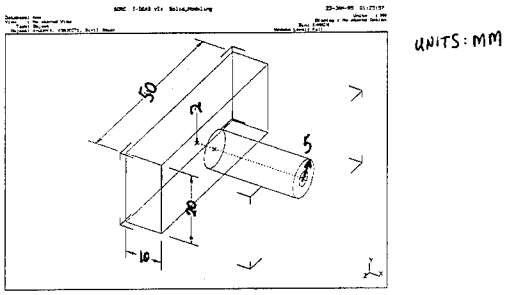


Figure 4: The geometry of a rectangular waveguide to coaxial converter.

Waveguide to Coaxial Converter

Another example that we have analyzed is a rectangular waveguide to coaxial cable converter as shown in Fig. 4. By using the finite elements, particularly the tetrahedral elements, the discretization can be made conforming to the problem geometry conveniently. Once again, the whole process of discretization is done automatically by using an automatic tetrahedral mesher. The final finite element mesh which is used in the analysis is shown in Fig. 5. In this mesh, there are total 6524 elements, and the smallest element length is 0.1. Since the formulation is unconditionally stable, the time step used in the calculation is based upon the average element length, which corresponds to $c\delta t = 2.6$. A much bigger time step than would be possible using the conditionally stable algorithms. Finally, the steady state field distribution for frequency at 10GHz is shown in Fig. 6.

References

[1] A. C. Cangellaris, C. C. Lin, and K. K. Mei, "Point-matched time domain finite element methods for electromagnetic radiation and scattering," IEEE Trans. Antennas Prop., AP-35, pp. 1160-1173, 1987.

[2] O. C. Zienkiewicz and K. Morgan, *Finite elements and approximation*, John Wiley & Sons, New York, 1983.

[3] J. F. Lee and Z. Sacks, "Whitney elements time domain methods", Invited paper, To appear in IEEE Trans. Magnetics, May 1995.

[4] G. Strang and G. J. Fix, *An analysis of the finite element method,* Englewood Cliffs, NJ:Prentice Hall, 1973.

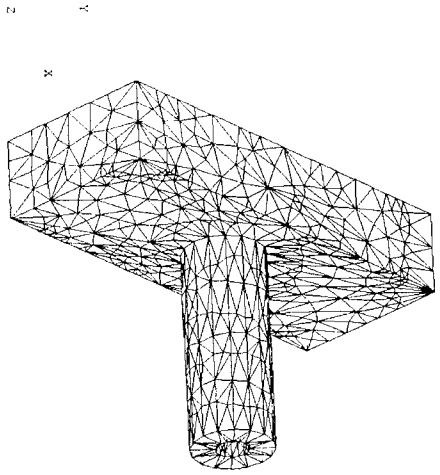


Figure 5: The finite element mesh of a rectangular waveguide to coaxial converter.

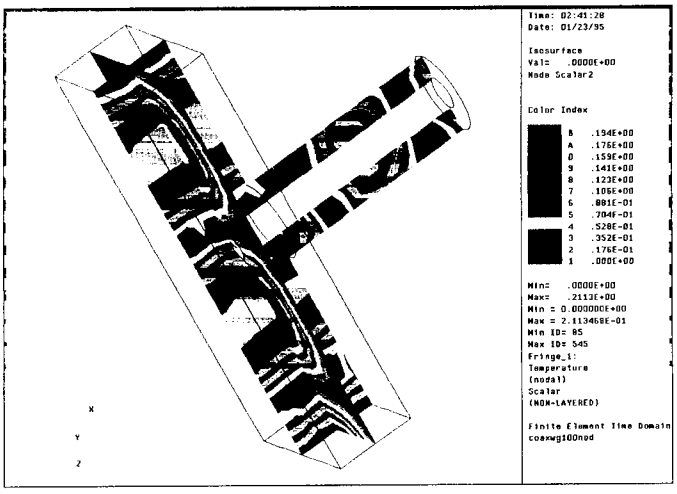


Figure 6: The field distribution for the waveguide to coaxial converter at 10 GHz.

An FDTD/FVTD 2D-algorithm to Solve Maxwell's Equations

Jei S. Chen, John V. Prodan, and Kane S. Yee
Lockheed Palo Alto Research Laboratories
Palo Alto, California

Abstract

A recently devised finite difference and finite volume time domain hybrid scheme [1], has simplified the process for calculating the electromagnetic scattering for a large class of 2-D, exterior volume, scattering problems. The computational grid is conformal to the object. The class of problems we address in this paper is the scattering of an incoming plane Gaussian pulse by various 2-D objects, either in free space or above a ground plane. It is the purpose of this paper to review the hybrid finite difference time domain (FDTD) and the finite volume time domain (FVTD) algorithms in a 2-D setting and to show how relatively easy it is to generate the conformal grid to which we can apply our time domain algorithm. In addition, examples of the kinds of calculations that can be done with this code for this class of objects will be presented.

Introduction

The technique of conformal time domain calculation in electromagnetics is not very old. It started with a paper by R. Holland [2] on the time domain discretization of Maxwell's equations in general non-orthogonal coordinates. The application of the surface-curve integral form of the Maxwell's equations to derive difference equations [3, 4, 5], instead of the FDTD in rectangular form, gives the freedom of numerically solving Maxwell's equations on a grid without an explicit coordinate system. The use of the integral forms (surface-curve and volume-surface) of Maxwell's equations was exploited by Madsen and Ziolkowski [6]. The time domain conformal techniques are now more developed [6, 7, 8], however 3-D conformal calculations are still not widely used. (In fact, most of the conformal calculations are in 2-D [5, 9, 10]). Recently, Holland [11] gave a very detailed discussion of the 2-D conformal calculation based mainly on the surface-curve integral form of Maxwell's equations. A glance at the content of that paper shows that even the 2-D conformal calculations are far from trivial. This complication of the 2-D conformal calculation, however, seems to be substantially eased with the newly advanced FDTD/FVTD hybrid [1]. In fact, since the announcement of the FDTD/FVTD in the 1993 PIERS conference [12], the 2-D FDTD/FVTD have been found to be simple to implement and yields good results for some applications [13, 14]. In this paper we specialize our 3-D FDTD/FVTD technique for 2-D calculations. It will be shown, with examples, that it is now quite easy to do conformal 2-D time domain calculations. The calculation is further simplified with the substitution of the traditional radiation boundary condition (RBC) by a newly discovered tapered damping technique near the outer computational boundary.

A brief discussion of the general relations on which the FDTD and FVTD algorithms are based will be given as well as the general philosophy for creating the grid. The 2-D relationships needed for the TM and TE cases will then be developed. (For the 2-D case, all the field variables are independent of the z-coordinate.) A somewhat expanded description of the boundary conditions for the TE case will be presented since they are a little more involved than those for the TM case. In addition, we have implemented a new radiation boundary condition which will be briefly described. Computational results for three "representative" objects will be given for the TM case. In 2-D problems, where computer memory is not a serious concern, one can easily generate time and spatial displays of field values and energy densities as well as cross section data. Electromagnetic energy density maps, at two different time steps, for a s-duct and a faceted object sitting above a ground plane are presented along with the RCS calculations for a circular cylinder.

The FDTD and the FVTD relations

There are four relationships that form the core algorithms for the FDTD and FVTD techniques. These are the line-surface integral and surface-volume integral forms of both Ampere's and Faraday's laws, given by:

$$-\int_A \frac{\partial \vec{B}}{\partial t} \cdot d\vec{a} = \int_{\partial A} \vec{E} \cdot d\vec{l} \qquad \text{Faraday's Law (line-surface)} \qquad (1a)$$

$$\int_A \frac{\partial \vec{D}}{\partial t} \cdot d\vec{a} = \int_{\partial A} \vec{H} \cdot d\vec{l} \qquad \text{Ampere's Law (line-surface)} \qquad (1b)$$

$$-\int_V \frac{\partial}{\partial t}\vec{B}\, dv = \int_{\partial V} \hat{n} \times \vec{E}\, da \qquad \text{Faraday's Law (surface-volume)} \qquad (2a)$$

$$\int_V \frac{\partial}{\partial t}\vec{D}\, dv = \int_{\partial V} \hat{n} \times \vec{H}\, da \qquad \text{Ampere's Law (surface-volume)} \qquad (2b)$$

We refer to the line integral in equation (1a) as the electric circulation; the line integral in equation (1b) as the magnetic circulation; the surface integral in equation (2a) as the electric vorticity; and the surface integral in equation (2b) as the magnetic vorticity. The (generalized) FDTD algorithm is developed from the discretization of Equations 1, while the FVTD algorithm is based on the discretization of Equations 2. In specializing to 2 dimensions, we take the volume, in Eqs. 2, to be prisms with height equal to Δz, and the trace of a prism in the x-y plane to be a curve.

Grid construction

A conformal grid is used to model the objects, eliminating the concerns that rise when a rectilinear staircasing grid is used. While the grid is conformal, it is not necessarily orthogonal. Examples of some objects are shown in Figures 1a-1d, together with the possible grids. Figure 1a depicts the grid for a PEC ogive; Fig. 1b shows a grid for an s-duct; the grid for a PEC circular cylinder is shown in Fig 1c; and Fig. 1d shows a grid for a faceted PEC object sitting above a ground plane.

For the most part, the grids are formed by translating (either horizontally or vertically) sections of the objects' boundary curve. In some cases, e.g., between the object and the ground plane in Fig. 1d, instead of a pure translation, the boundary curve can be extended from the object to the ground plane (which is also the computational boundary) by scaling the grid from the side of the object, so that the number of cells would be the same. (Care needs to be taken to ensure that the Courant condition is still satisfied for these "reduced size" cells.) The grid should be constructed such that the slope of the grid lines where the conformal part "transitions" to the rectangular grid is not excessive (~45° or less is advised). The reason for this requirement is to try to maintain accuracy in the updating of the electric field. The electric field vector is assigned at the vertices of the cells, while the magnetic vector is assigned at the cell center. (Figure 1e shows the positions of the field nodes in a blow-up of the upper right section of the grid shown in Fig. 1c.) To update the electric field, either the magnetic circulation or vorticity is needed, depending on the polarization. If the transition slope is too large, the centroid of the contour (formed by connecting the open circles in Fig. 1e) used to calculate the magnetic circulation (needed to update the electric field in the TM case) will not coincide with an electric vertex. (For the TE case, it is the centroid of the volume about which the magnetic vorticity is calculated that should to be coincident with the electric vertex.) If near coincidence can be maintained, then numerical accuracy of the update will be of 2^{nd} order, otherwise only 1^{st} order accuracy is achieved.

The TM case

For the TM case, the 2-D fields consist of the following: the z-component of the electric field, Ez, and the x- and y-components of the magnetic field, Hx and Hy. All the field components are only functions of x, y, and t.

The electric nodes are located at the grid points (i,j), with coordinates given by (vex(i,j),vey(i,j)). The magnetic nodes are located at (i+1/2,j+1/2), with coordinates given by (vmx(i+1/2,j+1/2), vmy(i+1/2,j+1/2)). To update the electric field at an electric node (i,j) (see Fig. 2a), the magnetic circulation is calculated and the FDTD algorithm is used.

The z-direction magnetic circulation, cirm(i,j), is:

$$\vec{H}(j1) \bullet (vmx(i+1/2,j-1/2) - vmx(i-1/2,j-1/2), vmy(i+1/2,j-1/2) - vmy(i-1/2,j-1/2)) +$$
$$\vec{H}(i2) \bullet (vmx(i+1/2,j+1/2) - vmx(i+1/2,j-1/2), vmy(i+1/2,j+1/2) - vmy(i+1/2,j-1/2)) +$$
$$\vec{H}(j2) \bullet (vmx(i-1/2,j+1/2) - vmx(i+1/2,j+1/2), vmy(i-1/2,j+1/2) - vmy(i+1/2,j+1/2)) +$$
$$\vec{H}(i1) \bullet (vmx(i-1/2,j-1/2) - vmx(i-1/2,j+1/2), vmy(i-1/2,j-1/2) - vmy(i-1/2,j+1/2)) \qquad (3)$$

To update the magnetic vector at the magnetic node (i+1/2,j+1/2), the electric vorticity is needed and the FVTD algorithm is used. For the required volume, we take a prism of height Δz, whose cross-section is shown

in Fig. 2b . The relation between the unit outward (surface) normal $\hat{n}$, the unit tangent vector $\hat{t}$, and the unit vector along the z-direction $\hat{z}$, is given by: $\hat{n} \times \hat{t} = \hat{z}$. These three vectors $\hat{n}$, $\hat{t}$ and $\hat{z}$ form a right handed orthogonal triad. The finite volume algorithm is applied to this prism in order to update the magnetic vector at the magnetic node (i+1/2,j+1/2). The contribution from the top and the bottom surfaces cancel. Denoting the length of a side by δ, the area vector of a lateral surface is given by: $\vec{A} = \hat{n}A = \hat{n}\delta\Delta z$. The electric vorticity at the lateral surfaces is found by computing $\vec{A} \times \vec{E}$ for each of the sides as follows:

$$\vec{A}(j1) \times \vec{E}(j1)$$
$$= A(j1)\hat{n} \times (E_z \hat{z}) = -\Delta z \delta E_z \hat{t} = -\Delta z E_z(\delta \hat{t})$$
$$= -\Delta z E_z(j1)\ \{\hat{x}(vex(i+1,j) - vex(i,j)) + \hat{y}(vey(i+1,j) - vey(i,j))\} \qquad (4a)$$

similarly,

$$\vec{A}(i2) \times \vec{E}(i2)$$
$$= -\Delta z E_z(i2)\ \{\hat{x}(vex(i+1,j+1) - vex(i+1,j)) + \hat{y}(vey(i+1,j+1) - vey(i+1,j))\} \qquad (4b)$$

$$\vec{A}(j2) \times \vec{E}(j2)$$
$$= -\Delta z E_z(j2)\ \{\hat{x}(vex(i,j+1) - vex(i+1,j+1)) + \hat{y}(vey(i,j+1) - vey(i+1,j+1))\} \qquad (4c)$$

$$\vec{A}(i1) \times \vec{E}(i1)$$
$$= -\Delta z E_z(i1)\ \{\hat{x}(vex(i,j) - vex(i,j+1)) + \hat{y}(vey(i,j) - vey(i,j+1))\} \qquad (4d)$$

The electric vorticity, $\vec{v}\,ore^n(i+1/2,j+1/2)$ over the lateral faces is the sum of the above four expressions.

Once the electric vorticity is known, the magnetic vector can be updated by

$$\vec{H}^{n+1/2}(i+1/2,j+1/2) = \vec{H}^{n-1/2}(i+1/2,j+1/2) - \frac{\Delta t}{\mu \Delta v}\,\vec{v}\,ore^n(i+1/2,j+1/2) \qquad (5a)$$

Similarly, knowing the magnetic circulation, the z-component of the electric field can be updated by:

$$E_z^{n+1}(i,j) = E_z^n(i,j) + \frac{\Delta t}{\varepsilon \Delta a}\,cirm^{n+1/2}(i,j) \qquad (5b)$$

In the above two expressions, Δv is the volume of the prism, i.e., the area shown in Fig. 2b multiplied by the height Δz; Δa is the area enclosed by the J1-I2-J2-I1 loop shown in Fig. 2a. The superscripts indicate the time step index.

The TE case

For the TE case, the 2-D fields consist of the following: the z-component of the magnetic field, Hz, and the x- and y-components of the electric field, Ex and Ey. As before, these field components are only functions of x, y, and t.

To update the magnetic field at a magnetic node (i+1/2,j+1/2), the electric circulation is computed and the FDTD algorithm is used. Referring to Fig. 3a , the z-direction electric circulation, cire(i+1/2,j+1/2), is;

$$\vec{E}(j1) \bullet (vex(i+1,j) - vex(i,j),\ vey(i+1,j) - vey(i,j)) +$$
$$\vec{E}(i2) \bullet (vex(i+1,j+1) - vex(i+1,j),\ vey(i+1,j+1) - vey(i+1,j)) +$$
$$\vec{E}(j2) \bullet (vex(i,j+1) - vex(i+1,j+1),\ vey(i,j+1) - vey(i+1,j+1)) +$$
$$\vec{E}(i1) \bullet (vex(i,j) - vex(i,j+1),\ vey(i,j) - vey(i,j+1)) \qquad (6)$$

To update the electric vector at the (interior) electric node (i,j), FVTD is used and the magnetic vorticity is required. For the relevant volume, we take a prism of height Δz, whose cross-section is shown in Fig. 3b. As

before, the unit outward normal $\hat{n}$, the unit tangent vector $\hat{t}$, and the unit vector along the z-direction $\hat{z}$, form a right handed orthogonal triad and are related by $\hat{n} \times \hat{t} = \hat{z}$. The finite volume algorithm is applied to this prism in order to provide the update of the electric vector at the electric node (i,j). The contribution from the top and the bottom surfaces cancel. Again, denoting the length of a side by δ, the area vector of a lateral surface is given by $\vec{A} = \hat{n}A = \hat{n}\delta\Delta z$. The magnetic vorticity at the lateral surfaces is found by evaluating $\vec{A} \times \vec{H}$ for each of the sides as follows:

$$\vec{A}(j1) \times \vec{H}(j1) = A(j1)\hat{n} \times H_z(j1)\,\hat{z}$$
$$= -\Delta z \delta H_z(j1)\,\hat{t} = -\Delta z H_z(j1)\,(\delta \hat{t})$$
$$= -\Delta z H_z(j1)\,\{\hat{x}[vmx(i+1/2,j-1/2) - vmx(i-1/2,j-1/2)] + \hat{y}[vmy(i+1/2,j-1/2 - vmy(i-1/2,j-1/2)]\}; \quad (7a)$$

similarly,

$$\vec{A}(i2) \times \vec{H}(i2)$$
$$= -\Delta z H_z(i2)\,\{\hat{x}[vmx(i+1/2,j+1/2) - vmx(i+1/2,j-1/2)] + \hat{y}[vmy(i+1/2,j+1/2 - vmy(i+1/2,j-1/2)]\}, \quad (7b)$$

$$\vec{A}(j2) \times \vec{H}(j2)$$
$$= -\Delta z H_z(j2)\,\{\hat{x}[vmx(i-1/2,j+1/2) - vmx(i+1/2,j+1/2)] + \hat{y}[vmy(i-1/2,j+1/2 - vmy(i+1/2,j+1/2)]\}, \quad (7c)$$

$$\vec{A}(i1) \times \vec{H}(i1)$$
$$= -\Delta z H_z(i1)\,\{\hat{x}[vmx(i-1/2,j-1/2) - vmx(i-1/2,j+1/2)] + \hat{y}[vmy(i-1/2,j-1/2 - vmy(i-1/2,j+1/2)]\}. \quad (7d)$$

The magnetic vorticity, $\vec{v}\text{orm}^{n+1/2}(i,j)$ over the lateral faces is the sum of the above four expressions.

Once the electric circulation is known, we can update the z-component of the magnetic field using

$$H_z^{n+1/2}(i+1/2,j+1/2) = H_z^{n-1/2}(i+1/2,j+1/2) - \frac{\Delta t}{\mu \Delta a}\,\text{cire}^n(i+1/2,j+1/2) \quad (8a)$$

and knowing the magnetic vorticity, the electric vector can be updated by

$$\vec{E}^{n+1}(i,j) = \vec{E}^n(i,j) + \frac{\Delta t}{\varepsilon \Delta v}\,\vec{v}\text{orm}^{n+1/2}(i,j). \quad (8b)$$

In the above two equations, Δa is the area enclosed by the contour J1-I2-J2-I1 shown in Fig. 3a and Δv is the volume of the prism of height Δz and base shown in Fig. 3b.

PEC boundary condition simulation for the TE wave

The boundary condition simulation for the TE wave is somewhat more complicated than the case for the TM wave, since electric nodes are located at the boundary of the scatterer. The magnetic field at the point **P** (see Fig. 4) is updated with the FDTD algorithm. At the points **1** and **4**, only the tangential components of the electric field are known (through the boundary condition). In order to get the electric circulation along the edge **2→1** and **4→3**, the component of the electric field along those edges, at the midpoints, is needed. (In the following, the electric fields are evaluated at the time step $n\Delta t$.)

We obtain the component along each of these edges in the following manner. Let $\hat{t}$ now be the unit tangent along **2→1**, $\hat{N}$ be the unit normal at the point **1** and $\hat{T}$ the unit tangent along the surface at point **1**. From the boundary condition, the tangential electric field, $\hat{T} \cdot \vec{E}(1)$ is known. The component of the field along $\hat{n}_S$, the unit normal to the line **PQ**, is given by $\hat{n}_S \cdot \vec{E}(a)$ and can be obtained by means of the FDTD algorithm. Approximating the electric vector at a by the average of the fields at points **1** and **2**, we have

$$\vec{E}(a) \cdot \hat{T} \approx 1/2\,[\vec{E}(1) + \vec{E}(2)] \cdot \hat{T}. \qquad (9a)$$

Breaking $\vec{E}(a)$ into components tangent and normal to the surface results in

$$\vec{E}(a) = \hat{T}\,[\vec{E}(a) \cdot \hat{T}] + \hat{N}\,[\hat{N} \cdot \vec{E}(a)], \qquad (9b)$$

and then forming the scalar product of (9b) and $\hat{n}_S$, we have

$$\hat{n}_S \cdot \vec{E}(a) = [\hat{n}_S \cdot \hat{T}]\,[\vec{E}(a) \cdot \hat{T}] + [\hat{n}_S \cdot \hat{N}]\,[\hat{N} \cdot \vec{E}(a)] \qquad (9c)$$

Solving for the component of the field along the normal, this final expression can be rewritten as,

$$\hat{N} \cdot \vec{E}(a) = \frac{1}{\hat{n}_S \cdot \hat{N}}\,\{\hat{n}_S \cdot \vec{E}(a) - [\hat{n}_S \cdot \hat{T}]\,[\vec{E}(a) \cdot \hat{T}]\}. \qquad (9d)$$

Equation (9d) is the relation that is needed to find the component of $\vec{E}$ along $2 \rightarrow 1$ (i.e., in the $\hat{t}$ direction). Dotting $\hat{t}$ into Eq. (9b) results in

$$\hat{t} \cdot \vec{E}(a) = [\hat{t} \cdot \hat{T}]\,[\vec{E}(a) \cdot \hat{T}] + [\hat{t} \cdot \hat{N}]\,[\hat{N} \cdot \vec{E}(a)] \qquad (10)$$

where the right hand side can now be evaluated. A similar procedure is used to generate the component of the field along $4 \rightarrow 3$.

Outer boundary condition simulation

Until quite recently, all the radiation boundary simulations near the outer boundary of the computation volume were based on the outgoing behavior of the scattered field. The most popular radiation boundary condition (RBC) approximations in electromagnetic calculations are the Mur RBC [15] or the Liao RBC [16]. We have discovered, however, a rather robust approximation near the outer boundary to simulate artificial damping of the scattered field in the neighborhood of this boundary. We called this technique "tapered damping" and the mathematical details describing this method are given in [17].

The procedure needed to implement this technique is very simple. The outer boundary of the computational volume in our problem is roughly one to two wavelengths away from the smallest box containing the scatterer, approximately the same distance away as when the Mur RBC is used. Several layers next to the outer boundary are introduced (see Figs. 5a and 5b) and labeled zones 1 through N. Extending across these zones, we define a tapered function:

$$\mathrm{Tab(ibd)} = \cos((\pi/3)(N+1-\mathrm{ibd})/N), \qquad (11)$$

where ibd=1,2, ..., N is the zone number from the outer boundary. In addition, a function tap(i,j), defined over the **entire** computational space, is introduced such that:

tap(i,j) = 1 if the point (i,j) does not belong to any of the zones
tap(i,j) = Tab(ibd) if the point (i,j) belongs to the zone ibd.

The function tap(i,j) takes on nonnegative values less than or equal to 1. (The above particular choice of Tab, is **not** meant to imply that this is the only one that should be used. Many such functions could be constructed (such that their values taper smoothly from 1 to a value less than 1) that would probably serve just as well. Extensive investigation has yet to be done to see if an "optimum" function exists.)

The calculational procedure is as follows:

1. Set the values of the scattered electric vector located at the outer boundary to be zero and never update them.
2a. Update the scattered magnetic field variables by the appropriate algorithm (i.e., either FDTD or FVTD) for a lossless medium.
2b. Multiply each magnetic field variable by the value of a magnetic tapered function at that point.
3a. Update the electric field variable by the appropriate algorithm for a lossless medium.
3b. Multiply each electric variable by the value of an electric tapered function at that point.

In the limited testing that we have done using this damping technique, we have found it to be reasonably robust (the results have been relatively insensitve to the particular choice of taper function) and certainly much simplier to implement than the Mur RBC. The best results seem to be obtained if the magnetic and electric tapered functions are the same. In addition, this method seems to be more amenable to efficient implementation on some of the massively parallel computing architectures, than is the Mur RBC. (This is due to the fact that the application of the technique is basically just a multiplication of the array holding the electric or magnetic field variables by another array, a process that is very efficient in parallel machines. No special treatment needs to be given to the values near the outer boundary.)

Computational results

As an illustration of our new FDTD/FVTD hybrid, we present calculations (TM case) for three different objects: an s-duct, a PEC circular cylinder and a faceted target sitting over a ground plane. (See Figs. 1b, 1c and 1d, respectively, for examples of what the grids for these objects would look like.) The calculations were carried out with the tapered damping RBC, with N = 10 (see Eq. 11 above). For the s-duct and the faceted object, energy density calculations were made and the results at two different time steps are shown. For the circular cylinder, we present the RCS calculation along with the theoretical value.

The display of the electromagnetic energy density for the s-duct at two different time steps is shown in Figs. 6a and 6b. For these two pictures, the gaussian pulse was incident from the lower left side at 30° from the horizontal, and first struck the duct at a time index of ~ 12. In Fig. 6a, the energy density at a (approximate) time index of 32 is shown. The scattering due to the impedance mismatch of the duct can be clearly seen as well as the energy that made it into the duct. Figure 6b shows the energy density at a time step of ~270. (The gaussian pulse has travelled past the duct by time step ~125.) The energy that made it inside the duct has now had time to travel the length of the duct (ricocheting off the walls), reflect off the back wall and is now broadcasting from the inlet. (There is still some energy rattling around in the duct for another 200 time steps!)

Figures 7a and 7b show the energy density maps for a gaussian pulse scattering off of a faceted PEC object that is sitting over a ground plane. The pulse is incident from the upper left hand side of the picture (60° from the horizontal). (Since this is a TM wave, the electric field vector is normal to the page.) Figure7a shows a snapshot of the energy density approximately 8 time steps after the pulse first strikes the object. The specular reflection off the leading facet can be seen (it is propagating back toward the upper left), as well as the diffracted energy that has scattered off the front tip and leading upper "corner". The point of contact between the pulse and the long facet of the body is also quite visible, due to the fact that the magnetic field has a substantial component parallel to the objects' surface for this incident angle. (In the lower left corner, the point of contact between the incident pulse and the ground plane is also evident.) The energy density after another 24 time steps is shown in Fig. 7b. The point of contact between the primary pulse and the object has now moved to the "trailing" corner, with the specular relection from the main facet clearly visible. (It is comforting to note that the angle of reflection equals the angle of the incidence!) At the left side of the object, we can see that the wave that was reflecting off the ground plane has struck the front tip and lower facet. In addition, the energy from the main pulse that had scattered off the upper leading facet earlier, can be seen in the upper left (it is spreading out as it propagates away from the body). A series of these snapshots can be (and has been) put together to form a movie depicting how the pulse is scattered off various parts of the body. (A final note pertaining to this object is that when the movie was viewed, no scattering could be seen coming off the computational boundary, indicating that this new RBC is doing its job!)

The results from a bistatic RCS calculation at 300 MHz for the infinite PEC circular cylinder are shown in Fig. 8a and 8b. The cylinder has a radius of 1 meter. The grid used for this calculation follows the scheme of Fig. 1c, with the cell size approximately 0.05 meters on a side. The following are the more detailed information for these calculations (please also refer to Fig. 1c):

$\Delta x = .05m$;

Incident plane wave is a Gaussian enveloped sinusoidal pulse;

The computational region has lower indices (1,1) and upper indices (101,101);

Point 1 has the indices (31,31); and point 3 has the indices (71,71); the center of the circle has the indices (51,51).

The number of damping zones in the outer boundary is 10; and the tapered damping function is $\cos\{\pi/3(10+1-ibd)/10\}$ (please refer to Fig. 5a).

We start our calculation shortly before the pulse arrived at the scatterer (our PEC cylinder). Calculation stops when the time signal is insignificant. The time domain data for the electric field and the magnetic field in the neighborhood (two zones) of the scatterer are retained and Fourier transformed to yield frequency domain data. We use the far field frequency domain representation of the scattered field for the TM case for $r >> 1$ [19, p.374]:

$$E_z^s=\frac{\exp(-jkr)}{r^{1/2}}\frac{j}{4}\left[\frac{2j}{\pi k}\right]^{1/2}\int_C\left\{\exp(jk\hat{u}\bullet\vec{r}')\frac{\partial E_z^s}{\partial n'}-E_z^s jk(\hat{u}\bullet\hat{n}')\exp(jk\hat{u}\bullet\vec{r}')\right\}dc' \quad ; \qquad (12)$$

where C is a closed curve enclosing the scatterer; $\hat{u}$ is the unit vector in the direction of observation; $\hat{n}'$ is the unit outward pointing normal to the curve C; and $\vec{r}'$ is the point of integration. Making use of $\frac{\partial E_z^s}{\partial n'}=\hat{n}'\bullet\nabla E_z^s$ and the Maxwell's equations

$\frac{\partial E_z}{\partial x}=j\omega H_y$ *and* $\frac{\partial E_z}{\partial y}=-j\omega H_x$, (12) becomes

$$E_z^s=\frac{\exp(-jkr)}{r^{1/2}}\frac{j}{4}\left[\frac{2j}{\pi k}\right]^{1/2}\int_C\left\{\exp(jk\hat{u}\bullet\vec{r}')j\omega\mu\hat{t}'\bullet H^s-E_z^s jk(\hat{u}\bullet\hat{n}')\exp(jk\hat{u}\bullet\vec{r}')\right\}dc' \quad ; \qquad (13)$$

where $\hat{t}'$ is the unit tangent along the curve in the counter-clockwise.
The 2-D bistatic RCS is defined as

$$\sigma=2\pi\lim_{r\to\infty} r\frac{\left|E_z^s\right|^2}{\left|E_z^i\right|^2} . \qquad (14)$$

Similar expression to (13) can be derived for the TE case and the RCS defined in term of the z-component of the scattered magnetic field.

These results show good agreement with the known results based on the exact series solution [18]. For comparison purpose we also show the calculations with the stair-casing FDTD code. The improvement of our conformal algorithm over the stair-casing FDTD for this circular cylinder is self-evident.

Conclusion

We have shown that an easy to implement, conformal finite difference technique, based on the integral forms of Ampere's and Faraday's laws, can now be used to calculate the scattering from a variety of 2-D objects. The conformal grids for these objects are produced in a relatively simple manner, adding to the potential utility of this technique. (Even objects over a ground plane can be modeled easily.) The method includes a new RBC that, not only, is easy to implement but seems to provide excellent "absorption" of the scattered wave at the outer computational boundary.

The data generated by the code is presentable in a variety of ways, including RCS (scattering widths), field amplitude versus time plots and energy density maps. Results (RCS) for a circular cylinder show good agreement with theory. Energy density displays for two objects have also been shown. Displays of this type can provide a wealth of qualitative (and perhaps quantitative) information on the nature of the scattering process.

References:

1. Kane S. Yee and J. S. Chen "Conformal Hybrid Finite Difference Time Domain and Finite Volume Time Domain," submitted to IEEE Trans. on Antennas and Propagation.

2. R. Holland, "Finite-difference solutions of Maxwell's equations in generalized non orthogonal coordinates", *IEEE Trans. Nuc. Sci.*, Vol. NS-30, pp.4589-4591, 1983.

3. T. Weiland, "On the numerical solution of Maxwell's equations and applications in the field of accelerator physics. " *Particle Accelerators*, Vol. 15, pp. 245-292, 1984

4. K. S. Yee, " Numerical solution to Maxwell's equations with non-orthogonal grids," Proc. of 1st Review of Numerical Electromagnetic Codes," Jan. 1985.

5. K. S. Yee, "Numerical solution to Maxwell's equations with non-orthogonal grids", Lawrence Livermore National Laboratory Technical Report, UCRL-93268, April,1987.

6. N. K. Madsen and R. W. Ziolkowski, " Numerical solution of Maxwell's equations in the time domain using irregular nonorthogonal grids, " *Wave Motion*, Vol. 10, pp.583-596. Dec., 1988.

7. K. S. Yee, J. S. Chen and A. H. Chang, "Conformal Finite Difference Time Domain (FDTD) with Overlapping Grids", *IEEE Trans. Antennas Propag.*, Vol. 40, No. 9, pp. 1068-1075, Sept. 1992.

8. N. K. Madsen, "Divergence Preserving Discrete Surface Integral Methods for Maxwell's Curl Equations Using Non-Orthogonal Unstructured Grids", Lawrence Livermore National Laboratory UCRL JC-109787, Feb. 1992.

9. K. K. Mei, A. Cangellaris, and D. J. Angelakos, " Conformal time domain finite-difference method," *Radio Sci.* Vol. 19, no. 5, pp1145-1147, 1984

10. R. Holland, V. P. Cable, and L. Wilson, "RCS calculation by finite volume time domain (FVTD) techniques," Lockheed Aeronautical Systems Co., Rep Lg-90ER013, Nov., 1990.

11. R. Holland, " Pitfalls of Staircase Meshing," *IEEE Transactions on Electromagnetic Compatibility*, Vol. 35, N4, pp434-439, Nov., 1993

12. K. S. Yee, J. S. Chen, and C. H. Chan, "Conformal Hybrid Finite Difference Time Domain and Finite Volume Time Domain," PIERS, July, 1993.

13. C. H. Chan and J. T. Elson, " A Vertex Based Finite-Volume Time-Domain Method for Analyzing Waveguide Discontinuities, " *Microwave and Guided Wave Letters*, Oct. ,1993.

14. J. T. Elson, C. H. Chan, L. Tsang, and K. S. Yee, " Observation of Backscattering Enhancement in Time with a Hybrid FVTD/FDTD Method," submitted for publication

15. G. Mur, "Absorbing Boundary Conditions for Finite-Difference Approximations of the Time-Domain Electromagnetic Field Equations," *IEEE Trans. Electromag. Compat.*, Vol. EMC-23, pp. 1073-1077, Nov. 1981.

16. Z. P. Liao, H. L. Wong, B. P. Yang and Y. F. Yuan, "A transmitting boundary for transient wave analysis," *Scientia Sinica* (series A.) 27(10), pp. 1063-76, 1984.

17. Jei S. Chen, and Kane S. Yee, " Artificial tapered damping near the outer computational boundary," to be submitted to IEEE for publication.

18. G. T. Ruck, editor, Radar Cross Section Handbook, Vol. 1, Ch. 4, New York, Plenum Press, 1970.

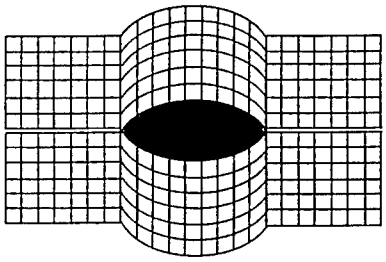


Figure 1a. The grid for a "lens"

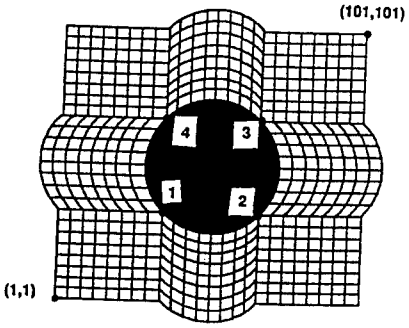


Fig. 1c The grid for a circular cylinder

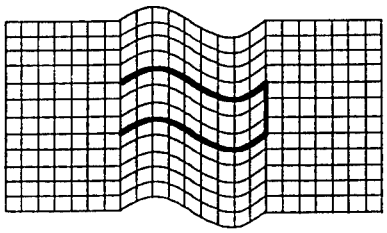


Figure 1b. The grid for a s-duct

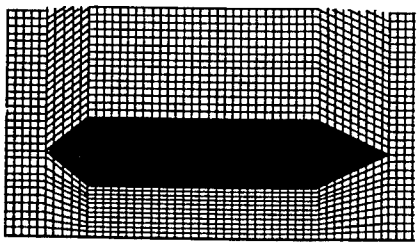
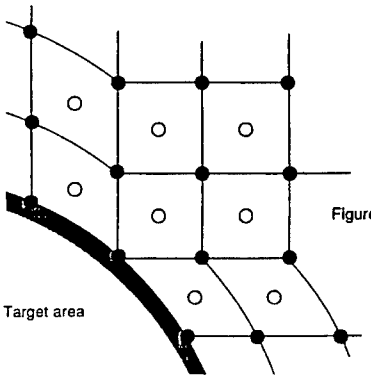


Fig. 1d The grid for an object with a ground plane



● Electric field nodes

○ Magnetic field nodes

Figure 1e. Placement of electric field and magnetic field nodes on a sample grid

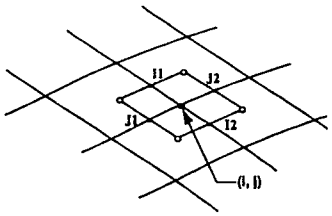


Figure 2a. The contour to update the electric field with the FDTD algorithm (TM case)

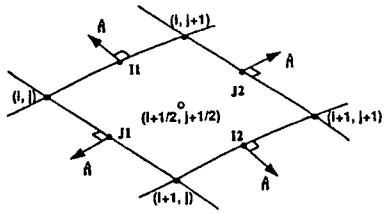


Figure 2b. The base of the prism to update the magnetic field vector with the FVTD algorithm (TM case)

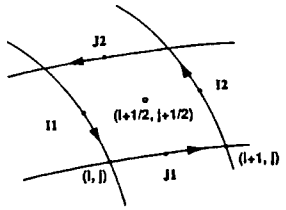


Figure 3a. The contour to update the magnetic field with the FDTD algorithm (TE case)

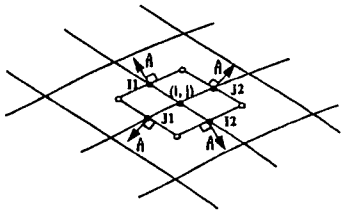


Figure 3b. The base of the prism to update the electric field vector with the FVTD algorithm (TE case)

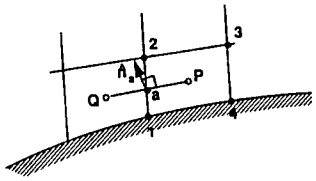


Figure 4. Positions of field points in the updating of the magnetic field at the point P

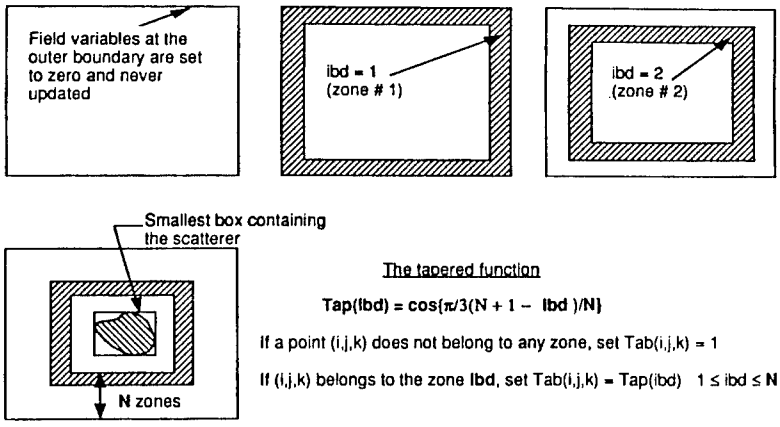


Figure 5a. Tapered damping zones at the outer boundary -- rectangular damping zones

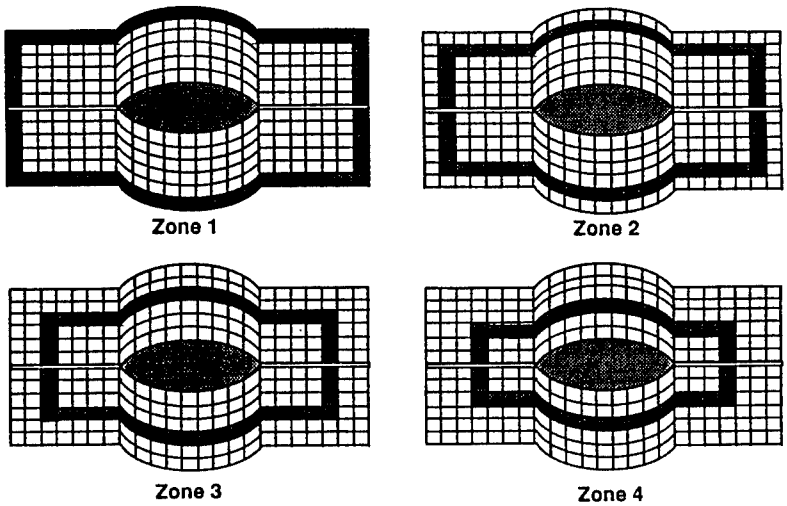
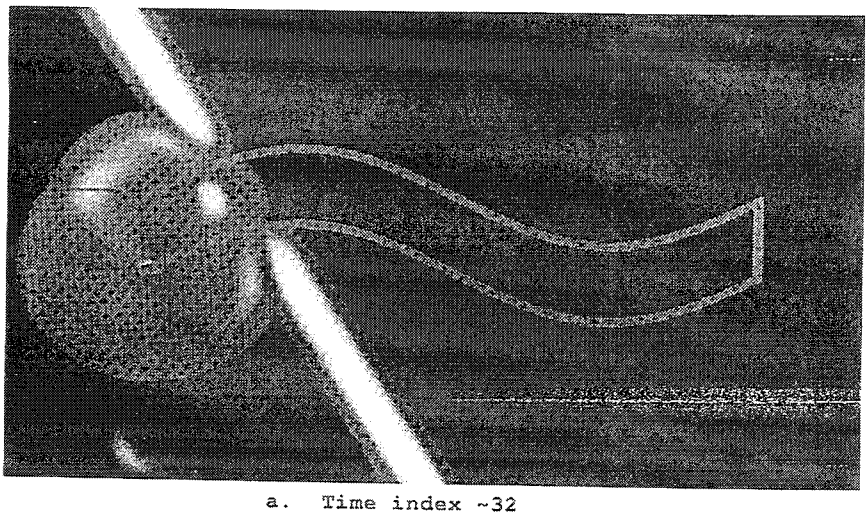
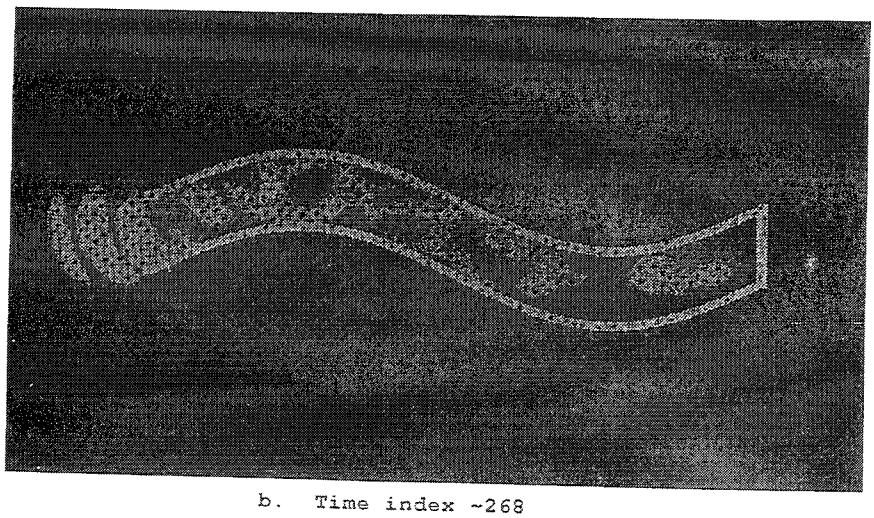


Figure 5b. Tapered damping zones at the outer boundary -- non-rectangular damping zones

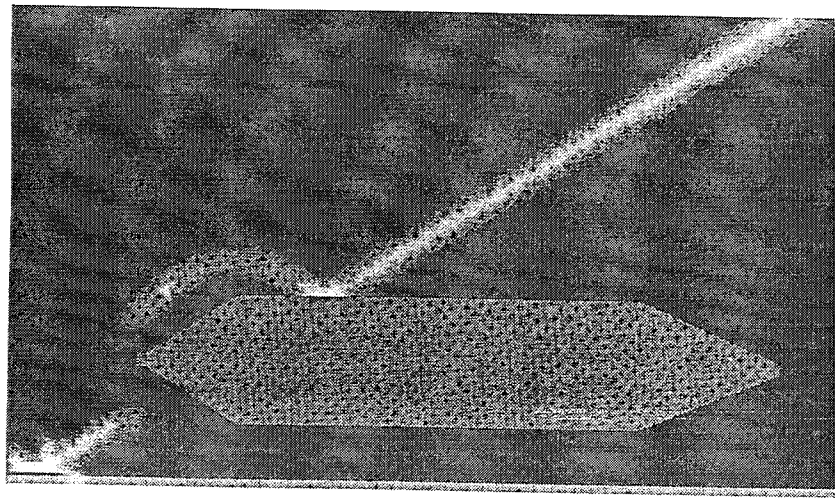


a. Time index ~32

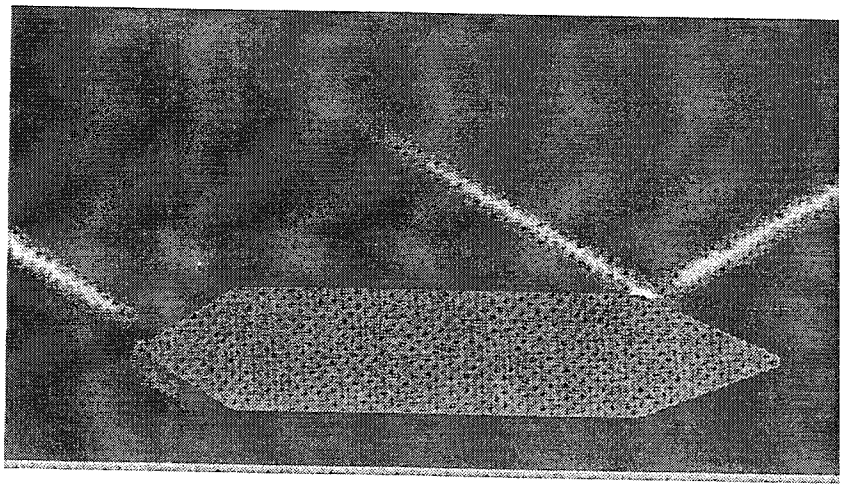


b. Time index ~268

Figure 6. Gaussian pulse incident on an S-duct



a. Time index ~24



b. Time index ~48

Figure 7. Gaussian pulse incident on a faceted object sitting above a ground plane

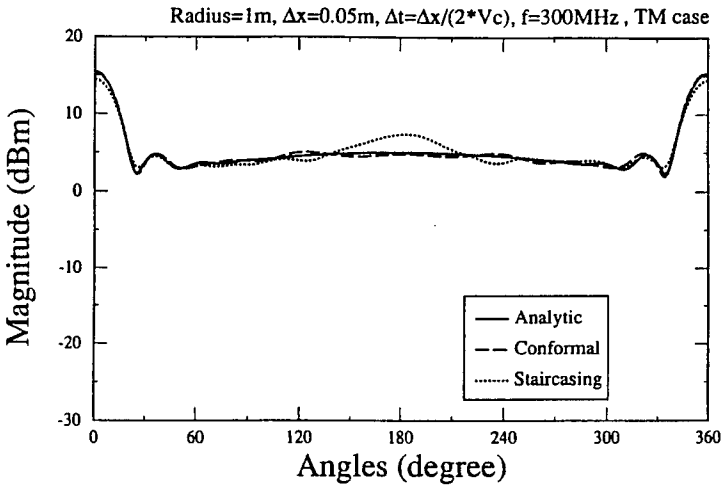


Figure 8a. Bistatic RCS for a PEC Circular Cylinder (TM)

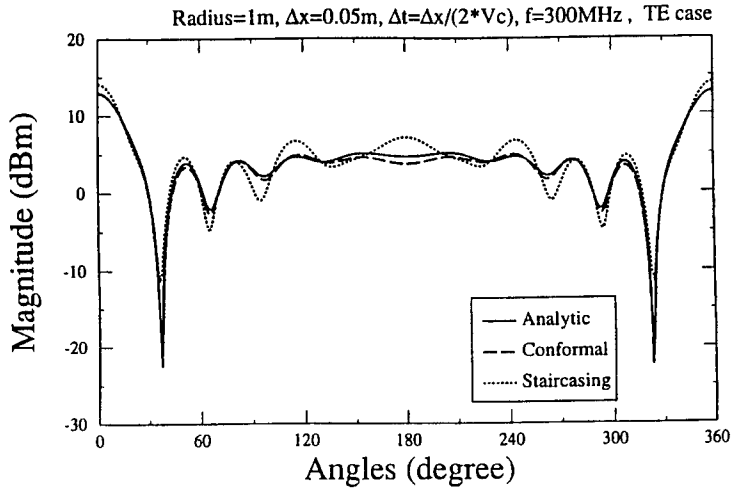


Figure 8b. Bistatic RCS for a PEC Circular Cylinder (TE)

SPECTRAL FINITE METHODS FOR THE SIMULATION OF ELECTROMAGNETIC INTERACTIONS WITH ELECTRICALLY LONG STRUCTURES

Andreas C. Cangellaris and Douglas Hart
Electromagnetics Laboratory
Department of Electrical and Computer Engineering
University of Arizona, Tucson, AZ 85721, USA
Tel: 602-621-4521, Fax: 602-621-2999
e-mail: cangellaris@ece.arizona.edu

Abstract

Spectral methods, in conjunction with domain decomposition techniques, are shown to be powerful candidates for the electromagnetic analysis of electrically long structures using differential equation-based formulations. Through the modeling of simple problems with known analytic solution, spectral methods are shown to exhibit the exponential accuracy required for the solution of structures spanning hundreds of wavelengths in at least one dimension. Furthermore, it is shown how such accuracy can be obtained with operation costs and storage much lower than those required of standard finite element approximations to achieve such accuracy.

1. Introduction

Domain decomposition techniques have been proposed recently for the modeling of electromagnetic wave interactions with electrically large structures. One specific domain decomposition approach splits the structure into smaller regions in which numerical solutions are computed separately with "basis" excitations on the partitions between the regions [1,2]. Then, field continuity at the partitions is invoked to obtain the solution in the entire structure subject to a specific excitation. The key merits of such an approach are: a) its inherent parallelism, making it ideal for implementation on massively parallel machines; and b) the fact that the solutions in each region can be developed using the most suitable numerical technique (analytical, differential-equation based, or integral-equation based).

Unfortunately, it can be shown that for those regions for which finite techniques (finite element or finite difference) are required, the numerical discretization needs to use a number of nodes per wavelength dictated by the electrical size of the entire structure in order to keep numerical dispersion at a minimum. The source of this difficulty is the numerical dispersion present in discrete approximations of wave phenomena. More specifically, it was shown in [3] that the relative rms discretization error in the finite element approximation of Helmholtz's equation is:

$$\|e\|_0 \leq C(hk)^{m+1}(kd) \tag{1}$$

where m is the degree of the interpolating polynomials, h is the grid size, d is the characteristic dimension of the discretized domain, k is the wavenumber, and C is a constant dependent on geometry and boundary conditions. The important implication of (1) is that as the electrical size of the domain increases, the discretization error increases. This result, as well as the impact of boundary conditions, was demonstrated also in [4,5]. To illustrate its importance, consider a $200\lambda \times 2\lambda \times 2\lambda$ structure. From [4], a resolution of 30 nodes per wavelength would be necessary for acceptable accuracy if quadratic finite elements are used. With the structure decomposed into 100 $2\lambda \times 2\lambda \times 2\lambda$ regions, the number of unknowns in each region will be 648,000!

In an attempt to deal with this issue we examine in this paper the advantages that the so-called spectral methods offer in improving the accuracy of differential-equation based wave simulations. Spectral methods have been used succesfully over the past twenty years for improving the numerical accuracy of numerical simulations of fluid dynamical problems. An excellent presentation of the fundamentals behind spectral methods, as well as a complete bibliography up to the end of the past decade can be found in [6].

To present the fundamentals of spectral methods, we concentrate on simple implementations of spectral approximations of the scalar Helmholtz equation in one and two dimensions. Boundary value problems with known analytic solutions are solved in order to demonstrate the exponential accuracy of spectral methods. Their implementation in conjunction with domain decomposition techniques is examined also. We continue with a discussion of the basic procedures necessary for the computationally efficient implementation of spectral methods. Finally, we identify specific areas of further research toward the establishment of spectral methods as legitimate candidates for the numerical modeling of electromagnetic wave phenomena in electrically large structures.

2. Spectral Approximation of the Helmholtz Equation

Spectral methods may be thought of as the extension of the method of separation of variables to the solution of non-separable problems. The underlying idea is to represent the solution to a problem as a truncated series of smooth functions of the independent variables. The critical point in this representation is that the functions used are such that the expansion converges faster than algebraically (i.e. the error caused by truncating the expansion after N terms goes to zero faster than any finite power of $1/N$ as $N \rightarrow \infty$). Furthermore, this *exponential* rate of convergence is not dependent on the boundary conditions; it dependes only on the smoothness of the solution.

As shown in [6], expansions in terms of eigenfunctions of singular Sturm-Liouville problems exhibit such exponential convergence. Eigenfunctions singular Sturm-Liouville problems include the families of Chebyshev polynomials, Legendre polynomials, Laguerre polynomials, etc. [7]. Expansions of the unknown solution using these classes of orthogonal polynomials are, then, expected to converge exponentially independently of the type of boundary conditions imposed on the boundaries of the computational domain. This convergence behavior should be contrasted to Fourier series representations of functions. It is well known that the Fourier series representation of $f(x)$ in the domain $0 \leq x < 2\pi$ converges rapidly only if the function is both smooth *and periodic*.

To present the fundamentals of spectral methods, let us consider the following one-dimensional boundary value problem:

$$\frac{d^2U}{dx^2} + k^2(x)U = 0, \quad 0 < x < L; \quad U(0) = 0, \quad U(L) = 1 \tag{2}$$

where $k^2(x) = \omega^2\mu(x)\epsilon(x)$. In (2) it is assumed that the material properties $\epsilon(x)$ and $\mu(x)$ are smooth functions of position so that $U(x) \in C^\infty$. However, it must be mentioned that for those cases where $\epsilon(x)$ and/or $\mu(x)$ exhibit discontinuities, spectral methods are still applicable. For example, in the spirit of domain decomposition techniques, a media interface across which ϵ and/or μ exhibit a jump is used as a geometry decomposition boundary. With the change of variables $\xi = 2x/L - 1$, the domain $0 \leq x \leq L$ is mapped onto the domain $-1 \leq \xi \leq 1$. The unknown field $U(\xi)$ is represented as the Lagrangian interpolant through the $N + 1$ points

$$\xi_n = \cos\frac{\pi n}{N}, \qquad n = 0, 1, \ldots, N \tag{3}$$

For this selection of points, the interpolation polynomials turn out to be the Chebyshev polynomials, $T_n(\xi) = \cos(n\cos^{-1}\xi)$. More specifically, the approximation, $\hat{U}$, of U takes the form

$$\hat{U}(\xi) = \sum_{n=0}^{N} a_n T_n(\xi) \tag{4}$$

where

$$a_n = \frac{2}{N}\frac{1}{c_n}\sum_{j=0}^{N}\frac{\hat{U}_j T_n(\xi_j)}{c_j} \tag{5}$$

with $\hat{U}_j = \hat{U}(\xi = \xi_j)$, $j = 0, 1, 2, \ldots, N$ and c_n defined as follows:

$$c_n = \begin{cases} 1, & \text{if } n \neq 0, N; \\ 2, & \text{otherwise.} \end{cases} \tag{6}$$

Even though there are several ways of obtaining a discrete approximation to (2) in the spirit of Galerkin's approach, we choose the collocation approach (often called *pseudospectral approximation*) for this example. More specifically, we require that the equation is satisfied exactly at the interpolation points ξ_n in (3). Toward this, we need the approximation of the second derivative of U at the collocation points. Using the notation

$$\frac{d^p \hat{U}(\xi)}{d\xi^p}\Big|_{\xi=\xi_k} = \sum_{j=0}^{N} \hat{U}_j (D_p)_{k,j} \tag{7}$$

to represent the p*th* derivative of U at $\xi = \xi_k$, direct differentiation of Chebyshev polynomials results in the following expressions:

$$(D_1)_{kj} = \frac{c_k}{c_j} \frac{(-1)^{j+k}}{\xi_k - \xi_j} \quad (k \neq j) \tag{8a}$$

$$(D_1)_{jj} = -\frac{\xi_j}{2(1-\xi_j^2)}, \quad (D_1)_{00} = \frac{2N^2+1}{6} = -(D_1)_{NN} \tag{8b}$$

and

$$D_p = (D_1)^p \tag{9}$$

In Section 4 we will show that this direct calculation of the matrix representation of the derivative operator is not necessary, and a more computationally efficient procedure for calculating the derivatives at the collocation points can be effected.

Using (4),(5),(8) and (9) with $p = 2$ in (2), a collocation procedure leads to a linear system of equations for the unknown coefficients $\hat{U}_j$. From (8) it is clear that the resulting matrix is full. Consequently, the value of N required for good numerical accuracy becomes an issue of concern. Clearly, the issue here is to obtain a relationship of the form of (1) for the number of expansion functions (or the number of collocation points) per wavelength required to achieve a desirable degree of accuracy. Toward this objective, the following result is useful:

$$\sin(M\pi\xi + \psi) = 2\sum_{n=0}^{\infty} \frac{1}{c_n} J_n(M\pi) \sin\left(\frac{n\pi}{2} + \psi\right) T_n(\xi), \tag{10}$$

$-1 \leq \xi \leq 1$, where $J_n(z)$ is the Bessel function of order n. Recalling the asymptotic form $J_n(z) \sim (1/\sqrt{2\pi n})(ez/n)^n$ as $n \to \infty$ [8], it is clear that $J_n(M\pi) \to 0$ exponentially fast as $n > M\pi$. This result suggests that Chebyshev approximations to time-harmonic wave solutions will start converge rapidly when the number of polynomials retained per wavelength is greater than π. In other words, a heuristic rule for the resolution requirements of Chebyshev expansions is at least four collocation points per wavelength.

In Figure 1 we plot the L_∞ error, $\|U - \hat{U}\|_\infty$, in the solution of problem (2) versus the number of collocation points for a homogeneous region with $k = 2\pi$. The length of the domain (in wavelengths) is used as a parameter. In addition to supporting the aforementioned sampling rule, the plots illustrate clearly the exponential convergence of the spectral approximation. For example, for the case $L = 9.7\lambda$, 7 polynomials per wavelength resulted in accuracy better than 10^{-7}. In comparison, a linear finite element solution of this problem with a resolution of 80 nodes per wavelength (i.e., $\sim$ 780 degrees of freedom) exhibits an error of $\sim 10^{-3}$.

The extension to two dimensions is straightforward. For example, consider the scalar Helmholtz equation for the electric field $\vec{E}(x,y) = \hat{z}E(x,y)$ associated with the two-dimensional TM modeling of electromagnetic wave phenomena in a z-independent medium

$$\frac{\partial}{\partial x}\left(\mu^{-1}(x,y)\frac{\partial E}{\partial x}\right) + \frac{\partial}{\partial y}\left(\mu^{-1}(x,y)\frac{\partial E}{\partial y}\right) + \omega^2 \epsilon(x,y)E = 0 \tag{11}$$

over the rectangular domain $(0 \leq x \leq L_1, 0 \leq y \leq L_2)$ with Dirichlet boundary conditions $E(x=0,y) = 0$, $E(x = L_1, y) = E_0(y)$, $E(x, y = 0) = 0$, $E(x, y = L_2) = 0$. With the change of variables $\xi = (2/L_1)x - 1$, $\eta = (2/L_2)y - 1$ the domain is transformed to the square region $(-1 \leq \xi \leq 1, 1 \leq \eta \leq 1)$ and (11) becomes:

$$\frac{\partial}{\partial \xi}\left(\frac{1}{L_1^2 \mu(\xi,\eta)}\frac{\partial E}{\partial \xi}\right) + \frac{\partial}{\partial \eta}\left(\frac{1}{L_2^2 \mu(\xi,\eta)}\frac{\partial E}{\partial \eta}\right) + \frac{\omega^2 \epsilon(\xi,\eta)}{4} E = 0 \tag{12}$$

The spectral approximation of the field is written as:

$$\hat{E}(\xi,\eta) = \sum_{m=0}^{M}\sum_{n=0}^{N} a_{mn} T_m(\xi) T_n(\eta) \tag{13}$$

where

$$a_{mn} = \frac{4}{MN}\frac{1}{c_n c_m}\sum_{i=0}^{M}\sum_{j=0}^{N}\frac{\hat{E}_{ij} T_m(\xi_i) T_n(\eta_j)}{c_i c_j} \tag{14}$$

and $\hat{E}_{ij}$ are the field values at the (i,j)th node of the grid $\{\xi_i \otimes \eta_j;\ \ \text{i=0,1,2,}\ldots,M,\ \ \text{j=0,1,2,}\ldots,N\}$, with $\xi_i = \cos(i\pi/M)$, $\eta_j = \cos(j\pi/N)$. As in the 1D-case, the interpolation points are used as collocation points also for a pseudospectral approximation of the equation.

For a numerical example in two dimensions, we used the boundary condition

$$E(x = L_1, y) = E_0(y) = \sin(\pi y/L_2)$$

for the boundary-value problem of (11) with $\mu = \mu_0$, $\epsilon = \epsilon_0$ and $\lambda = 1$. Thus, we simulated a standing wave pattern for the first TE_x mode in a shorted parallel-plate waveguide. For the case $L_2 = 4\lambda$, $L_1 = 5.3\lambda$, a 32×32 spectral approximation (~ 7 polynomials per wavelength) exhibits an error of $\|E - \hat{E}\|_\infty \sim 10^{-8}$, in agreement with the resolution rule mentioned above.

3. Spectral Methods and Domain Decomposition

To examine the performance of spectral methods in conjunction with domain decomposition techniques, we consider the following problem. The one-dimensional Helmholtz equation is solved in a homogeneous domain with $k = 2\pi$ (or $\lambda = 1$) of length L_m with Dirichlet boundary conditions $U(0) = 0$ and $U(L_m) = 1$. To develop the solution, the domain is decomposed in m subdomains, each of length $L = 3.7\lambda$. (For this special geometry all subdomains are the same.) Thus, $L_m = mL$. For m subdomains there exist $m-1$ subdomain boundaries which effect the decomposition of the domain. Let Q_i, $i = 1, 2, \ldots, m-1$, be the value of U at these boundaries. Let $Q_0 = U(0) = 0$ and $Q_m = U(L_m) = 1$. Within each subdomain we solve the following two problems:

Problem 1.

$$\frac{d^2U_a}{dt^2} + k^2 U_a = 0, \quad 0 < t < L; \quad U_a(0) = 0, \quad U_a(L) = 1 \tag{15}$$

Problem 2.

$$\frac{d^2U_b}{dt^2} + k^2 U_b = 0, \quad 0 < t < L; \quad U_b(0) = 1, \quad U_b(L) = 0 \tag{16}$$

Thus, the solution, $U^{(i)}$, in the ith subdomain can be written in terms of U_a, U_b and the values of U at the subdomain interfaces $i-1$ and i as:

$$U^{(i)}(x) = Q_{i-1}U_b + Q_i U_a, \quad (i-1)L \le x \le iL \tag{17}$$

Enforcement of the continuity of the normal derivative across domain decomposition boundaries results in a linear system of equations for the unknowns Q_i, $i = 1, 2, \ldots, m-1$. We note here that the spectral representation of the unknown field allows for an "exact" (within the approximation of the truncation of the expansion) calculation of the derivative even at the boundary points. This implies that the normal derivative continuity condition is also enforced with spectral accuracy.

In Figure 2 the L_∞ error is plotted versus the number of subdomains M. A comparison is made between a pseudospectral approximation (lower cluster of points) and a linear finite element approximation (upper cluster of points). For the pseudospectral approximation, 32 grid points were used within the 3.7λ

subdomain for the numerical solution for U_a and U_b. This resulted in a $\sim 10^{-12}$ accuracy in the numerical field and $\sim 10^{-10}$ accuracy in the numerical derivative calculated at the decomposition boundaries. For the linear finite element approximation, a resolution of 100 nodes per wavelength was used, which resulted in a $\sim 10^{-2}$ accuracy in the numerical derivatives at the decomposition boundaries. Clearly, the error of the finite element solution becomes unacceptable beyond the case of $M > 15$, assuming that an L_∞ error of less than 0.1 is desirable. (For the wave simulations studied in this paper, an L_∞ error of ~ 0.1 would result in an L_2 error better than 10^{-2}.) On the other hand, the error in the pseudospectral approximation is negligible even for the case of $M = 49$ or a domain $\sim 180\lambda$ long.

4. Efficient Numerical Implementation of Spectral Methods

Spectral approximations result in full matrices, a highly undesirable property for the solution of 2D and 3D problems. For example, for a true 3D application of spectral techniques, a $32 \times 32 \times 32$ grid will result in a full matrix of dimension $\sim 10^6$! However, using the fast transform properties of Chebyshev polynomials, and in conjunction with appropriate iterative techniques, one can solve the spectral equations with operation costs and storage comparable to those of standard finite element approximations to the problem with the same degrees of freedom [6].

To illustrate this point, let $\mathbf{K_{sp}}$ be the matrix resulting from the spectral approximation of the 1D problem in Section 2. In matrix form, the resulting linear system of equations is $\mathbf{K_{sp}}\hat{\mathbf{U}} = \mathbf{f}$, where $\hat{\mathbf{U}}$ is the vector of unknowns $\hat{U}_j$, and $\mathbf{f}$ is the forcing vector. Also, let $\mathbf{K_f}$ be the matrix resulting from a finite element or a finite difference approximation of the same problem using the same number of degrees of freedom. $\mathbf{K_f}$ is then used as a preconditioner for an iterative solution of the problem:

$$\hat{\mathbf{U}}^{(n+1)} = \hat{\mathbf{U}}^{(n)} - \mathbf{K_f}^{-1}\left(\mathbf{K_{sp}}\hat{\mathbf{U}}^{(n)} - \mathbf{f}\right), \quad n = 0, 1, \ldots \tag{18}$$

Since the number of degrees of freedom in spectral approximations is small, the sparse matrix $\mathbf{K_f}$ can be inverted efficiently. Therefore, most of the computational labor in (18) is associated with the multiplication $\mathbf{K_{sp}}\hat{\mathbf{U}}^{(n)}$. However, this multiplication can be effected in $O(N \log_2 N)$ operations instead of $O(N^2)$ operations as explained next.

Notice that we can write $\mathbf{K_{sp}} = \hat{\mathbf{D}}_{\mathbf{sp}} + \omega^2\mathbf{P}$, where $\hat{\mathbf{D}}_{\mathbf{sp}}$ is the matrix representation of the differentiation operations in Helmholtz's operator and P is a diagonal matrix. Thus, the operation $\hat{\mathbf{D}}_{\mathbf{sp}}\hat{\mathbf{U}}^{(n)}$ effects the calculation of appropriate derivatives at the N collocation points. Instead of direct multiplication, this calculation can be done using Fourier transforms. This becomes immediately clear if the result $T_n(\xi_j = \cos(\pi j/N)) = \cos(\pi jn/N)$ is used in (5) to cast it in the form:

$$a_n = \frac{2}{N}\frac{1}{c_n}\sum_{j=0}^{N}\frac{\hat{U}_j}{c_j}\cos\frac{\pi jn}{N}, \quad n = 0, 1, \ldots, N \tag{19}$$

From (19) it is clear that the coefficients a_n can be calculated using the FFT in $O(N \log_2 N)$ operations (assuming N is a power of 2). Once the a_n's are available, the derivatives of order p at the collocation points can be calculated using the following result [6]

$$\frac{d^p\hat{U}(\xi_j)}{d\xi^p} = \sum_{n=0}^{N} b_n^{(p)}\cos\frac{\pi nj}{N}, \quad j = 0, 1, 2, \ldots, N \tag{20}$$

where, $b_n^{(0)} = a_n$, $(0 \le n \le N)$, and for for $p > 0$ it is

$$c_n b_n^{(p)} = b_{n+2}^{(p)} + 2(n+1)b_{n+1}^{(p-1)}, \quad (0 \le n \le N-2) \tag{21a}$$

with

$$b_N^{(p)} = 0, \quad b_{N-1}^{(p)} = 2Nb_N^{(p-1)} \tag{21b}$$

From (20) the calculation of the derivative can be effected in $O(N \log_2 N)$ operations using the FFT, while from (21) the calculation of the pth derivative requires pN calculations. Therefore, the iterative process in (19) is an $O(N \log_2 N)$ process.

The extension of the aforementioned arguments to two and three dimensions is straightforward. However, it is appropriate to recall here the fact that for multiple dimensions most of the computational efficiency of transform methods comes not from the FFT but from the separability of multidimensional transforms. For example, for the two-dimensional case with an $M \times N$ Chebyshev grid, the aforementioned matrix multiplication requires about $NM(\log_2 N + \log_2 M)$ operations if N and M are powers of 2.

5. Conclusions

In summary, this paper has reviewed the fundamentals of spectral methods and has demonstrated the exponential accuracy they can provide to the numerical solution of elliptic boundary value problems associated with wave phenomena. This exponential (or spectral) accuracy is essential for the numerical modeling of wave interactions in structures that span hundreds of wavelengths. It was shown that, taking advantage of the availability of fast transforms for spectral eigenfunction expansions and using finite-difference or finite-element preconditioning, highly accurate solutions can be generated with computational cost slightly higher than that required for a finite element solution of the problem using the same number of degrees of freedom. However, for the finite element method alone to achieve the accuracy of the spectral methods, it will require higher-order interpolation functions, and the number of degrees of freedom in each dimension will need to be about an order of magnitude larger than that for the spectral approximation.

Future work will concentrate on the implementation of the spectral method to non-rectangular geometries and three-dimensional problems. In addition, the implementation of truncation boundary conditions in the spectral approximation of radiation and scattering problems will be considered.

ACKNOWLEDGEMENT

This work was supported by the National Science Foundation, under Grant ECS-9224946.

REFERENCES

[1] C.T. Spring and A.C. Cangellaris, "Parallel Implementation of Domain Decomposition Methods for the Electromagnetic Analysis of Guided Wave Systems," *J. Electromagnetic Waves and Applications*, in press.

[2] R. Lee and V. Chupongstimun, "A Partitioning Technique for the Finite Element Solution of Electromagnetic Scattering from Electrically Large Dielectric Cylinders," *IEEE Trans. Antennas & Propag.*, vol. 42, pp. 737-741, May 1994.

[3] A. Bayliss, C.I. Goldstein and E. Turkel, "On Accuracy Conditions for the Numerical Computation of Waves," *J. of Comput. Physics*, vol. 59, p. 396, 1985.

[4] A.C. Cangellaris and R. Lee, "On the Accuracy of Numerical Wave Simulations Based on Finite Methods," *J. of Electromagnetic Waves and Applications*, vol. 6, pp. 1635-1653, December 1992.

[5] R. Lee and A.C. Cangellaris, "A Study of Discretization Error in the Finite Element Approximation of Wave Solutions," *IEEE Trans. Antennas and Propag.*, vol. 40, pp. 542-549, May 1992.

[6] C. Canuto, M.Y. Hussaini, A. Quarteroni, and T.A. Zang, *Spectral Methods in Fluid Dynamics*, Springer-Verlag, Berlin Heidelberg, 1988.

[7] R. Courant and D. Hilbert, *Methods of Mathematical Physics*, Vol. 1, Interscience, New York, 1953.

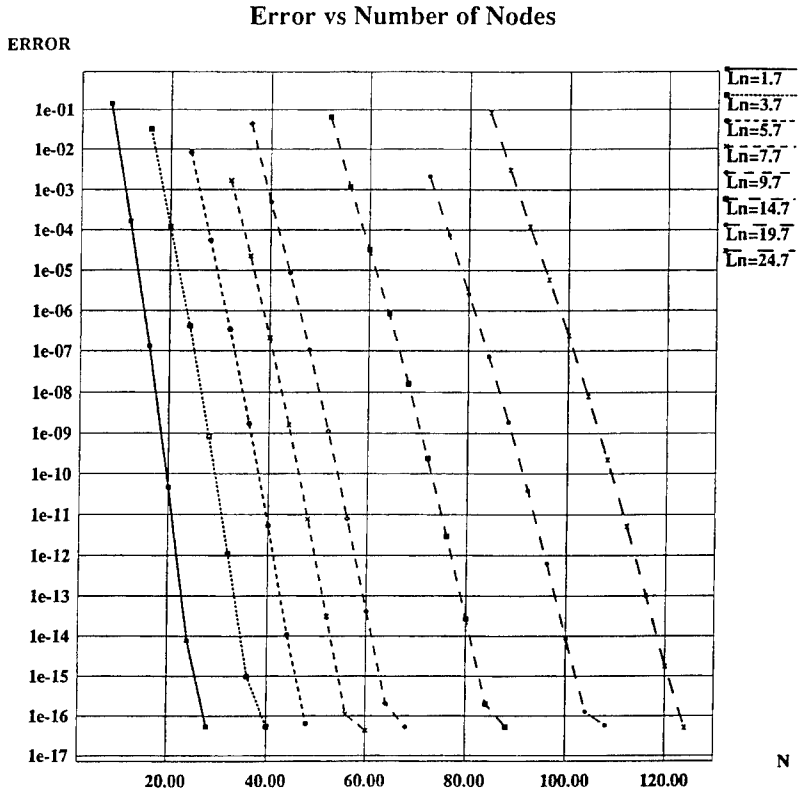


Figure 1. L_∞ error versus number of collocation points for the pseudospectral solution of the one-dimensional Helmholtz equation with Dircichlet boundary conditions. The length of the domain (in wavelengths) is used as parameter.

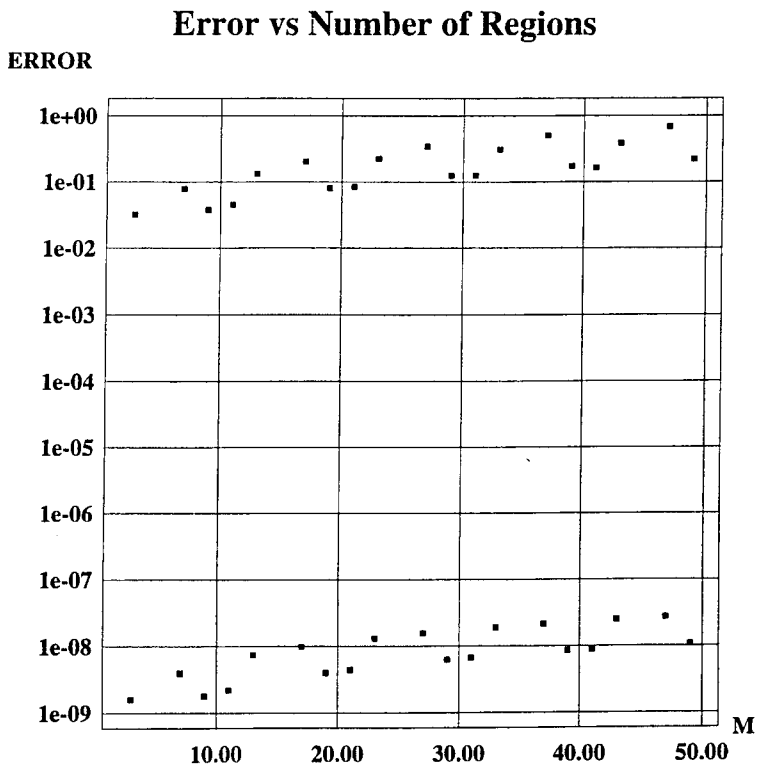


Figure 2. L_∞ error versus number of subdomains for the solution of the one-dimensional Helmholtz equation. The top cluster of points is for a linear finite element solution of the problem with 370 degrees of freedom per subdomain. The bottom cluster of points is for a pseudospectral solution with 32 degrees of freedom per subdomain.

AUTHOR INDEX

VI = Volume I
VII = Volume II

Abe, N.M. VI-66
Ahuja, V. VI-513
Albanese, R. VI-350
Ali, A.S. VII-1000, 1040
Ames, B. VI-127
Anastassiu, H.T. VII-1142
Andersh, D.J. VII-1111, 1134, 1142
Antilla, G.E. VII-1193
Arlguel, S. VII-672
Arkadan, A.A. VI-394
Aubert, H. VII-672
Aubrey, T.A. VII-873
Azu, C. VI-403
Baca, E.A. VI-418
Bagby, J.S. VI-216
Baginski, M.E. VI-8
Bai, L. VI-302
Bajon, D. VII-672
Balakrishnan, N. VII-680
Barrios, A. VII-784
Baudrand, H. VII-672
Beggs, J.H. VI-418
Belcher, W.R. VII-873
Bhalla, R. VII-1118
Blakely, B. VII-710
Blocher, T. VI-29, 294, 418
Boag, M. VI-614
Boyer, D.B. VII-824
Brauer, J. VII-1054
Breakall, J.K. VII-1025, 1033
Breed, G.A. VII-1017
Brodskyn, H.O. VI-66
Burkholder, R.J. VII-1126, 1134
Cangellaris, A.C. VI-498, VII-1280
Car, D.D. VII-848
Cardoso, J.R. VI-66
Cha, C.C. VII-695, 702
Chang, H.S. VII-962
Chaudhuri, S.K. VII-937
Chamberlin, K. VII-790
Chatterjee, A. VII-1212
Chen, J.S. VI 453, VII-1266
Cheng, G. VII-702
Cheng, Y.B. VI-378
Cheng, Z. VI-75
Cheung, P. VII-951
Chew, W.C. VI-482, 576, 629
Chou, H.T. VII-1134
Christensen, M.C. VII-1111
Christopher, S. VII-664, 680
Chu, S.T. VII-937
Colby, P.C. VI-164
Cook, G. VII-847
Corrington, L. VII-801
Cosnuau, A. VII-856
Crow, J.A. VI-45
Cugini, J.V. VI-143
Cummings, K.E. VII-724
Dai, J.F. VI-302
D'Angelo, J. VII-1163
David, R.S. VII-889
De La Bourdonnaye, A. VII-856
De Medeiros, L.H.A. VII-1094
Dembert, B. VI-621
Dimbylow, P.J. VI-240
Du, J.Y. VII-993
Dunn, D.B. VII-898
Duval, S.E. VII-1000
Dyck, D.N. VI-358
Elsherbeni, A.Z. VI-260, 542
Eme, B. VII-847
Engquist, B. VI-172
Erdley, T.A. VII-1025
Eremin, Y. V. VI-6, VII-925
Eswarappa, C. VI-13
Evans, J.A. VI-126
Fang, J. VI-504
Fast, S.A. VII-798
Fatemi, E. VI-172
Fath, J. VII-1134
Feliziani, M. VI-334
Ferraro, A.J. VII-970
Ferrières, X. VII-856
Fijany, A. VI-592
Fox, G.C. VII-702
Fresa, R. VI-350
Fröhlich, J. VI-584
Gao, S. VI-75
Gao, Y. VII-687
Gedera, M.B. VII-1194
Gerace, G.C. VI-49, VII-898, 904
Giarolla, M.H. VI-66
Girdinio, P. VII-1047
Gnos, M. VI-81
Goggans, P.M. VI-542
Golsberry, T.G. VII-979
Goorjian, P.M. VI-472
Gopinath, A. VII-951
Gordon, R.K. VI-559
Gothard, G.K. VI-189
Gribbons, M. VI-498
Hadi, M.F. VII-767
Hafner, Ch. VI-584
Hall, W.F. VII-839, 1185
Hamandi, L. VII-864
Hamilton, L.R. VI-606, VII-1177
Hantman, B. VI-118, 135
Hart, D. VII-1280
Haupt, R.L. VI-211, VII-1000
Henderson, L.W. VI-245
Hicks, R.G. VI-155
Hill, K.C. VII-1220
Hoefer, W.J.R. VI-13
Holland, R. VI-308
Holloway, C.L. VII-1040
Houshmand, B. VII-718
Hu, Q VI-75
Huffman, J.A. VII-1009
Ivakhnenko, V.I. VI-181, VII-929
Itoh, T. VII-718
Jackson, R. VI-118
Jarrlel, Jr. G.W. VI-8
Jensen, M.A. VI-592, VII-732
Johansson, N.M. VII-1085
Johnson, L. VII-710
Joseph, R.A. VI-151
Joseph, R.M. VI-476
Judkins, J.B. VII-957
Jurgens, D.E. VI-276, VII-710
Kanai, Y. VI-342
Karty, J.L. VII-1103
Kashiwa, T. VI-342
Katehi, L.P.B. VI-568
Katz, D.S. VI-476
Kelley, D.F. VI-526
Kesler, O.B. VI-21
Kienberger, T.L. VI-276
Kim, J.J. VI-21
King, A.S. VII-872
Kingsland, D.M. VI-490
Kluskens, M. VII-910
Kochlar, R. VII-710
Kopylov, Y.V. VI-234
Koschmieder, T.H. VII-798
Kost, A. VI-58
Kotulski, J.D. VII-848
Kragalott, M. VII-910
Krauss, T. VII-695
Kukk, A.V. VII-929
Kunz, K.S. VI-425, 431
Kuo, C.N. VII-718
Labelle, J. VI-118, 135
Langdon, H.S. VI-465
Larsson, J.A. VI-286
Latini, E. VI-334
Leca, P. VII-856
Lee, J.F. VI-490, VII-1054, 1258
Lee, R. VII-864
Lee, S.K. VI-498
Lee, S.W. VII-1111
Lemak, C. VII-801
Leuchtmann, P. VI-81
Ling, H. VII-1118
Lippincott, W. VII-910
Liu, J. VII-687
Liu, Z. VI-75
Liu, Z.M. VII-873
Lizalek, G. VII-1054
Ljung, S. VI-286
Logan, J. VI-410
Long, L.N. VI-513
Lowther, D.A. VI-358

Lu, C.C. VI-576
Luebbers, R.J. VI-445, 465, 526
Ma, Y.C. VII-1193
Madsen, N. VII-847
Mallasch, P. VI-551
Maloney, J.G. VI-430, VII-724
Manella, A. VII-1047
Maradei, F. VI-334
Marhefka, R.J. VI-245
Martone, R. VI-350
Matekovits, L. VI-600
McCowen, A. VI-2, 229
McGee, J. VI-403
McKaughan, M.E. VI-224
Medgyesi-Mitschang, L.N. VII-1194
Metker, S.E. VII-1009
Meyers, J.P. VI-49
Miano, G. VII-753
Michielssen, E. VI-614
Miller, E.K. VII-1151, 1202
Miyakawa, M. VI-342
Miyazaki, Y. VII-1062
Mohammadian, A. VII-839
Mohammed, O.A. VI-386, VII-1228
Mohan, A.S. VII-873
Molinari, G. VII-1047
Mooney, J.E. VI-98
Mortensen, G.E. VII-702
Mrozowski, M. VI-534
Murphy, R.K. VI-109
Neto, A.G. VII-672
Nicolas, A. VII-1070
Nicolas, L. VII-1070
Norgard, J. VI-29
Nutter, B. VI-224
Okoniewski, M. VI-534, VII-762
Orefice, M. VI-600
Orlov, N. V. VI-6, VII-925
Osher, S. VI-172
Ottusch, J.J. VI-606, VII-1177
Özgüner, F. VII-864
Packer, M.J. VI-252
Palaniswamy, S. VII-1185
Pan, G.W. VII-993
Park, C. VI-321
Pascher, W.W. VII-943
Passaro, A. VI-66
Pathak, P.H. VII-1134
Paulus, R.A. VII-809
Pearlman, R. VII-1194
Penney, C.W. VI-445
Perez, R. VI-323
Pesta, A. VI-29, 294
Peterson, A.F. VII-1077
Pflug, D.R. VI-268
Piket-May, M. VII-767
Pirinoli, P. VI-600
Popov, A.V. VI-195
Prakash, V.V.S. VII-680
Prather, W.D. VI-202
Pregla, R. VII-943
Prodan, J.V. VII-1266
Putnam, J.M. VII-848, 1194
Rahmat-Samii, Y. VI-592, VII-732
Raizer, A. VII-1094
Ramanujam, P. VI-321
Randall, W.M. VI-224
Rappaport, C.M. VII-898
Rao, S.M. VI-189
Reiß, K. VI 29, 37
Reuter, C.E. VI-476
Riggs, L. VI-8, 98
Riley, D.J. VI-435
Rockway, J. VI-410
Roedder, J.M. VII-1103
Rong, R. VI-358
Ross, D.C. VII-1142
Roux, F.X. VII-856
Rowell, C. VII-839
Rozenberg, V. VI-6
Rubinacci, G. VI-350
Russell, L. VI-410
Russenschuck, S. VI-366
Ryan, F.J. VII-816, 824
Sabbagh, H.A. VI-109, 135
Sabetfakhri, K. VI-568
Sacks, Z.S. VI-490
Saitoh, Y. VI-342
Sanford, J.R. VII-1085
Schinke, M. VI-29, 37
Schuster, J.W. VI-445
Schwartz, D. VI-410
Sega, R. VI-29
Seifert, M. VI-29, 294
Serpico, C. VII-753
Sezginer, A. VI-482
Shang, J.J.S. VII-1220
Shankar, V. VII-839, 1185
Shapiro, J.J. VII-1025
Sheikh, Q.M. VI-45
Shen, J. VI-58
Shen, X. VII-702
Shimizu, D.T. VII-762
Shirley, B.L. VI-430
Siarkiewicz, K. VI-118, 155
Sibul, L.H. VII-987
Silberberg, Y. VI-472
Singer, H. VII-881
Singh, A.K. VII-664, 680
Smith, C.E. VI-260
Song, J.M. VI-629
Souza, J.R. VII-648
Soyka, M. VI-403
Speciale, R.A. VII-639, 656
Stalzer, M.A. VI-606, VII-1177
Steich, D. VII-847
St. John, R. VI-308
Stuchly, M.A. VI-534, VII-762
Stuchly, S.S. VI-534
Subramaniam-Sivanesan, S. VI-394
Sykulski, J.K. VI-378
Taflove, A. VI-476, VII-775
Tam, D. VI-403
Tanaka, K. VII-1062
Taylor, Jr., C.D. VI-260
Terzuoli, Jr., A.J. VI-49, VII-898, 904
Thiele, E.T. VI-476
Toyama, K. VI-342
Treece, J.C. VII-109
Tripathi, V. VII-962
Tsitsopoulos, A.P. VI-252
Tsukamoto, T. VI-342
Tudziers, C. VII-881
Turley, R.S. VI-606, VII-1177
Turner, C.D. VI-435
Tyrtyshnikov, E.E. VI-181, VII-929
Üler, G.F. VI-386, VII-1228
Vann, L.D. VI-216
Vecchi, G. VI-600
Veliz, R.O. VII-648
Verolino, L. VII-753
Villone, F. VII-753
Visher, J.L. VI-606, VII-1177
Volakis, J.L. VII-1142, 1212
Wahlgren, B. VI-286
Wallace, C.B. VI-202
Wandzura, S.M. VI-606, VII-1170, VII-1177
Warren, D.E. VI-268
Wang, D.S. VII-1194
Wang, J. VII-687
Weedon, W.H. VI-482
Weisshaar, A. VII-962
Welch, C. VII-801
Werner, D.H. VII-964, 970, 1009
Werner, P.L. VII-970
Wheless, C.S. VI-89
Wheless, Jr., W.P. VI-89, 202
Whitcomb, C. VI-127
Wilkes, D.L. VII-695
Wille, L.T. VII-889
Wilton, D.R. VII-1077
Wolstenholme, D.J. VII-904
Woo, L.W. VI-109, 135
Wu, M. VI-75
Wu, Z. VI-504
Yao-bi, J.L. VII-1070
Ye, C. VI-75
Yee, K.S. VI-453, VII-1241, 1266
Yeremin, A.Y. VII-929
Yip, E. VI-621, 710
Young, J.S. VII-1025, 1033
Young, R.K. VII-979, 987
Zamarashkin, N.L. VII-926
Zolotarev, I.P. VII-830
Zimmerman, M. VI-551
Ziolkowski, R.W. VII-748, 957
Zook, B.J. VII-740